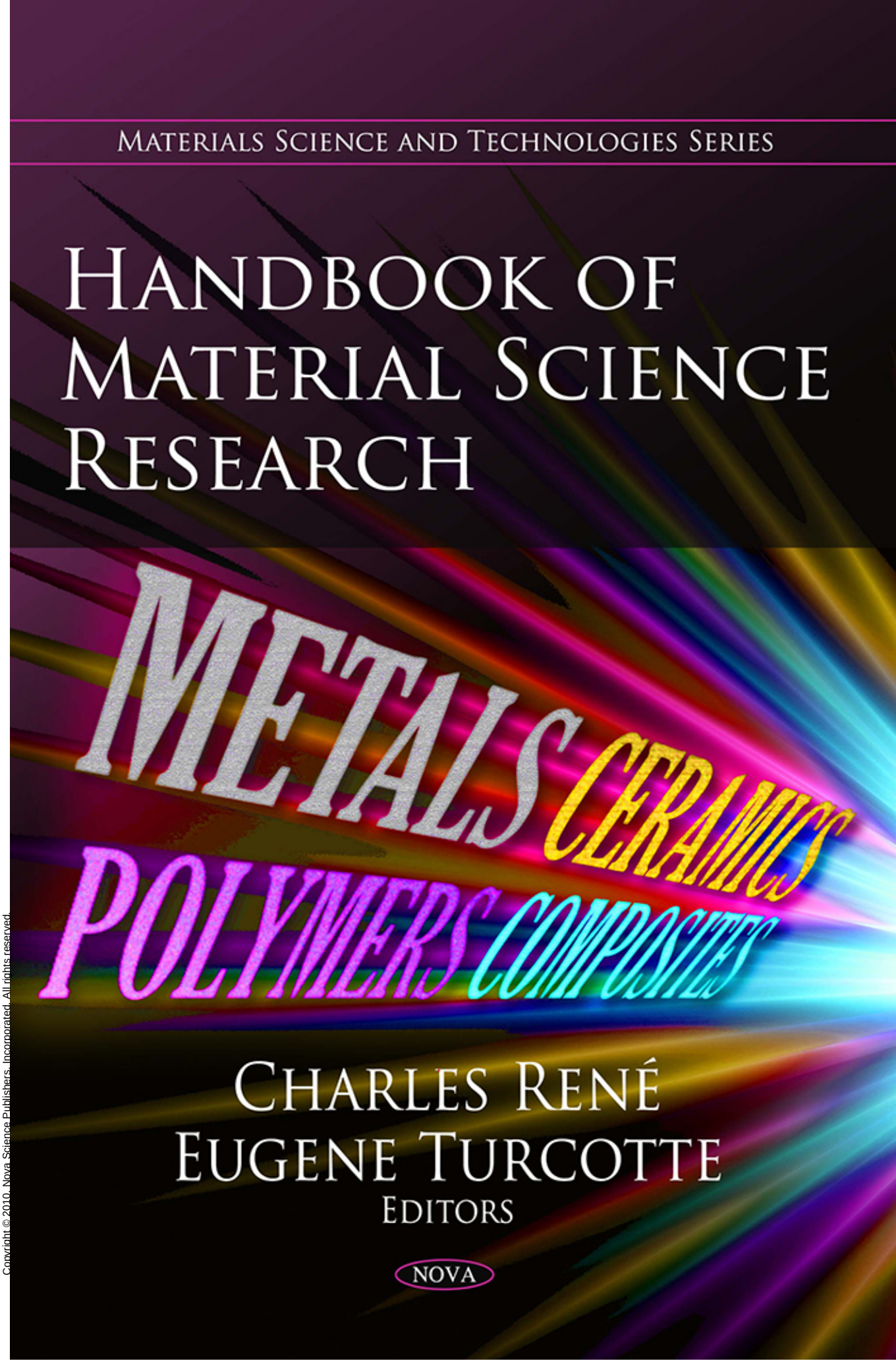


Copyright © 2010. Nova Science Publishers, Incorporated. All rights reserved.

Handbook of Material Science Research, Nova Science Publishers, Incorporated, 2010. ProQuest Ebook Central,

Copyright © 2010. Nova Science Publishers, Incorporated. All rights reserved.

Handbook of Material Science Research, Nova Science Publishers, Incorporated, 2010. ProQuest Ebook Central,

MATERIALS SCIENCE AND TECHNOLOGIES SERIES

HANDBOOK OF MATERIAL SCIENCE RESEARCH

Copyright © 2010. Nova Science Publishers, Incorporated. All rights reserved.

No part of this digital document may be reproduced, stored in a retrieval system or transmitted in any form or by any means. The publisher has taken reasonable care in the preparation of this digital document, but makes no expressed or implied warranty of any kind and assumes no responsibility for any errors or omissions. No liability is assumed for incidental or consequential damages in connection with or arising out of information contained herein. This digital document is sold with the clear understanding that the publisher is not engaged in

Handbook of Material Science Research, Nova Science Publishers, Incorporated, 2010. ProQuest Ebook Central,

MATERIALS SCIENCE AND TECHNOLOGIES SERIES

Magnetic Properties of Solids
Kenneth B. Tamayo (Editor)
2009. ISBN: 978-1-60741-550-3

Mesoporous Materials: Properties, Preparation and Applications
Lynn T. Burness (Editor)
2009. ISBN: 978-1-60741-051-5

Physical Aging of Glasses: The VFT Approach
Jacques Rault
2009. ISBN: 978-1-60741-316-5

Physical Aging of Glasses: The VFT Approach
Jacques Rault
2009. ISBN: 978-1-61668-002-2 (Online Book)

Graphene and Graphite Materials
H. E. Chan (Editor)
2009. ISBN: 978-1-60692-666-6

Dielectric Materials: Introduction, Research and Applications
Ram Naresh Prasad Choudhary and Sunanda Kumari Patri
2009. ISBN: 978-1-60741-039-3

Handbook of Zeolites: Structure, Properties and Applications
T. W. Wong
2009. ISBN: 978-1-60741-046-1

Strength of Materials
Gustavo Mendes and Bruno Lago (Editors)
2009. ISBN: 978-1-60741-500-8

Photoionization of Polyvalent Ions
Doris Möncke and Doris Ehrt
2009. ISBN: 978-1-60741-071-3

Building Materials: Properties, Performance and Applications
Donald N. Cornejo and Jason L. Haro (Editors)
2009. ISBN: 978-1-60741-082-9

Copyright © 2010. Nova Science Publishers, Incorporated. All rights reserved.

Handbook of Material Science Research, Nova Science Publishers, Incorporated, 2010. ProQuest Ebook Central,

Concrete Materials: Properties, Performance and Applications
Jeffrey Thomas Sentowski (Editor)
2009. ISBN: 978-1-60741-250-2

Corrosion Protection: Processes, Management and Technologies
Teodors Kalniņš and Vilhems Gulbis (Editors)
2009. ISBN: 978-1-60741-837-5

Corrosion Protection: Processes, Management and Technologies
Teodors Kalniņš and Vilhems Gulbis (Editors)
2009. ISBN: 978-1-61668-226-2 (Online Book)

Handbook on Borates: Chemistry, Production and Applications
M.P. Chung (Editor)
2009. ISBN: 978-1-60741-822-1

Physical Aging of Glasses: The VFT Approach
Jacques Rault
2009. ISBN: 978-1-61668-002-2

Handbook of Photocatalysts: Preparation, Structure and Applications
Geri K. Castello (Editor)
2009. ISBN: 978-1-60876-210-1

Smart Polymer Materials for Biomedical Applications
Songjun Li , Ashutosh Tiwari, Mani Prabaharan and Santosh Aryal (Editors)
2010. ISBN: 978-1-60876-192-0

Definition of Constants for Piezoceramic Materials
Vladimir A. Akopyan, Arkady Soloviev, Ivan A. Parinov and Sergey N. Shevtsov
2010. ISBN: 978-1-60876-350-4

Organometallic Compounds: Preparation, Structure and Properties
H.F. Chin (Editor)
2010. ISBN: 978-1-60741-917-4

Surface Modified Biomedical Titanium Alloys
Aravind Vadiraj, M . Kamaraj
2010. ISBN: 978-1-60876-581-2

Composite Laminates: Properties, Performance and Applications
Anders Doughett and Peder Asnarez (Editors)
2010. ISBN: 978-1-60741-620-3

Copyright © 2010. Nova Science Publishers, Incorporated. All rights reserved.

Handbook of Material Science Research, Nova Science Publishers, Incorporated, 2010. ProQuest Ebook Central,

Shape Memory Alloys: Manufacture, Properties and Applications
H. R. Chen (Editor)
2010. ISBN: 978-1-60741-789-7

Piezoelectric Materials: Structure, Properties and Applications
Wesley G. Nelson (Editor)
2010. ISBN: 978-1-60876-272-9

Titanium Alloys: Preparation, Properties and Applications
Pedro N. Sanchez (Editor)
2010. ISBN: 978-1-60876-151-7

Organosilanes: Properties, Performance and Applications
Elias B. Wyman and Mathis C. Skief (Editors)
2010. ISBN: 978-1-60876-452-5

Piezoceramic Materials and Devices
Ivan A. Parinov (Editor)
2010. ISBN: 978-1-60876-459-4

High Performance Coatings for Automotive and Aerospace Industries
Abdel Salam Hamdy Makhlouf (Editor)
2010. ISBN: 978-1-60876-579-9

Fundamentals and Engineering of Severe Plastic Deformation
Vladimir M. Segal, Irene J. Beyerlein, Carlos N. Tome, Vladimir N. Chuvildeev and Vladimir I. Kopylov
2010. ISBN: 978-1-61668-190-6

Fundamentals and Engineering of Severe Plastic Deformation
Vladimir M. Segal, Irene J. Beyerlein, Carlos N. Tome, Vladimir N. Chuvildeev and Vladimir I. Kopylov
2010. ISBN: 978-1-61668-458-7 (Online Book)

Amidation of Cellulose Materials
Nadege Follain
2010. ISBN: 978-1-61668-196-8

Amidation of Cellulose Materials
Nadege Follain
2010. ISBN: 978-1-61668-494-5 (Online Book)

Lanthanide–Doped Lead Borate Glasses for Optical Applications
Joanna Pisarska and Wojciech A. Pisarski
2010. ISBN: 978-1-61668-292-7

Copyright © 2010. Nova Science Publishers, Incorporated. All rights reserved.

Handbook of Material Science Research, Nova Science Publishers, Incorporated, 2010. ProQuest Ebook Central,

Lanthanide–Doped Lead Borate Glasses for Optical Applications
Joanna Pisarska and Wojciech A. Pisarski
2010. ISBN: 978-1-61668-736-6

Piezoelectric Ceramic Materials: Processing, Properties, Characterization, and Applications
Xinhua Zhu
2010. ISBN: 978-1-61668-418-1

New Developments in Materials Science
Ekaterine Chikoidze and Tamar Tchelidze (Editors)
2010. ISBN: 978-1-61668-852-3

New Developments in Materials Science
Ekaterine Chikoidze and Tamar Tchelidze (Editors)
2010. ISBN: 978-1-61668-907-0 (Online Book)

Handbook of Material Science Research
Charles René and Eugene Turcotte (Editors)
2010. ISBN: 978-1-60741-798-9

Innovative Materials for Automotive Industry
Akira Okada
2010. ISBN: 978-1-61668-237-8

Copyright © 2010. Nova Science Publishers, Incorporated. All rights reserved.

Handbook of Material Science Research, Nova Science Publishers, Incorporated, 2010. ProQuest Ebook Central,

Copyright © 2010. Nova Science Publishers, Incorporated. All rights reserved.

Handbook of Material Science Research, Nova Science Publishers, Incorporated, 2010. ProQuest Ebook Central,

MATERIALS SCIENCE AND TECHNOLOGIES SERIES

HANDBOOK OF MATERIAL SCIENCE RESEARCH

CHARLES RENÉ
AND
EUGENE TURCOTTE
EDITORS

Copyright © 2010. Nova Science Publishers, Incorporated. All rights reserved.



Nova Science Publishers, Inc.
New York

Handbook of Material Science Research, Nova Science Publishers, Incorporated, 2010. ProQuest Ebook Central,

Copyright © 2010 by Nova Science Publishers, Inc.

All rights reserved. No part of this book may be reproduced, stored in a retrieval system or transmitted in any form or by any means: electronic, electrostatic, magnetic, tape, mechanical photocopying, recording or otherwise without the written permission of the Publisher.

For permission to use material from this book please contact us:
Telephone 631-231-7269; Fax 631-231-8175
Web Site: http://www.novapublishers.com

NOTICE TO THE READER

The Publisher has taken reasonable care in the preparation of this book, but makes no expressed or implied warranty of any kind and assumes no responsibility for any errors or omissions. No liability is assumed for incidental or consequential damages in connection with or arising out of information contained in this book. The Publisher shall not be liable for any special, consequential, or exemplary damages resulting, in whole or in part, from the readers' use of, or reliance upon, this material. Any parts of this book based on government reports are so indicated and copyright is claimed for those parts to the extent applicable to compilations of such works.

Independent verification should be sought for any data, advice or recommendations contained in this book. In addition, no responsibility is assumed by the publisher for any injury and/or damage to persons or property arising from any methods, products, instructions, ideas or otherwise contained in this publication.

This publication is designed to provide accurate and authoritative information with regard to the subject matter covered herein. It is sold with the clear understanding that the Publisher is not engaged in rendering legal or any other professional services. If legal or any other expert assistance is required, the services of a competent person should be sought. FROM A DECLARATION OF PARTICIPANTS JOINTLY ADOPTED BY A COMMITTEE OF THE AMERICAN BAR ASSOCIATION AND A COMMITTEE OF PUBLISHERS.

Additional color graphics may be available in the e-book version of this book.

LIBRARY OF CONGRESS CATALOGING-IN-PUBLICATION DATA

Handbook of material science research / [edited by] Charles René and Eugene Turcotte.
p. cm.
Includes index.
ISBN 978-1-61122-536-5 (e-Book)
1. Materials science. I. René, Charles. II. Turcotte, Eugene.
TA404.2.H36 2009
620.1'1--dc22

2009031995

Published by Nova Science Publishers, Inc. ✦ New York

Copyright © 2010. Nova Science Publishers, Incorporated. All rights reserved.

Handbook of Material Science Research, Nova Science Publishers, Incorporated, 2010. ProQuest Ebook Central,

CONTENTS

Preface		**xi**
Chapter 1	Dielectric Spectroscopy of Dipolar Glasses and Relaxors *Juras Banys*	**1**
Chapter 2	Modification of Steel's Microhardness by Compression Plasma Flows *N. N. Cherenda and V. V. Uglov*	**125**
Chapter 3	Percolation Processes in Cuprate Composites as Low-Dimensional Systems *Katsukuni Yoshida*	**173**
Chapter 4	Dielectric and Ultrasonic Spectroscopy of Quasi Two-Dimensional $CuInP_2(S_XSe_{1-X})_6$ Mixed Crystals *V. Samulionis, J. Banys, J. Macutkevic and Yu.Vysochanskii*	**213**
Chapter 5	Unravelling XDT: Studies of Some Rare, but Violent, Explosions with Statistical Crack Mechanics *John K. Dienes*	**271**
Chapter 6	Magnetic Properties of Layered Titanium Dichalcogenides Intercalated with 3d- and 4f-metals *N. V. Baranov and V. G. Pleschov*	**295**
Chapter 7	Energetic Materials: Crystallization and Characterization *A.E.D.M. van der Heijden and R.H.B. Bouma*	**323**
Chapter 8	Electrodeposition and Corrosion Properties of Zn-Co and Zn-Co-Fe Alloy Coatings *J.M.C. Mol, Z.F. Lodhi, A. Hovestad, L. 't Hoen – Velterop, H. Terryn, and J.H.W. de Wit*	**347**
Chapter 9	Quasi One-dimensional CdSe Nanowires: Growth, Structure, and Polarized Photoluminescence *C.X. Shan, D.Z. Shen, and X.W. Fan*	**369**

Copyright © 2010. Nova Science Publishers, Incorporated. All rights reserved.

Handbook of Material Science Research, Nova Science Publishers, Incorporated, 2010. ProQuest Ebook Central,

Chapter 10 The Structure and Morphology of Electrodeposited Nickel-Cobalt Alloy Powders **395**
D.M. Minić, L. D. Rafailović, J. Wosik and G.E. Nauer

Chapter 11 A Systematic Procedure to Predict Explosive Performance and Sensitivity of Novel High-Energy Molecules in ADD, ADD Method-1 **417**
Soo Gyeong Cho

Chapter 12 The Development of Co-based Bulk Metallic Glasses **433**
Ding Chen and Gou-zhi Ma

Chapter 13 Control of Microstructures by Heat Treatments and High-Temperature Properties in High-Tungsten Cobalt-Base Superalloys **445**
Manabu Tanaka and Ryuichi Kato

Chapter 14 Pt-Co Supported on Polypyrrole-Multiwalled Carbon Nanotubes as an Anode Catalyst for Direct Methanol Fuel Cells **459**
Lei Li

Chapter 15 Graph-Skein Modules of Three-Manifolds **473**
Nafaa Chbili

Chapter 16 Evaluation of Metal Fatigue Characteristics Considering the Effect of Defects **491**
Tatsujiro Miyazaki and Hiroshi Noguchi

Index **517**

Copyright © 2010. Nova Science Publishers, Incorporated. All rights reserved.

Handbook of Material Science Research, Nova Science Publishers, Incorporated, 2010. ProQuest Ebook Central,

PREFACE

This book reviews the four classes of materials science, the study of each of which are also considered separate fields: metals, ceramics, polymers and composites. The application of materials science in energetic materials, like explosives and oxidizers, is also an important topic, and thus is extensively reviewed in this book. Furthermore, the microhardness of steel and the various testing methods in polymers is analyzed. Specifically, the Vickers microhardness of iron, carbon steels and high-alloyed steels are reviewed. Other chapters in this book explore the process of percolation in cuprate composites. Recently, extensive interest has been focused on the percolation processes in superconducting cuprates, of which physical properties are strongly characterized by the low-dimensional aspects of the crystal structures. Bulk metal glasses (BMGs) are also examined, which are currently the focus of intense research in the world because of their excellent properties and potential applications as engineering materials and functional devises. Other chapters in this book focus on electrodeposition and corrosion properties of zinc-cobalt and zinc-cobalt-iron, the structure and morphology of electrodeposited nickel-cobalt alloy powders, the control of microstructures by heat treatments and high-temperature properties, and the evaluation of fatigue strength methods for machine designs.

Chapter 1 - In this chapter, the main basics of ferroelectrics phase transitions is presented. This is compared with the main features of the dipolar galsses and relaxors.

The method of dielectric spectroscopy is explained including very broad frequency range which requires different techniques – simple capacitance method, coaxial line, waveguides. The method of the calculation of the distribution function of the relaxtion times is presented.

The results of investigation of dielectric dispersion of BP_xBPI_{1-x} mixed crystals are presented. The dielectric dispersion is analysed in terms of distribution of relaxation times. Anomalous broad and asymmetric distribution of relaxation times of betaine phosphite crystals with small admixture of betaine phosphate below and around T_c clearly differs from usual observed in ferroelectrics. From the distribution of relaxation times the parameters of a double well potential of the hydrogen bonds, the local polarization distribution function and average (macroscopic) polarization has been extracted. Unusual behaviour of an average asymmetry constant has been observed in BP_xBPI_{1-x} with $0.15 \leq x \leq 0.5$.

Results of the broadband dielectric spectroscopy of five various solid solutions of $PbMg_{1/3}Nb_{2/3}O_3$-$PbSc_{1/2}Nb_{1/2}O_3$-$PbZn_{1/3}Nb_{2/3}O_3$ (PMN-PSN-PZN) are presented. Dielectric spectra of these solutions were investigated in a broad frequency range from 20 Hz to 100 THz by a combination of dielectric spectroscopy (20Hz-53 GHz), time-domain THz

Copyright © 2010. Nova Science Publishers, Incorporated. All rights reserved.

Handbook of Material Science Research, Nova Science Publishers, Incorporated, 2010. ProQuest Ebook Central,

spectroscopy (0.1-0.9 THz) and infrared reflectivity (20–3000 cm^{-1}). Very strong and broad dielectric relaxation observed below phonon frequencies was analyzed in terms of distribution of relaxations times, using Tichonov regularization method. It revealed slowing down of the longest relaxation and the mean relaxation times in the agreement with the Vogel-Fulcher law and the Arrhenius law, respectively. Creation of polar nanoregions below the Burns temperature is manifested by appearance of the dielectric relaxation in the THz range, by temperature dependence of the A_1 component of the ferroelectric soft mode and by splitting of all polar modes in the infrared spectra. The A_1 component of the soft mode exhibits a minimal frequency near 400 K and the authors suggest that this temperature corresponds to the temperature, where the polar nanoregions percolate.

Chapter 2 - The main results of the influence of compression plasma flows' impact on the Vickers microhardness of iron, carbon steels and high-alloyed steels are presented in this chapter. The data from a variety of investigation techniques including X-ray diffraction, Mössbauer spectroscopy, Auger electron spectroscopy, Rutherford backscattering spectroscopy, scanning electron microscopy, etc. are used for the interpretation of microhardness results. Different approaches to steel hardening by compression plasma flows are demonstrated: direct treatment, surface alloying by mixing of a "coating-substrate" system and surface alloying by injection of an additional component into a plasma flow. The findings showed that direct treatment was effective for modification of iron and carbon steels (or low-alloyed steels) providing the microhardness increased up to 8–18 GPa. Alloying by compression plasma flows allows the formation of a hardened surface layer with the thickness of up to ~ 20 μm possessing high thermal stability both in carbon and high-speed steels. The role of the main hardening mechanisms is discussed.

Chapter 3 - Recently, extensive interest has been focused on the percolation processes in superconducting cuprates, of which physical properties are strongly characterized by the low-dimensional aspects of the crystal structures. This review article concerns the percolation processes in cuprate composites. Two cases of the composites having different scales (micron and nanometer) of the structural ingredients are discussed in reference to the percolation processes and the space dimension. First, the authors describe the percolation processes observed for Ag-added Bi-based cuprates. This composite is an eccentric composite in the sense that two kinds of ingredient grains considerably differ from each other in their particulate morphology; the Bi-based cuprate grain being in two-dimensional lamella and Ag grain being roundish. How to characterize materials is also discussed in terms of the percolation process, where the percolation threshold and the critical exponents in association with the space dimension are key issues. Finally, the authors describe microscopic processes concerning a two-dimensional percolation in the mixed-crystalline cuprates of Pr-substituted $R Ba_2Cu_3O_7$ (*R*Pr-123, *R*= rare earth). A nonclassical percolation occurs in this system, where a crystal-unit-cell placed in special configurations can be converted by an electron orbital hybridization into different type of cell, creating virtual percolation thresholds and causing the ionic size effect on the superconductor-insulator transition.

Chapter 4 - In this chapter, the broadband (20 Hz – 1.2 GHz) dielectric spectroscopy results of mixed $CuInP_2(S_xSe_{1-x})_6$ crystals are presented. In these crystals two contributions in dielectric spectra was successfully separated – at higher temperatures and low frequencies high copper ions conductivity and at higher frequencies and low temperatures order-disorder effects in copper and indium sub lattices. Critical increasing of the conductivity activation energy E_A and conductivity σ_0 was observed in intermediate concentration of sulphur and

Copyright © 2010. Nova Science Publishers, Incorporated. All rights reserved.

Handbook of Material Science Research, Nova Science Publishers, Incorporated, 2010. ProQuest Ebook Central,

selenium. A new dipolar glasses were discovered - $CuInP_2(S_xSe_{1-x})_6$ with x=0.4-0.8. Influence of small amount of selenium to dielectric dispersion of $CuInP_2S_6$ is more significant than corresponding amount of sulphur to dielectric dispersion of $CuInP_2Se_6$. Coexistence of ferroelectric order and dipolar glass disorder observed at low temperatures in $CuInP_2S_6$ with small admixture of selenium (2 %). Phase diagram boundary between dipolar glass disorder and ferroelectric order was examined and relaxor-like behaviour was discovered for $CuInP_2(S_{0.25}Se_{0.75})_6$. Ultrasonic spectroscopy was performed in the frequency range of 10-30 MHz using pulse-echo time of flight method. The critical ultrasonic anomalies at phase transitions in pure and mixed $CuInP_2(S_xSe_{1-x})_6$ crystals are observed. The polarization relaxation time was estimated from ultrasonic data in the vicinity of phase transitions. Phase diagram of phase transitions in these mixed crystals obtained from ultrasonic investigations corresponds to that obtained from dielectric spectroscopy. It was shown that $CuInP_2S_6$ layered crystals have extremely high elastic nonlinearity across layers. Elastic nonlinearity increases near phase transition temperature. Ultrasonic method was applied to detect and investigate piezoelectric sensitivity. It appeared that these layered crystals are good piezoelectric in low temperature ferroelectric phase and can be used as ultrasonic transducers . In paraelectric phase the piezoelectric sensitivity can be induced by external DC bias electric field directed along polar axis due to electrostriction.

Chapter 5 - The impact tests for propellant sensitivity reported by Jensen, Blommer and Brown (JBB) were anomalous in several respects. First, 12 out of 50 impacts at moderate speeds led to especially violent explosions (XDT) while the remaining 38 produced only mild deflagrations (DEF). XDT generally occurred following impact at speeds *lower* than those leading to shock-to-detonation (SDT), which occurred in the 22 shots at speeds above 2500fps. Moreover, the violent reactions occurred at relatively late times, in excess of 30 microseconds after impact, rather than the 5 microseconds typically associated with SDT. Finally, the blast pressure associated with the violent explosions was even higher than in SDT and the cratering was more profound. Since these results defied explanation by the mechanisms associated with classical detonation theory, the process was termed XDT. In XDT shock heating was considered negligible, as further evidenced by the late reaction time.

This report summarizes some mechanisms postulated by the author during the last 30 years to explain the observations of JBB and other violent but non-repeatable reactions in propellants and explosives. The fundamental assumption herein is that defects occur at random and that heating of these defects following impact may lead to reactive hot spots. More specifically, it is postulated that the defects are shear cracks in which interfacial sliding leads to frictional heating that, in turn, causes vigorous reactions that may culminate in violent explosions. Our analysis shows, however, that a single hot spot will not result in violent explosion since rapid expansion of the gas-filled cavities reduces the gas pressure enough to quench the reaction. Thus, the authors conclude that interactions of defects is responsible for the observed violence.

Three types of interactions are thought to contribute to the suddenness of the violence. In one, pulses from reactions in one defect enhance the pressure in adjoining defects and this feeds back to the first defect, initiating a divergent oscillation. Such interactions have been observed in special simulations. Further, growing cracks can intersect to form larger, more unstable, cracks, and a large enough number of intersections can result in a network of cracks that supports violent reactions. This is thought to occur when the concentration of cracks exceeds the percolation threshold, causing a violent reaction. Finally, the authors hypothesize

Copyright © 2010. Nova Science Publishers, Incorporated. All rights reserved.

Handbook of Material Science Research, Nova Science Publishers, Incorporated, 2010. ProQuest Ebook Central,

that radiation between connected cracks can cause the heat produced by chemical reactions to spread extremely rapidly, leading to violent explosions.

Chapter 6 - Layered structure of titanium dichalcogenides TiX_2 (X = S, Se, Te) allows to intercalate various guest atoms, in particular, with non-full filled 3*d* or 4*f* electron shells into space between X-Ti-X tri-layers and to obtain the quasi two-dimensional systems with alternate layers of magnetic and non-magnetic atoms. Different magnetic states ranging from spin-glass like behavior up to states with three-dimensional magnetic order are observed in M_xTiX_2 intercalated by 3d-transition (M) metals. The methods of the preparation of compounds intercalated with 3*d* and rare-earth (R) metals and the results of the crystal structure and magnetic properties investigations for M_xTiX_2 and R_xTiX_2 systems are presented and discussed. The values of the magnetic moments of intercalated M and R atoms and the presence of various magnetic states in compounds are considered as depending on both the chemical constituents and on the concentration of inserted atoms.

Chapter 7 - The application of energetic materials, like explosives and oxidizers, in munition or propellants, requires basic knowledge of the properties of the energetic ingredients. It is known that the sensitivity of energetic materials towards external stimuli like shock initiation, is predominantly determined by the presence of crystalline imperfections like inclusions, voids and dislocations in the crystalline energetic materials. Crystallization of energetic materials allows the control of mean particle size, particle shape and product quality. Specifically the improved product quality has been demonstrated to yield significantly less sensitive energetic materials when applied in a polymer-bonded explosive. This contribution gives a comprehensive review on the crystallization and characterization of various energetic materials and their application in insensitive munition. The review concludes with a future outlook on this area of research.

Chapter 8 - Cadmium (Cd) has been extensively used as an excellent corrosion protective coating for steel components in aerospace, automotive, electrical and fasteners industries. However, Cd is banned due to its toxic nature and strict environmental regulations. In this study, the electrodeposition mechanism and kinetics, coating morphology and corrosion resistance of alternative, electrodeposited Zinc-Cobalt (Zn-Co) and Zinc-Cobalt-Iron (Zn-Co-Fe) alloys have been investigated. Coatings with relatively high amounts of Co are very difficult to achieve due to anomalism associated with their deposition and are therefore not much reported so far. In this research Zn-Co and Zn-Co-Fe alloys with varying amount of Co (2 to 40 wt-%) and Fe (up to 1 wt-%) are electrodeposited and the effects of variation of process parameter settings (i.e. cathodic polarization, current density, temperature and electrolyte composition) on the electrodeposition mechanism and kinetics are investigated. The microstructure of the alloy coatings changed significantly with the variation in Co content in the deposits. The barrier and sacrificial corrosion protection provided by the coatings were investigated with a variety of electrochemical techniques and industrial accelerated tests. It was found that the sacrificial properties and the protection range decreases with increasing Co content in the alloy. For the highest Co content in the alloy, the coating may become more noble to steel and loses its sacrificial protection. The barrier resistance of the coatings increases with the increase of Co content in the alloy coating. Both Zn-Co and Zn-Co-Fe alloys with high Co content (> 32 wt-% Co) showed excellent barrier properties. An intermediate region of compositions can be distinguished in which the coatings would provide a good combination of sacrificial and barrier resistance properties and also a reasonable protection range.

Copyright © 2010. Nova Science Publishers, Incorporated. All rights reserved.

Handbook of Material Science Research, Nova Science Publishers, Incorporated, 2010. ProQuest Ebook Central,

Chapter 9 - In this chapter, the authors would like to provide a brief overview of the literature on the growth and characterization of quasi-1D CdSe nanostructures, and the overview will be divided into three parts: 1. The preparation of metastable 1D CdSe nanostructures; 2. Controlled growth of CdSe nanowires; 3. Polarized photoluminescence of individual CdSe nanowires.

Chapter 10 - Nanostructured nickel and cobalt alloy powder deposits from three different electrolyte compositions were obtained by electrodeposition from an ammonium sulfate-chloride solution in a galvanostatic regime. The influence of current density and the Ni^{2+}/Co^{2+} ratio in the bath on the microstructure and phase composition of the Ni-Co deposits were studied by SEM and X-ray diffraction methods. Both, bath composition and current density influence strongly the deposit growth mechanism as well as the deposit composition, microstructure, grain size and surface morphology. When electrodeposition was performed at high overpotentials, far from equilibrium conditions, face-centered cubic (FCC) mixtures of Ni and Co were generated while at low overpotentials, as well as at higher content of cobalt in the electrolyte, hexagonal close packed (HCP) of Co was formed with a lower rate of hydrogen evolution. The increase in the concentration of HCP phase in the nanocrystalline deposits was caused by increasing the overall Co content in the materials prepared as well as by decreasing deposition current density.

Differential scanning calorimetry (DSC) and X-ray diffraction analysis were used to examine the effects of structural changes on magnetic properties of the nanocrystalline powders electrochemically obtained in the temperature interval from room temperature to 650°C. Each stage of the structural changes caused corresponding changes in the magnetic permeability for the alloys prepared.

Chapter 11 - In order to derive novel high-energy molecules (HEMs) efficiently, the authors have recently established a systematic procedure to predict explosive performance and sensitivity of a HEM candidate of which a two-dimensional chemical sketch has been given. This procedure, which the authors called ADD Method-1, includes three theoretical steps, i.e. (1) calculation of molecular structure and energy, (2) computation of molecular descriptors, and (3) estimation of explosive performance and sensitivity. In calculating molecular structure and energy, the authors have utilized density functional theories in a quantum mechanical program. Once accurate three-dimensional molecular structure and molecular energy at that structure were calculated, heat of formation and density, two important molecular descriptors in estimating explosive performance, have been computed. Constitutional molecular descriptors including oxygen balance, cycles, and rotatable bonds, which will be used as input variables in estimating impact sensitivity, have been computed directly from a two-dimensional molecular structure. In a final step, explosive performance has been estimated with the Cheetah program, while impact sensitivity has been predicted with a knowledge-based neural network method.

Chapter 12 - Bulk metal glasses (BMGs) are currently the focus of the intense research in the world because of their excellent properties and potential applications as engineering materials and functional devices. Owing to their disordered structure, metallic glasses possess several unique properties that make them attractive for tribological, magnetic and mechanical applications. Most recently, with the development of new Co-based BMG with the highest strength (the compressive true strength is up to 5500 MPa) and unique magnetic characterization, Co-based BMG has become a hot topic in the new material field.

Copyright © 2010. Nova Science Publishers, Incorporated. All rights reserved.

Handbook of Material Science Research, Nova Science Publishers, Incorporated, 2010. ProQuest Ebook Central,

In this review, the preparation, factors contributing to glass-forming ability (GFA), mechanical and magnetic properties, and practical strategies for pinpointing compositions with optimum glass -forming ability of Co-based BMGs were presented. Furthermore, some potential investigation field and application condition about the new BMGs alloys system were also discussed. Our goal is to illustrate the major issues for Co-based BMG, from progressing to structures to properties and applications and from the fundamental science to viable industrial applications.

Chapter 13 - Cobalt-base HS-21 (L-605) alloy has high strength and good oxidation resistance at high temperatures, and is widely used for high-temperature components including blades, vanes and combustor parts in the hot sections of jet engines. In this study, effects of microstructures on the creep-rupture properties were investigated on the heat-treated specimens of the HS-25 (L-605) type heat-resistant alloys containing about 14 to 20% (mass %) tungsten (W) at 1089 and 1311 K. Serrated grain boundaries which were formed by precipitation of W-rich phase and M_6C carbide by heat treatment, improved rupture strength without significant loss of creep ductility. Ageing for 1080 ks (300 h) at 1273 K (1000℃) caused similar precipitates on grain boundaries and in grains, and also increased rupture strength in the specimens with normal straight grain boundaries. Improvement of the rupture properties by heat treatments was remarkable in the alloys with the higher W content at 1089 K, while such heat treatments were effective in relatively short-term creep at 1311 K. In the non-aged specimens with straight grain boundaries, the rupture strength increased with increasing W content at 1311 K, although the rupture strength was not improved largely with increasing W content at 1089 K. The principal strengthening mechanism in these alloys was attributed to the strengthening of grain boundaries and grains by precipitates of W-rich phase and carbide phases in addition to solid-solution strengthening by W atoms. The strengthening of grains by high-temperature ageing was comparable with the strengthening by serrated grain boundaries in the high-tungsten cobalt-base alloys at 1089 K. Fracture surfaces of specimens with serrated grain boundaries and those of aged specimens were ductile grain-boundary fracture surfaces with small dimples and ledges, while the non-aged specimens with straight grain boundaries exhibited brittle grain-boundary facets at 1089 K.

Chapter 14 - Direct methanol fuel cells (DMFCs) have attracted considerable attention as portable power sources due to their simple system design, low operating temperature, convenient fuel storage and supply. However, poor methanol oxidation at the anode is one of main challenges to limit DMFC applications. In order to solve this challenge, a novel catalyst, Pt-Co alloy supported on polypyrrole (PPy)-multiwalled carbon nanotubes (MWCNTs), was prepared by chemical reduction method. PPy-MWCNTs as catalyst support was prepared by *in situ* polymerization of pyrrole onto MWCNTs. Pt-Co nano-scaled particles with narrow particle size distribution about 2-4nm were uniformly co-deposited onto the PPy-MWCNTs. The physical characterizations of catalyst and catalyst support were measured by SEM, TEM, EDS and XRD, respectively. The electrochemical properties of Pt-Co/PPy-MWCNT catalyst were tested by using cyclic voltammetry, CO stripping voltammetry, and chronoamperometry measurements. It was found that the partial over-oxidation treatment of catalyst support enhanced the catalytic activity of Pt-Co catalyst for methanol oxidation. Under the same Pt loading and experiments conditions, the Pt-Co/PPy-MWCNT catalyst after the over-oxidation activation shows higher catalytic activity toward methanol oxidation compare to commercial Pt-Ru/C catalyst, and potential application for direct methanol fuel cells.

Copyright © 2010. Nova Science Publishers, Incorporated. All rights reserved.

Handbook of Material Science Research, Nova Science Publishers, Incorporated, 2010. ProQuest Ebook Central,

Chapter 15 – Our main purpose is to introduce the theory of graph-skein modules of three-manifolds. This theory associates to each oriented three-manifold *M* an algebraic object (a module or an algebra) which is defined by considering the set of all ribbon graphs embedded in *M* modulo local linear skein relations. This idea is inspired by Przytycki's theory of skein modules which is also known as algebraic topology based on knots. Historically, this theory appeared as a generalization of the quantum invariants of links in the three-sphere to links in an arbitrary three-manifold. In this paper, the authors review the construction of the Kauffman bracket skein module and investigate its relationship with our graph-skein modules. The authors compute the graph-skein algebra in few cases. As an application they introduce new criteria for symmetries of spatial graphs which improve some results obtained earlier. The proof of these criteria is based on some easy calculation in the graph-skein module of the solid torus.

Chapter 16 - When the fatigue strength is evaluated for machine designs, fatigue evaluation methods and fatigue data which match physical phenomena and the design conditions need to be chosen properly. Generally, fatigue tests are performed under stress controlled conditions and ΔK controlled conditions. Because the load condition is closely associated with crack closure phenomena, the differences of the load conditions cause the differences of the crack propagation and non-propagation behavior. Then, the fatigue crack is divided into a small and long one depending on a plastic zone size at a crack tip. The propagation and non-propagation characteristics of the small crack are different from those of the long one. Therefore, it should be noted that the fatigue data under the stress controlled conditions are different from those under the ΔK controlled conditions, and the propagation and non-propagation characteristics of the small crack are different from those of the long one. The authors proposed the evaluation methods for the fatigue strength of specimens with the various dimensional cracks and notches and applied the methods to the predictions of the fatigue life reliability and the fatigue limit reliability of the inhomogeneous materials. In this paper, it is mentioned that the propagation and non-propagation characteristics of the fatigue crack depends on the relative plastic zone size and the load conditions, and the simple forms which are obtained by formulating these characteristics under a constant stress controlled condition are introduced. Then, their applications to predictions of fatigue life reliability and fatigue strength reliability at $N = 10^7$ of aluminum cast alloy JIS AC4B-T6 which contains various stress concentration parts are roughly introduced.

Copyright © 2010. Nova Science Publishers, Incorporated. All rights reserved.

Handbook of Material Science Research, Nova Science Publishers, Incorporated, 2010. ProQuest Ebook Central,

Copyright © 2010. Nova Science Publishers, Incorporated. All rights reserved.

Handbook of Material Science Research, Nova Science Publishers, Incorporated, 2010. ProQuest Ebook Central,

In: Handbook of Material Science Research
Editors: C.s René and E. Turcotte, pp.1-124
ISBN 978-1-60741-798-9
© 2010 Nova Science Publishers, Inc.

Chapter 1

DIELECTRIC SPECTROSCOPY OF DIPOLAR GLASSES AND RELAXORS

Juras Banys
Department of Radiophysics Vilnius University,
Vilnius, Lithuania

ABSTRACT

In this chapter, the main basics of ferroelectrics phase transitions is presented. This is compared with the main features of the dipolar galsses and relaxors.

The method of dielectric spectroscopy is explained including very broad frequency range which requires different techniques – simple capacitance method, coaxial line, waveguides. The method of the calculation of the distribution function of the relaxtion times is presented.

The results of investigation of dielectric dispersion of BP_xBPI_{1-x} mixed crystals are presented. The dielectric dispersion is analysed in terms of distribution of relaxation times. Anomalous broad and asymmetric distribution of relaxation times of betaine phosphite crystals with small admixture of betaine phosphate below and around T_c clearly differs from usual observed in ferroelectrics. From the distribution of relaxation times the parameters of a double well potential of the hydrogen bonds, the local polarization distribution function and average (macroscopic) polarization has been extracted. Unusual behaviour of an average asymmetry constant has been observed in BP_xBPI_{1-x} with $0.15 \leq x \leq 0.5$.

Results of the broadband dielectric spectroscopy of five various solid solutions of $PbMg_{1/3}Nb_{2/3}O_3$-$PbSc_{1/2}Nb_{1/2}O_3$-$PbZn_{1/3}Nb_{2/3}O_3$ (PMN-PSN-PZN) are presented. Dielectric spectra of these solutions were investigated in a broad frequency range from 20 Hz to 100 THz by a combination of dielectric spectroscopy (20Hz-53 GHz), time-domain THz spectroscopy (0.1-0.9 THz) and infrared reflectivity (20–3000 cm^{-1}). Very strong and broad dielectric relaxation observed below phonon frequencies was analyzed in terms of distribution of relaxations times, using Tichonov regularization method. It revealed slowing down of the longest relaxation and the mean relaxation times in the agreement with the Vogel-Fulcher law and the Arrhenius law, respectively. Creation of polar nanoregions below the Burns temperature is manifested by appearance of the dielectric relaxation in the THz range, by temperature dependence of the A_1 component of the

Copyright © 2010. Nova Science Publishers, Incorporated. All rights reserved.

Handbook of Material Science Research, Nova Science Publishers, Incorporated, 2010. ProQuest Ebook Central,

ferroelectric soft mode and by splitting of all polar modes in the infrared spectra. The A_1 component of the soft mode exhibits a minimal frequency near 400 K and we suggest that this temperature corresponds to the temperature, where the polar nanoregions percolate.

1. OVERVIEW

1.1. Ferroelectrics

If the spontaneous polarization of a material between crystallographically equivalent configurations is possible to reorient by an external electric field, then, in analogy to ferromagnetics, one speaks about ferroelectrics. Thus, it is not the existence of the spontaneous polarization alone, but also its "switchability" by an external field defines a ferroelectric material.

1.1.1. Ginzburg-Landau Theory

The Ginzburg-Landau theory is equivalent to a mean field theory considering the thermodynamic entity of the dipoles in the mean field of all the others. It is reasonable if the particular dipole interacts with many other dipoles. The theory introduces an order parameter P, i.e. the polarization, which, for a second order phase transition, diminishes continuously to zero at the phase transition temperature T_c [2]. Close to the phase transition, therefore, the free energy may be written as an expansion of powers of the order parameter. All the odd powers of P do not occur because of a symmetry reasons:

$$F(P,T) = \frac{1}{2} g_2 P^2 + \frac{1}{4} g_4 P^4 + \frac{1}{6} g_6 P^6 . \tag{1.1}$$

The highest expansion coefficient (here g_6) needs to be larger than zero because otherwise the free energy would approach minus infinity for large P. All coefficients depend on the temperature and in particular the coefficient g_2. Expanding g_2 in a series of T around the Curie temperature Θ which is equal to or less than the phase transition temperature T_c, we can approximate:

$$g_2 = \frac{1}{C}(T - \Theta) . \tag{1.2}$$

where C is Curie-Weiss constant. Stable states are characterized by minima of the free energy with the necessary and sufficient conditions:

$$\frac{\partial F}{\partial P} = P(g_2 + g_4 P^2 + g_6 P^4) = 0 , \tag{1.3}$$

and

Copyright © 2010. Nova Science Publishers, Incorporated. All rights reserved.

Handbook of Material Science Research, Nova Science Publishers, Incorporated, 2010. ProQuest Ebook Central,

$$\frac{\partial^2 F}{\partial P^2} = \frac{1}{\varepsilon(0)} = g_2 + 3g_4 P^2 + 5g_6 P^4 > 0 . \tag{1.4}$$

Two cases are to distinguish: (i) $g_4 > 0 \Rightarrow g_6 = 0$, which corresponds to a phase transition of the second order, and (ii) $g_4 < 0 \Rightarrow g_6 > 0$, which is related with a phase transition of the first order. In both cases, the trivial solution $P = 0$ exists, representing the paraelectric phase. Inserting Equation (1.2) into (1.4) it becomes obvious that above T_c the coefficient g_2 needs to be larger than zero in order to obtain stable solutions. A comparison of Equation (1.2) and (1.4) shows that the g_2 is expressed by the permittivity $\varepsilon(0)$, for which the Curie-Weiss law is found:

$$\varepsilon(0) = \frac{C}{T - \Theta} . \tag{1.5}$$

Second Order Phase Transition

For $T < \Theta$, a spontaneous polarization exists. It can easily be shown that the Curie temperature Θ is equal to the phase transition temperature T_C. The spontaneous polarization depends on the distance from the phase transition temperature with a square root law:

$$P = \sqrt{\frac{T_c - T}{C g_4}} . \tag{1.6}$$

For $T > T_c$, a minimum is found for $P_2 = 0$. At $T = T_c$, this minimum shifts continuously to final values of the polarization. The temperature dependence of the permittivity in the ferroelectric phase is obtained by inserting Equation (1.6) into (1.4):

$$\left.\frac{1}{\varepsilon(0)}\right|_{T<T_c} = 2\frac{T_c - T}{C} . \tag{1.7}$$

The slope of the inverse permittivity below the T_c is just twice of the slope above the T_c.

First Order Phase Transition

If the expansion coefficients are chosen as $g_4 < 0$ and $g_6 > 0$, the stable states will again be found from Equation (1.3):

$$P^2 = \frac{1}{2g_6}\left(|g_4| + \sqrt{g_4^2 - 4C^{-1}(T - \Theta)g_6}\right) . \tag{1.8}$$

Inserting Equation (1.8) into (1.1) results in the free energy as a function of polarization and of temperature. At high temperatures the free energy assumes a parabolic shape with a minimum corresponding to a stable paraelectric phase. On cooling, secondary minima at

Copyright © 2010. Nova Science Publishers, Incorporated. All rights reserved.

Handbook of Material Science Research, Nova Science Publishers, Incorporated, 2010. ProQuest Ebook Central,

finite polarizations become visible. Their energy level at the beginning, however, is higher than that at $P = 0$. In this regime, the paraelectric phase is stable and the ferroelectric phase is metastable. Lowering the temperature further, at $T = T_C$, all three minima of the free energy are at the same level. Below T_C, F becomes negative and favors a finite spontaneous polarization. In the temperature regime between T_C and Θ, the paraelectric phase coexists with the ferroelectric phase with the paraelectric phase being metastable. Somewhere on cooling through this regime, the first order phase transition to the ferroelectric state will occur with a corresponding jump of the spontaneous polarization from zero to a finite value. The permittivity in the ferroelectric phase is given by:

$$\left.\frac{1}{\varepsilon(0)}\right|_{T<T_c} = \frac{T-\Theta}{C} + \frac{3g_4}{2g_6}\left(|g_4| + \sqrt{g_4^2 - 4C^{-1}(T-\Theta)g_6}\right) + \frac{1.25}{g_6}\left(|g_4| + \sqrt{g_4^2 - 4C^{-1}(T-\Theta)g_6}\right)^2 \cdot \tag{1.9}$$

1.1.2. Soft Mode Concept

The atoms of a crystal vibrate around their equilibrium position at finite temperatures. There are lattice waves propagating with certain wavelengths and frequencies through the crystal [3]. The characteristic wave vector $\vec{q}$ can be reduced to the first Brillouin zone of the reciprocal lattice, $0 \le q \le \pi/a$, where a is the lattice constant.

In every lattice there are three modes with different frequencies belonging to one longitudinal and two transverse branches of the acoustic phonons. A vibration of the atoms perpendicular to the propagation corresponds to a transverse wave, a vibration in the direction of the propagation corresponds to a longitudinal wave. The acoustic phonons have an elastic nature. All atoms vibrate as a linear chain independent of the number of different atoms per lattice cell. The sound velocity v_s gives the wavelengths of the acoustic phonons; therefore, no coupling of acoustic phonons with electromagnetic waves exists ($v_s << v_{\text{Light}}$).

In case of the non-primitive lattices with different atoms in the elementary cell, the sub-lattices can vibrate against each other. A vibration with a frequency $\omega \neq 0$ becomes possible even for the wave vector q=0. The opposite movement of neighboring atoms evokes large dipole moments allowing a coupling to electromagnetic waves.

In general, each mode of the phonon dispersion spectra is collectively characterized by the relating energy, i.e. the frequency and wave vector, and is associated with a specific distortion of the structure.

The local electric field in ionic crystals leads to a splitting of the optical vibration modes. The longitudinal mode frequency is shifted to higher frequencies while the transverse mode frequency is shifted to lower frequencies. The softening of the transverse modes is caused by a partial compensation of the short-range lattice (elastic) forces on the one hand and the long-range electric fields on the other hand. This effect is strongest at the zone center [3]. If the compensation is complete, the transverse optic mode frequency becomes zero when the temperature is decreased, ω_{TO} ($T \rightarrow T_c$) $\rightarrow$ 0, and the soft phonon condenses out so that at T_c a phase transition to a state with spontaneous polarization takes place (ferroelectric phase transition). At the zone center (wave vector is 0) the wavelength of the TO mode is infinite ($\lambda_0 \rightarrow \infty$), i.e. the region of homogeneous polarization becomes infinite. In the case of the softening of the TO mode the transverse frequency becomes zero and no vibration exists anymore ("frozen in").

Copyright © 2010. Nova Science Publishers, Incorporated. All rights reserved.

Handbook of Material Science Research, Nova Science Publishers, Incorporated, 2010. ProQuest Ebook Central,

A linear relation (Cochran law) between ω^2_{TO} and T at the zone center is found suggesting that the temperature dependence of the optic mode frequency relates to the phase transition [4]:

$$\omega_{TO}^2 = A_{cr}\left|T - T_C\right| \tag{1.10}$$

in accordance with the Lyddane-Sachs-Teller relation:

$$\frac{\varepsilon(T,0)}{\varepsilon_{\infty f}} = \frac{\omega_{LO}^2}{\omega_{TO}^2(T)}. \tag{1.11}$$

where $\varepsilon_{\infty f}$ is the contribution of the all higher modes and electronic polarization, ω_{LO} is the longitudinal optic mode frequency, and ε (T, 0) is contribution of presented mode.

1.1.3. Dielectric Dispersion in Ferroelectrics

In general, the polarization vector, due to the moment of various types of polarization, may be unable to follow the change of the field. As a result, $\varepsilon^*(\omega) = \varepsilon'(\omega) - i\varepsilon''(\omega)$ is complex. The Kramers-Kroning relations functionally relate the real and imaginary parts of the permittivity:

$$\varepsilon'(\omega) - \varepsilon_\infty = \frac{2}{\pi}\mathrm{P}_p\int_0^\infty \frac{\omega'\varepsilon''(\omega')}{(\omega')^2 - \omega^2}d\omega', \tag{1.12}$$

$$\varepsilon''(\omega) = \frac{2}{\pi}P_p\int_0^\infty \frac{\omega(\varepsilon'(\omega') - \varepsilon_\infty)}{(\omega')^2 - \omega^2}d\omega', \tag{1.13}$$

where P_p indicates Cauchy's principal part of the integral, ω' is an integration variable. In an external electric field, a molecule with permanent dipole moments undergoes an orientation. In an alternating field, the orientation depends on the frequency and causes a dielectric dispersion. The classical theory of the dielectric dispersion for polar liquids, which occurs mainly through the reorienatation of the noninteracting permanent dipoles, was developed by Debye [5]. In the Debye model, the relaxing polarization P_r is assumed to decay after step removal of the electric field according to the following equation:

$$\frac{dP_r}{dt} = -\frac{1}{\tau}P_r(t), \tag{1.14}$$

where τ corresponds to the relaxation time. The equilibrium polarization vanishes after switching off the electric field. The normalized macroscopic relaxation function $\Phi(t)$ describes the decay of the relaxing polarization and is expressed as simple exponent in the framework of the Debye model:

Copyright © 2010. Nova Science Publishers, Incorporated. All rights reserved.

Handbook of Material Science Research, Nova Science Publishers, Incorporated, 2010. ProQuest Ebook Central,

$$\Phi(t) = e^{-\frac{t}{\tau}}. \tag{1.15}$$

The relation between the complex permittivity and the function $\Phi(t)$ was first derived by Kubo [6]:

$$\frac{\varepsilon^*(\omega) - \varepsilon_{\infty r}}{\varepsilon(0) - \varepsilon_{\infty r}} = \int_0^\infty -\frac{d\Phi(t)}{dt} e^{-i\omega t} dt\,. \tag{1.16}$$

The dielectric permittivity ε^* of the Debye model can be derived from $\Phi(t)$ with Kubo relation (1.16):

$$\varepsilon^*(\omega) = \varepsilon_{\infty r} + \frac{\varepsilon(0) - \varepsilon_{\infty r}}{1 + i\omega\tau} = \varepsilon_{\infty r} + \frac{\Delta\varepsilon}{1 + i\omega\tau}, \tag{1.17}$$

where $\Delta\varepsilon$ is the contribution of the relaxation process to the static permittivity, $\varepsilon_{\infty r}$ is the contribution of the phonon modes and electronic polarization. Dielectric dispersion in pure ferroelectrics is Debey like or very similar to it [7].

1.2. Dipolar Glasses

1.2.1. Introduction

Orientational glasses are crystalline materials that transform from a high-temperature crystalline phase into a low-temperature glassy state. Analogous to the spin glasses (for a review see Ref. [8]), randomly substituted impurity ions (or molecules) that carry a moment are located on a topologically ordered lattice. These moments have orientational degrees of freedom and they interact with one another. The dominant exchange interaction can be of electrostatic dipolar, quadrupolar or octupolar, or of elastic quadrupolar nature. In the latter case, the interaction is mediated via lattice strains. Due to site disorder and anisotropic interactions, the orientational disorder is cooperatively frozen-in.

The use of the term "glass-state" suggests some similarity with canonical glasses such as vitreous silica. Indeed, the orientational glasses exhibit relaxation dynamics similar to those observed in canonical glasses. In addition, the low-temperature thermodynamic, elastic and dielectric properties are characteristic of amorphous systems. The advantage of orientational glass is that they can be modeled in terms of a Hamiltonian.

Figure l.1 shows mixtures of two orientationally ordered compounds A and B that exhibit a disordered low-temperature state. Well-known examples are mixtures of ferroelectric and antiferroelectric compounds such as rubidium ammonium dihydrogen phosphate (RADP) [9] and mixtures of the elastically ordered KCN and NaCN [10]. In RADP, a frustrated ground state is believed to occur via the competing electric interactions. In NaCN:KCN, it seems plausible that the random fields suppress a long-range elastic order [11]: random strains are introduced by the volume difference of the impurity atoms that cause quenched elastic relaxations of the neighbouring ions.

Copyright © 2010. Nova Science Publishers, Incorporated. All rights reserved.

Handbook of Material Science Research, Nova Science Publishers, Incorporated, 2010. ProQuest Ebook Central,

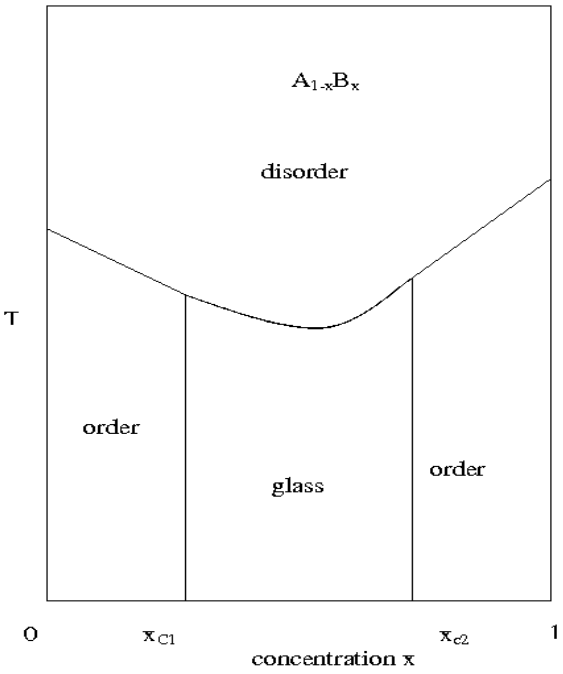


Figure 1.1. Schematic x-T phase diagram of two orientationally ordered compounds.

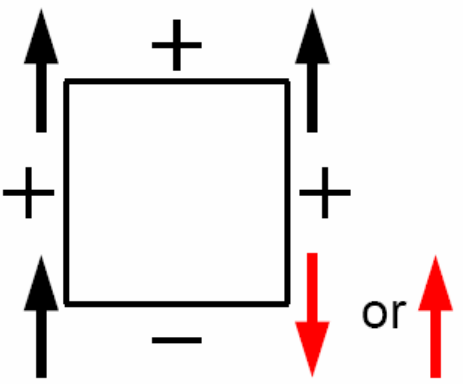


Figure 1.2. A toy model which shows frustration. If the interaction on the bond is a "+", the spins are parallel and if it is a "-" they are antiparallel. Clearly all these conditions can not be met so there is competition or "frustration".

1.2.2. Models of Spin Glasses

Because dipolar glass concept arises from the spin glasses, several ideas about spin glass must here mentioned. The spin glasses are magnetic systems in which the interactions between the magnetic moments are "in conflict" due to with some frozen-in structural disorder (Figure1.2). Thus, no conventional long-range order can be established. Nevertheless, these systems exhibit a "freezing transition" to a state with a new kind "order" in which the spins are aligned in random directions. The nature of this new kind of order, and

Copyright © 2010. Nova Science Publishers, Incorporated. All rights reserved.

Handbook of Material Science Research, Nova Science Publishers, Incorporated, 2010. ProQuest Ebook Central,

thus its appropriate theoretical description, is still heavily debated, as well as the character of freezing transition: is it a new type of phase transition [12] or failure to establish a complete thermal equilibrium during observation time? Number challenging questions arise here. Usually, the ordered phase is characterized by an order parameter (see Section 1.1.1.). What is the order parameter for spin glasses? The ordered phase generally has a lower symmetry than the corresponding disordered phase. Is there a "broken symmetry" here?

And many other more or less fundamental questions arise [8]. These questions are in generally actual also for dipolar glasses. Is still a mater of debate whether or not the relaxation times and spin glass correlation length diverge at freezing temperature T_0 signifying a phase transition, or just become large and finite. If there is a phase transition, we can define a spin glass (Edwards-Anderson) order parameter [12]:

$$q_{EA} = [\langle S_i \rangle_T^2]_{av}, \tag{1.18}$$

which is nonzero below T_0. Here $< >_T$ denotes a statistical mechanics average and $[\ ]_{av}$ is a configurational average over random interactions.

The standard "random bond" problem is formulated as such the Hamiltonian:

$$H = -\frac{1}{2}\sum_{ij} J_{ij} S_i S_j - F_{ex}\sum_i S_i^z , \tag{1.19}$$

where the last term characterizes interaction between the external magnetic field and spins, the first term characterizes an interplay between the spins, and the exchange constant are randomly chosen according to a fixed distribution $P(J_{ij})$. This choice is Gaussian in the Edwards-Anderson model [12]:

$$P(J_{ij}) = \frac{\exp[-(J_{ij} - \bar{J})^2 / 2(\Delta J)^2]}{\sqrt{2\pi}(\Delta J)}. \tag{1.20}$$

From the Hamiltonian (1.19) Edwards and Anderson [12] for susceptibility such a relation obtained:

$$\chi = \frac{C}{T_c} - O(T_c - T)^2 , \tag{1.21}$$

here O is a constant. This law predicts a sharp cusp at T_c. The cusp is linear on one side but quadratic on the lower side. Indeed, similar cusp is observed in spin glasses [13]. This cusp can be destroyed by an external magnetic field. Sherington and Kirkpatrick [14] proposed that the mean-field theory of the spin glasses should to be exact solutions of a infinite-range in the Edwards and Anderson model in which the probability distribution $P(J_{ij})$ is the same for all pairs of spins no matter how far they are apart. This is clearly an unphysical assumption, but the infinite-range model agrees fairly well with experiment, so it seems sensible to try in

Copyright © 2010. Nova Science Publishers, Incorporated. All rights reserved.

Handbook of Material Science Research, Nova Science Publishers, Incorporated, 2010. ProQuest Ebook Central,

analogous approach for spin glasses. The Hamiltonian in the Sherington-Kirkpatrick (SK) model is the same as one is in Equation (1.19).

Applying the replica trick and the steepest descent method one arrives at the following equations for the magnetization $m_{mgn}(T) \equiv <<S_i>>_j$ per site and for the Edwards-Anderson order parameter $q_{EA}(T)$ [14]:

$$m_{mgn}(T) = \frac{1}{\sqrt{2\pi}} \int_{-\infty}^{\infty} ds e^{-\frac{s^2}{2}} \tanh[\eta_{ef}(s)/(k_B T)], \tag{1.22}$$

$$q_{EA}(T) = \frac{1}{\sqrt{2\pi}} \int_{-\infty}^{\infty} ds e^{-\frac{s^2}{2}} \tanh^2[\eta_{ef}(s)/k_B T], \tag{1.23}$$

where k_B is Boltzman constant, $\eta_{ef}(s)$ is an effective mean field given by

$$\eta_{ef}(s) = \bar{J} m_{mgn} + \Delta J q_{EA}^{\frac{1}{2}} + F_{ex}. \tag{1.24}$$

From Eq. (1.21) we can obtain the susceptibility:

$$\chi = \frac{1 - q_{EA}(T)}{k_B T - \bar{J}(1 - q_{EA}(T))}. \tag{1.25}$$

The Oresic and Pirc (OP) [15] model is an anisotropic version of the SK model. The dipoles are assumed to be arranged in one dimensional chains, with a ferroelectric coupling K between nearest neighbors in each chain. An SK type long-range random bond interaction, with zero mean, $\bar{J}$ =0, exists between all pairs of spins (within a chain and between chains). Consequently the OP model predicate such Hamiltonian:

$$H = -\frac{1}{2} \sum_{i,j} K_{ij} S_i S_j - \frac{1}{2} \sum J_{ij} S_i S_j - F_{ex} \sum_i S_i. \tag{1.26}$$

There is no known closed form solution for this model. Oresic and Pirc used a numerical recursion method [15].

1.2.3. Random Bond-random Field Theory

The essential difference between the magnetic spin glasses and dipolar glasses is the fact that in this last group of materials an intrinsic random field is generated by substitutional impurities. Lattice distortions cannot give rise to random magnetic fields unless time-reversal symmetry is broken. In view of this, the formation of the dipole glass phase can be understood in terms of the frustrated correlation between the dipoles and the strong coupling via random fields. In addition, in dipolar glasses tunnelling can play an important role, therefore Hamiltonian (1.18) must be so overwritten [16]:

Copyright © 2010. Nova Science Publishers, Incorporated. All rights reserved.

Handbook of Material Science Research, Nova Science Publishers, Incorporated, 2010. ProQuest Ebook Central,

$$H = -\frac{1}{2}\sum_{ij} J_{ij} S^z{}_i S^z{}_j - \Omega \sum_i S_i^x - \sum_i f_i S_i^z - F_{ex} \sum_i S_i^z \,, \tag{1.27}$$

here the second term denotes influence of tunnelling effects and the third one is the interaction with random field. In the framework of random bond – random field (RBRF) theory the random fields f_i are distributed according to the Gaussian law:

$$P(f_i) = \frac{\exp[-(f_i - \bar{f})^2 / 2(\Delta f)^2]}{\sqrt{2\pi}(\Delta f)} \,. \tag{1.28}$$

For the case of various mixed crystals groups both ΔJ and Δf depend on the concentration x characterizing the composition of the glasses as in the case of $Rb_{1-x}(NH_4)_xH_2PO_4$ (RADP). The simplest concentration dependence typically has the form [16]:

$$\Delta f = 4x(1-x)\Delta f_{\max} \,, \tag{1.29}$$

and similar behaviour can be assumed for the variance ΔJ. From replica symmetric solutions R. Pirc and co-authors [16] obtained the polarization P:

$$P = \int_{-\infty}^{\infty} dx \frac{e^{-x^2/2}}{\sqrt{2\pi}} \frac{2}{Z(x)} \int_{-\infty}^{\infty} dy \frac{e^{-y^2/2}}{\sqrt{2\pi}} \frac{B_z}{B} \sin(B/(k_B T)) \,, \tag{1.30}$$

and the dielectric susceptibility χ in zero field:

$$\chi = (r - o_q)/(k_B T) \,, \tag{1.31}$$

where

$$o_q = \int_{-\infty}^{\infty} dx \frac{e^{-x^2/2}}{\sqrt{2\pi}} [\frac{2}{Z(x)} \int_{-\infty}^{\infty} dy \frac{e^{-y^2/2}}{\sqrt{2\pi}} \frac{B_z}{B} \sinh(B/(k_B T)]^2 \,, \tag{1.32}$$

$$r = \int_{-\infty}^{\infty} dx \frac{e^{-x^2/2}}{\sqrt{2\pi}} [\frac{2}{Z(x)} \int_{-\infty}^{\infty} dy \frac{e^{-y^2/2}}{\sqrt{2\pi}} ((\frac{B_z}{B})^2 \sin(B/(k_B T)) + k_B T \frac{\Omega^2}{B^3} \sin(B/(k_B T)]^2 \,, \tag{1.33}$$

$Z(x)$ is partition function, the vector $\boldsymbol{B}$=(Ω, 0, …, $(\bar{J}^2 q + \Delta f)^{1/2} x + \bar{J}(r-q)^{1/2} y + F_{ex}$). Since by assumption also $\bar{J}$ =0 in Eq. (1.20) the polarization will be strictly zero at all temperatures. The behaviour of the order parameter q_{EA} and the dielectric susceptibility χ the authors [16] obtained numerically. For a finite value of Δf the pseudo-spin-glass transition smeared out and the order parameter q_{EA} remains nonzero at all temperatures. One might

Copyright © 2010. Nova Science Publishers, Incorporated. All rights reserved.

Handbook of Material Science Research, Nova Science Publishers, Incorporated, 2010. ProQuest Ebook Central,

argue that the random-field variance Δf acts as an effective ordering "field" for the order parameter q_{EA} without inducing an average polarization P. This is the main difference between the transition smearing by a random field Δf and a homogeneous field E. As a result the onset of a glass phase is not determined by the appearance of a nonzero value of $q_{EA}(T)$. However, it is well known [8] that the replica symmetric solution we have presented becomes unstable below the Almeida-Thouless temperature. This instability also occurs in the presence of random fields and is usually associated with the onset of nonergodicity. The Almeida-Thouless temperature T_{AT} is given by [16]:

$$(\frac{k_B T_{AT}}{\Delta J})^2 = \int_{-\infty}^{\infty} \frac{dx}{\sqrt{2\pi}} e^{-x^2/2} [1 - \tanh^2(\eta_{ef}(s)/(k_B T)]^2 \ . \qquad [1.34]$$

1.3. Ferroelectric Relaxors

1.3.1. Introduction

Relaxor ferroelectrics or relaxors are a class of disordered crystals possessing peculiar structure and properties. At high temperature they exist in a non-polar paraelectric phase, which is similar in many respects to the paraelectric phase of normal ferroelectrics. Upon cooling they transform into the ergodic relaxor state in which polar regions of nanometer scale with randomly distributed directions of dipole moments appear. This transformation which occurs at the so-called Burns temperature (T_B) [1] cannot be considered a structural phase transition because it is not accompanied by any change of crystal structure on the macroscopic or mesoscopic scale. Nevertheless, the polar nanoregions affect the behaviour of the crystal dramatically, giving rise to unique physical properties. For this reason the state of crystal at $T < T_B$ is often considered as the new phase different from the paraelectric one.

At temperatures close to T_B the polar nanoregions are mobile and their behaviour is ergodic. On cooling, their dynamics slows down enormously and at a low enough temperature, T_0 (typically hundreds degrees below T_B), the polar nanoregions in the canonical relaxors become frozen into a nonergodic state, while the average symmetry of the crystal still remains cubic.

Similar kind of nonergodicity is characteristic of a dipole glass (or spin glass) phase. The existence in relaxors of an equilibrium phase transition into a low-temperature glassy phase is one of the most interesting hypotheses which has been intensively discussed. Freezing of the dipole dynamics is associated with a large and wide peak in the temperature dependence of the dielectric permittivity with characteristic dispersion observed at all frequencies practically available for dielectric measurements (Figure1.3). This peak is of the same order of magnitude as the peaks at the Curie point in the ordinary ferroelectric perovskites, but in contrast to ordinary ferroelectrics it is highly diffused and its temperature T_m ($> T_0$) shifts with frequency due to the dielectric dispersion. Because of the diffuseness of the dielectric anomaly and the anomalies in the temperature dependences of some other properties, relaxors are often called (especially in early literature) the "ferroelectrics with diffuse phase transition", even though no transition into ferroelectric phase really occurs. The nonergodic relaxor state existing below T_0 can be irreversibly transformed into a ferroelectric state by a strong enough external electric field. This is an important characteristic of relaxors which

Copyright © 2010. Nova Science Publishers, Incorporated. All rights reserved.

Handbook of Material Science Research, Nova Science Publishers, Incorporated, 2010. ProQuest Ebook Central,

distinguishes them from typical dipole glasses. Upon heating the ferroelectric phase transforms to the ergodic relaxor one at the temperature T_C which is very close to T_0. In many relaxors the spontaneous (i.e. without the application of an electric field) phase transition from the ergodic relaxor into a low-temperature ferroelectric phase still occurs at T_C and thus the nonergodic relaxor state does not exist.

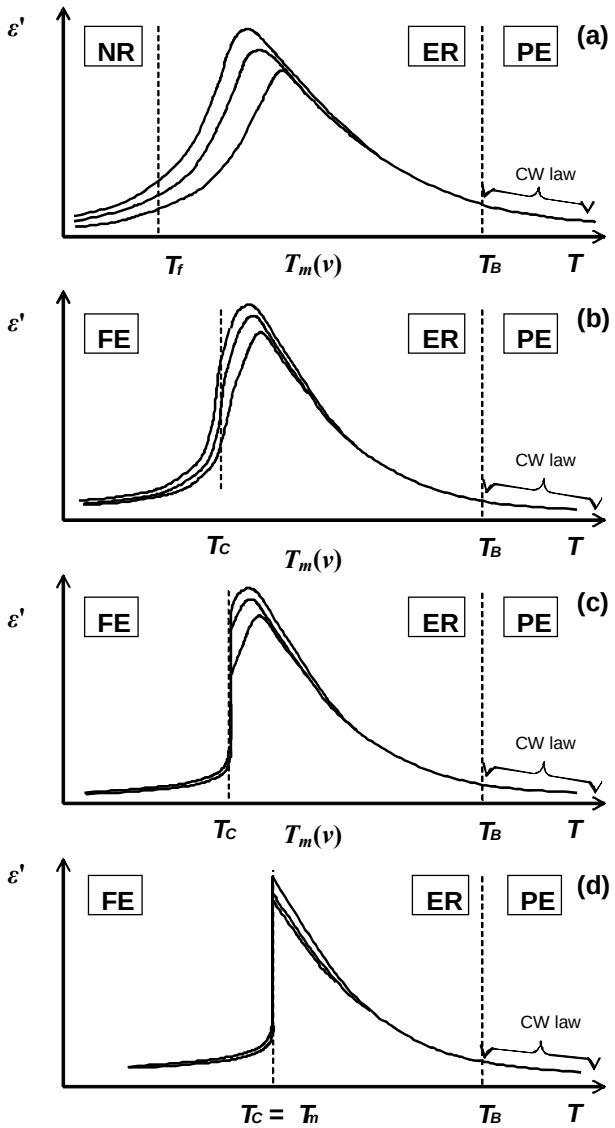


Figure 1.3.Different possibilities for the temperature evolution of structure and dielectric properties in compositionally disordered perovskites: (a) canonical relaxor; (b) crystal with a diffuse relaxor-to-ferroelectric transition at $T_C < T_m$; (c) crystal with a sharp relaxor-to-ferroelectric transition at $T_C < T_m$; (d) crystal with a sharp relaxor-to-ferroelectric transition at $T_C = T_m$. The temperature dependences of the dielectric constant at different frequencies ν are schematically shown. the crystallographically equivalent sites, is the common feature of relaxors.

Copyright © 2010. Nova Science Publishers, Incorporated. All rights reserved.

Handbook of Material Science Research, Nova Science Publishers, Incorporated, 2010. ProQuest Ebook Central,

Compositional disorder, i.e. the disorder in the arrangement of different ions on the crystallographically equivalent sites, is the common feature of relaxors. The relaxor behaviour was first observed in the perovskites with disorder of non-isovalent ions, including the stoichiometric complex perovskite compounds, e.g. $Pb(Mg_{1/3}Nb_{2/3})O_3$ (PMN) [17] or $Pb(Sc_{1/2}Ta_{1/2})O_3$ (PST) [18] (in which Mg^{2+}, Sc^{3+}, Ta^{5+} and Nb^{5+} ions are fully or partially disordered in the B-sublattice of the perovskite ABO_3 structure) and nonstoichiometric solid solutions, e.g. $Pb_{1-x}La_x(Zr_{1-y}Ti_y)_{1-x/4}O_3$ (PLZT) [19, 20] where the substitution of La^{3+} for Pb^{2+} ions necessarily leads to vacancies on the A-sites. Recently an increasing amount of data reported has shown that many homovalent solid solutions, e. g. $Ba(Ti_{1-x}Zr_x)O_3$ (BTZ) [21, 22] and $Ba(Ti_{1-x}Sn_x)O_3$ [23] can also exhibit relaxor behaviour. Other examples of relaxor ferroelectrics are complex perovskites $Pb(Zn_{1/3}Nb_{2/3})O_3$ (PZN) $Pb(Mg_{1/3}Ta_{2/3})O_3$ (PMT), $Pb(Sc_{1/2}Nb_{1/2})O_3$ (PSN), $Pb(In_{1/2}Nb_{1/2})O_3$ (PIN), $Pb(Fe_{1/2}Nb_{1/2})O_3$ (PFN), $Pb(Fe_{2/3}W_{1/3})O_3$ (PFW) and the solid solutions: $(1-x)Pb(Mg_{1/3}Nb_{2/3})O_3 - xPbTiO_3$ (PMN-PT), $(1-x)Pb(Zn_{1/3}Nb_{2/3})O_3 - xPbTiO_3$ (PZN-PT), PMN-PSN, PMN-PZN.

Although relaxor ferroelectrics were first reported nearly half a century ago, this field of research has experienced a revival of interest in recent years.

1.3.2. Compositional Order-disorder Phase Transitions and Quenched Disorder in Complex Perovskites

As mentioned above, the disordered distribution of different ions on the equivalent lattice sites (i.e. compositional disorder, also called chemical, ionic or substitutional disorder) is the essential structural characteristic of relaxors. The ground state of the complex perovskites should be compositionally ordered, e.g. in the $A(B'_{1/2}B''_{1/2})O_3$ compounds each type of the cations, B' or B", should be located in its own sublattice, creating a superstructure with complete translational symmetry. This is because the electrostatic and elastic energies of the structure are minimized in the ordered state due to the difference in both the charge and the size of B' and B" ions. The thermal motion is capable of destroying the order at a certain nonzero temperature (T_t). This occurs in the form of structural phase transition, the order parameter (compositional long-range order) of which can be measured by the X-ray or other diffraction methods. Such kind of phase transitions had been known long ago (e.g. in many metallic alloys) and was also discovered comparatively recently at T_t ~1500 K in PST, PSN [24] and several other complex perovskites. Ordering implies the site exchange between B' and B" cations via diffusion. It is a relaxation process with a nearly infinite characteristic time at low temperatures, but at 1500 K it can be quite fast. As a result, in some perovskites (e.g. in PST, PSN, PIN), by annealing at temperatures around T_t and subsequent quenching, one can obtain the metastable states with different states at low temperatures. In some other materials (e.g. in PFN and PMN) the compositional disorder cannot be changed by any heat treatment because the relaxation time of ordering is too long. However in all known relaxors, at T_B and below, the compositional order is frozen (quenched), i.e. cannot vary during practically reasonable time.

In the real complex perovskite crystals and ceramics the quenched compositional disorder is often inhomogeneous, e.g. small regions of the ordered state are embedded in a disordered matrix. These regions can be regarded as a result of incomplete compositional order-disorder phase transformation or as quenched phase fluctuations. In the prototypical relaxor PMN this kind of inhomogeneous structure always exists and cannot be changed by any heat treatment.

Copyright © 2010. Nova Science Publishers, Incorporated. All rights reserved.

Handbook of Material Science Research, Nova Science Publishers, Incorporated, 2010. ProQuest Ebook Central,

In $Pb(B'_{1/2}B''_{1/2})O_3$ perovskites the ordering of B-site ions converts the disordered PE $Pm\bar{3}m$ structure into the ordered $Fm\bar{3}m$ structure in which B' ions alternate with B'' ions along the <100> directions (1:1 ordering). In the ordered phase of many non-ferroelectric $A(B^{2+}_{1/3}B^{5+}_{2/3})O_3$ perovskites, B^{2+} ions alternate with two B^{5+} ions along the <100> directions (1:2 ordering). The type of ordering in lead-containing relaxor perovskites, $Pb(B^{2+}_{1/3}B^{5+}_{2/3})O_3$, has been the subject of debates. In the early works only inhomogeneous ordering (ordered regions within disordered surroundings) was found in the samples studied. High-resolution electron microscopy of PMN revealed nano-size (~ 2-5 nm) regions in which the ordering of 1:1 type ($Fm\bar{3}m$) was observed (see e.g. Refs.25, 26). These chemical nanoregions give rise to the week superlattice reflections (so-called F-spots). The results of anomalous X-ray scattering measurements [27] showed that the chemical nanoregions in PMN exhibit an isotropic shape and a temperature-independent (as expected for the quenched order) size in the temperature interval of 15 - 800 K. Alternating Mg^{2+} and Nb^{5+} ions, i.e the same type of ordering as in the ordered $Pb(B'_{1/2}B''_{1/2})O_3$ perovskites, were initially supposed to exist in these regions. This structural model was called "space charge model" because it implies the existence of the negatively charged compositionally ordered non-stoichiometric nanoregions, and the positively charged disordered non-stoichiometric matrix. Later, by means of appropriate high-temperature treatments, Davies and Akbas [28] were able to increase the size of chemical nanoregions and obtained highly 1:1 ordered samples without the disordered matrix in the PMT and modified PMN ceramics. The existence of such ordering in overall stoichiometric samples is obviously inconsistent with the space charge model. The results of X-ray energy dispersive spectroscopy with a nanometer probing size revealed that the Mg/Nb ratio is the same in the chemical nanoregions as in the disordered regions of PMN [29], which also disagrees with the space charge model. A charge-balanced "random-site" model has been suggested in which one of the B-sublattices is occupied exclusively by B^{5+} ions while the other one contains a random distribution of B^{2+} and B^{5+} ions in a 2:1 ratio so that the local stoichiometry is preserved [28].

The degree of compositional disorder can greatly influence the ferroelectric properties. For example, the disordered PIN crystals are relaxor ferroelectrics, but in the ordered state, they are antiferroelectrics with a sharp phase transition [30, 31], confirming the general rule that the relaxor behaviour can only be observed in disordered crystals. The possibility for real perovskite samples to have different states of compositional disorder, depending on crystal growth or ceramic sintering conditions, should be taken into account in research work.

1.3.3. Relaxors in the Ergodic State

The paraelectric phase of all perovskite ferroelectrics has the cubic $m\bar{3}m$ average symmetry, but locally the ion configuration can be distorted, i.e. the ions are not located in the special crystallographic sites of the ideal perovskite structure. For example, in the classical ferroelectrics $BaTiO_3$, the random displacements of Ti cations along the <111> directions caused by the multiple-well structure of potential surface were found [32, 33]. Such kind of displacements is due to the hybridization between electronic states of cations and the 2*p* states of oxygen (and should not exist in the case of purely ionic bonds). This effect is an important factor for the ferroelectric instability [34] and is also expected to occur in perovskite relaxors. Moreover, owing to the different sizes of the compositionally disordered cations and the random electric fields created because of the different charges of these cations in relaxors, all

Copyright © 2010. Nova Science Publishers, Incorporated. All rights reserved.

Handbook of Material Science Research, Nova Science Publishers, Incorporated, 2010. ProQuest Ebook Central,

ions are expected to be displaced from special positions. These shifts should exist in the paraelectric phase and also at lower temperatures.

Permanent uncorrelated displacements of ions from the high-symmetry positions of the (fully or partially compositionally disordered) cubic perovskite-type structure were indeed found in relaxors at temperatures much higher, as well as lower, than T_B. They are shown schematically in Figure 1.4.

The displacements of Pb^{2+} were detected in PMN [35, 36, 37], PZN, PSN, PST, PIN, PFN, PZN-PT and PMN-PT with small x by X-ray and neutron diffraction (see Refs.38, 39, 40 and references therein). To describe the Pb distribution, a spherical layer model has been proposed [37] according to which the shifts of ions are random both in length and direction so that they are distributed isotropically within the spherical layer centred on the special Pb site. The typical radius of the sphere is ~0.3 $\overset{o}{\text{A}}$. It decreases slightly with increasing temperature. The off-symmetry displacements of Pb ions in PMN were found to vanish at $T > 925$ K [37] (for other relaxors no data up to so high temperatures are available). The spherical layer model for Pb displacements in PMN was confirmed by the NMR investigations [41] and by the pulsed neutron atomic pair-distribution function (PDF) analysis [42]. Note that the significant random off-centring of Pb ions in perovskites is not the result of compositional disorder. It was also found in the paraelectric phase of the ordinary perovskite $PbZrO_3$ [43]. On the other hand, in the PMN-PT solid solution with x=0.4 which is still compositionally disordered, the Pb displacements from the special perovskite positions were not observed at $T > T_C$ [40].

According to neutron diffraction data [36, 38, 44] the shifts of oxygen ions in the planes parallel to the corresponding faces of the perovskite cubic cell are isotropic (in PMN the shifts are close to 0.2 $\overset{o}{\text{A}}$). The oxygen ions are also shifted (by about 0.06 $\overset{o}{\text{A}}$ in PMN) in the perpendicular direction so that the distribution of shifts forms two rings parallel to the face of the cube. The displacements of B-site ions (Nb^{5+}, Mg^{2+}, Zn^{2+} etc.) from the ideal positions were not noticed in diffraction experiments [38, 44] (some authors found small seemingly isotropic displacements of about 0.1 $\overset{o}{\text{A}}$ in PMN [36]). Nevertheless the investigations of the extended X-ray absorption fine structure (EXAFS) and the pre-edge regions of absorption spectra revealed the off-centre random displacements of Nb in the direction close to <110> in PMN, PZN, PSN and PIN [45]. These displacements are not sensitive to the change of temperature (in the range of 290-570 K), nor to the degree of compositional disorder (in PSN and PIN). The pulsed neutron PDF studies confirm [42] that the Nb displacements (in PMN at room temperature) are comparatively small (much smaller than in $KNbO_3$).

In the canonical relaxors such as PMN, the average crystal symmetry seems to remain cubic with decreasing temperature but the local structure changes. In addition to the uncorrelated local distortions described above, the clusters of ferroelectric order (i.e. polar nanoregions) appear at $T < T_B$ ($T_B \approx 620$ K in PMN). Due to their extremely small (nanometric) size, these polar nanoregions cannot be detected from the profiles of the X-ray and neutron diffraction Bragg peaks.

Other experiments are needed to validate their existence.

The first experimental (although indirect) evidence for the polar nanoregions came from the temperature dependences of the optic refraction index (n) which appear to be linear

Copyright © 2010. Nova Science Publishers, Incorporated. All rights reserved.

Handbook of Material Science Research, Nova Science Publishers, Incorporated, 2010. ProQuest Ebook Central,

at $T > T_B$, as shown in Figure 1.5 [46]. At lower temperatures, a deviation from linearity was observed which was attributed to the variation of n induced (via quadratic electrooptic effect) by local spontaneous polarization inside the polar nanoregions.

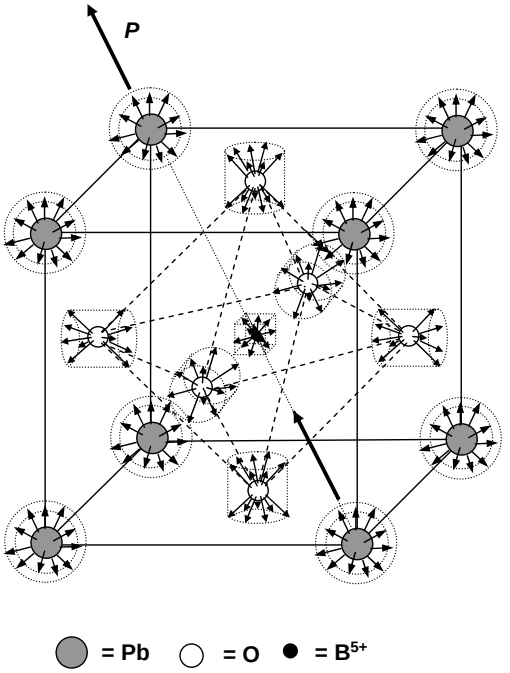


Figure 1.4. Typical uncorrelated ion displacements (shown by arrows) in the unit cells of the lead-containing complex perovskite relaxor. Thick arrows show the direction of the local spontaneous polarisation P caused by the correlated displacements of ions inside polar nanoregions.

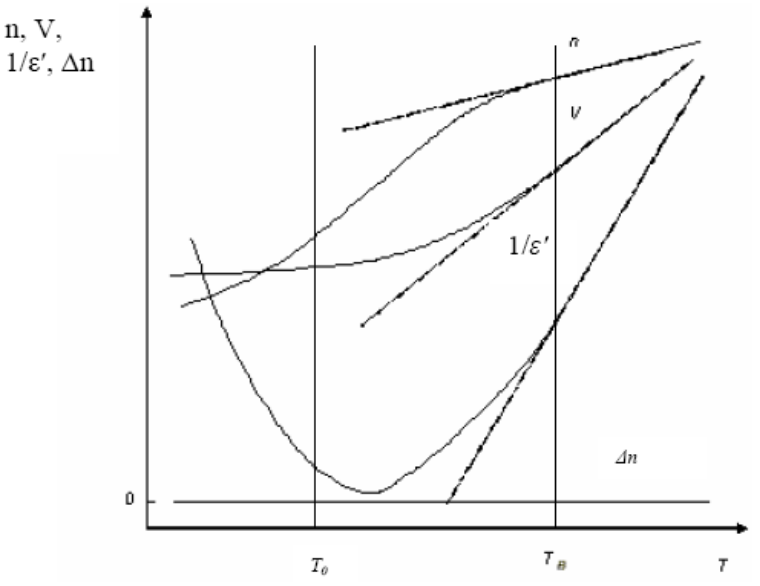


Figure 1.5. Typical temperature dependences of the refractive index, n, unit cell volume, V, reciprocal dielectric permittivity, $1/\varepsilon'$ and birefringence, Δn, in the canonical relaxor.

Copyright © 2010. Nova Science Publishers, Incorporated. All rights reserved.

Handbook of Material Science Research, Nova Science Publishers, Incorporated, 2010. ProQuest Ebook Central,

The existence of polar nanoregions was later confirmed by elastic diffuse neutron and X-ray scattering around the reciprocal lattice points [47, 48, 49, 50]. In the PMN crystals, significant diffuse scattering appears at $T < T_B$ with the intensity increasing with decreasing temperature. This effect resembles the scattering caused by ferroelectric critical fluctuations, but an important difference (found in synchrotron X-ray experiments [50]) is that the shape of wavevector dependence of scattering intensity at large distances from the reciprocal lattice point deviates from the Lorentzian. This means [50] that the polar nanoregions are more compact than the usual ferroelectric critical fluctuations and have better defined borders. The correlation length (ξ_C) of the atomic displacements contributing to the diffuse scattering, which is a measure of the size of polar nanoregions, can be derived from the experiment: it is inversely proportional to the width of the diffuse (Lorentzian) peak. According to the recent high-resolution neutron elastic diffuse scattering study of PMN [51], the size of the emerging polar nanoregions is very small (ξ_C is around 1.5 nm) and practically temperature independent at high temperatures. The perovskite unit cell parameter being ~ 0.4 nm, each polar nanoregions is practically composed of only a few unit cells. Below about 300 K, ξ_C begins to grow on cooling, reaching ~ 7 nm at 10 K. The most significant growth is found around T_0. Qualitatively the same behaviour was observed in the bulk of PZN crystals but the size of polar nanoregions is larger: they grow from ~7 nm at high temperatures to ~18 nm at 300 K [52, 53]. From the analysis of the relation between ξ_C and the integrated intensity of scattering, it was concluded [51] that the number of polar nanoregions also increases on cooling, but in contrast to the temperature evolution of ξ_C, the increase begins right from T_B and at $T \approx T_0$ a sharp decrease of this number occurs (presumably due to the merging of smaller polar nanoregions into larger ones). Below T_0 the number of polar nanoregions remains practically the same at any temperature.

Emergence of polar nanoregions below T_B was also observed in the PMN crystal by means of transmission electron microscopy (TEM) [26], but their size was an order of magnitude larger than that determined from the neutron diffuse scattering, probably because of the influence of electron beam irradiation.

The directions of ionic displacements responsible for the spontaneous dipole moment of polar nanoregions were investigated in several works. By means of dynamic structural analysis of diffuse neutron scattering in PMN crystals it was found that the B-site cations (Nb and Mg) and the O anions are displaced with respect to the Pb cations in the opposite directions along the body diagonal (i.e. the [111] direction) of the perovskite unit cell, forming a rhombohedral polar structure [54]. The rhombohedral *R*3*m* symmetry was also derived from the analysis of ion-pair displacement correlations obtained by an X-ray diffuse scattering technique [55], but according to this study, O displacements deviate from the body diagonal and remain parallel to the <110> direction. The shape of polar nanoregions was found to be ellipsoidal [55]. The same shape was revealed by TEM [13].

Besides the structural features, many properties of relaxors can be adequately explained on the basis of the idea of polar nanoregions. For example, in contrast to ordinary ferroelectrics, where a sharp anomaly of specific heat is known to appear at a phase transition, in relaxors such anomaly is smeared over a wide temperature range and thus is hardly distinguishable from the background of the lattice contribution. The excess specific heat (total minus lattice contribution) has been determined in PMN and PMT crystals using precise adiabatic and thermal relaxation techniques [56]. It appears as a diffuse symmetric maximum

Copyright © 2010. Nova Science Publishers, Incorporated. All rights reserved.

Handbook of Material Science Research, Nova Science Publishers, Incorporated, 2010. ProQuest Ebook Central,

located within the same temperature interval where polar nanoregions nucleate and grow (between 150 and 500 K in PMN). Therefore the anomaly is likely to be caused by the formation of polar nanoregions and/or by dipolar interactions among them.

Brillouin spectra of PMN-PT at $T >> T_C$ revealed significant relaxation mode (central peak), which was, attributed to the thermally activated fast (10 - 100 GHz) relaxation of polar nanoregions [57]. The intensity and the width of the peak increase with decreasing temperature indicating an increase of the number of polar nanoregions and a slowing-down of their dynamics, respectively. The hypersonic damping was also observed. It increases upon cooling, and is attributed to the scattering of acoustic mode by polar nanoregions [57]. Polar nanoregions can be thought as unusually large dipoles which direction and/or magnitude are dependent on an external electric field. Therefore the related properties are expected to be unusual. Indeed, at those temperatures where polar nanoregions exist, relaxors are characterized by giant electrostriction [58, 59, 60], remarkable electrooptic effect [59] and extremely large dielectric permittivity.

Even though no unambiguous structural confirmations for the phase transition at T_B are known, the anomalies of properties at this temperature were reported. In the course of thermal cycling of PMN and PMN-PT crystals annealed after growth, a narrow maximum of the acoustic emission activity is observed (and decreases with the increase of number of cycles) in the vicinity of T_B [61]. Not only the temperature dependence of the refraction index deviates from linearity at $T < T_B$ (as discussed above in this section), but the temperature dependences of the reciprocal dielectric permittivity, lattice parameter [60] (see Figure 1.6) and (consequently) thermal strain [61] also do the same.

Little is known about the relation between the chemical nanoregions and the polar nanoregions in relaxors, although such relation can *a priori* be expected. Based on the TEM data, it was concluded that polar nanoregions in PMN may contain chemical nanoregions inside and in this case the regions in which polar nano regions and chemical nanoregions overlap remain non-polar [26]. In the framework of the theoretical models discussed further, the chemical nanoregions can be considered as one of the factors influencing the formation and behaviour of polar nanoregions, but not necessarily the determining factor.

Copyright © 2010. Nova Science Publishers, Incorporated. All rights reserved.

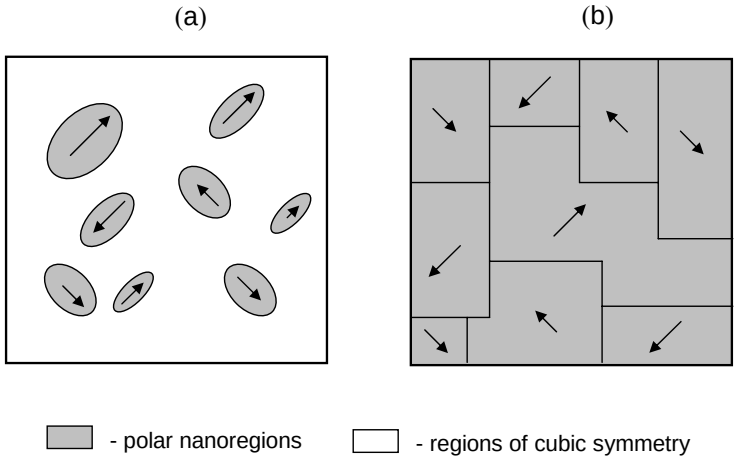


Figure 1.6. Schematic representation of polar nanoregions in relaxors according to the different models.

Handbook of Material Science Research, Nova Science Publishers, Incorporated, 2010. ProQuest Ebook Central,

Although the very existence of polar nanoregions in relaxors seems to be doubtless, the cause and mechanisms of their formation are not conclusively understood. At temperatures higher than T_B, the structure and properties of relaxors closely resemble those of normal displacive ferroelectrics. When a relaxor becomes compositionally ordered after the high-temperature annealing (without changing the chemical composition), a sharp ferro- or antiferroelectric phase transition is observed. These facts seemingly suggest that the relaxor crystal tends to be ferro- or antiferroelectric at low temperatures, but the quenched compositional disorder somehow prevents the normal transition into the phase with macroscopic ferroelectric or antiferroelectric order from happening. Instead, the polar nanoregions appear. There exist different approaches to explain the formation of polar nanoregions. All of them can be schematically subdivided into two categories. The models of the first category [62-65] consider the polar nanoregions as a result of local "phase transitions" or phase fluctuations so that the crystal consists of nanosize polar islands embedded into a cubic matrix in which the symmetry remains unchanged (as shown in Figure 1.6a). The models of the second category assume the transition to occur in all regions of the crystal and the crystal consists of low-symmetry nanodomains separated by the domain walls but not by the regions of cubic symmetry [66, 67] (the example is shown in Figure 1.6b). Note that these two situations can hardly be distinguished experimentally by structural examinations [68] because the local symmetry of cubic matrix is not expected to be cubic and the thickness of domain walls (i.e. the regions where polarization is not well-defined) is comparable with the size of nanodomains.

The second category is represented by the random-field model proposed by Westphal, Kleemann and Glinchuk (WKG model) [66, 69], who applied the results of a theoretical work by Imry and Ma [70] to the relaxors. It was shown in Ref. 70 that in the systems with a continuous symmetry of order parameter, a second-order phase transition should be destroyed by quenched random local fields conjugate to the order parameter. Below the Curie temperature the system becomes broken into small-size domains (analogy of polar nanoregions) instead of forming a long-range ordered state. It should be emphasized that this model does not consider the trivial case of the local spontaneous polarization , which is, directed parallel to the quenched field when the field is strong enough. Instead the situation is determined by the interplay of the surface energy of domain walls and the bulk energy of domains in the presence of arbitrary weak random fields [70].

For displacive transitions, continuous symmetry means that the spontaneous deformation is incommensurate with the paraelectric lattice. However, this is not the case for the perovskite ferroelectrics in which the spontaneous deformation and the polarization (order parameter) are aligned along definite crystallographic directions (e.g. the <111> directions for the rhombohedral phase). Nevertheless, when the number of allowed directions is large (e.g. eight for the rhombohedral phase), the symmetry of order parameter can be considered quasi-continuous and the approach appears to be applicable. The disordered distribution of the heterovalent ions inherent to compositionally disordered structure (e.g. Nb^{5+} and Mg^{2+} ions in PMN) provides the source for quenched random electric fields.

Ishchuk [67] analysed the thermodynamic potential in the framework of Landau phenomenological theory for the systems in which the energies of the ferroelectric and antiferroelectric phases are close to each other. It was shown that the state with coexisting ferroelectric and antiferroelectric domains might have lower thermodynamic potential than the homogeneous (ferroelectric or antiferroelectric) state. This effect is due to the interactions

Copyright © 2010. Nova Science Publishers, Incorporated. All rights reserved.

Handbook of Material Science Research, Nova Science Publishers, Incorporated, 2010. ProQuest Ebook Central,

(electrostatic and elastic) between the ferroelectric and antiferroelectric domains. It was suggested that relaxors are just the crystals in which this effect occurs. In other words, the nonpolar regions, coexisting with polar nanoregions (ferroelectric domains), are the domains of antiferroelectric structure.

The best-known model of the first category was developed in the early works by Isupov and Smolenskii [63, 71]. Due to the compositional disorder the concentrations of different ions (e.g. Mg^{2+} and Nb^{5+} in PMN) are subject to quenched spatial fluctuations. As the ferroelectric phase transition temperature (T_C) depends on the concentration, spatial fluctuations of local T_C are expected. It was suggested that upon cooling, local ferroelectric phase transitions occur first in those regions where T_C is higher, whereas the other parts of the crystal remain in the paraelectric phase. Therefore, polar nanoregions are simply the regions with elevated Curie temperature.

Several other models use the microscopic approach and consider the structural evolution and formation of polar nanoregions in terms of interatomic interactions. The ferroelectric lattice distortion in the ordinary perovskites is known to be determined by a delicate balance between the electrostatic (dipole-dipole) interactions and the short-range repulsions. Hybridization between the oxygen 2*p* states and electronic states of cations (covalent bonding) is able to change this balance, influencing thereby the phase transition temperature [34]. In the compositionally ordered (translationally symmetric) crystals, exactly the same forces affect all the atoms of a certain type because they have the same coordination neighbourhood. In the case of compositional disorder, the ions of different types may be found in the neighbouring unit cells on the same crystallographic positions (e.g. in the B-sublattice of PMN, both Mg and Nb ions are the nearest neighbours of Nb ions). The interatomic interactions which would cause ferro- or antiferroelectric order in the compositionally ordered state become random in this case, and as a result, the long-range polar order is disturbed. The models described below emphasize the importance of different interactions: the interactions under random local electric fields only (including dipole-dipole interactions) [62], the dipole-dipole interactions together with random short-range repulsions [72] or random covalent bonding [42].

In the random field theory developed for relaxors by Glinchuk and Farhi (GF model) [62] the transition is regarded as an order-disorder one, i.e. at high temperature the crystal is represented by a system of reorientable dipoles (dipoles caused by the shifts of ferroactive ions from their ideal perovskite positions). These random-site dipoles are embedded in highly polarizable "host lattice" (the high polarizability is due to the transverse optic soft mode existing in relaxors). The dipole-dipole interactions are indirect (they occur via the host lattice) and random. Nevertheless, according to the theory, they should lead to uniformly directed local fields and thus to ferroelectric ordering at low temperature (in contrast to direct dipole-dipole interactions which can lead to a dipole glass state). Thus to explain the absence of macroscopic ferroelectric order in relaxors, additional sources of random local electric fields are considered. These additional fields can be static (coming from quenched compositional disorder, lattice vacancies, impurities and other imperfections) or dynamic (associated with shifts of non-ferroactive ions from the special positions). In contrast to the fields considered in the WKG model, these fields should be rather large (larger than critical value) to destroy the long-range ferroelectric order. The ferroelectric order parameter, phase transition temperature T_C, linear and nonlinear dielectric susceptibilities are calculated within the framework of statistical theory using the distribution function for local fields. It is found

Copyright © 2010. Nova Science Publishers, Incorporated. All rights reserved.

Handbook of Material Science Research, Nova Science Publishers, Incorporated, 2010. ProQuest Ebook Central,

that depending on the model parameters (concentration of dipoles, other field sources and the host lattice correlation length), the low-temperature phase can be ferroelectric, dipole glass or mixed ferroglass. In the temperature interval between T_C and T_B, the short-range clusters may appear, in which the reorientable dipoles are ferroelectrically correlated (i.e. polar nanoregions). In the ferroglass state these clusters coexist with the macroscopic regions in which the dipoles are coherently ordered.

The GF model for relaxors is the extension of the analogous theory for incipient ferroelectrics with off-centre impurities (e.g. $KTaO_3$:Li, Nb, or Na). In the later case the off-centre impurities are the interacting dipoles. Due to their small concentration the crystal can be considered as the system of identical dipoles with the random long-range interactions. In the case of complex perovskite relaxors, the dipole concentration cannot be considered small. The random interactions of different (short-range) nature are also involved and thus the dipoles are not identical. It was first recognized in the model [63, 72]. In this model, the polar nanoregions are the result of local condensation of the soft phonon mode. The consideration is based on the model of coupled anharmonic oscillators which is often applied to ordinary ferroelectrics. The effective Hamiltonian is given by the sum of Hamiltonians of the individual unit cells:

$$H = \sum_l \left[0.5\Pi_l^2 + A_l\xi_l^2 + B_l\xi_l^4 - \sum_{l'} \upsilon_{ll'}\xi_l < \xi_{l'} > \right], \tag{1.35}$$

where Π_l and ξ_l are the generalized momentum and coordinate of the soft mode displacements, A_l and B_l are parameters of one-particle potential, which are determined by the interactions (mainly short-range repulsive) between ions of the l-th unit cell, and $\upsilon_{ll'}$ are parameters characterizing the interactions (long-range dipole-dipole) between different cells. In the translationally invariant crystal, all the parameters, A_l, B_l, and $\upsilon_{ll'}$, would be the same. In the case of compositional disorder they are different. The distribution function for these parameters is introduced in the model. This distribution gives rise to the spatial distribution of local "Curie temperature" T_C. Polar nanoregions appear in the regions with enhanced local T_C. The model parameters are linked to the parameters of real structure (in particular, the size of ions). Based on the crystal composition, this model is able to predict quantitatively the degree of "diffusion" of the transition, i.e. the extent of temperature interval in which the polar nanoregions develop before the crystal transform into the low-temperature nonergodic phase. In particular, the degree of diffusion increases with increasing difference in the radii of ions in the ferroactive sublattice (A or B perovskite sublattice) or with increasing compositional disorder in this sublattice. On the other hand, the diffusion is much less sensitive to the disorder in the non-ferroactive sublattice. The influence of the degree of compositional disorder on T_C is also explained. Based on the arguments similar to those used in the original model [63] it was recently suggested [73] that, because of the randomness of microscopic forces responsible for the onset of spontaneous polarization, each polar nanoregion can consist of unit cells polarized in different directions. This model of "soft nanoregions" also implies that, due to thermally activated reorientations of some unit cells inside polar nanoregion, not only the direction (as believed before), but also the magnitude of the spontaneous dipole moment of individual polar nanoregion can strongly change with time

Copyright © 2010. Nova Science Publishers, Incorporated. All rights reserved.

Handbook of Material Science Research, Nova Science Publishers, Incorporated, 2010. ProQuest Ebook Central,

(due to fluctuations or under the external field), while the size of polar nanoregion remains the same.

The Hamiltonian considered in the model by Egami [42] consists of two terms,

$$H = H_1 + H_2 \tag{1.36}$$

The first term is written in a standard form:

$$H_1 = -\sum_{ij} J_{ij} \vec{S}_i \cdot \vec{S}_j \,, \tag{1.37}$$

where $\vec{S}_i$ is the local polarization caused by the displacement of *i*-th Pb ion from its special position c of many Pb-containing relaxor, J_{ij} describes the random interaction between local polarizations mediated by oxygen and B-site ions. It is explained that in PMN the Pb ions cannot form the covalent bonds with those O ions which are bonded to Nb. On the other hand, Mg ions create purely ionic bonds and do not prevent the Pb-O bonding. Consequently the direction towards Mg is an "easy" direction for Pb displacement. This directional dependence of the energy of Pb displacements resembles the crystalline anisotropy in magnetic systems. It is random in compositionally disordered crystal and can be described by H_2 model Hamiltonian. This model was established to account for the relaxor properties in ergodic relaxor as wall as in nonergodic relaxor phases, but the appearance of polar nanoregions was not derived.

Timonin [64] suggested that the ergodic phase in relaxors is an antilog of Griffiths phase theoretically predicted long ago (but not yet experimentally found) for dilute ferromagnetics. Ferroelectric clusters of various sizes (i.e. polar nanoregions) appear in this model at $T < T_C$ (where T_C is the Curie temperature for non-dilute crystal) and specific non-exponential relaxation is predicted.

Specific temperature evolution of polar nanoregions can be explained in terms of the phenomenological kinetic theory of phase transitions in compositionally disordered crystals [65]. The emergence of polar nanoregions, i.e. the region of polar crystal symmetry within the cubic surrounding, should be accompanied by the creation of electric and elastic fields around polar nanoregions, which increase the total energy of the system. Due to the similar effects in the compositionally ordered crystals undergoing a first-order phase transition, the regions of the new phase (nuclei) are not stable. They tend to grow if their size is larger than the critical one or disappear otherwise. As follows from the theory [65], in disordered crystals the nuclei of the new phase can be stable and the equilibrium size of newly formed nuclei can be arbitrary small. The polar nanoregions in relaxors are really small (contain several unit cells) and stable can be regarded as such kind of nuclei. The theory predicts that polar nanoregions begin to appear in the paraelectric phase at T_B as a result of local "phase transitions" (e.g. condensation of phonon soft mode). Upon cooling, the number of polar nanoregions increases but the equilibrium size of each polar nanoregions remains unchanged within a certain temperature interval just below the temperature at which it appears. Upon further cooling, the polar nanoregions grows slowly with decreasing temperature while remaining in a stable equilibrium, and finally at $T = T_C$, becomes metastable so that the size of polar nanoregions increases steeply due to phase instability. In other words, the behaviour predicted by this

Copyright © 2010. Nova Science Publishers, Incorporated. All rights reserved.

Handbook of Material Science Research, Nova Science Publishers, Incorporated, 2010. ProQuest Ebook Central,

model is the same as experimentally observed in PMN. But this theory is unable to describe quantitatively the real behaviour at $T < T_C$, because it does not take into account the interactions between different polar nanoregions, which are obviously significant at low temperatures. It was further explained [63, 74] that depending on the model parameters (in particular, the mean T_C and the width of the distribution of local transition temperatures), a sharp phase transition can occur, resulting in large ferroelectric domains at $T < T_C$ (in the case of a small width and a comparatively high T_C) or the transition is diffuse and the low-temperature polar regions are of nanometer size. The dipole-dipole interactions between them can lead to the formation of a glass-type phase at a certain temperature T_0 . The intermediate situations are also possible with moderately diffused transition and mesoscopic polar regions (domains).

1.3.4. Glassy Nonergodic Relaxor Phase

Sharp peak of hypersonic dumping is observed at T_0 [75]. However, no other evidence of the structural phase transition at T_0 has been detected. The average cubic symmetry of PMN at low temperatures was confirmed in many structural studies by the absence of any splitting of X-ray and neutron Bragg reflections (which means that the shape of unit cell is cubic) as well as by the analysis of the intensities of the reflections (which are sensitive to the positions of atoms in the cell). For instance, in Refs. 37, 68, the unit cell was determined to be cubic by X-ray and neutron powder diffraction experiments performed down to 5 K, but due to the limited number of reflections analysed, the positions of atoms and the thermal parameters could not be refined simultaneously. In Refs. 76, 77 the analysis of a large number of reflections obtained from X-ray diffraction of PMN single crystals confirmed the $Pm\bar{3}m$ space group in the range of 100 – 300 K. The cubic structure is also confirmed by the absence of birefringence [78, 79].

Even though the structural phase transition in PMN is not definitely observed, some important structural changes not affecting the average symmetry are still found. With decreasing temperature, the average size of polar nanoregions increases significantly around T_0. The synchrotron X-ray scattering revealed the emergence of very weak and wide ½(hk0) superlattice reflections (α spots) in the vicinity of T_0 [80]. These reflections were attributed to the antiferroelectric nanoregions formed by the correlated anti-parallel (static or dynamic) displacements of Pb ions along the <110> directions with a magnitude of ~ 0.2 $\overset{o}{\text{A}}$. Significant enhancement of the intensity of α spots below T_0 is believed to arise from an increase in the total number of the antiferroelectric nanoregions, whose average size of ~ 30 $\overset{o}{\text{A}}$ (determined from the width of reflections) remains constant down to the lowest measured temperature of 10 K [80]. Antiferroelectric nanoregions appear to be different from polar nanoregions and chemical nanoregions, and unrelated to either of them [80].

Relaxors show nonergodic behaviour resembling the behaviour of spin (or dipole) glasses. In the high-temperature (ergodic) phase of glasses, the spins (or dipoles, which can be considered as pseudospins) are weakly correlated and free to rotate, so that after any excitation (e.g. after application and removal of an external field) the system quickly comes back to the state with the lowest free energy, i.e. the state with zero total magnetization. It is always the same state regardless of the initial conditions (i.e. the strength and direction of the field in our example). At lower temperatures, due to the correlations between spins, the free

Copyright © 2010. Nova Science Publishers, Incorporated. All rights reserved.

Handbook of Material Science Research, Nova Science Publishers, Incorporated, 2010. ProQuest Ebook Central,

energy surface has very many minima of almost the same depth separated by energy barriers of different heights (each minimum corresponds to a specific configuration of spins). In the glass phase, some of these barriers are so high that the time needed to overcome them is larger than any practically reasonable observation time. Therefore, during this time the system cannot reach all the configuration states, and consequently, the usual thermodynamic averaging and the time averaging give different results, i.e. the system is in a nonergodic state. On its way to a new state of minimum free energy required by the changed external conditions, the system should pass many barriers of different heights. This leads to a process with a wide distribution of relaxation times. The maximum relaxation time from this distribution may be so large (infinite for an infinite crystal) that the system cannot effectively reach the equilibrium. As a result, the state and the physical properties of the material depend on the history (i.e. the external field applied, the temperature variations, the observation time, etc.). In particular, substantial ageing effects should be observed, i.e. the change of properties with time spent by the sample at certain fixed external thermodynamic parameters (temperature, field, etc.).

All the main (mutually related) characteristics of nonergodic behaviour typical of spin glasses, i.e. anomalously wide relaxation spectrum, ageing, dependence of the thermodynamic state on the thermal and field history of a sample, are observed in relaxors at temperatures around and below T_0. Slow relaxation manifests itself also in other properties related to the local and/or macroscopic polarization. In particular, the relaxation of optical linear birefringence induced in PMN by a weak ($E < E_{cr}$) external electric field was studied [78] (E_{cr} is the critical field needed to induce the transition to the ferroelectric phase). The results were successfully described in terms of Chamberlin's approach to dynamic heterogeneity [81], implying a broad relaxation spectrum. Application of a strong ($E > E_{cr}$) d.c. field to the PMN crystal at $T < T_0$ results in a near logarithmic decay of dielectric permittivity [82] and a slow evolution of X-ray Bragg peaks reflecting the change of crystal symmetry [83]. The effects of ageing of susceptibility in the nonergodic relaxor phase of PMN and in the typical spin glass phase were found to be very similar (and much stronger than in typical dipole glasses) [84]. The other examples are the splitting in the temperature dependences of the field-cooled and zero-field-cooled quasistatic dielectric permittivity in PMN and PLZT [85, 86] and the $P(E)$ hysteresis loops.

The ergodicity is clearly broken in relaxors at low temperatures, but this does not necessarily mean that relaxors are really dipole glass systems. Many other systems may also be nonergodic [87]. In particular, an ordinary ferroelectric phase is also nonergodic, but its potential landscape contains only a few minima (which are symmetric and correspond to the different directions of spontaneous polarization). As a result, the properties are easily distinguishable from those of nonergodic spin glass (or relaxor) phase. Wide relaxation spectrum and ageing phenomena are absent in the ideal ferroelectric crystal. But in the compositionally disordered perovskite crystal the situation is very different and different explanations for the nonergodic behaviour are possible. For instance, the above-mentioned results of investigations of birefringence [81] were explained by domain wall displacements, rather than by the reorientations of dipoles [78]. Furthermore, some peculiarities of the relaxor behaviour have never been observed in spin and dipole glasses. In particular, the Barkhausen jumps during poling process (detected optically in PMN) are not compatible with the glassy reorientation of dipoles, which takes place on a microscopic length scale and hence should be continuous and monotonic [66]. Field-induced ferroelectric phase and ferroelectric

Copyright © 2010. Nova Science Publishers, Incorporated. All rights reserved.

Handbook of Material Science Research, Nova Science Publishers, Incorporated, 2010. ProQuest Ebook Central,

hysteresis loops have not been observed in typical dipole glasses. Thus, the nature of the nonergodic phase in relaxors remains the subject of intensive discussion. In particular, the WKG model suggests that the low-temperature phase of canonical relaxors is a ferroelectric state, but broken into nanodomains by quenched random fields. Note also that in terms of compositional disorder, relaxors are frozen in a metastable state. The degree of compositional disorder can depend on thermal prehistory. This is also an effect of nonergodicity. However, at temperatures around T_B and below, the compositional disorder remains unchanged on the experimental time scales (i.e. frozen), and at the same time, the motion of dipoles (at $T > T_0$) is fast. Thus, when considering the subsystem of dipoles at $T > T_0$, one can believe that the crystal reaches the equilibrium and the phase is effectively ergodic. On the other hand, if the sample has been annealed during experiment at high temperatures (~700 K or higher) the possible effects of nonergodicity related to the compositional disorder should be taken into account.

The important feature of the nonergodic relaxor state is that it can be irreversibly transformed to the phase with the ferroelectric dipole order when poling by an electric field larger than the critical strength (E_{cr} increases with decreasing temperature and in PMN the minimal E_{cr} is about 1.7 kV/cm [79]). This feature points to the common nature of relaxor and normal ferroelectrics. The ferroelectric hysteresis loops, which are known to be the determinative characteristic of ferroelectric phase, are observed in relaxors with the values of remnant polarization and coercive field typical of normal ferroelectrics. Pyro- and piezoelectric effects are also observed after poling. X-ray diffraction [83, 88] and optical [79] investigations of poled PMN crystals showed that the field-induced phase has the rhombohedral 3m symmetry, i.e. the same symmetry as in several normal perovskite ferroelectrics. On the other hand, locally the structure is inhomogeneous, i.e. different from normal ferroelectric structure. The traces of cubic phase were observed at low temperature by X-ray diffraction experiments in poled PMN crystal [83]. The NMR investigations of PMN crystal poled by a field almost two times as large as E_{cr}, revealed that only about 50% of Pb ions are displaced parallel to the [81] poling direction in a ferroelectric manner, while the other 50 % exhibit spherical layer-type displacements characteristic of paraelectric phase [41]. The size and number of antiferroelectric nanoregions found in PMN in the unpoled state remain unchanged in the ferroelectric phase [78].

1.3.4. Theoretical Description of Nonergodic Phase in Relaxors

Early works on relaxors (e.g. the composition fluctuations model by Smolenskii and Isupov [89, 90] and the superparaelectric model by Cross [91]) considered the polar nanoregions to be relatively independent noninteracting entities. It was later understood that the specific nonergodic behaviour of relaxors at low temperatures cannot be explained without taking into account the interactions among polar nanoregions and/or quenched random local fields existing in the compositionally disordered structure. The interactions among polar nanoregions may lead to anomalous slowing-down of their dynamics (nonergodicity effects) or, when becoming frustrated, even to the formation of the glass state in which the dipole moments of individual polar nanoregions are randomly fixed in different directions. Note that these interactions are of dipole-dipole nature and can be considered as dynamic local fields. Additionally polar nanoregions can be influenced (or probably even fixed) by quenched local random fields stemming from the compositional disorder or other types of lattice defects.

Copyright © 2010. Nova Science Publishers, Incorporated. All rights reserved.

Handbook of Material Science Research, Nova Science Publishers, Incorporated, 2010. ProQuest Ebook Central,

Some of these theories can explain the transition from the ergodic to nonergodic relaxor state. In particular, in the GF model, the polar nanoregions naturally appear in the temperature interval between the paraelectric and the low-temperature dipole glass or mixed ferroglass phase. In the WKG model, the formation of polar nanoregions as well as the transition to the nonergodic relaxor state is described to the quenched random fields exclusively.

However, the mechanisms leading to the formation of polar nanoregions at high temperatures are not necessarily responsible for their freezing and for the development of the low-temperature nonergodic state. The formation and freezing of polar nanoregions are possibly two distinct phenomena requiring different approaches. The "semi-microscopic" models [92-94] of glass state in relaxors describe only the latter phenomenon, while polar nanoregions are believed to be already-existing objects and the mechanisms of their formation are not examined.

In the spherical random-bond-random-field (SRBRF) model proposed by Pirc and Blinc [93, 94], the Hamiltonian is formally written with Eqs. (1.36) and (1.37), but the meanings of the parameters are different from those discussed above. Pseudospins $\vec{S}_i$ proportional to the dipole moments of polar nanoregions are introduced so that the relation

$$\sum_i (\vec{S}_i)^2 = 3N \tag{1.38}$$

is satisfied (N is the number of pseudospins in the crystal). It is assumed that each component of $\vec{S}_i$ can fluctuate continuously and take any value, i.e.

$$-\infty < S_{i\mu} < +\infty \,. \tag{1.39}$$

J_{ij} [in Eq. (1.37)] are the random interactions (bonds) between polar nanoregions which are assumed to be infinitely ranged. The second term in the Hamiltonian [in Eq. (1.36)] describes the interaction of pseudospins with quenched random electric fields $\vec{f}_i$

$$H_2 = -\sum_i \vec{f}_i \cdot \vec{S}_i \tag{1.40}$$

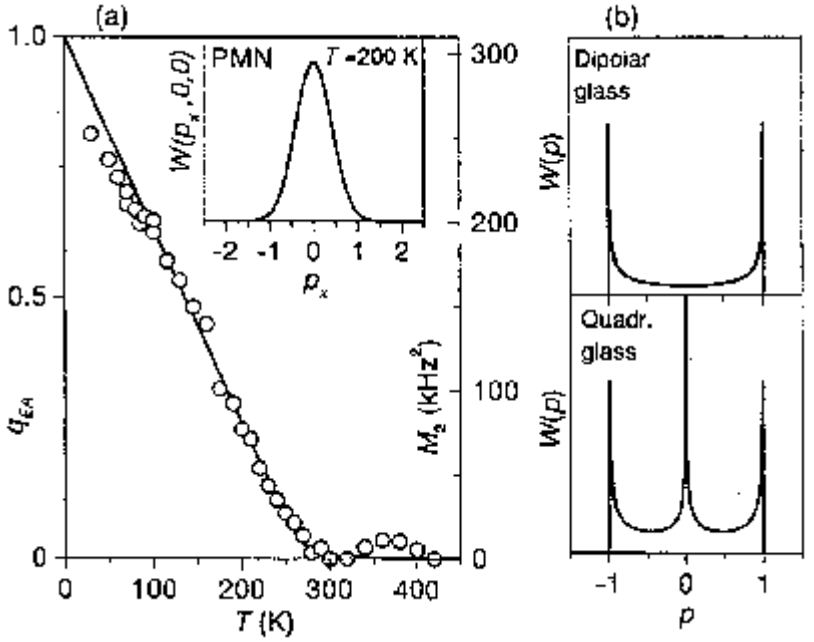
Both random bonds J_{ij} and random fields $\vec{f}_i$ obey the (uncorrelated) Gaussian probability distributions with a variance of ΔJ and Δf, respectively. The mean value of the distributions equals $\overline{J}$ (for random bonds) and zero (for random fields). In the absence of random fields ($\Delta f = 0$), if $\overline{J} > \Delta J$, the theory predicts the transition from the paraelectric phase (in the model this phase is equivalent to the ergodic relaxor phase) into an inhomogeneous ferroelectric phase with a nonzero spontaneous polarization; if $\overline{J} < \Delta J$, the system transforms, at a well-defined temperature $T = \Delta J/k_B$, from the paraelectric to a spherical glass phase without long range order, and the glass order parameter (which is equivalent in this model to the well-known Edwards-Anderson order parameter, q_{EA}) decreases linearly from 1 at $T = 0$ to zero at $T = \Delta J/k_B$. The presence of random fields ($\Delta f \neq 0$)

Copyright © 2010. Nova Science Publishers, Incorporated. All rights reserved.

Handbook of Material Science Research, Nova Science Publishers, Incorporated, 2010. ProQuest Ebook Central,

destroys the phase transition so that q_{EA} remains nonzero at $T = \Delta J/k_B$, and approaches zero when the temperature further increases. Figure 1.7 (a) shows the temperature dependence of q_{EA} determined experimentally from the NMR data of PMN (q_{EA} is shown to be proportional to the second moment, M_2, of the frequency distribution corresponding to the narrow ^{93}Nb NMR line) [94]. The solid line represents the fit with the parameters $\bar{J}/k_B$ = 20 K and $\Delta f/J^2$ = 0.002, confirming the applicability of the model.

The local polarization distribution function $W(\vec{p})$ (where $\vec{p} = <\vec{S}>$) predicted by the model and determined experimentally from the NMR line shape also appears to be the same as shown in the inset of Figure 1.7 (a) [94]. The $W(\vec{p})$ shape observed in dipolar and quadrupolar glasses look very different, as shown in Figure 1.7 (b). These results suggest that the nonergodic relaxor phase in PMN cannot be described as a dipolar or quadrupolar glass. It is a new type of glass which can be called "spherical cluster glass" [95]. The SRBRF model is also able to explain the dielectric non-linearity in PMN. The dynamic version of SRBRF model describing the dispersion of liner and non-linear dielectric susceptibility has been developed [96]. In the coupled SRBRF-phonon model [97], the coupling of polar nanoregions with soft TO phonons leads to the modification of interactions among polar nanoregions. The effect of pressure on the relative stability of different phases in relaxors is explained.



Reprinted figure with permission from [94]. Copyright 1999 by the American Physical Society.

Figure 1.7. (a) Temperature dependence of the Edwards-Anderson glass order parameter q_{EA} in PMN. The solid line is the fit to the "spherical random bond random field" (SRBRF) model. The inset shows the local polarization distribution function $W(\vec{p})$ along the p_x-axis according to the SRBRF model.

(b) Examples of the $W(p)$ functions for dipolar ($k_BT/\bar{J}$ =0.85, $\Delta f/(\Delta J)^2$=1) and quadrupolar ($k_BT/\bar{J}$ =0.5, $\Delta f/(\Delta J)^2$=0.1) glasses are shown for comparison.

Copyright © 2010. Nova Science Publishers, Incorporated. All rights reserved.

Handbook of Material Science Research, Nova Science Publishers, Incorporated, 2010. ProQuest Ebook Central,

Vugmeister and Rabitz [92, 98] considered in their model the hopping of polar nanoregions in multi-well potentials. The polar nanoregions exist in a highly polarizable paraelectric phase host lattice with a displacive dielectric response. The theory takes into account the broad distribution of the potential barriers controlling polar nanoregions dynamics and the effect of interactions between polar nanoregions mediated by highly polarizable host. These two aspects are described in terms of the local field distribution function. In this model, the dipole glass freezing is believed to be accompanied by the critical ferroelectric slowing-down. It is shown that the true glass state in which all dipoles (polar nanoregions) are frozen is not achieved in relaxors: the degree of the local freezing is rather small even at low temperatures. The role of the critical slowing-down is shown to be significant in the dynamics of the system due to the closeness of ferroelectric instability. In other words, relaxors can be considered incipient ferroelectrics. This explains their very large dielectric permittivity. In the framework of this model, the shape of the frequency-dependent permittivity as a function of temperature in typical relaxors is explained qualitatively. The glasslike freezing of the dynamics of polar nanoregions is characterized by the non-equilibrium spin-glass order parameter, the temperature behaviour of which is consistent with the NMR experiments (shown in Figure 1.7). The kinetics of the electric field induced transition from the nonergodic relaxor to ferroelectric phase was also successfully reproduced [99] (while the glass models experience difficulties in explaining this transition).

As mentioned above, the models so far discussed here consider polar nanoregions (pseudospins) to be already-existing entities. In order to describe the process of their formation and development (which begins from $T_B >> T_0$), other models are needed. Recently, it has been proposed that quenched random fields give rise to the formation of polar nanoregions in the paraelectric phase, as prescribed by the WKG model, and then, upon further cooling, the crystal undergoes a transition into the spherical cluster glass state due to random interactions between polar nanoregions [94]. Alternatively, some other models can be used to describe the formation of SRBRF pseudospins, in particular, the soft nanoregions model [81] [which justifies the fulfilment of condition (24)] together with the kinetic model [67].

Despite the remarkable progress achieved in the recent years, fundamental physics of the relaxors remains a fascinating puzzle. Some key questions, such as what the origin of relaxor behaviour is, still have no definite answers. Several theoretical models have been proposed; some of them contradict each other. Further experiments have to be performed in order to prove or reject these models, while new and more satisfactory theories are yet to be worked out. With their complex structures and intriguing properties, relaxors represent truly a frontier of research in ferroelectrics and related materials, offering great opportunities both for fundamental research and for technological applications.

1.4. Dielectric Dispersion in Disordered Materials

As already was mentioned, in pure ferroelectrics the relaxation dielectric dispersion often is of Debye-like (1.17). However, in disordered solids, such as dipolar glasses, relaxors and more others, as rule dielectric dispersion is much broader than 1.14 decades as should be from the Debye formula [100]. The plausible assumption is that relaxation dielectric dispersion

Copyright © 2010. Nova Science Publishers, Incorporated. All rights reserved.

Handbook of Material Science Research, Nova Science Publishers, Incorporated, 2010. ProQuest Ebook Central,

$\varepsilon^*(\omega) = \varepsilon' - i\varepsilon''$ in disordered materials can be represented as a superposition of the independent individual Debye-like processes:

$$\varepsilon'(\nu) = \varepsilon_{\infty r} + \Delta\varepsilon \int_{-\infty}^{\infty} \frac{f(\tau) d \lg \tau}{1 + (\omega\tau)^2}, \tag{1.41}$$

$$\varepsilon''(\nu) = \Delta\varepsilon \int_{-\infty}^{\infty} \omega\tau \frac{f(\tau) d \lg \tau}{1 + (\omega\tau)^2}. \tag{1.42}$$

These two expressions actually are the Fredholm integral equations of the first kind for the relaxation time distribution f(τ) definition. Such integral equations are known to be an ill-posed problem. Such normalization condition for f(τ) must fulfilled:

$$\int_{-\infty}^{\infty} f(\tau) d \lg(\tau) = 1. \tag{1.43}$$

From the distribution function the decay function $\Phi(t)$ can be calculated:

$$\Phi(t) = \int_{-\infty}^{\infty} f(\ln(\tau)) e^{-\frac{t}{\tau}} d \ln(\tau). \tag{1.44}$$

1.4.1. Various Predefined Dielectric Relaxation Functions

Simplistic solutions way of Eqs. (1.41) and (1.42) is the guess such the f(τ) function that integrals in formulas (1.41) and (1.42) can be integrated exactly. A most popular predefined distribution of relaxation times is the Cole-Cole distribution [101]:

$$f(\tau) = \frac{\sin(\alpha_{CC}\pi)}{\cosh\left[(1-\alpha_{CC})\ln(2\pi\tau_{CC}/\tau)\right] - \cos(\alpha_{CC}\pi)}, \tag{1.45}$$

there $0 \le \alpha_{CC} \le 1$ are the parameters of width of Cole-Cole distributions functions, τ_{CC} is the mean and most probable Cole-Cole relaxation time. From Eqs. (1.41), (1.42) and (1.45) easily can be obtained:

$$\varepsilon^* = \varepsilon_{\infty r} + \frac{\Delta\varepsilon}{1 + (i\omega\tau_{CC})^{1-\alpha_{CC}}}. \tag{1.46}$$

This formula is used very often; extremely often for various preliminary (and therefore often narrowband) dielectric studies of new materials. However, for the prototypical relaxors PMN and SBN and for the prototypical dipolar glasses DRADP Cole-Cole it is not valid, here some authors use two or more Cole-Cole functions. Another example of an empirical symmetric function for $\varepsilon''(\omega)$ is the Fuoss-Kirkwood equation [102] which is generalized form of Debye response and formulated directly for imaginary part of $\varepsilon^*(\omega)$:

Copyright © 2010. Nova Science Publishers, Incorporated. All rights reserved.

Handbook of Material Science Research, Nova Science Publishers, Incorporated, 2010. ProQuest Ebook Central,

$$\varepsilon^{"}(\omega) = \varepsilon"_{p}(\sec h(m\ln(\omega\tau)) = \frac{2\varepsilon"_{p}(\omega\tau)^{m}}{1+(\omega\tau)^{2m}}, \tag{1.47}$$

where ε''_p is the value of $\varepsilon''(\omega)$ at the peak frequency ω_p. In this case, $\varepsilon''_p = m*\Delta\varepsilon/2$ and $\omega_p = 1/\tau$. Equation implies (1.47) power laws with exponent $-m$ at high frequencies and m at low frequencies. In this case, the distribution function is:

$$f(\tau) = \frac{m}{\pi}\frac{\cosh(\frac{m\pi}{2})\cosh(mo)}{\cos^2(\frac{m\pi}{2}) + \sinh^2(mo)}, \quad o=\log(\tau_p/\tau). \tag{1.48}$$

For dielectric dispersion in relaxors is enough popular so called (also symmetric) "box" or "step" distribution function [103]:

$$f(\tau) = \frac{\Delta\varepsilon}{\ln(\frac{\tau_1}{\tau_2})} \quad \text{for } \tau_2<\tau<\tau_1$$

and

$$f(\tau)=0 \text{ for } \tau>\tau_1 \text{ or } \tau<\tau_2. \tag{1.49}$$

The integrals in Eqs. (1.41) and (1.42) with a uniform distribution function can be transformed into the following expression:

$$\varepsilon^{*}(\omega) = \varepsilon_{\infty r} + \frac{\Delta\varepsilon}{\ln(\tau_1/\tau_2)}[\frac{1}{2}\ln(\frac{(\tau_1/\tau_2)^2 + (\tau_1\omega)^2}{1+(\tau_1\omega)^2}) - i\arctan(\frac{\omega\tau_1(\tau_1/\tau_2 - 1)}{(\omega\tau_1)^2 + \tau_1/\tau_2})]. \tag{1.50}$$

This relationship predicate extremely fast (in comparison with otherwise predefined functions) alternation of ε'' around the frequencies $1/\tau_1$ and $1/\tau_2$, however such a behaviour of imaginary part of dielectric permittivity until now is not observed in any materials, therefore discrepancy of fit around mentioned frequencies is significant and essential [103]. Consequently such uniform distribution function is extremely rough approach of natural distributions of relaxation times. When possible to use such rough approach? In the range of frequencies that satisfy condition $\frac{1}{\tau_1} << \nu << \frac{1}{\tau_2}$ the exact solution of Eq. (1.50) gives very simple and easily applicable in practice predictions for both real and imaginary parts of the dielectric function:

Copyright © 2010. Nova Science Publishers, Incorporated. All rights reserved.

Handbook of Material Science Research, Nova Science Publishers, Incorporated, 2010. ProQuest Ebook Central,

$$\varepsilon'(\omega) = \varepsilon_{\infty r} - \frac{\Delta\varepsilon}{\ln(\tau_1/\tau_2)}\ln(\omega\tau_2),$$

$$\varepsilon''(\omega) = \frac{\pi}{2}\frac{\Delta\varepsilon}{\ln(\tau_1/\tau_2)} \tag{1.51}$$

These formulas are usable for various narrowband measurements [104] and for broadband measurements of anomalous broad dielectric dispersion [103, 105). In the first case, such analysis is clearly shoddy, in another case - speculative. Indeed parameters in formulas (1.51) $\varepsilon_{\infty r}$, τ_2 can easily be obtained from enough high-frequency data, however two parameters $\Delta\varepsilon$ and τ_1 remain unknown. Authors of [105] were assumed that $\Delta\varepsilon$ alternate according to the Curi-Weiss law (1.7) and were obtained unusual big values of times $\tau_1 \approx 10^{64}$ s at low temperatures. Clearly to examine this fact total lifetime is too short. Another misapprehension is that Eq. (1.51) is useful around and below T_0 [103]. It is clearly visible from Eq. (1.51) that at T_0 $\varepsilon''(\omega)$ should be equal to zero, and consequently such analysis here become brute.

The simplest case of the asymmetric distribution function is the Cole-Davidson distribution function [106]:

$$f(\tau) = \frac{\sin(\gamma\pi)}{\pi}\left(\frac{\tau}{\tau_{CD}-\tau}\right)^{\gamma} \text{ for } \tau<\tau_{CD}, \tag{1.52}$$

and

$f(\tau)=0$ for $\tau>\tau_{CD,}$

where τ_{CD} is the most probable relaxation time of the Cole-Davidson distribution function and $0 < \gamma \leq 1$ parameter of asymmetry of this functions. From Eqs. (1.41), (1.42) and (1.52) we have [106]:

$$\varepsilon^* = \varepsilon_{\infty r} + \frac{\Delta\varepsilon}{(1+i\omega\tau)^{\gamma}}. \tag{1.53}$$

This function describes well dielectric properties of polar liquids, for example, dielectric properties of water mixture of ethanol [107].

More general descriptions of the broad and asymmetric dielectric dispersion is the combination of the Cole-Cole and the Cole-Davidson– Havriliak-Negami function [108]:

$$\varepsilon^* = \varepsilon_{\infty r} + \frac{\Delta\varepsilon}{(1+(i\omega\tau\quad)^{1-\alpha_{CC}})^{\gamma}}. \tag{1.54}$$

Copyright © 2010. Nova Science Publishers, Incorporated. All rights reserved.

Handbook of Material Science Research, Nova Science Publishers, Incorporated, 2010. ProQuest Ebook Central,

Havriliak and Negami [109] derived the distribution function $f(\tau)$ by means of complex analysis:

$$f(\tau) = \frac{1}{\pi} \frac{(\frac{\tau}{\tau_{HN}})^{(1-\alpha_{CC})\gamma} \sin(\gamma\theta)}{((\frac{\tau}{\tau_{HN}})^{2(1-\alpha_{CC})} + 2(\frac{\tau}{\tau_{HN}})^{(1-\alpha_{CC})} \cos(\pi(1-\alpha_{CC})) + 1)^{\gamma/2}}, \quad (1.55)$$

with

$$\theta = \arctan(\frac{\sin(\pi(1-\alpha_{CC}))}{(\frac{\tau}{\tau_{HN}})^{1-\alpha_{CC}} + \cos(\pi(1-\alpha_{CC}))}). \quad (1.56)$$

Considerably beyond the author of [110] it was establish that in Eq. (1.56) must an additional term of π append if argument of arctan functions is negative. The Havrilak-Negami function describes enough correct dielectric response of widely class of disordered materials. S. Havriliak and S. J. Havriliak [111] have analyzed approximately 1000 sets of experimental data using unbiased statistical methods and the relaxation function commonly referred to as the Havriliak-Negami function. This function is widely used for investigations of dielectric response of relaxors [112] and dipolar glasses [113]. However, dielectric response of well-known dipolar glasses DRADP is not compatible with the Havriliak-Negami functions [114]. A very important problem is physical meaning of Havriliak-Negami functions and its parameters. The experimental data shows that α_{CC} and γ are strictly dependent on temperature, structure, composition and other controlled physical parameters. However, in many works the obtained parameters α_{CC} and γ commented very little (only how the form of dielectric dispersion is related with these parameters). When experimental data is of good quality (and only one relaxation process manifest) change of dielectric dispersion form is visual from dielectric spectra $\varepsilon^*(\omega)$. Only several attempt have been made to understand the physical meaning of Havriliak-Negami dielectric response functions [115-117].

In time-domain frequently used so-called "stretched exponential" or the Kolrausch-Williams-Watts (KWW) function [100]:

$$\Phi(t) = \exp[-(\frac{t}{\tau_{WW}})^{\beta}]. \quad (1.57)$$

Dielectric function then is:

$$\varepsilon^*(\omega) = \Delta\varepsilon \int_0^{\infty} [-\frac{d\Phi(t)}{dt}] e^{-i\omega t} dt, \quad (1.58)$$

and distribution of relaxation times is:

Copyright © 2010. Nova Science Publishers, Incorporated. All rights reserved.

Handbook of Material Science Research, Nova Science Publishers, Incorporated, 2010. ProQuest Ebook Central,

$$f(\tau) = \frac{1}{\pi}\int e^{-x} e^{4\cos(\pi\beta)} \sin(u\sin(\pi\beta))dx \text{, with } u = (\frac{x\tau}{\tau_0})^{\beta}. \quad (1.59)$$

Many physical models of KWW dielectric dispersions are proposed: localized state model, proton model, dipole interaction model and more others [118]. So that KWW function physical meaning is better understood than physical meaning of others predefined functions. Recently the empirical relationship between the KWW and Havriliak-Negami functions was discovered [119]:

$$\ln[\frac{\tau_{HN}}{\tau_{WW}}] = 2.6(1-\beta)^{0.5} e^{-3\beta},$$

$$\alpha_{CC}\gamma = \beta^{1.23}. \quad (1.60)$$

So that physical meaning of the Havriliak-Negami distributions sometimes can be related with physical meaning of the KWW models. There are many other predefined functions of distribution of relaxation times such as: Joncher [120], Rajagopal [121], Dissado-Hill [122], Curie-von Schweindler [123] and others.

We can conclude that various predefined dielectric functions dominate in dielectric spectroscopy, but physical meaning of these functions is not clear until now and discrepancy from fit often is significant and essential, so that such approach in many works is only blunt (and often bad) description of experimental data. Another calculating methods must be used in dielectric spectroscopy of disordered solids.

1.4.2. Distribution of Relaxation Times in Disordered Solids

Solving of integral equations (1.41) and (1.42) without any *a priori* assumption about distribution form is most adequate broadband dielectric spectroscopy calculating technique. Several methods can be used here. One way is the use of the inverse Fourier transform of Eqs. (1.41) and (1.42) as suggested by Franklin and de Bruin [124] and later improved by Liedermann and Loidl [125]. This method has the usual problems of discrete Fourier transforms: truncation, aliasing and computing rounding error effects, noisy data, and the need of the data points to be available at frequencies located at equidistant short intervals on a logarithmic scale. Another method is such Eqs. (1.41) and (1.42) can be inverted by discretizing the distribution function into a sum of N contributions or bins, each characterized by a pair (τ_k ,f_k). The dielectric loss can then be written as:

$$\varepsilon''(\omega) = \sum_{k=1}^{N} \frac{f_k \omega \tau_k}{1+\omega^2\tau_k^2}. \quad (1.61)$$

Colonomos and Gordon [126] used this concept along with the Simplex method of optimization for analyzing experimental dielectric data from isoamyl bromide. Imanishi et al. [127] with the histogram method, found the distribution of relaxation times by discretizing it and using an iterative method in order to minimize the differences between the observed and

Copyright © 2010. Nova Science Publishers, Incorporated. All rights reserved.

Handbook of Material Science Research, Nova Science Publishers, Incorporated, 2010. ProQuest Ebook Central,

calculated values of $\varepsilon''(f_i)$ where f_i are the measurement frequencies and choosing the discrete relaxation times as $\tau_i = 1/2\pi f_i$. However these methods are very sensitive to measurements accuracy. Global problem of these methods optimizations criterion i.e. minimization of such functional:

$$\delta\varepsilon'' = \sum_{i=1}^{N} [\varepsilon''_{obs}(\omega_i) - \varepsilon''_{cal}(\omega_i)]^2 . \tag{1.62}$$

It is very well known that for ill-posed problems such functional diverge. In order to eliminate such negative effect Bello et al. [127] adapted to dielectric spectroscopy simulated annealing direct signal analysis (SADSA) method. This method is enough powerful, however containing several defects. A most general method to solving ill-posed problems is Tichonov regularization [129]. Until present only several attempt have be made to apply this method to dielectric spectroscopy [130-132 and others].

Distribution function of relaxation time f (τ) and it temperature dependence provide very gripping information about collective phenomena in disordered dielectrics. When distribution function f (τ) is known and E (τ) is unambiguous continuous function, then distribution of random fields f (E) can be calculated according to well known mathematic relation [133]:

$$f(\tau) = F(E(\tau)\left|\frac{dE(\tau)}{d\tau}\right| \tag{1.63}$$

2. BROADBAND DIELECTRIC SPECTROSCOPY

2.1. Low Frequency Measurements

In the low frequency (20 Hz – 1 MHz) range, capacitance C_c and tangent of losses tgδ = ε″/ε′ of the sample was measured with the LCR meter HP4284. For all measurements the silver past was used for contacts. Complex dielectric permittivity was calculated from the plane capacitor formulas [134]:

$$\varepsilon' = \frac{(C'_{css} - C_{c0})d}{\varepsilon_0 S_s} + 1, \tag{2.1a}$$

$$tg\delta = \frac{C'_{css} tg\delta_{ss} - C_{c0} tg\delta_0}{C'_{css} - C_{c0}}, \tag{2.1b}$$

where C'_{css} and $tg\delta_{ss}$ are capacitance and tangent of losses of the systems with the sample, C_{c0} and $tg\delta_0$ are capacitance and tangent of losses of the systems without the sample, d is height of the sample, S_s is the area of the sample, ε_0 is the dielectric permittivity of vacuum. The area of the sample was much larger as quadrate of height d^2 so that the fringing field effects were in all performed experiments insignificant. The temperature was measured with

Copyright © 2010. Nova Science Publishers, Incorporated. All rights reserved.

Handbook of Material Science Research, Nova Science Publishers, Incorporated, 2010. ProQuest Ebook Central,

copper-constantan thermocouple, which one stub was at the sample and another put into ice and water mixture. Measurements were performed during continuous temperature variation with typical rate of 0.5 K/min for relaxors and dipolar glasses; for ferroelectrics typical rate was 0.05 K/min near a phase transition temperature and 0.5 K/min far from a phase transition temperature. All measurements were performed on cooling and heading but most of presented results are on cooling. For heading in all experiments was used home made furnace, for cooling in most experiments was used liquid nitrogen.

2.2. High Frequency Measurements

The coaxial technique is the most convenient for the dielectric spectroscopy of solids in the 1 MHz – 3 GHz frequency range. The specimen was placed at the end of the coaxial line between the inner conductor and the short piston and forms a capacitor. Such a configuration allows us to easily place the capacitor into temperature-control device. Coaxial lines are broadband lines. From the low-frequency end they can use at any frequency. From the superhigh-frequency end the condition of propagation of the main TEM-wave limits application of the coaxial lines. This condition is given by [134]:

$$\lambda_{00} > \pi(r_3 + r_4), \tag{2.2}$$

where r_3 and r_4 are the radii of the inner and outward conductors of the coaxial line, λ_{00} is the length of electromagnetic waves.

2.2.1. Experimental Details

Most of high frequency experiments were performed with a coaxial dielectric spectrometer [135]. The core of this coaxial spectrometer make complex reflection coefficient measurement unit P4-11. This unit contain: microwave sweeps oscillator (600 MHz –1.25 GHz), frequency converter (to frequency range 1 MHz – 650 MHz), amplitude and phase detectors. The complex reflection coefficient $R^*(\nu, T)$ is obtained by amplifying the incident and reflected signals by a frequency converter and detected by synchronous amplitude and phase detectors. Subsequently this core was improved: with a home made digital-analogical converter and frequency measurement unit Ч3-66 computer control of the oscillator sweeping frequency was realized. More details about this spectrometer are in [134]. In this work, also several data are presented with were measured with the more modern devices namely with Agilient 8714 ET (300 kHz – 3GHz) and Agilient 4291 B (1 MHz-1.8 GHz).

Inhomogeneities of the line and distortion in a high-frequency part of the spectrometer (influence of which increases with the increase of frequency) can be taken into account using a computer and digital processing of information by an analysis of the six-port between the capacitor and the output planes of the directional couples. The linear eight-port can be described by a scattering matrix $\|U_{ri}\|$ of the complex coefficients $U_{ri}=b_r/a_i$, relating a reflected signal b_r from the input signal a_i at input i. The indicator of the setup measures the reflection factor R_m (i. e., the ratio of outcoming signals from the measuring and referenced output $R_m=b_3/b_4$).

For an ideal reflectometer setup ($R_2=R_3=R_4=0$):

Copyright © 2010. Nova Science Publishers, Incorporated. All rights reserved.

Handbook of Material Science Research, Nova Science Publishers, Incorporated, 2010. ProQuest Ebook Central,

$$R_m = \frac{U_{12}U_{31}}{P_{42}} R = o_k R\,, \tag{2.3}$$

where the coefficient o_k can be found by calibrating the spectrometer using a shot with R= -1. In general, one should solve the set of linear equations:

$$\begin{Vmatrix} a_1 \\ a_2 \\ a_3 \\ a_4 \end{Vmatrix} \times \|U\| = \begin{Vmatrix} b_1 \\ b_2 \\ b_3 \\ b_4 \end{Vmatrix} \tag{2.4}$$

which respect to b_1, b_2, b_3, and b_4. Taking into account the fact that $a_1=R_1b_1$, $a_3=R_3b_3$ and $a_4=R_4b_4$, one find the relation between the measured reflection factor R_m and the reflection coefficient R:

$$R_m^* = \frac{o_{k1}R^* + o_{k2}}{o_{k3}R^* + 1}\,. \tag{2.5}$$

The coefficients o_{k1}, o_{k2} and o_{k3} are composed from products and sums of the elements of the scattering matrix U_{ri} and the reflection factors from the mixers R_3 and R_4. At every frequency they are determined by measuring the reflection R^i_m from the tree calibration samples (from short and open-circuit lines, and from a sample of known permittivity and small loss (TiO_2, $CaTiO_3$). Using Equation (2.5) for every sample, one obtains a set of three complex linear equations, from which one finds the coefficients k_1, k_2 and k_3. More details about calibration are presented in [7].

The dielectric spectra are obtained from the results of the measurements of the complex reflection coefficient $R^*(v, T)$ of the TEM-wave in the coaxial line loaded with the sample in the measuring capacitor. From the complex reflection coefficient $R^*(v, T)$ the complex dielectric permittivity $\varepsilon^*(v, T)$ was obtained according to the formulas presented in Subsection 2.2.2.

2.2.2. Complex Dielectric Permittivity Estimation

Complex reflection coefficient R^* is related with the impedance of measuring capacitor Z^*_{ss} and the systems impedance Z_0:

$$R^* = \frac{Z^*_{ss} - Z_0}{Z^*_{ss} + Z_0}\,. \tag{2.6}$$

For complex capacitance $C_c^* = C_c' - iC_c''$ of the planar capacitor the relation (2.1a) can be generalized in such a form:

Copyright © 2010. Nova Science Publishers, Incorporated. All rights reserved.

Handbook of Material Science Research, Nova Science Publishers, Incorporated, 2010. ProQuest Ebook Central,

$$\varepsilon' - i\varepsilon'' = \frac{d}{\varepsilon_0 S_s}(C_c' - iC_c'') + 1. \tag{2.7}$$

Between the complex impedance Z_{ss} and the complex capacitance C_c^* is a well known relation:

$$Z_{ss} = \frac{1}{\omega(C_{css}' + iC_{css}'')}. \tag{2.8}$$

From Eqs. (2.6), (2.7) and (2.8) we obtain the formulas for the real and imaginary parts of the complex dielectric permittivity ε^*:

$$\varepsilon' = \frac{d}{\varepsilon_0 S_s}\left(\frac{-2R\sin\varphi}{\omega Z_0(1+2R\cos\varphi+R^2)} - C_{c0}\right) + 1, \tag{2.9a}$$

$$\varepsilon'' = \frac{d}{\varepsilon_0 S_s}\frac{1-R^2}{\omega Z_0(1+2R\cos\varphi+R^2)}. \tag{2.9b}$$

Afore-cited equations are for a quasistatic capacitor in which capacitance is independent of frequency and the electric field is homogeneous in the sample, just as it is when the dimensions of the capacitors are much smaller in comparison to a wavelength λ_{00} of the exciting electric field. However, with the increase of frequency the electric field in the sample become non-homogeneous and is given by:

$$E = A_k J_0[2\pi/\lambda_{00}(\varepsilon_0\mu_0\varepsilon')^{1/2} r], \tag{2.10}$$

where A_k is the constant, depending on the dimensions of the capacitor, r is the distance from the center of a capacitor along the radius, J_0 is the Bessel function of the first kind of zero order, and μ_0 is the vacuum magnetic permittivity. Finding the zeros of the Bessel function, the radii r_1, r_2, r_3, …, where the field between electrodes of the capacitor is equal to zero, can be obtained. The radius r_1 is given by:

$$r_1 \approx \frac{2.405\lambda_{00}}{2\pi(\varepsilon_0\mu_0\varepsilon')^{1/2}}. \tag{2.11}$$

Taking the radius of the sample $r \le 0.1\ r_1$, one finds the conditions of the quasi-stationary electric field distribution in the capacitor:

$$r \le \frac{0.24\lambda_{00}}{2\pi(\varepsilon_0\mu_0\varepsilon')^{1/2}}. \tag{2.12}$$

Copyright © 2010. Nova Science Publishers, Incorporated. All rights reserved.

Handbook of Material Science Research, Nova Science Publishers, Incorporated, 2010. ProQuest Ebook Central,

In this case, a dynamic capacitor, which takes into account inhomogeneous distribution of the electric field in the sample, should be used. Consider now the propagation of electromagnetic waves in the capacitor, which is formed by the cylindrical sample, placed at the end of the coaxial line between the inner conductor and short piston. The harmonic field of frequency ω excites the line, and the main monochromatic TEM-wave propagates along the line without variation along the coordinates z and φ. The wave has only the components of the electromagnetic field E_z and H_φ. In the cylindrical system of coordinates, with the center at the axis of the line, the components E_z and H_φ are given by [7]:

$$E_z = -i(2\pi/\lambda_{00})^2 \mu_0 (\varepsilon'\mu_0)^{1/2} AJ_0[2\pi r/\lambda_{00}(\varepsilon'\mu_0)^{1/2}], \tag{2.13}$$

$$H_\varphi = -(2\pi/\lambda_{00})^2 \varepsilon'\mu_0 AJ_0'[2\pi r/\lambda_{00}(\varepsilon'\mu_0)^{1/2}], \tag{2.14}$$

where J'_0 is the derivate of the Bessel function J_0.

The impedance of the capacitor under study is given by:

$$Z = \frac{d}{2\pi r}\frac{E_z}{H_\varphi}. \tag{2.15}$$

Thus be comparison Eqs. (2.8), (2.13), (2.14), (2.15) we obtained the capacitance of dynamic capacitor [7]:

$$C_c = \frac{\varepsilon'^{1/2} rJ_1(\frac{2\pi}{\lambda_{00}}\varepsilon'^{1/2} r)}{(\frac{2\pi}{\lambda_{00}})dJ_0(\frac{2\pi}{\lambda_{00}}\varepsilon^{1/2} r)}. \tag{2.16}$$

when the quasi-stationary conditions (2.12) are fulfilled, the relationship (2.16) becomes equal to (2.1).

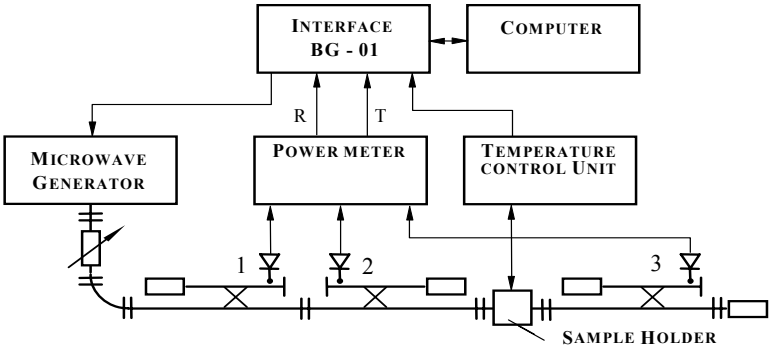


Figure 2.1. Dielectric spectrometer setup for reflection and transmission measurements in the centimetre and milimetre ranges.

Copyright © 2010. Nova Science Publishers, Incorporated. All rights reserved.

Handbook of Material Science Research, Nova Science Publishers, Incorporated, 2010. ProQuest Ebook Central,

2.3. Method of Thin Cylindrical Rod in Rectangular Waveguide

2.3.1. Microwave Reflectivity and Transmission Measurements

For dielectric measurements in the centimetre and millimetre microwave ranges method of thin cylindrical rod in rectangular waveguide was used [7]. Moduli of microwave reflection and transmission coeficients were measured with automatic dielectric spectrometer (Figure 2.1). Using generators (ГКЧ-61 for wave range 8 - 12 GHz, Р2-65 for range 26 - 37 GHz and Р2-68 for range 37 - 53 GHz) as variable frequency sources, and changing only the waveguide terminanting with a matched load, method under study was applied to measurements of moduli of microwave reflection and transmission coeficients in the frequncy range from 8 GHz to 53 GHz. Bandwith of the range is dependent as microwave oscilator bandwith and waveguide wall width. Power meter Я2Р-70 is used for reflection, transmission and supporting power measurements. Coupling between computer and measurements equipment realize the interface BG-01 of prof. A. Brilingas. In the interface unit there are digital analogical converters, which used to alternate of generators sweeping frequency. Generators sweeping frequency dependence of digital analogical converters signal level $\nu = f(N_{DAC})$ was measured with frequency cell and described as a third order polynomial (apart ГКЧ-61, where this function is linear). Frequency measurements errors were less then 0,2% in the centre of range and 1% in the edges of range.

Frequency dependencies of reflection R and transmission T_{tr} moduli were measured in all bandwidth of selected range at several hundred points, additionally for each point values was measured on several scan and averaged. Next curves $R=R(\nu)$ and $T_{tr}=T_{tr}(\nu)$ has been sleek, for selected frequencies results was saved in computer. Such processing of results allows to reduce an influence of the random errors and to improve accuracy and plausibility of the method.

The sample of cylindrical shape was placed in centre of the wide waveguide wall parallel to the electrical field of the main TE_{10} modes. A special sample holder was used. In this sample holder a slot for pistons was made. In the piston for sample was made notch, witch are used for contacts between sample and waveguide. Two others pistons were used for calibration of reflections and transmissions. This method allow to reject destruction of waveguide channel, and additionally, allow chance to verify a calibration during experiment.

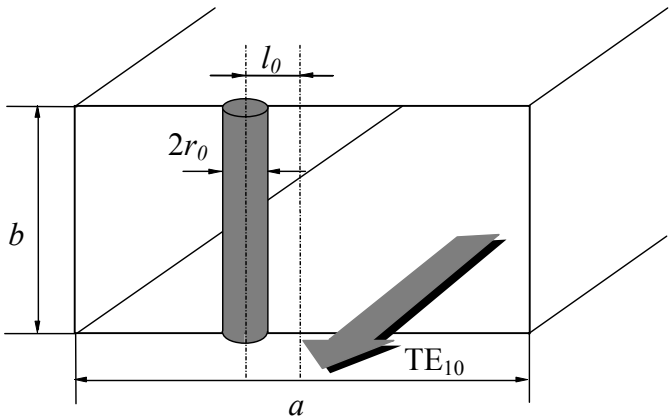


Figure 2.2. Thin cilindrical road in rectangular waveguide.

Copyright © 2010. Nova Science Publishers, Incorporated. All rights reserved.

Handbook of Material Science Research, Nova Science Publishers, Incorporated, 2010. ProQuest Ebook Central,

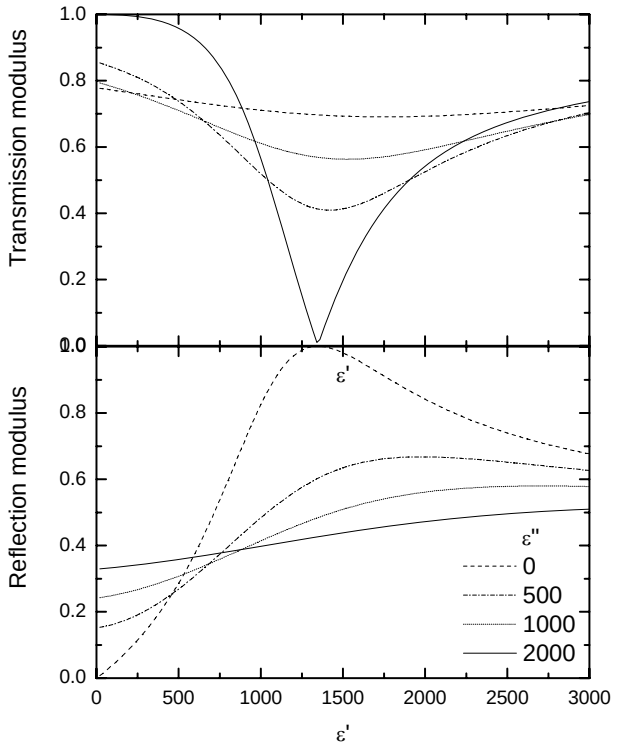


Figure 2.3. Microwave transmission and reflection coeficients moduli dependence from dielectric permittivity of sample, when ν = 10 GHz, radius of sample r = 100 □m.

2.3.3. Calculation of Complex Dielectric Permittivity

Microwave reflection R^* and transmission T^*_{tr} the complex coefficients are dependent from parameters of waveguide systems (width of the wall a), frequency of the microwave, complex dielectric permittivity ε^* and the radius r of a sample. Complex dielectric permittivity $\varepsilon^*(\nu)$ can be estimated from nonlinear equations $\varepsilon^* = f(R^*)$ or $\varepsilon^* = f(R, T_{tr})$.

Cylindrical form sample was placed in the centre of broader wall (or with distance l_0) parallel to the electrical field of main mode TE_{10} (Figure 2.2). When a sample is thin enough ($\alpha_0 = 2\pi r/\lambda_{00} \ll 1$), the complex reflection coefficient is [7]:

$$R^* = -\frac{4(\varepsilon^* - 1)J_1(\beta_0)}{\pi\Delta_1\sqrt{\left(\frac{2a}{\lambda_{00}}\right)^2 - 1}}, \tag{2.17}$$

$$\Delta_1 = \varepsilon^* J_1(\beta_0)\left[H_0^{(2)}(\alpha_0) + 2\sum_{m=1}^{\infty}(-1)^m H_0^{(2)}(2\pi ma/\lambda_{00})\right] - \sqrt{\varepsilon^*}J_0(\beta_0)H_1(\alpha_0),$$

Copyright © 2010. Nova Science Publishers, Incorporated. All rights reserved.

Handbook of Material Science Research, Nova Science Publishers, Incorporated, 2010. ProQuest Ebook Central,

where J_0, J_1 are the Bessel functions, H_1, $H_0^{(2)}$ are the Hankel fuctions, $\beta_0 = k_0(\varepsilon)^{,1/2}r$, a is the with of waveguide walls.

When a distance from the sample axis to centre of a waveguide wall is l_0, then another expression for complex reflectivity is used [7]:

$$R^* = -\frac{4\sqrt{\varepsilon^*}\cos^2\frac{\pi l_0}{a}}{\pi\sqrt{\left(\frac{2a}{\lambda_{00}}\right)^2 - 1}}\frac{J_1(\beta_0)}{\Delta_2}, \tag{2.18}$$

$$\Delta_2 = -\sqrt{\varepsilon^*}J_0'(\beta_0)\left[H_1^{(2)}(\alpha_0) + 2\sum_{m=1}^{\infty}H_0^{(2)}(2\pi ma/\lambda_{00})\right] - \sum_{m=0}^{\infty}H_0^{(2)}\left[(2m+1)a + 2l_0\right]2\pi/\lambda_{00} -$$

$$-\sum_{m=0}^{\infty}H_0^{(2)}\left[(2m+1)a - 2l_0\right]2\pi/\lambda_{00} - J_0(\beta_0)H_1^{(2)'}(\alpha_0).$$

For sample with enough big radius, when condition α_0 « 1 is not fulfil, more complicated expression for complex reflectivity modulus is used [7]:

$$R^* = -\frac{4(\varepsilon^*-1)}{\pi\sqrt{\left(\frac{2a}{\lambda_{00}}\right)^2 - 1}}\left[\frac{J_1(\beta_0)}{\Delta_1} + \frac{\alpha_0 J_2(\beta_0)}{\Delta_3}\right],$$

$$\Delta_3 = -\sqrt{\varepsilon^*}J_1(\beta_0)\left[H_1^{(2)}(\alpha_0) + \sum_{m=1}^{\infty}\lambda_{00}\frac{(-1)^m}{\pi ma}H_0^{(2)}(2\pi ma/\lambda_{00})\right] + \varepsilon^* J_1'(\beta_0)H_1(\alpha_0) \tag{2.19}$$

.

Better abruptness of curves $R = R(\varepsilon')$ and $T_{tr} = T_{tr}(\varepsilon')$ is for coeficients values $0{,}2 < R < 0{,}85$ (Figs. 2.3 and 2.4).

When dielectric permittivity is higher, this correction becomes considerable.

When losses in the sample is zero then the wave TE_{10} crystal full reflected (Figure 2.3.), for frequency of microwave is:

$$\nu_0 = \frac{c}{2\pi r\sqrt{\varepsilon}}, \tag{2.20}$$

there c is the light velocity in vacuum. When dielectric losses increase, the reflection and transmission coefficients dependence from a real part of dielectric permittivity becomes more shalower, together decrease the accuracy of the method, extremely at $\nu > \nu_0$.

For calculating the complex dielectric permittivity the Niuton method was used, which the allows alternating nonlinear equations system:

Copyright © 2010. Nova Science Publishers, Incorporated. All rights reserved.

Handbook of Material Science Research, Nova Science Publishers, Incorporated, 2010. ProQuest Ebook Central,

$$R = f_1(\varepsilon', \varepsilon'')$$
$$T_{tr} = f_2(\varepsilon', \varepsilon'') \tag{2.21}$$

into linear. The complex dielectric permittivity ε^* limits and their initial values were choosed aproximately by comparision of high-frequency and THz measurements results. Iteration calculation was stoped, when

$$R - f_1(\varepsilon', \varepsilon'') < \delta_{\text{ac}} \text{ and } T_{tr} - f_2(\varepsilon', \varepsilon'') < \delta_{\alpha\chi}; \tag{2.22}$$

there $\delta_{\alpha\chi}$ is the acuracy of calculations. Usualy $\delta_{\alpha\chi}$ is selected around 0,001, calculation with better acuracy is meaningless, because measurements accuracy is less. More information about this method is in [7].

2.3.4. Sample Preparation

For thin cylindrical road in rectangular waveguide the method requeres the samples of cylindrical shape and of height equal to narrow waveguide wall. The samples were prepareted according to measurements methodology requirement, that values of microwave reflection and transmission moduli would be not less then 0.2 and not higher then 0.85. As usual, the samples were cut from enough big piece and further manually polished until desirable dimension. Shape of the investigated specimens were nearly cilindrical and effective radius r_{ef} was calculated according to formula:

$$r_{ef} = \sqrt{\frac{S}{\pi}} \tag{2.23}$$

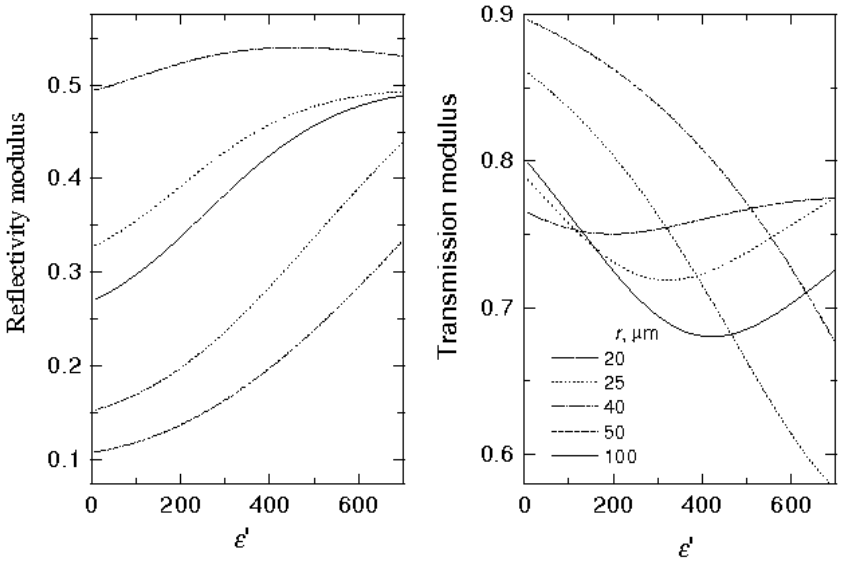


Figure 2.4. Microwave transmission and reflection coefficients moduli dependence from dielectric permittivity and radius of a sample, when ν = 53 GHz, losses of sample ε'' = 400 .

Copyright © 2010. Nova Science Publishers, Incorporated. All rights reserved.

Handbook of Material Science Research, Nova Science Publishers, Incorporated, 2010. ProQuest Ebook Central,

2.4. Dielectric Data Analysis

2.4.1. Tichonov Regularization Method

Treating integral Equations (1.41) and (1.42) numerically one has to perform the discretization which leads to the linear non homogeneous algebraic equation set. In the matrix notation it can be represented as:

$$A\vec{X} = \vec{T}\,. \tag{2.24}$$

Here the components T_n ($1 \le n \le$ N) of the vector $\vec{T}$ represent the dielectric spectrum $\{\varepsilon'_i,\ \varepsilon''_i\}$ ($1 \le i \le$ N/2) recorded at some frequencies ω_i. We used equidistant frequency intervals in the logarithmic scale ($\Delta\lg \tau_m = \text{const}$). The vector $\vec{X}$ with components X_m ($1 \le m \le$ M) stands for the relaxation time distribution f (τ_m) which we are looking for. We used equidistant time intervals in the logarithmic scale as well ($\Delta\lg \tau_m = \text{const}$). The symbol A stands for the kernel of the above matrix equation. It represents the matrix with elements obtained by the direct substitution of ω_i and τ_m values into the kernels of integral equations (1.41) and (1.42). In order to increase the accuracy in the case of noisy data, usually the number of frequency point's ω_i exceeds the number of relaxation times τ_m at which the distribution is calculated. Thus, the number of equations in Eq. (2.24) exceeds the number of variables (the number of the vector $\vec{X}$ components). Due to that fact that Equation (2.24) cannot be solved directly, and it has to be replaced by the following minimization problem:

$$\Phi_0 = \left\|\vec{T} - A\vec{X}\right\|^2 = \min\,. \tag{2.25}$$

Here and further we shall use the following vector norm notation $\left\|\vec{V}\right\| = \vec{V}^T\vec{V}$ where the superscript ^{T} indicates the transposed vector or matrix.

Due to the ill-posed nature of the integral Fredholm equations the above minimization problem is ill-posed as well, namely, its solution is a rather sensitive to small changes of the vector $\vec{T}$ components (the dielectric spectrum $\varepsilon^*(\omega)$ which are the input of the considered problem. That is why the above minimization problem can not be treated without some additional means. Following the Tikhonov regularization procedure we replace the functional Φ_0 by the following modified expression:

$$\Phi(\alpha_R) = \left\|\vec{T} - A\vec{X}\right\| + \alpha_R^2\left\|R\vec{X}\right\|, \tag{2.26}$$

where the additional regularization term is added. The symbol R stands for the regularization matrix, and α_R is the regularization parameter. It plays the same role as a filter bandwidth when smoothing noisy data. The less is the value of the regularization parameter in minimization problem (2.26) the more solutions satisfy this equation within the experimentally recorded dielectric spectrum errors, and the more the solution becomes unstable itself. While increasing this parameter we deviate from the actual relaxation time

Copyright © 2010. Nova Science Publishers, Incorporated. All rights reserved.

Handbook of Material Science Research, Nova Science Publishers, Incorporated, 2010. ProQuest Ebook Central,

distribution which we are looking for. Thus, in order to get the satisfactory result we have to add as many additional conditions as possible. First, we know that all relaxation time distribution components have to be positive ($X_n > 0$). Next, sometimes it is possible to obtain the rather reliable static permittivity $\varepsilon(0)$ or the limit high-frequency dielectric permittivity $\varepsilon_{\infty r}$. In this case it is worth to restrict the above minimization problem fixing some of these values or both.

2.4.2. Debye Program

Usually the minimization problem (2.26) is solved numerically by means of the least squares problem technique [147]. Prof. A. Matulis developed the Debye program for the numerical solution of restricted minimization problem (2.26) and the calculation of the relaxation time distribution. In this subsection we give some details of this numerical program. Actually the program implements the simplified version of Provencher algorithm [148] adapted to integral Equations (1.41) and (1.42) case. As it was already mentioned in Subsection 2.6.1., the equidistant discretization in the logarithmic scale with steps

$$\Delta\lg(\omega/2\pi)=h_\nu,\ \Delta\lg\tau=h_T \tag{2.27}$$

was used. The kernel matrix components are:

$$A_{nm}=h_T(1+(\omega_n\tau_m)^2)^{-1},\ n\le N/2$$

$$A_{nm}=\omega_n\tau_m h_T(1+(\omega_n\tau_m)^2)^{-1},\ n\ge N/2. \tag{2.28}$$

When the shift $\varepsilon_{\infty r}$ is known and fixed, it is subtracted from data vector replacing $\varepsilon'_i \to \varepsilon'_I$-$\varepsilon_{\infty r}$. In the opposite case, when the shift $\varepsilon_{\infty r}$ is not fixed, it is added to the $\vec{X}$ vector as its first component. In this case, the additional first $\{1, \cdot\cdot, 1, 0,\cdots, 0\}^T$ column is added to the kernel matrix.

The regularization matrix

$$R = R_0 = \begin{pmatrix} h_T^2 & 0 & 0 & 0 & \dots & 0 \\ 1 & -2 & 1 & 0 & \dots & 0 \\ 0 & 1 & -2 & 1 & \dots & 0 \\ \dots & \dots & \dots & \dots & \dots & \dots \\ 0 & \dots & 0 & 1 & -2. & 1 \\ 0 & \dots & 0 & 0 & 0 & h_T^2 \end{pmatrix} \tag{2.29}$$

corresponding to the calculation of the second order derivative was used. The first and last components proportional to h^2_T were adjusted during the simulation. In the case with not fixed shift $\varepsilon_{\infty r}$ value the above regularization matrix was replaced by

Copyright © 2010. Nova Science Publishers, Incorporated. All rights reserved.

Handbook of Material Science Research, Nova Science Publishers, Incorporated, 2010. ProQuest Ebook Central,

$$R = \begin{pmatrix} h_T^2 & 0 \\ 0 & R_0 \end{pmatrix}. \tag{2.30}$$

When the static permittivity $\varepsilon(0)$ is fixed there is the additional equality condition:

$$\varepsilon_{\infty r}+\int f(\tau)d\lg(\tau)=\varepsilon(0) \tag{2.31}$$

which relaxation time distribution has to obey. The discrete version of this condition can be presented as $E^T \vec{X} = e$ with

$$e=\varepsilon(0)-\varepsilon_{\infty r},\ E^{\mathrm{T}}=h_T\{1/2,\ 1,\ \ldots,\ 1,\ 1/2\} \tag{2.32}$$

in the case with fixed $\varepsilon_{\infty r}$, and

$$e=\varepsilon(0)\ E^{\mathrm{T}}=h_T\{1/h^{-1}{}_{\mathrm{T}},\ 1/2,\ \ldots,\ 1,\ 1/2\} \tag{2.33}$$

in the opposite case.

Thus, we have to solve the minimization problem with linear equality and inequality constraints:

$$\Phi(\alpha_R) = \left\|\vec{T} - A\vec{X}\right\| + \alpha_R^2 \left\|R\vec{X}\right\|, \tag{2.34a}$$

$$\vec{E}^T \vec{X} = e, \tag{2.34b}$$

$$X_n \geq 0. \tag{2.34c}$$

The standard way of treating such a problem is the exclusion of the equality constraint, and reduction of the remaining minimization problem with inequality constraints to the LDP (*Least Distance Programming*) problem [147]. The exclusion of the equality constraint is performed as follows. First, the scalar constraint (2.34b) is formally replaced by its matrix analog:

$$\Xi^T \vec{X} = e \tag{2.35}$$

with $M \times M$ matrix $\Xi=(\vec{E},\ 0)$ and M-component vector $\vec{e}^{\,T} = \{e \quad 0\}$. Next, the RQ decomposition is performed:

$$\Xi = (K_1 K_2)\begin{pmatrix} F_F & 0 \\ 0 & 0 \end{pmatrix}. \tag{2.36}$$

Copyright © 2010. Nova Science Publishers, Incorporated. All rights reserved.

Handbook of Material Science Research, Nova Science Publishers, Incorporated, 2010. ProQuest Ebook Central,

Here symbol K_1 stands for M-component vector, and K_2 is the $M\times(M\text{-}1)$ matrix. Those two objects together from the unitary matrix:

$$\begin{pmatrix} \vec{K}_1^T \\ K_2^T \end{pmatrix}\left(\vec{K}_1 \quad K_2\right) = I_I . \tag{2.37}$$

Here I_I is the unitary matrix.

Now inserting Eq. (2.36) into Eq. (2.35), and denoting:

$$\vec{X} = (\vec{K}_1 \quad K_2)\begin{pmatrix} X_1^E \\ \vec{X}_2^E \end{pmatrix} = \vec{K}_1 X_1^E + K_2 \vec{X}_2^E , \tag{2.38}$$

we obtain:

$$X_1^E = F_F{}^{-1} e , \tag{2.39}$$

and reduce the initial minimization problem to the problem with inequality constraints only:

$$\Phi(\alpha_R) = \left\| (\vec{T} - A\vec{K}_1 F_F{}^{-1} e) - AK_2 \vec{X}_2^E \right\| + \alpha_R{}^2 \left\| RK_1 F_F{}^{-1} e + RK_2 \vec{X}_2^E \right\|^2 = \min \tag{2.40a}$$

$$(K_2 \vec{X}_2^E)_n \geq -(\vec{K}_1)_i F_F{}^{-1} e \tag{2.40b}$$

for shorter vector $\vec{X}_2^E$ (with $(M\text{-}1)$ components).

The reduction of the above problem to LDP is based on the QR-decomposition:

$$AK_2 = Q_0 L, \tag{2.41}$$

followed by twofold singular value decompositions (SVD):

$$RK_2 = J\Psi\Im^T , \tag{2.42a}$$

$$C\Im\Psi^{-1} = QSW^T . \tag{2.42b}$$

Here matrices Q_0, J, $\Im$, Q, W are orthogonal ($Q^{\mathrm{T}}{}_0 Q_0$=I, etc.), matrices Ψ and S are diagonal matrix elements Ψ_n, S_n, correspondingly, and the matrix C is upper triangular.

The substitution:

$$\vec{X}_2^E = \Im\Psi^{-1}\{W\lambda^{-1} - J^T R\vec{K}_1 F_F{}^{-1} e\} \tag{2.43}$$

Copyright © 2010. Nova Science Publishers, Incorporated. All rights reserved.

Handbook of Material Science Research, Nova Science Publishers, Incorporated, 2010. ProQuest Ebook Central,

changes minimization problem (2.33) into the following one:

$$\Phi(\alpha_R) = \left\|\zeta - S\vec{\lambda}\right\| + \alpha_R^2 \left\|\vec{\lambda}\right\| = \min, \tag{2.44a}$$

$$(D\vec{\lambda})_n \geq -d_{dn}, \tag{2.44b}$$

where

$$D = K_2 \Im \Psi^{-1} W, \tag{2.45a}$$

$$d_d = \{K_2 \Im \Psi J^T - I\} \vec{K}_1 \mathrm{P}_m{}^{-1} e, \tag{2.45b}$$

$$\zeta = Q^T \{Q_0^T \vec{T} + (C\Im\Psi^{-1} J^T - Q_0{}^T A)\vec{K}_1 P_m{}^{-1} e\}. \tag{2.45c}$$

The main advantage of the obtained minimization problem is that both functional parts are composed of the diagonal components only. Thus, it can be easily rewritten in the single diagonal form:

$$Norm = \left\|\vec{\zeta}\right\| = \min, \tag{2.46a}$$

$$(D\widetilde{S}^{-1})_n \geq -(\vec{d} + D\widetilde{S}^{-1}\widetilde{\vec{\kappa}})_n, \tag{2.46b}$$

where the symbol $\widetilde{S}$ stands for diagonal matrix with the components $\widetilde{S}_n = \sqrt{S_n^2 + \alpha_R^2}$, $\widetilde{\vec{\kappa}}$ is the vector with components $\widetilde{\kappa}_n = \kappa_n S_n / \widetilde{S}_n$, and

$$\widetilde{\vec{\lambda}} = \widetilde{S}^{-1}(\vec{\zeta} + \widetilde{\vec{\kappa}}). \tag{2.47}$$

Final minimization problem (2.53) can be solved by LDP technique. When the vector $\vec{\zeta}$ is found the vector $\vec{X}$ (actually the relaxation time distribution) is obtained by means of Eqs. (2.46), (2.42), (2.38), and (2.37).

In the case when ε(0) is not fixed there is no Eq. (2.34b), and the algorithm is more simple. It can be easily obtained from the previous one formally assuming that $\vec{K}_1 = 0$ and $K_2 = I_I$.

The Debye program is written in C++ as a SDT (*Single Document Interface*) program for the Windows environment. The LDP subroutine was rewritten from the Fortran version given in [147], the matrix decomposition subroutines were taken from [149]. Up to now we used to set the regularization parameter manually.

Copyright © 2010. Nova Science Publishers, Incorporated. All rights reserved.

Handbook of Material Science Research, Nova Science Publishers, Incorporated, 2010. ProQuest Ebook Central,

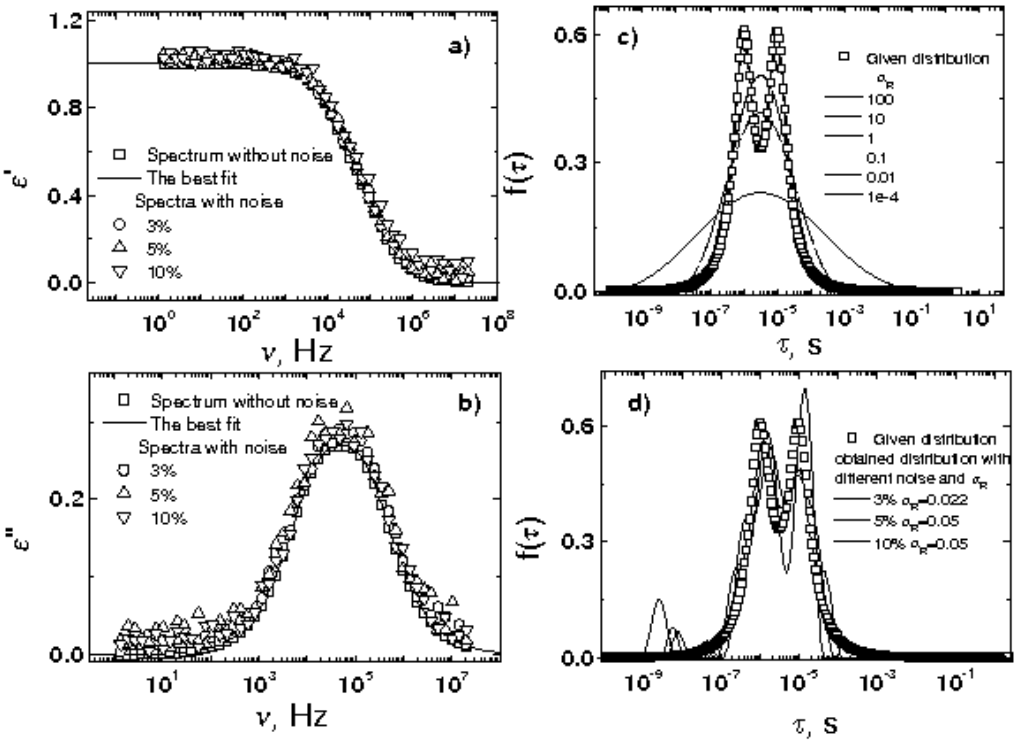


Figure 2.5. Frequency dependence of real (a) and imaginary (b) parts of dielectric permittivity and the corresponding double-peaked Cole-Cole reference relaxation time distribution function (c, points), calculated distribution function with different α_R without noise (c, different lines) and calculated distribution function from the dielectric spectra with different noise (d).

2.4.3. Simulation Results

In order to illustrate the usefulness of proposed method we performed the following numerical experiment. We prepared some fixed distributions of the relaxation times, generated the corresponding dielectric spectra adding some noise to it, and then tried to reveal the relaxation time distribution using the Debye program with various regularization α_R parameters chosen. For this purpose we used rather popular distributions given by the Cole-Cole (1.45) and (1.46) and Havriliak-Negami (1.54), (1.55), (1.56) formulas. The main advantage of these expressions is that the exact analytical expressions for the corresponding dielectric spectrum are known. Besides, we made the numerical experiments with simple distributions composed of single and multiple triangular and square shapes. The results are presented in Figs. 2.7 and 2.8.

Inspecting Figure 2.5 were the results obtained with the Cole-Cole distribution are presented one may to conclude that in the absence of noise the relaxation time distributions can be revealed quite successfully either in the case of a single or double peak, although the regularization parameter cannot be chosen rather small in order to avoid the appearance of the artificial peaks. The addition of some noise doesn't change the situation drastically.

The form of the distribution can be obtained successfully even with the noise levels up to 10%. It is also seen that the regularization parameter has to be increased in the case of the larger noise levels.

Copyright © 2010. Nova Science Publishers, Incorporated. All rights reserved.

Handbook of Material Science Research, Nova Science Publishers, Incorporated, 2010. ProQuest Ebook Central,

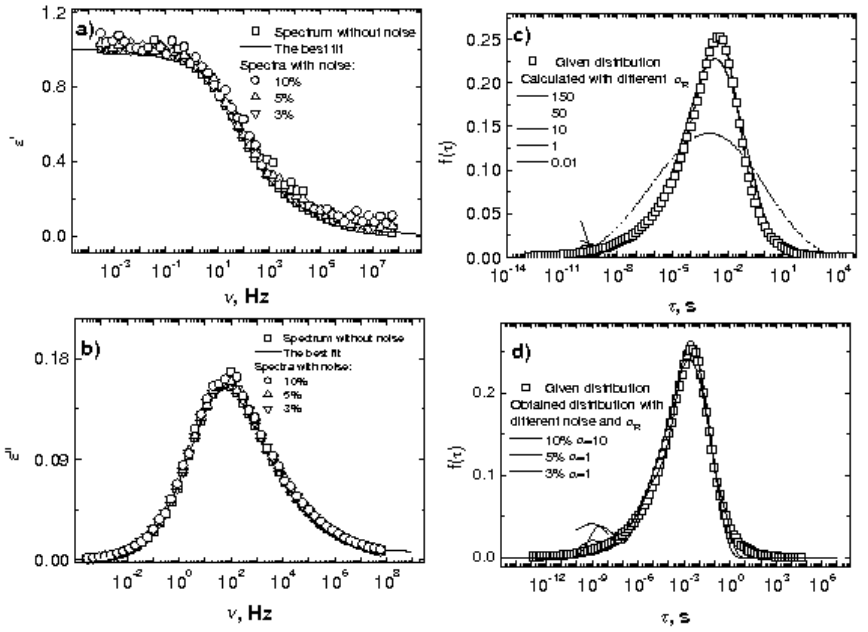


Figure 2.6. Frequency dependence of real (a) and imaginary (b) parts of dielectric permittivity and the corresponding Havriliak-Negami reference relaxation time distribution function (c, points), calculated distribution function with different α_R without noise (c, different lines) and calculated distribution function from the dielectric spectra with different noise (d).

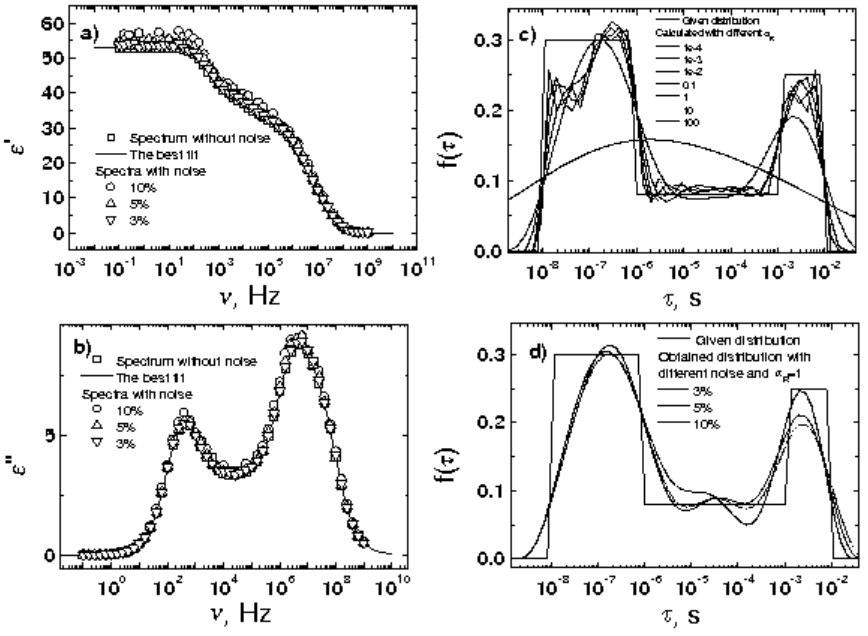


Figure 2.7. Frequency dependence of real (a) and imaginary (b) parts of dielectric permittivity and the corresponding triple-rectangular reference relaxation time distribution function (c, points), calculated distribution function with different α_R without noise (c, different lines) and calculated distribution function from the dielectric spectra with different noise (d).

Copyright © 2010. Nova Science Publishers, Incorporated. All rights reserved.

Handbook of Material Science Research, Nova Science Publishers, Incorporated, 2010. ProQuest Ebook Central,

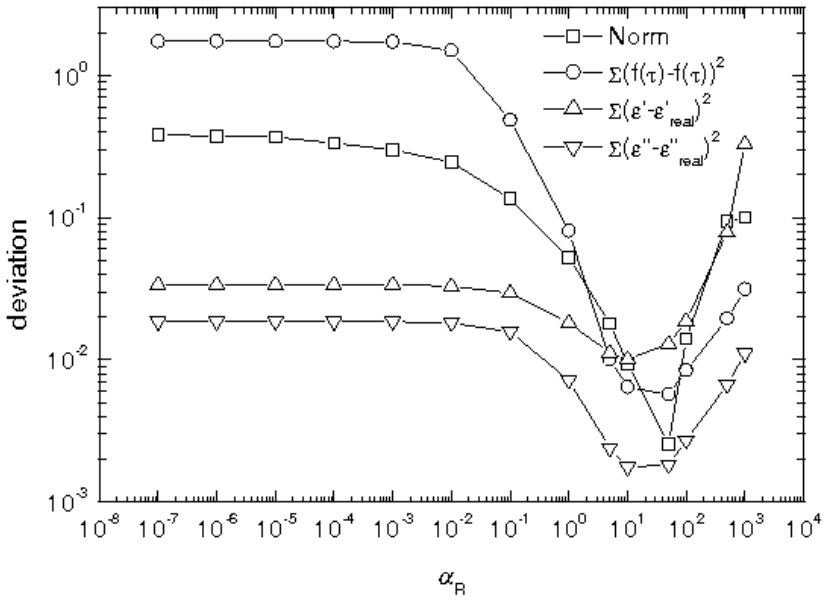


Figure 2.8. The α_R dependence of various deviation values for single Cole-Cole process with gaussian noise.

The results of similar experiments with the Havriliak-Negami distribution are presented in Figure 2.6. The main idea of the Havriliak-Negami distribution lays in the fact that it enables to model the non-symmetric relaxation time distributions. Comparison of these results with shown in Figure 2.5 results indicates that distribution asymmetry does not affects its definition essentially. Also, same calculations have been made for the simulated dielectric spectra with triangle and rectangular shapes of distribution function. From these simulations (see for example Figure 2.7) we can conclude, that it is not possible to obtain the exact shape of the distribution function, due to sharp edges, but general features of the spectra have been revealed.

2.4.4. The Reguliarization Parameter

The results presented in the previous section show that the regularization parameter α_R is crucial for the shape of the distribution function of the relaxation times. Too small values for α_R result in artificial physically meaningless structures in f (τ), while too large α_R tends to oversmoth the shape of f (τ) and suppress information. When applying the Tikhonov regularization technique the proper choice of the regularization parameter α_R is the main problem.

To find out how to chose proper α_R the following calculations have been performed. The following criteria for α_R have been chosen:

1. Deviation of the calculated spectra of dielectric permittivity from the given spectra of dielectric permittivity for the real and imaginary parts of permittivity;
2. Deviation of the calculated distribution function of the relaxation times from the given distribution of the relaxation times;
3. The NORM parameter.

Copyright © 2010. Nova Science Publishers, Incorporated. All rights reserved.

Handbook of Material Science Research, Nova Science Publishers, Incorporated, 2010. ProQuest Ebook Central,

From the 1st deviation we can see which dielectric spectra fits experimental results in the best way and is easiest to calculate (for routine calculations during fitting procedure). 2nd shows how close we are to the given distribution, but this parameter is not suitable for the experimental investigations, when we do not know initially the shape of the distribution function. 3rd or NORM parameter also gives information how close we are from the given distribution of the relaxation times. Such calculations have been performed and results are presented in Figure 2.8.

We can see that all curves have clearly expressed minimum, and what is the most important – NORM minimum coincides with minimum in deviation of the relaxation times distribution function. The minimum of the deviation of the real and imaginary parts of dielectric permittivity is not so clearly expressed. Because usually from the experimental data we do not know the shape of distribution function, most important is the parameter NORM. Such calculations have been performed with a different noise level and different distribution functions.

Thus, from all presented curves we can see that the best choice for regularization parameter is before it begins to increase. This happens for all three criteria.

3. DYNAMICS OF PHASE TRANSITIONS OF BPXBPI1-X MIXED CRYSTALS

3.1. Influence of Small Amount of Betaine Phosphate Admixture to Dielectric Dispersion of Betaine Phosphite Crystals

3.1.1. Introduction

Betaine phosphate (BP) $(CH_3)_3NCH_2COOH_3PO_4$ and betaine phosphite (BPI) $(CH_3)_3NCH_2COOH_3PO_3$ are molecular crystals consisting of the amino acid betaine as the organic, and phosphoric and phosphorous acids, respectively, as the inorganic component. The structure of both compounds is very similar [150-152] (Figs. 3.1, 3.2). The inorganic components (PO_4 or PO_3 groups) are linked by hydrogen bonds to form quasi-one-dimensional chains along the monoclinic b-axis. The betaine molecules are arranged almost perpendicular to this chains along the *a*-direction and are linked by one (BPI) or two (BP) hydrogen bonds to the inorganic group.

Both compounds, BPI and BP, undergo a phase transition from a paraelectric high-temperature phase with the space group $P2_1/m$ to an antiferrodistortive phase with the space group $P2_1/c$ at 355 K (BPI) and 365 K (BP), respectively. In the high-temperature phase the PO_4 or HPO_3 groups and the betaine molecules are disordered. They both order in the antiferrodistortive phase, but the hydrogen atoms linking PO_4 or HPO_3 groups remain disordered. Ordering of these hydrogen atoms induces the phase transition into the ferroelectric or antiferroelectric phase. BPI experiences a transition into a ferroelectric ordered low-temperature phase with space group $P2_1$ at 220 K. BP shows two further structural transitions at 86 K into a ferroelectric intermediate phase of $P2_1$ symmetry [153] and at 81 K into an antiferroelectric low-temperature phase with doubling of the unit cell along the crystallographic *a*-direction. The temperature dependence of the dielectric permittivity of both compounds shows evidence for a quasi-one dimensional behaviour. The

Copyright © 2010. Nova Science Publishers, Incorporated. All rights reserved.

Handbook of Material Science Research, Nova Science Publishers, Incorporated, 2010. ProQuest Ebook Central,

coupling between the electric dipolar units within the chains is much stronger than that one between dipolar units in neighboring chains [150, 153]. Antiferroelectric order is established in BP at T_C = 81 K [154] in such a way that the O–H···O bonds order ferroelectrically within the one-dimensional chains whereas neighboring chains are linked antiferroelectrically [151]. In BPI, however, neighboring chains are linked ferroelectrically below T_C = 216 K [155]. Deuteration of hydrogen-bonded ferroelectrics leads to significant changes of the dielectric properties and shifts the phase transition temperature to higher values [151]. This isotope effect has already been studied in deuterated crystals of the betaine family, namely betaine phosphate (DBP) and betaine phosphite (DBPI) [154, 156].

The low-frequency dielectric measurements of DBPI showed [156] that the transition temperature is shifted up to 297 K. Deuterated BP (DBP) shows only two phase transitions at 365 and 119 K, respectively. This gives strong evidence that the hydrogen bonds play an important role in the ferroelectric and antiferroelectric transition.

The results of broadband dielectric spectroscopy of BPI have been reported elsewhere [157]. The ferroelectric dispersion in the vicinity of T_C has been observed in 100 MHz – 77 GHz frequency range. The characteristic minimum of ε' appears at 9 GHz indicating a critical slowing-down in the microwave region. The ferroelectric dispersion has been described with the Debye formula.

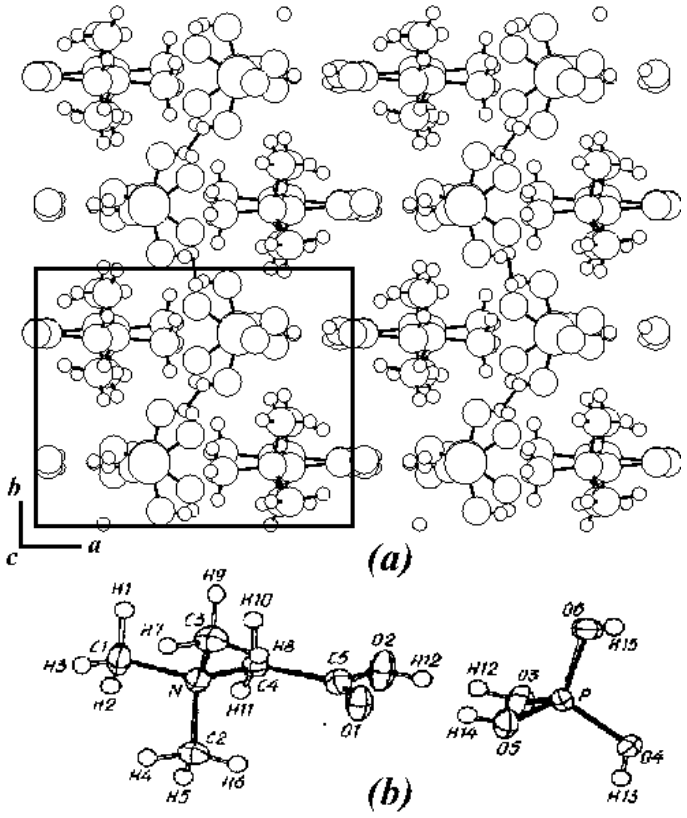


Figure 3.1. Projection of the BP structure in the (ab) plane at 299 K (a). At the bottom - plot of the betaine phosphate molecule at 150 K (b). After [150].

Copyright © 2010. Nova Science Publishers, Incorporated. All rights reserved.

Handbook of Material Science Research, Nova Science Publishers, Incorporated, 2010. ProQuest Ebook Central,

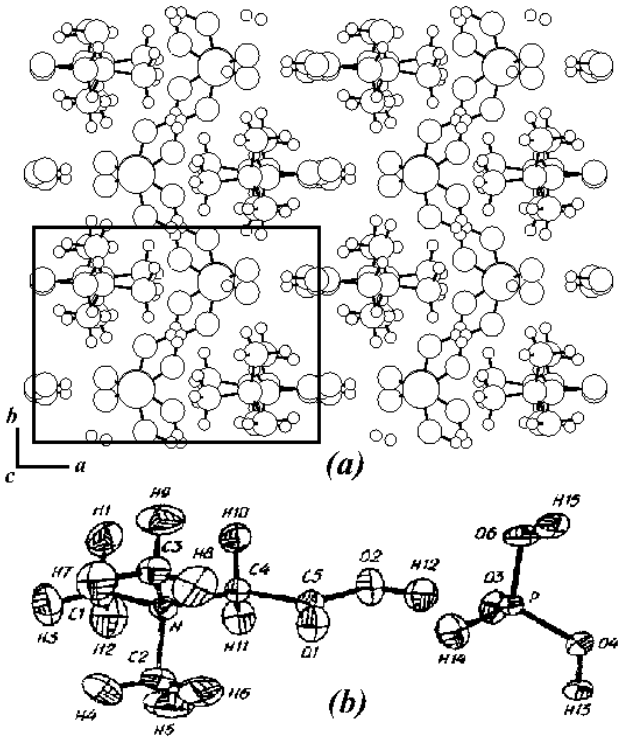


Figure 3.2. Projection of the BPI structure in the (ab) plane at 295 K (a). At the bottom - plot of the betaine phosphite molecule at 295 K (b). After [151].

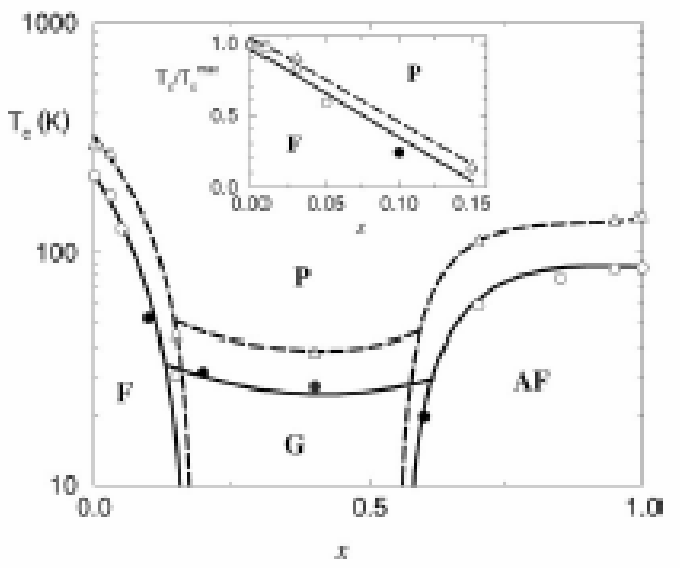


Figure 3.3. (T, x) phase diagram of the solid solutions of BP_xBPI_{1-x} represented by circles and DBP_xDBPI_{1-x} drawn by triangles. **F**, **AF**, **G**, and **P** denote the ferroelectric, antiferroelectric, spin-glasses, and paraelectric phases, respectively. Inset shows the **F**-**P** part of the phase diagram plotted using normalized temperature from [163].

Copyright © 2010. Nova Science Publishers, Incorporated. All rights reserved.

Handbook of Material Science Research, Nova Science Publishers, Incorporated, 2010. ProQuest Ebook Central,

The obtained relaxation frequency $\nu_r = (2\pi\tau_{CC})^{-1}$ on approaching T_C varies according to $\nu_r = 0.36$ (T - -218) GHz in the paraelectric phase and decreases to 2.4 GHz at T_C. It was found that there is an additional contribution to the static dielectric permittivity besides the contribution of the soft relaxational mode. Its origin is unknown so far [157]. The spontaneous polarization in the vicinity of T_C of BPI has been investigated in the reference [158]. The spontaneous polarization saturates at 2.3 μC/cm^2.

The high-frequency dielectric properties of BP have been studied in a range between 10 MHz and 400 GHz [159]. The dielectric data obtained in this frequency range can be explained on the basis of a simple Debye - relaxation with a critical slowing down of the relaxation rate on approaching T_{C2}. Similar results have been obtained for deuterated BP.

The BP_xBPI_{1-x} system was extensively studied experimentally [160-162] and theoretically [163] it is established that the low-temperature part of the (T, x) phase diagram of the BP_xBPI_{1-x} system consist mainly of (i) the ferroelectric phase for $0 \le x \le 0.1$, (ii) antiferroelectric phase for $0.65 \le x \le 1$, and (iii) so called glass phase for $0.1 \le x \le 0.65$ (Figure 3.3).

The main difference between the nondeuterated BP_xBPI_{1-x} and deuterated DBP_xDBPI_{1-x} systems phase diagrams is discrepancy in the absolute values of the phase transition temperature T_c, which is higher for deuterated crystals within the whole interval of x. Both compounds show an abrupt decrease in T_c at small x with ferroelectricity completely destroyed at $x > 0.1$. The considerable increase in T_c when hydrogen in hydrogen bonded ferroelectrics is replaced by deuterium was described within the framework of a model, which takes into account the bilinear coupling between the tunneling protons and displacements of the electron shells of the neighboring PO_4 groups [164].

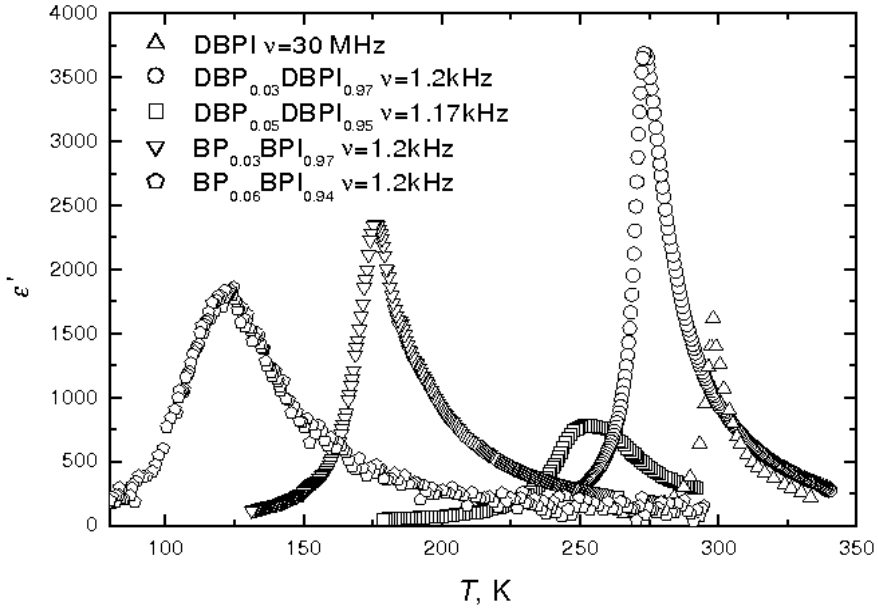


Figure 3.4. Temperature dependence of dielectric permittivity of betaine phosphite with smal admixture of betaine phoshpate at low frequecies, DBPI data is from [165].

Copyright © 2010. Nova Science Publishers, Incorporated. All rights reserved.

Handbook of Material Science Research, Nova Science Publishers, Incorporated, 2010. ProQuest Ebook Central,

3.1.2. Ferroelectric Phase Transition Region

The temperature dependence of dielectric permittivity of betaine phosphite with smal admixture of betaine phoshpate at low frequencies (indeed this dielectric permittivity is static) in ferroelectric phase transition region is presented in Figure 3.4.

On increasing of concentration of betaine phosphate a sharp peak of low frequencies dielectric permittivity changes to more flat. Temperature dependencies of the complex dielectric permittivity $\varepsilon^* = \varepsilon' - i\varepsilon''$ of all investigated BP_xBPI_{1-x} crystals at several frequencies in the ferroelectric phase transition region are shown in Figure 3.5. The characteristic minimum of ε' appears at 1 GHz only in $DBP_{0.03}DBPI_{0.97}$ crystals (Figure 3.5), this indicating a critical slowing down in $DBP_{0.03}DBPI_{0.97}$ as in other H-bonded ferroelectrics [7, 165]. There is a strong dielectric dispersion around and below ferroelectric phase transition temperature T_c in wide frequency range. At higher frequencies (above 1 MHz) temperature of dielectric permittivity maximum T_m strongly increase with increasing frequencies.

Two regions of the dielectric dispersion of deuterated compounds were observed in the vicinity of the Curie temperature (Figure 3.6c and 3.6d). In these compounds the ferroelectric dispersion regions is from about 1 MHz and up to millimeter waves. Simultaneously with the ferroelectric dispersion an additional dielectric relaxation phenomenon was observed at low frequencies below 1 MHz. The proximity of the H_2O melting point to T_C temperature allows linking this anomaly with the influence of humidity. But this effect is observed in two different compounds $DBP_{0.03}DBPI_{0.97}$ and $DBP_{0.05}DBPI_{0.95}$, also in the dielectric spectra of pure DBPI [165] with different T_C. Therefore, the nature of this phenomenon must be admitted as unknown.

At higher temperatures ($T > T_C$) the ferroelectric dispersion is only in microwave region (Figure 3.6). On cooling the broadening of dielectric dispersion has been observed. In the ferroelectric phase, at lower temperatures the ferroelectric dielectric dispersion of all presented crystals (Figure3.6) is very broad (from about 1 MHz to 100 GHz). The Cole-Cole diagrams of deuterated compounds are shown in Figure 3.7. In this diagrams clearly two dielectric dispersion can be separated. However, the Cole-Cole fit is not always adequate for both dielectric dispersions.

Copyright © 2010. Nova Science Publishers, Incorporated. All rights reserved.

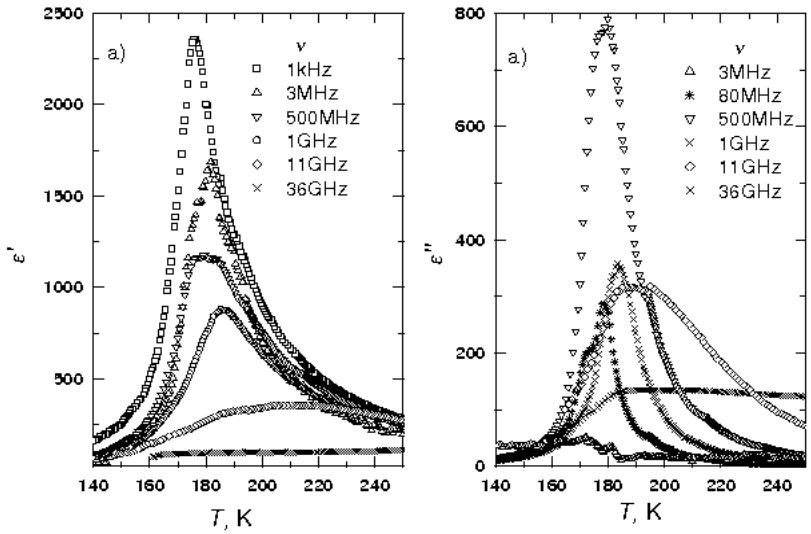
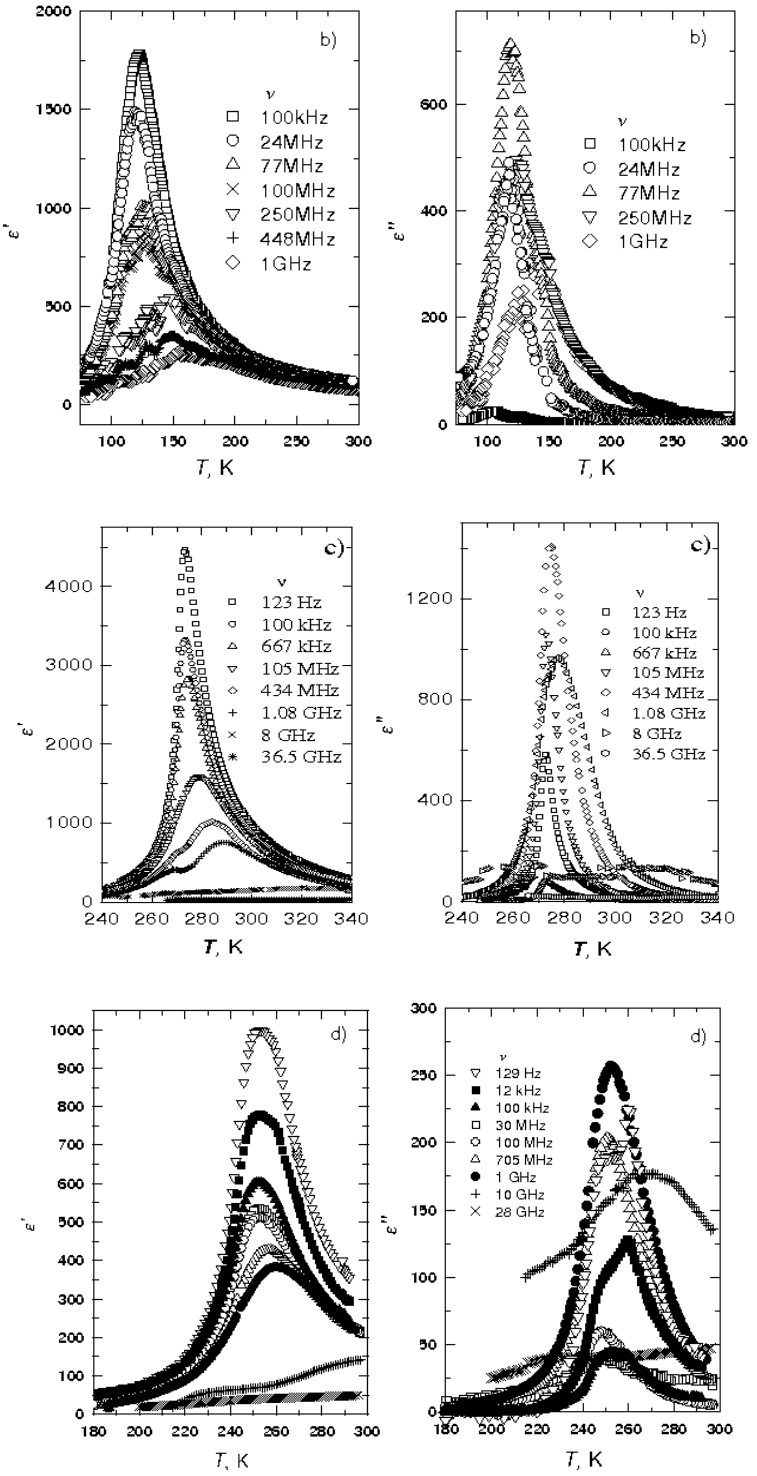


Figure 3.5 (Continues).

Handbook of Material Science Research, Nova Science Publishers, Incorporated, 2010. ProQuest Ebook Central,



Copyright © 2010. Nova Science Publishers, Incorporated. All rights reserved.

Reprinted figures with permission from [166]. Copyright 2001 by the IOP publishing Ltd.

Figure 3.5. Temperature dependence of complex dielectric permittivity ε^* of mixed BP_xBPI_{1-x} crystals: a) $BP_{0.03}BPI_{0.97}$, b) $BP_{0.06}BPI_{0.94}$, c) $DBP_{0.03}DBPI_{0.97}$ d) $DBP_{0.05}DBPI_{0.95}$ at several frequencies in the region of the ferroelectric phase transition.

Handbook of Material Science Research, Nova Science Publishers, Incorporated, 2010. ProQuest Ebook Central,

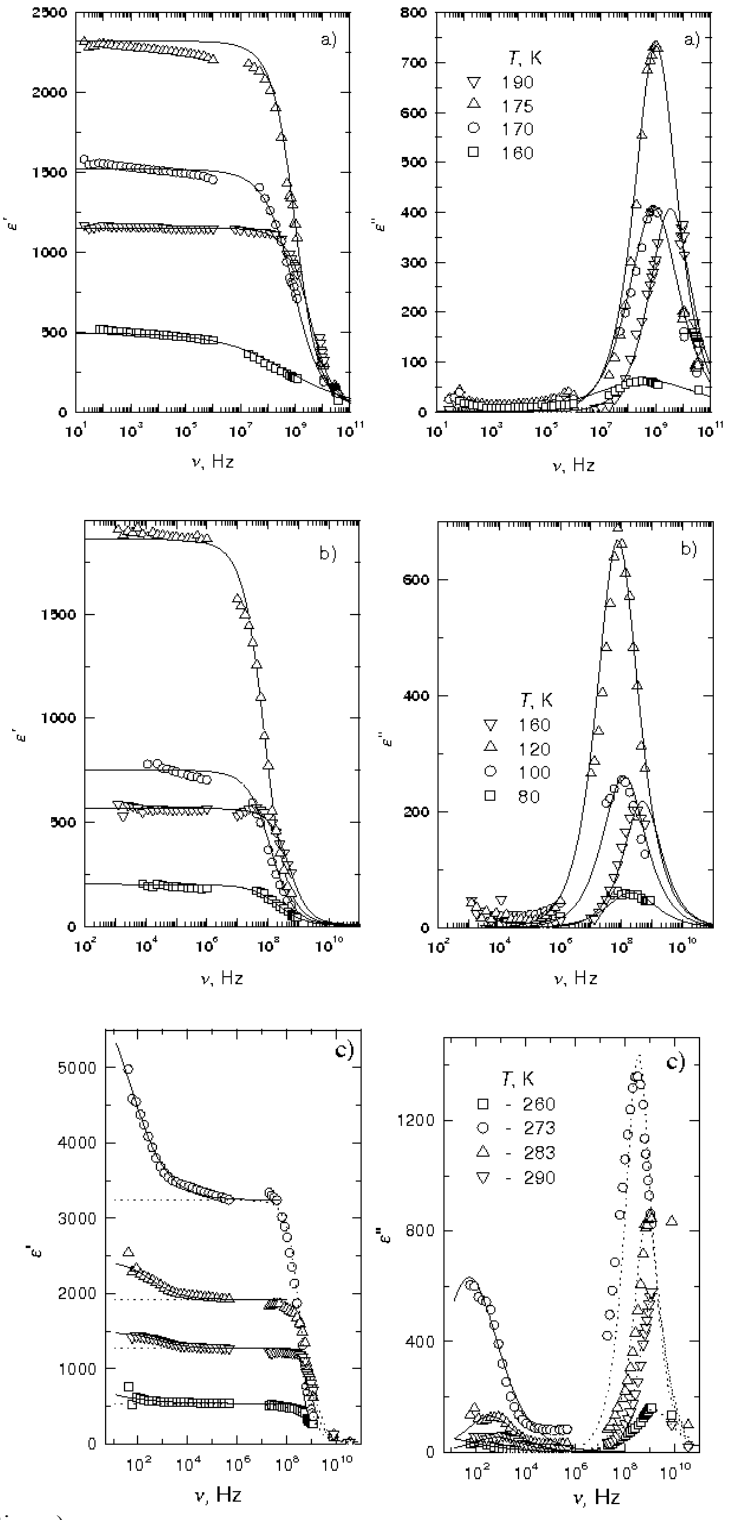
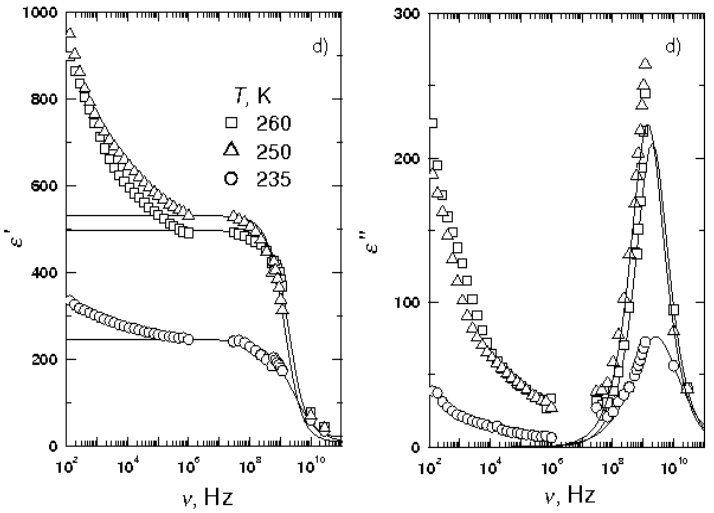


Figure 3.6 (Continues).

Copyright © 2010. Nova Science Publishers, Incorporated. All rights reserved.

Handbook of Material Science Research, Nova Science Publishers, Incorporated, 2010. ProQuest Ebook Central,



Reprinted figures with permission from [166, 175]. Copyright 2001 by the IOP publishing Ltd.

Figure 3.6. Frequency dependence of complex dielectric permittivity ε^* of mixed BP_xBPI_{1-x} crystals: a) $BP_{0.03}BPI_{0.97}$, b) $BP_{0.06}BPI_{0.94}$, c) $DBP_{0.03}DBPI_{0.97}$ d) $DBP_{0.05}DBPI_{0.95}$ at several temperatures in the region of the ferroelectric phase transition. The solid lines are the best fit according to Eqs. (1.41) and (1.42) (apart $DBP_{0.03}DBPI_{0.97}$ low frequency dielectric dispersion – according to Eq. (1.46)).

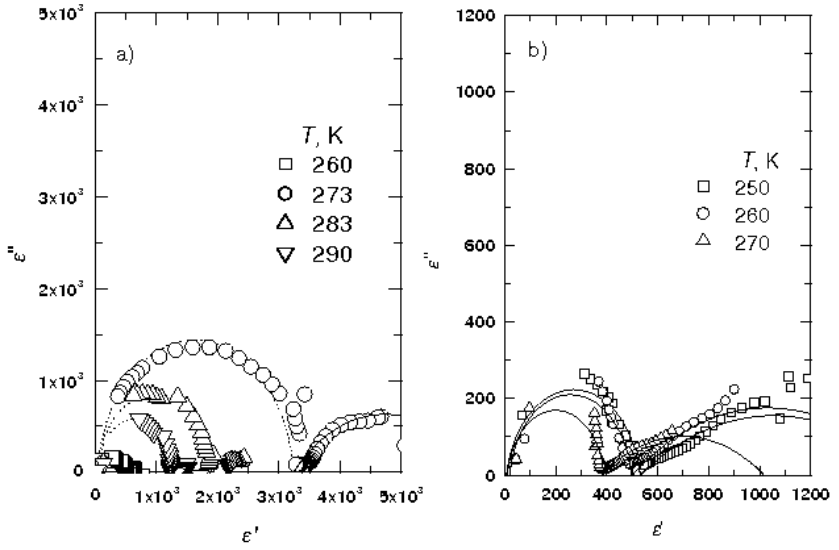


Figure 3.7. Cole–Cole diagrams of a) $DBP_{0.03}DBPI_{0.97}$ and b) $DBP_{0.05}DBPI_{0.95}$ crystals at the different temperatures. The lines are the best fit according to Eq. (1.46).

The experimental data were described with the Cole-Cole formula (1.46). The Cole-Cole parameters of ferroelectric dispersion are presented in Figure 3.8. Only the parameter $\varepsilon_{\infty r}$ does not vary with temperature. Dielectric dispersion looks like the Debye type dispersion only at higher temperatures ($T >> T_C$). On cooling the parameter of distribution of relaxation times α_{CC} of all investigated ferroelectrics increased. Extremely high value for ferroelectrics α_{CC}

Copyright © 2010. Nova Science Publishers, Incorporated. All rights reserved.

Handbook of Material Science Research, Nova Science Publishers, Incorporated, 2010. ProQuest Ebook Central,

reaches at $T < T_c$ that display extremely broad distribution of relaxation times. This clearly differs from the monodispersive character, observed in BPI [157] (α_{CCmax}=0.04), DBPI [165] (α_{CCmax}=0.12) and $DBP_{0.01}DBPI_{0.99}$ (α_{CCmax}= 0.2) [166], while α_{cc} deviate from its zero value only near T_C. The temperature dependence of the relaxation frequency ν_r=1/(2πτ_{CC}) shows a minimum, this indicating the critical slowing down in the presented crystal. Such non-typical (for ferroelectrics) and not so easily understood behaviour of distributions width α_{CC} show that the Cole-Cole formula is not suitable for dielectric dispersion below T_c in presented crystals (for enough high α_{CC} and usual mean τ_{CC} the shortest relaxation times of Cole-Cole distribution of relaxation times loss it physical meaning).

The quasi-one-dimensional Ising model was used to fit the relaxator strength of ferroelectric dispersion [159]:

$$\Delta\varepsilon = \frac{C}{T}\left[\exp\left(-\frac{2J_{\parallel}}{k_B T}\right) - \frac{J_{\perp}}{k_B T}\right]^{-1}, \tag{3.1}$$

where $J_{\parallel}$ and $J_{\perp}$ are the nearest neighbor intrachain and the effective mean field interchain coupling constants. From the best fit (the solid line in Figure 3.8 c) obtained parameters are presented in Table 3.1.

The temperature dependence of the relaxation frequency shows a curvature in the high temperature phase (Figure 3.8 b). The temperature dependence of the relaxation frequency according to the quasi one-dimensional Ising model [159] is given by:

$$\nu_r = \nu_\infty \exp\left(-\frac{\Delta U}{k_B T}\right)\left[\cosh\left(\frac{2J_{\parallel}}{k_B T}\right)\right]^{-1}\left[\exp\left(-\frac{2J_{\parallel}}{k_B T}\right) - \frac{J_{\perp}}{k_B T}\right], \tag{3.2}$$

where ΔU is the activation energy for the reorientation of the dipole, and ν_∞ is the attempt frequency. Using the parameters $J_{\parallel}$ and $J_{\perp}$ obtained by means of Eq. (3.1), the best fit according to Eq. (3.2) results to the values presented in Table 3.1.

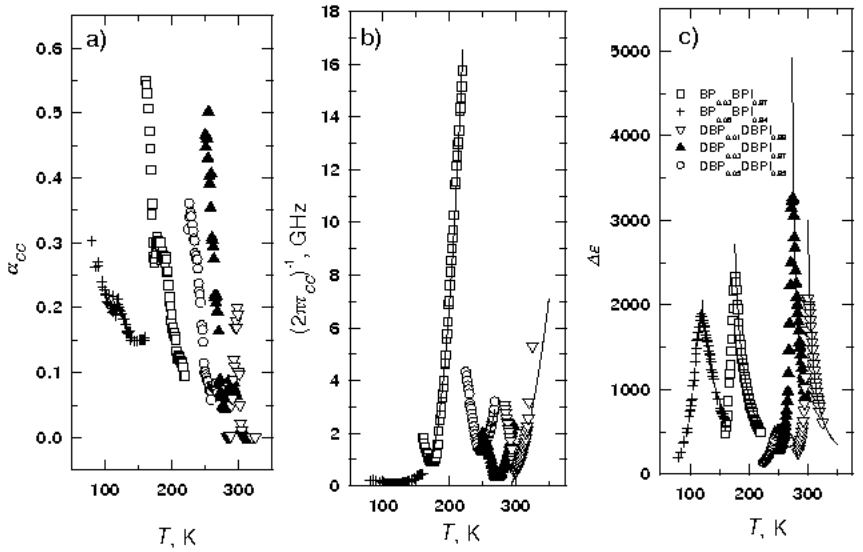
Also the low frequency dielectric relaxation of deuterated compounds was successfully described using the Cole–Cole formula (solid lines in Figures 3.7a and 3.7b). The fit parameters τ_{CCLF} and $\Delta\varepsilon_{LF}$ are presented in Figure 3.9. The contribution of all higher frequency modes and electronic polarization for this relaxation was described as $\varepsilon_{\infty rLF} = \Delta\varepsilon + \varepsilon_{\infty r}$. The distribution parameter α_{ccLF} does not show distinct temperature dependence and fluctuates around 0.41 mean values for $DBP_{0.03}DBPI_{0.97}$ [167] crystals and around 0.6 for $DBP_{0.05}DBPI_{0.95}$ crystals. The mean relaxation time rises intensively approaching T_C, indicating the slowing down phenomenon. The relaxation frequency reaches the minimum value 53 kHz at 273 K in the case of $DBP_{0.03}DBPI_{0.97}$ and 66 kHz at 255 K in the case of $DBP_{0.05}DBPI_{0.95}$.

The distribution of relaxation times has been calculated directly from dielectric spectra according to the formulas (1.41) and (1.42) and method described in Section 2.6. Various values of the Tikhonov regularization parameters were found as optimal for various chemical concentrations, however the differences were not big and mean optimal value was obtained as 4. The distributions of relaxation times of investigated ferroelectrics are presented in Figure

Copyright © 2010. Nova Science Publishers, Incorporated. All rights reserved.

Handbook of Material Science Research, Nova Science Publishers, Incorporated, 2010. ProQuest Ebook Central,

3.10. In the ferroelectric phase the non-symmetric distribution of relaxation times has been obtained. Anomalous (for ferroelectric) asymmetric distribution of relaxation times has been obtained for $DBP_{0.05}DBPI_{0.95}$ crystals. Until presented such asymmetric distributions has been observed only in highly disordered dielectrics, for example in dipolar glasses [160].



Reprinted figures with permission from [166, 175]. Copyright 2001, 1998 by the IOP publishing Ltd..

Figure 3.8. Temperature dependencies of the ferroelectric relaxation fit parameters α_{CC} (a), $v_r=(2\pi\tau_{CC})^{-1}$ (b) and $\Delta\varepsilon$ (c). The solid line is the best fit of quasi-one-dimensional Ising model. $DBP_{0.01}DBPI_{0.99}$ crystals data is from [166].

Copyright © 2010. Nova Science Publishers, Incorporated. All rights reserved.

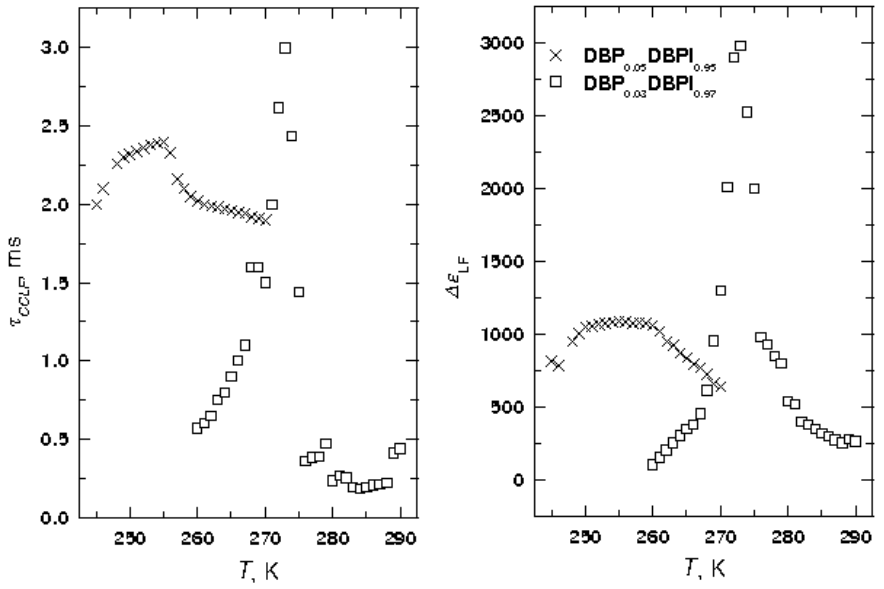


Figure 3.9. Temperature dependence of the additional relaxation fit parameters $\Delta\varepsilon_{LF}$ a) and τ_{CCLF} b).

Handbook of Material Science Research, Nova Science Publishers, Incorporated, 2010. ProQuest Ebook Central,

Table 3.1. Parameters of quasi-one-dimensional Ising models of BP_xBPI_{1-x} mixed crystals

	ν_∞, THz	$\Delta U/k_B$, K	$J_{\|}/k_B$, K	$J_\perp/k_B$, K	$J_{\|}/J_\perp$	C, K	P_0, $\mu C/cm^2$	T_{CIsing}, K
BPI from [158]	-	-	270	21	12.8	5946	2.53	226.7
$BP_{0.03}BPI_{0.97}$	10.3	757	170	19.9	8.54	15060	1.89	161.93
$BP_{0.06}BPI_{0.94}$	0.65	481	86	15	5.73	28296	-	94
BP from [159]	0.82	30	84	-7.5	-11.2	12500	-	-
DBPI from [165]	-	-	187	80	2.33	-	-	290
$DBP_{0.01}DBPI_{0.99}$ from [166]	3.89	1093	230	61	3.77	9692	2.6	293
$DBP_{0.03}DBPI_{0.97}$	0.77	630	234	46.4	5.05	13570	0.32	267.4
$DBP_{0.05}DBPI_{0.95}$	8.58	1378	193	30	6.45	13520	-	202
DBP from [159]	1.2	210	196	-9.1	21.5	-	-	-

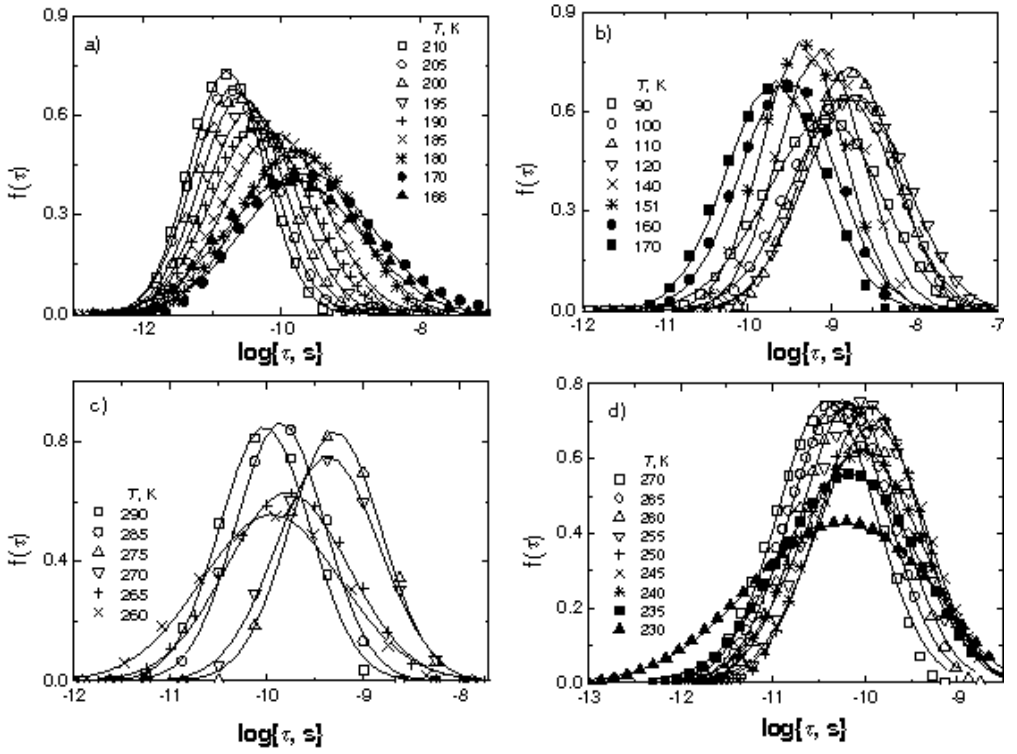


Figure 3.10. Distribution of relaxation times of mixed ferroelectric BP_xBPI_{1-x} crystals: a) $BP_{0.03}BPI_{0.97}$, b) $BP_{0.06}BPI_{0.94}$, c) $DBP_{0.03}DBPI_{0.97}$ d) $DBP_{0.05}DBPI_{0.95}$ obtained from dielectric spectra (points). The solid lines are best fits according to Eq. (3.7).

We consider proton moving in asymmetric double-well potential. The movement consists of fast oscillations in one of the minima with occasional thermally activated jumps between the minima. Here we neglect quantum tunneling, which is significant for protons at low temperatures. The jump probability is governed by the Boltzmann probability of overcoming

Copyright © 2010. Nova Science Publishers, Incorporated. All rights reserved.

Handbook of Material Science Research, Nova Science Publishers, Incorporated, 2010. ProQuest Ebook Central,

the potential barrier between the minima. It was shown that the relaxation time of an individual hydrogen bond dipole in such [168] a system is given by:

$$\tau = \tau_0 \frac{\exp[E_b / k_B (T - T_0)]}{2\cosh(A / 2k_B T)}. \tag{3.3}$$

This equation is similar to the Vogel-Fulcher one, except the dominator, which accounts for the asymmetry A of the local potential produced by the mean field influence of all the other dipoles. Thus, the local polarization p (time-averaged dipole moment) of an individual O-H…O bond is given by the asymmetry parameter A [168]:

$$p=\tanh(A/2k_BT). \tag{3.4}$$

We further consider that the asymmetry A and the potential barrier E_b of the local potential of the O-H...O bonds both are randomly distributed around their mean values A_0 and E_{b0} according to the Gaussian law resulting in the distribution functions:

$$f(E_b) = \frac{1}{\sqrt{2\pi}\sigma_{Eb}} \exp(-\frac{(E_b - E_{b0})^2}{2\sigma_{Eb}^2}), \tag{3.5}$$

with

$$f(A) = \frac{1}{\sqrt{2\pi}\sigma_A} \exp(-\frac{(A - A_0)^2}{2\sigma_A^2}), \tag{3.6}$$

where σ_{Eb} and σ_A are the standard deviations of E_b and A, respectively, from their mean values.

The distribution function of relaxation times is then given by:

$$f(\ln\tau) = \int_{-\infty}^{\infty} w(A) w[E_b(A,\tau)] \frac{\partial E_b}{\partial(\ln\tau)} dA, \tag{3.7}$$

where $E_b(A, \tau)$ is the dependence of E_b on A for a given τ, derived from Eq. (5).

Fits with the experimentally obtained relaxation-time distributions were performed simultaneously for seven different temperatures using the same parameter set: $\tau_0=5*10^{-12}$ s for $BP_{0.03}BPI_{0.97}$, $4.32*10^{-12}$ s for $BP_{0.06}BPI_{0.94}$, $1*10^{-12}$ s for $DBP_{0.03}DBPI_{0.97}$ and $DBP_{0.05}DBPI_{0.95}$ crystals; and $T_{01} = 0$ K (as it should be for the ferroelectric phase transition). The results are presented in Figure 3.10 as solid lines. The average local potential asymmetry A_0, average potential barrier E_{b0} and the standard deviations σ_A and σ_{Eb} are temperature dependent as demonstrated in Figure 3.11. At $T > T_C$ $A_0=0$ for all temperatures and standard deviation of asymmetry is very small ($\sigma_A/k_B \approx 0.9$ K). Only in the case of $BP_{0.06}BPI_{0.94}$ crystals average asymmetry is non-zero at $T > T_C$. In the ferroelectric phase on cooling average asymmetry A_0 and standard deviation σ_A strongly increased. At the same temperature

Copyright © 2010. Nova Science Publishers, Incorporated. All rights reserved.

Handbook of Material Science Research, Nova Science Publishers, Incorporated, 2010. ProQuest Ebook Central,

the ratio A_0 and σ_A strongly decreased with increasing of betaine phosphate concentration. However in all presented ferroelectrics the average asymmetry A_0 is strongly higher as standard deviation σ_A. In the paraelectric phase on cooling average potential barrier E_{b0} and the standard deviation σ_{Eb} increase, this strongly correlated with curvature of temperature dependence of the mean Cole-Cole relaxation time and adequate use of quasi-one-dimensional Ising models.

In all (except $DBP_{0.05}DBPI_{0.95}$) compounds the temperature dependence of average potential barrier E_{b0} have maximum at T_C, this strongly correlated with slow down of phase transitions dynamics.

The spontaneous polarization of BP_xBPI_{1-x} mixed crystals was measured by the pyroelectric method. A pyroelectric current was also observed above the phase transition temperature. It indicates the existence of some space charge in the crystal. The spontaneous polarization was calculated by integration of the pyroelectric coefficient below the temperature, corresponding to the peak of pyroelectric current. In Figure 3.12 the spontaneous polarization temperature dependence is presented. We compare obtained spontaneous polarization values with presented early [162] (in Figure 3.12 presented as line with triangles). A small amount of BP reduces the ferroelectric phase transition temperature significantly. The maximum value of the spontaneous polarization is very similar (1.8 $\mu C/cm^2$) to presented in [162] for $BP_{0.03}BPI_{0.97}$ – 1.8 $\mu C/cm^2$ and to BPI (1.6 $\mu C/cm^2$) in [158]. The influence of the BP amount to spontaneous polarization in non-deuterated mixed $BP_{1-x}BPI_x$ crystals is more inconsiderable than in deuterated samples DBP_xDBPI_{1-x}, for which a significant decrease of $(P)_{max}$ was observed already for $x > 0.03$ [167]. Different approaches, as in [158], were used to describe the temperature behaviour of the spontaneous polarization in betaine phosphite with small admixture of betaine phosphate. In the first approach we started from the classical state equation.

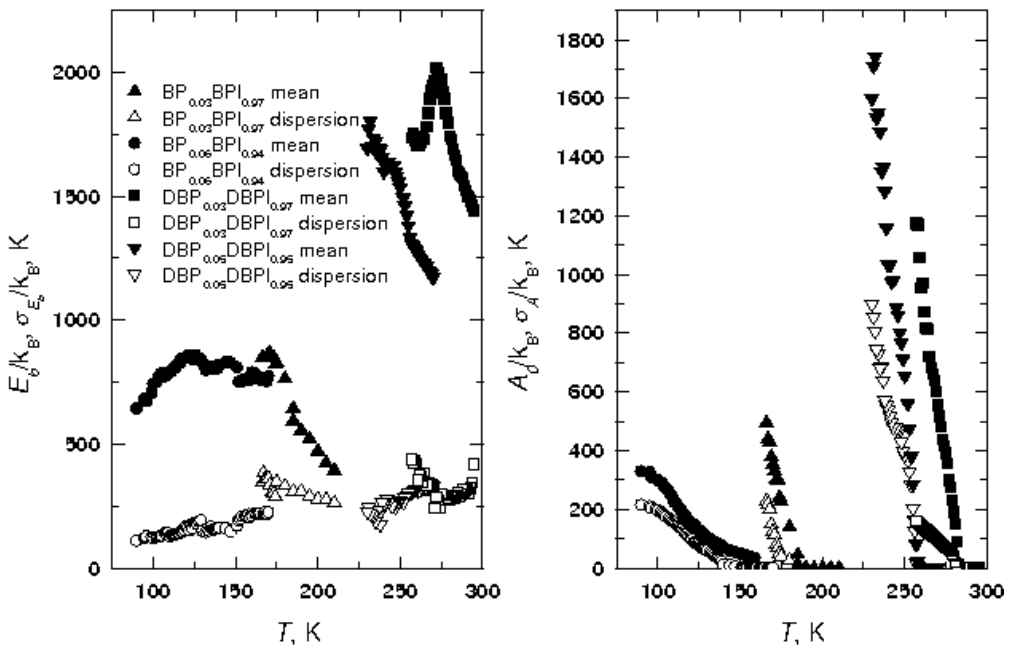


Figure 3.11. Temperature dependence of the mean values E_{b0}, A_0 and standard deviations σ_{Eb}, σ_A of mixed BP_xBPI_{1-x} crystals.

Copyright © 2010. Nova Science Publishers, Incorporated. All rights reserved.

Handbook of Material Science Research, Nova Science Publishers, Incorporated, 2010. ProQuest Ebook Central,

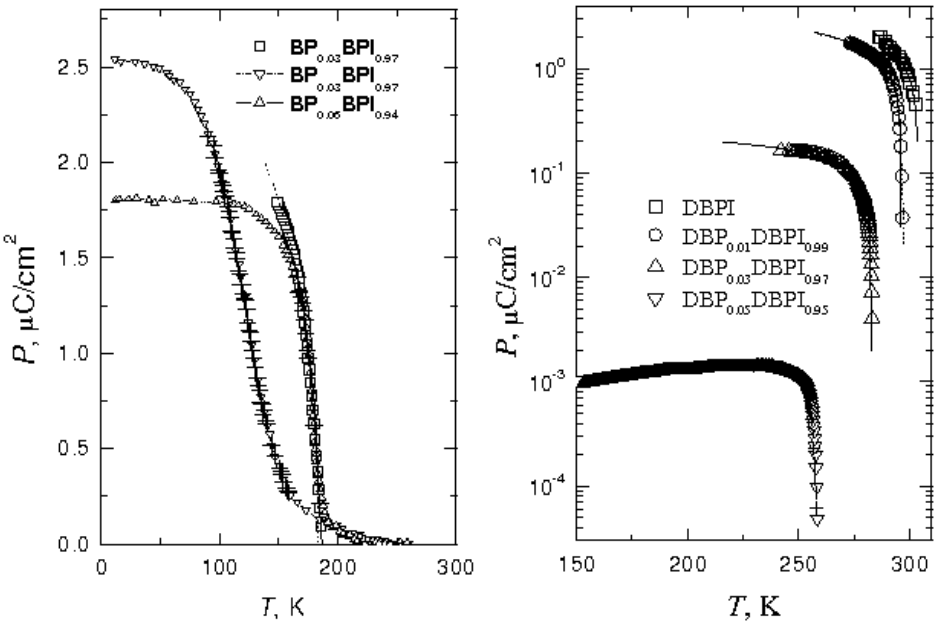


Figure 3.12. Temperature dependence of spontaneous polarization P of mixed BP_xBPI_{1-x} crystals a) protonated and b) deuterated crystals. Experimental data of DBPI are from [165], $DBP_{0.01}DBPI_{0.99}$ from [169], $BP_{0.03}BPI_{0.97}$ and $BP_{0.06}BPI_{0.94}$ (line plus points) from [162]. Solid lines are the best fit according to formulas (3.12), (3.15), dotted according to (3.9) formula.

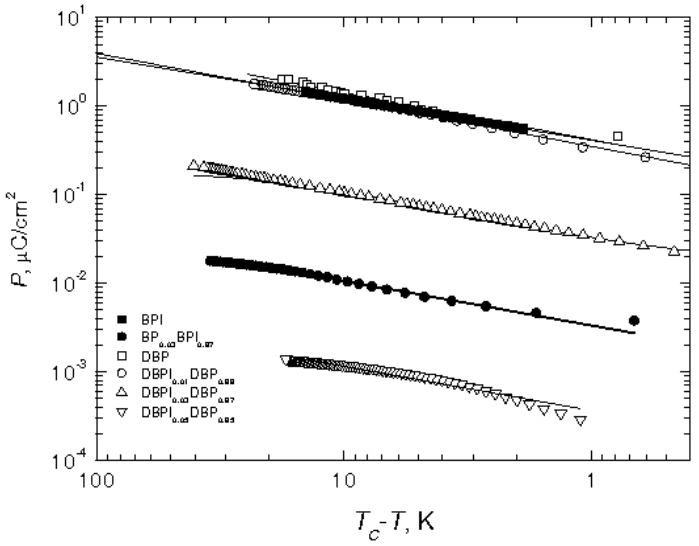


Figure 3.13. A log-log plot of $P= P(T_C-T)$. Experimental data of BPI are from [158], DBPI from [165], $DBP_{0.01}DBPI_{0.99}$ from [169], $BP_{0.06}BPI_{0.94}$ from [162].

In this case, the temperature dependence of P should fulfill the formula [158]:

$$T = T_C - \beta_{cl}P^2 - \gamma_{cl}P^4. \quad (3.8)$$

Copyright © 2010. Nova Science Publishers, Incorporated. All rights reserved.

Handbook of Material Science Research, Nova Science Publishers, Incorporated, 2010. ProQuest Ebook Central,

Table 3.2. Parameters of various models of spontaneous polarization temperature behaviour of BP_xBPI_{1-x} mixed crystals

		Classical state equation		Critical exponent equation
	T_C, K	β_{cl}, Km^4/C^2	γ_{cl}, Km^8/C^4	β_C
BPI from [158]	226.9	5.05×10^4	4.33×10^7	0.47
$BP_{0.03}BPI_{0.97}$	183.6	6.75×10^4	1.13×10^8	0.502
DBPI from [165]	303.58	5.73×10^4	-3.7×10^7	0.53
$DBP_{0.01}DBPI_{0.99}$ from [169]	299	6.61×10^4	2.24×10^7	0.52
$DBP_{0.03}DBPI_{0.97}$	282.53	4.68×10^6	3.02×10^{12}	0.50
$DBP_{0.05}DBPI_{0.95}$	258.41	1.19×10^6	4.34×10^{12}	0.49

The best fit of BP_xBPI_{1-x} crystals data was obtained for parameters presented in Table 3.2. According to the quasi-one-dimensional Ising model the spontaneous polarization can be expressed as follows [158]:

$$P = n_n\mu_d<\sigma_{sp}> = P_0<\sigma_{sp}>, \tag{3.9}$$

where μ_d is the effective dipole moment of the deuterated bond, n_n is the number of dipoles per unit volume, P_0 is the maximum value of spontaneous polarization while all dipoles are oriented in the same direction, $<\sigma_{sp}>$ is the average spin variable given by the self-consisting condition:

$$<\sigma_{sp}>=\frac{\sinh\dfrac{J_\perp<\sigma_{sp}>}{k_BT}}{\left[\sinh^2\dfrac{J_\perp<\sigma_{sp}>}{k_BT}+\exp\left(-\dfrac{4J_\parallel}{k_BT}\right)\right]^{1/2}}. \tag{3.10}$$

For the analysis of the temperature dependence of the spontaneous polarization in the frame of this model, we solved Eq. (3.11) for different temperatures and then corresponding amplitudes (Table 3.1) was found. Figure 3.12 shows also results of these calculations. The small value of P_0 signifies that the density of dipoles, which participate in ferroelectrical ordering processes, is sensitive to BP amount ($P_0 = 2.53$ μC/cm^2 for BPI [158]). According to the quasi-one-dimensional Ising model the transition temperature $T_{C\,\mathrm{Ising}}$ is determined by the condition:

$$k_BT_{C\,\mathrm{Ising}}\exp\left(-\frac{2J_\parallel}{k_BT_{C\,\mathrm{Ising}}}\right)=J_\perp. \tag{3.11}$$

Obtained corresponding temperatures $T_{C\,\mathrm{Ising}}$ are presented in Table 3.1 with the parameters obtained from the best fits. The ratio $J_\parallel/J_\perp$ in protonated mixed crystals strongly

Copyright © 2010. Nova Science Publishers, Incorporated. All rights reserved.

Handbook of Material Science Research, Nova Science Publishers, Incorporated, 2010. ProQuest Ebook Central,

increase with increasing the betaine phosphate concentration, in deuterated crystals this dependence is less expressed. However, in both cases the quasi-one-dimensional Ising model on increasing the betaine phosphate concentration becomes invalid. The mismatch with the real phase transition temperature T_C - $T_{C\,\mathrm{Ising}}$ is small only at BP concentration ≤ 0.03 and shows that the phase transition under investigation is not purely a second order phase transition. At higher betaine phosphate concentration (0.05 and more) we can not describe with the Ising model formulas together all dependencies: $P(T)$, $\Delta\varepsilon(T)$ and ν (T), because mismatch between T_C - $T_{C\,\mathrm{Ising}}$ become significant. This becomes understandable from the later presented experimental results that the spontaneous polarization shows a remarkable distribution for concentration of betaine phosphite at ≥ 0.03. The quasi-one-dimensional Ising model presupposes homogeneity and cannot describe non-homogeneous ferroelectrics. However in nature crystals (including ferroelectrics and the same "pure" betaine phosphite) without impurities not exist. A fundamental query is what must be concentration of impurities that discrepancy from the quasi-one-dimensional Ising behaviour becomes significant and essential. In the case of betaine phosphate the answer is 5 %.

Figure 3.13 presents the temperature dependence of the spontaneous polarization as a log-log plot. The various values of critical exponent was obtained (Table 3.2), this parameter of deuterated compounds strongly decreases with increasing of betaine phosphate concentration.

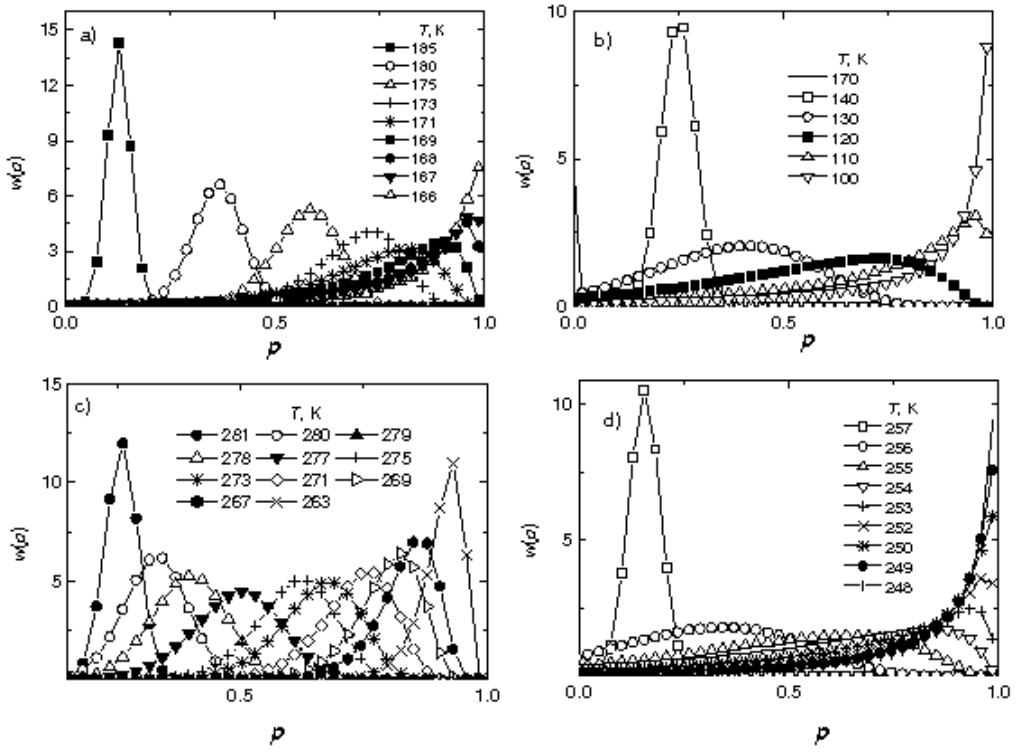


Figure 3.14. Distribution of local polarizations $w(p)$ of mixed BP_xBPI_{1-x} crystals: a) $BP_{0.03}BPI_{0.97}$, b) $BP_{0.06}BPI_{0.94}$, c) $DBP_{0.03}DBPI_{0.97}$ d) $DBP_{0.05}DBPI_{0.95}$ at several temperatures. Points are guide for eye.

Copyright © 2010. Nova Science Publishers, Incorporated. All rights reserved.

Handbook of Material Science Research, Nova Science Publishers, Incorporated, 2010. ProQuest Ebook Central,

From the distribution function $w(A)$ of the local potential asymmetry the distribution function $w(p)$ of the local polarization of the hydrogen bonds can be deduced:

$$w(p) = \frac{2k_B T}{\sqrt{2\pi}\sigma_A(1-p^2)} \exp[-\frac{[a\tanh(p) - a\tanh(p_0)]}{2\sigma_A^2/(2k_B T)^2}], \tag{3.12}$$

which transforms in the form known for the RBRF (see Subsection 1.2.3) [168] model when substituting:

$$\sigma_A = 2\bar{J}\sqrt{q_{EA} + \Delta f}\,, \tag{3.13}$$

and

$$A_0 = 2\Delta J\bar{p}\,. \tag{3.14}$$

Here $\bar{p}$ is the average polarization. The calculated distribution functions $w(p)$ of the local polarization are presented in Figure 3.14. As we can see, they behave exactly as expected for an inhomogeneous ferroelectric [170].

Knowing the distribution function $w(p)$, both the average (macroscopic) polarization can be calculated. The calculated average polarization values are presented in Figure 3.12. At is possible to see the calculated average polarization is the best fit for experimental results. We can conclude, that the extraction of continuous relaxation times distribution of the Debye fundamental processes directly from the broadband dielectric spectra allows better understanding dynamic phenomena in betaine phosphite crystals with a small admixture of the betaine phosphate.

$$\bar{p} = \int_{-1}^{1} pw(p)dp\,, \tag{3.15}$$

and the Edwards-Anderson glass order parameter

$$q_{EA} = \int_{-1}^{1} p^2 w(p)dp \tag{3.16}$$

3.1.3. Coexistence of Ferroelectric Order and Dipolar Glass Disorder

At temperatures much lower than T_C, the dielectric dispersion effects can be observed in the low-frequency dielectric response of the betaine phosphite with a small admixture of betaine phosphate (Figure 3.15). The same effect has been observed in pure BPI [171] and DBPI [165]. The main difference with the pure BPI is a local maximum of ε'' in the ferroelectric phase.

Copyright © 2010. Nova Science Publishers, Incorporated. All rights reserved.

Handbook of Material Science Research, Nova Science Publishers, Incorporated, 2010. ProQuest Ebook Central,

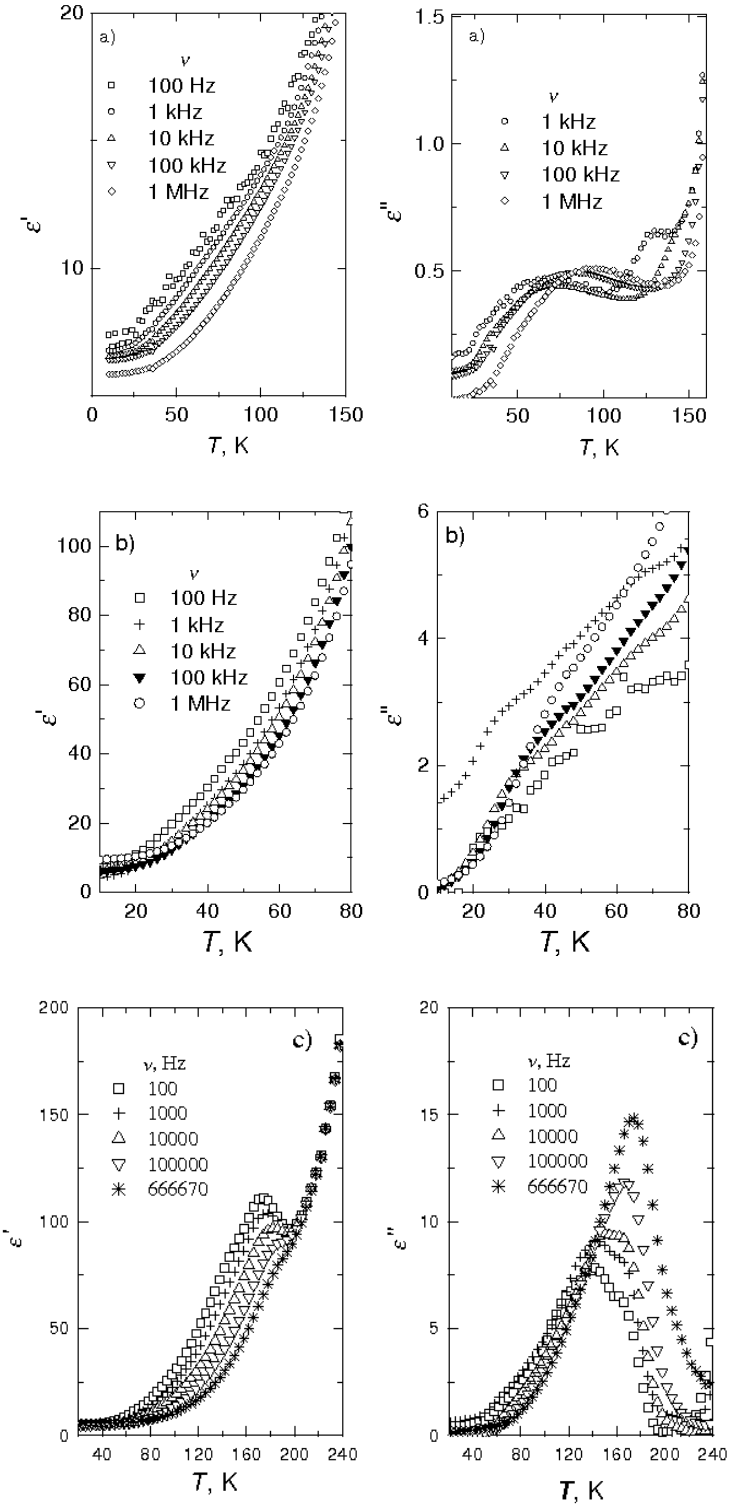
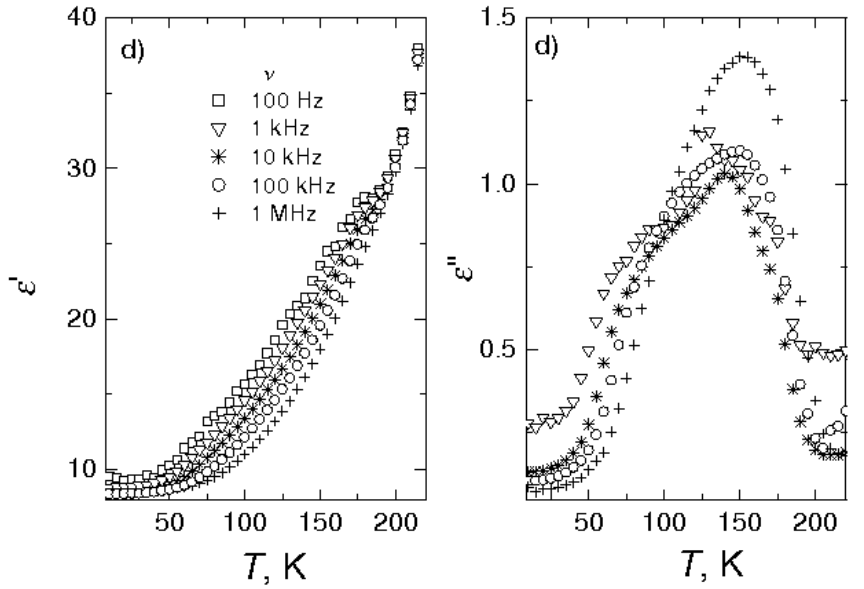


Figure 3.15 Continues.

Copyright © 2010. Nova Science Publishers, Incorporated. All rights reserved.

Handbook of Material Science Research, Nova Science Publishers, Incorporated, 2010. ProQuest Ebook Central,



Reprinted figures with permission from [175]. Copyright 1998 by the IOP publishing Ltd.

Figure 3.15. Temperature dependences of complex dielectric permittivity ε^* of mixed BP_xBPI_{1-x} crystals: a) $BP_{0.03}BPI_{0.97}$, b) $BP_{0.06}BPI_{0.94}$, c) $DBP_{0.03}DBPI_{0.97}$ d) $DBP_{0.05}DBPI_{0.95}$ at the different frequencies in the low temperature region.

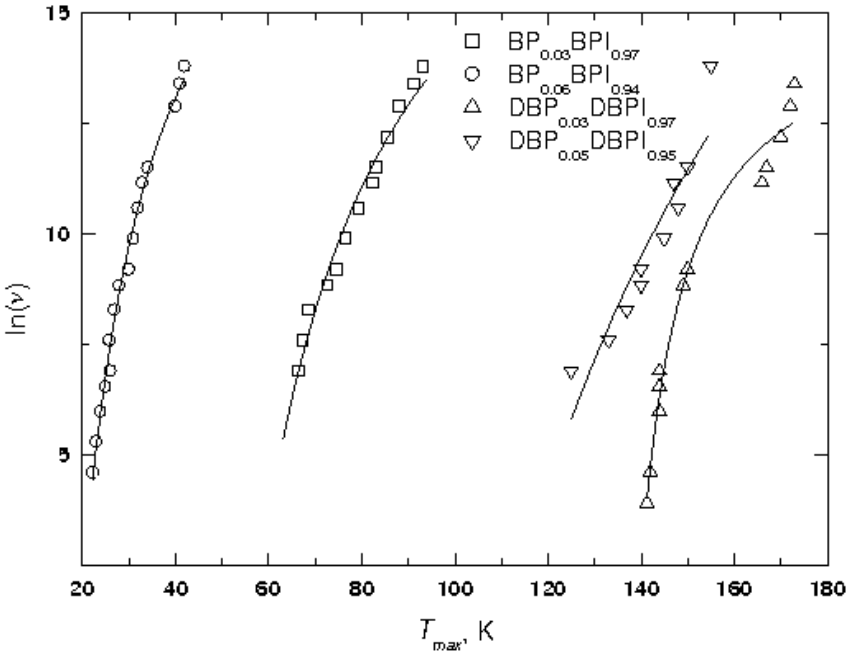


Figure 3.16. The measured frequencies ν versus T_m.

Copyright © 2010. Nova Science Publishers, Incorporated. All rights reserved.

Handbook of Material Science Research, Nova Science Publishers, Incorporated, 2010. ProQuest Ebook Central,

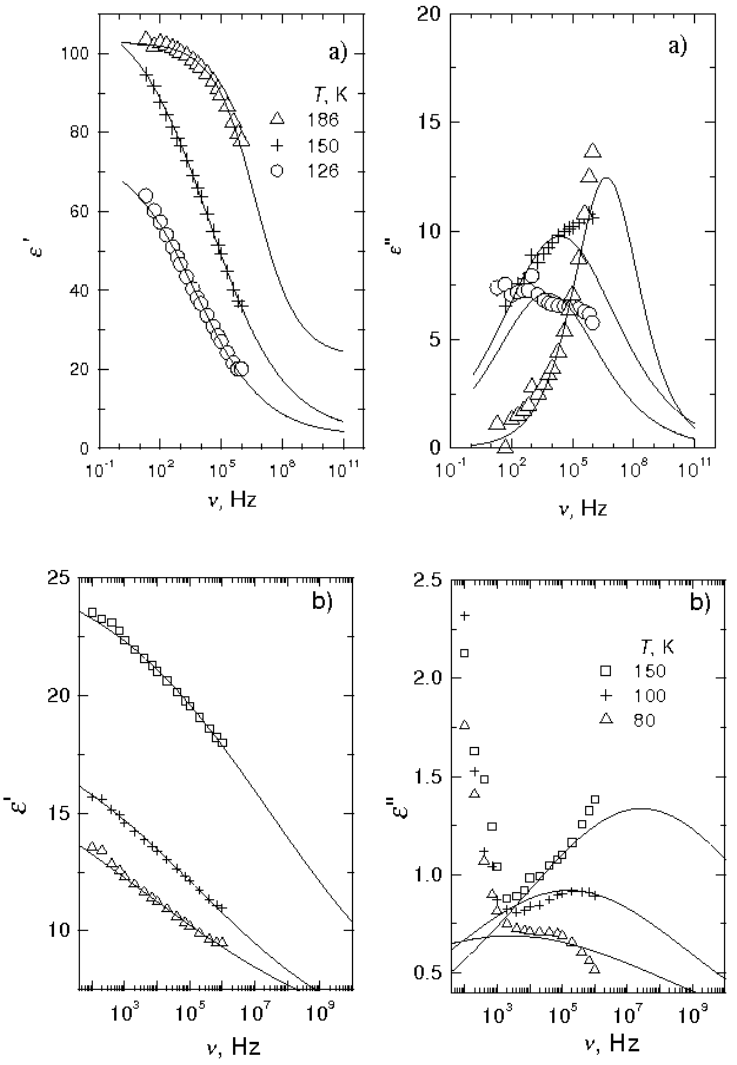


Figure 3.17. Frequency dependence of complex dielectric permittivity ε^* of mixed DBP_xDBPI_{1-x} crystals: a) $DBP_{0.03}DBPI_{0.97}$ and b) $DBP_{0.05}DBPI_{0.95}$ at several temperatures in the region of the dipolar glass phase transition.

This local maximum value of ε'' decreases with increasing frequency. This behaviour have been described by the Vogel-Fulcher relationship [172]:

$$\nu = \nu_0 e^{-\frac{E_t}{k_B(T_m - T_{0t})}}, \tag{3.17}$$

where T_m is the temperature at which the measured imaginary part of dielectric permittivity ε'' passes through a maximum, ν_0 is the frequency approached with $T_m \to \infty$; E_t is the activation energy, T_{0t} is the freezing temperature.

The best fit of ν with the Vogel-Fulcher equation is shown as a solid line in Figure 3.16. Obtained parameters are presented in Table 3.3.

Copyright © 2010. Nova Science Publishers, Incorporated. All rights reserved.

Handbook of Material Science Research, Nova Science Publishers, Incorporated, 2010. ProQuest Ebook Central,

Table 3.3. Parameters of Vogel-Fulcher law (3.17) of BP_xBPI_{1-x} ferroelectrics

	v_0, GHz	E_t/k_B, K (eV)	T_{0t}, K
$BP_{0.03}BPI_{0.97}$	7.33	558 (0.048)	30
$BP_{0.06}BPI_{0.94}$	2.12	293 (0.025)	5
$DBP_{0.03}DBPI_{0.97}$	0.004	118 (0.01)	130
$DBP_{0.05}DBPI_{0.95}$	0.59	537 (0.046)	25

Table 3.4. Parameters of the Vogel-Fulcher law (3.18) of DBP_xDBPI_{1-x} ferroelectrics

	τ_0, s	E_f, K (eV)	T_0, K
$DBP_{0.03}DBPI_{0.97}$	3.43×10^{-12}	1297 (0.112)	73
$DBP_{0.05}DBPI_{0.95}$	1.87×10^{-12}	1015 (0.088)	25

The frequency dependence of ε′ and ε″ in several temperatures provide clear evidence that the ε″ frequency dependence is much broader than 1.14 decades as it should be for the Debye-type dispersion (Figure 3.17).

This indicates a very wide distribution of the relaxation times. The freezing phenomena in betaine phosphite with a small admixture betaine phosphate reveal the characteristics of a transition into a dipolar glass state: the slowing down of the dipolar degrees of freedom exhibits a broad distribution of the relaxation rates, with the width of the distribution exceeding by orders of magnitude the width of a monodispersive Debye process.

The experimental data of deuterated compounds were fitted with the same Cole–Cole function (solid lines in Figure 3.17). Because the dielectric dispersion of protonated compounds is extremely broad, calculating of any parameters cannot be fulfilled. The temperature dependence of the fit parameters α_{cc}, $\Delta\varepsilon$, τ_{cc} and $\varepsilon_{\infty r}$ (only in the case of $DBP_{0.05}DBPI_{0.95}$ crystals the value $\varepsilon_{\infty r}$=4.38 is not vary with temperatures) are shown in Figure 3.18. The relaxation time distribution parameter α_{CC} increases intensively with decreasing temperature in the region 210 to 180 K, and fluctuates around a mean value of 0.75 for $DBP_{0.03}DBPI_{0.97}$ crystals and 0.85 for $DBP_{0.05}DBPI_{0.95}$ crystals below 170 K. This means an extremely broad distribution of relaxation times (the corresponded dielectric dispersion is much broader as our measurement frequency range). Two maxima in the temperature dependence of relaxator strength of $DBP_{0.03}DBPI_{0.97}$ crystals (at 170 and 150 K) indicate the complicated dynamics of the deuteron subsystem in these crystals. The mean relaxation time diverge according to the Vogel-Fulcher law [173]:

$$\tau = \tau_0 e^{\frac{E_f}{k_B(T-T_0)}}, \tag{3.18}$$

and obtained parameters are presented in Table 3.4.

In the case of $DBP_{0.05}DBPI_{0.95}$ crystals both freezing temperatures T_0 and T_{0t} are the same, however in the case of $DBP_{0.05}DBPI_{0.95}$ crystals $T_{0t} > T_0$, this is caused by calculating errors and in fact these both freezing temperatures can be not the same if the freezing dynamics is complicated enough. To extract the freezing temperature is another way [174].

Copyright © 2010. Nova Science Publishers, Incorporated. All rights reserved.

Handbook of Material Science Research, Nova Science Publishers, Incorporated, 2010. ProQuest Ebook Central,

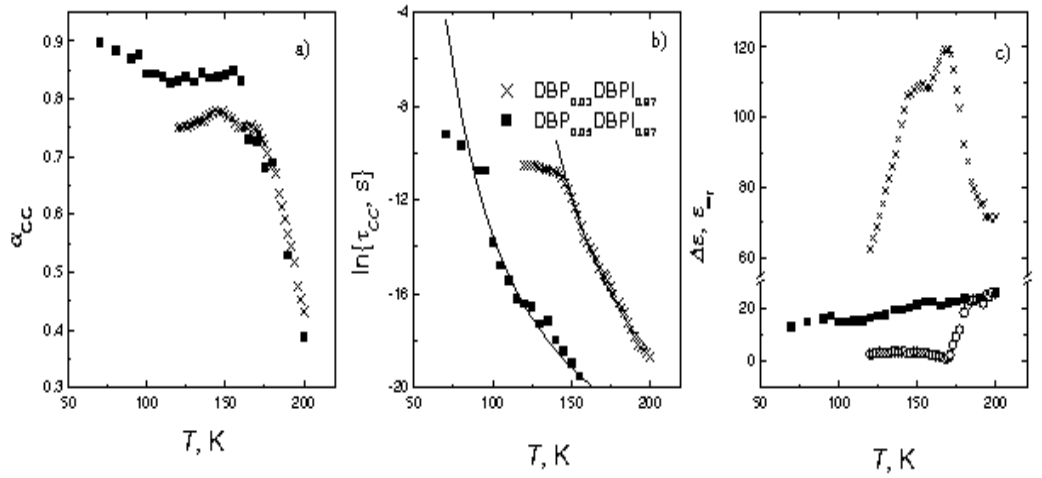


Figure 3.18. Temperature dependences of the low-temperature relaxation fit parameters α_{cc} a), $\Delta\varepsilon$ (b) and τ_{cc} (c).

Further we will briefly describe this method of Z. Kutnjak and write several critical remarks about it. In first step, a reduced dielectric permittivity is defined as

$$\delta_\delta = \frac{\varepsilon'(\nu,T) - \varepsilon_{r\infty}}{\varepsilon'(0,T) - \varepsilon_{r\infty}}. \tag{3.19}$$

Again, an assumption is made that the distribution of the relaxation times f (τ) is limited between lower and upper cutoffs τ_1 and τ_2. For each fixed value of δ_δ must be obtained a characteristic temperature-frequency profile in the (T, ν) plane. In the second step, the dependence ν (T) must be analyzed by Eq. (3.17). Obtained parameter T_{0K} is the temperature, as the static (non-dependent from frequency) dielectric permittivity is observed only at ν = 0. This parameter is the same freezing temperature T_0. However, no information about distribution function f (τ) and it temperature dependence this method provide, except freezing temperature. Therefore, such analysis, as in [175] gives not much information about the freezing dynamics.

We can conclude that, similarly to DRADA [176] crystals, also BP_xBPI_{1-x} and DBP_xDBPI_{1-x}crystals exhibit a phase with coexisting ferroelectric and dipolar glass order at lower temperatures, where part of protons (or deuterons) is frozen–in along the one–dimensional chains.

3.2. $BP_{1-x}BPI_x$ – An Unusual Dipolar Glass

3.2.1 Introduction

The middle part of the phase diagram of $BP_{1-x}BPI_x$ [160, 162, 177-179] (0.9 > x > 0.3) which was known until now is characterized by a glassy behaviour at low temperatures. Dielectric measurements [160,177-180] revealed proton glass behaviour for x = 0.85, 0.80, 0.60, 0.50, and 0.40. Very recently, a systematic study of the dielectric properties of

Copyright © 2010. Nova Science Publishers, Incorporated. All rights reserved.

Handbook of Material Science Research, Nova Science Publishers, Incorporated, 2010. ProQuest Ebook Central,

compounds of the series $(BP)_{1-x}(BPI)_x$ was presented [179] in the paraelectric phase, and compared with the predictions of three microscopic models: the quasi-one-dimensional Ising model without disorder [181-183], the Sherrington-Kirkpatrick model [14] and the quasi-one-dimensional random-bond random-field Ising model [15]. From the analysis of the static permittivity, parameters were determined characterizing the dipolar interactions and the random electric fields in these systems. Only in one of the compounds with the lowest admixture of the betaine phosphite x = 0.15 a behaviour consistent with a quasi one-dimensional glass phase was found. There was no evidence of the quasi-one-dimensional behaviour for compounds with a higher concentration of BPI except for nearly pure ferroelectric BPI. In fact, the other compounds with a glass phase were rather well fitted by the three-dimensional RBRF Ising model with the inclusion of random fields. In these compounds, the random fields are of greater importance than the random bonds. It was suspected that substitutional disorder leads to a more isotropic dielectric behaviour where interchain and intrachain couplings are similar in magnitude. The Almeida-Thouless temperatures were estimated for all the compounds with a glass phase and found to be close to the temperature where the real part of the low-frequency dielectric permittivity has its maximum.

Magnetic resonance proved to be one of the most appropriate techniques for the study of local proton or deuteron order and dynamics [184-187]. Deuteron glasses were carefully analyzed by deuteron NMR (nuclear magnetic resonance) where the local deuteron order is monitored by the nuclear quadrupole coupling. However, there is no direct study of the proton order in a proton glass by H^1 NMR up to now because it is difficult to resolve local proton order from the chemical shift data.

Recently authors of references [184-187] reported on direct studies of the local proton order by means of high-resolution ESR (electron spin resonance) measurements as CW and pulsed ENDOR (electron nuclear double resonance), ESE (electron spin echo) and ESEEM (electron spin echo envelope modulation) on the PO_3^{2-} paramagnetic probe in the γ-irradiated proton glasses $BP_{0.15}$ $BPI_{0.85}$ and $BP_{0.40}$ $BPI_{0.60}$. Hydrogen bonds link the phosphite and phosphate groups to the quasi one-dimensional chains along the crystallographic b-direction. The authors of references [186] showed that the protons in these bonds order glasslike. The ENDOR line shape of these protons is a direct mirror of the local polarization distribution $w(p)$. This allows a very detailed comparison with the theoretical models such as the one- and three-dimensional random-bond random-field Ising glass model because for one given temperature one has not only one single measuring point as for the static permittivity but an entire order parameter distribution curve. The experimental Edwards-Anderson glass order parameter obtained as the second moment of $w(p)$ showed a temperature dependence that is characteristic for a proton glass with the strong random fields. The random bond parameters $\Delta J / k_B = 30$ K and 25 K, respectively, for x = 0.85 and x = 0.60 were taken in accordance to glass temperatures T_G indicated by dielectric results. The unusual strong random fields represented by $\sqrt{\Delta} f / k_B = 79$ K and 103 K, respectively, reflect the relatively strong distortions of the proton double well potentials in the hydrogen bonds adjacent to substituted phosphate sites.

Also the stable inorganic PO_3^{2-} radical, studied in the several solid solutions of $BP_{1-x}BPI_x$ with ESR techniques, is created only at the HPO_3 but not at the PO_4 fragments. Consequently, the ESR experiment in the mixed crystals can be performed only at the HPO_3 sites. On the

Copyright © 2010. Nova Science Publishers, Incorporated. All rights reserved.

Handbook of Material Science Research, Nova Science Publishers, Incorporated, 2010. ProQuest Ebook Central,

other hand, beyond all doubt, the authors of reference [185] may presuppose from experiences in pure betaine phosphite that measurements of the PO_3^{2-} probe give really representative evidence of the proton configuration at HPO_3 sites without noticeable distortions due to the radical formation. Therefore, in the phosphite-rich compositions of $BP_{1-x}BPI_x$, where the phosphate units may be understood as substitutional defects, the measured proton configurations at the PO_3^{2-} probe are more or less representative for the general proton behaviour. In the phosphate-rich $BP_{1-x}BPI_x$ compositions, however, the statistically incorporated HPO_3 fragments have to be considered as substitutional defects, which create internal stochastic electric fields. From ENDOR studies of the PO_3^{2-} paramagnetic probe on the phosphate-rich side of the $BP_{1-x}BPI_x$ solid solution we got experimental evidence that the protons in the hydrogen bonds of a PO_4 - HPO_3 - PO_4 segment see an asymmetric double well potential which is a demonstration of the polar defect character of this segment. The polarity of the defect segment along the b-direction depends on which left or right side of the zigzag chain the HPO_3 defect is incorporated. It is of importance that the polarity can change under the influence of an ordering field. The same conclusion may be drawn for a PO_4 – defect in a HPO_3 chain.

The correspondence of the experimental order parameter distribution function with the simulations could considerably be improved if a non-zero mean $\bar{J}/k_B = 160K$ and 212 K of the random bond interaction and a tunneling energy Ω/k_B =250 K, respectively, were considered in the three-dimensional RBRF Ising model. Additionally, in order to obtain a better agreement with the experimental $W(p)$ behaviour the variance of the random fields had to be reduced from $\sqrt{\Delta f}/k_B = 79$ K and 103 K at temperatures above $\bar{J}/k_B$ to values $\sqrt{\Delta f}/k_B$=60 K and 61 K below $\bar{J}/k_B$. This reduction of the random field magnitude is caused by the reorientation of the polar defect units under the influence of an ordering field as mentioned above.

At T_0 =144 K and 160 K, far above the glass transition temperature, the results indicate a smeared transition into a phase with a mean long-range order in the proton chains but with strong fluctuations of the local order parameters. This additional phase transition is also reflected in a temperature anomaly of the electron spin-lattice relaxation indicating a singular anomaly in the phonon system [188-190]. It was shown that the infrared active optical mode at 560 cm^{-1} experiences a critical damping by interacting with a critical soft mode related to the mentioned transition. This ENDOR and electron spin-lattice relaxation results were recently confirmed by infrared measurements [190]. Both the measurements show that the transition is not of local but of collective nature. Consequently, one comes to the conclusion that for the solid solutions $BP_{1-x}BPI_x$ with compositions x = 0.05, 0.15, 0.30, 0.60, 0.85, 0.94 an intermediate phase exists between the antiferrodistortive paraelectric phase and the orientational glass phase. This new phase shows a regular proton order within the phosphate-phosphite chains and is supposed to be of quasiferroic or cluster like nature. Though there are indications to a proton glass behaviour, the local measurements showed that the system is more complex. It experiences transitions from a high-temperature non-polar, non-ferroelastic phase to a paraelectric antiferrodistortive phase, followed by an intermediate phase with a long-range proton order before the system becomes glasslike with respect to the proton order.

Very recently the dielectric permittivity measurements of $BP_{0.15}BPI_{0.85}$ in a wide frequency spectrum were published and presented a new type of data analysis [132]. Solving

Copyright © 2010. Nova Science Publishers, Incorporated. All rights reserved.

Handbook of Material Science Research, Nova Science Publishers, Incorporated, 2010. ProQuest Ebook Central,

the integral equation for the permittivity with the Tikhonov regularization technique, this method allows extracting the distribution of the relaxation times and resolves multiple dynamical processes. The dielectric relaxation spectrum is described in terms of an ensemble of the Debye processes with a continuous relaxation time distribution f (τ). Having obtained f (τ) one can then seek a physical interpretation in the τ domain rather than in the frequency domain. The dipole-freezing phenomena result in a broad asymmetrical distribution of the relaxation times. The authors of [132] demonstrated that the parameters of the double-well potentials of the hydrogen bonds, the local polarization distribution function and the glass order parameter can be extracted from the dielectric measurements.

It will be demonstrated that besides magnetic resonance techniques the dielectric spectroscopy coupled with the data analysis presented above is another appropriate tool to determine microscopic glass parameters. Because there do not exist peculiarities as such with the magnetic resonance line shape for short relaxation times, the dielectric spectroscopy gives interesting results for low temperatures, especially. The measurements give further indications for a special kind of an intermediate phase between the paraelectric and glassy state for a wider range of compositions as already concluded from ENDOR and electron spin-lattice time measurements [184-190]. Dielectric spectroscopy gives the new interesting result that the non-zero mean value of the random bond interaction $\bar{J}/k_B$ vanishes for very low temperatures. One can suspect that it is related with the real glass transition into the low-temperature non-ergodic glassy phase.

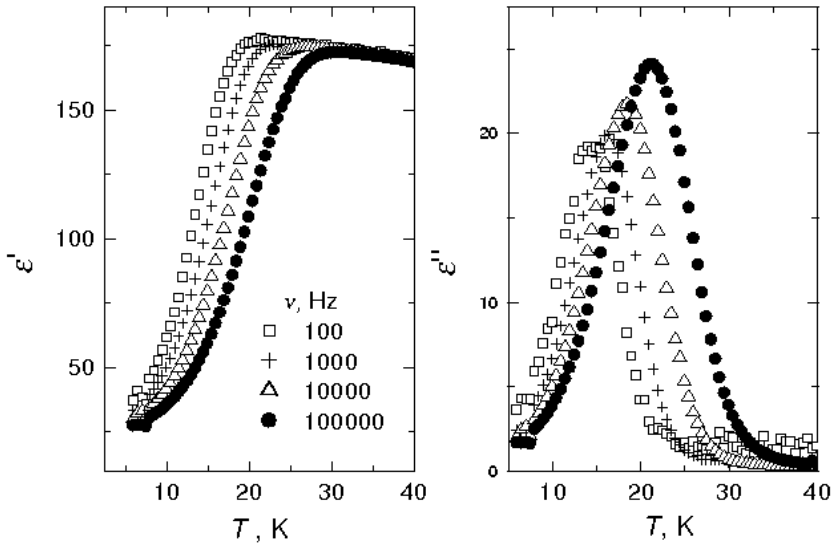
3.2.2. Comparison of the Results with the Dipolar Glass Model

For all mixed crystals under study no anomaly in ε' indicating a polar phase transition can be detected down to the lowest temperatures (Figure 3.19). In the temperature region below 100 K the dispersion effects dominate the dielectric response in the frequency range under study. The temperature behaviour of ε' and ε'' seems to be typical for glasses: with decreasing measurement frequency the maximum of ε' shifts to lower temperatures followed by the maximum of ε''. At fixed temperatures the frequency dependence of ε' and ε'' provides clear evidence that the frequency dependence of ε'' is much broader than for the Debye dispersion (Figure 3.20).

As it is possible to see from experiments, of the relaxation times distribution is over three decades, especially at low temperatures. Each one of the traditional models is strictly fixed with respect to the shape of the relaxation-time distribution function. The Cole-Cole formula assumes symmetrically shaped distribution of the relaxation times, but the real distribution function can be different from this. In order to get information that is more precise about the real relaxation-time distribution function, a special approach has been developed. The distribution of relaxation times of BP\BPI dipolar glass has been calculated from dielectric spectra according to formulas (1.41) and (1.42) and method described in Section 2.6. We considered the value of α_R = 4 as the best one for our experiment. The relaxation time distributions of the mixed crystals under study calculated from the experimental dielectric spectra at different temperatures are presented in Figure 3.21 as points. The relaxation-time distribution significantly broadens at low temperatures, as it is typical for dipolar glasses. On cooling the distribution of relaxation times become more asymmetric.

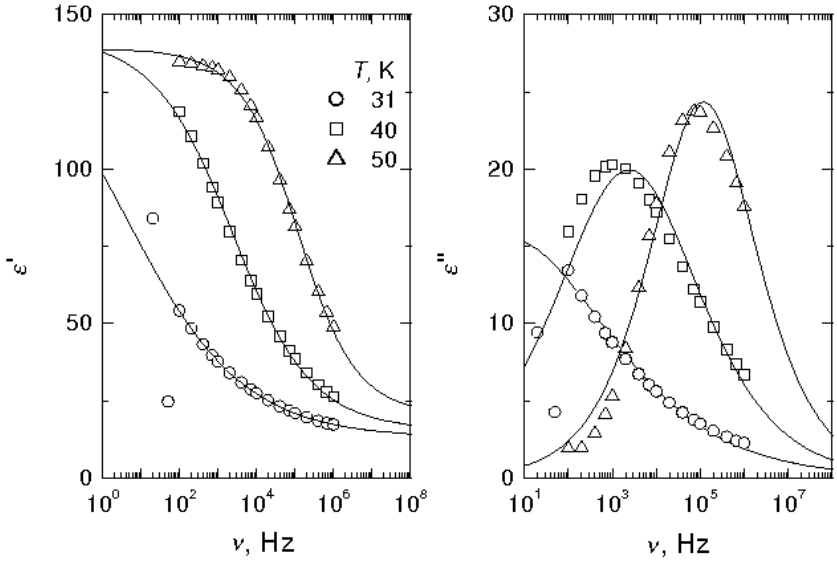
Copyright © 2010. Nova Science Publishers, Incorporated. All rights reserved.

Handbook of Material Science Research, Nova Science Publishers, Incorporated, 2010. ProQuest Ebook Central,



Reprinted figure with permission from [191]. Copyright 2006 by the American Physical Society.

Figure 3.19. Temperature dependence of complex dielectric permittivity of $BP_{0.3}BPI_{0.7}$ crystals.



Reprinted figure with permission from [191]. Copyright 2006 by the American Physical Society.

Figure 3.20. Frequency dependence of complex dielectric permittivity of $DBP_{0.3}DBPI_{0.7}$ crystals.

For dipolar glasses, it is usually assumed that the proton motion in the double well O-H···O potentials is randomly frozen-out at low temperatures, implying a static quenched disorder [174]. But due to the ''built-in'' disorder, always present in the off-stoichiometric solid solutions, there are a variety of environments for the O-H···O bonds. This leads to a distribution of the microscopic parameters of the bonds and, consequently, a distribution of dynamic properties such as the dipolar relaxation times when quenching takes place.

Copyright © 2010. Nova Science Publishers, Incorporated. All rights reserved.

Handbook of Material Science Research, Nova Science Publishers, Incorporated, 2010. ProQuest Ebook Central,

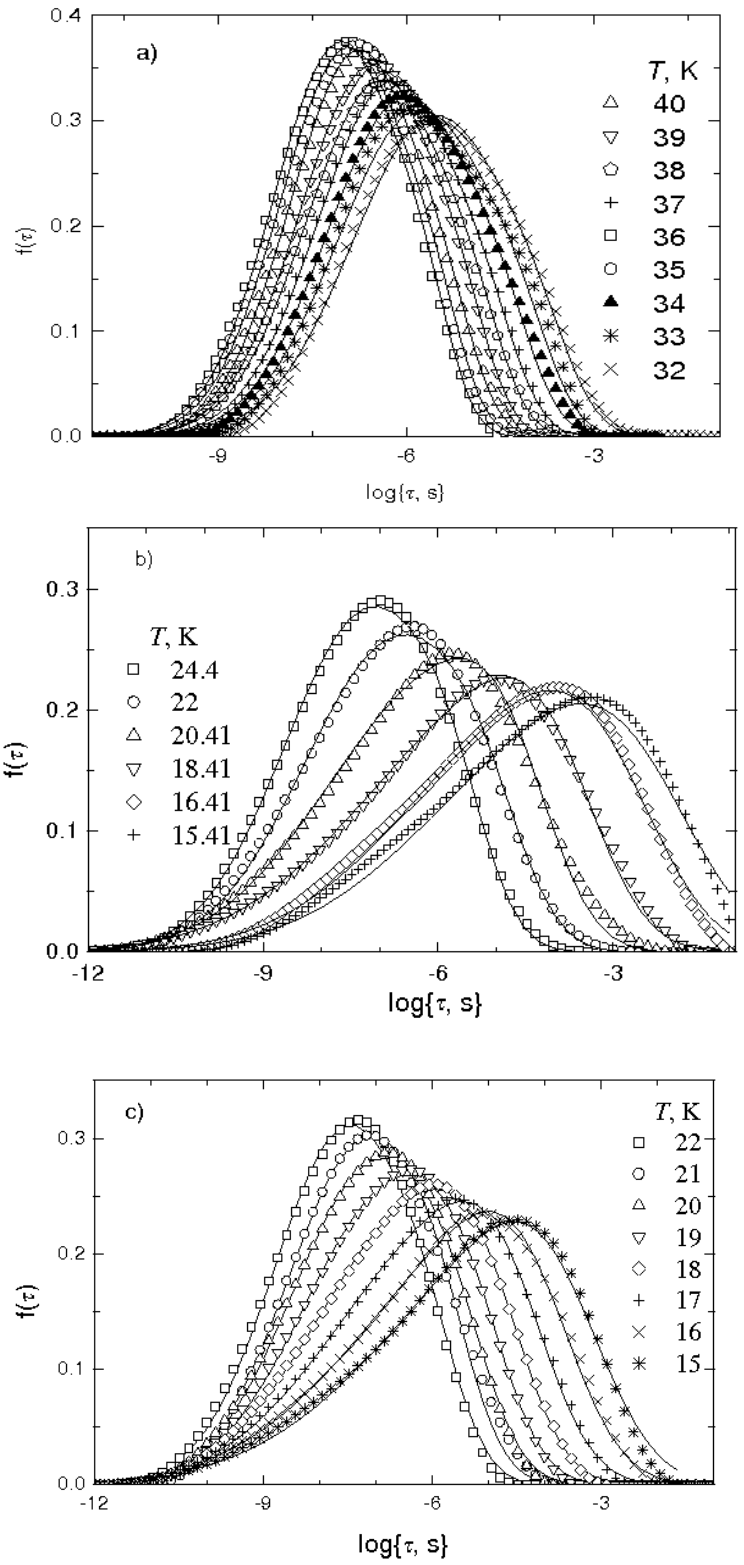
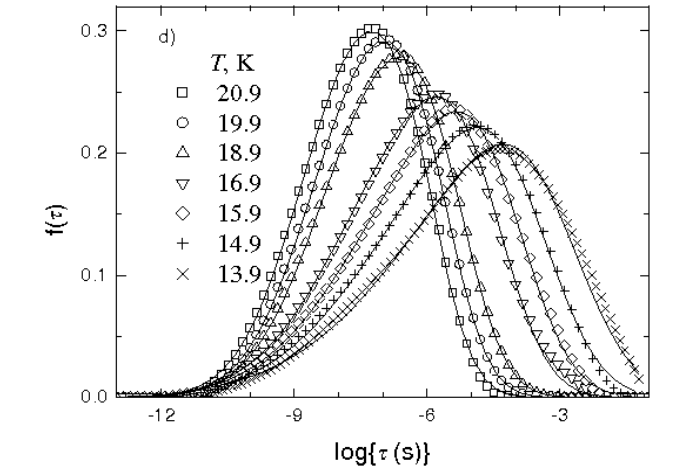
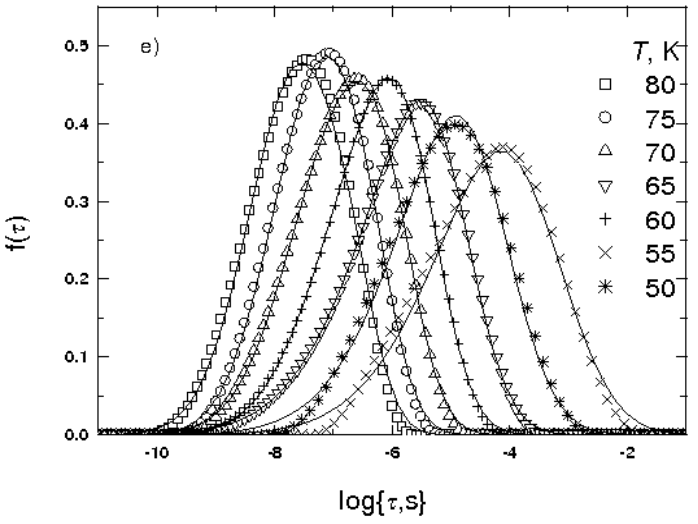


Figure 3.21 Continues.

Copyright © 2010. Nova Science Publishers, Incorporated. All rights reserved.

Handbook of Material Science Research, Nova Science Publishers, Incorporated, 2010. ProQuest Ebook Central,





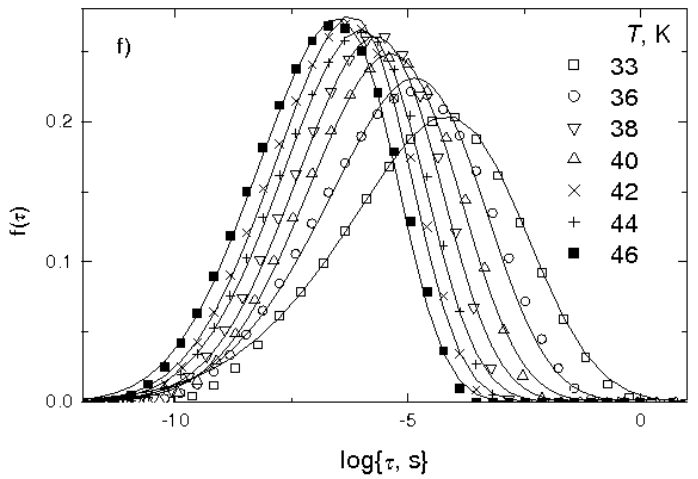
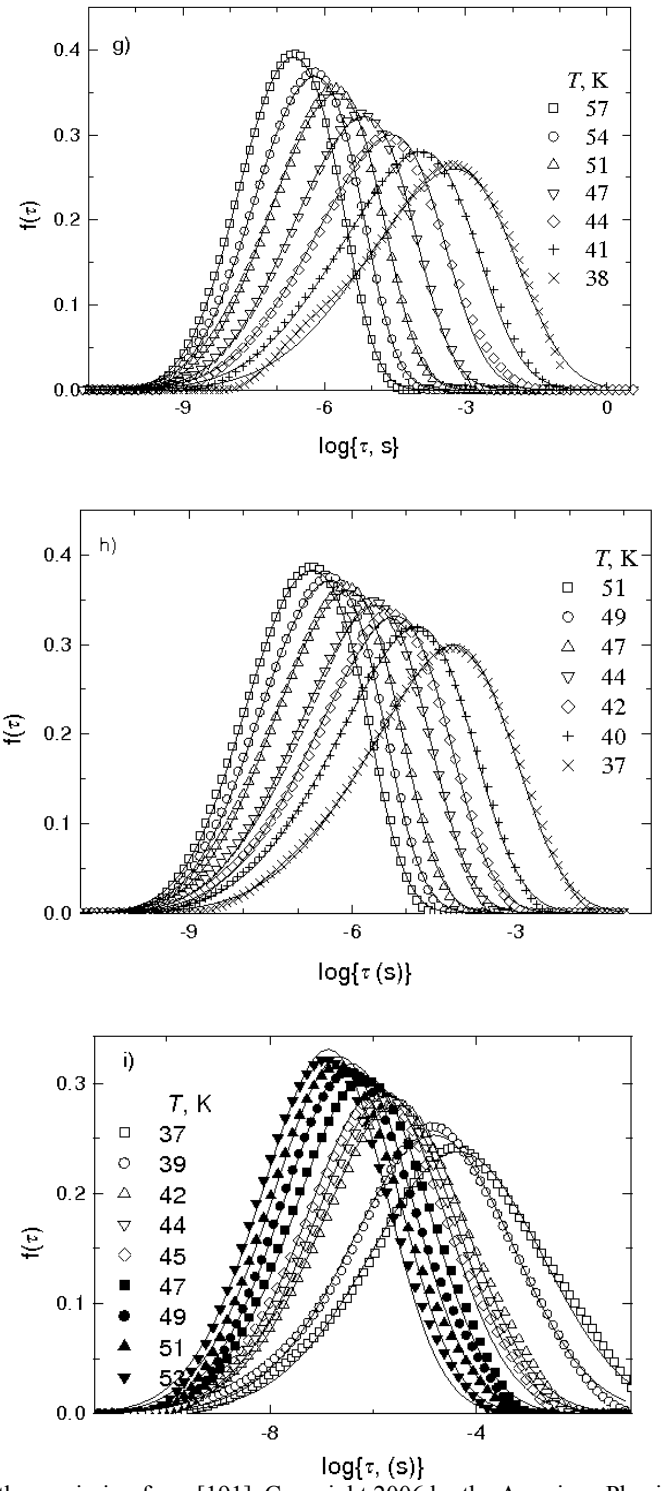


Figure 3.21 Continues.

Copyright © 2010. Nova Science Publishers, Incorporated. All rights reserved.

Handbook of Material Science Research, Nova Science Publishers, Incorporated, 2010. ProQuest Ebook Central,

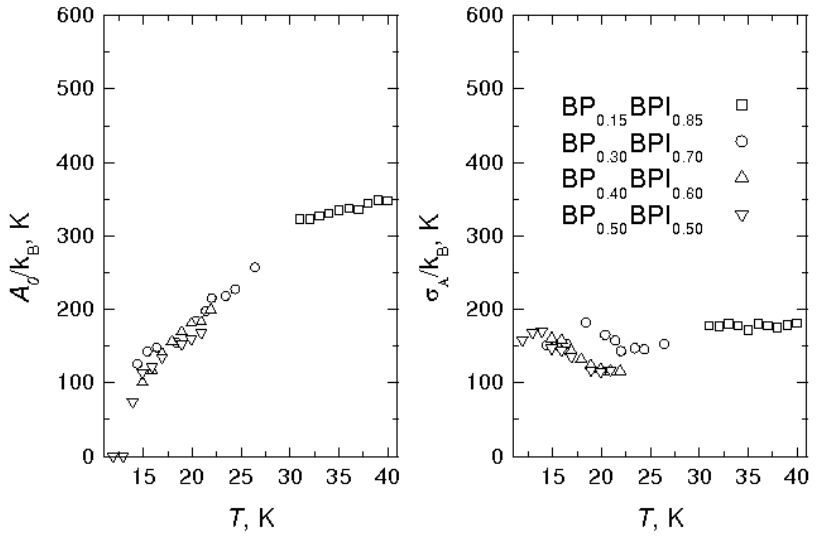


Reprinted figure with permission from [191]. Copyright 2006 by the American Physical Society.

Figure 3.21. Distribution of relaxation times of betaine phosphate betaine phosphite dipolar glasses: a) $BP_{0.15}BP_{0.85}$ b) $BP_{0.3}BPI_{0.7}$, c) $BP_{0.4}BPI_{0.6}$, d) $BP_{0.5}BPI_{0.5}$, e) $DBP_{0.15}DBP_{0.85}$, f) $DBP_{0.25}DBPI_{0.75}$, g) $DBP_{0.3}DBPI_{0.7}$, h) $DBP_{0.4}DBP_{0.6}$, i) $DBP_{0.5}DBPI_{0.5}$.

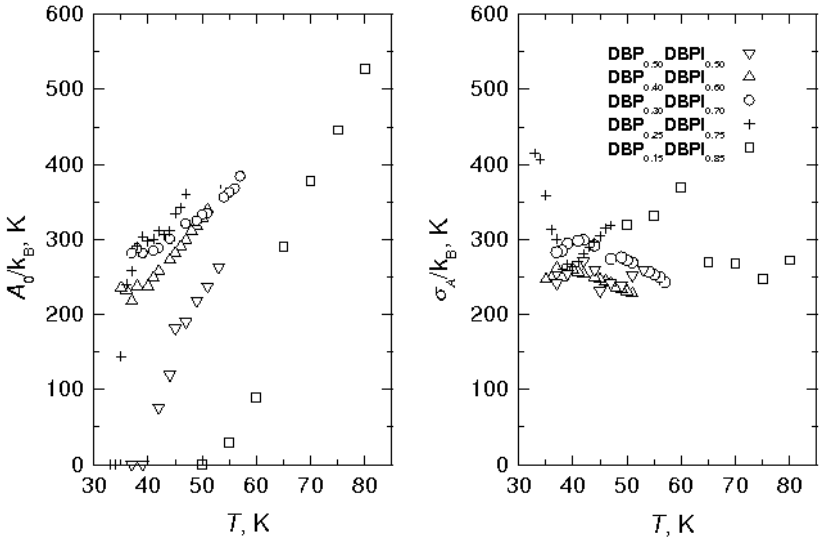
Copyright © 2010. Nova Science Publishers, Incorporated. All rights reserved.

Handbook of Material Science Research, Nova Science Publishers, Incorporated, 2010. ProQuest Ebook Central,



Reprinted figure with permission from [191]. Copyright 2006 by the American Physical Society.

Figure 3.22. Temperature dependencies of the average local potential asymmetry A_0 and the standard deviation σ_A of protonated crystals.



Reprinted figure with permission from [191]. Copyright 2006 by the American Physical Society.

Figure 3.23. Temperature dependencies of the average local potential asymmetry A_0 and the standard deviation σ_A of deuterated crystals.

Fits with the experimentally obtained relaxation-time distributions shown in Figure 3. 21 were performed simultaneously for all the considered temperatures. For one given crystal, only one parameter set τ_0, T_0, E_{b0}/k_B, and σ_E/k_B shown in Tables 3.5 and 3.6 was used for all the temperatures, whereas A_0 and σ_A appeared to be temperature dependent. The fit results are presented in Figure 3.21 as solid lines. The temperature dependencies of the average local potential asymmetry A_0 and the standard deviation σ_A are shown in Figs. 3.22 and 3.23.

Copyright © 2010. Nova Science Publishers, Incorporated. All rights reserved.

Handbook of Material Science Research, Nova Science Publishers, Incorporated, 2010. ProQuest Ebook Central,

Table 3.5. Parameters τ_0, T_0, E_b, σ_{Eb} for different protonated BP_xBPI_{1-x} crystals

x	τ_0, s	T_0, K	E_{b0}/k_B, K	σ_{Eb}/k_B, K
0.15	$5.5*10^{-12}$	5	490.9	32.5
0.3	$3.1*10^{-10}$	3.8	205.3	28.9
0.4	$1.7*10^{-10}$	2.6	187.5	26.5
0.5	$1.3*10^{-11}$	1.7	228.2	31.5

Reprinted table with permission from [191]. Copyright 2006 by the American Physical Society.

Table 3.6. Parameters τ_0, T_0, E_{b0}, σ_{Eb} for different deuterated DBP_xDBPI_{1-x} crystals

x	τ_0, s	T_0, K	E_{b0}/k_B, K	σ_{Eb}/k_B
0.15	$1*10^{-9}$	20.5	390.4	55.4
0.25	$9.6*10^{-11}$	8.1	425.2	72.6
0.3	$2.9*10^{-11}$	9.6	568	57
0.4	$5.1*10^{-11}$	9.8	459	49.6
0.5	$2.3*10^{-10}$	12.2	360.1	84.3

Reprinted table with permission from [191]. Copyright 2006 by the American Physical Society.

The temperature dependence of the widths σ_A of the random asymmetry distribution of the local potentials is rather weak in the temperature range under study. However, in contradiction to usual proton glasses the average asymmetry A_0 of the local potentials of the hydrogen bonds is nonzero and remarkably temperature dependent. At the upper end of the studied temperature region, the average asymmetry A_0 is clearly larger than the widths σ_A of the random asymmetry distribution. At lower temperatures, A_0 becomes smaller than σ_A, but A_0 does disappear only for very low temperatures. This behaviour is quite surprising and has not yet been observed for other dipolar glasses.

With former electron-nuclear double resonance (ENDOR) measurements of the protonated samples $BP_{0.15}BPI_{0.85}$ [184-185] and $BP_{0.40}BPI_{0.60}$ [186], the RBRF glass parameters have been determined to be $\Delta J/k_B$ = 30 K, $\bar{J}/k_B = 160K$, $\sqrt{\Delta f}/k_B = 4$ and $\Delta J/k_B$ = 25 K, $\bar{J}/k_B = 200K$, $\sqrt{\Delta f}/k_B = 6$, respectively, for temperatures above 90 K. Using Eqs. (3.13) and (3.14) with $\bar{p}$ = 1 and q_{EA} = 1, these parameter sets lead to σ_A/k_B = 134 K and 132 K, and A_0/k_B= 320 K and 400 K, respectively.

If we take into consideration that the dielectric data were measured at temperatures far below 90 K, then these values are in a reasonable agreement to that one fitting the dielectric relaxation-time distribution.

3.3.3. Discussion

Considering the dielectric studies of protonated and deuterated $BP_{1-x}BPI_x$ mixed crystals published until now in literature, at first glace these solid solutions seem to be typical representatives of the family of proton and deuteron glasses. In the middle region of composition, 0.9 > x >0.3, no anomaly in ε' indicating a polar phase transition can be detected down to lowest temperatures. The freezing phenomena reveal the characteristics of a transition into a dipolar glass state. In the temperature region below 100 K, dispersion effects

Copyright © 2010. Nova Science Publishers, Incorporated. All rights reserved.

Handbook of Material Science Research, Nova Science Publishers, Incorporated, 2010. ProQuest Ebook Central,

dominate the dielectric response in the frequency range below 1 MHz. The temperature behaviour is typical for glasses. With decreasing measurement frequency, the maximum of ε' shifts to lower temperatures followed by the maximum of ε''. At fixed temperatures, the frequency dependence of ε' and ε'' provides clear evidence that the frequency dependence of ε'' is much broader then for the Debye dispersion where the broadening increases considerably towards lower temperatures. The most probable dielectric relaxation time τ follows a Vogel-Fulcher law with the Vogel-Fulcher temperatures that are considerably higher for the deuterated crystals in comparison to that one of the protonated crystals.

But looking a bit more in detail, striking differences to the other proton glasses, e.g. of the KDP family, become apparent. The authors of reference [179] tried to interpret the temperature dependence of the static dielectric permittivity within the framework of the RBRF Ising model. They found that rather large random fields play an important role. But even more unusual, for reasonable fits they had to consider a rather large long-range order contribution $\bar{J}$ that is comparable to ΔJ. On the other hand, there are no characteristic differences of the quality of fits with the three- and one-dimensional RBRF models. On the other hand, not only for the ferroelectric and antiferroelectric compositions but also for the compositions that are known to behave glass-like, they got reasonable fits of the static permittivity using the quasi-one-dimensional Ising model of the one-dimensional dipole chains with intra-chain ferroelectric couplings stronger than inter-chain ones. The authors did not consider this interpretation any further because predictions resulted for antiferroelectric transitions at temperatures above 106 K did met show any sign of a transition is in ε' experiments.

Our results show that the situation in the $BP_{1-x}BPI_x$ mixed crystals is even more peculiar. For all compositions under study, the fits deliver an average asymmetry A_0 of the local potentials that is almost linearly temperature dependent with about the same slope. Extrapolating the A_0 behaviour of the protonated crystals to higher temperatures, the average interaction $\bar{J}$ given by Eq. (3.14) meets values $\bar{J}/k_B$ = 160 K and 212 K determined for $BP_{0.15}BPI_{0.85}$ and $BP_{0.40}BPI_{0.60}$, respectively, within the framework of the RBRF Ising model from ENDOR measurements. Obviously, these numbers are close to the intra-chain coupling parameter $J_\parallel$ in BP and BPI. At the same time, the random bond interactions $\Delta J/k_B = 30$ K and 25 K of both the crystals are much smaller then the random fields represented by $\sqrt{\Delta f}/k_B = 79$ K and 103 K, respectively, and both considerably smaller than the average ordering interaction $\Delta J/k_B$. Consequently, $BP_{0.15}BPI_{0.85}$ and $BP_{0.40}BPI_{0.60}$ do not behave like a true proton glass but undergo a transition into a phase with coexisting long-range and glassy order. However, there is no anomaly of the dielectric permittivity detectable at the corresponding transition temperatures.

For the other mixed crystals under study, the situation is similar. Above about 20 K and 60 K for the protonated and deuterated mixtures, respectively, the ordering average interaction $\bar{J}/k_B$ is larger then the disorder term $\sigma_A = 2\Delta J\sqrt{q_{EA} + \Delta f}$, i.e. the long-ranged order and glassy order do coexist below the temperature T_C, that is close to $\bar{J}/k_B$. For the protonated crystals, the transition temperatures from the paraelectric phase into the phase with coexisting long-range and glassy order were measured by ENDOR and spin-lattice

Copyright © 2010. Nova Science Publishers, Incorporated. All rights reserved.

Handbook of Material Science Research, Nova Science Publishers, Incorporated, 2010. ProQuest Ebook Central,

relaxation measurements [188]. They range from 160 K for $BP_{0.15}BPI_{0.85}$ to 110 K for $BP_{0.70}BPI_{0.30}$.

Above the transition temperature T_C, the long-range order disappears but the glassy order is retained. However, if one remembers the quasi-one-dimensional behaviour of the temperature dependence of the permittivity in ferroelectric betaine phosphite and antiferroelectric betaine phosphate characterized by a strong ferroelectric intra-chain coupling $J_{\parallel}$ but weak ferroelectric and antiferroelectric couplings $J_{\perp\perp} \approx \pm J_{\parallel}/10$ between chains, the above explanation seems to be to simple. As the estimated random bond interaction J is of the same order of magnitude as the inter-chain coupling $J_{\perp\perp}$, one must suspect a more annoyed order between chains. Unfortunately, local information like the asymmetry of the local potential concluded from the relaxation time distribution or the local polarization obtained by magnetic resonance experiments does allow any conclusion to the relative polarization directions of the chains. Therefore, parallel and antiparallel arrangements of chains are undistinguishable with these investigations. Consequently, the experimental results presented above allow only the conclusion about a certain ferroelectric order of the hydrogen bonds within the chains but nothing about the order between the chains, i.e. a ferroelectric chain arrangement cannot be distinguished from an antiferroelectric or commensurately modulated one.

On the other hand, even if we ignore the coupling between the chains and is consider them to be independent, at low temperatures some kind of order within the chains is expected in the form of rather large domains. Within the framework of the one-dimensional RFIM [192, 193], the system is disordered at T = 0 K but contains domains with typical size given by the Imry-Ma length

$$L_{IM} \approx 4\,\bar{J}^2\ /\Delta f. \tag{3.19}$$

with $\bar{J}/k_B \approx 220$ K and $\Delta f \approx 3600\ K^2$ the domain length within the chain results then to $L_{IM} \approx 50$ spin distances.

With a local measurement one sees ordered spins when the domain lifetime is longer than the time window of the measurement. The time window is with about 10^{-7} s for ENDOR and 10^{-2} s to 10^{-7} s for the dielectric spectroscopy such that this condition is fulfilled. As these domains are stabilized by the random fields caused by substituted phosphite groups in phosphate chains or vice versa, one may suspect that due to that appropriate couplings between neighboring chains become also stabilized leading to three-dimensional domains already at finite temperature.

As mentioned above, the transition from the paraelectric phase into this phase with coexisting long-range and glassy order is related to an anomaly of the phonon system [188-190], which gives strong evidence for a cooperative transition. At the same time, the temperature dependence of the static permittivity announces a kind of antiferroelectric transition at these temperatures. These together with all the other facts discussed above lead to the conclusion that for the whole composition range of $BP_{1-x}BPI_x$ a long-range ordered phase with a considerable degree of disorder does exist in the temperature range shown in Figs. 3.21 and 3.22. This phase is characterized by a ferroelectric order of the bridging protons or deuterons within the phosphate/phosphite chains but with a non-ferroelectric arrangement of neighboring chains.

Copyright © 2010. Nova Science Publishers, Incorporated. All rights reserved.

Handbook of Material Science Research, Nova Science Publishers, Incorporated, 2010. ProQuest Ebook Central,

The behaviour towards very low temperatures gives a novel surprise. As Figs. 3.22 and 3.23 show, the average asymmetry A_0 and herewith the ferroelectric interaction $\overline{J}$ within the chains decreases to lower temperatures. At 17 K and 40 K, for all the compositions of protonated and deuterated $BP_{1-x}BPI_x$, respectively, A_0 did cross σ_A, and became even smaller to lower temperatures. That means, the crystals are now in a phase with dominating glassy order. For certain compositions, A_0 goes to zero in the temperature range under study.

For the sake of clarity one must finally note, that the "local" measurements performed in the present work and in the former ENDOR papers do not give information about the entire order parameter but only about the sublattice order parameter within the chains. Consequently, the analysis of the sublattice order parameter behaviour within the framework of the three-dimensional RBRF Ising model is a contradiction in terms. The resulting model parameters ΔJ, $\overline{J}$, and Δf have to be considered as very questionable, or at the utmost, as a projection of the entire order parameter behaviour on the chain sublattice order behaviour. Keeping this in mind, the diminishing ferroelectric sublattice interaction $\overline{J}$ can be interpreted in the following manner. A finite sublattice polarization of the chains is only possible for a three-dimensional system. At temperatures only slightly lower than $\overline{J}/k_B$ the inter-chain couplings are strong enough to enforce a three-dimensional order behaviour. With lower temperatures the disordering forces between chains become more and more important, leading to a reduced ferroelectric chain sublattice polarization. Finally, the three-dimensional long-range order breaks down with the result that no chain sublattice polarization can exist anymore at finite temperatures. One can suspect that the disappearance of chain sublattice polarization marks the transition into the non-ergodic glassy state.

There is another possible explanation of the diminishing asymmetry parameter A_0. The methods used in this work to determine the effective distribution parameters of the H-bonds are based on the measurements of the dynamic response of the protons or deuterons in the distorted double well potential. While at the intermediate temperature it is quite likely that the large mean asymmetry A_0 in the distribution of the random fields is due to the fact that the dielectric spectroscopy cannot distinguish between the opposite polarizations of the domains, i.e. the actual distribution of the random fields has two maxima for opposite directions of the field rather than the simple Gaussian as it was assumed initially. Due to intra-chain ordering the majority of H-bonds are highly asymmetric and give the main contribution to the proton dynamics at intermediate temperatures. However at the lowest temperatures the protons or deuterons tend to freeze in the deep lower-energy minima of the asymmetric H-bonds, thus being effectively excluded from the dynamics. However, we know from the ENDOR results that the long-range order parameter has already the value $\overline{p}$ = 0.7 at 90 K such that it can hardly show a remarkable increase between 30 K and 15 K where A_0, determined with the dielectric spectroscopy, decreases drastically. Furthermore, the dielectric spectroscopy gives a value A_0/k_B = 350 K for $BP_{0.15}BPI_{0.85}$ at 40 K which is considerably larger than A_0/k_B = $\overline{p}$ ×2 $\overline{J}/k_B$ = 0.7×400 K = 280 K determined with ENDOR spectroscopy at 90 K. The corresponding long-range order parameter value is $\overline{p}$ = 350/400 = 0.88 at 40 K. Thus, we can ascertain that the dielectric spectroscopy gives correct parameters A_0 at low temperatures. Similar experimental results of another group of an at least partial erosion of the antiferroelectric order and a transition into a glassy state in a related mixed crystal (betaine

Copyright © 2010. Nova Science Publishers, Incorporated. All rights reserved.

Handbook of Material Science Research, Nova Science Publishers, Incorporated, 2010. ProQuest Ebook Central,

arsenate)$_{0.73}$(betaine phosphate)$_{0.27}$ at low temperatures can be considered as further confirmation of our observation [194].

The present theoretical models are not able to give a satisfactory description of these phenomena in our proton and deuteron glasses. However, one can hazard a guess that the observed transition from an inhomogeneous long-range ordered ferroic state to a glassy state at very low temperatures bears a certain resemblance to the long-puzzeling question of the self-generated disorder and glassines in structural glasses [195–198].

4. BROADBAND DIELECTRIC SPECTROSCOPY OF PMN-PSN-PZN RELAXORS

4.1. Dielectric Spectroscopy of PMN-PSN-PZN Ceramics

4.1.1. Introduction

Relaxor ferroelectrics have attracted considerable attention in recent years due to their unusual physical behaviour and excellent dielectric and electromechanical properties. Dielectric measurements of relaxors are very important for both fundamental investigations and applications. However most of such investigations are performed only in narrow frequency range [199-205, 105]. Often only increasing temperature of the dielectric permittivity maximum with increasing frequency is analyzed according to Eq. (3.17). As a rule, such investigations are based on various predefined formulas of distribution of relaxation times. Most popular predefined distribution of relaxation times is the Cole-Cole function (1.45) [206-208], however this model is good enough only for narrowband dielectric data of relaxors. On the other hand, two or more Cole-Cole functions describe better dielectric dispersion in relaxors, however a further drawback of such an approach is the inherent difficulty of separating processes with comparable relaxation times. Other predefined distribution functions: Davidson-Cole [209], Havriliak-Negami [112], Joncher, Kolraush-Wiliams-Watts and Curie-von Schweidler [210] analysis can not explain dynamics of polar nanoregions.

Broadband dielectric spectroscopy from Hz to THz region is needed for investigation of very wide dielectric relaxations in relaxors and because the broadband and THz technique is rather rare, only few relaxor ferroelectric systems PMN [211, 212], PST [213-215] and PLZT [216, 217] were investigated in microwave and THz range simultaneously. However, most of such investigations in frequency range between several GHz and several hundred GHz are performed with thin films at or below room temperature. We can predicate that dielectric dispersion of bulk relaxors at higher temperatures (near and below T_B) is rather unknown, because the dielectric dispersion at higher temperatures is reveals mainly in microwave and THz region. On the other hand, in literature there are many speculations about relaxor dynamics based on hypothesis about the dielectric dispersion between several GHz and several hundred GHz. The authors of [218] discovered two dielectric dispersions in relaxors, one from low frequencies to 1.8 GHz and another between 1.8 GHz and several hundred GHz, however no any data they have between 1.8 GHz and 100 GHz.

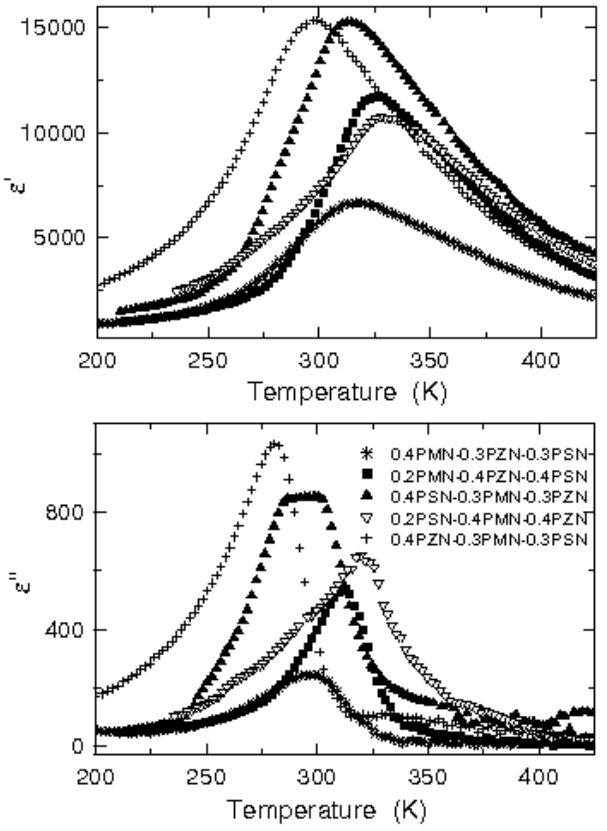
Dielectric and piezoelectric studies of solid solutions of relaxor ferroelectrics like PMN and PSN with normal ferroelectric $PbTiO_3$ revealed giant piezoelectricity (one order of

Copyright © 2010. Nova Science Publishers, Incorporated. All rights reserved.

Handbook of Material Science Research, Nova Science Publishers, Incorporated, 2010. ProQuest Ebook Central,

magnitude larger than in the best classical ferroelectrics like $PbZr_{1-x}Ti_xO_3$) for compositions near morphotropic phase boundary [219]. The paper of Park and Shrout [219] turned the attention of many physicists to the study of solid solutions of relaxor ferroelectrics with ferroelectrics. Monoclinic phase was observed on the morphotrophic phase boundary between the tetragonal and rhombohedral phases [220] and it was proposed that the easy rotation of polarization in the monoclinic phase is responsible for the giant piezoelectric coefficient in these systems [221].

Solid solutions of two relaxor ferroelectrics were investigated, although it was intuitively expected that such solid solutions will exhibit again a relaxor behaviour. The best-investigated system is PMN - PSN solid solution [222-226]. The relaxor behaviour was observed in both ordered and disordered forms of (1-x)PMN-(x)PSN for $x \leq 0.64$ [221, 222]. At higher levels of substitution, the dielectric response was dependent on the degree of order: disordered samples were relaxors and ordered samples exhibited normal ferroelectric behaviour. Such behaviour was explained within a Bragg-Wiliams approach by employing the random layer model. NMR study of PMN-PSN revealed that the spherical model of Pb displacements is unable to yield the observed distribution of the shortest Pb-O bond length [227].



Copyright © 2010. Nova Science Publishers, Incorporated. All rights reserved.

Reprinted figure with permission from [229]. Copyright 2006 by the American Physical Society.

Figure 4.1. Temperature dependence of complex dielectric permittivity of various PZN-PMN-PSN ceramics measured at 1 kHz.

Handbook of Material Science Research, Nova Science Publishers, Incorporated, 2010. ProQuest Ebook Central,

Ternary solid solutions of PSN-PZN-PMN relaxor ferroelectrics have been first synthesized and investigated by Dambekalne et al. [228]. The system was very well soluble and the dielectric data showed high values of permittivity (7000-30000). Investigated in this work ternary PSN-PZN-PMN solid solution was synthesized by solid state reactions from high grade oxides PbO_3, Nb_2O_5, MgO, ZnO, Sc_2O_3. The primary ingredients were homogenized and milled in agate ball mill for 8 hours in ethanol and dried at 250º C for 24 hours. The dried mixture was fired in platinum crucibles. To obtain sufficient homogeneous mixture of perovskite structure the synthesis was repeated three times: at first at 800º C, the second at 900º C, the third at 1000º C, 2 hours each. After each synthesis the mixture was milled in agate ball mill in ethanol, dried at 250º C for 24 hours, and the phase composition was analysed by X-ray diffraction. Detailed processing and sintering conditions are given in [228].

4.1.2. Broadband Dielectric Studies of PMN-PSN-PZN Ceramics

The temperature dependence of complex dielectric permittivity ε^* of all five investigated ceramics measured at 1 kHz is shown in Figure 4.1. Each composition shows just one maximum in $\varepsilon'(T)$ and $\varepsilon''(T)$ in the range of 280 and 330 K. The temperature dependences of complex dielectric permittivity ε^* at various frequencies show typical relaxor behaviour in all investigated ceramics (Figure 4.2). There is a broad peak in the real part of dielectric permittivity as a function of temperature. With increasing frequency in the wide frequency range from 20 Hz to 512 GHz, T_m increases, while the magnitude of the peak decreases.

Static permittivity of this ceramics is very high; the peak value of 0.4PZN-0.3PMN-0.3PSN ceramics is about 15,000 at frequencies lower than 0.1 kHz. There is a strong dielectric dispersion in the radio frequency region around and below T_m at 1 kHz. This dielectric dispersion does not obey the Debye theory [105]. At temperatures around and above its peak temperature (T'_m) of the dielectric absorption, the dielectric losses exhibit strong frequency dependence. The value of T'_m is much lower than that of T_m at the same frequency, the difference between T_m and T'_m increase on increasing frequency, that this difference is about 10 K at 129 Hz and about 250 K at 512 GHz. With increasing frequency, T'_m shifts to higher temperature and the magnitude of the dielectric absorption peak increases till about 1 GHz and then decrease. At frequencies below 1 GHz, with decreasing temperature, the dielectric absorption increases rapidly in the temperature region around T_m. At higher (above 1 GHz) frequencies the absorption temperature dependence is almost symmetric. The dielectric absorption is nearly independent of the frequency (in fact, the dielectric absorption shows a very diffuse dependence on the frequency) at a temperature much lower than T'_m. Permittivity remains of the order of 1,000 even in microwave range (4,500 for 0.2PSN-0.4PMN-0.4PZN ceramics at 11 GHz) and losses are also very high ($\tan\delta \approx 1$) at microwaves. It indicates that the main dielectric dispersion occurs in the microwave range.

The Vogel-Fulcher behaviour for the temperatures of the permittivity peaks, which is known to be one of the typical peculiarities of relaxors [200] Eq. (3.17), is also observed in our samples. From the Vogel-Fulcher analysis Eq. (3.17) follows that $\varepsilon(0)$ have maximum nearly at room temperature, however such analysis is not absolutely correct for relaxors as it is described below. On the other hand, the maximum of $\varepsilon(0)$ indicates some phase transition, which is really not observed in prototypical relaxors PMN. More appropriate assumption is that $\varepsilon(0)$ does not decrease on cooling.

Copyright © 2010. Nova Science Publishers, Incorporated. All rights reserved.

Handbook of Material Science Research, Nova Science Publishers, Incorporated, 2010. ProQuest Ebook Central,

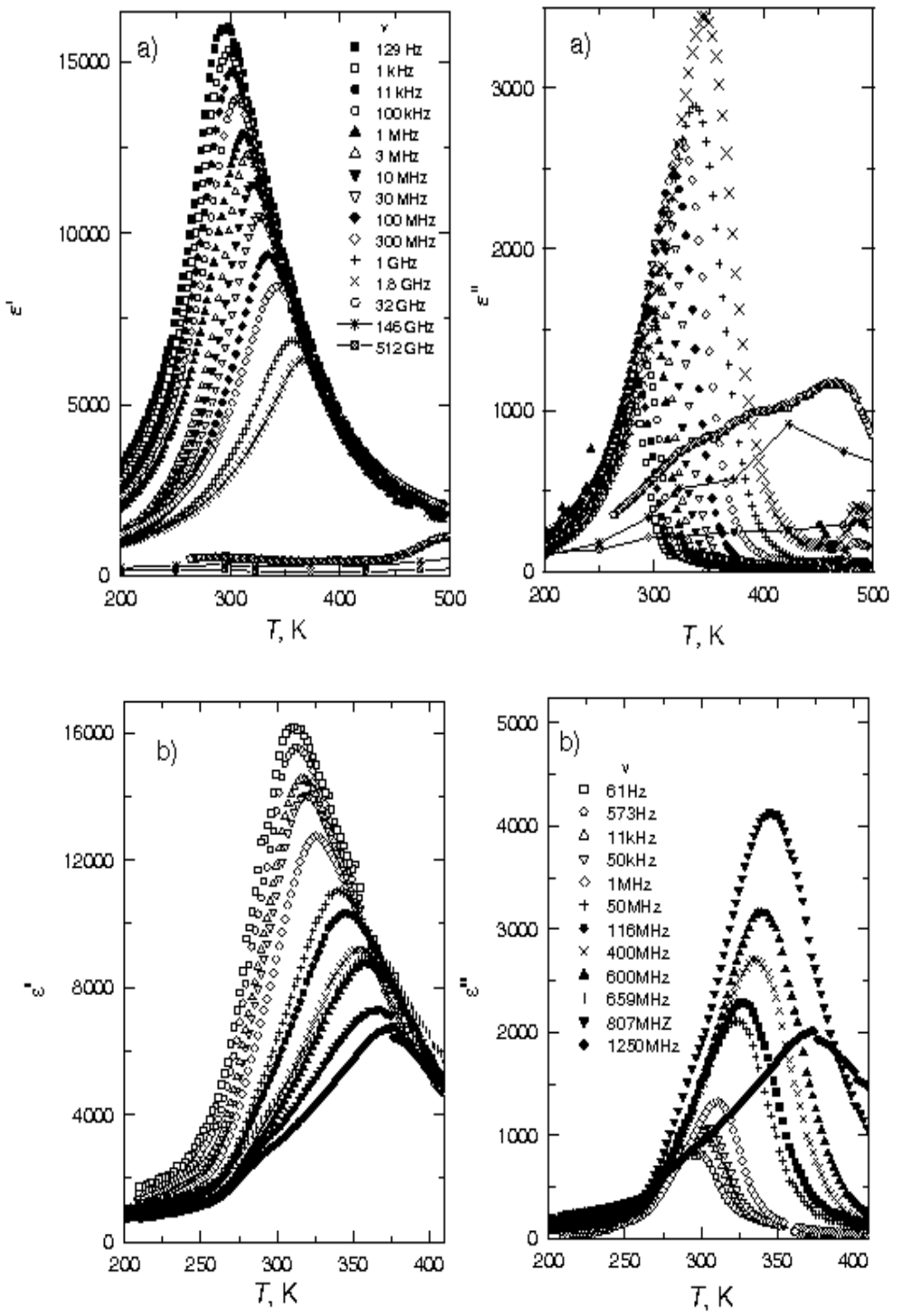


Figure 4.2. Continues.

Copyright © 2010. Nova Science Publishers, Incorporated. All rights reserved.

Handbook of Material Science Research, Nova Science Publishers, Incorporated, 2010. ProQuest Ebook Central,

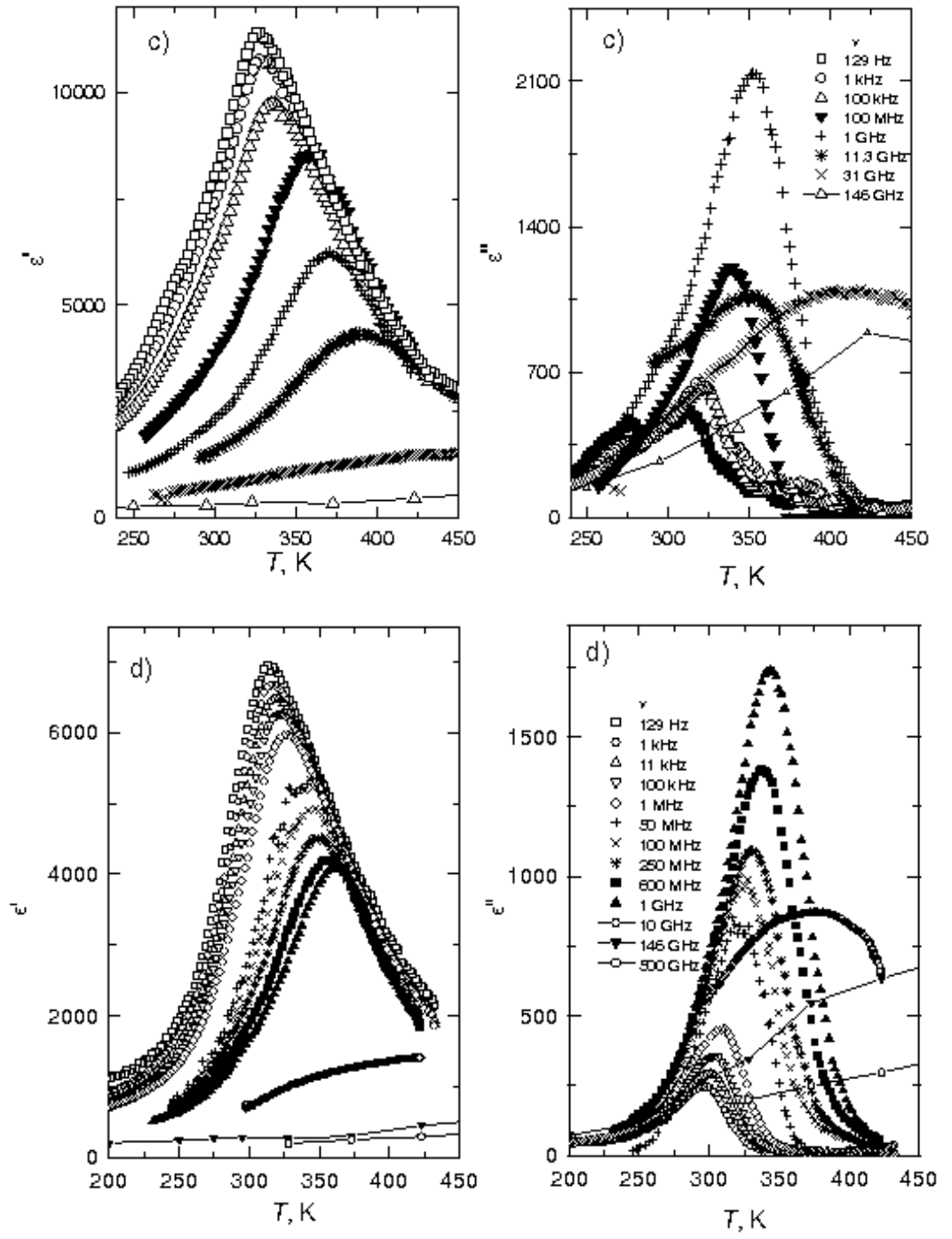
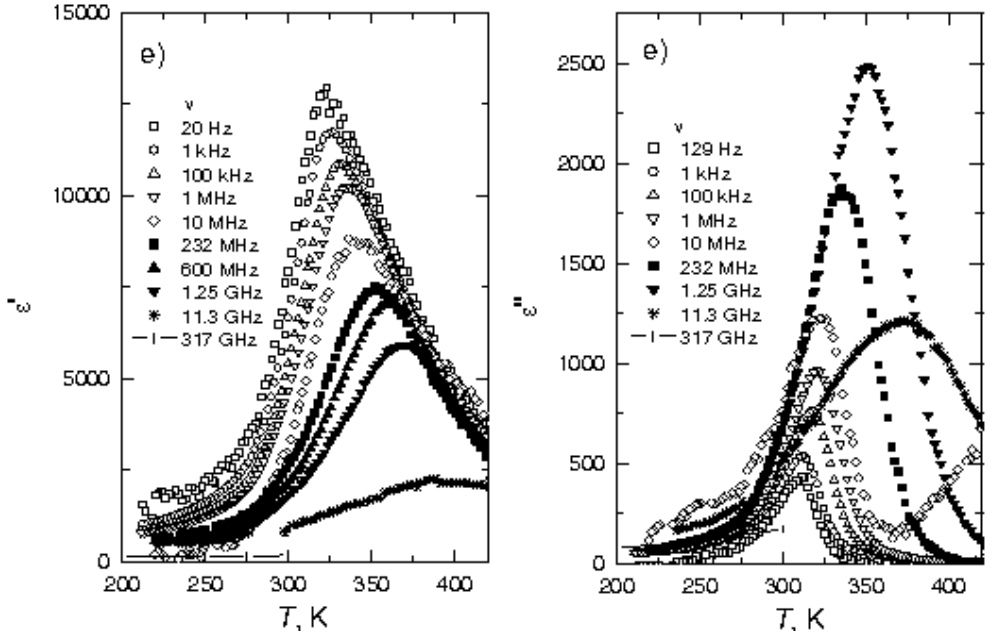


Figure 4.2. Continues.

Copyright © 2010. Nova Science Publishers, Incorporated. All rights reserved.

Handbook of Material Science Research, Nova Science Publishers, Incorporated, 2010. ProQuest Ebook Central,



Reprinted figure with permission from [229]. Copyright 2006 by the American Physical Society.

Figure 4.2. Temperature dependence of complex dielectric permittivity of various PZN-PMN-PSN ceramics (a) 0.4PZN-0.3PMN-0.3PSN, b) 0.4PSN-0.3PMN-0.3PZN, c) 0.2PSN-0.4PMN-0.4PZN, d) 0.4PMN-0.3PSN-0.3PZN, e) 0.2PMN-0.4PSN-0.4PZN) measured at different frequencies.

For understanding the dielectric relaxation, it is more convenient to use frequency plot of the complex permittivity at various representative temperatures (see Figure 4.3). One can see a huge change of dielectric dispersion with temperature in all investigated ceramics. At higher temperatures ($T \geq 400$ K), the dielectric loss dispersion it is clearly symmetric and is observed only at higher frequencies (more than 1 GHz). On cooling, the relaxation slows down and broadens. At temperatures around 300 K the relaxation becomes strongly asymmetric and very broad. On further cooling, the dielectric dispersion becomes so broad that we can see only part of this dispersion in our frequency range.

The symmetric dielectric dispersion at high temperatures can be easily described by the Cole-Cole formula (1.46). Temperature dependences of the Cole-Cole parameters obtained from the fit of all five investigated ceramics are presented in Figure 4.4. One can see qualitatively the same behaviour in all ceramics. The parameter α_{CC} is small (<0.2, however no Debye like dispersion really is observed in presented relaxors) only at higher temperatures. On cooling, this parameter increases (i.e. distribution of relaxation times broadens). The mean Cole-Cole relaxation time on cooling diverges according to the Vogel-Fulcher law (3.18). The obtained parameters are summarized in Table 4.1. The maximum of temperature dependences of $\Delta\varepsilon$ correspond to maximum of dielectric permittivity at lower frequencies, but real temperature dependences of static dielectric permittivity of relaxors cannot be obtained below T_m, because the dielectric dispersion is too broad and part of it appears below our experimental frequency limit. At lower temperatures, the Cole-Cole fit is no more appropriate, because the absorption peak is not symmetric, and even close to the freezing temperature the absorption $\varepsilon''(\nu)$ does not exhibit any clear maximum, so that the determination of the mean relaxation time τ_{CC} is not unambiguous (Figure 4.3, $T \leq 300$ K).

Copyright © 2010. Nova Science Publishers, Incorporated. All rights reserved.

Handbook of Material Science Research, Nova Science Publishers, Incorporated, 2010. ProQuest Ebook Central,

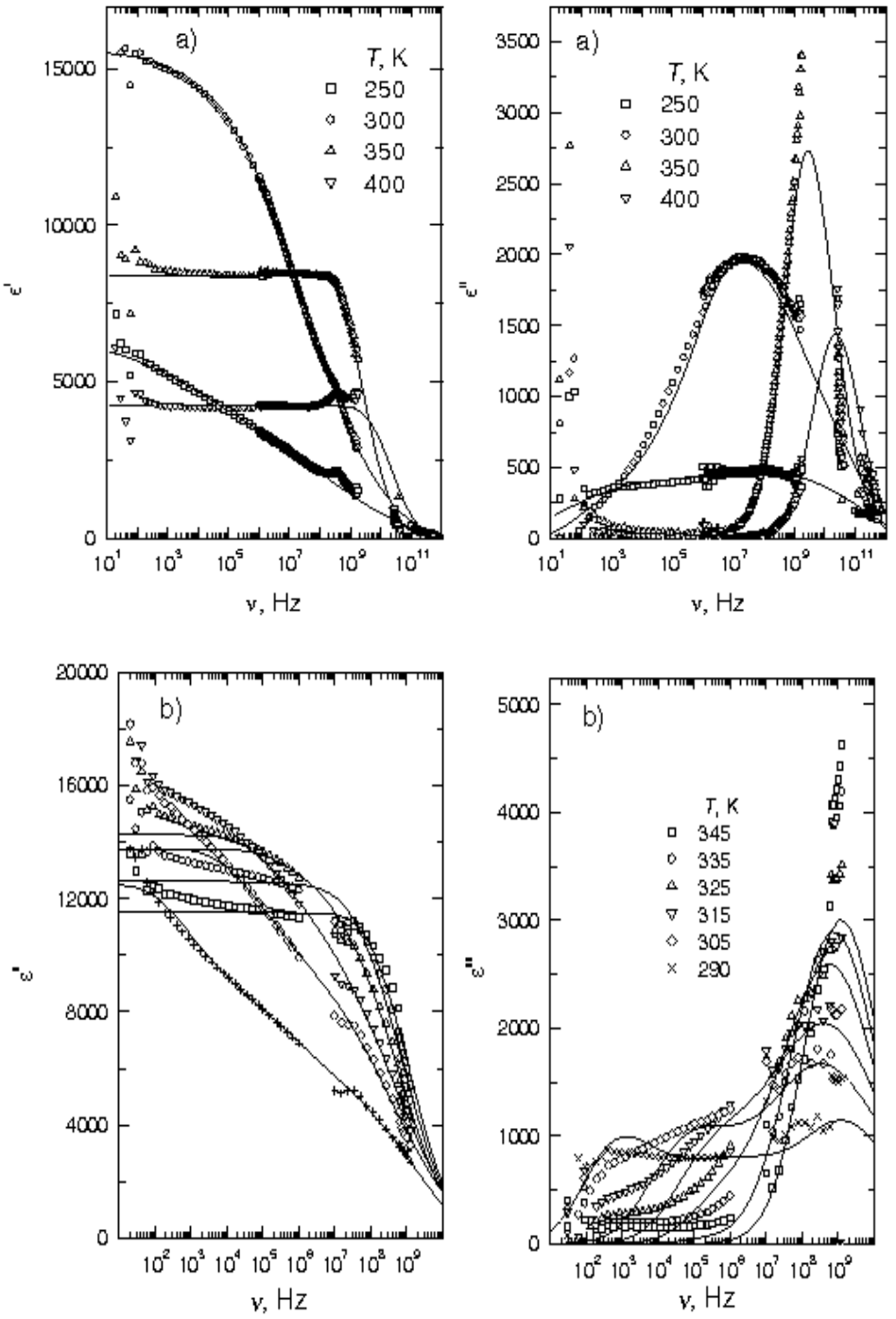


Figure 4.3. Continues.

Copyright © 2010. Nova Science Publishers, Incorporated. All rights reserved.

Handbook of Material Science Research, Nova Science Publishers, Incorporated, 2010. ProQuest Ebook Central,

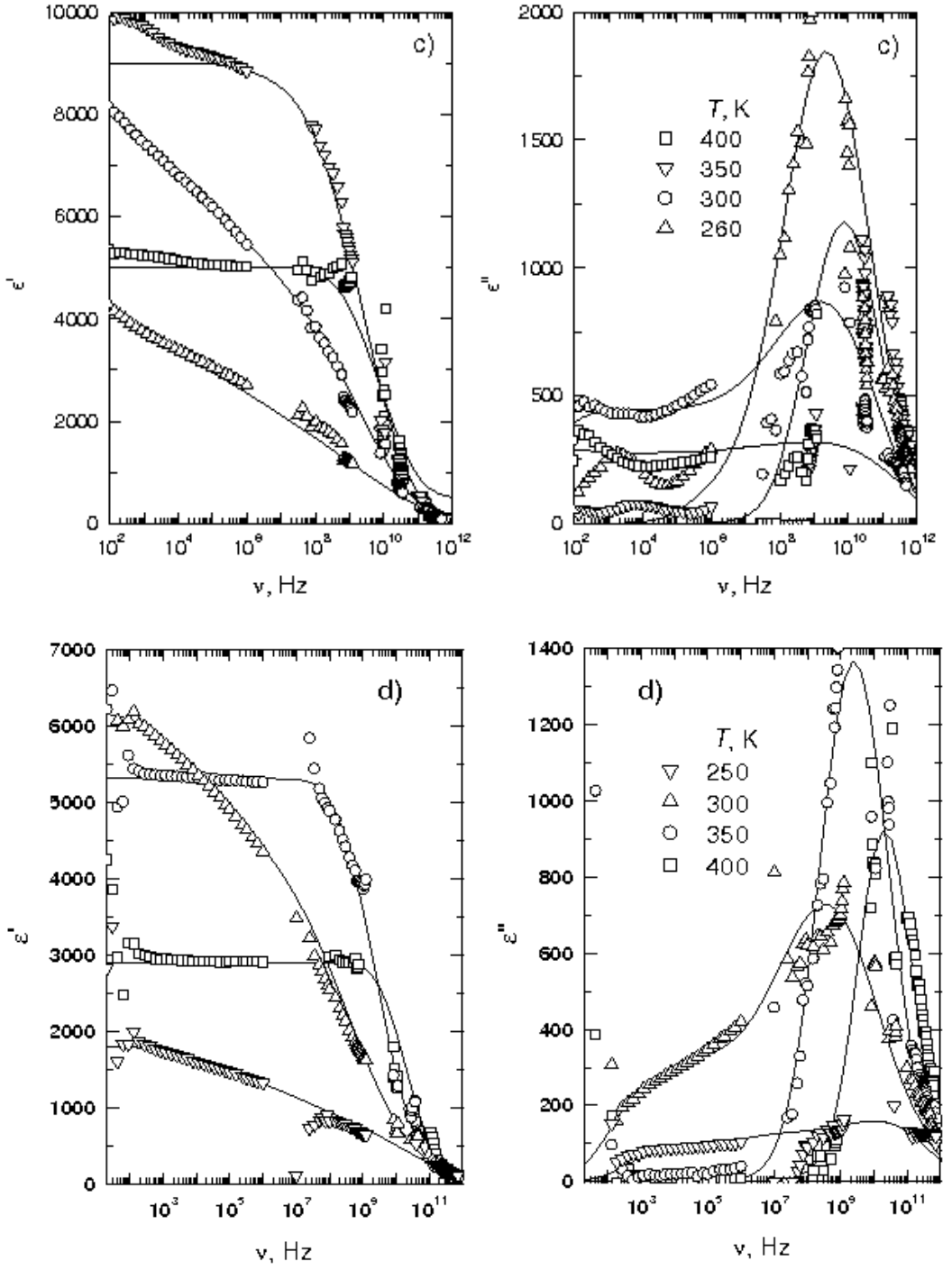
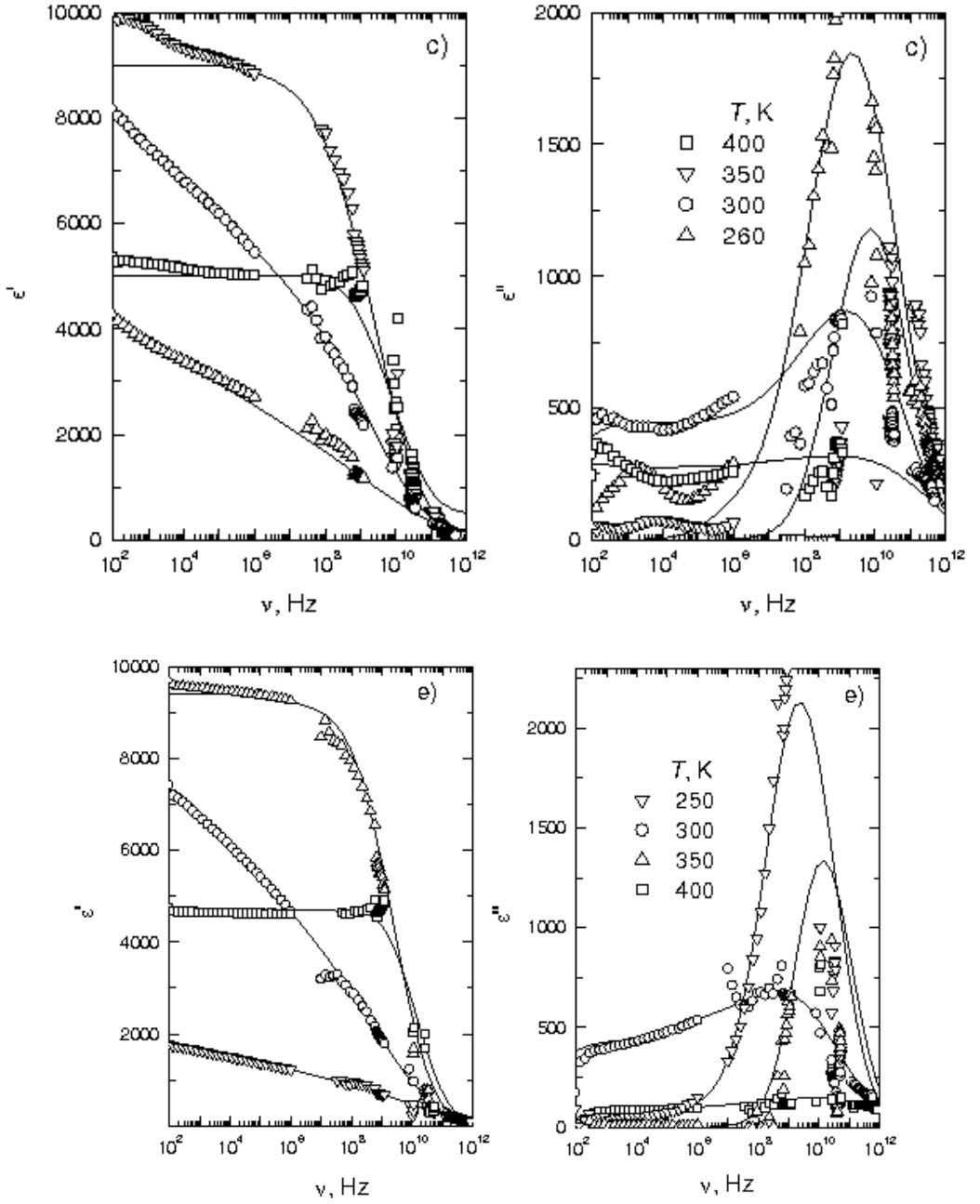


Figure 4.3. Continues.

Copyright © 2010. Nova Science Publishers, Incorporated. All rights reserved.

Handbook of Material Science Research, Nova Science Publishers, Incorporated, 2010. ProQuest Ebook Central,

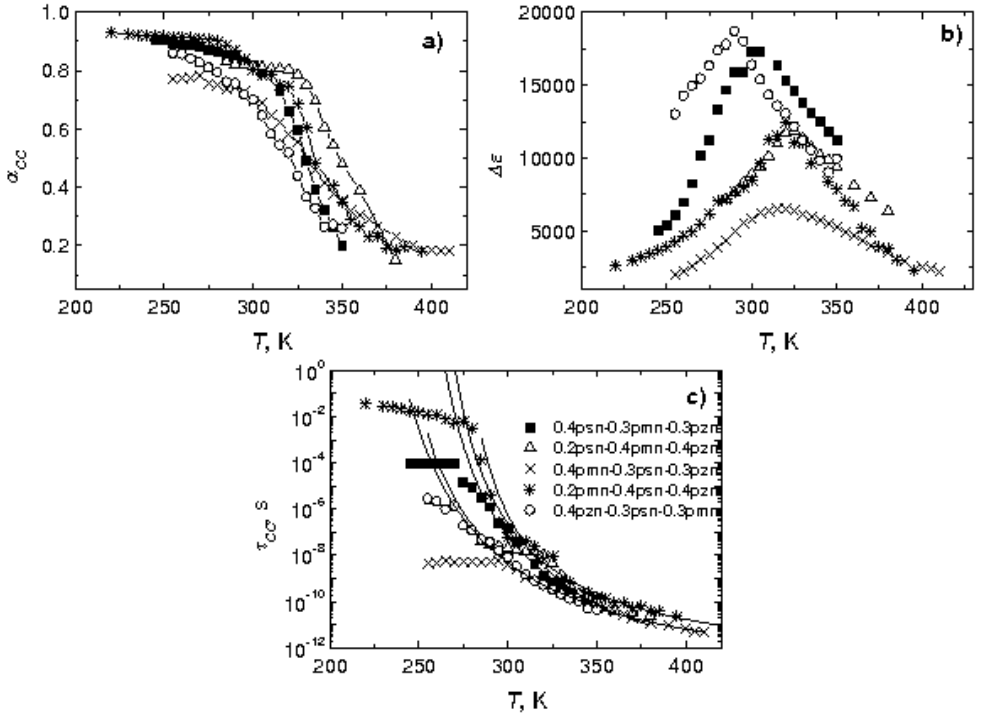


Reprinted figure (a) with permission from [229]. Copyright 2006 by the American Physical Society.

Figure 4.3. Frequency dependence of complex dielectric permittivity of various PZN-PMN-PSN ceramics (a) 0.4PZN-0.3PMN-0.3PSN, b) 0.4PSN-0.3PMN-0.3PZN, c) 0.2PSN-0.4PMN-0.4PZN, d) 0.4PMN-0.3PSN-0.3PZN, e) 0.2PMN-0.4PSN-0.4PZN) measured at different temperatures. The solid lines are the best fit according to Eqs. (1.41) and (1.42).

Copyright © 2010. Nova Science Publishers, Incorporated. All rights reserved.

Handbook of Material Science Research, Nova Science Publishers, Incorporated, 2010. ProQuest Ebook Central,



Reprinted figure with permission from [229]. Copyright 2006 by the American Physical Society.

Figure 4.4. Temperature dependence of Cole-Cole parameters a) α_{CC}, b) $\Delta\varepsilon$, c) τ_{CC} of the various PZN-PMN-PSN ceramics.

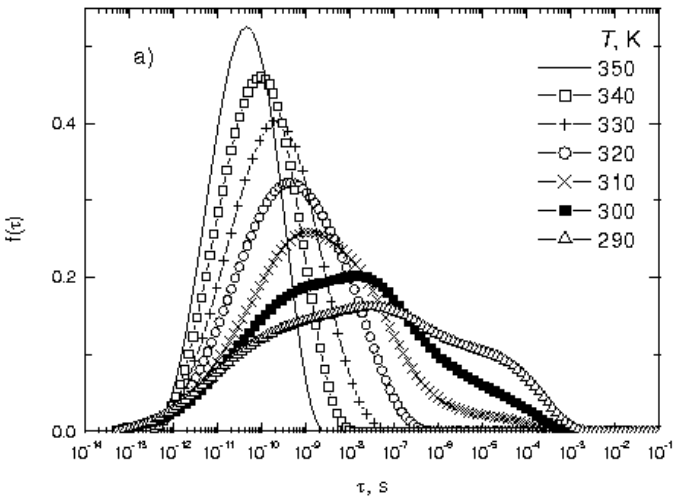


Figure 4.5. Continues.

Copyright © 2010. Nova Science Publishers, Incorporated. All rights reserved.

Handbook of Material Science Research, Nova Science Publishers, Incorporated, 2010. ProQuest Ebook Central,

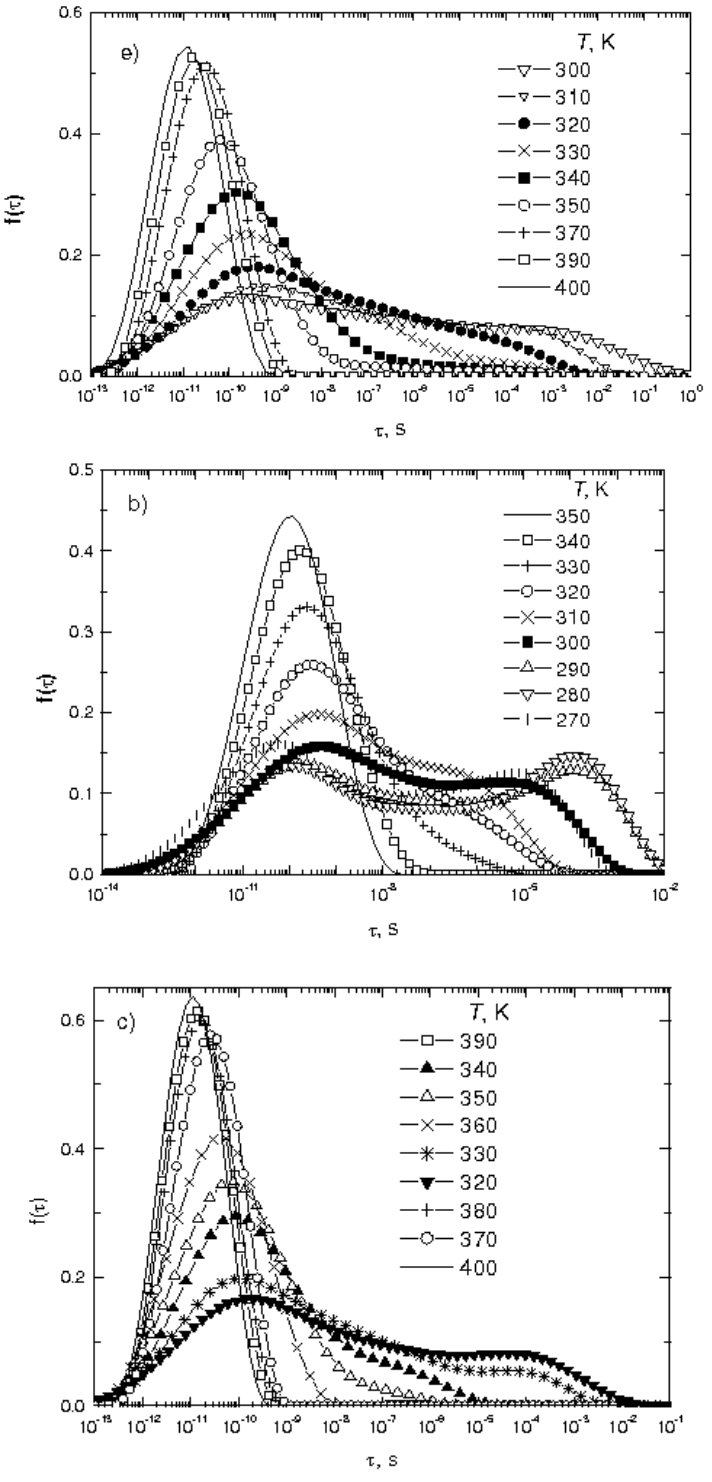
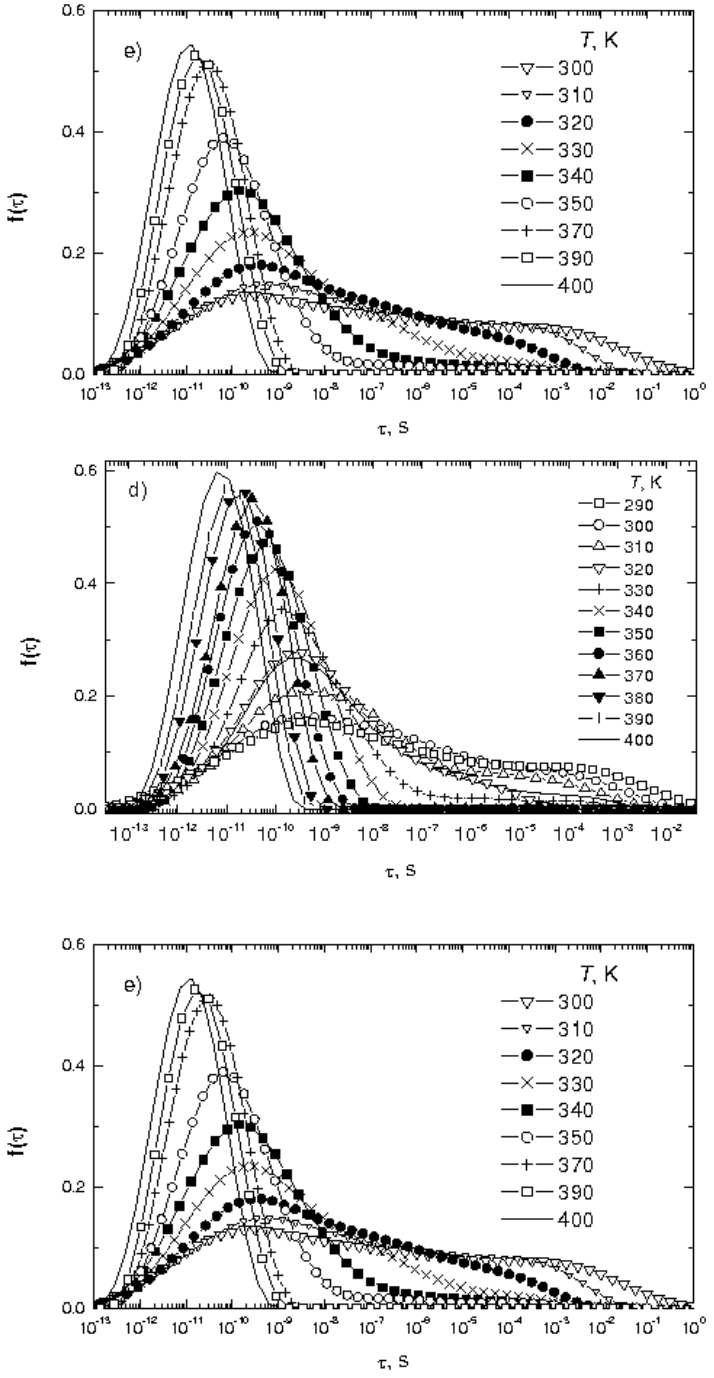


Figure 4.5. Continues.

Copyright © 2010. Nova Science Publishers, Incorporated. All rights reserved.

Handbook of Material Science Research, Nova Science Publishers, Incorporated, 2010. ProQuest Ebook Central,



Copyright © 2010. Nova Science Publishers, Incorporated. All rights reserved.

Reprinted figure (a) with permission from [229]. Copyright 2006 by the American Physical Society.

Figure 4.5. Distribution of relaxation times f (τ) of various PZN-PMN-PSN ceramics (a) 0.4PZN-0.3PMN-0.3PSN, b) 0.4PSN-0.3PMN-0.3PZN, c) 0.2PSN-0.4PMN-0.4PZN, d) 0.4PMN-0.3PSN-0.3PZN, e) 0.2PMN-0.4PSN-0.4PZN) calculated at different temperatures.

Handbook of Material Science Research, Nova Science Publishers, Incorporated, 2010. ProQuest Ebook Central,

Table 4.1. Parameters of the Vogel-Fulcher fit of mean relaxation time τ_{CC} of PMN-PSN-PZN ceramics

ceramics	τ_0, s	T_0, K	E_f/k_B, K
0.4PZN-0.3PMN-0.3PSN	10^{-14}	200	1297.4
0.4PSN-0.3PMN-0.3PZN	10^{-14}	231.5	1077
0.2PSN-0.4PMN-0.4PZN	10^{-14}	250	829
0.4PMN-0.3PSN-0.3PZN	$1.5*10^{-14}$	210	1150
0.2PMN-0.4PSN-0.4PZN	$6.27*10^{-14}$	241	892

Reprinted table with permission from [229]. Copyright 2006 by the American Physical Society.

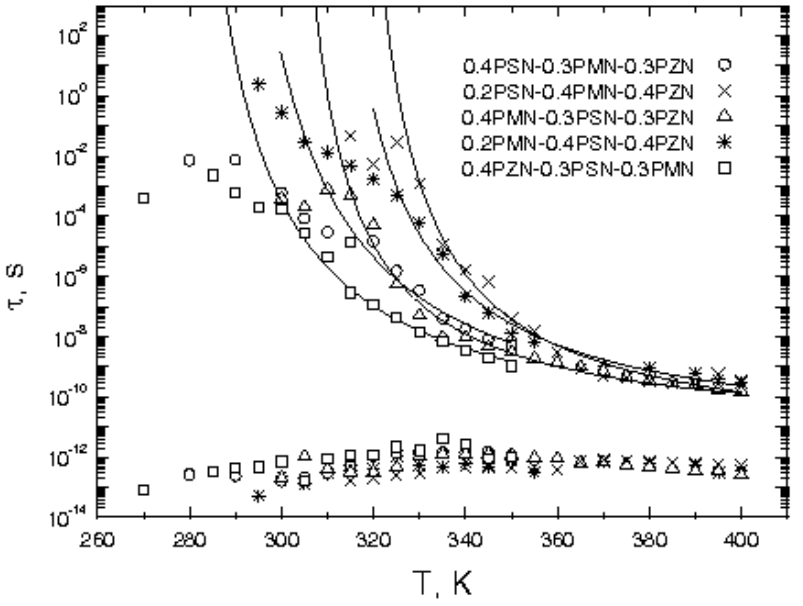
More general approach has to be used for determination of the real and continuous distribution function of relaxation times f (τ) by solving Fredholm integral equations (see Section 2.6). The regularization parameter 8 was found as optimal for all our investigated ceramics. Calculated distribution of the relaxation times f (τ) in PMN-PSN-PZN ceramics is presented in Figure 4.5. The temperature behaviour of f (τ) is qualitatively the same in all investigated ceramics. Symmetric and narrow distribution of relaxation times is observed at higher temperatures. On cooling the f (τ) function becomes asymmetrically shaped and a second maximum appears. The shortest and longest limits of the f (τ) function were calculated (level 0.1 of the maximum f (τ) was chosen for definition of the limits) at various temperatures (Figure 4.6). The longest relaxation time τ_{max} diverges according to the Vogel-Fulcher law (Figure 4.6) and the obtained parameters are presented in Table 4.2. All the shortest relaxation times have the same values 10^{-12} –10^{-13} s and are practically temperature independent within the accuracy of our analysis.

Both temperature dependences of τ_{max} and τ_{min} correspond very well to the results obtained in relaxor PLZT ceramics [251]. Distribution function f (τ) was determined only at rather high temperatures, when the relaxation time lies within our experimental frequency range. When the τ_{max} appears much below our frequency limit, we could not determine the static permittivity and therefore also τ_{max} unambiguously. It is also the reason, why the parameters of the Vogel-Fulcher fits in Tables 4.1 and 4.2 do not correspond to each other very well. τ_{max} values are determined less accurately and in a narrower temperature range than τ_{CC}. Therefore the parameters in Table 5.1 are more accurate. Nevertheless, one can expect that τ_{max} does not really diverge below T_0, because some dispersion remains also below the freezing temperature.

τ_{max} has probably very large but finite values below T_0 and follows most probably the Arrhenius law. Origin of the dielectric dispersion below the freezing temperature T_0 is rather non-trivial and will be discussed below together with explanation of THz dielectric relaxation above T_m. Nevertheless, we see qualitatively similar behaviour in all investigated samples: f (τ) has one maximum at high temperatures and it splits always near T_m into two parts. First one follows the Vogel-Fulcher law, while the second one is only slightly temperature dependent and remains in the range of 10^{-8} – 10^{-11} s. It is in contrast to dipolar glass systems, where only one f(τ) maximum was observed (see Section 3.2).

Copyright © 2010. Nova Science Publishers, Incorporated. All rights reserved.

Handbook of Material Science Research, Nova Science Publishers, Incorporated, 2010. ProQuest Ebook Central,



Reprinted figure with permission from [229]. Copyright 2006 by the American Physical Society.

Figure 4.6. Temperature dependences of the longest τ_{max} and shortest τ_{min} relaxation times in PZN-PMN-PSN ceramics.

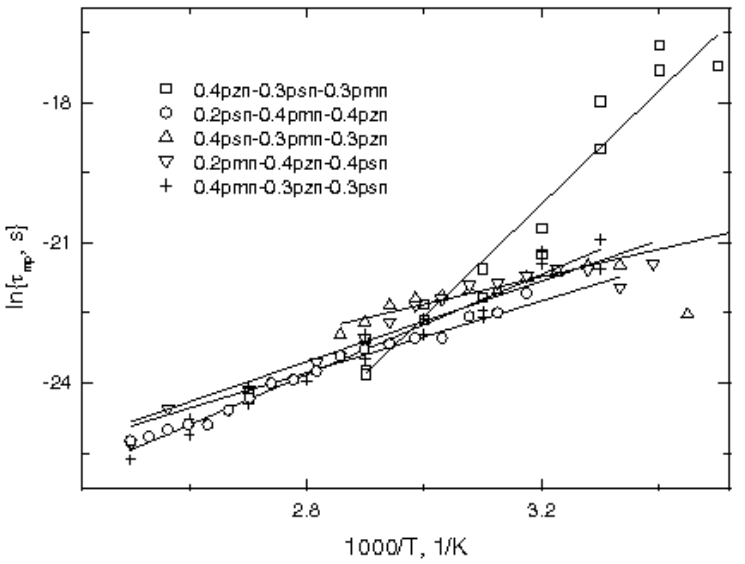


Figure 4.7. Temperature dependence of the most probable relaxation times τ_{mp} in PZN-PMN-PSN ceramics.

Copyright © 2010. Nova Science Publishers, Incorporated. All rights reserved.

Handbook of Material Science Research, Nova Science Publishers, Incorporated, 2010. ProQuest Ebook Central,

Table 4.2. Parameters of Vogel-Fulcher fit of longest relaxation time τ_{CC} of PMN-PSN-PZN ceramics

ceramics	τ_0, s	T_0, K	E_f/k_B, K
0.4PZN-0.3PMN-0.3PSN	$1.87*10^{-12}$	272.6	518
0.4PSN-0.3PMN-0.3PZN	$2.96*10^{-12}$	303.3	425.2
0.2PSN-0.4PMN-0.4PZN	$1.92*10^{-12}$	311.1	384.6
0.4PMN-0.3PSN-0.3PZN	$5.1*10^{-12}$	297	333.5
0.2PMN-0.4PSN-0.4PZN	10^{-12}	280.2	668.9

Reprinted table with permission from [229]. Copyright 2006 by the American Physical Society.

Table 4.3. Parameters of Arrhenius fit of most probable relaxation times τ_{mp}

ceramics	τ_0, s	E_a/k, K
0.4PZN-0.3PMN-0.3PSN	$2.79*10^{-26}$	12087.7
0.4PSN-0.3PMN-0.3PZN	$2.98*10^{-14}$	2942.4
0.2PSN-0.4PMN-0.4PZN	$1.06*10^{-15}$	3825.7
0.4PMN-0.3PSN-0.3PZN	$1.35*10^{-17}$	5365.8
0.2PMN-0.4PSN-0.4PZN	$3.4*10^{-16}$	4313.2

Non-physical small value of τ_0 of 0.4PZN-0.3PMN-0.3PSN ceramics correspond to abnormal high value of activation energy E_a and they both are caused by the measurements errors (this ceramics was measured in frequency range 1 MHz – 1.8 GHz by slightly another technique). On the other hand, the Arrhenius fit describes good enough the temperature dependence of most probable relaxation time in a temperature range where distributions were calculated. At the same time, the Arrhenius law validity at higher temperatures is unlikely because most probable relaxation time become smaller as 10^{-13} s, more appropriate assumption is that most probable relaxation time alternates only slightly above 400 K. The most probable relaxation time τ_{mp} obtained from the peak of distributions follows the Arrhenius law (4.11) (Figure 4.7).

4.1.3. THz Dielectric Spectra of PMN-PZN-PSN Ceramics

The broad-band dielectric spectra were obtained only up to 400 K, therefore Figure 4.5 shows f (τ) also only below this temperature. The answer to the question, how does the relaxation behave at higher temperatures, can be given by the THz dielectric spectroscopy, because the relaxation hardens into microwave and THz spectral range at high temperatures. Figure 4.8 shows the results of the time-domain THz transmission experiment obtained for 0.4PZN-0.3PSN-0.3PMN, 0.4PMN-0.3PSN-0.3PZN, 0.2PSN-0.4PZN-0.4PMN ceramics. The spectra of these PMN-PSN-PZN solid solutions exhibit qualitatively similar results.

One can see that the relaxation practically does not contribute into THz spectra below 40 K (permittivity is frequency-independent), dispersion is determined only by phonon contributions. Above 80 K, the low-frequency THz permittivity ε' and losses ε'' rise bringing evidence about the dielectric relaxation contribution into the spectra. ε' and ε'' continuously increase on heating to 523 K.

Simultaneously, the spectral range, where the sample is transparent, becomes narrower. Therefore, the spectrum at 523 K can be determined only up to 0.5 THz while the spectrum

Copyright © 2010. Nova Science Publishers, Incorporated. All rights reserved.

Handbook of Material Science Research, Nova Science Publishers, Incorporated, 2010. ProQuest Ebook Central,

taken at 20 K ends at 0.9 THz. Above 573 K, ε' and ε'' decreases on heating and finally no contribution of dielectric relaxation into complex permittivity is seen at 823 K.

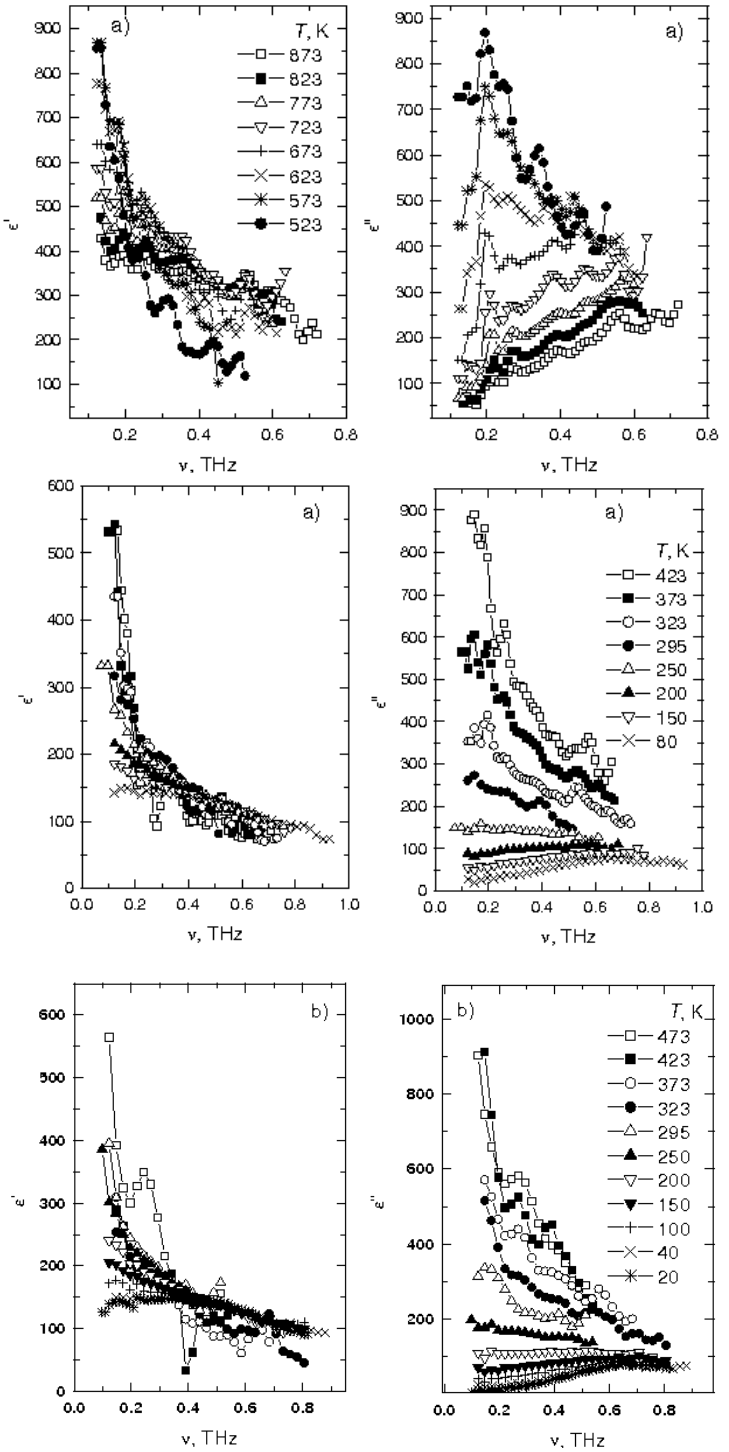
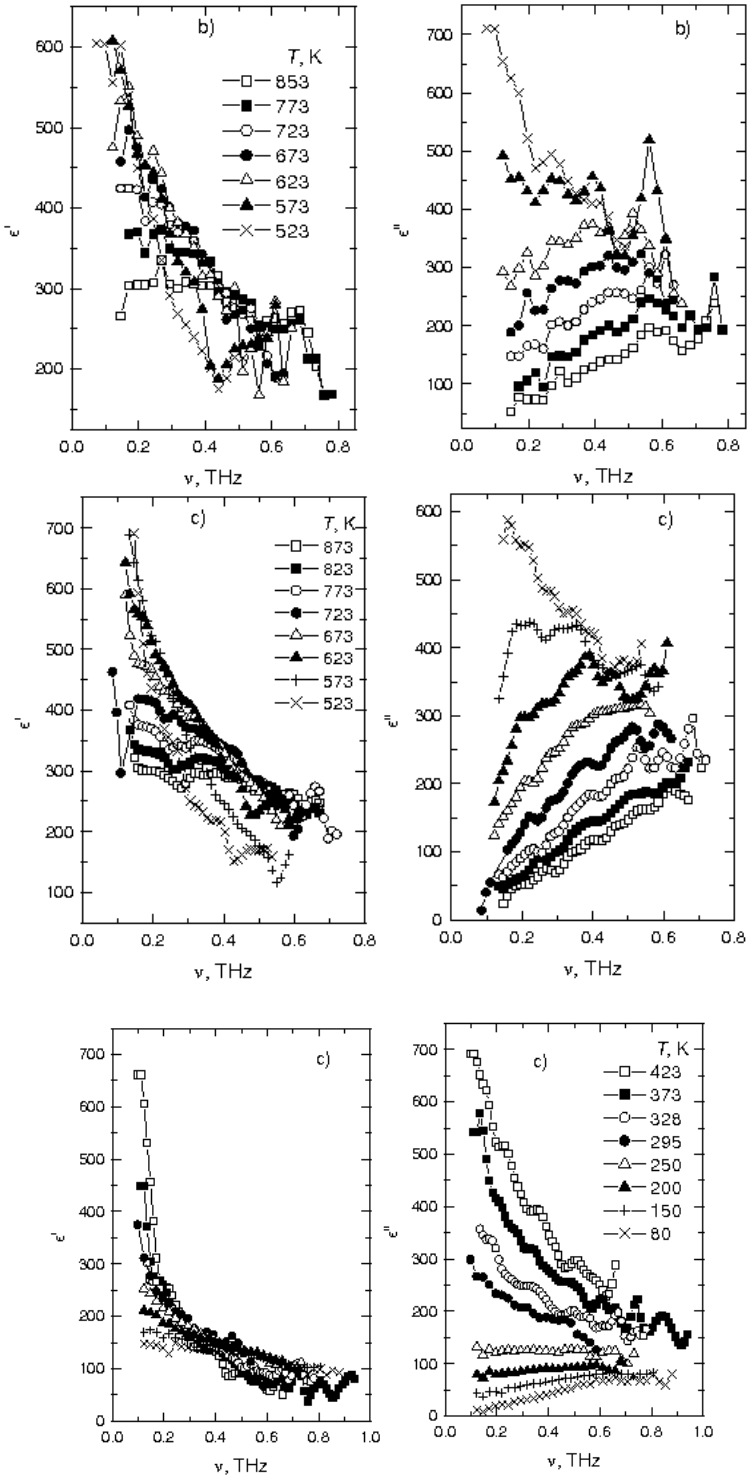


Figure 4.8. Continues.

Copyright © 2010. Nova Science Publishers, Incorporated. All rights reserved.

Handbook of Material Science Research, Nova Science Publishers, Incorporated, 2010. ProQuest Ebook Central,



Copyright © 2010. Nova Science Publishers, Incorporated. All rights reserved.

Reprinted figure with permission from [229]. Copyright 2006 by the American Physical Society.

Figure 4.8. Complex THz dielectric spectra of various PZN-PMN-PSN ceramics: a) 0.2PSN-0.4PZN-0.4PMN, b) 0.4PZN-0.3PMN-0.3PSN, c) 0.4PMN-0.3PSN-0.3PZN.

Handbook of Material Science Research, Nova Science Publishers, Incorporated, 2010. ProQuest Ebook Central,

The relaxation stems from dynamics of polar nanoregions and it is well known that the polar nanoregions start to appear below the Burns temperature T_B [1]. This temperature is not known in our solid solution system, but we assume that it has similar value as in pure PMN, i.e. near 600 K [1]. Note that ε' (below 200 GHz) and ε'' values are the highest at 523 K. This temperature is close to the Burns temperature in pure PMN. Nevertheless, one can see that the weak relaxation (decrease of $\varepsilon'(\omega)$ with frequency ω) is present in the spectra at least up to 773 K. The relaxation is the strongest at 523 K, because the relaxation has the highest relaxation frequency at this temperature. At lower temperatures the influence of relaxation into THz spectra weakens due to slowing down and broadening of dielectric relaxation.

Nevertheless, its contribution is seen in THz spectra at least down to 80 K, giving evidence that τ_{min} remains in the range 10^{-13} s down to this temperature. Nevertheless, one can see that the relaxation contribution gradually decreases on heating to 773 K, and finally no dielectric relaxation being seen at 823 K (Figure 4.8). Dielectric strengths of the relaxation decrease on heating above 523 K as a consequence of decrease in polar cluster concentration. It would mean that some polar clusters persist at least up to 773 K, i.e. the Burns temperature lies higher than in pure PMN. Note that similar behaviour, i.e. the unusual decrease in dielectric losses on heating above T_B was also observed in the PMN thin film ≈ 670 K [211].

This phenomenon was also explained by disappearance of the relaxation (central mode) and soft mode hardening above T_B [211] (see the discussion below).

Let us discuss the origin and temperature dependence of the distribution function f (τ) (Figure 4.5) together with the THz spectra. One symmetric and relatively narrow maximum is seen above 320 K in the THz and microwave range. The dielectric relaxation is caused predominantly by flipping, but also partially by breathing (i.e. fluctuations of the nanoregions volume) of polar nanoregions at high temperatures. At lower temperatures, the f (τ) function broadens and splits into two parts. The part at lower τ (probably mainly due to nanoregions flipping) anomalously slows down according to the Vogel-Fulcher law (see Figure 4.6) and disappears below freezing temperature T_0. The higher frequency part describes probably mainly breathing of the polar nanoregions. The breathing is temperature activated process, therefore it slows down on cooling according to the Arrhenius law. Large chemical disorder at the B perovskite sites causes random fields on disordered Pb atoms, which are most likely responsible for the anomalous broadening of f (τ) on cooling. Finally, f (τ) becomes almost flat between τ_{min} and τ_{max}. Below T_0, the τ_{max} shifts many orders of magnitude below our frequency range, therefore it was not evaluated from our spectra. Nevertheless, due to the expected increase of τ_{max} on cooling and due to the normalization condition (Eqs. (1.40) and (1.41)), one can expect decrease of both ε′ and ε″ at low temperatures. The THz dielectric spectra show influence of the dielectric relaxation down to at least 40 K. It means that τ_{min} remains almost constant in THz region down to very low temperatures. In other words, it means that there is a continuous distribution of activation energies for anharmonic hopping of Pb atoms from some maximum energy E_{max} essentially to 0. The energy E_{max} could be in principle obtained from the Arrhenius fit of $\tau_{max}(T)$ below T_0 , however such fit was not possible due to the lack of very low-frequency dielectric data. From the same reason f (τ) in Figure 5.5 was determined only above T_0.

The nature of the polar nanoregions and two-component dielectric relaxation is still under debate. Very recently Blinc et al. [262] suggested that ^{207}Pb NMR spectra give evidence for the two-component nature of relaxors - glassy matrix (corresponding to spherical displacements of Pb ions) and frozen polar nanoregions (due to the Pb displacements in the

Copyright © 2010. Nova Science Publishers, Incorporated. All rights reserved.

Handbook of Material Science Research, Nova Science Publishers, Incorporated, 2010. ProQuest Ebook Central,

[111] directions). These two components could be responsible also for the two-component dielectric relaxation [228]. Xu et al. [231] published recently some evidence that the polar nanoregions have polarizations along [110] directions, and that these clusters persist even in poled ferroelectric PZN with polarization along the [111] directions. Our opinion is that the two dielectric relaxation regions have origin in the flipping and breathing of the polar clusters, but the subject needs still further investigations.

4.1.4. Influence of AC Electric Field to Dielectric Dispersion of PMN-PSN-PZN Ceramics

The results of the dielectric experiments on the most studied relaxor system lead magnesium niobate PMN show that no long-range ferroelectric order is established in zero dc bias field. However, by cooling the PMN monocrystal in an electric field, higher than the critical field $E_C \approx 1.7$ kV/cm [232] or the PMN ceramics in a field higher than $E_C \approx 4$ kV/cm [233], a long-range ferroelectric phase is formed. Evidence that a dc electric field can induce such a transition came from an X-ray study [234]. Later, the electric-field–temperature (E-T) phase diagram of the PMN relaxor was proposed [84, 233, 235] based on the linear and nonlinear dielectric studies.

The sample was measured without a bias field in heating cycle and the results have been compared with the sample measured in different way: the sample was heated up, then poling field of 2 kV/cm was switched on and the sample was cooled down. After that, the bias field was switched off, and measurement was performed on heating. In other words two different measurements are compared: zero field heated (ZFH) measurement, field cooled and measured in ZFH. After each measurement a sample was heated to prevent history effects. Because no significant difference between zero field heated and zero field cooled data were observed [236], in this work we compare dielectric data on heading after poling with dielectric data on cooling without AC field (Figure4.2a). Obtained results of poled sample are presented in Figs. 4.9. Influence of external AC electric field to dielectric properties of investigated ceramics is significant. The real part of complex dielectric permittivity ε' decreases on temperature more than 10%. Very clearly, the field E = 2 kV/cm, induces net, albeit broadened, peaks in temperature dependence of both real part ε' and imaginary part ε'' of complex dielectric permittivity at T ≈ 244 K. Clearly they are superimposed on the usual broad background. Very similar anomaly observed in PMN in field headed [237] and in $KTaO_3$:Li crystals with x_{Li}=0.063 [238] on heading without field and after field cooled.

This anomaly is strongly related with relaxor-ferroelectric transition [239]. Such phenomenon can be explained according Andelman and Joanny's idea [240] that the external field helps privileged domains to grow up to macroscopic size. Interesting phenomenon observed by comparison frequency dependence after poling and without poling (Figure4.10). Inspection shows that the zero field frequency dependence of imaginary part ε'' of complex dielectric permittivity in frequency range 129 Hz – 1 MHz is almost linear function on a log-log scale, however the same dependence after poling is different: at lower frequencies value of losses is much smaller, clearly minimum at several kHz is expressed, and at higher frequencies difference between poled and unpoled sample losses become smaller. At this temperature (300 K) two maxima are clearly expressed in the distribution of relaxation times (Figure 4.5a) of unpoled sample. The long relaxation times maximum occurs mainly in the range of 10^{-5}-10^{-2} s. We can predicate that this part of distributions is mainly caused by

Copyright © 2010. Nova Science Publishers, Incorporated. All rights reserved.

Handbook of Material Science Research, Nova Science Publishers, Incorporated, 2010. ProQuest Ebook Central,

dielectric dispersion in the frequency range 10^2-10^6 Hz. Therefore, an influence of external electric field to distribution of relaxation times must by very significant [241].

The long-time maximum of distribution really not disappears after poling (as in [241]) because frequency dependence of losses show pronounced curvature (Figure4.10), however significant decrease of probability of relaxation time around 10^{-3} s must be observed so that pronounced minimum between two maxima in distributions must appear. Of course such consideration is speculative enough, because no measurements after poling at higher (above 1 MHz) frequencies were performed and therefore no real distributions of poled crystals can be calculated.

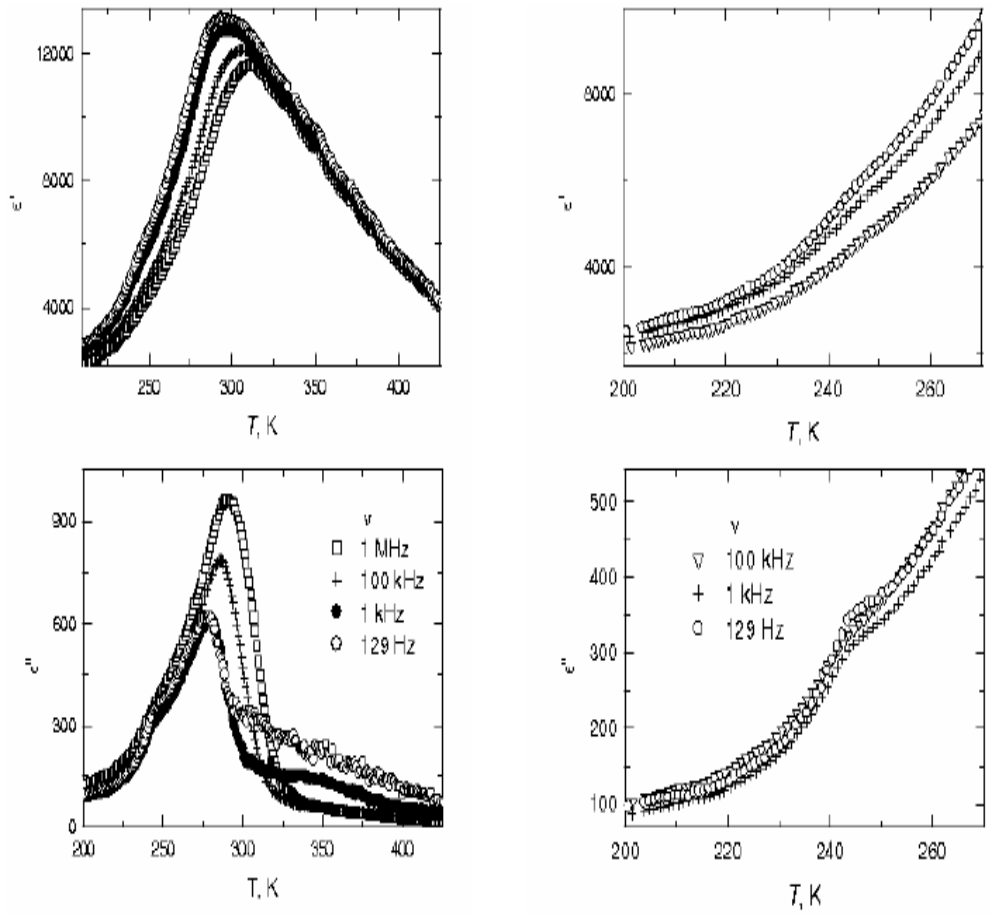


Figure 4.9. Temperature dependence of the real ε′ and the imaginary part ε″ of the dielectric permittivity of 0.4PZN-0.3PSN-0.3PZN ceramics at different frequencies, measured in ZFH, after 2kV/cm poling field cooled (on the right – enlarged scale around relaxor-ferroelectric transition temperature T=244 K).

Copyright © 2010. Nova Science Publishers, Incorporated. All rights reserved.

Handbook of Material Science Research, Nova Science Publishers, Incorporated, 2010. ProQuest Ebook Central,

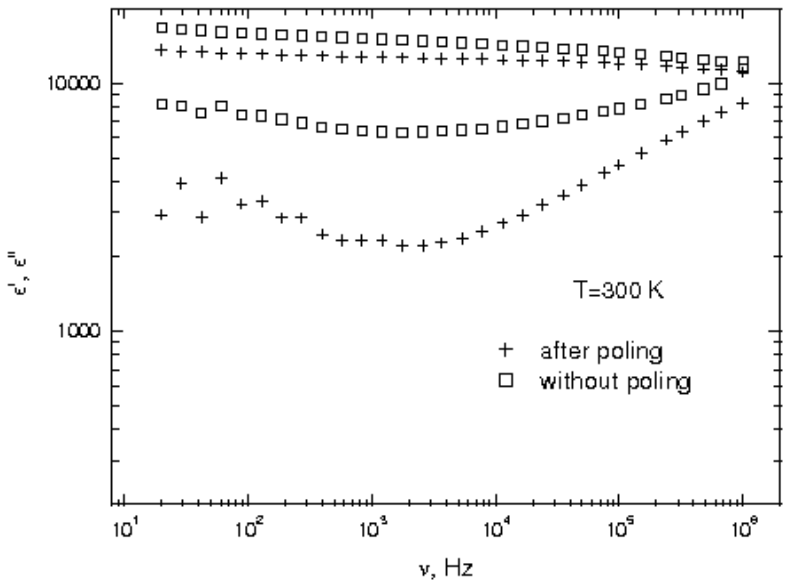


Figure 4.10. Frequency dependence of ε' and ε'' of poled and unpoled 0.4PZN-0.3PSN-0.3PMN ceramics.

4.2. Far-infrared Spectroscopy of PMN-PSN-PZN Ceramics

4.2.1. Infrared Reflectivity of PMN-PSN-PZN Ceramics

The data presented below were measured in the reflection mode using normal specular reflectance from the flat planar surface of a thick (i.e. opaque) sample, i.e. measuring the normal reflectivity $R(\omega)$. It is related to the isotropic relative complex permittivity $\varepsilon^*(\omega)$ by:

$$R(\omega) = \left| \frac{\sqrt{\varepsilon^*(\omega)} - 1}{\sqrt{\varepsilon^*(\omega)} + 1} \right|. \tag{4.1}$$

In all cases, when Eq. (4.1) holds, the complex permittivity $\varepsilon^*(\omega)$ can be in principle obtained in a standard way by the Kramers–Kronig analysis (by Eqs. (1.12) and (1.13) of broad-enough frequency range of reflectivity data, calculating the phase of complex reflectivity. In practice, a more accurate and convenient method is nowadays to use simple physically acceptable models for the dielectric function $\varepsilon^*(\omega)$ and fit them directly to the reflectivity spectrum. The dielectric function $\varepsilon^*(\omega)$ of a dielectric material usually contains contributions from the high-frequency electronic polarisation ε_∞, the polar phonons ε_{ph} and possibly of some dielectric relaxations ε_{dr}, which are particularly important in ferroelectrics, relaxors and all kinds of inhomogeneous materials (ceramics, composites) at lower frequencies. Frequency dependence in the IR polar-phonon region can be usually modeled as a sum of simple damped harmonic oscillator contributions

$$\varepsilon^*(\omega) = \varepsilon_\infty + \varepsilon_{ph} = \varepsilon_\infty + \sum_m \frac{S_m}{\omega_{Tom}^2 - \omega^2 + i\omega\gamma_{TOm}}, \tag{4.2}$$

Copyright © 2010. Nova Science Publishers, Incorporated. All rights reserved.

Handbook of Material Science Research, Nova Science Publishers, Incorporated, 2010. ProQuest Ebook Central,

where ω_{TOm}, γ_{TOm} and S_m denote the transverse optical (TO) m-th polar phonon mode frequency (it corresponds generally to the modulus of the m-th complex pole of the dielectric function), m-th TO-mode damping and (reduced) oscillator strength, respectively. For crystals with strong and overlapping polar modes (i.e. with substantial values of S_m), it is often necessary to replace the simple independent damped harmonic oscillator model by Eq. (5.2) by a more general factorised form of the dielectric function, using so-called generalized 4-parameter oscillator model [242], which, in addition to TO-mode parameters, allows independent and explicit adjustment of both the frequency ω_{LOm} and damping γ_{LOm} parameters of the m-th longitudinal optic (LO) mode:

$$\varepsilon^*(\omega) = \varepsilon_\infty \prod_j \frac{\omega_{LOj}^2 - \omega^2 + i\omega\gamma_{LOj}}{\omega_{TOj}^2 - \omega^2 + i\omega\gamma_{TOj}}. \tag{4.3}$$

The oscillator strength of the m-th mode, defined through ω_{LOm} and ω_{TOm} frequencies as:

$$S_m = \varepsilon_\infty \frac{\prod_j \omega_{LOj}^2 - \omega_{TOm}^2}{\prod_{j\neq m} \omega_{TOj}^2 - \omega_{TOm}^2} \tag{4.4}$$

is identical to that in equation (4.2) in cases when the Eqs. (4.2) and (4.3) are equivalent. In both cases, the static permittivity written as a sum of separate dielectric strengths $\Delta\varepsilon_m$ of all polar modes, can be further expressed through the oscillator strengths as:

$$\varepsilon(0) = \varepsilon_\infty + \sum_m \Delta\varepsilon_m = \varepsilon_\infty + \sum_m \frac{S_m}{\omega_{TOm}^2}. \tag{4.5}$$

The oscillator strength S_m is directly proportional to the squared effective charge associated with the corresponding mode eigenvector and it is thus characteristic of a given vibration type, irrespectively of its frequency. On the other hand, decrease ('softening') of ω_{TOm} to zero would lead to the divergence of the corresponding dielectric strength $\Delta\varepsilon_m$, and if, for example, the frequency of one (soft) mode follows the Cochran law (1.10) then equation (5.5) yields the Curie-Weiss-type (1.5) dielectric anomaly. For this reason, in the field of ferroelectricity it is usual to tabulate the dielectric strength of the m-th polar phonon $\Delta\varepsilon_m = S_m/\omega^2_{TOm}$ instead of the oscillator strength S_m.

In the literature another quantity is largely discussed about, so called mode-plasma frequency [243, 244] Ω_m, related to the oscillator strength S_m via:

$$\Omega_m^2 = -\frac{2}{\pi}\int_0^\infty \omega \,\mathrm{Im}\left[\frac{S_m}{\omega_{TOm}^2 - \omega^2 + i\omega\gamma_m}\right] d\omega = S_m. \tag{4.6}$$

The relation between Ω_m and the mode eigenvector is known to be given by a set of Born effective charges tensors for all in-equivalent ions in the unit cell. For example, the mode-plasma frequency associated with the mode strength in the $\varepsilon_{ii}(\omega)$ diagonal component of permittivity tensor is given by essentially linear relation

Copyright © 2010. Nova Science Publishers, Incorporated. All rights reserved.

Handbook of Material Science Research, Nova Science Publishers, Incorporated, 2010. ProQuest Ebook Central,

$$(\Omega_m)_{ii} = \frac{1}{\sqrt{\varepsilon_0 V_0}} \left| \sum_{kj} (Z_k^*)_{ij} m_k^{-1/2} (x_m)_{kj} \right|, \tag{4.7}$$

where i and j are Cartesian components, V_0 is the unit-cell volume, Z^*_k is the Born effective charges tensor of the ion k, m_k is its mass, and x_m is dimensionless eigenvector of the mass-reduced dynamical matrix associated with the m-th phonon mode normalized according to

$$\sum_{kj} (x_m)_{kj}^2 = 1 \tag{4.8}$$

with k going through all ions in the unit cell. The mode-plasma frequencies can be also expressed through the components of the mode-effective-charge vectors Z^{***}_m as defined by Gonze and Lee [243]

$$(\Omega_m)_{ii} = \frac{1}{\sqrt{\varepsilon_0 V_0}} \left| \sum_{kj} (Z_k^*)_{ij} m_k^{-1/2} (x_m)_{kj} \right|, \tag{4.9}$$

where $(Z^{**}_m)_i = M^{1/2}_m \Sigma_{kj} (Z^*_k)_{ij} m_k^{-1/2} (x_m)_{kj}$, $M^{-1}_m = \Sigma_{kj} m^{-1}_k (x_m)^2_{kj}$, or compared with the mode-effective-charge vectors Z^{***}_m introduced by Zhong et al. [244]

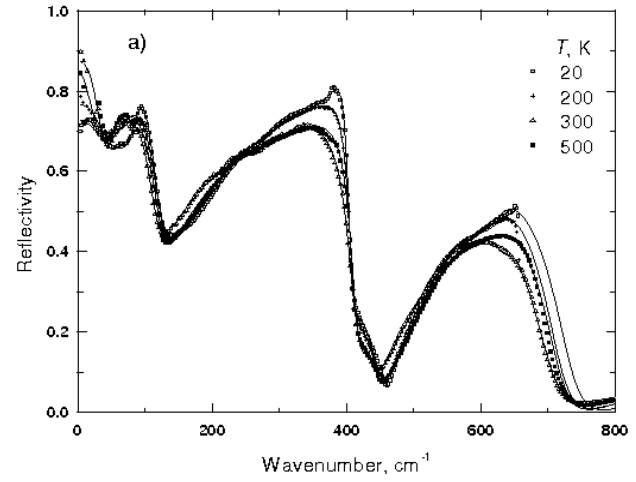
$$(Z_m^{***})_i = \sum_{kj} (Z_k^*)_{ij} (x_m)_{ij} \ . \tag{4.10}$$

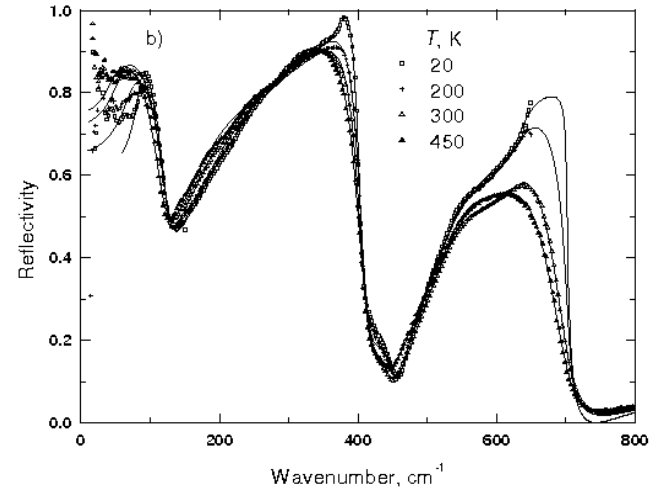
For particular simple structures, the phonon eigenvectors may be determined by symmetry so that all the three types of effective charges can be explicitly expressed through the mode-plasma frequencies. In general, however, none of them can be calculated from the mode-plasma frequencies alone without the a priori knowledge of the phonon eigenvectors. Among the various quantities that can be directly evaluated from the IR spectra, the mode-plasma frequencies Ω_m are in the closest relation to the phonon eigenvectors and are therefore convenient for phonon assignment and comparison with predictions from microscopic models. Isothermal IR and THz reflectivity spectra of all investigated PMN-PSN-PZN ceramics are shown in Figure4.11.

THz reflectivity was calculated from THz transmission spectra. The spectral range above 800 cm^{-1} is not shown because the reflectivity is flat at higher frequencies approaching the value given by the high-frequency permittivity ε_∞. IR and THz reflectivity spectra were fitted simultaneously using a generalized-oscillator model of the factorized form of the complex permittivity Eq. (4.3). The high-frequency permittivity ε_∞ resulting from electronic absorption processes was obtained from the frequency-independent room temperature reflectivity above the phonon frequencies.

Copyright © 2010. Nova Science Publishers, Incorporated. All rights reserved.

Handbook of Material Science Research, Nova Science Publishers, Incorporated, 2010. ProQuest Ebook Central,





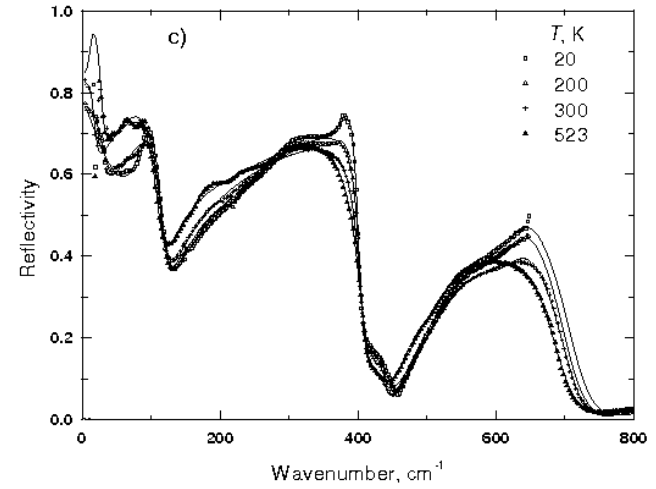
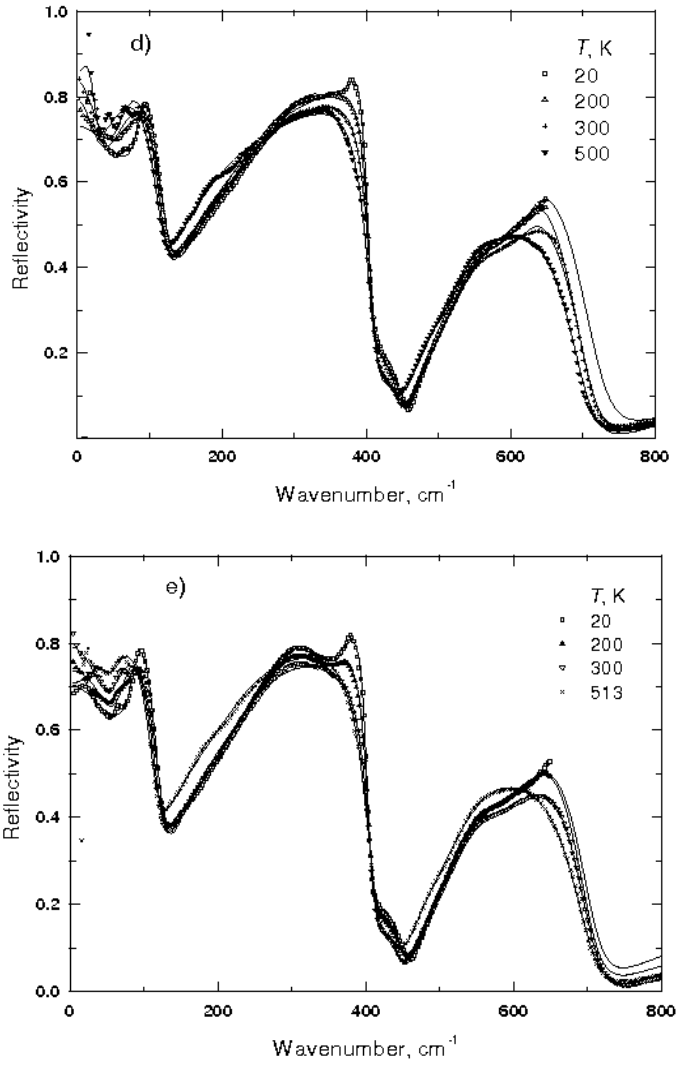


Figure 4.11. Continues.

Copyright © 2010. Nova Science Publishers, Incorporated. All rights reserved.

Handbook of Material Science Research, Nova Science Publishers, Incorporated, 2010. ProQuest Ebook Central,



Reprinted figure with permission from [229]. Copyright 2006 by the American Physical Society.

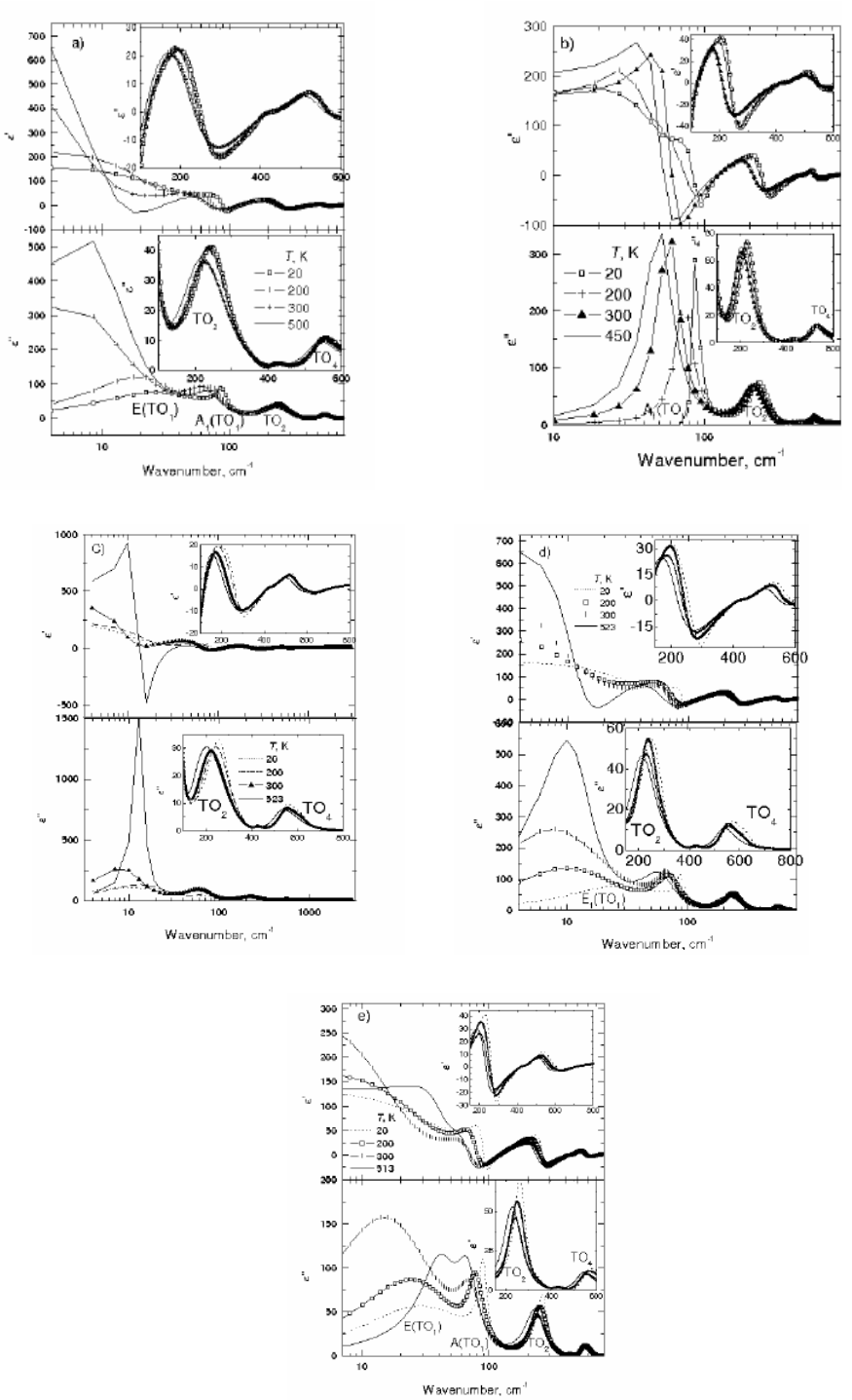
Figure 4.11. IR and THz reflectivity spectra of various PZN-PMN-PSN ceramics (a) 0.4PZN-0.3PMN-0.3PSN, b) 0.4PSN-0.3PMN-0.3PZN, c) 0.2PSN-0.4PMN-0.4PZN, d) 0.4PMN-0.3PSN-0.3PZN, e) 0.2PMN-0.4PSN-0.4PZN) at various temperatures. Solid lines are results of the fits.

Obtained values of ε_∞ are from 5.87 to 5.04 dependent from chemical composition and are comparable with the values of pure PMN – 5.87 [247] and PST – 5.67 [248]. The temperature dependence of ε_∞ is usually very small and was neglected in our fits.

Eight polar phonons were resolved below 150 K, and seven modes at higher temperatures. This is inconsistent with factor-group analysis for cubic and rhombohedral symmetry, where only 3 and 16 IR active modes are allowed in the IR spectra.

Copyright © 2010. Nova Science Publishers, Incorporated. All rights reserved.

Handbook of Material Science Research, Nova Science Publishers, Incorporated, 2010. ProQuest Ebook Central,



Reprinted figure with permission from [229]. Copyright 2006 by the American Physical Society.

Figure 4.12. Complex dielectric permittivity obtained from the fit of IR and THz spectra of various PZN-PMN-PSN ceramics (a) 0.4PZN-0.3PMN-0.3PSN, b) 0.4PSN-0.3PMN-0.3PZN, c) 0.2PSN-0.4PMN-0.4PZN, d) 0.4PMN-0.3PSN-0.3PZN, e) 0.2PMN-0.4PSN-0.4PZN). Points are guide for eye.

Copyright © 2010. Nova Science Publishers, Incorporated. All rights reserved.

Handbook of Material Science Research, Nova Science Publishers, Incorporated, 2010. ProQuest Ebook Central,

If we assume that the ceramics have macroscopically cubic symmetry with the polar nanoregions of rhombohedral symmetry, the IR probe is enough sensitive to see the local polar distortion, i.e. the polar modes from rhombohedral structure could be allowed in the spectra. Nevertheless, we do not see all the modes allowed in the rhombohedral phase because some of them could be weak and/or overlapped with others due to their finite widths.

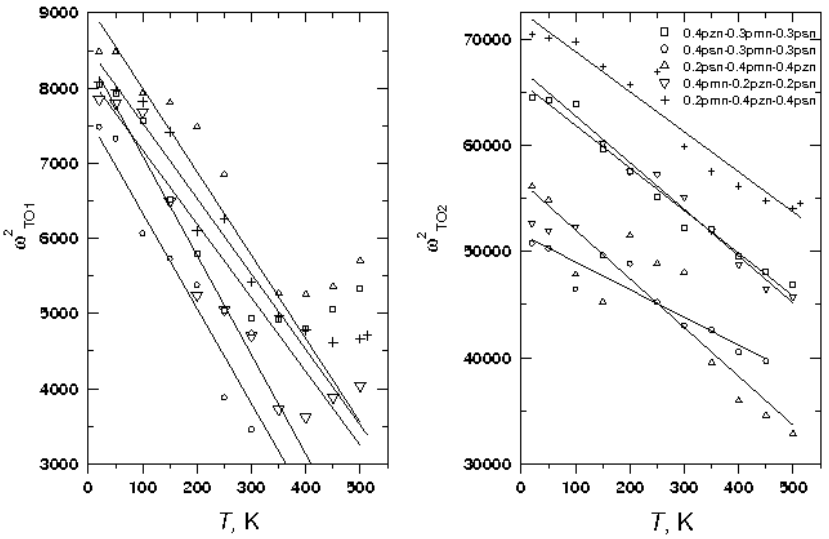
Real and imaginary parts of $\varepsilon^*(\omega)$ obtained from the fits of IR reflectivity and THz dielectric spectra are shown in Figure 4.12. The low-frequency part of the IR and THz spectrum was fitted with an overdamped oscillator. Of course, this model cannot completely fit the microwave relaxation (see Section 4.1.2.), but it can roughly describe the high-frequency wing of microwave relaxation seen in THz spectra. Dielectric contribution of the overdamped oscillator increases with temperature, because the relaxation frequency of the microwave relaxation hardens and comes into THz range.

4.2.2 Phonon Modes of PMN-PSN-PZN Ceramics

Interesting phonon anomalies were observed in all investigated ceramics. Most of phonon frequencies exhibit softening on heating, the most remarkable softening is seen by the lowest frequency TO_1 phonon. Similar soft TO_1 modes were observed in PMN and PST. This mode was explained as a ferroelectric soft mode in polar nanoregions [211, 212], which softens close to the Burns temperature. The soft mode frequency follows the Cochran law (1.10). Obtained parameters of the fits according to Eq. 1.10 are presented in Tables 4.4 and 4.5.

The T_{cr1} of TO_1 mode fluctuates between 600 and 860 K, but it is really difficult to speculate that these temperatures correspond to the Burns temperature, because the experimental TO_1 frequencies start to increase already above 400 K. Nevertheless, it is worth to note, that in 0.4PZN-0.3PMN-0.3PSN, 0.2PSN-0.4PMN-0.4PSN and 0.4PMN-0.3PZN-0.3PSN ceramics the dielectric relaxation (in other words, the polar clusters) disappears above 773 K which corresponds more less to T_{cr} of first two ceramics from the Cochran law for TO_1 mode and is significantly different from T_{cr} of 0.4PMN-0.3PZN-0.3PSN ceramics.

Copyright © 2010. Nova Science Publishers, Incorporated. All rights reserved.



Reprinted figure with permission from [229]. Copyright 2006 by the American Physical Society.

Figure 4.13. Cochran fit to a) TO_1 and b) TO_2 modes in various PZN-PMN-PSN ceramics.

Handbook of Material Science Research, Nova Science Publishers, Incorporated, 2010. ProQuest Ebook Central,

Table 4.4. Parameters of the Cochran's fit of TO_1 modes in PZN-PMN-PSN ceramics

compounds	A, cm^2/K	T_{cr1}, K
0.4PZN-0.3PMN-0.3PSN	11.12	747
0.4PSN-0.3PMN-0.3PZN	12.66	599
0.2PSN-0.4PMN-0.4PZN	11.1	820
0.4PMN-0.3PSN-0.3PZN	13.22	636
0.2PMN-0.4PSN-0.4PZN	10.05	859

Reprinted table with permission from [229]. Copyright 2006 by the American Physical Society.

Table 4.5. Parameters of Cochran's fit of TO_2 modes in PZN-PMN-PSN ceramics

compounds	A, cm^2/K	T_{cr1}, K
0.4PZN-0.3PMN-0.3PSN	40.15	1641
0.4PSN-0.3PMN-0.3PZN	26.15	1975
0.2PSN-0.4PMN-0.4PZN	45.97	1231
0.4PMN-0.3PSN-0.3PZN	37.57	1901
0.2PMN-0.4PSN-0.4PZN	37.76	1922

Reprinted table with permission from [229]. Copyright 2006 by the American Physical Society.

Non-complete softening of TO_1 mode was observed in all previously studied perovskite relaxors [249]. For example, in pure PMN [213] the soft mode followed the Cochran law up to 450K and it leveled off at higher temperatures.

Recently, Toulouse et al. [250] investigated PZN relaxor by means of Raman scattering and reported about a new critical temperature near 470 K, which he called "temperature of local phase transition" or temperature of creation of polar nanoregions. According to Toulouse at al. the Burns temperature is just temperature, below which the anharmonic vibration of Pb atoms becomes slower than the frequency of F_{1u} soft mode. Dkhil et al. [251] reported also about a new critical temperature T_l located between the Burns T_B and the freezing T_0 temperature. They observed rise of diffuse scattering in PMN below $T_l \approx 400$ K as well as plateau in temperature dependent lattice constant between T_l and T_0. Unfortunately, we did not study IR reflectivity spectra above 500 K due to limit of our furnace. For the investigation of $TO_1(T)$ above T_B is more suitable and more accurate far IR transmission spectroscopy of relaxor thin films deposited on transparent substrate like sapphire or MgO [210]. We speculate that the T_l temperature corresponds to temperature, below which the polar clusters percolate. The effective soft mode cannot completely soften in the system of non-percolated clusters [250] due to rise of effective soft phonon frequency in the composite of polar clusters with non-polar matrix. Therefore, the leveling off (or even increase) of soft mode frequency is seen above $T_l \approx 400$ K.

Surprisingly, the TO_2 mode frequency also softens on heating and follows the Cochran law (Figure 4.13b). This mode is so called Slater mode describing predominantly vibration of B atoms against oxygen octahedral [253]. The B sites exhibit large chemical disorder (4 various atoms of different valency!) and T_{cr2} temperature can correspond to temperature, where the B site atoms can theoretically migrate, because T_{cr2} is close to the temperature of compositional order-disorder phase transitions (see Subsection 1.3.2.). The list of polar mode

Copyright © 2010. Nova Science Publishers, Incorporated. All rights reserved.

Handbook of Material Science Research, Nova Science Publishers, Incorporated, 2010. ProQuest Ebook Central,

parameters in investigated PMN-PSN-PZN ceramics is summarized in Tables 4.6 (at 300 K) and 4.7 (at 20 K).

The parameters of investigated ceramics are very similar and comparison with pure PMN [245, 247] as well as with PST [252] or with PMN-PT [247, 253] shows that the spectra of all perovskite relaxors have the same features: original three F_{1u} cubic perovskite modes are split due to lower symmetry in polar nanoregions. The most remarkable splitting is seen in the soft mode at 20 K. Its A_1 component has frequency near 90 cm^{-1}, while the E component is heavily damped and has frequency near 20 cm^{-1}. Detail assignment of polar modes in perovskite relaxors was recently thoroughly discussed [247]: the modes below 100 cm^{-1} are so called Last modes [256] expressing predominantly the vibration of rigid BO_6 octahedra against Pb atoms.

Table 4.6. Polar modes parameters of PMN-PSN-PZN ceramics at 300 K

ceramics	ω_{TO}, cm^{-1}	γ_{TO}, cm^{-1}	ω_{LO}, cm^{-1}	γ_{LO}, cm^{-1}	$\Delta\varepsilon$
0.4PZN-0.3PMN-0.3PSN	70.2	57.1	118.2	39.4	59.2
	228.4	168.3	410.5	22.5	17.5
	296.2	317.3	291.2	479.6	0.8
	431.2	44.3	444.7	33.8	0.1
	548.3	101	711.8	56.7	1.6
	623.1	78	615.8	92.3	0.1
0.4PSN-0.3PMN-0.3PZN	58.8	23.6	124.9	36.8	132.3
	207.4	90.7	408.4	30.4	19
	296.2	258.9	291.2	426.9	0.5
	443.6	82.6	450.3	44.1	0.1
	527.9	89.1	701.7	46.9	1.7
	627.9	101.1	625.8	154.9	0.02
0.2PSN-0.4PMN-0.4PZN	68.8	54.9	118.6	32.7	63.94
	219.2	200.7	407.2	23.2	17.54
	282.2	277	277.9	438.5	0.8
	425.5	43.6	440.6	35.3	0.1
	544.5	110.8	709.9	65.2	1.4
	629.1	80.7	621.2	114.7	0.08
0.4PMN-0.3PSN-0.3PZN	68.6	33	110.7	31	49.5
	234.8	119.9	404.5	21.6	17.3
	292	307.2	289.3	418	0.5
	434.1	56.5	445.1	39	0.1
	547.3	87.6	703.8	60.3	1.6
	620.1	72.4	610.2	101.4	0.1
0.2PMN-0.4PSN-0.4PZN	73.6	37.8	108.2	27.8	31
	244.7	90.2	402.8	22.5	14.9
	299.6	492.5	296.1	514.6	0.5
	429.4	47.4	442.2	38.3	0.1
	541.7	89.7	697.3	55.2	1.5
	628.5	95.8	616.4	150.1	0.1

Part reprinted table with permission from [229]. Copyright 2006 by the American Physical Society.

Copyright © 2010. Nova Science Publishers, Incorporated. All rights reserved.

Handbook of Material Science Research, Nova Science Publishers, Incorporated, 2010. ProQuest Ebook Central,

Table 4.7. Polar modes parameters of PMN-PSN-PZN ceramics at 20 K

ceramics	ω_{TO}, cm^{-1}	γ_{TO}, cm^{-1}	ω_{LO}, cm^{-1}	γ_{LO}, cm^{-1}	assignment
0.4PZN-0.3PMN-0.3PSN	17.5	17.5	23.2	56.9	E component of TO_1
	91.7	29.5	119.1	27.4	A_1 component of TO_1
	266.6	170.4	404.7	19.2	E component of TO_2
	296.2	340.6	294.2	441.9	A_1 component of TO_2
	358.3	112.8	352	88.1	From Brillouin zone boundary
	405.7	62.1	447.9	37.9	Resonance between E LO_2 and A_1 LO_2 - see Ref. 290
	533.2	105.5	735.4	41.9	E component of TO_4
	623.9	100.6	615.7	137	A_1 component of TO_4
0.4PSN-0.3PMN-0.3PZN	25.4	18.4	35.7	49.3	E component of TO_1
	86.5	9.9	125.4	35.1	A_1 component of TO_1
	225.3	94.1	405.2	20.5	E component of TO_2
	296.2	161.8	291.2	423.6	A_1 component of TO_2
	368.2	96.9	348.3	87.1	From Brillouin zone boundary
	443.6	82.5	450.3	27.6	Resonance between E LO_2 and A_1 LO_2 - see Ref. 290
	527.9	102.1	701.7	2.9	E component of TO_4
	627.9	60.5	625.8	71.3	A_1 component of TO_4
0.2PSN-0.4PMN-0.4PZN	17.4	16.3	32.1	55.3	E component of TO_1
	95.1	20.4	114.2	21.7	A_1 component of TO_1
	236.1	240.9	395.2	18.2	E component of TO_2
	282.5	79.1	277.9	280.2	A_1 component of TO_2
	381.1	31.4	362.3	238.5	From Brillouin zone boundary
	408.3	303.8	443.5	60.4	Resonance between E LO_2 and A_1 LO_2 - see Ref. 290
	551.3	31.6	709.9	231.3	E component of TO_4
	628.1	63.5	621.2	147.5	A_1 component of TO_4
0.4PMN-0.3PSN-0.3PZN	29.4	21.2	39.5	59.5	E component of TO_1
	88.2	19.2	118.7	32.4	A_1 component of TO_1
	241.4	157.2	406.8	14.7	E component of TO_2
	292	111.4	289.3	440.1	A_1 component of TO_2
	379.4	80.1	354.1	84.5	From Brillouin zone boundary
	434.3	55.7	444.4	18.4	Resonance between E LO_2 and A_1 LO_2 - see Ref. 290
	568.2	89.2	703.8	60.3	E component of TO_4
	626.4	66.7	610.2	107.4	A_1 component of TO_4
0.2PMN-0.4PSN-0.4PZN	17.5	17.5	23.2	50.3	E component of TO_1
	88.3	26.1	121.1	25.8	A_1 component of TO_1
	263.7	68.5	404.2	17.8	E component of TO_2
	296.2	411.7	294.2	442.7	A_1 component of TO_2
	365.1	95.7	351.3	85.8	From Brillouin zone boundary
	405.7	65.5	447.9	50.1	Resonance between E LO_2 and A_1 LO_2 - see Ref. 290
	552.1	80	733.1	164.4	E component of TO_4
	623.9	62.5	615.7	108.6	A_1 component of TO_4

Part reprinted table with permission from [229]. Copyright 2006 by the American Physical Society.

Copyright © 2010. Nova Science Publishers, Incorporated. All rights reserved.

Handbook of Material Science Research, Nova Science Publishers, Incorporated, 2010. ProQuest Ebook Central,

Two modes between 200 and 300 cm^{-1} are A_1 and E components of so called Slater modes [255] (vibration of B atoms against O_6 octahedra) and the modes above 500 cm^{-1} are Axe modes [256] (bending of the O_6 octahedra).

The mode near 350 cm^{-1} is activated in the spectra only due to local order in the B sites and express the mutual B atoms vibrations. Hlinka et al. [258] recently used the effective medium approximation for the evaluation of room temperature IR reflectivity spectra of PMN and showed that this approach can be used for determination of anisotropic dielectric functions (i.e. also of parameters of modes of different symmetries) in polar nanoregions. It follows from this analysis that the mode near 430 cm^{-1} (seen also in our spectra), is not real polar phonon but just apparent mode which appears in the IR spectra as consequence of resonances between two longitudinal mode frequencies [249].

Figure 4.12 shows the broad maximum of $\varepsilon''(\omega)$ near 30 cm^{-1} which is the E component of the soft mode. This mode softens to about 20 cm^{-1} at 200 K, however at higher temperatures is this mode overlapped by the dielectric relaxation which approaches this frequency range and which is seen as a peak near 7 cm^{-1}. The E mode probably disappears from the spectra above the Burns temperature, where only triple degenerate F_{1u} mode is allowed.

CONCLUSION

Two different systems have been presented in this chapter. One system is typical dipolar glass - BP – BPI, such as other well known dipolar glasses, for example RADP. Another system is typical relaxors, such as PMN or disordered PSN. Different summary can be made for these systems:

(i) Mixed betaine phosphite betaine phosphate crystals

a) A small amount of antiferroelectric betaine phosphite changes dielectric dispersion of betaine phosphite substantially. Broad and asymmetric distribution of relaxation times of these crystals around the ferroelectric phase transition temperature T_c clearly differs from usually observed in ferroelectrics. Local polarization of these ferroelectric shows pronounced distribution even at low temperatures. At very low temperatures ($T << T_c$) the coexistence of ferroelectric order and dipolar glass disorder in these ferroelectrics is observed.

b) The non-zero mean value $\bar{J}/k_B$ of the random bond interaction of mixed $BP_{1-x}BPI_x$ crystals with x=0.15-0.5 vanishes for very low temperatures. It is related with the transition into the low-temperature non-ergodic glassy phase.

(ii) PMN-PSN-PZN relaxors

a) Creation of polar nanoregions below the Burns temperature in PMN-PSN-PZN ceramics manifests by appearance of the dielectric relaxation in THz range, by temperature dependence of the A1 component of the ferroelectric soft mode and by splitting of all polar modes in the infrared spectra. The Burns temperature of PMN-

Copyright © 2010. Nova Science Publishers, Incorporated. All rights reserved.

Handbook of Material Science Research, Nova Science Publishers, Incorporated, 2010. ProQuest Ebook Central,

PSN-PZN ceramics is about 700-800 K. It is higher than previously declared for PMN crystals.

b) Two dielectric relaxation regions of ferroelectric relaxors PMN-PSN-PZN were successfully separated. The short relaxation times region appears at the Burns temperature in THz spectra and on cooling it heavily slows down according to the Arrhenius law. Breathing of the polar nanoregions causes this region. The long relaxation times region appears close to room temperature and, on cooling it slows down according to the Vogel-Fulcher law and disappears below freezing temperature. Flipping of the polar nanoregions causes this relaxation.
c) The long relaxation times region is strongly affected by strong external electrical DC field. Such electrical field induces relaxor-ferroelectric transition in 0.4PZN-0.3PMN-0.3PSN ceramics at T = 244 K.
d) The Last mode in PMN-PSN-PZN ceramics, expressing the vibration of rigid BO6 octahedra against Pb atoms, is the ferroelectric soft mode inside the polar nanoregions. It critical temperature corresponds to the Burns temperature. Softening of A1 component of the Last mode vanishes above 400 K, below this temperature the polar nanoregions percolate.
e) Frequency of the Slater mode, describing vibration of B atoms against the oxygen octahedral, also softens on heating and follows the Cochran law. Critical temperature of the Slater mode is of 1200-1900 K order and it is the temperature of compositional order-disorder phase transitions.

The low frequency part, or freezing behaves very similarly for the both systems – dipolar glasses and relaxors. Concluding we can state, that we have the same dipolar glass state, only the material is approaching this dipolar glass state differently – in one case by the order – disorder scenario, in other by displacive scenario. The first case is dipolar glass in usual notation, the second case is relaxor [259]. Both cases have extremely broad distribution of the relaxation times, especially around and below the freezing temperature.

Copyright © 2010. Nova Science Publishers, Incorporated. All rights reserved.

REFERENCES

[1] G. Burns and F. H. Dacol, Solid State Commun. 48, 853 (1983), G. Burns and F. H. Dacol, *Phys. Rev*. B 28, 2527 (1983).
[2] C. Kittel, *Introduction to Solid State Physics*, Wiley, New York, (1996).
[3] L. Brillouin, *Wave Propagation in Periodic Structures*, Dover Publications, New York, (1953).
[4] W. Cochran, *Phys. Rev. Lett*. 3, 412 (1959).
[5] P. Debye, *Polar molecules,* Dover, New York (1954).
[6] R. Kubo, *J. Phys. Soc. Jpn*. 12, 570 (1957).
[7] J. Grigas, *Microwave dielectric spectroscopy of ferroelectrics and related materials*, Gordon and Breach Science Publ., OPA Amsterdam (1996).
[8] K. Binder, A. P. Young, *Rev. Mod. Phys*. 58, 802 (1986).
[9] E. Courtsen, *Phys. Rev. Lett*. 52, 69 (1984).
[10] F. Lüty and J. Ortiz-Lopez, *Phys. Rev. Lett*. 50, 1289 (1983).

Handbook of Material Science Research, Nova Science Publishers, Incorporated, 2010. ProQuest Ebook Central,

[11] K. H. Michel, *Phys. Rev. Lett*. 57, 2188 (1987).
[12] S. F. Edwards and P. W. Anderson, *J. Phys.* F 5, 965 (1975).
[13] V. A. Cannella and J. A. Mydosh, *Phys, Rev*. B 6, 4220 (1972).
[14] D. Sherington and S. Kirkpatrick, *Phys. Rev*. Lett. 35, 1972 (1975).
[15] M. Oresic and R. Pirc, *Phys, Rev*. B 47, 2655 (1993).
[16] R. Pirc, B. Tadic and R. Blinc, *Phys. Rev*. B 36, 8607 (1987).
[17] G. A Smolenskii, V. A. Isupov, A. I. Agranovskaya and S. N. Popov, *Sov. Phys. Solid State* 2, 2584 (1961).
[18] F. Chu, N. Setter and A. K. Tagantsev, *J. Appl. Phys.* 74, 5129 (1993).
[19] X. Dai, Z. Xu and D. Viehland, *Phil. Mag.* B 70, 33 (1994).
[20] A. Krumins, T. Shiosaki and S. Koizumi, *Jpn. J. Appl. Phys*. Pt. 1 33, 4940 (1994).
[21] Ph. Sciau, G. Calvarin and J. Ravez, *Solid State Commun*. 113, 77 (2000).
[22] A. Simon, J. Ravez and M. Maglione, *J. Phys.: Condens. Matter* 16, 963 (2004).
[23] N. Yasuda, H. Ohwa and S. Asano, *Jpn. J. Appl. Phys*. Pt. 1 35, 5099 (1996).
[24] C. G. F. Stenger and A. J. Burggraaf, *Phys. Stat. Solidi* (a) 60, 653 (1980).
[25] C. Boulesteix, F. Varnier, A. Llebaria and E. Husson, *J. Solid State Chem.* 108, 141, (1994).
[26] M. Yoshida, S. Mori, N. Yamamoto, Y. Uesu and J. M. Kiat, *Ferroelectrics* 217, 327 (1998).
[27] A. Tkachuk and H. Chen, *Ferroelectrics* 253, 1 (2001).
[28] P. K. Davies and M. A. Akbas, *J. Phys. Chem. Solids* 61, 159 (2000).
[29] H. Z. Jin, J. Zhu, S, Miao, X. W. Zhang and Z. Y. Cheng, *J. Appl. Phys.* 89, 5048 (2001).
[30] A. A. Bokov, I. P. Raevskii and V. G. Smotrakov, *Sov. Phys. Solid State* 26, 1708 (1984).
[31] A. A. Bokov, M. A. Leshchenko, M. A. Malitskaya and I. P. Raevski, *J. Phys.: Condens. Matter* 11, 4899 (1999).
[32] R. Comes, M. Lambert, and A. Guinier, *Acta Crystallogr*. B 26, 244 (1970).
[33] E. A. Stern, *Phys. Rev. Lett.* 93, 037601 (2004).
[34] R. E. Cohen, *Nature* 358, 136 (1992).
[35] P. Bonneau, P. Garnier, E. Husson and A. Morell, *Mat. Res. Bull* 24, 201 (1989).
[36] P. Bonneau, P. Garnier, G. Calvarin, E. Husson, J. R. Gavarri, and A. Morell, *J. Solid State Chem*. 91, 350 (1991).
[37] S. Vakhrushev, S. Zhukov, G. Fetisov and V. Chernyshov, *J. Phys.: Condens. Matter* 6, 4021 (1994).
[38] K. Fujishiro, T. Iwase, Y. Uesu, Y. Yamada, B. Dkhil, J. M. Kiat, S. Mori and N. Yamamoto, *J. Phys. Soc. Japan* 69, 2331 (2000).
[39] B. Dkhil, J. M. Kiat, G. Calvarin, G. Baldinozzi, S. B. Vakhrushev and E. Suard, *Phys, Rev*. B 65, 024104 (2001).
[40] S. G. Zhukov, V. V. Chernyshev and S. B. Vakhrushev, *Ferroelectrics* 235, 143 (1999).
[41] R. Blinc, V. Laguta and B. Zalar, *Phys. Rev. Lett*. 91, 247601 (2003).
[42] T. Egami, *Ferroelectrics* 267, 101 (2002).
[43] S. Aoyagi, Y. Kuroiwa, A. Sawada, H. Tanaka, I. Harada, E. Nishibori, M. Takata and M. Sakata, *J. Phys. Soc. Jpn* 71, 2353 (2002).
[44] Y. Uesu, Y. Yamada, K. Fujishiro, H. Tazawa, S. Enokido, J. M. Kiat and B. Dkhil, *Ferroelectrics* 217, 319 (1998).

Copyright © 2010. Nova Science Publishers, Incorporated. All rights reserved.

Handbook of Material Science Research, Nova Science Publishers, Incorporated, 2010. ProQuest Ebook Central,

[45] V. A. Shuvaeva, I. Pirog, Y. Azuma, K. Yagi, K. Sakaue, H. Terauchi, I. P. Raevskii, K. Zhuchkov and M. Yu. Antipin, *J. Phys.: Condens. Matter* 15, 2413 (2003).
[46] G. Burns and F. H. Dacol, *Solid State Commun.* 48, 853 (1983).
[47] S. B. Vakhrushev, B. E. Kvyatkovsky, A. A. Nabereznov, N. M. Okuneva and B. P. Toperverg, *Ferroelectrics* 90, 173 (1989).
[48] A. Nabereznov, S. Vakhrushev, B. Dorner, D. Strauch and H. Moudden, *Eur. Phys. J.* 11, 13 (1999).
[49] S. Vakhrushev, A. Nabereznov, S. K. Sinha, Y. P. Feng and T. Egami, *J. Phys. Chem. Solids* 57, 1517 (1996).
[50] K. Hirota, Z. G. Ye, S. Wakimoto, P. M. Gehring and G. Shirane, *Phys. Rev*. B 65, 104105 (2002).
[51] G. Xu, G. Shirane, J. R. D. Copley and P. M. Gehring, *Phys. Rev*. B 69, 064112 (2004).
[52] D. La-Orauttapong, J. Toulouse, J. L. Robertson and Z. G. Ye, *Phys. Rev*. B 64, 212101 (2001).
[53] C. Stock, R. J. Birgeneau, S. Wakimoto, J. S. Gardner, W. Chen, Z. G. Ye and G. Shirane, *Phys. Rev*. B 69, 094104 (2004).
[54] S. B. Vakhrushev, A. A. Naberezhnov, N. M. Okuneva and B. N. Savenko, *Phys. Solid State* 37, 1993 (1995).
[55] N. Takesue, Y. Fujii and H. You, *Phys. Rev*. B 64, 184112 (2001).
[56] Y. Moriya, H. Kawaji, T. Tojo and T. Atake, *Phys. Rev. Lett.* 90, 205901 (2003).
[57] F. M. Jiang and S. Kojima, Phys. Rev. B 62, 8572 (2000); *Appl. Phys. Lett.* 77, 1271 (2000).
[58] V. V. Lemanov, N. K. Yushin, E. P. Smirnova, A. V. Sotnikov, E. A. Tarakanov and A. Yu. Maksimov, *Ferroelectrics* 134, 139 (1992).
[59] K. Uchino, *Ferroelectrics* 151, 321(1994).
[60] J. Zhao, A. E. Glazounov, Q. M. Zhang and B. Toby, *Appl. Phys. Lett.* 72, 1048 (1998).
[61] E. Dul'kin, I. P. Raevskii and S. M. Emel'yanov, *Phys. Solid State* 45, 158 (2003).
[62] M. D. Glinchuk and R. Farhi, *J. Phys.: Condens. Matter* 8, 6985 (1996).
[63] A. A. Bokov, *JEPT* 84, 994 (1997).
[64] P. N. Timonin, *Ferroelectrics* 199, 69 (1997).
[65] A. A. Bokov, Phys. Solid State 36, 19(1994); *Ferroelectrics* 190, 197 (1997).
[66] V. Westphal, W. Kleemann and M. D. Glinchuk, *Phys. Rev. Lett.* 68, 847 (1992).
[67] V. M. Ishchuk, *Ferroelectrics* 255, 73 (2001).
[68] N. de Mathan, E. Husson, G. Calvarin, J. R. Gavarri, A. W. Hewat and A. Morell, *J. Phys.: Condens. Matter* 3, 8159 (1991).
[69] W. Kleemann, *Int. J. Mod. Phys.* B 7, 2469 (1993).
[70] Y. Imry and S. K. Ma, *Phys. Rev. Lett.* 35, 1399 (1975).
[71] V. A. Isupov, *Ferroelectrics* 289, 131 (2003).
[72] A. A. Bokov, *Ferroelectrics* 131, 49 (1992).
[73] A. A. Bokov and Z. G. Ye, *Phys. Rev*. B 66, 064103 (2002).
[74] Y. Bing, A. A. Bokov, Z. G. Ye, B. Noheda and G. Shirane, *J. Phys.: Condens. Matter* 17, 2493 (2005).
[75] C. S. Tu, V. H. Schmidt and I. G. Siny, *J. Appl. Phys.* 78, 5665 (1995).
[76] A. Verbaere, Y. Piffard, Z. G. Ye and E. Husson, *Mat. Res. Bull.* 27, 1227 (1992).
[77] A. R. Lebedinskaya and M. F. Kupriyanov, *Phase Transitions* 75, 289(2002).
[78] W. Kleemann and R. Lindner, *Ferroelectrics* 199, 1 (1997).

Copyright © 2010. Nova Science Publishers, Incorporated. All rights reserved.

Handbook of Material Science Research, Nova Science Publishers, Incorporated, 2010. ProQuest Ebook Central,

[79] Z. G. Ye and H. Schmid, *Ferroelectrics* 145, 83 (1993).
[80] A. Tkachuk and H. Chen, Fundamental Physics of Ferroelectrics 2003, AIP Conference Proceedings 677, 55 (2003).
[81] R. V. Chamberlin, *Europhys. Lett.* 33, 545 (1996).
[82] E. V. Colla, E. Yu. Koroleva, N. M. Okuneva and S. B. Vakhrushev, *Phys. Rev. Lett.* 74, 1681 (1995).
[83] S. B. Vakhrushev, J. M. Kiat, and B. Dkhil, *Solid State Commun*. 103, 477 (1997).
[84] E. V. Colla, L. K. Chao, M. B. Weissman and D. Viehland, *Phys. Rev. Lett.* 85, 3033 (2000).
[85] A. Levstik, Z. Kutnjak, C. Filipic, and R. Pirc, *Phys. Rev*. B 57, 11204 (1998).
[86] Z. Kutnjak, C. Filipic, R. Pirc, A. Levstik, R. Farhi and M. Marssi, *Phys. Rev*. B 59, 294, (1999).
[87] R. G. Palmer, *Adv. Phys.* 31, 669 (1982).
[88] G. Calvarin, E. Husson and Z.-G. Ye, *Ferroelectrics* 165, 349 (1995).
[89] G. A. Smolenskii, *J. Phys. Soc. Jpn.* 28, (Supl.) 26 (1970).
[90] V. V. Kirillov and V. A. Isupov, *Ferroelectrics* 5, 3 (1973).
[91] L. E. Cross, *Ferroelectrics* 76, 241 (1987); 151, 305 (1994).
[92] B. E. Vugmeister and H. Rabitz, *Phys. Rev*. B 57, 7581 (1998).
[93] R. Pirc and R. Blinc, *Phys. Rev*. B 60, 13470 (1999).
[94] R. Blinc, J. Dolinsek, A. Gregorovic, B. Zalar, C. Filipic, Z. Kutnjak, A. Levstik and R. Pirc, *Phys. Rev. Lett.* 83, 424 (1999).
[95] W. Kleemann, J. Dec, R. Blinc, B. Zalar and R. Pankrath, *Ferroelectrics* 267, 157 (2002).
[96] R. Pirc, R. Blinc and V. Bobnar, *Phys. Rev*. B 63, 0542203 (2001).
[97] R. Blinc, V. Bobnar and R. Pirc, *Phys. Rev*. B 64, 132103 (2001).
[98] B. E. Vugmeister and H. Rabitz, Phys. Rev. B 61, 14448 (2000).
[99] B. E. Vugmeister and H. Rabitz, *Phys. Rev*. B 65, 024111 (2001).
[100] A. K. Jonscher, *Dielectric relaxation in solids*, Chelsea Dielectric Press, London (1983).
[101] K. S. Cole and R. H. Cole, *J. Chem. Phys*. 9, 341 (1941).
[102] R. M. Fuoss and J. G. Kirkwood, *J. Am. Chem. Soc*. 63, 385 (1941).
[103] V. Porokhonskyy, Ph. D. Thesis, Prague (2004).
[104] Z. Y. Cheng, R. S. Katiyar, X. Yao and A. S. Guo, *Phys. Rev*. B 55, 8165 (1997).
[105] S. Kamba, V. Porokhonskyy, A. Pashkin, V. Bovtun, and J. Petzelt, J. C. Nino, S. Trolier-McKinstry, M. T. Lanagan, and C. A. Randall, *Phys. Rev*. B 66, 054106 (2002).
[106] D. W. Davidson and R. H. Cole, *J. Chem. Phys*. 19, 1484 (1951).
[107] J. Z. Bao, *J. Chem. Phys*. 104, 4441 (1996).
[108] S. Havriliak, S. Negami, *J Polym. Sci*. C 14, 99 (1966).
[109] S. Havriliak, S. Negami, *Polyme*r 8, 161 (1967).
[110] R. Zorn, *J. Polym Sci. Pol. Phys*. 37, 1043 (1999)
[111] S. Havriliak, S. J. Havriliak, *J. Non-Cryst Solids* 172, 297 (1994).
[112] S. A. Seo, K. H. Noh, S. I. Kwun, J. Korean. *Phys. Soc*. 35, 496 (1999).
[113] H. Ries, R. Böhmer, I. Fehst and A. Loidl, *Z. Phys. B-Cond. Matter* 99, 401 (1996).
[114] B. G. Kimm, J. J. Kimm, H. M. Jang, *Phys. Rev*. B 60, 7170 (1999).

Copyright © 2010. Nova Science Publishers, Incorporated. All rights reserved.

Handbook of Material Science Research, Nova Science Publishers, Incorporated, 2010. ProQuest Ebook Central,

[115] R. R. Nigmatullin, V. A. Goncharov, Ya. E. Ryabov, Extended abstract of the XXVII congress Ampere, 251 (1994).
[116] R. R. Nigmatullin, Y. E. Ryabov, *Phys. Solid State* 39, 87 (1997).
[117] J. H. Calderwood, IEEE Transactions on Dielectrics and Electrical Insulation 10, 1006 (2003).
[118] H. Kliem, IEEE Transactions on Dielectrics and Electrical Insulation 12, 709 (2005).
[119] F. Alvarez, A. Alegria, and J. Colmenero *Phys. Rev.* B 44, 7306 (1991).
[120] A. K. Jonscher, *Colloid Polym. Sci*. 253, 231 (1975).
[121] K. L. Ngai, G. B. Wright (Eds.), *Relaxations in Complex Systems*, North-Holland, Amsterdam (1991).
[122] L. A. Dissado and R. M. Hill, *Proc. Roy. Soc*. London 390, 131180 (1983).
[123] A. K. Jonscher, *Nature* 267, 673 (1977).
[124] A. D. Franklin and H. J. de Bruin, *Phys. Stat. Solidi* A 75, 647 (1983).
[125] K. Liedermann and A. Loidl, *J. Non-Cryst. Solids* 155, 26 (1993).
[126] P. Colonomos and R. G. Gordon, *J. Chem. Phys*. 71, 1159 (1979).
[127] Y. Imanishi, K. Adachi, and T. Kotaka, *J. Chem. Phys*. 89, 7593 (1988).
[128] A. Bello and E. Laredo, M. Grimau, *Phys. Rev*. B 60, 12764 (1999).
[129] A. V. Tichonov, *DAN SSSR*, 153, 3 (1963).
[130] H. Schäfer, E. Sternin, R. Stannarius, M. Arndt, and F. Kremer, *Phys. Rev. Lett.* 76, 2177 (1996).
[131] R. Pelster, T. Kruse, H. G. Krauthäuser, G. Nimtz and P. Pissis, *Phys. Rev*. B 57, 8763 (1998).
[132] J. Banys, S. Lapinskas, A. Kajokas, A. Matulis, C. Klimm, G. Völkel, and A. Klöpperpieper, *Phys. Rev*. B 66, 144113 (2002).
[133] V. A. Stephanovich, M. D. Glinchuk, B. Hilczer and E. V. Kirichenko, *Phys. Solid State* 44, 799 (2002).
[134] A. Brandt, *Isledovanie dielektrikov na sverchvysokich castotach*, Fizmatgiz, Moskva (1963).
[135] A. Brilingas, R. L. Davidovich, J. Grigas, S. Lapinskas, M. A. Medkov, V. Samulionis and V. Skritskii, *Phys. Stat. Sol*. (a) 96, 101 (1986).
[136] D. H. Auston, and M. C. Nuss, *IEEE J. Quantum Electron*. 24, 184 (1988).
[137] X. C. Zhang, X. F. Ma, Y. Jin, T. M. Lu, E. P. Boden, D. P. Phelps, K. R. Stewart, and C. P. Yakymyshyn, *Appl. Phys. Lett.* 61, 3080 (1993).
[138] P. R. Smith, D. H. Auston, and M. C. Nuss*, IEEE J. Quantum Electron* 24, 255 (1988).
[139] X. C. Zhang, B. B. Hu, J. T. Darrow, and D. H. Auston, *Appl. Phys. Lett*. 56, 1011 (1990).
[140] Ch. Fattinger, and D. Grischkowsky, *Appl. Phys. Lett*. 53, 1480 (1988).
[141] D. H. Auston, K. P. Cheung, and P. R. Smith, *Appl. Phys. Lett*. 45, 284 (1984).
[142] D. H. Auston, K. P. Cheung, J. A. Valdmanis, and D. A. Kleinman, *Phys. Rev. Lett*. 53, 1555 (1984).
[143] G. Grüner (ed.), *Millimeter and Submillimeter Wave Spectroscopy of Solids*, Chap. 2, p. 7, Springer-Verlag, Berlin Heidelberg (1998).
[144] M. van Exter, Ch. Fattinger, and D. Grishkowsky, *Opt. Lett.* 14, 1128 (1989).
[145] Q. Wu, and X. C. Zhang, *Appl. Phys. Lett*. 68, 1604 (1996).
[146] R. J. Bell, *Introductory Transform spectroscopy*, Academic press, New York (1972).

Copyright © 2010. Nova Science Publishers, Incorporated. All rights reserved.

Handbook of Material Science Research, Nova Science Publishers, Incorporated, 2010. ProQuest Ebook Central,

[147] C. L. Lawson, R. J. Hanson, *Solving Least Squares Problems,* SIAM, Philadelphia, (1995).
[148] S. W. Provencher, *Comput. Phys. Commun*. 27, 213 (1982).
[149] W. H. Press, *Numerical recipes in C*, University press, Cambridge, (1992).
[150] I. Fehst, M. Paasch, S. L. Hutton, M. Braune, R. Böhmer, A. Loidl, M. Dörfel, Th. Narz, S. Haussühl and G. J. Mcintyre, *Ferroelectrics* 138, 1 (1993).
[151] W. Schildkamp and J. Spilker, *Z. Kristalogr.* 168, 159 (1984).
[152] H. Ebert, S. Lanceros - Mendes, G. Schaack and A. Klöpperpieper, *J. Phys.: Condens. Matter*. 7, 9305 (1995).
[153] M. L. Santos, J. M. Kiat, A. Almeida, M. R. Chaves, A. Klöpperpieper and J. Albers, *Phys. Stat. Solidi* (a) 189, 371 (1995).
[154] J. Albers, A. Klöpperpieper, H. J. Rother and K. H. Ehses, *Phys. Stat. Solidi* (a) 74, 553 (1982).
[155] J. Albers, A. Klöpperpieper, H. J. Rother, and S. Hausshühl, *Ferroelectrics* 81, 27 (1988).
[156] H. Bauch, J. Banys, R. Böttcher, A. Pöppl, G. Völkel, C. Klimm and A. Klöpperpieper, *Ferroelectrics* 163, 59 (1995).
[157] R. Sobiestianskas, J. Grigas, Z. Czapla and S. Dacko, *Phys. Stat. Solidi* (a) 136, 223 (1993).
[158] R. Cach, S. Dacko and Z. Czapla, *Phys. Stat. Solidi* (a) 148, 585 (1995).
[159] G. Fischer, H. J. Brückner, A. Klöpperpieper, H. G. Unruh and A. Levstik, *Z. Phys. B - Condensed Matter* 79, 301 (1990).
[160] H. Ries, R. Böhmer, I. Fehst and A. Loidl, *Z. Phys. B: Condens. Matter* 99, 401 (1996).
[161] J. Banys, C. Klimm, G. Völkel, H. Bauch, and A. Klöpperpieper, *Phys. Rev*. B 50, 751 (1994).
[162] Ml. Santos, Mr. Chaves, A. Almeida, A. Klöpperpieper, He. Muser, J. Albers, *Ferroelectrics Let*. 15, 17 (1993).
[163] J. Banys, P. J. Kundrotas, C. Klimm, A. Klöpperpieper, G. Völkel, *Phys. Rev*. B 61, 3159 (2000).
[164] A. Bussmann-Holder and K. H. Michel, *Phys. Rev. Lett.* 80, 2173, (1998).
[165] J. Banys, R. Sobiestianskas, C. Klimm, and G. Völkel, *Lithuan. J. Phys*. 37, 505 (1997).
[166] J. Banys, C. Klimm, G. Völkel, A. Kajokas, A. Brilingas and J. Grigas, *J. Phys.: Condens. Matter.* 13, 1773, (2001).
[167] J. Banys, J. Macutkevic, C. Klimm, G. Völkel, A. Kajokas, A. Brilingas, and J. Grigas, *Phys. Stat. Solidi* (a) 201, 602 (2004).
[168] J. Dolinsek, D. Acron, B. Zalar, R. Pirc, R. Blinc, and R. Kind, *Phys. Rev*. B 54, R6811 (1996).
[169] J. Banys, A. Kajokas, A. Brilingas, J. Grigas, G. Völkel and C. Klimm, *Ferroelectrics* 258, 113 (2001).
[170] R. Blinc, B. Zalar, A. Gregorovic, R. Pirc and M.D. Glinchuk, *Ferrolectrics* 240, 207 (2000).
[171] H. Bauch, J. Banys, R. Böttcher, C. Klimm, A. Klöpperpieper, G. Völkel, *Phys. Stat. Solidi* (b) 187, K81 (1995).
[172] J. L. Tholence, Solid. State Commun. 35, 113 (1980). A. K. Tagantsev, *Phys. Rev. Let.* 72, 1100 (1994).
[173] H. Fogel, Z. Phys. 22, 645 (1921). G. S. Vulcher, *J. Am. Ceram. Soc*. 8, 339 (1925).

Copyright © 2010. Nova Science Publishers, Incorporated. All rights reserved.

Handbook of Material Science Research, Nova Science Publishers, Incorporated, 2010. ProQuest Ebook Central,

[174] Z. Kutnjak, R. Pirc, A. Levstik, I. Levstik, C. Filipič, R. Blinc and R. Kind, *Phys. Rev*. B 50, 12421 (1994).
[175] J. Banys, A. Kajokas, C. Klimm, G. Völkel and A. Klöpperpieper, *J. Phys.: Condens. Matter* 10, 8389 (1998).
[176] Z. Trybula, V. H. Schmidt and J. E. Drumheller, *Phys. Rev*. B 43, 13762 (1992).
[177] S. L. Hutton, I. Fehst, R. Böhmer, M. Braune, B. Mertz, P. Lunkenheimer, and A. Loidl, *Phys. Rev. Lett.* 66, 1990 (1991).
[178] M. L. Santos, J. C. Azevedo, A. Almeida, M. R. Chaves, A. R. Pires, H. E. Müser, and A. Klöpperpieper, *Ferroelectrics* 108, 1969 (1990).
[179] J. M. B. Lopes dos Santos, M. L. Santos, M. R. Chaves, A. Almeida, and A. Klöpperpieper, *Phys. Rev*. B 61, 8053 (2000).
[180] J. Banys, C. Klimm, G. Völkel, H. Bauch, and A. Klöpperpieper, *Phys. Rev*. B. 50, 16751 (1994).
[181] A. V. de Carvalho and S. R. Salinas, *J. Phys. Soc. Jpn*. 44, 238 (1978).
[182] R. Blinc, B. Žekš, A. Levstik, C. Filipič, J. Slack, M. Burgar, I. Zupančič, L. A. Shuvalov, and A. I. Baranov, *Phys. Rev. Lett*. 43, 231 (1979).
[183] R. Blinc and F. C. Sa Baretto, *J. Chem. Phys*. 72, 6031 (1980).
[184] H. Bauch, G. Völkel, R. Böttcher, A. Pöppl, H. Schäfer, J. Banys, and A. Klöpperpieper, *Phys. Rev*. B 54, 9162 (1996).
[185] G. Völkel, H. Bauch, R. Böttcher, A. Pöppl, H. Schäfer, and A. Klöpperpieper, *Phys. Rev*. B 55, 12151 (1997).
[186] G. Völkel, N. Alsabbagh, J. Banys, H. Bauch, R. Böttcher, M. Gutjahr, D. Michel, and A. Pöppl, in Adv. in Solid State Phys. 42, pp. 241-251, edited by B. Kramer Springer-Verlag, Berlin Heidelberg (2002).
[187] A. Pöppl, G. Völkel, J. Hoentsch, S. Orlinski, and A. Klöpperpieper, *Chem. Phys. Lett.* 224, 233 (1994).
[188] J. Banys, A. Pöppl, G. Völkel, J. Simon, J. Hoentsch, and A. Klöpperpieper, *Lithuanian Journ. of Phys.* 36, 409 (1996).
[189] R. Böttcher, A. Pöppl, G. Völkel, J. Banys, and A. Klöpperpieper, *Ferroelectrics* 208, 105 (1998).
[190] J. Banys, S. Kamba, A. Klöpperpieper, and G. Völkel, *Phys. Stat. Solidi* (b) 231, 581 (2002).
[191] J. Banys, J. Macutkevic, S. Lapinskas, C. Klimm and G.Voelkel, *Phys Rev* B. 73, 144202 (2006).
[192] T. Nattermann, in *Spin Glasses and Random Fields*, edited by A.P. Young, Directions in Condensed Matter Physics 12 World Scientific, Singapore (1998).
[193] D. S. Fisher, P. Le Doussal, and C. Monthus, *Phys. Rev*. E 64, 066107 (2001).
[194] M. Manger, S. Lanceros-Mendez, G. Schaack and A. Klöpperpieper, *J. Phys.: Condens. Matter* 8, 4617 (1996).
[195] A. A. Pastor, V. Dobrosavljevic, M. L. Horbach, *Phys. Rev.* B 66, 014413 (2002).
[196] V. G. Rostiashvili, G. Migliorini, and T. A. Vilgis, *Phys. Rev*. E 64, 051112 (2001).
[197] M. Tarzia and A. Coniglio, arXiv:cond-mat/0506485 v1 20 Jun. 2005.
[198] V. G. Rostiashvili and T. A. Vilgis, arXiv:condmat/ 9911280 v2 22 Nov. 1999.
[199] A. A. Bokov, Y. H. Bing, W. Chen, Z. G. Ye, S. A. Bogatina, I. P. Raevski, S. I. Raevskaja, *Phys. Rev*. 68, 052102 (2003).
[200] D. Viehland, S. J. Jang, L. E. Cross, M. Wuttig, *Phys. Rev*. 46 8003 (1992).

Copyright © 2010. Nova Science Publishers, Incorporated. All rights reserved.

Handbook of Material Science Research, Nova Science Publishers, Incorporated, 2010. ProQuest Ebook Central,

[201] E. V. Cola, E. Yu. Koroleva, N. M. Okuneva and S. B. Vakruchev, *J. Phys.: Condens. Matter* 4, 3671 (1992).
[202] O. Bidault, C. Perrin, C. Caranoni, N. Mengui, *J. Appl. Phys*. 90, 4115 (2001).
[203] Y. L. Wang, S. S. N. Bharadwaja, A. K. Tagantsev, N. Setter, *Journal of the European Ceramic Society* 25, 2521 (2005).
[204] S. M. Huang, C. D. Feng, L. D. Chen, Q. Wang, *J. Am. Ceram. Soc*. 89, 328 (2006).
[205] S. Saha, T. P. Sinha, *Phys. Rev*. B 65, 134103 (1993).
[206] J. L. Dellis, I. P. Raevski, S. I. Raevskaja, L. A. Reznitchenko, *Ferroelectrics* 318, 169 (2005).
[207] D. Viehland, S. Jang, L. E. Cross, *Philos. Mag*. B 64, 335 (1991).
[208] A. Khodorov, A. Tsotsorin, *Ferroelectrics* 299, 121 (2004).
[209] J. Malecki, B. Hilcher, *Key Eng. Mat*. 92, 181 (1994).
[210] W. Kleemann, R. Lindner, *Ferroelectrics* 199, 1 (1997).
[211] V. Bovtun, S. Kamba, A. Pashkin, M. Savinov, P. Samoukhina, J. Petzelt, I. P. Bykov, M. D. Glinchuk, *Ferroelectrics* 298, 23 (2004).
[212] S. Kamba, M. Kempa, V. Bovtun, J. Petzelt, K. Brinkman, and N. Setter, J. *Phys.: Condens. Matter* 17, 3965 (2005).
[213] F. Chu, N. Setter, C. Elissalde, and J. Ravez, *Mat. Sci. Eng*. B 38, 171 (1996).
[214] V. Bovtun, V. Porokhonskyy, J. Petzelt, M. Savinov, J. Endal, C. Elissalde, and C. Malibert, Ferroelectrics 238, 17 (2000).
[215] S. Kamba, M. Berta, M. Kempa, J. Hlinka, J. Petzelt, K. Brinkman, and N. Setter, *J. Appl. Phys*. 98, 074103 (2005).
[216] S. Kamba, V. Bovtun, J. Petzelt, I. Rychetski, R. Mizaras, A. Brilingas, J. Banys, J. Grigas, M. Kosec, *J. Phys.: Condens. Matter* 12, 497 (2000).
[217] I. Rychetsky, S. Kamba, V. Porokhonskyy, A. Pashkin, M. Savinov, V. Bovtun, J. Petzelt, M. Kosec and M. Dressel, *J. Phys.: Condens. Matter* 15, 6017 (2003).
[218] E. Buxaderas, M. Savinov, M. Kempa, S. Veljko, S. Kamba, J. Petzelt, R. Pankrath and S. Kapphan, *J. Phys.: Condens. Matter* 17, 653 (2005).
[219] S. E. Park and T. S. Shrout, *J. Appl. Phys*. 82, 1804 (1997).
[220] B. Noheda, *Current Op. Sol. St. Mat. Sci*. 6, 27 (2002).
[221] N. Fu, R. E. Cohen, *Nature* 403, 281 (2000) and references therein.
[222] L. Farber, P. Davies, *J. Am. Ceram. Soc*. 86, 1861 (2003).
[223] I. P. Raevski, S. A. Prosandeev, S. M. Emelyanov, F. I. Savenko, I. N. Zakharchenko, O. A. Bunina, A. S. Bogatin, S. I. Raevskaja, E. S. Gagarina, E. V. Sahkar and L. Jastrabik, *Integrated Ferroelectrics* 53, 475 (2003).
[224] I. P. Raevski, S. M. Emelyanov, F. I. Savenko, I. N. Zakharchenko, O. A. Bunina, M. A. Malitskaya, A. S. Bogatin, E. V. Sahkar, *Ferroelectrics* 285, 283 (2003).
[225] K. Bormanis, A. I. Burkhanov, A. V. Alpatov, M. Dambekalne, A. Kalvane, A. Sternberg, and A. V.Shil'nikov, *Ferroelectrics* 318, 209 (2005).
[226] E. P. Smirnova, S. E. Aleksandrov, K. A. Sotnikov, A. A. Kapralov, A. B. Sotnikov, *Phys. Sol. State* 45, 1305 (2003).
[227] D. H. Zhou, G. L. Hoatson, R. L. Vold, F. Fayon, *Phys. Rev*. B 69, 134104 (2004).
[228] M. Dambekalne, K. Bormanis, A. Sternberg and I. Brante, *Ferroelectrics* 240, 221 (2000).
[229] J. Macutkevic, S. Kamba, J. Banys, A. Brilingas, A. Pashkin, J. Petzelt, K. Bormanis and A. Sternberg, *Phys. Rev.* B 74, 104106 (2006)

Copyright © 2010. Nova Science Publishers, Incorporated. All rights reserved.

Handbook of Material Science Research, Nova Science Publishers, Incorporated, 2010. ProQuest Ebook Central,

[230] R. Blinc, V. V. Laguta, B. Zalar, and J. Banys, *J. Mat. Sci*. 41, 27 (2006).
[231] Xu. Guangyong, Z. Zhong, Y. Bing, Z. G. Ye, and G. Shirane, *Nature Materials* 5, 134 (2006).
[232] R. Sommer, N. K. Yushin, and J. J. van der Klink, *Phys. Rev.* B 48, 13 230 (1993).
[233] 233 O. Bidault, M. Licheron, E. Husson, and A. Morell, *J. Phys.: Condens. Matter* 8, 8017 (1996).
[234] H. Arndt, F. Sauerbier, G. Schmidt, and L. A. Shebanov, *Ferroelectrics* 79, 145 (1988).
[235] E. V. Colla, E. Yu. Koroleva, A. A. Nabereznov, and N. M. Okuneva, *Ferroelectrics* 151, 337 (1994).
[236] J. Banys, J. Macutkevic, A. Brilingas, V. Samulionis, K. Bormanis, A. Sternberg, V. Zauls, *Material Science Forum* 514, 216 (2006).
[237] V. Westphal, W. Kleemann, M. D. Glinchuk, *Phys. Rev. Lett*. 68, 847 (1992).
[238] H. Schremer, W. Kleemann, and D. Rytz, *Phys. Rev. Lett*. 62, 1896 (1989).
[239] V. Bobnar, Z. Kutnjak, R. Pirc, and A. Levstik, *Phys. Rev.* B 60, 6420 (1999).
[240] D. Andelman and J. F. Joanny, *Phys. Rev.* B 32, 4818 (1985).
[241] J. Banys, J. Macutkevic, R. Grigalaitis and W. Kleemann, *Phys. Rev*. B 72, 024106 (2005).
[242] F. Gervais, in Infrared and Millimeter Waves, edited by K.J. Button, Vol. 8, Chapter 7 (Academic Press, New York, 1983), pp. 279–339.
[243] J. Onstott and G. Lucovsky, *J. Phys. Chem. Solids* 31, 2171 (1970).
[244] G. Lucovsky, R. M. Martin and E. Burnstein, *Phys. Rev*. B 4, 1367 (1971).
[245] X. Gonze and Ch. Lee, *Phys. Rev*. B 55, 10355 (1997).
[246] W. Zhong, R. D. King-Smith and D. Vanderbilt, *Phys. Rev. Lett*. 72, 3618 (2004).
[247] S. A. Prosandeev, E. Cockayne, B. P. Burton, S. Kamba, J. Petzelt, Yu. Yuzyuk, R. S. Katiar and S. B. Vakhrushev, *Phys. Rev*. B 70, 134110 (2004).
[248] J. Hlinka, T. Ostapchuk, D. Noujni, S. Kamba and J. Petzelt, cond-mat/0510273.
[249] J. Hlinka, J. Petzelt, S. Kamba, D. Noujni, and T. Ostapchuk, Phase Transitions 79, 41 (2006).
[250] J. Toulouse, F. Jiang, O. Svitelskiy, W. Chen, and Z. G. Ye, *Phys. Rev*. 72, 184106 (2005).
[251] B. Dkhil, J. M. Kiat, G. Calvarin, G. Baldinozzi, S. B. Vakhrushev, and E. Suard, *Phys. Rev*. B 65, 024104 (2002).
[252] I. Rychetsky and J. Petzelt, *Ferroelectrics* 303, 137 (2004).
[253] J. C. Slater, *Phys. Rev*. 78, 748 (1950).
[254] J. Petzelt, E. Buixaderas, and A. V. Pronin, *Mater. Sci.Eng*. B 55, 86 (1998).
[255] S. Kamba, E. Buixaderas, J. Petzelt, J. Fousek, J. Nosek, and P. Bridenbaugh, *J. Appl. Phys*. 93, 933 (2003).
[256] J. T. Last, *Phys. Rev*. 105, 1740 (1957).
[257] J. D. Axe, *Phys. Rev*. 157, 429 (1957).
[258] J. Hlinka, T. Ostapchuk, D. Noujni, S. Kamba, and J. Petzelt, *Phys. Rev. Lett*. 96, 027601 (2006).
[259] R.Pirc, R.Blinc, private communication.

Copyright © 2010. Nova Science Publishers, Incorporated. All rights reserved.

Handbook of Material Science Research, Nova Science Publishers, Incorporated, 2010. ProQuest Ebook Central,

In: Handbook of Material Science Research
Editors: C. René and E. Turcotte, pp.125-172
ISBN 978-1-60741-798-9
© 2010 Nova Science Publishers, Inc.

Chapter 2

MODIFICATION OF STEEL'S MICROHARDNESS BY COMPRESSION PLASMA FLOWS

N. N. Cherenda and V. V. Uglov*
Belarusian State University,
Department of Solid State Physics, Minsk, Belarus

ABSTRACT

The main results of the influence of compression plasma flows' impact on the Vickers microhardness of iron, carbon steels and high-alloyed steels are presented in this chapter. The data from a variety of investigation techniques including X-ray diffraction, Mössbauer spectroscopy, Auger electron spectroscopy, Rutherford backscattering spectroscopy, scanning electron microscopy, etc. are used for the interpretation of microhardness results. Different approaches to steel hardening by compression plasma flows are demonstrated: direct treatment, surface alloying by mixing of a "coating-substrate" system and surface alloying by injection of an additional component into a plasma flow. The findings showed that direct treatment was effective for modification of iron and carbon steels (or low-alloyed steels) providing the microhardness increased up to 8–18 GPa. Alloying by compression plasma flows allows the formation of a hardened surface layer with the thickness of up to ~ 20 μm possessing high thermal stability both in carbon and high-speed steels. The role of the main hardening mechanisms is discussed.

1. INTRODUCTION

Microhardness measurements are widely used for mechanical characterization of materials due to relative simplicity and short testing time. At the same time it can be used as an investigation technique providing information about the structure and processes taking place in the surface layer, e.g., for detection of interphase precipitation in micro-alloyed steels [1] or even as a method for dating ancient steel samples [2]. Microhardness is also used for

* Nezavisimosti ave. 4, 220030 Minsk, Belarus.

Copyright © 2010. Nova Science Publishers, Incorporated. All rights reserved.

Handbook of Material Science Research, Nova Science Publishers, Incorporated, 2010. ProQuest Ebook Central,

the investigation of a steels response to different types of surface layer modification techniques.

Chemicothermal treatment was one of the first hardening techniques used in industry for improvement of steel's operational characteristics [3]. Its main drawback is a large treatment time. The use of treatment techniques based on ion, electron, plasma and laser beams allows us to shorten processing time up to a few hours or even tens of minutes. One can mention the following well-studied techniques: ion implantation [4, 5], electron beam treatment [6], different types of plasma nitriding and carburizing [7-9], plasma immersion ion implantation [10-12], laser treatment and laser nitriding [13, 14]. In the last decades reduction of beam weapons programs and development of new fusion reactors have given use to new prospective types of surface treatment techniques based on high power fluxes (~10^5-10^{11} W/cm^2): high-power ion beams (HPIB) [15], high-current electron beams (HCEB) [16] and intense pulsed plasma beams (IPPB) [17] which can diminish processing time up to minutes. Nowadays these techniques cannot fully substitute for traditionally used techniques of steel hardening. But the possibility of new metastable structures formation, a nanostructures synthesis, and discovery of new effects can solve problems arising in mechanical engineering and new industries such as nuclear power engineering, aerospace industry, etc.

1.1. Some Peculiarities of Microhardness Testing

Before reviewing the results obtained, some peculiarities of the most widespread Vickers microhardness testing application for the investigation of materials treated by HPIB, HCEB and IPPB have to be considered.

It is known that the Vickers microhardness value is load dependent [18-20]. It is called the indentation size effect (ISE). The ISE appeared at loads less than 100 g [18]. Diminishing of the load usually results in a microhardness increase [18], though the microhardness decrease or its complex variation with changes in load can be found [19]. Only at loads greater than 500 g standard (macro) hardness or the bulk Vickers hardness can be received [18]. The following reasons for this effect are discussed in the literature: external vibrations, polishing hardening, a limit of optical system resolution, greater elastic recovery of the indentation print for a smaller load, work hardening during indentation, pile-up or sink-in around the print, etc. [18, 19]. Some corrections should be made to receive a bulk (or absolute) microhardness value independent of the ISE. One of the first ISE corrections was made by Meyer [18, 19]:

$$P = Ad^m, \tag{1}$$

where P - applied load, d – indentation diagonal length, A and m – constants. In fact, this equation usually does not describe all observed variations of the microhardness dependence. That is why several authors proposed other corrections. A short review of them can be found in [18] and for stainless steel in [19].

The thickness of the surface layer modified by different types of treatment technique can be significantly less than the indenter penetration depth during microhardness testing. That is why the microhardness value will be the superposition of different layers microhardness. To

Copyright © 2010. Nova Science Publishers, Incorporated. All rights reserved.

Handbook of Material Science Research, Nova Science Publishers, Incorporated, 2010. ProQuest Ebook Central,

receive the microhardness value close to the microhardness of the modified layer it is necessary to diminish the indenter load. But it results in the increase of the ISE influence. In this case one of the simplest ways to avoid interpretation errors during the comparison of experimental data is to compare microhardness values at equal depths of the indenter penetration. It should be noted that the harder the material is, the greater the ISE effect is [18]. At the same time it is hard to avoid possible errors due to the ISE in data interpretations. The ISE effect has many causes and most of them can arise during treatment or during a change of treatment regimes.

If the thickness of the modified layer is comparable with the indenter penetration depth models for determination of the films and coatings microhardness value can be useful for finding the modified layer average microhardness [21].

A high energy absorbed by the surface layer during treatment by HPIB, HCEB and IPPB can lead to its melting and formation of developed surface roughness due to a high cooling rate [22]. The formed asperities size can be the same order of magnitude as *d*. Surface roughness will influence the microhardness value and can be taken into account by adding an item to the hardness dependence on the indenter penetration depth [20, 23]. The following correction was suggested in [20]:

$$\frac{H_r}{H_0} = 1 + \frac{2{,}4\pi}{\sin\Theta}(\eta R\sigma)\frac{\sigma}{r}, \qquad (2)$$

where H_r- microhardness value of a rough surface, H_0- microhardness value of a smooth surface (bulk hardness), $\Theta=18^o$ for the Vickers indenter, η- the number density of asperity, R- statistic average radius of all asperity summits, σ- mean-square deviation of the asperity height distribution, r- radius of the indenter projected area at the surface (the indentation print size). One can see that ($\eta R\sigma$) increase results in the microhardness value increase and at the same time in the growth of the ISE influence.

1.2. High-Power Ion Beams

Different types of accelerators can be used for HPIB generation: TEMP [24-26], TONUS [15, 27-31], ETIGO [32], ANACONDA [25, 33], RHEPP-I [34] etc. Generated pulsed ion beams of low-Z ions (H,C,O) have the following typical parameters: the accelerating energy varies in the range of 0.01-10 MeV, the current in a pulse – 5-1000 kA, the energy density – 1-100 J/cm^2 per pulse, the pulse duration - 10^{-9}-10^{-6} s, the ion range – 0.1-10 μm [15, 25, 28].

HIPIB irradiation induces rapid heating with a high temperature gradient, leading to melting, evaporation, formation of thermal stress and shock waves. High cooling rates (10^8-10^{11} K/s) can cause amorphous layer formation and a synthesis of nanocrystalline and metastable phases, providing improved corrosion, wear and hardness properties [15, 25, 30, 31, 34]. The chemical influence of an implanted impurity is usually negligible – its concentration does not exceed 10^{-5} at.% in the implanted layer. Grains refinement and phase transformations in the melted layer can be one of the reasons for surface hardening [25]. For example, HPIB processing of AISI 4620 steel at the ANACONDA accelerator after 10 pulses at the energy density of 5 J/cm^2 showed 1.4 times microhardness increase [25]. The thickness

Copyright © 2010. Nova Science Publishers, Incorporated. All rights reserved.

Handbook of Material Science Research, Nova Science Publishers, Incorporated, 2010. ProQuest Ebook Central,

of the melted layer was ~ 1 μm and the heat-affected layer ~ 5μm. Surface texturing which can influence the microhardness value is usually accompanied by a rapid melt–resolidification process. The initial surface roughness R_a can either increase or decrease. Samples of AISI 4620 steel polished to R_a≈0.1 μm and processed at the ANACONDA reveal smoothing over micron-scale lengths, accompanied by crater formation and large-scale (>10 μm) roughening [25]. Tool steels processed by TEMP showed R_a of 1 μm after treatment. Polished surfaces are roughened to this R_a whereas rougher surfaces are smoothed to this value [25].

Significant enhancement of mechanical properties have been observed not only on the treated surface and the near-surface layer but also at greater depths of hundreds of micrometers [15, 24, 25, 27-31]. It is one of the main features of HPIB processing. A similar long-range effect was observed during pulsed metal ion implantation [35]. The main reason for it is generation of shock waves with the initial pressure magnitude in the range of 2-14 GPa [15, 28, 36]. Evaporation and ionization of the near-surface layer by HPIB result in generation of an ablated plasma jet adiabatically spreading with velocity 10^5–10^7 cm/s in the direction normal to the treated surface [24]. This process generates a very strong recoil impulse directed into a treated sample. The recoil impulse forms an intense compression wave in the target. The propagation of shock waves in metals leads to enhanced diffusion, growth of point defects and dislocations density in the target. Thus the strengthening mechanism can be similar to normal work-hardening with a fast deformation rate [36]. As a result, microhardness increases to the depth of about 50-100 μm. For example, microhardness measured along the cross-section of R6M5 steel (AISI M2 analogue) treated by HPIB at the TEMP accelerator with the ion current density of 60 A/cm^2 increases to the depth of 50 μm [24]. Similar result was received for this steel by its processing at the TONUS accelerator with the ion current density of 80 A/cm^2 [27].

Materials processing by the TONUS accelerator revealed bimodal microhardness distribution along the cross-section depth [15, 24, 28-31]. If the energy density exceeds some critical value which is target material dependent (~ 3-4 J/cm^2 per pulse or the ion current density greater than 100 A/cm^2), besides the surface microhardness peak a second peak can be observed at the depth of (40-100)R_0, where R_0 is the carbon ions range (~ 1μm) with the energy of 0.4 MeV [28]. This effect was found for pure α-iron [15, 31], R6M5 steel [29, 30], beryllium [30], etc. The same effect was found for 316L stainless steel processed at the TEMP accelerator [26]. The microhardness value of both peaks increases with the ion current density growth. Microhardness distribution along the cross-section correlates with dislocation density distribution along the depth. This effect is explained by shock wave propagation peculiarities and is described in detail in [15].

An advantage of this technique over ion implantation is that HPIB provide a modification of about one or two orders of magnitude deeper layer. HPIB possess more electrical efficiency than lasers though vacuum and X-rays shielding are necessary for processing. There is no need for a background plasma and magnetic field for HPIB propagation in comparison with HCEB.

Copyright © 2010. Nova Science Publishers, Incorporated. All rights reserved.

Handbook of Material Science Research, Nova Science Publishers, Incorporated, 2010. ProQuest Ebook Central,

1.3. High-Current Electron Beams

The modification of materials by HCEB, as in case of HPIB, is mainly based on superfast heating, melting and evaporation followed by generation of shock waves, superfast solidification. The main parameters of HCEB generated by different types of accelerators (direct-action vacuum diodes and plasma filled diodes mainly) are summarized in [16]: the acceleration energy – 5-300 keV, the beam current density – 10^1-10^3 A/cm^2, the pulse duration – 0.05-2000 μs, the beam energy density – 10^{-2} – $2 \cdot 10^2$ J/cm^2.

Lately low energy HCEB (the acceleration voltage does not exceed ~ 50 kV, the pulse duration 0.5-5 μs) are more widely spread [16, 37-39]. The low accelerating voltage allows to avoid problems with X-ray shielding. In [37] it was shown that low energy HCEB processing (20 keV, 0.8 μs, 2-2.5 J/cm^2) of pure iron led to formation of an extended (~100 μm) non-uniformly hardened zone with the microhardness maximum ~1.1 GPa located at the depth of a ~20 μm. The thickness of a heat affected zone where the maximum temperature exceeds the recrystallization temperature varies in the range of ~5-20 μm depending on beam parameters [37, 38]. The thickness of the melted layer is in the range of 0.7-2.5 μm [37]. It means that hardening is caused by a combined effect of melting, recrystallization and shock waves. As in case of HPIB dislocation density distribution is close to microhardness distribution along the cross-section [37]. The increase of the number of pulses leads to the microhardness increase at the cross-section depth greater 20 μm. The energy density growth (up to 5.2 J/cm^2) results in bimodal microhardness distribution along the depth [16, 31, 37]. The first maximum at the surface is associated with microstructure changes in the melted layer and the second - with shock waves [16].

Low-energy HCEB processing of carbon steels results in hardening only if the melt thickness is over some critical value [37]. This was explained by the existence of the minimum critical grain size for the original phase (~1 μm) necessary for nucleation of martensitic crystals [37]. Thus, steel 45 (0.45 % C, 0.27 % Si, 0.65 % Mn, 0.25 % Cu, 0.25 % Ni, 0.25 % Cr in wt. %) originally having the ferritic–pearlitic structure is not hardened after HCEB processing (1 μs, 2.5 J/cm^2) because the melt thickness is noticeably below the critical value. Hardening of the prequenched steel 45 is substantially different in character [37-39]. In this case an extended (~200 μm) hardened zone with two microhardness maxima along the cross-section is formed. The microhardness of the first maximum is up to ~16 GPa. The microhardness in the second maximum increases with the growth of the pulses number and can reach the same value. Processing of high-alloyed steels results in phase composition changes in the melted layer [40, 41]. For example, HCEB treatment of S6-5-2 high-speed steel (AISI M2 analogue) leads to partial or full dissolution (depending on beam parameters) of M_6C type carbide in a layer with the thickness of 1 μm and to the growth of austenite content [40]. These effects resulted in the wear resistance growth [40]. At the same time one could expect a surface layer hardness decrease. Similar behaviour of Cr-rich AISI D2 steel was observed in [41]: the microhardness decrease in a thin melted layer. At the same time shock waves generated during processing provided the microhardness increase far below the surface heat affected zone up to 450 μm. That is why the nanohardness measurement of the surface layer of HCEB processed D2 steel reveal a hardness value decrease only [42]. To avoid formation of a soft surface layer in this type of steels convenient e-beam treatment can be used [43, 44].

Copyright © 2010. Nova Science Publishers, Incorporated. All rights reserved.

Handbook of Material Science Research, Nova Science Publishers, Incorporated, 2010. ProQuest Ebook Central,

Typical parameters of high energy HCEB (the acceleration energy - up to 300 keV, the pulse duration - 5-250 μs) allow to form a deep melted layer in steels with the thickness of up to 200 μm [45, 46]. Hardening will be mainly determined by temperature distribution in the surface layer. In quenched carbon steel U7A (AISI W1 analogue) irradiated by HCEB (10 μs, 170 keV, 40-150 J/cm^2) three main surface layers with a modified structure were found [45]: a zone hardened from melt, a zone hardened from a solid state and a tempered zone. In the first zone microhardness had the maximum value of 10.2 GPa at the depth of 15-20 μm (40 J/cm^2). The energy density increase (150 J/cm^2) resulted in the growth of the first zone thickness up to 200 μm. The hardening degree was noticeably lower in this case. Cooling rate decrease was the main reason for this effect [45]. The microhardness behaviour in the other zones correlated with temperature distribution in the surface layer. The second zone corresponded to the temperature region between critical temperature A_{c3} and tempering temperature [45]. When an unquenched steel was irradiated the tempering zone was absent [45, 47]. High energy HCEB treatment of Cr-rich DIN 1.4922 steel revealed formation of a hardened layer with the thickness of up to 70 μm [46]. The formation of the wavy surface structure was found. The average roughness was reduced by the factor of ~2 after 20 pulses, while no effect on microhardness was observed within statistical fluctuations. At the same time the increase of the pulses number as well as the increase of the beam energy or pulse duration can cause microhardness reduction [46].

Though microstructure changes in the heat affected zone are considered to be the main reason for hardening during high energy HCEB treatment shock waves generated during a beam impact can also be a cause of hardening. Thin (0.615 mm) specimens of quenched carbon steels U10A (1 % C, 0.25 % Si, 0.2 % Mn, 0.15 % Cr in wt. %) and U7A were irradiated by high energy HCEB (350 keV, 0.1 μs, 63 J/cm^2) [47]. Three microhardness maxima along a cross-section were found. The first maximum was formed by hardening due to high temperature quenching; the second one was formed by a combined mechanism, i.e., by shock waves hardening followed by the effect of high temperatures, and the third one, located near the rear side of the target, was formed by the shock waves mechanism as well, but the material in this region was not subjected to heating. The reason for such behaviour is the following. If the target thickness is small, a shock wave may reach the rear surface of the target with insignificant attenuation, reflect from this surface, arrive at the face surface and reflect again. In this case even if the amplitude of the incident wave is below the yield point, the material, nevertheless, can be modified in wave reflection zones where the wave amplitude increases during its reflection and may exceed the yield point [47]. At the same time the pulse duration in this experiment is much lower than typical pulse duration of high energy HCEB. It seems to be the main reason for a relatively small thickness of the melt layer and an increased influence of shock waves.

1.4. Intense Pulsed Plasma Beams

IPPB as well as HPIB and HCEB supply enough energy to the surface in a short period of time to provide its ablation, superfast heating, melting and high cooling rates. But the main advantage of plasma beam is that it can transport some material species, thus changing chemical composition of the surface. The influence of these species on structural and mechanical properties changes will depend on the species concentration, material and

Copyright © 2010. Nova Science Publishers, Incorporated. All rights reserved.

Handbook of Material Science Research, Nova Science Publishers, Incorporated, 2010. ProQuest Ebook Central,

treatment parameters. Different plasma generator types can be used for steel hardening: a rod plasma injector [17, 48-50], a plasma coaxial gun [51-54], plasma focus device [55] etc. A short review of some of them and their parameters can be found in [17].

Experiments carried out on a rod plasma injector showed that nitrogen plasma treatment (~ 1 μs, 5-6 J/cm^2) resulted in surface hardening of different carbon steels [48]. For example, a significant increase of microhardness by the factor of 2 was observed for steel 65 (0.63% C, 0.28 % Si, 0.74 % Mn, 0.02 % P, 0.025 % S, 0.09 % Cr, <0.01 % Mo, 0.05 % Ni, 0.03 % Al, 0.3 % Cu, <0.01 % V in wt. %). The microhardness value of 20 GPa for it was reported. Such a value may appear due to the use of a very small load for testing (10 g). Most of samples were previously tempered. That is why the influence of quenching effects during treatment on hardening increased. The thickness of the melted layer according to numerical simulation was ~ 1.5 μm. At the same time treatment with the same parameters of argon plasma resulted in a small increase or sometimes in the microhardness decrease [48]. The main cause of surface hardening during nitrogen plasma treatment was formation of nitrogen containing phases such as γ_N nitrogen-expanded austenite and ε-Fe_3N [48-50], though the detected nitrogen concentration was very small. Nitrogen distribution along the depth had the maximum (~ 3.5 at.%) at the surface [48], showing that the main nitrogen transport mechanism was diffusion from residual atmosphere into a heated substrate. The maximum depth of nitrogen distribution was 0.6-0.8 μm [48].

Treatment of high-alloyed steel AISI 321 at this type of plasma generators leads to its microhardness decrease after 1 pulse [49]. A further increase of the number of pulses causes an increase of nitrogen concentration and almost a linear increase of microhardness close to the initial value by the mechanism of interstitial solid solution hardening [49]. It was supposed that with a further increase in the nitrogen content microhardness could increase above the initial value.

Plasma treatment resulted in formation of cracks and craters on the surface [48]. According to [49], to avoid severe damage the practical threshold of the power incident on the surface can be ~10 MW/cm^2 for most metals. This requirement limits the total energy delivered in a single pulse to 10 J/cm^2 in case of 1 μs duration and to 1 J/cm^2 in case of 100 ns duration.

Coaxial plasma generators can provide a much higher energy density (up to 3000 J/cm^2 [51]) and discharge duration (up to ~10^2-10^3 μs [51]). For materials modification the energy density does not exceed 10-30 J/cm^2 [52-54]. Treatment of carbon steels, low-alloyed and high-alloyed steels at the PROSVET accelerator with nitrogen plasma (10-30 J/cm^2, 2-5 μs, the ion energy - up to 2 keV) results in 2-5 times microhardness increase for all investigated types of steel [52, 53]. Approximately 2 times increase of microhardness was achieved for previously quenched samples. The thickness of the hardened layer was up to 30 μm [52, 53]. The maximum microhardness value for carbon steel 45 was achieved after 5 pulses. Some decrease of microhardness with a larger number of pulses was observed. This was explained by partial annealing of the defect structure under material heating by the previous pulses [52]. R_a investigations showed the same type of dependence on the number of pulses but no correlations between microhardness and roughness were made in this work. The maximum R_a was equal to 1.1 μm. Processing of samples with R_a > 1 μm led to the decrease of surface roughness. The same tendency was found in [25] for HPIB.

A similar dependence of microhardness on the number of pulses was found for different types of steel processed at the MK200 accelerator (2-50 μs, the incident flux specific power -

Copyright © 2010. Nova Science Publishers, Incorporated. All rights reserved.

Handbook of Material Science Research, Nova Science Publishers, Incorporated, 2010. ProQuest Ebook Central,

up to 10^7 W/cm^2, the ions energy - 2-6 keV) [54, 56]. In these experiments surface hardening was also observed for all investigated steels. Microhardness depended on irradiation regimes, a type of steel and samples preliminary processing as in the previous cases. The formation of a columnar structure inside the surface layer was reported [54, 56]. It looked like cells of different shapes in the cross-section parallel to the surface. Cell walls possessed a dislocation structure and in case of complex alloys were decorated with fine-grained precipitates. This structure can be one of hardening causes [54, 56]. One more interesting effect is the formation of bimodal microhardness distribution along the cross-section of 12H18N10T steel (0.12 % C, 18 % Cr, 10% Ni, 0.7% Ti, 0.8 % Si, 2 % Mn, 0.3% Cu in wt.%) processed at the power density greater than 10^6 W/cm^2 [39, 54, 56]. The first peak of microhardness corresponded to the modified layer. The second peak was observed at a significantly greater depth (up to 40 μm) and correlated with a high dislocation density region. Both peaks were located at progressively greater depths as the power density increased.

One can see that all techniques reviewed in this chapter have common features providing steels microhardness changes. If pulse ion, electron and plasma sources can be considered simply as sources of energy, then processes occurring in the surface layer are the same. Energy is used to melt the surface layer, sometimes dissolving the second phases, then quenching at a high speed takes place due to rapid conduction of heat into the bulk of the material. At the same time the hardening degree, as well as some peculiarities of hardness behaviour along the depth, will be strongly dependent on the energy delivered to the surface and pulse duration. Besides, plasma processing can provide chemical composition changes of the surface layer. In this chapter different approaches to steels hardening by compression plasma flows (~100 μs, the absorbed energy density 5-40 J/cm^2) will be considered: direct treatment, surface alloying by mixing of a "coating-substrate" system and surface alloying by injecting an additional component into a plasma flow.

2. EXPERIMENTAL

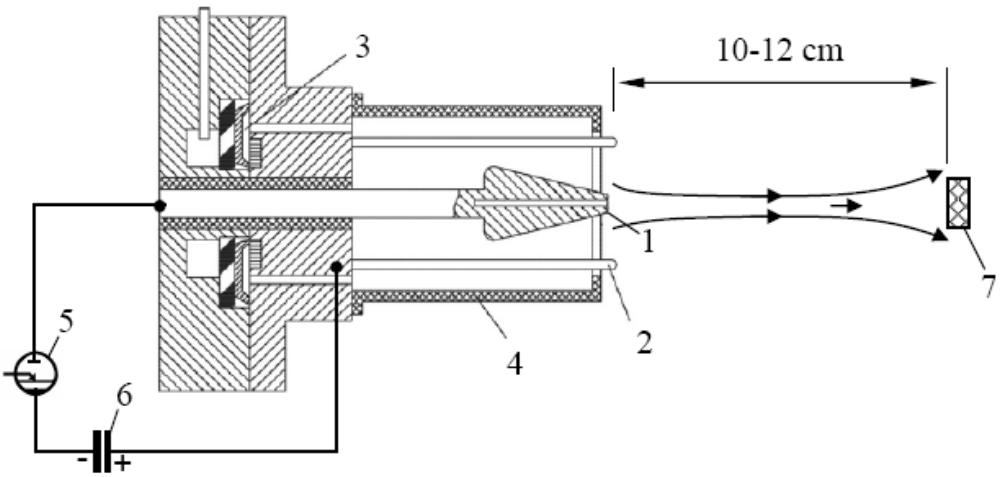
Compression plasma flows (CPF) were obtained using a gas-discharge magneto-plasma compressor of compact geometry (MPC) powered with the capacitive storage of 1200 mF, operating at the initial voltages from 3 to 5 kV (Figure 1). This is a coaxial type of plasma generators in which plasma produced during the interelectrode gap breakdown is accelerated in the discharge device by the Ampere force and outflows from the discharge unit. The discharge duration in the MPC amounts to ~100 μs and the peak value of the discharge current can reach 100 kA. The velocity of the leading front of the plasma flow and its pressure both depend on the MPC initial parameters and the derivative of the total discharge current. The length of the plasma flow is about 10 - 12 cm. The formation of the contraction (compression) zone in the middle of the plasma flow is a peculiarity of MPC accelerator (Figure 1). The diameter of the plasma flow in this zone is ~ 1 cm. Compression of the plasma flow takes place due to the interaction of the longitudinal component of the discharge current 'swept away' from the discharge device with the intrinsic azimuth magnetic field. The flow diverges in half-angles from 5 to 15°. The plasma velocity in the compression flow amounts to $(4\text{-}7)\cdot 10^6$cm/s, depending on the initial parameters of acceleration. The

Copyright © 2010. Nova Science Publishers, Incorporated. All rights reserved.

Handbook of Material Science Research, Nova Science Publishers, Incorporated, 2010. ProQuest Ebook Central,

concentration and temperature of electrons in the field of the maximum contraction reach (1-10)·10^{17} cm^{-3} and 1-3 eV. The pressure of the plasma flow on the treated surface is ~ 10^6 Pa.

The energy absorbed by the surface layer can vary by changing the plasma-forming gas pressure, the distance between electrodes and a sample, the capacitive storage initial voltage and number of pulses. Nitrogen or hydrogen were used in the MPC as a plasma-forming gas. The pressure in the preevacuated vacuum chamber was 10^{-3} Pa. The experiments were performed in a ''residual gas'' mode at which the vacuum chamber was filled with a plasma-forming gas. The pressure of the plasma-forming gas (*P*) varied in the range of 400–4000 Pa, the distance between the cathode and a sample – in the range of 6-12 cm and the capacitive storage initial voltage – in the range of 3-4 kV. According to calorimetric measurements the value of the energy density absorbed by the sample surface (*Q*) during processing varied in the range of 5-45 J/cm^2 per pulse. The number of pulses (*n*) varied in the range of 1-9. The time interval between pulses was 30-40 s. Some samples before CPF treatment were coated with Zr, Ti, Cr, Mo using vacuum cathodic arc deposition. The thickness of the Zr coating was 2.3 μm, Cr – 1.0 μm, Mo – 0.5 μm. The Ti coating thickness varied in the range of 0.5-5.0 μm.



a.



b.

Figure 1. Scheme of the MPC (a) and discharge unit (b): 1– cathode, 2 – anodes, 3 – gas valve, 4 – outer cover, 5 – ignitron, 6 – capacitor bank, 7 - sample.

Copyright © 2010. Nova Science Publishers, Incorporated. All rights reserved.

Handbook of Material Science Research, Nova Science Publishers, Incorporated, 2010. ProQuest Ebook Central,

Samples of the following materials were investigated: Armco-iron (<0.025 wt. % of C); carbon steel 3 (0.2% C, 0.2% Si, 0.5% Mn); carbon steel 40 (0.39% C, 0.52% Mn, 0.19% Si, 0.02% S, 0.01% P in wt. %); carbon steel U8A (0.8% C, 0.3% Mn, 0.2% Si, <0.2% Cr, <0.2% Cu, <0.2% Ni, <0.02% S, <0.02% P in wt. %) – AISI W1 analogue; stamp steel H12M (11.8% Cr, 1.5% C, 0.5 % Mo, 0.25% Si, 0.23% V, in wt.%) – AISI D2 analogue; high-speed steel R6M5 (0.8% C, 6.0% W, 5.0% Mo, 4.1% Cr, 1.9% V, 0.5% Co in wt. %) – AISI M2 analogue; high-speed steel R18 (0.8% C, 18.7% W, 4.3% Cr, 1.9% V, in wt.%) – AISI T1 analogue. Two types of U8A samples were used: in as-delivered condition and quenched. U8A samples were quenched at 1070 K for 3 minutes with subsequent cooling in mineral oil. R6M5 and R18 high-speed steel samples were subjected to hardening quenching at 1123 K in NaCl for 1 minute and at 1513 K in BaCl for 1 minute with final two-folded annealing at 833 K for 30 minutes. All samples were ground before processing. Samples of steel 3 and H12M were additionally polished with diamond paste (the grains size- up to 0.5 μm).

Microhardness of samples *H* was measured by means of the PMT-3 microhardmeter with the Vickers indenter under the load *P* ranging from 50 to 200 g using the conventional expression:

$$H = 1854 \frac{P}{d^2}, \tag{3}$$

where *d* – indentation diagonal length in μm. The loading (unloading) time was equal to 4 s, time under the load – 15 s.

The phase composition of samples was investigated using the X-ray diffraction analysis (XRD) in the Bragg- Brentano geometry with Cu Kα radiation at the DRON4 diffractometer. The calculated X-ray penetration depth in iron was 0.7-1.2 μm for $2\theta=30^o$-50° assuming the absorption of 75% of X-ray energy. The glancing X-ray diffraction analysis (GXRD) using Cu Kα radiation was carried out at the SEIFERT 3003 diffractometer with the HUBER SMC 9000 goniometer for the investigation of the surface layer phase composition. The glancing angle amounted to 3°. The investigation of phase composition was also carried out by ^{57}Fe conversion electron Mössbauer spectroscopy (CEMS) at room temperature using ^{57}Co/Rh source. CEMS study allows to identify phase composition from a layer with the thickness of 0.1 μm. The investigation of deeper layers (up to 10 μm) of modified samples was performed using X-ray Mössbauer spectroscopy (XMS) by registration of characteristic radiation. The obtained spectra were evaluated numerically using the MOSMOD program assuming distribution of hyperfine magnetic fields and quadrupole splitting [57]. A relative concentration of the observed phases was estimated by calculating the area under the corresponding subspectra. The concentration profiles of elements were measured by Auger electron spectroscopy (AES) using PHI-660 (Perkin Elmer) combined with 3.5 keV Ar ions sputtering. Rutherford backscattering analysis (RBS) of He ions with the energy of 6 MeV at the High Voltage Engineering tandetron system was also used. A high energy of helium ions allowed to increase a yield of ions scattered on light impurities. The SIMNRA program was used for spectra deconvolution [58]. Surface and cross-section morphology was studied by scanning electron microscopy (SEM) and optical microscopy (OM). SEM investigations were conducted at LEO1455VP microscope with the energy-dispersive Röntec microanalyzer. OM investigations were carried out at the NEOPHOT 21 microscope. The cross-section was

Copyright © 2010. Nova Science Publishers, Incorporated. All rights reserved.

Handbook of Material Science Research, Nova Science Publishers, Incorporated, 2010. ProQuest Ebook Central,

prepared by cutting samples using the "ABRASIMET" cutting machine with subsequent grinding by SiC paper of a different grain size (the minimum grain size - 17 μm) and polishing by diamond paste (the minimum particle size – 3 μm) and alumina particles (the minimum particle size – 0.05 μm). After that cross-sections were etched in a nitric or a picric acid alcoholic solution.

3. CPF TREATMENT OF ARMCO-IRON

CPF treatment of Armco-iron samples was carried out in nitrogen atmosphere with the following parameters Q=7-17 J/cm^2, n=1-9, P=400 Pa. The element analysis showed nitrogen penetration into the surface layer of samples (Figure 2). The maximum nitrogen concentration of 20 at.% was observed on the surface. The estimated penetration depth (or the depth at which the nitrogen concentration was greater than the instrumental error) was ~ 4-5 μm. Q increase up to 17 J/cm^2 did not significantly affect nitrogen distribution. One can see that nitrogen distribution has a diffusion-like shape. To prove it some estimation was made.

The one-dimensional equation of thermal conductivity was used to estimate the surface layer temperature during treatment by a compression plasma flow (Q=12 J/cm^2) [59]:

$$\frac{\partial}{\partial x}\left(k(T)\frac{\partial T}{\partial x}\right)=c(T)\rho\frac{\partial T}{\partial t}, \tag{4}$$

where $T(x, t)$ – temperature, $k=k(T)$ – thermal conductivity of the material, $c=c(T)$ – thermal capacity, ρ – density of the material, x – depth, t - time. This task was considered in the area $0\le x\le l$ and $0\le t\le 2\tau$, where l – sample thickness, τ – pulse duration. Entry and boundary conditions were the following:

$$T\big|_{x=l}=T\big|_{t=0}=T_0, \tag{5}$$

$$\left.\frac{\partial T}{\partial x}\right|_{x=0}=\frac{h}{k}\left(T\big|_{x=0}-\theta\right), \tag{6}$$

$$\theta=\begin{cases}T_m, t\le\tau\\ T_0, t>\tau\end{cases}, \tag{7}$$

where h – heat exchange factor, T_m – temperature of a plasma flow ($5\cdot10^4$K), T_0 – room temperature.

The results of the calculation showed that the temperature of the surface layer with the thickness of 20 μm for ~100 μs was greater than $2\cdot10^3$ K and could reach $3.5\cdot10^3$ K [59]. The cooling rate according to this estimation is of the order of 10^7 K/s. Nitrogen distribution $C_N(x,t)$ can be calculated assuming a constant source of impurity C_0 and using the solution of the Fick second law and conventional boundary conditions [60]:

Copyright © 2010. Nova Science Publishers, Incorporated. All rights reserved.

Handbook of Material Science Research, Nova Science Publishers, Incorporated, 2010. ProQuest Ebook Central,

$$C_N(x,t) = C_0 erfc \frac{x}{2\sqrt{D_N t}}, \quad (8)$$

where the nitrogen diffusion coefficient in the temperature range of 1811-2023 K can be estimated as $D_N = 2.86 \cdot 10^{-7} \exp\left(-\frac{61090}{RT}\right)$ [61].

Calculated nitrogen distribution ($T=2\cdot10^3$ K, t=100 μs, $D_N=10^{-8}$ m^2/s) is shown in Figure 2. One can see that calculated distribution is close enough to experimental. Thus, diffusion of nitrogen from residual atmosphere is the main reason for nitrogen penetration into a sample.

SEM findings showed the formation of a cellular structure on the surface of treated samples [62, 63]. The average cell size was 400 nm. It is hard to say whether such a structure can influence microhardness as it was shown in [54, 56] because no investigations of the dislocation structure of the surface layer were carried out. A similar cellular structure with the same cell size was also found for steel U8A and steel 40 after CPF treatment.

Investigations of cross-section morphology revealed that the modified layer consisted of two main zones (Figure 3). The first zone (the melted layer) contained dispersed grains. *Q* increase in the range of 7-17 J/cm^2 resulted in the growth of the melted layer thickness from 2 μm to 20 μm. The zone consisted of ferrite and martensite grains (inside the former austenite grains). The second zone (the heat-affected zone) consisted of columnar ferrite grains with the width of ~ 1-2 μm and the length of ~15 μm which was equal to the thickness of the zone. The thickness of the zone did not depend on *Q*. The number of pulses increase did not affect the modified layer thickness but influenced the size of this layer constituents.

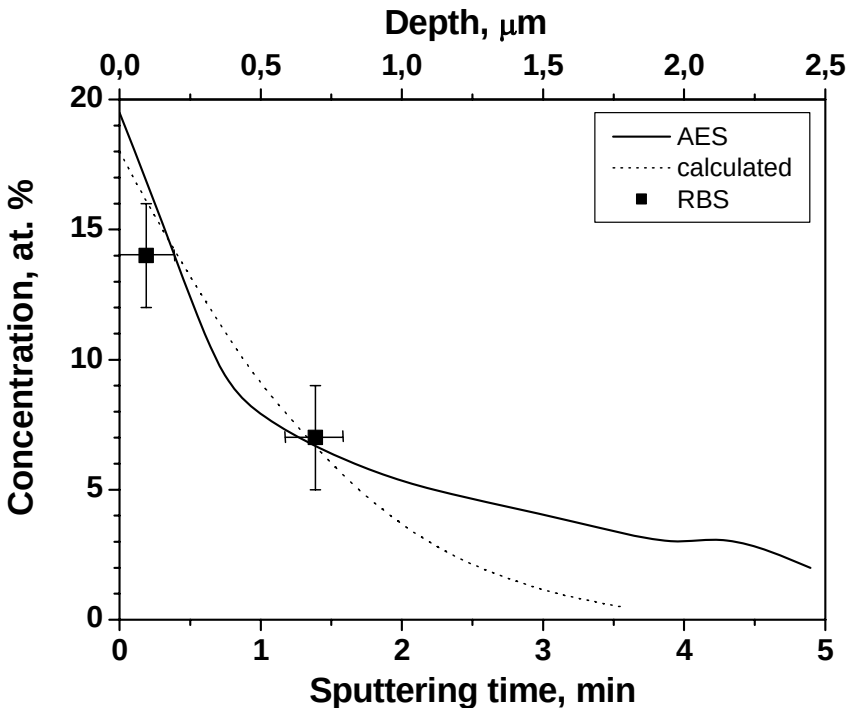


Figure 2. Nitrogen distribution in an Armco-iron sample treated by one pulse of CPF at 12 J/cm^2.

Copyright © 2010. Nova Science Publishers, Incorporated. All rights reserved.

Handbook of Material Science Research, Nova Science Publishers, Incorporated, 2010. ProQuest Ebook Central,

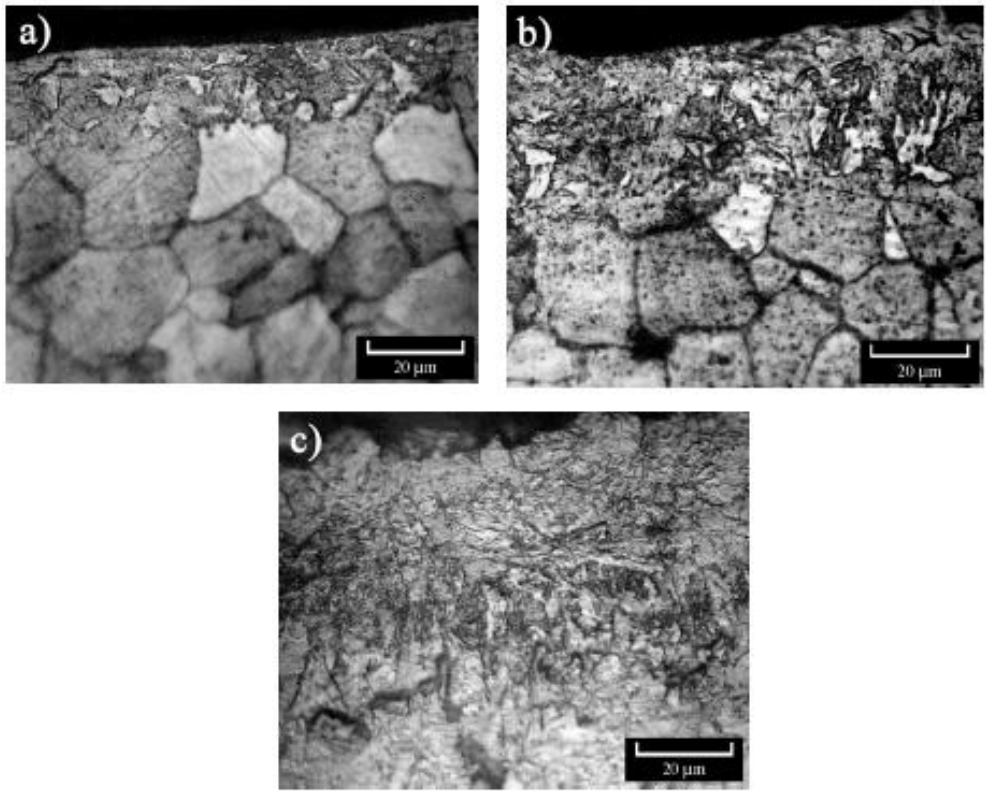


Figure 3. Cross-section OM images of Armco-iron samples treated by one pulse of CPF at 7 J/cm^2 (a), 12 J/cm^2 (b), 17 J/cm^2 (c) [62].

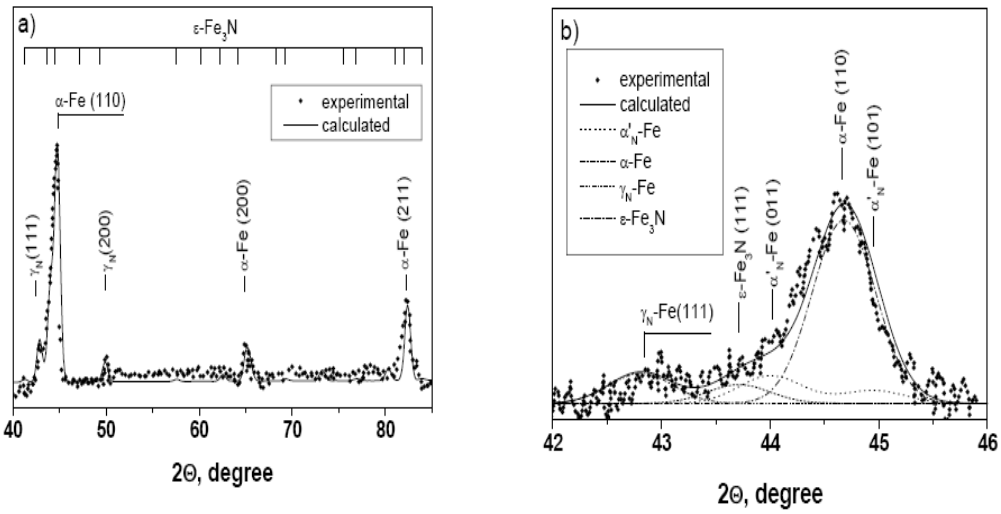


Figure 4. XRD routine (a) and precision (b) patterns of an Armco-iron sample treated by one pulse of CPF at 12 J/cm^2.

Copyright © 2010. Nova Science Publishers, Incorporated. All rights reserved.

Handbook of Material Science Research, Nova Science Publishers, Incorporated, 2010. ProQuest Ebook Central,

XRD investigations (Fig4a) showed that the analyzed layer consisted of ferrite (α-Fe) and nitrogenous austenite (γ_N-Fe). More precise investigations allowed to suppose a nitrogenous martensite (α'_N-Fe) and ε-$Fe_{2+x}N$ ($0 \le x \le 1$) type of nitride formation (Fig 4b). The mean volume fraction of these phases in the surface layer with the thickness of ~ 1 μm was 70 % α-Fe, 15 % α'_N-Fe, 13 % ε-Fe_3N, 2 % - γ_N-Fe. The iron based solid solutions lattice parameter was independent of treatment regimes thus one could conclude that the nitrogen content in these phases was constant. This is in agreement with the data of the element composition analysis.

CEMS and XMS investigations confirm the XRD data (Figure 5). The CEMS analysis (Fig 5a) showed formation of nitrogenous austenite and two phases the parameters of which being compared with the known data [64, 65] allowed to identify them as ε-$Fe_{3.2}N$ and ε-$Fe_{2.5}N$. The mean volume fraction of phases in the layer with the thickness of ~ 0.1 μm was 30 % - γ_N-Fe, 14% α-Fe, 40 % ε-$Fe_{3.2}N$, 16 % ε-$Fe_{2.5}N$. Thus a thin surface layer mainly consisted of nitrogen containing phases. The increase of the analyzed depth (Figure 5b) led to diminishing of a nitrogen containing phases volume fraction. The layer with the thickness of ~ 10 μm consisted of 90% α-Fe and 10% ε-Fe_3N. This is in agreement with nitrogen distribution along the depth.

The results of Armco-iron microhardness measurements treated by CPF in nitrogen atmosphere are presented in Figure 6a. All treatment regimes provide the microhardness increase. The maximum value of 10.8 GPa is obtained at the surface after 9 pulses of CPF treatment. Microhardness of all samples has its maximum at the surface and decreases with the growth of the indentation depth. At the depth (4 μm) the maximum value is ~ 5 GPa which is close to the microhardness value of the ferrite-nitrides mixture (3.5-5.0 GPa) [66]. Such microhardness behaviour is typical of steels nitrided or nitrocarburized by means of different techniques due to formation of the surface compound layer [12, 67]. A close correlation between the embedded impurities depth profile and the hardness depth profile can be found [8, 68]. The ISE effect can also lead to such a type of microhardness behaviour but due to a heterogeneous structure and phase composition of the surface layer the influence of this effect is hard to analyze.

Copyright © 2010. Nova Science Publishers, Incorporated. All rights reserved.

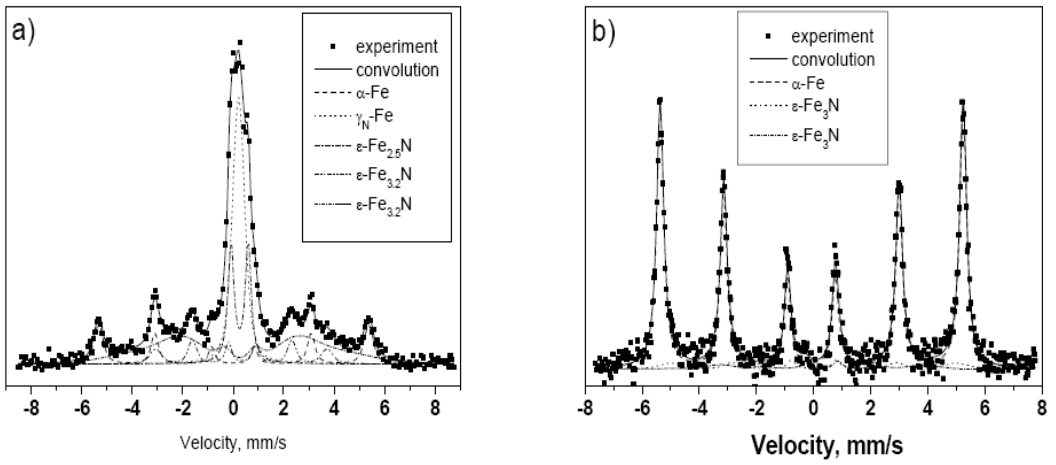


Figure 5. CEMS (a) an XMS (b) spectra of an Armco-iron sample treated by one pulse of CPF at 12 J/cm^2.

Handbook of Material Science Research, Nova Science Publishers, Incorporated, 2010. ProQuest Ebook Central,

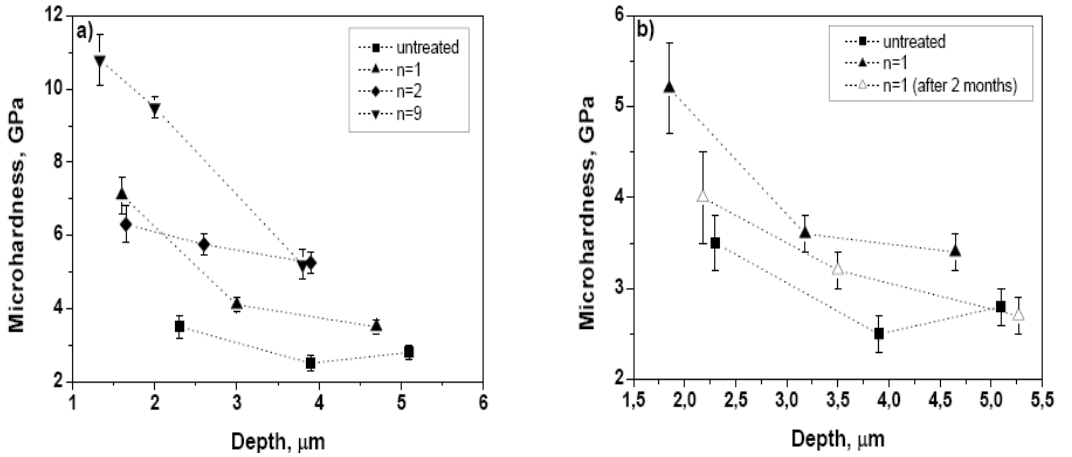


Figure 6. Microhardness dependence on the indentation depth of samples treated by CPF in nitrogen atmosphere at 12 J/cm^2(a) and hydrogen atmosphere at 14 J/cm^2 (b).

Investigations of the phase composition, element composition, surface and cross section morphology allow to suppose the following hardening mechanisms: an increase of surface roughness, grain-boundary hardening, solid solution hardening, dispersion hardening and phase composition changes. To investigate the role of phase composition changes additional experiments on CPF treatment in hydrogen atmosphere were carried out (Figure 6b). XRD and CEMS investigations did not reveal any phase composition changes after such treatment.

Surface roughness investigations using a profilometer showed that CPF treatment resulted in R_a increase. In the range of n=1-5 R_a was equal to 2±1 μm. This value is close to R_a found in [25, 52]. At n=9 R_a was equal to 7±1 μm. R_a growth is connected with large energy absorbed by the surface layer, boiling of a material with subsequent superfast cooling and craters formation. At the same time indenter prints were made in areas with almost equal R_a=2±1 μm, free of craters and other heterogeneities. That is why the roughness increase can provide the microhardness increase but by the same value for all treatment parameters.

Cross-section morphology investigations do not allow to determine the grain size in the melted layer. But it should be at least one order of magnitude less than before treatment. This effect could also be the reason for hardening. The thickness of the melted layer after CPF treatment at Q=12 J/cm^2 was 6-7 μm. It means that all microhardness measurements were made in this layer. Thus the microhardness value growth at the depth of ~ 4 μm (Fig 6a) could be connected with grain boundary hardening (or the increased dislocation density). At the same time testing of samples treated in hydrogen atmosphere showed that after two months microhardness of a treated sample was close to that of in untreated one. The grain structure of the melted layer did not change at that time. Thus one can conclude that in case of Armco-iron treatment by CPF the influence of the grain-boundary hardening mechanism does not seem to be significant. A similar conclusion can be drawn for a surface roughness influence. Due to the above reason the influence of the dislocation density on microhardness may be excluded though the dislocation structure was not examined. The microhardness decrease with time can be connected with hydrogen leaving the surface layer, thus ceasing hardening mechanisms such as solid solution hardening or stopping dislocations by impurities agglomeration. Solid-solution hardening after treatment in nitrogen atmosphere can give an

Copyright © 2010. Nova Science Publishers, Incorporated. All rights reserved.

Handbook of Material Science Research, Nova Science Publishers, Incorporated, 2010. ProQuest Ebook Central,

almost constant contribution in hardening for all treatment regimes because no crystal lattice distortion of iron based solid solutions was found.

The increase of the nitrogen content and thus the nitrogen containing phases concentration [49] as well as formation of a more developed defects structure [37-39] can be causes of the microhardness increase with *n* growth.

The analysis of the observed data showed that the main hardening mechanisms in case of one pulse of CPF treatment in nitrogen atmosphere could be dispersion hardening – pinning of dislocations by nitride precipitates in the melted layer and a change of the phase composition, e.g. nitrogenous martensite formation. The other hardening mechanisms can give some contribution but the comparison of the data in Figure 6a and Fig 6b showed that treatment in nitrogen atmosphere provided a greater microhardness increase than treatment in hydrogen atmosphere.

4. CPF Treatment of Carbon Steels

4.1. Direct Treatment

CPF treatment of carbon steels U8A and steel 40 samples was carried out in nitrogen atmosphere with the following parameters Q=7-17 J/cm^2, n=1-5, P=400 Pa. The analysis of elements distribution in the modified layer showed that nitrogen had a diffusion-like shape as in case of Armco-iron with the maximum concentration of 16-30 at. % at the surface depending on treatment parameters and a material (Figure 7). These values are close to the values of the maximum nitrogen concentration of 20-25 at. % obtained by laser nitriding of an iron-based material [69]. At the same time in [69] similar nitrogen profiles were received for iron, carbon steels and austenitic stainless steel exhibiting no dependence on the carbon content.

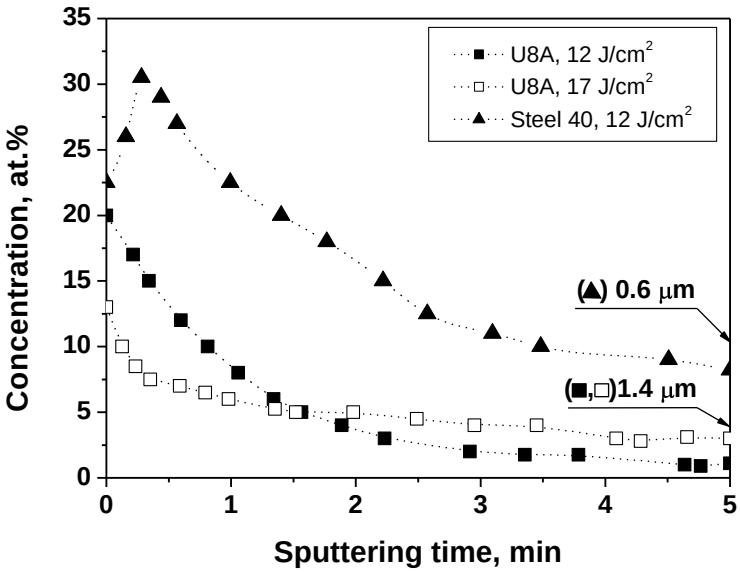


Figure 7. AES nitrogen profile in steels samples treated by one pulse of CPF.

Copyright © 2010. Nova Science Publishers, Incorporated. All rights reserved.

Handbook of Material Science Research, Nova Science Publishers, Incorporated, 2010. ProQuest Ebook Central,

In contrast to these results CPF treatment results in deeper nitrogen penetration in case of Armco-iron samples (Figure 2) than in case of carbon steels (Figure 7). Thus the increase of carbon content and presence of alloying elements can diminish the nitrogen diffusion depth. The comparison of nitrogen depth profiles for carbon steels with a different carbon concentration showed that other reasons would also influence nitrogen distribution, for example the grain boundaries area, otherwise the nitrogen concentration in U8A steel (with a greater carbon content) should be higher than in steel 40 and nitrogen penetration depth should be less. The carbon content in the analyzed layer of both steels was almost constant for all treatment regimes.

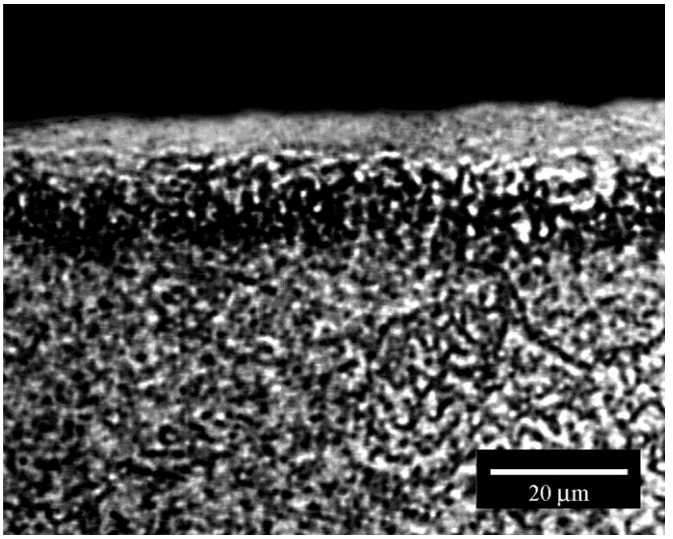


Figure 8. Cross-section OM image of U8A steel sample treated by one pulse of CPF at 12 J/cm^2.

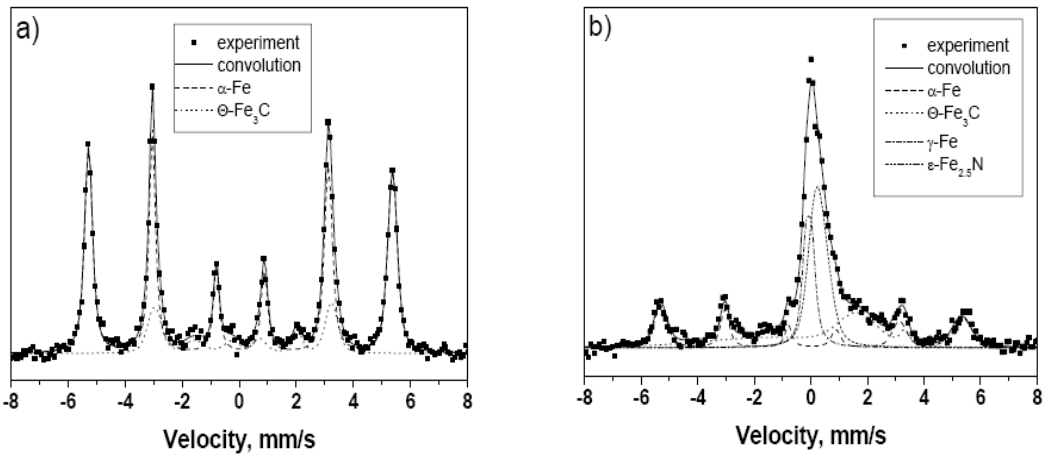


Figure 9. CEMS spectra of U8A steel samples before (a) and after treatment by one pulse of CPF at 12 J/cm^2.

Copyright © 2010. Nova Science Publishers, Incorporated. All rights reserved.

Handbook of Material Science Research, Nova Science Publishers, Incorporated, 2010. ProQuest Ebook Central,

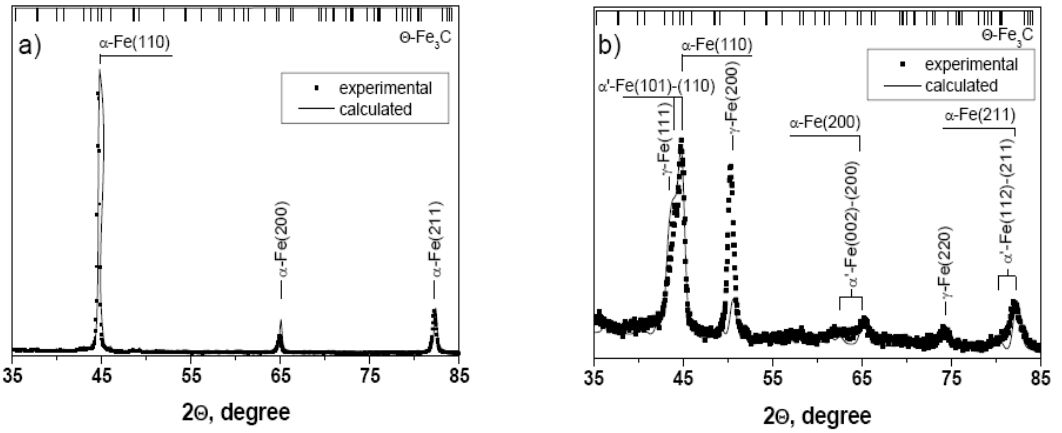


Figure 10. XRD patterns of U8A steel sample before (a) and after (b) CPF treatment by one pulse at 12 J/cm^2.

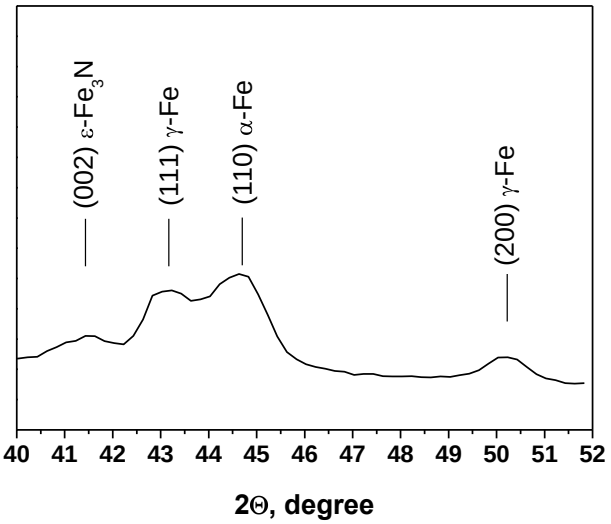


Figure 11. GXRD pattern of U8A steel sample treated by one pulse of CPF at 12 J/cm^2.

The modified layer of carbon steels consists of two main zones as in case of Armco-iron. The first zone has dispersed grains crystallized at a high cooling rate in the melted layer, while the second zone consists of columnar grains. For samples of U8A steel the thickness of the first zone is about 10 μm (Figure 8). According to the data of the metallographic analysis it consists of austenite, martensite, carbides and nitrides. The microhardness of this zone measured at the load of 50 g at the cross-section is 14.3±0.7 GPa. The thickness of the second zone is about 12 μm. Its main phase constituents (in an untreated steel too) are divorced pearlite with an increased density of cementite precipitates in comparison with the first zone. Its precipitates are located transversely to the surface. The size of θ-Fe_3C precipitates is 0.4-0.6 μm. The same size of cementite precipitates was observed before treatment. The microhardness of this zone is 8.8±0.5 GPa. The microhardness in the bulk of the sample is 5.9±0.6 GPa.

Copyright © 2010. Nova Science Publishers, Incorporated. All rights reserved.

Handbook of Material Science Research, Nova Science Publishers, Incorporated, 2010. ProQuest Ebook Central,

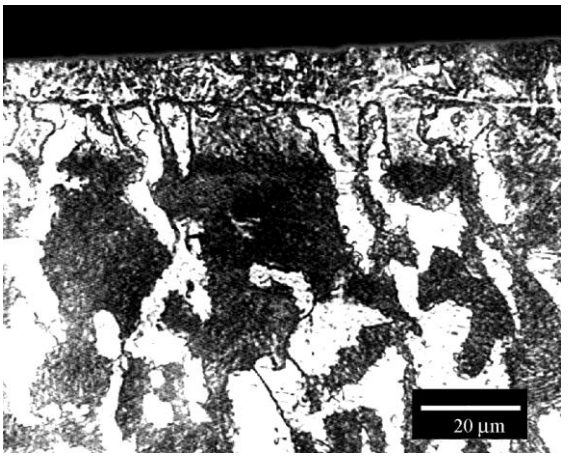


Figure 12. Cross-section OM image of steel 40 sample treated by one pulse of CPF at 12 J/cm^2.

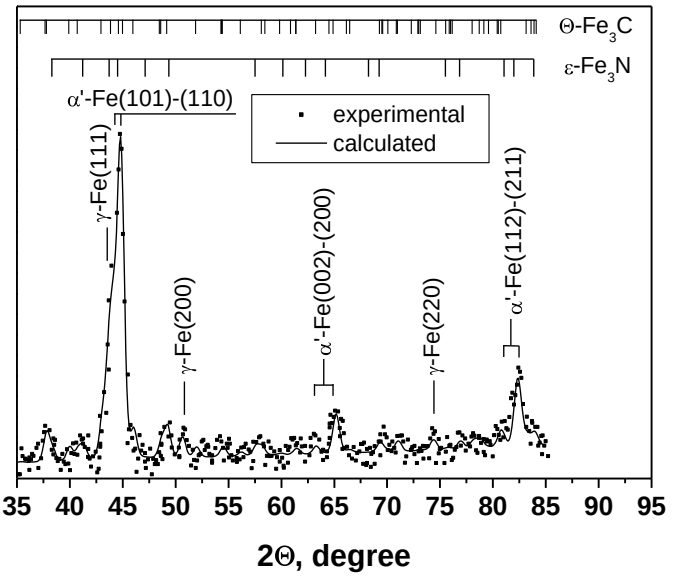


Figure 13. XRD patterns of steel 40 sample treated by one pulse of CPF at 12 J/cm^2.

The CEMS and XRD analyses confirmed the presence of phase constituents in the first zone. CEMS data showed the formation of the phase with the isomer shift of -0.07 mm/s and quadrupole splitting of 0.21 mm/s which can be attributed to austenite [64] and formation of ε-$Fe_{2.5}N$ (Figure 9). The mean volume fractions of these phases in the layer with the thickness of 0.1 μm are 18 % and 32%, respectively. The presence of ferrite (24 %) is also observed. The fraction of cementite diminishes to 26 % in comparison with that in the untreated sample (Figure 9). The XRD analysis showed the presence of ferrite, martensite, cementite and austenite in the layer with the thickness of ~ 1μm (Figure 10). The GXRD analysis confirmed formation of ε-$Fe_{2+x}N$ type nitride (Figure 11). The comparison of AES, CEMS and XRD data showed that martensite was formed in the layer beyond the surface layer enriched with

Copyright © 2010. Nova Science Publishers, Incorporated. All rights reserved.

Handbook of Material Science Research, Nova Science Publishers, Incorporated, 2010. ProQuest Ebook Central,

nitrogen. Insufficient concentration of impurities in this layer for austenite stabilization at room temperature seems to be the main reason for this effect.

The findings showed that CPF impact on U8A steel results in cementite dissolution in the melted layer. Carbon from dissolved cementite as well as nitrogen can stabilize austenite in the surface layer after cooling. Carbon can also take part in martensite formation during cooling of the melted layer. Formation of martensite, dispersed nitride and carbide precipitates can be the main reasons for the surface layer microhardness increase.

The formed structure possesses enhanced thermal stability. Twenty minutes vacuum annealing at 430 K of U8A steel sample treated by one pulse of CPF at 12 J/cm^2 does not show the microhardness decrease, though this temperature is critical for mechanical properties of an untreated steel. At the temperature of 900 K the microhardness of the sample was equal to 8.5±0.5 GPa. This temperature is close to the minimal temperature of stable austenite existence. Thus annealing can lead to a partial transformation of the austenite-martensite structure into the initial pearlite structure resulting in the microhardness decrease. The initial microhardness (~6 GPa) as well as the initial structure were observed after annealing at 1020 K.

Metallographic investigations showed that the first zone in treated steel 40 with the thickness of 15 μm consisted of martensite with different dispersity (Fig 12). Besides, XRD showed austenite and ε-nitride formation in the surface layer of this zone (Fig 13). The second zone with the same thickness had a structure close to the structure of the bulk. It consisted of pearlite and ferrite grains. A more detailed analysis discovered martensite and troostite structures with the size of 0.2 μm. Microhardness distribution along the corresponding cross-section is presented in Figure 14. In the first zone the microhardness value (load 50 g) can be as high as 9.0±0.6 GPa due to formation of dispersed martensite and surface nitrides. In the second zone martensite and troostite precipitates provide the mean microhardness value ~ 5 GPa.

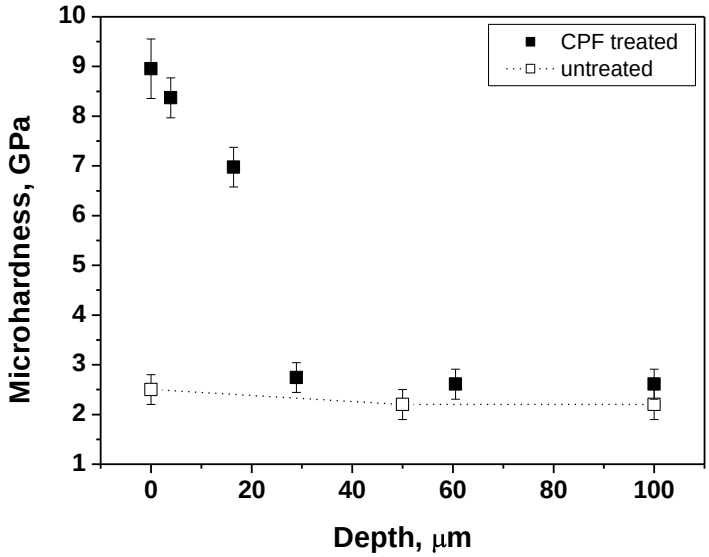


Figure 14. Microhardness distribution along the cross-section of steel 40 sample before and after treatment by one pulse of CPF at 12 J/cm^2.

Copyright © 2010. Nova Science Publishers, Incorporated. All rights reserved.

Handbook of Material Science Research, Nova Science Publishers, Incorporated, 2010. ProQuest Ebook Central,

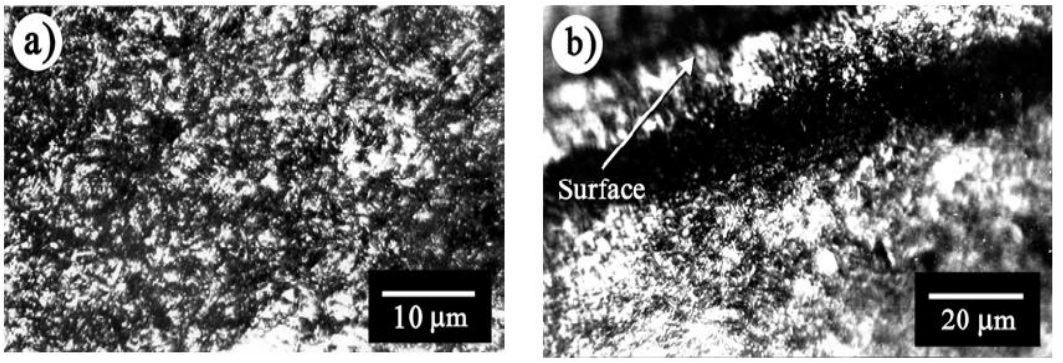


Figure 15. Cross-section OM images of quenched U8A steel sample before (a) and after CPF treatment by one pulse at 12 J/cm^2 (b).

CPF treatment of the preliminary quenched sample of U8A steel was carried out to investigate the influence of the preliminary heat treatment on mechanical properties. After quenching the structure of steel was a martensite and pearlite mixture (Figure 15 a). Its microhardness (load 50 g) was equal to 9.3±0.5 GPa. After CPF treatment (Figure 15 b) the microhardness in the first zone with the thickness of 10 μm was 18.0±0.8 GPa, which could be connected with an increased volume fraction of martensite according to XRD data. The microhardness of the second zone (a dark layer in the Figure 15 b) was 7.5±0.5 GPa. It resembled the tempered zone formed below the hardened layer after HCEB treatment of steels [45]. The microhardness in bulk was equal to the initial microhardness.

The observed data showed that the microhardness increase in carbon steels treated by one pulse CPF could mainly be connected both with the modification of the initial phase constituents of the steel structure and nitride precipitates formation. A further *n* increase could involve hardening mechanisms based on changes in the defects density.

4.2. Alloying By Mixing of a "Coating/Substrate" System

Mixing of a "coating/substrate" system by ion, electron, plasma and laser beams allows to alloy the substrate material with the coating elements. This process is of special interest in investigating nonequilibrium phase diagrams or in producing nonequilibrium, immiscible and metastable compounds the existence of which in equilibrium phase diagrams is forbidden. In contrast to well-known ion-beam mixing based on energy transfer in atomic elastic collisions [70] or on diffusion in thermal spikes [71], mixing with high energy fluxes can provide formation of deeper alloyed layers with the thickness of ~ 0.1 - 1 μm for HPIB, HCEB and IPPB with typical parameters [15, 72-75]. For GESA pulsed electron beam facility [76] and coaxial plasma generators [39, 56] the thickness of the alloyed layer can be even tens of micrometers. A greater thickness is achieved by a greater amount of energy supplied to the surface in a pulse and a greater discharge time because of the mixing mechanism which will be discussed later. The use of such technique for steels treatment leads to formation of surface layers with enhanced microhardness [56, 72, 73] and wear resistance [73]. Unlike HPIB and HCEB techniques treatment by IPPB allows to incorporate additionally atoms of a plasma-forming gas, thus expanding the number of compounds to be synthesized in the mixed layer.

Copyright © 2010. Nova Science Publishers, Incorporated. All rights reserved.

Handbook of Material Science Research, Nova Science Publishers, Incorporated, 2010. ProQuest Ebook Central,

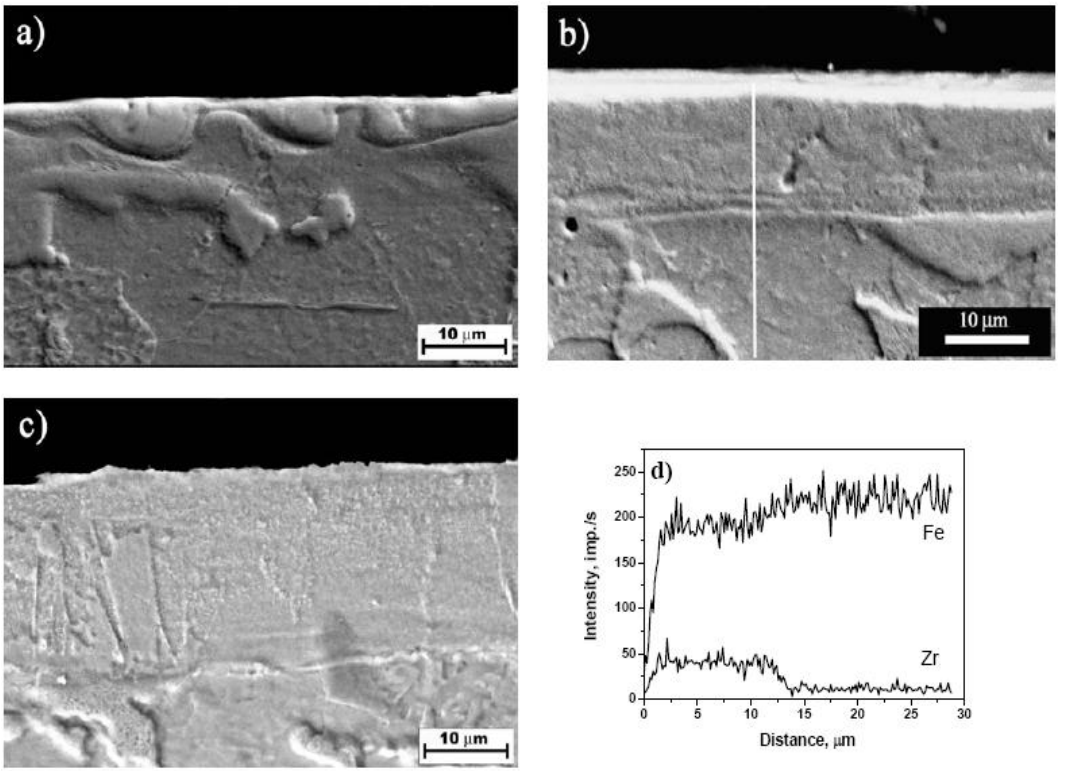


Figure 16. SEM images (a, b, c) and distribution of elements along the corresponding white line (d) of the Zr/steel samples cross-section after CPF treatment: Q=13 J/cm^2 and n=1 (a), Q=13 J/cm^2 and n=5 (b, d), Q=40 J/cm^2 and n=1 (c).

The following systems: Zr/steel 3, Cr/steel 3, Mo/steel 3 and Ti/steel 3 were examined to investigate the mixing process by CPF. Steel 3 is a hypoeutectoid steel with a ferrite-pearlite structure. A possibility of the element and phase composition control as well as mechanical properties control by varying treatment parameters can be illustrated by the example of the Zr/steel 3 system. The samples of this system were treated by CPF at Q=13-40 J/cm^2, n=1-5 and P=400 Pa.

The investigations of the samples cross-section using the energy-dispersive X-ray analysis showed that after treatment Zr was distributed along the whole melted layer (Figure 16). After one treatment pulse at 13 J/cm^2 the thickness of the melted layer was not constant and Zr had non-uniform distribution. Uniform Zr distribution along the depth was observed after five pulses of CPF treatment (Figure 16d). The growth of Q led to the increase of the mixed layer thickness up to 20 μm at 40 J/cm^2. The thickness of the coating was constant for all treated samples that is why one could expect a decrease of the alloying element concentration in the mixed (melted) layer with Q increase.

The element composition of the surface layer was investigated by means of both AES and RBS. Such an approach allows to receive reliable information on the concentration of light and heavier components as well as to determine the depth at which an element composition change takes place. According to AES data n increase led to the growth of the nitrogen concentration in the surface layer up to ~60 at.% (Figure 17). This large value can be connected with formation of blisters containing nitrogen. Blisters formation was found by

Copyright © 2010. Nova Science Publishers, Incorporated. All rights reserved.

Handbook of Material Science Research, Nova Science Publishers, Incorporated, 2010. ProQuest Ebook Central,

SEM analysis of surface morphology. These data also confirmed the supposition on the growth of the nitrogen concentration and the volume fraction of the nitrogen containing phase with *n* growth resulting in the microhardness increase of Armco-iron samples. At the same time the shape of nitrogen distribution was different from that received for iron and steels after direct CPF treatment. Its maximum coincided with the maximum of zirconium distribution.

AES data showed that the increase of *Q* or *n* led to the decrease of the zirconium concentration (Figure 17). Its concentration in layer below the surface nitrogen enriched layer diminished from 15 at. % to 3 at. %. This regularity was confirmed by RBS data (Figure 18). Three main layers in zirconium distribution could be found. The first layer contained zirconium surface segregation peak with the concentration of 20-25 at. % that was consistent with the data. The first layer thickness was about 0.1 μm. This layer also contained the maximum nitrogen concentration (Figure 17). The underlying layer lacked zirconium. This peculiarity of zirconium distribution was clearly seen after CPF treatment at Q=13 J/cm^2 and n=5. The thickness of this layer depended on treatment parameters. And in the third layer (the bulk of the mixed layer) the zirconium concentration became constant. The presence of the zirconium depleted layer could be connected with zirconium diffusion to the surface during crystallization from the melt. The formation of the zirconium containing surface phase can be the cause of diffusion. According to RBS analysis the maximum nitrogen penetration depth (at 13 J/cm^2) was about 0.6 μm.

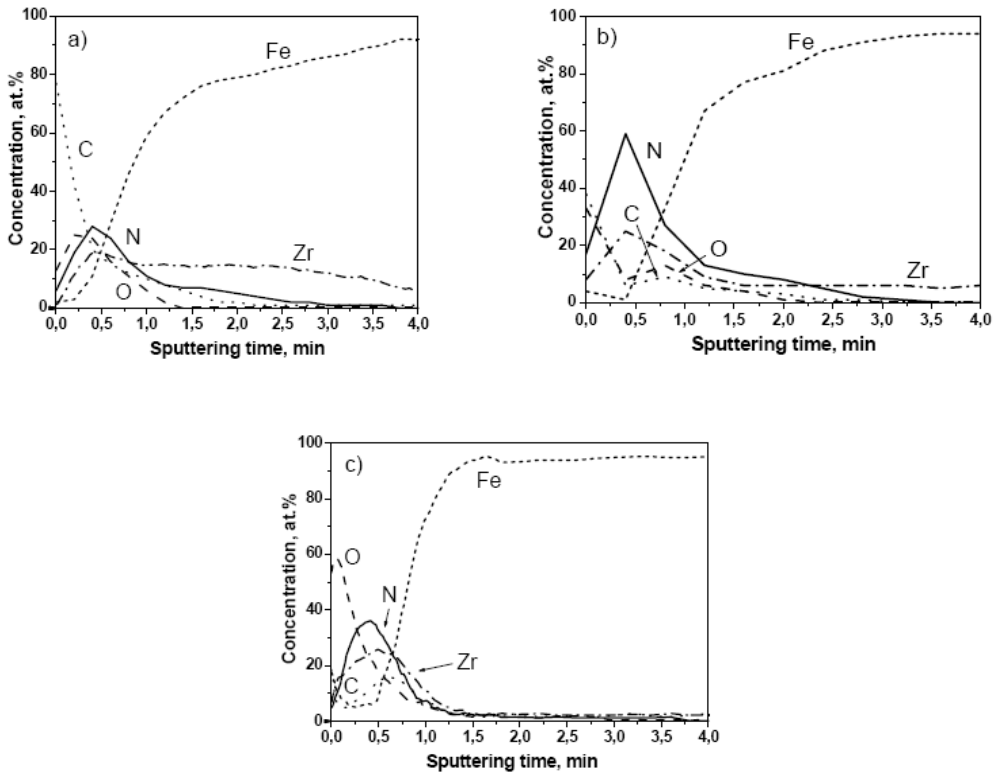


Figure 17. AES elements depth profiles in Zr/steel samples after CPF treatment: Q=13 J/cm^2 and n=1 (a), Q=13 J/cm^2 and n=5 (b), Q=40 J/cm^2 and n=1 (c).

Copyright © 2010. Nova Science Publishers, Incorporated. All rights reserved.

Handbook of Material Science Research, Nova Science Publishers, Incorporated, 2010. ProQuest Ebook Central,

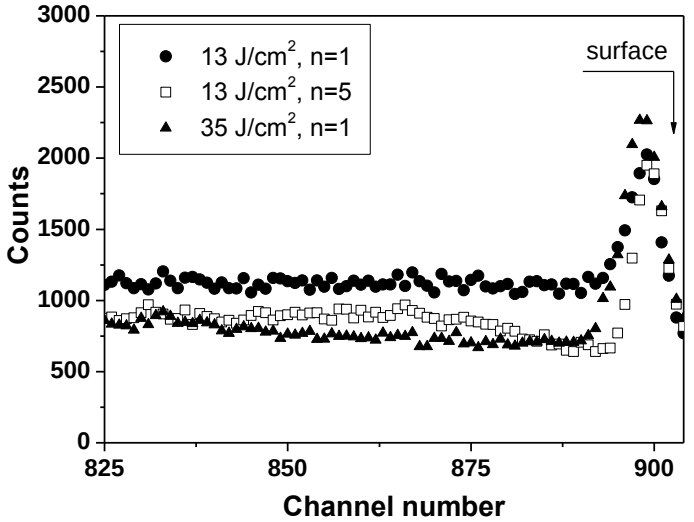


Figure 18. Part of RBS spectra corresponding to Zr distribution of Zr/steel samples after CPF treatment.

The decrease of the alloying element concentration with Q growth is connected with the following reasons. Q growth leads to the increase of the melted layer thickness. In case of a constant coating thickness the whole volume of the coating element will be distributed in the melted layer of a greater thickness resulting in the decrease of the alloying element concentration. In other words, the mean concentration of zirconium in the mixed layer after one treatment pulse can be estimated as:

$$\bar{c}_{Zr} \approx \frac{x_{Zr}}{x_{mix}}, \tag{9}$$

where x_{Zr} – thickness of the coating, x_{mix} – thickness of the mixed layer. For the treatment regime Q=13 J/cm^2 and n=1 $\bar{c}_{Zr}$ is equal to 19 at. %, for Q=40 J/cm^2 and n=1 $\bar{c}_{Zr}$ is equal to 11 at. %. The comparison with the experimental data showed that the concentration received using equation (9) was overestimated. The difference between the calculated and experimental concentration became greater with Q increase. The reason for such behaviour (and the second cause of the alloying element decrease) was ablation. Ablation resulted in the removal of the coating surface layer during CPF impact, thus diminishing the alloying element volume that could be redistributed in the mixed layer. The ablated mass increased with the growth of Q. Ablation was also the reason for the alloying element decrease in case of n growth.

The analysis of the alloying element redistribution showed that its diffusion or transport in conditions of a large concentration, temperature and pressure gradients did not provide penetration at the depth greater than a few micrometers [77]. The most probable reason for mixed layer formation was concentration-capillar and thermo-capillar (Marangoni) convection [78-81]. Convection whirls (see for example, Ref. [76]) appeared in the liquid phase in conditions of temperature and concentration gradients due to the dependence of surface tension on temperature and concentration lead to mixing in the melted surface layer containing both a coating and a substrate material. One can see that the thickness of the

Copyright © 2010. Nova Science Publishers, Incorporated. All rights reserved.

Handbook of Material Science Research, Nova Science Publishers, Incorporated, 2010. ProQuest Ebook Central,

melted layer should be greater than the coating thickness otherwise no mixing process will take place. It should also be noted that convection efficiency will depend on the liquid phase existence time [81]. Sources of high-energy fluxes that provide a high energy (for melting of the surface layer) and a relatively high time of the melt existence will be more effective in applying this alloying technique. That is why sources with a high discharge time and a high energy in pulse provide deep alloyed layers (see Ref. [39, 56, 76]).

The results of the Zr/steel 3 surface layer phase composition analysis are presented in Figure 19. One can see that CPF treatment in nitrogen atmosphere resulted in ZrN formation. Its formation is thermodynamically strongly favourable because of its formation enthalpy -372 kJ/mol [82] that is sufficiently lower than formation enthalpy of iron nitrides. That is why ZrN presence in the Zr/steel 3 system was expected after CPF treatment. AES data showed that even thin ZrN film could be expected on the surface (Figure 17c). ZrN formation determines peculiarities of elements distribution in the surface layer. On the one hand, ZrN formation leads to Zr diffusion from the bulk to the surface due to the difference in chemical potential, thus resulting in Zr depleted layer formation. On the other hand, it prevents nitrogen diffusion from atmosphere to the bulk of a sample, thus making nitrogen distribution different from that received for direct treatment of iron and steels. After CPF treatment with Q=13 J/cm^2 and n=1 Zr diffraction lines can be seen in the diffraction pattern. Q and n increase lead to their disappearance. At the same time according to AES data (Figure 17) the Zr concentration in the bulk of the mixed layer treated with Q=13 J/cm^2 and n=5 is ~ 6 at.%. The maximum solubility of Zr in α-Fe is ~ 0.1 at.% and in γ-Fe it is ~ 0.2 at.% [83]. That is why Zr not bounded in ZrN can form oversaturated solid solutions on the basis of α-Fe and γ-Fe, disperse Zr or Fe-Zr (Fe_2Zr) intermetallide precipitates that can not be revealed by XRD. Detailed investigations of the α-Fe lattice parameter showed its growth with the Zr concentration increase in the mixed layer.

Q increase led to the decrease of the ZrN content due to diminishing of the Zr concentration in the surface layer. The excess of nitrogen over zirconium led to stabilization of austenite at room temperature.

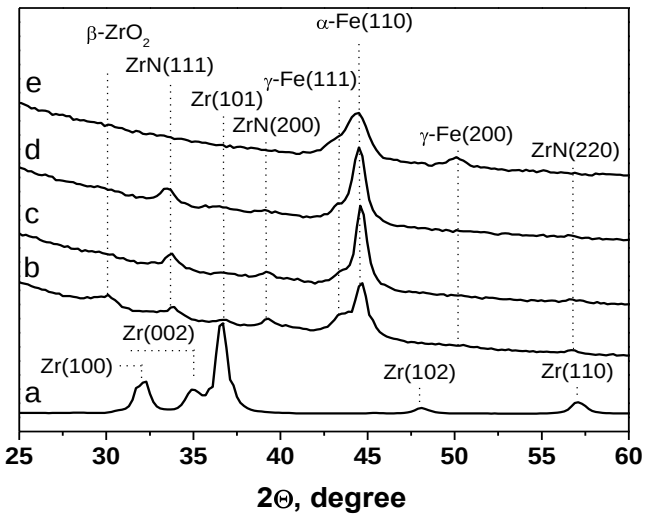


Figure 19. GXRD patterns of Zr/steel samples before (a) and after CPF treatment: Q=13 J/cm^2 and n=1 (b), Q=13 J/cm^2 and n=5 (c), Q=35 J/cm^2 and n=1 (d), Q=40 J/cm^2 and n=1 (e).

Copyright © 2010. Nova Science Publishers, Incorporated. All rights reserved.

Handbook of Material Science Research, Nova Science Publishers, Incorporated, 2010. ProQuest Ebook Central,

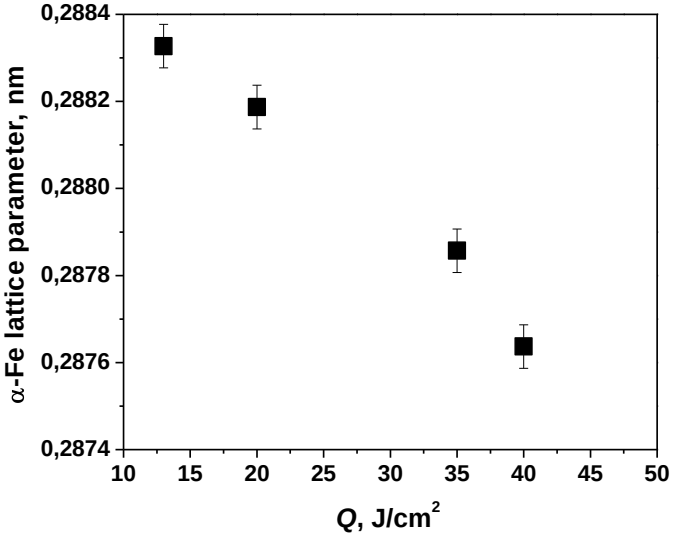


Figure 20. α-Fe lattice parameter dependence of Zr/ steel 3 samples treated by one pulse of CPF on Q.

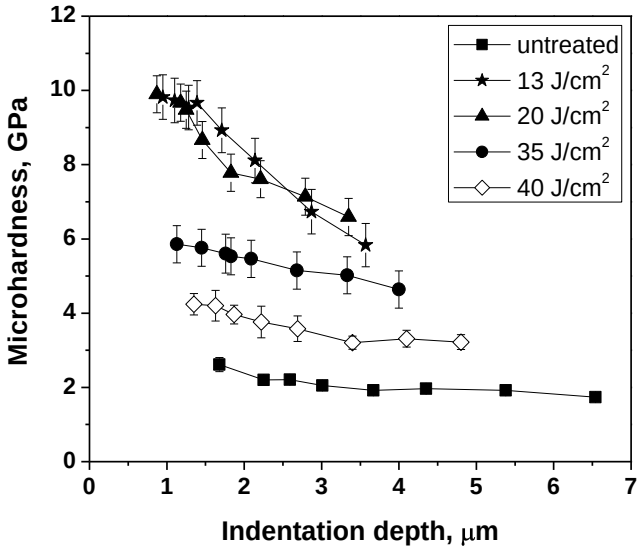


Figure 21. Microhardness dependence on the indentation depth of untreated steel 3 and Zr/steel 3 samples treated by one pulse of CPF.

Thus the structure of the mixed layer can be described as follows. A thin ZrN film may exist on the surface. The surface layer with the thickness of up to 0.6 μm contains ZrN precipitates, α-Fe(N,C,Zr) and γ-Fe(N,C,Zr). The whole mixed layer can contain α-Fe(C,Zr) and disperse precipitates of Zr or Fe-Zr intermetallide.

The analysis of the microhardness dependence on the indentation depth showed that the maximum microhardness was observed in samples with maximum zirconium concentration (Figure 21). This can have the following reasons.

Copyright © 2010. Nova Science Publishers, Incorporated. All rights reserved.

Handbook of Material Science Research, Nova Science Publishers, Incorporated, 2010. ProQuest Ebook Central,

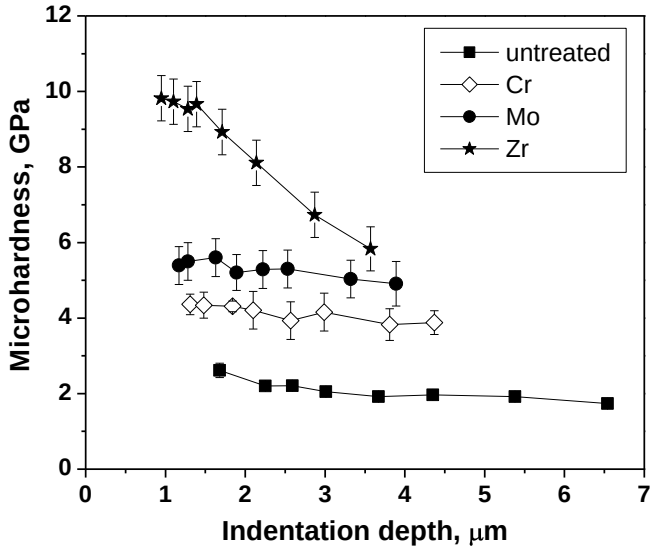


Figure 22. Microhardness dependence on the indentation depth of untreated steel 3 and steel 3 samples with different coatings treated by one pulse of CPF at 13 J/cm^2.

Firstly, the zirconium concentration increase results in the maximum ZrN content in the surface layer. That is why the microhardness of samples treated at Q=13 J/cm^2 and Q=20 J/cm^2 is greater at a smaller load. The comparison of the samples microhardness with different alloying elements also showed that the Zr alloyed surface layer had the largest microhardness (Figure 22). The investigation of the Mo/steel 3 and Cr/steel 3 systems phase composition after CPF treatment did not reveal nitrides formation [84, 85]. Though chromium nitrides are hard to be detected by XRD.

Secondly, the growth of the zirconium concentration led to distortion of the α-Fe crystal lattice. This can be the reason for a solid solution hardening mechanism which can be significant at the depth of about 1 μm and greater where no ZrN precipitates exist. It seems to be the main hardening mechanism for a sample treated at Q=35 J/cm^2 at the whole indentation depth and for samples treated at smaller energy at the indentation depth of 3-4 μm where influence of the ZrN containing layer is less significant. This mechanism also results in hardening of Mo and Cr alloyed steel 3 (Figure 22). The microhardness value is almost constant on the depth for these samples, which is consistent with the previous reasoning. The comparison of iron solid solutions lattice parameters changes (Table) showed that lattice distortion was proportional to the alloying element atom radius. Microhardness values at the indentation depth of 3-4 μm are in the same order (Figure 22).

Table. Lattice parameters of iron based solid solutions (a_α, a_γ) in samples alloyed with different elements by CPF (n=1, Q=13 J/cm^2) and ratio of atomic radia

Alloying element	a_α, nm	a_γ, nm	Δa, nm	r_{Me}/r_{Fe}
Zr	0,28833	-	0,00005	1,27
Mo	0,28745	0,36315	0,00005	1,11
Cr	0,28688	0,36005	0,00005	1,02

Copyright © 2010. Nova Science Publishers, Incorporated. All rights reserved.

Handbook of Material Science Research, Nova Science Publishers, Incorporated, 2010. ProQuest Ebook Central,

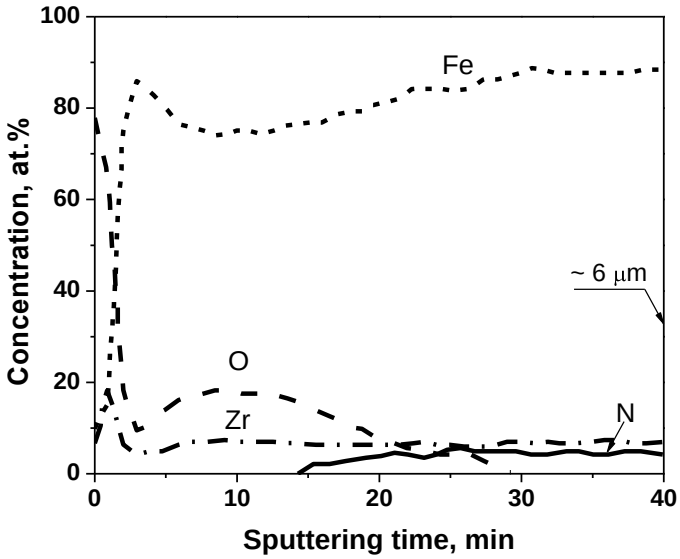


Figure 23. AES elements depth profiles in Zr/steel sample after CPF treatment and annealing at 1273 K.

The influence of other hardening mechanisms on the microhardness value is also possible. But dispersion hardening and solid solution hardening are more likely to occur. Partially it is proved by the fact that microhardness values of steel 3 sample treated by one pulse of CPF at Q=13 J/cm^2 is close to microhardness values of Zr/ steel 3 sample treated by one pulse of CPF at Q=40 J/cm^2 with the smallest Zr concentration.

Vacuum annealing in the temperature range of 473-1273 K of the Zr /steel 3 sample treated by CPF at Q=13 J/cm^2 and n=5 was carried out to investigate thermal stability of the structure and mechanical properties. The pressure of residual gases was less than 10^{-3} Pa. Annealing time was 30 min at each temperature. One can see that nitrogen redistribution into the depth and oxygen enrichment of the surface layer took place during annealing (Figure 23). Formation of the surface oxide can be a barrier for nitrogen diffusion to the surface. Thus it may be the reason for nitrogen redistribution into the bulk of the sample at the depth greater than 6 μm.

The phase composition analysis confirmed formation of zirconium oxide in the surface layer (Figure 24). The volume fraction of this phase in the analyzed layer increased with the growth of annealing temperature. β-ZrO_2 phase which was formed during CPF treatment (Figure 19) prevailed over α-ZrO_2 phase up to the annealing temperature of 1073 K. At greater temperature β-ZrO_2 still existed but a further oxide growth took place as α-ZrO_2. ZrN phase could be observed for all annealing temperatures but the intensity of its diffraction lines decreased with the growth of temperature. Partial dissolution of this phase in the oxide rich surface layer could be the reason for this effect. At the same time nitrogen diffused to the bulk could form ZrN precipitates in a deeper layer. The growth of annealing temperature also resulted in the decrease of the α-Fe lattice parameter (Figure 25) that could be connected with decomposition of the α-Fe supersaturated solid solution. The lattice parameter was still larger than that of the untreated steel 3 (0.28694 nm) even at the highest annealing temperature. The γ-Fe diffraction line disappeared at the temperature greater than 673 K.

Copyright © 2010. Nova Science Publishers, Incorporated. All rights reserved.

Handbook of Material Science Research, Nova Science Publishers, Incorporated, 2010. ProQuest Ebook Central,

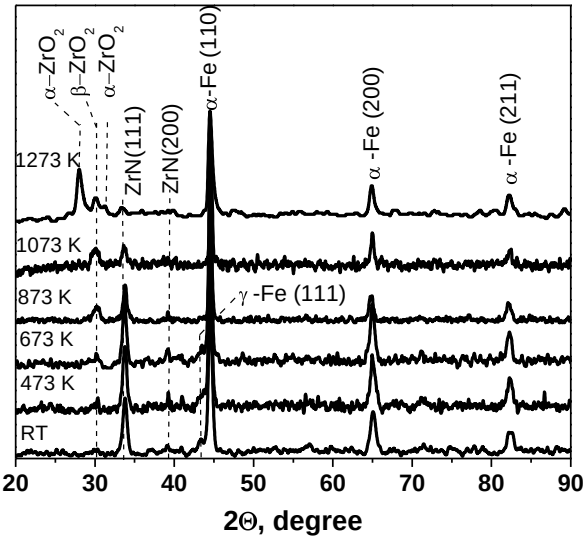


Figure 24. XRD patterns of Zr/steel sample after CPF treatment and after annealing at different temperatures.

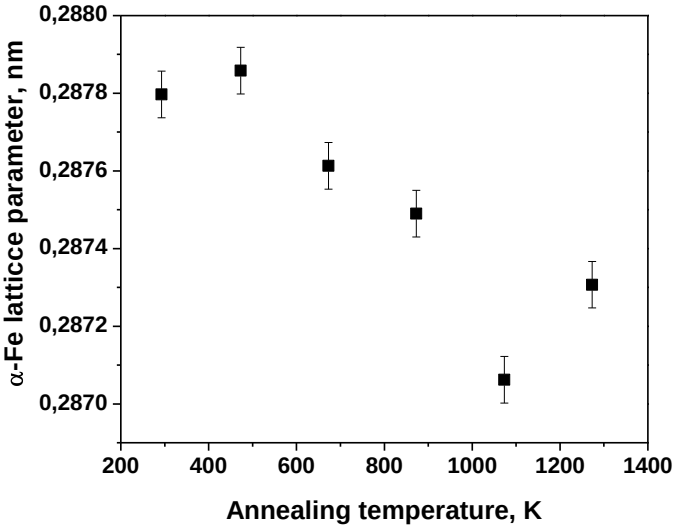


Figure 25. α-Fe lattice parameter dependence of Zr/ steel 3 sample treated by CPF on annealing temperature.

The SEM analysis of the sample cross-section did not reveal significant differences in Zr distribution after annealing (Figure 26). Annealing led to formation of lamellar pearlite in the mixed layer. Pearlite was not found in the mixed layer after treatment due to its dissolution because the temperature of the surface layer was higher than Θ-Fe_3C melting temperature (1923 K). Annealing at the temperature greater than 996 K (the maximum temperature of pearlite transformation) will lead to pearlite formation due to release of carbon from the α-Fe supersaturated solid solution. Decomposition of the supersaturated solid solution will lead to

Copyright © 2010. Nova Science Publishers, Incorporated. All rights reserved.

Handbook of Material Science Research, Nova Science Publishers, Incorporated, 2010. ProQuest Ebook Central,

Zr atoms leaving from it. Zr can take part in formation of disperse precipitates (Zr, ZrC, ZrN) shown in insert of Figure 26a with the size up to 100 nm.

Microhardness measurements were carried out in the load range of 50-200 g. Then microhardness values at the depth of 4 μm were chosen for comparison (Figure 27). Figure 27 showed that a significant microhardness decrease of a Zr /steel 3 sample treated by CPF was observed after annealing at the temperature greater than 1073 K. Microhardness behaviour of the treated sample in the temperature range of 293-1073 K was close to that of the untreated steel sample (but in the range of the measurement error). In both cases the same drop of the microhardness value was observed in this temperature range. It could be caused by the sample bulk (unaffected by CPF treatment) influence on the measured microhardness value according to the classic rule that the indentation depth should be less 0.1 of the testing object thickness. In our case the chosen indentation depth is ~ one third of alloyed layer.

It is known that steel 3 preserves its mechanical properties at temperatures less than 473 K [86], which is consistent with the received results. Earlier it was shown that dispersion hardening and solid solution hardening were the main mechanisms of the microhardness increase in the surface layer after CPF treatment of Zr / steel 3 samples. According to the XRD analysis a significant decrease of ZrN phase in the surface layer as well as the α-Fe lattice parameter decrease were observed after annealing at the temperature greater than 673 K while the microhardness value changed in the range of the measurement error up to the temperature of 1073 K. The formation of disperse Zr-containing particles due to decomposition of the α-Fe supersaturated solid solution was a possible reason for microhardness value retaining. The increase of annealing temperature up to 1273 K can lead to coagulation of earlier formed dispersed particles, thus diminishing the effect of dispersion hardnening. At the same time one can see that the mixed layer of the Zr/ steel 3 system has a high hardness value up to the temperature of 1073 K that is greater even than the upper temperature of high-speed steels mechanical properties stability.

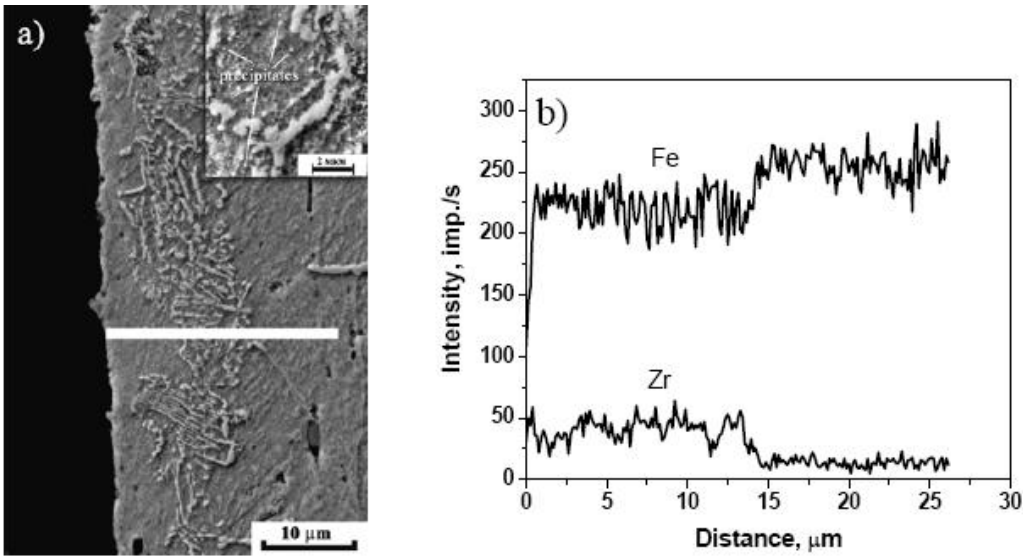


Figure 26. SEM image (a) and distribution of elements along the corresponding white line (b) of Zr/steel sample after CPF treatment and annealing at 1273 K.

Copyright © 2010. Nova Science Publishers, Incorporated. All rights reserved.

Handbook of Material Science Research, Nova Science Publishers, Incorporated, 2010. ProQuest Ebook Central,

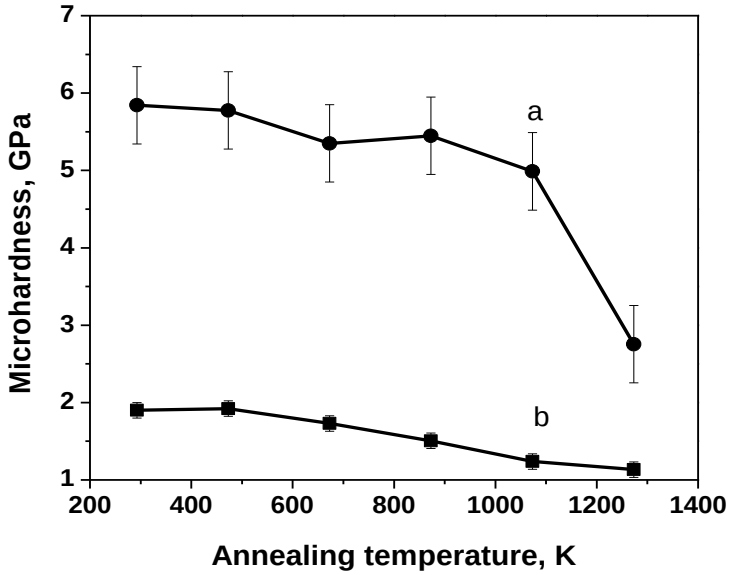


Figure 27. Microhardness dependence of steel 3 sample (a) and Zr/steel sample after CPF treatment (b) on annealing temperature.

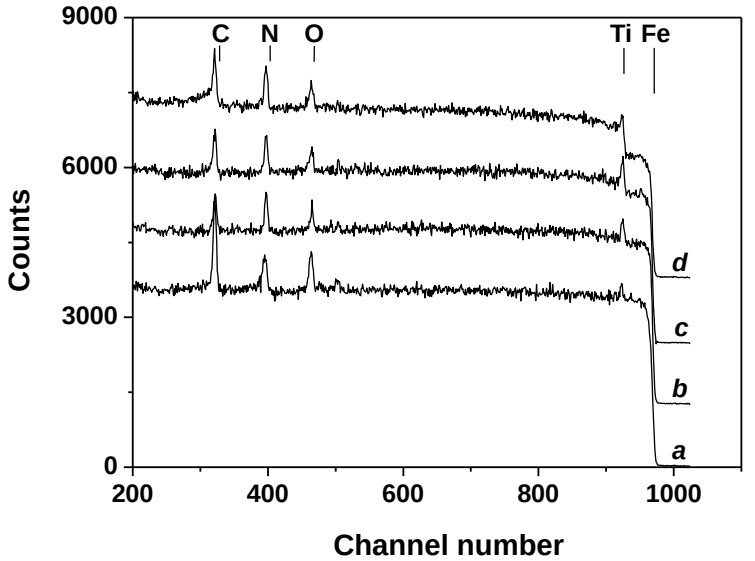


Figure 28. RBS spectra of the Ti/steel 3 system samples with the coating thickness of 0.5 μm (a), 1.2 μm (b), 2.5 μm (c), 5.0 μm (d) treated by CPF.

The previous experiments showed that the concentration of the alloying element did not exceed ~ 15 at.% (Figure 17). The growth of the number of pulses or the energy transferred to a sample per pulse led to the decrease of the alloying element concentration. Another way of an alloying element concentration change is a variation of the coating thickness. The increase of the coating thickness allows to rise the concentration of the alloying element, thus expanding the range of synthesized alloys. This tendency can be observed by analyzing data

Copyright © 2010. Nova Science Publishers, Incorporated. All rights reserved.

Handbook of Material Science Research, Nova Science Publishers, Incorporated, 2010. ProQuest Ebook Central,

on plasma flow treatment of "coating/substrate" systems with a different coating thickness [56]. The influence of CPF treatment on the phase and element composition of the "Ti coating / steel 3" system with the coating thickness of 0.5, 1.2, 2.5 and 5.0 μm was investigated to analyze a possibility of the alloying element growth in the mixed layer. CPF treatment was carried out by three pulses of compression plasma flows to provide homogeneity of the mixed layer. Q was ~13 J/cm^2 per pulse.

The element composition analysis showed that the growth of the coating thickness led to the increase of the Ti concentration in the bulk of the mixed layer (Figure 28). The corresponding concentration for the coating thickness of 0.5, 1.2, 2.5 and 5.0 μm amounted to 4.0±0.3 at. %, 8.0±0.6 at. %, 15.0±0.8 at. % and 30 ± 1 at. %, respectively. These data are in good agreement with the results of the energy-dispersive X-ray microanalysis (3±1 at. %, 11±2 at. %, 14±2 at. % and 31±3 at. %, respectively). Thus, one could find almost a linear dependence of the Ti concentration on the Ti coating thickness in the used range of experimental parameters. RBS spectra also contained carbon, nitrogen and oxygen peaks that appeared due to diffusion of vacuum chamber residual atmosphere elements into samples during treatment. At the same time the distribution type of nitrogen and oxygen in samples was not diffusion-like. The thickness of the surface layer containing nitrogen and oxygen was about 50- 70 nm. The nitrogen concentration in this layer was about 20-25 at. % and was almost constant for all treated samples. The distribution of titanium was not uniform in the surface layer. The Ti distribution had a surface segregation peak (just in the layer containing light impurities). The underlying layer (up to ~ 0.4 μm) lacked titanium. Possible reasons for such alloying element behaviour were discussed above.

The change of the alloying element concentration in the surface layer influences its phase composition (Figure 29). The XRD analysis showed a shift of α-Fe diffraction lines to smaller angles with the growth of the titanium concentration. A possible reason for this effect is formation of a supersaturated α-Fe(Ti) solid solution where Ti atoms substitute Fe atoms in the bcc lattice. Ti solubility in α-Fe does not exceed 2.9 at.% even at 773 K in equilibrium conditions [83]. In our case α-Fe(Ti) is the only phase that can be seen by XRD if the Ti concentration is not greater than 8 at.% except for TiO_2 phase (from the thin surface layer) that can be seen at low angles for all treated samples. A further increase of the Ti concentration up to 15 at.% led to formation of TiN with a (200) preferred orientation. The element composition analysis showed that the nitrogen concentration in the surface layer was almost constant as well as the thickness of the nitrogen containing layer for all samples. Thus, the appearance of TiN diffraction peaks was connected with the growth of the Ti concentration. The increase of the Ti concentration up to 30 at.% led to the growth of the TiN volume fraction and precipitation of Fe_2Ti phase.

The change of the phase composition and quenching effects result in the microhardness increase (Figure 30). The treated samples with the titanium concentration up to 8 at. % showed 1.6 times microhardness increase in comparison with an untreated steel sample. Microhardness of these samples does not depend on the indentation depth (the curves b,c in Figure 30). The supersaturated α-Fe(Ti) solid solution is the only phase that can be seen in diffraction patterns of these samples (except for very small intensity TiO_2 diffraction lines). Thus solid solution hardening seems to be the main hardening mechanism for samples with the Ti concentration up to 8 at.%. At the same time no difference in the microhardness value of samples containing 4 at.% and 8 at.% was found. It can be connected either with a smaller Ti atom radius in comparison with that of Zr which provides a larger microhardness increase

Copyright © 2010. Nova Science Publishers, Incorporated. All rights reserved.

Handbook of Material Science Research, Nova Science Publishers, Incorporated, 2010. ProQuest Ebook Central,

during formation of the supersaturated α-Fe solid solution (Figure 21) or with the action of other factors that were not revealed in the experiment.

The TiN phase formation causes the microhardness increase up to 5.5 GPa at a smaller indentation depth (the curves e,d in Figure 30) due to dispersion hardening in the thin surface layer. The increase of the Ti concentration up to ~30 at.% lead to formation of Fe_2Ti precipitates in the mixed layer, providing a further microhardness increase in the bulk (3.8 GPa at the depth of 4.5 μm for the curve e in Figure 30). Thus, as in the previous case solid solution hardening and dispersion hardening can be the main mechanisms of the mixed layer microhardness increase. At the same time the main hardening mechanism of this system depends on the concentration of an alloying element: solid solution hardening – up to 8 % of Ti, both solid solution hardening and dispersion hardening – at a higher Ti concentration.

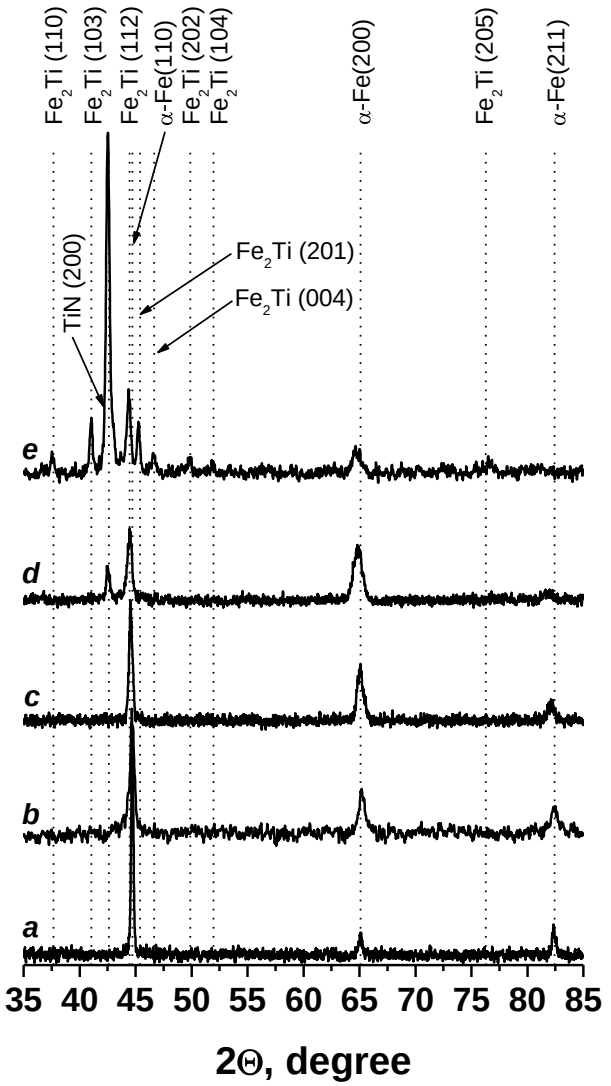


Figure 29. XRD patterns of the initial steel 3 sample (a) and samples of the Ti/steel 3 system with the coating thickness of 0.5 μm (b), 1.2 μm (c), 2.5 μm (d), 5.0 μm (e) treated by CPF.

Copyright © 2010. Nova Science Publishers, Incorporated. All rights reserved.

Handbook of Material Science Research, Nova Science Publishers, Incorporated, 2010. ProQuest Ebook Central,

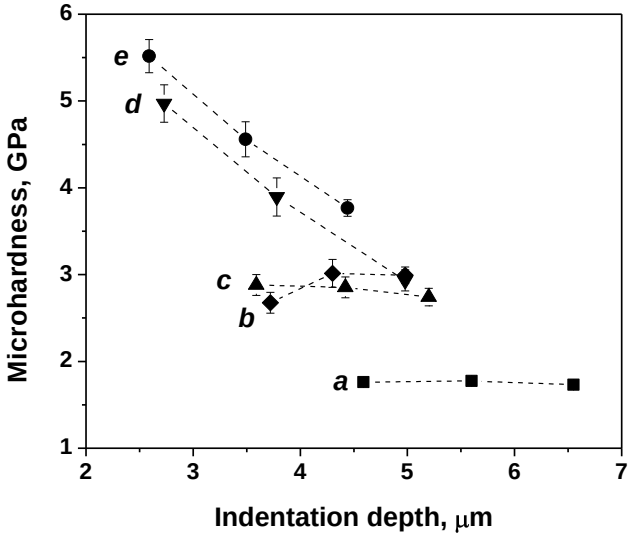


Figure 30. Microhardness dependence on the indentation depth of the initial steel 3 sample (a) and samples of the Ti/steel 3 system with the coating thickness of 0.5 μm (b), 1.2 μm (c), 2.5 μm (d), 5.0 μm (e) treated by CPF.

One can see that the variation of treatment parameters and the coating thickness in the "coating/substrate" system subjected to CPF treatment results in the formation of a range of alloys in a steel surface layer with the controlled element and phase composition as well as mechanical properties. Such an approach allows to modify mechanical, corrosion, magnetic and other properties of a steel surface layer by corresponding choice of alloying elements. The microhardness of the surface layer will be mainly determined by a type of alloying element and its concentration.

4.3. Alloying by Injection of an Additional Component into a Plasma Flow

Earlier it was found that the injection of a metal powder into a compression plasma flow led to deposition of a metal containing thin film on the silicon surface [87]. The film consisted of a spherical particles monolayer, up to 200 nm in size, bounded to each other. A combined technique consisting in simultaneous CPF treatment and thin film deposition using CPF can be also used for alloying of the surface layer with a component injected into the plasma flow. The mechanism of the alloying layer formation is the following [88]. The injection of the metal powder into the plasma flow results in its melting and evaporation. At the same time the interaction of CPF with the sample surface leads to the formation of the shock-compressed plasma layer near the treated surface throughout discharge duration. It consists of target material ablation products and elements of the plasma flow. Clusterization of cooling vapour in the near surface layer and clusters deposition on the crystallized surface take place after plasma shell disintegration [89, 90]. Thus, the formation of a thin film containing elements of the injected component and elements of the sample takes place on the sample surface. The next CPF pulse will result in mixing of the thin film with the surface sample layer and formation of a new film. This approach was used for alloying of steel 3 with tungsten by injecting a tungsten powder (~70 μm) into a nitrogen plasma flow [88].

Copyright © 2010. Nova Science Publishers, Incorporated. All rights reserved.

Handbook of Material Science Research, Nova Science Publishers, Incorporated, 2010. ProQuest Ebook Central,

The findings of this experiment showed that after one pulse of CPF treatment a thin film consisting of spherical particles with the size of 100 - 200 nm bound to each other was formed on the steel surface. The film contained 20-40 at.% of tungsten. After three pulses the steel surface layer was alloyed with ~10-20 % of tungsten and contained up to ~ 10 at.% of carbon. The increased value of the carbon concentration was explained by carbon redistribution to the surface from the bulk and carbon diffusion from residual gases. The phase composition analysis revealed formation of doped austenite and tungsten carbides Fe_3W_3C and WC. Fe_3W_3C is the main hardening carbide of a high-speed steel and WC is a material for a hard alloy. According to the data of the element composition analysis tungsten carbides were mainly located in the deposited film while austenite could be present in the whole analyzed layer. The increase of the pulse number led to the growth of WC and doped austenite due to deeper penetration of tungsten and nitrogen into the bulk of the material and due to the growth of the carbon concentration. Phase and structure transformations resulted in the microhardness increase up to 8 GPa after CPF treatment with Q=18 J/cm^2 and n=3. This value is close to the microhardness value of high-alloyed steels. A significant microhardness increase was explained by tungsten carbides formation in the alloyed layer [88].

5. CPF TREATMENT OF HIGH-ALLOYED STEELS

5.1. Direct Treatment

High-alloyed steels possess more complicated phase composition. R6M5 and R18 high-speed steels consist of α-Fe doped with alloying elements, M_6C, MC and $M_{23}C_6$ carbides (M: Fe, W, Cr, Mo, V). Cr_7C_3 and $Cr_{23}C_6$ are the main hardening carbides of H12M steel. Mechanical properties of these steels after treatment will mainly depend on the CPF influence on these phases. Steel samples were subjected to CPF treatment with Q=5-17 J/cm^2 and n=1-5. The nitrogen pressure for R6M5 and H12M steel samples was 400 Pa. R18 steel samples were treated in the pressure range of 400-4000 Pa. Treatment conditions for R18 steel samples at 400 Pa corresponds to Q=5 J/cm^2. The growth of nitrogen pressure should lead to diminishing of Q value though calorimetric measurements were not conducted for such a type of experiment.

The element composition analysis showed that nitrogen depth profiles exhibited a well-known system consisting of the near-surface compound layer containing nitrides and a deeper diffusion layer obtained after nitrogen treatment (Figure 31). For R18 steel nitrogen distributions had a similar character but strongly differed in the penetration depth. Besides, the surface nitrogen concentration in the sample treated at P=2.7 kPa and n=1 differed from the surface nitrogen concentration in other samples. This could be connected with the presence of a contaminating carbon layer on the surface and subsequent normalization of the atomic concentration to 100 %. The growth of the nitrogen pressure in the vacuum chamber (in the range of 0.4-2.7 kPa) resulted in the increase of the nitrogen content in the surface layer and in the increase of the nitrogen penetration depth. The growth of the pulse number at P=2.7 kPa also led to the increase of the nitrogen content in the surface layer. The maximum concentration of nitrogen (33 at.%) is observed in the sample treated at P=2.7 kPa and n=5. A further increase of P can result in the decrease of the nitrogen content because the excess of

Copyright © 2010. Nova Science Publishers, Incorporated. All rights reserved.

Handbook of Material Science Research, Nova Science Publishers, Incorporated, 2010. ProQuest Ebook Central,

nitrogen atoms in the vacuum chamber will be an obstacle for plasma flow spreading. The nonlinear dependence of the nitrogen concentration on the pressure of nitrogen was already observed during laser nitriding of an austenitic stainless steel [91]. Thus, one could expect the nonlinear dependence of mechanical properties on the nitrogen pressure. RBS investigations showed that the maximum nitrogen penetration depth was about 350-400 nm in case of treatment with P=2.7 kPa and n=5 [59]. Alloying elements significantly diminished nitrogen penetration depth in comparison with that in Armco-iron and carbon steels (Figure 2 and 7). The phase and element composition of R6M5 and R18 is quite similar except for the Mo and W content. A greater tungsten content in R18 steel can slightly decrease the nitrogen diffusion depth but the order of the penetration depth will be just the same. That is why one can expect similar nitrogen distribution and nitrogen penetration depth in R6M5 steel.

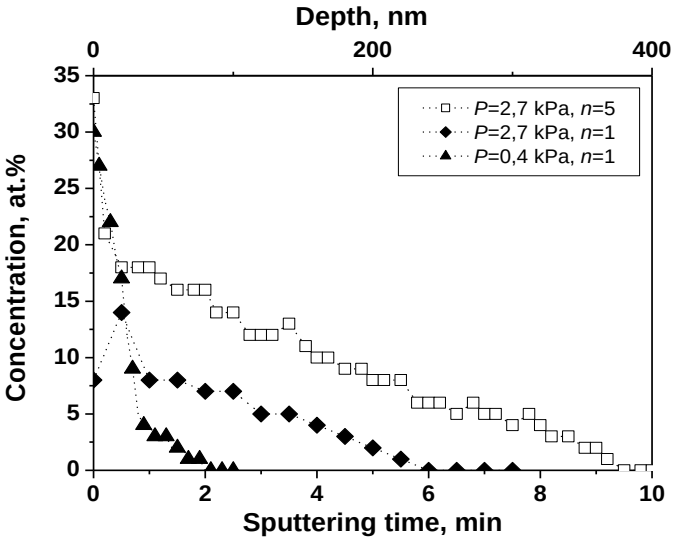


Figure 31. Nitrogen AES depth profiles in R18 steel treated by CPF at different regimes. [59].

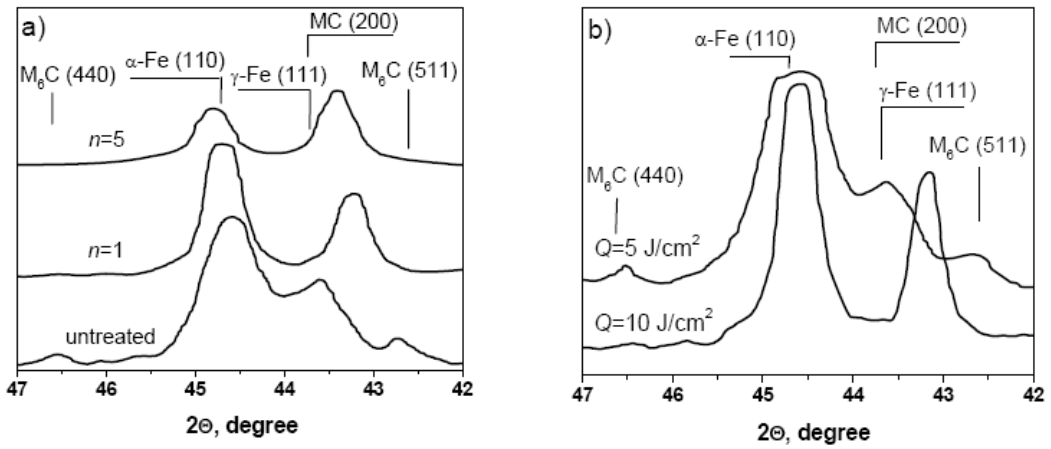


Figure 32. XRD patterns of R6M5 steel before and after CPF treatment at 13 J/cm^2 with a different number of pulses (a) and after one pulse of CPF treatment at different Q (b) [59].

Copyright © 2010. Nova Science Publishers, Incorporated. All rights reserved.

Handbook of Material Science Research, Nova Science Publishers, Incorporated, 2010. ProQuest Ebook Central,

The results of the phase composition analysis before and after treatment are presented in Figure 32-34. One can see that the diffraction pattern of R6M5 steel in the initial state (Figure 32a) contains diffraction lines of α-Fe, M_6C and MC – the main carbides in high-speed steels. Treatment even by one pulse of CPF at Q=13 J/cm^2 resulted in dissolution of M_6C and MC carbides in the analyzed layer (Figure 32a). The temperature of M_6C dissolution is 1573 K. The temperature evaluation in the surface layer during treatment showed much higher values [59]. Full or partial dissolution of hardening carbides can be seen for H12M and R18 steels after treatment (Figure 33, 34). CPF treatment also led to austenite formation. One can see the presence of residual austenite diffraction lines after treatment by one pulse (Figure 32a). At room temperature the existence of γ-Fe phase can be stabilized by nitrogen incorporated into the f.c.c. lattice. A similar effect can be obtained by incorporating Cr, which is present in steel, into the f.c.c. lattice. Dissolution of Cr-containing carbides during treatment of H12M steel led to a full transformation of the b.c.c iron lattice into the f.c.c lattice (Figure 33). In contrast to H12M steel the (111) γ-Fe diffraction line of R6M5 steel is shifted into the area of smaller 2θ angles as in case of expanded nitrogenous austenite formation [92]. Expanded austenite is usually observed after nitriding austenite stainless steels with a high Cr concentration [92, 93]. A significant shift of the (200) γ-Fe diffraction line is also typical of expanded austenite [92] because nitrogen should mainly be located in octahedral pores of the f.c.c. lattice [94]. In our case the position of the (200) γ-Fe diffraction line is in good agreement with standard data. The shift of the (111) γ-Fe line and lattice distortion can be mainly connected with incorporation of W, Mo and V atoms from dissolved carbides into the iron f.c.c. lattice. From Figure 33 one can see that Cr incorporation into γ-Fe lattice does not cause strong lattice distortion due to Cr and Fe atoms isomorphism. Thus, according to the obtained diffraction patterns the formation of the γ-Fe phase doped with alloying elements can be assumed. The increase of *n* led to the growth of the austenite diffraction line intensity, i.e. the growth of the austenite content in the analyzed layer.

Copyright © 2010. Nova Science Publishers, Incorporated. All rights reserved.

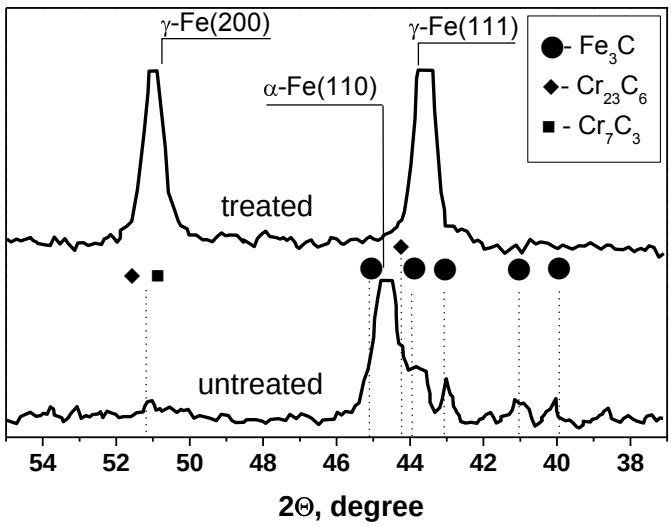


Figure 33. XRD patterns of H12M steel before and after 1 pulse of CPF treatment at *Q*=17 J/cm^2.

Handbook of Material Science Research, Nova Science Publishers, Incorporated, 2010. ProQuest Ebook Central,

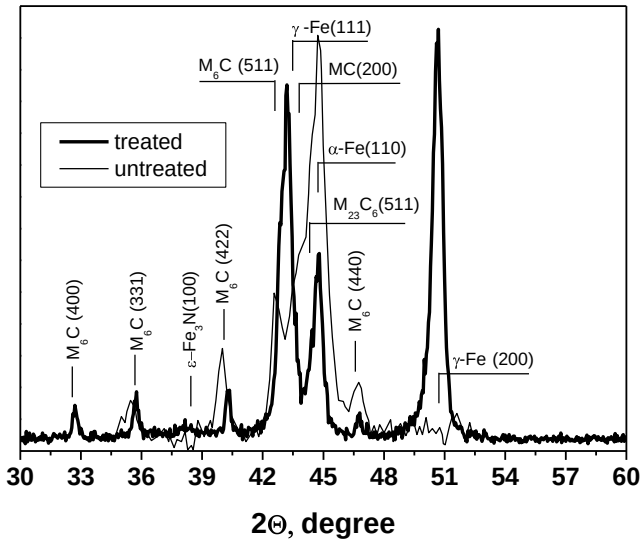


Figure 34. XRD patterns of R18 steel before and after 5 pulses of CPF treatment at P=2.7 kPa [59].

The main reason for the observed effects is the energy absorbed by the surface layer during the CPF impact. Treatment at Q=5 J/cm^2 did not almost change the phase composition of R6M5 steel (Figure 32b). While treatment at Q=10 J/cm^2 resulted again in austenite formation, MC and M_6C carbides dissolution.

A weak line of ε-$Fe_{2+x}N$ or ε-Fe_{2+x}(N, C) was found in the diffraction pattern of the R18 steel sample containing the maximum quantity of nitrogen (Figure 34). The nitrogen concentration in a thin compound layer (Figure 31) lies in the limits of the nitride stoichiometry change. Therefore, in spite of a relatively high concentration of nitrogen in the surface layer only a small part of nitrogen atoms can take part in nitride formation. The concentration of nitrogen in austenite can be as much as 12 at. % [91]. That is why nitride formation can be expected in the thin surface compound layer and in the diffusion zone in which the nitrogen concentration exceeds this value. At the same time the presence of alloying elements in the f.c.c. lattice can change the limit of the nitrogen content in austenite. The total depth of the layer that can contain nitride precipitates is ~ 100 nm (Figure 31). Nitrogen atoms are more likely to be incorporated into austenite in a deeper layer or can form nitrides with different elements.

The investigation of R6M5 steel cross-section morphology showed that the thickness of the modified layer increased with the growth of n and Q [59]. In case of CPF treatment at 5 J/cm^2 the thickness of the modified layer is approximately 9 μm (Figure 35a). This layer contains M_6C carbides of a smaller size than those in the bulk of the layer. The increase of Q resulted in the growth of the modified layer thickness up to 12 μm (Figure 35b). This layer can be divided into two main sublayers. The first sublayer with the thickness ~ 6 μm contains small inclusions of MC carbide (Figure 35c). This sublayer includes the surface layer with the thickness of ~ 1 μm (X-rays analyzing depth) containing no carbides at all. MC carbide is considered insoluble in high-speed steels, while in steels containing only vanadium it dissolves at the temperature of 1373 K. These data are also in agreement with those of the

Copyright © 2010. Nova Science Publishers, Incorporated. All rights reserved.

Handbook of Material Science Research, Nova Science Publishers, Incorporated, 2010. ProQuest Ebook Central,

phase analysis (Figure 32). The size of MC carbide increases with the depth. No M_6C carbides were found in this sublayer. Small M_6C carbides appeared only in the second sublayer with the thickness of ~ 6 μm.

The observed changes in the phase composition of a high-alloyed steel strongly influence its microhardness (Figure 36-38). The growth of energy absorbed by the surface layer due to Q or n led to the microhardness decrease because of hardening carbides dissolution. Only the R6M5 steel sample treated with the lowest energy used Q=5 J/cm^2 possesses the same value of microhardness (in the limits of the error) in comparison with the initial one (Figure 36b). The formation of alloyed austenite after CPF treatment can also influence the microhardness value. At the same time partial or full carbides dissolution in the surface layer seems to be the most probable cause of the microhardness drop.

The change of the nitrogen pressure in the vacuum chamber during treatment due to Q change also strongly affects hardness of R18 steel samples [59]. The maximum hardness decrease is observed in the sample treated at P=2.7 kPa and n=5 (Figure 38). Formation of ε-$Fe_{2+x}N$ nitride (Figure 34) does not compensate the influence of M_6C and MC carbides partial dissolution on the microhardness value. The microhardness dependence on the nitrogen pressure has a nonlinear character [59]. The increase of P up to 4 kPa weakens the effect of a compression plasma flow on samples and prevents a microhardness significant decrease [59].

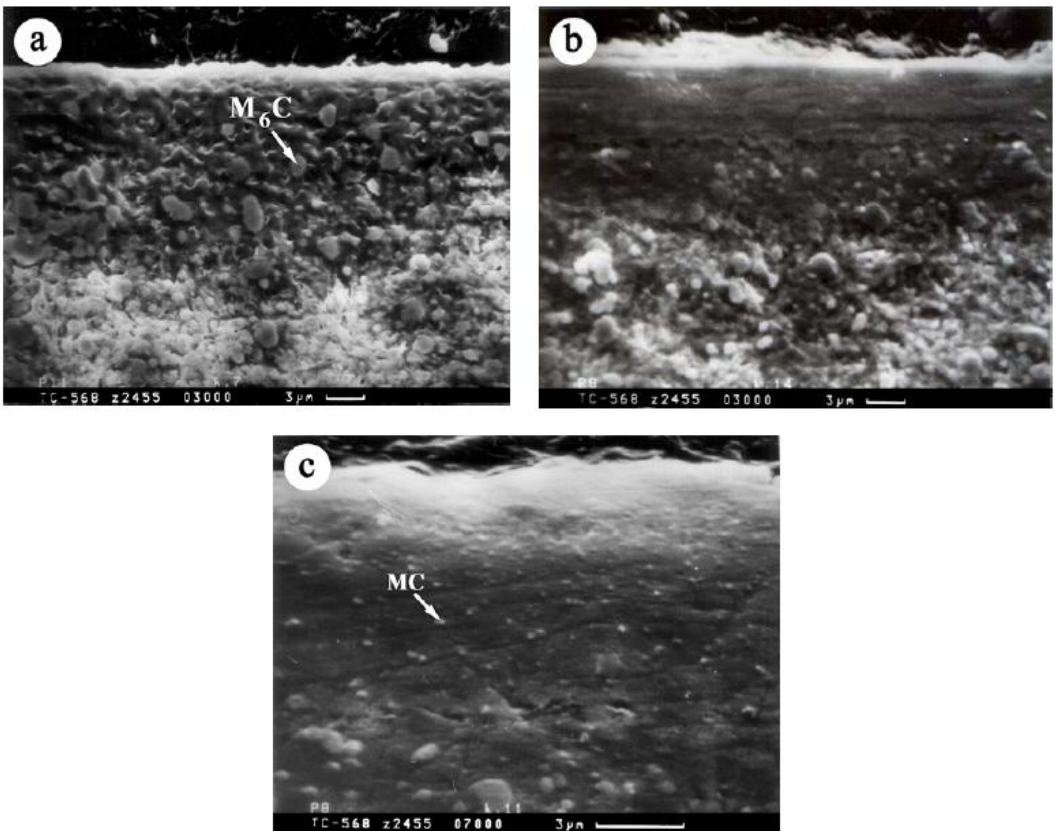


Figure 35. SEM images of the R6M5 steel cross-section after one pulse of CPF treatment at Q=5 J/cm^2 (a) and at Q=10 J/cm^2 (b, c) [59].

Copyright © 2010. Nova Science Publishers, Incorporated. All rights reserved.

Handbook of Material Science Research, Nova Science Publishers, Incorporated, 2010. ProQuest Ebook Central,

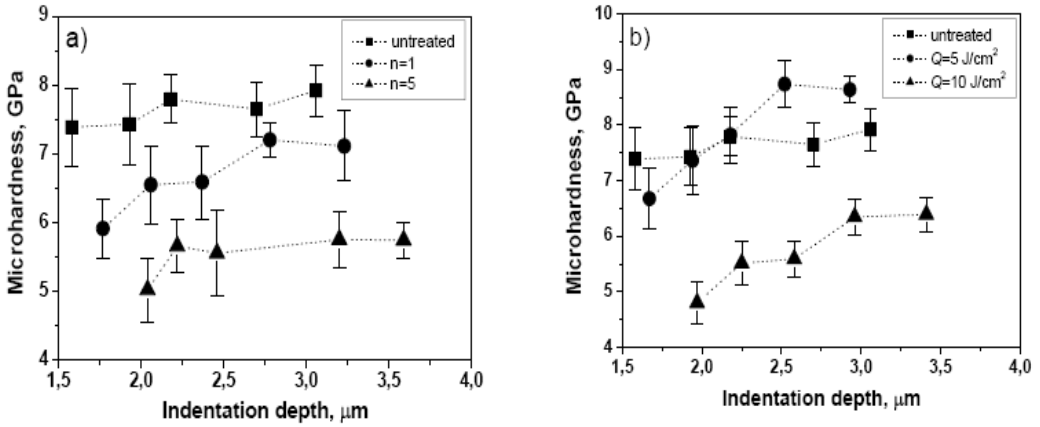


Figure 36. Microhardness dependence on the indentation depth of R6M5 steel samples before and after CPF treatment at 13 J/cm^2 with a different number of pulses (a) and after one pulse of CPF treatment at different Q (b) [59].

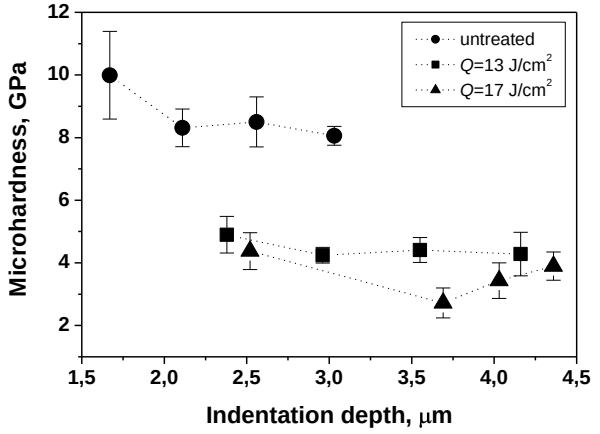


Figure 37. Microhardness dependence on the indentation depth of H12M steel samples before and after one pulse of CPF treatment at different Q.

CPF treatment mainly leads to the decrease of high-speed steels microhardness. At the same time CPF treatment as a high temperature quenching process could be a substitute for conventional quenching of high-speed steels. The usual tasks of conventional quenching are dissolution of secondary carbides and formation of high-alloyed austenite.

Subsequent annealing resulted in austenite→martensite transformation and precipitation of disperse carbide particles determining high hardness of this type of steels. One can see that one hour annealing in air at 873 K of the R18 steel sample previously treated with five pulses of CPF at P=2.7 kPa resulted in the microhardness increase up to 12.4±0.6 GPa, which 1.5 times greater than the microhardness value of a steel sample subjected to conventional heat treatment (Figure 38). During CPF treatment the temperature of the surface layer is two times higher at least than during conventional quenching, that is why the residual austenite content and carbide dissolution rate should be greater. Thus, after annealing one can expect an increase of the number of dispersed carbides with a smaller size resulting in the microhardness increase.

Copyright © 2010. Nova Science Publishers, Incorporated. All rights reserved.

Handbook of Material Science Research, Nova Science Publishers, Incorporated, 2010. ProQuest Ebook Central,

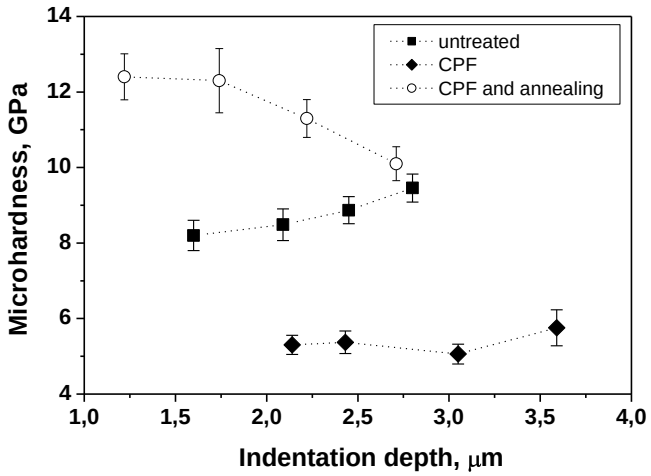


Figure 38. Microhardness dependence on the indentation depth of untreated R18 steel sample and samples after CPF treatment (P=2.7 kPa, n=1) and subsequent annealing.

Nitrogen CPF treatment resulted in a substantial modification of the initial structure of high-speed steels. High temperature quenching is the main effect appeared during the interaction of a compression plasma flow with a high-alloyed steel surface. This effect resulted in partial dissolution of hardening carbides and formation of alloyed austenite. Carbides dissolution leads to the microhardness decrease though the presence of austenite improves the friction coefficient behaviour [59].

5.2. Alloying by Mixing of a "Coating/Substrate" System

The microhardness drop after CPF treatment of a high-alloyed steel can be compensated by incorporating an additional component providing high hardness of the surface layer. This approach was used for the modification of R6M5 high-speed steel tribological properties [95]. Zr coating deposition of 1.87 μm thickness with subsequent CPF treatment at Q=13 J/cm^2 and n=1-5 was carried out [95]. The nitrogen pressure was 400 Pa. Annealing in air at the temperature of 873 K for 1 hour was carried out to examine thermal stability of the modified layer. This temperature limits the operation ability of R6M5 steel tools [96].

The RBS analysis showed the same regularities of the alloying element distribution as in case of the CPF treated Zr/steel 3 system described earlier [95]. The increase of energy absorbed by the surface layer per pulse as well as the number of pulses led to more uniform redistribution of components inside the modified layer and to a decrease of the zirconium concentration [95]. Zirconium had a surface peak with the concentration of 20-25 at. % which could be connected with ZrN formation in the thin surface layer [95].

The results of the phase composition analysis are presented in Figure 39. One can see that CPF treatment of Zr/R6M5 samples results in ZrN formation. ZrN phase remains in the surface layer after annealing. In the XRD pattern of the Zr/M2 sample treated by one pulse of CPF one can see a diffraction line of zirconium and a diffraction line of Fe_2Zr (2Θ=40.6^o). Both of these diffraction lines disappeared at n=5. In comparison with the Zr/steel 3 system

Copyright © 2010. Nova Science Publishers, Incorporated. All rights reserved.

Handbook of Material Science Research, Nova Science Publishers, Incorporated, 2010. ProQuest Ebook Central,

(Figure 19) a higher content of Zr and Fe_2Zr is connected with saturation of α-Fe and γ-Fe solid solutions with W, Mo and V atoms from dissolved carbides. Thus, the concentration of Zr that can take part in formation of these solid solutions diminishes and the rest of Zr atoms that do not form ZrN will form Fe_2Zr or Zr phase. The presence of Zr after one pulse of treatment can also be connected with nonuniform mixing.

Changes in the structure of the surface layer after CPF treatment cause changes in microhardness (load 100 g) behaviour (Figure 40). CPF treatment by one pulse slightly increases microhardness (1.2 times) due to ZrN formation. A further increase of the pulse number results in the microhardness decrease. The Zr concentration decrease and dissolution or partial dissolution of hardening carbides MC and M_6C are the main reasons for this effect. The microhardness decrease is not compensated by formation of hard ZrN nitrides at this treatment regime. Annealing does not influence microhardness of a CPF treated sample while an untreated R6M5 sample shows the microhardness drop. The latter effect is usually observed in a high-speed steel at the temperature of ~ 873 K and higher due to the decay of martensite and coagulation of disperse carbide particles [96].

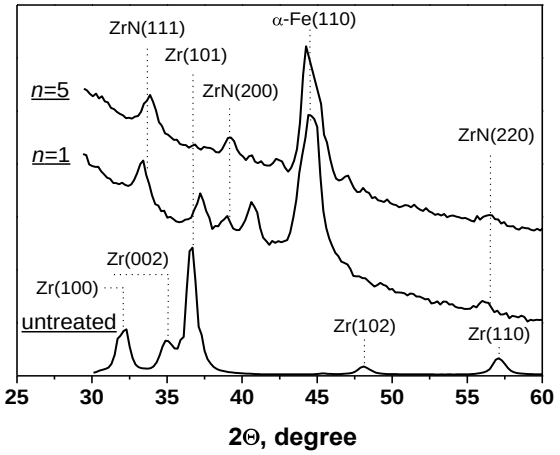


Figure 39. XRD patterns of Zr/R6M5 steel samples before and after CPF treatment at Q=13 J/cm^2) [95].

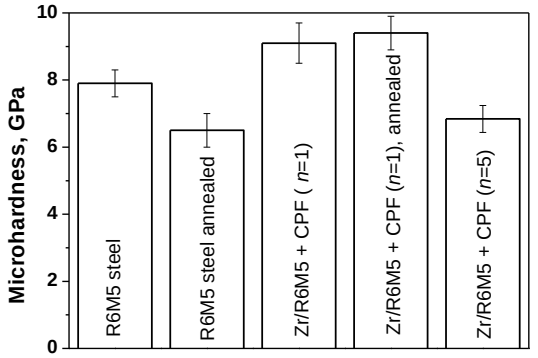


Figure 40. Microhardness of R6M5 steel and Zr/R6M5 steel samples after CPF treatment at Q=13 J/cm^2 and annealing [95].

Copyright © 2010. Nova Science Publishers, Incorporated. All rights reserved.

Handbook of Material Science Research, Nova Science Publishers, Incorporated, 2010. ProQuest Ebook Central,

CPF treatment in nitrogen atmosphere of Zr/R6M5 steel results in formation of ZrN nitrides in the surface layer. Nucleation of hard stable nitrides allows us to avoid the microhardness decrease due to dissolution of hardening carbides and to expand the operation temperature range of tools made of R6M5 steel.

6. CONCLUSION

Compression plasma flows treatment is a promising technology of materials' properties modification. Its main advantages are a short treatment time, a possibility of surface layer formation with pre-determined element and phase composition. CPF can be effectively used for formation of metastable phases and alloys containing immiscible elements. A small treatment area and nonuniformity of the plasma flow along the treated surface are the main drawbacks of CPF generated by MPC. These drawbacks can be overcome by the use of wider plasma flows generated by quasi-stationary high-current plasma accelerators [97] and by the increase of the number of pulses.

Microhardness of the surface layer of steels treated by CPF is mainly dependent on a type of steel, preliminary heat treatment, CPF treatment parameters and a used CPF treatment technique. Formation of nitrogen containing phases leads to hardening of iron with a small carbon concentration. Microhardness of carbon steels after direct CPF treatment depends on the initial phase constituents as well as on nitrogen containing phases. Changes in the initial phase composition and their concentration in high-alloyed steels mainly determine microhardness behaviour after direct CPF treatment. Thus, elements and phases that determine microhardness of steel are also in charge of the microhardness change after CPF processing.

Direct CPF treatment is a very effective processing technique for the modification of low-alloyed carbon steels. For example, microhardness of the surface layer of the preliminary quenched U8A steel can be as high as 18 GPa after treatment. This value is even higher than the microhardness value of high-speed steels. Alloying of the surface layer by CPF with any element (or elements) that can be preliminarily deposited allows the formation of a surface layer with a thickness of up to ~ 15 μm possessing high thermal stability and with properties usually unattainable for low-alloyed steels. In this case a type of alloying element and its concentration determine a hardening mechanism of the surface layer. The alloying element concentration can be changed either by the CPF treatment parameters change or by the change of the preliminarily deposited coating thickness. In general the choice of elements to be alloyed allows us to modify a wide range of surface layer properties: mechanical, tribological, magnetic, corrosion, etc.

Direct CPF treatment results in the microhardness decrease of high-alloyed steels due to dissolution of hardening carbides. At the same time a modified layer possesses a low friction coefficient ~ 0.2 even in conditions of dry friction [59]. Thus, direct CPF treatment can be used for the modification of tools made of high-alloyed steels depending on a tool application. For example, CPF treated rams made of R6M5 steel were tested at the Belarusian automobile works. Industry tests showed a twofold increase of the tool lifetime. A similar result—7 times increase of the lifetime of a cutting tool made of hard alloy—was found after CPF treatment of the tool. The microhardness drop of a high-alloyed steel after treatment can

Copyright © 2010. Nova Science Publishers, Incorporated. All rights reserved.

Handbook of Material Science Research, Nova Science Publishers, Incorporated, 2010. ProQuest Ebook Central,

be overcome by subsequent annealing. Thus, CPF treatment can be used as a high temperature quenching process for high-speed steels. A combined influence of CPF and subsequent annealing at 873 K for 1 hour allows us to increase the microhardness of the R18 steel surface layer up to 12.5 GPa. Another way for formation of hardened, wear-resistant, low-friction and thermally stable layers in tools made of high-speed steel is alloying by CPF mixing of a "coating/substrate" system [95].

The review of the data obtained on steel treatment at different types of coaxial plasma generators [52-54, 56] and the findings on CPF treatment show that the microhardness increase of high-alloyed steels can be obtained by direct treatment at the discharge time not greater than ~ 10^0-10^1 μs (considering the same energy absorbed by the surface layer and one or a few plasma pulses). A smaller discharge time leads to smaller dissolution of carbides during the impact of a plasma pulse due to a smaller diffusion time while the increase of the discharge time enhances an effect of the mixing process due to the growth of the liquid phase convection time. CPF with a comparatively high discharge period and a greater thickness of the melted layer will be more effective in the surface layer alloying by "coating/substrate" system mixing than HPIB and low energy HCEB with the conventional range of 10^{-9}-10^{-6} μs pulse time.

Thus compression plasma flows can be effectively used for hardening of steels and forming surface layers possessing enhanced operation abilities.

ACKNOWLEDGMENTS

The authors are grateful to Dr. Sc. V.M. Astashynski and Dr. A.M. Kuzmitski for assistance in samples treatment by compression plasma flows. The assistance of Dr. V.V. Astashynski, Dr. A.K. Stalmashonak, Yu.V. Sveshnikov, and A.V. Punko in investigations carried out is greatly acknowledged.

REFERENCES

[1] Campos, S.S.; Morales, E.V.; Kestenbach, H.-J. *Mater. Char.* 2004, *52*, 379– 384.
[2] Jiménez, J. M.; Bravo, E.; Criado, A. J.; Arévalo, R.; Dietz, C.; Martínez, J. A.; Criado, A. J. *Mater. Char*. 2004, *52*, 145– 151.
[3] Yugai, S. S.; Kleiner, L. M.; Shatsov, A.A. *Met. Sci. Heat Treat.* 2006, *48*(*3-4*), 122-126.
[4] Li, M.; Knystautas, E. J.; Krishnadev, M. *Surf. Coat. Technol*. 2001, *138*, 220-228.
[5] Wilbur, P.J.; Davis, J.A.; Wei, R.; Vajo, J.J.; Williamson, D.L. *Surf. Coat. Technol.* 1996, *83*, 250-256.
[6] Panzer, S.; Müller. M. *Härterei-Technische Mitteilungen*. 1988, *43*(*2*), 103-111.
[7] Kim, S.K.; Yoo, J.S.; Priest, J.M.; Fewell. M.P. *Surf. Coat. Technol.* 2003, *163-164*, 380-385.
[8] Cheng, Z.; Li, C.X.; Dong, H.; Bell, T. *Surf. Coat. Technol*. 2005, *191*, 195-200.
[9] Bell, T.; Li, C. X. *Int. Heat Treat. Surf. Eng.* 2007, *1*(*1*), 34-38.

Copyright © 2010. Nova Science Publishers, Incorporated. All rights reserved.

Handbook of Material Science Research, Nova Science Publishers, Incorporated, 2010. ProQuest Ebook Central,

[10] Mändl, S.; Richter, E.; Günzel, R.; Möller, W. *Nucl. Instrum. Methods Phys. Res.* 1999, *B148*, 846-850.
[11] Collins, G.A.; Hutchings, R.; Short, K.T.; Tendys, J. *Surf. Coat. Technol.* 1998, *103-104*, 212-217.
[12] Mukherjee, S.; Charaborty, J.; Gupta, S.; Paole, P.M.; John, P.I.; Rao, K.R.M.; Manna, I. *Surf. Coat. Technol*. 2002, *156*, 103-109.
[13] Schaaf, P.; Illgner, C.; Landry, F.; Lieb, K.-P.; *Surf. Coat. Technol*. 1998, *100-101*, 404-407.
[14] Majumdar, J. D.; Manna, I. *Sādhanā*. 2003, *28* (*3-4*), 495–562.
[15] Boiko, V. I.; Valyaev, A. N.; Pogrebnyak, A. D. *Physics-Uspekhi*. 1999, *42*(*11*), 1139-1166.
[16] Pogrebnyak, D.; Proskurovskii, D. I. *Phys. Stat. Sol*. 1994, *a145*, 9-49.
[17] Werner, Z.; Piekoszewski, J.; Szymczyk, W. *Vacuum*. 2001, *63*, 701-708.
[18] Iost, R.; Bigot. J. *Mater. Sci.* 1996, *31*, 3573-3577.
[19] Chicot, D.; Roudet, F.; Soom A.; Lesage, J. *Surf. Eng.* 2007, *23* (*1*), 32-39.
[20] Gao, Y. X.; Fana, H. *J. Mater. Sci.* 2002, *37*, 4493 – 4498.
[21] Chicot, D.; Lesage, J. *Thin Solid Films*. 1995, *254*, 123-130.
[22] Pimenov, V.N.; Dyomina, E.V.; Ivanov, L.I.; Maslyaev, S.A.; Gribkov V.A. *J. Nucl. Mater.* 2002, *307–311*, 95–99.
[23] Weiss, W.-J. *Phys. Stat. Sol*. 1987, *a99*, 491-501.
[24] Remnev, G.E.; Isakov, I.F.; Opekounov, M.S.; Matvienko, V.M.; Ryzhkov V.A. *Surf. Coat. Technol.* 1999, *114*, 206–212.
[25] Rej, D.J.; Davis, H.A.; Olson, J.C.; Remnev, G.E.; Zakoutaev, A.N. *J. Vac. Sci. Technol.* 1997, *A15*(*3*), 1089-1097.
[26] Wang, X.; Lei, M.K.; Zhang, J.S. *Surf. Coat. Technol.* 2007, *201*, 5884–5890.
[27] Isakov, I.F.; Ligachev, A.E.; Pogrebnjak A.D.; Remnev, G.E. *Nucl. Instrum. Methods Phys. Res*. 1987, *B 28*, 37-40.
[28] Pogrebnjak, A.D.; Shablya, V.T.; Sviridenko, N.V.; Valyaev, A.N.; Plotnikov, S.V.; Kylyshkanov, M.K. *Surf. Coat. Technol*. 1996, *111*, 46–50.
[29] Pogrebnjak, A.D.; Remnev, G.E.; Romanov, I.G. *Nucl. Instrum. Methods Phys. Res.* 1989, *B43*, 41-45.
[30] Valyaev, A.N.; Kylyshkanov, M.K.; Pogrebnjak, A.D.; Valyaev, A.A.; Plotnikov, S.V. *Vacuum*. 2000, *58*, 53-59.
[31] Pogrebnjak, A.D.; Ladysev, V.S.; Pogrebnjak, N.A.; Michaliov, A.D.; Shablya, V.T. *Vacuum.* 2000, *58*, 45-52.
[32] Yatsui, K.; Tokuchi, A.; Tanaka, H.; Ishizuka, H.; Kawai, A.; Sai, E.; Masugata, K.; Ito, M.; Matsui. M. *Laser Part. Beams*, 1985, *3*, 119-127.
[33] Rej, D.J.; Davis, H.A.; Nastasi, M.; Olson, J.C.; Peterson, E.J. *Nucl. Instrum. Methods Phys. Res.* 1997, *B 127/128*, 987-991.
[34] Renk, T.J.; Buchheit, R.G.; Sorensen, N.R.; Cowell Senft, D.; Thompson, M.O.; Grabowski, K. S. *Phys. Plasmas*. 1998, *5*(*5*), 2144-2150.
[35] Sharkeev, Y.P.; Gritsenko, B.P.; Fortuna, S.V.; Perry, A.J. *Vacuum*. 1999, *52*, 247-254.
[36] Hao, S.Z.; Qin, Y.; Mei, X.X.; Gao, B.; Zuo, J.X.; Guan, Q.F.; Dong, C.; Zhang, Q.Y. *Surf. Coat. Technol.* 2007, *201*, 8588–8595.
[37] Proskurovsky, D.I.; Rotshtein, V.P.; Ozur, G.E.; Ivanov, Yu.F.; Markov. A.B. *Surf. Coat. Technol.* 2000, *125*, 49–56.

Copyright © 2010. Nova Science Publishers, Incorporated. All rights reserved.

Handbook of Material Science Research, Nova Science Publishers, Incorporated, 2010. ProQuest Ebook Central,

[38] Proskurovsky, D.I.; Rotshtein, V.P.; Ozur, G.E. *Surf. Coat. Technol.* 1997, *96*, 117-122.
[39] Perry, A. J.; Matossian. J. N. *Metall. Mater. Trans.* 1998, *29A*, 593-610.
[40] Ivanov, Yu.; Matz, W.; Rotshtein V.; Gunzel, R.; Shevchenko, N. *Surf. Coat. Technol.* 2002, *150*, 188–198.
[41] Hao, S.; Gao, B.; Wu, A.; Zou, J.; Qin Y. *Nucl. Instrum. Methods Phys. Res.* 2005, *B240*, 646–652
[42] Dong, C.; Wu, A.; Hao, S.; Zou, J.; Liu, Z. *Surf. Coat. Technol.* 2003, *163-164*, 620–624.
[43] Song, R.G.; Zhang, K.; Chen, G.N. *Vacuum*. 2003, *69*, 513–516.
[44] Song, R.G.; Zhang, K.; Chen, G.N. *Surf. Coat. Technol.* 2002, *157*, 1-4.
[45] Markov, A.B.; Rotshtein, V.P. *Nucl. Instrum. Methods Phys. Res.* 1997, *B132*, 79-86.
[46] Koppitz, T.; Jung, P.; Müller, G.; Weisenburger, A.; Futakawa, M.; Ikeda, Y. *J. Nucl. Mater.* 2005, *343*, 92-100.
[47] Markov, A. B. *Russ. Phys. J.* 1999, *42*(*3*), 293-298.
[48] Sartowska, B.; Piekoszewski, J.; Waliś, L.; Szymczyk, W.; Stanis, J. *Vacuum.* 2005, *78*, 181-186.
[49] Piekoszewski, J.; Werner, Z.; Langner, J.; Waliś, L. *Surf. Coat. Technol.* 1998, *106*, 228-233.
[50] Sartowska, B.; Piekoszewski, J.; Waliś, L.; Senatorski, J.; Stanisławski, J. *Surf. Coat. Technol*. 2007, *201*, 8295–8298.
[51] Tereshin, V.I. *Plasma Phys. Control. Fusion*. 1995, *37*, A177-A190.
[52] Garkusha, I.E.; Byrka, O.V.; Chebotarev, V.V.; Derepovski, N.T.; Müller, G. *Vacuum*. 2000, *58*, 195-201.
[53] Tereshin, V.I.; Bandura, A.N.; Bovda, A.M.; Brown, I.G.; Byrka, O.V. *Rev. Sci. Instrum*. 2002, *73*(*2*), 831-833.
[54] Kalin, B.A.; Yakushin, V.L.; Pol'skii, B.I. *Russ. Phys. J.* 1994, *37*(*5*), 491-505.
[55] Lepone, A.; Kelly, H.; Lamas, D.; Márquez, A. *Appl. Surf. Sci.* 1999, *143*, 124-134.
[56] Kalin, B.A.; Yakushin, V.L.; Vasiliev, V.I.; Tserevitinov, S.S. *Surf. Coat. Technol.* 1997, *96*, 110-116.
[57] Rancourt, D.G.; Ping, J.Y. *Nucl. Instrum. Methods Phys. Res.* 1991, *B58*, 85–97.
[58] Mayer, M. *Nucl. Instrum. Methods Phys. Res.* 2002, *B 194*, 177–186.
[59] Cherenda, N.N.; Uglov, V.V.; Anishchik, V.M.; Stalmashonak, A.K.; Astashinski, V.M. *Surf. Coat. Technol.* 2006, *200*, 5334 – 5342.
[60] Pavlov, P.V.; Hohlov, A.F. *Solid state Physics*; Vishaya shkola: Moscow, 2000; p. 494. (in Russian).
[61] Fromm, E.; Gebhardt, E. *Gases and carbon in metals*; Metallurgiya: Moscow, 1980; p. 712. (in Russian).
[62] Uglov, V.V.; Anishchik, V.M.; Astashynski, V.V.; Sveshnikov, Yu.V.; Rumianceva, I.N. *Surf. Coat. Technol.* 2004, *180-181*, 633–636.
[63] Uglov, V.V.; Anishchik, V.M.; Astashynski V.V.; Rumianceva, I.N. *High Temp. Mater. Process*. 2004, *8*(*2*), 233-244.
[64] Kopcewicz, M.; Jagielski, J.; Turos, A.; Williamson, D.L. *J. Appl. Phys.* 1992, *71*, 4217-4226.
[65] Jiraskova, Y. J.; Havlíček, S.; Schneeweiss, O.; Peřina, V.; Blawert, C. *Magn. Magn. Mater.* 2001. *234*, 477-488.
[66] Kontorovich, I.E. *Journal of technical physics*. 1950, *20*(*1*), 53-65. (in Russian).

Copyright © 2010. Nova Science Publishers, Incorporated. All rights reserved.

Handbook of Material Science Research, Nova Science Publishers, Incorporated, 2010. ProQuest Ebook Central,

[67] Nolan, D.; Leskovsek, V.; Jenko, M. *Surf. Coat. Technol.* 2006, *201*, 182–188.
[68] Miola, E.J.; de Souza, S.D.; Olzon-Dionysio, M.; Spinelli, D.; Soares, M.R.F. *J. Magn. Magn. Mater*. 1998, *A256*, 60-68.
[69] Schaaf, P.; Landry, F.; Han, M.; Carpene, E.; Lieb, K.-P. Hyperfine Interactions. 2002, *139/140*, 307–314.
[70] Mayer, J.W.; Tsaur, B.Y.; Lau, S.S.; Hung, L-S. Nucl. Instrum. Methods. 1981, *182/183*, 1-13.
[71] Miotello, A.; Kelly, R. *Nucl. Instrum. Methods Phys. Res.* 1997, *B122*, 458-469.
[72] Pogrebnjak, A.D.; Bratushka, S.; Boyko, V.I.; Shamanin, I.V.; Tsvintarnay, Yu.V. *Nucl. Instrum. Methods Phys. Res.* 1998, *B145*, 373-390.
[73] Rotshtein, V.P.; Ivanov, Yu.F.; Markov, A.B.; Proskurovsky, D.I.; Karlik, K.V. *Surf. Coat. Technol.*, 2006, *200*, 6378–6383.
[74] Yan, S.; Le, X.Y.; Zhao, W.J.; Shang, Y.J.; Wang, Y.; Xue, J. *Surf. Coat. Technol*. 2007, *201*, 4817–4821.
[75] Werner, Z.; Piekoszewski, J.; Barkcz, A.; Grötzschel, R.; Prokert, F. *Nucl. Instrum. Methods Phys. Res.* 2001, *B175-177*, 767-771.
[76] Mueller, G.; Engelko, V.; Weisenburger, A.; Heinzel, A. *Vacuum*. 2005, *77*, 469–474.
[77] Uglov, V.V.; Anishchik, V.M.; Cherenda, N.N.; Stalmashonak, A.K.; Astashinski, V.M. *High Temp. Mater. Process.* 2004, *8*, 605-615.
[78] Tarasova, T.V. *Met. Sci. Heat Treat.* 2002, *44*(*3-4*), 124-127.
[79] Velde, O.; Gritzki, R.; Grundmann, R. *Int. J. Heat Mass Tran.* 2001, *44*, 2751-2762.
[80] Astapchik, S.A.; Bereza, N.A. *Physics of metals and physical metallurgy*. 2007, *103*(*1*), 3-14.(in Russian).
[81] Budovskih, E.A.; Sarichev, V.D.; Simakov, V.P.; Nosarev, P.S. *Physics and chemistry of materials treatment.* 1993, *1*, 59-66. (in Russian).
[82] Hoch, M.; Dingledy, D.; Johnston, H. *J. Am. Chem. Soc.* 1955, *77*, 304-306.
[83] Lyakishev, N.P. Ed. *Binary metal systems phase diagrams*; Mashinostroenie: Moscow, 1997; Vol. 2, p. 1024. (in Russian).
[84] Uglov, V.V.; Anishchik, V.M.; Cherenda, N.N.; Stalmashonak, A.K.; Astashinski, V.M. *Vacuum*. 2005, *78*, 489–493.
[85] Uglov, V.V.; Cherenda, N.N.; Anishchik, V.M.; Stalmashonak, A.K.; Astashinski, V.M. *Vacuum*. 2007, *81*, 1341-1344.
[86] Lahtin, U.M.; Rahstadt, A.H. Eds. *Thermal treatment in machine-building*; Mashinostroenie: Moscow, 1980; p. 783. (in Russian).
[87] Astashynski, V.M.; Ananin, S.I.; Askerko, V.V.; Kostyukevich, E.A.; Kuzmitski, A.M.; Uglov, V.V.; Cherenda, N.N.; Anishchik, V.M.; Sveshnikov, Yu.V.; Astashynski, V.V.; Kvasov, N.T.; Danilyuk, A.L.; Punko, A.V. *Vacuum*. 2005, *78*, 157-160.
[88] Uglov, V.V.; Anishchik, V.M.; Cherenda, N.N.; Sveshnikov, Yu.V.; Astashynski, V.M. *Surf. Coat. Technol.* 2008, *202*, 2439-2442.
[89] Tsytovich, V.N. *JETP*. 2007, *104*(*2*), 279-295.
[90] Tsytovich, V.N.; Morfill, G.E. *Plasma Phys. Rep.* 2002, *28*(*3*), 195-201.
[91] Han, M.; Landry, F.; Lieb, K.-P.; Schaaf, P. *Appl. Phys.* 1999, *A69*, S795-S797.
[92] Ozturk, O.; Williamson, D.L. *Surf. Coat. Technol.* 2002, *158-159*, 288-294.
[93] Wang, L.; Xu, X.; Yu, Z.; Hei, Z. *Surf. Coat. Technol.* 2000, *124*, 93-96.
[94] Xu, X.; Yu, Z.; Wang, L.; Qiang, J.; Hei, Z. *Surf. Coat. Technol.* 2003, *162*, 242-247.

Copyright © 2010. Nova Science Publishers, Incorporated. All rights reserved.

Handbook of Material Science Research, Nova Science Publishers, Incorporated, 2010. ProQuest Ebook Central,

[95] Cherenda, N.N.; Uglov, V.V.; Anishchik, V.M.; Stalmashonak, A.K.; Astashinski, V.M. *Vacuum*. 2007, *81*, 1337–1340.
[96] Geller, Y.A. *Tool steels*; Metallurgiya: Moscow, 1983; p. 527. (in Russian)
[97] Astashynski, V.M.; Ananin, S.I.; Askerko, V.V.; Kostyukevich, E.A.; Kuzmitski, A.M. *Surf. Coat. Technol.* 2004, *180-181*, 392–395.

Reviewed by Dr. Sc. A.P. Laskovnev, Physicotechnical Institute of the Belarus National Academy of Sciences, Minsk, Belarus.

Copyright © 2010. Nova Science Publishers, Incorporated. All rights reserved.

Handbook of Material Science Research, Nova Science Publishers, Incorporated, 2010. ProQuest Ebook Central,

In: Handbook of Material Science Research
Editors: C. René and E. Turcotte, pp.173-212
ISBN 978-1-60741-798-9
© 2010 Nova Science Publishers, Inc.

Chapter 3

PERCOLATION PROCESSES IN CUPRATE COMPOSITES AS LOW-DIMENSIONAL SYSTEMS

Katsukuni Yoshida
Graduate School of Energy Science,
Kyoto University, Kyoto, Japan

ABSTRACT

Recently, extensive interest has been focused on the percolation processes in superconducting cuprates, of which physical properties are strongly characterized by the low-dimensional aspects of the crystal structures. This review article concerns the percolation processes in cuprate composites. Two cases of the composites having different scales (micron and nanometer) of the structural ingredients are discussed in reference to the percolation processes and the space dimension. First, we describe the percolation processes observed for Ag-added Bi-based cuprates. This composite is an eccentric composite in the sense that two kinds of ingredient grains considerably differ from each other in their particulate morphology; the Bi-based cuprate grain being in two-dimensional lamella and Ag grain being roundish. How to characterize materials is also discussed in terms of the percolation process, where the percolation threshold and the critical exponents in association with the space dimension are key issues. Finally, we describe microscopic processes concerning a two-dimensional percolation in the mixed-crystalline cuprates of Pr-substituted RBa$_2$Cu$_3$O$_7$ (RPr-123, R= rare earth). A nonclassical percolation occurs in this system, where a crystal-unit-cell placed in special configurations can be converted by an electron orbital hybridization into different type of cell, creating virtual percolation thresholds and causing the ionic size effect on the superconductor-insulator transition.

Copyright © 2010. Nova Science Publishers, Incorporated. All rights reserved.

1. INTRODUCTION

Percolation is a critical phenomenon where the structure and properties of the system largely change when the concentration of structural ingredients in the system exceeds a critical value, i.e. percolation threshold. This phenomenon provides a prototypical model of

Handbook of Material Science Research, Nova Science Publishers, Incorporated, 2010. ProQuest Ebook Central,

the usual phase transitions, and its concept has been proved useful for understanding the relationship between structures and physical properties of materials. Of late, extensive interest has been focused on the percolation processes in superconducting cuprates, physical properties of which are strongly characterized by the low-dimensional aspects of the crystal structures.

This review article concerns the percolation processes in composites as comprising cuprate compounds. Two cases of the structures having different scales (micron and nanometer) of the structural ingredients will be discussed in reference to the percolation processes and the space dimension. Applications will also be shown on how to characterize materials in terms of the percolation theory, where the critical exponents and the percolation threshold with reference to the space dimension are key issues. The main part of the present article consists of four sections (Sects. 2~5).

In Section 2, we review the general nature of the percolation process involving the critical behavior of structural and physical quantities. A generalized effective medium model will also be presented to describe realistic percolation transition as observed for actual materials. Section 3 describes macroscopic percolation processes in polycrystalline mixtures consisting of lamellar grains of superconducting Bi-based cuprate (Bi-2223) and particulates of Ag phase. In this system two types of percolation processes take place for clustering of the grains in size of microns: two-dimensional clustering of superconducting lamellar grains of Bi-2223 and three-dimensional clustering of Ag particulates. Moreover, the clustering of Bi-2223 involves two processes: the first is two-dimensional growth of the cluster with increasing volume fraction of Bi-2223 phase, and the second is the superconducting cluster-extension assisted by the weak-link between adjacent superconducting Bi-2223 grains. In section 4, how to characterize the structure of the composites is described in terms of the percolation factors such as the percolation threshold, critical exponents, morphology of structural ingredients, and textural symmetry of the systems. Section 5 is devoted to the microscopic percolation process in mixed crystalline compound $R_{1-x}Pr_x Ba_2Cu_3O_{7-\delta}$ (*R*Pr-123, *R*=rare earth element), that consists of crystal unit cells of $RBa_2Cu_3O_{7-\delta}$ (*R*-123) and $PrBa_2Cu_3O_{7-\delta}$ (Pr-123). The superconductivity in *R*Pr-123 is well featured by two-dimensionality, where the internal Josephson coupling in the direction of the *c* axis is quite subtle owing to the presence of Pr. The percolation in the nanometric mixed crystalline medium exhibits nonclassical behavior, where the orbital hybridization of electrons in the CuO_2 plane plays an important role. This phenomenon will shed a light on a new aspect of the cuprate superconductivity.

2. PERCOLATION PROCESSES IN TWO-PHASE COMPOSITES

2.1. Percolation Transition and the Critical Behavior of Physical Properties

In Sec. 2, an overview of the percolation processes is presented in order to help the discussion throughout the article. In a mixture consisting of two kinds of particles, we can see variously sized aggregations (clusters) of the same kind of particles, where the particles are connected (or contacted) with each other in each clusters. As the concentration (x) of the particles increases, the number of clusters and their size will also increase. With increasing x,

Copyright © 2010. Nova Science Publishers, Incorporated. All rights reserved.

Handbook of Material Science Research, Nova Science Publishers, Incorporated, 2010. ProQuest Ebook Central,

the cluster has a chance to interlink with a neighboring cluster of the same kind by adding a new particle. The cluster grows with increasing speed by undergoing repeatedly this incorporation process. When x attains a critical concentration x_c, this process eventually creates a single huge cluster extending throughout the medium [1]; if the medium is boundless, this percolation cluster will extend infinitely. This occurrence is called "percolation transition". Owing to repetition of the cluster-incorporation process, a fractal structure is built in the percolation cluster. The critical concentration x_c is the percolation threshold at which the percolation transition takes place. Therefore, the percolation phenomenon is a highly geometrical phenomenon and can be a prototype of the actual transition phenomena in matter.

When the structural elements (e. g. particles) are distributed in a discrete lattice medium, two types of percolation is formed: the site-percolation when each element is placed on the lattice point, and the bond-percolation when each element is placed between adjacent lattice points. As displayed in Table 1, the percolation threshold x_c depends on the lattice type, the percolation type (site or bond) and the space dimensionality (2D or 3D) of the system. In general, higher dimensionality of the lattice and higher configuration around the element yield a lower percolation threshold, because of the high degree of freedom in creating connection between two elements.

Table 1. Percolation thresholds x_c for the first-nearest-neighbor connection, and critical exponents for discrete media having lattice structures; β, γ, ν denote critical exponents relevant to the percolation probability (P), mean cluster size (S) and correlation length (ξ), respectively [2–4]

Lattice	Site x_c	Bond x_c	β	γ	ν
Square	0.5927	1/2*			
Triangular	1/2*	$2\sin(\pi/18)$*	5/36*	43/18*	4/3*
Honeycomb	0.6962	$1-2\sin(\pi/18)$*			
Simple Cubic	0.3116	0.2488			
bcc	0.246	0.1803	0.42	1.796	0.88
fcc	0.198:	0.119			
Diamond	0.428	0.388			

* Exact values.

Table 2. Percolation threshold f_c (volume fraction) and transport exponents t and s observed for continuum media (metal-insulator composites) having symmetric texture; the exponents are applicable not only to continuum media but also to discrete lattices in spite of different thresholds x_c; the equation $t=s$ holds for 2D

Dimension	Threshold f_c	Exponent t	Exponent s
2D	0.5	1.1~1.3[a]	1.1~1.3[a]
3D	~0.15[b]	~2.0[b, c]	0.7~0.73[a, d, e]

[a]Ref. 5, [b]Ref. 1, [c]Ref. 6, [d]Ref. 7, [e]Ref. 8.

Copyright © 2010. Nova Science Publishers, Incorporated. All rights reserved.

Handbook of Material Science Research, Nova Science Publishers, Incorporated, 2010. ProQuest Ebook Central,

Statistical quantities relevant to the percolation transition show the critical behavior that appears as a power law featured by critical exponents. The percolation probability P ($x \geq x_c$) defined by the probability with which an arbitrarily chosen site (bond) belongs to the percolation cluster crossing through the system, the correlation (connectivity) length ξ defined as the average root mean square distance between occupied sites belonging to the same cluster, and the mean cluster size S are expressed as follows:

$$P \propto \left(x - x_c\right)^{\beta} \tag{1}$$

$$\xi \propto \left|x - x_c\right|^{-\nu} \tag{2}$$

$$S \propto \left|x - x_c\right|^{-\gamma}. \tag{3}$$

These critical exponents are independent of the lattice structure, but strongly depend on the space dimension (2D, 3D). Among them, the exponent ν of the correlation length closely relates to the transport phenomena in the system, as will be shown later.

More realistic is the percolation in continuum media corresponding to actual materials. It is convenient to use the volume fraction f of a phase constituting a medium, instead of the concentration x. Let us consider a two-phase composite consisting of phase a and phase b, where the grains of phases a and b are almost the same in morphology and have almost the same size. If the ingredient grains distribute randomly, then the textural pattern becomes symmetric, that is, the textural pattern at a volume fraction f_a=1–f_b =q is equivalent to the pattern appearing at f_a=1–q, exhibiting a correspondence between positive and negative (reversed) pictures. In such ideal texture, the percolation threshold is found as f_c=0.5 for 2D and f_c=0.15 for 3D. Table 2 lists the percolation parameters for such continuum media having symmetric texture. The exponent t and s give the power law of transport properties (conductivity and dielectric constant), as will be described in the next subsection.

2.2. Power Law Based on the Scaling Hypothesis and Structure Model for Critical Exponent

Following the percolation transition, the critical behavior emerges not only for the structural quantities such as P, ξ, S, but also for the transport properties such as the conductivity σ and the dielectric constant ε. The critical behavior of such properties can be derived from the scaling hypothesis [9–11]. With this approach, we consider below the critical behavior of conductivity (σ) of a composite consisting of phases a and b having conductivities σ_a and σ_b (σ_a>σ_b) and volume fraction f_a (f_b=1–f_a). .

First of all, the effective conductivity normalized with σ_a is assumed to be a function of f_a–f_c and the ratio σ_b / σ_a only in the neighborhood of the critical point f_c, and besides these quantities are assumed to be scaled with a parameter λ having appropriate exponents (the notation β used below is utterly different from the one given in Table 1 and Eq. (1)), as expressed by:

Copyright © 2010. Nova Science Publishers, Incorporated. All rights reserved.

Handbook of Material Science Research, Nova Science Publishers, Incorporated, 2010. ProQuest Ebook Central,

$$\frac{\sigma}{\sigma_a}\lambda = Q\left[\left(\frac{\sigma_b}{\sigma_a}\right)\lambda^{\alpha}, (f_a - f_c)\lambda^{\beta}\right]. \tag{4}$$

By putting λ as

$$\lambda = (f_a - f_c)^{-1/\beta}, \tag{5}$$

the scaling function $Q(\sigma_b/\sigma_a, \lambda, f_a\text{-}f_c)$ can be reduced to a new scaling function $F(x)$ as expressed by

$$\sigma = \sigma_a (f_a - f_c)^t F_+\left[\frac{\sigma_b}{\sigma_a}(f_a - f_c)^{-(t+s)}\right] \quad \text{for} \quad f_a > f_c, \tag{6}$$

$$\sigma = \sigma_a (f_c - f_a)^t F_-\left[\frac{\sigma_b}{\sigma_a}(f_c - f_a)^{-(t+s)}\right] \quad \text{for} \quad f_a < f_c, \tag{7}$$

where $F(x)$ is given by $F[\ldots]$, and the exponents α and β were rewritten as

$$\alpha = \frac{t+s}{t}, \quad \beta = \frac{1}{t}. \tag{8}$$

The reduced scaling functions $F_+(x)$ and $F_-(x)$ satisfy the following conditions:

$$F_+(0) > 0, \; F_-(0) = 0. \tag{9}$$

Thus, Eqs. (6) and (7) are expanded for $\sigma_b/\sigma_a << 1$ as follows:

$$\sigma = \sigma_a (f_a - f_c)^t F_+(0) + \sigma_b (f_a - f_c)^{-s}\left(\frac{\partial F_+}{\partial x}\right)_{x=0} + \cdots \text{ for } f_a > f_c, \tag{10}$$

$$\sigma = \sigma_b (f_c - f_a)^{-s}\left(\frac{\partial F_-}{\partial x}\right)_{x=0} + \cdots \text{ for } f_a < f_c. \tag{11}$$

From them, we have the simple power law for $\sigma_b/\sigma_a \sim 0$:

$$\sigma \propto (f_a - f_c)^t \quad \text{for } f_a > f_c, \tag{12}$$

$$\sigma \propto (f_c - f_a)^{-s} \quad \text{for } f_a < f_c. \tag{13}$$

Copyright © 2010. Nova Science Publishers, Incorporated. All rights reserved.

Handbook of Material Science Research, Nova Science Publishers, Incorporated, 2010. ProQuest Ebook Central,

When phase *a* is a superconductor and phase *b* is a normal conductor (or insulator), the ratio $\sigma_b/\sigma_a = 0$ holds below the critical temperature T_c. Eqs. (11) and (13) are applied also to this case ($f_a<f_c$). When phase *a* is a normal conductor and phase *b* is an insulator, the dielectric constant ε also follows the power law equivalent to Eq. (13):

$$\varepsilon \propto \left(f_c - f_a\right)^{-s} \quad \text{for} \quad f_a < f_c. \tag{14}$$

A general case when the ratio σ_b/σ_a is untrivial will be discussed later in reference to a deviation from the above power law (Sec. 4).

The power laws, Eqs. (12)~(14), for the properties σ and ε have been experimentally confirmed for a variety of materials. However, strangely, the properties observed for actual metal-insulator media are found to obey the power law not in the neighborhood of f_c, but also over wider range of f ($f_c \le f \le 1$, or $0 \le f \le f_c$) [1, 6, 7]. How to explain this extended critical behavior seems to have still remained as a problem to be solved.

Now, let us discuss geometrical features of the percolation structure in the discrete system. Figure 1 (a) shows an infinite cluster after undergoing the percolation transition for the triangle lattice site-percolation, where all the finite clusters are eliminated [12]. The infinite cluster wears numerous dangling dead-end branches. By removing these branches, we obtain a backbone of the cluster, as depicted in Figure 1(b); such a backbone was observed also for realistic materials like a metallic thin-film [13]. The backbone is networked with meshes, sizes of which decrease with increasing x in proportion to the correlation length ξ (Eq. (2)). The transport properties are governed by such network, through which the current or heat flows. By further inspecting the mesh of the backbone, the current path is found to consist of current bypasses and narrow necks crucial to the current passing.

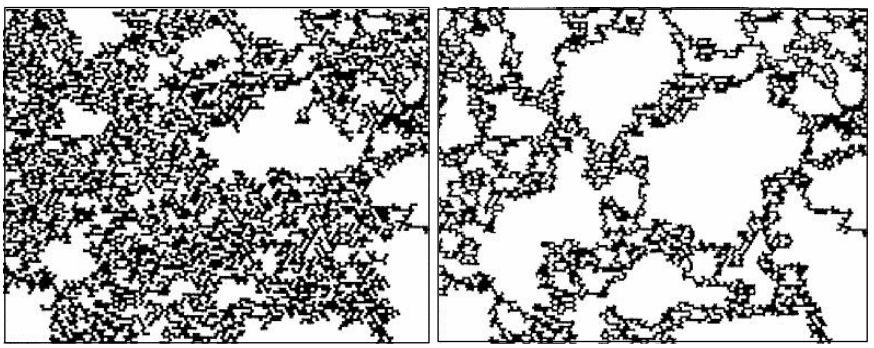


Figure 1. (a) Single infinite cluster in the triangle lattice site-percolation system (x=0.52), where the background comprising numerous finite clusters is eliminated; (b) the backbone of the infinite cluster, emerging as a network [12].

Copyright © 2010. Nova Science Publishers, Incorporated. All rights reserved.

Handbook of Material Science Research, Nova Science Publishers, Incorporated, 2010. ProQuest Ebook Central,

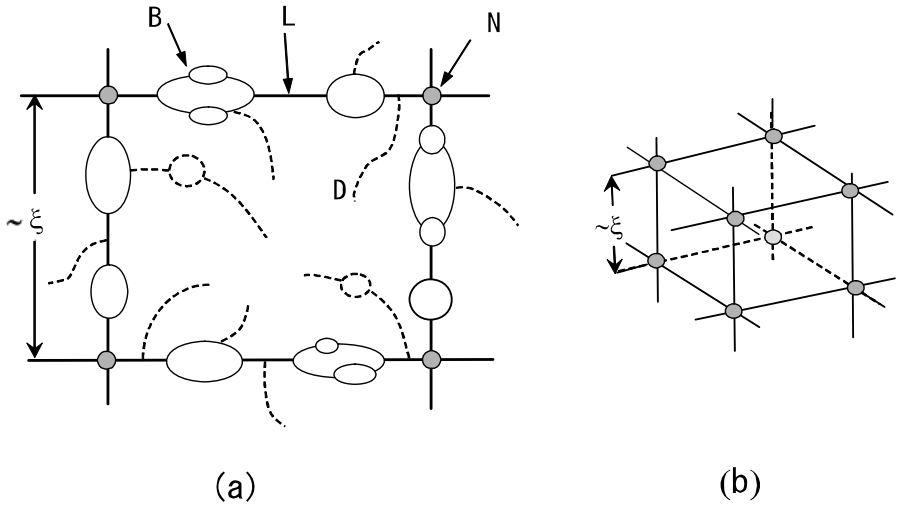


Figure 2. (a) Links-blobs-nodes model for the percolation cluster constructing a network with a unit size in proportion to ξ; L, B, N, D denote links, blobs, nodes, and dead-end branches, respectively; (b) conducting network (3D) based on the links-blobs-nodes model .

The structure observed for the cluster is simply modeled by the links-nodes-blobs geometry [11, 14-16]. Figure 2(a) illustrates this model, where the backbone consists of links (L), blobs (B) and nodes (N). The link is a singly connected path that is crucial for passing the current, and the blob is a group of bypasses (multi-connected part). The node is the crossing point of the links, and determines the unit of mesh. Of particular importance is the link, because the current path between two neighboring nodes can't work when the link is cut off.

The dangling branches D occupy a large part of the cluster (compare Figs. 1(a) and (b)), but give no contribution to the transport properties (except when the current is alternating with high frequency). However, the dead-end branch plays, in spite of the name, a role as an active edge for growing the cluster; which can grow by linking a dead-end branch with the nearest one, thereby a mesh (or a blob) being newly created

Now let us consider a conducting network (Figure 2(b)) and discuss what the exponent t means. The length of a segment between two neighboring nodes is proportional to the correlation length ξ, and the corresponding resistance per unit length along this segment will be given by $(x-x_c)^{-\chi}$, which means that the backbone becomes thick as x increases departing from x_c, lowering the resistance along this segment. The structural factor that strongly governs the resistance is the population of the links, which are the narrowest parts and so bear the most part of the resistance. The link population over the correlation length ξ has been found to be proportional to $(x-x_c)^{-1}$ [17], to which the resistance is substantially proportional. In addition, the conductivity σ is proportional also to the density of nodes in the unit area of the cross section perpendicular to the current. Then, the conductivity in d-dimensional space is expressed, using Eq. (2), as follows:

$$\sigma \propto \left(x - x_c\right)^{+\chi} \xi^{-(d-1)} \approx \left(x - x_c\right)^{+1} \xi^{+1} \xi^{-(d-1)} \propto \left(x - x_c\right)^{(d-2)\nu+1}. \qquad (15)$$

Copyright © 2010. Nova Science Publishers, Incorporated. All rights reserved.

Handbook of Material Science Research, Nova Science Publishers, Incorporated, 2010. ProQuest Ebook Central,

Thus, we obtain t:

$$t \approx (d-2)\nu + 1 . \tag{16}$$

From this formula and the power exponent ν in Table 1, we estimate t as $t \approx 1.88$ for 3D and $t \approx 1$ for 2D, which well approximate to the experimental values of t as listed in Table 2. As for another exponent s, no convincing model seems to have been established, but the equivalency $t=s$ is proved to hold for 2D.

2.3. Generalized Effective Medium Model Describing the Percolation Transition

The effective properties, that is, the overall physical properties of an inhomogeneous medium can be described by use of the effective medium concept. An advantage of this idea is that it can represent even the percolation transition. According to Bruggeman model (BM) for two-phase composite (3D) consisting of particles of phase a and phase b, the effective conductivity (σ^*) is given by the following equation [18, 19]:

$$\frac{\sigma^* - \sigma_a}{2\sigma^* + \sigma_a} f_a + \frac{\sigma^* - \sigma_b}{2\sigma^* + \sigma_b} f_b = 0 . \tag{17}$$

For conductor-insulator composites ($\sigma_a \neq 0$, $\sigma_b = 0$), Eq. (17) gives the percolation transition at $f_a = 1/3$:

$$\sigma^* = \frac{3}{2}\sigma_a \left(f_a - \frac{1}{3} \right). \tag{18}$$

However, Eq. (18) only gives linear dependence ($t=1$) on f_a and therefore does not represent well the critical behavior of σ^* observed for actual materials.

Another contrasting model is Maxwell model (or Maxwell-Garnett model, MGM) for dispersion composites like suspension (or emulsion), where dispersed particles (phase a) are embedded in the continuum matrix (phase b) [20]:

$$\frac{\sigma^* - \sigma_b}{\sigma^* + 2\sigma_b} = f_a \frac{\sigma_a - \sigma_b}{\sigma_a + 2\sigma_b} . \tag{19}$$

However, this model can't represent the percolation transition.

These conventional models (BM and MGM) seem to be quite unsatisfactory for investigation the relationship between the effective properties and realistic structures of media; MGM assumes only that isolated particles are embedded in the continuum matrix,

Copyright © 2010. Nova Science Publishers, Incorporated. All rights reserved.

Handbook of Material Science Research, Nova Science Publishers, Incorporated, 2010. ProQuest Ebook Central,

while BM provides no structural information other than considering that the medium has a completely random structure. Realistic structures in materials will have more complicated features intermediate between the simplified structures presumed in BM and MGM [21]. In order to remedy such deficiency in BM and MGM, a generalized effective medium model that considers more realistic structures and unites BM and MGM has been developed, as described below [1, 21, 22].

The effective conductivity $\sigma^*$is defined as

$$\boldsymbol{\sigma}^* \cdot \langle \boldsymbol{E}(\boldsymbol{r}) \rangle = \langle \boldsymbol{\sigma}(\boldsymbol{r}) \cdot \boldsymbol{E}(\boldsymbol{r}) \rangle \quad , \tag{20}$$

where the bracket stands for the volume average, $\boldsymbol{E}(\boldsymbol{r})$ is the electric field (vector) dependent on position $\boldsymbol{r}$, and $\boldsymbol{\sigma}(\boldsymbol{r})$ is the conductivity (tensor) intrinsic to the constituent phase. Further, $\boldsymbol{\sigma}(\boldsymbol{r})$ consists of position-independent part $\boldsymbol{\sigma}_0$ and dependent part $\delta\boldsymbol{\sigma}(\boldsymbol{r})$:

$$\boldsymbol{\sigma}(\boldsymbol{r}) = \boldsymbol{\sigma}_0 + \boldsymbol{\delta\sigma}(\boldsymbol{r}) \ . \tag{21}$$

We introduce $\boldsymbol{s}(\boldsymbol{r})$ that can involve all the spatial fluctuation of $\boldsymbol{E}(\boldsymbol{r})$ and $\boldsymbol{\sigma}(\boldsymbol{r})$, as follows:

$$\boldsymbol{s}(\boldsymbol{r}) \cdot \boldsymbol{E}_0 = \boldsymbol{\delta\sigma}(\boldsymbol{r}) \cdot \boldsymbol{E}(\boldsymbol{r}), \tag{22}$$

where $\boldsymbol{E}_0$ is a uniform electric field. Using these equations, we obtain the formula for σ^* (21):

$$\boldsymbol{\sigma}^* = \boldsymbol{\sigma}_0 + \langle \boldsymbol{s}(\boldsymbol{r}) \rangle \cdot \left\langle \boldsymbol{\delta\sigma}(\boldsymbol{r})^{-1} \cdot \boldsymbol{s}(\boldsymbol{r}) \right\rangle^{-1} . \tag{23}$$

Thus, if $\boldsymbol{s}(\boldsymbol{r})$ is known, then $\boldsymbol{\sigma}^*$ is determined. To obtain an exact expression of $\boldsymbol{s}(\boldsymbol{r})$ from first principles by using the equation of the current continuity (div $\boldsymbol{J}(\boldsymbol{r})$=0) needs to solve a many-body potential problem [21]. However, the problem can be transformed into one body problem by introducing a phenomenological idea, i. e. the effective medium, as described below.

Let us consider a constituent like a grain which is embedded in a uniform matrix having $\boldsymbol{\sigma}_0$. When a uniform field $\boldsymbol{E}_0$ is applied to the matrix, $\boldsymbol{E}$ is induced in this constituent. Equation (22) describes the relationship between $\boldsymbol{E}_0$ and $\boldsymbol{E}$, and therefore $\boldsymbol{s}(\boldsymbol{r})$ is obtained by solving the boundary-value problem as to the potential in the isolated constituent [21]. The self consistent condition is that the matrix itself is regarded as the effective medium to be obtained, that is, $\boldsymbol{\sigma}_0$=$\boldsymbol{\sigma}^*$. Therefore, this condition is rewritten from Eq. (23) as:

$$\langle \boldsymbol{s}(\boldsymbol{r}) \rangle = 0 \, . \tag{24}$$

In a two-phase composite consisting of phases *a* and *b*, we can observe some morphological features of the mixed constituents (grains) [21]: (1) A grain of phase *a* is surrounded by other grains of phase *b*; (2) Its inverse geometry; (3) Neither grain *a* nor grain *b* is surrounded by a single phase alone as presumed in BM. We can represent such geometry

Copyright © 2010. Nova Science Publishers, Incorporated. All rights reserved.

Handbook of Material Science Research, Nova Science Publishers, Incorporated, 2010. ProQuest Ebook Central,

in terms of four types of cells A, B, C, D, as depicted in Figure 3; A and B refer to (1) and (2); C and D refer to (3). For each of these cells, we can obtain $\boldsymbol{s}(\boldsymbol{r})$ from Eq. (22) [21, 22]. The effective medium can be represented by the aggregation of these cells with volume fractions F_A, F_B, F_C, F_D. By applying the self-consistent condition, i. e. Eq. (24), we can obtain a formula of $\boldsymbol{\sigma}^*$.

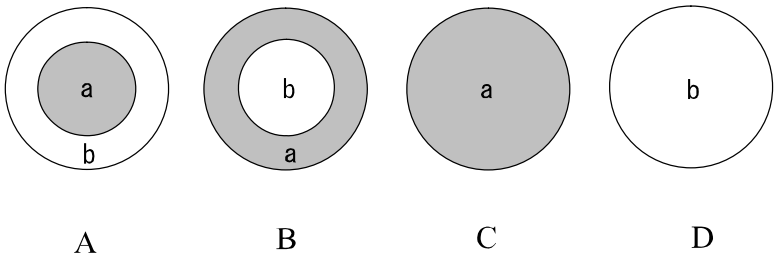


Figure 3. Four types of cells as structural elements in the medium consisting of phases *a* and *b*.

Here, for simplicity, we consider only two types of cells A and B [1]; the more general formulation considering all of the cells A, B, C, D has been given in Ref. 21. In order to make the model flexible for applying actual materials, we consider structural parameters α_1 and α_2 which control the range where the cells A and B coexist, as follows:

$$\alpha_1 \le \boldsymbol{f}_a \le \alpha_2 \quad (0 \le \alpha_1 \le \alpha_2 \le 1). \tag{25}$$

This condition means also that A-cells alone exist for $0 \le f_a \le \alpha_1$ and B-cells alone exist for $\alpha_2 \le f_a \le 1$. From Eq. (24), we derive the following equation for σ^*:

$$\frac{\sigma_a + 2\sigma_b + \gamma_A(\sigma_b - \sigma_a)}{(2\sigma^* + \sigma_b)(\sigma_a + 2\sigma_b) + 2\gamma_A(\sigma_b - \sigma^*)(\sigma_a - \sigma_b)}\boldsymbol{F}_A + \frac{\sigma_b + 2\sigma_a + \gamma_B(\sigma_a - \sigma_b)}{(2\sigma^* + \sigma_a)(\sigma_b + 2\sigma_a) + 2\gamma_B(\sigma_a - \sigma^*)(\sigma_b - \sigma_a)}\boldsymbol{F}_B = \frac{1}{3\sigma^*} \tag{26}$$

$$\boldsymbol{F}_A = \frac{\gamma_B - \boldsymbol{f}_b}{\gamma_A + \gamma_B - 1}, \tag{27}$$

$$\boldsymbol{F}_B = \frac{\gamma_A - \boldsymbol{f}_a}{\gamma_A + \gamma_B - 1}, \tag{28}$$

$$\gamma_A = \boldsymbol{f}_a \quad (0 \le f_a \le \alpha_1), \tag{29}$$

$$\gamma_B = \boldsymbol{f}_b = 1 - \boldsymbol{f}_a \quad (\alpha_2 \le f_a \le 1). \tag{30}$$

Copyright © 2010. Nova Science Publishers, Incorporated. All rights reserved.

Handbook of Material Science Research, Nova Science Publishers, Incorporated, 2010. ProQuest Ebook Central,

For $\alpha_1 \le f_a \le \alpha_2$,

$$\gamma_A = \boldsymbol{f}_a + (3 - \alpha_1 - 2\alpha_2)\left(\frac{\boldsymbol{f}_a - \alpha_1}{\alpha_2 - \alpha_1}\right)^2 + (\alpha_1 + \alpha_2 - 2)\left(\frac{\boldsymbol{f}_a - \alpha_1}{\alpha_2 - \alpha_1}\right)^3, \quad (31)$$

$$\gamma_B = 1 - \boldsymbol{f}_a + (2\alpha_1 + \alpha_2)\left(\frac{\boldsymbol{f}_a - \alpha_2}{\alpha_2 - \alpha_1}\right)^2 + (\alpha_1 + \alpha_2)\left(\frac{\boldsymbol{f}_a - \alpha_2}{\alpha_2 - \alpha_1}\right)^3. \quad (32)$$

Equation (26), which is a quadratic equation of σ* and so gives an analytical solution, is applicable to complicated structures where two phases are in tangled textures. This model , which is sometimes called "structure-oriented percolation model" [23, 24], is also capable of determining the percolation threshold f_c by choosing the cell coexisting region (α_1, α_2); f_c is not a given parameter in this model. Besides, this model can derive the conventional models BM and MGM as special cases [1, 21]:

(a) At the limit (α_1, α_2)→(1,1), Eq. (26) straightforwardly gives Eq. (19), i. e. MGM of the case when phase *a* is granular and phase *b* is matrix.

(b) At the limit (α_1, α_2)→(0,0), Eq.(26) straightforwardly gives the reversed MGM of the case when phase *a* is matrix and phase *b* is granular.

(c) If we can put (γ_A, γ_B) → (1, 1) or (0, 0), regardless of Eqs. (29)~(32), then Eq. (26) straightforwardly gives BM, i. e. Eq. (17).

Figure 4 demonstrates the comparison of the theoretical and experimental results [1]. The solid curves are illustrated by the present model and compared with experimental observation for bulky samples (3D) of the composite Nb-Al_2O_3, which were prepared by hot-press sintering at 1200°C under the pressure 430 kg/cm^2 in a vacuum atmosphere [1, 25–27]. The theoretical curves well reproduce the experimental result showing the percolation threshold f_c=0.16, which is quite close to the value typical to 3D random systems (Table 2). The present model has been applied to a variety of practical materials [1, 8, 24, 28–34], and a review of the relevant models has been given in Ref. 23. In Sec. 4, this model will be again used for characterizing cuprate composites.

2.4. Summary

The percolation processes in the clustering of structural ingredients in two-phase composites are overviewed, with enhancement on the importance of the percolation transition and the critical behavior depicting the power laws of structural quantities and physical properties. The percolation threshold f_c (or x_c) and the critical exponents β, γ, ν concerning the percolation probability, cluster size, and the correlation length are largely dependent on the dimensionality (2D, 3D) of the media. These quantities closely relate with the power law of the physical properties such as electrical conductivity. The power law is founded on the basis of the scaling hypothesis, and its exponent *t* is theoretically obtained from the backbone network model of the percolation cluster. Finally, a generalized effective medium model that

Copyright © 2010. Nova Science Publishers, Incorporated. All rights reserved.

Handbook of Material Science Research, Nova Science Publishers, Incorporated, 2010. ProQuest Ebook Central,

is applicable to more complex structures in two-phase composites than implied by BM and MGM is described, demonstrating a realistic percolation transition.

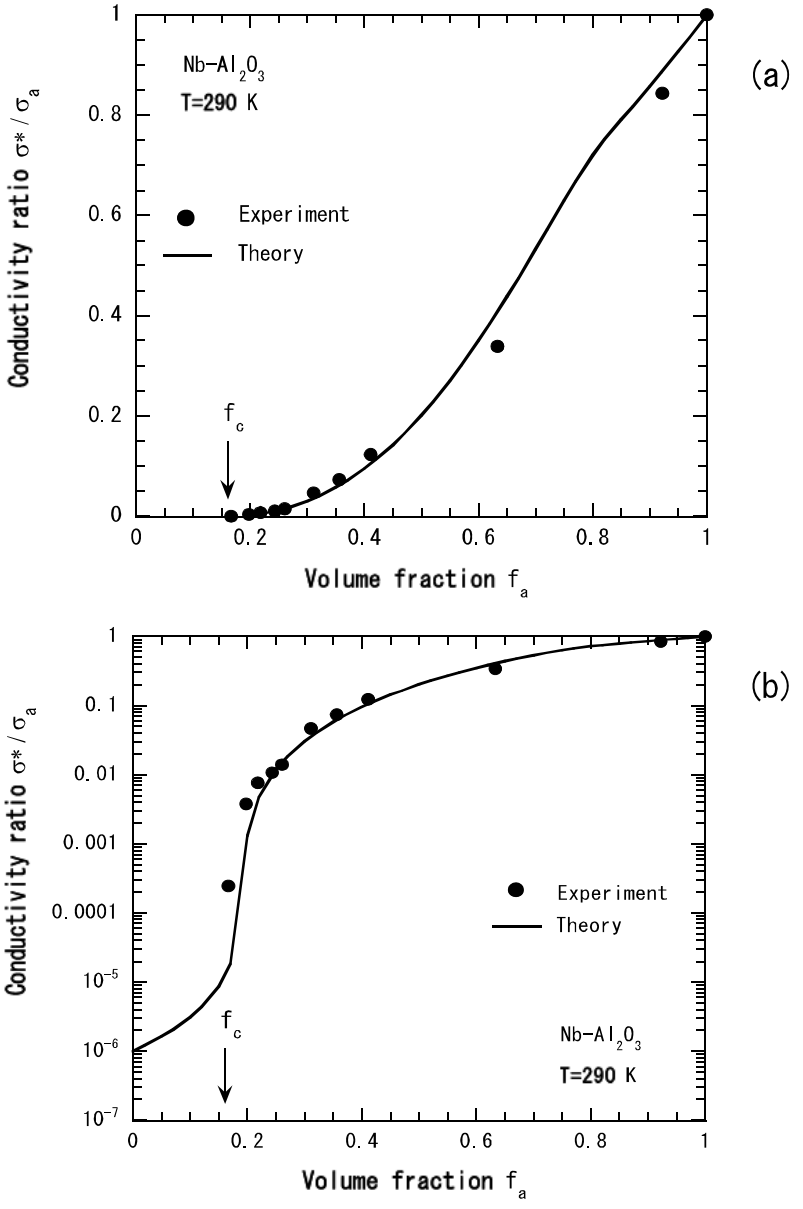


Figure 4. (a) Experimental (solid circle) and theoretical (solid curve) comparison for the effective conductivity σ^* (normalized with σ_a) as a function of f_a, and (b) the logarithmic plot of σ^*, giving f_c=0.16; the calculation was made for α_1=0 and α_2=0.83, by considering cells A and B only (Fig. 3); the experimental data were obtained for a typical metal-insulator composite Nb-Al_2O_3 (f_a is for Nb phase) [1, 8, 25, 26].

Copyright © 2010. Nova Science Publishers, Incorporated. All rights reserved.

Handbook of Material Science Research, Nova Science Publishers, Incorporated, 2010. ProQuest Ebook Central,

3. PERCOLATION PROCESSES OF CLUSTERING IN CUPRATE COMPOSITE Ag-ADDED Bi-2223

3.1. Anisotropic Structure of Bi-Based Cuprate (Bi-2223) and Properties of Two-Phase Composite Ag-Added Bi-2223

In this section we describe the percolative behavior of constituent phases in the composite of Ag-added $(Bi, Pr)_2Sr_2Ca_2Cu_3O_{10}$ (BiPb-2223). At the beginning, for considering space dimensional aspects, we focus on the cuprate compound BiPb-2223 itself. This compound becomes superconducting below the critical temperature (onset) T_c=110 K; the dopant Pb is used to create a single phased compound substantially identical to $Bi_2Sr_2Ca_2Cu_3O_{10}$ (Bi-2223). In spite of the presence of Pb, from now on, we will refer BiPb-2223 to as Bi-2223 simply. Such Bi-based cuprates are generally expressed in a general form as $Bi_2Sr_2Ca_{n-1}Cu_nO_{4+2n+\delta}$ (referred to as BSCCO, from now on). This stoichiometric form gives several kinds of compounds according to n: $Bi_2Sr_2CuO_6$ for n=1 (Bi-2201, T_c=8, 20, 30 K), $Bi_2Sr_2CaCu_2O_8$ for n=2 (Bi-2212, T_c=80~95 K) and $Bi_2Sr_2Ca_2Cu_3O_{10}$ for n=3 (Bi-2223, T_c=107, 110 K). The different values of T_c for the same compound are due to the sample quality that depends on heat treatments (annealed or no-annealed) or furnace atmosphere in the sample preparation. The number n just equals the number of CuO_2 planes in a half of the crystal unit cell, as shown in Figure 5. Those compounds are well known to be extremely anisotropic in structures and properties in comparison with other types of high-T_c cuprates. The superconductivity is propagated along the two-dimensional sheets of CuO_2 planes.

The structural anisotropy is obvious from the crystallographic structure, as depicted for Bi-2223 in Figure 5. In this compound, the lattice constants are 5.413 Å along either of *a*- or *b*-axis, and 37.1 Å along the *c*-axis. For measuring the anisotropy in physical properties, we employ the ratio (γ) of the directionally dependent London's penetration depths λ_c/λ_{ab} or that of coherence lengths ξ_{ab}/ξ_c. The observed values are γ=30~50 for Bi-2223 [35, 36], while γ ≈7 for Y-123 with T_c=92.4 K [37]. The anisotropy ratio for Bi-2223 is much greater than that for Y-123, indicating the outstanding anisotropy in Bi-2223. This strong anisotropy brings the two-dimensional character in Bi-2223. In spite of its high value of T_c, which makes us expect high potential of applications, this remarkable anisotropy largely restricts practical applications of Bi-2223, because its anisotropy considerably reduces the flux pinning force and the irreversibility field $H^*(T)$ at temperatures near T=77 K, thereby lowering the critical current density J_c. Owing to this disadvantage, Bi-2223 (H^*≈0.2 T at 77 K [38]) is being superseded by Y-123 (H^*≈7 T at 77 K [38]) in power applications; the latter is far less anisotropic, and so can retain a high critical current density at even T=77K. However, Bi-2223 still remains as an excellent superconductor in comparison with conventional ones like $NbSn_3$ and NbTi, when used at sufficiently low temperatures below 30 K.

Another salient feature is the presence of Bi_2O_2 layers in the crystal of BSCCO (regardless of n), as depicted in Figure 5. This layer consists of a double sheet of Bi-O planes, and the coupling between Bi-O planes is made only by van der Waals force, which is considerably weak in comparison with the usual chemical bonding. Therefore, the crystal of BSCCO is easily cleaved at Bi_2O_2 layer, and the grain becomes two-dimensional lamella. The easy cleavage of the grain is exploited in fabricating the superconducting wire of Bi-2223 by the powder-in-tube method (PIT). When the Ag-tube sheathing the powder of Bi-2223 grains

Copyright © 2010. Nova Science Publishers, Incorporated. All rights reserved.

Handbook of Material Science Research, Nova Science Publishers, Incorporated, 2010. ProQuest Ebook Central,

is swaged to a thread, the grains are highly oriented by virtue of the cleavage, giving an advantage in fabricating the superconducting wire. Figure 6 illustrates lamellar grains of Bi-2223 (or other BSCCO), where Bi-2223 grains are uniquely oriented like a stack of playing cards sliding sideway.

Another compound $Bi_2Sr_2CaCu_2O_8$ (Bi-2212) has smaller potential for power applications than Bi-2223 has. However, this compound occupies a unique position in providing valuable information for basic understanding of the high-T_c superconductivity, since Bi-2212 can easily be single phased and crystallized without dopant Pb, giving an extremely flat cleavage-surface that is fit for observing phenomena on atomic scales.

The addition of Ag to high-T_c cuprates has an advantage of introducing some ductility in the brittle cuprates without degrading the intrinsic superconductivity because of its chemical inertness to cuprate compounds [39]. For example, although under a restricted condition, a beneficial influence of Ag-addition on the critical current density J_c has occasionally been found [40]; when the sample fabrication involves mechanical deformation, the ductile Ag-phase will assist the deformation for texturally compacting the composite, which may lead to improvement of J_c under appropriate condition [40, 41] . However, in spite of the chemical inertness of Ag to the cuprates, its addition has been found to exert a marked influence on the thermodynamic processes in the synthesis and sintering in the sample preparation [42–46]. Therefore, without special conditions, the Ag-addition makes the stoichiometry of the compounds unstable to yield impurity phases during the fabrication process [42, 43]. Reflecting this situation, the Ag-addition has often been found to result in deterioration of the overall superconductivity [42, 47–49].

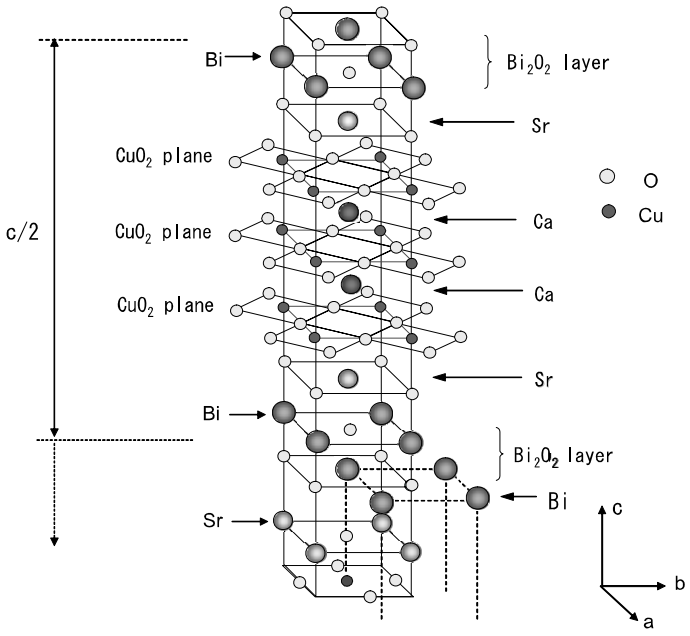


Figure 5. Crystallographic structure of $Bi_2Sr_2Ca_2Cu_3O_{10}$ (Bi-2223); a half of the crystal unit cell is designated by c/2, and another half with the same structure is repeated from Bi_2O_2 layer by shifting the (*a*, *b*)-abscissa by (a/2, b/2), as indicated by the broken lines at the bottom.

Copyright © 2010. Nova Science Publishers, Incorporated. All rights reserved.

Handbook of Material Science Research, Nova Science Publishers, Incorporated, 2010. ProQuest Ebook Central,

It should be emphasized that Ag-added Bi-2223 (Bi-2223/Ag) is an eccentric composite in the sense that two kinds of ingredient grains considerably differ from each other in their particulate morphology; the cuprate grain being in two-dimensional lamella (Figure 3-2) and Ag grain being roundish without such low-dimensionality.

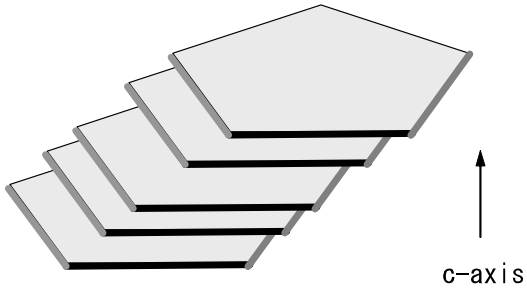


Figure 6. Sliding of two-dimensional lamellar grains of Bi-2223 (or other BSCCO) having cleavage planes (Bi_2O_2), each grain being so oriented that the *c*-axis is perpendicular to the cleavage surface (schematic).

3.2. Preparation of Two-Phase Composite Ag-Added Bi-2223 and the Superconducting Characters

The starting material was a powder of the compound with nominal composition $Bi_{1.8}Pb_{0.4}Sr_2Ca_2Cu_{3.2}O_{10}$ (Bi-2223). This compound was synthesized by a coprecipitated-oxalates method, and the particle size of its powder was several tens of micrometers [50]. The powder was ground to smaller particle size, sintered at 850°C for 48 hours in air, and pulverized. The X-ray diffraction (XRD) measurement showed that the resultant powder consisted almost entirely of the high-T_c compound Bi-2223 phase, though a small amount of Bi-2201 was recognized together with a faint trace of impurity phase Bi-3221 [42]. The powder was then thoroughly mixed with Ag_2O powder in appropriate amount, and ground again. The weight fraction of Ag_2O ranged from 0 to 90 %. The mixture was then cold pressed into a rectangular parallelepiped slab. The slab was sintered at 840°C for 120 hours in air, and subsequently it was removed from the furnace to air cool. After the sintering, no deformation was applied to the specimens. The additive Ag_2O decomposed above about 250°C to yield metallic Ag-phase. The XRD patterns of the resultant composites were almost the same as that of the presintered powder described before, except for the newly appearing spectra of the Ag phase, indicating the additive Ag did not react with the cuprate itself. No deformation was applied. The dimensions of the composite samples were $15\times7.5\times1.0$ mm^3. The electrical conductivity was measured by the conventional four-probe method.

The composite Ag-added Bi-2223 (Bi-2223/Ag) comprises not only Bi-2223 and Ag phases, but also pores. Figure 7 exhibits the correlation among the volume fractions of Ag-phase (f_A), that of Bi-2223 (f_B) and the porosity f_p in the composite [50]; where $f_A+f_B+f_p=1$. The volume fractions f_A and f_B were determined by measuring the density of the sintered sample and the weight % of Ag_2O on the assumption that the evaporation of Ag atoms when Ag_2O was decomposed was negligible. The densities adopted were 10.5 g/cm^3 for Ag phase and 6.44 g/cm^3 for Bi-2223 ($Bi_{1.8}Pb_{0.4}Sr_{2.0}Ca_{2.0}Cu_{3.2}O_{10.}$) phase. The porosity was determined

Copyright © 2010. Nova Science Publishers, Incorporated. All rights reserved.

Handbook of Material Science Research, Nova Science Publishers, Incorporated, 2010. ProQuest Ebook Central,

from the equation $f_p=1-f_A-f_B$. Both f_B and f_p linearly decrease with increasing f_A. The negative slope of f_p indicates that the Ag phase fills in the pores among the Bi-2223 grains, and thereby the sample becomes texturally compact and mechanically ductile.

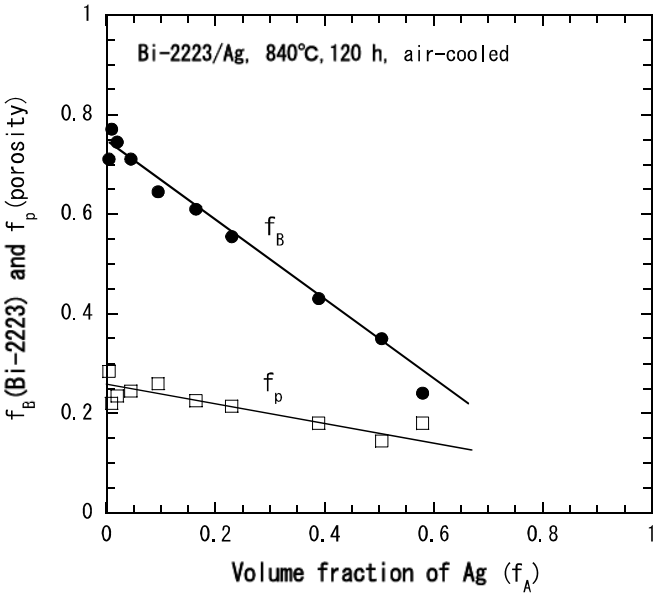


Figure 7. Volume fractions of Bi-2223 (f_B) and porosity (f_p) depending on the volume fraction of Ag phase (f_A) in the composite Bi-2223/Ag.

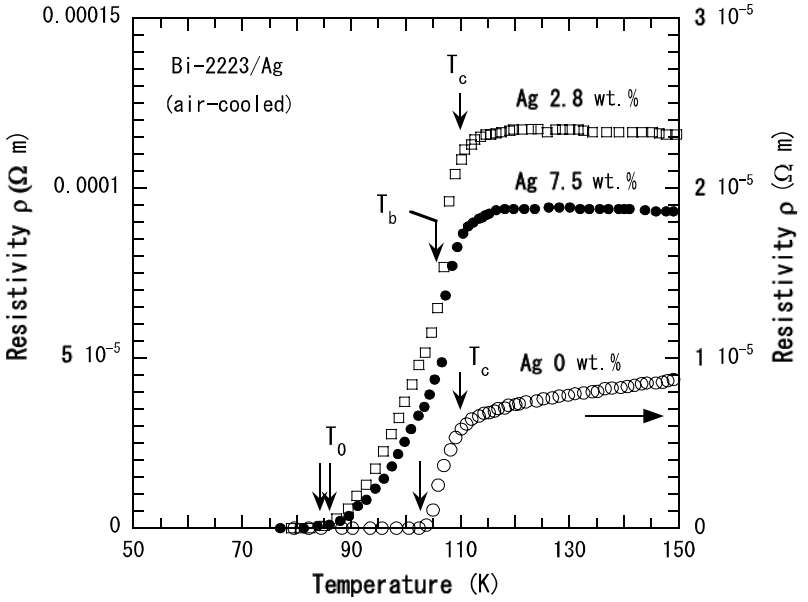


Figure 8. Resistivity ρ vs. temperature for Bi-2223/Ag with Ag 0, 2.8, and 7.5 wt.%, where T_c indicates onset temperature, T_0 zero-resistance temperature, T_b curve-bend temperature; the curve for Ag 0 wt. % should be read on the right hand scale (indicated by an arrow), while others on the left hand scale; the samples were air-cooled after the sintering at T= 835°C.

Copyright © 2010. Nova Science Publishers, Incorporated. All rights reserved.

Handbook of Material Science Research, Nova Science Publishers, Incorporated, 2010. ProQuest Ebook Central,

Figure 8 shows the effect of Ag-addition on the resistivity ρ of the composites with Ag wt. % ranging from 0 to 7.5 % [42, 43]. After sintering at 835°C for 120 hours in air, the samples were removed from the furnace to cool at room temperature (air-cooled). For the unadded sample (Ag 0 wt. %), the resistivity ρ falls off in the transition range from the onset temperature T_c (=110 K) to the zero resistance temperature T_0 (=104 K), and besides exhibits a metallic behavior above T_c, increasing linearly with increasing T. In contrast, Ag-addition even with a small amount as low as 2.8 wt. % causes a considerable change in ρ, degrading the superconductivity; note the difference in reading scales on the left and right sides. In spite of the same onset temperature, the resistivity at T_c markedly rises up more than ten times that of the unadded sample, and the zero-resistance temperature T_0 shifts to much lower temperature (T=88 K). Of interest is that the further Ag-addition (7.5 wt.%) does not yield such considerable change as stated above; appropriate rescaling of the curve of 7.5 wt.% can entirely overlap with that of 2.8 wt.% [42]. This fact indicates that the precipitation of metallic Ag-phase itself is insignificant, but its addition, even in small amount, plays a catalyzing role in invoking the precipitation of impurity phases at the grain boundary of Bi-2223 [42, 43]. These curves of 2.8 and 7.5 wt.% undergo two stages of variation; a sharp falling-off from T_c, which indicates granular superconductivity inside the grains, is followed by a bend at T_b, subsequently a long tail being formed. The bend and the tail describe a change in the resistivity at the grain boundary. The presence of this bend supports the view that a less conductive impurity phase such as Bi-2201 (when becoming amorphous) emerges at the grain boundary of Bi-2223 [42]. The change in ρ caused by the Ag-addition is largely depends on the cooling rate after the sintering, being enhanced by increasing cooling rate [42, 44]. Further Ag-addition (Ag 7.5 wt.%) turns the normal conducting part above T_c to decrease in magnitude, because clustering of metallic Ag grains proceeds with the further addition, so that the conductive contribution from this phase becomes obvious; the Bi-2223 is much less conducting at the room temperature, as will be shown later.

Although not shown here, the superconducting degradation due to the impurity-phase precipitation at the grain boundary has also been observed from the diamagnetic behavior of the same samples [42, 43]. The precipitation of such impurity phase largely interrupts the superconducting connection among Bi-2223 grains, as will be discussed in Sec. 4. However, the precipitation seems to reach the ceiling at a stage of low Ag content.

3.3. Percolative Clustering of Ag Grains in Composite Bi-2223/Ag and the Power Low

Figure 9 shows the dependence of the resistivity ρ of Bi-2223/Ag on the volume fraction f_A of the Ag-phase at T=290 K and 77 K [50]. At the room temperature (290 K), Bi-2223 phase is a normal conductor having the resistivity of nearly four orders of magnitude higher than that of the Ag-phase. A salient feature in the dependence curve is the appearance of a shoulder that shows a steep falling off around a critical point $f_{A,c}$ =0.25, where ρ is reduced by a factor of approximately 10^3. This considerable change in ρ is caused by the percolation transition, in which the clustering of the Ag grains begins to spread throughout the sample [50].

Copyright © 2010. Nova Science Publishers, Incorporated. All rights reserved.

Handbook of Material Science Research, Nova Science Publishers, Incorporated, 2010. ProQuest Ebook Central,

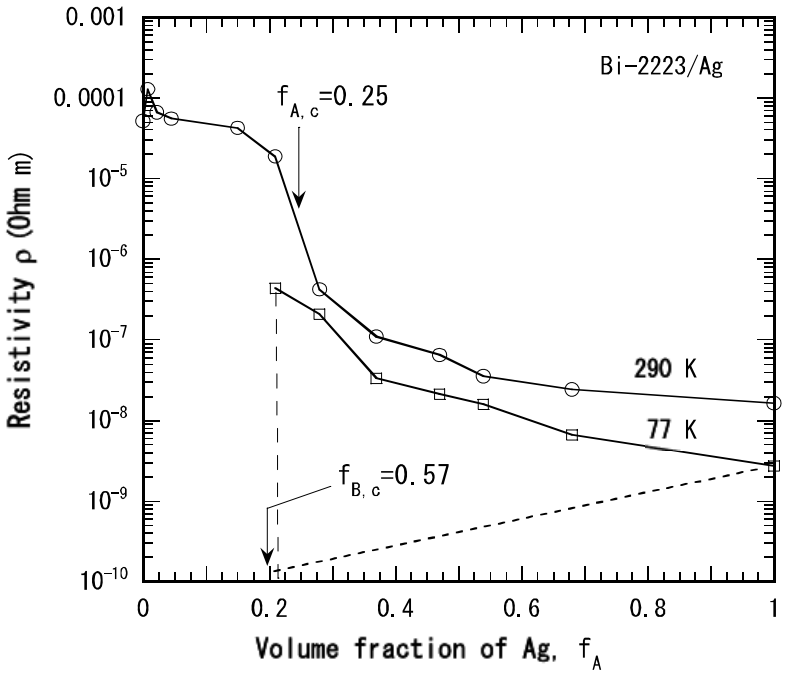


Figure 9. Dependence of the resistivity ρ on the volume fraction f_A of Ag-phase in the composite Bi-2223/Ag at T=290 K and 77 K; $f_{A,c}$ and $f_{B,c}$ indicate the percolation threshold for Ag-phase and for Bi-2223 phase, respectively; $f_{B,c}$ is obtained by use of Fig. 7; the samples were air-cooled after the sintering at T=840°C for 120 h .

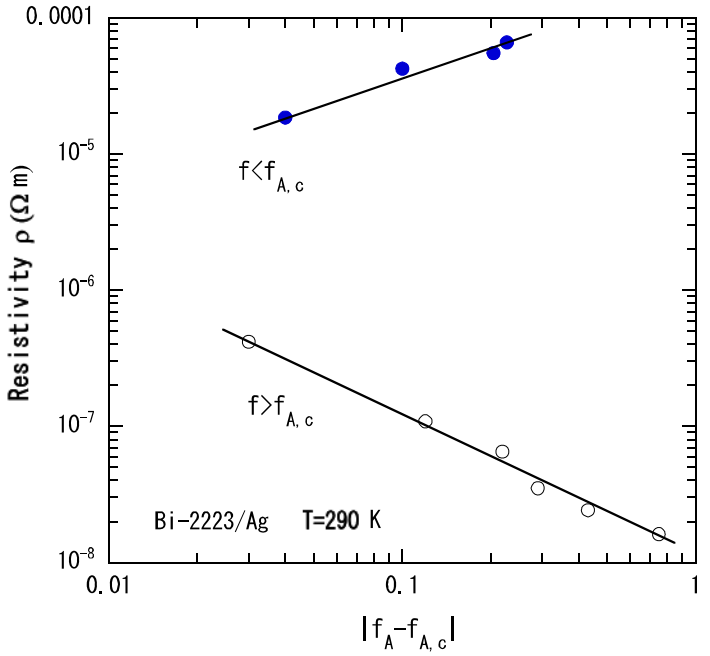


Figure 10. Power law for the resistivity of Bi-2223/Ag with respect to (f_A–$f_{A,c}$) at T=290 K; $f_{A,c}$=0.25, t =1.11 ($f_A > f_{A,c}$) for the lower line and s=0.66 ($f_A < f_{A,c}$) for the upper line [50].

Copyright © 2010. Nova Science Publishers, Incorporated. All rights reserved.

Handbook of Material Science Research, Nova Science Publishers, Incorporated, 2010. ProQuest Ebook Central,

On the other hand, the resistivity at T=77 K suddenly soars up from zero to a high value when f_A exceeds about 0.2 (f_B=0.57), indicating a break in an infinite cluster of the superconducting Bi-2223; the infinite cluster means such a cluster as extending from end to end in the sample. In spite of the temperature lower than T_c=110 K, the subsequent decrease in ρ seems strange, since the decrease in volume fraction f_B of superconducting Bi-2223 (i.e. increase in f_A) should normally raise ρ, as depicted by the broken line in Figure 9. This dependence curve for T=77 K is almost the same as that of T=290 K, implying that even at 77 K the resistivity entirely depends on the percolative behavior of the Ag-phase, and hence the contribution from the superconducting cluster to the overall conduction is concealed. The disappearance of the superconducting contribution is relevant to the way of clustering of lamellar grains of Bi-2223 (see Figure 6), having a low degree of freedom in clustering, due to morphological low dimensionality of the grains. This problem will be discussed again in Sec. 4.

Returning to the resistivity at T=290 K, which reflects the behavior of the clustering Ag-phase, we discuss here the power law observed for ρ at this temperature. From Eqs. (12) and (13) (Sec.2), the power low for the resistivity ρ is expressed as follows:

$$\rho \propto \left(f_{A,c} - f_A\right)^s \quad \text{for } f_A < f_{A,c}, \tag{33}$$

$$\rho \propto \left(f_A - f_{A,c}\right)^{-t} \quad \text{for } f_A > f_{A,c}, \tag{34}$$

where $f_{A,c}$ indicates the percolation threshold for Ag-phase. For the highly random structure, the exponents t and s is expected to take the universal values, which depends only on the spatial dimension, but are independent of the details of structures. These universal values are $t\approx2$ and $s\approx0.7\sim0.73$ for 3D systems, and $t = s= 1.1\sim1.3$ for 2D systems, as displayed in Table 2.

Figure 10 displays a logarithmic plot of the resistivity at T=290 K as a function of $\Delta f \equiv f_A - f_{A,c}$. The power law seems to hold for both the cases $f_A < f_{A,c}$ and $f_A > f_{A,c}$. The percolation threshold $f_{A,c}$ and the exponent t (or s) can be determined simultaneously in the following way. First, a certain value of $f_{A,c}$ is appropriately chosen, and then t (or s) is calculated by the least squares fitting, which gives a minimum residual R for which the trial line of ρ as a function of Δf most appropriately fits the data. This procedure is repeated by varying the value of $f_{A,c}$, giving a series of values of R. When R takes the minimum in the series, then the corresponding values of $f_{A,c}$ and t (or s) are the ones that we finally determine [1, 51].

Thus we obtain the following values: $f_{A,c}$=0.25 ±0.01, t=1.11 ± 0.05 for $f_A > f_{A,c}$, and s=0.66 ± 0.05 for $f_A < f_{A,c}$ [50]. The experimental s almost agrees with the expected value, i. e., the universal one (s=0.7 for 3D). However, the experimental t largely deviates from the universal one (t=2.0 for 3D). Of interest is that such deviation of t is commonly observed for other kind of cuprate composites, as displayed in Table 3. The data shown there were obtained by measuring the electrical resistivity, although the last case in Table 3 is for the thermal conductivity. Most of the values observed for t are much less than the universal one for 3D, and in contrast, most of those observed for s are close to the universal one for 3D. The observed values of t seem to approximate even to the universal value for the 2D case, for which t=1~1.3. This strange variance is associated with the problem of whether the single

Copyright © 2010. Nova Science Publishers, Incorporated. All rights reserved.

Handbook of Material Science Research, Nova Science Publishers, Incorporated, 2010. ProQuest Ebook Central,

power low as given by Eqs. (33) and (34) are validated for the present case. This problem will be discussed in detail in Sec. 4.

3.4. Clustering of Bi-2223 Grains in Composite Bi-2223/Ag and the Power Low

Now let us turn to the issue on the clustering process of superconducting grains (Bi-2223) in the composite, where Bi-2223 grains become superconducting at temperatures lower than T_c=110 K. When the superconducting path consisting of Bi-2223 grains is segmented stepwise with decreasing f_B (i. e. increasing f_A), the resistivity ρ should increase from zero with increasing f_A, as indicated by the broken line in Figure 9. Nevertheless, even at 77 K, the resistivity entirely depends on the percolative behavior of the normal conducting Ag-phase as seen for T=290 K, concealing the contribution from the superconductivity of Bi-2223.

However, by lowering the temperature further, the superconducting contribution comes to appear. Figure 11 demonstrates how the resistivity changes its dependence on $(f_{B,c}-f_B)$, according as T decreases from 77K [56]. The dependence curve changes from a decreasing function of $(f_{B,\,c}-f_B)$ at T=77K to an increasing function at T=35 K, undergoing the intermediate transition expressed by combination of a decreasing and an increasing functions of $(f_{B,c}-f_B)$; qualitatively, a decreasing function of $(f_{B,c}-f_B)$ is also a decreasing function of f_A. The increasing part in each curve discloses a behavior of the superconducting clusters. This increasing part is enhanced with decreasing T, and eventually the resistivity ρ turns into a monotonically increasing function, expressing the power law relevant to the superconducting clusters. Forming of the superconducting clusters is largely featured by two factors; one is the change in the volume fraction f_B of Bi-2223, and another is the T-dependent weal-link superconductivity at the grain boundary of Bi-2223 grains.

Table 3. Experimental observation of the percolation threshold $f_{A,c}$ and the exponents t ($f_A > f_{A,c}$) and s ($f_A < f_{A,c}$) with respect to the volume fraction f_A of Ag (or Au) phase; the data were obtained by measuring the electrical resistivity, except for the last case of the thermal conductivity, and the present work refers to Refs. 50, 56

Composites	$f_{A,\,c}$	t	s	Refs.
$YBa_2Cu_3O_7$/Au (297K)	0.23	0.73	0.71	[52]
$YBa_2Cu_3O_7$/Ag (300 K)	0.19	1.6	0.7	[53]
$YBa_2Cu_3O_7$/Ag (300 K)	0.20	0.79	1.4	[54]
Bi-2212/Ag (300 K)	0.168	1.1		[55]
Bi-2223/Ag				
Resistivity (290 K)	0.25	1.11	0.66	[50]
Resistivity* (35 K)	$f_{B,\,c}$=0.57*		1.2*	[56]
Bi-2223/Ag**	0.25			
Thermal cond. (30K)		1.08	0.63	[57]

* The quantities for T=35 K were determined with respect to the volume fraction (f_B) of Bi-2223.

** The samples used for measuring the thermal conductivity [57] were the same as used for measuring the resistivity [50].

Copyright © 2010. Nova Science Publishers, Incorporated. All rights reserved.

Handbook of Material Science Research, Nova Science Publishers, Incorporated, 2010. ProQuest Ebook Central,

The spatial extension of the clustering can be analyzed in reference to the percolation process. As will be explained in Sec, 4, the resistivity ρ at T=35 K obeys the following power law:

$$\rho \propto \left(f_{\mathrm{B,c}} - f_{\mathrm{B}}\right)^{s} \quad \text{for} \quad f_{\mathrm{B}} < f_{\mathrm{B,c}}. \tag{35}$$

The exponent s and the percolation threshold $f_{\mathrm{B,c}}$ are determined at the same time in the way previously described; f_{B}=0.57 and s=1.2 [56]. Those values are well approximate to those of the ideal 2D system, for which $f_{\mathrm{B,c}}$=0.5 and s=1.1 ~1.3 (Table 2). From this result, we may say that the cluster of Bi-2223 grains extends two-dimensionally with increasing f_{B} rather than three-dimensionally, in contrast to the Ag-phase clustering. The Bi-2223 grain is in shape of a lamella as shown before (Figure 6), and its low degree of freedom in connecting with each other will be responsible for creating such low-dimensional cluster.

3.5. Summary

The Ag-added Bi-2223 (Bi-2223/Ag) is an eccentric composite in the sense that two kinds of ingredient grains considerably differ in their particulate morphology; the cuprate grain being in two-dimensional lamella (Figure 6) and Ag grain being roundish without such low-dimensionality.

The cluster of Ag phase has been found to percolate through the medium at the percolation threshold $f_{\mathrm{A,c}}$=0.25 (volume fraction of Ag), which is rather close to the threshold expected for the three-dimensional percolation. However, the critical exponent t has been observed as t=1.11, which approximates even to the universal value expected for 2D systems, while another exponent s is found to be s=0.66, which refers to the universal value for 3D systems. This variance is seen in common with other kinds of Ag (Au)-added cuprate composites. The observed variance seems to concern an effect of the conductivity ratio for Bi-2223 and Ag phases, and will be elucidated in the next section.

The clustering of Bi-2223 phase shows more anomalous behavior especially at temperature as low as T=77 K, exhibiting no contribution from the superconducting clusters, in spite of the temperature below T_{c}=110 K. However, as T is lowered, the superconducting feature appears stepwise, and eventually the power low with respect to ($f_{\mathrm{B,c}} - f_{\mathrm{B}}$) for Bi-2223 emerges at T=35 K, giving s=1.2. This behavior implies an effect of the superconducting weak-link between Bi-2223 grains, as will be demonstrated in the next section.

4. Characterization of Composites in Terms of Percolation

4.1. Effect of Conductivity Ratio on the Power Law

In this section we discuss how to characterize the composites in terms of the percolation theory. First we start with the foregoing issue on the power law for the Ag-phase in composite Bi-2223/Ag at room-temperature. The power law at issue is featured by t = 1.11 ($f_{\mathrm{A}} > f_{\mathrm{A,c}}$), and s = 0.66 ($f_{\mathrm{A}} < f_{\mathrm{A,c}}$) together with $f_{\mathrm{A,c}}$ = 0.25 [50]. The value of s almost agrees with the

Copyright © 2010. Nova Science Publishers, Incorporated. All rights reserved.

Handbook of Material Science Research, Nova Science Publishers, Incorporated, 2010. ProQuest Ebook Central,

expected value, i. e., the universal one (s=0.7 for 3D), but the observed t largely deviates from the universal one (t =2.0 for 3D). This discrepancy is observed in common with other cuprate composites (Table 3). The small values observed for t seem as if implying the universal value for 2D systems (see Table 3). This problem on the power law can be addressed from the scaling theory described in Sec. 2.

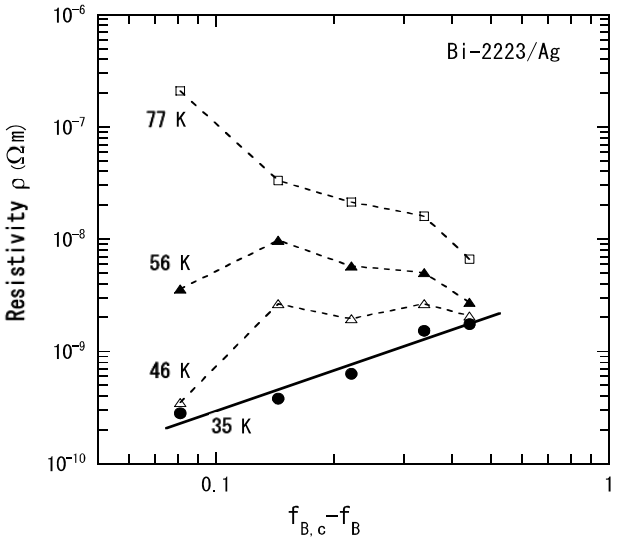


Figure 11. Transitional change of the resistivity ρ on lowering T from 77 K to 35 K, and the power law appearing at T=35 K, giving power exponent s=1.2; f_B is the volume fraction of Bi-2223 phase and the percolation threshold is $f_{B,c}$=0.57.

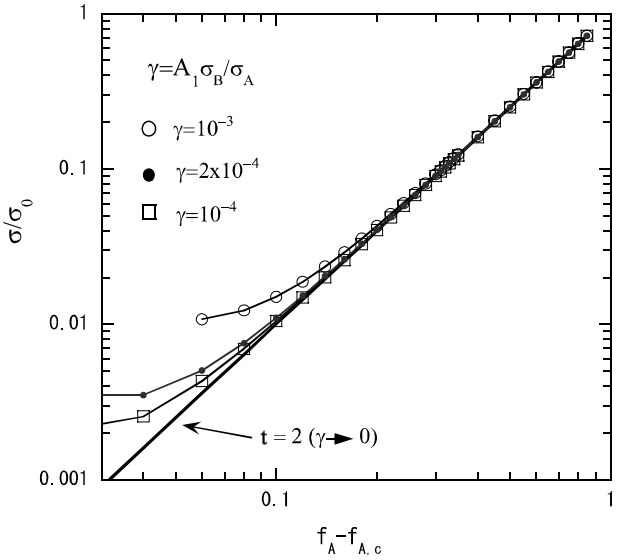


Figure 12. Deviation from the simple power law of the conductivity, calculated up to the second term including $A_1(\sigma_B/\sigma_A)$ in Eq. (38), where $\gamma=A_1\sigma_B/\sigma_A$ and $\sigma_0=\sigma_A F_+(0)$, and the curves are displayed for such a range of $(f_A-f_{A,c})$ as justifying the expansion in Eq. (38); the linear line refers to the simple power law with exponent t =2, which is given by the limit $\gamma\to 0$.

Copyright © 2010. Nova Science Publishers, Incorporated. All rights reserved.

Handbook of Material Science Research, Nova Science Publishers, Incorporated, 2010. ProQuest Ebook Central,

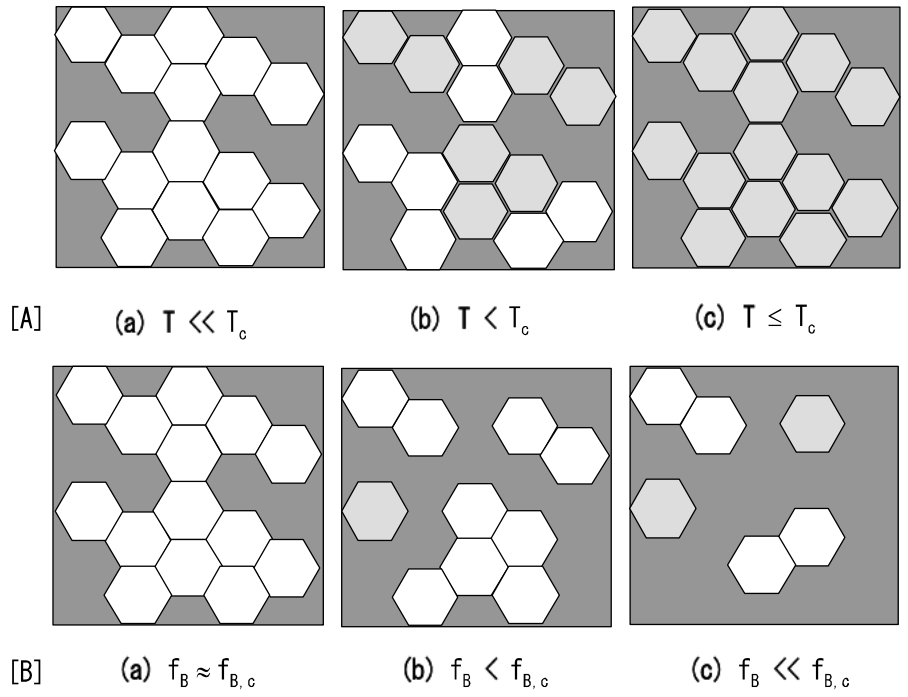


Figure 13. Two clustering-processes of superconducting grains: [A] Weak-link network extension of superconducting grains (light gray) by lowering temperature T [(c)→(b)→(a)], where grains are colored white when connected by the weak-ink at the gain boundary; [B] Growth of the superconducting cluster (white) with increasing f_B [(c) →(b) →(a)] at a sufficiently low temperature ($T << T_c$); isolated and connected grains of the superconducting phase are indicated by light gray and white, respectively; the dark background indicates the non-superconducting phase.

This strange variance implies that the single power low as given by Eqs. (33) and (34) is inapplicable to the present case. This problem is associated with the conductivity ratio σ_B/σ_A (<1) in composite of a good conductor A (Ag-phase) and a bad conductor B (Bi-2223 phase); in the present case, the Bi-2223 phase is a bad conductor because of the room temperature (290 K). For the composites listed in Table 3, the ratio σ_B/σ_A at room temperature is of the order of 10^{-4} to 10^{-3}. For such untrivial values of the ratio, the composite will no longer be regarded as a genuinely conductor-insulator mixture.

Let us examine the effect of the conductivity ratio on the power law [10, 50, 57–59]. Equations (6) and (7) in Sec, 2 are rewritten as Eq. (36), where the notation ± refers the ranges $f_A \geq f_{A,c}$ and $f_A \leq f_{A,c}$:

$$\sigma_{\pm} = \sigma_A \left| \boldsymbol{f}_A - \boldsymbol{f}_{A,c} \right|^t \boldsymbol{F}_{\pm} \left[\left| \boldsymbol{f}_A - \boldsymbol{f}_{A,c} \right|^{-(t+s)} \left(\frac{\sigma_B}{\sigma_A} \right) \right]. \tag{36}$$

When σ_B/σ_A is sufficiently small ($1>>\sigma_B/\sigma_A \neq 0$), so that

Copyright © 2010. Nova Science Publishers, Incorporated. All rights reserved.

Handbook of Material Science Research, Nova Science Publishers, Incorporated, 2010. ProQuest Ebook Central,

$$\left(\frac{\sigma_{\mathrm{B}}}{\sigma_{\mathrm{A}}}\right) < \left| f_{\mathrm{A}} - f_{\mathrm{A,c}} \right|^{t+s}, \tag{37}$$

the scaling function F can be expanded for such $\sigma_{\mathrm{B}}/\sigma_{\mathrm{A}}$ and (f_{A}–$f_{\mathrm{A,c}}$), as follows [50]:

For $f_{\mathrm{A}} > f_{\mathrm{A,c}}$,

$$\sigma_{+} = \sigma_{\mathrm{A}} \left(f_{\mathrm{A}} - f_{\mathrm{A,c}} \right)^{t} \left[F_{+}(0) + A_{1} \left(\frac{\sigma_{\mathrm{B}}}{\sigma_{\mathrm{A}}} \right) \left(f_{\mathrm{A}} - f_{\mathrm{A,c}} \right)^{-(t+s)} + A_{2} \left(\frac{\sigma_{\mathrm{B}}}{\sigma_{\mathrm{A}}} \right)^{2} \left(f_{\mathrm{A}} - f_{\mathrm{A,c}} \right)^{-2(t+s)} \cdots \right]$$

, (38)

and for $f_{\mathrm{A}} < f_{\mathrm{A,c}}$,

$$\sigma_{-} = \sigma_{\mathrm{A}} \left(f_{\mathrm{A,c}} - f_{\mathrm{A}} \right)^{-s} \left[B_{1} \left(\frac{\sigma_{\mathrm{B}}}{\sigma_{\mathrm{A}}} \right) + B_{2} \left(\frac{\sigma_{\mathrm{B}}}{\sigma_{\mathrm{A}}} \right)^{2} \left(f_{\mathrm{A,c}} - f_{\mathrm{A}} \right)^{-(t+s)} \cdots \right], \tag{39}$$

where the coefficients A_1(>0), B_1 (>0), B_2 (<0) and A_2 relate to the derivative of $F_{\pm}$ (x) with respect to x [50]. At the limit $\sigma_{\mathrm{B}}/\sigma_{\mathrm{A}} \rightarrow 0$, Eqs (38) and (39) are reduced to the simple power law, i. e. Eqs. (34) and (33) in terms of the resistivity ρ.

Figure 12 displays the logarithmic plot of Eq. (38) relevant to the exponent t, where the calculation is made up to the second term including $A_1 \sigma_{\mathrm{B}}/\sigma_{\mathrm{A}}$ ($\equiv\gamma$); the third term relevant to $(\sigma_{\mathrm{B}}/\sigma_{\mathrm{A}})^2$ and the higher ones are neglected. The curves are displayed for such a range of (f_{A}–$f_{\mathrm{A,c}}$) as is justified for the expansion of Eq. (38). The straight line refers to the limit $\sigma_{\mathrm{B}}/\sigma_{\mathrm{A}} \rightarrow 0$, giving t=2. For finite $\gamma \neq 0$, the plot appears nonlinear. Of particular interest is that according as the conductivity ratio $\sigma_{\mathrm{B}}/\sigma_{\mathrm{A}}$ (or γ) increases, the plotted curve inclines downward. Each of the non-linear curves can be approximately expressed by a linear line obtained by a numerical method based on the least square fitting, and thereby an effective exponent t* can be obtained from such an assigned line [50]. From the above result, it is concluded that the power law is sensitive to the value of the ratio $\sigma_{\mathrm{B}}/\sigma_{\mathrm{A}}$, and the effective exponent t* decreases with increasing $\sigma_{\mathrm{B}}/\sigma_{\mathrm{A}}$. Therefore, the low value of t (=1.11) is not resulted from the 2D percolation process, but from the 3D process involving untrivial contribution from the ratio $\sigma_{\mathrm{B}}/\sigma_{\mathrm{A}}$ ($\neq 0$).

However, a problem on another exponent s rises as to why, in spite of the untrivial ratio $\sigma_{\mathrm{B}}/\sigma_{\mathrm{A}}$, the exponent s is insensitive to $\sigma_{\mathrm{B}}/\sigma_{\mathrm{A}}$, taking the value ranging from 0.66 to 0.71 (Table 3), which are almost equal to the universal ones (s=0.7–0.73) in the 3D systems. Let us examine the case for $f_{\mathrm{A}} < f_{\mathrm{A,c}}$. The parenthesis […] in Eq. (39) does not include the constant term independent of the ratio, and the correction yielding a deviation from the single power law is given by the second term including $(\sigma_{\mathrm{B}}/\sigma_{\mathrm{A}})^2$, instead of the term including $(\sigma_{\mathrm{B}}/\sigma_{\mathrm{A}})$. Thus, the contribution from the conductivity ratio is less significant in this range $f_{\mathrm{A}} < f_{\mathrm{A,c}}$, yielding s insensitive to the conductivity ratio.

Copyright © 2010. Nova Science Publishers, Incorporated. All rights reserved.

Handbook of Material Science Research, Nova Science Publishers, Incorporated, 2010. ProQuest Ebook Central,

4.2. Clustering Processes of Superconducting Bi-2223 Phase

Here we discuss the clustering processes of Bi-2223 phase when it is superconducting. In this case, the power law becomes observable when the temperature is lowered down to T=35 K (Figure 11). In Eq. (39), the labels A and B can be exchanged, since the phase B (Bi-2223) is designated here as a good conductor. Since the Bi-2223 phase is superconducting, the conductivity ratio σ_A/σ_B reaches zero as $\sigma_B \to \infty$. Then, Eq. (40) is straightforwardly obtained from Eq. (39) by exchanging the labels:

$$\sigma_{-} = \sigma_0 \left(f_{B,c} - f_B \right)^{-s} \text{ for } f_B < f_{B,c}, \tag{40}$$

where $\sigma_0 \equiv \sigma_A B_1$.

Therefore, the exponent s is now free from the correction due to the conductivity ratio, and the value of s straightforwardly reflects the space dimension, that is, the observed s=1.2 indicates that the clustering of Bi-2223 phase has two-dimensional extension. This dimensionality accords with that implied by the observed percolation threshold $f_{B,c}$ =0.57, which is close to the threshold for the ideal 2D case (Table 2 in Sec.2).

Figure 13 schematically illustrates two clustering-processes of the superconducting grains. One process (Figure 13 [A]) concerns the weak-link network extension of superconducting clusters, where the cuprate grains are connected by the superconducting weal-link at the grain boundary. This weak-link connection spatially proceeds as T decreases [(c)→(b)→(a)] to extend the superconducting cluster at a given volume fraction f_B. Another process concerns the cluster growth with increasing f_B (Figure 13 [B]). As illustrated in [B], at sufficiently low temperatures, the superconducting grains are electrically connected by the weak link, and this percolative cluster is segmented stepwise by decreasing f_B (or increasing f_A). This situation refers to the case at T=35 K (Figure11), where the power law for the Bi-2223 phase is obvious. At temperatures as high as 77 K ($T<T_c$), the superconducting cluster near the threshold $f_{B,c}$, as depicted by Fig. 13 [A]-(b), are substantially divided into smaller pieces, owing to extremely faint weal-link at the grain boundary, so that the superconducting contribution is concealed. The intermediate transition observed in Figure 11 will be resulted from a combination of these processes.

The low-dimensional percolation process of the Bi-2223 cluster is closely related to the morphology of the Bi-2223 grain itself. As depicted in Figure 14, owing to the lamella shape of Bi-2223 grains (Figure 6), the degree of freedom of connection between the grains is geometrically restricted, giving two-dimensional extension of the clusters. The composite we have investigated is an eccentric material in the sense that two constituent phases are considerably different in morphology of the clusters. Therefore, some spatial buffer is requisite to mediate these morphologically disparate phases to form the percolative texture as described so far. The porosity with relatively high value as shown in Figure 7 will play a complementary role as such a buffer in the composite.

Copyright © 2010. Nova Science Publishers, Incorporated. All rights reserved.

Handbook of Material Science Research, Nova Science Publishers, Incorporated, 2010. ProQuest Ebook Central,

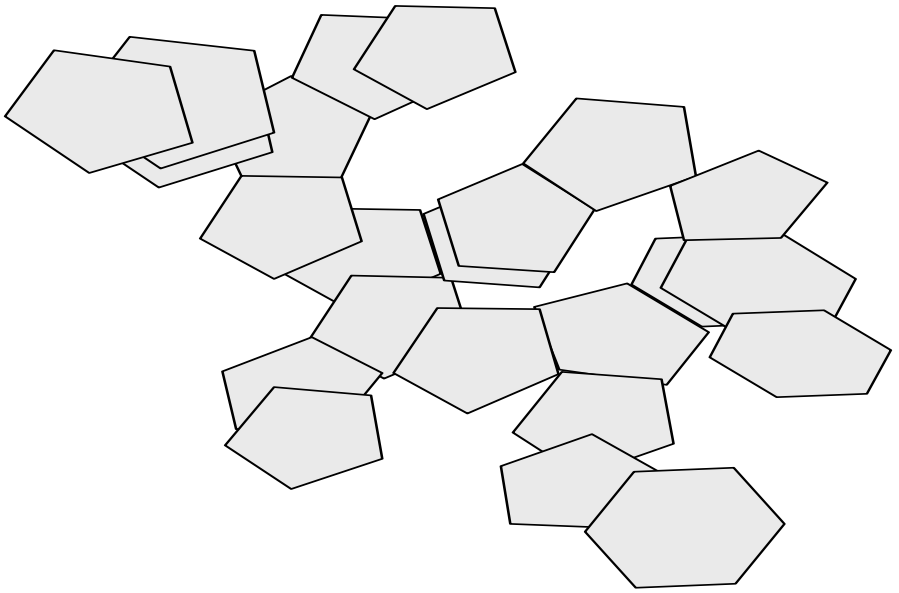


Figure 14. Two-dimensional clustering (schematic) of Bi-based cuprate grains, where the degree of freedom in connection of grains is low.

4.3. Textural Asymmetry Affecting the Percolation Threshold

The symmetry of the texture in a two-phase (*a*, *b*) composite means that the textural pattern at a given volume fraction $f_a = q$ is equivalent to the pattern at $f_a = 1-q$, the former and the latter being in the positive-negative relationship. Then, the percolation threshold $f_{b,c}$ with respect to the volume fraction f_b equals the threshold $f_{a,c}$ with respect to f_a. However, as seen for the Bi-2223/Ag composite, when the constituent phases are morphologically different, the texture becomes noticeably asymmetric, and one of the thresholds $f_{b,c.}$ is in variance with another $f_{a,c.}$ Therefore, in the characterization of composites, the structural dimensionality (2D or 3D) cannot be determined only from the observation of f_c. Such an asymmetric structure is more frequently seen for composites when a constituent phase granularly disperses; the most typical case is the dispersion structure of MGM, as describe in Sec. 2.

Figure 15 displays an effect of the granularity of conducting phase *a* on the effective conductivity σ^* of a metal-insulator composite (3D). The calculation was made by using the generalized effective medium model, i. e. Eq. (26) described in Sec. 2 [21]. As described there, the parameters α_1 and α_2 give a range where complex cells A and B coexist (Figure 3). As α_1 increases, the A-cells (i. e. granularity of phase *a*) keep existing up to a higher f_a. The percolation threshold f_c, indicating a sharp rise of σ^*, shifts to higher side of f_a, according as the granularity of the phase *a* lasts up to higher f_a, and can exceed even f_a=0.5 in spite of 3D. This result demonstrates that such high value of the percolation threshold as exceeding f_c=0.5 does not always indicate that the system is two-dimensional.

Copyright © 2010. Nova Science Publishers, Incorporated. All rights reserved.

Handbook of Material Science Research, Nova Science Publishers, Incorporated, 2010. ProQuest Ebook Central,

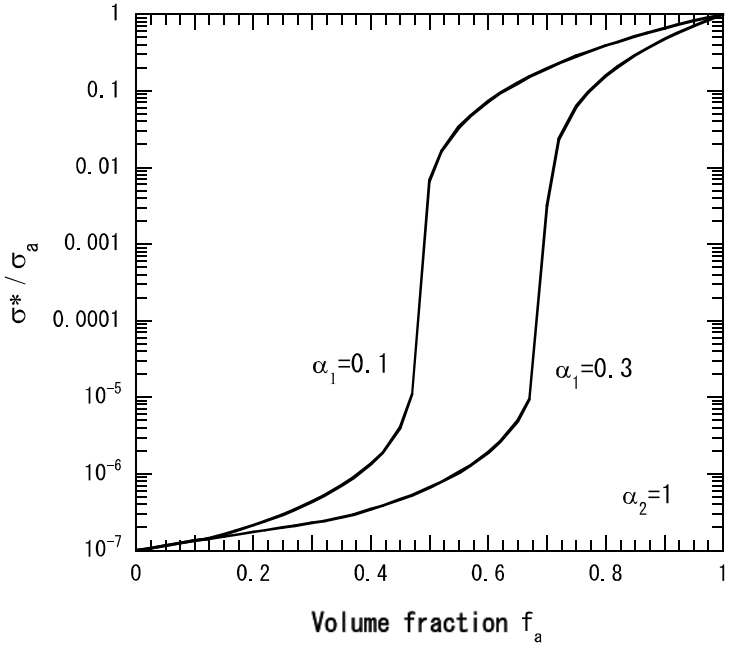


Figure 15. The effective conductivity σ^* (normalized with σ_a) depending on the degree of granularity of the conducting phase (phase *a* with volume fraction f_a), calculated from the effective medium model for 3D composite, i. e. Eq. (26) in Sec. 2 [1, 21]; as α_1 increases, granularity of phase *a* (cell A) lasts over a wider range of f_a, yielding higher percolation threshold f_c.

4.4. Summary

How to characterize the composite materials has been discussed in terms of the percolation factors: the percolation threshold, the power law exponents, *t* and *s*, and morphology of ingredient grains. On the basis of the scaling theory, the deviation of observed *t* from the universal value expected for the three-dimensional percolation is found to come from an effect of untrivial resistance-ratio for the two phases, but another exponent *s* is proved to be insensitive to the ratio. From this analysis, the clustering of Ag phase is found to be three dimensional, in spite of the low value of observed exponent *t*. As for Bi-2223 phase, the clustering is largely influenced by the superconducting weak-link together with the two-dimensional lamella shape of the grain. The cluster growing of Bi-2223 involves two processes: one is the extension of the weak link network, and another is the two-dimensional cluster growth with increasing volume fraction of Bi-2223 phase. The textural asymmetry in two-phase composites also largely affects the percolation transition. This effect is typically seen for the dispersion structure including a granular phase *a*. According to the generalized effective medium model (Sec.2), the percolation threshold f_c, is found to shift to higher side of f_a, according as the granularity of a conducting phase lasts up to higher f_a, It is pointed out that high value of the percolation threshold as exceeding f_c=0.5 does not always indicate low-dimensionality of the system.

Copyright © 2010. Nova Science Publishers, Incorporated. All rights reserved.

Handbook of Material Science Research, Nova Science Publishers, Incorporated, 2010. ProQuest Ebook Central,

5. MICROSCOPIC PERCOLATION PROCESS IN MIXED-CRYSTALLINE COMPOUND $R_{1-x}Pr_xBa_2Cu_3O_{7-\delta}$ (R: RARE EARTH)

5.1. Two-Dimensionality of the Superconducting Paths in Nanocomposite $R_{1-x}Pr_xBa_2Cu_3O_{7-\delta}$

In this section we focus on a microscopic percolation process, which has been found in the compound $R_{1-x}Pr_xBa_2Cu_3O_{7-\delta}$ (RPr-123) [60, 61, 62]; R denotes Y and rare earth elements (Gd, Nd, etc). This compound can be regarded as a mixed crystalline nanocomposite that consists of crystal unit cells of $RBa_2Cu_3O_{7-\delta}$ (R-123) and $PrBa_2Cu_3O_{7-\delta}$ (Pr-123). The nanostructural intermixture between two compounds R-123 and Pr-123 can easily be formed, because they are isostructural, as exhibited in Figure 16. The structure of R-123 can be converted into that of Pr-123 by only substituting Pr for rare earth element R. Of interest is that in spite of the crystallographic isostructure, the bulk of R-123 is good conductor and also becomes superconducting below the critical temperature $T_c = 92\sim96$ K, while that of Pr-123 is insulator having semiconductor-like resistivity as a decreasing function of temperature T. The superconductivity in R-123 is realized in the CuO_2 planes, to which mobile holes are provided from the CuO chains. The superconductivity suppression in Pr-123 is ascribable to localization of the mobile holes around Pr-site , which is caused by the hybridization between orbitals of Pr-4f and O-2p in the CuO_2 plane [63, 64, 65].

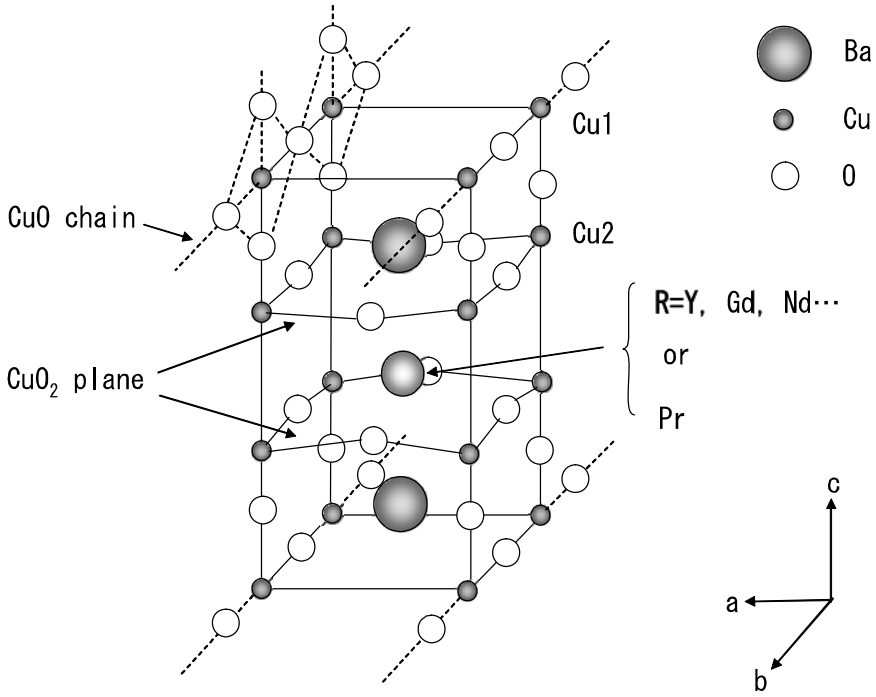


Figure 16. Crystal structure of $RBa_2Cu_3O_7$ (R-123) with CuO_2 planes and CuO chains; replacing R with Pr converts the crystal unit cell into that of $PrBa_2Cu_3O_7$ (Pr-123).

Copyright © 2010. Nova Science Publishers, Incorporated. All rights reserved.

Handbook of Material Science Research, Nova Science Publishers, Incorporated, 2010. ProQuest Ebook Central,

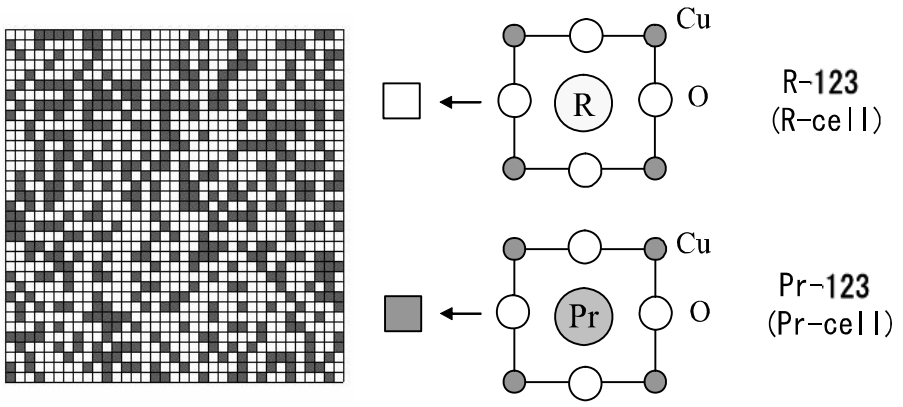


Figure 17. Percolation structure consisting of crystal unit-cells of *R*-123 (white squares) and Pr-123 (dark squares) in *R*Pr-123 when viewed from the *c*-axis direction, where each of unit cells depicted on the right hand side is represented by the CuO_2 plane with the site of *R* or Pr [60, 62, 69].

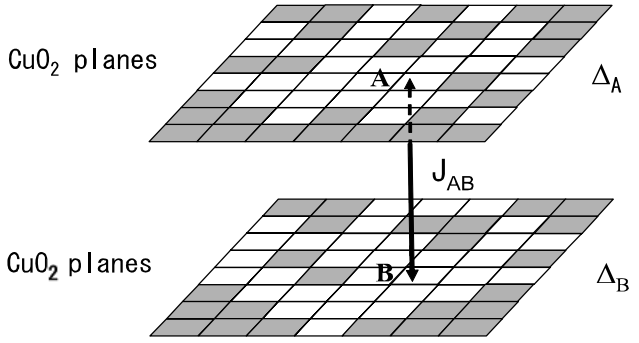


Figure 18. Tunneling Josephson current J_{AB} between upper and lower superconducting networks (white parts) on the sheets consisting of CuO_2 planes, where the upper and lower CuO_2 planes belong to upper and lower crystal-unit-cells adjoining each other along the *c*-axis direction; the gap parameters Δ_A and Δ_B at positions A and B become smaller with increasing *x*, so that J_{AB} also is weakened; this situation is also the case when upper and lower CuO_2 planes belong to the same unit cells ($\Delta_A=\Delta_B$).

In the compound *R*Pr-123, as the concentration *x* of Pr (or unit cell Pr-123) increases, the superconductivity degrades, and eventually disappears at a critical point x_c (superconductor-insulator (S-I) transition). The S-I transition due to Pr-doping was first observed for YPr-123, for which $x_c = 0.55$ [66]. The transition point x_c is dependent on ionic radius (r_i) of the rare earth *R*, decreasing with increasing r_i [62, 67, 68]. The superconductivity suppression caused by substituting Pr for *R* is associate with the foregoing localization of mobile holes around Pr ion. However, understanding of how the S-I transition occurs on increasing *x* and how the ionic radius r_i plays a role in determining the transition point x_c has been a long standing issue. Recently, a light has been shed on this issue to unveil the basis of this phenomenon in terms of a nonclassical percolation [62]; where the crystal-unit-cell of *R*-123 changes with the aid of the orbital hybridization its identity when adjoining unit-cells of Pr-123 (Pr cell), so that virtual percolation thresholds (x_2, x_1) are created instead of the classical thresholds (x_{pc2},

Copyright © 2010. Nova Science Publishers, Incorporated. All rights reserved.

Handbook of Material Science Research, Nova Science Publishers, Incorporated, 2010. ProQuest Ebook Central,

x_{pc1}) [60]. This nonclassical percolation model can explain the S-I transition coupled with the ionic size effect [62].

Before addressing this issue, let us inspect whether the superconducting sheet consisting of CuO_2 planes in *R*Pr-123 is electronically two-dimensional as it looks. In *R*Pr-123, the unit cells of *R*-123 and Pr-123 (Figure 16) are arrayed in the *a*-*b* plane (CuO_2 sheet) normal to the *c*-axis direction, and the crystal axes of these cells are commonly oriented to the same directions. Figure 17 exhibits a two-dimensional array of these unit cells when viewed from the *c*-axis direction [60]. The clusters of *R*-123 crystal unit cells (*R* cells) are denoted by white squares and those of Pr-123 unit cells (Pr cells) are denoted by gray squares. The CuO_2 sheet just underlies this pattern. The superconductivity is propagated along this two-dimensional CuO_2 sheet. However, the superconductivity is known to occur in also the normal direction (*c*-axis) in bulk *R*-123. Such superconductivity will be caused by the intrinsic Josephson tunneling between upper and lower CuO_2 sheets; the upper and lower CuO_2 planes constituting the sheets may belong to the same crystal unit of *R*-123 or to different unit cells of adjoining each other along the *c*-axis direction. If the tunneling is stout in the *c*-axis direction, the superconductivity in *R*Pr-123 will exhibit three-dimensional character. However, this prepossessed view will be ruled out in Pr-substituted cuprates from the following reason.

The Josephson tunneling current J_t is caused by the phase difference (θ_1–θ_2) between superconducting banks (labeled 1 and 2), between which a thin insulator layer is sandwiched:

$$J_t = J_0 \sin(\theta_1 - \theta_2) \ . \tag{41}$$

The maximum tunneling current J_0 depends on the gap parameters Δ_1 and Δ_2 of the superconducting banks [70], and for T=0 K it is expressed as:

$$J_0 = \frac{2}{eR_n} \frac{\Delta_1 \Delta_2}{(\Delta_1 + \Delta_2)} K\left(\frac{|\Delta_1 - \Delta_2|}{\Delta_1 + \Delta_2} \right), \tag{42}$$

where R_n is the normal tunneling resistance when the banks on the both sides are normal conductors, and $K(x)$ is the first type elliptic function of x. If $\Delta_1 = \Delta_2 = \Delta(T)$ and $T \neq 0$ K, then J_0 is given by Ambegaokar and Baratoff 's formula [71]:

$$J_0 = \frac{\pi}{2} \frac{\Delta(T)}{eR_n} \tanh\left[\frac{\Delta(T)}{2k_B T} \right] . \tag{43}$$

When T=0 K and $\Delta_1 \approx \Delta_2$, Eq. (42) is reduced to a simple form:

$$J_0 \cong \frac{\pi}{eR_n} \frac{\Delta_1 \Delta_2}{(\Delta_1 + \Delta_2)} \ . \tag{44}$$

This formula indicates that according as the gap parameter of the banks decreases, the tunneling current J_0 decreases. The issue is now turned to the gap parameters in the percolative structure.

Copyright © 2010. Nova Science Publishers, Incorporated. All rights reserved.

Handbook of Material Science Research, Nova Science Publishers, Incorporated, 2010. ProQuest Ebook Central,

In the inhomogeneous structure (Figure 17), the gap parameter is no longer uniquely determined, varying from place to place in the CuO_2 sheet. This position dependent gap-parameter $\Delta(r)$ will be smaller in a smaller area of the superconducting cluster, as illustrated in Figure 18. In other words, with increasing x, the superconducting cluster becomes thin so that $\Delta(r)$ at a given position will become small. Thereby the tunneling coupling between A and B becomes weak. Thus, the superconducting CuO_2 sheet in *R*Pr-123 is well defined as being two dimensional. This means also that the inhomogeneous mixed-crystalline structure in *R*Pr-123 (Figure 17) can be regarded as a two-dimensional site-percolation system.

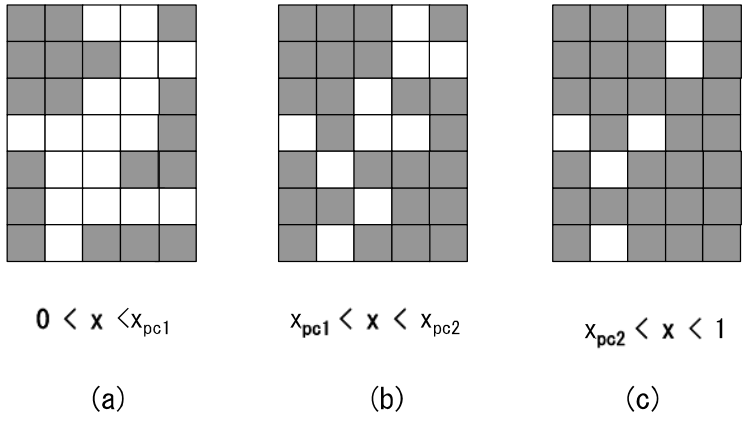


Figure 19. Conducting paths characteristic of the range of Pr-concentration x in the two dimensional site percolation structure consisting of crystal unit cells (more strictly CuO_2 planes) of *R*-123 (white) and Pr-123 (dark gray); in the classical scheme, the first and second percolation thresholds are x_{pc1}=0.407 (≈0.41) and x_{pc2}=0.5927 (≈0.59) [60, 62].

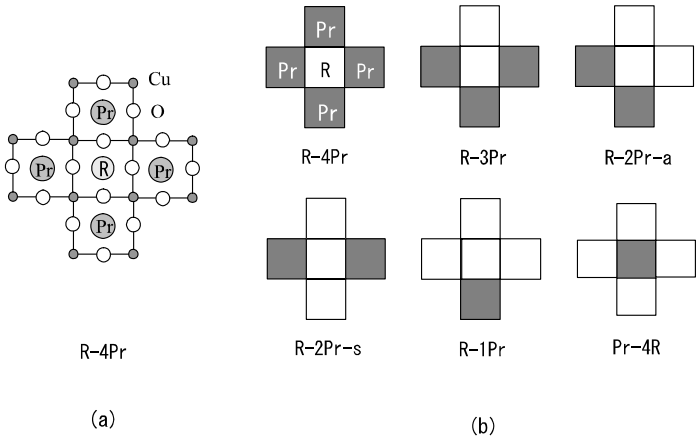


Figure 20. Configurations of CuO_2 planes in crystal unit-cells of *R*-123 and Pr-123 when the centered cell (CuO_2 plane) can be converted; (a) *R*-123 cell is surrounded by Pr-123 cells, and (b) various types of configurations for the cell conversion (Pr-4*R* is the reversion of *R*-4Pr) [60, 62].

Copyright © 2010. Nova Science Publishers, Incorporated. All rights reserved.

Handbook of Material Science Research, Nova Science Publishers, Incorporated, 2010. ProQuest Ebook Central,

5.2. Model of Nonclassical Percolation with the Aid of Orbital Hybridization in the Nanostructure of *R*Pr-123

In the classical scheme, the '*go* board' pattern as displayed in Figure 17 represents a typical two-dimensional site percolation structure with the first percolation threshold x_{pc1}=0.407 (≈0.41) and the second one x_{pc2}=0.5927 (≈0.59) [60]. As schematically shown in Figure 19, in the region $x < x_{pc1}$, the conducting path (type 1) is made of *R*-123 cells (white squares) which join each other at their lateral faces; the first nearest connection between adjoining *R*-123 cells. In the higher region $x_{pc2} > x > x_{pc1}$, the conducting path (type 2) is built by joining *R*-123 cells not only with the first nearest-neighbor connection but also with the second nearest-neighbor one [60]. In the highest region $x > x_{pc2,}$ the path of type 2 is broken. We assume here that the unit cell of Pr-123 plays as a block against the superconducting current (or Josephson tunneling), because of Coulomb blockade due to the holes locally trapped by the orbital hybridization around Pr site. The superconducting current is assumed to pass along these conducting paths consisting of *R*-123 cells; more precisely, the superconductivity is propagated along the path made of the CuO_2 planes of *R*-123 cells [60].

The above nanostructure system is more pregnant in physics than the classical system, of which structural ingredients are mechanically tiled as in bricklaying. A basic feature of the system is the orbital sharing between adjacent crystal unit cells of *R*-123 and Pr-123. Now we show below a case of $Y_{1-x}Pr_xBa_2Cu_3O_{7-\delta}$ (YPr-123), i. e., the nanocomposite consisting of Y-123 and Pr-123.

As depicted in Figure 20 (from now on, we put *R*=Y), when an isolated unit-cell of Y-123 adjoins four Pr-cells at lateral faces (Y-4Pr), the O-2*p* orbital in CuO_2 plane of the centered Y-123 cell is shared with the surrounding Pr-cells. Then the orbitals $2p_\pi$ of O ions will hybridize with the 4*f* orbitals of Pr ions, so that the centered Y-123 cell (i. e., its CuO_2 planes) will lose its initial electronic identity, that is, the holes will be localized also around the centered Y-123 cell. Then this centered cell changes into a different cell that behaves as if it were a Pr-123 cell [62]. On the other hand, when an isolated Pr-123 cell adjoins four Y-123 cells at lateral faces (Pr-4*R*), the O-2p orbitals in CuO_2 plane are shared with all of them, and the $4f$-$2p_\pi$ hybridization initially realized in the centered Pr-123cell may be released so that this centered will also be converted into a different cell behaving as if it were a Y-123 cell [62]; however, this is not the case with larger ionic size of *R* having 4*f* electrons. Therefore the effective concentration x^* of Pr (or effective fraction x^* of substantial Pr-cells including the converted cells) is given by the formula [62]:

$$x^* = x + x^4(1-x) - x(1-x)^4 . \tag{45}$$

The effective critical point x_2 for the S-I transition as described in Subsection 5.1 is then approximately obtained from the solution of the equation $x^*=x_{pc2}$ [62]. On the other hand, the solution of $x^*=x_{pc1}$ with regard to the first percolation threshold indicates a characteristic point x_1 which appears in the diamagnetic susceptibility as a function of x [62]. It should be noticed that these solutions are approximate to the exact values of x_2 and x_1, because the cell conversion stated above introduce incompleteness more or less in the structural randomness of the percolation system. From now on, these two types of critical points (x_2, x_1) relevant to x_{pc2} and x_{pc1} are referred to as virtual percolation thresholds.

Copyright © 2010. Nova Science Publishers, Incorporated. All rights reserved.

Handbook of Material Science Research, Nova Science Publishers, Incorporated, 2010. ProQuest Ebook Central,

Figure 21 exhibits the experimental observation of the virtual percolation thresholds (x_2 and x_1) for YPr-123 at T=4.2 K; the thresholds emerge as characteristic points in the diamagnetic susceptibility χ as a function of x [60, 69]. It is to be noted that the dependence of χ on the ac magnetic field h is considerable in the range bounded by the virtual thresholds x_2 and x_1, instead by the classical thresholds x_{pc2} and x_{pc1}. The locations of x_2 and x_1 in the curve have been observed to remain visible up to temperature as high as 30 K [62]. Although the samples were polycrystalline, as is the case for most of the experimental studies on the S-I transition in *R*Pr-123, the deteriorative influence from the grain boundary will be concealed, because the superconductivity itself inside the grain is highly depraved owing to the presence of Pr [62].

The virtual percolation thresholds calculated from Eq. (45) are x_2=0.566 and x_1=0.435, which are quite close to the experimental values x_2=0.55 and x_1=0.44 in Figure 21. The computer simulation on the site percolation structure undergoing the cell conversion was also performed to find these virtual thresholds, giving x_2=0.554 and x_1=0.446, which are a little closer to the experimental values [62].

The above experimental result supports the present model based on the cell conversion, which explains the extremely localized behavior of the superconductivity that reflects the percolation on the nanometer scale. This implies from this behavior that the current path as narrow as the crystal unit cell is capable of propagating the superconductivity. This surprising feature is seen also for other Pr-substituted cuprate *R*Pr-123, though the virtual thresholds x_2 and x_1 change, depending on the ionic size of *R*. Probably the superconducting coherency in such small area might be sustained by the Cu(2) spin lattice in the CuO_2 sheet embracing *R*-123 and Pr-123 cells as the background of the superconducting path [62].

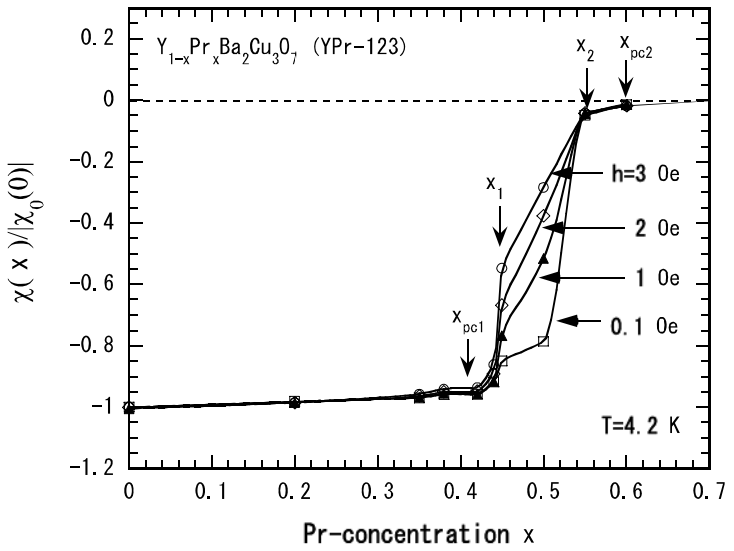


Figure 21. Diamagnetic susceptibility χ (normalized with the value at x=0 and h=0.1 Oe) as a function of x for YPr-123 at T=4.2 K; x_{pc2} and x_{pc1} are the classical percolation thresholds and x_2 and x_1 are virtual percolation thresholds (observed as x_2=0.55 and x_1=0.44); h indicates ac magnetic fields (rms).

Copyright © 2010. Nova Science Publishers, Incorporated. All rights reserved.

Handbook of Material Science Research, Nova Science Publishers, Incorporated, 2010. ProQuest Ebook Central,

5.3. Effect of Ionic Size on the Superconductor-Insulator Transition in *R*Pr-123

The model described above, as it stands, is inapplicable to more general case of *R*Pr-123 when *R* has a larger ionic size, because the S-I transition takes place at a lower value of x_2 for a larger ionic size. Recently, in order to resolve this ionic size effect, the nonclassical percolation model has been developed into a more general form by extending the configuration for the cell conversion due to $4f$-$2p_\pi$ hybridization [62].

Figure 20 depicts the configurations (*R*-*n*Pr) for converting the centered *R*-123 cell in contact with *n* Pr cells. The rare earth elements such as Nd, Eu, Gd have 4*f* orbitals in contrast to Y without 4*f* orbital. As the ionic radius *r* of *R* increases, the 4*f* orbital will also spatially extend. This will make the hybridization between *R*-4*f* and O-2p orbitals occur in cooperation with neighboring 4*f* orbitals from Pr ions [62]. Different to the case of YPr-123, for *R* having 4*f* orbitals extending large, the reverse configurations Pr-n*R* (Figure 20 (b)) are assumed to be ineffective for releasing the hybridization around the centered Pr-123 cell, and are neglected below. The centered *R*-123 cell is more easily converted by increasing the ionic size of *R* into a different cell behaving as if it were Pr-123 cell. This is explained by the view that the number of the configurations pertaining to the cell conversion increases stepwise with increasing ionic size of *R*.

The virtual thresholds x_2 and x_1 are approximately estimated from the effective concentration equation in the form [62]:

$$x^* = x + \sum_{n=1}^{4} k_n C_n (1-x)^{5-n} x^n \qquad (4 \geq n \geq 1)\,, \tag{46}$$

where C_4=1, C_3=C_1=4 and C_2=6, and the coefficient k_n denotes the contribution from the configuration *R*-*n*Pr to the cell conversion, and takes 1 or 0 according to the ionic size, as displayed in Table 4; as for *R*-2Pr, however, k_2=2/3 or 1/3 for *R*-2Pr-a or *R*-2Pr-s. The thresholds x_2 and x_1 are obtained by putting x^*=x_{pc2} and x^*=x_{pc1} in Eq. (46) [62].

Table 4. Ionic size of rare earth R^{3+} and assignment of configurations *R*-*n*Pr and coefficients k_n to classified ionic size; for details, see Ref. 62

	Class 1	Class 2	Class 3	Class 4
Ionic radius (Å) of R^{3+} (eightfold configuration)	Nd: 1.11	Eu: 1.07, Sm:1.08	Gd: 1.05	Y: 1.02 Ho:1.02 Dy: 1.03
Configurations for cell conversion	*R*-4Pr, *R*-3Pr, *R*-2Pr-a, *R*-2Pr-s	*R*-4Pr, *R*-3Pr, *R*-2Pr-a	*R*-4Pr, *R*-3Pr	*R*-4Pr, Pr-4*R*
Coefficients k_n	k_4=k_3=k_2=1, k_1=0	k_4=k_3=1, k_2=2/3, k_1=0	k_4=k_3=1, k_2=k_1=0	k_4=1 and see Eq.(45) k_3=k_2=k_1=0

Copyright © 2010. Nova Science Publishers, Incorporated. All rights reserved.

Handbook of Material Science Research, Nova Science Publishers, Incorporated, 2010. ProQuest Ebook Central,

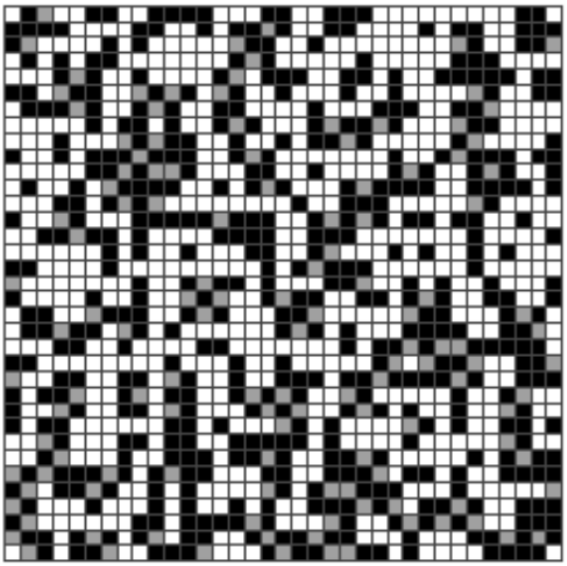


Figure 22.The nonclassical percolation structure subjected to the cell conversion due to *R*-4Pr and *R*-3Pr at x=0.4 (Class 3 in Table 4); the white and dark squares are *R*-123 cells and Pr-123 cells, respectively, and the light gray squares are converted *R*-123 cells; the periodic boundary condition was applied: the case of Class 1is demonstrated in Ref. 62.

In addition, the simulation on the computer-generated percolation structure involving the cell conversion for various configurations (Figure 20) has been performed under the periodic boundary conditions [62]. The simulated values of x_2 and x_1 are found to be a little closer to the experimental values than the calculated ones, as shown below. Figure 22 exhibits a pattern produced by a computer simulation for the nonclassical percolation structure subjected to the cell conversion due to configurations *R*-4Pr and *R*-3Pr at x=0.4 (Class 3, *R*=Gd). Owing to the cell conversion, the nonsuperconducting region (dark part) is noticeably extended, giving lower percolation threshold x_2. Such extension of the nonsuperconducting region is the most considerable for the configurations *R*-4Pr, *R*-3Pr, *R*-2Pr-a, *R*-2Pr-s (Class 1 in Table 4), yielding much lower x_2 [62].

The values of x_2 for Class 1–4 (Table 4) have been obtained from the nonclassical percolation model by calculation (x_2^{cal}) and simulation (x_2^{sim}). Those are compared with experimental values (x_2^{ex}) as below (the results are detailed in Ref. 62), where three values in a parenthesis indicate (x_2^{ex}, x_2^{cal}, x_2^{sim}) : (0.3–0.32, 0.33 0.3) for Class 1; (0.35–0.42, 0.37, 0.4) for Class 2; (0.45, 0.46, 0.45) for Class 3; (0.55–0.57, 0.57, 0.55) for Class 4. It may be said that theoretical values due to the model are in agreement with experimental values.

Finally, the cell conversion due to the orbital hybridization creates another effect with respect to the diamagnetism. With the aid of the 4*f*-2*p* hybridization, the magnetic moment of the R^{3+} in the converted cell will also take part in the superexchange interaction with neighboring Pr^{3+} (or such converted R^{3+}) via the oxygen (*R*-O-Pr), and thereby substantially contribute to the spatial spread of the antiferromagnetic ordering region with respect to Pr^{3+} [62]. Therefore, the Néel critical point x_N(Pr) at which Néel temperature T_N(Pr) begins to rise will also decrease with decreasing x_2.

Copyright © 2010. Nova Science Publishers, Incorporated. All rights reserved.

Handbook of Material Science Research, Nova Science Publishers, Incorporated, 2010. ProQuest Ebook Central,

5.4. Summary

The superconductivity in the mixed-crystalline nanostructure of *R*Pr-123 is largely featured by the CuO_2 orbital sharing between the crystal unit cells of *R*-123 and Pr-123; thereby the electronic identity of the relevant cells is not necessarily retained. Of particular importance is the $4f$-$2p_\pi$ orbital hybridization in the CuO_2 plane occurring when *R*-123 cell adjoins the Pr-123 cells. By the hybridization, such *R*-123 cell is changed into a different cell behaving as if it were Pr-123 cell, so that this converted cell gives no contribution to the superconductivity. For *R* having larger ionic size, the cell conversion occurs for the centered *R*-123 cell alone, but takes various types of cell configurations according to the ionic size: *R*-4Pr, *R*-3Pr, *R*-2Pr-a, *R*-2Pr-s, *R*-1Pr. The cell conversion changes the fraction of superconducting cells, creating virtual percolation thresholds: the second threshold x_2 giving the S-I transition and the first threshold x_1. The number of the configurations for cell conversion increases with increasing ionic size, yielding the ionic size effect on the S-I transition.

The antiferromagnetic ordering due to Pr^{3+} spins is also influenced by the cell conversion, because the spin of R^{3+} in the converted cell also takes part in the superexchange interaction with that of Pr^{3+} via the relevant O ion. Hence, the critical concentration x_N of Pr, at which Néel temperature begins to rise, decreases with decreasing x_2.

Finally, the nonclassical percolation model based on the idea of the cell conversion with the aid of $4f$-$2p_\pi$ hybridization provides comprehensive understanding of the S-I transition coupled with the ionic size effect in *R*Pr-123.

6. CONCLUSIONS

In this review article, the percolation processes have been shown to yield various transport phenomena in the cuprate compounds with close reference to the space dimension (2D or 3D) and the scale resolution (order of micron or nanometer) of the structural inhomogeneity in the media. First, as a macroscopic percolation system, we focused on Ag-added Bi-2223 composite. This type of composite (Bi-2223/Ag) is an eccentric composite in the sense that two kinds of ingredient grains considerably differ from each other in their particulate morphology; the cuprate grain being in two-dimensional lamella and Ag grain being roundish without such low-dimensionality. Next, as a microscopic percolation system, we focused on mixed-crystalline compound *R*Pr-123, which consists of two kinds of crystal unit cells *R*-123 and Pr-123. In this system, genuinely two-dimensional percolation takes place in the sheet consisting of CuO_2 planes. The percolation process appears to be nonclassical, where the crystal unit cell loses its electronic identity under special configuration of unit cells, being converted by the $4f$-$2p$ hybridization into different type of the unit cell. The contents and conclusions described in Sections 2–5 are summarized as follows.

In Sec.2, the percolation processes on the growth of clustering of structural ingredients in two-phase composites are overviewed, with enhancement on the significance of the percolation transition and the critical behavior depicting the power laws of structural quantities and physical properties. The power laws are derived from the scaling hypothesis

Copyright © 2010. Nova Science Publishers, Incorporated. All rights reserved.

Handbook of Material Science Research, Nova Science Publishers, Incorporated, 2010. ProQuest Ebook Central,

pertain to the phase transitions, and the transport critical exponent t, which strongly depends on the space dimension, can closely be related to the network structure in the percolation structure. In addition, a generalized effective medium model based on structural features of two-phase composites is described for explaining the percolation transition observed for actual meta-insulator composites.

As exhibited in Sec. 3, in the Ag-added Bi-2223 composites, the cluster of Ag phase has been found to percolate through the medium at the percolation threshold $f_{A,c}$=0.25 (volume fraction of Ag), which is rather close to the threshold expected for the ideal 3D percolation. However, the critical exponent t has been observed as t=1.11, which implies as if the composite were a 2D system, while another exponent s is found to be s=0.66 indicative of a 3D system. This observed variance is ascribable to an effect of untrivial conductivity ratio for Bi-2223 and Ag phases. The clustering of Bi-2223 phase shows more anomalous behavior especially at temperature as high as T=77 K, exhibiting no sign of the superconductivity, in spite of T lower than T_c=110 K. However, as T is lowered further, the superconducting contribution appears stepwise, and eventually shows the power low with respect to the volume fraction f_B of Bi-2223. This behavior is explained in terms of the superconducting weak-link between adjacent grains.

As shown in Sec. 4, how to characterize the composites has been discussed in terms of the percolation factors: the percolation threshold, the power law exponents, t and s, and morphology of ingredient grains. The deviation of observed t from the universal value expected for the 3D percolation is found to come from an effect due to untrivial conductivity-ratio of the two phases, but another exponent s is found to be insensitive to the ratio. From this analysis, the clustering of Ag phase is found to be three dimensional, in spite of the low value of observed t. As for superconducting Bi-2223 phase, the clustering is largely influenced by the superconducting weak-link together with the two-dimensional lamella shape of the grain. The cluster growing of Bi-2223 involves two processes: One is the extension of the weak link network, and another is the two-dimensional cluster growth with increasing volume fraction of Bi-2223 phase. The textural asymmetry in two-phase composites also largely affects the percolation transition. As demonstrated by a generalized effective-medium model, the above effect is typically seen for the dispersion structure including a granular phase.

As described in Sec. 5, when going into a more microscopic percolation system as realized in the mixed-crystalline compound RPr-123, we can see a quite different scene realized there. In this nanometric compound, the superconducting clusters are thinned by the presence of Pr, so that the relevant gap parameters in the CuO_2 sheets are reduced, resulting in faint Josephson-coupling between adjacent sheets. Therefore, the superconductivity is well characterized as being two-dimensional, and so the compound RPr-123 itself is regarded as a two-dimensional site percolation system. The percolation process there is largely featured by the CuO_2 orbital sharing between the crystal unit cells of R-123 and Pr-123. This orbital sharing can convert, by invoking the $4f$-$2p_\pi$ hybridization, the R-cell adjoining Pr-cells into a different cell behaving as if it were Pr-cell. This cell conversion creates virtual percolation thresholds x_2 and x_1. Construction of the superconducting path is largely affected by this cell conversion, and the S-I transition is determined by the virtual percolation threshold x_2. The cell conversion becomes easy as the ionic size of R^{3+} increases, giving the ionic size effect of the S-I transition. This nonclassical percolation can also describe the behavior of the Néel

Copyright © 2010. Nova Science Publishers, Incorporated. All rights reserved.

Handbook of Material Science Research, Nova Science Publishers, Incorporated, 2010. ProQuest Ebook Central,

point for the antiferromagnetism of Pr^{3+}. The above nonclassical percolation model implies that the localized superconductivity can be realized in extremely small area in the cuprates.

ACKNOWLEDGMENTS

The present author would like to thank the students and the staff at his laboratory in Graduate School of Energy Science, Kyoto University for their collaboration and helps during the course of the studies reviewed in this article. The author would also like to appreciate the support for the studies from Institute of Atomic Energy, Kyoto University (currently renamed Institute of Advanced Energy), where a part of the studies was implemented.

REFERENCES

[1] Yoshida, K. *J. Phys. Soc. Jpn*. 1990, *vol. 59*, 4087-4095.
[2] Essam, J. W. (1972). Percolation and Cluster Size (Chap. 6). In C. Dom, and M. S. Green (Eds.), *Phase Transition and Critical Phenomena* Vol. 2, London; Academic Press Inc.
[3] Stauffer, D. and Aharony, A. (1992). Introduction to Percolation Theory (2nd ed.). London, Washington, DC; Taylor and Francis.
[4] Bunde, A. and Havlin, S. (1991). Percolation I. In A. Bunde, and S. Havlin (Eds.), *Fractals and Disordered Systems,* Berlin, New York, London, Paris, Tokyo; Springer-Verlag.
[5] Straley, J. P. (1983). Scaling Predictions for Physical Properties. In G. Deutscher., R. Zallen, and J. Adler (Eds.), *Percolation Structures and Processes*: Israel Physical Society and American Institute of Physics.
[6] Adler, D.; Flora, L. P., and Senturia, S. D. *Solid State Com.,* 1973, *vol. 12,* 9-12.
[7] Grannan, D. M.; Garland, J. C.; Tanner, D. B., *Phys. Rev. Lett.* 1981, *vol. 46,* 375-378.
[8] Yoshida, K. *Jpn. J. Appl. Phys.*, 1991, *vol. 30,* 3482-3483.
[9] Straley, J. P. J. *Phys. C*, 1976, *vol. 9,*783-795.
[10] Bergman, D. J.; Imry, Y. *Phys. Rev. Lett.* 1977, *vol. 39,* 1222-1225.
[11] Stanley, H. E. *J. Phys. A*, 1977, *vol. 10*, L211-L220.
[12] Yoshida, K. *Materia Japan*, 1994, *vol. 33*, 133-137.
[13] Kapitulnik, A.; Deutscher, G., Phys. Rev. Lett., 1982, *vol. 49*, 1444-1448.
[14] Skal, A.; Shklovskii, B. I. *Soviet Phys. Semicond*., 1975, *vol. 8*, 1029.
[15] de Gennes, P. G. *J. Physique Lett.*, 1976, *vol. 37*, L1.
[16] Coniglio, A. *Phys. Rev. Lett.,* 1981, *vol. 46*, 250-253.
[17] Coniglio, A. J. *Phys. A,* 1982, *vol.* 15, 3829-3844.
[18] Bruggeman, D. A. G., *Ann. Phys., Lpz.,* 1935, *vol. 24*, 636.
[19] Landauer, R., *J. Appl. Phys.*, 1952, *vol. 23*, 779-784.
[20] Maxwell, J. C., *A Treatise on Electricity and Magnetism* (Chap. IX): Dover Pub. Inc.: New York, 1954, *vol*.1; reproduction of the 3rd Edition, published by the Clarendon Press in 1891).
[21] Yoshida, K. *Philos. Mag. B*, 1986, *vol. 53*, 55-67.

Copyright © 2010. Nova Science Publishers, Incorporated. All rights reserved.

Handbook of Material Science Research, Nova Science Publishers, Incorporated, 2010. ProQuest Ebook Central,

[22] Yoshida, K. *J. Phys. C,* 1982, *vol. 15*, L87-L91; *ibid.* 1983, *vol. 15*, L1023.
[23] Lux, F., *J. Materials Science*, 1993, *vol. 28*, 285-301.
[24] Zivkovic, Lj.; Nikolic, Z.; Boskovic, S; Miljkovic, M, *J. Alloys and Compounds,* 2004, *vol. 373,* 231-236.
[25] Yoshida, K,; Tomii, Y.; Ueda, S., *Jpn. J. Appl. Phys.*, 1988, *vol. 27,* 2224-2226.
[26] Yoshida, K., *Fractals,* 1996, *vol. 4*, 175-180.
[27] Yoshida, K.; Ueda, S., *Material Science Res. Inter.*, 1995, *vol. 1*, 114-119.
[28] Garncarek, Z.; Piasecki, R.; Borecki, J.; Maj, A.; Sudol, M., *J. Phys. D,* 1996, *vol. 29*, 1360-1366.
[29] He, Y.; Wei, Y.; Zheng, G.; Yu, M.; Liu, M., *J. Appl. Phys.,*1997, vol. *82,* 3408-3413.
[30] Piasecki, R.; Ziembik, Z.; Waclawek, W.: Zabkowska-Waclawek, M., *phys. stat. sol. (a),* 1991, *vol. 123*, K145-K148.
[31] Piasecki, R.; Ziembik, Z.; Waclawek, W.: Zabkowska-Waclawek, M., *phys. stat. sol. (a),* 1991, *vol. 128,* K109-K112.
[32] Bera, S. K.; Chaudhuri, S.; Pal, A. K., *J. Phys. D,* 2000, *vol. 33,* 2320-2326.
[33] Gerber, A.; Grenet, T.; Cyrot, M.; Beille, J., *Phys. Rev. Lett.,* 1990, *vol. 65,* 3201-3204.
[34] Yoshida, K., *J. Phys. Soc. Jpn.,* 1990, *vol. 59*, 4405-4411.
[35] Matsubara, H,; Tanigawa, T.; Ogawa, T.; Yamashita, H.; Kinoshita, M.; Kawai, T., *Phys. Rev. B*, 1992, *vol. 45,* 7414.
[36] Li, Q.; Suenaga, M.; Hikita, T.;Sato, K., *Phys. Rev. B*, 1992, *vol.46*, 5857-5860.
[37] Gallagher, W. J., *J. Appl. Phys.,* 1988, *vol. 63*, 4216-4219.
[38] Larbalestier, D.; Gurevich, A.: Feldmann, D. M.; Polyanskii, A., *Nature,* 2001, *vol. 414*, 368-377.
[39] Jin, S.; Sherwood, R. C.; Tiefel, T. H., Kammlott, G. W.; Fastnacht, R. A.,; Davis, M. E.; Zahurak, S. M., *Appl. Phys. Lett.* 1988, *vol. 52,* 1628-1630.
[40] Gao, W.; Sande, J. B. V., *Physica C,* 1991, *vol. 181*, 105-120.
[41] Malik, M. K.; Nair, V. D.; Biswas, A. R.; Raghavan, R. V., *Appl. Phys. Lett.*, 1988, *vol. 52,* 1525-1527.
[42] Yoshida, K.; Sano, Y.; Tomii, Y., *Supercond. Sci. Technol.,* 1995, *vol. 8*, 329-335.
[43] Yoshida, K.; Sano, Y.; Tomii, Y., *Physica B*, 1994, *vol. 194-196,* 1949-1950.
[44] Yoshida, K., *physica status solidi (a)*, 1996, *vol. 153*, K5-K7.
[45] Jones, T. E.; Schindler, J. W.; Boss, R. D.; Thibado, P. M.; McGinnis, W. C., *Phys. Rev. B*, 1990, *vol. 41*, 7197.
[46] Wu, N. L.; Chang, Y. C., *Jpn. J. Appl. Phys.*, 1990, *vol. 29*, L563-L565.
[47] Düzgün, İ.; Karaca, İ.; Öztürk, A.; Çelebi, S., *Physica C,* 2006, *vol. 436*, 93-98.
[48] Bolat, S.; Çelebi, S.; Gencer, A.; Cömert, H.; Yanmaz, E., *J. Alloys and. Compounds,* 1998, *vol. 269*, 1-6.
[49] Karaca, I.; Çelebi, S.; Varilci, A.; Malik, A. I., *Supercond. Sci. Technol.* 2003, *vol. 16*, 100-104.
[50] Yoshida, K.; Sano, Y.; Tomii, Y., *Physica C,* 1993, *vol. 206*, 127-132.
[51] Yoshida, K., *J. Phys. Soc. Jpn.,* 1990, *vol.* 59, 1518-1519.
[52] Xiao, G.; Streitz, F. H.; Cieplak, M. Z.; Bakhshai, A.; Gavrin, A.; Chien, C. L., Phys. Rev. B, 1988, vol. 38, 776-779.
[53] Dwir, B.; Pavuna, D.; Affronte, M.; Berger, H.; Tholence, J. L., *J. Supercond.,* 1989, *vol. 2*, 419-426.
[54] Lin, J. J.; Chen, T. M., *Z. Phys. B,* 1990, *vol. 81*, 13-17.

Copyright © 2010. Nova Science Publishers, Incorporated. All rights reserved.

Handbook of Material Science Research, Nova Science Publishers, Incorporated, 2010. ProQuest Ebook Central,

[55] Lin, J. J.; Chen, T. M., *Jpn. J. Appl. Phys.*, 1991, *vol. 30*, L1256-L1259.
[56] Yoshida, K.; Matsukawa, M.; Noto, K., *Materials Lett.,* 1998, *vol. 36,* 7-10.
[57] Matsukawa, M.; Tatezaki, F.; Ogasawara, H.; Noto, K.; Yoshida, K., *J. Phys. Soc. Jpn.,* 1995, *vol. 64*, 164-169.
[58] Lin, J. J., Phys. Rev. B, 1991, vol. 44, 789-794.
[59] Ikebe, M.; Fujishiro, H., *J. Low Temp. Phys.*, 1999, *vol. 117*, 1289-1293.
[60] Yoshida, K., *Phys. Rev. B*, 1999, *vol. 60*, 9325-9328.
[61] Yoshida, K., *Physica B*, 2000, *vol. 284-288*, 644-646.
[62] Yoshida, K., *Phys. Rev. B*, 2007, *vol. 76*, 024514/1-7.
[63] Fink, J.; Nucker, N.; Romberg, H.; Alexander, M,; Maple, M. B.; Neumeier, J. J.; Allen, J. W., *Phys. Rev. B,* 1990, *vol. 42*, 4823-4826.
[64] Jostarndt, H. D.; Walter, U.; Harnischmacher, J.; Kalenborn, J.; Severing, A.; Holland-Moritz, E., *Phys. Rev. B,* 1992, *vol. 46,* 14872-14882.
[65] Fehrenbacher, R.; Rice, T. M., *Phys. Rev, Lett.*, 1993, *vol. 70,* 3471-3474.
[66] Soderholm, L.; Zhang, K.; Hinks, D. G.; Beno, M. A.; Jorgensen, J. D.; Segre, C, U.; Schuller, I. K., *Nature (London),* 1987, *vol. 328*, 604-605.
[67] Yang, H. D.; Chen, P. F.; Hsu, C. R; Lee, C. W.; Li, C. L.; Peng, C. C., *Phys. Rev. B*, 1991, vol. 43, 10568.
[68] Xu, Y.; Guan, W., *Appl. Phys. Lett.*, 1991, *vol. 59*, 2183.
[69] Yoshida, K. (2008). Transport Properties Due to Structural Inhomogeneity in Superconducting Cuprates Doped with Cations. In T. Watanabe (Ed.), *Leading-Edge Superconductivity Research Developments*, New York; Nova Science Publishers. Inc.
[70] Barone, A.; Paternò, G., *Physics and Applications of the Josephson Effect*; John Wiley and Sons, Inc.: New York, 1982.
[71] Ambegaokar, V.; Baratoff, A., *Phys. Rev. Lett.,* 1963, *vol. 10*, 486-489.

Copyright © 2010. Nova Science Publishers, Incorporated. All rights reserved.

Handbook of Material Science Research, Nova Science Publishers, Incorporated, 2010. ProQuest Ebook Central,

In: Handbook of Material Science Research
Editors: C. René and E. Turcotte, pp.213-269
ISBN 978-1-60741-798-9
© 2010 Nova Science Publishers, Inc.

Chapter 4

DIELECTRIC AND ULTRASONIC SPECTROSCOPY OF QUASI TWO-DIMENSIONAL $CuInP_2(S_XSE_{1-X})_6$ MIXED CRYSTALS

V. Samulionis[1], J. Banys, J. Macutkevic[1] and Yu.Vysochanskii[2]
[1]Vilnius University,Vilnius, Lithuania
[2]Uzhgorod University, Uzhgorod, Ukraine

ABSTRACT

In this chapter, the broadband (20 Hz – 1.2 GHz) dielectric spectroscopy results of mixed $CuInP_2(S_xSe_{1-x})_6$ crystals are presented. In these crystals two contributions in dielectric spectra was successfully separated – at higher temperatures and low frequencies high copper ions conductivity and at higher frequencies and low temperatures order-disorder effects in copper and indium sub lattices. Critical increasing of the conductivity activation energy E_A and conductivity σ_0 was observed in intermediate concentration of sulphur and selenium. A new dipolar glasses were discovered - $CuInP_2(S_xSe_{1-x})_6$ with x=0.4-0.8. Influence of small amount of selenium to dielectric dispersion of $CuInP_2S_6$ is more significant than corresponding amount of sulphur to dielectric dispersion of $CuInP_2Se_6$. Coexistence of ferroelectric order and dipolar glass disorder observed at low temperatures in $CuInP_2S_6$ with small admixture of selenium (2 %). Phase diagram boundary between dipolar glass disorder and ferroelectric order was examined and relaxor-like behaviour was discovered for $CuInP_2(S_{0.25}Se_{0.75})_6$. Ultrasonic spectroscopy was performed in the frequency range of 10-30 MHz using pulse-echo time of flight method. The critical ultrasonic anomalies at phase transitions in pure and mixed $CuInP_2(S_xSe_{1-x})_6$ crystals are observed. The polarization relaxation time was estimated from ultrasonic data in the vicinity of phase transitions. Phase diagram of phase transitions in these mixed crystals obtained from ultrasonic investigations corresponds to that obtained from dielectric spectroscopy. It was shown that $CuInP_2S_6$ layered crystals have extremely high elastic nonlinearity across layers. Elastic nonlinearity increases near phase transition temperature. Ultrasonic method was applied to detect and investigate piezoelectric sensitivity. It appeared that these layered crystals are good piezoelectric in low temperature ferroelectric phase and can be used as ultrasonic transducers . In paraelectric phase the piezoelectric sensitivity can be induced by external DC bias electric field directed along polar axis due to electrostriction.

Copyright © 2010. Nova Science Publishers, Incorporated. All rights reserved.

Handbook of Material Science Research, Nova Science Publishers, Incorporated, 2010. ProQuest Ebook Central,

1. DIELECTRIC INVESTIGATION OF PHASE TRANSITIONS IN PURE $CuInP_2S_6$ AND $CuInP_2Se_6$ CRYSTALS

1.1. Phase Transitions in $CuInP_2S_6$ and $CuInP_2Se_6$ Crystals

$CuInP_2S_6$ crystals studied in the present work represent an unusual example of a collinear two-sublattice ferrielectric system [1-3]. This crystal illustrates the general features of cooperative dipole effects within a lamellar chalcogenophosphate. Here a first-order phase transition of the "order–disorder" type from the paraelectric to the ferrielectric phase is realized (T_c = 315 K), accompanied by anomalous behaviour of its physical properties. The symmetry reduction at the phase transition (C2/c → Cc) occurs due to ordering in the copper sublattice and displacement of cations from the centrosymmetric positions in the indium sublattice. This conclusion also was supported by the Raman investigation of $CuInP_2S_6$ [4]. The spontaneous polarization arising at the phase transition to the ferrielectric phase is perpendicular to the layer planes. These thiophosphates consist of lamellae defined by a sulphur framework in which the metal cations and P - P pairs fill the octahedral voids; within a layer, the Cu, In, and P-P form triangular patterns [5] (Figure1.1). The cation off-centering, 1.6 Å for Cu^{I} and 0.2 Å for In^{III}, may be attributed to a second-order Jahn-Teller instability associated with the d^{10} electronic configuration. The lamellar matrix absorbs the structural deformations via the flexible P_2S_6 groups while restricting the cations to antiparallel displacements that minimize the energy costs of dipole ordering. Each Cu ion can occupy two different positions. The Cu, In or Cr and P - P form triangular patterns within the layer. Relaxational rather than resonant behaviour is indicated by the temperature dependence of the spectral characteristics, in agreement with X-ray investigations. It was suggested that a coupling between P_2S_6 deformation modes and Cu^{I} vibrations enables the copper ion hopping motions that lead to the loss of polarity and the onset of ionic conductivity in this material at higher temperatures [4]. The ionic conductivity of $CuInP_2S_6$ has been already preliminary investigated [6] in the frequency range from 1 Hz to 1 MHz. Only few frequencies have been measured. It was found that σ_{DC} follows the Arrhenius law with the activation energy E_A = 0.73 eV.

Other dielectric and Raman measurements [4] confirmed the first order, order-disorder phase transition nature in $CuInP_2S_6$, and showed a huge influence of the conductivity at higher temperatures on low-frequency dielectric properties. Also two different mechanisms of polarization have been found at low frequencies. Preliminary ultrasonic and piezoelectric studies were carried out in small, prepared by solid-state reactions, $CuInP_2S_6$ crystals [7]. New investigations concerning ultrasonic velocity, attenuation and second harmonic generation in large $CuInP_2S_6$ crystals grown by Bridgman method are presented in [8]. It was shown, that the extremely large value of nonlinear elastic coefficient exists for longitudinal waves propagating across the layers. In the presented crystals the ultrasonic velocity exhibits a critical slowing down which gives accompanied by the attenuation peaks in the phase transition region. The nonlinear elastic parameter substantially increases at the phase transition temperature. Results of the Raman investigations under pressure [9] indicate the phase transition at about 4 GPa, which is inferred to be of the first-order (from a monoclinic to trigonal structural).

Copyright © 2010. Nova Science Publishers, Incorporated. All rights reserved.

Handbook of Material Science Research, Nova Science Publishers, Incorporated, 2010. ProQuest Ebook Central,

The selenium analogue $CuInP_2Se_6$ is a relatively new addition to this class of chalcogenophosphate materials. Calorimetric evidence for the occurrence of a broad phase transition between 220 and 240 K in this compound was given in paper [10]. A single-crystal X-ray diffraction study showed that the high- and low-temperature structures of $CuInP_2Se_6$ (trigonal space group *P*-31*c* and *P*31*c*, respectively) are very similar to those of $CuInP_2S_6$ in the paraelectric and ferrielectric phases, with the Cu^I off-centering shift being smaller in the former than in the latter [10-11]. There the thermal evolution of the cell parameters of $CuInP_2Se_6$ was obtained by full profile fits to the X-ray diffractograms. Both cell parameters a and c slightly increase on cooling, only at T=226 K a parameters show a local minimum. This behaviour is quite different from the anomalous increases found in the cell parameters of $CuInP_2S_6$ when heating through the transition [2, 12]. The important feature of selenides is the higher covalence degree of their bonds. Evidently, for this reason the copper ion sites in the low-temperature phase of $CuInP_2Se_6$ are displaced only by 1.17 Å from the middle of the structure layers in comparison with the corresponding displacement 1.58 Å for $CuInP_2S_6$ [1, 2, 5]. These facts enable to assume the potential relief for copper ions in $CuInP_2Se_6$ to be shallower than for its sulphide analog. Presumably, for this reason the structural phase transition in the selenide compound is observed at lower temperature than for the sulphide compound. Neutron powder power simulations show that neutron reflections are stronger in a $CuInP_2Se_6$ structure with Cu atoms in off-center rather than on-center sites. Whether or not these dipoles adopt a polar arrangement as in $CuInP_2S_6$ until now is not yet clear. However these neutron investigations are rough, because performed with samples contained substantial impurities of $CuInSe_2$ and Cu_3PSe_4.

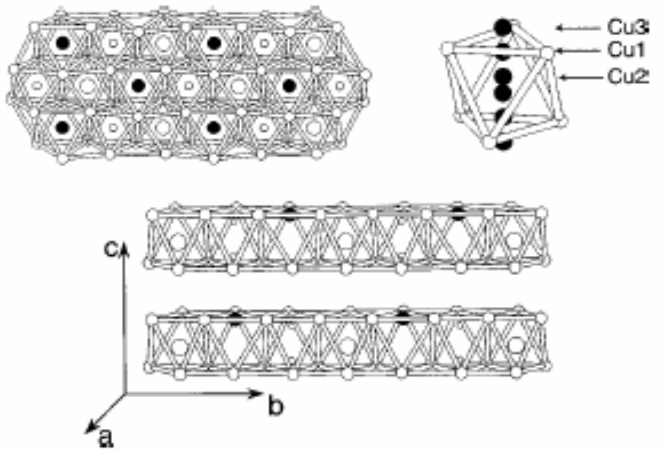


Figure 1.1. Top left: Projection onto the *a*-*b* plane of the $CuInP_2S_6$ structure showing the triangular sublattices formed by the copper and indium cations and the P-P pairs. Top right: A sulfur octahedral cage showing the various types of copper sites: the off-center Cu1, the almost central Cu2, and Cu3 in the interlayer space. At *T*>315, a twofold axis through the center doubles the number of sites per CuS6; two off-center sites become inequivalent when unequally occupied at *T*<315 K. Bottom: Two layers of CuInP2S6 shown in the ferroelectric phase (*T*<315 K). The up (down) shifted Cu^I (In^{III}) ions are represented by the larger black (white) circles in the octahedra; the smaller white circles are the *P*. The monoclinic lattice parameters at room temperature are *a*=56.0956(4) Å, *b*=510.5645 Å, *c*=513.6230(9) Å, and *β*=5107.101(3)° from [4].

Copyright © 2010. Nova Science Publishers, Incorporated. All rights reserved.

Handbook of Material Science Research, Nova Science Publishers, Incorporated, 2010. ProQuest Ebook Central,

The phase transitions in considered compounds are triggered by the cooperative freezing of intersite copper motions. This cooperative dipolar behaviour is supposed [13] to arise from the presence of an off-centring displacement caused by an electronic instability in the form of a second order Jahn–Teller (SOJT) effect related to the d^{10} electronic configuration of the cations Cu^{+}. A SOJT coupling, involving the localized d^{10} states forming the top of the valence band and the s–p states of the bottom of the conduction band, is predicted to yield such an instability. Through photo-electron spectroscopy measurements was given evidence for a strong redistribution of the density of states at the top of the valence band [13]. By combining these data with band-structure calculations were shown [13] that these changes are mainly ascribable in the redistribution of the Cu partial density of electron states, related to the off-centred position of the d^{10} cations in the ferrielectric phase.

In addition to earlier mentioned role of Cu^{+} ions, for the $M_2P_2S_6$ layered compounds the highest valence bands are known [14] also to be formed by the (P–P) p-bonding states and S 3p nonbonding levels, while the lowest conduction bands are constituted mostly by the (P–P) p-antibonding and the S p-bonding and antibonding states. Therefore, the optical absorption edge in $CuInP_2S_6$ crystals also can be formed by the electronic transitions between the (P–P) p-bonding and antibonding states. The redistribution of copper atoms over different positions in a multiwell potential results in the essential nonequivalence of P_2S_6 structural groups, enabling the S–P and P–P bond lengths, as well as S–P–S and S–P–P angles to be varied within a certain interval. This is confirmed by a substantial increase of damping of $(P_2S_6)^{4-}$ anion internal stretching and valence vibrations lines in Raman spectra with temperature increase above the phase transition to the paraelectric phase [4, 15]. Also, the copper cation hopping motion results in the variation of the S–P and P–P bond characteristics, leading to the optical absorption edge smearing, and, thus, to the deviation from the spectral dependence, typical for the direct transitions, in the ferrielectric phase and the appearance of exponential absorption tails in the paraelectric phase of $CuInP_2S_6$ [16]. Similar rise of the Urbach optical absorption edge width at transition into paraelectric phase was observed for the $CuInP_2Se_6$ compound [17].

The temperature dependence of the Urbach absorption edge energy width *w* reflects the step of a disordering in the paraelectric phase. The smearing of the absorption edge is caused by intense temperature-dependent hopping of copper ions between potential wells as well as due to their penetrating into the interlayer van der Waals space at high temperatures, which promotes the ionic conductivity. The relaxational dynamics of Cu^{+} cations determines the essential anharmonicity of internal vibrations of $(P_2S_6)^{4-}$ anions, which by means of electron-phonon interaction modifies the (P–P) p-bonding and antibonding states, participating in the formation of the valence band top and the conduction band bottom. High values of the exponential absorption edge energy width *w* (above 100 meV) are typical for glassy semiconductors [16, 17]. Perhaps at $T > T_c$ certain "glassy behaviour" occurs resulting in the sharp absorption edge broadening due to strong electron-phonon interaction and the smeared tails of the density of electronic states in the gap.

1.2. Dielectric Studies of $CuInP_2S_6$ and $CuInP_2Se_6$ Crystals

Dielectric properties of $CuInP_2Se_6$ crystals were investigated in [18, 19]. In [19] temperature dependence of the dielectric permittivity was investigated at 10 kHz frequencies.

Copyright © 2010. Nova Science Publishers, Incorporated. All rights reserved.

Handbook of Material Science Research, Nova Science Publishers, Incorporated, 2010. ProQuest Ebook Central,

At these frequencies for all temperatures tgδ > 1 i. e. the main contribution in the dielectric permittivity is caused the conductivity and contacts.

From those very questionable data authors discover two phase transitions: a second-order one at T_i = 248 K and a first-order transition at T_c = 236 K in $CuInP_2Se_6$ crystals. Extremely questionable from this results is the first-order transition, because the real part of dielectric permittivity ε′ changes only 14%. There no static dielectric permittivity was obtained, therefore no adequate temperature of phase transitions they can estimate. In [18] the dielectric permittivity was investigated in wide frequencies range 20 Hz – 600 MHz, however, the authors at higher frequencies performed experiment too fast so that only several experimental points are obtained around the phase transition temperature. At low frequencies, they did not separate contributions of contact effects and of bulk conductivity; therefore no any conductivity parameters are obtained there. Authors of [18] observed only second phase transition at T_c = 234 K. However this results is very questionable because measurements were performed clearly very fast and the phase transition dynamics was strongly affected by the transport phenomena via strong temperature gradient. Until present no data about the conductivity distinguished from the contact effects and no static dielectric permittivity were obtained for both $CuInP_2S_6$ and $CuInP_2Se_6$. The phase transition dynamics of this crystal until presented is also not known.

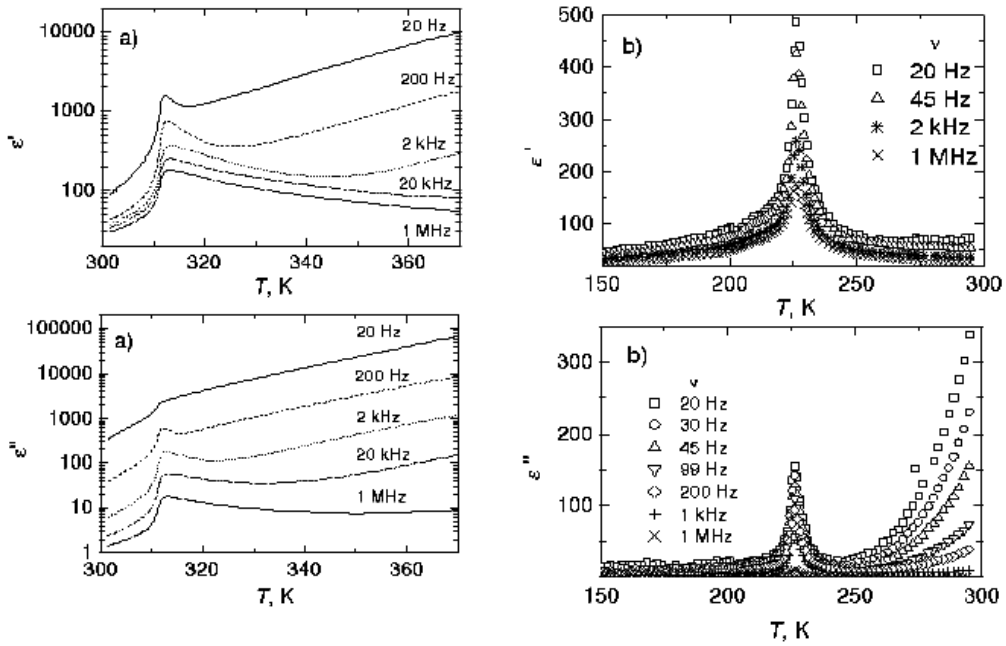


Figure 1.2. Temperature dependence of complex dielectric permittivity of: a) $CuInP_2S_6$ and b) $CuInP_2Se_6$ crystals measured at low frequencies.

Copyright © 2010. Nova Science Publishers, Incorporated. All rights reserved.

Handbook of Material Science Research, Nova Science Publishers, Incorporated, 2010. ProQuest Ebook Central,

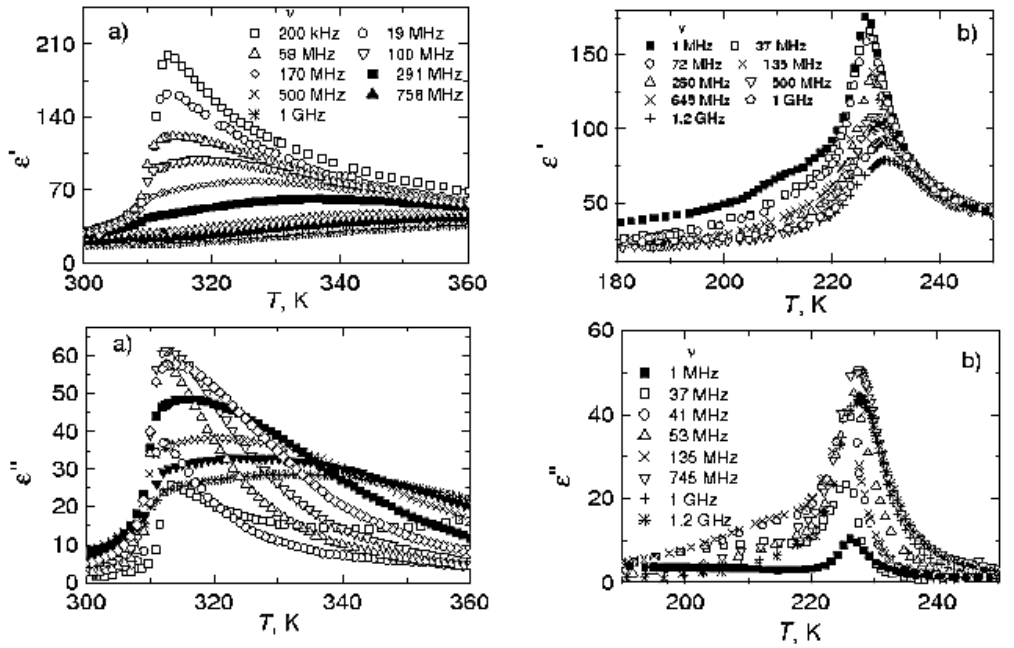


Figure 1.3.Temperature dependence of complex dielectric permittivity of: a) $CuInP_2S_6$ and b) $CuInP_2Se_6$ crystals measured at higher frequencies.

Our results of low-frequency dielectric measurement of $CuInP_2S_6$ and $CuInP_2Se_6$ are presented in Figure 1.2. At low frequencies the dielectric losses increase with increasing temperature and cause increase of the real part of the dielectric permittivity. Such an effect is mainly caused by the high ionic conductivity as it was already shown previously [6]. From the Figure 1.2 it is possible to see that the real part of the dielectric permittivity already corresponds to the static one caused by the soft mode at 1 MHz because at that frequency ε'' is already much smaller then ε'. In contrast to [19] $tg\delta < 1$ for $CuInP_2Se_6$ at all frequencies around the phase transition temperature T_c.

Temperature dependence of the dielectric permittivity of $CuInP_2S_6$ and $CuInP_2Se_6$ crystals at several higher frequencies are shown in Figure 1.3. The ferroelectric dispersion in the vicinity of T_c begins at about 1 MHz and ranges up to the GHz region. The characteristic minimum of ε' of $CuInP_2S_6$ crystals appears at 111 MHz indicating a critical slowing down typical for the order-disorder phase transitions, for example H - bonded ferroelectrics [20]. The ferroelectric dispersion of $CuInP_2S_6$ crystals nearly vanishes at 1 GHz. The value of a residual dielectric permittivity of $CuInP_2S_6$ crystals of $\varepsilon' = 14$ shows that high-frequency modes makes a noticeable contribution to the dielectric permittivity.

In $CuInP_2Se_6$ crystals even at higher measured frequency (1.2 GHz) the temperature dependence of dielectric permittivity is significant so that the relaxation dielectric dispersion must by appear at higher frequencies. Therefore, the dielectric dispersion is much broader in $CuInP_2Se_6$ than in it sulphur analogue $CuInP_2S_6$ around the phase transition temperature. The dielectric dispersion not vanishes in $CuInP_2Se_6$ crystals even substantially below transitions temperature T_c = 225 K. A characteristic additional peak around T = 210 K obviously is

Copyright © 2010. Nova Science Publishers, Incorporated. All rights reserved.

Handbook of Material Science Research, Nova Science Publishers, Incorporated, 2010. ProQuest Ebook Central,

caused of domain wall motion contributions. However no any anomaly is really observed above the phase transition temperature T_c = 225 K (Figs.1.2b and 1.3b).

The frequency dependence of the real and imaginary parts of dielectric permittivity of both crystals (Figure 1.4) under study shows that the dielectric dispersion can be described by the Cole-Cole formula: :

The soft mode parameters τ_{CC}, $\Delta\varepsilon$ and α_{CC} have been calculated according to the Cole-Cole formula (1.1) from the experimental results. As can be seen from Figure 1.4, the dielectric dispersion of $CuInP_2S_6$ crystals shows the Debye type nature, and only close to T_c parameter α_{CC} increases up to 0.2. The Cole-Cole parameter relaxation times distribution α_{CC} of $CuInP_2Se_6$ crystals show huge temperature dependence – on cooling it strongly increase and arise enough big (for ferroelectrics) value 0.4.

Much more interesting temperature behaviour has been observed for $\Delta\varepsilon$ and $\varepsilon_{\infty r}$ of $CuInP_2S_6$ crystals. The value of $\varepsilon_{\infty r}$ slightly increases on approach of T_c from 8 to 7.5. As can be seen from Figure 1.5, the reciprocal $\Delta\varepsilon$ temperature dependence looks like obeys the Curie-Weiss law in the paraelectric phase.

Also the same should be valid for the relaxation time temperature dependence - or the soft mode $\nu_r = 1/2\pi\tau_{CC}$. Usually for the order-disorder phase transitions ν_r *shows linear dependence an temperature:*

$$\nu_r = B_r(T-T_C). \tag{1.2}$$

But in the case of $CuInP_2S_6$ crystals the square root of the mode frequency is linear temperature-dependent.

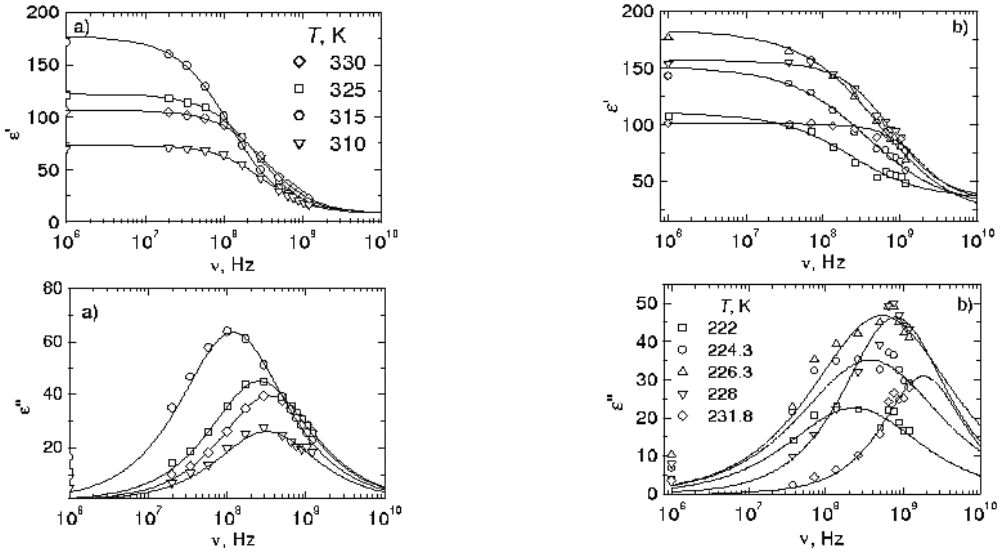


Figure 1.4. Frequency dependence of complex dielectric permittivity of: a) $CuInP_2S_6$ and b) $CuInP_2Se_6$ crystals measured at different temperatures.

Copyright © 2010. Nova Science Publishers, Incorporated. All rights reserved.

Handbook of Material Science Research, Nova Science Publishers, Incorporated, 2010. ProQuest Ebook Central,

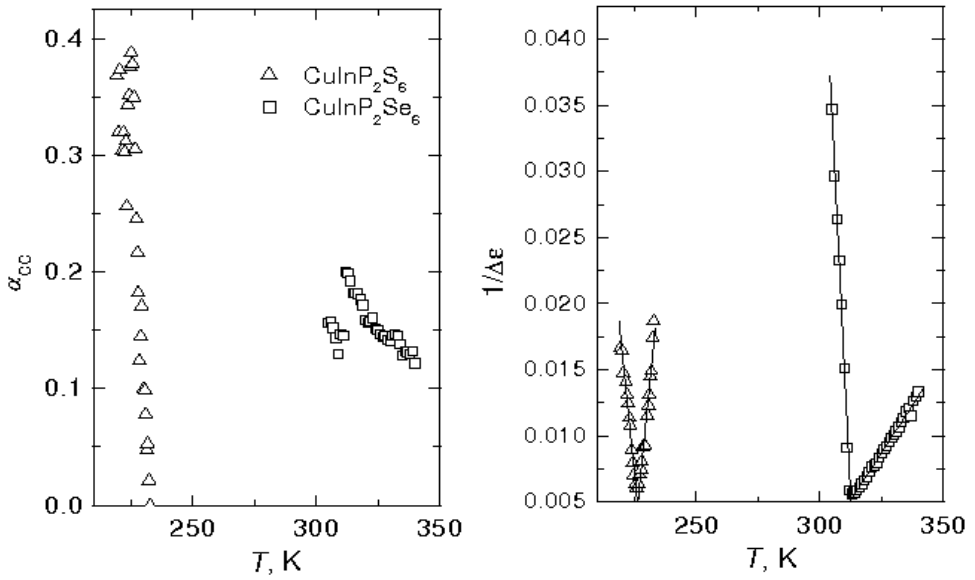


Figure 1.5. Temperature dependence of the Cole-Cole parameters: α_{CC} and $1/\Delta\varepsilon$ of $CuInP_2S_6$ and $CuInP_2Se_6$ crystals. The lines are the best fit according to Ciuri-Weiss law.

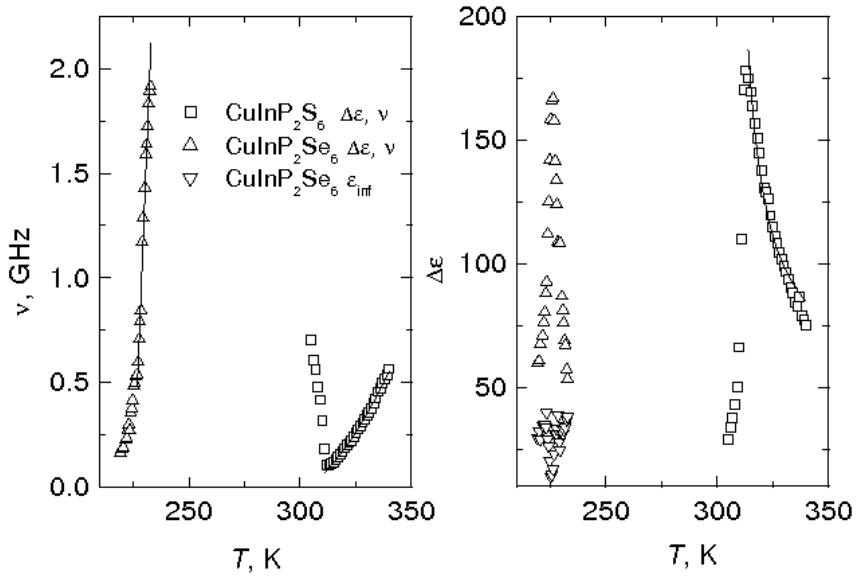


Figure 1.6. Temperature dependence of the Cole-Cole parameters: ν_r and $\Delta\varepsilon$ of $CuInP_2S_6$ and $CuInP_2Se_6$ crystals. The lines are the best fit according to (1.3) and (1.4) in $CuInP_2S_6$ case and according to (1.2) in $CuInP_2Se_6$ case.

Such a temperature behaviour is predicted for the one dimensional Ising model with the phase transition temperature $T_{c1} = 0$ K. So the results above give us a strong hint that the temperature behaviour of the soft mode is strongly one dimensional. Due to the structure of the crystal it seems that Cu atoms are placed in one-dimensional chains, and the motion of Cu

Copyright © 2010. Nova Science Publishers, Incorporated. All rights reserved.

Handbook of Material Science Research, Nova Science Publishers, Incorporated, 2010. ProQuest Ebook Central,

atoms in the double minima potential gives the main contribution to the dielectric permittivity.

$$\varepsilon^* = \varepsilon_{\infty r} + \frac{\Delta\varepsilon}{1+(i\omega\tau_{CC})^{1-\alpha_{CC}}}. \tag{1.1}$$

In such case to describe the dynamic and static dielectric properties is possible with the modified one-dimensional Ising model. In this model, the interaction between neighbouring dipoles in one-dimensional chains is treated exactly whereas all additional (weak) interactions are taken into account by a mean field approximation. The treatment of this system yields for the static dielectric permittivity in the disordered phase The quasi-one-dimensional Ising model was used to fit the relaxator strength of ferroelectric dispersion [21]:

$$\Delta\varepsilon = \frac{C}{T}\left[\exp\left(-\frac{2J_{\parallel}}{k_B T}\right) - \frac{J_{\perp}}{k_B T}\right]^{-1}, \tag{1.3}$$

where $J_{\parallel}$ and $J_{\perp}$ are the nearest neighbor intrachain and the effective mean field interchain coupling constants.

The temperature dependence of the relaxation frequency shows a curvature in the high temperature phase . The temperature dependence of the relaxation frequency according to the quasi one-dimensional Ising model [21] is given by:

$$\nu_r = \nu_{\infty}\exp\left(-\frac{\Delta U}{k_B T}\right)\left[\cosh\left(\frac{2J_{\parallel}}{k_B T}\right)\right]^{-1}\left[\exp\left(-\frac{2J_{\parallel}}{k_B T}\right) - \frac{J_{\perp}}{k_B T}\right], \tag{1.4}$$

where ΔU is the activation energy for the reorientation of the dipole, and ν_{∞} is the attempt frequency. Using the parameters $J_{\parallel}$ and $J_{\perp}$ obtained by means of Eq. (1.3), the best fit according to Eq. (1.4) results to the values of $CuInP_2S_6$ crystals: $J_{\perp}/k_B = 86.9$ K, $J_{II}/k_B = 172.3$ K, $C = 1131.2$ K, $\nu_{\infty} = 6.8 \times 10^{11}$ Hz, $\Delta U/k_B = 1459.4$ K. According to the quasi-one-dimensional Ising model it is possible to calculate the phase transition temperature from these values. The transition temperature $T_{C\,\mathrm{Ising}}$ is determined by the condition:

$$k_B T_{C\,\mathrm{Ising}}\exp\left(-\frac{2J_{\parallel}}{k_B T_{C\,\mathrm{Ising}}}\right) = J_{\perp}. \tag{1.5}$$

The obtained value of the phase transition temperature 163 K shows that the observed phase transition in $CuInP_2S_6$ is the first order one. The frequency of the soft relaxational mode of $CuInP_2Se_6$ crystals in the paraelectric phase follows the classical law Eq. (1.1) with the parameters T_c=225 K and B_r=0.265 GHz/K. The temperature dependence of the parameter $\varepsilon_{\infty r}$ of $CuInP_2Se_6$ shows a pronounced minimum in the vicinity of the phase transition temperature.

Copyright © 2010. Nova Science Publishers, Incorporated. All rights reserved.

Handbook of Material Science Research, Nova Science Publishers, Incorporated, 2010. ProQuest Ebook Central,

Thus, the dielectric spectra of $CuInP_2S_6$ and $CuInP_2Se_6$ can be divided into two parts: the low-frequency part, which is determined by the conductivity effects and high-frequency part, where the dielectric dispersion caused by the relaxational soft mode appears. The temperature behaviour of the soft mode of $CuInP_2S_6$ clearly shows a quasi-one-dimensional character. The Ising model describes the temperature behaviour of the soft mode in $CuInP_2S_6$ crystals very well. We can strictly predicate that in $CuInP_2Se_6$ crystals only one phase transition – ferroelectric at T_c=225 K is observed. Recently this predication is confirmed by very accurate calorimetric studies [22]. The ordering of Cu ions in the double minima potential is the reason of the phase transition in both $CuInP_2S_6$ and $CuInP_2Se_6$ crystals. More about the phase transition dynamics in $CuInP_2Se_6$ crystals we will discuss in Section 1.3.

1.2. Investigation of Ionic Conductivity in Mixed $CuInP_2(S_xSe_{1-x})_6$ Crystals

1.2.1. Introduction

In spite of many research efforts, the mechanism of fast ionic conduction in solids is not understood completely yet because of the difficulty in separating the contribution of the ion concentration and mobility from the measured conductivity. Many factors affect ionic conductivity, i. e. defect concentrations [23], unit cell free volume [24], the size and charge of the dopant and mobile ions [25], their mobility, association and ordering of points defects [23], grain boundary diffusion and segregation of secondary phase [26]. Many studies of ionic conductivity have been reported for oxides, but less for non-oxide materials. Recently studies of conductivity of the mixed crystals $CuCr_{1-x}V_xSe_2$ show an important role of unit cell size in determining Cu^+-cationic conductivity compared with a chemical bond character [27]. The structure of both crystals families $CuCr_{1-x}V_xSe_2$ and $CuInP_2(S_xSe_{1-x})_6$ is very similar: they are layered crystals with strong ionic-covalent bonds between metal and chalcogenide ions and enough weak Van-der-Waals forces between triple layers. Recent X-ray studies of $CuInP_2(S_xSe_{1-x})_6$ mixed crystals show [28] a minimum of unit cell volume at around x=0.5. X-ray studies of $CuCr_{1-x}V_xSe_2$ crystals show one minimum of unit cell volume at x=0.25 [27]. Because an ionic conductivity of both $CuInP_2S_6$ and $CuInP_2Se_6$ crystals is high enough, we can expect also the high ionic conductivity in the mixed crystals $CuInP_2(S_xSe_{1-x})_6$. Further we will describe the conductivity properties of $CuInP_2(S_xSe_{1-x})_6$ crystals.

1.2.2. Ionic Conductivity of Mixed $CuInP_2(S_xSe_{1-x})_6$ Crystals

The results as usual were analyzed within standard formalisms referred to as complex impedance Z^*, complex admittance Y^*, complex permittivity ε^* and complex modulus M^*. The measured values Z^* and Y^* depend on geometry of the sample (sample area and thickness for a parallel plate cell) so it is necessary to express the electrical properties of the material in terms of intensive quantities, which are dielectric permittivity, electrical modulus, and electrical conductivity. We will start from dielectric permittivity. The temperature dependence of complex dielectric permittivity ε^* of mixed $CuInP_2(S_{0.02}Se_{0.98})_6$ crystals at low frequencies are presented in Figure 1.7. For this crystal and for pure crystals $CuInP_2S_6$ and $CuInP_2Se_6$ (Figs.1.2) (and for other mixed crystal under study) at higher temperatures the real and imaginary parts are strongly increasing on heating, this effect was already observed in pure $CuInP_2S_6$ and $CuCrP_2S_6$ [5] crystals, and was explained by high ionic conductivity.

Copyright © 2010. Nova Science Publishers, Incorporated. All rights reserved.

Handbook of Material Science Research, Nova Science Publishers, Incorporated, 2010. ProQuest Ebook Central,

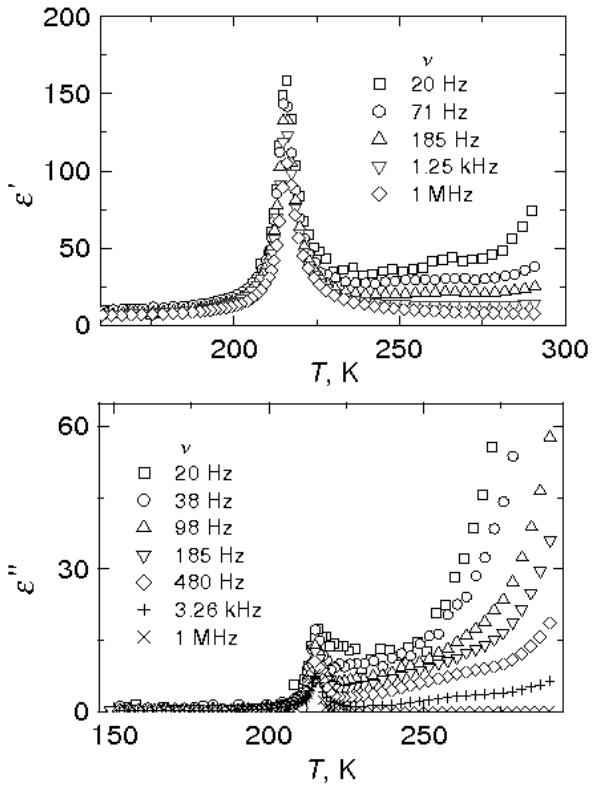


Figure 1.7. Temperature dependence of complex dielectric permittivity of $CuInP_2(Se_{0.98}S_{0.02})_6$ crystals measured at low frequencies.

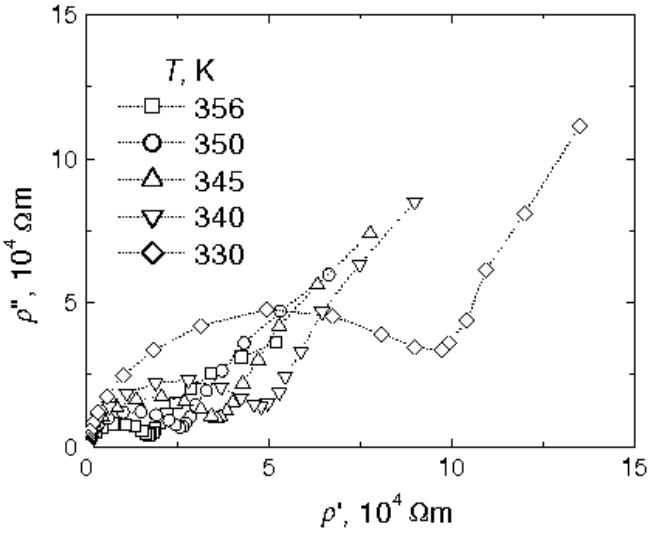


Figure 1.8. The Cole-Cole diagram of $\rho^*=\rho'-i\rho''$ for $CuInP_2S_6$ crystals at different temperature. Lines are guide for eyes.

Copyright © 2010. Nova Science Publishers, Incorporated. All rights reserved.

Handbook of Material Science Research, Nova Science Publishers, Incorporated, 2010. ProQuest Ebook Central,

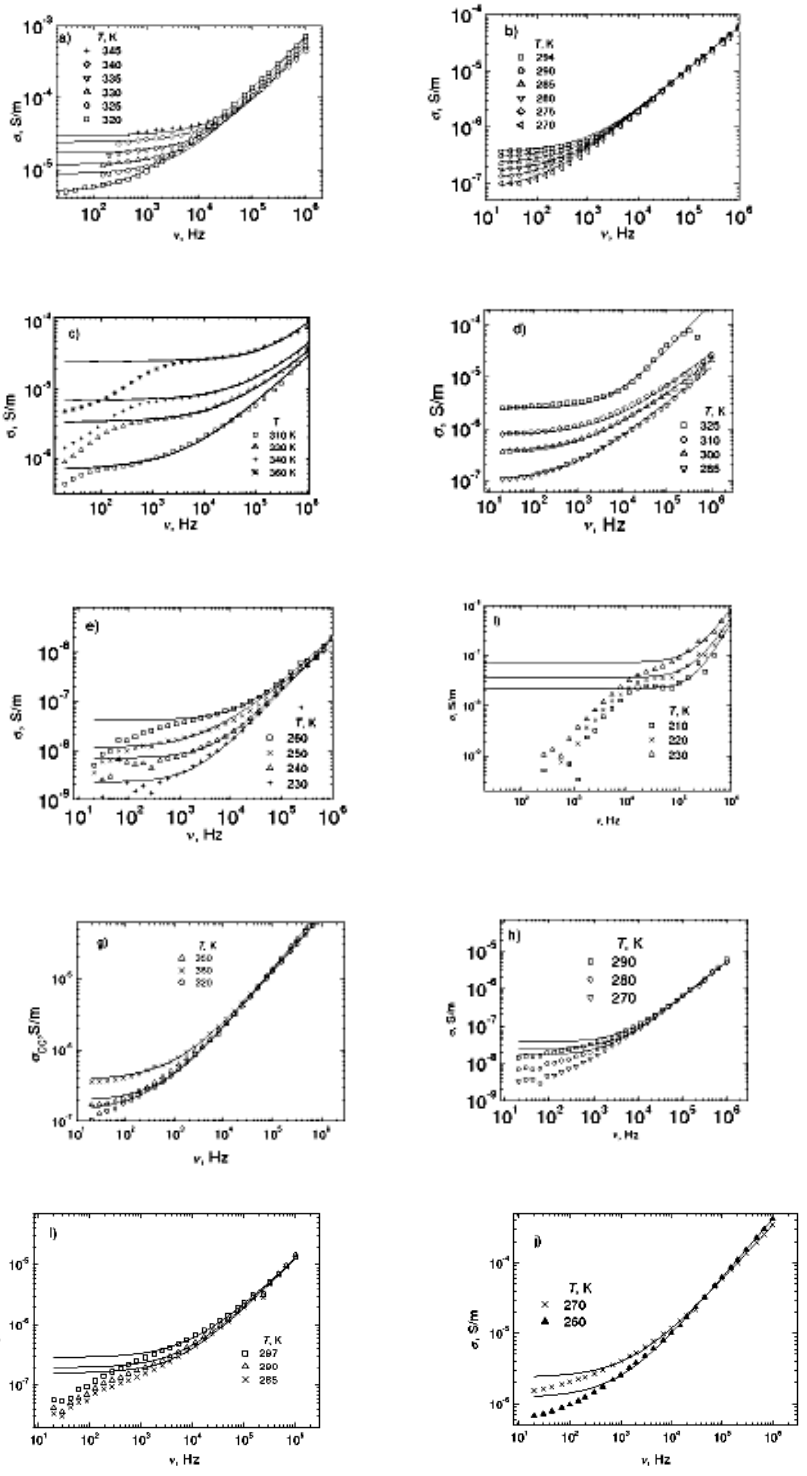


Figure 1.9. Frequency dependence of σ for $CuInP_2(S_xSe_{1-x})_6$ mixed crystals at different *x*: 1 a), 0 b), 0.98 c), 0.8 d), 0.7 e), 0.6 f), 0.5 g), 0.4 h), 0.1 i) 0.02 j).

Copyright © 2010. Nova Science Publishers, Incorporated. All rights reserved.

Handbook of Material Science Research, Nova Science Publishers, Incorporated, 2010. ProQuest Ebook Central,

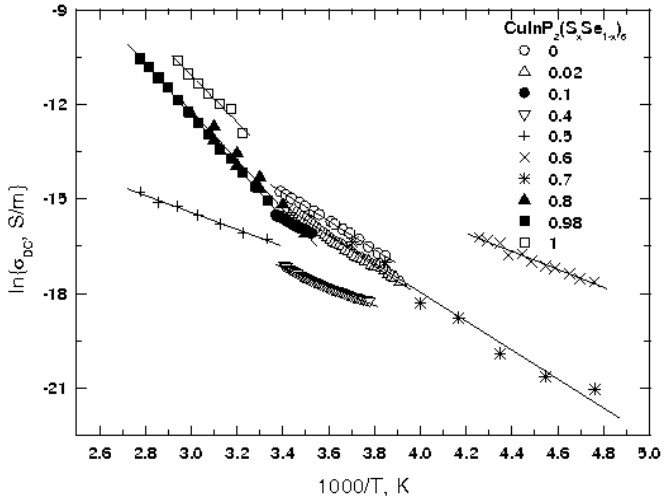


Figure 1.10. 1/*T* dependence of σ_{DC} for $CuInP_2(S_xSe_{1-x})_6$ crystals.

At lower temperatures, the maximum of both ε' and ε'' temperatures dependencies is observed. This maximum is caused by a phase transition, which we will discuss in the next paragraph. Two formalisms such as electric conductivity and electric modulus [29] have been employed to study the ion dynamics in solids under ac electric field. However, there is a debate on which of these formalisms provides better insights into the phenomena of ion dynamics [30]. In this work we compare both formalism. Undeniable fact is that $M''(\omega)$ is actually advantageous because it displays differences that are essentially invisible in $\sigma'(\omega)$. The complex electric modulus spectra represent a measure of distribution of ion energies or configurations in the disordered structure and also describe the electrical relaxation of ionic solids as a microscopic property of these materials. Recently authors of [29] from a stochastic transport theory obtained ratio of the electrical modulus relaxation time and microscopic relaxation time, this ratio is dependent from high-frequency dielectric permittivity and temperature.

At low frequencies, the conductivity phenomena dominate in the dielectric spectra. With such a high value of conductivity, the blocking contact effect can play an important role. To distinguish the volume conductivity from contact effect we calculated a specific resistance:

$$\rho' = \frac{\varepsilon''^2}{\varepsilon'^2 + \varepsilon''^2} \frac{1}{\varepsilon_0 \omega}, \tag{1.6}$$

$$\rho'' = \frac{\varepsilon'^2}{\varepsilon'^2 + \varepsilon''^2} \frac{1}{\varepsilon_0 \omega}. \tag{1.7}$$

The half circle at higher frequencies and lower values of ρ^* are caused by the bulk conductivity of crystal, and the bigger values ρ^* are already influenced by contacts (Figure

Copyright © 2010. Nova Science Publishers, Incorporated. All rights reserved.

Handbook of Material Science Research, Nova Science Publishers, Incorporated, 2010. ProQuest Ebook Central,

1.8) [31]. The contact influence is playing an important role at higher temperatures and lower frequencies.

So, it is extremely important to extract bulk conductivity from the experimental data. The electric conductivity σ has been calculated according to equation:

$$\sigma = \omega\varepsilon_0\varepsilon''. \tag{1.8}$$

The obtained results are presented in Figure 1.9. At low frequencies, random distribution of the ionic charge carriers via activated hopping gives rise to a frequency independent conductivity (dc conductivity). At higher frequencies, conductivity exhibits dispersion, increasing roughly in a power law fashion and eventually becoming almost linear at even higher frequencies.

The additional low-frequency dispersion region due to the electrode effects characterizes the high-temperature conductivity spectra of the Cu ion conducting materials. However this effect, as already has been described, is important only at higher temperatures and low frequencies (Figure 1.8).

The frequency behaviour of σ has been analyzed using Almond-West type power law with single exponent [32]:

$$\sigma = \sigma_{DC} + D\omega^g, \tag{1.9}$$

where σ_{DC} is the DC conductivity and $D\omega^g$ is the σ_{AC} conductivity. Such fit describe good dynamic properties of conductivity of all presented mixed crystals. Obtained dependencies $\ln(\sigma_{DC}(1/T))$ are presented in Figure 1.10.

Dc conductivity is closely related with ions hopping frequency ω_p [32]:

$$\sigma_{DC}=D\omega^g{}_p. \tag{1.10}$$

Hopping frequency ω_p is such temperature function:

$$\omega_p= \omega_e\exp(-\Delta E_j/k_BT), \tag{1.11}$$

there ΔE_j is the ions hopping activation energy, ω_e is the effective ions hopping frequency. From Eqs. (1.9), (1.10) and (1.11) we can easily obtain the relationship between ions hopping activation energy ΔE_j and ions conductivity energy $E_A - g^* \Delta E_j=E_A$. Because in the crystals under study $g < 1$, both mobility of ions and it density is temperature and sulphur concentration function.

From obtained values of σ_{DC} at different temperatures (Figure 1.10) it was possible to calculate the activation energy E_A and σ_0 of the conductivity according to the Arrhenius law:

$$\sigma = \sigma_0\exp(-E_A/k_BT). \tag{1.12}$$

Copyright © 2010. Nova Science Publishers, Incorporated. All rights reserved.

Handbook of Material Science Research, Nova Science Publishers, Incorporated, 2010. ProQuest Ebook Central,

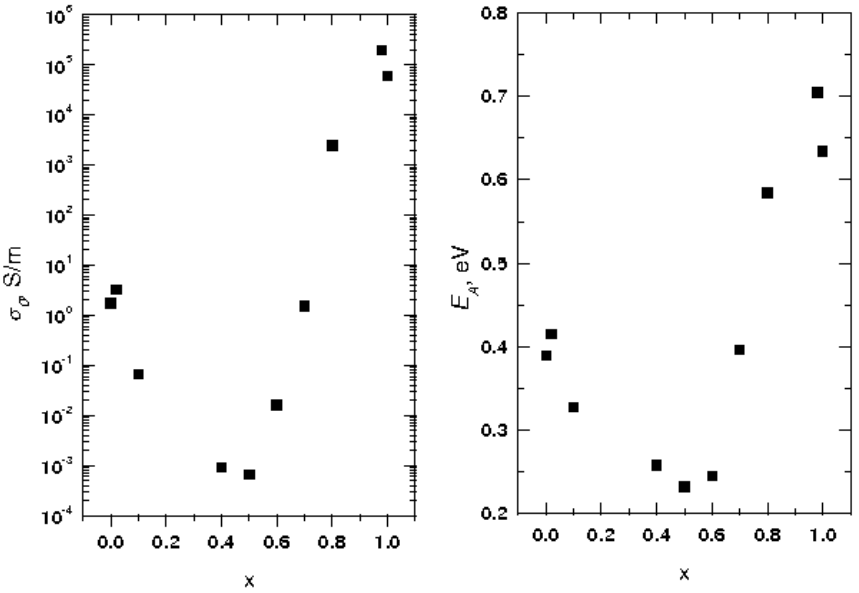


Figure 1.11. Activation energy E_A and σ_0 dependence of sulphur concentration x.

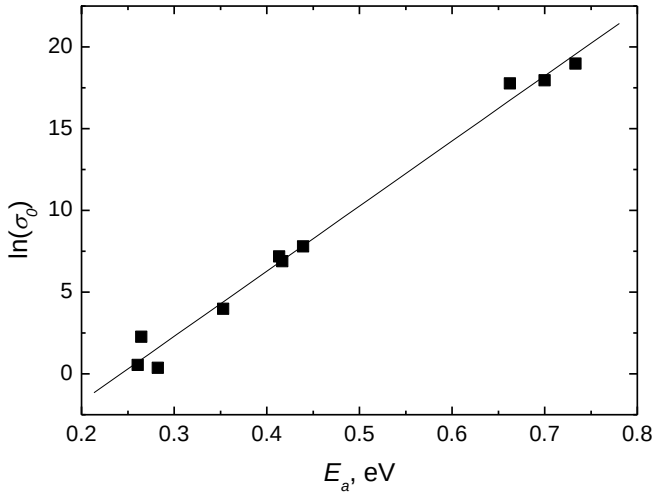


Figure 1.12. σ_0 dependence of activation energy E_A.

Calculated parameters of mixed crystals are presented in Figure 1.11. The obtained values for $CuInP_2S_6$ crystals (E_A/k_B = 7357.4 K (E_A = 0.635 eV), $\sigma_0 = 5.9 \times 10^4$ S/m) are similar as in [6]. For $CuInP_2Se_6$ crystals the obtained activation energy is much smaller E_A/k_B = 4507.1 K (0.389 eV) and σ_0 = 1.75 S/m. This confirms that the potential relief for copper ions in $CuInP_2Se_6$ is shallower than for its sulfide analog. Such values of activation energy clearly differ from larger gap semiconductive $CuInP_2S_6$ (2.8 eV) and $CuInP_2Se_6$ (1.8 eV) crystals. As it was already explained in the case of $CuInP_2S_6$ crystals, such high values of conductivity are caused by Cu ions, which can move in the crystal lattice [4, 6]. Activation

Copyright © 2010. Nova Science Publishers, Incorporated. All rights reserved.

Handbook of Material Science Research, Nova Science Publishers, Incorporated, 2010. ProQuest Ebook Central,

energy E_A and σ_0 dependence on sulphur concentration have pronounced minimum at $x = 0.5$. In the mixed crystals, the copper cation hopping motion occurs in local potential, determined by different combinations of nearest chalcogen atoms. Here also strong delay of electron density of states into the gap appears - even small replacing atoms S↔Se, as on $CuInP_2S_6$, so at $CuInP_2Se_6$ side, induces strong compositional disordering of the crystal lattice and smearing of the optical absorption edge. In the paraelectric phase, the exponential absorption edge energy width w has maximum value at the middle of concentration interval, i. e. at 325 K w increases from about 105 meV at $x = 0$ till about 150 meV at $x = 0.5$, and after w decreases to about 130 meV at $x = 1$ [16, 17]. By this obviously could be explained the minimum value of the activation energy for the conductivity E_a in the middle of concentration interval for $CuInP_2(Se_xS_{1-x})_6$ the solid solutions. The minimum of conductivity σ_0 is strongly correlated with the unit cell volume minimum observed in [28] and can be explained by extending of the channels for Cu cations movement when sulphur is replaced by selenium.

σ_0 correlates with activation energy E_a as $\sigma_0=\sigma_{00}\exp(E_A/k_BT_{MN})$ [33], where σ_{00} is often called as Meyer-Neldel pre exponential factor and T_{MN} Meyer-Neldel temperature (Figure 1.12). Obtained parameters for $CuInP_2(S_xSe_{1-x})_6$ crystals are $\sigma_{00}=6.37*10^{-5}$ S/m, $T_{MN}=290.6$ K. Conductivity σ generally can be described so:

$$\sigma = \sigma_0 e^{\frac{E_a}{k_B T_{MN}} - \frac{E_a}{k_B T}}. \tag{1.13}$$

One sees immediately that for a Meyer-Neldel temperature T_{MN}, the conductivity becomes independent of the activation energy. Therefore, in presented crystals family conductivity near room temperature vary only slightly in comparison with drastic variation of σ_0.

The conductivity of mobile ions can be related to the electrical modulus, $M^*(\omega)$, which a defined as reciprocal of the complex permittivity:

$$M^*(\omega) = \frac{1}{\varepsilon^*(\omega)} = \frac{\varepsilon' - i\varepsilon''}{|\varepsilon|^2} = M + iM'', \tag{1.14}$$

in analogy with the mechanical shear and tensile modulus being the complex reciprocals of the shear and tensile compliances. Frequency dependence of complex electrical modulus can be described by the integral equation:

$$M^* = M_\infty\left(1 - \int_0^\infty e^{-i\omega t}\left(-\frac{d\varphi}{dt}\right)dt\right). \tag{1.15}$$

The function $\varphi(t)$ gives the time evolution of the electric field within the material.

If $\varphi(t)$ is a single exponential decay $e^{-t/\tau}$, that Eq. (1.15) become the Debye like formula. The authors [30] found that a good description of the electrical relaxation behaviour of ionic solids and liquids was obtained using Eq. (1.15) together with KWW function [34]:

Copyright © 2010. Nova Science Publishers, Incorporated. All rights reserved.

Handbook of Material Science Research, Nova Science Publishers, Incorporated, 2010. ProQuest Ebook Central,

$$\Phi(t) = \exp[-(\frac{t}{\tau_{WW}})^{\beta}]. \tag{1.16}$$

Dielectric function then is:

$$\varepsilon^*(\omega) = \Delta\varepsilon\int_0^{\infty}[-\frac{d\Phi(t)}{dt}]e^{-i\omega t}dt\,. \tag{1.17}$$

The Cole-Cole function Eq. (1.1) is substantiality unsuitable for description frequency dependence of the complex electrical modulus $M^*(\omega)$, because both high-frequency and low-frequency limits of the Cole-Cole approach diverge [30].

The isothermal frequency spectra of M' and M'' of $CuInP_2S_6$, $CuInP_2Se_6$ and mixed crystals $CuInP_2(S_{1-x}Se_x)_6$ are presented in Figure 1.13. The low-frequency value of M' is almost zero and represents a lack of the restoring force for the electric field induced by mobile copper ions. As frequency increases, each ion moves a shorter and shorter distance until finally the electric field changes so rapidly that the ions only oscillate within the confinements of their potential energy wells. As a result, M' increases to a maximum asymptotic value $M(\infty) = 1/\varepsilon(\infty)$.

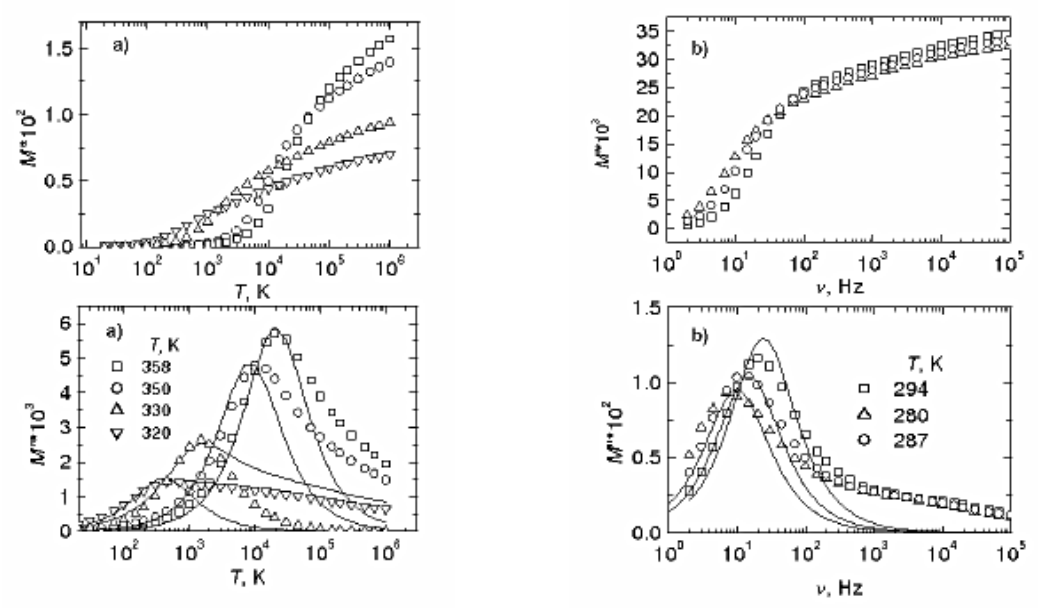


Figure 1.13 continues.

Copyright © 2010. Nova Science Publishers, Incorporated. All rights reserved.

Handbook of Material Science Research, Nova Science Publishers, Incorporated, 2010. ProQuest Ebook Central,

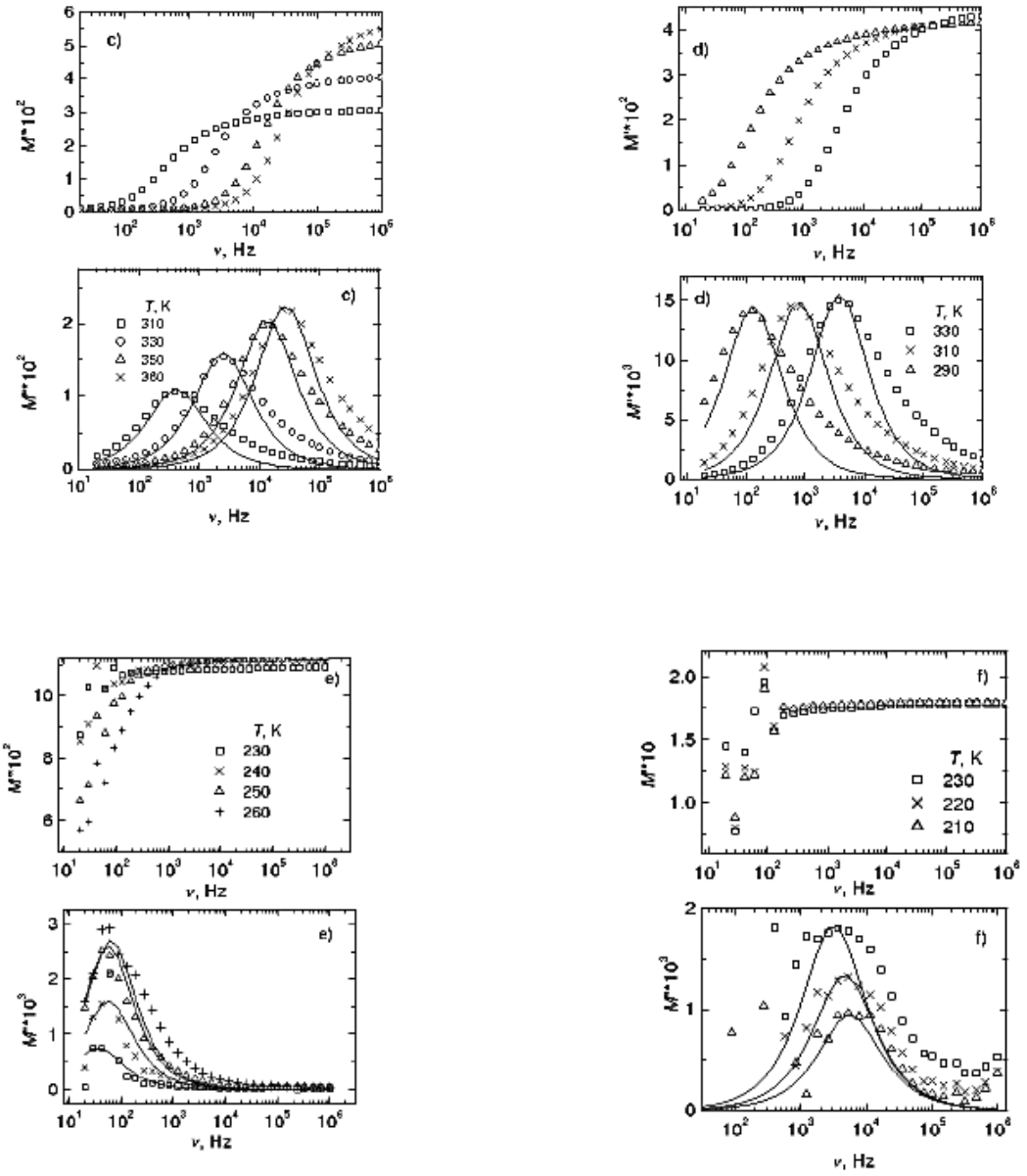


Figure 1.13 continues.

Copyright © 2010. Nova Science Publishers, Incorporated. All rights reserved.

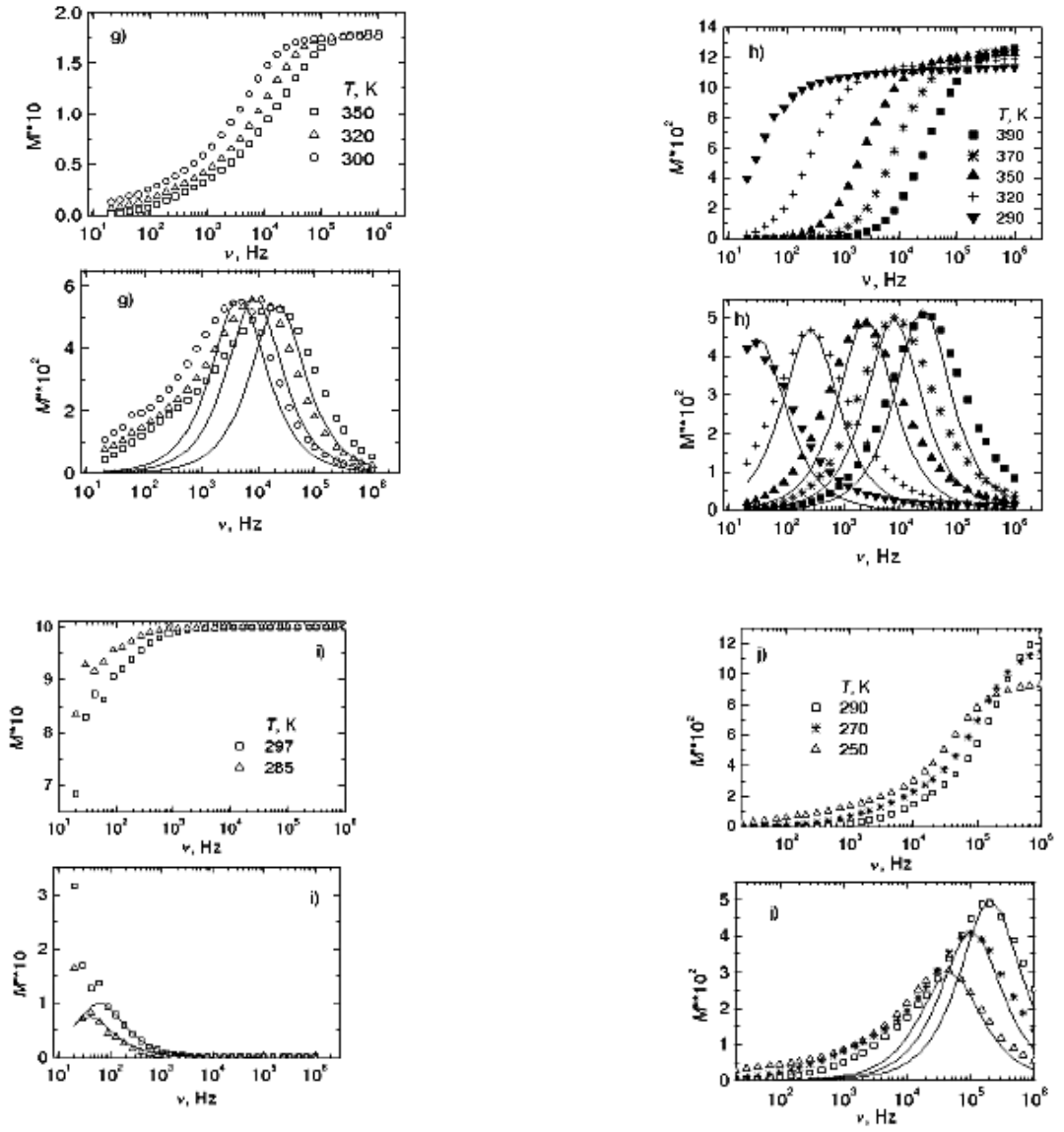


Figure 1.13. Plots of the isothermal frequency spectra of M' and M'' of $CuInP_2(S_xSe_{1-x})_6$ mixed crystals at different x: 1 a), 0 b), 0.98 c), 0.8 d), 0.7 e), 0.6 f), 0.5 g), 0.4 h), 0.1 i) 0.02 j). The solid lines are best fit according to (4.11), with $\varphi(t)$ single exponential decay function.

The spectra of M'' show a slightly asymmetric peak centered in the dispersion region of M'. For frequencies to the left of the M'' peak ($\omega\tau_\sigma < 1$) most ions are mobile over long distances and are able to decay the applied electric field. For frequencies to the right of the M'' peak ($\omega\tau_\sigma > 1$), most ions are spatially confined in their potential wells and are unable to decay the applied electric field. The region where the peak occurs ($\omega\tau_\sigma = 1$) is indicative of the transition from long-range to short-range ion mobility and the peak frequency corresponds to the average electric field (or conductivity) relaxation time, $1/\tau_\sigma$. The broadening in the

Copyright © 2010. Nova Science Publishers, Incorporated. All rights reserved.

Handbook of Material Science Research, Nova Science Publishers, Incorporated, 2010. ProQuest Ebook Central,

modulus spectra indicates a cooperative motion of mobile ions, especially in the higher frequency range.

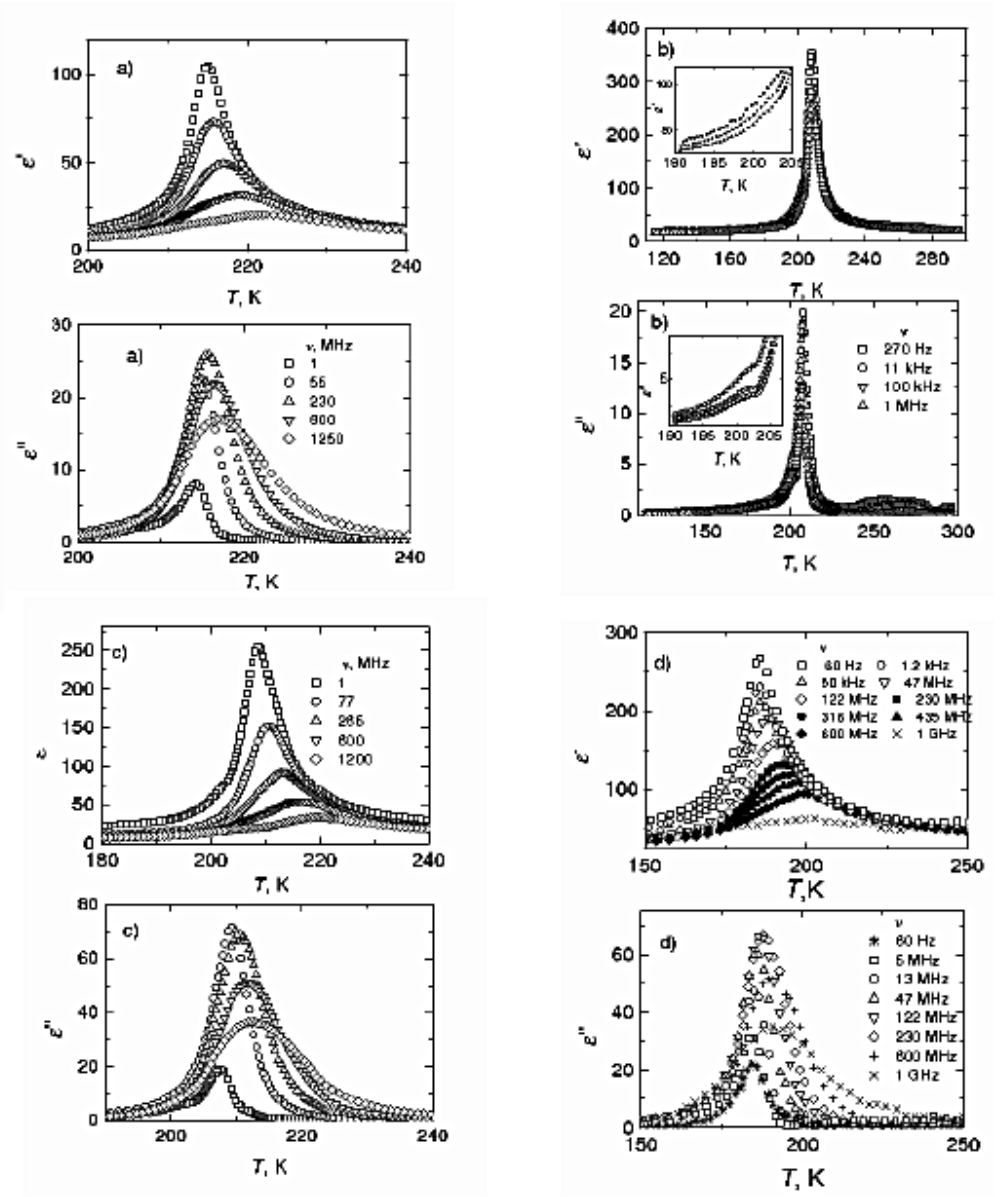


Figure 1.14. Temperature dependence of complex dielectric permittivity of $CuInP_2(S_xSe_{1-x})_6$ ferrielectrics with different *x*: a) 0.02; b) (at lower frequencies) and c) at (higher frequencies) 0.05; d) 0.1.

Copyright © 2010. Nova Science Publishers, Incorporated. All rights reserved.

Handbook of Material Science Research, Nova Science Publishers, Incorporated, 2010. ProQuest Ebook Central,

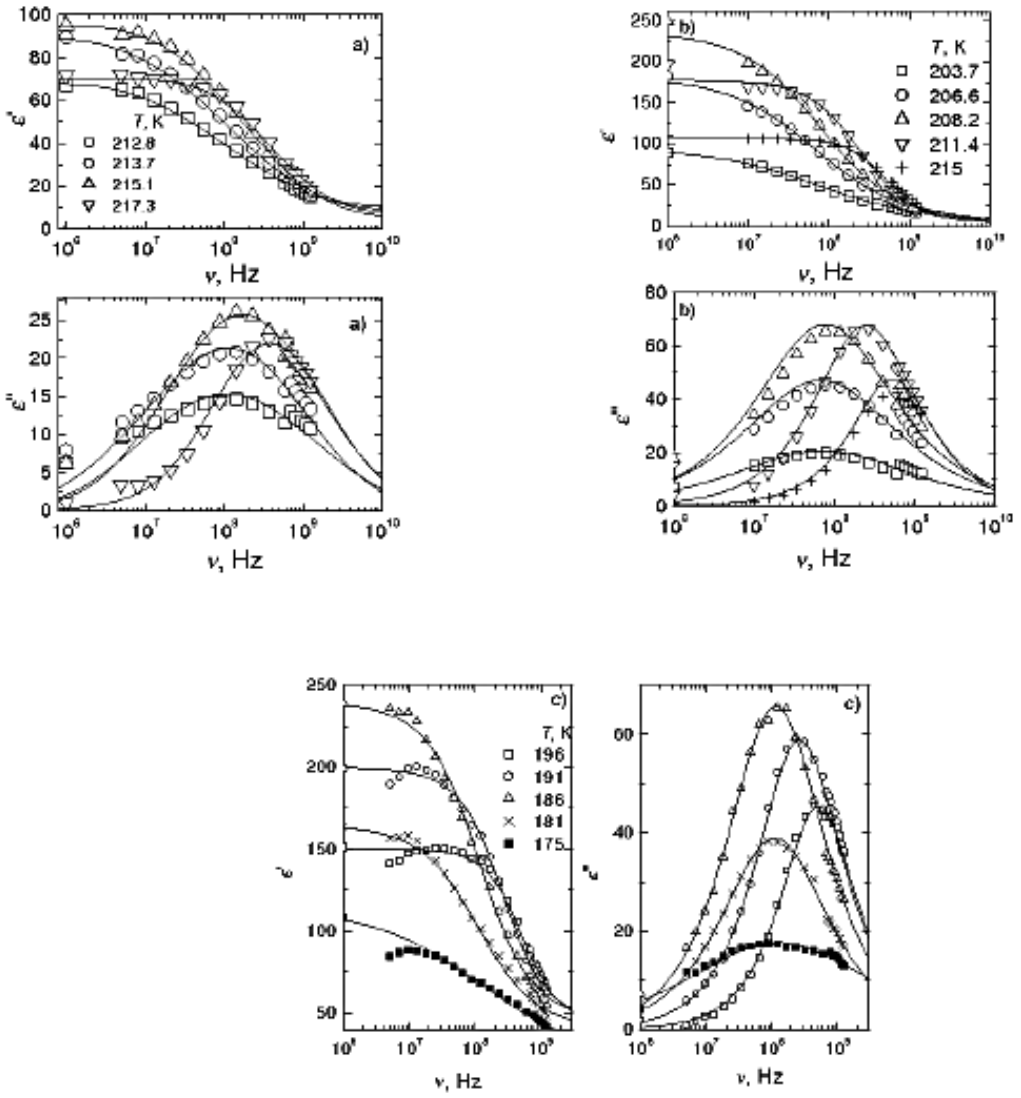


Figure 1.15. Frequency dependence of complex dielectric permittivity of $CuInP_2(S_xSe_{1-x})_6$ ferrielectrics with different *x*: a) 0.02; b) 0.05; c) 0.1.

1.3. Dynamics of Phase Transitions in Mixed $CuInP_2(SxSe_1\text{-}x)_6$ Crystals

1.3.1. Influence of Small Amount of Sulphur to Dielectric Dispersion in $CuInP_2Se_6$ Crystals

As already have been mentioned, a small admixture of impurities can changes properties of ferroelectrics. Here we will present dielectric properties of ferrielectric $CuInP_2Se_6$ crystals with a small admixture of sulphur (2-10 %). The temperature dependence of dielectric permittivity ε^* of $CuInP_2(S_{0.02}Se_{0.98})_6$, $CuInP_2(S_{0.05}Se_{0.95})_6$ and $CuInP_2(S_{0.1}Se_{0.9})_6$ crystals at several frequencies are presented in Fig 1.14. A small amount of sulphur (2%) changes the temperature of the maximum of dielectric permittivity significantly (from about 225 K to 216

Copyright © 2010. Nova Science Publishers, Incorporated. All rights reserved.

Handbook of Material Science Research, Nova Science Publishers, Incorporated, 2010. ProQuest Ebook Central,

K). For further increasing of sulphur admixture the temperature of the maximum of dielectric permittivity strongly decrease. Such a behaviour already observed in [35], however at only one frequency 10 kHz. The temperature of dielectric permittivity peak T_m of all crystals under study show pronounced frequency dependence in frequency range 10 MHz –1.2 GHz. At low frequencies an additional break in temperature dependence of losses ε″ appears at T=203 K in $CuInP_2(S_{0.05}Se_{0.95})_6$ crystals (Figure 1.14b). This additional anomaly is strongly correlated with a weak breaking of dielectric permittivity ε' at the same temperature and also was already observed in [35]. There a hypothesis was put that this breaking is caused by a jump from intermediate to ferrielectric phase. However, the low-frequency dielectric dispersion is broad enough both above and below 203 K, therefore such effect is rather dynamic than static and probably is caused by the ferroelectric domain dynamics.

The temperature behaviour of the dielectric dispersion of $CuInP_2Se_6$ crystals with a small admixture of sulphur (Figure 1.15) is very similar to the dielectric dispersion of pure $CuInP_2Se_6$ crystals. At higher temperatures ($T >> T_c$) the dielectric dispersion reveals in 10^8 - 10^{10} Hz frequency range. With decreasing temperature the dielectric dispersion become broader and appears at lower frequencies. At lower temperatures

($T << T_c$) the dielectric dispersion remains in wide frequency range and only its strength decreases on cooling. More information about the phase transition dynamics can be obtained by analysis the dielectric dispersion with the Cole-Cole formula (1.1). Obtained parameters are presented in Figure 1.16. The Cole-Cole parameters of all presented compounds show the similar behaviour: the Cole-Cole distribution parameter α_{CC} strongly increases on cooling, reciprocal dielectric strength $1/\Delta\varepsilon$ show a minimum at ferroelectric phase transition temperature, the soft mode frequency $\nu_r=1/(2\pi\tau_{CC})$ slows down on cooling in the paraelectric phase.

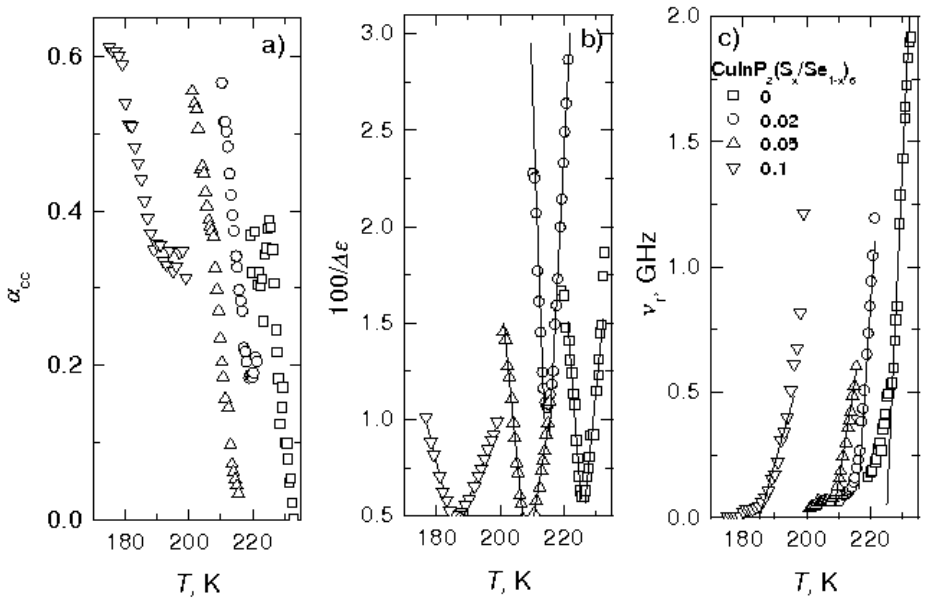


Figure 1.16. Temperature dependence of the Cole-Cole parameters a) α_{cc}; b) $1/\Delta\varepsilon$; c) ν_r for $CuInP_2(S_xSe_{1-x})_6$ ferrielectrics with x is 0.02-0.1.

Copyright © 2010. Nova Science Publishers, Incorporated. All rights reserved.

Handbook of Material Science Research, Nova Science Publishers, Incorporated, 2010. ProQuest Ebook Central,

Table 1.1. Parameters of phase transition dynamic of $CuInP_2Se_6$ crystals with small admixture of sulphur

	C_p, K	C_F, K	C_p/C_F	B, MHz/K	T_c, K
$CuInP_2Se_6$	591.7	444.4	1.33	271.9	225
$CuInP_2(Se_{0.98}S_{0.02})_6$	309.6	215.9	1.43	193.4	215.7
$CuInP_2(Se_{0.95}S_{0.05})_6$	980.3	591.7	1.66	79.3	208.2
$CuInP_2(Se_{0.9}S_{0.1})_6$	2380.9	1562.5	1.52	44.4	185

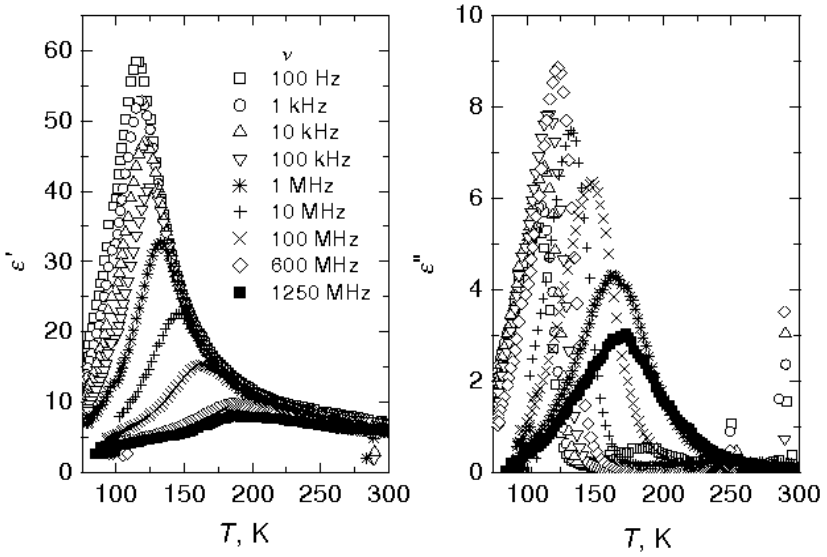


Figure 1.17. Temperature dependence of complex dielectric permittivity of $CuInP_2(S_{0.25}Se_{0.75})_6$ relaxors.

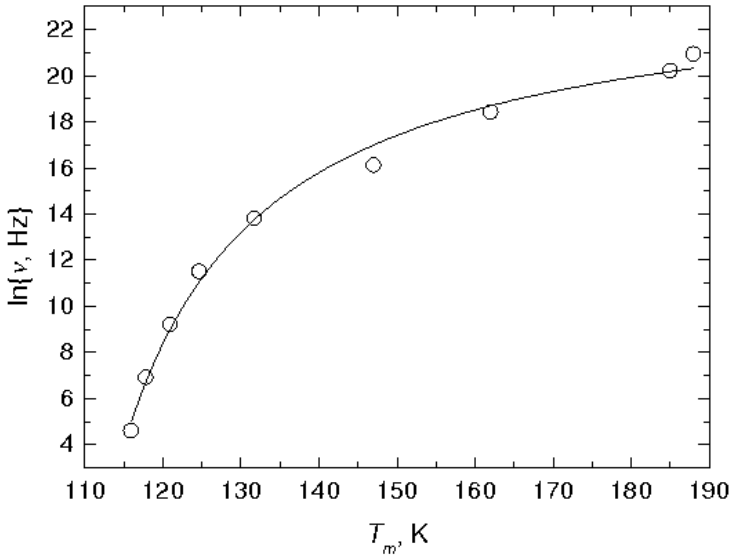


Figure 1.18. The measured frequencies ν versus T_m.

Copyright © 2010. Nova Science Publishers, Incorporated. All rights reserved.

Handbook of Material Science Research, Nova Science Publishers, Incorporated, 2010. ProQuest Ebook Central,

Temperature dependence of the dielectric strength $\Delta\varepsilon$ and the soft mode frequency were fitted with Eqs. (1.1) and (1.2), respectively. Obtained parameters are presented in Table 1.1. For all the compounds the C_p/C_F ratio is about 1.5, for the second order phase transitions this ratio must be 2, for the first order one higher than 2. It is possible that in these crystals between paraelectric and ferroelectric phase an additional incommensurate phase exist. However, in all presented crystals no any anomalies above the main (ferroelectric) anomalies were observed (Figure 1.14).

Below the main anomalies in $CuInP_2Se_6$ (Figure 1.3b) and $CuInP_2(Se_{0.95}S_{0.05})_6$ (Figure 1.15b) crystals the additional dielectric anomalies really were observed, however they are caused by ferroelectric domain dynamics. Therefore, probably the contribution of ferroelectric domain dynamics effectively raises the dielectric strength $\Delta\varepsilon$ in the ferroelectric phase and together C_F.

1.3.2. Crossover between Ferroelectric Order and Dipolar Glass Disorder

In recent years, the search for relaxor ferroelectrics or relaxor antiferroelectrics in Pb-excluded substances has been a popular subject because they are widely applicable. A probable way to discover new relaxors is inspection of both antiferroelectric-glass and ferroelectric-glass phase boundaries of very known mixed crystals families. Recently the relaxor-like behaviour as an embryo of the glass is proposed in the antiferroelectric-glass phase boundary region of DRADP crystals family where the growth of glass ordering is shown in quite a different pattern from that of the ferroelectric-glass phase boundary region [36]. The temperature dependences of the complex dielectric permittivity ε^* at various frequencies of $CuInP_2(Se_{0.75}S_{0.25})_6$ crystals show typical relaxor behaviour (Figure 1.17). There is a broad peak in the real part of dielectric permittivity as a function of temperature. With increasing frequency in the wide frequency range from 20 Hz to 1.25 GHz, T_m increases, while the magnitude of the peak decreases. There is a strong dielectric dispersion in a radio frequency region around and below T_m at 1 kHz. This dielectric dispersion does not obey the Debye theory [37].

At temperatures around and above its peak temperature (T'_m) of the dielectric absorption, the dielectric losses exhibit a strong frequency dependence. The value of T'_m is much lower than that of T_m at the same frequency. The position of the maximum of dielectric permittivity is strongly frequency-dependent; no certain static dielectric permittivity can be obtained below and around dielectric permittivity maximum temperature T_m at 1 kHz. This behaviour has been described by the Vogel-Fulcher relationship [38]:

$$\nu = \nu_0 e^{-\frac{E_t}{k_B(T_m - T_{0t})}}, \tag{1.18}$$

where T_m is the temperature at which the measured imaginary part of dielectric permittivity ε'' passes through a maximum, ν_0 is the frequency approached with $T_m \to \infty$; E_t is the activation energy, T_{0t} is the freezing temperature. (Figure 1.18). Obtained parameters are ν_0=38.34 GHz, E_f /k_B=370 K, T_{0t}=96.8 K. The dielectric dispersion of $CuInP_2(S_{0.25}Se_{0.75})_6$ crystals show strong temperature dependence (Figure 1.19): at higher temperatures the dielectric dispersion is only in 10^7 – 10^{10} Hz region, on cooling the dielectric dispersion becomes broader and more asymmetric, strongly asymmetric and very broad dielectric dispersion is observed below

Copyright © 2010. Nova Science Publishers, Incorporated. All rights reserved.

Handbook of Material Science Research, Nova Science Publishers, Incorporated, 2010. ProQuest Ebook Central,

and around dielectric permittivity maximum temperature T_m at 1kHz. The Cole-Cole formula (1.1) can describe such dielectric dispersion only at higher temperatures, because it predefined symmetric shape of the dielectric dispersion. This is clearly visible in Figure 1.19, where the Cole-Cole fit represents as dot line. Obtained Cole-Cole parameters of presented crystals are showed in Figure 1.20.

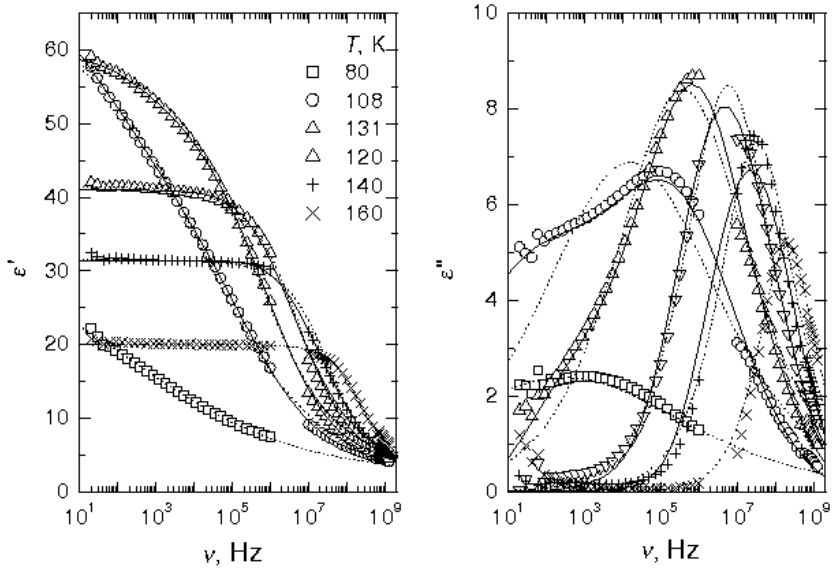


Figure 1.19. Frequency dependence of complex dielectric permittivity of $CuInP_2(S_{0.25}Se_{0.75})_6$ relaxors.

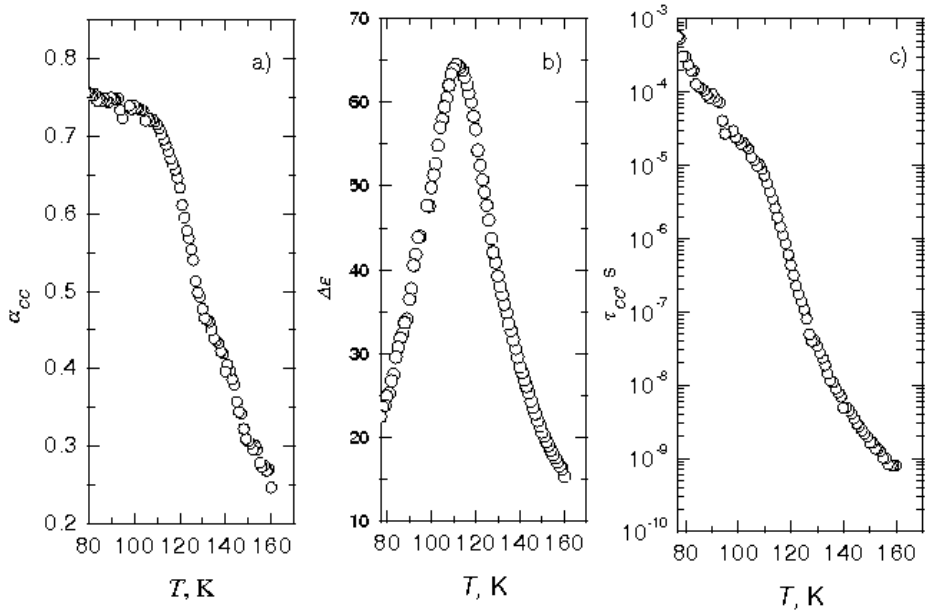


Figure 1.20. Temperature dependence of the Cole-Cole parameters a) α_{cc}; b) $\Delta\varepsilon$; c) τ_{CC} of $CuInP_2(S_{0.25}Se_{0.75})_6$ relaxors.

Copyright © 2010. Nova Science Publishers, Incorporated. All rights reserved.

Handbook of Material Science Research, Nova Science Publishers, Incorporated, 2010. ProQuest Ebook Central,

On cooling distribution of Cole-Cole parameter of relaxation times α_{CC} and mean relaxation time τ_{cc} strongly increase. The dielectric strength $\Delta\varepsilon$ has maximum near 111 K, however this maximum is not caused by some phase transition, because Cole-Cole formula becomes at low temperatures no adequate. For extracting distributions of relaxation times, the method described in next section has been used.

1.3.3. Dielectric Dispersion in Disordered Materials

As already was mentioned, in pure ferroelectrics the relaxation dielectric dispersion often is of Debye-like. However, in disordered solids, such as dipolar glasses, relaxors and more others, as rule dielectric dispersion is much broader than 1.14 decades as should be from the Debye formula [34]. The plausible assumption is that relaxation dielectric dispersion $\varepsilon^*(\omega) = \varepsilon' - i\varepsilon''$ in disordered materials can be represented as a superposition of the independent individual Debye-like processes:

$$\varepsilon'(\nu) = \varepsilon_{\infty r} + \Delta\varepsilon \int_{-\infty}^{\infty} \frac{f(\tau) d \lg \tau}{1+(\omega\tau)^2}, \tag{1.19}$$

$$\varepsilon''(\nu) = \Delta\varepsilon \int_{-\infty}^{\infty} \omega\tau \frac{f(\tau) d \lg \tau}{1+(\omega\tau)^2}. \tag{1.20}$$

These two expressions actually are the Fredholm integral equations of the first kind for the relaxation time distribution f(τ) definition. Such integral equations are known to be an ill-posed problem. Such normalization condition for f(τ) must fulfilled:

$$\int_{-\infty}^{\infty} f(\tau) d \lg(\tau) = 1. \tag{1.21}$$

From the distribution function the decay function $\Phi(t)$ can be calculated:

$$\Phi(t) = \int_{-\infty}^{\infty} f(\ln(\tau)) e^{-\frac{t}{\tau}} d \ln(\tau). \tag{1.22}$$

1.3.4. Various Predefined Dielectric Relaxation Functions

Simplistic solutions way of Eqs. (1.21) and (1.22) is the guess such the f(τ) function that integrals in formulas (1.19) and (1.20) can be integrated exactly. A most popular predefined distribution of relaxation times is the Cole-Cole distribution [39]:

$$f(\tau) = \frac{\sin(\alpha_{CC}\pi)}{\cosh\left[(1-\alpha_{CC})\ln(2\pi\tau_{CC}/\tau)\right] - \cos(\alpha_{CC}\pi)}, \tag{1.23}$$

Copyright © 2010. Nova Science Publishers, Incorporated. All rights reserved.

Handbook of Material Science Research, Nova Science Publishers, Incorporated, 2010. ProQuest Ebook Central,

there $0 \le \alpha_{CC} \le 1$ are the parameters of width of Cole-Cole distributions functions, τ_{CC} is the mean and most probable Cole-Cole relaxation time. From Eqs. (1.21), (1.19) and (1.20) easily can be obtained:

$$\varepsilon^* = \varepsilon_{\infty r} + \frac{\Delta\varepsilon}{1+(i\omega\tau_{CC})^{1-\alpha_{CC}}}. \tag{1.24}$$

This formula is used very often; extremely often for various preliminary (and therefore often narrowband) dielectric studies of new materials. However, for the prototypical relaxors PMN and SBN and for the prototypical dipolar glasses DRADP Cole-Cole it is not valid, here some authors use two or more Cole-Cole functions. Another example of an empirical symmetric function for $\varepsilon''(\omega)$ is the Fuoss-Kirkwood equation [40] which is generalized form of Debye response and formulated directly for imaginary part of $\varepsilon^*(\omega)$:

$$\varepsilon''(\omega) = \varepsilon''_p(\sec h(m\ln(\omega\tau)) = \frac{2\varepsilon''_p(\omega\tau)^m}{1+(\omega\tau)^{2m}}, \tag{1.25}$$

where ε''_p is the value of $\varepsilon''(\omega)$ at the peak frequency ω_p. In this case, $\varepsilon''_p = m*\Delta\varepsilon/2$ and $\omega_p = 1/\tau$. Equation implies (1.25) power laws with exponent $-m$ at high frequencies and m at low frequencies. In this case, the distribution function is:

$$f(\tau) = \frac{m}{\pi}\frac{\cosh(\frac{m\pi}{2})\cosh(mo)}{\cos^2(\frac{m\pi}{2})+\sinh^2(mo)}, \quad o=\log(\tau_p/\tau). \tag{1.26}$$

For dielectric dispersion in relaxors is enough popular so called (also symmetric) "box" or "step" distribution function [41]:

$$f(\tau) = \frac{\Delta\varepsilon}{\ln(\frac{\tau_1}{\tau_2})} \quad \text{for } \tau_2<\tau<\tau_1$$

And

$$f(\tau)=0 \text{ for } \tau>\tau_1 \text{ or } \tau<\tau_2. \tag{1.27}$$

The integrals in Eqs. (1.19) and (1.20) with a uniform distribution function can be transformed into the following expression:

Copyright © 2010. Nova Science Publishers, Incorporated. All rights reserved.

Handbook of Material Science Research, Nova Science Publishers, Incorporated, 2010. ProQuest Ebook Central,

$$\varepsilon^*(\omega) = \varepsilon_{\infty r} + \frac{\Delta\varepsilon}{\ln(\tau_1/\tau_2)}\left[\frac{1}{2}\ln\left(\frac{(\tau_1/\tau_2)^2 + (\tau_1\omega)^2}{1+(\tau_1\omega)^2}\right) - i\arctan\left(\frac{\omega\tau_1(\tau_1/\tau_2 - 1)}{(\omega\tau_1)^2 + \tau_1/\tau_2}\right)\right]. \tag{1.28}$$

This relationship predicate extremely fast (in comparison with otherwise predefined functions) alternation of ε'' around the frequencies $1/\tau_1$ and $1/\tau_2$, however such a behaviour of imaginary part of dielectric permittivity until now is not observed in any materials, therefore discrepancy of fit around mentioned frequencies is significant and essential [41]. Consequently such uniform distribution function is extremely rough approach of natural distributions of relaxation times. When possible to use such rough approach? In the range of frequencies that satisfy condition $\frac{1}{\tau_1} << \nu << \frac{1}{\tau_2}$ the exact solution of Eq. (1.28) gives very simple and easily applicable in practice predictions for both real and imaginary parts of the dielectric function:

$$\varepsilon'(\omega) = \varepsilon_{\infty r} - \frac{\Delta\varepsilon}{\ln(\tau_1/\tau_2)}\ln(\omega\tau_2),$$

$$\varepsilon''(\omega) = \frac{\pi}{2}\frac{\Delta\varepsilon}{\ln(\tau_1/\tau_2)}. \tag{1.29}$$

These formulas are usable for various narrowband measurements [42] and for broadband measurements of anomalous broad dielectric dispersion [41, 43]. In the first case, such analysis is clearly shoddy, in another case - speculative. Indeed parameters in formulas (1.29) $\varepsilon_{\infty r}$, τ_2 can easily be obtained from enough high-frequency data, however two parameters $\Delta\varepsilon$ and τ_1 remain unknown. Authors of [43] assumed that $\Delta\varepsilon$ alternate according to the Curi-Weiss law and obtained unusual big values of times $\tau_1 \approx 10^{64}$ s at low temperatures. Clearly to examine this fact total lifetime is too short. Another misapprehension is that Eq. (1.29) is useful around and below T_0 [41]. It is clearly visible from Eq. (1.29) that at T_0 $\varepsilon''(\omega)$ should be equal to zero, and consequently such analysis here become brute.

The simplest case of the asymmetric distribution function is the Cole-Davidson distribution function [44]:

$$f(\tau) = \frac{\sin(\gamma\pi)}{\pi}\left(\frac{\tau}{\tau_{CD} - \tau}\right)^{\gamma} \text{ for } \tau<\tau_{CD}, \tag{1.30}$$

and $f(\tau)=0$ for $\tau>\tau_{CD}$,
where τ_{CD} is the most probable relaxation time of the Cole-Davidson distribution function and $0 < \gamma \leq 1$ parameter of asymmetry of this functions. From Eqs. (1.19), (1.20) and (1.30) we have [44]:

Copyright © 2010. Nova Science Publishers, Incorporated. All rights reserved.

Handbook of Material Science Research, Nova Science Publishers, Incorporated, 2010. ProQuest Ebook Central,

$$\varepsilon^* = \varepsilon_{\infty r} + \frac{\Delta\varepsilon}{(1+i\omega\tau)^{\gamma}}. \tag{1.31}$$

This function describes well dielectric properties of polar liquids, for example, dielectric properties of water mixture of ethanol [45].

More general descriptions of the broad and asymmetric dielectric dispersion is the combination of the Cole-Cole and the Cole-Davidson– Havriliak-Negami function [46]:

$$\varepsilon^* = \varepsilon_{\infty r} + \frac{\Delta\varepsilon}{(1+(i\omega\tau\quad)^{1-\alpha_{CC}})^{\gamma}}. \tag{1.32}$$

Havriliak and Negami [47] derived the distribution function $f(\tau)$ by means of complex analysis:

$$f(\tau) = \frac{1}{\pi}\frac{(\frac{\tau}{\tau_{HN}})^{(1-\alpha_{CC})\gamma}\sin(\gamma\theta)}{((\frac{\tau}{\tau_{HN}})^{2(1-\alpha_{CC})} + 2(\frac{\tau}{\tau_{HN}})^{(1-\alpha_{CC})}\cos(\pi(1-\alpha_{CC})) + 1)^{\gamma/2}}, \tag{1.33}$$

with

$$\theta = \arctan(\frac{\sin(\pi(1-\alpha_{CC}))}{(\frac{\tau}{\tau_{HN}})^{1-\alpha_{CC}} + \cos(\pi(1-\alpha_{CC}))}). \tag{1.34}$$

Considerably beyond the author of [48] it was establish that in Eq. (1.34) must an additional term of π append if argument of arctan functions is negative. The Havrilak-Negami function describes enough correct dielectric response of widely class of disordered materials. S. Havriliak and S. J. Havriliak [49] have analyzed approximately 1000 sets of experimental data using unbiased statistical methods and the relaxation function commonly referred to as the Havriliak-Negami function. This function is widely used for investigations of dielectric response of relaxors [50] and dipolar glasses [51]. However, dielectric response of well-known dipolar glasses DRADP is not compatible with the Havriliak-Negami functions [52]. A very important problem is physical meaning of Havriliak-Negami functions and its parameters. The experimental data shows that α_{CC} and γ are strictly dependent on temperature, structure, composition and other controlled physical parameters. However, in many works the obtained parameters α_{CC} and γ commented very little (only how the form of dielectric dispersion is related with these parameters). When experimental data is of good quality (and only one relaxation process manifest) change of dielectric dispersion form is visual from dielectric spectra $\varepsilon^*(\omega)$. Only several attempt have been made to understand the physical meaning of Havriliak-Negami dielectric response functions [53-55].

Copyright © 2010. Nova Science Publishers, Incorporated. All rights reserved.

Handbook of Material Science Research, Nova Science Publishers, Incorporated, 2010. ProQuest Ebook Central,

In time-domain frequently used so-called "stretched exponential" or the Kolrausch-Williams-Watts (KWW) function [34]:

$$\Phi(t) = \exp[-(\frac{t}{\tau_{WW}})^{\beta}]. \tag{1.35}$$

Dielectric function then is:

$$\varepsilon^*(\omega) = \Delta\varepsilon\int_0^{\infty}[-\frac{d\Phi(t)}{dt}]e^{-i\omega t}dt, \tag{1.36}$$

and distribution of relaxation times is:

$$f(\tau) = \frac{1}{\pi}\int e^{-x}e^{4\cos(\pi\beta)}\sin(u\sin(\pi\beta))dx, \text{ with } u = (\frac{x\tau}{\tau_0})^{\beta}. \tag{1.37}$$

Many physical models of KWW dielectric dispersions are proposed: localized state model, proton model, dipole interaction model and more others [56]. So that KWW function physical meaning is better understood than physical meaning of others predefined functions. Recently the empirical relationship between the KWW and Havriliak-Negami functions was discovered [57]:

$$\ln[\frac{\tau_{HN}}{\tau_{WW}}] = 2.6(1-\beta)^{0.5}e^{-3\beta},$$

$$\alpha_{CC}\gamma = \beta^{1.23}. \tag{1.38}$$

So that physical meaning of the Havriliak-Negami distributions sometimes can be related with physical meaning of the KWW models. There are many other predefined functions of distribution of relaxation times such as: Joncher [58], Rajagopal [59], Dissado-Hill [60], Curie-von Schweindler [61] and others.

We can conclude that various predefined dielectric functions dominate in dielectric spectroscopy, but physical meaning of these functions is not clear until now and discrepancy from fit often is significant and essential, so that such approach in many works is only blunt (and often bad) description of experimental data. Another calculating methods must be used in dielectric spectroscopy of disordered solids.

1.3.5. Tichonov Regularization Method

Treating integral Equations (1.19) and (1.20) numerically one has to perform the discretization which leads to the linear non homogeneous algebraic equation set. In the matrix notation it can be represented as:

Copyright © 2010. Nova Science Publishers, Incorporated. All rights reserved.

Handbook of Material Science Research, Nova Science Publishers, Incorporated, 2010. ProQuest Ebook Central,

$$A\vec{X} = \vec{T}. \tag{1.39}$$

Here the components T_n ($1 \le n \le$ N) of the vector $\vec{T}$ represent the dielectric spectrum $\{\varepsilon'_i, \varepsilon''_i\}$ ($1 \le i \le$ N/2) recorded at some frequencies ω_i. We used equidistant frequency intervals in the logarithmic scale ($\Delta \lg \tau_m$ = const). The vector $\vec{X}$ with components X_m ($1 \le m \le$ M) stands for the relaxation time distribution f (τ_m) which we are looking for. We used equidistant time intervals in the logarithmic scale as well ($\Delta \lg \tau_m$ = const). The symbol A stands for the kernel of the above matrix equation. It represents the matrix with elements obtained by the direct substitution of ω_i and τ_m values into the kernels of integral equations (1.19) and (1.20). In order to increase the accuracy in the case of noisy data, usually the number of frequency point's ω_i exceeds the number of relaxation times τ_m at which the distribution is calculated. Thus, the number of equations in Eq. (1.39) exceeds the number of variables (the number of the vector $\vec{X}$ components). Due to that fact that Equation (1.39) cannot be solved directly, and it has to be replaced by the following minimization problem:

$$\Phi_0 = \left\| \vec{T} - A\vec{X} \right\|^2 = \min . \tag{1.40}$$

Here and further we shall use the following vector norm notation $\left\| \vec{V} \right\| = \vec{V}^T \vec{V}$ where the superscript ^{T} indicates the transposed vector or matrix.

Due to the ill-posed nature of the integral Fredholm equations the above minimization problem is ill-posed as well, namely, its solution is a rather sensitive to small changes of the vector $\vec{T}$ components (the dielectric spectrum $\varepsilon^*(\omega)$ which are the input of the considered problem. That is why the above minimization problem can not be treated without some additional means. Following the Tikhonov regularization procedure we replace the functional Φ_0 by the following modified expression:

$$\Phi(\alpha_R) = \left\| \vec{T} - A\vec{X} \right\| + \alpha_R^2 \left\| R\vec{X} \right\|, \tag{1.41}$$

where the additional regularization term is added. The symbol R stands for the regularization matrix, and α_R is the regularization parameter. It plays the same role as a filter bandwidth when smoothing noisy data. The less is the value of the regularization parameter in minimization problem (2.26) the more solutions satisfy this equation within the experimentally recorded dielectric spectrum errors, and the more the solution becomes unstable itself. While increasing this parameter we deviate from the actual relaxation time distribution which we are looking for. Thus, in order to get the satisfactory result we have to add as many additional conditions as possible. First, we know that all relaxation time distribution components have to be positive ($X_n > 0$). Next, sometimes it is possible to obtain the rather reliable static permittivity $\varepsilon(0)$ or the limit high-frequency dielectric permittivity $\varepsilon_{\infty r}$. In this case it is worth to restrict the above minimization problem fixing some of these values or both.

Copyright © 2010. Nova Science Publishers, Incorporated. All rights reserved.

Handbook of Material Science Research, Nova Science Publishers, Incorporated, 2010. ProQuest Ebook Central,

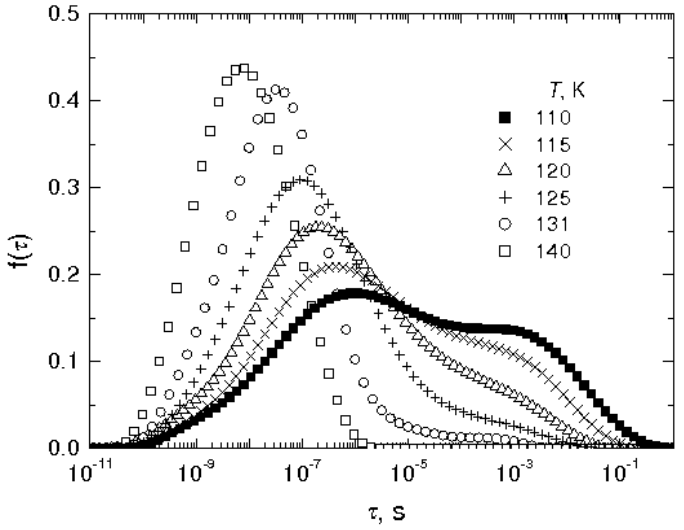


Figure 1.21. Distributions of relaxation times of $CuInP_2(S_{0.25}Se_{0.75})_6$ relaxors.

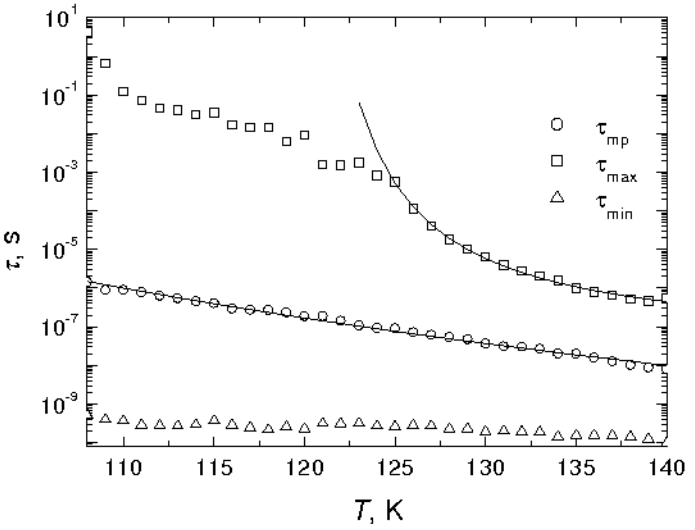


Figure 1.22. Temperature dependence of characteristic times of $CuInP_2(S_{0.25}Se_{0.75})_6$ relaxors.

1.3.6. Distribution of the Relaxtion Times

The calculated distribution of relaxation times of $CuInP_2(S_{0.25}Se_{0.75})_6$ crystals are presented in Figure 1.21. The symmetric and narrow dielectric dispersion observed only at higher temperature $T >> T_m$ (at 1 kHz), on cooling the distributions becomes broader and more asymmetric so that below T_m (at 1 kHz) second maximum appears. Such a behaviour of distributions already was observed in prototypical relaxors PMN [62].

From calculated distributions of relaxation times the most probable relaxation time τ_{mp}, longest relaxation time τ_{max} and τ_{min} shortest relaxation times (level 0.1 was chosen as sufficient accurate) has been obtained (Figure 1.22). The shortest relaxation time τ_{min} is about

Copyright © 2010. Nova Science Publishers, Incorporated. All rights reserved.

Handbook of Material Science Research, Nova Science Publishers, Incorporated, 2010. ProQuest Ebook Central,

0.1 ns and it increases slowly with the increasing of temperature. The longest relaxation time τ_{max} diverges according to the Vogel-Fulcher law (1.18). The obtained parameters are τ_0 = 2.52*10^{-8} s, E_f/k_B = 60.5 K (0.0052 eV), T_0 = 118.9 K, however the most probable relaxation time diverges with good accuracy according to the Arrhenius law:

$$\tau_{\max} = \tau_0 \exp[-\frac{E_a}{k_B T}], \tag{1.42}$$

with the parameters τ_0 = 4.6*10^{-16} s and E_a/k_B = 2365.3 K (0.203 eV).

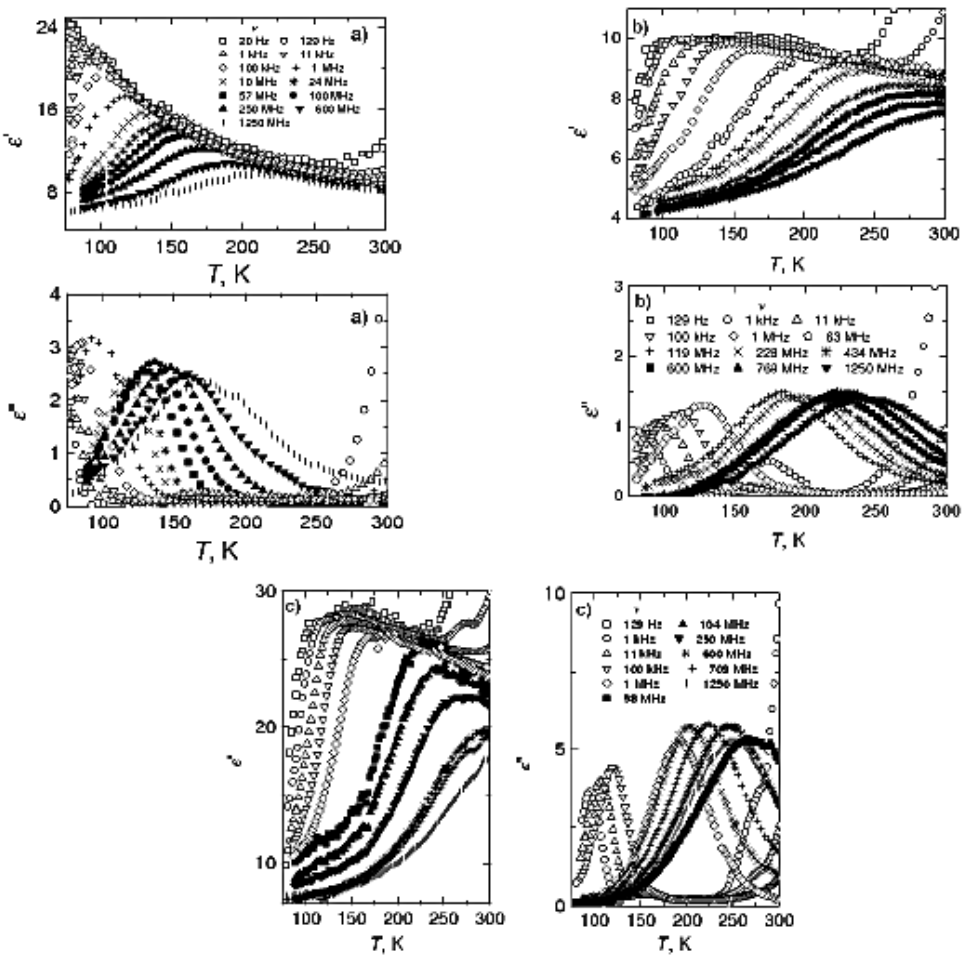


Figure 1.23. Temperature dependence of complex dielectric permittivity of CuInP2(SxSe1-x)6 dipolar glasses with different x: a) 0.4; b) 0.7; c) 0.8.

Copyright © 2010. Nova Science Publishers, Incorporated. All rights reserved.

Handbook of Material Science Research, Nova Science Publishers, Incorporated, 2010. ProQuest Ebook Central,

At this sulphur concentration (25%) the authors of [35] suggested morphotropic phase boundary between the paraelectric phases C2/c (characteristic for $CuInP_2S_6$) and P-31c (characteristic for $CuInP_2Se_6$) or accordingly ferrielectric phases Cc and P31c. Nevertheless, $CuInP_2(S_{0.25}Se_{0.75})_6$ crystals must contain much defects, they are origin of the relaxor nature of the investigated crystals. To confirm the relaxor nature of $CuInP_2(S_{0.25}Se_{0.75})_6$ crystals some additional experiments must be performed, for example dielectric hysteresis loops measurements.

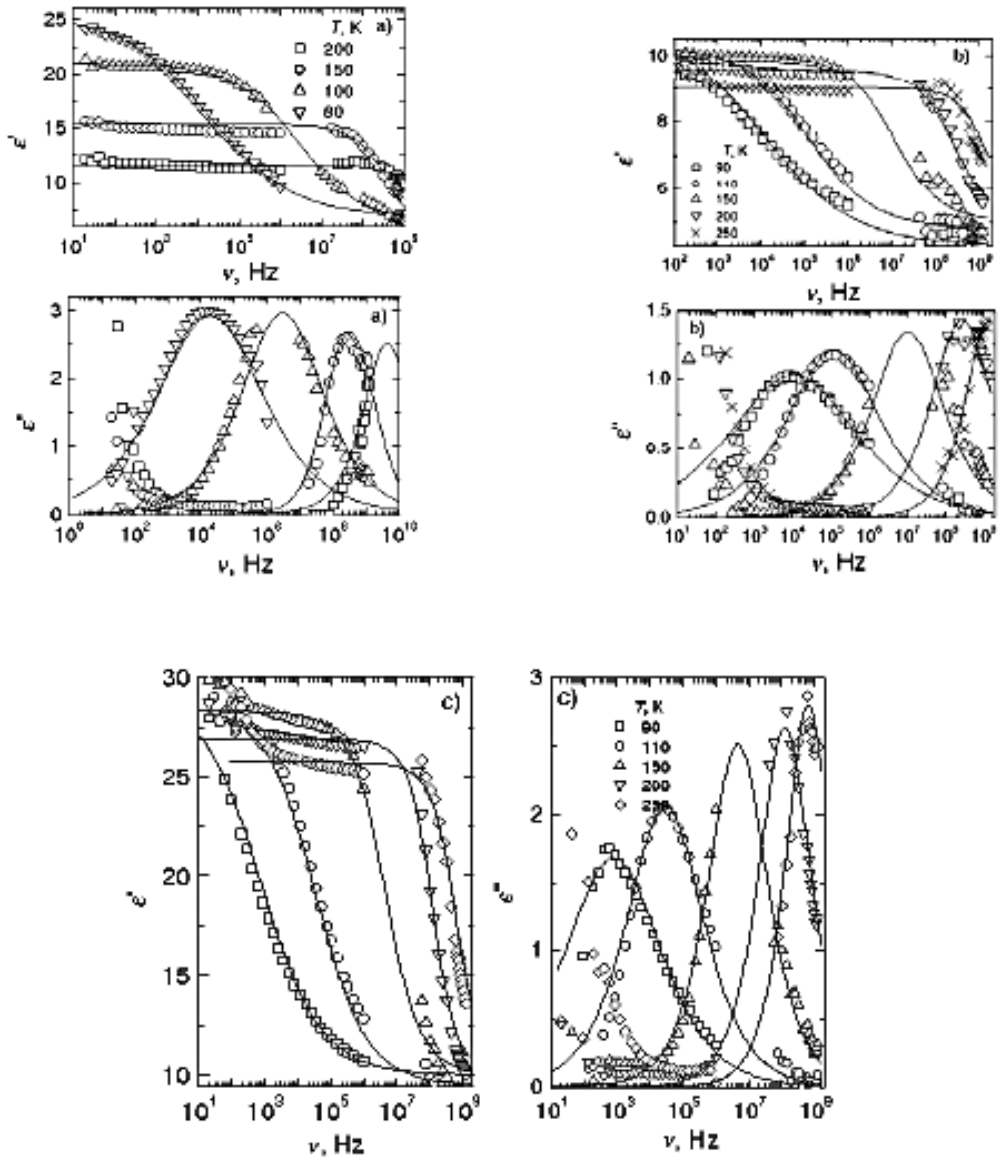


Figure 1.24. Frequency dependence of complex dielectric permittivity of $CuInP_2(Se_{1-x}S_x)_6$ dipolar glasses with different *x*: a) 0.4; b) 0.7; c) 0.8.

Copyright © 2010. Nova Science Publishers, Incorporated. All rights reserved.

Handbook of Material Science Research, Nova Science Publishers, Incorporated, 2010. ProQuest Ebook Central,

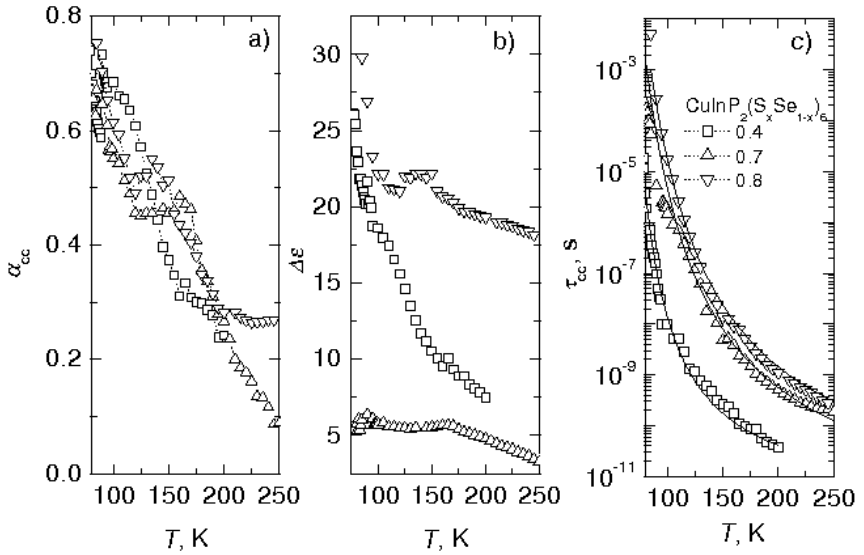


Figure 1.25. Temperature dependence of the Cole-Cole parameters: a) α_{CC} ,b) $\Delta\varepsilon$, c) τ_{CC} for $CuInP_2(Se_{1-x}S_x)_6$ dipolar glasses. The solid lines are the best fit according to Eq. (1.18).

Table 1.2. Parameters of Vogel-Fulcher law of $CuInP_2(S_xSe_{1-x})$ dipolar glasses

	τ_0, s	E_f/k_B, K	T_0, K
$CuInP_2(S_{0.4}Se_{0.6})_6$	2.29e-12	433.9	50
$CuInP_2(S_{0.7}Se_{0.3})_6$	1.07e-12	1089.8	21.9
$CuInP_2(S_{0.8}Se_{0.2})_6$	1.27e-12	1228.9	24.9

1.3.7. Dipolar Glass Disorder in Mixed $CuInP_2(S_xSe_{1-x})_6$ Crystals with x=0.4-0.8

Real and imaginary parts of the complex dielectric permittivity of $CuInP_2(S_xSe_{1-x})_6$ crystals with x=0.4-0.8 are shown in Figure 1.23 as a function of temperature for several frequencies. It's easy to see a wide dispersion of the complex dielectric permittivity extending from 260 K to the lowest temperatures.

On cooling in the static dielectric permittivity of $CuInP_2(S_{0.4}Se_{0.6})_6$ crystals is observed so called cusp, which is characteristic for spin glasses. In other compounds this cusp is completely destroyed by the strong random fields. The maximum of the real part of dielectric permittivity shifts to higher temperatures with increase of the frequency together with the maximum of the imaginary part and manifest the behaviour typical for the dipolar glasses. The dielectric dispersion is symmetric of all crystals under study so that it can easily be described by the Cole-Cole formula (1.24) (Figure 1.24).

Obtained Cole-Cole parameters are presented in Figure 1.25. On cooling, the parameter α_{CC} strongly increases and reaches extremely high value about 0.7 at $T < 100$ K for all investigated compounds. The mean relaxation time τ_{CC} on cooling strongly increases according to the Vogel-Fulcher (1.18) law. The parameters of this law are presented in Table 1.2.

We can conclude that $CuInP_2(S_xSe_{1-x})_6$ crystals with x=0.4-0.8 are dipolar glasses.

Copyright © 2010. Nova Science Publishers, Incorporated. All rights reserved.

Handbook of Material Science Research, Nova Science Publishers, Incorporated, 2010. ProQuest Ebook Central,

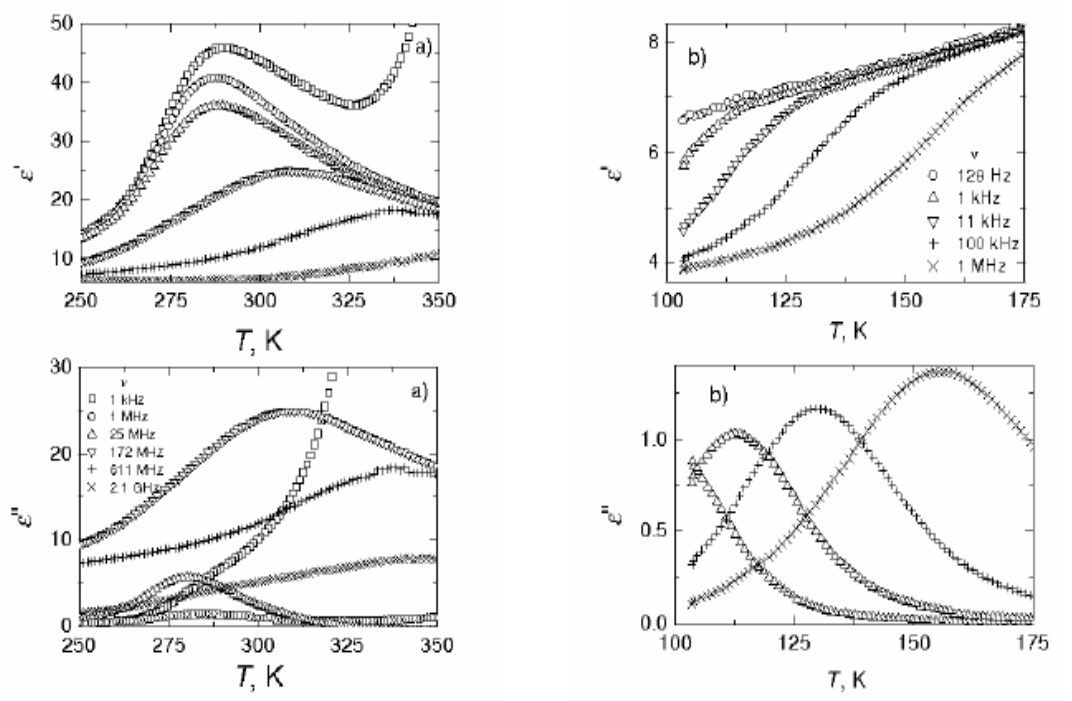


Figure 1.26. Temperature dependence of complex dielectric permittivity of $CuInP_2(S_{0.98}Se_{0.02})_6$ inhomogeneous ferroelectrics: a) high temperature anomaly b) low temperature anomaly.

1.3.8. Influence of Small Amount of Selenium to Dielectric Dispersion in $CuInP_2S_6$ Crystals

Temperature dependence of the dielectric permittivity of $CuInP_2S_6$ crystals with a small amount of selenium (2%) is presented in Figure 1.26. A small amount of selenium changes dielectric properties of $CuInP_2S_6$ crystals significantly: the temperature of the main dielectric anomaly shift from about 315 to 289 K, the maximum value of the dielectric permittivity ε' significantly decreases from about 180 to 40 (at 1 MHz), at higher frequencies (from about 10 MHz) the peak of dielectric permittivity becomes frequency- dependent in $CuInP_2(S_{0.98}Se_{0.02})_6$ crystals and a critical slowing down disappears. An additional dielectric dispersion appears at low frequencies and at low temperatures.

Such a behaviour is very similar to behaviour of betaine phosphite with a small amount of betaine phosphate and in RADA [63] crystals, where a proposition that at low temperatures a coexistence of the ferroelectric order and dipolar glass disorder appears was proposed. Therefore we can conclude that $CuInP_2(S_{0.98}Se_{0.02})_6$ crystals also exhibit at low temperatures a coexistence of ferroelectric and dipolar glass disorder. Dielectric dispersion $\varepsilon^*(\nu)$ of $CuInP_2(S_{0.98}Se_{0.02})_6$ crystals at several frequencies is presented in Fig. 1.26. Dielectric dispersion at higher temperatures (until about 180 K)

Copyright © 2010. Nova Science Publishers, Incorporated. All rights reserved.

Handbook of Material Science Research, Nova Science Publishers, Incorporated, 2010. ProQuest Ebook Central,

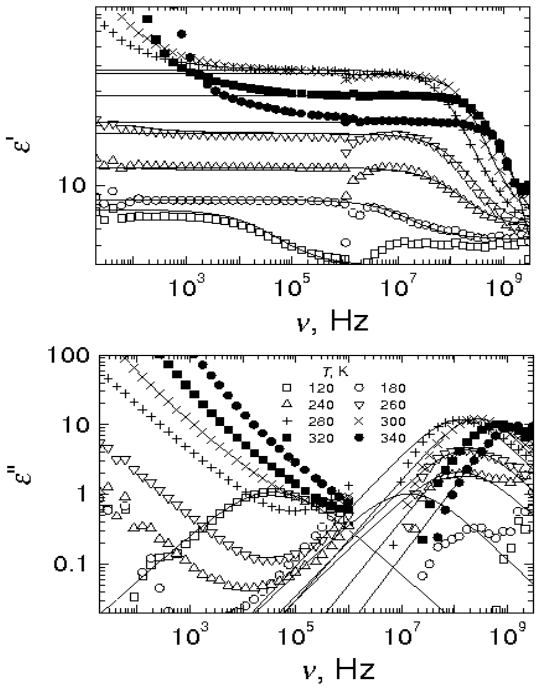


Figure 1.27. Frequency dependence of complex dielectric permittivity of $CuInP_2(S_{0.98}Se_{0.02})_6$ inhomogeneous ferroelectrics:

reveals from 10 MHz. At low temperatures, the maximum of frequency dependences of losses moves to lower frequencies (T = 120 K). The dielectric dispersion looks as symmetric so that it can be correctly described by the Cole-Cole formula (1.24). The Cole-Cole parameters are shown in Figure 1.26. The parameters of the Cole-Cole distribution of relaxation α_{CC} strongly increase on cooling and reach 0.43 at T = 100 K (Figure 1.26 a). In the temperature region 250 K – 170 K an undesirable plateau appears in dependence under study. The cause of this plateau is so that the Cole-Cole fit is not suitable in this temperature region, this can easily be seen from frequency-dependent losses ε'' (Figure 1.26) at T = 180 K. In this temperature region, two contributions in dielectric spectra dominate. The temperature dependence of fit parameters $\Delta\varepsilon$ and frequency $\nu_r=1/2\pi\tau_{CC}$ is presented in Figure 1.26b and 1.26c. These dependences of both $CuInP_2S_6$ and $CuInP_2(S_{0.98}Se_{0.02})_6$ crystals in the paraelectric phase show a similar curvature, the phase transition dynamics in pure $CuInP_2S_6$ was successfully described by the quasi-one-dimensional Ising model, therefore this model can be fit in the case of $CuInP_2(S_{0.98}Se_{0.02})_6$. The obtained parameters for this crystal are: $J_\perp/k_B$ = 70 K, J_{II}/k_B = 143.6 K, C = 1370.6 K, $\nu_\infty = 2 \times 10^{13}$ Hz, $\Delta U/k_B$ = 2647.7 K. The ratio of J_{II} and $J_\perp$ of both crystals is very similar, but the difference T_C-T_{Cising} decreases in $CuInP_2(S_{0.98}Se_{0.02})_6$ crystals (become 55 K). Consequently, in the paraelectric phase the phase transition dynamics of both crystals under study is similar. Differences become notable below the T_c. The frequency ν_r below the T_c increases only in a narrow temperature region, further on cooling a significant decreasing of frequencies ν_r is observed. This decreasing can be easily explained by the Fogel-Vulcher law (1.18). The obtained parameters are $\tau_0 = 3.77*10^{-11}$ s, E_f/k_B = 1077.5 K (0.093 eV), T_0 = 28 K. Consequently at low temperatures coexistence of the ferroelectric order and dipolar glass disorder is observed in $CuInP_2(S_{0.98}Se_{0.02})_6$ crystal.

Copyright © 2010. Nova Science Publishers, Incorporated. All rights reserved.

Handbook of Material Science Research, Nova Science Publishers, Incorporated, 2010. ProQuest Ebook Central,

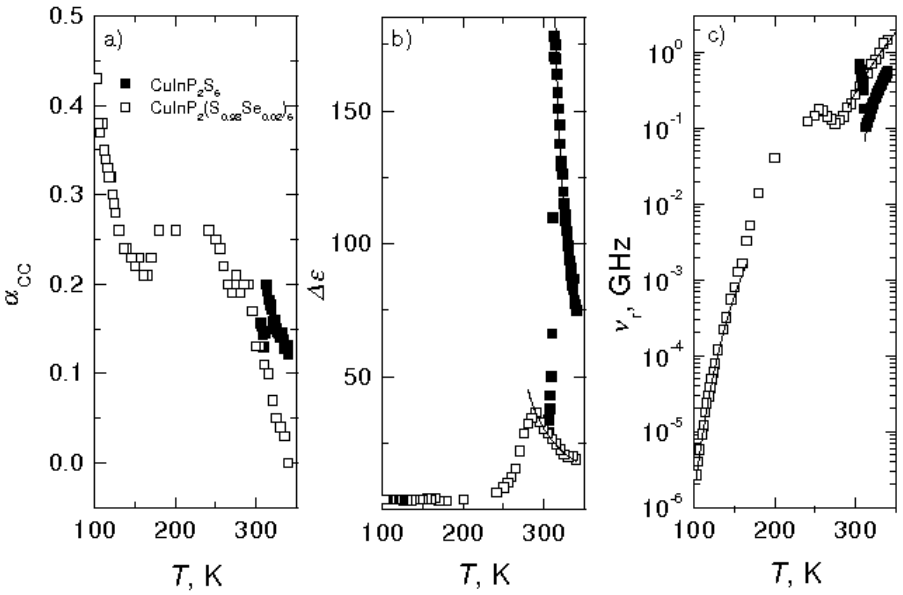


Figure 1.28. Temperature dependence of the Cole-Cole parameters a) α_{cc}; b) $\Delta\varepsilon$; c) ν_r for $CuInP_2(S_{0.98}Se_{0.02})_6$ inhomogeneous ferroelectric. The solid lines are the best fit according to Eqs. (1.4), (1.5) (at higher temperatures) and (1.18) (at lower temperatures).

2. ULTRASONIC SPECTROSCOPY OF PHASE TRANSITIONS IN $CuInP_2(S_XSE_{1-X})_6$ MIXED CRYSTALS

2.1. Introduction to Ultrasonic Behavior at the Ferroelectric Phase Transition

Usually the ultrasonic attenuation and velocity behavior near ferroelectric phase transition is described by Landau-Khalatnikov theory [64-66]. Here we shortly present the main features of this theory.

The elastic constant evaluated from ultrasonic experiment is the real part of the complex frequency dependent elastic constant $c^*(\varpi)$. For temperatures close to, but below phase transition temperature T_c in ferroelectric materials, ω can be compared to the inverse relaxation time of order parameter (polarization), so that dispersion can affect the value of $c^*(\varpi)$. In this case, from Landau-Khalatnikov theory in the ferroelectric phase:

$$c(\varpi) = c_\infty - \frac{c_\infty - c_0}{1+\varpi\tau}, \tag{2.1}$$

where c_∞ - is the elastic constant at high frequencies and c_0 is the static value of the elastic constant in the low remperature phase.

From the general theory of elasticity:

Copyright © 2010. Nova Science Publishers, Incorporated. All rights reserved.

Handbook of Material Science Research, Nova Science Publishers, Incorporated, 2010. ProQuest Ebook Central,

$$v^2 = \frac{\mathrm{Re}\, c^*}{\rho} = v^2{}_\infty - \frac{v^2{}_\infty - v^2{}_0}{1+\varpi^2\tau^2}, \tag{2.2}$$

$$\alpha = \frac{\varpi \,\mathrm{Im}\, c^*}{2\rho v_0{}^3} = \frac{v_\infty{}^2 - v_0{}^2}{2v_0{}^3}\frac{\varpi^2\tau}{1+\varpi^2\tau^2}. \tag{2.3}$$

In order to get expressions for the ferroelectric phase , the free energy dencity of a proper uniaxial ferroelectric without piezoeffect in the ferroelectric phase can be written as

$$F = F_0 + \frac{A}{2}(T-T_c)P^2 + \frac{\beta}{4}P^4 + \frac{\gamma}{6}P^6 + guP^2 + \frac{1}{2}c_\infty u^2, \tag{2.4}$$

where A, β, γ are Landau coefficients, g is appropriate electrostriction tensor component, u is the elastic strain component and P is polarization. Using the equation of equilibrium the static elastic constant can be straightforwardly calculated as:

$$c = c_\infty - \frac{2g^2}{\beta + 2\gamma P^2}, \tag{2.5}$$

Usually ΔP indused by strain is less than the static value of polarization P_0 and the P in (2.5) can be changed to:

$$P_0 = \frac{-\beta + [\beta^2 - 4\alpha\beta(T-T_c)]^{0.5}}{2\gamma}. \tag{2.6}$$

Then we get:

$$c = c_0 - \frac{2g^2}{\beta(1+\frac{T_c - T}{n})^{0.5}}, \tag{2.7}$$

where $n = \beta^2/4A\gamma$. Rewriting (2.7) in the form $\Delta c = c_\infty - c_0 = \rho v_\infty{}^2 - \rho v_0{}^2$ (where ρ is mass density, one finds in the ferroelectric phase that:

$$v_\infty{}^2 - v_0{}^2 = \frac{2\rho g^2}{\beta(1+(T_c - T)/n)^{0.5}}. \tag{2.8}$$

Inserting (2.8) in equations (2.2) and (2.3) and assuming the value of v_∞ equal to the ultrasonic velocity in the paraelectric phase v_{para} we obtain simple expressions for ultrasonic velocity and attenuation in ferroelectric material near phase transition:

Copyright © 2010. Nova Science Publishers, Incorporated. All rights reserved.

Handbook of Material Science Research, Nova Science Publishers, Incorporated, 2010. ProQuest Ebook Central,

$$v^2 = v_\infty{}^2 - \frac{2\rho g^2}{\beta(1+(T_c-T)/n)^{0.5}} \frac{1}{1+\varpi^2\tau^2} \tag{2.9}$$

$$\alpha = = \frac{2g^2}{2v_0{}^3\beta(1+(T_c-T)/n)^{0.5}} \frac{\varpi^2\tau}{1+\varpi^2\tau^2} \tag{2.10}$$

The polarization relaxation time according to the Landau theory increases approaching to T_c

$$\tau = \frac{\tau_0}{T_c - T} \ . \tag{2.11}$$

As one can see from (2.9), (2.10) and (2.11) at phase transition is the downward step of ultrasonic velocity and attenuation maximum which appears when $\varpi\tau = 1$. The behavior of ultrasonic velocity and attenuation in ferroelectric phase away from transition is mainly defined by Landau free energy expansion coefficients. In paraelectric phase ultrasonic velocity and attenuation is caused by polarization fluctuations [67].

2.2. Ultrasonic Studies of $CuInP_2S_6$ and $CuInP_2Se_6$ and Mixed $CuInP_2(S_xSe_{1-x})_6$ Crystals

Ultrasonic investigations were performed by automatic computer controlled pulse-echo method [68] and the main results are presented in papers [7,8,69-71]. In pure $CuInP_2S_6$ crystals ultrasonic measurements were carried out using longitudinal mode in direction of polar c-axis across layers.

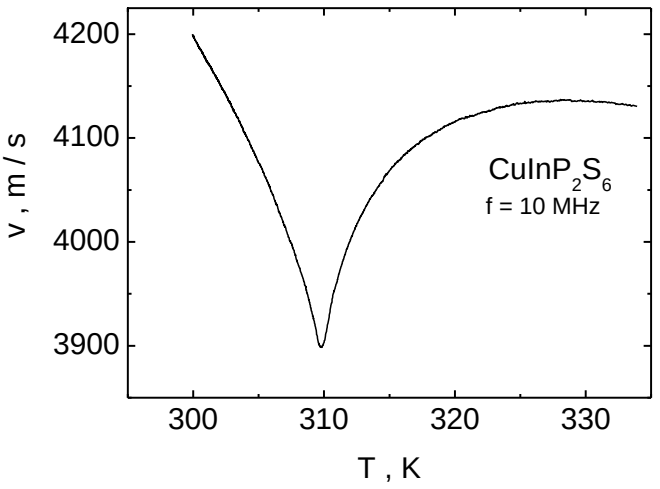


Figure 2.1. The temperature dependence of longitudinal ultrasonic velocity measured along z-axis in $CuInP_2S_6$ crystal at 10 MHz frequency.

Copyright © 2010. Nova Science Publishers, Incorporated. All rights reserved.

Handbook of Material Science Research, Nova Science Publishers, Incorporated, 2010. ProQuest Ebook Central,

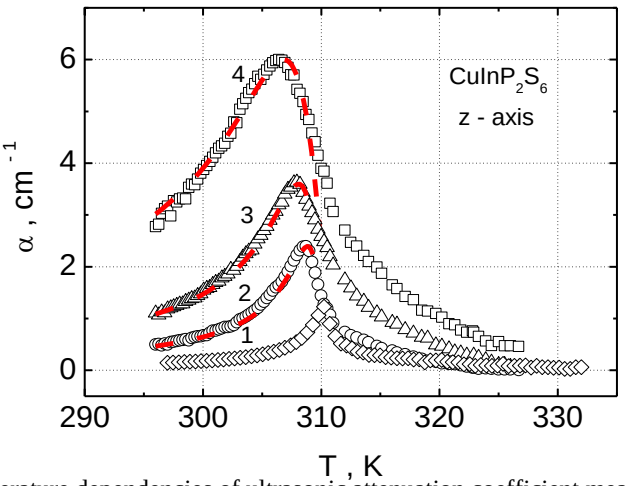


Figure 2.2. The temperature dependencies of ultrasonic attenuation coefficient measured along z-axis in $CuInP_2S_6$ crystal at 10 (1), 20 (2), 30 (3) and 50 (4) MHz frequencies.

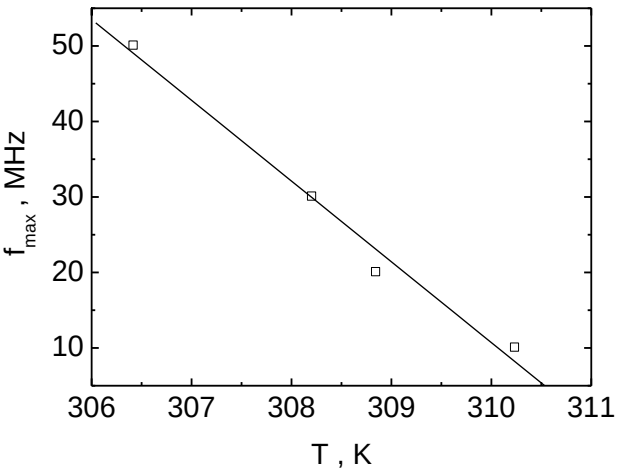


Figure 2.3. The temperature dependence of f_{max}.

The temperature dependence of longitudinal ultrasonic velocity along ferroelectric z-axis, which is directed across the layers, in Bridgman method grown $CuInP_2S_6$ sample exhibits minimum near phase transition temperature near 310 K (Figure 2.1). The data were collected in cooling cycle. It should be noted, that the thermal hysteresis of about 2 K is observed in heating cycle, what shows the first order nature of phase transition in $CuInP_2S_6$ compound [71]. In the low temperature phase velocity behavior is unusual because ultrasonic velocity increase to the value which exceeds the ultrasonic velocity in the paraelectric phase. Such behavior could be explained by the influence of fourth order term Au^2P^2 which should be added in Landau free energy expansion (2.7). In this case the following contribution to c_∞ appears:

$$C_\infty = c_\infty + AP^2 . \qquad (2.12)$$

Copyright © 2010. Nova Science Publishers, Incorporated. All rights reserved.

Handbook of Material Science Research, Nova Science Publishers, Incorporated, 2010. ProQuest Ebook Central,

As one can see such contribution could considerably increase ultrasonic velocity in the ferroelectric phase. The influence of the fourth order term was observed and in other feooelectric materials [72-73].

The velocity minimum is accompanied by ultrasonic attenuation peak. With frequency increasing from 10 to 50 MHz, attenuation maximum shifts to lower temperatures (Figure 2.2), showing the relaxation behaviour with relaxation time increasing when approaching the transition temperature.

The temperature and frequency dependencies of ultrasonic attenuation near PT in ferroelectric phase generally can be desribed by simplified result of Landau-Chalatnikov theory obtained from eq.(2.9):

$$\alpha = 2\alpha_{\max}\frac{\omega\tau}{1+\omega^2\tau^2}, \qquad (2.13)$$

here α_{max} - the attenuation coefficient at maximum, ω - the angular frequency of elastic wave and $\tau = \tau_0/(T_c - T)$ - the polarisation relaxation time, which increases critically approaching T_c. The peak of ultrasonic attenuation appears when condition $\omega\tau = 1$ fulfilled. In this case: $\omega\tau_o = T_c - T$. It means that for higher frequencies α_{max} is reached at lower T. From the slope of the dependence $\omega_{max}/2\pi = f_{max} = f(T)$, the value of $\tau_0 = 1.4*10^{-8}$ s/K can be easily obtained (see Figure 2.3). The intersection of this curve with abscise axis gives the T_c = 310.8 K. Using these parameters the theoretical dependencies $\alpha = f(T)$ were calculated for all frequencies and are shown in Figure 2.2 by dot lines. In paraelectric phase the long tails of anomalous ultrasonic attenuation were observed (see Figure 2.2) what is determined by polar clusters existing far above of the phase transition point. Existence of such clusters we observed in our piezoelectric measurements because the long tail of piezosensitivity exists and in the paraelectric phase [7]. It could be also influence of impurities and dislocations in the crystal lattice.

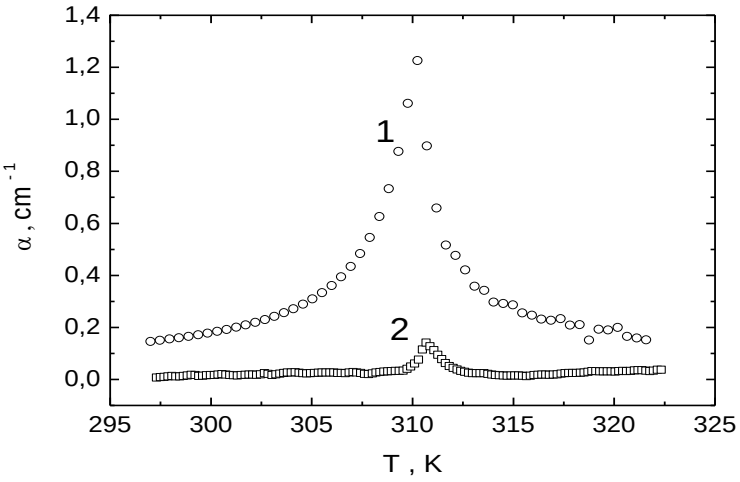


Figure 2.4. The temperature dependences of longitudinal ultrasonic attenuation along (1) c-axis and normal (2) to c-axis in $CuInP_2S_6$ crystal.

Copyright © 2010. Nova Science Publishers, Incorporated. All rights reserved.

Handbook of Material Science Research, Nova Science Publishers, Incorporated, 2010. ProQuest Ebook Central,

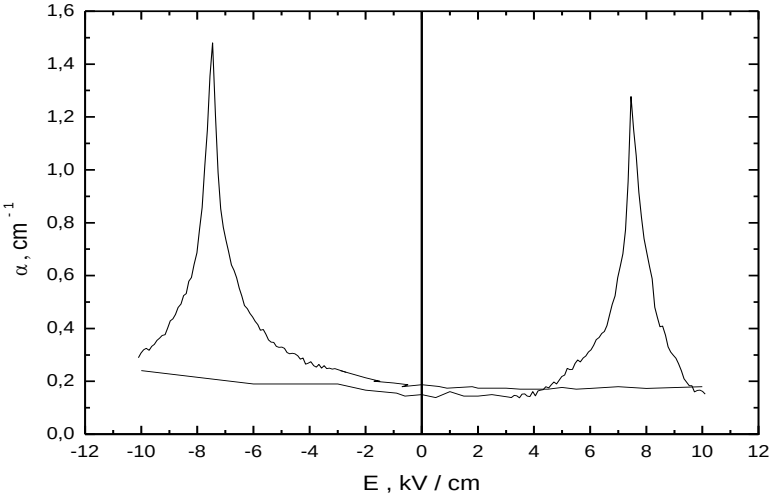


Figure 2.5. The DC field dependencies of longitudinal ultrasonic attenuation in $CuInP_2S_6$ crystal along c-axis.

The layered $CuInP_2S_6$ crystals show very large anisotropy of elastic behavior. This was confirmed by measuring longitudinal ultrasonic attenuation across and along the layers. In the direction along layers the ultrasonic attenuation peak was much smaller than measured across layers i.e. along the c-axis. Such anisotropy could be explained by the difference of electrostriction tensor components g according to equation (2.10). The peak of critical ultrasonic attenuation is proportional to g^2 and in polar direction the active electrostriction tensor component should be g_{33} and perpendicular to c-axis the corresponding electrostriction tensor component should be g_{31} or g_{32}. The peak values of longitudinal ultrasonic attenuation along and normal to c-axis are 1.2 cm^{-1} and 0.12 cm^{-1} as it is seen from Figure2.4, respectively. The corresponding electrostriction tensor components should differ by factor more than 3. Also the anisotropy of ultrasonic velocity in low temperature phase can influence the peak value of attenuation. Ultrasonic velocity at room temperature along layers is larger than in direction across layers [74].

The ultrasonic attenuation has a maximum not only at the phase transition temperature but also near coercive field in polarization reversal procedure. For ultrasonic measurements the sample was cut from the same Bridgemen grown crystals and had length of 1 mm in direction of c-axis. Longitudinal ultrasonic wave was excited in this $CuInP_2S_6$ sample along polar c-axis and ultrasonic attenuation was measured under polarization reversal conditions at 303 K temperature in order to reduce coercive field. In this case the smaller voltage could be applied on the sample in order to diminish heating. The dependencies of ultrasonic attenuation were recorded by processing the 10 MHz signal on receiving lithium niobate transducer, together with voltage, which was applied on the crystal. Dependencies of $\alpha = f(E)$ are shown in Figure 2.5. As one could see the longitudinal attenuation maxima were observed near DC field close to coercive. The peak values of ultrasonic attenuation were close to those which were obtained in our previous measurements of critical ultrasonic attenuation at phase transition in $CuInP_2S_6$ [7]. Therefore it could be guessed that here also ultrasonic attenuation

Copyright © 2010. Nova Science Publishers, Incorporated. All rights reserved.

Handbook of Material Science Research, Nova Science Publishers, Incorporated, 2010. ProQuest Ebook Central,

is caused by relaxation of polarization according Landau-Khalatnikov mechanism [64-65] and the polarization relaxation time increases in the vicinity of coercive field.

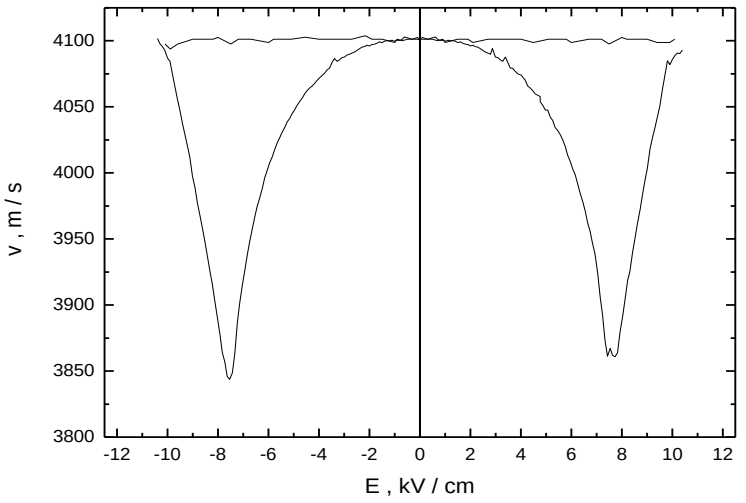


Figure 2.6. The DC field dependencies of ultrasonic velocity in $CuInP_2S_6$ crystal along c-axis.

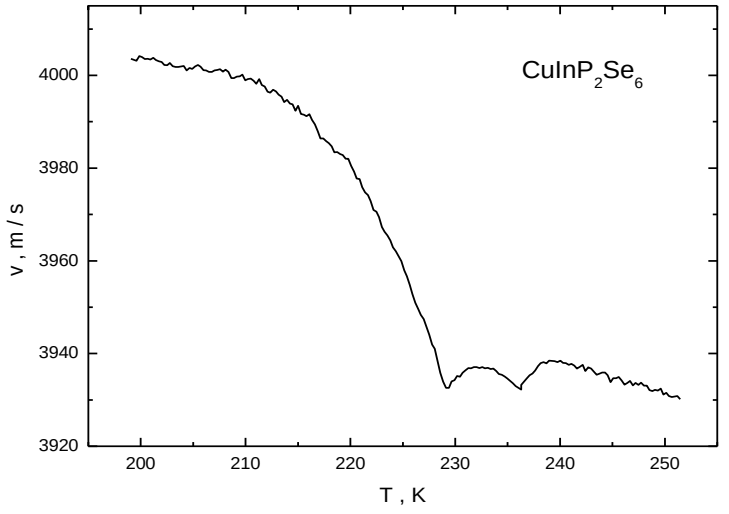


Figure 2.7. The temperature variation of longitudinal ultrasonic velocity measured along c-axis in $CuInP_2Se_6$ crystal at 10 MHz frequency.

Similar anomalies were obtained and for velocity of longitudinal ultrasonic wave. Velocity changes were recorded when voltage was slowly varied at the same temperature 303 K as for ultrasonic attenuation measurements. The clear ultrasonic velocity minima appeared at coercive field (Figure2.6). The small asymmetry can be explained by electric contacts which can change DC field in the volume of the sample.

Copyright © 2010. Nova Science Publishers, Incorporated. All rights reserved.

Handbook of Material Science Research, Nova Science Publishers, Incorporated, 2010. ProQuest Ebook Central,

Pure perfect $CuInP_2Se_6$ and mixed $CuInP_2(S_xSe_{1-x})_6$ crystals is impossible to obtain by Bridgemen method. By the method of chemical transport reactions only thin plates of these materials are available. Therefore in ultrasonic experiments we used layered samples as stacks from 8-10 plates glued in such way that longitudinal ultrasound could propagate across layers in order to increase sample length. For pure $CuInP_2Se_6$ plates to obtain perfect stacks was difficult because of bad quality surfaces but still we succeeded to measure ultrasonic velocity in the phase transition region. Temperature dependence of longitudinal ultrasonic velocity in pure $CuInP_2Se_6$ crystal is shown in Figure 2.7.

The velocity minimum at 225 K coincides with dielectric anomaly but we observed also small another minimum near 335 K. Ultrasonic investigation of piezoelectric sensitivity has shown that piezoelectric sensitivity do not disappear at 225 K (it only has a minimum there) but completely disappears close to 335 K [74]. Such behavior could be caused by the existence of intermediate phase existing in temperature interval of 225 -235 K.

In mixed $CuInP_2(S_xSe_{1-x})_6$ crystals we performed longitudinal ultrasonic velocity and attenuation measurements along c-axis. It was shown that addition small amount of Se in $CuInP_2S_6$ crystal strongly influence the ultrasonic behaviour and phase transition temperature. The phase transition temperature decreases and ultrasonic velocity and attenuation anomalies at the transition also decreases and broadens. As it was mentioned, above samples for ultrasonic experiments usually were made as stacks from several plates glued together, therefore to obtain reliable results at higher than 10 MHz frequencies was very difficult and we made measurements only at 10 MHz frequency.

The temperature dependencies of longitudinal ultrasonic attenuation (α) and relative velocity ($\Delta v/v$) measured at 10 MHz are shown in Figure2.6 (a,b) for $CuInP_2(S_{1-x}Se_x)_6$ crystals with different Se contents 0.02, 0.05 and 0.1. For the sample with 2% Se, attenuation and velocity anomalies were sharp and well defined as in the case of pure $CuInP_2S_6$ crystal [7]. In virgin samples with 0.05 and 0.1 Se content, the ultrasonic anomalies broadened and almost vanished during cooling. After cooling down to 120 K and long time keeping the sample at low temperature, the anomalies became more pronounced, especially when crystals were cooled down with applied DC field. Previous dielectric investigations showed significant broadening of dielectric anomalies for crystals with >5% Se [75], and for the compound with 30% typical dipolar glass dielectric dispersion was found. To our opinion the glassy state, which emerges in these compounds, is responsible for such nonergodic ultrasonic behaviour. The results in Figure2.6 for crystals with 5% and 10% Se contents are shown on heating cycle after cooling with applied DC field. As it was shown above, the ultrasonic behaviour at the ferroelectric phase transition is described by interaction of the order parameter (polarization) with the ultrasonic waves according to the relaxation theory of Landau-Khalatnikov (Eq. 2.10), which implies a critical increase of the order parameter relaxation time. Consequently, after substitution S by Se the ultrasonic velocity and attenuation anomalies decrease and broaden showing that the relaxation time increases. The increase of relaxation time can be explained by the existence of a diffused phase transition and the glassy state, which does not contradict the observed non-ergodic behaviour. The temperatures of attenuation maxima are corresponding to the temperatures of dielectric anomalies. The increase of ultrasonic attenuation with temperature above the transition is attributed to the interaction of ultrasonic wave with mobile copper ions, because ionic conductivity is high enough at elevated temperatures [6]. In crystals with Se content >0.1 no critical ultrasonic anomalies were observed. Non ergodic broad changes of attenuation could

Copyright © 2010. Nova Science Publishers, Incorporated. All rights reserved.

Handbook of Material Science Research, Nova Science Publishers, Incorporated, 2010. ProQuest Ebook Central,

be seen, but it can be attributed to the influence of gluing material and ultrasonic experiments can be made in these mixed crystals only if larger samples will be grown. In Se rich mixed $CuInP_2(S_xSe_{1-x})_6$ crystals the scenario of anomalous ultrasonic behavior is very similar to that of sulphur rich solid solutions.

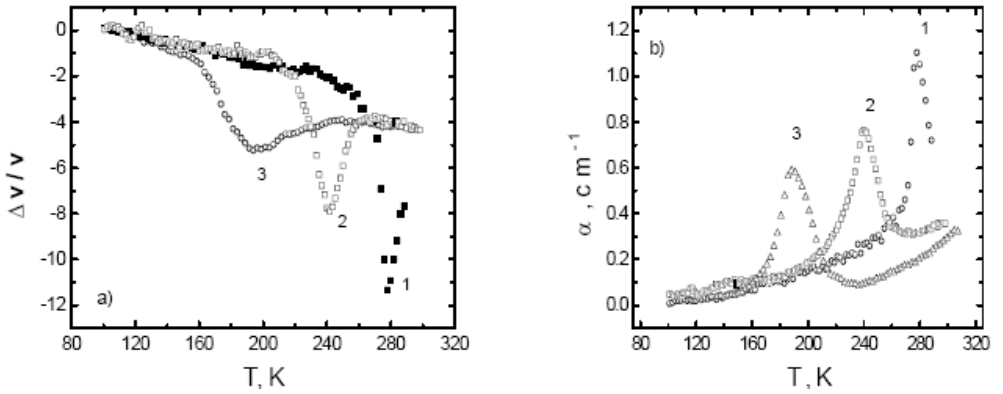


Figure 2.8. The temperature dependencies of ultrasonic velocity (a) and attenuation (b) along c-axis in $CuInP_2(S_{1-x}Se_x)_6$ crystals with different Se content 0.02 (1), 0.05 (2) and 0.1 (3).

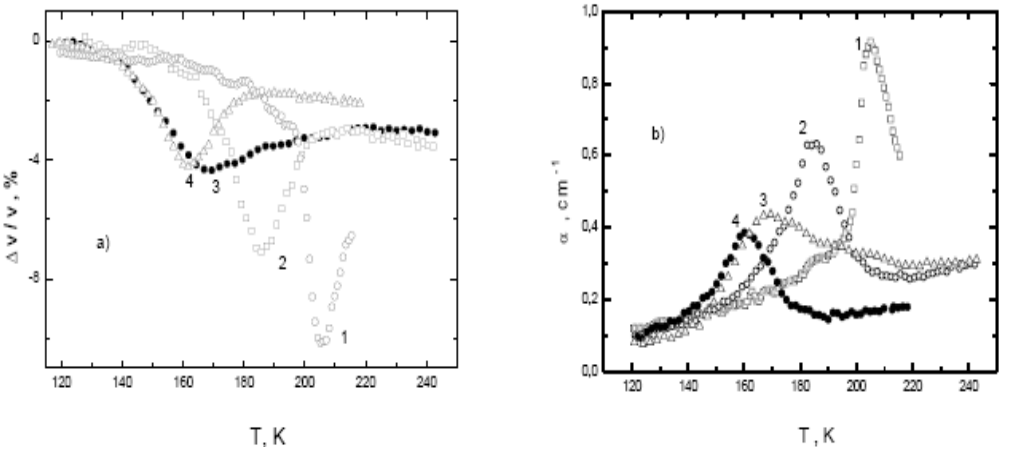


Figure 2.9. The temperature dependencies of ultrasonic velocity (a) and attenuation (b) along c-axis in $CuInP_2(S_xSe_{1-x})_6$ crystals with different S content 0.05 (1), 0.1 (2), 0.2 (3) and 0.25 (4).

In polarised samples, the anomalies of longitudinal ultrasonic velocity and attenuation along c-axis were observed in crystals with 5%, 10%, 20% and 25% sulphur content and are shown on heating cycle after cooling with the applied DC field (Figure 2.7). The temperature dependences of ultrasonic velocity show that there are minima near temperatures T=205 K for 5% for sample; T=185 K for 10% sample, T=185 K in 20% in crystal and T_2=160 K for $CuInP_2(S_{0.25}Se_{0.75})_6$. Velocity minima correspond the attenuation peaks. As one can see the attenuation peaks decrease with increasing S content. After substitution Se by S the ultrasonic velocity and attenuation anomalies decrease and widen showing that the polarisation relaxation time increases as in the case of selenium rich mixed crystals. But in Se rich crystals lowering of the phase transition temperature is more gradual. The increase of

Copyright © 2010. Nova Science Publishers, Incorporated. All rights reserved.

Handbook of Material Science Research, Nova Science Publishers, Incorporated, 2010. ProQuest Ebook Central,

relaxation time can be explained by the existence of a diffused phase transition and the glassy state. The gradual increase of velocity in low temperature phases (below 140 K) is determined by the temperature dependence of ultrasonic velocity following the behaviour of the square of order parameter.

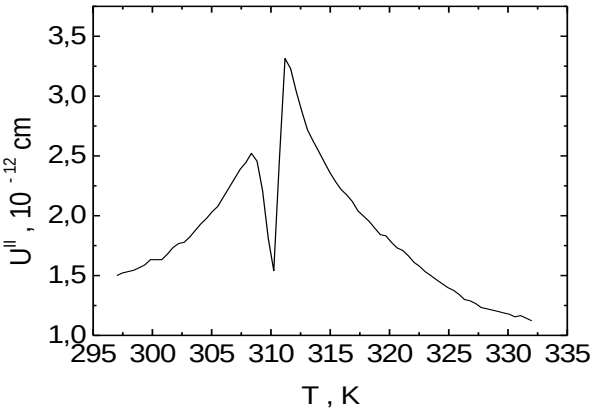


Figure 2.10. The temperature dependence of the second longitudinal ultrasonic harmonic measured along *c*-axis in $CuInP_2S_6$ crystal.

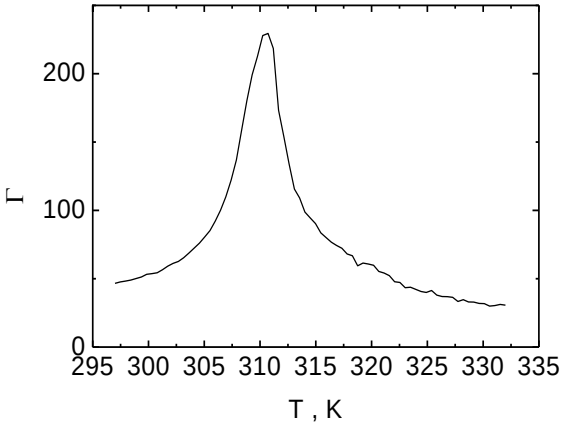


Figure 2.11. The temperature variation of nonlinear parameter along *c*-axis of $CuInP_2S_6$ crystal.

2.3. Nonlinear Elastic Properties of Layered $CuInP_2S_6$ Crystals

Much information about the system can be obtained from nonlinear effects investigations. Very interesting results have been obtained in second longitudinal ultrasonic harmonic experiments in layered $CuInP_2S_6$ crystals. We measured the temperature dependencies of the second harmonic amplitude i.e. elastic displacement u_2 at 20 MHz frequency across and along the layers of the crystal. The values of elastic displacement u_2 were calculated from RF voltage appearing on receiving transducer similarly as in our previous investigations [76-77].

Copyright © 2010. Nova Science Publishers, Incorporated. All rights reserved.

Handbook of Material Science Research, Nova Science Publishers, Incorporated, 2010. ProQuest Ebook Central,

It was shown, that the extremely large amplitude of the second harmonic was observed for longitudinal waves propagating across the layers (along *c*-axis) at room temperature. The amplitude u_2 was noticeably less when measured along the layers, normal to *z*-axis. The signal of second harmonic increased with temperature below T_c. The temperature dependence of the amplitude of the second ultrasonic harmonic measured on 20 MHz frequency is shown in Figure 2.8. There are two peaks of u_2. One is below PT temperature; another is in the paraelectric phase. The minimum is situated near the temperature where the peak of ultrasonic attenuation at input of 10 MHz frequency exists (see Figure2.2). The temperature dependence of nonlinear elastic parameter can be calculated from our obtained second harmonic results and ultrasonic attenuation data. It is well known, that the amplitude of the second harmonic u_2 can be described by the following equation [78]:

$$u_2 = \frac{\Gamma \omega^2 u_1^{\,2}}{16 V^2 \alpha_1} [\exp(-2\alpha_1 x) - \exp(-4\alpha_1 x)] \ , \tag{2.14}$$

where: *x*-length of the sample, Γ-nonlinear parameter, α_1- attenuation coefficient at the 10 MHz excitation frequency, u_1- the displacement amplitude at the input of the sample, *V*-velocity of the ultrasonic wave, ω-angular frequency. In our case*:* x = 0.49 cm, $u_1 = 5\times10^{-9}$ cm (this value was estimated from RF voltage on exciting 10 MHz frequency transducer). According to written above equation (2), using velocity, attenuation and the second harmonic amplitude data, the temperature dependence of nonlinear parameter Γ was calculated. This dependence is shown in Figure 2.11. The value of nonlinear parameter at room temperature is about 50, what exceeds the nonlinear coefficient of other layered materials $KY(MoO_4)_2$ and $Si_{20}Te_{80}$ [79]. The peak of nonlinear parameter near PT can be explained by the soft mode, as in case of ferroelectric SbSI [76]. The anisotropy of nonlinear elastic properties arises from large anisotropy of bonding forces, determined by anharmonicity of appropriate longitudinal phonon modes.

The increase of elastic nonlinearity was observed also near coercive field when DC bias field was applied along c-axis of $CuInP_2S_6$ crystal. We measured the temperature variation of the second harmonic amplitude i.e. elastic displacement u_2 at 20 MHz frequency according to the above described method. The DC bias field dependence of the amplitude of the second ultrasonic harmonic measured at 20 MHz frequency is shown in Figure 2.12. It is clearly seen from this figure that the elastic nonlinearity increases, similarly as near the phase transition, because a peak of the second harmonic is observed at E_c.

The DC bias field dependence of the nonlinear elastic parameter Γ can be calculated from obtained second harmonic and ultrasonic attenuation data. For simplicity we assumed that attenuation quadratic depends on frequency. In our case*:* x = 0.1 cm, $u_1 = 5\times10^{-9}$ cm (this value was estimated from the radio frequency voltage on the exciting 10 MHz transducer). The DC bias field dependence of the nonlinear parameter Γ (Figure 2.13) was calculated according to equation (2.14), using values of velocity V = 4100 m/s (the velocity change is relatively small as seen from Figure 2.6), attenuation and second harmonic data from Figures 2.5 and 2.12. As it was shown in [80] room temperature value of nonlinear elastic parameter $\Gamma \sim 50$ is the largest for materials found in literature [79], in DC bias field nonlinear elastic parameter increases even more and reaches values as high as 250. Such large nonlinearity of $CuInP_2S_6$ suggests possible applications in nonlinear signal processing devices.

Copyright © 2010. Nova Science Publishers, Incorporated. All rights reserved.

Handbook of Material Science Research, Nova Science Publishers, Incorporated, 2010. ProQuest Ebook Central,

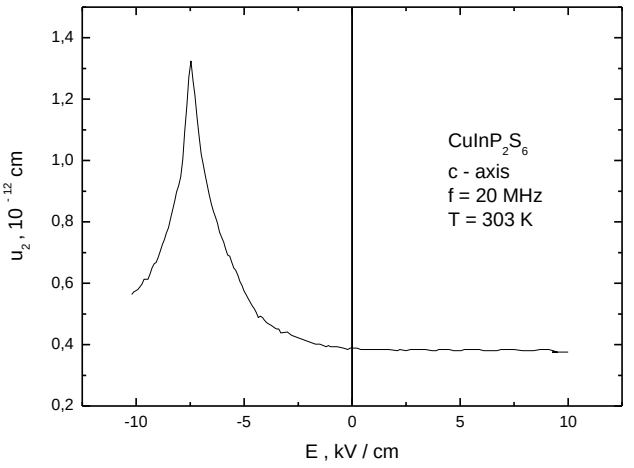


Figure 2.12. The DC bias field dependence of the second ultrasonic harmonic amplitude in $CuInP_2S_6$ layered crystal.

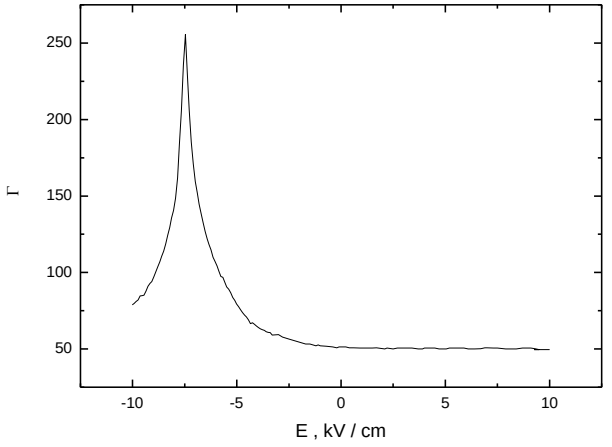


Figure 2.13. The DC field dependence of nonlinear elastic parameter in $CuInP_2S_6$ crystal at T = 303 K.

2.3. Ultrasonic Method for Investigation of Piezoelectric and Ferroelectric Properties of $CuInP_2S_6$, $CuInP_2Se_6$ and Mixed $CuInP_2(S_xSe_{1-x})_6$ Crystals

The pulse-echo ultrasonic method allows investigating piezoelectric and ferroelectric properties of layered crystals. Also this method can be used for indication of ferroelectric phase transitions. The main feature of ultrasonic method is to detect piezoelectric signal by thin plate of material under investigation. The simplified experimental set up is shown in Figure2.14. Here radio frequency pulse excites lithium niobate ultrasonic transducer T_1. Ultrasonic wave passes fussed quartz buffer (QB) and excites $CuInP_2S_6$ plate. The electric signal appears only if plate is piezoelectric or in the paraelectric phase piezoelectricity can be induced by applied DC voltage (U_{DC}) due to electrostriction. By this method we investigated $CuInP_2S_6$ family layered crystals. The advantage of this ultrasonic method is that it was

Copyright © 2010. Nova Science Publishers, Incorporated. All rights reserved.

Handbook of Material Science Research, Nova Science Publishers, Incorporated, 2010. ProQuest Ebook Central,

possible to apply high frequency ultrasonic wave and relaxations which usually appears in comparatively conductive crystals it was possible to avoid. Usually $CuInP_2S_6$ family crystals are grown as good surface quality plates and it is possible to use such samples without polishing.

The c-cut $CuInP_2S_6$ thin sample, was attached to quartz buffer in order to detect piezoelectric signal when short ultrasonic pulse of 10 MHz frequency was applied. At 320 K temperature no signal was detected, showing that the crystal was not piezoelectric. After application of DC bias field the signal of 10 MHz was observed in cooling down at about 312 K and increased with temperature decreasing. In heating run the DC field was removed. After such polarization procedure the temperature dependencies of piezoelectric signal U_p appearing on polarized $CuInP_2S_6$ plate was measured. The variation of U_p is shown in Figure 2.15. The presence of step in $U_p = f(T)$ shows that the phase transition near T_c=312 K is of the first order. Here in our experiment we are measuring voltage arising on piezoelectric plate when longitudinal stress from ultrasonic wave is applied. In this case piezoelectric coefficient g_{33} appears in piezoelectric equations $E_3 = g_{33}T_{33}$. The tensor relation of piezoelectric coefficients implies that: $g = d\ \varepsilon_t^{-1}$. According to [81] piezoelectric coefficient d in piezoelectric crystal: $d \sim \eta_0/(T_c-T)$. Assuming dielectric permittivity can be approximated by Curie low, quite reasonable assumption could be made, that the amplitude of our ultrasonically detected signal varies with temperature in the same manner as order parameter η_0.

In the low temperature phase quite reasonable dependencies of the amplitude piezoelectric signal on DC electric field were obtained. In this case DC field was slowly changed and the sample was at constant field for two minutes. The coercive field is about 11 kV/cm at room temperature and it is smaller than obtained in [2] where coercive field was about 77 kV/cm in AC field of 50 Hz frequency. Our measurements are in almost static field and of course the coercive field is smaller. It is interesting to note that at fields near coercive field the amplitude of piezoelectric signal changes with time, when time increases the coercive field decreases. The coercive field also decreases with temperature and at T = 303 K it is of 7.5 kV/cm as one could see from Figure 2.16.

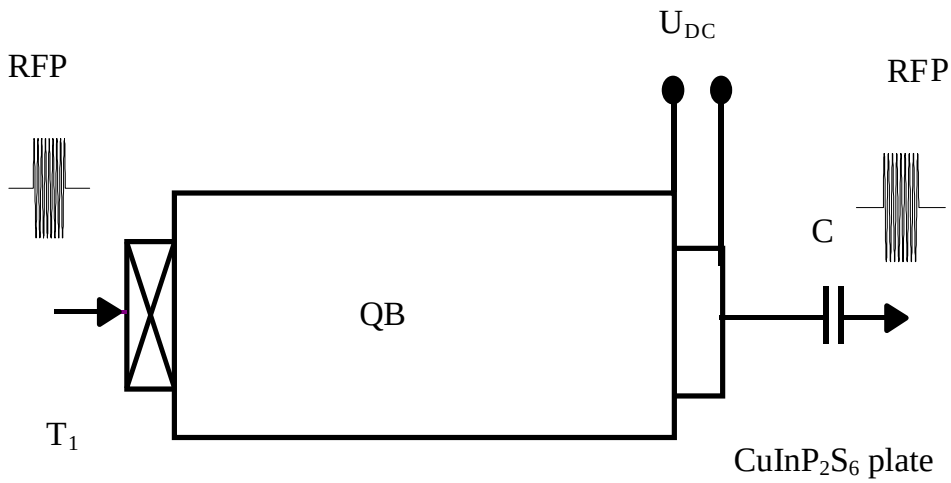


Figure 2.14. Experimental set up for piezoelectric test using pulse-echo ultrasonic system

Copyright © 2010. Nova Science Publishers, Incorporated. All rights reserved.

Handbook of Material Science Research, Nova Science Publishers, Incorporated, 2010. ProQuest Ebook Central,

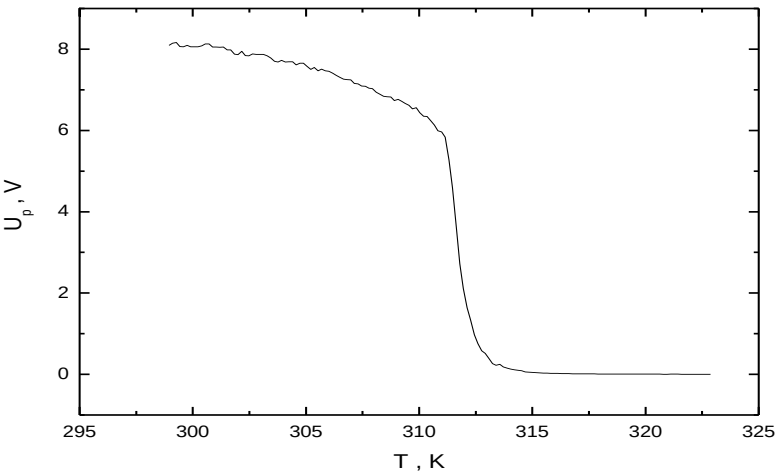


Figure 2.15. The temperature dependencie of ultrasonically detected piezoelectric signal in $CuInP_2S_6$ crystal. In cooling the 10 kV/cm bias field was applied.

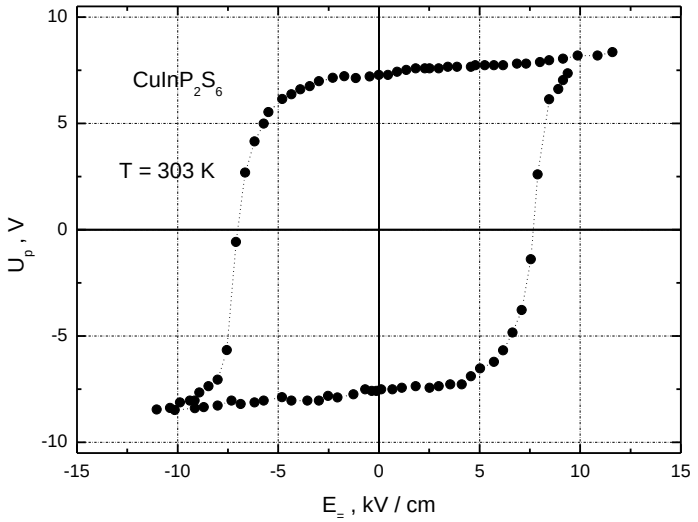


Figure 2.16. The DC field dependence of piezoelectric signal amplitude in $CuInP_2S_6$ crystal at T = 303 K.

It is necessary to note that above the phase transition we detect piezoelectric signal and it shows that some polarization tail remains in the paraelectric phase. This remnant polarization can cause additional ultrasonic attenuation above phase transition (see part 2.1). Therefore such ultrasonic method is very sensitive for detecting even small deviations in centrosymetric lattice.

Another example of application of this method is investigation of piezoelectric sensitivity of pure $CuInP_2Se_6$ crystalline plates [69]. In order to determine temperature interval of the existence of a piezoeffect in $CuInP_2Se_6$ we also made direct experiment on the same thin 0.16 mm plate vibrating as a piezoelectric transducer and attached to quartz buffer. The

Copyright © 2010. Nova Science Publishers, Incorporated. All rights reserved.

Handbook of Material Science Research, Nova Science Publishers, Incorporated, 2010. ProQuest Ebook Central,

temperature dependence of detected by such $CuInP_2Se_6$ transducer signal is shown in Figure 2.17. At low temperature we observed comparatively large signal. In heating cycle signal has a minimum at 226 K, increases in the intermediate phase ($T_2<T<T_1$) then has another drop down and completely disappears in the paraelectric phase (above T = 240 K). This investigation confirms existence of intermediate phase and another phase transition which was observed in ultrasonic velocity experiments (see Figure 2.7).

In mixed $CuInP_2(S,Se)_6$ crystals temperature dependencies of ultrasonically detected signals are shown in Figure 2.18.

The piezoelectric signal vanishes in the paraelectric phase what is the indication that in this phase the crystal is centrosymetric [82]. The phase transition temperature decreases when S content increases. The intermediate phase also appears in Se rich mixed crystals.

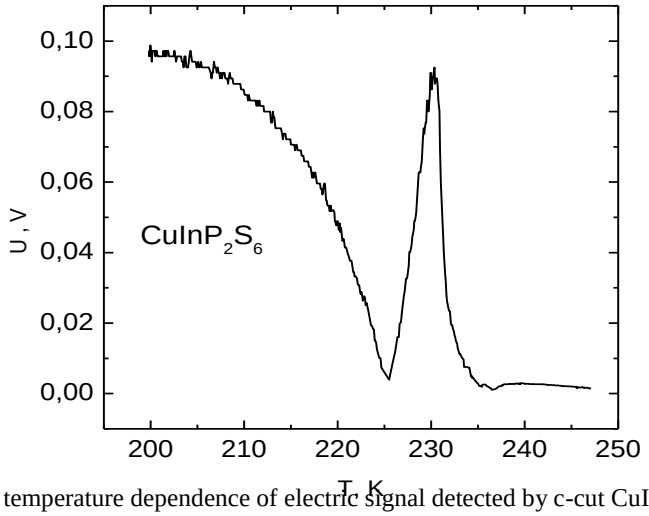


Figure 2.17. The temperature dependence of electric signal detected by c-cut $CuInP_2Se_6$ plate.

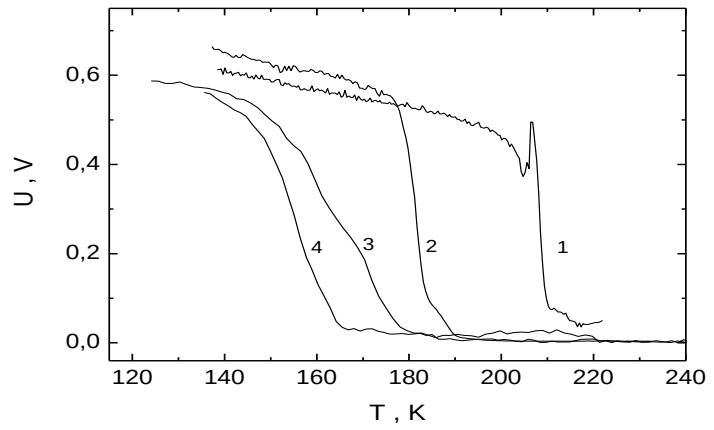


Figure 2.18. The temperature dependences of ultrasonically detected piezoelectric signal in polarised $CuInP_2(S_xSe_{1-x})_6$ c-cut plates: x=0 (1), 0.05 (2), 0.1 (3), 0.2 (4) and 0.25 (5).

Copyright © 2010. Nova Science Publishers, Incorporated. All rights reserved.

Handbook of Material Science Research, Nova Science Publishers, Incorporated, 2010. ProQuest Ebook Central,

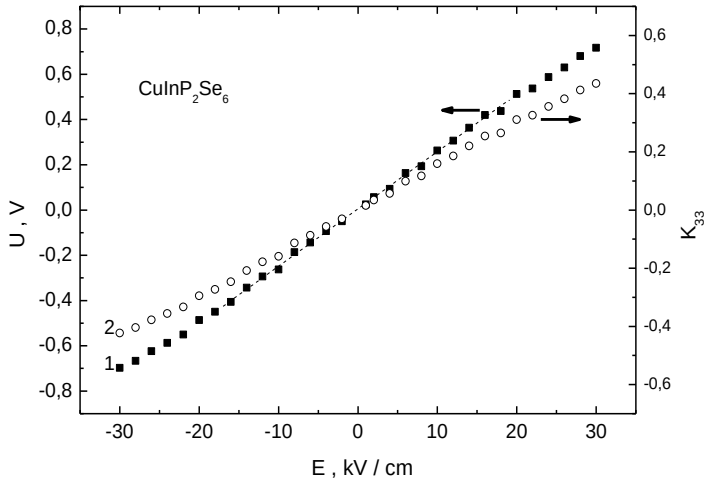


Figure 2.19. The ultrasonic signal detected by c-cut plate (1) and electromechanical coupling constant K_{33} (2) as a function of DC electric field applied along c-axis of $CuInP_2Se_6$ crystal.

Piezoelectric sensitivity in centrosymetric crystal can be induced by external DC electric field [82-84]. Pure $CuInP_2Se_6$ crystals at room temperature belong to the centrosymetric point group. And as one can see from Figure 2.17 they did not show piezosensitivity. But the applied DC field strongly raises the detected ultrasonic signal on the $CuInP_2Se_6$ transducer. The only possible explanation is that the electrostriction causes such behaviour. The results for such $CuInP_2Se_6$ thin plate transducer, which worked on 20 MHz frequency, are shown in Figure2.19. The linear dependence of ultrasonically detected piezoelectric signal holds for fields 20 kV/cm (see dashed line, which is guide to eye) and only under higher fields slight deviation from linearity appears. In the same figure electromechanical coupling coefficient is also shown. The electromechanical coupling coefficient at chosen value of DC electric field was obtained from another namely resonance- antiresonance measurement, and it was supposed that for other DC field values proportionality U_p and K_{33} holds [81]. The values of electromechanical coupling K_{33} at DC field 30 kV/cm can be reached as high as 0.45, which correspond to $K^2_{33} \approx 20\%$. It is necessary to note that in our experiment we used thin $CuInP_2Se_6$ plates without any mechanical cut and treatment. This is advantage of such layered crystals that they can be obtained as thin plates with quite good surfaces and comparatively large DC electric field can be applied without electric breakdown. The similar results of DC bias field induced piezosensitivity due to electrostriction were obtained and in other mixed crystals of $CuInP_2S_6$ family at room temperature. Therefore possible applications of such layered crystals in DC field controlled ultrasonic transducers are foreseen.

CONCLUSION

a) The temperature behaviour of the soft mode of $CuInP_2S_6$ shows quasi-one-dimensional character.
b) One ferroelectric phase transition is observed in $CuInP_2Se_6$ crystals at T_c = 225 K.

Copyright © 2010. Nova Science Publishers, Incorporated. All rights reserved.

Handbook of Material Science Research, Nova Science Publishers, Incorporated, 2010. ProQuest Ebook Central,

c) Critical decreasing of conductivity activation energy E_A and conductivity σ_0 in intermediate concentration of sulphur and selenium is caused by strong random fields, which appear in the mixed $CuInP_2(S_xSe_{1-x})_6$ crystals. The minimum of conductivity σ_0 at x = 0.5 is strongly correlated with a unit cell volume minimum and can be explained by extending the channels for Cu cations movement, when sulphur replaced by selenium. σ_0 correlates with activation energy E_a very well according to Meyer-Neldel law. The Meyer-Neldel temperature for $CuInP_2(S_xSe_{1-x})_6$ mixed crystals is 290.6 K.

d) A small admixture of sulphur ($x \leq 0.02$) reduces ferroelectric phase transition temperature significantly but not changes character of the phase transition.

e) In intermediate concentration of selenium and sulphur (x = 0.4-0.8) the temperature behaviour of dielectric dispersion shows evidence of dipolar glass behaviour.

f) In boundary region between the dipolar glass disorder and ferroelectric order the relaxor-like behaviour is observed for $CuInP_2(S_{0.25}Se_{0.75})_6$ crystals. Critical slowing down of the longest relaxation times according to the Vogel-Fulcher law and slowing down of the most probable relaxation time according to the Arrhenius law manifest this behaviour.

g) A small admixture of selenium ($x \geq 0.98$) change phase transition dynamics of $CuInP_2S_6$ so that at low temperatures the coexistence of ferroelectric order and dipolar glass disorder is observed in these crystals.

h) Ultrasonic velocity and attenuation anomalies due to interaction of ultrasonic with polarisation were observed in $CuInP_2S_6$, $CuInP_2Se_6$ and mixed $CuInP_2(S_xSe_{1-x})_6$ crystals. These anomalies are determined by phase transitions in these crystals.

i) It was shown that $CuInP_2S_6$, crystals are highly anisotropic. The attenuation maxima at phase transition differs more than ten times when measured along and across layers.

j) The layered $CuInP_2S_6$ crystals exhibit extremely large elastic nonlinearity. Nonlinear elastic coefficient F for longitudinal ultrasonic waves propagating across layers at room temperature is >50 and it is the largest value from known materials. The elastic nonlinearity even more increases near the phase transition temperature and in the vicinity of coercive field under polarization reversal conditions.

k) Under polarization reversal conditions, near the coercive field, the critical increase of attenuation and decrease of velocity of longitudinal ultrasonic waves propagating along polar direction of $CuInP_2S_6$ crystals.

l) The layered $CuInP_2S_6$ family crystals in low temperature phase exhibit piezoelectric effect which vanishes in the high temperature paraelectric phase, We used ultrasonic method in order to establish piezosensitivity in $CuInP_2S_6$ family crystals. It was shown that such ultrasonic method is very sensitive for indication of ferroelectric phase transitions. In ferroelectric phase polarization reversal was observed and values of coercive field were measured. In the paraelectric phase piezoesensitivity due to electrostriction was observed in DC bias electric field applied along c-axis in layered $CuInP_2S_6$ family crystals. The polarized quazi –two dimensional $CuInP_2S_6$ crystals can be used as ultrasonic transducers. In the paraelectric phase these crystals can work as DC electric field controlled electrostrictive ultrasonic transducers.

Copyright © 2010. Nova Science Publishers, Incorporated. All rights reserved.

Handbook of Material Science Research, Nova Science Publishers, Incorporated, 2010. ProQuest Ebook Central,

REFERENCES

[1] V. B. Cajipe, J. Ravez, V. Maisonneuve, A. Simon, C. Payen, R. Von der Muhll and J. E. Fischer, *Ferroelectrics* 223, 43 (1999).

[2] V. Maisonneuve, V. B. Cajipe, A. Simon, R. Von der Muhll, and J. Ravez, *Phys. Rev*.B 56, 10860 (1997).

[3] X. Bourdon, A. R. Grimmer, V. B. Cajipe, *Chem. Mater*. 11, 2680, (1999).

[4] Yu. M. Vysochanskii, V. A. Stephanovich, A. A. Molnar, V. B. Cajipe, and X. Bourdon, *Phys. Rev*. B. 58, 9119 (1998).

[5] V. Maisonneuve, M. Evain, C. Payen, V. B. Cajipe, and P. Molinie, *J. Alloys and Compdounds* 218, 157 (1995).

[6] V. Maisonneuve, J. M. Reau, Ming Dong, V. B. Cajipe, C. Payen, and J. Ravez, *Ferroelectrics* 196, 257 (1997).

[7] V. Samulionis, J. Banys, Yu. Vysochanskii and V. Cajipe, *Ferroelectrics* 257, 113 (2001).

[8] J. Banys, J. Macutkevic, V. Samulionis, A. Brilingas and Yu. Vysochanskii, *Phase Transitions* 77, 345 (2004).

[9] A. Grzechnik, V. B. Cajipe, C. Payen and P. F. McMillan, *Solid State Commun*. 108, 43 (1998).

[10] X. Bourdon, V. Maisonneuve, V. B. Cajipe, C. Payen, J. E. Fischer, *J. Alloys Compd*. 283, 122 (1999).

[11] X. Bourdon, PhD Thesis, Universite de Nantes, (1998).

[12] A. Simon, J. Ravez, V. Maisonneuve, C. Payen, and V. B. Cajipe, *Chem. Matter*, 6, 1575 (1994).

[13] V. Fagot-Revurat, X. Bourdon, F. Bertran, V. B. Cajipe, and D. Maltere, *J. Phys. Cond. Matter.* 15, 595 (2003).

[14] C. Calareso, V. Grasso, F. Neri, and L. Silipigni, *J. Phys.: Condens. Matter* 9, 4791 (1997).

[15] Yu. M. Vysochanskii, A. A. Molnar, V. A. Stephanovich, V. B. Cajipe and X. Bourdon, *Ferroelectrics* 226, 443 (1997)

[16] I. P. Studenyak, V. V. Mitrovcij, Gy. Sh. Kovacs, M. I. Gurzan, O. A. Mykajlo, Yu. M. Vysochanskii, V. B. Cajipe, *Phys. Stat. Solidi* (b) 236, 678 (2003).

[17] I. P. Studenyak, O. A. Mykajlo, V. O. Stephanovich, M. I. Gurzan, Yu. M. Vysochanskii, V. B. Cajipe, *Phys. Stat. Solidi* (a) 198, 487 (2003).

[18] J. Banys, V. Samulionis, V. B. Cajipe and Yu. Vysochanskii, *Ferroelectrics* 257, 163 (2001).

[19] Y. M. Vysochanskii, A. A. Molnar, M. I. Gurzan, V. B. Cajipe, X. Bourdon, *Solid State Commun*. 115, 13 (2000).

[20] J. Grigas, *Microwave dielectric spectroscopy of ferroelectrics and related materials*, Gordon and Breach Science Publ., OPA Amsterdam (1996).

[21] G. Fischer, H. J. Brückner, A. Klöpperpieper, H. G. Unruh and A. Levstik, *Z. Phys. B - Condensed Matter* 79, 301 (1990).

[22] http://www.chem.sci.osaka-u.ac.jp/lab/micro/report/2004/2004res02.html.en

[23] S. Dikmen, P. Shuk, M. Greenblatt, *Solid State Ionics* 126, 89 (1999).

Copyright © 2010. Nova Science Publishers, Incorporated. All rights reserved.

Handbook of Material Science Research, Nova Science Publishers, Incorporated, 2010. ProQuest Ebook Central,

[24] T. Yao, Y. Uchimoto, M. Kinuhata, T. Inagaki, H. Yoshida, *Solid State Ionics* 132, 189 (2000).
[25] H. Hayashi, H. Inaba, M. Matsuyama, N. G. Lan, M. Dokiya, H. Tagawa, *Solid State Ionics* 122, 1 (1999).
[26] J. Huan, L. Jiang, L. Zhe, Z. Xin, H. Tianmin, S. Wenhui, *Solid State Ionics* 126, 277 (1999).
[27] R. F. Almukhametov, R. A. Yakshibayev, R. M. Kutusheva, A. Amineva, *Solid State Ionics* 158, 409 (2003).
[28] Yu. M. Vysochanskii, L. Beley, S. Perechinskii, M. Gurzan, O. Molnar, O. Mykajlo, V. Tovt, V. Stephanovich, *Ferroelectrics* 298, 361 (2004).
[29] K. L. Ngai and C. León, *Phys. Rev*. B 60, 9396 (1999).
[30] C. T. Moynihan, *J. Non. Cryst. Solids*, 172-174, 1395 (1994).
[31] M. Gödickemeier, B. Michel, A. Orliukas, P. Bohac, K. Sasaki, L. Gauckler, H. Heiunrich, P. Swander, G. Kostorz, H. Hofman, and O. Frei, *J.Matter.Res*. 9, 1228 (1994).
[32] D. Almond, G. K. Duncan, A. R. West, *Solid State Ionics* 8, 159 (1983).
[33] W. Meyer and H. Neldel, *Z. Tech. Phys*. (Leipzig) 12, 588 (1937).
[34] A. K. Jonscher, *Dielectric relaxation in solids*, Chelsea Dielectric Press, London (1983).
[35] Yu. M. Vysochanskii, A. A. Molnar, M. I. Gurzan and V. B. Cajipe, *Ferroelectrics* 257, 147 (2001).
[36] E. Matsuhita and K. Takahashi, *Jpn. J. Appl. Phys*. 41, 7184 (2002).
[37] S. Kamba, V. Porokhonskyy, A. Pashkin, V. Bovtun, and J. Petzelt, J. C. Nino, S. Trolier-McKinstry, M. T. Lanagan, and C. A. Randall, *Phys. Rev*. B 66, 054106 (2002).
[38] J. L. Tholence, Solid. State Commun. 35, 113 (1980). A. K. Tagantsev, *Phys. Rev. Let.* 72, 1100 (1994).
[39] K. S. Cole and R. H. Cole, *J. Chem. Phys*. 9, 341 (1941).
[40] R. M. Fuoss and J. G. Kirkwood, *J. Am. Chem. Soc*. 63, 385 (1941).
[41] V. Porokhonskyy, Ph. D. Thesis, Prague (2004).
[42] Z. Y. Cheng, R. S. Katiyar, X. Yao and A. S. Guo, *Phys. Rev*. B 55, 8165 (1997).
[43] S. Kamba, V. Porokhonskyy, A. Pashkin, V. Bovtun, and J. Petzelt, J. C. Nino, S. Trolier-McKinstry, M. T. Lanagan, and C. A. Randall, *Phys. Rev*. B 66, 054106 (2002).
[44] D. W. Davidson and R. H. Cole, *J. Chem. Phys*. 19, 1484 (1951).
[45] J. Z. Bao, *J. Chem. Phys*. 104, 4441 (1996).
[46] S. Havriliak, S. Negami, *J. Polym. Sci*. C 14, 99 (1966).
[47] S. Havriliak, S. Negami, *Polymer* 8, 161 (1967).
[48] R. Zorn, *J. Polym Sci. Pol. Phys.* 37, 1043 (1999)
[49] S. Havriliak, S. J. Havriliak, *J. Non-Cryst Solids* 172, 297 (1994).
[50] S. A. Seo, K. H. Noh, S. I. Kwun, *J. Korean. Phys. Soc.* 35, 496 (1999).
[51] H. Ries, R. Böhmer, I. Fehst and A. Loidl, *Z. Phys. B-Cond. Matter* 99, 401 (1996).
[52] B. G. Kimm, J. J. Kimm, H. M. Jang, *Phys. Rev*. B 60, 7170 (1999).
[53] R. R. Nigmatullin, V. A. Goncharov, Ya. E. Ryabov, Extended abstract of the XXVII congress Ampere, 251 (1994).
[54] R. R. Nigmatullin, Y. E. Ryabov, *Phys. Solid State* 39, 87 (1997).

Copyright © 2010. Nova Science Publishers, Incorporated. All rights reserved.

Handbook of Material Science Research, Nova Science Publishers, Incorporated, 2010. ProQuest Ebook Central,

[55] J. H. Calderwood, IEEE Transactions on Dielectrics and Electrical Insulation 10, 1006 (2003).
[56] H. Kliem, IEEE Transactions on Dielectrics and Electrical Insulation 12, 709 (2005).
[57] F. Alvarez, A. Alegria, and J. Colmenero *Phys. Rev*. B 44, 7306 (1991).
[58] A. K. Jonscher, *Colloid Polym*. Sci. 253, 231 (1975).
[59] K. L. Ngai, G. B. Wright (Eds.), *Relaxations in Complex Systems*, North-Holland, Amsterdam (1991).
[60] L. A. Dissado and R. M. Hill, *Proc. Roy. Soc*. London 390, 131180 (1983).
[61] A. K. Jonscher, *Nature* 267, 673 (1977).
[62] R. Grigalaitis, J. Banys, A. Kania, A. Slodczyk, *J. Phys*. 4 128, 127 (2005).
[63] S. L. Hutton, I. Fehst, R. Böhmer, M. Braune, B. Mertz, P. Lunkenheimer, and A. Loidl, *Phys. Rev. Lett.* 66, 1990 (1991).
[64] L.D. Landau I.M. Khalatnikov. *Sov. Phys*. (Doklady), (in Russian), 96, 459 (1954).
[65] V. Valevicius, V. Samulionis and J. Banys. *J. Alloys and Compounds*, 211/212, 369 (1994).
[66] V. Samulionis, J. Banys and G.Volkel. *J. Alloys and Compounds*, 310, 173 (2000).
[67] A.P. Levaniuk. *Sov. Phys*. (JETF) 49, 1309 (1965).
[68] V. Valevicius V. Samulionis, J. Banys and A. Brilingas. J. de Physique IV, 6, C8-405 (1996).
[69] V. Samulionis Yu. Vysochanskii and V. Cajipe. *Ferroelectrics*, 295, 21 (2003).
[70] V. Samulionis J. Banys Yu. Vysochanskii and I.P. Studeniak. *Ferroelectrics* 185, 135 (2006).
[71] V.Samulionis, J.Banys and Yu.Vysochanskii. *J.Phys.IV France* 126 139 (2005).
[72] Valevicius V., Samulionis V., Banys J., Grigas J., and Yagi T.: *Ferroelectrics*,156, 365 (1994).
[73] 73 R. Sobestijanskas, J. Grigas, V.Samulionis and E. F. Andreyev. *Phase transitions*. 29. 167 (1991).
[74] V. Samulionis and J. Banys. *J. Europ. Cer. Soc*. 25, 2543 (2005).
[75] Banys J., Grigalaitis R., Macutkevic J., Brilingas A., Samulionis V., Grigas J., and Vysochanskii Yu.: *Ferroelectrics* 318, 2005,163-168.
[76] V. Samulionis, V. Kunigelis and M. Girshovicius. *Sov.Phys* (JETF) 61, 1941 (1971).
[77] V. Samulionis, V. Valevichius, J. Grigas and Yu. Vysochanskii, *Ferroelectrics,* 105, 397 (1990).
[78] L.K. Zarembo and V.A.Krasilnikov. *Sov. Phys. Uspekhi*, 13, 778 (1971).
[79] L.A. Kulakova. *Physics of the Solid State*, 43, 1468 (2001).
[80] V. Samulionis and Yu. Vysochanskii. Proceedings of the World Congress on Ultrasonics (Paris), 279 (2003).
[81] B,A. Strukov, A.P. Levaniuk. *Physics of ferroelectric phenomena in crystals*. Moscow, 1995, in Russian , p. 117.
[82] V. Samulionis, J. Banys and Yu.Vysochanskii. *Materials Science Forum*, 514, 230 (2005).
[83] V.Samulionis, J.Banys and Yu Vysochanskii. *Ferroelectrics*, 348: 526 (2007).
[84] V. Samulionis, Yu. Vysochanskii. Proceedings of the International Congress on Ultrasonics, Vienna, April 9-13, 2007, doi:10.3728/ICUltrasonics.2007.Vienna.1554_ samulionis

Copyright © 2010. Nova Science Publishers, Incorporated. All rights reserved.

Handbook of Material Science Research, Nova Science Publishers, Incorporated, 2010. ProQuest Ebook Central,

Copyright © 2010. Nova Science Publishers, Incorporated. All rights reserved.

Handbook of Material Science Research, Nova Science Publishers, Incorporated, 2010. ProQuest Ebook Central,

In: Handbook of Material Science Research
Editors: C. René and E. Turcotte, pp.271-293
ISBN 978-1-60741-798-9
© 2010 Nova Science Publishers, Inc.

Chapter 5

UNRAVELLING XDT: STUDIES OF SOME RARE, BUT VIOLENT, EXPLOSIONS WITH STATISTICAL CRACK MECHANICS

John K. Dienes
Los Alamos National Laboratory, NM, USA

ABSTRACT

The impact tests for propellant sensitivity reported by Jensen, Blommer and Brown (JBB) were anomalous in several respects. First, 12 out of 50 impacts at moderate speeds led to especially violent explosions (XDT) while the remaining 38 produced only mild deflagrations (DEF). XDT generally occurred following impact at speeds *lower* than those leading to shock-to-detonation (SDT), which occurred in the 22 shots at speeds above 2500fps. Moreover, the violent reactions occurred at relatively late times, in excess of 30 microseconds after impact, rather than the 5 microseconds typically associated with SDT. Finally, the blast pressure associated with the violent explosions was even higher than in SDT and the cratering was more profound. Since these results defied explanation by the mechanisms associated with classical detonation theory, the process was termed XDT. In XDT shock heating was considered negligible, as further evidenced by the late reaction time.

This report summarizes some mechanisms postulated by the author during the last 30 years to explain the observations of JBB and other violent but non-repeatable reactions in propellants and explosives. The fundamental assumption herein is that defects occur at random and that heating of these defects following impact may lead to reactive hot spots. More specifically, it is postulated that the defects are shear cracks in which interfacial sliding leads to frictional heating that, in turn, causes vigorous reactions that may culminate in violent explosions. Our analysis shows, however, that a single hot spot will not result in violent explosion since rapid expansion of the gas-filled cavities reduces the gas pressure enough to quench the reaction. Thus, we conclude that interactions of defects is responsible for the observed violence.

Three types of interactions are thought to contribute to the suddenness of the violence. In one, pulses from reactions in one defect enhance the pressure in adjoining

Copyright © 2010. Nova Science Publishers, Incorporated. All rights reserved.

Handbook of Material Science Research, Nova Science Publishers, Incorporated, 2010. ProQuest Ebook Central,

defects and this feeds back to the first defect, initiating a divergent oscillation. Such interactions have been observed in special simulations. Further, growing cracks can intersect to form larger, more unstable, cracks, and a large enough number of intersections can result in a network of cracks that supports violent reactions. This is thought to occur when the concentration of cracks exceeds the percolation threshold, causing a violent reaction. Finally, we hypothesize that radiation between connected cracks can cause the heat produced by chemical reactions to spread extremely rapidly, leading to violent explosions.

INTRODUCTION

Results of the test program of Jensen, Blommer and Brown (JBB) [1] were of interest to the U.S. Navy and to Los Alamos because neither initiation of the explosions nor their extreme violence could be explained with classical detonation theory. These explosions, dubbed XDT by JBB, occurred when test cylinders were fired against a steel target at less than 2500 fps. The temperature rise due to shock heating at the threshold velocity is estimated as 6C, not nearly enough to initiate a significant reaction in a homogenous reactive material. At higher speeds the reactions were prompt and resembled shock to detonation (SDT). The XDT explosions differed from SDT in four important respects: (1) they occurred at relatively low velocities; (2) the reactions occurred at relatively late times; (3) the adjacent blast wave was more violent than observed in SDT (which occurred consistently following impacts at above 2500fps); and (4) the violent reactions occurred in only 12 out of 50 shots. Radiographs of the cylindrical projectiles at late times showed that they deformed into a shape like that of a fried egg, sunny side up, in the absence of an early explosion. Thus, an appropriate theory would need to account for large deformations rather than the simple uniaxial compression often associated with shock and detonation waves. A full simulation would also account for macroscopic radial cracking of the cylinders.

An explanation for this anomalous behavior can be found in the behavior of defects that evolve into hot spots that, in turn, coalesce and undergo a nearly simultaneous reaction. Many kinds of defects can be observed in real materials, but for theoretical purposes they are generally idealized as spherical holes or cracks. We tend to think of the spherical holes as occurring in ductile materials and cracks as occurring in brittle materials, but this somewhat oversimplifies the real behavior of some materials; it is not practical or even possible to address this subject fully here. The emphasis in this review is, rather, on the behavior of explosive grains held together by a binder. Such grains are often brittle and, hence, tend to form sharp cracks at sufficiently high stress. With this idealization it is possible to account for the anomalous behavior in the tests of JBB. A conceptual overview of the XDT process is shown in Figure 1. When the relative velocity of the faces of a shear crack is high, frictional heating can raise the local temperature very rapidly, thereby initiating melting in many materials and a reaction in explosive grains. The delay in the full XDT explosion, then, is explained by the time for heating to diffuse from the crack surface into a significant volume of material. The extreme violence is due to the nearly simultaneous reaction over a large volume because of hot spot interactions, including pressure waves, convection and radiation transported between cracks that become connected so as to form a network that is above the percolation threshold. Finally, only if the existing cracks are large enough or numerous

Copyright © 2010. Nova Science Publishers, Incorporated. All rights reserved.

Handbook of Material Science Research, Nova Science Publishers, Incorporated, 2010. ProQuest Ebook Central,

enough to interact will the explosion have the violence of XDT. Another chance element is associated with crack orientation, for only shear cracks with certain orientations grow with sufficient shearing stress and speed to induce the heating necessary for initiation. Recall that the theory of hot spots requires that they be of sufficient size that they will not quench because of thermal diffusion, so crack tip heating can be ruled out as a relevant mechanism.

These ideas were addressed quantitatively by the author in a variety of studies at Los Alamos in the years since the tests of JBB, and quantitative analysis has tended to support the conjectures described above. The scenario presented here is sufficiently complex, however, that the many issues that are raised here could not be fully addressed within the scope of our very limited effort. Still, the subject is considered to be of sufficient importance that a continuing effort would be justified. We believe that large masses of explosive or propellant are more sensitive than the (small) samples usually tested because the chance that a combination of the number and size of defects exceeds the critical value is greater in larger samples. This size effect (quantified below) is well known in many fields of engineering, but is not always recognized in connection with reactive solids. It is reported by Green et al [2], for example. I have heard it argued that there is no size effect because of the plasticity of reactive materials. This appears to me fallacious and dangerous since most explosives tend to be brittle (though the binder may make the mixture viscoelastic, even rubbery). Though explosive accidents are rare, the consequences can be severe; thus, a theory that accounts for the probability of occurrence should be of general interest.

The scenario proposed here is complex in several respects and required a variety of new concepts to address them. These are summarized briefly here and elaborated on in the sections that follow. First, large deformations are involved, so it is fortunate that a general theory for the kinematics of arbitrarily large deformations has evolved in recent years. The approach is based on a mathematical theorem, polar decomposition, which allows any deformation to be separated into a strain (technically, a stretch) and a rotation. The deformation theory has only been fully developed in recent years, but begins with the theorem of Autonne [3]. In our application it is extended to allow for the behavior of an ensemble of defects, which are treated in a statistical manner. The theory allows us to superimpose the deformations due to elasticity; plasticity; opening, shear, and coalescence of cracks; and, in fact, whatever kinds of mechanical behavior are present in the material of interest. This can be considered a generalization of the well-known *superposition of strain rates* common in plasticity. We have also made use of the theory of penny-shaped cracks, a term coined by the British and well developed in the literature. Heating and thermal diffusion in the neighborhood of sliding crack faces is straightforward in many respects, but it is likely that melting occurs in XDT, and motion of the melting interface requires special consideration. Melting at the interface of shear cracks is not well-known in engineering materials, but it is observed in geophysics in features known as pseudotachylytes. The rate of shear-crack growth has been the subject of intense research in recent years by Rosakis [4] and colleagues, but it appears to be well established now that this speed can be supersonic (intersonic, in the jargon). In addressing XDT it is proposed that hot products of reaction could open a crack and cause it to grow in an unstable fashion, possibly at high speed. To calculate the speed of cracks during XDT we have taken a different approach than solving the PDEs of elasticity, the classical method, because we are interested in the behavior of an ensemble of cracks under the very erratic, time-varying, stress which occurs in our simulations. Solving the PDEs for the growth of an ensemble of cracks would be computationally impractical. Thus, crack

Copyright © 2010. Nova Science Publishers, Incorporated. All rights reserved.

Handbook of Material Science Research, Nova Science Publishers, Incorporated, 2010. ProQuest Ebook Central,

behavior is idealized by using the method of generalized coordinates, taking the crack opening and radius as degrees of freedom. This gives results for crack speed and dynamic behavior that are in general agreement with more exact theory insofar as comparison is possible, and solving the appropriate ODEs is not computationally burdensome. Thus, we can treat extremely large numbers of cracks in our finite-element simulations of XDT. A major concern here is that cracks filled with reacting gases will be initially unstable but grow at such a rapid rate that the gas pressure drops precipitously, causing the heating and reactions to quench. Thus, to explain XDT we were motivated to see whether an instability could develop as a result of crack interactions. Using the theory of crack dynamics described above we simulated the response of interacting cracks and found that, indeed, an instability would develop when the provocation was sufficient, i.e., the initial pressure pulse was sufficiently intense. Other kinds of interaction are possible. Cracks can intersect to form larger cracks, and the heat can be shared between them. If this occurs radiatively, the process can be faster than convective mixing. This seems a likely occurrence in the late stages of XDT, though no radiation calculations have been carried out.

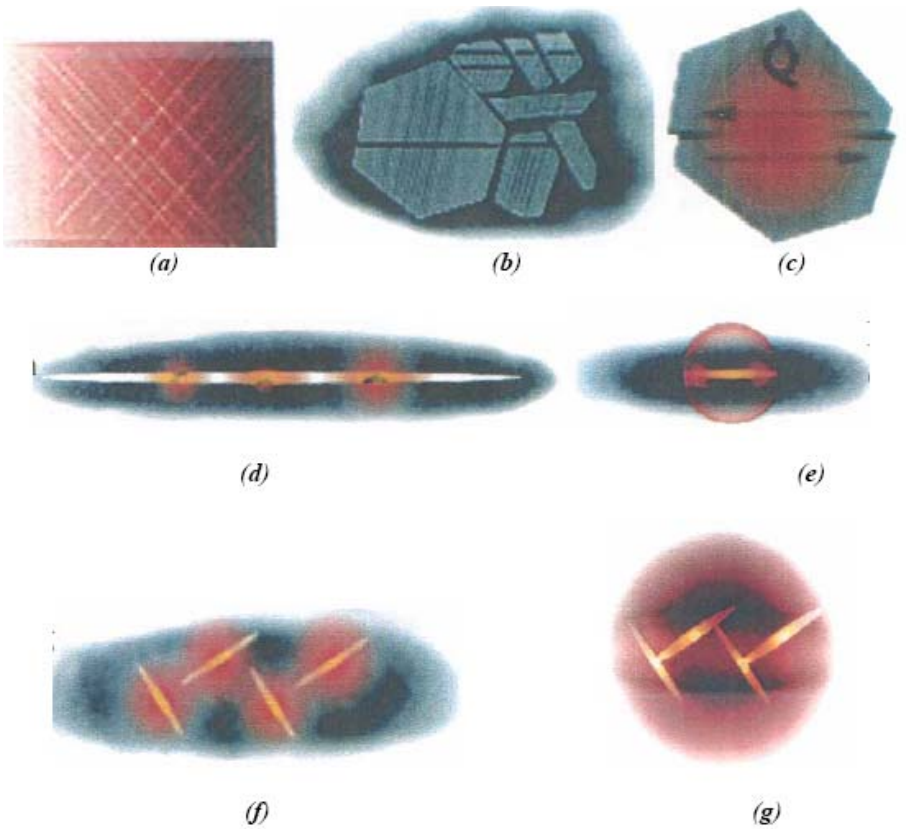


Figure 1. Overview of the stages involved in initiation according to SCRAM. (a) shear cracks form under shock; (b) cracks grow easily inside explosive grains, but are inhibited by binder; (c) cracks grind and generate frictional heat; (d) grains initiate near crack surfaces; (e) burned gases open cracks creating high-pressure zone. Opening is inhibited by inertia, stiffness, and damping; (f) burning increases general pressure, accelerating burn in adjoining hot spots; (g) cracks coalesce at percolation threshold.

Copyright © 2010. Nova Science Publishers, Incorporated. All rights reserved.

Handbook of Material Science Research, Nova Science Publishers, Incorporated, 2010. ProQuest Ebook Central,

Experiments to test the various scenarios suggested above are needed to understand better the XDT process. The problem with unravelling XDT experimentally is that it is very rapid and probably very complex and, and the details of hot-spot behavior are difficult to observe. The writer has proposed that much can be learned by testing a mixture of explosive with an inert organic such as sugar and the usual binders, a PBMIX [5]. Then the damaged material can be recovered and partially reacted grains can be examined to assess the transients. This should provide insights into the nature of the defects, their instabilities, reactions, and interactions. Informal discussions of such experiments have been encouraging, but no concrete plan has evolved at this time.

Responding to the assertion of Von Holle and Martin [6] that "initial formation of hot spots has never been completely understood," it is believed possible to establish the mechanics governing the initial formation of hot spots by testing of the type reported by JBB supplemented by tests of the type proposed above. (Neither is our view as pessimistic as that of Birk et al. [7], who claim that a "combustion process dependent on failing structural integrity is nearly impossible to predict.") The methods described here are based on sound but more advanced principles than those traditionally used. In combination with good test data, predictions of sensitivity and the effects of environment, aging, temperature, and damage should be possible. In particular, size effects are thought to be vital in munitions safety, but are rarely quantified. We believe that SCRAM provides a rigorous underlying theoretical framework to quantify risk that complements testing, which is costly indeed when large volumes are involved.

XDT-THE ANOMALOUS EXPLOSIONS OF JENNINGS, BLOMMER AND BROWN

The test series reported by JBB [1] was of particular interest because it was the first to describe the peculiar XDT phenomenology on the basis of a large number of impacts at varying speeds. These tests involved impact of propellant cylinders against a steel plate at speeds from 1000 to 3200 fps, with explosive reactions of 3 very different types clearly identified: SDT, DEF, and XDT. Their Figure 4 charts the blast overpressure versus impact speed, and shows that the explosions are grouped in the 3 distinct categories identified above. At speeds above 2500 fps shock to detonation (SDT) dominated (22 shots), but below that speed the reactions were different. It was demonstrated that any misalignment of the cylinder axes from the velocity vector was small and had negligible effect. In 12 out of 50 shots violent explosions occurred (XDT), while in the remaining 38 shots only mild deflagrations (DEF) were observed. The blast-wave overpressure was observed with a pair of pressure gages and averaged about 55 psi following XDT, and was not affected by impact speed, while it averaged only about 45 psi following SDT, also independent of impact speed. (The XDT overpressures were considered underestimates.) Following DEF, however, the overpressure increased about linearly with impact speed, but never exceeded 30 psi. It appears clear that three different phenomena were involved, a conclusion supported by the high-speed photography and radiographs illustrating the explosions. It is striking that 2 impacts at 1575 fps produced entirely different blast pressure and profiles after 15 μs (JBB Figs. 7 and 8), while before that time the shapes are identical; the DEF produced a blast of 8 psi while the

Copyright © 2010. Nova Science Publishers, Incorporated. All rights reserved.

Handbook of Material Science Research, Nova Science Publishers, Incorporated, 2010. ProQuest Ebook Central,

XDT blast was 80 psi. The DEF shot had a fried-egg shape at 30 μs while the XDT radiograph showed an explosion at the same time. However, SDT occurred within about 5μs, as illustrated in their Figure 10. At 50μs the DEF showed a pancake remaining, while the XDT reaction was terminated. Furthermore, their Figure 9 showed that the crater produced by SDT was much greater than by DEF. Thus we have the 4 anomalies: different responses to identical impacts at the lower speeds; exceptional overpressure and cratering in the case of XDT; later explosion times in XDT than SDT; and relatively quick reactions in XDT (though much later than SDT). (In a personal visit the author saw high speed films (100,000 frames per second) in which the reaction occurred between frames.) It should be emphasized that these tests had extensive instrumentation: laser speed diagnostics, blast gauges, Cordin camera, flash X-ray, crater measurements, and manganin gauges in the target [8].

Numerous test programs have shown evidence that different samples of propellants and explosives can react quite differently under the same circumstances (insults). The literature on this is far too extensive and diverse for a review to be practical, and much of it is not open. It is worth noting, however, that the drop tests often used to test different formulations show scattered responses to similar impacts.

STATISTICAL CRACK MECHANICS (SCRAM)

It has been assumed since the time of Prandtl and Reuss that it is valid to superimpose the strain rates due to elastic and plastic strain rates to obtain the total strain rate in a ductile material, and thereby to formulate a constitutive law. This concept is used in most formulations of finite-element and hydro codes. It can be generalized, and that is one of the hallmarks of SCRAM. If materials contain cracks, and especially if the material is somewhat brittle, additional contributions to the strain rate arise from crack opening, shear and growth. Other defects such as spherical voids and shear bands may contribute to the strain rate as well, but in Statistical Crack Mechanics we have been concerned primarily with crack behavior. Extension to other defects is certainly possible. In any case, we make use of a generalized version of the superposition of strain rates to develop a constitutive law that accounts for brittle behavior. A mathematical demonstration of the validity of this concept has been put forth by Dienes [9] using arguments that apply for arbitrarily large material deformations. (Experimental validation of this concept would be useful, but would be particular to the defects in the materials tested.) Since it is derived theoretically, the basis for Generalized Superposition of Strain Rates (GSSR) is quite different from the approach in plasticity wherein superposition is merely *assumed* to be valid. (Originally, the Prandtl-Reuss idea was hypothesized to avoid discontinuous behavior when a material transitions from the elastic to the plastic state.) The fundamental notion in SCRAM is that the various defects are separated in space, so that their effects can be added. Interactions of defects can be addressed, but this gets much more sophisticated. (Such ideas are allowed for in the work of Kachanov [10].) In addition, the need for a good treatment of large deformation is important in connection with XDT and is alluded to above in the discussion of JBB, which includes deformation of a right cylinder into the shape of a fried egg, and beyond in extreme cases.

Copyright © 2010. Nova Science Publishers, Incorporated. All rights reserved.

Handbook of Material Science Research, Nova Science Publishers, Incorporated, 2010. ProQuest Ebook Central,

Large Deformations

The possibility of an exact theory of large deformation arises from the Polar Decomposition Theorem, which allows us to separate any deformation into a stretch and a rotation. This is discussed in most modern books on continuum mechanics, but we have been extending the theory to include accurate means for computing the strain and stress rates necessary for very general damage calculations, Dienes [9]. Briefly, an arbitrary deformation $\mathbf{F} = \left(\partial \mathbf{x_i} / \partial \mathbf{X_j}\right)$ can be separated into a stretch and a rotation by **F=VR**. Here $x_i(X_j, t)$ denotes the coordinates of a particle initially at X_i and **D** is the symmetric part of the velocity gradient $\mathbf{G} = \dot{\mathbf{x}}_{\mathbf{i,j}}$. Rates of strain and rotation are defined by $\hat{\boldsymbol{\varepsilon}} = \mathbf{VDV}$ and $\boldsymbol{\Omega}$. The circumflex denotes a generalized tensor rate that accounts for material rotation, $\hat{\mathbf{A}} = \dot{\mathbf{A}} + \mathbf{A}\Omega - \breve{\mathbf{z}}\Omega$, which we call a polar rate. The strain rate is thereby related to the stretching, **D**, a quantity of central importance in finite element and finite difference calculations. Accounting for large material rotation may seem unnecessarily sophisticated, but numerical calculations of large deformation may become unstable if the rates are not computed rigorously in finite-element programs, and very large deformations are experienced in most impact calculations. This approach is taken by Taylor and Flanagan [11] in their PRONTO code. **D** is the sum of contributions from elastic and plastic behavior and, in our extended theory, contributions from crack opening, shear, and growth, as well as some other special terms. We have also found in unpublished results that the computing grid is more stable when polar rates are used. The constitutive relations are not used in this form in calculations, but mathematically rearranged to express the stress rate in terms of other running variables.

In the derivation of a theory for the generalized superposition of strain rates, GSSR, the strain rates are of two kinds. The first kind includes those contributions that are treated as continuous: elastic, plastic, viscous, and high-pressure equation of state. The second kind accounts for strain rates due to defect dynamics, and these involve statistical concepts. Thus we can write

$$\mathbf{D} = \mathbf{D}^e + \mathbf{D}^p + \mathbf{D}^v + \mathbf{D}^{hp} + \mathbf{D}^c + \mathbf{D}^g . \tag{1}$$

The first four terms on the right represent stretching due to elastic, plastic, visco-elastic-plastic, and high-pressure behavior. These are considered continuum terms. The high-pressure term accounts only for isotropic nonlinear behavior since the linear portion of the elastic deformation is included in the elastic term, but it may depend on internal energy. (We are not ready for anisotropic high-pressure terms.) The fifth and sixth terms account for crack behavior, which depends on crack statistics, to be discussed below. The fifth term accounts for the changing compliance due to cracks, and its contribution depends on whether cracks are open or closed. It is controlled by the normal component of traction, positive (tensile) for open cracks and negative (compressive) for shear cracks. Cracks with different orientations respond differently, and thereby contribute to anisotropic damage. The sixth term accounts for the effect of growing cracks, which may be small or very large. If the shear cracks are growing very rapidly they induce very large change in temperature, and in our calculations

Copyright © 2010. Nova Science Publishers, Incorporated. All rights reserved.

Handbook of Material Science Research, Nova Science Publishers, Incorporated, 2010. ProQuest Ebook Central,

often cause sharp spikes of temperature and melting. In some cases the reactive heating precludes a return to near normal temperature. The rate of growth of shear cracks can be very large, on the order of $\sqrt{2}$ times the speed of shear waves, Rosakis [4].

The elastic stretching and the elastic strain rate are proportional $\left(\hat{\boldsymbol{\varepsilon}}^{\mathbf{e}} = \mathbf{V}\mathbf{D}^{\mathbf{e}}\mathbf{V}\right)$, and this strain rate is proportional to the stress rate. This last term is linear in $\dot{\boldsymbol{\sigma}}$, so the equation can be solved for $\dot{\boldsymbol{\sigma}}$ and the result used to update the stress, which thereby depends on both continuum and crack behavior. The plastic stress rate may involve a hardening term, commonly represented by a back stress $\boldsymbol{\alpha}$ in kinematic hardening theory, i.e., $\hat{\boldsymbol{\alpha}} = b\,\hat{\boldsymbol{\varepsilon}}^{p}$, where *b* is the hardening modulus. The difference $\boldsymbol{\sigma} - \boldsymbol{\alpha}$ is treated by the von Mises theory in the usual way, with special iterations to force the stress onto the (movable) yield surface. The theory is discussed in detail by Dienes [12,13].

Statistics

In SCRAM the statistics of cracks, and the consequent behavior of an ensemble of cracks, are simplified and made tractable by assuming an initially exponential distribution of crack sizes. This distribution is well known in geophysics, but it is not the only one, as discussed, for example, by Scholtz [14]. The exponential has great mathematical appeal because it makes the growth of an ensemble of cracks tractable, as well as theories of coalescence and calculation of the percolation threshold. Specifically, it is assumed that the initial number density of cracks that exceed c in radius at a particular orientation is given by

$$L = L_0\, e^{-c/\bar{c}}, \tag{2}$$

where $\bar{c}$ denotes the average crack size, and L_0 is the number density of cracks with the particular orientation. It is also assumed that the cracks are penny-shaped, a very convenient shape for the mathematical analysis of deformation. The stability has been studied extensively by Zuo and Dienes [15], who investigated the effect of interfacial friction in shear cracks and showed that it can account for the difference in compressive and tensile strength of brittle materials, which is typically in excess of a factor of eight. Crack orientation can be defined by its normal, $\boldsymbol{\Omega}$**.** Often it can be assumed that the initial crack statistics are independent of orientation, and then L=N/2π, with N the total number of cracks per unit volume. Though this may be the case initially for certain dynamic problems, crack growth will generally depend on crack orientation and in that case the density L and mean crack size $\bar{c}$ will be time dependent. Some materials are initially anisotropic, and then L_0 will be variable. This is especially the case for oil shale, which led to some interesting results, Dienes [16]. In shales there are numerous bedding cracks, which tend to make the material much weaker in the transverse direction and to enhance damage in the bedding planes. It is also the case for materials that are rolled, such as beryllium or steel, but the effects are generally much smaller than for shales. In an analysis of the effect of a spherical charge exploded in oil shale it was found that the resulting cavity was aspirin shaped and, surprisingly, no amount of

Copyright © 2010. Nova Science Publishers, Incorporated. All rights reserved.

Handbook of Material Science Research, Nova Science Publishers, Incorporated, 2010. ProQuest Ebook Central,

(computational) anisotropic elasticity or plasticity would account for this effect. However, accounting for the enhanced growth of cracks in the bedding planes did allow us to account precisely for the added displacement normal to the bedding planes. In explosives and propellants cracking may depend on the pressing, casting, or pouring that occur during fabrication.

As cracks grow they may coalesce, and the coalescence may inhibit further growth, or may not, depending on the details of the intersections. In SCRAM the late stage cracks are assumed to fall into two categories that we call *active* and *inactive*. Active cracks continue to grow with sufficient stress, but inactive cracks do not grow because they have intersected enough other cracks that their tips are quite blunted. A conceptual diagram of the resulting crack geometry is shown in Figure 2. Actual diagrams of real crack intersections are reproduced by Dienes [13,17] but of course these are only diagrams of plane sections. They show intersections of two kinds that we call T and X cracks for obvious reasons. T cracks are often inactive and X cracks active, though full 3D analysis might show exceptions. The mathematical theory of coalescence statistics is described by Dienes [13,17].

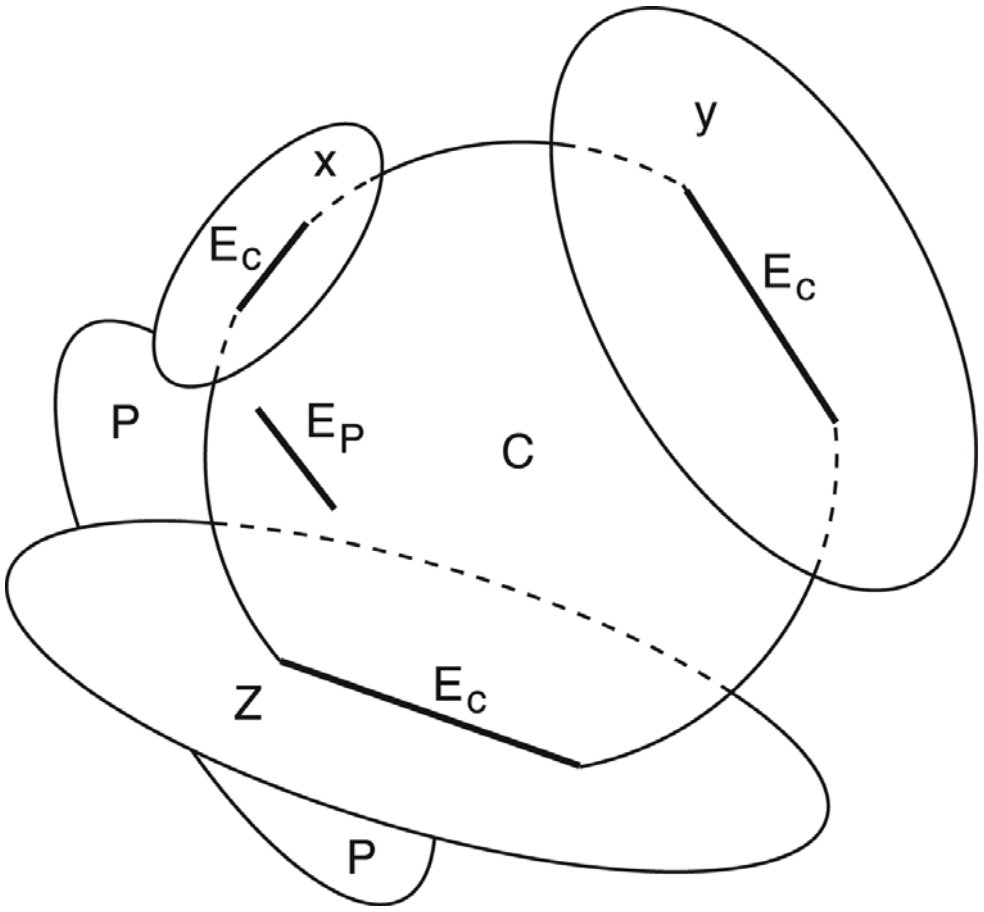


Figure 2. Crack C grows until it intersects X, Y, and Z, cracks that cause C to transition from an unstable to a stable (inactive) crack as a result of the blunting. Crack P intersects C, but has little effect on the behavior of C in this approach. Fluids (reaction products in explosives and propellants, oil or water in reservoirs) can readily penetrate connected cracks, which largely control the permeability.

Copyright © 2010. Nova Science Publishers, Incorporated. All rights reserved.

Handbook of Material Science Research, Nova Science Publishers, Incorporated, 2010. ProQuest Ebook Central,

It is possible to obtain analytic solutions for a variety of statistical problems by probability methods. In particular, the crack distribution in the bulk can be inferred from observations on a plane cut by a geometrical construction that leads to a certain integral [Dienes, 18]. For example, a certain Bessel function distribution in two dimensions is uniquely related to the exponential distribution in three dimensions. Another issue concerns material failure. When the distribution of crack sizes reaches a critical value the cracks form unbounded networks, an example of the percolation threshold addressed in statistical physics, and the material loses its strength. One relatively straightforward approximation to determine when spall occurs, for example, is to determine the Projected Area Per Unit Area (PAPUA) of the cracks that cross a given plane on that plane. This involves a certain integral that can be readily put in analytic form for the assumed exponential distribution of crack sizes [Dienes, 17]. When PAPUA reaches unity, failure has occurred in this approximation, a condition that can be written

$$PAPUA = 4\pi N\ \bar{c}^3 = 1. \tag{3}$$

A more elaborate analysis is required to determine the average "size" of a crack network for a random distribution of cracks. Here size refers to an integer counting the number of cracks in the network. When this size becomes infinite we say that the percolation threshold has been attained. This depends on crack size and number density, and on the maximum number of intersections that a crack can be expected to sustain, denoted by α. A general theory has been published [Dienes, 17] assuming a random distribution of penny-shaped cracks, and results are given for integer values of α. Intuitively, we would expect the real value of α to lie between 3 and 4, and we can, in fact, find evidence that gives a value of α for various materials at failure [Zhurkov and Kuksenko, 19], and that average value is determined to be 3.34.

This approach to damage resolves a paradox that the writer discussed at one time with Professor McClintock, the observation that critical strain seems to be a better criterion for failure than ultimate stress, though the latter is more standard. That is, strain to failure seems to be independent of temperature and strain rate, while the stress at failure varies widely with these environmental variables. This observation is inconsistent, for example, with standard fracture theory, which develops a critical failure stress. (In fact, the failure criterion involves the stress intensity factor, the product of stress and the square root of crack size.) In the current network approach to failure, the network is a geometric quantity (a statistical entity) that is not concerned with how the network was formed (stress distribution, its rate and the temperature) but only on the crack pattern, which is intimately involved with the strain. Thus, strain-to-failure as a failure criterion is a natural outcome. The work of Zhurkov and Sanfirova [20] confirms that the strain rate and time to failure are both governed by an Arrhenius law in such a way that *the product is independent of stress and temperature* and the product is, in fact, the strain to failure. It seems curious that this point is not made in their article. It is relevant that the peak stress in a PBX is shown to be independent of strain rate and temperature in Figure 5 of Dienes, Zuo, and Kershner [5].

Copyright © 2010. Nova Science Publishers, Incorporated. All rights reserved.

Handbook of Material Science Research, Nova Science Publishers, Incorporated, 2010. ProQuest Ebook Central,

Crack Stability and Speed

The theory of crack stability has been so widely studied since the time of Griffith in the 1920s that any attempt at review would be presumptuous. Much of the early work focused on 2D cracks with a practical concern for the strength of steel plates, but more general geometries were addressed beginning in the 50s. In particular, the analysis of penny-shaped cracks is useful when concerned with solids such as rock masses and bulk propellants or explosives. This idealization has been widely studied (Sack, Sneddon, Segedin, Keer and others) as referenced by Zuo and Dienes [15], who went on to combine those results and account for interfacial friction in a generalized fracture criterion. This is crucial in our modeling of XDT. Penny-shaped cracks are more physically realistic than two-dimensional cracks as the defects in continuum damage, and we can model many statistical features such as their effect on compliance, coalescence, and the percolation threshold. In our modeling it is assumed that cracks are either open or closed, and can change from one kind to the other depending on the normal component of traction. Previous studies of the stability of closed penny-shaped cracks have ignored interfacial friction, but this is a crucial feature in our modeling of XDT; a more general discussion is given in the following paragraph.

Without frictional sliding there is no significant heating, and the friction drastically changes the stability. (Occasionally, it is suggested that crack-tip heating is responsible for initiation, but the volume that is heated is extremely small, and the heating due to plasticity is not significant. On the other hand, the heating due to frictional sliding in cracks can be very large and is readily estimated; this heated area is much larger than the tip area.) The importance of friction is illustrated by the difference in compressive and tensile strength of such materials as rock, cement, and explosives. Typically, the compressive strength is 5 to 15 times the tensile strength. The reasons for this are somewhat controversial, as discussed by Scholz [14], but it is readily explained by considering the effect of interfacial friction, as discussed in Appendix A.

Dynamic crack growth is a crucial aspect of SCRAM, and represented by the last term of Eq. 1, $\mathbf{D}^g$. This subject has been reviewed by Freund [21] and it is known that it depends on the stress intensity factor as he describes in detail for two-dimensional cracks. A subject of considerable recent interest is the growth rate of shear cracks, as reviewed by Rosakis [4]. Such cracks can run at $\sqrt{2}$ times the speed of shear waves, and there is thought to be only transient behavior for crack speeds between this upper limit and the Rayleigh speed. The subject has been investigated extensively by analytic, experimental, and numerical methods, and their conclusions are in general agreement, though the treatment is a little shaky because of the complex behavior of interfacial friction. The consequences of friction and melting can be observed in the pseudotachylytes found in rocks following earthquakes, as described by Scholz [14] and Rosakis [4]. Measured crack speeds approaching the theoretical limit have been reported in recent years, especially in connection with the Izmit earthquake. The subject is complicated by the effects of friction, which are complex, since the actual interfacial friction is not necessarily uniform, as assumed by Zuo and Dienes [15] in applying classical crack theory, but may involve local slip as proposed by Heaton in connection with earthquakes [22] and investigated by numerous recent authors, especially Rice [23], who provides a concise summary. The possibility of observing or calculating the dynamic behavior of shear cracks in explosive grains seems remote because of the complex nature of the materials, their opacity, the small volume involved, chemical reactions, phase changes,

Copyright © 2010. Nova Science Publishers, Incorporated. All rights reserved.

Handbook of Material Science Research, Nova Science Publishers, Incorporated, 2010. ProQuest Ebook Central,

and the danger of explosions. However, quenched tests of a PBMIX as proposed by Dienes et al [5] would shed some light on the transient phenomena at the interface.

A THEORETICAL APPROACH TO XDT AND HMX SENSITIVITY

There is a long history concerning the mechanism of explosive sensitivity, beginning perhaps with Frank-Kamenetsky [24]. Generally, one is concerned with the growth of hot spots, but there are numerous kinds of hot spots and many theoretical approaches. Broadly, they can be divided into 4 categories: hydrodynamic, elastic-plastic, viscoelastic, and brittle. Various mechanisms have been listed by Field et al [25] (Table 1) and these have attracted a wide range of approximations. It was proposed by Dienes at a 1982 China Lake meeting [26] that another candidate is the shear crack, a mechanism that explains the four anomalies observed by JBB: statistical fluctuations in test results, extreme violence of XDT, variable sensitivity at sub-SDT velocities, and delayed blast, as well as the size effect of Green et al (op cit). In that first work impact simulations were performed with the crack growth algorithm included in the constitutive law, but not friction or reactive heating. Impact calculations were performed with the Los Alamos SALE hydro-code. Crack sliding effects were introduced into a post-processor that determined the resultant heating and integrated the Frank-Kamentsky equation dynamically. This determined whether runaway heating occurred in the explosive. Heating only occurred in shear cracks; when cracks opened, heating terminated. Of course, cracks with different orientations heated differently. The most critical orientation of the 9 accounted for were at 45 degrees to the direction of impact. Thus, only a small fraction of the cracks present in a propellant (or explosive) are important as hot spots. It is worth noting that the first calculations did not account for plasticity and were not able to account for the extreme deformation at the edge of the fried–egg shape discussed above. However, when plasticity was incorporated into the calculation the deformation became realistic.

Table I

The Hot-Spot Mechanisms Cited by Field et al (in condensed form)
Adiabatic compression of cavity gases
Heating of solid adjacent to collapsing cavity
Viscous heating of binder between grains
Friction between impacting surfaces
Localized adiabatic shear*
Heating at crack tips
Heating at dislocation pile ups
Spark discharge
Triboluminescent discharge
Decomposition followed by Joule heating of metallic elements

*Adiabatic shear is sometimes considered to be similar to shear cracking, but there are essential difference in the details, with the former involving a thermal softening instability and the latter a strictly mechanical instability involving competition of strain energy and surface energy. Adiabatic shear involves continuous displacement across the unstable zone, while shear cracks involve discontinuous displacement.

Copyright © 2010. Nova Science Publishers, Incorporated. All rights reserved.

Handbook of Material Science Research, Nova Science Publishers, Incorporated, 2010. ProQuest Ebook Central,

The success of this approximate simulation encouraged us to develop a more complete simulation in which heating and chemistry were incorporated into SCRAM, which was then embedded in the SANDIA finite element code PRONTO developed by Taylor and Flanagan [11]. This very versatile test bed for different constitutive behaviors accounts for large deformation using the polar rates described above. The calculations [27] were axisymmetric, as were the cylinder tests of JBB. (A later version accounted for three-dimensional behavior, but here we were concerned with only two.)

A crucial concern in the PRONTO calculations was the effect of melting at crack interfaces due to rapid frictional heating. This molten layer is very thin but crucial because it lowers the frictional heating and can mitigate the reaction process. This caused some anguish when the issue first arose, but on further consideration it was concluded that the molten layer is typically so thin that the viscous heating at the high strain rates obtained is a crucial factor. Though some critics note that melting has not been observed, the calculations show that so little material has melted (submicron layers) that its existence would not be obvious in *post mortem* examination. Such heating is known in geology and is observed in pseudotachylites and possibly in slickensides. In the final version of the heating algorithm the thickness of the molten layer is computed dynamically, and heating due to plasticity in the cooler layer beyond the melt is also accounted for. This requires some sophisticated treatment of the boundary conditions, but it is not prohibitive. The one-dimensional heat equation (heat flow normal to the crack) is integrated by the Crank-Nicholson method and solved by Gauss-Seidel, but it is worth noting that it is important to provide sufficient zones to account for conduction far (many zones) from the heating source. It is also important that the zones used in integrating the heat equation in the neighborhood of a crack be much finer than in the continuum calculations, but it is not prohibitive to run both calculations at the same time step.

Calculations reported at a Vanderbilt Workshop [Dienes,28] show the deformation following impact of a typical JBB test and numerous diagnostics. Contour plots of stiffness, crack size and temperature were shown as well as plots of the growth of crack temperature. The crack temperatures can vastly exceed the continuum temperature, and, of course, are much larger for cracks at 45 degrees to the impact direction than for other directions computed. Input data was varied to examine the effect of ductility. In particular, it was found that temperature history is very sensitive to the effective surface energy of the material. (Effective surface energy represents the energy required for crack growth, with low energy representing brittle behavior. The surface energy in [28] represents an average energy for the composite, and accounts for the effect of the binder, which holds the brittle grains together. The individual grains are very brittle, having a surface energy of about 50 ergs/cm^2.) For a surface energy, γ, of 650 ergs/cm^2 the temperature rise is rapid and unlimited after 60μs, and not very different for $\gamma = 1300$, but if γ is raised to 1950 the temperature rise hardly exceeds 200C. This agrees with the intuitive insight that increasing toughness, reflected here by γ, reduces sensitivity. Another way of improving ductility is to reduce the average flow stress, Y. (Recall that the strain rate is the sum of contributions from plasticity and crack growth, as well as some other contributions not relevant here.) In some regions of the test cylinder, halving the flow stress makes little difference, while in others it changes a runaway temperature rise to one that does not exceed 200C in the spikes, and does not exceed 100C at late time. The effect of impact speed was considered by computing crack temperature for impact speeds of 400, 500, 600 and 700m/s. At the lower speeds the crack temperature never

Copyright © 2010. Nova Science Publishers, Incorporated. All rights reserved.

Handbook of Material Science Research, Nova Science Publishers, Incorporated, 2010. ProQuest Ebook Central,

rose more than 50C, while at 600m/s there was a high spike in temperature but it dropped back to 50 C at late times. At 700m/s the temperature ran away at 47μs, never to return, suggesting local initiation, but not necessarily XDT because actual burn might be quenched by crack growth. The effect of crack size was also explored. The average radius of our penny-shaped cracks was normally 50μ in these calculations, but in one calculation it was increased locally from 50 to 150μ. This changed the peak temperature rise, a brief spike, from 50C into a runaway. It may be mentioned here that the Frank-Kamentsky equations in these calculations did not put limitations on temperature rise, so that it tends to run away when temperature rises above 1500K. Adding depletion, burn dynamics and other real processes would limit the temperature; these Vanderbilt calculations were only exploratory. Details of the theory and calculation are given by Dienes [27].

Burn

The calculations described above can describe initiation and perhaps sensitivity, but the actual reactive burn and subsequent explosion require a more detailed description of the chemical and physical processes at late times. That is, how do the heat conduction, melting, and reaction in the solid lead to gas phase processes that cause the major release of energy? And when the crack grows, what will prevent the drop in internal pressure to avoid quenching. There are several issues here that require individual treatment. First, how can we deal with crack dynamics in a practical way when the crack is driven by internal pressure associated with the products of combustion. Normally crack dynamics is treated by integrating the continuum (elastic) equations of motion, but this becomes difficult, probably quite impractical, when large numbers of cracks combine their effects in a burning explosive. We are faced with the possibility of crack interactions, and this would become outlandishly complex when the full test cylinder is modeled. It will be shown below that crack dynamics can be modeled with ODEs. A second challenge is to examine crack interactions in order to understand how a very rapid explosion can develop, as opposed to a deflagration, which can also occur (4 out of 5 in JBB). These 2 subjects have been treated separately in different papers. They are summarized in the paragraphs below.

Treating crack dynamics theoretically has traditionally been done by solving the governing elastic equations (PDEs) analytically, or with approximations, or numerically. In the case of XDT so many issues are involved that this approach is not viable if we are to consider the entire process of XDT. Thus we take an approach pioneered by Fermi in which the continuum (fluid) dynamics is approximated with selectively chosen degrees of freedom that represent the motion in an approximate manner, and use the method of generalized coordinates. Fermi had good success with this in examining the late stages of Rayleigh-Taylor instability [29], in which spikes form from an initially smooth perturbation. Unfortunately, this result was not published in the open literature and its importance has been obscured by the more modern approach of numerically integrating the continuum equations with supercomputers. Rayleigh-Taylor instability in solids was explored by Miles and Dienes [30] and spike formation was addressed Dienes [31], who was able to account for dissipative effects in the materials, and their effect on stability. For crack dynamics the degrees of

Copyright © 2010. Nova Science Publishers, Incorporated. All rights reserved.

Handbook of Material Science Research, Nova Science Publishers, Incorporated, 2010. ProQuest Ebook Central,

freedom are taken to be crack opening and crack growth by Dienes [32], and the material deformation is assumed to be that of the classic Mode I crack. The equations of motion are

$$\frac{d}{dt}\left(A_{ij}\dot{q}_j\right)-\frac{1}{2}A_{kl,i}\dot{q}_k\dot{q}_l+C_i=Q_i\,, \tag{4}$$

where q_1 denoted crack opening and q_2 crack radius. The mass matrix is

$$\mathbf{A}=\pi^2\frac{7-12\nu+8\nu^2}{120(1-\nu)^2}\rho\begin{pmatrix}4q_2{}^3 & q_1q_2{}^2\\ q_1q_2{}^2 & 24q_1{}^2q_2\end{pmatrix}, \tag{5}$$

with the generalized elastic forces

$$C_1=2Kq_1q_2\,,\ C_2=Kq_1{}^2\,,\quad K=\frac{\pi^2}{3}\frac{\mu}{1-\nu}\,, \tag{6a,b,c}$$

and the generalized external forces

$$Q_1=\frac{4\pi}{3}pq_2{}^2\,,\quad Q_2=\frac{8\pi}{3}pq_1q_2-4\pi\gamma q_2\,. \tag{7a,b}$$

The symbols ν and μ represent the usual elastic constants, p, the pressure less the far field traction, and γ the effective surface energy. It is shown in the paper that these equations lead to reasonable approximations to crack opening, speed, and stability for arbitrary far-field stress and internal pressure. For example, in the steady state the crack speed is

$$\dot{q}_2=\dot{c}\left(5-8\theta\left(\theta-\sqrt{\theta^2-1}\right)\right)^{1/2},\ \dot{c}^2=\frac{8}{5}\frac{1-\nu}{7-12\nu+8\nu^2}\frac{\mu}{\rho},\ \theta=\frac{5\sqrt{\pi}}{\sqrt{48\gamma}}\frac{p\sqrt{c}}{\sqrt{K}}, \tag{8a,b,c}$$

where the constant $\dot{c}$ has the dimensions of a speed and the parameter θ is a sort of dimensionless stress intensity factor. It turns out that $\dot{c}$ is indeed the peak crack speed, since for θ large this expression leads to $\dot{q}_2=\dot{c}$. For $\theta=5/4$ the velocity vanishes, so this lower value corresponds to the critical condition when the crack is marginally stable, behavior like that described by Freund [21], but here we have the effect of dynamical pressure in a simple form. These equations are solved numerically in SCRAM to account for the dynamics of the crack networks.

These results were used by Dienes and Kershner [33] to examine how crack interactions might enhance burning, which would otherwise be quenched as crack opening and radius increase, rapidly dropping the pressure in the crack. As an initial venture into the problem it seemed propitious to deal with only a single crack, and to represent the effects of the

Copyright © 2010. Nova Science Publishers, Incorporated. All rights reserved.

Handbook of Material Science Research, Nova Science Publishers, Incorporated, 2010. ProQuest Ebook Central,

neighbors by imposing a periodic driving pressure on a single crack. The result proves to be rather classical in the sense of nonlinear mechanics in that low pressures do not lead to instability, but sufficiently large pressure results in an oscillatory instability. To address this issue we require a burning algorithm.

The results of Ward, Son, and Brewster (WSB) provide a basis for relating the burn rate of HMX to pressure and temperature [34]. HMX is a major component of many explosives and propellants, so this is a useful estimate, but the HMX grains are generally mixed with a small amount of binder, which may affect the explosions somewhat, either enhancing or weakening them. In this exploratory simulation the chemical effect of the binder is neglected. The WSB theory does not allow for an explicit computation of pressure, but our paper [33] shows how their equations can be used to determine the pressure when the volume is an oblate ellipsoid with q_1 and q_2 the minor and major axes. The normal component of traction in the far field can simply be added to the internal pressure to determine p so long as the crack is thin, as shown by Dienes [13] in Appendix A. Calculations of crack dynamics for the cases of a sinusoidal far-field stress of 100 MPa and 400 MPa are compared in Figs. 4 and 5 of the paper [33]. It may be seen that crack radius alternates between periods of stability and rapid growth in the high stress calculation, while it is stable in the more modest stress level (100 Mpa) calculation. Additional figures are provided to show the effects of various pulse shapes and partial burning.

To test the validity of this algorithm we compared preliminary theoretical results to a high-precision experiment of Mulford et al [35] in which successive shocks were produced by impact of a two-material flyer plate against a slab of PBX 9501 (95% HMX). The first material in the flyer plate to impact is Kel-F and the second is Vistal, a much denser material. The material velocity in the PBX was measured with wires embedded in a strong magnetic field at 11 locations spaced about 0.5mm apart. The two shocks coalesce at about 1.3 μs. There is no observable effect of reaction following the first shock, but the second initiates a reaction that increases the particle velocity from 0.76 to 0.94mm/μs.

The experiment was simulated with HYDROX, a plane-wave shock-hydrodynamics finite-difference code developed by Shaw and Straub [36]. The material response is characterized by the SCRAM algorithm and the required mechanical properties for PBX 9501 were determined by Dienes [37] based on unpublished data of D. Wiegand. In this as in most SCRAM work we account for the behavior of cracks with 9 different orientations, which can be thought of as the 3 aligned with the orthogonal faces of a cube plus the 6 diagonals associated with its 12 edges. However, only the cracks with the 4 orientations at 45 degrees to the impact direction are activated in axisymmetric impact, and those have the same behavior. In this calculation the reactive behavior was controlled by the solid reaction described by the Frank-Kamenetskii equations up to the ignition point, and the subsequent reaction was described by the chemistry of WSB.

The issue concerning which crack orientations are most critical for initiation, and what number of crack orientations is needed for an accurate calculation, was addressed by Dienes et al in a brief shock symposium paper [38]. In that study cracks whose normals had orientations ranging from 47.5 to 87.5 degrees in 5 degree increments were considered for 4 values of static friction coefficient, 0.1, 0.5, 1.0, and 1.2. For the 2 lowest values of friction, all orientations were unstable at high enough stress except 87.5 degrees. However, as the friction was increased the range of unstable orientations narrowed, and for μ=1 instability

Copyright © 2010. Nova Science Publishers, Incorporated. All rights reserved.

Handbook of Material Science Research, Nova Science Publishers, Incorporated, 2010. ProQuest Ebook Central,

occurred for only the 5 orientation bins centered at 67.5 degrees, i.e., only 40% of the possible orientations on the unit sphere may be unstable at very high stresses. Calculations of the effect of crack orientation on particle velocity in the configuration of Mulford et al [35] showed that the peak material velocity for crack normals at an angle of 55 degrees were higher than for 45 degrees, the value used in the original calculations, and higher than for cracks at 70 and 80 degrees [5].

Direct evidence for the effect of crack orientation is given in photographs published by Howe et al [39] of TNT filled 105mm shells impacted at several velocities by a flat plate against the side, as illustrated in Figure 3. At high speeds violent explosions were initiated, but at the lower speeds the shells were recovered, sectioned, polished and etched. Two kinds of cracks were revealed: some long shear cracks at 45 degrees to the impact direction showed no evidence of reaction; some small cracks that were highly blackened, which we take to be evidence of residual carbon from reactions, had normals at about 75 degrees to the impact direction, consistent with the calculations described above. The crack configuration is idealized in a sketch of Dienes et al [5]. Preliminary calculations were carried out, but because of the uncertainties in TNT properties, errors produced by running a 2-dimensional idealization of a 3-dimensional test, and other finite-element approximations, we concluded that the agreement with the test result was suggestive but did not unambiguously demonstrate validation of the model.

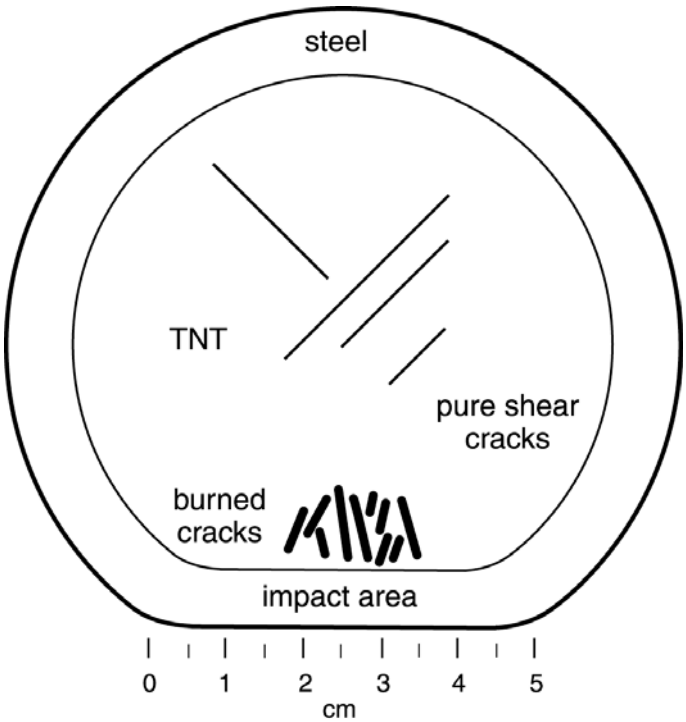


Figure 3. Sketch of the cracks observed inside a TNT-filled artillery shell impacted by a flyer plate at 440 m/s, based on photographs from Howe et al [39]. The pure shear cracks show no evidence of reaction, and are perfectly plane. The dark cracks are thought to provide evidence of frictional heating and subsequent reactions. SCRAM calculations have reproduced these effects qualitatively.

Copyright © 2010. Nova Science Publishers, Incorporated. All rights reserved.

Handbook of Material Science Research, Nova Science Publishers, Incorporated, 2010. ProQuest Ebook Central,

In really detailed calculations we would have cracks at a large number of orientations present at the right number density, but such a calculation might be premature until we have complete materials data and more confidence that all the important physical processes have been accounted for. Tests of a mixture of HMX and sugar (PBMIX) with the appropriate binder as proposed by Dienes [5] would go a long way toward generating the required confidence. The concept is that the mixture would not react enough to cause an explosion, but the nature of the hot spots and subsequent burn could be observed by sectioning the recovered mixture. Recall that numerous initiation mechanisms have been proposed, but none have been confirmed, so more definitive evidence for hot spot mechanism(s) is certainly needed.

To summarize the current status of verification and validation of the initiation and burn model, the reaction calculations in the solid state were verified by comparing with published results of Cook [40] and Linan and Williams [41] and the burn has been validated by comparing with the experiment reported by Mulford et al [35], recalling that the burn model is based on experimental data of WSB. The SCRAM calculations were limited to one-dimensional hydrodynamics, however, and only the single crack orientation at 45 degrees, entered into the calculation. The 4 shear orientations are equivalent as a result of symmetry, so the interactions between real cracks with different orientations near the same plane are not accounted for. Nevertheless, some crack interactions are accounted for since burning cracks in adjacent cells influence each other. Thus, interactions are probably more important than what we have accounted for.

Experimental evidence for the effect of orientation on initiation is provided by the results of Howe et al [39] which showed that long shear cracks at 45 degrees to the impact direction suffered no reaction, while those that show evidence of reaction (blackening) are nearly aligned with the impact direction. These crack behaviors actually occurred in different sections of the shell, so the comparison has been clarified by combining them into a single figure [5].

CONCLUSION

The tests of JBB exposed a number of issues concerning the response of propellants to dynamic loads. In particular, they showed that (1) vigorous explosions (XDT) can occur for impact speeds below those that initiate SDT; (2) these violent explosions occur intermittently, with 80% of the impacts resulting in mild deflagrations (DEF); (3) the blast pressure is well above that for SDT; and (4) the reactions are delayed, occurring in the neighborhood of 30μs rather than 5μs for SDT. These unexpected results suggest that propellants, and possibly explosives as well, can release their energy in surprising ways, and we are concerned that the same mechanical insult can lead to different levels of violence. This phenomenon is also discussed by Keefe based on his card gap tests [42]. In addition, it is worth noting that the XDT observed by Green et al [2] shows that large samples are more sensitive than small ones, an important size effect that they do not discuss, but one that can be explained as a consequence of percolation theory applied to crack networks. It is proposed here that the statistical behavior is a consequence of the dynamics of crack networks, and that fracture theory combined with probability concepts can play a role in exposing the random nature of the initiation process. To support this hypothesis, a general theory of dynamic deformation

Copyright © 2010. Nova Science Publishers, Incorporated. All rights reserved.

Handbook of Material Science Research, Nova Science Publishers, Incorporated, 2010. ProQuest Ebook Central,

has been developed that accounts for extreme stretching and rotation, for growth and interaction of defects, for the statistical nature of crack networks, and for reactions and phase changes within these defects. These developments have been reported in a rather wide variety of forums, and are reviewed here to show where we stand and where progress may be made.

The mathematical methods described here are thought to be appropriate, and the physical models plausible, but the results cannot be considered definitive at this point. Some of the outstanding issues follow. The generalized superposition of strain rates (GSSR) is a productive way of describing the behavior of an ensemble of defects that are too numerous to treat individually. The treatment of typical defects in SCRAM allows us to study defect thermochemistry on a subgrid with dimensions so small that there can be a hundred cells in a micron, while the governing cracks can extend from 40 to 400 microns, or more. The overall finite-element grid can be many centimeters across. Thus, our method allows us to account for a wide range of scales. A statistical theory allows us to account for coalescence of growing cracks and the formation of crack networks. The effect of crack orientation is found to be significant, and cracks nearly parallel to the impact direction appear to be most sensitive. The initial heating of cracks begins with sliding of the interfaces of closed (penny-shaped) cracks, continues with melting, is superceded by reactive heating in the manner of Frank-Kamenetsky, is followed by reactive burn following Ward, Son, and Brewster and, if sufficient crack interaction occurs, a fast explosion takes place at late times. We do not consider it to be a detonation because it does not propagate as a wave but, rather, occurs in the bulk with numerous crack interactions, possibly supported by radiation. The process is thought to start with very rapid growth of shear cracks in the explosive grains, which are brittle, but crack growth can continue through the binder with large cracks behaving as though they are in a tougher material. Phases of rapid crack growth cause significant bursts of heating due to friction. Carrying out simulations with greater resolution might improve the accuracy, but we believe that this would be premature until the proposed mechanisms are validated more definitively.

The various theoretical processes described above are all reported in the literature, but not collectively or with XDT in mind. To demonstrate experimentally that they actually combine in a manner something like that described here would require capturing the process before complete reaction of the bulk material. It seems plausible that this could be accomplished by mixing explosive grains with sugar, or some other inert simulant, in an appropriate binder as discussed by Dienes et al [5]. A few cracked grains containing reaction products would identify shear cracking, whereas sliding with reaction between adjacent grains would reveal a different heating mechanism, as would crack-tip heating. Observations of defect interactions would be crucial.

Violent accidental explosions are rare, but well-worth avoiding. Laboratory tests are useful, but large masses of reactive material are more vulnerable than laboratory samples and the scale effects are unknown. A better understanding of initiation mechanisms would allow the vulnerability of full-scale systems (rockets, submarines, aircraft, ships) to be quantified and quite possibly suggest designs leading to safer configurations. The idea that networks of cracks can be responsible for violent explosions of the kind observed in XDT, but also in fast and slow cook-off, drop tests, card gap tests, and such, has received very little attention. If research in this new direction becomes promising, it may well allow us to quantify probabilities of explosive reaction as a function of sample size and other relevant parameters.

Copyright © 2010. Nova Science Publishers, Incorporated. All rights reserved.

Handbook of Material Science Research, Nova Science Publishers, Incorporated, 2010. ProQuest Ebook Central,

APPENDIX

Comparison of Tensile and Compressive Strength

Criteria for the stability of penny-shaped cracks are summarized by Zuo and Dienes [15]. We consider here only the case of one-dimensional stress. The critical condition for stability of a penny-shaped crack in tension is

$$\sigma_{11}{}^2 c < \frac{\varsigma}{(1-\nu/2)}\ ,\ \ \zeta = \frac{\pi}{2}\frac{2-\nu}{1-\nu}\gamma\mu$$

where ν is Poisson's ratio; γ, the effective surface energy; and μ the shear modulus. For compression the solution of Segedin can be supplemented to include friction by subtracting the friction stress τ from the far-field stress σ_{11}, with the resulting stability condition given by

$$(\sigma-\tau)^2\, c < \varsigma\,,\ \ \tau = \sigma_{11}\cos\alpha\sin\alpha\,,\ \ \sigma = \bar{\mu}\sigma_{11}\cos^2\alpha\,,$$

where $\bar{\mu}$ denotes the coefficient of friction and α is the angle of the crack normal with the direction of the imposed stress σ_{11}. Then the ratio of critical compressive to tensile stress is given by

$$\frac{\sigma_c}{\sigma_t} = \frac{\sqrt{1-\nu/2}}{\cos\alpha\left(\sin\alpha - \bar{\mu}\cos\alpha\right)},$$

independent of crack size. This ratio depends on the angle of the compression crack. It has a minimum when the angle of the compression crack has the value $\alpha = \pi/4 + \beta/2$, where $\tan\beta = \bar{\mu}$, i.e.,

$$\frac{\sigma_c}{\sigma_t} = \frac{2\sqrt{1-\nu/2}}{\sqrt{1+\bar{\mu}^2}-\bar{\mu}}.$$

This compares the conditions for incipient damage in compression and tension. For $\bar{\mu}=1$, the ratio is $4.83\sqrt{1-\nu/2}$. As discussed in the text, ultimate failure occurs when the cracks coalesce at the percolation threshold, a condition that depends on crack statistics rather than initial instability. Note that this result is quite different from that for ductile materials, for which tensile and compressive yield conditions are nearly the same. This approach to compressive failure of brittle materials accounts only for self-similar crack growth, while actual compressive failure of explosives and propellants is difficult to characterize because of the risk of explosion when interface sliding begins. If this ratio of strengths seems low, it may

Copyright © 2010. Nova Science Publishers, Incorporated. All rights reserved.

Handbook of Material Science Research, Nova Science Publishers, Incorporated, 2010. ProQuest Ebook Central,

be noted that the coefficient of friction between fresh new surfaces may well exceed unity, and is quite probably greater than the usual values tabulated in handbooks, which involve dirty, dissimilar surfaces with little cohesion. The goal here is to provide a framework for a general theory rather than to fit any specific data. A broad perspective for geologic materials is provided by Scholz [14], but the behavior of (organic) explosive grains may be quite different and deserves a special treatment. A recent useful paper by Biegel, Sammis, and Rosakis [43] discusses some of the complexities in an explosive simulant, Homalite.

REFERENCES

[1] Jensen, R.C.; Blommer, E.J.; Brown, B. "An Instrumented Shotgun Facility To Study Impact Initiated Explosive Reactions", Seventh Symposium (International) on Detonation, J.M.Short, Ed., Naval Suface Weapons Center, White Oak, 1982.

[2] Green, L.G.; James, E.; Lee, E.L.; Chambers, E.S.; Tarver, C.M.; Westmorland, C.; Weston, A.M.; Brown, B. "Delayed detonation in propellants from low velocity impact", In: Short, J.M. (Ed.), Proc. of the 7th Symp on Detonation, pp. 254-264, 1982.

[3] Autonne, M.L. "Sur les groupes lineares, reels, et orthogonaux", *Bull. Soc. Math*. France, 30, pp 121-130, 1902.

[4] Rosakis, A.J. "Intersonic shear cracks and fault ruptures", *Adv. Phys*. 51, 4, pp 1189-1257, 2002.

[5] Dienes, J.K.; Zuo, Q.H.; and Kershner, J.D. "Impact Initiation of Explosives and Propellants via Statistical Crack Mechanics", *J. Mech. Phys. Solids*, pp1237-1275, 2006.

[6] Von Holle, W.; and Martin C.; "Safe Handling of Insensitive High Explosive Weapon Subassemblies at the Pantex Plant", DNFSB/TECH24, 1999.

[7] Birk, A.; Baker, D.; Kooker, R.; Lieb, S.; Stegall and Delaney J. "Nondetonative Explosions and Burning of Composition-B Explosive", Twelfth Symposium (International) on Detonation, 2002.

[8] Blommer, E.J.; "A Manganin Gauge Technique for Propellant Impingement Pressure-Time Histories", Propulsion Systems Hazards Subcommitee Meeting, CPIA Publication 356, 1 pp 205-223, 1982.

[9] Dienes, J. K.; "Finite Deformation of Materials with an Ensemble of Defects", Los Alamos Report LA-13994-MS, 2004. (Available on GOOGLE)

[10] Kachanov, M.; "Elastic Solids with Many Cracks and Related Problems", Advances in Applied Mechanics, Academic Press, San Diego, CA, 1994.

[11] Taylor, L. M.; and Flanagan D. P. "Pronto 3D--A Three-Dimensional Transient Solid Dynamics Program", SAND87-1912, Sandia National Laboratories, 1989.

[12] Dienes, J. K. "The Effect of Finite Rotation on a Problem in Plastic Deformation", Proc. Bell International Symposium on Plasticity, University of Oklahoma, Norman, OK, 1984.

[13] Dienes, J. K.; "Theory of Deformation, Vol. II – Physical Theory", Los Alamos National Laboratory Report LA-11063-MS, Vol. II, 1989.

[14] Scholz, C.H. The Mechanics of Earthquake Faulting, Cambridge University Press, Cambridge, UK, 2002.

Copyright © 2010. Nova Science Publishers, Incorporated. All rights reserved.

Handbook of Material Science Research, Nova Science Publishers, Incorporated, 2010. ProQuest Ebook Central,

[15] Zuo, Q.H.; and Dienes, J.K. "On the stability of penny-shaped cracks with friction: the five types of brittle behavior", *Int. J. Solids Structures*, 42/5-6 pp 1309-1326, 2004.
[16] Dienes, J.K. "On the effect of anisotropy in explosive fragmentation", In: Einstein, H.H. (ed), Rock Mechanics from Research to Application, Proceedings of the 22nd US Symposium on Rock Mechanics, M.I.T., Cambridge, MA, 1981.
[17] Dienes, J. K. "On the Mean Cluster Size of a Network of Cracks", *J. Structural Control*, 13, 169-189, 2005. DOI: 10.1002/stc.126
[18] Dienes, J.K. "Inferring Three-Dimensional Crack Statistics from Two-Dimensional Data", *Adv. Appl. Math*. 24, pp 57-64, 2000.
[19] Zhurkov, S.N.; and Kuksenko, V.S. "The micromechanics of polymer fracture," *Int. J. Fracture,* II, 4, pp 629-639, 1975.
[20] Zhurkov, S.N.; and Sanfirova, T.P. "Relation Between Strength and Creep of Metals and Alloys", Soviet Physics, English Translation, 3, 5, pp1586-1592, 1957.
[21] Freund, L.B. Dynamic Fracture Mechanics, Cambridge University Press, NYC, NY, 1990.
[22] Heaton, T.H. "Evidence for and implicatrions of self-healing pulses of slip in earthquake rupture", *Phys. Earth Planet. Inter*., 64, 1-20, 1990.
[23] Rice, J.R. "New perspectives on cracks and fault dynamics", In: Aref, H., Phillips, J.W. (eds.), Mechanics for a New Millennium: Proceedings of the ICTAM 2000, Kluwer Academic Publishers, Dordrect, Netherlands, 2000.
[24] Frank-Kamenetsky, A.A.; "On the mathematical theory of thermal explosions", Acta Physicochimica URSS 16, pp 357-361, 1942.
[25] Field, J.E.; Bourne, N.K.; Palmer, S.J.P.; and Walley, S.M. "Hot-spot ignition mechanisms for explosives and propellants", *Phil. Trans. R. Soc*. A339, pp 269-283, 1992.
[26] Dienes, J. K. "A Frictional Hot-Spot Theory for Propellant Sensitivity," Proc. 1982 JANNAF Propulsion Systems Hazards Meeting, China Lake, CA, 1982.
[27] Dienes, J. K. "A Unified Theory of Flow, Hot Spots, and Fragmentation with an Application to Explosive Sensitivity", in High-Pressure Shock Compression of Solids II, Springer-Verlag, NYC, NY, Lee Davison et al, (eds,), 1996.
[28] Dienes, J.K. "Statistical Crack Mechanics and Explosive Hot Spots," Workshop on Propellant Ignition Micromechanics (via ESD, Impact, or Friction), United States Army Research Office, Nashville, Tennessee, pp 89-99, 1991.
[29] Fermi, E. Los Alamos Report LA-1927, 1956, Collected papers 2, Univ. Chicago Press, Chicago, IL, No. 244, 1966.
[30] Miles, J. W.; and Dienes, J. K. "Taylor Instability in a Viscous Liquid," General Atomic Report GA-7253, July 1966, *Phys. Fluids*, 9, 12, pp 2518-2519, 1966.
[31] Dienes, J. K. "The Method of Generalized Coordinates and an Application to Rayleigh-Taylor Instability", *Phys. Fluids*, 21, 5, pp 736-744,1978.
[32] Dienes, J. K. "Crack dynamics via Lagrange's equations and generalized coordinates," *Acta Mech*. 148, pp 79-92, 2001.
[33] Dienes, J. K.; and Kershner, J.D. "Crack dynamics and explosive burn via generalized coordinates*," J. Comput-Aided Mater*, 7, pp 217-237, 2001.
[34] Ward, M.J.; Son, S.F.; and Brewster, M.Q. "Steady deflagration of HMX with simple kinetics: a gas phase chain reaction model," *Combust. Flame*, 114, pp 556-558, 1998.

Copyright © 2010. Nova Science Publishers, Incorporated. All rights reserved.

Handbook of Material Science Research, Nova Science Publishers, Incorporated, 2010. ProQuest Ebook Central,

[35] Mulford, R.N.; Sheffield S.A; and Alcon, R.A. "Initiation of Preshocked High Explosives PBX 9404, PBX 9502, PBX 9501, Monitored with In-Material Magnetic Gauging," Proceedings of the Tenth International Detonation Symposium, Boston, MA, pp. 459-467, 1991.

[36] Shaw, M.S. and Straub, G.K. "HYDROX, A One Dimensional Lagrangian Hydrodynamics Code", Los Alamos Report LA-8642-M, 1981.

[37] Dienes, J. K. "Strain-Softening via SCRAM", Los Alamos Report LA-UR-98-3620, 1998.

[38] Dienes, J. K.; Middleditch, J.; Zuo, Q.H.; and Kershner, J.D. "On the Role of Crack Orientation in Brittle Failure and the Formation of Hot Spots", 13th APS SCCM Conference in Portland, OR, Los Alamos report LA-UR-03-4004, 2003.

[39] Howe, P.M.; Gibbons, G.G.; Weber, P.E. "An experimental investigation of the role of shearing initiation of detonation", In: Short,, J.M., and Deal, W.E., (Ed.) Proc. of the 8th Symp. On Detonation, pp 294-306, 1985.

[40] Cook, G.B., "The initiation of explosion in solid secondary explosives", *Proc. R. Soc. London* A 246, pp 154-160, 1958.

[41] Linan, A.; and Williams, F.A. "Theory of ignition of a reactive solid by constant energy flux", *Combust. Sci. Technol*. 3, pp 91-98, 1971.

[42] Keefe, R.L. "Delayed Detonation in Card Gap Tests", Seventh Symposium (International) on Detonation, J.M.Short, Ed., Naval Suface Weapons Center, White Oak, pp 265-272, 1982.

[43] Biegel, R.L.; Sammis, C.G.; and Rosakis, A.J. "An experimental study of the effect of off-fault damage on the velocity of a slip pulse", *J. Geophys. Res*., 113, B04302, doi10.1029/2007JB005234, 2008.

Copyright © 2010. Nova Science Publishers, Incorporated. All rights reserved.

Handbook of Material Science Research, Nova Science Publishers, Incorporated, 2010. ProQuest Ebook Central,

Copyright © 2010. Nova Science Publishers, Incorporated. All rights reserved.

Handbook of Material Science Research, Nova Science Publishers, Incorporated, 2010. ProQuest Ebook Central,

In: Handbook of Material Science Research
Editors: C. René and E. Turcotte, pp.295-322
ISBN 978-1-60741-798-9
© 2010 Nova Science Publishers, Inc.

Chapter 6

MAGNETIC PROPERTIES OF LAYERED TITANIUM DICHALCOGENIDES INTERCALATED WITH 3D- AND 4F-METALS

N. V. Baranov[1, 2] and V. G. Pleschov[1]
[1] Ural State University, Ekaterinburg, Russia
[2] Institute of Metal Physics,
Russian Academy of Science, Ekaterinburg, Russia

ABSTRACT

Layered structure of titanium dichalcogenides TiX_2 (X = S, Se, Te) allows to intercalate various guest atoms, in particular, with non-full filled 3*d* or 4*f* electron shells into space between X-Ti-X tri-layers and to obtain the quasi two-dimensional systems with alternate layers of magnetic and non-magnetic atoms. Different magnetic states ranging from spin-glass like behavior up to states with three-dimensional magnetic order are observed in M_xTiX_2 intercalated by 3d-transition (M) metals. The methods of the preparation of compounds intercalated with 3*d* and rare-earth (R) metals and the results of the crystal structure and magnetic properties investigations for M_xTiX_2 and R_xTiX_2 systems are presented and discussed. The values of the magnetic moments of intercalated M and R atoms and the presence of various magnetic states in compounds are considered as depending on both the chemical constituents and on the concentration of inserted atoms.

1. INTRODUCTION

For more than 30 years the layered compounds based on transition-metal (T) dichalconides have been a subject of particular interest for investigations in the field of physics and chemistry of two-dimensional state. The TX_2 (X = S, Se, Te) compounds have highly anisotropic physical properties and reveal unique electronic properties such as a variety of charge density wave (CDW) and superconducting transitions [1, 2]. Among the TX_2 compounds, a great attention was paid to the study of titanium dichalgogenides. The

Copyright © 2010. Nova Science Publishers, Incorporated. All rights reserved.

Handbook of Material Science Research, Nova Science Publishers, Incorporated, 2010. ProQuest Ebook Central,

TiX_2 (X = S, Se, Te) compounds consist of a hexagonal sheet of Ti atoms sandwiched between two similar sheets of chalcogen atoms, forming the basic X-Ti-X tri-layer. The sheets are coupled by relatively weak van der Waals (vdW) forces while the atoms within the sheet are coupled by strong covalent bonds [1.2]. As a result of this the TiX_2 compounds can be intercalated with foreign atoms and molecules (see Figure1) leading to significant changes in their crystal lattice, electrical and magnetic properties [3, 4] and making them technologically useful. In particular, some of intercalated materials are used for rechargeable high-energy-density lithium batteries [5] and for ion-selective electrodes [6].

The studies of the magnetic properties of TiX_2 compounds have shown that they are Pauli paramagnets with the susceptibility values $\chi \sim 10^{-6} - 10^{-5}$ emu/ mol at room temperature [7 – 9]. The intercalation of the TiX_2 matrixes with atoms exhibiting non-full filled 3*d* or 4*f* electron shells changes dramatically their magnetic behavior. Some TiX_2 compounds intercalated with atoms of 3d or rare earth metals manifest a spin-glass, cluster-glass state and ferromagnetic or anniferromagnetic order depending on the type and concentration of quest atoms as well as on the chalcogen type [3, 10-19].

In this chapter, the results of the crystal structure and magnetic properties investigations of M_xTiX_2 compounds intercalated with various 3*d* metals as well as with some rare earth metals are presented. Because of their layered structure the M_xTX_2 and R_xTiX_2 compounds can be considered as good objects for the study of mechanisms of the exchange interaction, magnetic anisotropy and formation of magnetic moments on the inserted atoms in quasi two-dimensional systems.

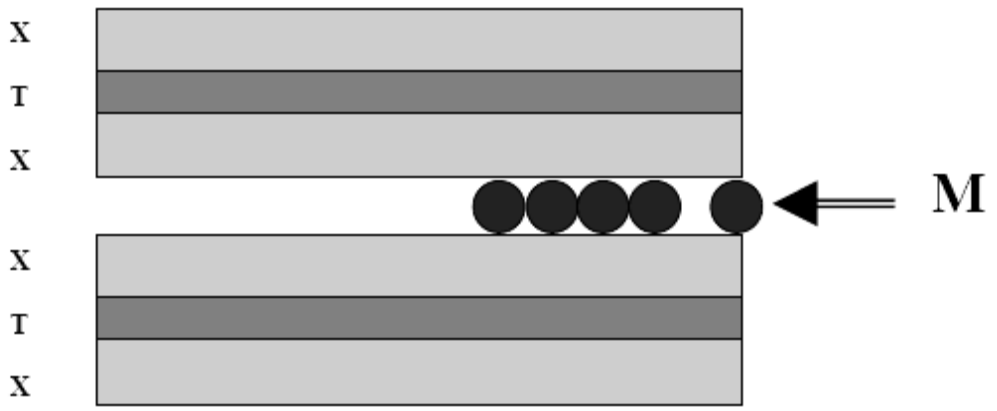


Figure 1. Scheme of the intercalation of M atoms into TX_2 (X = S, Se, Te).

2. Sample Preparation and Peculiarities of the Crystal Structure

An ampoule synthesis method is usually used for the preparation of polycrystalline M_xTiX_2 samples (M = V, Cr, Mn, Fe, Co, Ni). First the parent compound TiX_2 is synthesized by heat treatment of a mixture of the starting materials Ti and Se at temperature from 600 up to 900 °C during several days. In the second stage the mixtures of 3*d* metals and $TiSe_2$ powders are sealed in evacuated quartz tubes and annealed under the same conditions [13,

Copyright © 2010. Nova Science Publishers, Incorporated. All rights reserved.

Handbook of Material Science Research, Nova Science Publishers, Incorporated, 2010. ProQuest Ebook Central,

14]. For better homogeneity the obtained specimens can be milled again, compacted into pellets and then homogenized for several weeks followed by cooling down to room temperature through removal of the tube from the oven into air or dropping into water. In some cases, the samples are cooled slowly to room temperature in the furnace in order to achieve ordering effect of intercalated M ions and vacancies in the van der Waals (vdW) gaps [12, 20-21]. The polycrystalline Gd_xTiSe_2 [19] and Gd_xTiS_2 [23] compounds intercalated with gadolinium up to x=0.35 and x=0.05 respectively can be prepared by an ampoule synthesis as well. Another method was used to synthesize the intercalation compounds R_xTiSe_2 (R= Eu, Yb) with x up to x = 0.066. These compounds were prepared by thermal deintercalation of NH_4^+ and NH_3 from the ammonia containing precursors [24].

A chemical vapor transport technique with several carrier agents (I_2, Br_2, $IC1_2$) is mainly used for the preparation of TiX_2 single crystals. As reported by many authors (see Ref. 25 and Ref. 26, for instance), the single crystals of intercalated M_xTX_2 compounds can be prepared by the same method. The plate shape crystal with 5-50 mm^2 area and 0.03 – 0.05 mm thickness of some M_xTiS_2 and M_xTiSe_2 compounds are prepared depending on transport gas, size of ampoule, and temperature [25]. The chemical composition of each single crystal is needed to be determined separately since the intercalant concentration in crystals may differ substantially from that in starting M_xTiX_2 polycrystalline materials.

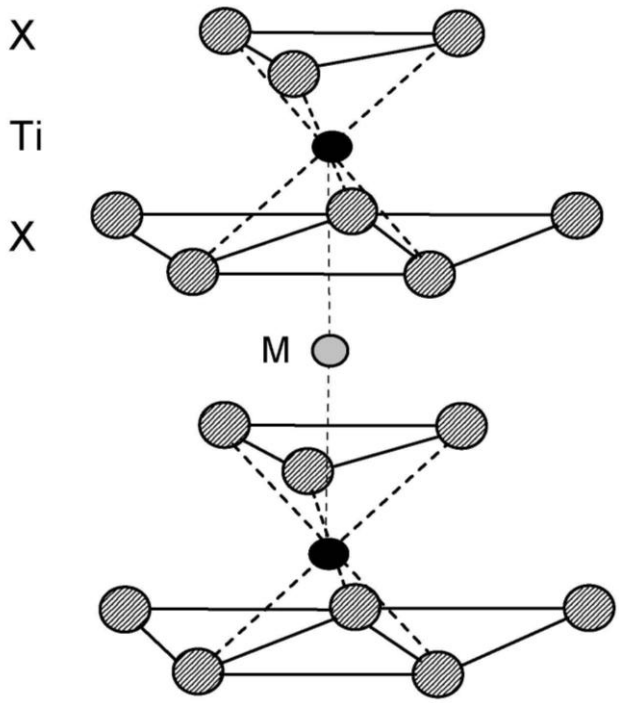


Figure 2. Scheme of the arrangement of chalcogen and titanium atoms in TiX_2 (X = S, Se, Te). Small light grey symbol indicates a possible octahedral position of M atom intercalated.

Copyright © 2010. Nova Science Publishers, Incorporated. All rights reserved.

Handbook of Material Science Research, Nova Science Publishers, Incorporated, 2010. ProQuest Ebook Central,

Table 1. Crystal lattice parameters a_0 and c_0, the c_0/a_0 ratio, the van der Waals gap width, $d_{X\text{-}X}$; the thickness of X-Ti-X sandwiches, $d_{X\text{-}Ti\text{-}X}$; the $d_{X\text{-}X} / d_{X\text{-}Ti\text{-}X}$ ratio for TiX_2 compounds (X= S, Se, Te) and ionic radii of X^{2-} ions [28]

Compound	a_0 (Å)	c_0 (Å)	$\frac{c_0}{a_0}$	$d_{\text{X-X}}$ (Å)	$d_{\text{X-Ti-X}}$ (Å)	$\frac{d_{X-X}}{d_{X-Ti-X}}$	r_{x} (Å)
TiS_2	3.407	5.695	1.672	2.426	3.269	0.742	1.82
$TiSe_2$	3.540	6.008	1.697	2.554	3.454	0.739	1.93
$TiTe_2$	3.766	6.491	1.724	2.717	3.774	0.719	2.11

The parent TiX_2 compounds, like many early transition-metal dichalcogenides, crystallize in the 1*T*-CdI_2 structure, which has a hexagonal close packing of anions with the Ti atoms in octahedral holes (shown in Figure2). Each Ti atom is surrounded by six chalgogen in a nearly octahedral coordination. The space group of this structure is $P\bar{3}m1$.

In some transition-metal dichalcogenides the transition metal layers may be shifted that leads to trigonal surrounding (2*H* – polytype). Between the weakly bonded TiX_2 sandwiches foreign atoms or molecules may be inserted in the empty holes formed by two adjacent *X* layers. The main structural characteristics of TiX_2 compounds are displayed in Table 1 [27].

As follows from Table 1, the minimal distance $d_{\text{X-X}}$ between positions of chalcogen atoms belonging to adjacent X-layers and corresponding to the van der Waals gap width increases for 12% when going from $TiSe_2$ to $TiTe_2$. At the fist glance, such an increase of $d_{\text{X-X}}$ may be considered as an indication of the reduction of the interaction between X-Ti-X tri-layers. However, as can be seen from the Table 1, the Te^{2-} ion exhibits an increased r_x value by about 16% in comparison with S^{2-} ion due to the larger spatial extension of 4*p*-orbitals. It means that despite the growth of the "geometrical" width $d_{\text{X-X}}$, the "physical" width of the of the v-d-W gap decreases when going from TiS_2 to TiT_2. Therefore, an increase of the interaction between X-Ti-X sandwiches can be expected with increasing atomic number of *X*, which implies the decrease of the compressibility of the lattice within $TiS_2 \rightarrow TiSe_2 \rightarrow TiTe_2$ series. The reduction of the "physical" width of the vdW gap with increasing atomic number of the chalcogen in TiX_2 matrixes may result in the reduction of a maximal concentration of the intercalated atoms.

Within the family of titanium dichalcogenides, the most attention was paid to the study of the crystal structure and physical properties of the $TiSe_2$ compounds because of the existence of a structural phase transition induced by a charge density wave (CDW) below the critical temperature $T_t \approx 200$ K [2, 9]. The phase transition into a commensurate ($2 \times 2 \times 2$) superlattice in $TiSe_2$ is observed to be accompanied by significant anomalies of the ultrasonic velocity, thermal expansion, electrical and optical properties [2, 9, 29-31]. All these observations show that both the lattice and electronic subsystems of $TiSe_2$ are strongly modified at the CDW transition. The mechanism of this transition remains unclear till now despite the extensive experimental and theoretical investigations performed during last three decades. The structural phase transitions associated with the CDW formation are also observed in other transition metal dichalgogenides, for instance, in $TaSe_2$ and $NbSe_2$ [1-2].

Copyright © 2010. Nova Science Publishers, Incorporated. All rights reserved.

Handbook of Material Science Research, Nova Science Publishers, Incorporated, 2010. ProQuest Ebook Central,

Unlike $TiSe_2$, the appearance of the CDW state in these compounds is accompanied by phase transitions to incommensurate superlattices.

The intercalation of 3*d* atoms between X-Ti-X sandwiches leads to a contraction or expansion of the averaged interlayer distance, depending on the type of the 3*d* metal and its concentration [4, 14-15]. The structure of sandwiches and geometry of the chalcogen surrounding of Ti atoms do not change appreciably at the intercalation. Figure 3 shows the variation of the lattice parameter c with increasing intercalant content for M_xTiSe_2 systems intercalated with 3*d* metals [15, 19].

As can be seen from Figure3, the intercalation of titanium diselenide by 3*d* metals leads in most cases to the contraction of the lattice along the *c* direction. A less pronounced contraction of the lattice perpendicular to the layers is observed in the case of the gadolinium intercalation [19]. The concentration dependence of the *c* parameter for Gd_xTiSe_2 system is displayed in Figure 3 as well. An exception from the general trend reveals the Mn_xTiSe_2 system. Unlike other 3*d* metal, the intercalation of Mn atoms into v-d-W gaps of $TiSe_2$ causes an increase of the *c* parameter. The contraction of the crystal lattice along the *c*-axis in M_xTiSe_2 compounds is ascribed by to the formation of covalent links between X–Ti–X layers via intercalated M-ions [4, 14-15]. According to the band structure calculations performed for some ordered M_xTiX_2 (X=S, Se) compounds, the 3*d*-electron states of M ions are hybridized with TiX_2 bands [32-33]. Photoelectron spectroscopy studies performed for some M_xTiX_2 systems have indeed revealed a strong hybridization of M 3*d* states with chalcogen *p* and Ti 3*d* states [33-36]. Moreover, the appearance of a narrow dispersionless band below the Fermi level in M_xTiSe2 compounds with M = Cr and Co is observed [33] in comparison with the parent compound $TiSe_2$. The main contribution to this additional band results from hybridized M 3*d* –Ti 3*d* states.

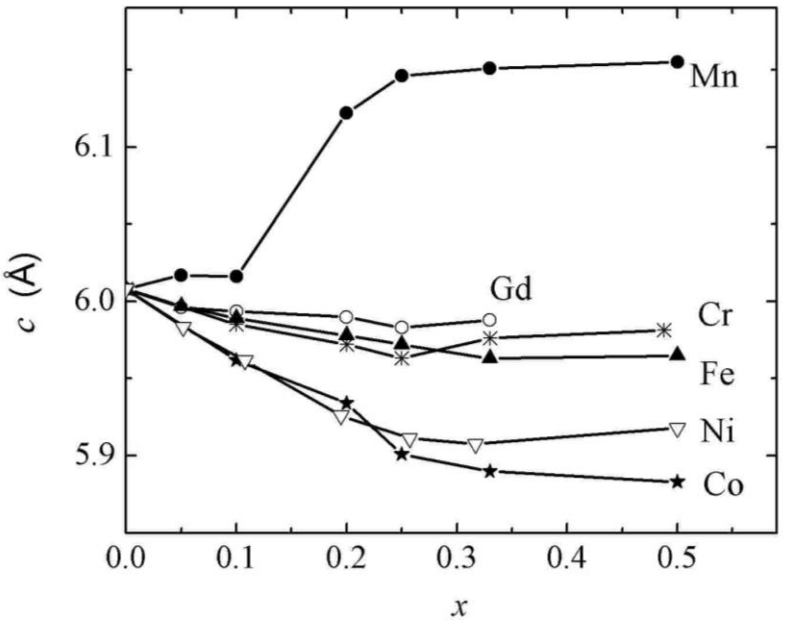


Figure 3. Concentration dependences of the lattice parameter *c* with for some M_xTiSe_2 systems intercalated with 3*d* metals.

Copyright © 2010. Nova Science Publishers, Incorporated. All rights reserved.

Handbook of Material Science Research, Nova Science Publishers, Incorporated, 2010. ProQuest Ebook Central,

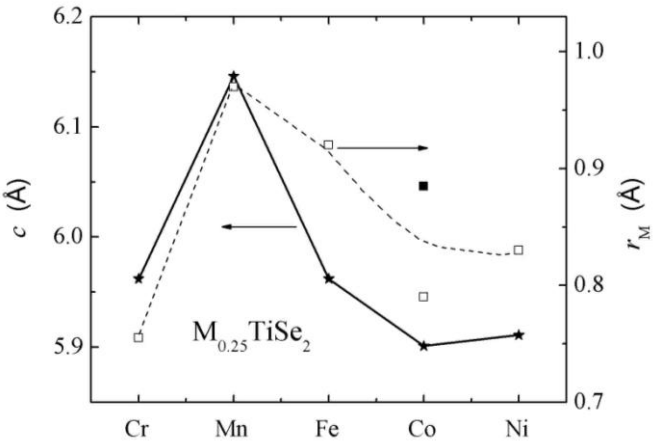


Figure 4. The *c* parameter of $M_{0.25}TiSe_2$ compounds and M ionic radii [28] as a function of the atomic number of the 3*d* metal intercalated. For cobalt, the *r* values are presented for both high-spin (■) and low-spin (□) states.

The influence of the intercalation of different 3*d* metals on the deformation of the lattice perpendicular to the layers is clear seen from Figure 4 which shows the variation of the *c* parameter of $M_{0.25}TiSe_2$ compounds as a function of the atomic number of the 3*d* metal intercalated. As it seen, the variation of the *c* parameter correlates with the change of the ionic radius in the series of 3*d* transition metals. The M 3*d* metals intercalated into $TiSe_2$, except for trivalent chromium, are divalent [4]. An analogous correlation between the interlayer spacing *c* and ionic radius of M metals was observed for M_xTiS_2 and M_xNbX_2 (X = S, Se) systems [4].

At high concentrations of intercalated M metals ($x \geq 0.25$), the superstructure formation can be observed in M_xTiSe_2 due to the ordering of the inserted atoms and vacancies in v-d-W gaps [12, 20]. Thus, the superstructure $2a_0 \times 2a_0\sqrt{3} \times 2c_0$ caused by the formation of Cr chains in the plane intercalated atoms was observed in Cr_xTiSe_2 at x = 0.25 (a_0 and c_0 are lattice parameters of the initial hexagonal lattice). At x = 0.33, the superstructure $a_0\sqrt{3} \times a_0\sqrt{3} \times 2c_0$ appears due to the formation of a network of Cr atoms between sandwiches. Sharp cooling of the samples prevents the superstructure formation in Cr_xTiSe_2 compounds at x < 0.5. The crystal structure of quenched Cr_xTiSe_2 samples at x < 0.5 is described by the same space group ($P\bar{3}m1$) as that of the parent $TiSe_2$ compound. At higher intercalant concentrations ($x \geq 0.5$), the superstructure $a_0 \times a_0\sqrt{3} \times 2c_0$ is found to appear in Cr_xTiSe_2 independent on the cooling rate. As it will be shown below, the distribution character of M atoms within v-d-W gaps may affect substantially the magnetic behavior of some M_xTX_2 compounds.

3. INFLUENCE OF THE 3*D* METAL INTERCALATION ON MAGNETIC PROPERTIES OF TiX_2 COMPOUNDS

Together with structural changes the intercalation of titanium dichalcogenides with 3d metal atoms modifies substantially the magnetic behavior of compounds. Unlike parent TX_2 matrixes, the intercalated M_xTX_2 compounds exhibit an anomalous behavior of temperature dependences of the magnetic susceptibility at low temperatures, which are indicative of the

Copyright © 2010. Nova Science Publishers, Incorporated. All rights reserved.

Handbook of Material Science Research, Nova Science Publishers, Incorporated, 2010. ProQuest Ebook Central,

appearance magnetically ordered states. The temperature dependence of the magnetic susceptibility of M_xTiX_2 in the paramagnetic state can be well described by the expression: $\chi = \chi_0 + C/(T-\Theta_p)$, where $\chi_0 = \chi_d + \chi_P$ includes the diamagnetic contribution and paramagnetic contribution from delocalized electrons. In many cases, the Pauli paramagnetic contribution χ_P from conduction electrons is suggested to be temperature independent when analyzing the total susceptibility behavior. However, as it known (see [37], for instance) this contribution may reveal the temperature dependence associated with the temperature change in the density of the electronic states at the Fermi level. The diamagnetic susceptibility χ_d which includes the contribution from the ions with full-filled electronic shells and Landau's diamagnetic contribution of free electrons is accepted to be constant. The second term in this expression describes the Curie-Weiss contribution; C is the Curie constant, Θ_p denotes the paramagnetic Curie temperature. The effective magnetic moment μ_{eff} of M ions in M_xTiX_2 is observed to be lower than the expected value $\mu_{eff} = g\mu_B[S(S+1)]^{1/2}$ calculated at g = 2 [37].

As will be shown below, different magnetic states may be observed in M_xTiX_2 depending on the kind and concentration of M ions as well as on the type of the TiX_2 matrix.

3.1. V_xTiX_2

The vanadium intercalated compounds V_xTiS_2 ($0 < x \leq 1$) are observed to exhibit a paramagnetic behavior within temperature range 4.2 – 300 K with the effective magnetic moment of around 0.6 μ_B per V atom [4, 38]. The paramagnetic Curie temperature shows negative values (Θ_p = -2 – -10 K), which may be indicative of the presence of the antiferromagnetic exchange interaction between 3*d* electrons of inserted vanadium atoms. For the titanium diselenide V_xTiSe_2 intercalated with vanadium up to x = 0.2, the effective magnetic moment is estimated to be 1.4 – 1.5 μ_B per V atom and Θ_p ~ - 3 K [13]. According to Ref.13, the lower values of μ_{eff} in comparison with expected 3.87 μ_B for V^{2+} may be attributed to the hybridization of V 3*d* states with electronic states of parent TiX_2 compounds.

3.2. Cr_xTiX_2

The effective magnetic moment per Cr atom intercalated between X-T-X sandwiches in Cr_xTiX_2 compounds are observed to vary from 3 μ_B up to 4.2 μ_B [10] (see Table 2), i.e. quite close to the calculated value μ_{eff} = 3.87 μ_B for Cr^{3+} with the spin value $S = 3/2$ и $g = 2$. The anomalies observed at low temperatures on the temperature dependences of the magnetic susceptibility of Cr_xTiS_2 were explained by the appearance of a long-range magnetic order at low temperatures. From the magnetization behavior under application of a magnetic field, the magnetic order of Cr_xTiS_2 compounds with $0 < x < 1$ was classified as a ferromagnetic one, while an antiferromagnetic order was suggested to exhibit in $CrTiS_2$ (x = 1) [10]. More detailed investigations of the magnetic state were performed for chromium intercalated titanium diselenide Cr_xTiSe_2 with intercalant concentrations within $0 < x \leq 0.6$ on the samples obtained at different cooling rate [16, 39]. Figure5 and Figure6 show the temperature dependences of the magnetic susceptibility of Cr_xTiSe_2 measured in a low-temperature region on a sample cooled in zero field (ZFC) or on a sample cooled in an applied field (FC).

Copyright © 2010. Nova Science Publishers, Incorporated. All rights reserved.

Handbook of Material Science Research, Nova Science Publishers, Incorporated, 2010. ProQuest Ebook Central,

Table 2. The effective magnetic moment μ_{eff}, the magnetic state at low temperatures and magnetic critical temperature T_{crit} for Cr_xTiX_2 (X = S, Se, Te)

Compound	x	0.1	0.2	0.25	0.33	0.5	References
Cr_xTiS_2	$\mu_{eff}(\mu_B)$	3,2	3,0				[10]
	Magnetic state			F	F	F	
	T_{crit} (K)	4		12	14	15–30	
Cr_xTiSe_2	$\mu_{eff}(\mu_B)$	3.4	3.1	3.3	3.5	3.6–3.8	[16, 39]
	Magnetic state	SG		CG	CG	AF	
	T_{crit} (K)	3		8	10	38	
Cr_xTiTe_2	$\mu_{eff}(\mu_B)$	4.1	3.9	4.1	3.8	4.2	[40]
	Magnetic state		SG	CG	CG	CG +FM	
	T_{crit} (K)		8	10	12	78	

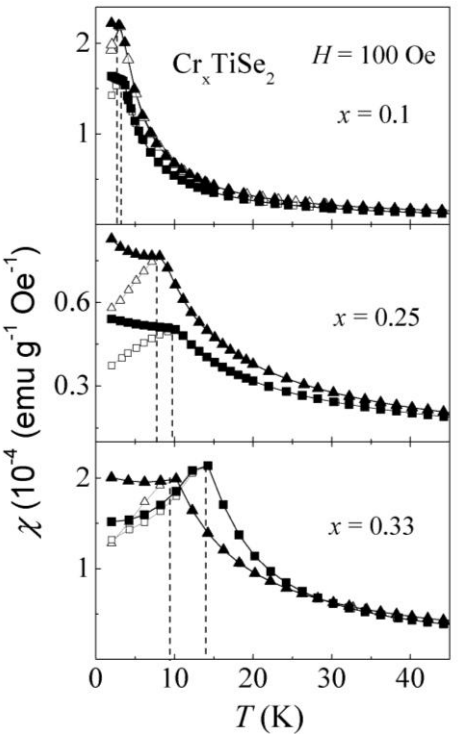


Figure 5. Temperature dependences of the magnetic susceptibility of the quenched (triangles) and slowly-cooled (sguares) samples of Cr_xTiSe_2 ($x \leq 0.33$) measured at FC (full symbols) and ZFC (open symbols) regimes.

Copyright © 2010. Nova Science Publishers, Incorporated. All rights reserved.

Handbook of Material Science Research, Nova Science Publishers, Incorporated, 2010. ProQuest Ebook Central,

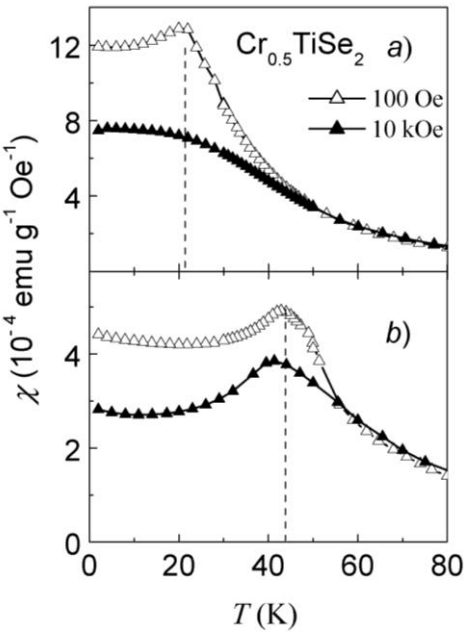


Figure 6. Temperature dependences of the magnetic susceptibility of the quenched (a) and slowly-cooled (b) samples of $Cr_{0.5}TiSe_2$ measured at heating in magnetic fields 100 Oe (Δ) and 10 kOe (▲).

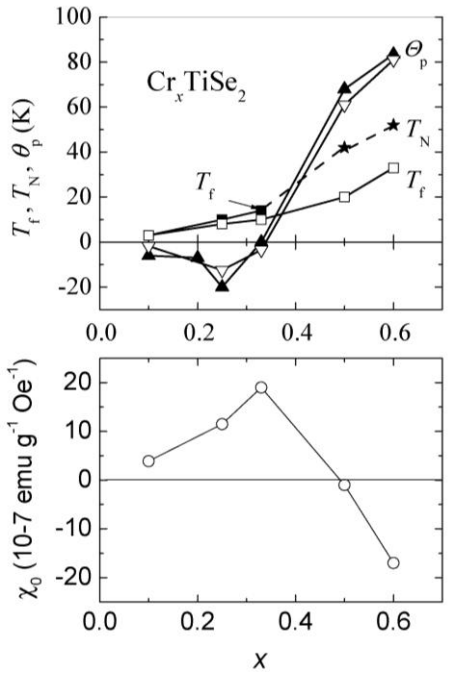


Figure 7. (a) Concentration dependence of the paramagnetic Curie temperature Θ_p (triangles), Neel temperature T_N (stars) and freezing temperature T_f (squares) for the slowly cooled (full symbols) and quenched (open symbols) samples of Cr_xTiSe_2.(b) The χ_0 contribution to the total magnetic susceptibility as a function of the intercalant content in Cr_xTiSe_2.

Copyright © 2010. Nova Science Publishers, Incorporated. All rights reserved.

Handbook of Material Science Research, Nova Science Publishers, Incorporated, 2010. ProQuest Ebook Central,

The Cr_xTiSe_2 compounds with the Cr concentration $x \leq 0.33$ show the susceptibility curves which may be indicative of a spin-glass ($x = 0.1$) or cluster-glass ($x = 0.25$; 0.33) behavior below the freezing temperature, T_f. At low intercalant concentration ($x \sim 0.1$), the freezing temperature does not depend on the cooling conditions of the samples after heat treatment, while the slowly cooled and quenched sample with $x > 0.25$ demonstrate essential difference in their T_f values. As is seen from Figure5 and Figure6, the critical temperatures for the slowly cooled Cr_xTiSe_2 samples are almost in twice increased in comparison with that for the quenched samples. Figure7a displays also the concentration dependence of the paramagnetic Curie temperature Θ_p which reflects the average of interspin exchange interactions. The paramagnetic Curie temperature shows negative values in the concentration range $0 < x < 0.33$, while Θ_p becomes positive with further growth of the Cr content reaching 82 K at $x = 0.6$. Such a behavior indicates the presence of competitive exchange interactions between 3*d* electrons of inserted Cr atoms. The values of Θ_p (see Figure7) as well as the effective magnetic moments of Cr ions are observed to be close for slowly cooled and quenched Cr_xTiSe_2 samples.

As is shown in Figure7b, the temperature-independent contribution χ_0 to the total magnetic susceptibility of slowly cooled Cr_xTiSe_2 samples changes non-monotonously with increasing Cr content. The intercalation of Cr up to $x = 0.33$ is accompanied by the growth of χ_0, which can be attributed to the increase of the Pauli paramagnetic contribution and, consequently, to the growth of the density of electronic states [16, 36]. Further Cr intercalation reduces the χ_0 value and changes its sign from positive to negative at $x > 0.5$, which implies the change of the electronic structure due to the intercalation. There is some correlation between the Θ_p and χ_0 behaviors: the positive Θ_p values are observed above $x = 0.33$ when χ_0 starts to decrease.

Unlike Cr_xTiSe_2 samples with low Cr concentrations ($x < 0.33$), the different cooling rate of highly-intercalated compounds ($x = 0.5$; 0.6) leads to significantly different behavior under application of a magnetic field. The shape of the field dependence of the magnetization for the slowly cooled $Cr_{0.5}TiSe_2$ sample (see Figure8) is typical of a first-order field-induced transition from the antiferromagnetic state to a ferromagnetic state with a noticeable hysteresis. The relatively low value of the critical AF–F transition field ($H_c \sim 10$ kOe) observed in $Cr_{0.5}TiSe_2$ indicates a weakness of the antiferromagnetic interlayer exchange interaction in comparison with the ferromagnetic intralayer exchange since neighbor Cr-layers are separated by non-magnetic Se-Ti-Se sandwiches. This is supported by the fact that the $Cr_{0.5}TiSe_2$ compound exhibits positive paramagnetic Curie temperature ($\Theta_p = 67$ K) despite the presence of the AF order below $T_N = 42$ K. The layered character of the AF structure in a slowly cooled $Cr_{0.5}TiSe_2$ sample was confirmed by the neutron diffraction study [22]. The high-field magnetization measurements performed for $Cr_{0.5}TiSe_2$ have shown that the magnetic moment per Cr ion in the saturated field-induced F-state is about 2.3 μ_B [16] which is in agreement with 2.4 μ_B derived from neutron diffraction data [22]. This saturation magnetic moment is lower than the value 3 μ_B which can be expected for localized 3*d* electrons of inserted Cr^{3+} ions. Therefore, the Cr 3*d* electrons in Cr_xTiSe_2 have presumably an intermediate regime, which is favorable for spin fluctuations. Despite the band character of the Cr 3*d* electrons which hybridize with Ti 3*d* electrons, they seem to remain rather localized. The quenching of the $Cr_{0.5}TiSe_2$ sample after heat treatment changes substantially the magnetic state and the magnetization process. As can be seen from Figure 8, the

Copyright © 2010. Nova Science Publishers, Incorporated. All rights reserved.

Handbook of Material Science Research, Nova Science Publishers, Incorporated, 2010. ProQuest Ebook Central,

magnetization curve for the quenched sample does not show any features characteristic for antiferromagnetically ordered compound.

The $M(H)$ dependence for this sample is analogous to that observed for the compound in a cluster-glass state. Such a change of the magnetic state of $Cr_{0.5}TiSe_2$ after quenching in comparison with a slowly cooled sample may result from the partial mutual substitution of Cr and Ti ions because of closeness of their ionic radii. The substitution of Ti for Cr in the vdW gap should lead to the weakening of the ferromagnetic exchange interaction within the Cr layer, while the substitution of Cr for Ti in the Se-Ti-Se sandwiches results apparently in the strengthening of the inter-layer exchange.

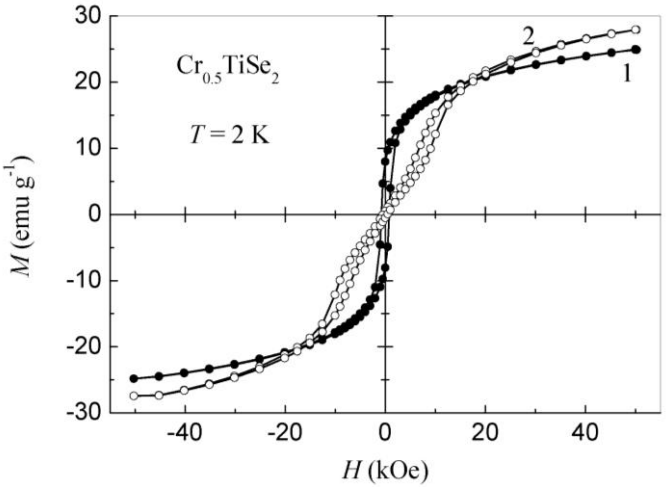


Figure 8. Field dependences of the magnetization measured at $T = 2$ K on quenched (1) and slowly-cooled (2) samples of $Cr_{0.5}TiSe_2$.

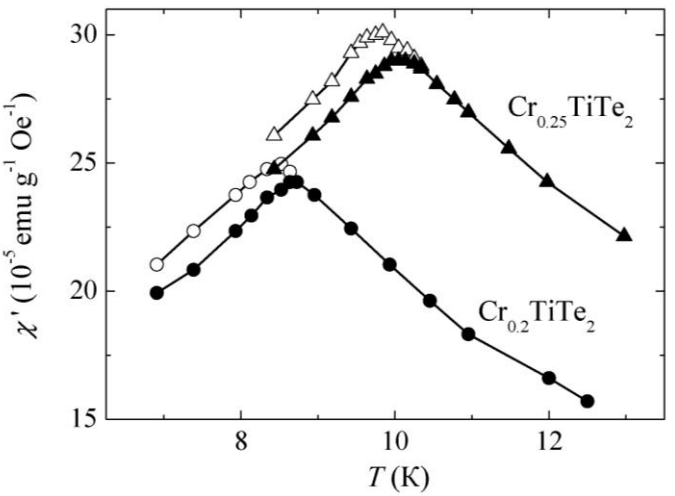


Figure 9. Temperature dependence of the real part of the ac-susceptibility of Cr_xTiSe_2 (x = 0.2; 0.25) measured at frequencies 8 Hz (open symbols) and 800 Hz (full symbols).

Copyright © 2010. Nova Science Publishers, Incorporated. All rights reserved.

Handbook of Material Science Research, Nova Science Publishers, Incorporated, 2010. ProQuest Ebook Central,

As in other M_xTiX_2, the intercalation of Cr up to $x = 0.33$ into $TiTe_2$ leads to appearance of the spin-glass or cluster-glass state below freezing temperatures $T_f \sim 8 – 12$ K [40]. The measurements of the ac-susceptibility of Cr_xTiTe_2 compounds have revealed the frequency dependence in the vicinity of T_f (shown in Figure9) as in other spin-glasses.

3.3. Mn_xTiX_2

Unlike other 3*d* metals the intercalation of TiX_2 with manganese is accompanied by the expansion of the crystal lattice in the basal plane as well as in the perpendicular direction [13, 17]. According to the ESR data the Mn ions intercalated into titanium disulfide are divalent [41]. However, the values of the effective magnetic moment of Mn in Mn_xTiS_2 и Mn_xTiSe_2 systems are observed to vary within 3.8 μ_B – 5.8 μ_B (see Table 3), i.e. lower than $\mu_{eff} = 5.92\ \mu_B$ for the Mn^{2+} ion with $S = 5/2$ and $g = 2$.

Magnetic susceptibility measurements performed for a single crystal of $Mn_{0.25}TiS_2$ have shown that this compound enters a spin-glass state with decreasing temperature below $T_f \sim 13$ K [43]. There is the lack of data in the literature in respect to magnetic properties of titanium ditelluride intercalated with manganese. The study performed in Ref. 17 has shown that depending on the Mn content the Mn_xTiSe_2 compounds with $0 < x \leq 0.5$ exhibit a spin-glass or cluster-glass behavior at low temperatures. As it follows from Figure10, the freezing temperature changes non-monotonously with Mn concentration in Mn_xTiSe_2. The negative paramagnetic Curie temperature increases in the absolute value with increasing *x* which is indicative of dominating antiferromagnetic exchange interaction between 3*d* electrons of inserted Mn ions.

The intercalation of Mn is observed to increase monotonously the temperature-independent term χ_0 of the total magnetic susceptibility of Mn_xTiSe_2 from $1.5 \cdot 10^{-6}$ emu g^{-1} Oe^{-1} at x = 0.1 up to $3.2 \cdot 10^{-6}$ emu g^{-1} Oe^{-1} at $x = 0.5$ [17]. As in other M_xTiX_2 compounds, this enhancement of χ_0 may by attributed to the growth of the density of electronic states (DOS) at the Fermi level (E_F).

Table 3. The effective magnetic moment μ_{eff}, the magnetic state at low temperatures and magnetic critical temperature T_{crit} for Mn_xTiX_2 (X = S, Se)

Compounds	*x*	0.1	0.2	0.25	0.33	0.5	References
Mn_xTiS_2	μ_{eff} (μ_B)	5.4	5.0	4.4–5.7	4.0	3.6	[18, 42,43]
	Magnetic state		SG	SG			
	T_{crit}(K)		12	6–13			
Mn_xTiSe_2	μ_{eff} (μ_B)	3.6		4.4		4.3	[13, 17, 18]
	Magnetic state	SG		CG		CG	
	T_{crit}(K)	< 2		10		5.8	

Copyright © 2010. Nova Science Publishers, Incorporated. All rights reserved.

Handbook of Material Science Research, Nova Science Publishers, Incorporated, 2010. ProQuest Ebook Central,

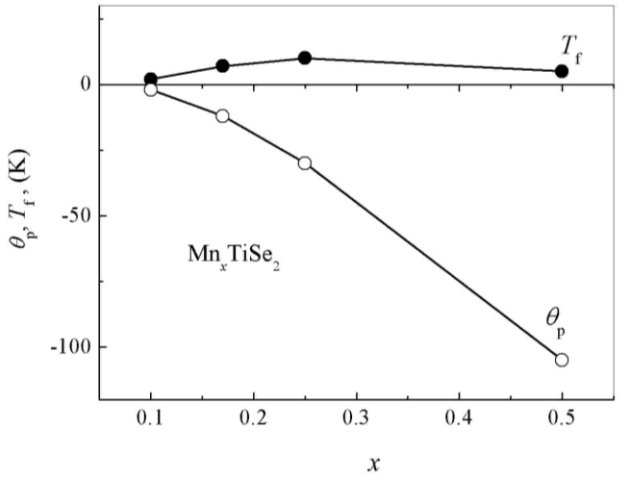


Figure 10. Concentration dependences of the paramagnetic Curie temperature Θ_p and freezing temperature T_f for Mn_xTiSe_2 compounds.

3.4. Fe_xTiX_2

Among the M_xTiX_2 systems, much attention was paid to the study of titanium disulfides and titanium diselenides intercalated with iron. At high Fe concentrations ($x \geq 0{,}5$) in Fe_xTiS_2 compounds, a long-range ferromagnetic order was observed below Curie temperatures T_C ~ 160 K – 160 K [4, 10], while the magnetic state of highly intercalated Fe_xTiSe_2 was classified as an antiferromagnetic one with the Neel temperatures up to 138 K [11,]. The main magnetic characteristics of Fe_xTiX_2 intercalates are collected in Table 4.

Table 4. The effective magnetic moment μ_{eff}, the magnetic state at low temperatures and magnetic critical temperature T_{crit} for Fe_xTiX_2 (X = S, Se, Te)

Compounds	x	0.1	0.2	0.25	0.33	0.5	1.0	References
Fe_xTiS_2	μ_{eff} (μ_B)	4.2	3.9	3.9	4.0	3.4		[4, 10]
	Magnetic state	SG	SG	CG	CG	F	F	
	T_{crit} (K)	24.5–32	41	52	57	84	160	
Fe_xTiSe_2	μ_{eff} (μ_B)	4.0	3.4	3.6		3.4		[11, 12, 18]
	Magnetic state	SG	SG	CG	CG (AF)	AF		
	T_{crit}(K)		24	62–89	60–68	129–138		
Fe_xTiTe_2	μ_{eff} (μ_B)	2.7		2.6				
	Magnetic state	SG		SG				
	T_{crit}(K)	12		18				

Copyright © 2010. Nova Science Publishers, Incorporated. All rights reserved.

Handbook of Material Science Research, Nova Science Publishers, Incorporated, 2010. ProQuest Ebook Central,

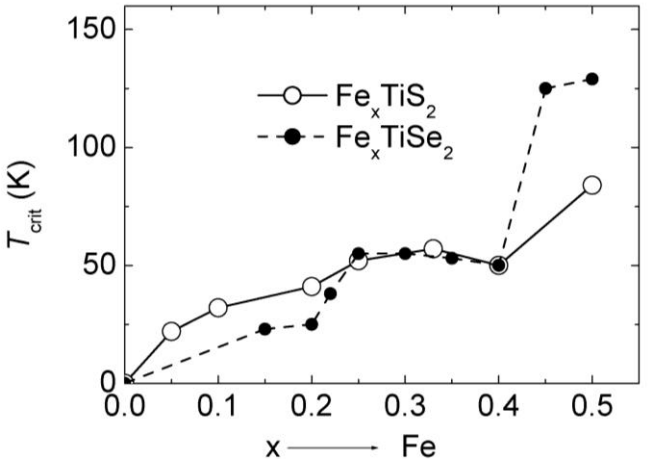


Figure 11. Concentration dependences of the magnetic critical temperatures for Fe_xTiS_2 [10] and Fe_xTiSe_2 [44] systems.

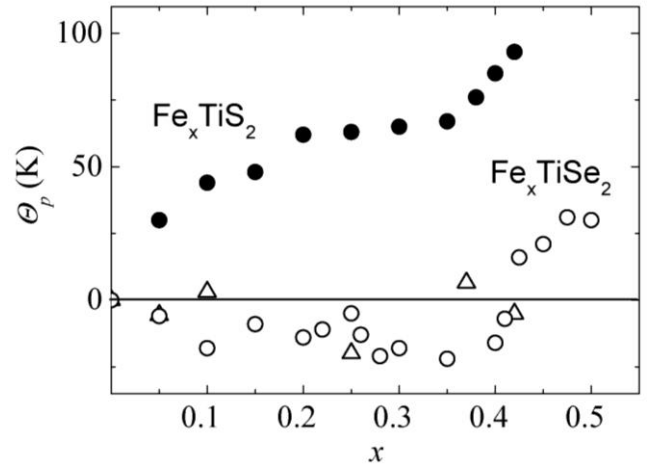


Figure 12. Paramagnetic Curie temperature of Fe_xTiS_2 (● – [18]) and Fe_xTiSe_2 (○ – [44], и (Δ – [34]) as a function of the Fe concentration.

In both Fe_xTiS_2 and Fe_xTiSe_2 systems, the spin-glass and cluster-glass behavior was revealed at low ($x < 0.2$) and intermediate ($0,2 < x < 0,4$) Fe concentrations respectively. As can be seen from Figure10, at ($0.2 < x < 0.4$) the freezing temperatures for both these systems do not differ substantially.

The measurements of the magnetic susceptibility on single crystalline samples of Fe_xTiS_2 have revealed the presence of a significant anisotropy, therefore, the Fe_xTiS_2 compounds with low Fe concentrations are considered as spin-glasses of the Ising type [45]. At $T < T_f$, the magnetic moments of Fe ions situated between S-Ti-S sandwiches are arranged perpendicular to the layers do to the influence of the crystal field. The paramagnetic Curie temperature of Fe_xTiS_2 is found to be positive in all concentration range, the value of Θ_p increases monotonously with increasing Fe content [44] (shown in Figure 12).

Copyright © 2010. Nova Science Publishers, Incorporated. All rights reserved.

Handbook of Material Science Research, Nova Science Publishers, Incorporated, 2010. ProQuest Ebook Central,

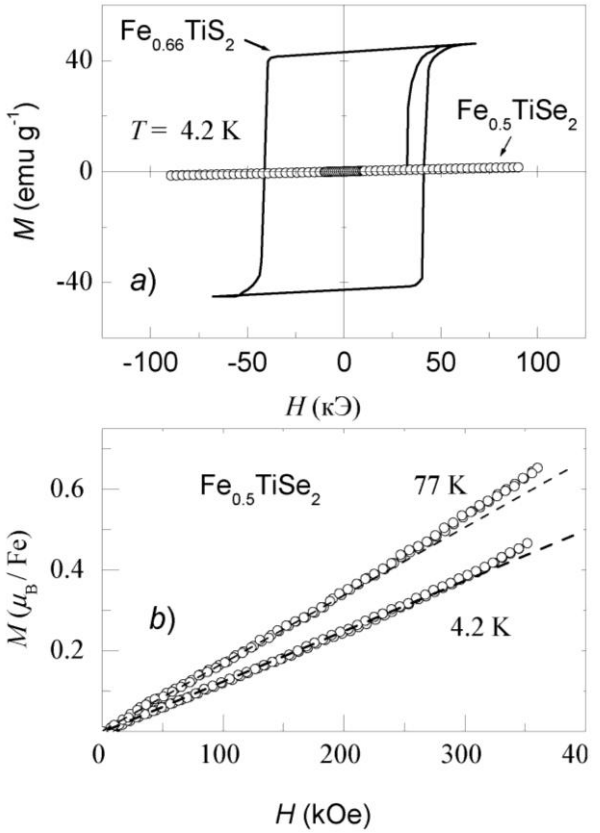


Figure 13. (a) Field dependences of the magnetization measured on a $Fe_{0.66}TiS_2$ single crystal [10] and on a polycrystalline $Fe_{0.5}TiSe_2$ sample at T = 4.2 K in steady magnetic fields. (b) Magnetization curves for $Fe_{0.5}TiSe_2$ measured in pulse fields at T = 4.2 K and 77 K.

These results indicate the dominance of the ferromagnetic exchange interaction between 3*d* electrons of Fe ions inserted into the TiS_2 matrix. The Fe_xTiSe_2 compounds exhibit more complicated behavior of Θ_p. As follows from Figure 12, the Θ_p values for Fe_xTiSe_2 are negative in the concentration range $0 < x \leq 0.4$ and vary within interval between -5 K and -40 K. At the further growth of the Fe concentration, the paramagnetic Curie temperature of Fe_xTiSe_2 becomes positive. This Θ_p versus x dependence results apparently from the competition of antiferromagnetic and ferromagnetic exchange interactions. It is worth to mention that $\Theta_p(x)$ dependence obtained for Fe_xTiSe_2 compounds is similar to that observed for Cr intercalated titanium diselenide (see Figure7a). In both these systems the paramagnetic Curie temperatures being negative below $x \sim 0.33 - 0.4$ become positive with further increasing intercalant concentration. Moreover, both Cr_xTiSe_2 and Fe_xTiSe_2 compounds with $x \geq 0.5$ exhibit an antiferromagnetic order. An attempt to describe the concentration dependence of Θ_p in Fe_xTiX_2 systems (X = S, Se) was made by Tazuke et al. [18] in the frame of a model of the Ruderman-Kittel-Kasuya-Yosida (RKKY) exchange which implies the indirect exchange interaction between localized 3*d* electrons of Fe atoms via conduction electrons. The calculation has shown that the experimental results can be quite well described in the RKKY – type model using the band structure data for TiS_2. These results show a dominant role of the RKKY-type exchange interaction in the formation of a magnetic order in

Copyright © 2010. Nova Science Publishers, Incorporated. All rights reserved.

Handbook of Material Science Research, Nova Science Publishers, Incorporated, 2010. ProQuest Ebook Central,

M_xTiX_2 compounds. The recent measurements of the magnetic circular dichroism (MCD) performed for Fe_xTiS_2 have revealed that the Fe 3*d* electrons acquire more itinerant character with increasing *x* [46]. Moreover, according to the MCD study of Fe_xTiSe_2 a small induced magnetic moment exists on Ti atoms due to the hybridization of Fe 3*d* and Ti 3*d* electronic states. These data show that the Ti atoms may be involved in the exchange interactions as well.

Figure 13 shows the field dependences of the magnetization for the ferromagnetic $Fe_{0.66}TiS_2$ compound having the Curie temperature $T_C \approx 140$ K [10] and for $Fe_{0.5}TiSe_2$ which exhibits an antiferromagneic order below 135 K [12]. The very broad hysteresis loop with the coercive field $H_c \sim 40 - 50$ kOe is obtained on a single crystal of $Fe_{0.66}TiS_2$ at low temperatures [10], which is indicative of a large magnetocrystalline anisotropy of Fe intercalated titanium disulfide. The strong ferromagnetic properties with a sharp hysteresis loop were recently observed at low temperatures on a single crystalline sample of the Fe intercalated $Fe_{0.25}TaS_2$ compound having a 2*H*-type structure [46].

The antiferromagnetic compound $Fe_{0.5}TiSe_2$ shows the linear change of the magnetization with variation of the field within -90 kOe $\leq H \leq +90$ kOe. However, the pulse-field magnetization measurements performed for this compound have revealed the deviation from the linearity starting from ~250 kOe, which may be associated with the beginning of a phase transition from the antiferomagnetic to the ferromagnetic state. Unlike the Cr_xTiSi_2 system, the change of the cooling conditions does not noticeably affect the main magnetic characteristics of Fe_xTiSe_2, despite the crystal structure of the samples with high ($x \sim 0.5$) iron concentrations depends on the cooling rate after heat treatment. According to X-ray diffraction data the crystal structure of the slowly cooled sample is monoclinic one. It can be described by the space group I 2/m and presented as a superstructure $\sqrt{3}a_0 \times a_0 \times 2c_0$ formed from the initial $TiSe_2$ structure by the ordering of Fe atoms inserted and vacancies in the vdW gaps. From the absence of observed external lines on the X-ray diffraction pattern, the quenched $Fe_{0.5}TiSe_2$ sample was determined to be of the same structure as the parent $TiSe_2$ matrix. However, despite the presence of such a difference in the crystal structure the magnetic susceptibility measurements have shown that the Neel temperatures of both the slowly cooled and quenched $Fe_{0.5}TiSe_2$ samples are close [39]. As to the Fe intercalation of the titanium ditelluride, the compound Fe_xTiTe_2 are found to exhibit a spin-glass behavior below $T_f = 12$ K and 18 K at $x = 0.1$ and 0.25 respectively.

The effective magnetic moments per Fe ion intercalated into TiS_2 and $TiSe_2$ are observed to vary with the Fe concentration between 4.0 – 4.2 μ_B for $x = 0.1$ and ~3.4 μ_B for $x = 0.5$ (see Table 4). These values are lower than $\mu_{eff} = 4.89\ \mu_B$ expected for a high-spin state of the Fe^{2+} ion with $g = 2$. A substantially lower μ_{eff} value (~2.6–2.7 μ_B) is observed for Fe ions intercalated into titanium ditelluride. The magnetization measurements performed for $Fe_{0.33}TiS_2$ in pulse fields up to 360 kOe have shown that the magnetization reaches in saturation a value ~ 2.6 μ_B per Fe ion [47]. It is worth to mention that the magnetic moment of Fe in the localized model should be equal to 4 μ_B and independent on the concentration. Therefore, the lower value of the saturation moment implies that the magnetic properties of these compounds can be rather described in the frame of an itinerant electron model than a localized model [47].

Copyright © 2010. Nova Science Publishers, Incorporated. All rights reserved.

Handbook of Material Science Research, Nova Science Publishers, Incorporated, 2010. ProQuest Ebook Central,

Table 5. The effective magnetic moment μeff, the magnetic state at low temperatures and magnetic critical temperature Tcrit for CoxTiX2 (X = S, Se, Te)

Compounds	x	0.05	0.1	0.2	0.25	0.30	0.33	0.5	References
Co_xTiS_2	μ_{eff} (μ_B)	2.1	2.1 2,5	2.0		1.0			[4, 38]
	Magnetic state	SG	SG	SG		SG			
	T_{crit}(K)	3	8	6.5		2.7			
Co_xTiSe_2	μ_{eff} (μ_B)	2.1	2.0 2,25	2.0 1,7	1.76	1.4	1.38		[39]
	Magnetic state		SG	SG	SG				
	T_{crit}(K)		10.5 7,5	7 4,5	7 5				
Co_xTiTe_2	μ_{eff} (μ_B)	1.3		0.6				0.9	[27]
	Magnetic state								
	T_{crit}(K)								

3.5. Co_xTiX_2

The Co intercalated Co_xTiS_2 compounds with the Co concentrations up to x = 0.4 are reported to exhibit a spin-glass like magnetic state at low temperatures (see Table 5). The freezing temperature shows a non-monotonous concentration dependence with the maximal value ~ 8 K at x = 0.15. The decrease of T_f with increasing Co content above x = 0.15 is ascribed to the reduction of the Co magnetic moment [38]. The effective magnetic moment per Co ion is observed to decrease from 2.1 μ_B at x = 0.05 up to 1 μ_B at x = 0.3. The reduction of μ_{eff} is suggested to result from the growth of the hybridization of Co 3*d* electrons with electronic states of the TiS_2 matrix as the intecalant content increases [38]. An analogous situation is observed in titanium diselenide intercalated with Co. The temperature dependences of the magnetic susceptibility of Co_xTiSe_2 compounds with the Co concentration up to x = 0.33 shows a pronounced peak at low temperatures which indicates the appearance of a spin-glass (cluster-glass) state [39]. The value of μ_{eff} changes from 2.1 μ_B at x = 0.05 down to 1.38 μ_B at x = 0.33. The magnetic susceptibility of the Co intercalated titanium ditelluride is studied in the paramagnetic region only [27]. As can be seen form Table 5, the μ_{eff} values in Co_xTiTe_2 are found to be within 0.6 – 1.3 μ_{eff}. It is worth to mention that the effective magnetic moment per Co ion intercalated into TiX_2 is almost in twice lower than the expected μ_{eff} = 3.87 μ_B for a high-spin state of Co^{2+} ion at g = 2, while the observed μ_{eff} values for other 3*d* metal ions (Cr^{3+}, Mn^{2+} и Fe^{2+}) are found to be about 3/4 of appropriate theoretical values (see above).

According to Ref.4, the reduced μ_{eff} values in Co_xTiX_2 may be caused by the fact that the Co^{2+} ions intercalated into TiX_2 matrixes are in a low-spin state $(d\varepsilon)^6(d\gamma)^1$ for which μ_{eff} is equal to 2.1 μ_B. Another reason which my lead to reduced μ_{eff} values is the above mentioned hybridization 3*d* electrons of intercalated ions with Ti 3*d* states and *p* states of chalcogen ions in TiX_2.

Copyright © 2010. Nova Science Publishers, Incorporated. All rights reserved.

Handbook of Material Science Research, Nova Science Publishers, Incorporated, 2010. ProQuest Ebook Central,

3.6. Ni_xTiX_2

The intercalation of Ni into titanium disulfide does not lead to appearance of magnetically ordered states at $0 < x < 0.5$. These compounds are observed to be paramagnetic (P) down to $T = 2$ K [10]. At higher concentrations ($0.5 \leq x \leq 0.75$) the Ni_xTiS_2 compounds show the behavior characteristic of weak ferromagnets with Curie temperatures 10 – 17 K. The investigation of Ni intercalated compounds based on the titanium diselenide Ni_xTiSe_2 with interacalant concentration up to $x = 0.5$ has shown [48] that these compounds remain paramagnetic with decreasing temperature down to 2K (see Figure14).

As follows from the inset in Figure14, the temperature dependences of the inverse susceptibility for Ni_xTiSe_2 has a pronounced non-monotonic character unlike the $\chi^{-1}(T)$ curves for the compounds intercalated by other 3*d* metals, which are nonlinear but monotonic above their ordering temperatures. As is shown in Ref. 48, the $\chi^{-1}(T)$ dependences for Ni_xTiSe_2 compounds can be quite well described by expression $\chi(T) = \chi_0(T) + C\,(T - \Theta_p)^{-1}$, in which both terms are temperature dependent. The part of the first term associated with the Pauli paramagnetic contribution is suggested to vary as T^2 [48]. The competition of two temperature-dependent contributions to the total magnetic susceptibility gives rise to non-monotonous change of the inverse susceptibility. It should be mentioned that unlike Ni_xTiSe_2 compounds, for which an appreciable growth of χ_0 is observed with increasing temperature, the paramagnetic contribution from conduction electrons to the total magnetic susceptibility of M_xTiSe_2 compounds intercalated by other 3*d* metals (M=Cr, Mn, Fe, Co) was suggested to be temperature-independent (see above).

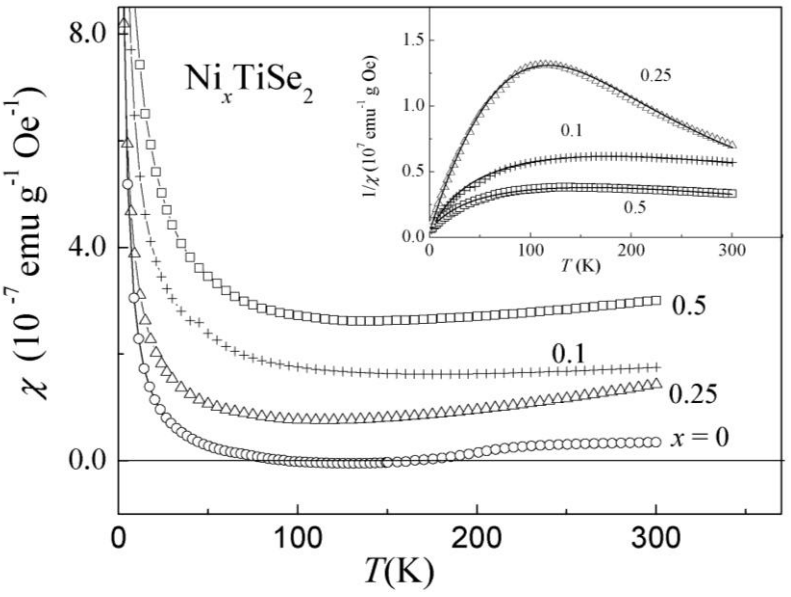


Figure 14. Temperature dependence of the magnetic susceptibility of Ni_xTiSe_2 at various Ni content. Inset: $\chi-1$ versus T curves for Ni-intercalated compounds (solid lines obtained by fitting).

Copyright © 2010. Nova Science Publishers, Incorporated. All rights reserved.

Handbook of Material Science Research, Nova Science Publishers, Incorporated, 2010. ProQuest Ebook Central,

Table 6. The effective magnetic moment μ_{eff}, the magnetic state at low temperatures and magnetic critical temperature T_{crit} for Ni_xTiX_2 (X = S, Se)

Compounds	*x*	0.1	0.2	0.25	0.33	0.5	References
Ni_xTiS_2	μ_{eff} (μ_B)		0.11		0.1		[10]
	Magnetic state	P	P	P	P	F	
	T_{crit}(K)					12	
Ni_xTiSe_2	μ_{eff} (μ_B)	0.3		0.17	0.16	0.18	[48]
	Magnetic state	P		P	P	P	
	T_{crit} (K)						

The last may be caused by the fact that the temperature dependence of χ_0 is masked in these compounds by the large Curie–Weiss term and, therefore, cannot be revealed so distinctly as in the Ni_xTiSe_2 case. It should be noted, that the increase of the DOS due to the NI intercalation derived from the susceptibility measurements of Ni_xTiSe_2 is supported by the low-temperature specific heat data [48].

As follows from the Table 6, the effective magnetic moment per Ni ion in Ni_xTiS_2 and Ni_xTiSe_2 compounds is observed to be significantly lower than the calculated value μ_{eff} = 2.83 μ_B for the Ni^{2+} ion with $g = 2$.

The maximal value of μ_{eff} = 0.3μ_B is obtained for x=0.1; with further growth of the Ni content, the value of μ_{eff} decreases and remains almost unchanged (0.16μ_B−0.18μ_B) within the concentration range $0.25 \leq x \leq 0.5$. The paramagnetic Curie temperatures of Ni_xTiSe_2 compounds with Ni content up to x = 0.5 are negative with absolute values of about 1–4 K, which implies the presence of a small antiferromagnetic exchange interaction between 3*d* electrons of Ni. There are no available data in the literature in respect of the magnetic properties of Ni intercalated titanium ditelluride.

3.7. The Formation of Magnetic Moments and Magnetic Ordering in M_xTiSe_2 Depending on the Type of M Ions Intercalated

As follows from the above presented results, the intercalation of 3d atoms into the vdW gaps between X-Ti-X sandwiches in TiX_2 layered compounds affects substantially the crystal and electronic structure as well the magnetic state of the compounds. The appearance of an additional M band is accompanied by deformations of the crystal lattice due to the hybridization of 3d electrons of inserted ions with electronic states of the TiX_2 matrix. Figure 14 shows the relative change of the interlayer distance $(c - c_0)/c_0$ and the contribution χ_0 to the total magnetic susceptibility of M_xTiSe_2 compounds as a function of the atomic number of the 3d metal intercalated at x = 0.1 (c_0 = 6.008 Å is the lattice parameter of the parent $TiSe_2$ compound).

Copyright © 2010. Nova Science Publishers, Incorporated. All rights reserved.

Handbook of Material Science Research, Nova Science Publishers, Incorporated, 2010. ProQuest Ebook Central,

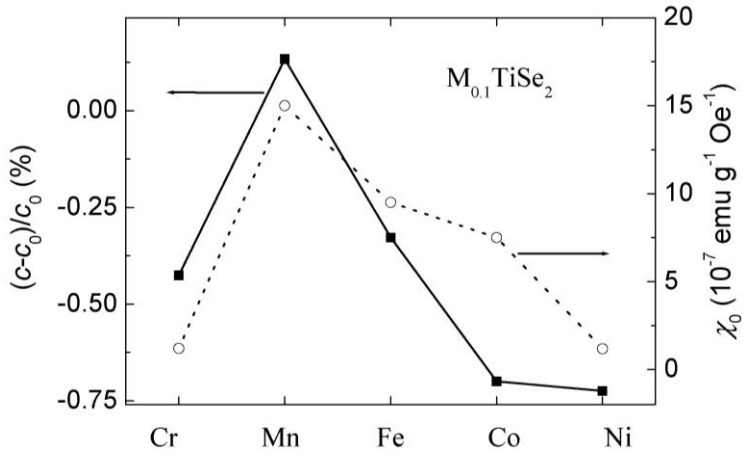


Figure 15. The $(c - c_0)/c_0$ and χ_0 values for $M_{0.1}TiSe_2$ compounds as a function of the atomic number of M atoms intercalated.

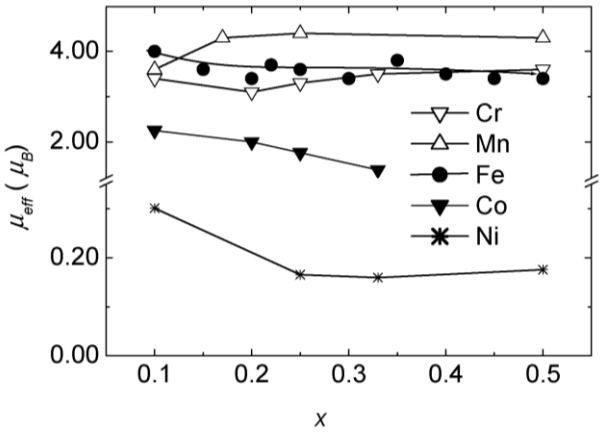


Figure 16. Concentration dependences of the effective magnetic moment calculated per M atom for M_xTiSe_2 compounds. The data for Fe_xTiSe_2 are taken from Ref. 18.

As can be seen, both the deformation of the lattice along the *c* direction and the χ_0 value show a non-monotonous change with increasing atomic number of 3*d* metal intercalated. This correlation shows that the density of electronic states at E_F in $M_{0.1}TiSe_2$ compounds depends on the deformation degree of the crystal lattice, i.e. on the hybridization of 3*d* electrons of M atoms with electronic bands of $TiSe_2$. The maximal value of χ_0 and DOS at E_F in the case of the Mn intercalation is indicative of lower hybridization degree of 3*d* electrons of inserted Mn ions with Ti 3*d* and Se 4*p* electronic states of the $TiSe_2$ matrix in comparison with other 3*d* metals. The decrease of χ_0 when going from manganese to nickel indicates the reduction of DOS at E_F, which can be attributed to the growth of the hybridization degree of M 3*d* electrons with electronic states of $TiSe_2$. The hybridization was confirmed by X-ray photoemission and X-ray absorption spectroscopy studies of some M_xTiX_2 compounds [33-36]. As it was mentioned above, the increase of the intercalant content up to $x = 0.25$ in all M_xTiSe_2 systems except Mn_xTiSe_2 leads to the contraction of the crystal lattice in the

Copyright © 2010. Nova Science Publishers, Incorporated. All rights reserved.

Handbook of Material Science Research, Nova Science Publishers, Incorporated, 2010. ProQuest Ebook Central,

direction perpendicular to the layers, which may be associated with the increase of the hybridization of M 3*d* electrons with $TiSe_2$ bands. One can suggest that the change of the hybridization caused by the growth of the intercalant content will affect the magnetic moment of M atoms intercalated. Analysis of the data on magnetic properties of M_xTiSe_2 systems with various guest 3*d* atoms shows that except of the Mn intercalation the μ_{eff} value per M atom in M_xTiSe_2 compounds decreases with increasing concentration up to $x = 0.25$ indeed. It is clear seen from the concentration dependences of μ_{eff} presented in Figure16. It is worth to mention that in the frame of the localized model the effective magnetic moment in M_xTiSe_2 should be invariable with increasing M content.

There are several factors which may affect the magnetic moment of M atoms intercalated between X-Ti-X trilayers in M_xTiX_2 with the change of the intercalant concentration: i) the change in the hybridization of 3*d* electrons of M atoms with *p* electronic states of the chalgogen and with 3*d* states of Ti; ii) the change of the width of the additional M band; iii) the change of DOS at E_F; iv) the change in the orbital and spin contributions to the total magnetic moment. Figure17a. shows the effective magnetic moments per M atom calculated by using the expression $\mu_{eff}^{theor} = 2\mu_B[S(S+1)]^{1/2}$ and the $\mu_{eff}^{\exp}$ values determined from the paramagnetic susceptibility data for $M_{0.25}TiSe_2$ as a function of the atomic number (Z) of M atoms. For chromium, the μ_{eff}^{theor} value corresponds to Cr^{3+} ion, while other M atoms are accepted to be in divalent states M^{2+}.

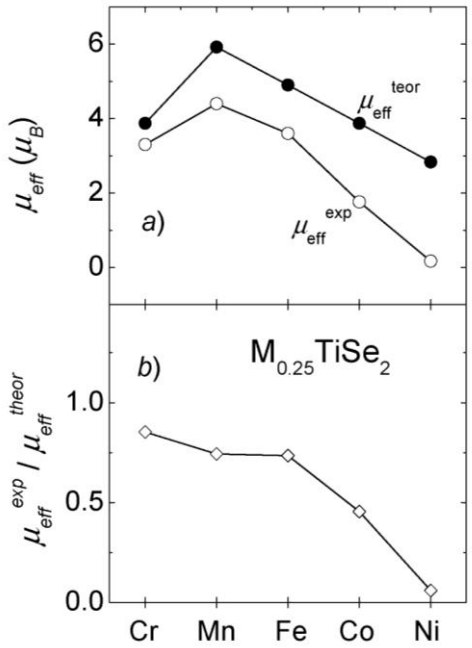


Figure 17. (a) The effective magnetic moment $\mu_{eff}^{\exp}$ observed on M ions in M0.25TiSe2 compounds as a function of the atomic number. The values μ_{eff}^{theor} are the expected spin-only values. (b) The $\mu_{eff}^{\exp} / \mu_{eff}^{theor}$ ratio as a function of the atomic number of M metal.

Copyright © 2010. Nova Science Publishers, Incorporated. All rights reserved.

Handbook of Material Science Research, Nova Science Publishers, Incorporated, 2010. ProQuest Ebook Central,

As follows from Figure17a, there is some correlation between the behavior of the expected and observed effective magnetic moments with increasing atomic number of 3*d* elements. However, the observed values of μ_{eff} for all 3*d* metals intercalated into $TiSe_2$ are obtained to be lower than μ_{eff}^{theor}. Moreover, as it clear seen from Figure17b, the ratio between μ_{eff}^{theor} and $\mu_{eff}^{\exp}$ increases with increasing atomic number of M atoms. Such a behavior supports the conjecture about the increase of the hybridization degree of 3*d* electrons of inserted M atoms with 3*d* electrons of titanium and *p* electrons of chalcogen ions as *Z* increases. This suggestion is supported by the data on the Pauli paramagnetic contribution to the total magnetic susceptibility, which indicates that the DOS value at the Fermi level in M_xTiSe_2 decreases starting from Mn (see Figure15). This last result may also be indicative of a shift of the position of M 3*d* electron states towards low energies when the M atomic number increases. The effective magnetic moment of M atoms intercalated into M_xTiX_2 seems to be controlled by the hybridization degree with TX_2 bands and can not be described in a model of localized moments. It should be noted, that the study of magnetic properties of Cr_xTiSe_2 under application of a hydrostatic pressure has revealed a distinct reduction of the saturation magnetic moment per Cr atom with decreasing interatomic distances [16], which supports the conclusion about a non-localized nature of magnetism in M_xTiX_2 compounds. Despite the band character of the 3*d* electrons of the inserted M atoms they seem to remain rather localized and are favorable for spin fluctuations. As it known [49], the physical properties of such systems may be influenced by spin fluctuations. One can suggest that the magnetic moment per M atom inserted in the TiX_2 matrix is characterized by both the amplitude of the local spin density and the spatial extension of the spin correlation, which are apparently dependent on the type and concentration of the M metal as well as on the hybridization degree of M 3*d* states with $TiSe_2$ bands.

A reach variety of the magnetic states in M_xTiX_2 systems is suggested to result from the competition between intralayer exchange interaction of the RKKY type and interlayer exchange interactions of the 3*d* electrons of the M atoms inserted. The intralayer exchange is mediated by conduction electrons, bearing in mind a metallic type of the in-plane conductivity observed in many M_xTiX_2 [3, 9]. Because of the substantially lower conductivity in the direction perpendicular to the layers, which is a common feature ofM_xTiX_2 compounds, and the larger distance between M ions situated in neighbors M layers, the interlayer exchange interaction may be characterized as being of superexchange type, which occurs presumably through intervening chalcogen atoms. Nevertheless, the Ti 3*d* electrons are probably also involved in the interlayer M–M exchange interaction, since the band-structure calculations [50] and neutron diffraction data [12] indicate the possible magnetic polarization of the Ti sublattice.

The comparison of the behavior of two antiferromagnetic compounds $Cr_{0.5}TiSe_2$ and $Fe_{0.5}TiSe_2$ shows that the critical field of the phase transition from the antiferromagnetic to ferromagnetic state in $Fe_{0.5}TiSe_2$ (Figure13b) exceeds significantly (by more than 20 times) the AF-F critical transition field in a slowly cooled $Cr_{0.5}TiSe_2$ sample (Figure8). This is because of the presence of different exchange interactions within the layers of inserted Fe and Cr atoms. According to neutron diffraction studies [22] the Cr magnetic moments exhibit a dominating ferromagnetic arrangement within layers and antiferromagnetic exchange in the perpendicular direction. The lower energy of the interlayer exchange in comparison with

Copyright © 2010. Nova Science Publishers, Incorporated. All rights reserved.

Handbook of Material Science Research, Nova Science Publishers, Incorporated, 2010. ProQuest Ebook Central,

intralayer one results in a low critical field (~ 10 kOe) which is needed to destroy the antiferromagnetic order in $Cr_{0.5}TiSe_2$. In distinction from Cr intercalated titanium diselende, the $Fe_{0.5}TiSe_2$ compound exhibits an AF order of Fe moments within layer. Therefore, the large value of the critical field (~ 350 kOe) which induces the AF-F transition in this compound is determined by the strong antiferromagnetic intralyer exchange interaction between magnetic moments of Fe atoms situated in the same layer.

4. MAGNETIC PROPERTIES OF TITANIUM DICHALCOGENIDES INTERCALATED WITH RARE EARTHS

There is lack of data in the literature about titanium dichalcogenides intercalated with rare-earth (R) elements. Works available in this direction are devoted mainly to study of incommensurate layered compounds $(RS)_{1+\delta}TS_2$ (with T = Nb , Ta) [51-54] where the individual structural RS fragments contain rare earth elements. Most of these compounds reveal a metallic behavior, and 4*f* shell occupation corresponds to that of the free R^{3+} ion. The R^{3+} valence of majority of rare-earth ions in misfit-layer compounds $(RS)NbS_2$ was derived from magnetic susceptibility measurements [51-53] as well as from photoelectron spectroscopy data [54, 55]. Some $(RS)_{1+\delta}TS_2$ systems are observed to exhibit an antiferromagnetic order with the Neel temperature in few Kelvin [51-53]. The R_xTiS_2 compounds intercalated with mixed-valence rare earths Yb and Eu [24] via liquid ammonia technique are observed to contain in the vdW gap the R ions in both R^{2+} and R^{3+} states. According to Ref. 55, the electronic spectra of Eu_xTiSe_2 could not be described in a rigid-band model and the hybridization effects of Eu 5*d* electrons with Ti 3*d* and Se 2*p* states should be taken into account. Because of the more localized character of the unfilled 4*f* electron shell of R ions in comparison with 3d electrons of M metals one can expect that the magnetism of R_xTiSe_2 compounds will have more pronounced two-dimensional character than in the case of 3d-metal intercalation.

The study of the Gd intercalated titanium diselenide has shown that all Gd_xTiSe_2 compounds ($0 < x \leq 0.33$) in the temperature range from 10 up to 350 K exhibit a paramagnetic behavior [19]. The value of μ_{eff} per Gd ion is found to be equal ~7.9 μ_B which is close to 7.94 μ_B for the free Gd^{3+} ion unlike M_xTiSe_2 compounds intercalated with 3*d* metals, where reduced values of μ_{eff} and their pronounced concentration dependence are observed (see above). This means that the 4*f* electrons of the Gd ion remain well localized in the $TiSe_2$ matrix unlike 3*d*-electrons of M ions in M_xTiX_2. Bearing in mind an invariability of the effective moment calculated per Gd ion in Gd_xTiSe_2 one can suggest that the Ti valence in these compounds remains constant at the intercalation. The paramagnetic Curie temperatures are observed to be negative for Gd_xTiSe_2, which is indicative of a dominating antiferromagnetic Gd-Gd exchange interaction. For all Gd_xTiSe_2 at $x \leq 0.33$, the absolute value of θ_p was estimated to be about of 11 K. Since the 4*f* electrons of Gd ions are well localized this exchange interaction is apparently indirect and may be mediated by conduction electrons or by intervening ions. The electrical resistivity of Gd_xTiSe_2 ($x \leq 0.33$) exhibits a metallic behavior. Therefore, the indirect exchange interaction via conduction electrons of the RKKY type is suggested to determine the magnetic behavior of Gd_xTiSe_2 [19].

Copyright © 2010. Nova Science Publishers, Incorporated. All rights reserved.

Handbook of Material Science Research, Nova Science Publishers, Incorporated, 2010. ProQuest Ebook Central,

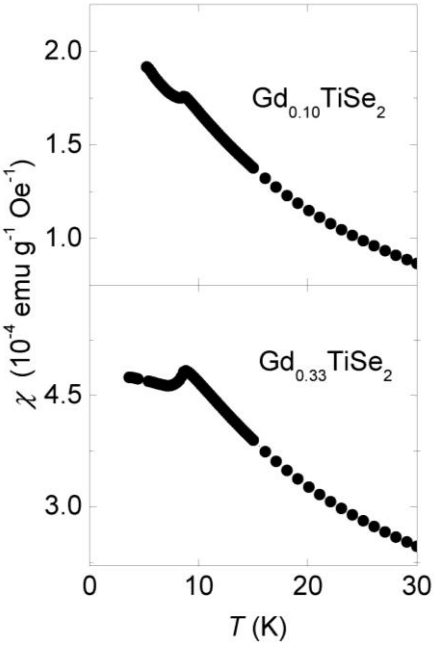


Figure 18. Temperature dependences of the magnetic susceptibility for $Gd_{0.1}TiSe_2$ (a) and $Gd_{0.33}TiSe_2$.

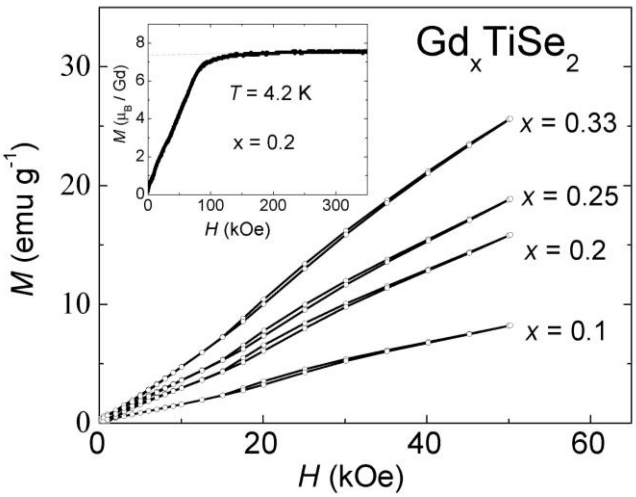


Figure 19. Field dependences of the magnetization of Gd_xTiSe_2 with various intercalant concentration at T = 2 K. Inset shows the magnetization curve for $Gd_{0.2}TiSe_2$ measured in pulse fields at T = 4.2 K.

In a low-temperature region, a distinct anomaly is observed around 9 K on the temperature dependencies of the *dc*-susceptibility of Gd_xTiSe_2 compounds (see Figure18). The maximum of χ shifts toward lower temperatures with increasing magnetic field. Together with negative values of the paramagnetic Curie temperature such a behavior may be associated with antiferromagnetic (AF) ordering of Gd magnetic moments in Gd_xTiSe_2 below the Neel temperature $T_N \approx 9$ K. The suggestion about the presence of the AF order in Gd_xTiSe_2 is confirmed by the measurements of magnetization curves which are displayed in

Copyright © 2010. Nova Science Publishers, Incorporated. All rights reserved.

Handbook of Material Science Research, Nova Science Publishers, Incorporated, 2010. ProQuest Ebook Central,

Figure19. As can be seen, all $M(H)$ dependences measured at 2 K, i. e. below the magnetic ordering temperature, exhibit the change in their slope and an appreciable hysteresis in the vicinity of a critical field $H_c \approx 18$ kOe.

The value of H_c was estimated by using the maximum of dM/dH dependences. This critical field may be associated with a spin-flop like transition within subsystem of Gd magnetic moments. Such a low critical transition field is indicative of a relatively weak energy of the antiferromagnetic exchange interaction between 4*f* electrons of Gd ions and suggests the presence of an appreciable anisotropy. Bearing in mind zero orbital moment of Gd one can suggest that this anisotropy originates in the anisotropy of the exchange interaction because of a quasi two-dimensional character of the crystal structure and substantial anisotropy of the conductivity of $TiSe_2$ based compounds [1-3]. The H_c value as well as the Neel temperature of Gd_xTiSe_2 does not show a strong concentration dependence from $x = 0.1$ up to $x = 0.33$. As is seen from Figure19, the steady fields of 50 kOe are not sufficient to achieve the saturation. The inset in Figure19 presents the magnetization curve for $Gd_{0.2}TiSe_2$ measured in pulsed fields below T_N. At $T = 4.2$ K, the magnetization of this compound is observed to saturate when the applied field exceeds a value $H_s \sim 90$ kOe. The extrapolation of the $M(H)$ curve measured at 4.2 K from high fields to $H = 0$ allowed to estimate the magnetization value per Gd ion.

The estimation has given a value $\sim 7.3 \pm 0.3\ \mu_B$ which is close to $\mu_{Gd} = gJ\ \mu_B = 7\ \mu_B$ for the free Gd^{3+} ion. This result together with the value of μ_{eff} supports the conclusion that the 4*f* electrons of Gd ions remain localized in Gd_xTiSe_2 unlike 3*d* electrons of 3*d* metals in M_xTiSe_2.

5. CONCLUDING REMARKS

The above consideration shows that the intercalation of 3*d* or 4*f* atoms substantially modifies the crystal structure, electronic structure and magnetic properties of layered TiX_2 compounds. Because of their layered structure the M_xTX_2 compounds can be considered as good objects for the study of mechanisms of the exchange interaction, magnetic anisotropy and formation of magnetic moments on the inserted atoms. The paramagnetic susceptibility measurements of M_xTiX_2 have revealed an increase of the Pauli contribution with increasing intercalant content up to x=0.25, which is indicative of the growth of the density of electronic states at the Fermi level. The value of the effective magnetic moment of 3d ions in all M_xTiX_2 compounds are observed to be lower than spin-only moments $\mu_{eff}^{theor} = 2\mu_B[S(S+1)]^{1/2}$. The difference between the observed $\mu_{eff}^{\exp}$ and calculated μ_{eff}^{theor} values is found to increase with increasing atomic number of M atoms. The effective magnetic moment of M atoms intercalated into M_xTiX_2 seems to be controlled by the hybridization degree with TX_2 bands and can not be described in a model of localized moments. The results are also indicative of a shift of the position of M 3*d* electron states towards low energies when the M atomic number increases. Unlike 3d metal the magnetic moment of rare earth atoms in R_xTiX_2 does not change at the intercalation. The 4*f* electrons of R ions intercalated into TiX_2 matrixes are suggested to remain well localized.

Copyright © 2010. Nova Science Publishers, Incorporated. All rights reserved.

Handbook of Material Science Research, Nova Science Publishers, Incorporated, 2010. ProQuest Ebook Central,

Titanium dichalcogenides intercalated with 3*d* or 4*f* metals show various magnetic states depending on the type and concentration of inserted atoms as well as on the type of chalcogen in the TiX_2 matrix. At the intercalant concentrations lower than x = 0.25, the M_xTiX_2 compounds may reveal a spin-glass or cluster-glass behavior, while a three-dimensional ferromagnetic or antiferromagnetic order can be obtained at higher intercalant concentrations with magnetic ordering temperatures up to ~ 160 K. The different types of magnetic ordering were also in dichalcogenides of other transition metals TX_2 (T = Nb, Ta, Zr) [56-59]. At low temperatures, some Fe_xTS_2 compounds (T = Ti, Ta) are found to exhibit permanent magnetic properties with broad hysteresis loops [10, 46]. The measurements of the electrical resistivity under application of a magnetic field for intercalated M_xTiS_2 compounds (M = Mn, Fe, Co, Ni) [60, 61] have revealed the giant magnetoresistance effect ($|\Delta\rho/\rho|$ ~ 30-40 %) in Mn intercalated compounds with the intercalant concentration x ~ 0.05 at low temperatures. It would be interesting to extend the temperature interval where such compounds have a magnetic order toward room temperatures. The recent investigation [62] has shown that the magnetic critical temperatures of the TX_2 based compounds can be increased when together with the intercalation the partial substitution of M atoms for T atoms in a TX_2 matrix will be performed. Thus, the Curie temperature about 600 K was observed for the $Fe_{0.25}(Ta_{0.5}Fe_{0.5})S_2$ compound in which the half of Ta atoms in S-Ta-S sandwiches is substituted by Fe atoms [62]. These Fe atoms within Ta layers play apparently a role of exchange "bridges" between the layers of Fe atoms situated in the vdW gaps, which results in strengthening of the interlayer exchange interaction.

The recent achievements in the synthesis methods of nanomaterials have revealed a possibility to obtain the TiS_2 [63] and $TiSe_2$ nanotubes [64]. The study of these materisals which belong to a new class of non-carbon nanotubes focuses primarily on their use as materials for rechargeable batteries and hydrogen storage. However, one can suggest that the intercalation of such nanotubes with 3*d* and 4*f* metals will allow obtaining new nanomagnets with interesting properties.

Copyright © 2010. Nova Science Publishers, Incorporated. All rights reserved.

REFERENCES

[1] Wilson, J. A.; Yoffe A. D. *Adv. Phys.* 1969, 18, 193-335.
[2] Wilson, J. A.; Di Salvo, F. J.; Mahajan, S. *Adv. Physics*. 2001, 50, 1171-1248.
[3] Friend, R. H.; Yoffe, A. D. *Adv. Phys*. 1987, 36, 1-94
[4] Inoue, M.; Hughes, H. P., Yoffe, A. D. *Adv. Phys.* 1989, 38, 565-604.
[5] Julien C.; Nazri G.-A. Solid State Batteries*: Materials Design and Optimization;* Springer-Verlag: New York, LLC, 1994; Ch.6-7
[6] Velikanova, T. V.; Titov, A. N.; Malkova, M. A *J. Analytical Chemistry* 2001, *56*, 666-670.
[7] Bernard, L.; Glaunsinger W.; Colombet P. *Solid State Ionics* 1985, *17*, 81–89.
[8] de Boer, D. K. G.; van Brugger, C. F.; Bus G. W.; Coehoorn R.; Haas C.; Sawatzky, G. A. *Phys. Rev*. B 1984, 29, 6797-6809.
[9] Di Salvo F. J.; Moncton, D. E. ; Waszczak J.V. J. *Phys. Rev*. B 1976, 14, 4321-4328.
[10] Negishi, H.; Shoube, A.; Takahashi, H.; Ueda, Y.; Sasaki, M.; Inoue, M. *J. Magn. Magn. Mater*. 1987, 87, 179-186.

Handbook of Material Science Research, Nova Science Publishers, Incorporated, 2010. ProQuest Ebook Central,

[11] Huntley, D. R.; Sienko, M. J.; Hiebl, K. J. *Solid State Chem*. 1984, 52, 233-243.
[12] Calvarin, G.; Gavarri, J. R.; Buhannic, M. A.; Colombet, P.; Danot, M. *Rev. Phys. Appl.* 1987, 22, 1131-1138.
[13] Tazuke, Y.; Takeyama, T. J. *Phys. Soc. Jpn*. 1997, 66, 827–830.
[14] Kuranov A. V.; Pleschov, V. G.; Titov, A. N.; Baranov, N. V.; Krasavin L. S. *Phys. Solid State* 2000, 42, 2029-2032.
[15] Toporova, N. V.; Maksimov, V. I.; Pleschov, V. G.; Titov, A. N.; Baranov, N. V. *Phys. Met. Metallogr*. 2005, 99(Suppl.1), S50-S52.
[16] Pleschov, V. G.; Baranov, N. V.; Titov, A. N.; Inoue K.; Bartashevich, M. I.; Goto, T. J. *Alloys Comp*. 2001. 320, 13-17.
[17] Maksimov, V. I.; Baranov, N. V.; Pleschov, V. G., Inoue, K. J. *Alloys Comp*. 2004, 384, 33-38.
[18] Tazuke, Y.; Miyashita, T.; Nakano, H.; Sasaki R. *Phys. Stat. Sol*. C 2006, 3, 2787–2790.
[19] Sherokalova, E. M.; Pleschov, V. G.; Baranov, N. V.; Korolev, A .V. *Phys. Lett*. A. 2007, 369, 236-242.
[20] Arnaud, Y.; Chevreton, M. J. *Solid State Chem*. 1981, 36, 151-160.
[21] Gu, B.; Song, Q.; Ni, J. J. *Appl. Phys*. 1999, 85, 819-824.
[22] Baranov, N. V.; Titov, A. N.; Maksimov, V. I.; Toporova, N.V.; Daoud-Aladine, A.; Podlesnyak A.. J. *Phys. Condens. Matter*. 2005, 17, 5255-5262.
[23] Li, D.; Qin, X. Y.; Zhang J. J. *Mater. Res*. 2006, 21, 480-483.
[24] Hsu, S. P.; Glaunsinger, W. G. *Mat. Res. Bull*. 1986, 21**,** 1063-1072.
[25] Inoue, M.; Negishi H. J. *Phys. Soc. Jpn*. 1984, 53, 943–946.
[26] Kuznetsova, T.; Titov, A.; Yarmoshenko, Yu.; Kurmaev, E.; Postnikov, A.; Pleschev, V. *Phys. Rev*. B 2005, 72, 085418.
[27] Pleschev, V. G.; Titov, A. N.; Titova, S. G. *Physics of the Solid State* 2003, 45, 433-437.
[28] Shannon, R. D. *Acta Cryst*. A 1976, 32, 751-767.
[29] Woo, K.C.; Brown, F. C.; McMillan, W. L.; Miller, R. J.; Schaffman, M. J.; Sears, M. P. *Physical Review* B 1976, 14, 3242-3247.
[30] Rossnagel, K.; Kipp, L.; Skibowski, M. *Phys. Rev*. B 2002, 65, 235101.
[31] Li, G.; Hu, W. Z.; Qian, D.; Hsieh, D.; Hasan, M. Z.; Morosan, E.; Cava, R. J.; Wang, N. L. *Phys. Rev. Lett*. 2007, 99, 027404.
[32] Yamasaki, T.; Suzuki, N.; Motizuki, K. *J. Phys. C: Solid State Phys.* 1987, ***20*****,** 395-404
[33] Titov, A. N.; Kuranov, A. V.; Pleschev, V. G.; Yarmoshenko, Yu. M.; Yablonskikh, M. V.; Postnikov, A. V.; Plogmann, S.; Neumann, M.; Ezhov, A. V.; Kurmaev, E. Z. *Physical Review* B 2001, 63, 035106
[34] Matsushita, T.; Suga, S.; Kimura, A.; Negishi, H.; Inoue, M. *Phys. Rev*. B 1999, 60, 1678-1686.
[35] Cui, Y.; Negishi, H.; Titova, S. G.; Shimada, K.; Ohnishi, A.; Higashiguchi, M.; Miura, Y.; Hino, S.; Jahir, A. M.; Titov, A.; Bidadi, H.; Negishi, S.; Namatame, H.; Taniguchi, M.; Sasaki, M. *Phys. Rev*. B. 2006, 73, 085111.
[36] Kuznetsova, T. V.; Titov, A.N.; Yarmoshenko, Yu. M.; Kurmaev, E. Z.; Postnikov, A. V.; Pleschev, V. G.; Eltner, B.; Nicolay, G.; Ehm, D.; Schmidt, S.; Reinert, F.; Hüfner, S. *Physical Review* B 2005, 72, 085418
[37] Vonsovsky, S. V. Magnetism; Wiley: New York, 1974. Ch.11.

Copyright © 2010. Nova Science Publishers, Incorporated. All rights reserved.

Handbook of Material Science Research, Nova Science Publishers, Incorporated, 2010. ProQuest Ebook Central,

[38] Tazuke, Y. In Recent Advances in Magnetism of Transition Metal Compounds. Ed. A. Kotani and N. Suzuki. World Scientific: Singapore - New Jersey-London-Hong Kong. 1993. P. 204-218.
[39] Maksimov, V.I. PhD Thesis; Ural State University: Ekaterinburg, 2006.
[40] Pleshchev, V. G.; Korolev, A.V.; Dorofeev, Yu. A. *Phys. Solid State*. 2004, 46, 280-293.
[41] Inoue, M.; Negishi, H. J. *Phys. Soc. Jap*. 1985, 54, 380–388.
[42] Tazuke, Y. J. *Magn. Magn. Mater*. 1995, 140–144, 155–156.
[43] Takase, K.; Kubota, Y.; Takano, Y.; Sasaki, M.; Inoue, M.; Sekizawa, K. Physica B 2000, 284–288, 1517–1518.
[44] Shintomi, M.; Tazuke, Y.; Tahakashi, H. *Mol. Cryst. Liq. Cryst*. 2000, 341, 27-32
[45] Satoh, T.; Tazuke, Y.; Miyadai, T.; Hoshi, K. J. *Phys. Soc. Jap*. 1988, 57, 1743–1750.
[46] Morosan, E.; Zandbergen, H. W.; Li, L.; Lee, M.; Checkelsky, J. G.; Heinrich, M., Siegrist, T.; Ong, N. P.; Caval, R. J. *Phys. Rev*. B 2007, 75, 104401.
[47] Negishi, H.; Koyano, M.; Inoue, M.; Sakakibara, T.; Goto, T. J. *Magn. Magn. Mater*. 1988, 74, 27–30.
[48] Baranov, N. V.; Inoue. K.; Maksimov, V. I.; Ovchinnikov, A. S.; Pleschov, V. G.; Podlesnyak, A.; Titov, A. N.; Toporova, N. V. *J. Phys.: Condens. Matter*. 2004, 16, 9243-9258.
[49] Moriya, T. Spin-fluctuations in the Itinerant Electron Magnetism; Springer: Berlin-Heidelberg, 1985.
[50] Postnikov, A.V.; Neumann, M.; Plogmann, St.; Yarmoshenko, Yu. M.; Titov, A. N.; Kuranov, A. V. *Comput. Mat. Sci*. 2000, 17, 450-454.
[51] Suzuki, K.; Enoki, T. *Solid State Commun*. 1991, *78*, 73-77.
[52] Pefiat, 0.; Rabu, P.; Meerschaut, A. *J. Phys.: Condens. Matter*. 1991, 3, 9929–9940.
[53] Zhou, W. Y.; Meetsma, A.; de Boer, J. L.; Wiegers, G. A. J. *Alloys Comp*. 1996, 233, 80-88.
[54] Suzuki, K.; Enoki, T.; Bandow, *Sh. Phys. Rev*. B 1993, 48, 11077–11085.
[55] Danzenbacher, S.; Molodtsov, S. L.; Koepernik, K.; Tomm, Y.; Laubschat, C. *Mol. Cryst. Liq. Cryst*. 2000, 341, 45-50.
[56] Hillenius, S. J.; Coleman, R. V. *Phys. Rev*. B 1979, 20, 4569-4576.
[57] Parkin, S. S. P.; Marseglia, E. A.; Brown, P. J. *J. Phys. C: Solid State Phys*. 1983, 16, 2765-2778.
[58] Checkelsky, J. G.; Lee, M.; Morosan, E.; Cava, R. J.; Ong N. P. *Phys. Rev*. B 2008, **77**, 014433.
[59] Buhannic, M. A.; Danot, M.; Colombet, P.; Dordor, P.; Fillion, G. *Physical Review* B 1986, 34, 4790-4795.
[60] Negishi, H.; Yamada, H.; Yuri, K.; Sasaki, M.; Inoue, M. *Phys. Rev*. B 1997, 56, 11144–11148.
[61] Negishi, H.; Kakita, S.; Yamada, H.; Negishi, S.; Sasaki, M.; Inoue, M. *Solid State Commun.* 1999, 112, 275–279.
[62] Wada, H.; Nozaki, H.; Sato, A.; Takada, K.; Sasaki, T. *J. Alloys and Comp*. 2004, *383*, 148-151.
[63] Chen, J.; Li, S. L.; Tao, Z. L.; Gao F. *Chem. Commun*. 2003, 980-981.
[64] Chen, J.; Tao, Z. L.; Li, S. L.; Fun, X. B.; Chou, Sh. L. *Adv. Mater*. 2003, 15, 1379-1382.

Copyright © 2010. Nova Science Publishers, Incorporated. All rights reserved.

Handbook of Material Science Research, Nova Science Publishers, Incorporated, 2010. ProQuest Ebook Central,

In: Handbook of Material Science Research
Editors: C. René and E. Turcotte, pp.323-345
ISBN 978-1-60741-798-9
© 2010 Nova Science Publishers, Inc.

Chapter 7

ENERGETIC MATERIALS: CRYSTALLIZATION AND CHARACTERIZATION

A.E.D.M. van der Heijden* and R.H.B. Bouma
TNO Defense, Security and Safety, Business Unit Protection,
Munition and Weapons,
Department of Energetic Materials, The Netherlands

ABSTRACT

The application of energetic materials, like explosives and oxidizers, in munition or propellants, requires basic knowledge of the properties of the energetic ingredients. It is known that the sensitivity of energetic materials towards external stimuli like shock initiation, is predominantly determined by the presence of crystalline imperfections like inclusions, voids and dislocations in the crystalline energetic materials. Crystallization of energetic materials allows the control of mean particle size, particle shape and product quality. Specifically the improved product quality has been demonstrated to yield significantly less sensitive energetic materials when applied in a polymer-bonded explosive. This contribution gives a comprehensive review on the crystallization and characterization of various energetic materials and their application in insensitive munition. The review concludes with a future outlook on this area of research.

INTRODUCTION

The majority of the crystalline materials is produced according to a certain synthesis process. The synthesis is usually followed by a crystallization process in order to fulfil specific product requirements regarding e.g. mean size, particle shape, purity, filterability, free-flowing properties, degree of agglomeration and storability of the crystals [1]. For explosives and oxidizers, generally referred to as energetic materials, additional demands have to be met with respect to their hazard properties (sensitivity towards impact, friction and

* Corresponding author: A.E.D.M. van der Heijden, P.O. Box 45, 2280 AA Rijswijk, The Netherlands. antoine.vanderheijden@tno.nl, tel +31 15 284 3774, fax +31 15 284 3974.

Copyright © 2010. Nova Science Publishers, Incorporated. All rights reserved.

Handbook of Material Science Research, Nova Science Publishers, Incorporated, 2010. ProQuest Ebook Central,

electrostatic discharge), thermal stability as well as their compatibility with other chemical substances. For an important part, these properties are affected or determined by the production technique by means of which these energetic materials have been produced. In order to meet the increasingly stringent product demands, the optimization of current production processes, the application of new production processes as well as the design of the production hardware, need to be addressed.

Apart from the 'conventional' energetic materials, like nitramines, also the synthesis and development of new energetic materials with enhanced performance and reduced sensitivity have a continued interest. Often the decision whether or not to pursue further development of a newly synthesized material is based on its thermal stability and hazard properties. These properties are generally determined using materials from synthesis processes that have not yet been optimized with respect to particle shape, mean size and purity, whereas these characteristics in many cases strongly affect the thermal stability and hazard properties. Efforts on (in first instance small scale) production techniques, in which often a crystallization step forms the final process, should therefore be included already in the development phase. Furthermore, new crystallization techniques might also be applied to the existing group of energetic materials, in order to further improve the properties of these 'conventional' materials.

Experimental work shows that the product quality of energetic materials plays an important role in the sensitivity of the energetic material, when applied as an ingredient in e.g. a polymer-bonded explosive (PBX), towards e.g. shock initiation [2,3]. Product quality comprises different aspects or characteristic properties of the material: particle shape, particle size distribution (mean size and width of the distribution), degree of agglomeration of the particles, purity (solvent/impurity content, presence of different polymorphs), density and the presence of structural defects (point defects, dislocations, grain boundaries), free-flowing properties, hazard properties, compatibility etc. [1]. This chapter will focus on the crystallization of energetic materials, their characterization and application in energetic formulations, either explosives or rocket propellants.

Copyright © 2010. Nova Science Publishers, Incorporated. All rights reserved.

CRYSTALLIZATION OF ENERGETIC MATERIALS

Different crystallization techniques are available to produce solid materials [4]. The ones most commonly applied are evaporative, cooling and drowning-out crystallization [5]. The application of melt crystallization is rather limited, since many energetic materials decompose close to their melting temperature. Exceptions are e.g. TNT and AN. Melt casting of TNT or TNT-based mixtures with other explosive materials like RDX, HMX and/or fuels like aluminium form a well-known family of conventional explosives.

During evaporative crystallization the solvent in which the energetic material is dissolved, is slowly removed by evaporation. This technique can be applied if the solubility of the solute hardly changes with temperature. Upon evaporation of the solvent, primary (spontaneous) nucleation occurs and the nuclei formed start to grow. The boiling zone at the top of the solution will be a continuous source of new nuclei since the supersaturation is the highest in that zone; growth of these particles will occur in the lower part of the crystallizer at more moderate levels of supersaturation. The crystals can be collected by filtration, after

Handbook of Material Science Research, Nova Science Publishers, Incorporated, 2010. ProQuest Ebook Central,

which the product is washed and dried. Instead of primary nucleation, also seed crystals can be added which act as nuclei for further growth of these seed crystals to the final product particles. The mean size of the crystals obtained by evaporative crystallization is of the order of several hundreds of micrometers.

Cooling crystallization is applied if the solubility of the solute shows a medium to strong dependence on temperature. For many substances the solubility increases with temperature. During cooling crystallization a (slightly under)saturated solution is cooled down according to a defined temperature profile, after which primary nucleation leads to the formation of crystalline nuclei which increase in size upon further cooling. Also in this case seed crystals may be added in order to avoid primary nucleation, e.g. in cases where a larger mean size of the final product is desired. Seeding, if applied at the proper moment in the crystallization process, allows a better control of the process, since primary nucleation is a statistical process which may introduce considerable batch-to-batch variations. After the final temperature has been reached, e.g. just below room temperature, the product is separated from the solution by means of a filtration process. Subsequently, the product is washed and dried. The final mean size of the crystals is of the order of several hundreds of micrometers.

Drowning-out crystallization, also referred to as solvent/non-solvent or anti-solvent crystallization, uses the addition of a non-solvent to a solution, or vice versa. The non-solvent and solvent need to be miscible, preferably over the complete concentration range. Upon mixing of the two solvents, a reduction in solubility of the solute dissolved in the solution leads to the nucleation of particles. Contrary to evaporative and cooling crystallization, the crystals formed during drowning-out crystallization hardly grow, since the nucleation process dominates the crystallization, due to the fact that locally relatively high supersaturation levels exist. If sufficient non-solvent is added, relatively high yields can be achieved, sometimes upto 90% or more. This is generally (much) higher compared to the yields that can be achieved by means of cooling and evaporative crystallization. A disadvantage is that generally large volumes of solvents are required and that the crystals tend to contain residual processing solvents because drowning-out crystallization is a rather rapid process, during which relatively high supersaturation levels occur. However, drowning-out crystallization generally leads to a much smaller mean size of the final product compared to evaporative and cooling crystallization, i.e. from the micron range upto several tens of microns, making it a valuable production technique depending on the application of the final product.

The crystallization technique, the solvents used, the processing conditions (stirrer rotation rate, cooling profile, evaporation rate, fines removal, seeding, etc.), geometry of the crystallization hardware, scale of operation etc. all influence the final product quality. Several illustrations are given in Figures 1-3. Figure 1 shows an example of crystals of hydrazinium nitroformate (HNF, $N_2H_5C(NO_2)_3$), produced by cooling crystallization from different organic solvents. HNF is a chlorine-free oxidizer with a higher performance than ammonium perchorate (AP) [6,7]. The pictures show needle shaped HNF crystals and the mean aspect ratio increases with increasing length of the carbon chain of the alcohol used as solvent (methanol, ethanol, 1- and 2-propanol). For application of HNF in solid composite propellant formulations, particles with a low aspect ratio are required in order to maximize the solid load in the propellant. For this application methanol is the preferred solvent to produce the HNF particles.

Copyright © 2010. Nova Science Publishers, Incorporated. All rights reserved.

Handbook of Material Science Research, Nova Science Publishers, Incorporated, 2010. ProQuest Ebook Central,

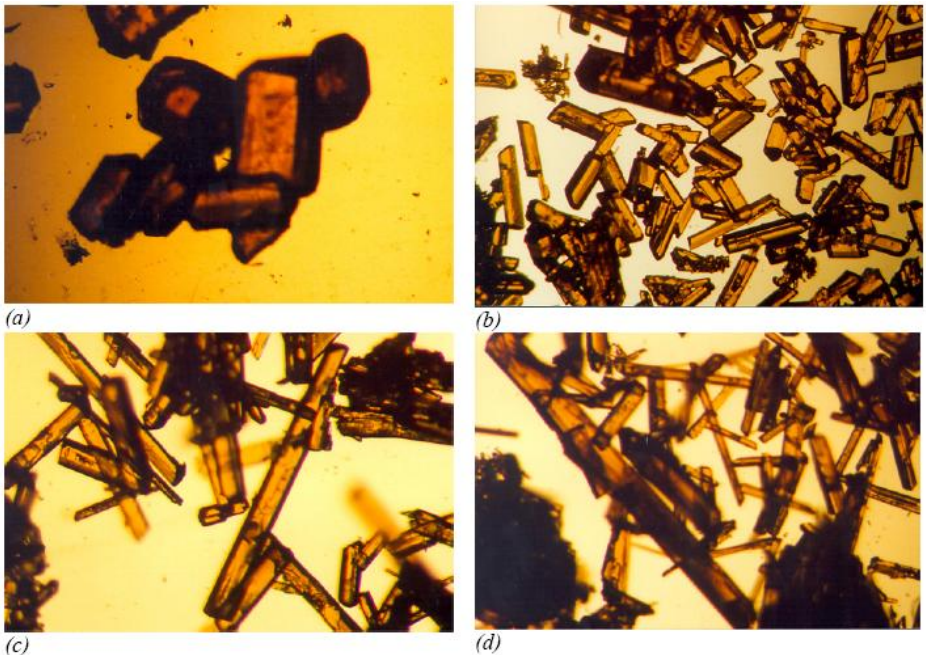


Figure 1. HNF crystals produced by means of cooling crystallization from (a) methanol, (b) ethanol, (c) 1-propanol and (d) 2-propanol. Clearly the influence of the solvent on the crystal shape is shown, going from an aspect ratio of 2-3 (in methanol) to 5-10 (in 1- and 2-propanol) [6, 7].

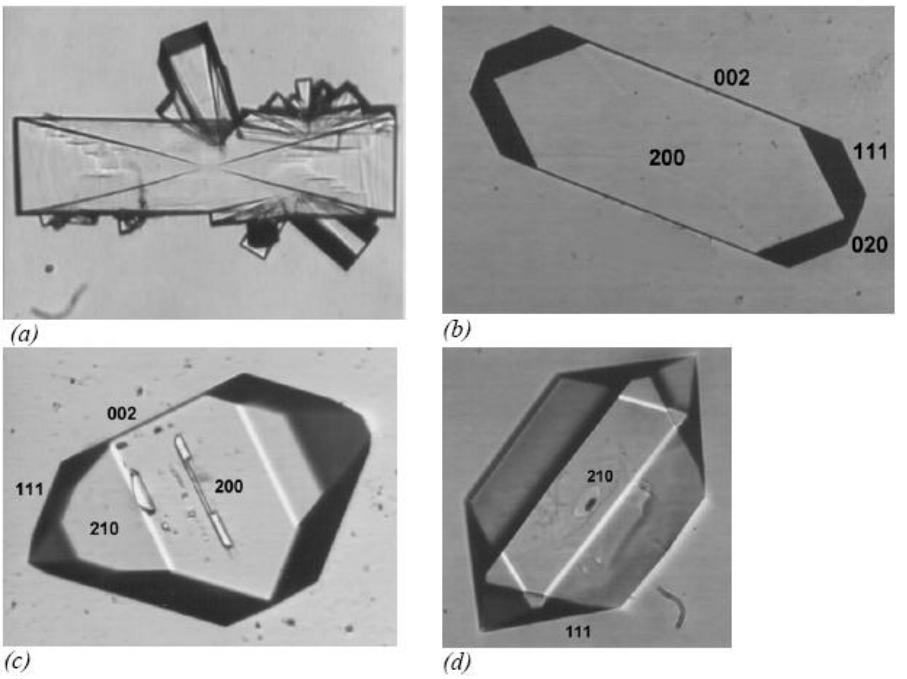


Figure 2. RDX crystallized (cooling crystallization) from (a) cyclohexanone without water, (b) cyclohexanone with water, (c) acetone and (d) γ-butyrolactone. The indices refer to different crystallographic faces of the RDX crystal [8, 9].

Copyright © 2010. Nova Science Publishers, Incorporated. All rights reserved.

Handbook of Material Science Research, Nova Science Publishers, Incorporated, 2010. ProQuest Ebook Central,

Figure 2 shows an example of the nitramine RDX (cyclotrimethylene trinitramine, $C_3H_6N_6O_6$), also crystallized from different solvents in stagnant solutions (cooling crystallization) [8]. For this example a clear influence of the solvent on the RDX crystal shape is observed. Especially the absence or presence of a small amount of water in cyclohexanone, leads to completely different shapes (compare Figure 2*(a)* and *(b)*). In the absence of water under specific supersaturation conditions, new crystals with a random orientation sprout from the crystals growing from the stagnant solution, as if 3-dimensional nucleation occurs randomly upon in particular the {200} crystal surfaces. This effect is not observed in cyclohexanone containing a small amount of water. The explanation for this effect might be related to a condensation reaction between TAX (hexahydro-1-acetyl-3,5-dinitro-1,3,5-triazine, a byproduct from the RDX synthesis) and cyclohexanone, during which water is formed [9]. The TAX-cyclohexanone condensation product could act as a blocking type impurity, interfering with the growth of the RDX crystal. Since the condensation reaction is an equilibrium reaction, the presence of water shifts the equilibrium to the side of the unreacted TAX and cyclohexanone, in this way preventing the condensation product to be formed and thus removing the blocking type impurity [9].

2,2',4,4',6,6'-Hexanitrostilbene (HNS) is an insensitive and thermally stable explosive. It decomposes at a temperature of ~319 ºC. HNS finds applications in boosters and detonators. Very fine HNS appears especially suited for exploding foil initiators. In order to obtain small particles, the continuous nucleation of new particles has to be the dominant process, rather than growth of these particles and a drowning-out, or solvent/non-solvent crystallisation process has been chosen. Figure 3 shows the HNS particles that are obtained by means of such a drowning-out crystallization technique [10]. For specific booster applications HNS particles are required with a very high specific surface area (5-25 m^2/g). The specific surface area of the HNS product shown in Figure 3 is ~14 m^2/g, as determined according to a BET analysis. The size of the particles ranges from 0.2-5 μm.

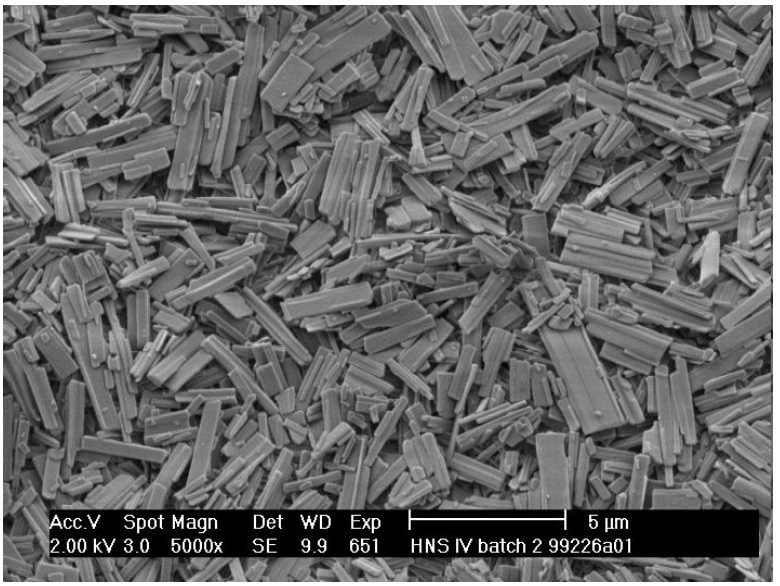
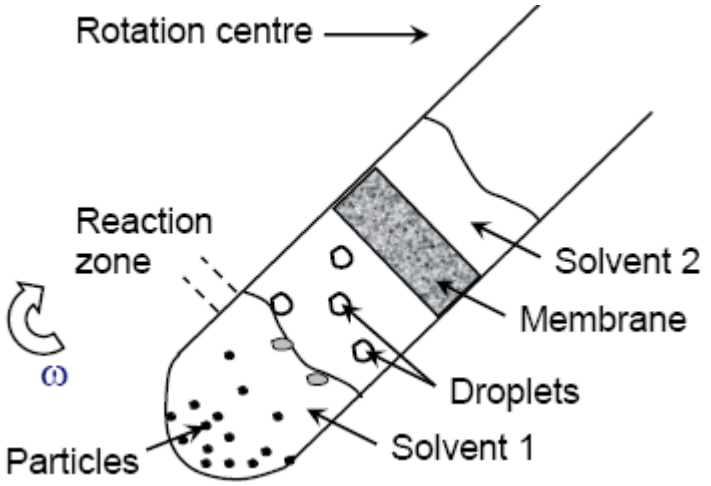


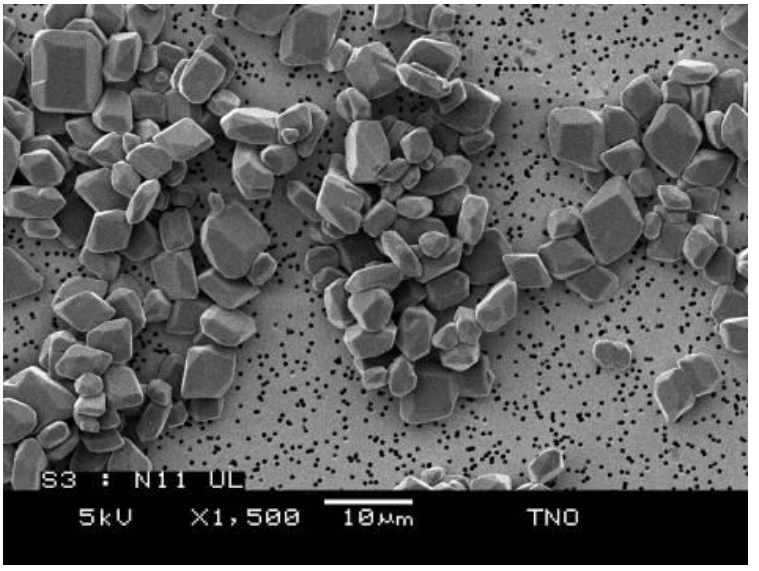
Figure 3. HNS crystals produced by means of drowning-out crystallization [10].

Copyright © 2010. Nova Science Publishers, Incorporated. All rights reserved.

Handbook of Material Science Research, Nova Science Publishers, Incorporated, 2010. ProQuest Ebook Central,



(a).



(b).

Figure 4. (a) Schematic picture of the ROCS technique. (b) Monodisperse RDX crystals produced by means of the ROCS process. The mean size of these RDX particles is approximately 5-10 μm [15].

The interest in nanotechnology and the fact that nanomaterials generally have properties significantly differing from conventionally sized particles of the same material, has led to the modification of existing or the development of new techniques to produce these kind of nanomaterials. Also for energetic materials efforts are undertaken to reduce the mean size below the micron [11-15]. It is expected that energetic nanomaterials have a higher product quality, as liquid inclusions, which generally have dimensions of a few microns or larger, cannot be formed in these nanomaterials. Generally, inclusions are also a source of other crystalline defects, like dislocations and grain boundaries. As a result of the expected absence of these kind of defects in the crystalline nanomaterials, a potential initiation source e.g. during shock loading, has been removed, making it more difficult to initiate the energetic

Copyright © 2010. Nova Science Publishers, Incorporated. All rights reserved.

Handbook of Material Science Research, Nova Science Publishers, Incorporated, 2010. ProQuest Ebook Central,

material. Based on this reasoning, it is expected that energetic nanomaterials are less sensitive compared to their conventionally sized counterparts. The propagation of a reaction however, tends to occur more readily in fine particles, as shown by failure diameters and run distance to detonation [16]. Nanoscale energetic materials may also find applications in microscale energy-demanding systems as actuation, ignition, propulsion and power [13].

Apart from a product quality point-of-view, the mean size of an explosive or oxidizer particle generally also affects its burning rate. Usually the smallest sizes applied in e.g. solid composite propellants are several microns. Ultrafine or nanometric versions of RDX were investigated by Pivkina et al. [11]: the nanometric version of RDX (~ 50 nm) was shown to have a twice as high burning rate (30 mm/s@10 MPa) compared to standard RDX (~ 50 μm, 15.1 mm/s@10 MPa). Pivkina et al. also showed that the thermal properties, as determined by means of DTA measurements at 20 ºC/min heating rate, of nanometric and micron-sized RDX are significantly different. The nanometric RDX and micron-sized RDX showed similar melting temperatures (~190 ºC), but a difference of 25 ºC between the temperature of the maximum energy release during RDX decomposition of the micron-sized powder and the nanopowder was measured, which remained unexplained [11].

Lee et al. [14] have developed a novel method for the preparation of submicron-sized HMX by a simple fast-cooling technique. The HMX particles have an average width of ~300 nm and length of ~1-2 μm. Raman spectroscopy and neutron powder diffraction showed that the submicron-sized HMX is the γ-polymorph with a polymorphic purity greater than 99% [14]. The usual commercially-produced form of HMX is β.

An example of a relatively new crystallization technique is ROtation – Conversion – Separation (ROCS) [17,18], which should allow a controlled production of very small (sub)micron particles (0.1-10 μm) with a narrow particle size distribution. ROCS is a 'high-*g*' technique, a form of process intensification by means of crystallization in an external centrifugal field and using membranes. A schematic picture of the ROCS technique is shown in Figure 4*(a)*. The process is strongly dominated by a continuous nucleation of new particles, which, as soon as they have been formed, hardly grow anymore. This ROCS method has been merged with the drowning-out crystallization technique, described above, in order to be able to apply this technique to the energetic material RDX. Figure 4*(b)* shows a SEM micrograph of the particles that have been produced by means of ROCS. Clearly monodispersed particles can be observed, having a mean size of 5-10 μm. It is expected that by optimizing the process conditions, it should be possible to reach submicron particles [15].

Another crystallization technique to obtain submicron size energetic particles is based on spray drying. A solution is pressed through a nozzle giving a mist of small droplets. The solvent within each droplet starts to evaporate, eventually initiating nucleation of the solute material. Figure 5 illustrates the submicron RDX particles that have been produced by spray drying [15].

Another example of the application of nanomaterials is the crystallization of RDX in the presence of nanometric aluminium particles, rather than macroscopically mixing the two powders [19,20]. This type of crystallization is expected to lead to a more intimate contact between the explosive and the fuel particle and hence an enhanced reactivity between these two materials in the decomposition processes during a detonation. An RDX/nano-aluminium nanocomposite is shown in Figure 6*(a)*.

Copyright © 2010. Nova Science Publishers, Incorporated. All rights reserved.

Handbook of Material Science Research, Nova Science Publishers, Incorporated, 2010. ProQuest Ebook Central,

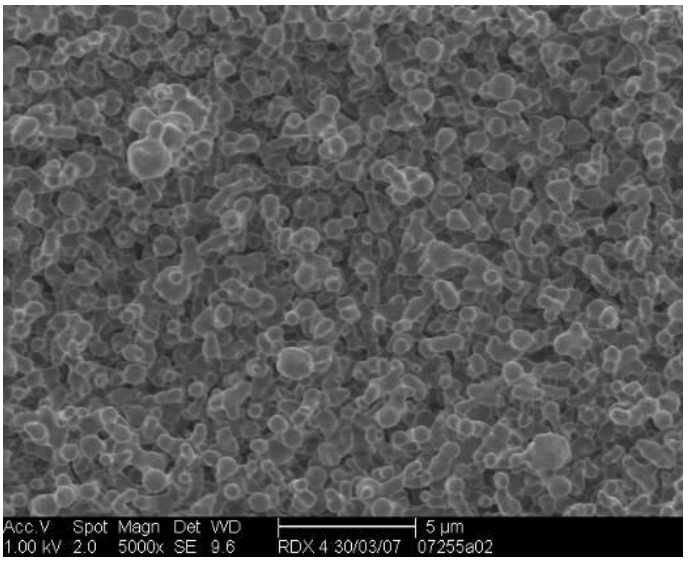


Figure 5. RDX crystals produced by means of the spray drying process. The size of the particles ranges from just below 1 µm to 2 µm [15].

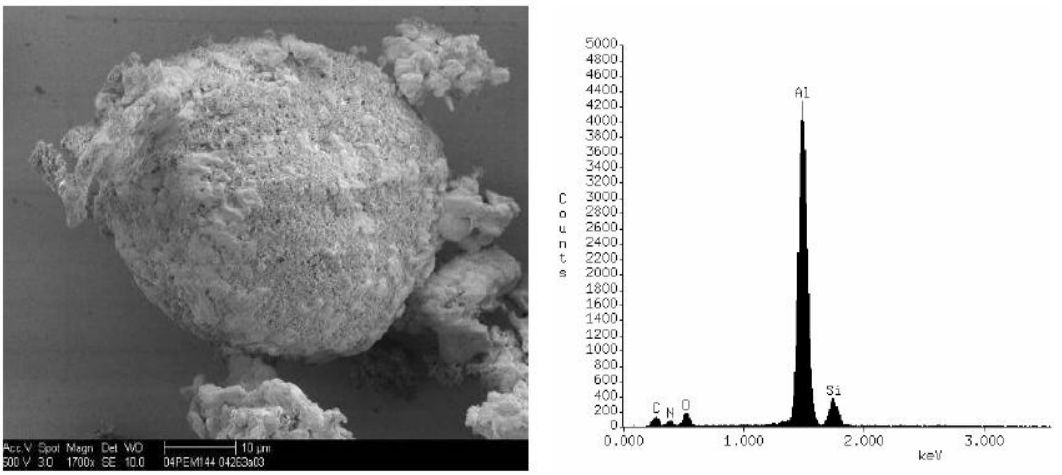


Figure 6. (a) Example of an RDX/nano-aluminium nanocomposite. (b) More detailed characterization by means of X-ray spectroscopy has shown evidence for the presence of aluminium in the particle shown on the left [20]. Peaks are found for C, N and O (originating from RDX) and Al. The Si peak is from the silicon sample holder. Acceleration voltage 15 kV, sampling time 100 s.

The nano-aluminium particles (mean size 40.7 nm) are attached to an RDX particle. The presence of aluminium in this particle was demonstrated by means of an X-ray spectrum, see Figure 6*(b)* [20].

Copyright © 2010. Nova Science Publishers, Incorporated. All rights reserved.

Handbook of Material Science Research, Nova Science Publishers, Incorporated, 2010. ProQuest Ebook Central,

Table 1. Overview of the product properties and consequences of product properties which determine the overall product quality of a material, as well as examples of analytical techniques that can be applied to assess or measure these product properties (and their potential consequences)

Property:	Affects:	Analytical tools:
Crystal size distribution	– Rheology / processability – Hazards – Maximum achievable solids loading – Shock sensitivity – Ballistic properties – Mechanical properties	– Particle size analyzers – Optical microscopy – Scanning electron microscopy
Particle shape / surface properties	– Rheology / processability – Maximum achievable solids loading – Shock sensitivity – Ballistic properties – Mechanical properties	– Scanning electron microscopy – Optical microscopy
Chemical purity	– Thermal stability – Compatibility – Reactivity – Hazards – Caking – Agglomeration – Storability (shelf-life) – Performance	– High performance liquid chromatography – Gas chromatography – Mass spectrometry (e.g. combined with thermal analyses) – Fourier transform infrared spectroscopy (e.g. combined with thermal analyses) – X-ray diffraction – Pycnometry (density)
Defect content	– Hazards – Shock sensitivity	– X-ray diffraction (structural defects) – Nuclear quadrupole resonance (NQR) – Optical microscopy (inclusions; limited to particles with sizes larger than ~50 μm) – Confocal scanning laser microscopy (micro-inclusions; limited to particles with sizes larger than ~50 μm)
Filterability	– Effectiveness of solid/liquid separation after production – Amount of adhering solvent(s)	– Particle size analyzers (size distribution) – Scanning electron microscopy (particle shape, agglomeration) – Liquid adsorption isotherms with gravimetric based equipment – Gas chromatography and/or high-performance liquid chromatography (residual solvent)

Copyright © 2010. Nova Science Publishers, Incorporated. All rights reserved.

Handbook of Material Science Research, Nova Science Publishers, Incorporated, 2010. ProQuest Ebook Central,

Table 1. (Continued)

Property:	Affects:	Analytical tools:
Free-flowing	– Dust formation (fine particles) – Caking – Electrostatic charging / dust explosions – Hazards	– Particle size analyzers – Scanning electron microscopy (agglomeration effects) – Determination of Hausner ratio, angle of repose, Carr's index – Moisture / residual solvent content (affect caking) – Caking tests / anti-caking agents – Dust explosion characteristics – Conductivity
Storability	– Shelf-life (functional and operational) – Caking – Hygroscopicity	– Thermal analysis – Moisture / residual solvent content (affect caking) – Determination of Hausner ratio, angle of repose, Carr's index – Caking tests / anti-caking agents – Liquid adsorption isotherms with gravimetric based equipment – Hygroscopic point
Hazards	– Impact sensitivity – Friction sensitivity – Electrostatic discharge	– Impact testing, e.g. Fall Hammer, Ballistic impact chamber – Friction testing – Electrostatic discharge testing
Thermal stability	– Processability – Storability (shelf-life) – Ageing	– Differential scanning calorimetry – Thermogravimetry/differential thermal analysis
Compatibility	– (Thermal) stability – Reactivity (with other materials) – Compatibility – Storability (shelf-life) – Hazards	– Differential scanning calorimetry – Thermogravimetry/differential thermal analysis – Vacuum stability test

CHARACTERIZATION OF ENERGETIC MATERIALS / COMPOSITIONS

The product quality of energetic materials comprises a broad spectrum of properties which generally can be assessed or measured by one or a few analytical techniques. Table 1 gives an overview of these product properties and consequences of these properties for e.g. down-stream processes, including examples of suitable characterization techniques. Some examples of characterization techniques have been shown already in the previous section, e.g. optical microscopy and SEM. These as well as other analytical techniques will be addressed in this section in more detail.

Figure 7 shows optical micrographs of RDX crystals, taken from different grades, that have been submerged in a refractive index matched liquid [2]. In this way, irregularities present at the surface of the crystals are ignored and only the inside of the crystals is

Copyright © 2010. Nova Science Publishers, Incorporated. All rights reserved.

Handbook of Material Science Research, Nova Science Publishers, Incorporated, 2010. ProQuest Ebook Central,

observed. The inclusions appear as dark spots against a bright background. Clearly differences in inclusion content can be observed.

Figure 8 shows results obtained with confocal scanning laser microscopy (CSLM), applied to different HMX (cyclotetramethylene tetranitramine, $C_4H_8N_8O_8$) grades [21]. By using CSLM in reflection mode, images of optical slices down to a thickness of about 0.5 μm can be made from a transparent object. Diffraction of the laser light will occur at locations with a local mismatch of the refractive index and on the image these locations will appear as bright spots against a dark background. Prior to CSLM characterization, the crystals are embedded in an epoxy resin, which is then cut and polished. To avoid surface artefacts due to the cutting and polishing steps in preparing the sample, the first slice is taken 15 μm below the surface of the HMX crystal. Each step in the *z*-direction is 0.5 μm deeper into the crystal. Each image covers an area of about 140×93 μm^2 and a depth of ~35 μm (70 slices). A two-dimensional mapping of the refractive index differences in this volume of a crystal is obtained by superimposing the images of the separate slices.

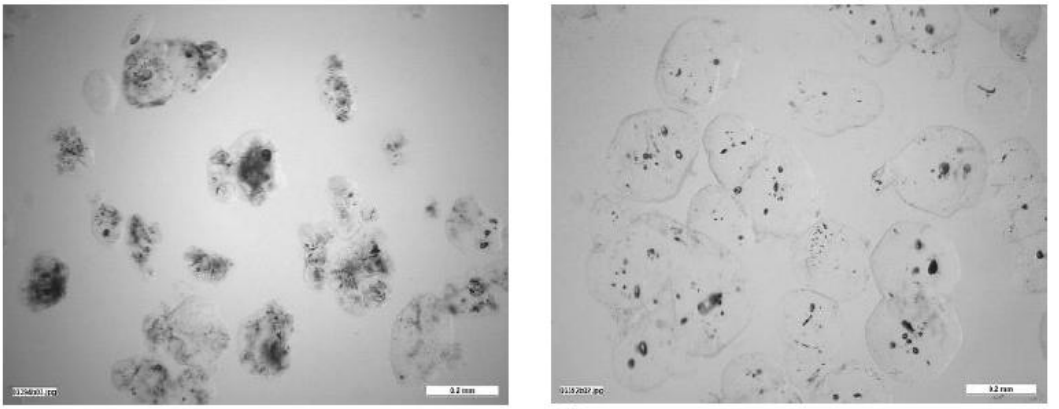


Figure 7. Optical micrographs of RDX crystals submerged in a refractive index matched liquid. (a) RDX, Class 1 and (b) I-RDX®, Class 1. I-RDX® is an insensitive version of RDX [2].

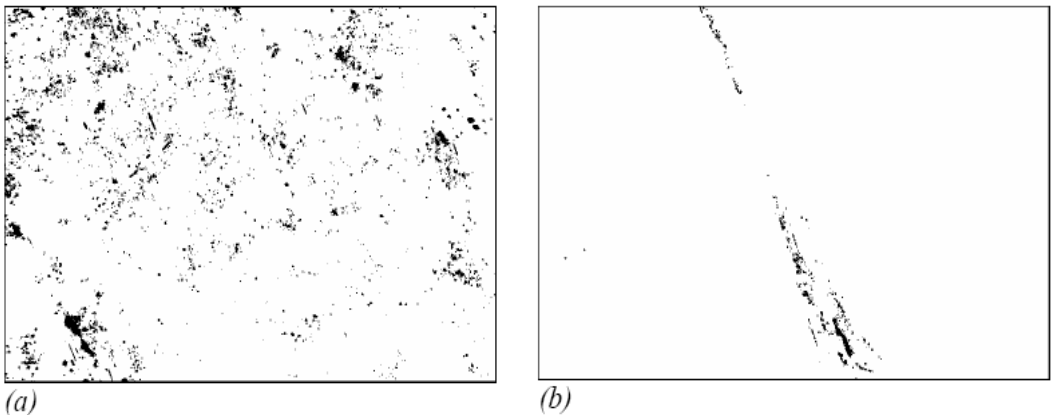


Figure 8. Confocal scanning laser microscopy (CSLM) applied to HMX. (a) Commercial HMX grade and (b) HMX crystallized from the commercial grade [21].

Copyright © 2010. Nova Science Publishers, Incorporated. All rights reserved.

Handbook of Material Science Research, Nova Science Publishers, Incorporated, 2010. ProQuest Ebook Central,

Table 2. Source of the RDX samples and shock initiation pressure of the PBXN-109 compositions prepared with either one of the seven RDX grades as determined with the NOL large scale gap test

Code	RDX source	Initiation pressure of PBXN-109 [kbar]
K1	BAe Royal Ordnance RDX	50.6
K2	Dyno reduced sensitivity RDX	52.4
K3	BAe OSI RDX	42.0
K4	Eurenco medium-insensitive RDX	22.1
K5	Eurenco insensitive RDX	46.6
K6	Dyno type II RDX	38.6
K7	ADI RDX	53.3

The images shown in Figure 8 have been inverted, now showing black spots against a bright background. The images clearly show a considerable difference between the commercial HMX grade and the HMX that has been crystallized starting from the commercial grade: the former grade contains many localized areas with 'clouds' of spots, whereas the latter grade contains only several, distributed spots. The size of the refractive index differences is estimated at ~ 2 μm. By means of scanning electron microscopy (SEM) of fractured HMX crystal surfaces, it was verified that the black spots in the CSLM images corresponded to micro-inclusions [21].

As insensitive types of RDX, e.g. I-RDX®, have become available, the important question is how to characterize the as-received energetic crystal, so prior to processing it to produce a PBX, in order to discriminate between different qualities of the explosive particles, i.e. a 'standard' or a reduced sensitivity version. This question has been studied in an international round-robin program dedicated to the characterization of RDX originating from seven different sources [22], see Table 2. It has been concluded that no single, definitive, and measurable property of the neat powder could be found yet, that is able to distinguish between higher and lower sensitivity qualities [23]. However, several techniques have been identified that are promising and appear to point in the right direction. These techniques comprise a relatively new ballistic impact test (ballistic impact chamber, BIC), nuclear quadrupole resonance (NQR) and a compressive stiffness test (CST), which will be discussed below.

The seven different RDX sources K1-K7, mentioned in Table 2, have been tested in a so-called Ballistic Impact Chamber (BIC) [24]. The BIC is an impact machine constructed with the objective to obtain information on the growth and extent of a reaction, by impacting explosives and propellants with the same impact condition and measuring their response [25,26]. The impact chamber has an internal diameter of 40 mm. It has a pressure gauge, two optic fibers to observe the start of reaction in the energetic material, and a 4.5 mm barrel opposite of the pressure gauge as automatic pressure relief. After placing a defined amount of loose RDX powder, the striker is put on top of the RDX pile. A laser is aligned horizontally just above the top surface of the striker and records the start of the deformation. A dropweight is released from 1.5 or 0.375 m, yielding an impact velocity at the position of the striker of 5.35 and 2.61 m/s, respectively [26]. The impact will accelerate the striker and squeeze the RDX powder between striker and anvil, until a reaction occurs. A schematic picture of the BIC device is shown in Figure 9.

Copyright © 2010. Nova Science Publishers, Incorporated. All rights reserved.

Handbook of Material Science Research, Nova Science Publishers, Incorporated, 2010. ProQuest Ebook Central,

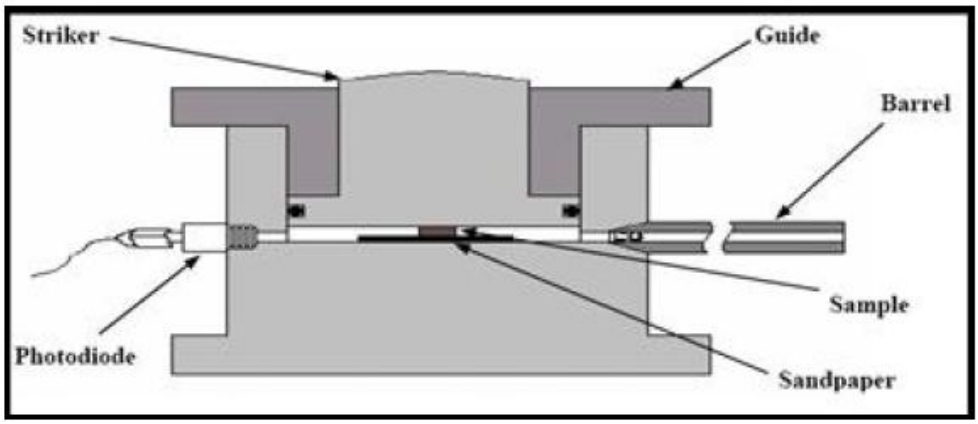


Figure 9. Schematic picture of the BIC device.

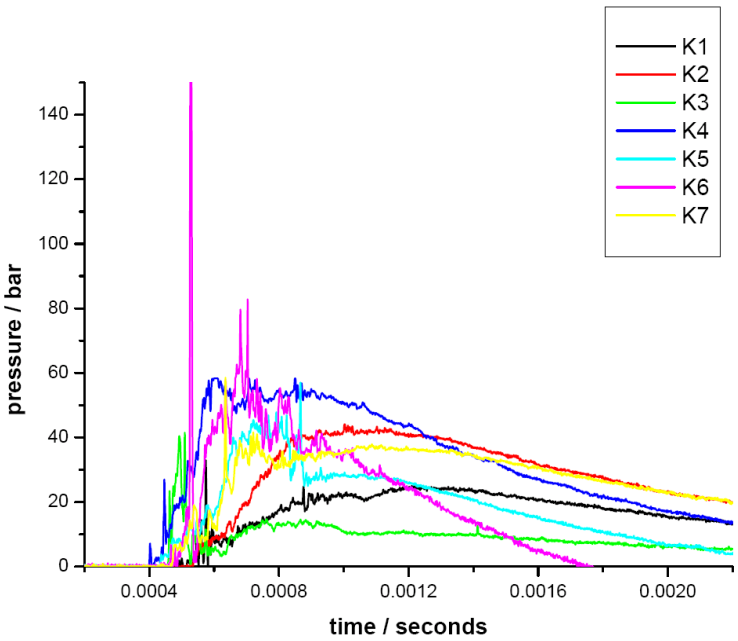


Figure 10. Pressure evolution in the BIC for seven different RDX qualities (K1-K7, see Table 2) and with a 10 kg dropweight impacting the striker and a 60 µl RDX sample at 5.35 m/s [24].

Figure 10 shows the pressure evolutions for 60 µl RDX samples K1-K7. More data, also using sample volumes of 40 and 80 µl, have been reported in [24]. Overall a gradual pressure build-up and decay occurs in the BIC which is due to the sample material decomposing while the volume below the striker decreases and increases again. The involved time scales are of the order 0.1 ms and comparable to numerical simulations that have been performed (not shown here, see [24]). Very strong pressure peaks are observed for K6 and K4, which coincide with the PBX compositions being the most susceptible to shock initiation (38.6 and 22.1 kbar, respectively; see Table 2). Actual maxima are even larger than shown as signals clip by exceeding the oscilloscope settings. K3, K5 and K7 show pressure peaks and an

Copyright © 2010. Nova Science Publishers, Incorporated. All rights reserved.

Handbook of Material Science Research, Nova Science Publishers, Incorporated, 2010. ProQuest Ebook Central,

irregular pressure build-up. K1 and K2 have a rather gradual pressure increase and decrease, coinciding with two PBX compositions that show a rather low susceptibility to shock initiation (50.6 and 52.4 kbar, see Table 2). The shock-insensitive crystals can be distinguished from the shock-sensitive RDX crystals by the shape of the pressure curve measured with the BIC. For the more shock-insensitive crystals (K7, K2, K1 and K5, see Table 2) a smooth pressure profile is observed or at most an irregular pressure build-up with late-time and not too strong pressure peaks. The more shock-sensitive crystals (K4, K6 and K3, see Table 2) with (sub)-micron defect structure, typically show a strong and fast pressure peak, before a pressure builds up in the BIC. Sometimes even more pressure peaks are distinguished. These fast rising pressure peaks are due to the shock wave travelling through air and is directly followed by the still high density reaction products reaching the pressure gauge.

The BIC data have been further substantiated by means of optical microscopy and scanning electron microscopy of the RDX samples. In optical microscopy the internal defect structure of the crystals is visualized by immersion into a liquid with a refractive index matching as closely as possible the refractive indices of the RDX crystal lattice, similar to the micrographs shown previously in Figure 7. Internal voids are present in all samples, although to a different extent, see Figure 11. Furthermore, samples K3, K4 and K6 are also not completely transparent and have a 'greyish' appearance. In earlier work [2] on RDX and HMX the absence of this grey appearance has been correlated to enhanced insensitivity. The RDX samples for the SEM observations have been prepared by cleaving RDX crystals with a scalpel. Particles taken from batches K3 and K4 completely shattered when trying to cleave them and these could not be further analysed with SEM. The same occurred with K6 and only after several attempts a cleaved crystal part was left and of sufficient quality for the SEM observations. In Figure 12 the optical and SEM micrographs of RDX crystals from batches K1, K2 and K6 are shown [27]. By comparison of SEM and optical microscopy, the 'greyish' appearance observed in the optical micrographs, has been attributed to internal defects with typical micron-sized features [21].

Another example of a promising characterization technique is Nuclear Quadrupole Resonance (NQR). NQR has been applied by Caulder *et al.* [28,29] to correlate the crystalline quality of energetic materials with their sensitivity towards shock initiation when applying these crystals in polymer-bonded explosives. A number of factors associated with crystal quality contribute to the NQR line width. Imperfections such as dislocations, voids, strain and impurities can be electrical sources that distort the electric field gradient at nearby quadrupolar nuclei and broaden the observed NQR line. With NQR the ^{14}N line widths of several samples have been measured to assess their crystal quality. The line widths have been compared and correlated with sample purity, particle size distribution and density. Also cast polymer bonded explosives containing either RDX or HMX were studied and compared with those of the powdered samples [30]. These results have been used to predict the shock sensitivity of CL-20 based explosives [29]. NQR linewidths are probably better indicators of overall crystal quality than any of the properties like purity, particle size distribution and density alone.

The correlation of NQR linewidth and shock initiation pressure of PBXN-109 is given in Figure 13 [23]. PBXN-109 contains 64 wt% RDX and for the NQR tests the same seven RDX lots summarized in Table 2 have been used. In Figure 13 the correlation of the NQR linewidth and the shock initiation pressure has been differentiated towards the RDX synthesis route, *i.e.*

Copyright © 2010. Nova Science Publishers, Incorporated. All rights reserved.

Handbook of Material Science Research, Nova Science Publishers, Incorporated, 2010. ProQuest Ebook Central,

the direct nitration (Woolwich process) and the acetic anhydride (Bachmann) process. The latter RDX may contain from 4 upto 17 wt% of HMX [31], which is expected to broaden the linedwidth in NQR. Also for the PBXN-109 formulations containing different RDX grades a trend can be observed that for smaller NQR linewidths a higher shock initiation pressure is found. It is worth mentioning that not all types of defects affect shock sensitivity to the same extent, which is probably why the Bachmann and Woolwich materials separate into two groups in Figure 13.

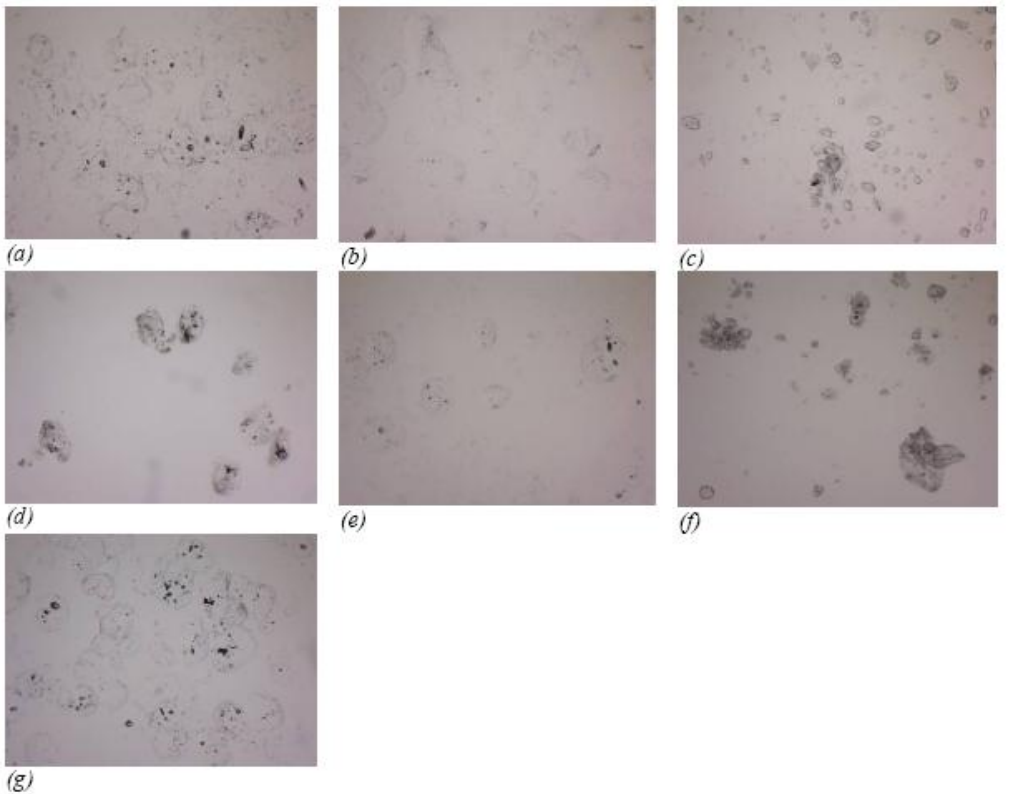


Figure 11. Optical micrographs of RDX samples (a) K1, (b) K2, (c) K3, (d) K4, (e) K5, (f) K6 and (g) K7.

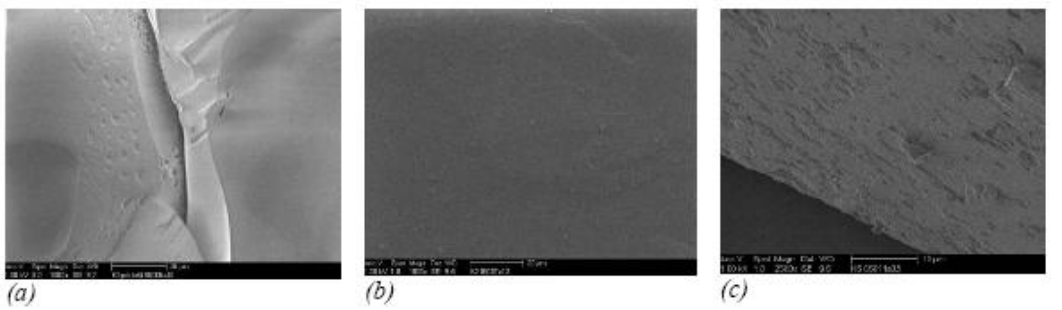


Figure 12. SEM micrographs of a cleaved RDX crystal taken from RDX source (a) K1, (b) K2 and (c) K6.

Copyright © 2010. Nova Science Publishers, Incorporated. All rights reserved.

Handbook of Material Science Research, Nova Science Publishers, Incorporated, 2010. ProQuest Ebook Central,

Differences in crystal quality can also be assessed by measuring the mechanical strength and fragmentation behaviour of crystals. These parameters have been studied for RDX crystals from grades with varying internal defects by means of a compressive stiffness test (CST), *i.e.* confined quasi-static compression, of 2 g samples [32]. The discrimination between commercial and reprocessed RDX batches could be revealed from the compaction curves as well as by the quantitative parameter of the initial secant modulus (ISM). The CST experiments have been combined with optical micrographs of the RDX batches in a refractive index matched liquid and density measurements. The results described and discussed in [32] indicate that the internal defects play a key role in the mechanical response of an ensemble of particles when subjected to an external load, whereas the effects resulting from external quality are limited.

Energetic materials like RDX and HMX are generally dispersed in a polymer matrix to produce a Polymer-Bonded eXplosive (PBX). In demonstrating the effect of the HMX crystal quality on shock sensitivity two studies have been carried out on exactly the same variety of HMX crystals: as-received or recrystallized from acetone and γ-butyrolactone at different processing conditions. In the first study the HMX particles (sieve fraction 250-425 μm) have been dispersed in a PBX and shock sensitivity has been studied with the water gap test [33]. The energetic filler content, particle size and PBX processing conditions have been carefully kept constant. The shock initiation pressure increased significantly from 4.1 to 6.8 GPa by increasing the HMX crystal density by recrystallization from 1.886 to 1.902 g/cm^3. In the second study a similar change in shock sensitivity has been found with the identical HMX qualities, only this time the HMX crystals (sieve fraction 355-425 μm) have been dispersed in a density-matched liquid and the shock sensitivity is studied by means of the flyer impact set-up [34,35]. In this study also a significant increase in shock initiation pressure was found from 7.0 GPa to 12 GPa for the commercial and reprocessed HMX, respectively [34].

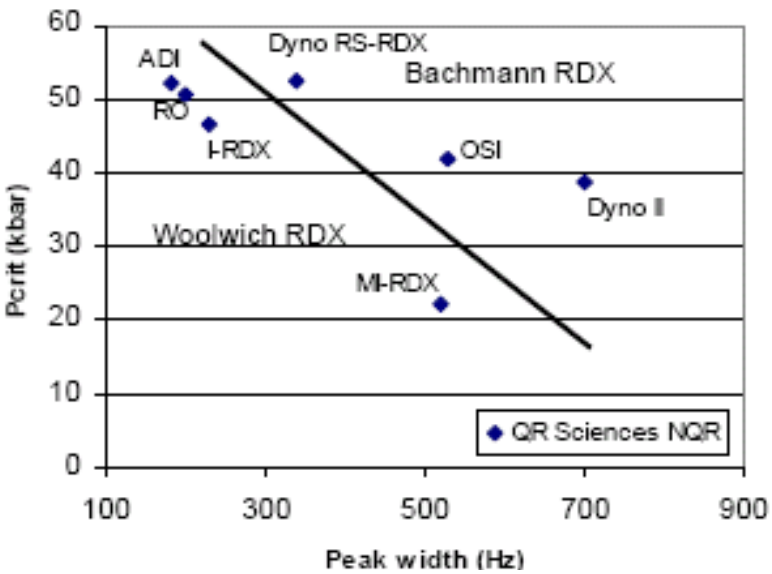


Figure 13. Correlation of shock sensitivity in NOL Large Scale Gap Test with NQR line width [23]. See also Table 2 for the critical initiation pressures.

Copyright © 2010. Nova Science Publishers, Incorporated. All rights reserved.

Handbook of Material Science Research, Nova Science Publishers, Incorporated, 2010. ProQuest Ebook Central,

Table 3. RDX/HMX/HTPB based PBX formulations, tested regarding their shock initiation characteristics as determined by means of flyer impact tests using the mega ampere pulser (MAP) set-up

Code	HMX type / content [wt%]	RDX type / content [wt%]	Binder [wt%]
PBX1	Coarse: commercial HMX / 60.8 Fine: comminuted HMX [a] / 15.2	–	24.0
PBX2	Coarse: commercial HMX / 60.8 Fine: comminuted HMX [b] / 15.2	–	24.0
PBX3	Coarse: reprocessed HMX / 60.8 Fine: comminuted HMX [a] / 15.2	–	24.0
PBX4	Coarse: reprocessed HMX / 60.8 Fine: comminuted HMX [b] / 15.2	–	24.0
PBX9	Fine: comminuted HMX [a] / 16.4	Coarse: I-RDX® / 65.6	18.0
PBX10	Fine: comminuted HMX [b] / 16.4	Coarse: reprocessed I-RDX® / 65.6	18.0

[a] Comminution by means of a rotor-stator system.

[b] Comminution by means of an annular gap mill.

Table 4. Shock initiation data of the PBXs tabulated in Table 3

Code	Critical flyer impact velocity [km/s]	Measured detonation velocity [km/s]	Shock initiation pressure [GPa]
PBX1	2.8 ± 0.2	7.9 ± 0.2	10
PBX2	4.1 ± 0.2	6.9 ± 0.2	18
PBX3	3.1 ± 0.2	7.6 ± 0.1	12
PBX4	4.5 ± 0.2	6.6 ± 0.4	20
PBX9	4.7 ± 0.3	7.5 ± 0.2	21
PBX10	> 6.0 ± 0.2	7.5 ± 0.2	> 31

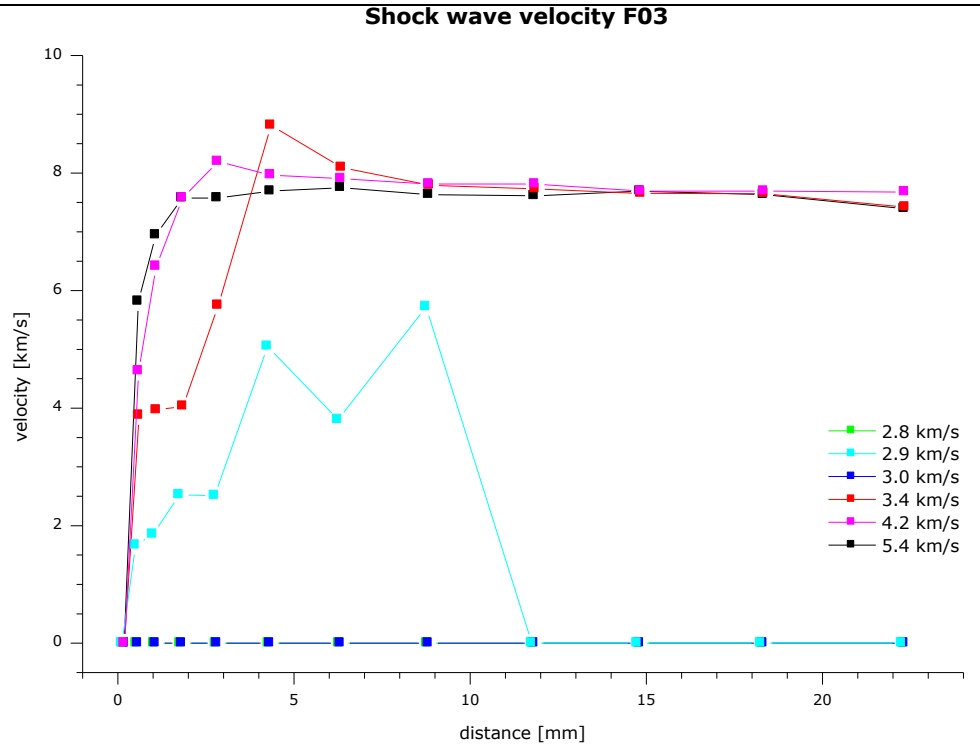
A more recent example is the effect of the source (manufacturer and/or production method) of RDX on the shock sensitivity of PBXN-109 as demonstrated in Table 2 [23,36]. PBXN-109 is a composition containing 64 wt% RDX, 20 wt% aluminium, and 16 wt% of hydroxyl-terminated polybutadiene (HTPB). Depending on the RDX source in the PBXN-109 composition, one can find a shock initiation pressure as low as 22 kbar or as high as 53 kbar. This variation is significant, see Table 2.

Reprocessing (by means of crystallization) of I-RDX® (already a reduced sensitivity RDX) and HMX has shown that, on a PBX level, again significant steps in insensitivity can be achieved. Figure 14 shows examples of the shock initiation data of RDX/HMX- and HMX-based PBXs according to the formulations mentioned in Table 3.

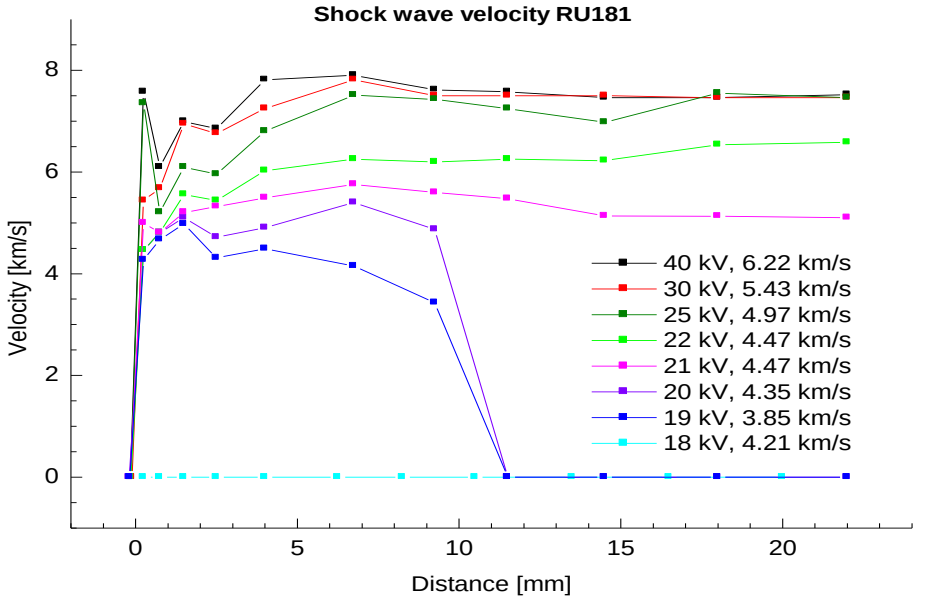
The RDX/HMX PBXs have been subjected to flyer plate impact tests using a so-called Mega Ampere Pulser (MAP) set-up. The test is based on a kapton flyer impact on a PBX sample, during which the shock-to-detonation transition or the decay of the input shock wave is monitored using fiber optics. Details of this shock initiation test set-up have been described elsewhere [37]. The results are illustrated for PBX9 in Figure 14*(b)* by plotting the detonation wave velocity versus distance in the PBX sample. By changing the MAP voltage, the impact velocity of the flyer impacting with the PBX sample can be varied and in this way the critical flyer impact velocity can be found which corresponds to the 'go/no go' level of the PBX tested.

Copyright © 2010. Nova Science Publishers, Incorporated. All rights reserved.

Handbook of Material Science Research, Nova Science Publishers, Incorporated, 2010. ProQuest Ebook Central,



(a).



(b).

Figure 14. Shock wave velocity as a function of distance in the PBX sample for (a) PBX3 and (b) PBX9, as determined by means of flyer impact tests using the mega ampere pulser (MAP) set-up.

In a positive test (‘go’), the PBX sample detonates and a stable shock wave velocity is found which corresponds to the detonation velocity. During a ‘no go’ the input shock wave decays to zero. The results show that the critical flyer impact velocity is 4.7 km/s for PBX9

Copyright © 2010. Nova Science Publishers, Incorporated. All rights reserved.

Handbook of Material Science Research, Nova Science Publishers, Incorporated, 2010. ProQuest Ebook Central,

and > 6.0 km/s for PBX10, thus indicating that PBX10 is significantly less sensitive towards shock initiation than PBX9 [38]. These critical flyer impact velocities correspond to critical initiation pressures of 21 GPa and > 31 GPa for PBX9 and PBX10, respectively (see Table 4). PBX9 and PBX10 both contain the same fine grade of HMX, but two different RDX grades: in PBX9 an I-RDX® produced by SME/France is used, whereas in PBX10 a reprocessed version of the I-RDX® is used. The reprocessed I-RDX® is produced by again crystallizing the RDX according to a cooling crystallization process. Both the I-RDX® and reprocessed version have been sieved to yield particle sizes in the range of 75-355 μm. The shock initiation data of PBX9 and PBX10 therefore also clearly demonstrate that the reprocessed I-RDX® turns out to be significantly less sensitive than the original I-RDX®.

Similar results with HMX/HTPB based PBXs have been obtained. These PBX formulations are also summarized in Table 3 (PBX1-PBX4). These PBXs consisted of coarse and fine HMX grades in an 80/20 wt% ratio. The coarse HMX grades were either a commercial HMX batch or a reprocessed one by recrystallizing the commercial HMX batch by means of a cooling crystallization process. Both coarse grades were sieved (75-180 μm), in order to avoid differences in particle size to affect the shock initiation test results. This time the PBXs consisted of an uncured HTPB/IDP 50/50 wt% mixture with a solid load of 76.0 wt% (compared to 82.0 wt% for PBX9 and PBX10). The shock initiation test of PBX3 is shown in Figure 14*(a)* to illustrate the results. The critical flyer impact velocities, measured detonation velocities and critical initiation pressures have been summarized in Table 4. Generally smaller particles tend to be less sensitive than larger particles. This is in agreement with the finding that PBX3 and PBX4 are less sensitive than PBX1 and PBX2, respectively, since PBX3 and PBX4 both contain the smallest of the two ground HMX grades investigated. Together with the sensitivity data shown above for I-RDX® and its reprocessed version, also these HMX results clearly show that the PBXs containing the reprocessed HMX (PBX2 and PBX4) are considerably less sensitive compared to the PBXs with the commercial HMX (PBX1 and PBX3).

Based on these experimental results, the conclusion appears justified that the limits in the insensitivity of I-RDX® and HMX have not yet been reached, and there is still margin for further improvement regarding the insensitiveness of these conventional explosives. It can be expected that in the near future similar investigations will be carried out with CL-20.

OUTLOOK

Some of the techniques mentioned previously appear promising in order to qualitatively and quantitatively assess the internal crystal quality of explosive particles. Qualitative techniques comprise e.g. optical microscopy and CSLM. Examples of quantitative techniques are NQR, BIC and density measurements. However, the reduction in mean particle size of energetic materials down to the sub-micron and nanoscale, poses new challenges to the energetic materials community regarding suitable analytical techniques to characterize these materials.

Not every compound lends itself to improvement in the particle characteristics because compounds like TATB and HNS have very limited solubility and one is mainly limited to using what is produced from the original synthesis, whereas RDX, HMX and CL-20 can be

Copyright © 2010. Nova Science Publishers, Incorporated. All rights reserved.

Handbook of Material Science Research, Nova Science Publishers, Incorporated, 2010. ProQuest Ebook Central,

manipulated to produce more desirable crystalline particles because they have substantial solubilities in a wide range of solvents. However, instead of using conventional solvents, the application of ionic liquids, a relatively new class of solvents, has recently led to improvements in the mean particle size and shape of TATB particles [39]. Parallel to the developments to produce reduced sensitivity versions of conventional explosive particles like RDX, HMX and in the near future presumably also CL-20, research is focused at the synthesis of new, intrinsically less sensitive energetic materials as well. As an example of these developments the high-energy density materials like nitrogen-rich compounds can be mentioned [40,41]. It will be important to realize that decisions to scale-up new energetic substances will be made on the basis of their hazard and thermal stability properties. Since these materials will be prepared on small scale, probably according to a sub-optimal process, the resulting hazard and thermal properties will also be sub-optimal. For future developments of new, intrinsically less sensitive energetic materials it is therefore recommended to include – already in the development phase – a crystallization step, next to the synthesis process. In this way a first step will be made towards a more optimized process, generally resulting in more reliable product properties.

Developments on the application of the computational chemical method ReaxFF have shown to successfully describe the thermal decomposition of RDX [42] and the initial chemical events in RDX upon interaction with a shock wave [43]. This as well as other modelling techniques hold promise as a tool to simulate the response of an energetic material either described as single molecules or as an ensemble of particles embedded in a binder matrix to e.g. temperature effects (decomposition, cook-off behaviour), shock waves, bullet/fragment impact etc. It will be interesting to see whether these modelling techniques will be able to simulate the interaction of e.g. shock waves with energetic crystals containing specific defects, like inclusions, dislocations or impurities and in this way to assess which type of defects or combination of defects determine the final sensitiveness of the energetic material. These results can then be used to modify existing or develop new crystallization techniques, including the design of the crystallization hardware, which reduce or avoid the formation of these types of defects in the explosive particles during their production.

Finally, experimental verification of the expected improvements in the insensitivity of energetic materials will still remain to be an important and crucial part of the research regarding the development and characterization of less sensitive energetic materials.

ACKNOWLEDGMENTS

We ackowledge The Netherlands Ministery of Defence and the European Office of Aerospace Research and Development (EOARD, Contract Number F61775-02-C4093) for financial support of a part of the work presented in this review. Dr Ruth Doherty (Department of Homeland Security, USA), Dr John F. Zevenbergen and Dr Koos L. Verolme (both TNO Defence, Security and Safety, The Netherlands) are gratefully acknowledged for careful reading and reviewing of the manuscript prior to publication.

Copyright © 2010. Nova Science Publishers, Incorporated. All rights reserved.

Handbook of Material Science Research, Nova Science Publishers, Incorporated, 2010. ProQuest Ebook Central,

REFERENCES

[1] A.E.D.M. van der Heijden and J.H. ter Horst, "Crystallization and product quality", in: "Energetic Materials – Particle Processing and Characterization", ed. U. Teipel, 2005, Wiley-VCH, Germany

[2] A.E.D.M. van der Heijden, R.H.B. Bouma and A.C. van der Steen, "Physico-chemical parameters of nitramines influencing shock sensitivity", Propellants, Explosives, Pyrotechnics 29 (2004) 304-313

[3] A.E.D.M. van der Heijden and R.H.B. Bouma, "Crystallization and characterization of RDX, HMX and CL-20", *Crystal Growth and Design* 4 (2004) 999-1007

[4] J.W. Mullin, in: "Crystallization", Butterworth-Heineman Ltd., Oxford, Great Britain, 3rd edition, 1993

[5] A.E.D.M. van der Heijden, "Crystallization and characterization of energetic materials", in: "Trends in Chemical Engineering", Research Trends, Poojopura, India, 1998

[6] H.F.R. Schöyer, W.H.M. Welland-Veltmans, J. Louwers, P.A.O.G. Korting, A.E.D.M. van der Heijden, H.L.J. Keizers and R.P. van den Berg, "Overview of the development of hydrazinium nitroformate", *Journal of Propulsion and Power* 18 (2002) 131-137

[7] W.H.M. Veltmans, A.E.D.M. van der Heijden, M.I. Rodgers and R.M. Geertman, "Improvement of hydrazinium nitroformate product characteristics", Proceedings 30th International Annual Conference of ICT, Karlsruhe, Germany

[8] J.H. ter Horst, R.M. Geertman, A.E.D.M. van der Heijden and G.M. van Rosmalen, "The influence of a solvent on the crystal morphology of RDX", *Journal of Crystal Growth* 198/199 (1999) 773

[9] J.H. ter Horst, "Molecular Modelling and Crystallization: Morphology, Solvent Effect and Adsorption", PhD Thesis, Delft University of Technology, 2000, Delft, The Netherlands

[10] C.A. van Driel, A.E.A. van Gijzel, A.E.D.M. van der Heijden, M.P. van Rooijen and W.C. Prinse, "Crystallization and characterization of HNS-IV", Proceedings of 33rd International Annual Conference of ICT, 2002, Karlsruhe, Germany

[11] A. Pivkina, P. Ulyanova, Y. Frolov, S. Zavyalov and J. Schoonman, "Nanomaterials for heterogeneous combustion", Propellants, Explosives, Pyrotechnics 29 (2004) 39-48

[12] Y. Frolov, A. Pivkina, P. Ulyanova and S. Zavyalov, "Nanomaterials and nanostructures as components for high-energy condensed systems", in: Proceedings 28th International Pyrotechnics Seminar, Adelaide, Australia, Nov. 2001, 305

[13] C. Rossi, K. Zhang, D. Estève, P. Alphonse, P. Tailhades and C. Vahlas, "Nanoenergetic materials for MEMS: a review", *J. Microelectromechanical Systems* 16 (2007) 919-931

[14] K.-Y. Lee, D.S. Moore, B.W. Asay and A. Llobet, "Submicron-sized gamma-HMX: 1. preparation and initial characterization", *Journal of Energetic Materials* 25 (2007) 161-171

[15] A.E.D.M. van der Heijden, R.H.B. Bouma, E.P. Carton, M. Martinez Pacheco, B. Meuken, R. Webb and J.F. Zevenbergen, "Processing, application and characterization of (ultra)fine and nanometric materials in energetic compositions", invited lecture at the

Copyright © 2010. Nova Science Publishers, Incorporated. All rights reserved.

Handbook of Material Science Research, Nova Science Publishers, Incorporated, 2010. ProQuest Ebook Central,

14th Shock Compression of Condensed Materials Conference, 31 July – 5 August, 2006, Baltimore MD, USA; AIP Conference Proceedings 845, 1121-1126

[16] D. Price, "Critical parameters for detonation propagation and initiation of solid explosives", NSWC TR 80-339, September 1981

[17] E. L. V. Goetheer, Z. Xiaojun, L. J. P. van den Broeke, H. W. Piepers, J. T. Keurentjes, A. A. Drinkenburg and A. W. Verkerk, "Method for preparing particles of a defined size in a reaction vessel", *European Patent* 1,536,881; 2005

[18] D. Verdoes and M. Nienoord, "New technologies for controlled production of submicron particles", Proceedings of the 16th International Symposium on Industrial Crystallization, edited by J. Ulrich, September 11-14, 2005, p 897-902

[19] A.E.D.M. van der Heijden, R.H.B. Bouma, A.C. van der Steen and H.R. Fischer, "Application and characterization of nanomaterials in energetic compositions", *Materials Research Society* Vol 800 (2004) AA5.6

[20] A.E.D.M. van der Heijden, C.P.M. Roelands, Y.L.M. Creyghton, E. Marino, R.H.B. Bouma, J.H.G. Scholtes and W. Duvalois, "Energetic (nano)materials: crystallization, characterization and insensitive plastic bonded explosives", *Propellants, Explosives, Pyrotechnics* 33 (2008) 25-32

[21] A.E.D.M. van der Heijden, W. Duvalois and C.J.M. van der Wulp, "Micro-inclusions in HMX crystals", Proceedings 30th International Annual Conference of ICT, 1999, Karlsruhe, Germany

[22] D. Watt, F. Peugeot, R. Doherty, M. Sharp, D. Tucker and D. Topler, "Reduced sensitivity RDX, where are we?", Proceedings 35th International Annual Conference of ICT, 2004, Karlsruhe, Germany

[23] R. Doherty and D. Watt, in: Insensitive Energetic Materials – Particles, Crystals and Composites, eds. U. Teipel and M. Herrmann, 2007, p109

[24] R.H.B. Bouma, A.G. Boluijt, H.J. Verbeek and A.E.D.M. van der Heijden, "On the impact testing of RDX crystals with different internal quality", *Journal of Applied Physics* 103 (2008) 093517

[25] C.S. Coffey and V.F. DeVost, Impact testing of explosives and propellants, *Propellants, Explosives, Pyrotechnics* 20 (1995) 105

[26] B. Meuken., M. Martinez Pacheco, H.J. Verbeek, R.H.B. Bouma and L. Katgerman, Shear initiated reactions in energetic and reactive materials, in: Multifunctional Energetic Materials, eds. N.N. Thadhani, R.W. Armstrong, A.E. Gash and W.H. Wilson (Materials Research Society Symposium Proceedings 896, Warrendale, PA, 2006) 0896-H06-06

[27] A.E.D.M. van der Heijden, R.H.B. Bouma and W. Duvalois, Characterization of insensitive energetic materials, in: Insensitive Energetic Materials – Particles, Crystals and Composites, eds. U. Teipel and M. Herrmann, 2007, p142

[28] S.M. Caulder, M.L. Buess, A.N. Garroway and P.J. Miller, "NQR line broadening due to crystal lattice imperfections and its relationship to shock sensitivity", 13th American Physical Society Topical Conference on Shock Compression of Condensed Matter, July 20 - 25, 2003, Portland, Oregon, USA

[29] S.M. Caulder, M.L. Buess and L.A. Nock, "An analytical study of the crystal quality of ε-hexanitrohexaazaisowurtzitane (CL-20) synthesized using several different crystallization techniques and intermediate precursors", *Science and Technology of Energetic Materials* 66 (2005) 406

Copyright © 2010. Nova Science Publishers, Incorporated. All rights reserved.

Handbook of Material Science Research, Nova Science Publishers, Incorporated, 2010. ProQuest Ebook Central,

[30] M.L. Buess and S.M. Caulder, "Factors affecting the NQR line width in nitramine explosives", *Applied Magnetic Resonance* 25 (2004) 383
[31] Detailed specification RDX (cyclotrimethylenetrinitramine), MIL-DTL-398D, 1996
[32] L. Ming, H. Ming, K. Bin, W. Maoping, L. Hongzhen and X. Rong, "Quality evaluation of RDX crystalline particles by confined quasi-static compression method", *Propellants, Explosives, Pyrotechnics* 32 (2007) 401
[33] A.E.D.M. van der Heijden and R.H.B. Bouma, "Shock sensitivity of HMX/HTPB PBX's: relation with HMX crystal density", Proceedings 29th International Annual Conference of ICT, 1998, Karlsruhe, Germany
[34] A.E.D.M. van der Heijden, R.H.B. Bouma and R.J. van Esveld, "Shock sensitivity of HMX based compositions", Proceedings 31st International Annual Conference of ICT, 2000, Karlsruhe, Germany
[35] R.H.B. Bouma and A.E.D.M. van der Heijden, "Evaluation of crystal defects by the shock sensitivity of energetic crystals suspended in a density-matched liquid", Proceedings 32nd International Annual Conference of ICT, 2001, Karlsruhe, Germany
[36] R. Doherty, "Minutes of the RS-RDX Round Robin (R4) Technical Meeting (ICT 2006)", MSIAC Report No. L-130, 2006
[37] W.C. Prinse, R.J. van Esveld, R. Oostdam, M.P. van Rooijen and R.H.B. Bouma, Proceedings of the 23rd International Congress on High-Speed Photography and Photonics, 20-25 September 1998, Moscow, Russia
[38] M. Herrmann, I. Mikonsaari, H. Krause, M. Kaiser, R. Hühn, M.H. Lefebvre, M. Alouaamari, C. Martin, A.E.D.M. van der Heijden, R.H.B. Bouma, J. Paap, I. Plaksin, J. Campos, R. Mendes, J. Ribeiro, J. Góis and S. Almada, "WEAG-Panel II-CEPA14 ERG114-009 Particle processing and characterization. Part IV: PBX-formulation and characterization", Proceedings 37th International Annual Conference of ICT, 2006
[39] A. Maiti, P.F. Pagoria, A.E. Gash, T.Y. Han, C.A. Orme, R.H. Gee and L.E. Fried, "Solvent screening for a hard-to-dissolve crystal", *Physical Chemistry Chemical Physics* 10 (2008) 5050-5056
[40] B.M. Rice, E.F.C. Byrd and W.D. Mattson, "Computational aspects of nitrogen-rich HEDMs", *Structure and Bonding* 125 (2007) 153-194
[41] D.M. Badgujar, M.B. Talawar, S.N. Asthana and P.P. Mahulikar, "Advances in science and technology of modern energetic materials: an overview", *Journal of Hazardous Materials* 151 (2008) 289-305
[42] A. Strachan, E.M. Kober, A.C.T. van Duin, J. Oxgaard and W.A. Goddard III, "Thermal decomposition of RDX from reactive molecular dynamics", *Journal of Chemical Physics* 122 (2005) 054502
[43] A. Strachan, A.C.T. van Duin, D. Chakraborty, S. Dasgupta and W.A. Goddard III, "Shock waves in high-energy materials: the initial chemical events in nitramine RDX", *Physical Review Letters* 91 (2003) 098301

Copyright © 2010. Nova Science Publishers, Incorporated. All rights reserved.

Handbook of Material Science Research, Nova Science Publishers, Incorporated, 2010. ProQuest Ebook Central,

Copyright © 2010. Nova Science Publishers, Incorporated. All rights reserved.

Handbook of Material Science Research, Nova Science Publishers, Incorporated, 2010. ProQuest Ebook Central,

In: Handbook of Material Science Research
Editors: C. René and E. Turcotte, pp.347-368
ISBN 978-1-60741-798-9
© 2010 Nova Science Publishers, Inc.

Chapter 8

ELECTRODEPOSITION AND CORROSION PROPERTIES OF ZN-CO AND ZN-CO-FE ALLOY COATINGS

J.M.C. Mol [1]*, Z.F. Lodhi [1,2], A. Hovestad [3], L. 't Hoen – Velterop [4], H. Terryn [2,5], and J.H.W. de Wit [1]

1. Delft University of Technology,
Department of Materials Science and Engineering, Delft, The Netherlands
2. M2i Materials Innovation Institute, Delft, The Netherlands
3. TNO Netherlands Organisation for Applied Scientific Research,
Eindhoven, The Netherlands
4. National Aerospace Laboratory NLR,
Amsterdam, The Netherlands
5. Vrije Universiteit Brussels, Department of Metallurgy,
Electrochemistry and Materials Science, Brussels, Belgium

Copyright © 2010. Nova Science Publishers, Incorporated. All rights reserved.

ABSTRACT

Cadmium (Cd) has been extensively used as an excellent corrosion protective coating for steel components in aerospace, automotive, electrical and fasteners industries. However, Cd is banned due to its toxic nature and strict environmental regulations. In this study, the electrodeposition mechanism and kinetics, coating morphology and corrosion resistance of alternative, electrodeposited Zinc-Cobalt (Zn-Co) and Zinc-Cobalt-Iron (Zn-Co-Fe) alloys have been investigated. Coatings with relatively high amounts of Co are very difficult to achieve due to anomalism associated with their deposition and are therefore not much reported so far. In this research Zn-Co and Zn-Co-Fe alloys with varying amount of Co (2 to 40 wt-%) and Fe (up to 1 wt-%) are electrodeposited and the effects of variation of process parameter settings (i.e. cathodic polarization, current density, temperature and electrolyte composition) on the electrodeposition mechanism and kinetics are investigated. The microstructure of the alloy coatings changed significantly with the variation in Co content in the deposits. The barrier and sacrificial corrosion protection provided by the coatings were investigated with a variety of

* E-mail: J.M.C.Mol@tudelft.nl.

Handbook of Material Science Research, Nova Science Publishers, Incorporated, 2010. ProQuest Ebook Central,

electrochemical techniques and industrial accelerated tests. It was found that the sacrificial properties and the protection range decreases with increasing Co content in the alloy. For the highest Co content in the alloy, the coating may become more noble to steel and loses its sacrificial protection. The barrier resistance of the coatings increases with the increase of Co content in the alloy coating. Both Zn-Co and Zn-Co-Fe alloys with high Co content (> 32 wt-% Co) showed excellent barrier properties. An intermediate region of compositions can be distinguished in which the coatings would provide a good combination of sacrificial and barrier resistance properties and also a reasonable protection range.

1. INTRODUCTION

Corrosion protective coatings form artificial intermediate layers between the corrosive environment and the underlying metal substrate. In general, the coatings can protect the metal substrates by two main mechanisms: sacrificial and barrier protection mechanisms. Cadmium (Cd) has been used extensively as a barrier and sacrificial coating for steel applications in aerospace, automobile, electrical and fasteners industries because of its excellent corrosion resistance and mechanical engineering properties [1-3]. However, Cd is banned due to its toxic nature and stringent environmental regulations [4]. Hence, due to restrictions on Cd, alternate coatings to Cd are being actively explored [2,5,6]. The application of a zinc (Zn) coating is recognized to provide excellent protection to steel against corrosion mainly because of its sacrificial behavior, by virtue of its low standard electrode potential (E_0 = -1.07V vs. SCE). It is reported [2,7] that the difference in the potential of the coating and the substrate acts as a driving force for the corrosion of the sacrificial coating and protection of steel under corroding conditions. Because of the relatively large difference in electronegativities of Zn and (AISI-4340) steel (E_0= -0.65V vs. SCE), rapid dissolution of Zn occurs under corroding conditions and reduces the coating life of pure Zn on steel, provided the coating is damaged. This problem of rapid dissolution has been mitigated by alloying Zn with cobalt (Co) and iron (Fe) that will bring the E_0 closer to that of the steel substrate and herewith reduces the driving force for dissolution and enhances the corrosion resistance for a longer period of time. However, most of the researchers and industries emphasize on using Zn-Co and Zn-Fe alloys with lower amount of Co and Fe in the alloys [8,9]. At present, the optimum content of Co and Fe in the coating and their protection mechanism are still matters of controversy. These Zn alloy coatings are anomalous in nature (i.e. the less noble element Zn deposits preferentially) and work well in combination with chromate passivation [10]. However, these coatings, with low alloying element contents, possess E_0 values near pure Zn and the potential difference remains large: therefore the coating is still prone to rapid dissolution. Besides, due to the restrictions on the use of chromates in the near future and having relatively less corrosion resistant properties in the unpassivated state, these coatings cannot be considered as true replacements for Cd. There is little information available in literature on Zn-Co and Zn-Co-Fe electrodeposition with Co contents higher than 10 wt-% and their corrosion resistance, perhaps due to the anomalism associated with these coatings [11-14].

This chapter summarizes our investigations into the deposition characteristics of a wide range of Zn-Co and Zn-Co-Fe alloys as well as the corresponding corrosion protection, also in comparison with Zn and Cd coatings.

Copyright © 2010. Nova Science Publishers, Incorporated. All rights reserved.

Handbook of Material Science Research, Nova Science Publishers, Incorporated, 2010. ProQuest Ebook Central,

Table 1. Compositions of the various Zn, Co and ZnCo alloys electrolytes used for deposition

Electrolyte	$ZnCl_2$ (g/L)	$CoCl_2.6H_2O$ (g/L)	Molar Ratio Zn^{2+} / Co^{2+}	$\%Co^{2+}$
1	0	237.9	1.0	0
2	150	0	1.1	100
3	150	100	1.1 / 0.42	27.6
4	150	150	1.1 / 0.63	36.4
5	150	180	1.1 / 0.75	40
6	150	202	1.1 / 0.85	44
7	138	237.93	1.0 / 1.0	50

Table 2. Electrolyte formulation and process parameter settings for electrodeposition of Cd

Electrolyte composition	Conditions of deposition
110g/l NaCN 32 g/l CdO 15-60 g/l Na_2CO_3	pH: 13.0 ± 0.2 Temperature: 25 °C Current Density: 3.5 A/dm^2
2-3 min. rinsing in flowing cold water and hot air dry	

2. EXPERIMENTAL

2.1. Base Material and Surface Preparation

All coatings except those for the MASTMAASIS test were electrodeposited on both sides of 5.0×2.5×1.0 cm samples made of AISI 4340 steel. The samples were degreased for 10 min at 70 °C in alkaline solution (containing 40 g/l NaOH, 20 g/l Na_2CO_3, 20 g/l Na-gluconate and 10 ml of non-ionic surfactant), then the samples were electro-cleaned anodically for 3 min at 3.0 A/dm^2 in alkaline solution containing 40 g/l NaOH, 20 g/l of Na_2CO_3 and 10 ml Merck brand surfactant. Before the deposition the samples were neutralized and activated in 10% HCl for 3 min and rinsed with demineralised water. After these preparation steps, the samples were immediately put in the electrolyte in order to avoid the formation of an oxide layer on the surface.

The electrolytes for depositing both Zn-Co alloys were freshly prepared from double distilled demineralised water and analytical grade reagents. In case of Zn-Co-Fe alloy deposition a very small amount of citric acid was added to the bath as a chelating agent in order to prevent the precipitation of $Fe(OH)_3$. The bath was free of additives such as levelers or brighteners. The electrodeposition was carried out in a 3.0 liters open mouth beaker. Two pure Co (99.5% pure) anodes were placed on both sides of the flat sample. The purpose of Co

Copyright © 2010. Nova Science Publishers, Incorporated. All rights reserved.

Handbook of Material Science Research, Nova Science Publishers, Incorporated, 2010. ProQuest Ebook Central,

as anodes is to replenish and maintain the Co^{2+} content of the electrolyte and to avoid formation of $Co(OH)_2$ during the deposition process. After plating, the samples were thoroughly washed with demineralised water and ethanol, then dried with hot air and weighed.

2.2. Electrolyte composition for Zn-Co electrodeposition studies

The composition of blank solution was KCl 186g/L (2.5M), H_3BO_3 = 30g/L (0.5M) and NH_4Cl = 20g/L. All electrodepositions given in Table 1 were carried out at a constant bulk pH of 3.6 at 35°C and the electrolyte was continuously stirred during deposition.

2.3. Electrodeposition Parameter Settings for Electrochemical Studies

Cd was electrodeposited under galvanostatic conditions at a current density of 3.5A/dm^2 from a cyanide bath. The bath temperature was maintained at 25°C and the electrodeposition was done without bath agitation for ~7 minutes in order to get a coating thickness of ~10μm. An overview of the electrolyte composition and plating parameters are presented in Table 2.

The Zn and Zn-Co-Fe alloy coatings studied by electrochemical techniques were electrodeposited from chloride salts. A detailed overview of the composition of the electrolytes and plating parameters is presented in Table 3.

The electrodeposition was carried out at a temperature of 35°C at 2.0 A/dm^2 for various durations of time in order to electrodeposit a range of compositions. The parameters were adjusted to obtain a coating layer of ~10μm thickness.

The deposits were analyzed by Scanning Electron Microscopy (SEM). The composition of the coatings was determined by using Energy Dispersive X-ray (EDX) analysis at 20-30kV, as shown in Table 4.

2.4. Zn-Co Electrodeposition Studies by Cathodic Polarization Measurements

Cathodic Potentiodynamic Polarization studies were carried out in a three-electrode cell. The cathode (high strength steel substrate) was immersed in aerated solutions (containing Zn, Co, ZnCo and blank solutions) as mentioned in the composition section above. Saturated Calomel Electrode (SCE) was used as an external reference electrode and a Luggin capillary was used to keep the reference electrode as close as possible to overcome the ohmic resistance. A platinum mesh anode was used to complete the cell. A Solarton 1286 computer controlled potentiostat was used to apply the potential ranging from –0.4V to –1.5V vs. SCE at a scan rate of 1mV/sec and the resulting current density was recorded.

Copyright © 2010. Nova Science Publishers, Incorporated. All rights reserved.

Handbook of Material Science Research, Nova Science Publishers, Incorporated, 2010. ProQuest Ebook Central,

Table 3. Electrolyte formulation and process parameter settings for electrodeposition of Zn and Zn-Co-Fe coatings

Electrolyte composition	Conditions of deposition
136 g/l (1.0M) $ZnCl_2$ 23.8-238 g/l (0.1-1.0M) $CoCl_2 \cdot 6H_2O$ * 6.3 g/l (0.05M) $FeCl_2$ 180g/l (2.5M) KCl 20g/l (0.4M) $(NH4)_2Cl$ 25g/l (0.5M) H_3BO_3	pH: 3.5 ± 0.2 Temperature: 35 °C Current Density: 2.0 A/dm^2

* Zinc deposition is carried out from the same electrolyte without the addition of $CoCl_2$.

Table 4. Coating specimen codes and typical compositions of Zn-Co-Fe alloys

Coating specimen code	Element content (wt-%)
Zn-Co-Fe-1	0.7 %Co +0.3 %Fe
Zn-Co-Fe-2	1.5 %Co+0.3%Fe
Zn-Co-Fe-3	2.5 %Co +0.5 %Fe
Zn-Co-Fe-4	3.5 %Co +0.5 %Fe
Zn-Co-Fe-5	5.5 %Co +0.5 %Fe
Zn-Co-Fe-6	18 %Co +1 %Fe*
Zn-Co-Fe-7	32 %Co +1 %Fe*
Zn-Co-Fe-8	35 %Co +1 %Fe*
Zn-Co-Fe-9	40 %Co +1 %Fe*

* ± 0.2 wt-% Fe

2.5. Electrochemical Studies of Sacrificial Properties of Zn-Co and Zn-Co-Fe Coatings

Open Circuit Potential (OCP, for 1 hour and 120 hours) measurements were performed in an Avesta cell containing a platinum counter electrode and Saturated Calomel Electrode (SCE) as a reference electrode. All potential values in this paper are referred to SCE, unless mentioned else.

For the OCP measurements the samples were immersed in neutral 0.6 M NaCl solutions for 1 hour and 120 hours under free corroding conditions and the open circuit potential was recorded. The solution was neither de-aerated nor agitated during the measurement time and was kept at a constant temperature of 25°C.

Copyright © 2010. Nova Science Publishers, Incorporated. All rights reserved.

Handbook of Material Science Research, Nova Science Publishers, Incorporated, 2010. ProQuest Ebook Central,

2.6. Electrochemical Studies of Barrier Properties of Zn-Co and Zn-Co-Fe Coatings

2.6.1. Potentiodynamic Polarization Measurements

For the Anodic Potentiodynamic polarization (APP) measurements, the samples were immersed in quiescent 0.6 M NaCl solutions for 1 hour to establish a relatively constant OCP value. Then the anodic polarization measurements were recorded starting at -0.13V vs. OCP and ending at +0.5V vs. OCP. The scan rate was 0.5 mV/sec and solutions were neither de-aerated nor agitated during tests.

In case of the Cathodic polarization measurements (CPP) measurements, after 1 hour immersion in 0.6 M NaCl solution for stabilizing the OCP value, the system was polarized cathodically from the OCP value to -1.8 V vs. SCE. From the polarization curves, the corrosion current density and the corrosion potential were measured and verified by using both Tafel and Butler-Volmer equation fitting with CorrView Software. The Tafel region was taken at least 50mV from the OCP and in case diffusion limiting currents were observed in the cathodic region this was taken into account by the Corrview Software.

2.6.2. Linear Polarization Measurements

With LPR measurements, the polarization resistance of a material is defined as the slope of the potential-current density ($\Delta E/\Delta I$) curve at the free corrosion potential, yielding the polarization resistance R_p that can be related (for reactions under activation control) to the corrosion current by the Stern-Geary equation, as presented in Equation 1:

$$Rp = \frac{B}{I_{corr}} = \frac{(\Delta E)}{(\Delta I)} \Delta \mathrm{E} \to 0 \tag{1}$$

In which: Rp is the polarization resistance, I_{corr} the corrosion current, B is the proportionality constant, which can be calculated according to Equation 2 from b_a and b_c, the slopes of the anodic and cathodic Tafel slopes respectively.

$$B = \frac{b_a \times b_c}{2.3(b_a + b_c)} \tag{2}$$

During LPR the potential was swept linearly from –15mV to +15mV vs. OCP at a scan rate of 0.17 mV/sec. The scan was repeated 30 times and before starting the scan the OCP of each coating was measured for 1 hour. This allows the changes in the corrosion resistance of the coatings to be observed throughout the immersion. The appropriate values of b_a and b_c were obtained from the sweeps and were used in the calculation of the polarization resistance.

Copyright © 2010. Nova Science Publishers, Incorporated. All rights reserved.

Handbook of Material Science Research, Nova Science Publishers, Incorporated, 2010. ProQuest Ebook Central,

2.7. Salt Spray Testing

Neutral salt spray tests were conducted on coated samples in accordance with ASTM-B117. The time taken to 5% red rust on the panel surface was used to assess the corrosion performance of the coating. A MASTMAASIS (Modified ASTM Acetic Acid Salt Intermittent Spray) test was conducted according to ASTM G85-Annex 2. The test was run for 1000 hours and the time to the first occurrence of red rust was used to asses the corrosion protection offered by the coatings. In both tests the time recorded may only help in making a comparison of various coatings performances and should not be interpreted as an absolute measure of corrosion resistance.

For the MASTMAASIS test high alloy Zn-Co, low alloy Zn-Co-Fe and Cd coatings of 10 μm thickness were electrodeposited on two types of high strength steel, i.e. 300M and AerMet100, panels. In order to obtain sufficient adhesion on the high strength steels a sulfuric acid based nickel-strike was applied before depositing the coatings. After deposition the coatings were passivated and hydrogen embrittlement relieved by heat-treatment at 190°C for 24 hours. The high alloy Zn-Co, 30 wt-% Co, coating was deposited from the bath given in Table 3 with 1.0 M $CoCl_2 \cdot 6H_2O$, but without Fe addition. Cd coatings were deposited industrially and in the laboratory from the bath given in Table 2. The low alloy Zn-Co-Fe, 1 wt-% Co and 1 wt-% Fe, coatings were deposited using the commercial non-cyanide Zincrolyte® NCZ-191 process (Cookson Electronics). These coatings were prepared both on laboratory scale and on industrial scale at a job coater. The Cd and low-alloy Zn-Co-Fe were passivated with a chromate conversion coatings (CCC) in a solution of 200 g/l $Na_2Cr_2O_7.H_2O$ and 10 ml/l H_2SO_4 at pH 1 and room temperature for 20 seconds. The passivated coatings were dried at 70°C for 1 hour. The high alloy Zn-Co alloy could not be passivated using this process. Additionally high alloy Zn-Co and low-alloy Zn-Co-Fe were passivated by a trivalent chrome based conversion coating (TCC) as a less hazardous and environmentally more benign alternative to the hexavalent chrome based CCC. The thick yellow TCC was applied using the commercial Permapass® 3095 process (Cookson Electronics) at pH 1.8 and 60°C for 60 s. The passivated coatings were dried at 100^{0}C for 1 hour.

3. RESULTS AND DISCUSSION

3.1. Zn-Co Electrodeposition Studies by Cathodic Polarization Measurements

Figure 1 shows the cathodic potentiodynamic polarization curves for zinc, cobalt and Zn-Co alloys (electrolytes 1 to 6) on steel substrate from their respective plating solutions, as given in Table 1 [11]. In case of pure zinc, at potentials below the rest potential (-0.59V) till –1.04V the current density does not increase the same way as it did for the blank electrolyte. As the potential reaches –1.05V, the current density increases abruptly and corresponds to the onset of zinc deposition. The current density continues to increase until it reaches –1.25V and beyond which a limiting stage appears. The limiting current density is found to increase with the increase in temperature and stirring rate of the electrolyte (not shown here). In case of cobalt, the electrodeposition starts at about –0.60V in the given electrolyte. The current

Copyright © 2010. Nova Science Publishers, Incorporated. All rights reserved.

Handbook of Material Science Research, Nova Science Publishers, Incorporated, 2010. ProQuest Ebook Central,

density increases markedly below –0.60V and continues to do so until it reaches –0.82V. At this potential the current density does not increase further and the deposition reaches its limiting stage.

In case of cathodic potentiodynamic polarization for the Zn-Co alloys (curves 3 to 6), the curves follow pure cobalt curve in region A beyond the rest potential. Nevertheless, the current density in region A is suppressed and the curves deviate from the cobalt curve with the increase of Zn^{2+} ions in electrolytes and with increasing cathodic potential. The presence of Zn^{2+} ions in electrolyte appears to be responsible for the suppression of current density. With the further increase in potential, as shown in curves 3 to 6, a critical potential (C_p) is observed. Below Cp, the current density decreases abruptly (marked as region B) and the deposition in this region suffers from severe inhibition, as shown by the drop in cathodic current density. With the increase in Zn^{2+}/Co^{2+} ratio in electrolyte the current density corresponding to C_p decreases and the Zn-Co alloy deposition curves also shift further away from the Co deposition curve in both regions A and B. The current density continues to decrease till the potential reaches –1.04V to –1.05V for bath 3 to 6 respectively, at which the current density increases distinctly (marked as region C). This sudden rise in current density indicates that whatever was the cause of mitigation is removed and the current density increases till –1.25V followed by a region of limiting current density.

The electrodeposition of Zn-Co alloys is a complex process that involves inhibition and anomalism in different potential regions. It is divided into three potential regions i.e. a normal deposition region A (positive to Zn deposition potential E^0_{Zn} = -1.05V), an anomalous deposition region C (negative to E^0_{Zn}) and the region B located in between. A critical potential C_p is also reported here subsequent to region A for the first time in the polarization curves (to our knowledge) beyond which the deposition is sharply mitigated.

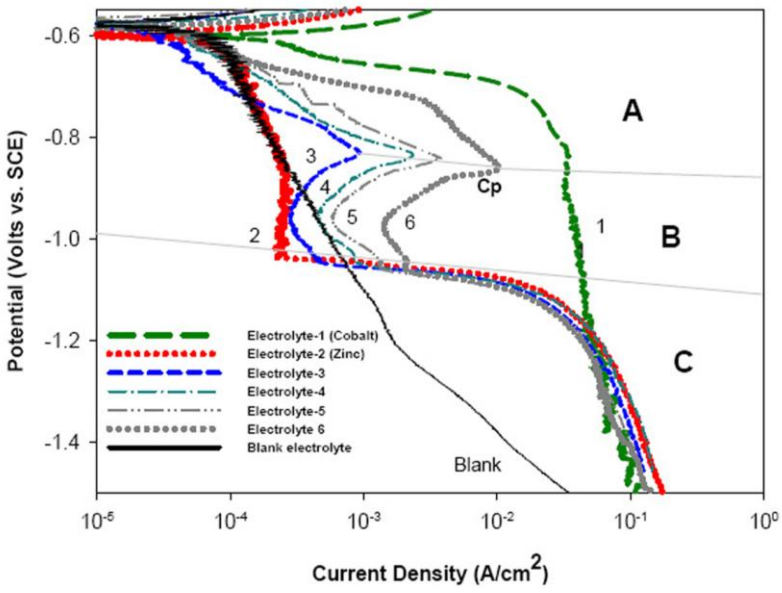


Figure 1. Cathodic potentiodynamic electrodeposition on steel substrate. The curves show changes in the deposition behavior with the variation in amount of Co^{2+} in the electrolyte. (curve 1) 100% Co, (curve 2) 100% Zn, (curve 3) 27.6 % Co, (curve 4) 36.4 % Co, (curve 5) 40 % Co and (curve 6) 44 % Co [11].

Copyright © 2010. Nova Science Publishers, Incorporated. All rights reserved.

Handbook of Material Science Research, Nova Science Publishers, Incorporated, 2010. ProQuest Ebook Central,

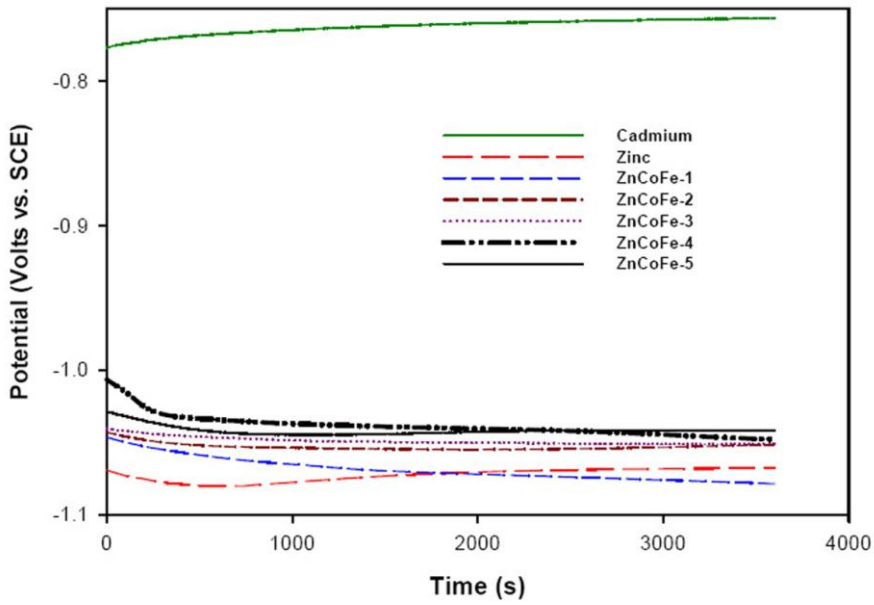


Figure 2. OCP curves of Cd, Zn and Zn-Co-Fe coatings 1 to 5 during 1 hour immersion in 0.6M NaCl solution at room temperature [14].

The deposition of Co starts around –0.6V through nucleation at a few active sites and increase steadily with potential until -0.75V mainly through growth mechanisms, also reported by other researchers [15,16]. In case of Zn deposition curve (between –0.80 to –1.04V), the current density remains lower than that for blank electrolyte. It appears that addition of Zn^{2+} in electrolyte has suppressed the other reduction reactions (mainly H^+ reduction). This suppression of H^+ reduction prior to –1.05V is related to the underpotential deposition (UPD) of zinc on steel substrate, as the UPD of Zn has previously been reported [18-26] on several substrates including steels. It is known that Zn has a lower exchange current density for H^+ reduction (i.e. in the order of $10^{-10.5}A/cm^2$) as compared to Fe (approximately $10^{-5.5}A/cm^2$) [27]. Therefore the low cathodic current density recorded in case of pure Zn deposition on steel substrate prior to –1.04V is due to UPD of Zn, which suppressed hydrogen evolution reaction (HER).

3.2. Electrochemical Studies of Sacrificial Properties of Zn-Co and Zn-Co-Fe Coatings

The corrosion resistance of Cd, Zn and a range of Zn-Co-Fe alloy coatings with a variation of Co (0.7-40 wt-%) and Fe (0.3-1.0 wt-%) in the deposits are studied and compared. The specimen codes and compositions of all Zn-Co-Fe alloy coatings, measured by EDX, are presented in Table 4.

The sacrificial properties of metal coatings are investigated by the measurement of the OCP with time. The OCP measurement results obtained in quiescent 0.6 M NaCl solutions are shown in Figures 2 and 3 for 1 hour of immersion and in Figure 4 for 120 hours of immersion [14].

Copyright © 2010. Nova Science Publishers, Incorporated. All rights reserved.

Handbook of Material Science Research, Nova Science Publishers, Incorporated, 2010. ProQuest Ebook Central,

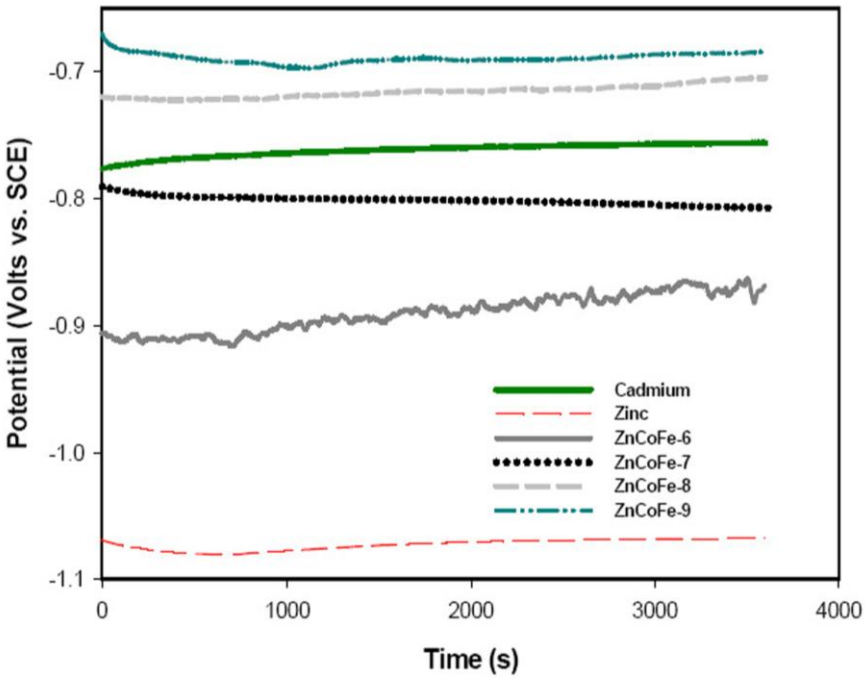


Figure 3. OCP curves of Cd, Zn and Zn-Co-Fe coatings 6 to 9 during 1 hour immersion in 0.6M NaCl solution at room temperature [14].

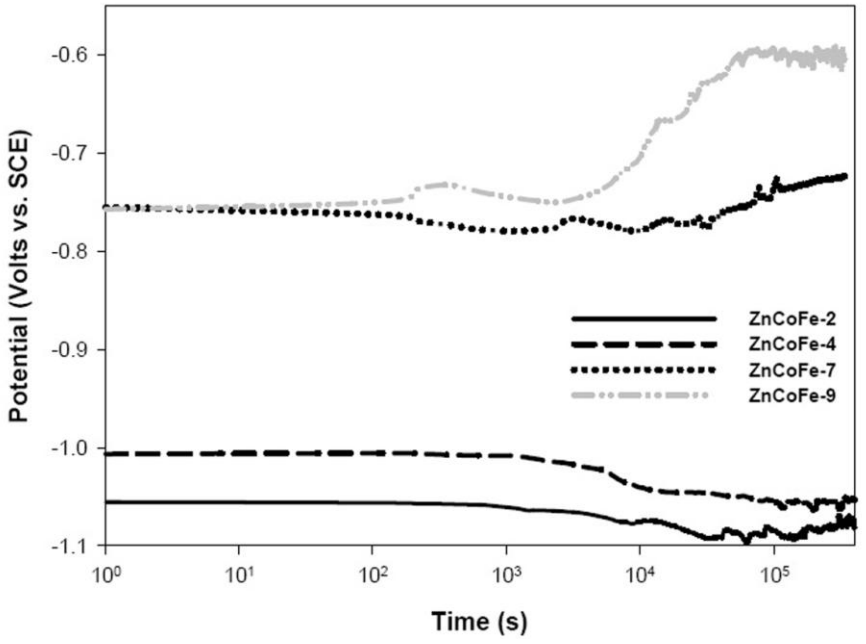


Figure 4. OCP curves of Zn-Co-Fe coatings 2, 4, 7 and 9 during 120 hours immersion in 0.6 M NaCl solution at room temperature [14].

Copyright © 2010. Nova Science Publishers, Incorporated. All rights reserved.

Handbook of Material Science Research, Nova Science Publishers, Incorporated, 2010. ProQuest Ebook Central,

An OCP value of -0.68V vs. SCE was measured for AISI 4340 steel in 0.6 M NaCl solutions. Figure 2 shows a comparison between Zn, Zn-Co-Fe alloy coatings 1 to 5 (with relatively low Co content between 1-7 wt-%) and a Cd coating. It is evident from Figure 2 that the OCP curves for Zn-Co-Fe alloys 1 to 5 are very close to that of the pure Zn. A large potential difference between these low Co content Zn-Co-Fe coatings and the steel substrate exists. In contrast to Figure 2, the OCP curves for Zn-Co-Fe alloys 6 to 9 (with relatively high Co content between 18-38 wt-%), shown in Figure 3, are closer to that of Cd. The potential difference between these Zn-Co-Fe alloys and steel is smaller compared to that between Zn and steel. With further increase of the Co content (> 40 wt-%) in the Zn-Co-Fe alloy the OCP becomes more noble than steel and would not be able to protect the steel sacrificially. In general, it is shown in Figures 2 and 3 that as the Co content of the Zn-Co-Fe alloys increases the OCP shifts towards more positive potential until it becomes electropositive to steel.

Figure 4 shows the evolution of the OCP for both low and high Co content Zn-Co-Fe alloys during immersion for 120 hours in 0.6 M NaCl solution [14]. It is shown that the OCP for Zn-Co-Fe-2 and Zn-Co-Fe-4 alloys did not change much compared to that for the 1 hour immersion measurement. In the case of the higher Co content Zn-Co-Fe-7 and Zn-Co-Fe-8 alloys the OCP has shifted to more positive potentials for longer exposure times. In case of Zn-Co-Fe-8 alloy the OCP has even shifted to a more positive value than steel. This indicates that after long immersion period the coatings have become more noble than steel.

The sacrificial behavior of various coatings can be predicted with reasonable accuracy by comparing their open circuit potentials with that of the substrate material (AISI 4340 steel) [2,7,28]. Table 5 shows that all coatings of interest are to some or more extent electronegative to steel (-0.68V vs. SCE in 0.6 M NaCl) and are expected to provide a certain degree of sacrificial protection to steel.

Table 5. Open circuit potential (OCP) and corrosion current density (i_{corr}) values after 1 hour of immersion in 0.6 M NaCl [14]

Coating specimen code	OCP (V vs. SCE) after 1hr	i_{corr} ($\mu A/cm^2$)
Cadmium	-0.79	2.6
Zinc	-1.07	4.4
Zn-Co-Fe-1	-1.07	5.1
Zn-Co-Fe-2	-1.06	7.3
Zn-Co-Fe-3	-1.05	6.4
Zn-Co-Fe-4	-1.05	4.8
Zn-Co-Fe-5	-1.04	2.8
Zn-Co-Fe-6	-0.81	4.3
Zn-Co-Fe-7	-0.78	0.6
Zn-Co-Fe-8	-0.76	0.4
Zn-Co-Fe-9	-0.70	0.2

Copyright © 2010. Nova Science Publishers, Incorporated. All rights reserved.

Handbook of Material Science Research, Nova Science Publishers, Incorporated, 2010. ProQuest Ebook Central,

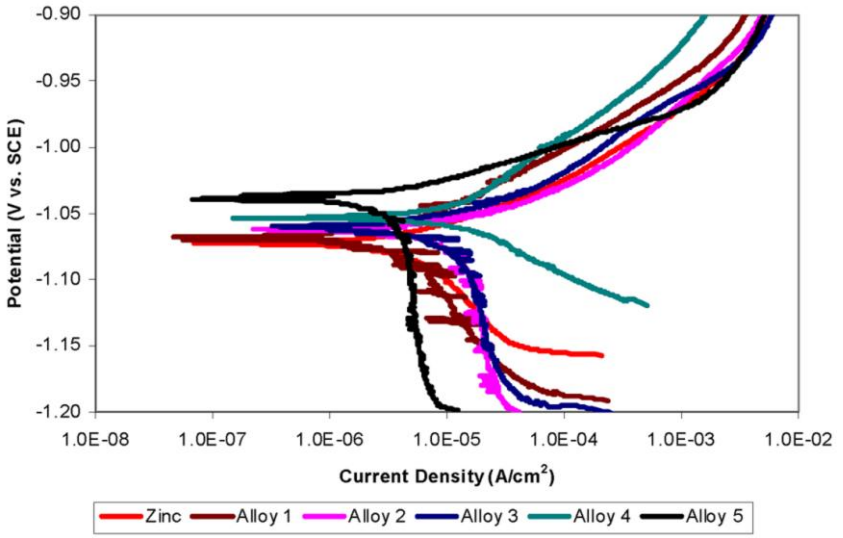


Figure 5. Polarization curves for Zn and Zn-Co-Fe coatings 1 to 5 after 1 hour immersion in 0.6 M NaCl solution at room temperature [14].

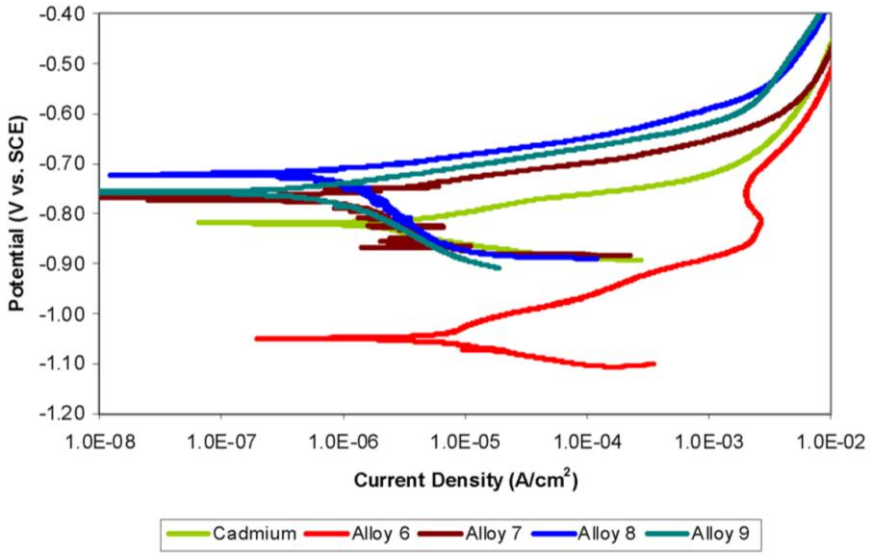


Figure 6. Polarization curves for Cd and Zn-Co-Fe coatings 6 to 9 after 1 hour immersion in 0.6 M NaCl solution at room temperature [14].

A large potential difference between the lower Co content Zn-Co-Fe coatings and the steel substrate exists. It can therefore be predicted from the relative potential difference that these coatings are highly sacrificial to steel and due to a large driving force these are prone to rapid dissolution in a corrosive environment, once the base steel substrate is exposed. After 120 hours of immersion in a 0.6M NaCl electrolyte the OCP value did not increase significantly which can be correlated to the relatively high Zn content and low alloying element concentration.

Copyright © 2010. Nova Science Publishers, Incorporated. All rights reserved.

Handbook of Material Science Research, Nova Science Publishers, Incorporated, 2010. ProQuest Ebook Central,

The potential difference between the higher Co content Zn-Co-Fe alloys and steel is smaller as compared to that between Zn and steel. Therefore it can be predicted that these Zn-Co-Fe alloy coatings would dissolve less rapidly than the lower Co content Zn-Co-Fe alloy coatings, provided the base steel substrate is exposed, and would protect the exposed steel substrate for a longer period of time. With further increase of the Co content (> 40 wt-%) in the Zn-Co-Fe alloy the OCP would become noble to steel and the coating would not be able to protect the steel sacrificially.

It is found that the OCP for Zn-Co-Fe-7 and Zn-Co-Fe-8 alloys has shifted to more positive potentials for longer exposure times. In case of Zn-Co-Fe-8 alloy the OCP has even shifted to a more positive value than steel. This indicates that after a long immersion time the coatings have become noble to steel. This shift in potential can be correlated to the selective dissolution of Zn from the alloy coating, leaving behind deposits that are rich in Co and causing ennoblement of the surface. This process is also known as the de-zincification mechanism and is reported by other researchers as well [2,29,30]. The ennoblement is a surface phenomenon and results in passivation of the surface. If a coating is scratched then the sacrificial nature of the coating will still be able to play a role.

3.3. Electrochemical Studies of Barrier Properties of Zn-Co and Zn-Co-Fe Coatings

3.3.1. Potentiodynamic Polarization Measurement

Anodic potentiodynamic polarization measurement (APP) are used to determine the barrier resistance of the coatings by measuring the corrosion current density. APP sweeps were carried out on all electrodeposited coatings (i.e. Cd, Zn, Co and Zn-Co-Fe alloys) after 1 hour immersion in 0.6 M NaCl solutions and shown in Figures 5 and 6 [14]. For each coating, a relatively large increase in current density is obtained for a small increase in polarization overpotential, indicating that they are essentially active in this environment. Corrosion current density values, presented in Table 5, were determined from the cathodic sweeps using Tafel extrapolation techniques.

In case of Zn-Co-Fe alloys 1 to 5 (with relatively low Co content), as shown in Figure 5 and Table 5, the corrosion current density is relatively high compared to Cd and is close to that of pure Zn. This suggests that they will provide less efficient barrier protection and will dissolve faster as compared to Cd under the corrosive conditions investigated. Figure 6 (and as listed in Table 5) shows a comparison of Cd and relatively high Co content Zn-Co-Fe alloys (18-40 wt-% Co) [14]. It is shown that alloy 6 (i.e. 18 wt-% Co) shows a relatively high corrosion current density compared to the other high Co content alloys and Cd. In particular, the Zn-Co-Fe alloys 7 to 9 (with Co content higher than 32 wt-%) show significantly lower corrosion current density values as compared to Zn-Co-Fe alloy 6, Zn and Cd coatings indicating a relatively low dissolution rate under the conditions investigated.

For Zn-Co-Fe alloys 7 and 9 the corrosion potential moves to more positive values. It is found during the cathodic polarization that from the corrosion potential to -1.25 V vs. SCE the main cathodic reaction responsible for the current density is the oxygen reduction that produces OH^- ions, also previously reported by Hinton and Wilson for zinc [31]. The cathodic reduction reaction results in a local increase of pH which is reported to facilitate the

Copyright © 2010. Nova Science Publishers, Incorporated. All rights reserved.

Handbook of Material Science Research, Nova Science Publishers, Incorporated, 2010. ProQuest Ebook Central,

formation of $Zn(OH)_2$ on the surface [29,31-34]. At -1.35 V, for pure zinc and Zn-Co-Fe alloys 1, 4 and 5, the cathodic current density varies with the potential in a complex manner. The reason for such a behavior is unknown but also found by other researchers [31]. It suggests that other reactions, in addition to oxygen reduction, are occurring on the surface.

In case of Cd the excellent corrosion behavior is due to the formation of a CdO layer on the surface, which prevents further dissolution. In aqueous environment the initial corrosion product layer observed on the surface of zinc coating is $Zn(OH)_2$ which is a good barrier layer and a poor semi conductor. However, in case of pure zinc and Zn alloys with lower alloying elements the hydroxide layer rapidly de-hydrates to form ZnO, which is voluminous, less adherent and a poor insulator. It is reported by several researchers [29,32-38] that the presence of (iron group metals) Co and Fe at the surface of the alloy contribute to an improved level of protection by increasing the stability of the hydroxide layer, avoiding formation of ZnO, then further forming ZnOHCl which is an insulator. The lower barrier resistance shown by pure Zn and Zn-Co-Fe alloys with lower Co content (alloys 1 to 5) can be attributed to the formation of a ZnO layer. The excellent barrier resistance of the Zn-Co-Fe 7 to 9 alloys can be attributed to the presence of $Zn(OH)_2$, which is a good barrier layer and a poor semi conductor. Furthermore, the dezincification process leaves behind Co at the surface and results in ennoblement of the surface, which also contributes to the barrier resistance as Co itself is very stable substance in a corrosive medium [2,7,30,35]. In addition, due to local pH rise Co may also further convert to $Co(OH)_2$ which is again very stable [32] and a very good insulator as well.

This is illustrated in Figure 7 that shows the anodic polarization behavior obtained for an electrodeposited pure Co coating on steel after 1 hour immersion in quiescent 0.6 M NaCl solution [14]. Figure 7 shows a clear passive corrosion behavior at relatively small anodic overpotential in contrast to the anodic behavior of the Zn-Co-Fe alloys with relatively high cobalt content level (30-40 wt-% Co). The passive region, corresponds to a relatively low dissolution rate by the formation of a stable oxide-hydroxide layer in near neutral solutions [32].

Figure 8 shows the potentiodynamic polarization curves for Zn-Co-Fe-2, 4, 7 and 9 alloys with extended immersion times of 120 hours in 0.6 M NaCl solutions [14]. Comparison of the anodic polarization curves for Zn-Co-Fe-2 and 4 alloys after 1 and 120 hours indicates that the curves do not change after immersion for 120 hours in the electrolyte and the corrosion current density remains relatively high, as presented in Table 6. The Zn-Co-Fe-7 alloy (with 32 wt-% Co) shows a further decrease in corrosion current density after 120 hours immersion compared to that after 1 hour of immersion only.

Table 6. Open circuit potential (OCP) and corrosion current density (i_{corr}) values after 120 hours of immersion in 0.6M NaCl [14]

Coating specimen code	OCP (V vs. SCE) after 120 hrs	i_{corr} ($\mu A/cm^2$)
Zn-Co-Fe-2	-1.08	4.1
Zn-Co-Fe-4	-1.04	3.9
Zn-Co-Fe-7	-0.72	0.1
Zn-Co-Fe-9	-0.64	1.1

Copyright © 2010. Nova Science Publishers, Incorporated. All rights reserved.

Handbook of Material Science Research, Nova Science Publishers, Incorporated, 2010. ProQuest Ebook Central,

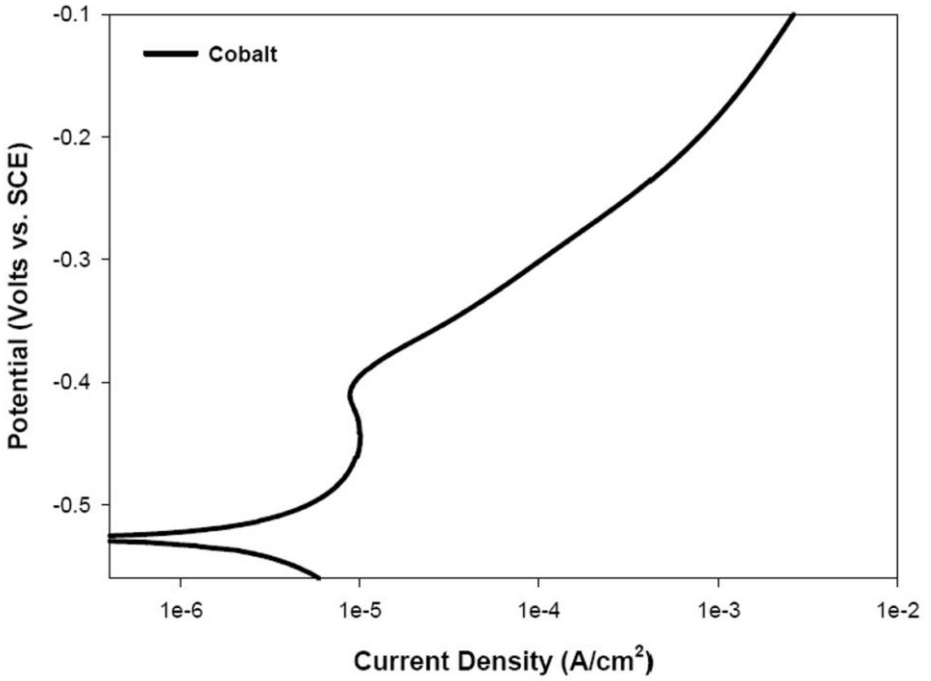


Figure 7. Polarization curve for a pure cobalt coating after 1 hour immersion in 0.6M NaCl solution at room temperature [14].

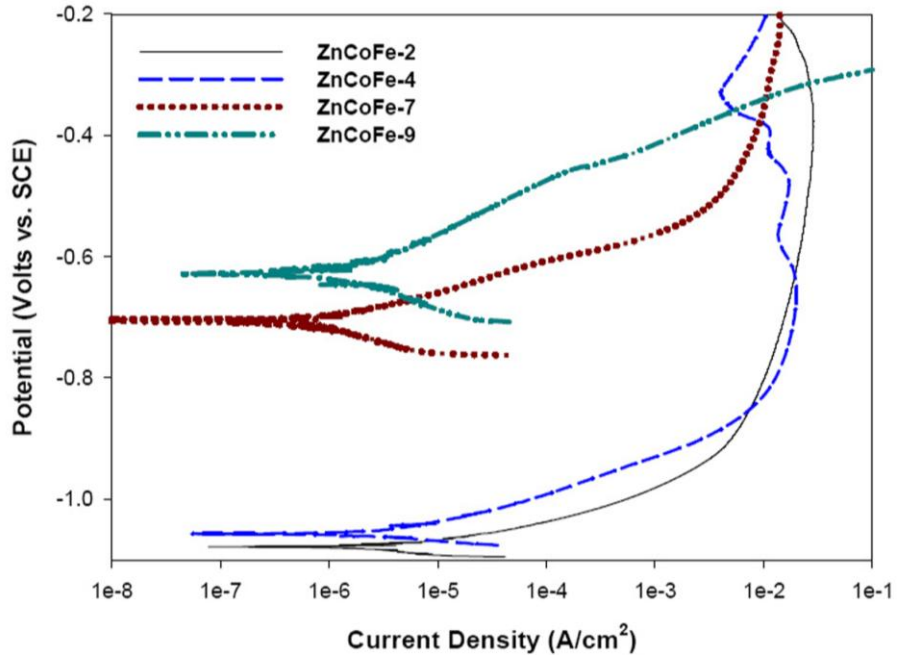


Figure 8. Polarization curves for Zn-Co-Fe coatings 2, 4, 7 and 9 after 120 hours immersion in 0.6 M NaCl solution at room temperature [14].

Copyright © 2010. Nova Science Publishers, Incorporated. All rights reserved.

Handbook of Material Science Research, Nova Science Publishers, Incorporated, 2010. ProQuest Ebook Central,

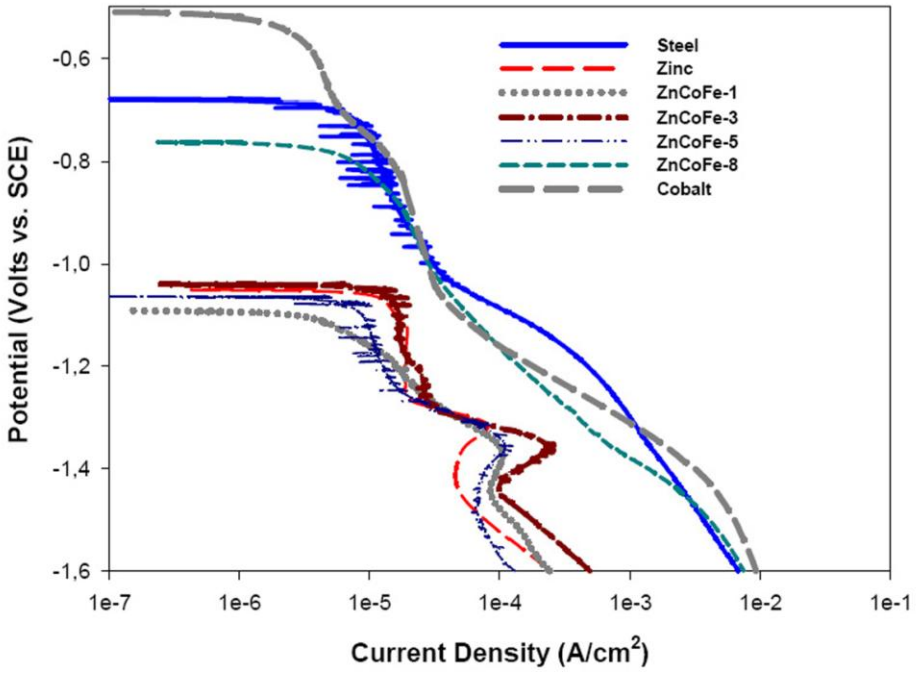


Figure 9. Cathodic polarization curves for steel, Co, Zn and Zn-Co-Fe coatings 1, 3, 5 and 8 obtained during immersion in 0.6 M NaCl solution at room temperature [14].

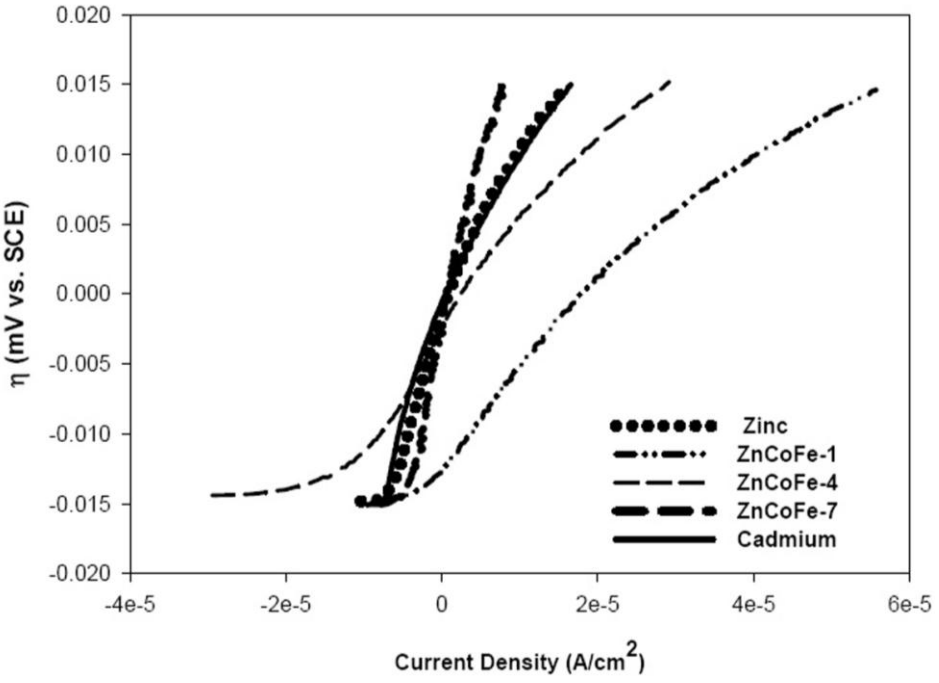


Figure 10. Linear polarization curves for Cd, Zn and Zn-Co-Fe coatings 1, 4 and 7 after 11 hours immersion in 0.6 M NaCl solution at neutral pH and room temperature [14].

Copyright © 2010. Nova Science Publishers, Incorporated. All rights reserved.

Handbook of Material Science Research, Nova Science Publishers, Incorporated, 2010. ProQuest Ebook Central,

The cathodic polarization curves obtained for Zn, Co and Zn-Co-Fe alloys are shown in Figure 9 [14]. The cathodic polarization curve for steel substrate is also shown in Figure 9 for comparison. The curves for Zn and Zn-Co-Fe alloys with relatively low Co contents (i.e. 1, 4, 5 wt-% Co) show similar cathodic behavior. These curves show a complex reduction behavior at -1.3V vs. SCE, also reported by other researchers [31]. The curves for the Zn-Co-Fe alloys with 40 wt-% Co show a cathodic polarization behavior that is similar to pure cobalt and steel.

3.3.2. Linear Polarization Measurements

Linear polarization measurements (LPR) studies are carried out on pure Cd, pure Zn and Zn-Co-Fe alloys. The resulting graphs of overpotential vs. current density for Cd, Zn and Zn-Co-Fe-1, 4 and 7 alloys after 11 hours of immersion in 0.6 M NaCl solutions are shown in Figure 10 [14]**.** The slopes of these lines yield the value of the polarization resistance (R_p). This overpotential vs. current density plot suggests that Cd and Zn-Co-Fe-7 alloy have a rather steep slope indicating very good barrier properties. The less steep slope in case of the Zn-Co-Fe-1 and Zn-Co-Fe-4 alloys indicates a poor barrier resistance against dissolution, herewith suggesting a higher corrosion rates for these alloys. Figure 11 shows the plot of polarization resistance values as a function of time for all above-mentioned coatings [14]. It is evident from Figure 11 that the polarization resistance is very high for Zn-Co-Fe alloys 2, 7 and 8. The resistance value increases further for Cd and Zn-Co-Fe-7 alloy with time under open circuit conditions. The polarization resistance for Zn-Co-Fe-1, 4 and 5 is lower and does not improve over a longer immersion period. It is noticeable that the resistance increases with increasing Co content with the exception of Zn-Co-Fe-2 alloy which shows excellent barrier properties.

3.4. Salt Spray Testing

The barrier resistance determined by the electrochemical techniques are further investigated by the Neutral salt spray tests. A comparison of corrosion performance for various coatings is given in Figure 12 [14]. Although less pronounced as in the electochemical measurement this test confirms the superior corrosion resistance for Cd and Zn-Co-Fe alloys 7, 8 and 9 with a high Co content compared to lower Co content alloys 1 to 5 and pure Zn.

The time to the first occurrence of red rust in the MASTMAASIS test is shown in Figure 13 for the various coatings [14]. It can be seen that the corrosion resistance of the trivalent chrome (TCC) passivated high alloy zinc coating is equal or better than the other tested coatings on both types of steel. Of the various Cd coatings only the industrial chromate (CCC) passivated coating on AerMet 100 gives a similar corrosion protection. Of the various low alloy Zn-Co-Fe coatings only the chromate (CCC) passivated coatings show an equal time to first red rust occurrence. However it has to be mentioned that the industrial low alloy Zn-Co-Fe coating were considerably thinner, i.e. 6-8 μm compared to 10 μm, than the other coatings. As the coating thickness strongly affects the time to red rust formation it can not be excluded that also trivalent chrome (TCC) passivated low alloy Zn-Co-Fe offers a similar corrosion protection as a trivalent chrome (TCC) passivated high alloy Zn-Co coating.

Copyright © 2010. Nova Science Publishers, Incorporated. All rights reserved.

Handbook of Material Science Research, Nova Science Publishers, Incorporated, 2010. ProQuest Ebook Central,

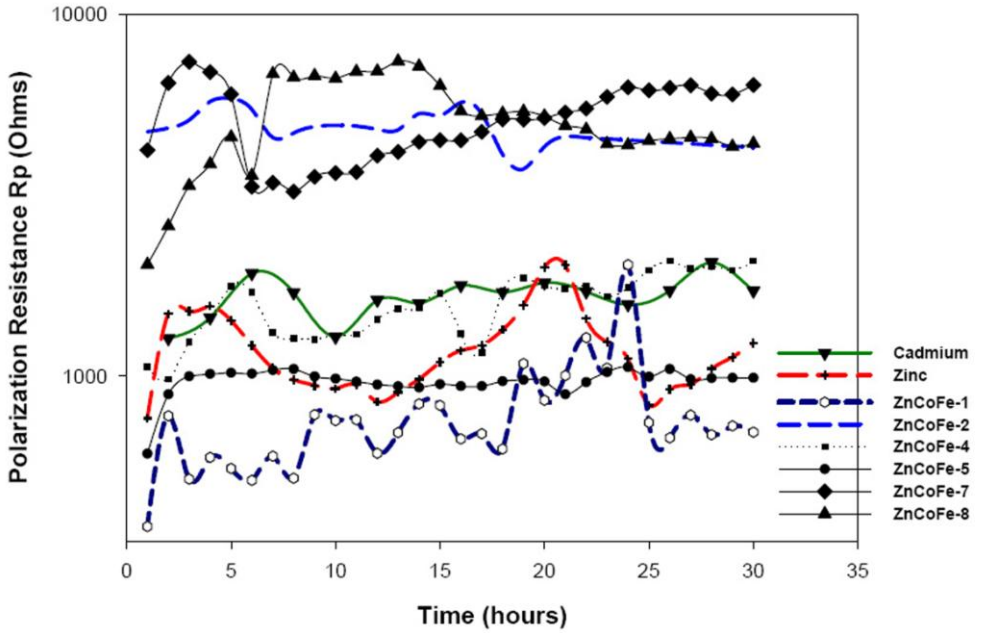


Figure 11. Plot of polarization resistance versus time for Cd, Zn and Zn-Co-Fe coatings 1, 2, 4, 5, 7 and 8 in 0.6 M NaCl solution at neutral pH and room temperature [14].

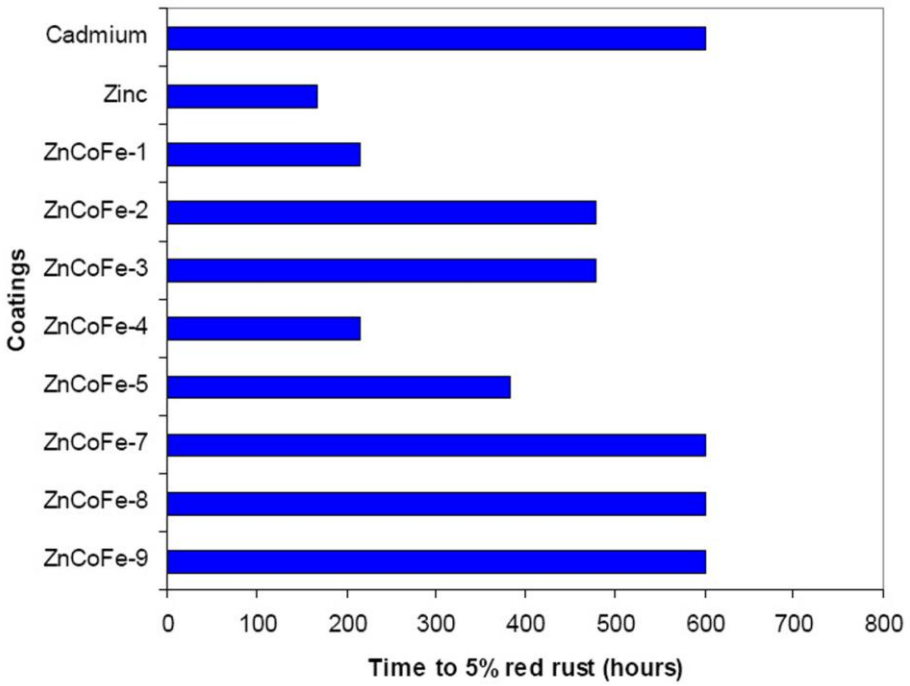


Figure 12. Comparison of the performance of coated steel sheet exposed to neutral salt fog, according to ASTM B117 (Average coating thickness ~10 μm) [14].

Copyright © 2010. Nova Science Publishers, Incorporated. All rights reserved.

Handbook of Material Science Research, Nova Science Publishers, Incorporated, 2010. ProQuest Ebook Central,

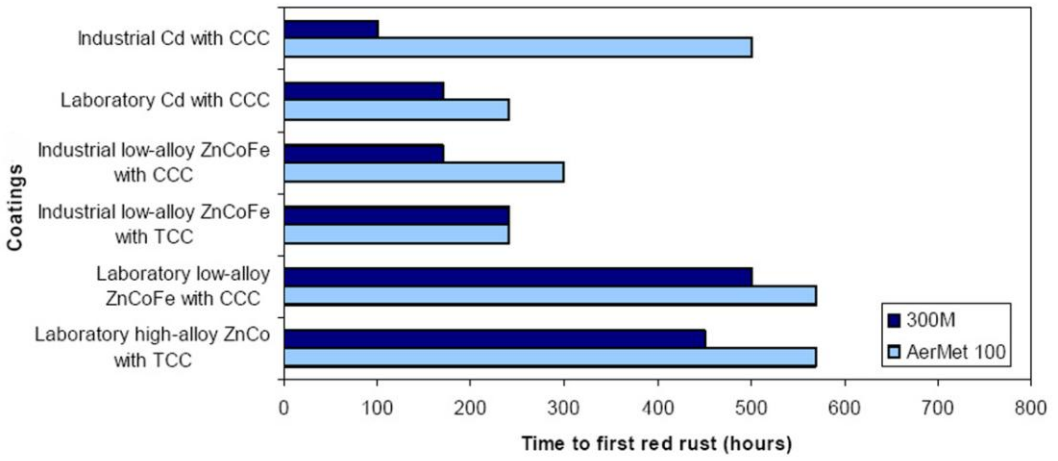


Figure 13. Time to first occurrence of red rust on high alloy Zn-Co, low alloy Zn-Co-Fe and Cd coatings on 300M and AerMet 100 steel in the MASTMAASIS test [14].

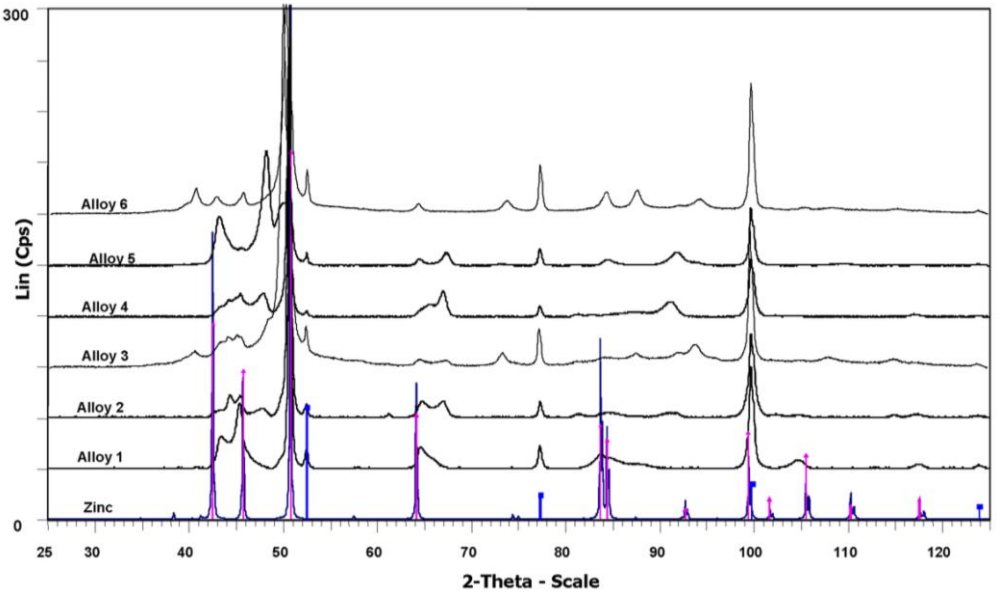


Figure 14. The XRD pattern of Zn and Zn-Co-Fe coatings 3 to 6 determined with CoK-α radiation [14].

3.5. X-ray Diffraction of Zn-Co-Fe Coatings

The presence of one or more phases on a coating surface can also influence the measured corrosion current density values. Higher corrosion current density values for the Zn-Co-Fe-alloys can be attributed to the presence of more phases of Zn-Co-Fe alloys on the surface as verified by the several peaks in the XRD patterns (shown in Figure 14) that indicate highly crystalline structures [14]. Some other researchers have also reported the presence of various phases in electrodeposited Zn-Ni alloys (Zn-Ni) with varying Ni contents [33].

Copyright © 2010. Nova Science Publishers, Incorporated. All rights reserved.

Handbook of Material Science Research, Nova Science Publishers, Incorporated, 2010. ProQuest Ebook Central,

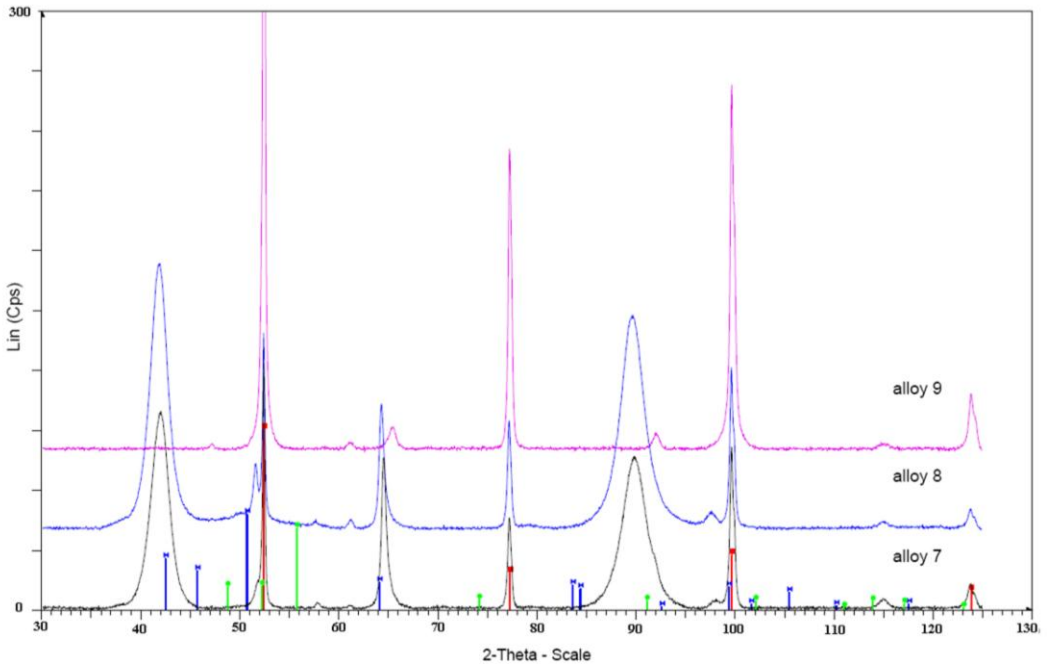


Figure 15. The XRD pattern of Zn-Co-Fe coatings 7 to 9 determined with CoK-α radiations [14].

As these local microstructural variations adopt different equilibrium potentials in aqueous solutions these are susceptible to local galvanic corrosion. On this basis it is expected that the corrosion rates of the single phase alloys is lower than the binary or multiphase alloys.

The lower corrosion current densities for the Zn-Co-Fe-alloys 2, 3 and 7-9 are related to the presence of a single phase. For Co contents higher than 30 wt-% the Zn-Co-Fe alloys consist of a single phase that contains nano-crystallites (unidentified), as shown by the peak broadening effects of XRD in Figure 15 [14].

4. CONCLUSIONS

It is usually considered that the inhibition of Fe-group metals occur subsequent to Nernst equilibrium potential corresponding to Zn. But it is noticed in this investigation that inhibition occurs a lot earlier than that. However, there are different reasons for inhibition or anomalism during deposition in different potential regions. In regions A and B, (usually considered the normal deposition region), the difference of work function values $\Delta\phi$ between the two metals (Zn/Fe or Zn/Co) causes UPD of Zn, which results in suppression of Co deposition and hydrogen reduction. The inhibition becomes severe subsequent to critical potential, which is due to UPD of Zn on discharged Co^{2+} or developed Co clusters at both the nucleation and growth stage. With an increase of Zn^{2+}/Co^{2+} ratio in the bath the critical potential shifts upwards (towards positive potential) and as a result the percentage of Co in deposit also decreases prior to the critical potential. In the potential region C, cathodic to Nernst equilibrium potential for Zn (known as the anomalous region), another mode of inhibition takes place during codeposition that results in a higher amount of Zn as compared to Co. In

Copyright © 2010. Nova Science Publishers, Incorporated. All rights reserved.

Handbook of Material Science Research, Nova Science Publishers, Incorporated, 2010. ProQuest Ebook Central,

this anomalous codeposition, the faster deposition kinetics of Zn as compared to that of Co is considered responsible. It is found that increasing the Co^{2+}/Zn^{2+} ratio (and operating temperature of the electrolyte) assist in overcoming the anomalism.

In the present investigation the corrosion resistance in terms of sacrificial properties of electrodeposited Zn-Co-Fe alloys (up to 40 wt-% Co and 1 wt-% Fe) was studied in 0.6M NaCl solution. The results of the Zn-Co-Fe alloy coatings were also related to those for electrodeposited zinc and cadmium coatings. It is found that Zn-Co-Fe alloys with relatively low Co content (< 7 wt-%) show OCP values near pure zinc and the potential values do not change significantly for immersion periods up to 120 hours. A large OCP difference between these coatings and steel results in a high driving force for dissolution if the coating is damaged and the underlying steel is exposed. A higher corrosion rate can be attributed to the presence of binary or multiphase regions present on the surface resulting in local galvanic corrosion. For the Zn-Co-Fe alloys with relatively high Co content (> 32 wt-%) the OCP was shown to be very close to that for a cadmium coating and the OCP difference between steel and the coatings is also lower (like that for cadmium) compared to the Zn-Co-Fe alloys with relatively low Co content. The Zn-Co-Fe coatings with relatively high Co content are supposed to protect the steel substrate for a longer period of time. However, due to the de-zincification mechanism, surface ennoblement with Co occurs and the OCP moved to significantly more positive values for longer immersion times.

The corrosion resistance determined by the electrochemical techniques are confirmed by salt spray testing showing the superior corrosion resistance for Cd and high Co content Zn-Co-Fe alloys and lower performance of alloys with lower Co contents and pure Zn both in unpassivated as trivalent or hexavalent chrome passivated.

ACKNOWLEDGMENTS

This research was carried out under the project number MC6.02122 in the framework of the Strategic Research program of the Materials Innovation Institute (M2i) in The Netherlands (www.m2i.nl).

REFERENCES

[1] H. Morrow, Cadmium Council Inc. Reston, Va., 1995, 201.
[2] K.R. Baldwin, C.J.E Smith, Trans. IMF, 1996, *74*, 202.
[3] ASM Handbook on Plating and Surface Finishing, Chapter 13, 2005, 36.
[4] W.H. Safranek, Plating Surf. Finish., 1997, 84, 45.
[5] E. Budman, R.R. Sizelove, Chemtech Finishing System Inc., Farmington Hills MI and McDermid Inc., Kearny NJ, 1993.
[6] G.D. Wilcox and D.R. Gabe, *Corros. Sci.*, 1993, *35*, 1251.
[7] K.R. Baldwin, M.J. Robinson, C.J.E. Smith, *Br. Corros. J.*, 1994, *29*, 209.
[8] Kirilova, I. Ivanov, St. Rashkov, *J. Appl. Electrochem.*, 1997, *27*, 1380.
[9] N.R. Short, A. Abibsi, J.K. Dennis, *Trans. Inst.*, 1986, *67*, 73.

Copyright © 2010. Nova Science Publishers, Incorporated. All rights reserved.

Handbook of Material Science Research, Nova Science Publishers, Incorporated, 2010. ProQuest Ebook Central,

[10] Brenner, *Electrodeposition of Alloys, Principles and Practice*, Chapter 30, Academic Press, New York, 1963, 194.
[11] Z.F. Lodhi, J.M.C. Mol, W.J. Hamer, H.A. Terryn, J.H.W. de Wit, *Electrochim. Acta*, 2007, *52*, 5444.
[12] Z.F. Lodhi, J.M.C. Mol, A. Hovestad, H. Terryn, J.H.W. de Wit, *Surf. Coat. Technol.*, 2007, *202*, 84.
[13] Z.F. Lodhi, F.D. Tichelaar, C. Kwakernaak, J.M.C. Mol, H. Terryn, J.H.W. de Wit, *Surf. Coat. Technol.*, 2008, *202*, 2755.
[14] Z.F. Lodhi, J.M.C. Mol, A. Hovestad, L. 't Hoen-Velterop, H. Terryn, J.H.W. de Wit, *Surf. Coat. Technol.*, 2009, *203*, 1415.
[15] M.Yunus, C. Capel-Boute, C.Decroly, *Electrochim. Acta*., 1965, *10*, 885-900.
[16] M. Alcala, M. Gomez, E. Valles, *J. Electroanal. Chem.*, 1994, *370*, 73.
[17] G. Roventi, T. Bellezze, R. Fratesi, *Electrochim. Acta*, 2006, *51*, 2691.
[18] M.J. Nicol and H.I. Philip *J. Electroanal. Chem.*, 1976, *70*, 233.
[19] J.H.O.J. Wijenberg, J.T. Stevels, J.H.W. De Wit, *Electrochim. Acta*, 1997, *43*, 649.
[20] T.Ohtsuka, A. Komori, *Electrochim. Acta*, 1998, *43*, 3269.
[21] P.Y.Chen, I-W.Sun, *Electrochim. Acta*, 2001, *46*, 1169.
[22] J-F. Hung, I-W. Sun, *J. Electrochem. Soc.*, 2004, *151*, C 8 .
[23] J. Vaes, J. Fransear, J.P. Celis, *J. Electrochem. Soc.*, 2002, *149*, C 567.
[24] D.M.Kolb, M. Przasnyski, H. Gerischer, *J. Electroanal. Chem.*, 1974, *54*, 25.
[25] J. Dogel, W. Freyland, *Phys. Chem. Chem. Phys*, 2003, *5*, 2484.
[26] J.O.M. Bockris, S.U.M. Khan, *Surface Electrochemistry*, Chapter 3, 376 Plenum press, New York, 1993.
[27] Z. Li, J. Cai and S. Zhou. *Trans. IMF*, 1999, *77*, 149.
[28] K.R. Baldwin, R.I. Bates, R.D. Arnell, C.J.E. Smith, *Corros. Sci.*, 1996, *38*, 155.
[29] K.R. Baldwin, M.J. Robinson, C.J.E. Smith, *Corros. Sci.*, 1994, *36*, 1115.
[30] M. Gravilla, J.P. Millet, H. Mazille, D. Marchandise, J.M. Cuntz, *Surf. Coat. Technol.*, 2000, *123*, 164.
[31] B.R.W. Hinton, L.Wilson, *Corros. Sci.*, 1985, 29, 967.
[32] M. Pourbaix, *Atlas of electrochemical equilibria in aqueous solutions*, NACE Publishing, Houston, 1974.
[33] Shibuya, T. Kurimoto, M. Kimoto, *Sumitomo Search*, 1985, 31, 75.
[34] F.J. Miranda, I.C.P. Margarit, O.R. Mattos, O.E. Barcia, R. Wiart, *Corrosion*, 1999, 732.
[35] T. Zhang, Y. Zhe-Long, A. Mao-Zhang, L. Wen-Liang, Z. Jing-Shuang, *Trans. IMF*, 1999, 77, 246.
[36] J.R. Vilche, K. Juttner, W.J. Lorentz, W.Kautek, W. Paatsch, M.H. Dean, U. Stimming, *J. Electrochem. Soc.*, 1989, 136, 3773.
[37] R. Ramanauskas, P. Quintana, P. Bartolo-Parez, L. Diaz-Ballote, *Corrosion*, 2000, 56, 588.
[38] N. Boshkov, K. Petrov, S. Vitkova, S. Nemska, G. Raichevsky, *Surf. Coat. Technol.*, 2002, 157, 171.

Copyright © 2010. Nova Science Publishers, Incorporated. All rights reserved.

Handbook of Material Science Research, Nova Science Publishers, Incorporated, 2010. ProQuest Ebook Central,

In: Handbook of Material Science Research
Editors: C. René and E. Turcotte, pp.369-393
ISBN 978-1-60741-798-9
© 2010 Nova Science Publishers, Inc.

Chapter 9

QUASI ONE-DIMENSIONAL CDSE NANOWIRES: GROWTH, STRUCTURE, AND POLARIZED PHOTOLUMINESCENCE

C.X. Shan*, D.Z. Shen, and X.W. Fan
Key Laboratory of Excited State Processes, Changchun Institute of Optics,
Fine Mechanics and Physics,
Chinese Academy of Sciences, Changchun, 130033, China

Cadmium selenide (CdSe) is an important II-VI compound semiconductor. It can be crystallized into hexagonal wurtzite or cubic zincblende structure. Table I shows some basic properties of this material. Because of its direct band gap and high quantum efficiency, CdSe has long been regarded as a promising candidate for applications in optoelectronic devices such as light-emitting devices [1], photodetectors [2], solar cells [3], and sensors [4]. Although much attention has been paid to CdSe, most of the research on CdSe has focused on zero-dimensional structures, such as quantum dots and nanocrystals. Especially, CdSe nanocrystals have attracted much attention in recent years because they have relatively high quantum efficiency and the emission spectrum of the nanocrystals can be adjusted to cover the whole visible range by just changing the size of the nanocrystals [5-8]. In 1990s, the research on CdSe had boomed thanks to the appearance of CdSe self-assembled quantum dots [9-11].

Quasi-one-dimensional (1D) nanoscaled semiconductors, such as nanowires, nanobelts, nanotubes, nanoneedles and nanorods (in brief, all the forms are called nanowires hereafter), have been subjects of intensive research since the detailed report on the discovery of carbon nanotubes [12]. What motivates the research is the unique properties proposed or demonstrated in these kinds of materials, such as possible high emission efficiency [13], super mechanical toughness [14], low lasing threshold [15], etc. Also nanowires can act as building blocks for a series of nano-scaled devices, such as light-emitting diodes, lasing diodes, photodetectors, field-effect transistors, gas-sensors and solar cells. However, compare

* Corresponding author: Changchun Institite of Optics, Fine Mechanics and Physics, Chinese Academy of Sciences, No.3888 Dongnanhu Road, Changchun, 130033, China. E-mail: phycxshan@yahoo.com.cn .

Copyright © 2010. Nova Science Publishers, Incorporated. All rights reserved.

Handbook of Material Science Research, Nova Science Publishers, Incorporated, 2010. ProQuest Ebook Central,

with the large numbers of reports on 0D quantum dots or nanocrystals, the reports on quasi-one-dimensional (1D) nanostructures are still very limited. Furthermore, most of the 1D nanostructures are prolonged nanocrystals or quantum rods with very small size (several nanometers in diameter and tens of nanometers in length) [16-18], while for the so-called nanowires with relatively large size (several tens of nanometers in diameter, and several tens of micrometers in length), still less reports can be found [19-24].

Table I. Some basic properties of CdSe

Molecular formula	CdSe
Color	Yellow to red
Molar mass	191.36 g/mol
Structure	Wurtzite (Hexagonal) or zincblende (Cubic)
Space group	$F\bar{4}3m - Td^2$ for zincblende structure $P6_3mc - C_{6V}^4$ for wurtzite strucure
Lattice constants	Wurtzite: a= 4.30 Å, c= 7.01 Å Zincblende: a= 6.05 Å
Density:	5.810 g/cm^3
Debye temperature	181.7 K
Melting point	1541 K
Effective mass	Electron: 0.13 m_0 Hole: 0.45 m_0
Band gap	Wurtzite: 1.84 eV (0 K), 1.74 eV (300 K) Zincblende: 1.75 eV (0 K), 1.67 eV (300 K)
Band gap temperature coefficient	-4.6×10^{-4} eV/K
Electron mobility	5000 cm^{2}V^{-1}S^{-1} at 80 K 660 cm^{2}V^{-1}S^{-1} at 300 K 200 cm^{2}V^{-1}S^{-1} at 800 K
Electron drift mobility	720 cm^{2}V^{-1}S^{-1} at 300 K
Hole mobility	40 cm^{2}V^{-1}S^{-1} at 300 K
Intrinsic carrier concentration	$n \approx p$, 6×10^{13}cm^{-3} at 800 K 6×10^{16}cm^{-3} at 1300 K

Copyright © 2010. Nova Science Publishers, Incorporated. All rights reserved.

Handbook of Material Science Research, Nova Science Publishers, Incorporated, 2010. ProQuest Ebook Central,

Phonon energy	TO: 23.0 meV, LO: 27.0 meV TA: 7.4 meV, LA: 13.6 meV
Second order elastic moduli	$c_{11} = 74.6GPa$ $c_{12} = 46.1GPa$ $c_{33} = 81.7GPa$ $c_{44} = 13.0GPa$ $c_{66} = 14.3GPa$
Young's Modulus	5×10^{11}dyne/cm^2
Thermal Expansion Coef. (500 K):	$\alpha_1=6.26\times10^{-6}$/K, $\alpha_3=4.28\times10^{-6}$/K
Electromechanical coupling factor	$k_{31} = 0.084$ $k_{33} = 0.195$ $k_{15} = 0.131$ $k_t = 0.124$
Dielectric constant	$\varepsilon^{\perp}(0) = 9.29$ at 300K $\varepsilon^{\perp}(0) = 9.15$ at 100K $\varepsilon^{\parallel}(0) = 10.16$ at 300K $\varepsilon^{\parallel}(0) = 9.29$ at 100K $\varepsilon^{\parallel}(\infty) = 6.30$ at 300K $\varepsilon^{\parallel}(\infty) = 6.30$ at 100K $\varepsilon^{\perp}(\infty) = 6.20$ at 300K $\varepsilon^{\perp}(\infty) = 6.20$ at 100K
Specific Heat:	0.49 J/gK
Thermal conductivity (at 25 ^{o}C):	0.04 W/cmK
Max. Transmittance (λ=2.5-15 μm):	$\geq$ 71 %
Refractive index (λ=10.6 μm):	2.4
Sound velocity	3.86 km/s (*l*), 1.54 km/s (*t*)

In this chapter, we'd like to provide a brief overview of the literature on the growth and characterization of quasi-1D CdSe nanostructures, and the overview will be divided into three parts: 1. The preparation of metastable 1D CdSe nanostructures; 2. Controlled growth of CdSe nanowires; 3. Polarized photoluminescence of individual CdSe nanowires.

Copyright © 2010. Nova Science Publishers, Incorporated. All rights reserved.

Handbook of Material Science Research, Nova Science Publishers, Incorporated, 2010. ProQuest Ebook Central,

I. THE PREPARATION OF METASTABLE 1D CDSE NANOSTRUCTURES

CdSe bulk crystals usually crystallize in hexagonal wurtzite phase under normal conditions, and CdSe films can be grown in zincblende form on GaAs substrate using metalorganic chemical vapor deposition (MOCVD) technique [25]. More importantly, most of the earlier reported CdSe nanowires are crystallized in wurtzite structure. Since ZnSe, the most frequently used compound to alloy with CdSe, nucleates in zincblende structure at normal conditions, it is of interest to obtain similar structured CdSe for synthesizing nano-heterostructures and alloy nanostructures with zincblende ZnSe.

Yang *et al.* prepared CdSe nanowires using a poly(vinyl alcohol) (PVA)-assisted ethylenediamine solvothermal method [26], the morphology of the CdSe nanowires are shown in Fig.1. The PVA used in the preparation process is favorable for the formation of nanowires. However, the CdSe nanowires was a mixture of wurtzite and zincblende phase.

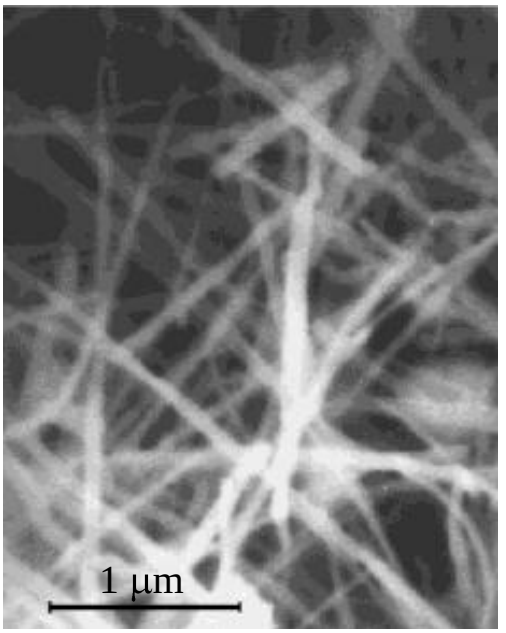


Figure 1. Scanning electron microscopy image of the CdSe nanowires reported by Yang *et al.* [26].

Zhao *et al.* prepared single-phased metastable zincblende CdSe nanowires in anode aluminum oxide (AAO) templates using a photochemical route [21]. In this route, porous AAO template with the pore size of about 80 nanometers was placed in aqueous solution containing cadmium salts ($CdCl_2$) and selenium (Na_2SeSO_3). Under the illumination of ultraviolet light, the Cd and Se precursor will react to form CdSe precipitates, and these precipitates will fill the pores of the AAO template. After growth, the AAO was removed by chemical etching. In this way, CdSe nanowires were resulted. The morphology of the CdSe

Copyright © 2010. Nova Science Publishers, Incorporated. All rights reserved.

Handbook of Material Science Research, Nova Science Publishers, Incorporated, 2010. ProQuest Ebook Central,

nanowires is shown in Fig.2. X-ray diffraction (XRD) reveals that the CdSe nanowires were crystallized in zincblende phase. However, the CdSe nanowires obtained in this way were polycrystalline in structure, comprised of mainly nano-scaled grains. In 2004, Ma *et al.* reported single-crystalline CdSe nanostructures for the first time [22]. The nanostructures they obtained is mostly saw-like shaped and some of them are belt-like shaped, the morphology of which is shown in Fig. 3.

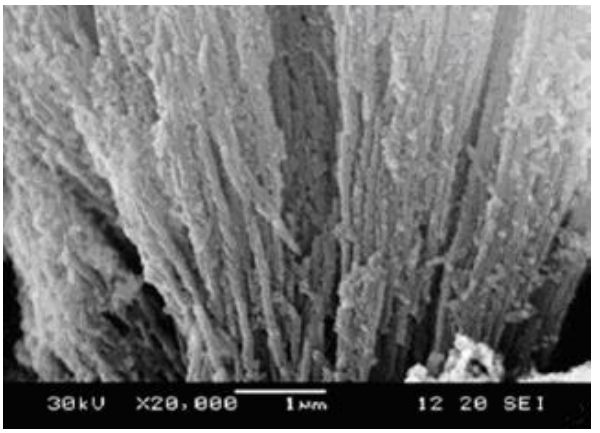


Figure 2. Scanning electron microscopy image of CdSe nanowires grown in AAO by Zhao *et al.* [21].

We have prepared pyramid-like shaped CdSe nanostructures on Si substrate using MOCVD technique by employing gold (Au) as catalysts [27], the morphology of these nanostructures can be seen in Figure 4. As shown in the figure, without Au catalysts, only roughly equiaxed crystal grains appear in the scanning electron microscopy (SEM) image, while high-density quasi-1D nanostructures can be achieved for the sample with Au catalyst. The above results indicate that the formation of the 1D nanostructures was catalyzed by gold. Higher magnification image of the nanostructures shows that they taper the diameter from the base to the tip significantly and their length is in the range of 3 to 10 μm; their base size varies with the length and can reach nearly 1 μm for the long ones. However, the tip, if not broken off, is always very sharp. The radius of curvature (tens of nanometers) of the tips is comparable to the characteristic size of commonly studied nanowires. To investigate the shape of the nanostructures in detail, the sample was tilted by 30˚ with respect to the electron beam, as shown in the inset in Figure 4(c). It clearly shows three sides, indicating the triangular pyramidal shape of the nanostructures. We note that besides the pyramids, there are always some equiaxed grains covering the substrate, as can be seen in Figure 4(b).

XRD diffraction of the samples covered with pyramid-shaped nanostructures gives two sets of peaks, corresponding to the two possible structures of CdSe, while the sample without Au catalyst give only one set of diffraction peaks corresponding to wurtzite CdSe, as shown in Figure 5. The peaks labeled by Miller indices (hkl) belong to the zincblende structure and those by hkl, without parentheses for distinction, to the wurtzite structure. The peak marked by "▼" is an artifact of the XRD equipment. The two peaks marked by "∗" are characteristic peaks of zincblende CdSe. One can see that the pattern of the sample containing only equiaxed grains show only characteristics peaks from wurtzite CdSe besides the diffraction

Copyright © 2010. Nova Science Publishers, Incorporated. All rights reserved.

Handbook of Material Science Research, Nova Science Publishers, Incorporated, 2010. ProQuest Ebook Central,

from the Si substrate, while that of the sample containing both pyramides and equaxed grains shows also two peaks at around 61.20^o and 67.45^o besides the characteristic peaks of wurtzite CdSe and Si substrate. The difference in the XRD patterns of the samples containing only equiaxed grains, and the samples containing both pyramids and equiaxed grains, suggests that the pyramids are zincblende while the grains are wurtzite in structure. The suggestion is verified by electron diffraction and photoluminescence (PL) measurements on individual pyramids as will be discussed in the following paragraph.

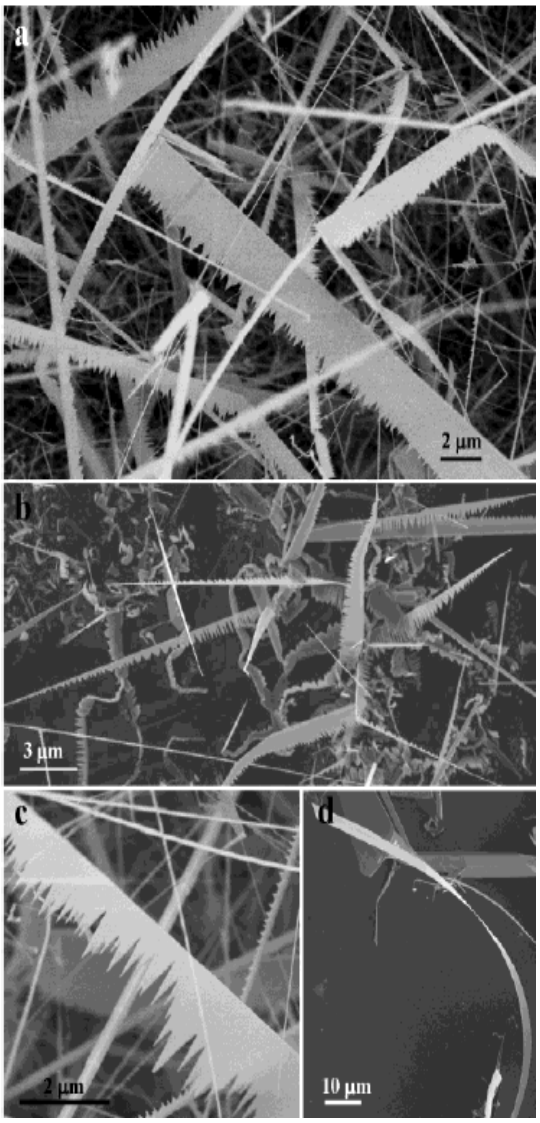


Figure 3. SEM images of CdSe nanosaws (a, b, c) and nanobelts (d) [22].

Copyright © 2010. Nova Science Publishers, Incorporated. All rights reserved.

Handbook of Material Science Research, Nova Science Publishers, Incorporated, 2010. ProQuest Ebook Central,

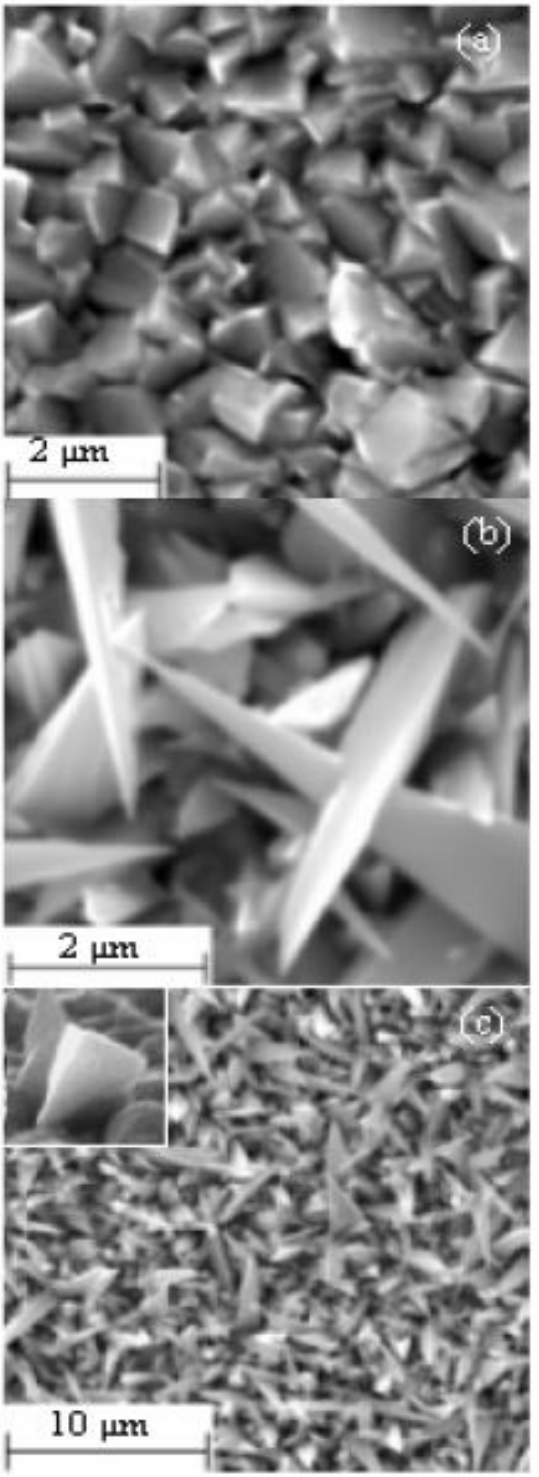


Figure 4. SEM images of CdSe deposited on Si without (a) and with Au catalyst (b); (c) shows the low-magnified SEM image of the image in (b), and the inset in (c) is an enlarged image of an individual CdSe pyramid taken by tilting the sample during the SEM measurement.

Copyright © 2010. Nova Science Publishers, Incorporated. All rights reserved.

Handbook of Material Science Research, Nova Science Publishers, Incorporated, 2010. ProQuest Ebook Central,

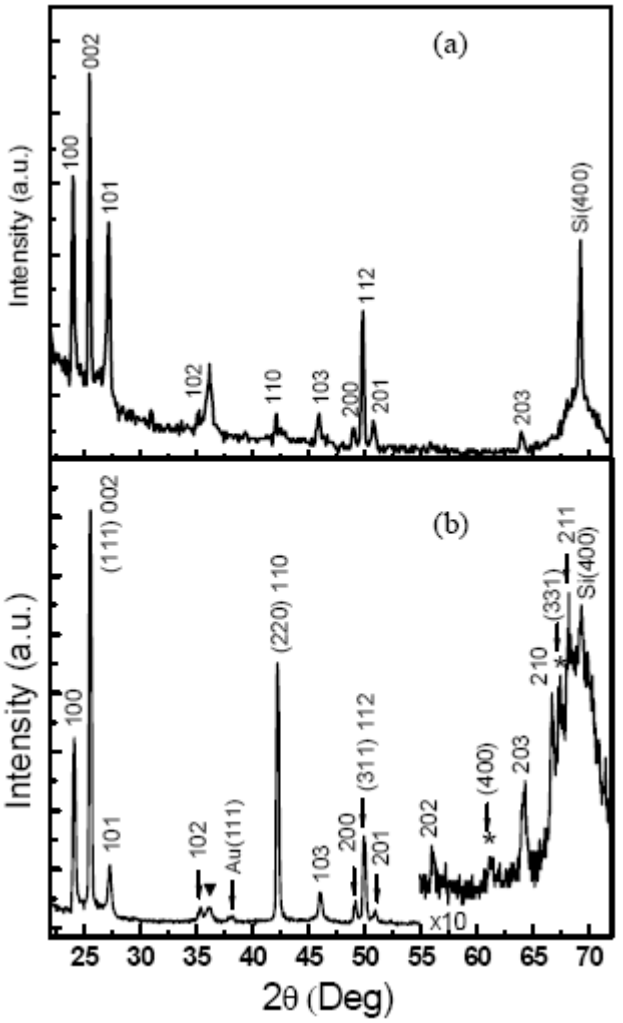


Figure 5. XRD patterns of the sample containing only equiaxed grains (a) and that of the sample containing both pyramids and equiaxed grains (b); the intensity in the range 55 to 72° of (b) was multiplied by 10 to bring out the weaker peaks. Note that Miller indices (hkl) in parentheses denote the diffraction peaks from cubic structure and hkl from hexagonal structure.

Figure 6(a) shows the transmission electron microscopy (TEM) image of a broken-off piece of a pyramid, and 3(b) shows the selected area electron diffraction (SAED) pattern of the pyramid near its very tip. This diffraction pattern, which can be identified unambiguously as the [011] zone of cubic zincblende CdSe, clearly demonstrates the single-crystalline cubic structure of the pyramids. The chemical composition of the pyramids was determined by energy-dispersive x-ray spectroscopy (EDX), from which a typical spectrum is shown in Figure 6(c). Only Cu, Cd and Se were found; of these the Cu peak originates from the TEM grid used. Quantitative analysis determines the atomic composition as 51.1% Cd and 48.9% Se, which is almost stoichiometric within experimental errors. The high resolution TEM image of the pyramids is shown in Figure 6(d), which confirms the single-crystalline zincblende structure of the CdSe pyramids.

Copyright © 2010. Nova Science Publishers, Incorporated. All rights reserved.

Handbook of Material Science Research, Nova Science Publishers, Incorporated, 2010. ProQuest Ebook Central,

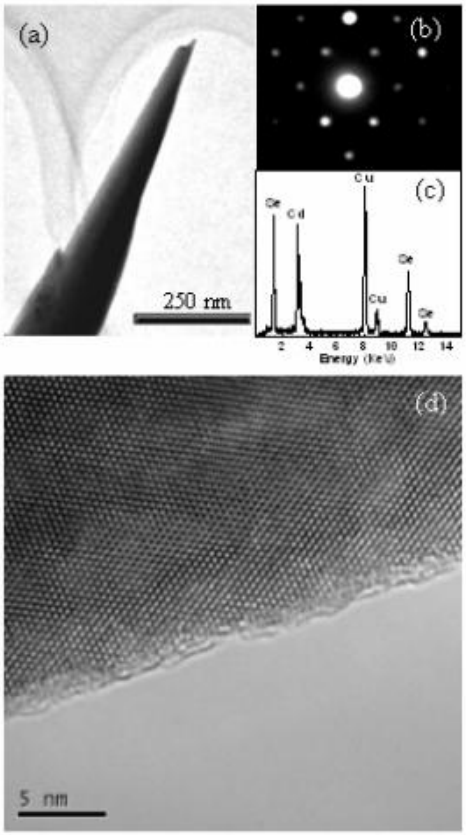


Figure 6. (a) TEM image of a portion of a CdSe pyramid, (b) SAED pattern of the pyramid, the beam is along the cubic [011] zone axis and (c) EDX spectrum of the pyramids, in which the Cu related peaks are from the grid used, (d) High-resolution TEM image of the pyramids.

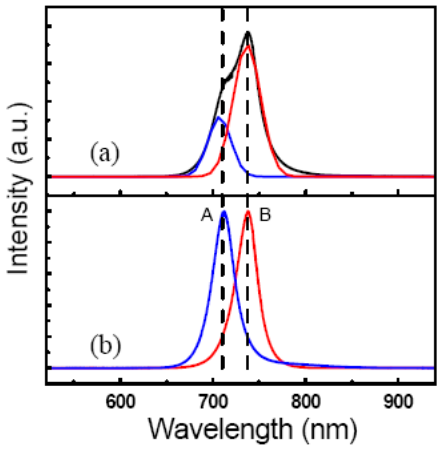


Figure 7. Room temperature PL spectra of the sample containing both equiaxed grains and pyramids (a) and the sample containing only equiaxed grains (peak Ain (b)) and an individual pyramid (peak B in (b)). In (a) the original peak can be fitted well by two Gaussian curves. The two vertical dashed lines show the alignment of the peaks in (a) and (b).

Copyright © 2010. Nova Science Publishers, Incorporated. All rights reserved.

Handbook of Material Science Research, Nova Science Publishers, Incorporated, 2010. ProQuest Ebook Central,

Under a high magnification microscope objective, it is possible to concentrate on individual pyramids and have their PL spectra measured. We found that even with the micro-PL setup, interference signal from the equiaxed grains underneath the pyramids could not be completely blocked off. Complete isolation of the pyramids from the grains was achieved by transferring a few pyramids from the as-synthesized samples to a bare Si wafer. The low density of the transferred pyramids ensured that only an individual pyramid was studied. A typical PL spectrum of the sample containing both equiaxed grains and pyramids is shown in Figure 7(a). For comparison, the spectrum of the sample containing only equiaxed grains (peak A) and an isolated pyramid (peak B) are also plotted in Figure 7(b). The spectrum in Figure 7(a) contains an asymmetric peak, which can be de-convoluted into two Gaussian curves located at 707 and 737 nm. The reported room temperature band gap of wurtzite CdSe is 1.738 eV and that of zincblende CdSe is 1.66 eV [28, 29]. The fact that the peak positions of peaks A and B are close to the reported band gaps lead us to assign them as the near-band-edge (NBE) emissions from wurtzite- and zincblende-structured CdSe, respectively; the former comes from the equiaxed grains and the latter from the pyramids. This assignment is consistent with the XRD pattern that has two sets of diffraction peaks, and can be further confirmed by noting that the spectrum of the wurtzite-structured equiaxed grains contains a single, nearly Gaussian peak at 711 nm and that of the individual pyramids also contains a single Gaussian peak, but at 738 nm, as shown in Figure 7(b).

The formation mechanisms of zincblende pyramids and the wurtzite grains appear different. We think that when the Si substrate was heated to the growth temperature (450 °C), the Au catalysts will aggregates into small islands, leaving areas between them depleted of Au. Aided by the catalytic reactions, zincblende-structured leaders emerge on the Au islands and grow rapidly along one direction. The growth of the leader is probably influenced more by kinetics than thermodynamics. Secondary thickening by overgrowth on the leaders results in the pyramids of zincblende structure [30]. Without catalysts, the growth is slower and nearly equiaxial. Because wurtzite structure is more stable for CdSe at normal conditions, equiaxed wurtzite grains are formed in the area without Au. Since both mechanisms occur at the same time but on different areas of the substrate, both zincblende pyramids and wurtzite equiaxed grains are obtained in the sample with Au catalyst, while only wurtzite equaxed grains are achieved in the sample without Au catalyst.

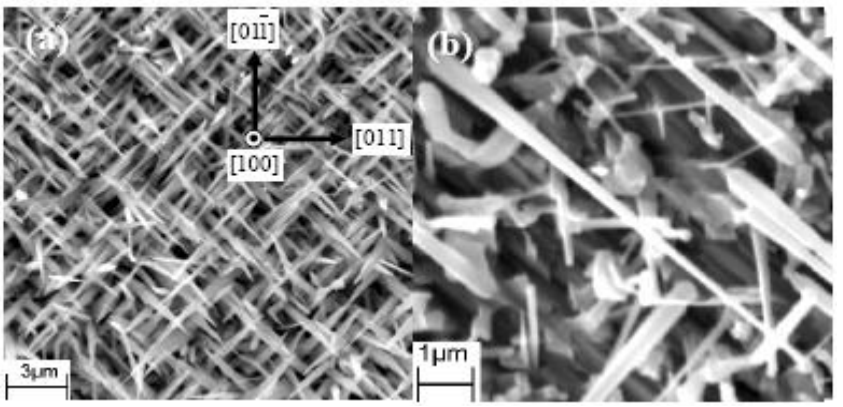


Figure 8. (a) Plan-view SEM image of the as-synthesized quasi-1D metastable zincblende CdSe nanostructures on GaAs (100) substrate. (b) A magnified image reveals the shape of the nanostructures.

Copyright © 2010. Nova Science Publishers, Incorporated. All rights reserved.

Handbook of Material Science Research, Nova Science Publishers, Incorporated, 2010. ProQuest Ebook Central,

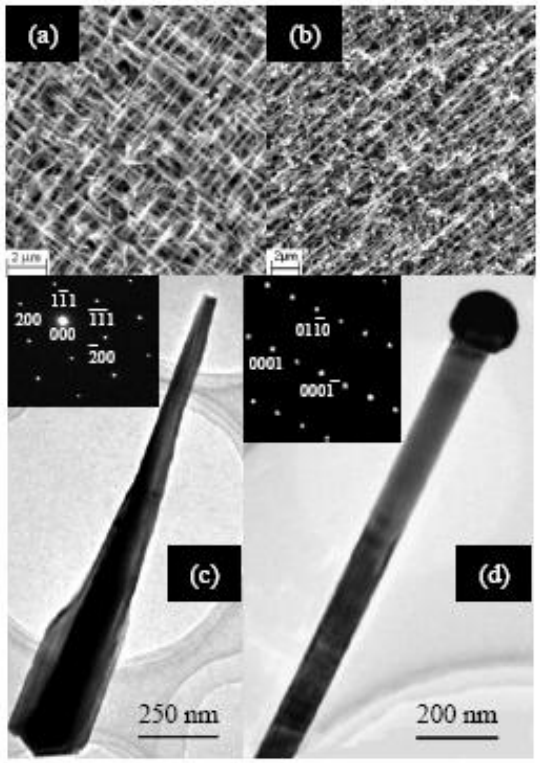


Figure 9. SEM images of the CdSe nanostructures grown at different temperatures, (a) 430°C, (b) 500°C; (c) and (d) are TEM images of individual nanoneedles (left) and nanorods (right), the inset shows the electron diffraction pattern of these two kinds of structures.

By selecting GaAs as the substrates, oriented 1D metastable zincblende CdSe nanostructures can be obtained [31], as shown in Figure 8. A high density of nanostructures, whose projected lengths on the substrate are orthogonal to each other, covers the substrate. Their projected lengths on the GaAs(100) substrate are along the <010> directions as shown in the plan-view image of Figure 8(a). By rotating and tilting the sample during SEM observations, it is found that the growth directions of the nanostructures possess four-fold symmetry and are about 45° to the surface normal. From these we deduce that they grow along the <110> directions of the substrate. To investigate the morphology of the nanostructures in more details, a magnified view of the nanostructures was shown in Figure 8(b). It is clear that the nanostructure tapers gradually from the bottom to the sharp tip, hence suggesting to us to call the resulting shape nanoneedles. The nanoneedles easily exceed 5 μm in length and are about 300 nm in diameter at the base, but the size at the tip is very small, about tens of nanometers.

II. Controlled Growth of CdSe Nanoiwres

It is generally accepted that the shape, structure, size and density of the nanowires exert vital influences on the physical properties of nanowires and their usefulness as nanodevices. However, a systematic study on controlled growth of CdSe nanowires has not yet appeared,

Copyright © 2010. Nova Science Publishers, Incorporated. All rights reserved.

Handbook of Material Science Research, Nova Science Publishers, Incorporated, 2010. ProQuest Ebook Central,

although a number of reports on the controlled growth of some other 1D nanostructures hve been demonstrated [32-36]. In this part, we report the realization of the controlled growth over the morphology, density, crystalline structure, and orientations of CdSe nanowires.

2.1. Morphology Control of CdSe Nanowires

The morphological control of the CdSe nanostructures described in this section is realized in a metal-organic chemical vapor deposition (MOCVD) technique by changing the growth temperature [37]. Figures 9(a) and 9(b) show the SEM images of the 1D CdSe nanostructures grown at 430°C and 500°C, respectively. For clarity, TEM image of individual representatives of the two kinds of nanostructures are shown in Figs.9(c) and 9(d). The nanostructures grown at 430°C have a very sharp tip and a wider base, with a width exceeding 300 nm in the base, and are about 5 μm in length. That is, the nanostructures grown at 430°C have a needle-like shape. The nanostructures grown at 500°C, on the other hand, are rather uniform, having a rod-like shape with a diameter about 70 nm and a length about 10 μm. Note that the bump at the head of the nanorods is the Au catalyst. One can see from the figure that needle-like nanostructures were formed at 430°C, while rod-like ones were formed at 500°C. Since all other growth parameters for the two samples were the same except temperatures, one can conclude that the shape of the 1D CdSe nanostructures can be varied by just changing the growth temperature. Note that the varied morphology of the CdSe nanostructures with growth temperature is not occasional, and several tens of growths have been carried out, and the same variation trend has been observed.

As for the mechanism for the different morphology, we think it can be understood as follows: When heated to 430 ^{o}C, the small sputtered Au islands act as nucleation sites for the growth of CdSe nanoneedles. Precursors absorbed on the Au islands grow into a leader at a rate much faster than those on the bare substrate, because of the lower nucleation energy of the former. The CdSe leader grows in a certain direction, such that only surfaces with relatively low formation energy are exposed. Secondary growth on the side surfaces of the leader, starting from its base, leads to the tapering form. The formation process of the nanorods is totally different. We note that a catalytic particle always appears at the tips of the nanorods, indicating a vapor-liquid-solid (VLS) growth mode. At 500 ^{o}C, the small Au islands had apparently melted and acted as catalysts of growth along a certain direction. Due to the much faster growth rate of the VLS mode, secondary thickening process becomes negligible; and thus uniform, rod-shaped nanowires are formed. Similar variation of the morphology with temperature has been observed in ZnO and GaN nanostructures, in which tapered needle-like structures were formed at low temperature, while uniform rods at high temperature [39,40].

2.2. Crystalline Structure Control of the CdSe Nanowires

The crystalline structure of the CdSe nanostructures can also be altered by changing the growth temperature [37]. The XRD patterns of the nanoneedles and nanorods are shown in Figure 10, in which the weak peak at 36.1^{o} is a spurious peak from the equipment. It is noted

Copyright © 2010. Nova Science Publishers, Incorporated. All rights reserved.

Handbook of Material Science Research, Nova Science Publishers, Incorporated, 2010. ProQuest Ebook Central,

that the nanorod sample was tilted during the measurement to avoid interference from the substrate. The pattern of the nanoneedles shows, besides those from the substrate, only the (200) and (400) peaks of zincblende structured CdSe, (JCPDS 19-0191), while that of the nanorods shows only peaks of wurtzite structured CdSe (JCPDS 77-2307). The above XRD data reveal that the nanoneedles are crystallized in zincblende structure while the nanorods in wurtzite structure.

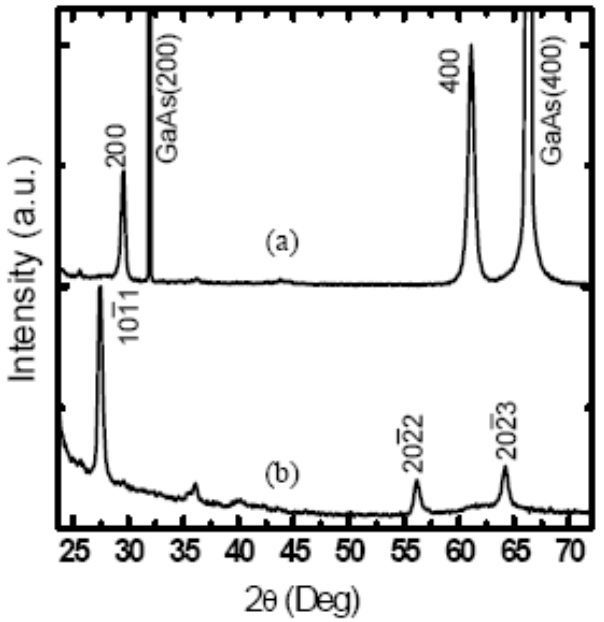


Figure 10. XRD patterns of the nanoneedles (a) and nanorods (b) [37].

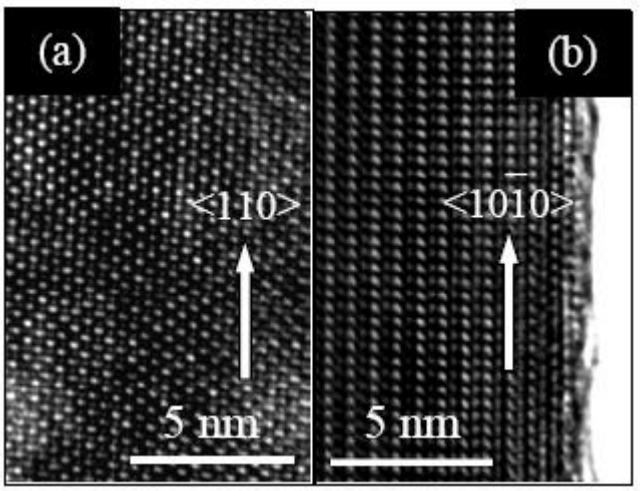


Figure 11. High-resolution TEM images of a nanoneedle (a) and a nanorod (b), the arrows indicate the growth directions of the nanostructures [37].

Copyright © 2010. Nova Science Publishers, Incorporated. All rights reserved.

Handbook of Material Science Research, Nova Science Publishers, Incorporated, 2010. ProQuest Ebook Central,

Figure 11 shows the lattice resolved images of these two types of nanostructures, in which that of the nanoneedle in Figure 11(a) can be indexed to the [111] zone of zincblende structure, while that of the nanorod in Figure 11(b) to the [$2\bar{1}\bar{1}0$] zone of wurtzite structure. The clear, spotty images demonstrate their single-crystalline structure. The growth directions of the two kinds of nanostructures, as deduced from the TEM measurements, are <110> for the zincblende nanoneedles and $<10\bar{1}0>$ for the wurtzite nanorods.

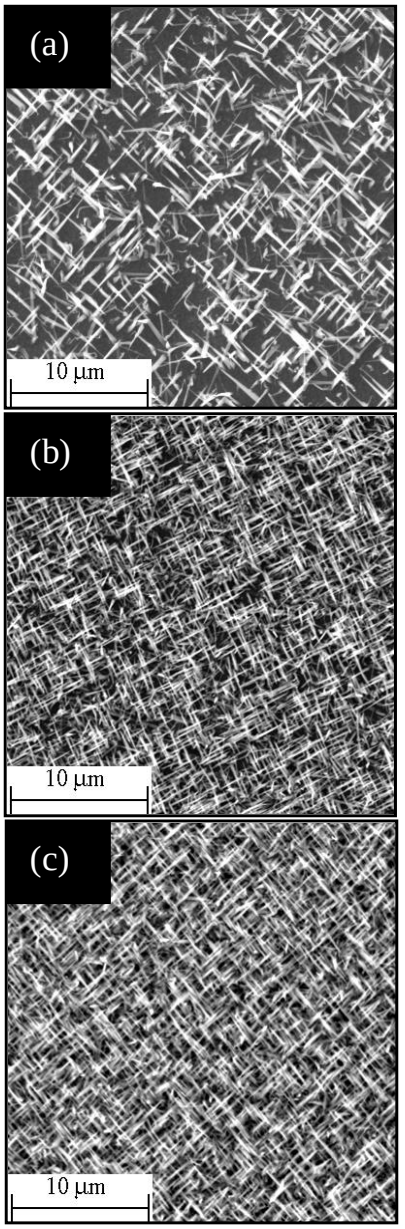


Figure 12. SEM images showing the density of CdSe nanoneedles grown under the same conditions, but the Au sputtering times of (a) 5 s, (b) 10 s, and (c) 15 s on GaAs (100) substrate [31].

Copyright © 2010. Nova Science Publishers, Incorporated. All rights reserved.

Handbook of Material Science Research, Nova Science Publishers, Incorporated, 2010. ProQuest Ebook Central,

Based on the above results, one can see that CdSe 1D nanostructures can be grown intentionally into either zincblende or wurtzite structure by changing the growth temperature in MOCVD system. The change of the crystal structure with temperature may be understood in terms of the growth kinetics. It is known that CdSe crystallizes overwhelmingly in wurtzite structure in bulk form at normal conditions, but it can be grown in zincblende thin films on GaAs substrates [28,40]. At lower growth temperature, 430°C in this case, the atoms do not have adequate thermal energy to get to the lowest-energy lattice sites; consequently, zincblende structured nanoneedle-like nanostructures are formed under the influence of the GaAs substrate. The condition is different at higher temperature, 500°C for example. The atoms have enough energy to get over the kinetic barrier to the minimum energy sites, and thermodynamics plays a more important role than kinetics. As a result, the more stable wurtzite structured CdSe nanorods are formed.

2.3. Control the Density of CdSe Nanowires

The formation of the 1D CdSe nanostructures was catalyzed by Au coating, therefore, it is natural that the density of the CdSe nanowires can be controlled by changing the thickness of the Au coating [31]. As shown in Figure 12, the density increases progressively as the sputtering time changed from 5 to 10 and to 15 s. Also shown in the figures, the size and shape of the nanoneedles are not significantly affected by the amount of Au used.

2.4. Growth Orientation Control of CdSe Nanowires

To build a nanodevice, in some cases the nanowire should be assembled in a certain pattern to form a network [41-43]. Therefore, not only should the synthesis yield aligned nanowires, it should also provide a control over their orientations. However, only very few reports on controlled orientation of nanowires of very limited material systems have been demonstrated [44-50]. Yang *et al*. [44], Maeda *et al*. [45] and Lee *et al*. [46] realized controlled orientations of carbon nanotubes by applying an electric or a magnetic field on the substrates during growth. Ge *et al*. prepared oriented Si nanowires by thermal evaporation method [47]. They showed that the projections of the Si nanowires grown on Si(100), (111) and (110) surfaces form rectangular networks, triangular networks, and parallel straight lines, correspondingly [47]. Zhang *et al.* have also prepared highly oriented ZnSe nanowires arrays on GaAs(100), (211)A, and (111) substrates, and found that the orientations of the nanowires can be controlled through the choice of the epitaxial substrate surface [48]. Orientation-controlled GaAs nanowires grown on Si substrate by molecular beam epitaxy have been demonstrated recently [49]. Ge nanowires with controllable orientations have also been grown epitaxially on Ge(111), (110) and (001) substrates by chemical vapor deposition method [50]. The studies so far have demonstrated the orientational control of only cubic structured nanowires. Whether the same control on hexagonal structured nanowires can be achieved is an interesting question, as the choices of readily available substrates for their epitaxial growth are more limited.

In this section, we show that highly oriented wurtzite CdSe nanowires can be epitaxially grown on zincblende structured GaAs substrates, and their orientations with respect to the

Copyright © 2010. Nova Science Publishers, Incorporated. All rights reserved.

Handbook of Material Science Research, Nova Science Publishers, Incorporated, 2010. ProQuest Ebook Central,

substrate normal can be controlled intentionally by choosing substrates with different surfaces [51].

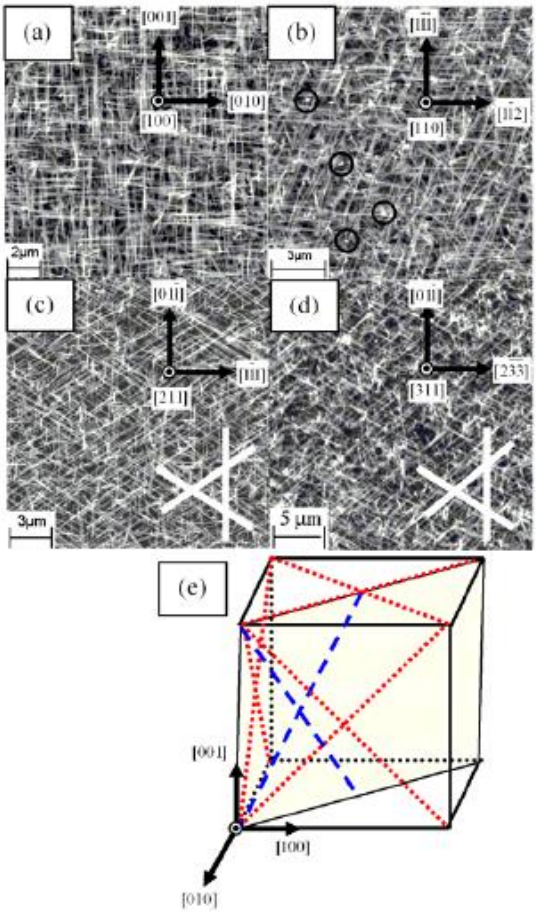


Figure 13. Plan-view SEM images of CdSe nanowires grown on different substrates, (a) GaAs(100), (b) GaAs(110), (c) GaAs(211)A, (d) GaAs(311)A. The insets show the geometrical relationship between the substrate orientations and the nanowire projections. The circles in (b) shows the projection of the nanowires grown perpendicularly on the substrate; (e) Schematic illustration of the orientation relationship between the substrate and the nanowires taking GaAs(110) as an example, where the dotted lines show the equivalent <110> directions, and the dashed lines indicate the projections of the <110> directions on (110) surface [51].

Typical plan-view SEM images of the CdSe nanowires are shown in Figs.13 (a)- 13(d). It is noted that the four samples were prepared in the same growth process. The insets show the relationship between the orientation of the substrate and the projections of the nanowires onto the substrate surface. For all the four samples, wire-like nanostructures with preferred orientations are observed on the substrates. The most remarkable feature of these nanowires lies in the geometrical relationship between their projections and the crystallographic orientations of the substrate surface. For the nanowires grown on GaAs(100) substrate, their projections show a perpendicular network in plan-view. By rotating and tilting the sample during SEM observations, it is found that the nanowires show four-fold symmetry, and their

Copyright © 2010. Nova Science Publishers, Incorporated. All rights reserved.

Handbook of Material Science Research, Nova Science Publishers, Incorporated, 2010. ProQuest Ebook Central,

length makes an angle of about 45° to the normal of the substrate. Therefore, they are deduced to grow along the four equivalent <110> directions of the substrate. It is known that there are six equivalent <110> directions in zincblende structures, but two of them lie in the (100) surface, the growth of nanowires along these two directions are hindered; the nanowires can only grow along the remaining four <110> directions. Therefore, a projection of four-folded symmetry is observed on GaAs(100) substrate. For the nanowires grown on GaAs(110), their projections make an angle of about 70° with each other, as shown in Figure 13(b). They are also found to form an angle of 60° with respect to [110]. The projections of the CdSe nanowires grown on GaAs(211)A show a triangular pattern on the substrate surface, as shown in Figure 13(c). The angles between the nanowires and the normal of the substrate are asymmetrical, some nanowires make an angle of 30° to the normal of the substrate, while others make a 73° angle. The CdSe nanowires grown on GaAs(311)A show a very similar geometry as those on GaAs(211)A. Their projections also appear in a triangular pattern, but the corresponding angles are 31° and 65°. The geometrical relationship between the nanowires and the substrates can be understood in terms of crystallography. Take the nanowires grown on GaAs(110) as an example. The six equivalent <110> directions are indicated by the dotted lines in Figure 13(e). Among the six equivalent directions, one lies in the (110) surface, the nanowires grown along this direction is hindered; another is perpendicular to the surface, the projections of the nanowires along this direction appear as bright spots, as marked by the open circles in Figure 13(b); the projections of the remaining four <110> directions are shown by the two dashed lines. The angle between the two lines can be calculated geometrically to be 70°, which is in good accordance with that observed 73° in SEM images.

III. Polarized Photoluminescence of Individual Wurtzite CdSe Nanowires

While PL measurements are often employed to study the electronic transitions of semiconductors, polarized spectra, which can provide additional information, are still less used. Polarized light emission or absorption is closely related to the symmetry of the wave functions [52]. Wurtzite CdSe is optically uniaxial, and a number of papers have demonstrated obtaining strong polarized spectra from spherical nanocrystals and prolonged quantum rods (generally less than ten nanometers in width) of CdSe [53-58]. As for the polarized PL study on 1D nanowires with larger size (usually tens of nanometers in width and several micrometers or more in length), only a few reports can be found [59-65]. However, most of them are focused on cubic structured materials [60-63], while for the polarization in wurtzite structured nanowires, very few reports can be found to the best of our knowledge [59,64,65]. The polarization in cubic nanowires is usually attributed to the contrast in dielectric constants between the nanowires and the surrounding media [61,62]. According to the classical electromagnetic theory, when the applied electric field is perpendicular to the axis of an isotropic cylindrical nanowire whose diameter is much smaller than the wavelength of light, the electric field inside the nanowire will be attenuated by a factor $2/(\varepsilon+1)$ from the external electric field, where ε is the dielectric constant of the nanowire relative to its surrounding medium. While when the applied electric field is parallel to the nanowire, the

Copyright © 2010. Nova Science Publishers, Incorporated. All rights reserved.

Handbook of Material Science Research, Nova Science Publishers, Incorporated, 2010. ProQuest Ebook Central,

internal field remains the same as the external one [66]. As a result, the polarized PL along the long axis direction is stronger than that along the short axis of the nanowires. For the PL polarization in wurtzite structured nanowires, Venugopal *et al.* found that the PL intensity reaches its maximum when the exciting field was perpendicular to the long axis (*c* axis) of CdSe nanobelts, and they thought that the selection rules in wurtizite structures are the cause for the polarization [64]. Qi *et al.* also found that maximum PL intensity was obtained when the exciting light polarizes perpendicularly to the long axis (*c* axis of the ensemble) in rod-shaped CdS quantum dot (QD) ensembles [67]. According to the selection rule, when the exciting light polarizes perpendicularly to the *c* axis of wurtzite structures, both A-exciton and B-exciton contributes to the PL; while when parallel, only B-exciton contributes [68]. In 1992, Efros has studied theoretically that the selective recombination can lead to polarization in wurtzite CdSe microcrystals [69]. However, Hsu *et al.* stated that the near-band-edge emission of ZnO nanorods has its minimum intensity when the exciting light polarizes perpendicular to the long axis (*c* axis), while maximum when parallel [65]. Their observations are totally different from what was observed in the abovementioned CdS QD ensembles and CdSe nanobelts [64,67]. They thought the polarization in their case may come from the dipole transition as observed in quantum rods [65]. However, dipole transition usually plays significant role in very small sized system, while their ZnO nanorods are 80- 120 nm and 10-20 μm in length, which is well beyond the quantum confinement region. Since the wurtzite structures are intrinsically uniaxial, the polarization mechanism is more complicated than that in zincblende systems. To explore the origin of the PL polarization in wurtzite structured nanowires and resolve the controversial observed in the above mentioned CdS QD ensembles, CdSe nanbelts and ZnO nanorods, PL polarization study on wurtzite structured nanowires growing along a direction other than *c* axis is necessary.

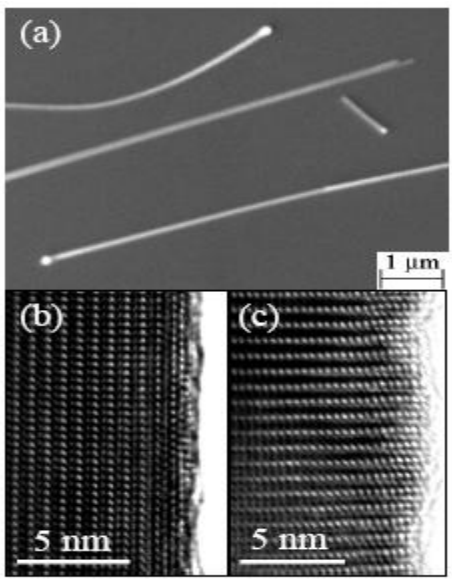


Figure 14. (a) SEM image of some nanowires transferred to a bare Si wafer, the low density of the transferred nanowires ensures the collection of the emission from a single nanowire; (b) and (c) show typical high-resolution TEM images of CdSe nanowires grown on GaAs(100) and GaAs(111)B, revealing their growth directions are along $<10\bar{1}0>$ and <0001>, respectively [70].

Copyright © 2010. Nova Science Publishers, Incorporated. All rights reserved.

Handbook of Material Science Research, Nova Science Publishers, Incorporated, 2010. ProQuest Ebook Central,

In this section we present the PL polarization study on individual wurtzite CdSe nanowires. It is found that the CdSe nanowires whether grown along or perpendicular to the *c* axis of wurtzite structure, show strong PL polarization, and that the excitation/ emission of the nanowires exhibit maximum intensity when the polarization of the exciting/ emission field *E* is parallel to the long axis of the nanowire, regardless the direction of its *c* axis. We think the dielectric contrast plays a dominating role in determining the PL polarization of our CdSe nanowires, while the role of crystallographic growth direction of the nanowires is negligible [70].

For the polarization measurement on individual nanowires, some of the as-grown nanowires were transferred to a bare Si wafer. The low density of the transferred nanowires and the high magnification microscope (50×) attached to the spectrometer ensure emission from individual nanowires were measured. A half-wave plate was used to rotate the polarization direction of the exciting 514.5 nm laser, and the emitted light passes through a polarization analyzer before entering the spectrometer.

Figure 14(a) shows a plan-view SEM image of the CdSe nanowires transferred to a Si wafer. As is evidenced, the nanowires are well separated on the Si wafer, which ensures the single-wire emissions were detected during the PL measurements. Figures 14(b) and 14(c) show the lattice images of CdSe nanowires grown on GaAs(100) and GaAs(111)B, and they are both obtained with the electron beam parallel to the [$2\bar{1}\bar{1}0$] direction of wurtzite structure. We examined about 10 nanowires on each substrate, and found that the nanowires grew exclusively along the $<10\bar{1}0>$ direction on GaAs(100), and most majority grew along the <0001> direction on GaAs(111)B. Xiong *et al.* have also grown wurtzite ZnS nanowires with two orthogonal growth directions by pulsed laser vaporization method [71]. The mechanism for how the substrate affects the growth direction of the nanowires is not clear, but Kuykendall *et al.* found that the growth direction of nanowires can indeed be affected by the substrate orientations, and they thought that the lattice matching between the substrate surface and the growth direction of the nanowires may be the cause [72].

Figure 15 shows the excitation polarization dependence of the nanowires, which was obtained by rotating the polarization direction of the exciting field by the half-wave plate. Figures 15(b) and 15(d) show the polarized PL spectra of the nanowires grown along the <0001> and $<10\bar{1}0>$ directions, respectively. The spectra compose of two emission bands, one at about 690 nm, and another broad peak at 800- 1000 nm. The peak at 690 nm comes from the near-band-edge emission, while the latter from the deep levels of the CdSe nanowires. In this section, only the polarization dependence of the NBE emissions is studied, while that of the deep level emission was omitted. It is noted that regardless of their growth directions, the PL of the nanowires reaches maximum intensity when the exciting light field E_{ex} is parallel to the long axis of the nanowires *l* (E_{ex} // *l*), and reaches minimum intensity when $E_{ex} \perp l$. Figures 15(a) and 15(c) present the dependence of the peak intensity on the excitation polarization angle for the nanowires grown along the <0001> and $<10\bar{1}0>$ directions. Note that $\theta = 0$ means the polarization of the excitation light is parallel to the length of the nanowires. The experimental data denoted by the rectangles can be well fitted by a $\cos^2\theta$ function, as shown by the solid line in the figure. As indicated in the figure, the two types of nanowires show the same excitation polarization dependence despite their different growth directions.

Copyright © 2010. Nova Science Publishers, Incorporated. All rights reserved.

Handbook of Material Science Research, Nova Science Publishers, Incorporated, 2010. ProQuest Ebook Central,

The emission polarization dependence of the CdSe nanowires was shown in Figure 16, which was obtained by rotating the analyzer in the emission path way, while maintaining the polarization of the excitation light parallel to the long axis of the nanowire. In Figs. 16(b) and 16(d), the PL spectra of individual CdSe nanowires with the emission light field parallel (E_{em} // l) and perpendicular ($E_{em} \perp l$) to the long axis of the nanowires are illustrated. The maximum emission intensity is obtained when E_{em} // l, while minium emission intensity is obtained when $E_{em} \perp l$ for both types of nanowires. The dependence of the emission intensity on emission polarization angle θ also follows a $\cos^2\theta$ law, as expected. It is noted that the polarizing effect of the optical elements involved on the polarization measurements of the nanowires can be neglected, since we found it only lead to an intensity modulation of less than about 25% (very small compared to the several fold changes shown in the spectra) when an unpolarized light source was tested under the same experimental conditions.

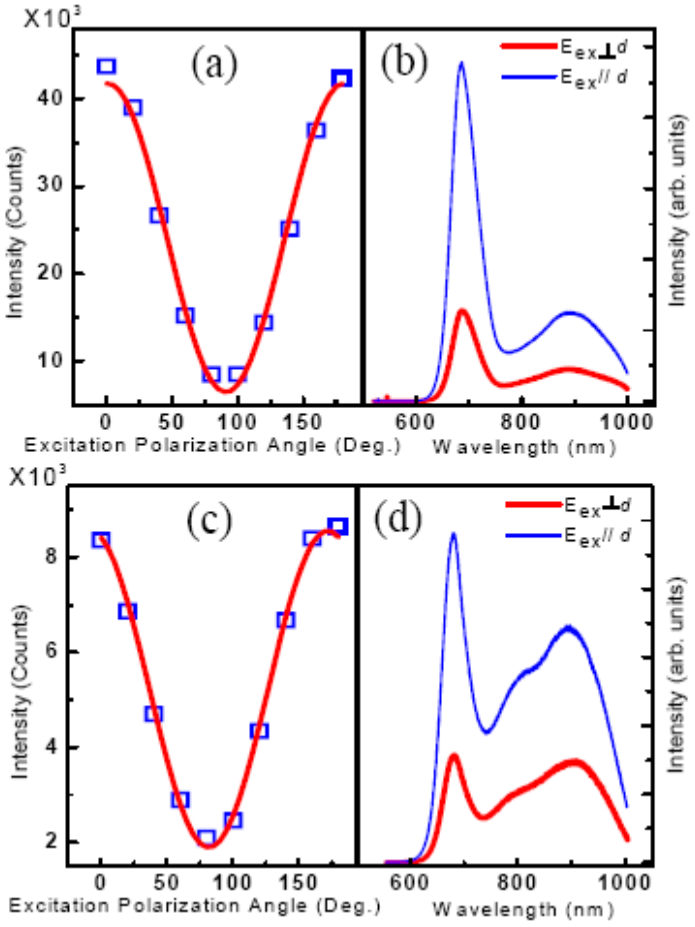


Figure 15. Emission spectroscopy of individual CdSe nanowires as a function of excitation polarization angle; (a) and (c) show room temperature PL peak intensity dependent on excitation polarization angle of a single nanowire grown along <0001> and $<10\bar{1}0>$, respectively. (b) and (d) show the PL spectra obtained with E_{ex}// d and $E_{ex} \perp d$. for nanowires grown along <0001> and $<10\bar{1}0>$, respectively [70].

Copyright © 2010. Nova Science Publishers, Incorporated. All rights reserved.

Handbook of Material Science Research, Nova Science Publishers, Incorporated, 2010. ProQuest Ebook Central,

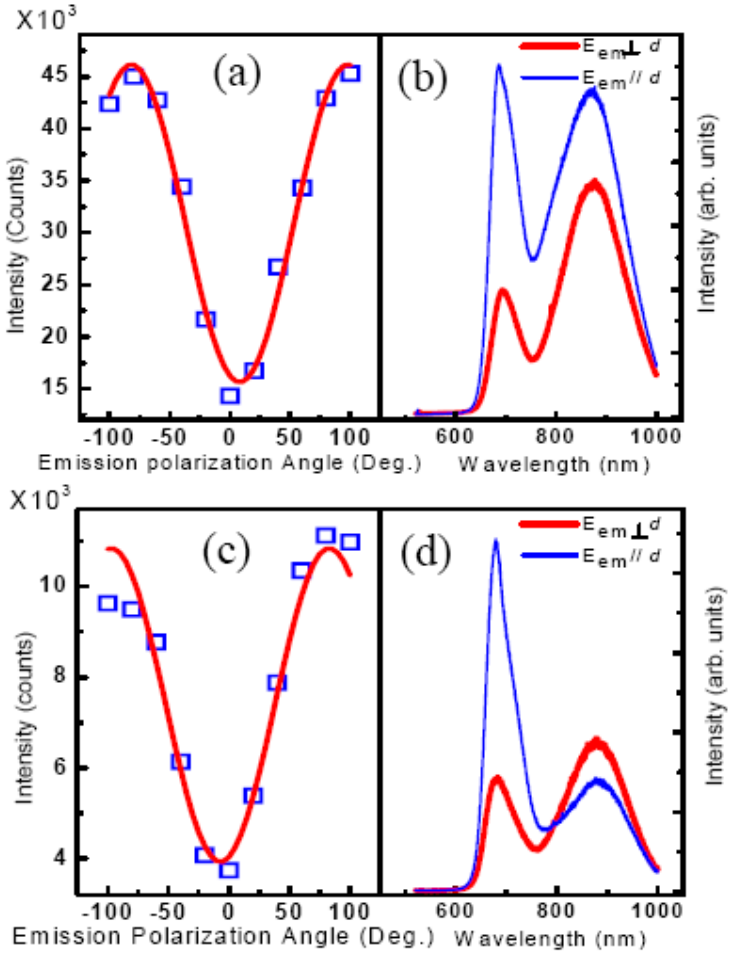


Figure 16. Emission spectroscopy of individual CdSe nanowires as a function of emission polarization angle; (a) and (c) show room temperature PL peak intensity dependent on emission polarization angle of a single nanowire grown along <0001> and $<10\bar{1}0>$, respectively. (b) and (d) show the PL spectra obtained with E_{em}// *d* and $E_{em}\perp$ *d*. for nanowires grown along <0001> and $<10\bar{1}0>$, respectively [70].

As shown in Figures 15 and 16, both the excitation and emission polarizations affect the PL intensity of the CdSe nanowires significantly. For the excitation polarization dependent PL spectra, whether the CdSe nanowires were grown along or perpendicularly to the *c* axis, they both have the maximum emission intensity when the polarization of the excitation light is parallel to the length of the nanowire, while have the minium intensity when perpendicular. Similarly, for the emission polarization dependent PL spectra, they both have maximum emission intensity when the polarization of the emission light is parallel to the length of the nanowire, while have the minium intensity when perpendicular. We have performed the polarization measurements on more than 10 nanowires for each type, and the same conclusion can be drawn. The above phenomena suggest to us that it is the shape, other than the intrinsic asymmetry of wurtzite lattice structure of CdSe nanowires that dominates the polarization. This conclusion is corroborated by the results of polarized photoconductivity and PL in many zincblende quantum dots or nanowires [52,60-63,73,74], which has no intrinsic optical

Copyright © 2010. Nova Science Publishers, Incorporated. All rights reserved.

Handbook of Material Science Research, Nova Science Publishers, Incorporated, 2010. ProQuest Ebook Central,

anisotropy. Therefore, just like those observed in InP and Si nanowires [61,62], the polarization observed in our experiments mainly come from the dielectric difference between the nanowires and their surroundings. The reason why our results differ from what observed in wurtzite CdSe nanobelts in Ref. 64 may lie in the following facts: The length of the nanobelts length in their case is ten to hundreds micrometers, the width is 0.1- 3 μm, and the exciting light is 647 nm. Because both their length and width are comparable or even larger than the exciting wavelength, the light will not be attenuated either parallel or perpendicular to the length of the nanobelts. As a result, just like the case in bulk materials, only selection rule contributes to the polarization. Therefore, maximum PL intensity was obtained when exciting light polarizes perpendicular to the *c* axis, and minimum when parallel. For the QD ensembles in Ref. 67, their length is 150 -200 nm, and the width is about 50 nm. Both dimensions was smaller than the exciting wavelength 354 nm, so the exciting light will be attenuated whether its plolarization direction is parallel or perpendicular to the long axis of the ensembles. As a result, the contribution form the dielectric contrast becomes negligible. For our nanowires the situation is different. The width of the CdSe nanowires (about 70 nm) is much smaller than the wavelength of the excitation light (514.5 nm), while the length (several micrometers) is larger than the excitation wavelength. Consequently, the light field is attenuated when the exciting field is perpendicular to the length of the nanowires, while it is not when parallel. Consequently, just as the situation in cubic nanowires, the dielectric contrast dominates the polarization in our case. We can speculate that when the width of the nanowires creases to a certain value which is comparative to or larger than 514.5 nm, the polarization may be dominated by the selection rules.

CONCLUSION

Due to the great efforts of many groups, significant advances in the growth and characterizations of quasi-1D CdSe nanowires have been acquired in recent years, for example, 1D CdSe nanostructures with various porphologies, such as nanorods, nanoneedles, nanopyramids, nanosaws, nanobelts, etc have been reported. However, there is still much room for the improvements despite of these progresses. One of the major obstacles in this field lies in that there are still very limited reports on the application of 1D CdSe nanowires as building blocks in optoelectronic devices. We hope that quasi-1D CdSe nanowires can find such applications in the near future.

REFERENCES

[1] N. Matsumura, H. Endo, and J. Saraie, *Phys. Stat. Sol*. (b) 229, 1039 (2002).
[2] K. W. Frese, Jr., *Appl. Phys. Lett.* 40, 275 (1982).
[3] C. F. Hermandez, D. J. Suh, B. Kippelen, and S. R. Marder, *Appl. Phys. Lett*. 85, 534 (2004).
[4] R.C. Somers, M.G. Bawendi, D.G. Nocera, *Chem. Soc. Rev*. 36, 579 (2007).
[5] X.G. Peng, L. Manna, W. Yang, J. Wlckham, E. Scher, A. Kadavalch, and A.P. Allvlsatos, *Nature* 404, 59 (2000).

Copyright © 2010. Nova Science Publishers, Incorporated. All rights reserved.

Handbook of Material Science Research, Nova Science Publishers, Incorporated, 2010. ProQuest Ebook Central,

[6] M. Bruchez, Jr., M. Moronne, P. Gin, S. Weiss, and A. P. Alivisatos, *Science* 281, 2013 (1998).
[7] C.B. Murray, D.J. Norris, M.G. Bawendi, *J. Am. Chem. Soc*. 115, 8706 (1993).
[8] T. Trindade, P. OBrien, *Adv. Mater*. 8, 161 (1996).
[9] S.H. Xin, P. D. Wang, A. Yin, C. Kim, M. Dobrowolska, J. L. Merz, and J. K. Furdyna, *Appl. Phys. Lett*. 69, 3884 (1996).
[10] C.S. Kim, M. Kim, J.K. Furdyna, M. Dobrowolska, S. Lee, H. Rho, L.M. Smith, H.E.Jackson, E.M.James, Y. Xin, N.D. Browning, *Phys. Rev. Lett*. 85, 1124 (2000).
[11] C.X. Shan, X.W. Fan, J.Y. Zhang, Z.Z. Zhang, X.H. Wang, Y.M. Lu, Y.C. Liu, D.Z. Shen, S.Z. Lu, *J. Crystal Growth* 265, 541 (2004).
[12] S. Iijima, *Nature* 354, 56 (1991).
[13] E.W. Wong, P. E. Sheehan, and C. M. Lieber, *Science* 277, 1971 (1997).
[14] J.D. Holmes, K. P. Johnston, R.C. Doty, and B.A. Korgel, *Science* 287, 1471 (2000).
[15] Y.Y. Wu, B. Messer, and P. D. Yang, *Adv. Mater*. (Weinheim, Ger.) 13, 1487 (2001).
[16] D. Katz, T. Wizansky, O. Millo, E. Rothenberg, T. Mokari, U. Banin, *Phys. Rev. Lett*. 89, 086801 (2002).
[17] K.T.Yong, Y.Sahoo, M.T.Swihart, P.N. Prasad, *Adv. Mater*. 18, 1978 (2006).
[18] A. Creti, M. Anni, M.Z. Rossi, G. Lanzani, G. Leo, F. Della Sala, L. Manna, M. Lomascolo, *Phys. Rev*. B 72, 125346 (2005).
[19] X.S. Peng, J. Zhang, X. F. Wang, Y. W. Wang, L. X. Zhao, G. W. Meng, and L. D. Zhang, *Chem.Phys.Lett*., 343, 470 (2001).
[20] D. S. Xu, X. S. Shi, G. L. Guo, L. L. Gui, and Y. Q. Tang, *J. Phys. Chem*. B 104, 5061 (2000).
[21] W. B. Zhao, J. J. Zhu, and H. Y. Chen, *Scripta Materialia* 50, 1169 (2004).
[22] C. Ma, Y. Ding, D. Moore, X.D. Wang, Z.L. Wang, *J. Am. Chem. Soc*. 126, 708 (2004).
[23] Y. Ding, C. Ma, Z.L. Wang, *Adv. Mater*. 16, 1740 (2004).
[24] C. Ma, Z.L. Wang, *Adv. Mater*.17, 2635 (2005).
[25] X.B. Zhang, S.K. Hark, *J. Crystal Growth* 234, 373 (2002).
[26] Q. Yang, K.B. Tang, C.R. Wang, Y.T. Qian, S.Y. Zhang, *J. Phys. Chem*. B 106, 9227 (2002).
[27] C.X. Shan, Z.Liu, C.M. Ng, S.K. Hark, *Appl. Phys. Lett*. 86, 213106 (2005).
[28] U. Lunz, J. Kuhn, F. Goschenhofer, U. Schussler, S. Einfeldt, C. R. Becker, and G. Landwehr, *J. Appl. Phys*. 80, 6861 (1996).
[29] J. R. Mei, and V. Lemos, *Solid State Commun*. 52, 785 (1984).
[30] C. C. Evans, *Whiskers*, (Mills and Boon Ltd, London, 1972), p14.
[31] C.X. Shan, Z. Liu, S.K. Hark, *Appl. Phys. Lett*. 87, 163108 (2005).
[32] G. Kipshidze, B. Yavich, A. Chandolu, J. Yun, V. Kuryatkov, I. Ahmad, D. Aurongzeb, M. Holtz, H. Temkin, *Appl. Phys. Lett.* 86, 033104 (2005).
[33] A.I. Hochbaum, R. Fan, R.R. He, P.D. Yang, *Nano Lett*. 5, 457 (2005).
[34] S.P. Ge, K.L. Jiang, X.X. Lu, Y.F. Chen, R.M. Wang, S.S Fan, *Adv. Mater.* 17, 56 (2005).
[35] C.W. Sun, H. Li, H.R. Zhang, Z.X. Wang, L.Q. Chen, *Nanotechnology* 16, 1454 (2005).
[36] B.T. Park, K. Yong, *Nanotechnology* 15, S365 (2004).
[37] C.X. Shan, Z. Liu, S.K. Hark, Nanotechnology, 16, 3133 (2005).
[38] H.M. Kim, T.W. Kang, K.S. Chung, *Adv. Mater.* 15, 567 (2003).

Copyright © 2010. Nova Science Publishers, Incorporated. All rights reserved.

Handbook of Material Science Research, Nova Science Publishers, Incorporated, 2010. ProQuest Ebook Central,

[39] X.Q. Meng, D.X. Zhao, J.Y. Zhang, D.Z. Shen, Y.M. Lu, Y.C. Liu, X.W. Fan, *Chem. Phys. Lett.* 407, 91 (2005).
[40] N. Smarth, H. Luo, J.K. Furdyna, S.B. Qadri, Y.R. Lee, A.K. Ramdas, N. Otsuka, *Appl. Phys. Lett.* 54, 2680 (1989).
[41] J. Zhou, Y. Ding, S. Z. Deng, L. Gong, N. S. Xiu, and Z. L. Wang, *Adv. Mater*. (Weinheim, Ger.) 17, 2107, (2005).
[42] C. X. Xu, X. W. Sun, C. Yuen, B. J. Chen, S. F. Yu, Z. L. Dong, *Appl. Phys. Lett*. 86, 011118, (2005).
[43] D. H. Wang, R. Kou, M. P. Gil, H. P. Jakobson, J. Tang, D. H. Yu, Y. F. Lu, *J. Nanosci. Nanotechnol.* 5, 1904 (2005).
[44] Q. Yang, C. Xiao, W. Chen, A. K. Singh, T. Asai, A. Hirose, *Diamond Relat. Mater*. 12, 1482, (2003).
[45] M. Maeda, C. K. Hyon, T. Kamimura, A. Kojima, K. Sakamoto, and K. Matsumoto, J. *J. Appl. Phys.* 44, 1585, (2005).
[46] K. H. Lee, J. M. Cho, and W. Sigmund, *Appl. Phys. Lett.* 82, 448 (2003).
[47] S. P. Ge, K. L. Jiang, X. X. Lu, Y. F. Chen, R. M. Wang, and S. S. Fan, *Adv. Mater*. (Weinheim, Ger.) 17, 56, (2005).
[48] X. T. Zhang, Z. Liu, Quan Li, Y. P. Leung, K. M. Ip, and S. K. Hark, *Adv. Mater*. (Weinheim, Ger.) 17, 1405, (2005).
[49] S. G. Lhn, J. I. Song, T. W. Kim, D. S. Leem, T. Lee, S. G. Lee, E. K. Koh, K. Song, *Nano Lett*. 7, 39 (2007).
[50] H. Adhikari, A. F. Marshall, C. E. D. Chidsey, P. C. Mclntyre, *Nano Lett*. 6, 318 (2006).
[51] C.X. Shan, Z. Liu, S.K. Hark, *Appl. Phys. Lett*. 90, 193123 (2007).
[52] V. Zwiller, L. Jarlskog, M. Pistol, C. Pryor, P. Castrillo, W. Seifert, L. Samuelson, *Phys. Rev*. B 63, 233301 (2001).
[53] E. Rabani, B. Hetenyi, B. J. Berne, L. E. Brus, *J. Chem. Phys*. 110, 5355 (1999).
[54] M. Artemyev, B. Möller, U. Woggon, *Nano Lett.* 3(4), 509 (2003).
[55] N. L. Thomas, E. Herz, O. Schőps, U. Woggon, M. V. Artemyev, *Phys. Rev. Lett*. 94, 016803 (2005).
[56] J. T. Hu, L. S. Li, W. D. Yang, L. Manna, L. W. Wang, A. P. Alivisatos, *Science* 292, 2060 (2001).
[57] X. Chen, A. Nazzal, D. Goorskey, M. Xiao, Z. A. Peng, X. G. Peng, *Phys. Rev.* B 64, 245304 (2001).
[58] S. A. Empedocles, R. Neuhauser, and M. G. Bawendi, *Nature* 399, 126 (1999).
[59] N. E. Hsu, W. K. Hung, Y. F. Chen, *J. Appl. Phys*. 96, 4671 (2004).
[60] J. Qi, A. M. Belcher, J. M. White, *Appl. Phys. Lett*. 82, 2616 (2003).
[61] J. F. Wang, M. S. Gudiksen, X. F. Duan, Y. Cui, C. M. Lieber, *Science* 293, 1455 (2001).
[62] D. D. D. Ma, S. T. Lee, J. Shinar, *Appl. Phys. Lett*. 87, 033107 (2005).
[63] M. P. Persson, and H. Q. Xu, *Phys. Rev*. B, 161310 (2004).
[64] R. Venugopal, P. I. Lin, C. C. Liu, Y. T. Chen, *J. Am. Chem. Soc*. 127, 11262 (2005).
[65] Z. Y. Fan, P. C. Chang, J. G. Lu, E. C. Walter, R. M. Penner, C. H. Lin, H. P. Lee, *Appl. Phys. Lett*. 85, 6128 (2004).
[66] L. D. Landau, E. M. Lifshitz, L. P. Pitaevskii, Electromagnetics of Continuous Media (Pergamon, Oxford, 1984), pp. 34-42.

Copyright © 2010. Nova Science Publishers, Incorporated. All rights reserved.

Handbook of Material Science Research, Nova Science Publishers, Incorporated, 2010. ProQuest Ebook Central,

[67] J. Qi, C. Mao, J. M. White, A. M. Belcher, *Phys. Rev*. B 68, 125319 (2003).
[68] D. Braun, W. W. Rűhle, C. T. Giner, J. Collet, *Phys. Rev. Lett*. 67 (17), 2335 (1991).
[69] A. L. Efros, *Phys. Rev*. B 46, 7448 (1992).
[70] C.X. Shan, Z. Liu, S.K. Hark, *Phys. Rev*. B 74, 153402 (2006).
[71] Q.H. Xiong, G. Chen, J. D. Acord, X. Liu, J. J. Zeng, H. R. Gutierrez, J. M. Redwing, L. C. Lew Yan Voon, B. Lassen, P. C. Eklund, *Nano Lett*. 4, 1663 (2004).
[72] T. Kuykendall, P.J. Pauzauskie, Y.F. Zhang, J. Goldberger, D. Sirbuly, J. Denlinger, P.D. Yang, *Nature Mater*. 3, 524 (2004).

Copyright © 2010. Nova Science Publishers, Incorporated. All rights reserved.

Handbook of Material Science Research, Nova Science Publishers, Incorporated, 2010. ProQuest Ebook Central,

Copyright © 2010. Nova Science Publishers, Incorporated. All rights reserved.

Handbook of Material Science Research, Nova Science Publishers, Incorporated, 2010. ProQuest Ebook Central,

In: Handbook of Material Science Research
Editors: C. René and E. Turcotte, pp.395-416
ISBN 978-1-60741-798-9
© 2010 Nova Science Publishers, Inc.

Chapter 10

THE STRUCTURE AND MORPHOLOGY OF ELECTRODEPOSITED NICKEL-COBALT ALLOY POWDERS

D.M. Minić[1], L. D. Rafailović[2], J. Wosik[3] and G.E. Nauer[3,4]

1. Faculty of Physical Chemistry,
University of Belgrade, Belgrade, Serbia
2. Physics of Nanostructured Materials, Faculty of Physics,
University of Vienna, Vienna, Austria
3. CEST, Kompetenzzentrum für
elektrochemische Oberflächentechnologie GmbH, Neustadt, Austria
4. Faculty of Chemistry,
University of Vienna, Vienna, Austria

Copyright © 2010. Nova Science Publishers, Incorporated. All rights reserved.

ABSTRACT

Nanostructured nickel and cobalt alloy powder deposits from three different electrolyte compositions were obtained by electrodeposition from an ammonium sulfate-chloride solution in a galvanostatic regime. The influence of current density and the Ni^{2+}/Co^{2+} ratio in the bath on the microstructure and phase composition of the Ni-Co deposits were studied by SEM and X-ray diffraction methods. Both, bath composition and current density influence strongly the deposit growth mechanism as well as the deposit composition, microstructure, grain size and surface morphology. When electrodeposition was performed at high overpotentials, far from equilibrium conditions, face-centered cubic (FCC) mixtures of Ni and Co were generated while at low overpotentials, as well as at higher content of cobalt in the electrolyte, hexagonal close packed (HCP) of Co was formed with a lower rate of hydrogen evolution. The increase in the concentration of HCP phase in the nanocrystalline deposits was caused by increasing the overall Co content in the materials prepared as well as by decreasing deposition current density.

Differential scanning calorimetry (DSC) and X-ray diffraction analysis were used to examine the effects of structural changes on magnetic properties of the nanocrystalline powders electrochemically obtained in the temperature interval from room temperature to

Handbook of Material Science Research, Nova Science Publishers, Incorporated, 2010. ProQuest Ebook Central,

650°C. Each stage of the structural changes caused corresponding changes in the magnetic permeability for the alloys prepared.

INTRODUCTION

From the earliest papers in the nanostructured material science [1] until nowadays and from widespread research over the past couple of decades, nanoscaled materials have attracted a lot of attention of scientists all over the world concerning both scientific as well as technological aspect [2-4]. Nanostructured materials provide an excellent opportunity to extend the understanding of the structure- property relations in solid materials [5-7] and also open an attractive potential for technological applications [5].

Many synthesis techniques for production of nanostructured materials have been developed like inert gas-condensation, ball-milling, severe plastic deformation, chemical vapor deposition and electrochemical deposition [3]. Although electrodeposition has been one of the methods using well known processes for synthesizing nanocrystalline materials, properties of nanocrystalline electrodeposits are less evaluated, especially for tribological application in nanoscale devices such as micro and nanoelectromechanical systems (MEMS and NEMS). The electrodeposition technique has significant advantages compared to other methods for synthesis of nanocrystalline materials; one of them is possibility of preparation of amorphous alloys [9]. Other important advantages are the easy preparation of materials of high purity exhibiting different structures and morphologies and the possibility of changing the composition and morphology within a broad range, adjusting only the deposition parameters [10,11].

Electrodeposited NiCo thin films have been intensively studied due to their application in MEMS [6]. Thin and thick NiCo films form important parts of magnetic-MEMS devices including sensors, microactuators or micromotors because of their excellent physical properties. Fine Ni, Co and Ni-Co alloy powders are required for developing magnetoresistive sensors in thick-film form [7].

Electrodeposition of Ni-Co powders from defined solutions; of Ni powders as well as of Co powders were established by the work of Calusaru [8]. Almost all metals can be obtained in powder form, but the method for obtaining such materials will be dependant on intended properties affected by their structure [10]. The electrolytic powder production method usually yields a product of requested chemical composition, high purity, which can be well pressed and sintered as we have show in previous papers [11-13].

The electrodeposition of Co has been far less studied compared to the Ni electrodeposition [14]. Electrolytic Co crystallizes with two modifications, the HCP, stable allotropic modification at temperatures below 417°C, and with the FCC form of lattice structure stable at higher temperatures. With increase of pH the structure becomes completely in the form of the HCP-phase and deposit texture depends mainly on solution pH [15]. The prevailing orientations and their stability with respect to the operative conditions are characterized in details for both sulphate [15] and chloride based electrolytes [16]. Cohen-Hyams et al. showed that the structure of electrodeposited Co significantly depends on the level of used overpotential [17]. When electrodeposition is performed far from equilibrium conditions, *i.e.*, at a higher overpotentials, FCC cobalt is deposited while at lower overpotentials HCP Co is formed with a lower rate of hydrogen evolution.

Copyright © 2010. Nova Science Publishers, Incorporated. All rights reserved.

Handbook of Material Science Research, Nova Science Publishers, Incorporated, 2010. ProQuest Ebook Central,

Recently several papers have been published on the effect of electrolyte composition and current density on the hardness of the electrodeposited iron group films [18] as well as on the chemical composition, structure, electric and magnetic properties and corrosive stability of thin electrodeposited nanocrystalline film [19,21-24]. Higher electrical resistivity of the electrodeposited CoNi alloys can be attributed to the smaller grain sizes, high defect densities, and impurity incorporation during electrodeposition [5].

Alloys of iron group metals, Fe, Co and Ni, have been considered as very good magnetic materials [19, 20, 25, 26, 30]. These alloys are known to possess much better permanent magnetic properties than pure metals.

In the present chapter the composition, the morphology and microstructure of Ni-Co powders galvanostatically deposited were investigated as well as their thermal stability and structural transformations in the temperature range from ambient to 600°C.

A differently composed Ni-Co alloys were prepared galvanostatically from ammonium sulfate-chloride solutions, containing different Ni^{2+}/Co^{2+} concentration ratios, Ni^{2+}/Co^{2+}= 4; Ni^{2+}/Co^{2+}= 1 and Ni^{2+}/Co^{2+}= 0.25 [total concentration 0.12 moldm^{-3} ($NiSO_4$+$CoSO_4$); 0.5moldm^{-3} NH_4Cl and 3.5 moldm^{-3} NH_4OH] at pH=10 in a glass cell with a volume of 1.0 dm^3 without stirring, thermostatically controlled at a temperature of 298 ± 1 K. Cu platelets placed in the center of the cell with a 1.0 cm^2 surface area and 0.2 cm thickness were used as working electrodes. A Ti plate covered with RuO_2/TiO_2 (10 cm^2 geometric area), placed close and parallel to the Cu-plate, was used as anode (DSA). The electrodeposition of the powder was performed with a constant current regime in the range of 40 - 450 mAcm^{-2} [11, 12].

Polarization measurements were performed using a computer controlled electrochemical system (PAR M 273A, software PAR M352/252, version 2.01) with a sweep rate of 1 mVs^{-1}. For the correction of the IR drop, current interrupt technique was used with a time of current interruption of 0.5 s. The counter electrode (Pt-foil) and the reference electrode (saturated calomel electrode, SCE) were placed in separate compartments. The Luggin capillary connecting the SCE to the electrolyte was positioned at a distance of 0.2 cm from the working electrode (copper rod, d = 0.4 cm). Before each experiment, the working electrode was polished using a 0.05 μm alumina impregnated polishing cloth.

Coulomb efficiencies were measured at different current densities by weighting the mass of the deposits at the copper platelets. The coulombs consumed for hydrogen evolution were calculated using Faraday's law [26].

For the surface morphology characterisation an XL 30 ESEM-FEG (environmental scanning electron microscope with field emission gun, FEI Company, Netherlands) was used. The 3D reconstruction of the specimen surface shown was characterized by Scanning Electron Microscope - SEM using MeX software from Alicona (A).

An alloy composition analysis was performed by ESEM using EDX software Genesis (USA). X-ray powder diffraction (XRD) analysis was carried out using a MRD diffractometer (Philips, NL) with CuKα radiation (40kV/30 mA). Step scan mode was utilized with 0.03º in 2θ per 1.15 s step. The angular 2θ range investigated was 30°-110°. Structural transformations of the alloy powders were determined upon annealing the samples at selected temperatures for 30 minutes in an argon atmosphere.

DSC measurements were performed at 10 mg samples using a DSC-204 C (Netzsch, D) in the temperature range of 25 to 600°C in argon atmosphere with a heating rate of 20 Kmin^{-1}. For magnetic measurements, the powders were pressed at 100 MPa into 40 mm long, 1 mm wide and 0.3-0.6 mm thick samples. The determination of the relative magnetic permeability

Copyright © 2010. Nova Science Publishers, Incorporated. All rights reserved.

Handbook of Material Science Research, Nova Science Publishers, Incorporated, 2010. ProQuest Ebook Central,

was performed using a modified Maxwell method, based on the action of an inhomogeneous magnetic field on the sample, using home-made equipment [13].

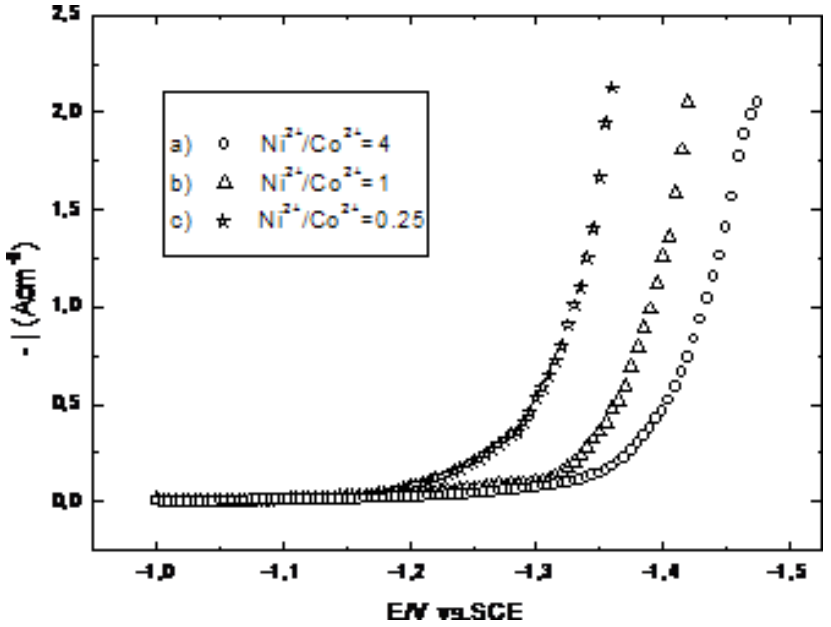


Figure 1. Polarization curves at the Cu-cathode for the different compositions of the electrolyte: a) $Ni^{2+}/Co^{2+}= 4$; b) $Ni^{2+}/Co^{2+} = 1$ and c) $Ni^{2+}/Co^{2+}=0.25$, sweep rate: 1mVs^{-1}.

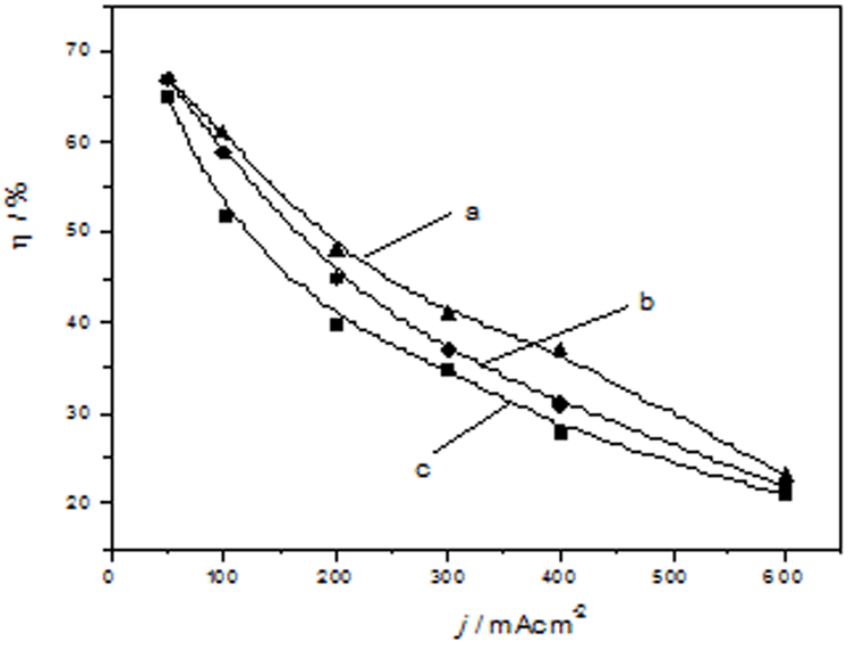


Figure 2. Current efficiency of the alloy deposition process at a Cu-cathode vs. the current density for different composition of electrolyte: a) $Ni^{2+}/Co^{2+}= 4$; b) $Ni^{2+}/Co^{2+}= 1$ and c) $Ni^{2+}/Co^{2+}=0.25$.

Copyright © 2010. Nova Science Publishers, Incorporated. All rights reserved.

Handbook of Material Science Research, Nova Science Publishers, Incorporated, 2010. ProQuest Ebook Central,

Figure 1 shows the polarization curves of the Cu-cathode for different compositions of the electrolyte. The shape and position of the polarization curves strongly depend on the electrolyte composition. Decreasing the amount of Co^{2+} and an increasing the amount of Ni^{2+} shift the position of corresponding polarization curves towards negative values of potentials, corresponding to the potential of the Ni/Ni^{2+} deposition of pure nickel. According to this polarization curves, current densities of 40- 400 $mAcm^{-2}$ were selected for deposition of the alloys, expecting the formation of non-compact deposits [39].

In our experiments a defined amount of Ni-Co alloy was possible to obtain only at current density, $j > 40$ $mAcm^{-2}$. However, in all bath compositions at current densities, $j< 65$ $mAcm^{-2}$, compact deposits were obtained. For higher current densities (>150 $mAcm^{-2}$), the deposits were in the form of powders that could be easily removed from the electrode surface. It should be mentioned that for higher current densities, hydrogen evolution was quite intensive providing conditions in which some amount of the powders drop into the cell. The trend for the hydrogen evolution reaction which is accomplished with alloy powder deposition reaction at the current density $j>150$ $mAcm^{-2}$ increases with a decrease of the amount of Ni^{2+} in the electrolyte suggesting that activity for the hydrogen evolution reaction increases with a decrease of the nickel content in the deposit.

The hydrogen evolution during deposition of the alloys affects the current efficiency, depending on the electrolyte composition as well as on the current density (Figure 2). In the current density range, where powders were deposited, the current efficiency decreases with the increasing the current density and with the decrease of the Ni^{2+} concentration in the electrolyte.

a. Morphology of Nanocrystalline Deposits Obtained from Bath of Different Composition

Figure 3 presents SEM micrographs (micrographs a-c) of the alloys, electrodeposited from electrolytes with three different Ni^{2+}/Co^{2+} concentration ratios (4, 1, 0.25, respectively) at a current density of $j = 65$ $mAcm^{-2}$, as well as the corresponding 3D SEM micrographs (micrographs i-iii). For current densities in the range between 65 and 400 $mAcm^{-2}$, deposits were obtained with the size of agglomerates varying from 5 μm to about 50 μm.

The deposit with the highest content of Ni^{2+} in the electrolyte (micrographs 3a and 3i) exhibits the cauliflower-like structure, consisting of small particles with an average radii <500nm, surrounded with diffusion zones and the deposition took place in spherically symmetrical way. For the ratio of $Ni^{2+}/ Co^{2+} = 1$ (micrographs 3b and 3ii), the morphology of the deposit is changed and the powder consists of particles also with cauliflower structure but exhibiting a different surface morphology, based on preferred oriented platelets (Figure 3b). Finally, the particles deposited from electrolyte with the highest content of $[Co^{2+}]$ (micrographs 3b and 3iii) show the platelet structure, also with preferred orientation and a size of the platelets in the μm range. Concluding, the morphology of electrodeposited alloy depends strongly of the electrolyte composition. The surface morphology of the deposits is determined by the nature of the electrochemically active ions or complexes and kinetics of the electrocrystallization processes. Overpotentials of 1.3 V are needed for the deposition of very disperse powder [29].

Copyright © 2010. Nova Science Publishers, Incorporated. All rights reserved.

Handbook of Material Science Research, Nova Science Publishers, Incorporated, 2010. ProQuest Ebook Central,

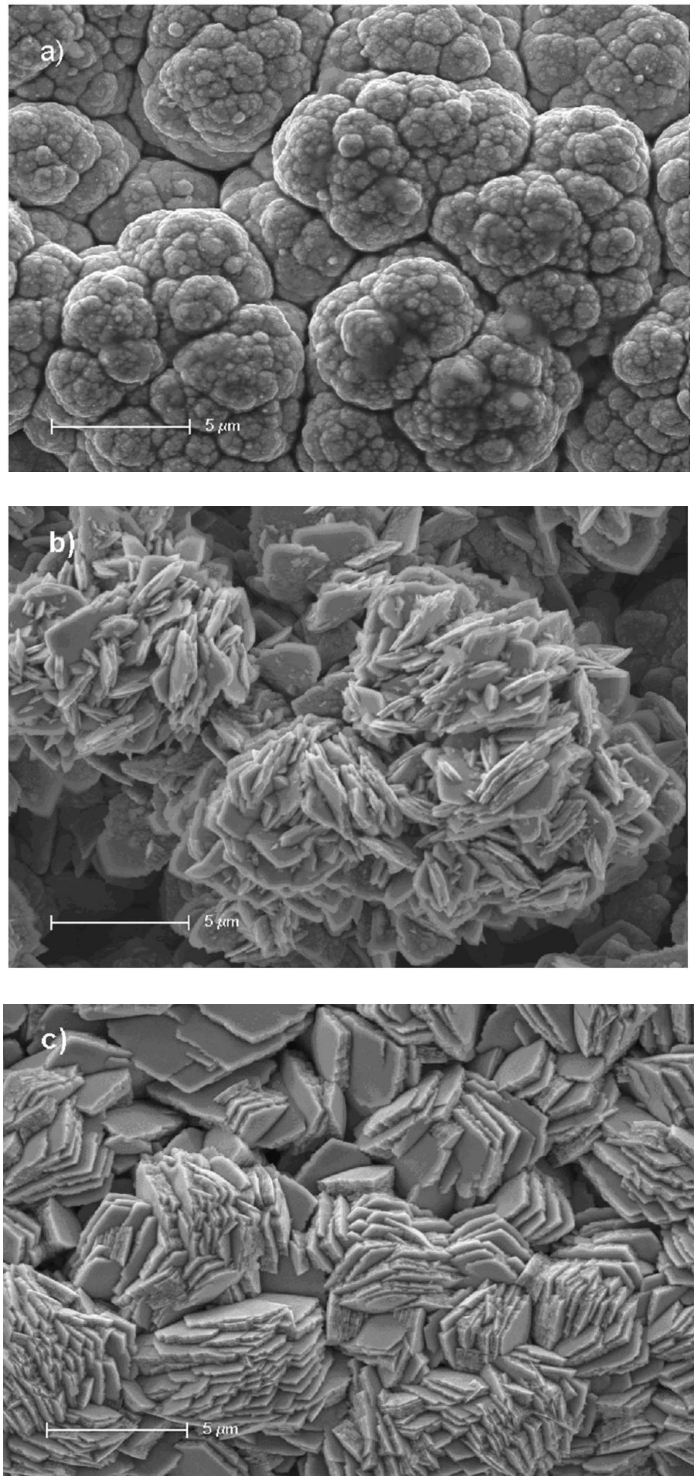


Figure 3. Continues.

Copyright © 2010. Nova Science Publishers, Incorporated. All rights reserved.

Handbook of Material Science Research, Nova Science Publishers, Incorporated, 2010. ProQuest Ebook Central,

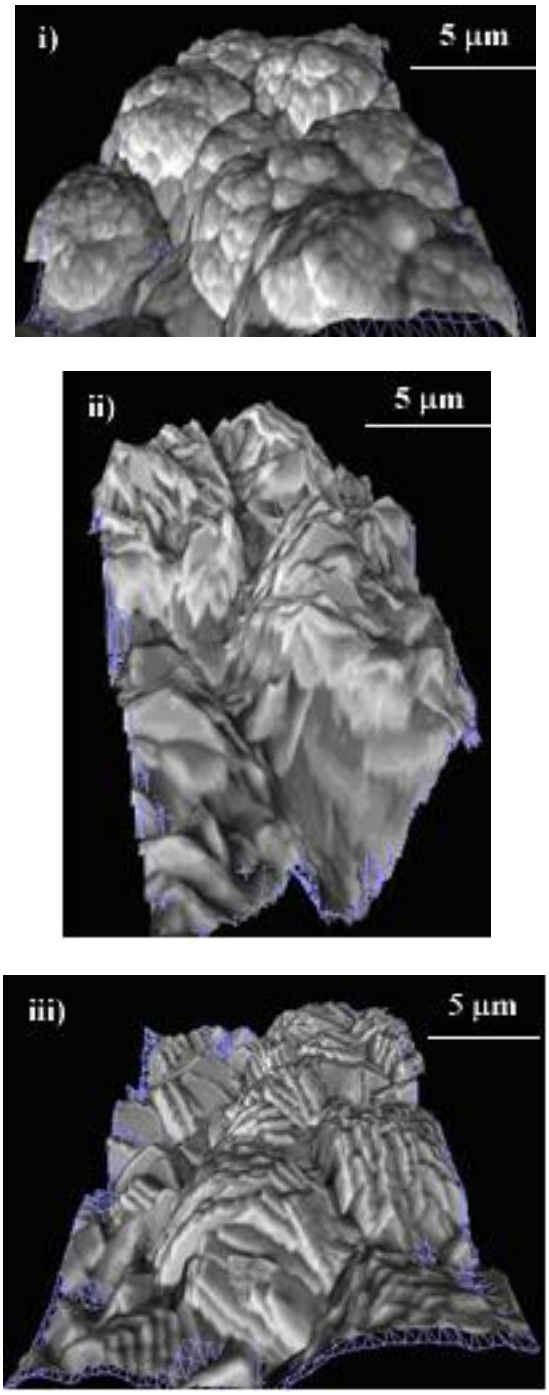


Figure 3. SEM micrographs of Ni-Co deposits galvanostatically prepared out of electrolyte with different Ni^{2+}/Co^{2+} ratio: a) 4; b) 1 and c) 0.25, at a current density of j=65 $mAcm^{-2}$; corresponding 3D SEM reconstructions (i-iii) of the surface of Ni-Co deposits.

Copyright © 2010. Nova Science Publishers, Incorporated. All rights reserved.

Handbook of Material Science Research, Nova Science Publishers, Incorporated, 2010. ProQuest Ebook Central,

Table 1. Roughness parameters of alloys deposited from electrolytes of different Ni^{2+}/Co^{2+} concentration ratio and at different current densities

Ni^{2+}/Co^{2+} Concentration ratio	Current density ($mAcm^{-2}$)	Ra µm	Rz µm	RS (μm^2)
4	65	1.0	4.7	1.64
1	65	3.0	13.1	1.98
1	220	1.1	5.2	1.38
1	400	1.0	6.5	1.62
0.25	65	0.7	4.7	1.64

The 3D dataset was calculated from two stereoscopic images obtained by tilting the sample stage in the ESEM at the eucentric point with an angle of 5°. It enables to carry out a 3D analysis directly from the digital images yielding profile and roughness measurements and also area analysis as well as volumetric measurements. The calculated roughness parameters are shown in Table 1. (Ra- mean roughness, Rz -the difference between the highest and the lowest point in the picture of defined scan, RS -active surface, the ratio of the real surface including topography to a projected surface of the measurements (a square with dimensions of 23x15 µm).

A concentration ratio Ni^{2+}/Co^{2+}= 4 and Ni^{2+}/Co^{2+}= 1, led to a surface with similar roughness values inspite of different morphology, (Figure3a) and (Figure 3c), respectively. In the case of concentration ratio Ni^{2+}/Co^{2+} = 1, the mean roughness of the deposit is almost 3 times higher than in the specimens with ratios of 4 or 0.25. Also, the active surface has a maximum at the ratio 1. An increase in the current density results in a decrease in roughness, since at higher current densities the amount of crystal nuclei on the surface in enhanced and dendritic growing is reduced in the initial period of deposition.

SEM micrographs of alloy powders deposited from electrolyte with concentration ratio Ni^{2+}/Co^{2+}= 1 at different current densities, j = 65 $mAcm^{-2}$ (Figure 4a), j = 220 $mAcm^{-2}$ (Figure 4b) and j = 400 $mAcm^{-2}$ (Figure 4c), show significant differences in the morphology as well as in the particle size. The increase of current density from j = 65 $mAcm^{-2}$ to j = 220 $mAcm^{-2}$ changes the morphology of deposit from the inlaid structure to the cauliflower-like structure with a finer grain size. Further increasing of current density shows no significant influence on particle size.

b. Chemical Composition of Nanocrystalline Deposits

The compositions of the alloys galvanostatically deposited, calculated for alloy samples of surfaces of 10μm^2 with an error of ± 2%, are summarized in Table 2.

According to the EDX results, the increase in current density leads to an increase of the Ni content in the deposits. At current density of j = 65 $mAcm^{-2}$, the content of cobalt in the alloys is always higher than in the electrolyte, as a consequence of the lower overpotential for the Co^{2+} reduction compared to Ni^{2+} as can be seen also from the polarization curves (Figure 1.b).

Copyright © 2010. Nova Science Publishers, Incorporated. All rights reserved.

Handbook of Material Science Research, Nova Science Publishers, Incorporated, 2010. ProQuest Ebook Central,

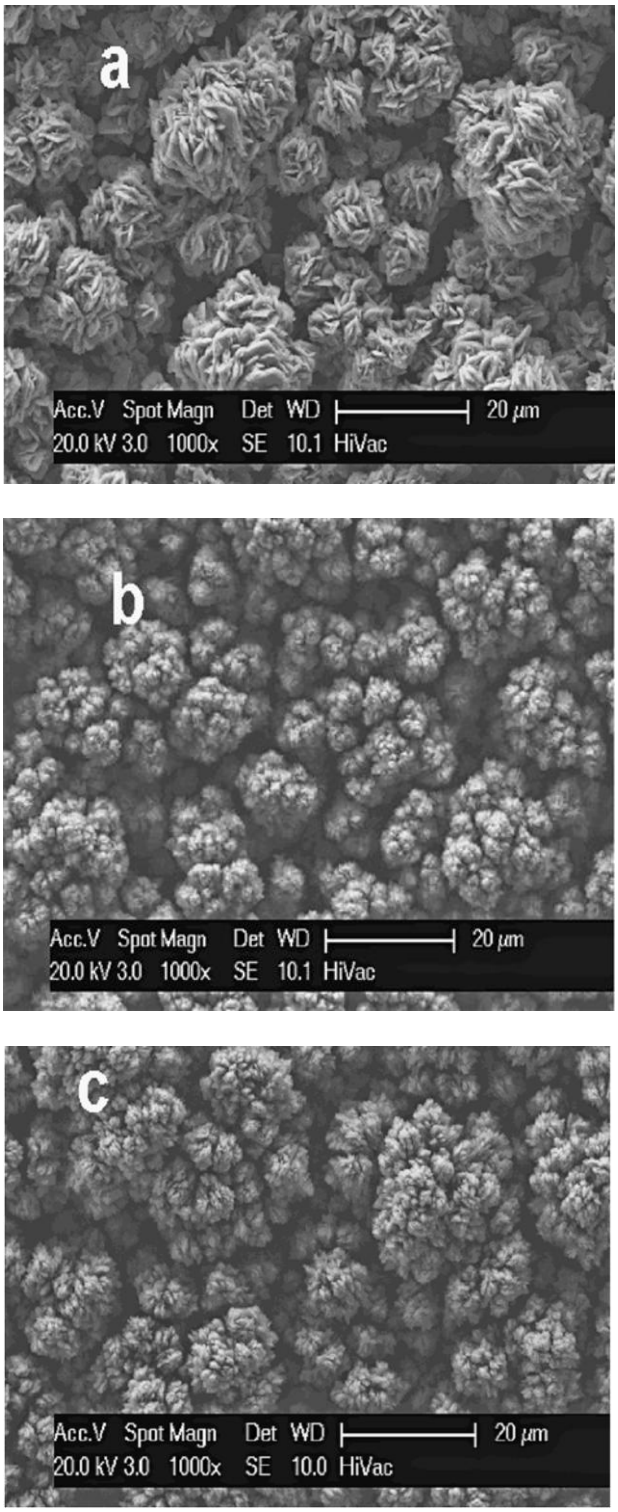

a
Acc.V Spot Magn Det WD 20 μm
20.0 kV 3.0 1000x SE 10.1 HiVac
b
Acc.V Spot Magn Det WD 20 μm
20.0 kV 3.0 1000x SE 10.1 HiVac
c
Acc.V Spot Magn Det WD 20 μm
20.0 kV 3.0 1000x SE 10.0 HiVac

Figure 4. SEM micrographs of deposits obtained from the electrolyte with concentration ratio Ni^{2+}/Co^{2+}= 1 at different current densities: a) 65, b) j=220 and c) j=400 $mAcm^{-2}$.

Copyright © 2010. Nova Science Publishers, Incorporated. All rights reserved.

Handbook of Material Science Research, Nova Science Publishers, Incorporated, 2010. ProQuest Ebook Central,

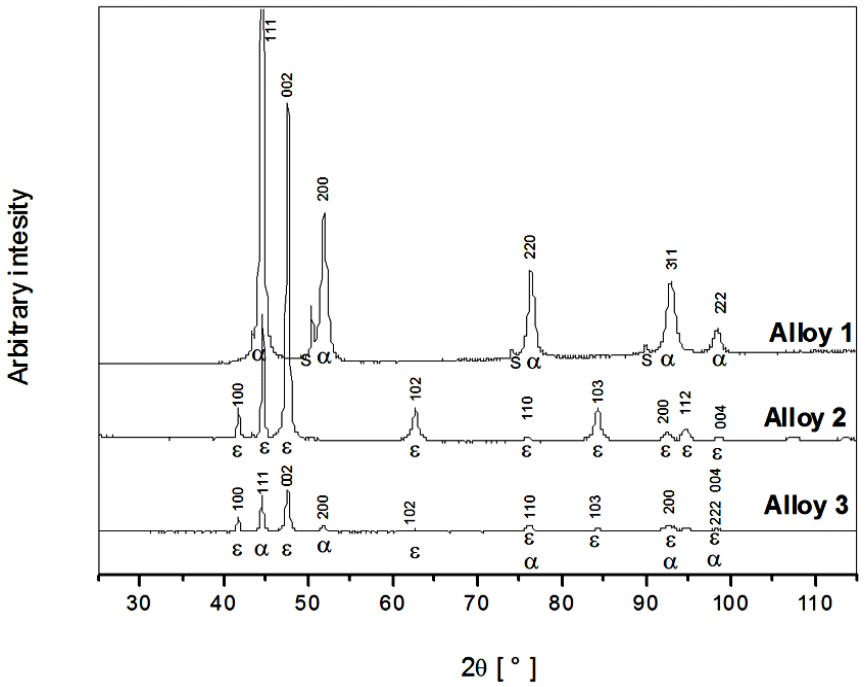


Figure 5. X-ray diffraction patterns of alloys 1, 2 and 3 experimental details as indicated in Table 2 (α-reflections attributed to the α-Ni; ε-reflections attributed to the ε-Co; S- reflection attributed to the Cu-substrate).

The deposits (alloys 3, 4 and 5) obtained from the electrolyte (Ni^{2+}/Co^{2+} = 1) at selected current densities, exhibit different compositions as well as structures. Increasing the current density shifts the ratio of nickel and cobalt in the alloys closer to the value of concentration of the corresponding ions in electrolyte. The phenomenon of anomalous co-deposition (characteristic for the electrodeposition of iron group metals) is very pronounced in the production of compact deposits. However in the case of powder deposition, anomalous co-deposition is much less pronounced, so that the composition of the alloy powder deposited at high current densitiy is almost similar to the concentration of the metal ions in the electrolyte (alloy 5).

c. Microstructure of the Ni-Co Nanocrystalline Deposits

The crystal structure, particle shape and size of the electrochemically obtained cobalt-nickel alloy deposits considerably depend on current density according to the ESEM analysis and X-ray diffraction patterns (Figure 5). Average grain sizes and lattice parameters were calculated from the peak broadening using Scherrer equation with Rietveld refinement method [27]. Powder particles obtained with the geometric size varying from 5 μm to about 50 μm were composed by fine nanosized crystallites (see Table 3). Crystal structure and composition of the deposits obey the phase diagram [28].

Copyright © 2010. Nova Science Publishers, Incorporated. All rights reserved.

Handbook of Material Science Research, Nova Science Publishers, Incorporated, 2010. ProQuest Ebook Central,

Table 2. Chemical composition of the alloys galvanostatically deposited out of electrolytes with the different ratios of Ni^{2+}/Co^{2+} and at different current densities

	Alloy 1	Alloy 2	Alloy 3	Alloy 4	Alloy 5
Ni^{2+}/Co^{2+} ratio in the electrolyte	4	0.25	1	1	1
Current density ($mAcm^{-2}$)	65	65	65	220	400
Ni content in alloy (At%)	80	5.5	33	40	43
Co content in alloy (At%)	20	94.5	67	60	57

Table 3. Phase composition, size of primary crystallites and cell parameters of the alloys electrodeposited, experimental details as in Table 2

Alloy/ current density	Crystal structure/Content (%)	Grain size (nm)	a (Å)	c (Å)	Cell volume ($Å^3$)
Alloy 1/ 65 $mAcm^{-2}$	FCC/100	13	3.5259		43.833
Alloy 2/ 65 $mAcm^{-2}$	HCP/100	20	2.5057	4.0690	22.126
Alloy 3/ 65 $mAcm^{-2}$	FCC/28 HCP/72	19 15	3.5291 2.5053	 4.0717	43.955 22.127
Alloy 4/ 220 $mAcm^{-2}$	FCC/71 HCP/27 amorphous phase/8	13 11	3.5296 2.4987	 4.0767	43.971 22.043
Alloy 5/ 400 $mAcm^{-2}$	FCC/82 HCP/3 amorphous phase/15	11 10	3.5329 2.4947	 4.1005	44.096 22.100

Figure 5 presents X-ray diffraction patterns of three alloys, electrodeposited at a current density of j =65 $mAcm^{-2}$, with 43 $mAhcm^{-2}$ Coulombs consumed and average sample thickness of (25±5) μm. The phase composition and average size of crystallites are summarized in Table 3.

As can be seen from the presented results (Figure 5, Table 3), a deposit obtained from the electrolyte with Ni^{2+}/Co^{2+} concentration ratio 4:1 (alloy 1) consists of α-Ni phase with face-centered cubic lattice (FCC phase, space group Fm3m, a=3.524Å, JCPDS 00-004-0850). The diffraction peaks of Cu with low intensity result from the substrate material. The average size of primary crystallites in the FCC phase was 13±2 nm. The alloy electrodeposited at the same current density with the ratio Ni^{2+}/Co^{2+} = 4 (alloy 2) contains the ε-Co phase with hexagonal close-packed lattice (HCP phase, space group P63/mmc, a=2.506Å, c=4.069Å, JCPDS 01-071-4239). With increasing Co content in the alloys (Table 3) the average size of crystallite

Copyright © 2010. Nova Science Publishers, Incorporated. All rights reserved.

Handbook of Material Science Research, Nova Science Publishers, Incorporated, 2010. ProQuest Ebook Central,

increases ranging from 13 to 19 nm for the FCC phase and from 15 to 20 nm for the HCP phase. The diffraction patterns of all three alloys deposited at relatively low current density for powder formation show a strong texture.

A detailed Rietveld's analysis revealed that Ni-Co alloys deposited from the electrolyte with the Ni^{2+}/Co^{2+} ratio of 1 at different current densities (alloys 3, 4 and 5), are composed of solid solutions of the both, cubic FCC phase and the HCP phase due to the mutual miscibility of Ni and Co in the range of concentration in the obtained deposits (Table 2). The increase of current density lead to the increase in the content of FCC phase in solid solution as well as the formation of significant amounts of amorphous phase.

An analysis of the diffractograms of the powdered alloys electrodeposited at j = 65, j = and j = 400 $mAcm^{-2}$ (alloys 3, 4 and 5) shows that the decrease of the current density results in pronounced crystallization and an increase of the size of crystallites as well as higher HCP content. Furthermore, it can be seen that the cell volume of the alloys (alloy 3-5) increases slightly with increasing current density. Alloy 1 (rich in Ni) and alloy 2 (rich in Co) exhibit cell volumes comparable to the theoretical values of Ni (43.8 $Å^3$) and Co (22.1 $Å^3$).

At lower current densities, the content of Co in the deposit consists only of HCP phase; with increasing current density the content of Co decreases by approximately 10 at%, but the concentration of the HCP phase is reduced down to 3 %. Beside an amorphous content of 8 - 15%, the rest of the Co is forming a solid solution within the Ni FCC phase, resulting in an increase of the cell volume (see Table 3). If the kinetics of the deposition process is fast, the powder can be obtained at low driving force [29], while a much larger driving force is needed for kinetically slow processes such as Ni and Co deposition, resulting in an electrodeposition process far from equilibrium conditions, *i.e.*, at high overpotentials, and formation of the FCC phase. At low overpotentials, a higher amount of Co as the HCP phase is formed.

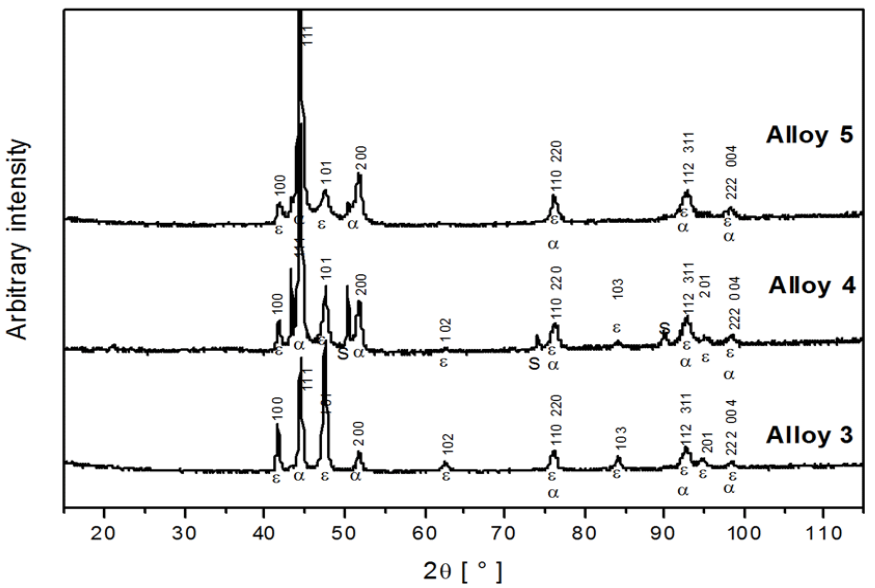


Figure 6. X-ray diffraction patterns of the alloys 3, 4 and 5, experimentally details as indicated in Table 2(α- reflections attributed to the α-Ni; ε-reflections attributed to the ε-Co; S- reflection attributed to the Cu-substrate).

Copyright © 2010. Nova Science Publishers, Incorporated. All rights reserved.

Handbook of Material Science Research, Nova Science Publishers, Incorporated, 2010. ProQuest Ebook Central,

d. Thermal Stability of Nanocrystalline Deposits

The thermal stability of alloys (prepared as powders out of electrolytes with concentration ratios in the bath Ni^{2+}/Co^{2+} = 4, alloy 1, and Ni^{2+}/Co^{2+} = 0.25, alloy 2, at j=65mAcm^{-2} was characterized by DSC analysis (temperature range from room temperature to 600°C) as well as by X-ray diffraction and SEM. For X-ray diffraction and SEM measurements, the samples were annealed in sealed evacuated quartz tubes at selected temperatures for 30 minutes, water quenched and than analyzed.

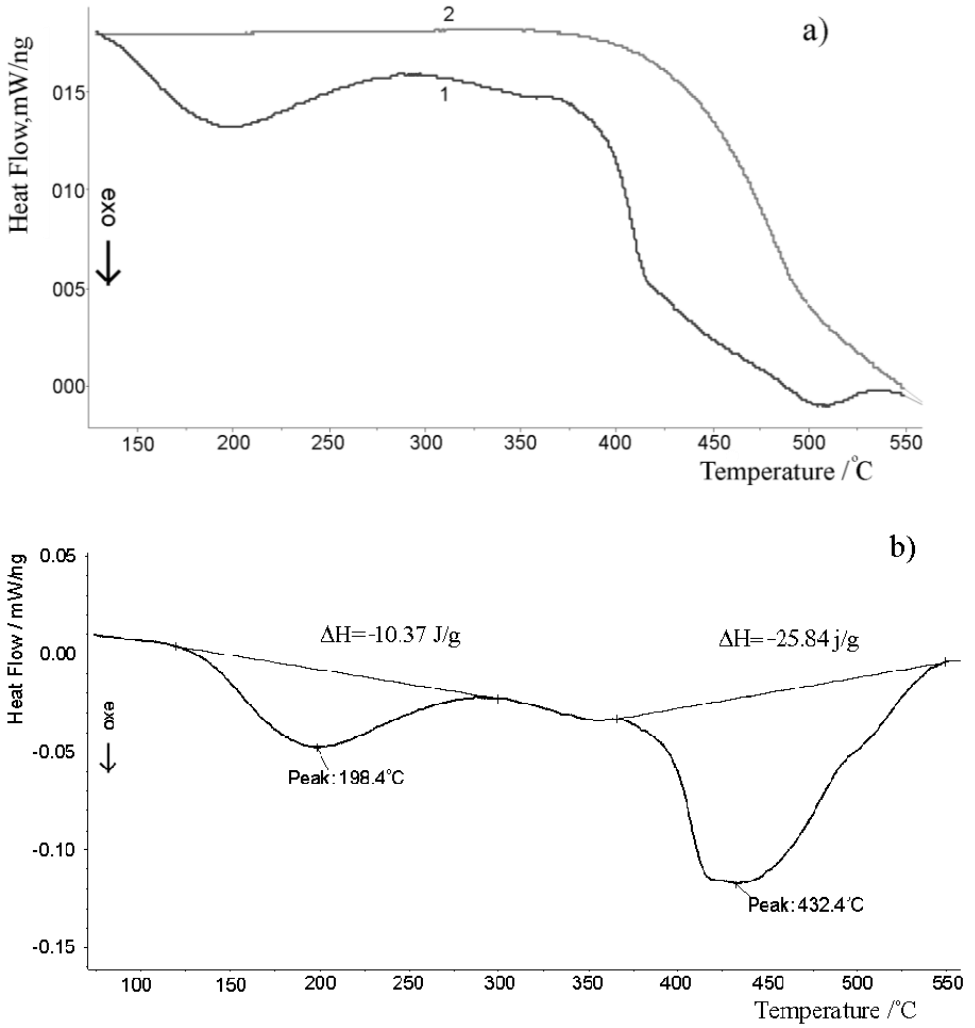


Figure 7. a) DSC traces showing the first run (curve 1) and second heating run (curve 2) of an as-prepared sample of alloy 1; heating rate 20 Kmin^{-}1; b) Heat flow difference of the alloy 1; heating rate 20 Kmin^{-1}, experimental details as in Table 2.

Since at the nanometer scale the atomic fraction of interfacial atoms is comparable to that in the perfect crystalline state, the structure of grain joints is unstable at room temperature and tends to evolve towards a more ordered state. Because the intercrystalline volume represents a region of stored excess energy with respect to the bulk of a grain, there is a significant driving

Copyright © 2010. Nova Science Publishers, Incorporated. All rights reserved.

Handbook of Material Science Research, Nova Science Publishers, Incorporated, 2010. ProQuest Ebook Central,

force for grain growth in nanocrystalline materials during heating. The structure of nanosized metals is thus thermodynamically unstable and shows a strong tendency to structural changes under annealing [31] or even at room temperature [32]. These changes typically affect the density of crystalline defects, grain size, crystallographic orientation and grain boundary structure [33]. The enthalpy release due to annealing of the nanocrystalline structure can be directly measured e.g. by DSC [34].

Thermal Stability of Alloy 1

The thermal behavior of the powder of alloy 1 (Ni^{2+}/Co^{2+} = 4, j = 65mAcm^{-2}) is depicted in DSC curves, Figure 7a. The first heating run (1) of an as-prepared sample shows a significant heat flow in comparison to the second heating run (2), measured after cooling the sample to ambient temperature, the heating run was repeated to obtain a baseline. By subtracting the DSC curve of the second run from the first one gives the heat released, Figure 7b [34]. The heat release associated with structural relaxation in the temperature range 120-300°C was ΔH= -10.3 J/g and for further structural transformations in the temperature range 380-530°C, released heat was ΔH=-25.8 J/g.

Structural transformations in Ni-Co deposits (alloy 1) induced by annealing at 250, 350 and 550°C are shown in the XRD (Figure 8). These temperatures have been chose according to DSC curve. The XRD patterns and Rietveld refinement analysis (Table 4) show only grain growth. No reflections related to cobalt or nickel oxides were detectable. A typical SEM micrograph of alloy 1 after annealing at 550°C is shown in Figure 9. The composition as well as the structure of the deposit was attained with no significant change even in particle size.

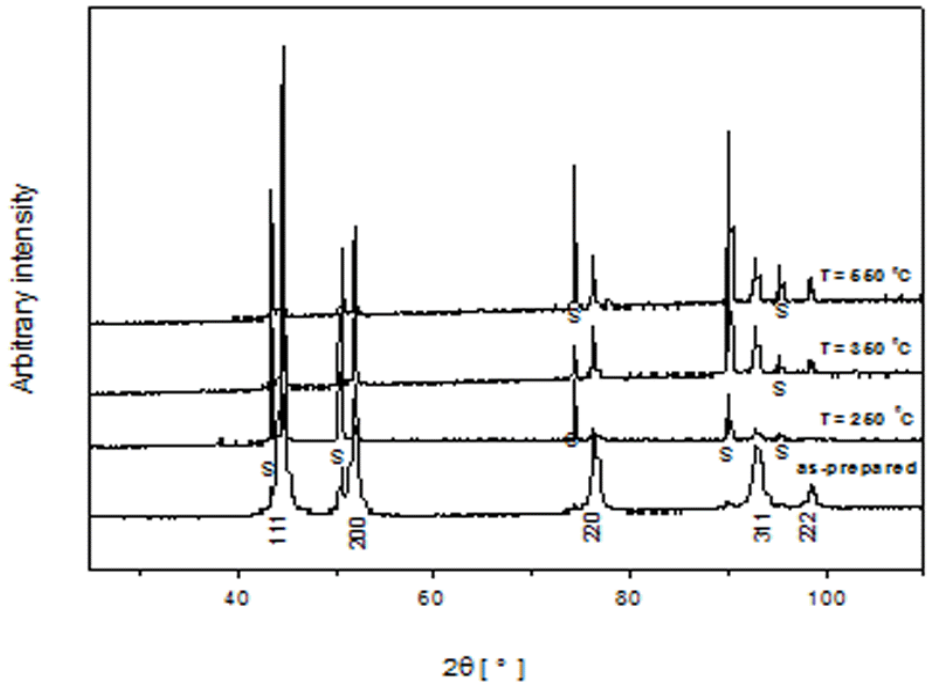


Figure 8. XRD patterns of alloy 1 as prepared and annealed at different temperatures.

Copyright © 2010. Nova Science Publishers, Incorporated. All rights reserved.

Handbook of Material Science Research, Nova Science Publishers, Incorporated, 2010. ProQuest Ebook Central,

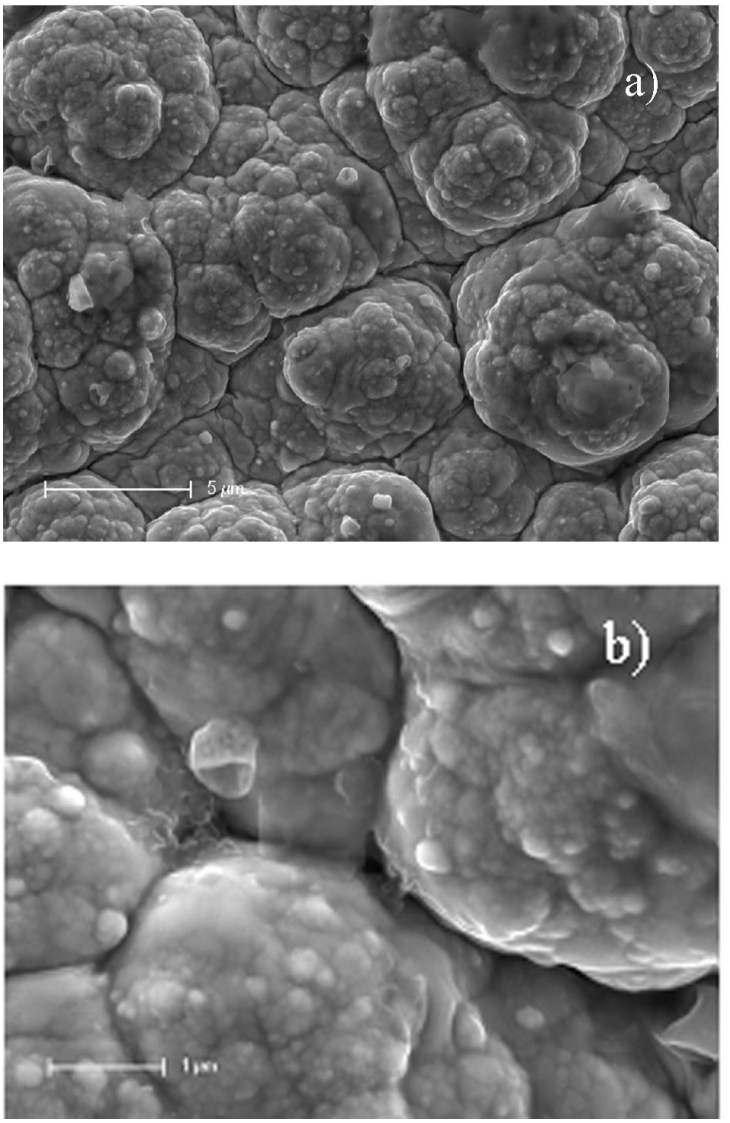


Figure 9. SEM micrographs of Ni-Co deposits on copper substrate prepared out of an electrolyte with concentration ratio $Ni^{2+}/ Co^{2+} = 4$, $j=65mAcm^{-2}$ upon annealing at 550°C; a) magnification 5000x b) magnification 20000x (SE, accelerating voltage 10kV).

As in many studies on the thermal stability of nanocrystalline materials [36], the Ni-Co alloy powder showed during heating exhibit a quasi-nucleation growth-process. When nanocrystalline deposits are brought to an elevated temperature, the nanometer-sized crystallites in the deposits start to grow in a random, non-uniform way and some of the present nanocrystallites appear as nuclei and preferentially start to grow at the expense of the surrounding nanocrystalline matrix. With increasing temperature, the grains become larger and the number of dislocations decreases considerably. The lattice constant of the FCC phase increases slightly with increased annealing temperature, resulting in large cell volumes compared to the theoretical FCC- Ni, probably due to the presence of 20 percentage of cobalt in the deposit (Table 4).

Copyright © 2010. Nova Science Publishers, Incorporated. All rights reserved.

Handbook of Material Science Research, Nova Science Publishers, Incorporated, 2010. ProQuest Ebook Central,

Table 4. Phase composition and size of crystallites of electrodeposited as well as annealed alloy 1 (prepared from electrolyte with concentration ion ratio Ni^{2+}/Co^{2+} = 4 at current density j=65mAcm^{-2})

Alloy	Crystal structure	Grain size (nm)	Lattice constant (Å)	Cell volume (Å^3)
Alloy 1 as prepared	FCC	13	3.5259	43.833
Alloy 1 annealed at 250°C	FCC	20	3.5274	43.891
Alloy 1 annealed at 350°C	FCC	47	3.5270	43.876
Alloy 1 annealed at 550 °C	FCC	57	3.5305	44.004

Thermal Stability of Alloy 2

The thermal behavior of the of Ni-Co powder of alloy 2 (electrolyte ratio Ni^{2+}/Co^{2+} =0.25, j=65mAcm^{-2}) shown on the DSC curve Figure 10 is characterized by an exothermic reaction indicating a stepwise process of structural relaxation and transformation of the alloy in the temperature range 300-550°C. The first exothermic feature in the temperature range 280-300°C can be attributed to structural relaxation process of the FCC phase. During grain growth, as the system moves from the condition of an as-prepared nanocrystalline sample of higher excess free energy to the condition of the annealed sample exhibiting lower excess of free energy, there is an enthalpy release of ΔH= -190.6 J/g) giving a measure of the thermal stability of the sample connected with the phase transformation from HCP to FCC structure.

Table 5. Phase composition and size of crystallites of electrodeposited and annealed alloy 2 (prepared from electrolyte with concentration ion ratio Ni^{2+}/Co^{2+} =0.25, at current density j = 65 mAcm^{-2})

Alloy	Crystal structure	Grain size (nm)	a (Å)	c (Å)	Cell volume (Å^3)
Alloy 2 As prepared	HCP	20	2.5057	4.0690	22.126
Alloy 2 annealed at 280°C	HCP	21	2.5071	4.0706	22.159
Alloy 2 annealed at 350 °C	HCP	19	2.5079	4.0714	22.177
Alloy 2 annealed at 550 °C	FCC HCP	50 7	3.5467 2.4790	 4.257	44.616 22.660

Copyright © 2010. Nova Science Publishers, Incorporated. All rights reserved.

Handbook of Material Science Research, Nova Science Publishers, Incorporated, 2010. ProQuest Ebook Central,

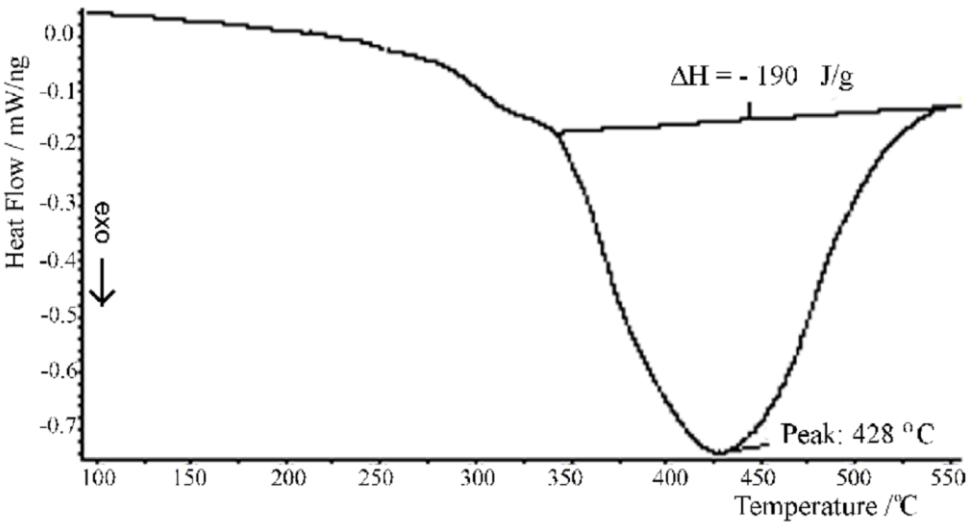


Figure 10. Heat flow difference of the alloy 2; heating rate 20 $Kmin^{-1}$; experimental details as in Table 2.

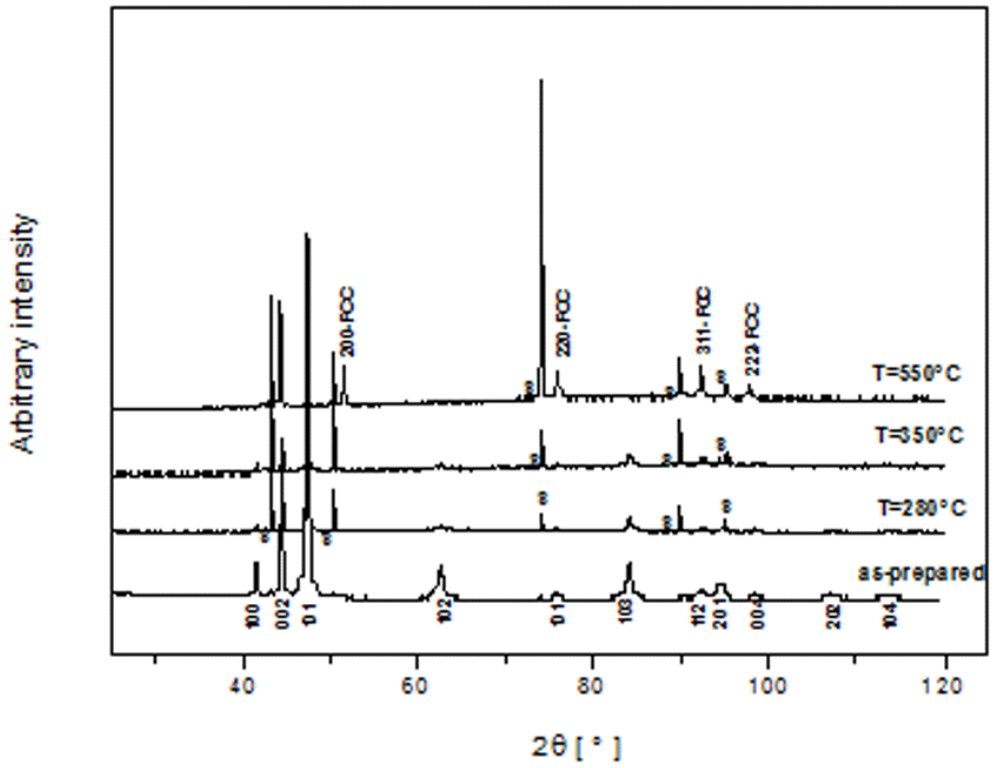


Figure 11. XRD patterns of alloy 2 as prepared as well as annealed at the different temperatures.

Copyright © 2010. Nova Science Publishers, Incorporated. All rights reserved.

Handbook of Material Science Research, Nova Science Publishers, Incorporated, 2010. ProQuest Ebook Central,

As in the case of alloy 1, based on the DSC curve (Figure 10) the analysis of structural transformations of Ni-Co deposits (alloy 2) induced by heating were carried out using samples annealed at temperatures of 280, 350 and 550°C.

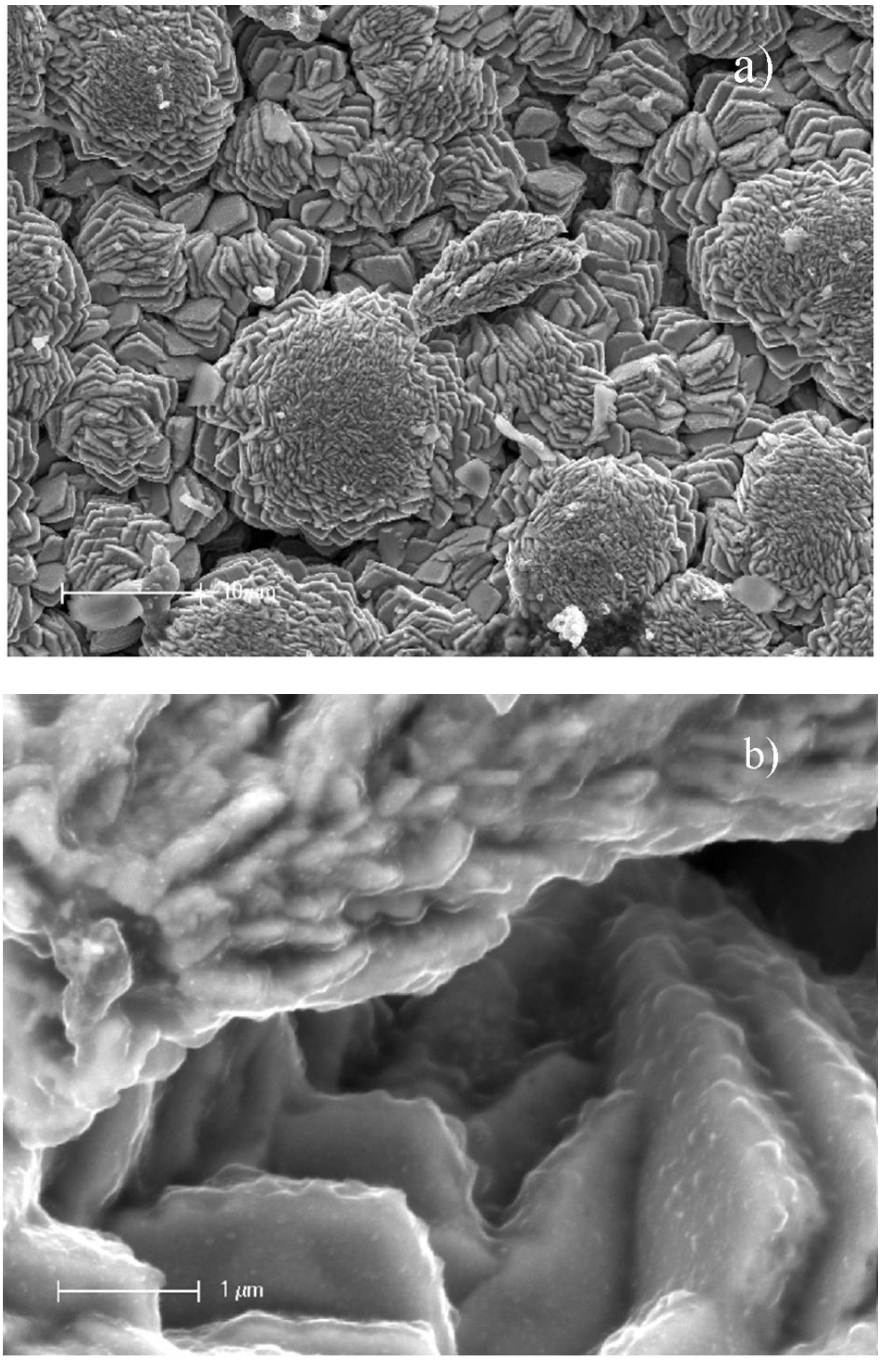


Figure 12. SEM micrographs of Ni-Co deposits on copper substrate prepared out of an electrolyte with concentration ratio Ni^{2+}/Co^{2+}= 0.25, j=65mAcm^{-2} (alloy 2) upon annealing at 550°C; a) magnification 2000 x, b) magnification 20000x (SE, accelerating voltage 10kV).

Copyright © 2010. Nova Science Publishers, Incorporated. All rights reserved.

Handbook of Material Science Research, Nova Science Publishers, Incorporated, 2010. ProQuest Ebook Central,

The XRD of the alloy 2 as prepared on the copper substrate showed only the reflections of a Co-like HCP pattern, see Fig 5. According to the X-ray diffraction analysis (Figure 11), during annealing the concentration of the HCP phase is continuously reduced and the reflection attributed to the FCC phase of Co appears, with a content of >70% in the sample, Table 5.

The grain size of the FCC phase significantly increases to 50 nm, while size of HCP phase decreases to 6.5 nm (Table 5). Annealing at temperatures of 280 and 350°C caused only slight difference of grain size and lattice constant (Table 5). However, the annealing at temperature of 550°C generated grain size and lattice constant changes due to the austenitic allotropic phase transformation at 422°C according to the phase diagram [28]. The HCP phase is more stable phase at room temperature, but back transformation to FCC phase after cooling did not occur. However, the austenitic phase transformation (HCP to FCC) temperature is a function of heating rate [37]. At this point, it is assumed that the allotropic transformation is connected with grain growth. The FCC phase is retained upon cooling to ambient temperature and with increasing temperature the content of HCP phase is reduced. Further investigations of structural transformation in electrodeposited nanocrystalline alloy sample with high content of Co are performed actually.

SEM micrographs of annealed alloy 2 are shown in Figure 12. The platelet structure is preserved; however, the top of the particles consists of the platelets with reduced size. Additionally, single particle grains are much better formed in comparison to the as-prepared sample (Figure 12-3c).

e. Magnetic Properties of Nanocrystalline Deposits

Electrodeposited nanostructured ferromagnetic materials such as Ni and Ni-Fe alloys exhibit desirable soft magnetic properties such as low coercivity, increased electrical resistivity and grain size independent saturation magnetization [37]. Magnetic saturation of electrodeposited ferromagnetic materials is only dependent on the composition [23]. The potential of cobalt based nanocrystalline alloys has attracted attention because of their higher saturation magnetization compared with Ni and permalloy (Ni-20wt%Fe) type electrodeposits.

The samples obtained after pressing were heated up to 600°C in an argon atmosphere in order to achieve the thermal stabilization of alloy structure. Upon application of a weak magnetic field, the magnetization increases rapidly to a high value called the saturation magnetization, which is in general a function of temperature. The relative magnetic permeability increases in the temperature range from 180 to 250°C for alloy 1 and to 430°C for alloy 2 with a peak value at 250°C (alloy 1) and 430°C (alloy 2). A decrease in the free volume, a decrease in the content minimal value of the chaotically distributed dislocations and a reduction in the content of microstrains took place in this temperature interval.

Copyright © 2010. Nova Science Publishers, Incorporated. All rights reserved.

Handbook of Material Science Research, Nova Science Publishers, Incorporated, 2010. ProQuest Ebook Central,

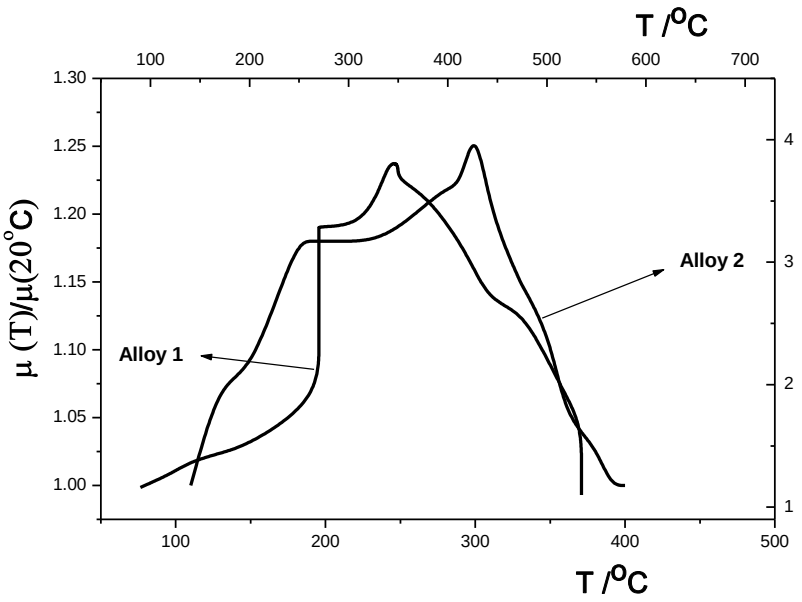


Figure 13. Temperature dependence of relative magnetic permeability of the powders of alloys.

The increase in magnetic permeability is a consequence of the described structural changes during heating. All of these features ensure greater mobility of the magnetic domain walls and their better directionality, consequently increasing the magnetic permeability. In the temperature range 250 to 370 °C the relative magnetic permeability of alloy 1 decreases rapidly, reaching Curie temperature at approximately 370°C, close to the value of pure Ni (627 K) [38]. The slightly higher value of the Curie temperature can be attributed to the content of Co in the sample (see Table 2.) The relative magnetic permeability for alloy 2 decreases in the temperature range of 420 to 525 °C. The Curie temperature of this sample is related to the relative high content of Ni, reducing the Curie temperature from the value of pure Co of 1388K [38] to the actual one.

CONCLUSION

The structures as well as morphology of the Ni-Co alloy powders galvanostatically deposited from ammonium nickel and cobalt sulfate solutions on Cu-cathodes depend on the deposition current density as well as the bath composition. FCC phase is the predominant phase in the alloy powders at the Ni rich side. A decrease in the Ni concentration in the alloy powders causes the increase in the concentration of HCP phase in the crystalline part of the powder. A decrease in the deposition current density results in an increased amount of the HCP phase in the powder and the crystal grain growth of FCC and HCP phases. HCP phase is the dominant phase in powders with a higher content of cobalt. Increase of the deposition current density in electrolytes with a concentration ratio $Ni^{2+}/Co^{2+} = 1$ leads to a decrease of HCP phase content in the powders, the crystal grains growth of the FCC phase and the transformation of the HCP phase into the FCC phase. A significant thermal effect upon

Copyright © 2010. Nova Science Publishers, Incorporated. All rights reserved.

Handbook of Material Science Research, Nova Science Publishers, Incorporated, 2010. ProQuest Ebook Central,

heating of nanocrystalline Ni-Co alloy powder deposits has been observed. In Co rich samples, structural changes during heating were attributed to the phase transformation of HCP to FCC. The relative magnetic permeability strongly depends on the Ni^{2+}/Co^{2+} ratio in the alloys, showing the strong influence of a material with low Curie temperature (Ni) on a material with a high Curie temperature (Co).

ACKNOWLEDGMENTS

The investigation was partially supported by the Ministry of Science and Environmental Protection of Serbia, under the following Project and 142025. The support by the I.K. "Experimental Materials Science – Nanostructured Materials", a college for PhD students at the University of Vienna is greatly appreciated by L.R.

REFERENCES

[1] H. Gleiter, Nanocrystalline materials, *Prog. Mater. Sci*.33(1989)223-315.
[2] R.P. Andres, R.S. Averback, W.L. Brown, L.E. Brus, W.A. Goddard III, S.G. Kaldor, *J. Mater. Res*. 4(1989) 704-736.
[3] M.A.Meyers, A. Mishra, D.J. Benson, *Progress in Materials Science* 51(2004) 427-556.
[4] U. Erb, *Nanost. Mater*. 6(1995)533-538.
[5] N. V. Myung, K. Nobe, *J. Electrochem. Soc*.148(2001)136-144.
[6] D.-Y.Park, K.S.Park, J.M.Ko,D.-H. Cho, S.H. Lim, W.Y.Kim, B.Y. Yoo, Myung N.V., *J. Electrochem. Soc*.153(2006)814-821.
[7] A. Bianco, G. Gusmano, R. Montanari, G. Montesperelli, E. Traversa, *Thermochimica Acta* 269/270(1995)117-132.
[8] A. Calusaru, Electrodeposition of Powders from Solutions, Elsevier, New York, (1979)USA.
[9] C.A.C. Souza, J.E. May, A.T. Machado, A.L.R. Tachard, E.D. Bidoia, *Surface and Coatings Technology*, 190(2005)75-82.
[10] K.I. Popov, M.G. Pavlović, "Electrodeposition of metal powders with controlled particle grain size and morphology", in Modern Aspects of Electrochemistry, Vol. 24, Edited by R.E. White, B.E. Conway, and J.O'M. Bockris, Plenum Press, New York (1993) Chapter 6.
[11] A. Maričić, M. Spasojević, L. Rafailović, V. Milovanović, L. Ribić-Zelenović, *Mat. Sci. Forum* 453/454(2004)411-416.
[12] L. Ribić-Zelenović, L. Rafailović, M. Spasojević, A. Maričić, *Sci. Sintering*, 38(2006)145-153.
[13] L. Ribić-Zelenović, L. Rafailović, M. Spasojević, A. Maričić, Physica B Condensed Matter 403(2008)2148-2154.
[14] A.Vicenzo, P.L.Cavallotti, *Electrochim. Acta* 49(2004)4079-4089.
[15] S.Armyanov, S.Vitkova, *Surf. Technol*.7(1978)319-329.
[16] J. Scoyer, R. Winand. *Surf. Technol*. 5(1977)169-204.

Copyright © 2010. Nova Science Publishers, Incorporated. All rights reserved.

Handbook of Material Science Research, Nova Science Publishers, Incorporated, 2010. ProQuest Ebook Central,

[17] T Cohen- Hyams, W.D. Kaplan, J. Yahalom, *Electrochem. Solid- State Lett*., 5(2002)75.
[18] H.Li, F. Ebrahimi, *Material Science and Eng*. A, 347(2003)93.
[19] S.H.Kim, K.T. Aust, U. Erb, F.Gonzales, G. Palumbo, *Scripta Mater*., 48(2003)1379-1384.
[20] E. Gómez, S. Pané, E. Vallés, *Electrochim. Acta* 51 (2005) 146-153.
[21] E. Gómez, S. Pané, X. Alcobe, E. Vallés, *Electrochim. Acta* 51(2006)5703-5709.
[22] D. Kim, D.Y .Park, B.Y.Yoo, P.T.A.Sumodjo, N.V. Myung, *Electrochim. Acta* 48 (2003) 819-830.
[23] N.V. Myung, D.-Y .Park, B.-Y.Yoo, P.T.A .Sumodjo, *J. of Magnetism and Mag. Mater*.265(2003)189-198.
[24] I.Z. Rahman, M.V. Khaddem-Mousavi, A.A.Gandhi, T.F.Lynch, M.A.Rahman, *J of Physics: Conference Series* 61(2007) 523-528.
[25] V.D. Jović, V. Maksimović, M.G. Pavlović, V. Maksimović, *J. Solid State Electrochem*. 10(2006)959-966.
[26] V.D. Jović, B.M. Jović, M.G. Pavlović, *Electrochim. Acta* 51(2006)5468-5477.
[27] H.Rietveld, *J.Appl. Crystallogr*. 2(1969)65-71.
[28] T.B. Massalski, Binary alloy phase diagrams, ASM International, *Materials Park*, OH,(1991) USA.
[29] K.I. Popov, S. S. Djokić, B.N. Grgur, Fundamental Aspects of Electrometallurgy, Kluwer Academic press, New York (2002) USA.
[30] G.M. Chow, Y.Y. Li, Y.K. Hwu, *Mater. Phys. Mech*.1 (2000) 67-72.
[31] F. Czerwinski, A. Zielinska-Lipiec, J.A. Szpunar, *Acta Mater*. 47(1999) 2553-2566.
[32] B. Bozzini, G. Giovannelli and P.L. Cavallotti, *J. Appl. Electrochem.* 30(2000)591-594.
[33] L. Peraldo Bicelli, B. Bozzini, C. Mele, L. D'Urzo, *Int. J. Electrochem. Sci.*, Vol. 3(2008)
[34] L.C. Chen, F. Spaepen, *J. Appl. Phys*. 69(1991)679-688.
[35] F.O.Méar, B. Lenk, Y. Zhang, A.L.Greer, *Scripta Mater*.,59(2008) 1243-1246.
[36] N. Wang, Z. Wang, K.T. Aust, U. Erb, *Acta Mater*. 45(1997)1655-1669.
[37] G. Hibbard, K. T. Aust, G. Palumbo, U.Erb, *Scripta Mater*. 44(2001)513-518.
[38] C. Kittel, Introduction to Solid State Physics, 8th Edition (2005) USA.
[39] D.M. Minić, The applied Electrochemistry, Faculty for Physical Chemistry, Belgrade (1996).

Copyright © 2010. Nova Science Publishers, Incorporated. All rights reserved.

Handbook of Material Science Research, Nova Science Publishers, Incorporated, 2010. ProQuest Ebook Central,

In: Handbook of Material Science Research
Editors: C. René and E. Turcotte, pp.417-431
ISBN 978-1-60741-798-9
© 2010 Nova Science Publishers, Inc.

Chapter 11

A SYSTEMATIC PROCEDURE TO PREDICT EXPLOSIVE PERFORMANCE AND SENSITIVITY OF NOVEL HIGH-ENERGY MOLECULES IN ADD, ADD METHOD-1

Soo Gyeong Cho*
High Explosives Group, Agency for Defense Development (ADD),
Daejeon, Korea

ABSTRACT

In order to derive novel high-energy molecules (HEMs) efficiently, we recently have established a systematic procedure to predict explosive performance and sensitivity of a HEM candidate of which a two-dimensional chemical sketch has been given. This procedure, which we called ADD Method-1, includes three theoretical steps, i.e. (1) calculation of molecular structure and energy, (2) computation of molecular descriptors, and (3) estimation of explosive performance and sensitivity. In calculating molecular structure and energy, we have utilized density functional theories in a quantum mechanical program. Once accurate three-dimensional molecular structure and molecular energy at that structure were calculated, heat of formation and density, two important molecular descriptors in estimating explosive performance, have been computed. Constitutional molecular descriptors including oxygen balance, cycles, and rotatable bonds, which will be used as input variables in estimating impact sensitivity, have been computed directly from a two-dimensional molecular structure. In a final step, explosive performance has been estimated with the Cheetah program, while impact sensitivity has been predicted with a knowledge-based neural network method.

Keywords: High-energy molecule; Explosive performance; Impact sensitivity; Molecular descriptor; Density; Heat of formation

∗ Corresponding author: P.O. Box 35-42, Daejeon, 305-600, Korea. Tel.: +82-42-821-3704; fax: +82-42-821-2390, E-mail address: soocho@add.re.kr.

Copyright © 2010. Nova Science Publishers, Incorporated. All rights reserved.

Handbook of Material Science Research, Nova Science Publishers, Incorporated, 2010. ProQuest Ebook Central,

1. INTRODUCTION

During recent years, the development of novel substances has become an important research area, probably due to the high profit if a novel substance is successfully developed. However, this type of research usually requires a tedious and expensive process. Sometimes, efforts often turn out to be in vain when the candidate that once looked promising delivers disappointing results in some aspects almost at the final stage of the test and evaluation. Furthermore, the efficiency of success in deriving new substances has been known to be quite low. For example, in the area of drugs, recent statistics show that only one drug reaches the market out of approximately five thousand trials [1]. Thus, to increase the profit of research, it should be of particular importance to increase the efficiency by selecting promising candidate molecules in the early stage. Nowadays, novel approaches of molecular modelling [2] and combinatorial chemistry [3] have been introduced to help researchers choose good candidate molecules with promising properties.

As in other research areas, there has been significant advancement in developing new HEMs in recent decades [4-5]. A number of new HEMs and relevant additive materials have been successfully synthesized. Some important HEMs worth mentioning are CL-20 (2,4,6,8,10,12-hexanitrohexaazaisowurtzitane), TNAZ (1,3,3-trinitroazetidine), NTO (3-nitro-1,2,4-triazole-5-one), and FOX-7 (1,1-diamino-2,2-dinitroethylene). To incorporate these new HEMs into military technologies, extensive formulation studies have been going on.

In a more recent and major achievement, Prof. Eaton of the University of Chicago succeeded in synthesizing octanitrocubane [6-7]. Dr. Christe reported the first synthesis of the pentanitrogen cation (N_5^+), only the third number of the N_n family [8-9]. Eaton's and Christe's discoveries have prompted theoretical chemists to investigate various polycyclic cage compounds and polynitrogen clusters including the N_8 molecules [10-14]. Although these theoretical studies will not provide synthetic methodologies to make them, they usually furnish good answers regarding whether they will be stable, once they have been synthesized, and will guide synthetic chemists by providing good visions concerning molecular structure and energy content. In addition, numerous new nitrogen-rich molecules have been actively pursued by synthetic chemists [15-20]. When judged against all this information, we are confident that there will be major breakthroughs in some HEM areas within a decade from now.

With our continuous interests in deriving new HEMs, we have recently proposed a systematic procedure to predict explosive performance and sensitivity of HEMs which do not have any experimental data available. Our approach is purely theoretical. The overall procedure is shown in Figure 1. In this procedure, we have tried to assemble prediction methods that we believe are practically the best in each step by considering both accuracy and computation speed. As we accumulate the results by applying this procedure to numerous HEMs, we will find advantages and limitations in each and in the overall steps. We are going to update the prediction method of each step, if a new scientific advance for the step emerges as a better one than the current method.

Copyright © 2010. Nova Science Publishers, Incorporated. All rights reserved.

Handbook of Material Science Research, Nova Science Publishers, Incorporated, 2010. ProQuest Ebook Central,

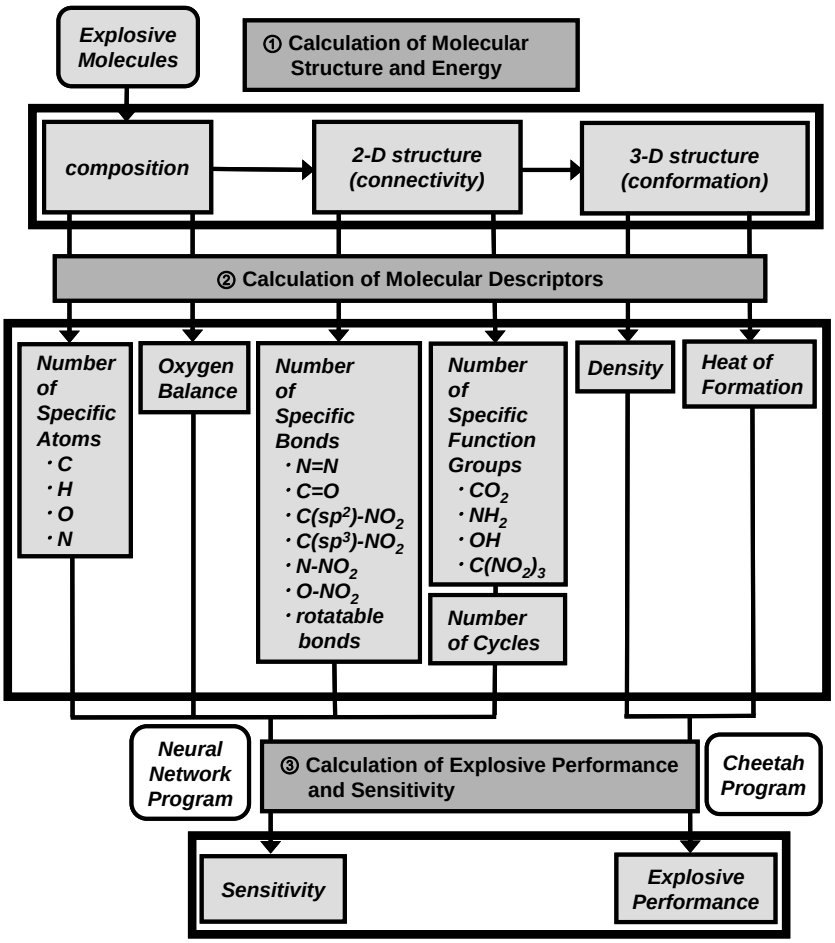


Figure 1. Overall procedure of ADD Method-1.

2. Calculation of Molecular Structure and Energy

Once a new HEM is presented with a two-dimensional structure, the first task of ADD Method-1 should be an accurate prediction of three-dimensional molecular structure. In principle, all the molecular descriptors should be derived at the global minimum where the molecule exists in the lowest energy [21]. However, obtaining the global minimum in the potential energy surface usually requires extensive conformational analyses even in molecules with a modest size. Sometimes, this step may require most of computational powers among the total steps of ADD Method-1. Thus, one has to be concerned with how extensive the conformational search should be performed, when a structurally complex molecule is presented. Computational efforts in this step is perhaps relieved significantly by (1) previous good knowledge of conformational preference in both main skeletons and side chains and (2) simplified modelling with model compounds. Employment of respectably high levels of computation theories is usually required to obtain accurate molecular structures and energies, but is often restricted by the availability of computational resources. Thus, the decision of calculational levels can be determined by a compromise between the accuracy requirement

Copyright © 2010. Nova Science Publishers, Incorporated. All rights reserved.

Handbook of Material Science Research, Nova Science Publishers, Incorporated, 2010. ProQuest Ebook Central,

and the computational power the user can put in. In ADD Method-1, we decide to utilize B3LYP/6-31G* level of density functional theory [22-24] in the GAUSSIAN series of programs [25], which is known to provide quite accurate results in estimating a variety of physicochemical properties.

3. CALCULATION OF MOLECULAR DESCRIPTORS

3.1. Density

According to our preliminary studies, density is probably the most important descriptor to predict the explosive performance accurately [26]. However, getting the right prediction of crystal patterns is one of the most difficult challenges in computational chemistry [27,28]. Many scientists in various research areas such as crystallography, biophysics, and supramolecules have been attempting to predict the crystal packing patterns including crystal densities based on the arrays of 3-D molecular network [29-35], but this prediction is still a formidable task and is known to have several huge hurdles in getting the job done in the right fashion. Although some applications have been found in the area of HEMs [36-40], this approach may not be performed routinely in molecular modelling of explosives at current stage. We also believe that this approach will not be a practical solution since it requires too much computational works and screening of HEM candidates has to deal with a large number of molecules at a time.

Up till now, many researchers in the HEM area still utilize the group additivity method (GAM), where the molar volume (including void) is obtained by summing up the volume of each atom or molecular fragment (group). In the estimation of densities of HEMs, the parameters developed by Stine were frequently utilized [41]. Stine developed 34 parameters representing specific types of atoms by compiling more than 2000 crystals. In 1998, Ammon and Mitchell developed 78 parameters corresponding to each group as well as atom by examining more than 11000 crystal structure data [42]. Professor Ammon revised his parameters in 2001, where 96 parameters were established from approximately 26,000 crystal structures [43].

Other approach to predict densities of HEMs is the calculation method based on the molecular volume. Professor Politzer developed a novel scheme to calculate densities by combining molecular volume and molecular surface electrostatic potential (MSEP) [44]. Professor Kim modified Politzer's scheme to calculate electrostatic potential on a simple van der Waals surface [45]. We applied this modified scheme to predict densities of 41 explosive molecules, which were selected through a variety of molecular types and density values [46]. Similar approach was also successfully applied to HEMs by others [47].

In ADD Method-1, both GAM with Ammon's parameters and MSEP were utilized. As seen in Figure 2, MSEP method appears to be slightly superior to GAM, but requires much more computational efforts. Using two completely different approaches may help the users in confirming the prediction process in deciding a very important molecular descriptor. One shortcoming of current GAM we have to mention is the inability of GAM to differentiate the densities of structural isomers.

Copyright © 2010. Nova Science Publishers, Incorporated. All rights reserved.

Handbook of Material Science Research, Nova Science Publishers, Incorporated, 2010. ProQuest Ebook Central,

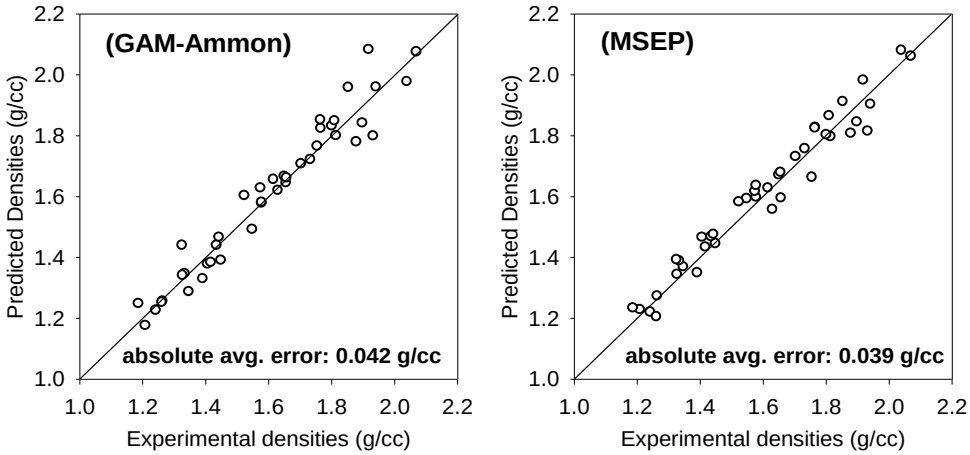


Figure 2. Plots of the densities predicted by GAM-Ammon (left) and by MSEP (right) against experimental densities.

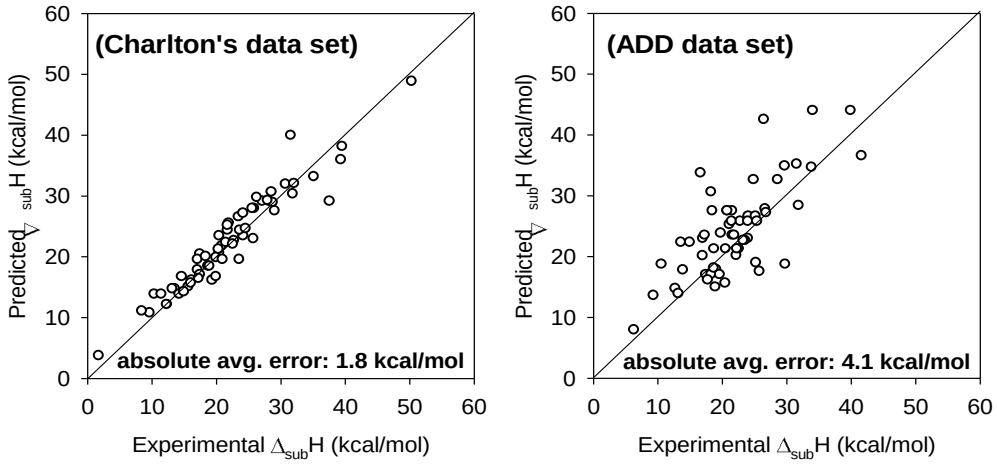


Figure 3. Plots of the predicted sublimation energies against the experimental ones. Tests have been performed at Charlton's data set (Left) and ADD data set (Right).

3.2. Heat of Formation

In the prediction of the heat of formation, at the current stage, we are following the scheme developed by Politzer and coworkers [48,49], in which density functional calculations at the BP86/6-31G** level [22-24], and empirical atomic correction terms were used. This requires additional geometry optimization at the BP86/6-31G** level, while our previous geometry and energy calculations are carried out at the B3LYP/6-31G* level. However, we have noticed that geometry optimizations at both levels provide similar molecular structures, and the additional calculation takes only a few steps to reach to the new optimized geometry. Politzer's scheme provided heat of formation in the gas phase. Since all the HEMs considered in this study are solid, sublimation energy should be subtracted.

Copyright © 2010. Nova Science Publishers, Incorporated. All rights reserved.

Handbook of Material Science Research, Nova Science Publishers, Incorporated, 2010. ProQuest Ebook Central,

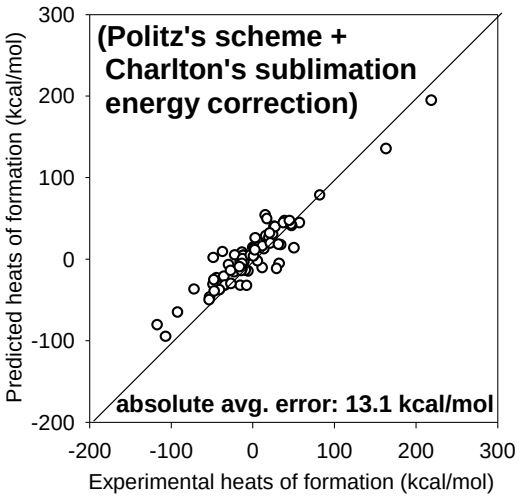


Figure 4. A Plot of the predicted heats of formation against the experimental ones in 72 nitro compounds.

In estimating sublimation energy, we employed a QSPR regression scheme developed by Charlton et al. [50], who used three simple molecular descriptors, i.e. carbon atom number, hydrogen bond donor, and hydrogen bond acceptor. According to the results of Charlton et al., their QSPR equation predicted sublimation energies of 62 compounds (Charlton's data set) to be an average error of 1.8 kcal/mol. Before applying this QSPR scheme to our work, we have validated this scheme with a data set of 58 compounds (ADD data set) where 40 nitro and 18 heterocyclic compounds are included. An average error in the ADD data set is 4.1 kcal/mol, which is much poorer than the one in the Charton's data set. This large discrepancy ensures us that the parameters and equations developed for general chemical compounds may not be transferred directly to HEMs. In the near future, we are planning to derive a new QSPR equation to be suitable for HEMs.

In order to validate the overall scheme in estimating the heats of formation in ADD Method-1, we have collected a variety of nitro compounds whose experimental heats of formation in the solid phase were known from the ICT database [51]. This data set consisted of 72 nitro compounds from (1) aromatic benzenes and heterocycles, and (2) aliphatic cyclic hydrocarbons, heterocycles, and (3) acyclic compounds. The result is depicted in Figure 4. The overall error in predicting heats of formation in the solid phase is estimated to be slightly greater than 13 kcal/mol. Of course, this error includes prediction error in sublimation energies. The current prediction error in heat of formation may not mislead the predicted explosive performance significantly, but there are substantial rooms to improve the accuracy of prediction errors including the one of sublimation energy.

3.3. Other Molecular Descriptors

Besides density and heat of formation, molecular descriptors required to be computed are all the descriptors used to estimate impact sensitivity in knowledge based neural network scheme. All these molecular descriptors are constitutional descriptors [52], which can be

Copyright © 2010. Nova Science Publishers, Incorporated. All rights reserved.

Handbook of Material Science Research, Nova Science Publishers, Incorporated, 2010. ProQuest Ebook Central,

computed from a 2-D chemical molecular structure without considering 3-D nature of a molecule. These include (1) the number of C, H, O, and N atoms, (2) the numbers of N=N, C=O, C(sp^2)-NO_2, C(sp^3)-NO_2, N-NO_2, O-NO_2, and rotatable bonds, (3) the number of CO_2, NH_2, OH, and C(NO_2)$_3$ groups, (4) ring cycles, and (5) oxygen balance. These 17 constitutional descriptors are used as input variables in estimating impact sensitivity (see Figure 1).

4. Calculation of Explosive Performance and Sensitivity

4.1. Explosive Performance

One of the important aspects researchers of HEMs are looking for is high explosive performance. Thus, it is of significant importance for modelling scientist to predict the explosive performance with reasonable accuracy. With numerous efforts given to this area, it is now generally accepted that accurate prediction is possible, provided that reasonably good values for the heat of formation and density are given [26,53]. In predicting explosive performance, the Cheetah program [54], which is probably one of the most well known programs, has been utilized in ADD Method-1. In calculating explosive performance in the Cheetah program, we assume that HEM is packed to 97% of theoretical maximum density, which is the crystal density we have obtained in the previous step. Either C-J pressure or detonation velocity is represented as the explosive performance, and is compared with corresponding value of well known HEMs such as TNT, 24-DNI (2,4-dinitroimidazole), RDX, HMX, and CL-20. These five HEMs may represent typical examples of their own performance.

One of the biggest problems in predicting explosive performance accurately is the quality of input data in heat of formation and density. We have found that the density value appears to affect the final performance seriously, but the value of the heat of formation influences in a modest way [55]. Figure 5 depicts the variation in detonation velocity and C-J pressure of HMX drawn as a relative scale by changing heat of formation and density in the Cheetah program [54]. The total variations shown in Figure 5 are 40 kcal/mol in heat of formation, and 0.20 g/cc in density, respectively. Rough computations may be prone to commit such errors. We arbitrarily classify the quality of input data as ‘excellent’, ‘reasonable, and ‘poor’ depending upon the magnitude of errors in Table 1. Figure 6 shows the estimation errors in the explosive performances of HMX according to the classification shown in Table 1. We have compared the predicted explosive performance of HMX with those of RDX and CL-20. HMX is known to be an explosive which is clearly superior to RDX and is definitely inferior to CL-20. As shown in Figure 6, if the quality of input data is ‘excellent’, the estimated explosive performances are quite close to the real ones, and are clearly distinguishable from those of explosive molecules in different levels. If the quality of input data is ‘reasonable’, one may still have the right understanding about what the performance will be, although the prediction results have some errors. On the other hand, the ‘poor’ input data sometimes mislead the users to have wrong information. As shown in ‘poor’ prediction of Figure 6, the predicted explosive performances of HMX are close to those of either RDX or CL-20, unless two conflicting errors are cancelled by chance.

Copyright © 2010. Nova Science Publishers, Incorporated. All rights reserved.

Handbook of Material Science Research, Nova Science Publishers, Incorporated, 2010. ProQuest Ebook Central,

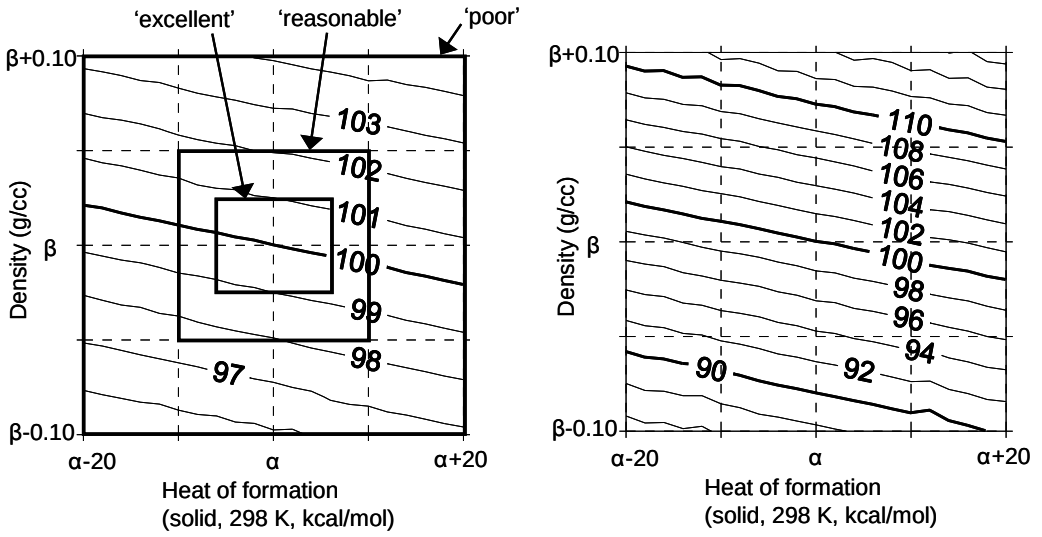


Figure 5. Variation of detonation velocity (left), and C-J pressure (right) of HMX due to the change of heat of formation and density (α=17.9 kcal/mol, β=1.905 g/cc).

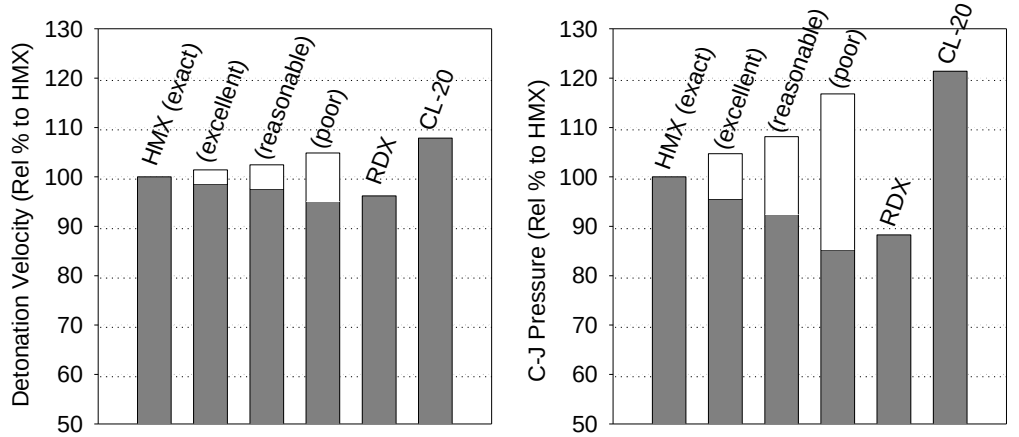


Figure 6. Variation of Predicted Detonation Velocity (left) and C-J Pressure (right) of HMX Due to the Quality of Input Data. White Blocks Show the Lower and Upper Limits of Prediction.

Table 1. Qualitative Classification of Input Data for Explosive Performance

classification	error range	remark
excellent	density: ±0.03 g/cc heat of formation: ±5 kcal/mol	goal to achieve
reasonable	density: ±0.05 g/cc heat of formation: ±10 kcal/mol	state-of-art computations
poor	density: ±0.10 g/cc heat of formation: ±25 kcal/mol	rough computations

Copyright © 2010. Nova Science Publishers, Incorporated. All rights reserved.

Handbook of Material Science Research, Nova Science Publishers, Incorporated, 2010. ProQuest Ebook Central,

4.2. Impact Sensitivity

Besides explosive performance, it is also of significant importance to quantify the sensitivities of new HEMs accurately. In contrast to the explosive performance, the sensitivities of HEMs are hardly correlated with several governing molecular descriptors in a reasonable fashion [56]. Thus, we believe that predicting the sensitivities of HEMs with a few molecular descriptors may not be a good approach. In addition, if one wants to utilize the impact sensitivity, published experimental values may not be trustworthy enough to use as reference values. These values are known to vary largely, when they are collected from various different sources, which use different experimental apparatus in different environments. Thus, bearing all these natures of sensitivities in mind, we feel that artificial neural network method may be one of the best methods in predicting the sensitivity of HEMs [57,58].

The pioneering work with knowledge-based approach was done by Nefati, Cense, and Legendre, who utilized a neural network method [59]. Netafi et al. utilized the database published by Storm, Stine, and Kramer [60,61], who archived impact sensitivities of more than 200 HEMs. We also have optimized new neural network architecture. We (1) collect 234 HEMs from the database of Storm et. al., (2) sketch 3-D structures of those molecules with the Cerius-2 molecular modeling program, (3) minimize those structures by using semi-empirical AM1 methods, and (4) calculate 39 different types of molecular descriptors [62]. A number of different sets have been constructed by combining these molecular descriptors to form an input layer of the neural network structure. We have found that the 17(constitutional parameters)-2-1 architecture provides the best result among those tested in our study (see Figure 7). With the optimized neural network architecture shown in Figure 7, we have calculated the correlation coefficient (r^2) and standard error of prediction (SEP) for each set. The overall SEP and r^2 values are 0.190 and 0.818, respectively. As also shown in Figure 8, the results in validation and test (unknown samples) sets are as good as those in the train set. We have checked whether this architecture depended upon the selection of different molecules in validation and test sets. These new predictions by switching molecules in validation and test sets have provided SEP and r^2 values which are quite similar to the original prediction.

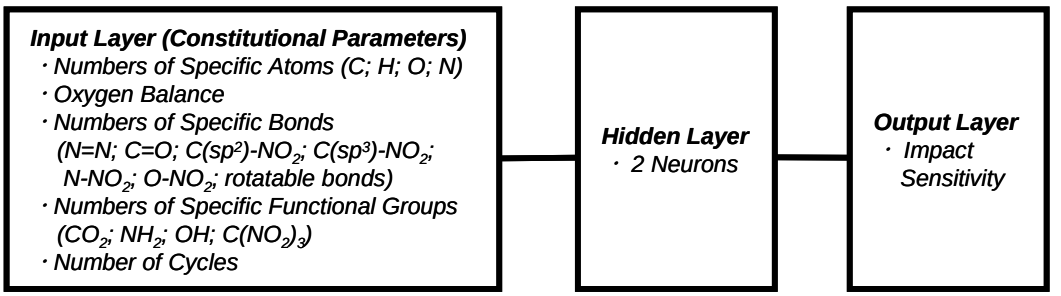


Figure 7. Neural network architecture (17-2-1) used for impact sensitivity prediction in ADD Method-1.

Copyright © 2010. Nova Science Publishers, Incorporated. All rights reserved.

Handbook of Material Science Research, Nova Science Publishers, Incorporated, 2010. ProQuest Ebook Central,

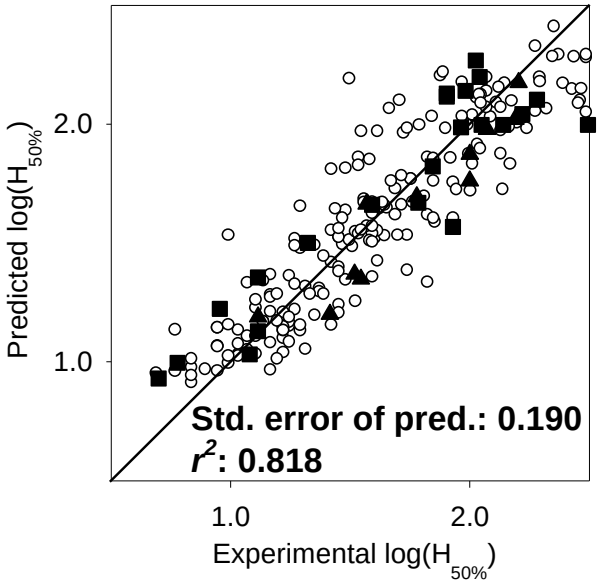


Figure 8. A plot of predicted impact sensitivities against experimental ones. Molecules in the training, validation, and test sets are marked as ○, ■, and ▲, respectively. Solid line represents perfect agreement between experiment and prediction.

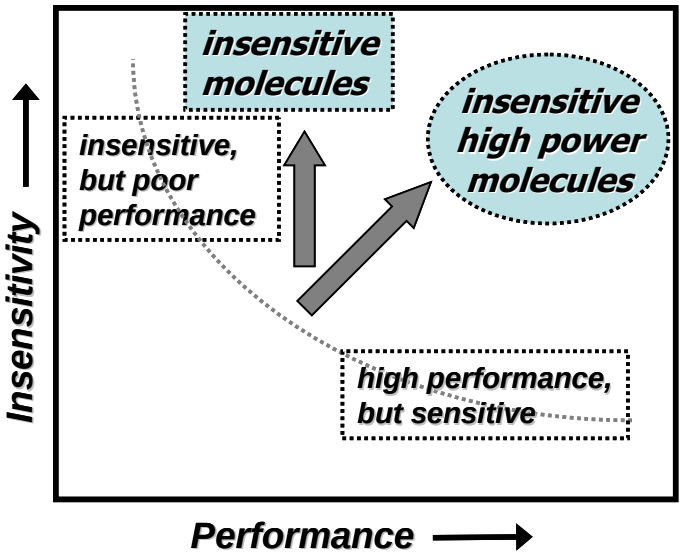


Figure 9. A general feature of a 2-D plot between explosive performance and sensitivity. Broken curve may reflect the technical limit of the current HEMs.

Copyright © 2010. Nova Science Publishers, Incorporated. All rights reserved.

Handbook of Material Science Research, Nova Science Publishers, Incorporated, 2010. ProQuest Ebook Central,

5. A Two-Dimensional Plot between Explosive Performance and Impact Sensitivity

It is very difficult for one to judge the usefulness of new HEMs by considering either explosive performance or sensitivity nature alone. We believe that the usefulness of new HEM candidates should be judged by a combination of explosive performance and sensitivity nature, although it may depend heavily upon the need of the users. We have devised a novel 2-D plot between explosive performance and insensitivity shown in Figure 9.

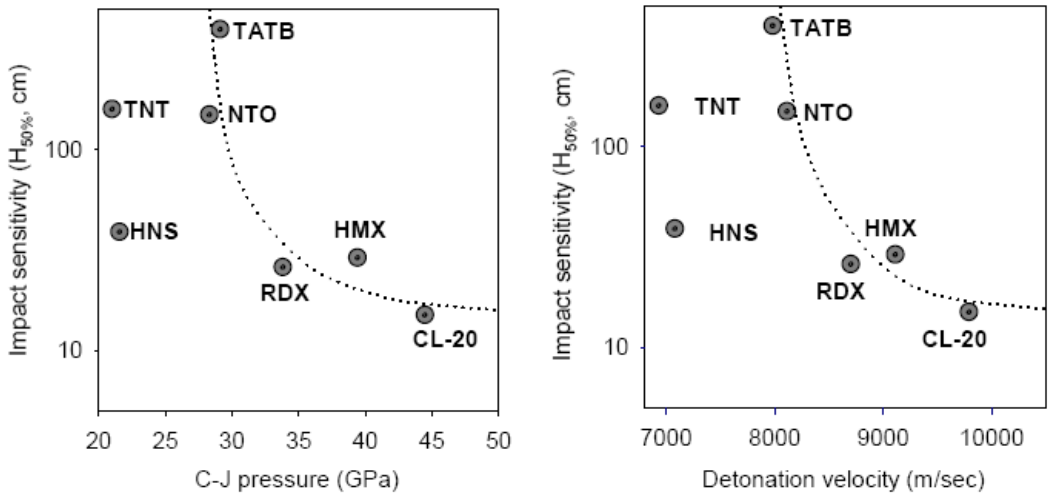


Figure 10. 2-D Plots between explosive performance and impact sensitivity. Explosive performance is represented by either C-J pressure (left) or detonation velocity (right).

This 2-D plot presents a relatively clear understanding regarding the technical status of each HEM. HEMs with high power, but are sensitive, reside in the area of the lower right side, while sensitive HEMs with less power form a region in the upper left side. When we connect well-known HEMs in current military application, a curve is drawn through insensitive explosives to highly powerful ones. This curve may represent a current technical boundary, which new HEM candidate should tackle to surpass in terms of explosive performance and insensitivity. If a new HEM candidate surpasses this curve to move toward right upper side, it should be considered as a really good candidate for an insensitive high power HEM. If the candidate resides in the upper region and break the curve to have more power than the current HEMs, it ought to be a good candidate for an insensitive HEM.

We have made spots in 2-D plots with well-known HEMs such as RDX, HMX, TNT, NTO, TATB, and CL-20. Explosive performance in the X-axis is represented by either C-J pressure or detonation velocity computed at the Cheetah program. Insensitivity in the Y-axis is illustrated by the impact sensitivity as a logarithm scale of $H_{50\%}$ predicted at a knowledge-based neural network method. 2-D plots with actual data are shown in Figure 10. As mentioned before, the spots of CL-20, HMX, and RDX, all of which have high power, but are relatively sensitive, position in the lower right corner of the plot. On the other hand, the spots of TATB and NTO, which are insensitive but less powerful, reside in the upper left side. Besides explosive performance and sensitivity, there are other numerous chemical and

Copyright © 2010. Nova Science Publishers, Incorporated. All rights reserved.

Handbook of Material Science Research, Nova Science Publishers, Incorporated, 2010. ProQuest Ebook Central,

explosive features considered in finding a good HEM. Thus, only good positioning in this 2-D plot may not ensure the HEM candidate to be a good one. However, *it is certain that the new candidate molecule should be removed early, if it is predicted to be in a poor position in this 2-D plot.*

6. CONCLUSION

During our recent extensive prediction studies, we decided to standardize our prediction methods, which we called ADD Method-1, to derive new HEMs. According to ADD Method-1, one is able to estimate explosive performance and safety nature of new HEM candidates which do not have any prior chemical information but a simple 2-D sketch. It calculates accurate 3-D molecular structure with high level quantum mechanical calculations, and computes molecular energy on the most stable geometry. Based on computed molecular geometry and energy, nineteen different molecular descriptors including heat of formation and density are computed. These molecular descriptors are used to compute explosive performance and impact sensitivity. Explosive performance is predicted by the Cheetah program, and the impact sensitivity is estimated by an artificial neural network method optimized in ADD. ADD Method-1 is currently a combination of high level quantum mechanical calculations and knowledge-based QSPR methods. We also attempted to increase our prediction accuracy by employing the so-called best known and well-proved techniques for each step. This may require some computational resources, and takes some time to perform all the steps. Our future intention is to change the calculational methods of all the steps to knowledge-based QSPR methods, which eventually enables the user to finish all the steps in less than an hour. When this fast, yet accurate prediction method is coupled with extensive new HEM search methods, we believe that the development of new HEMs will be greatly accelerated. Of course, although this method contains some knowledge-based methods, it can be applicable to any compound the properties of which the user has no prior information about.

Copyright © 2010. Nova Science Publishers, Incorporated. All rights reserved.

ACKNOWLEDGMENTS

Dr. Bang Sam Park who recently retired from the High Explosives Group (HEG) in ADD is gratefully acknowledged for his guidance and support in preparing all the hardware and software necessary for this study. The author also appreciates Drs. Jeong Kook Kim and Jin Rai Cho who previously guided, and Dr. Hyoun Soo Kim who currently guides HEG. They have given a full support to a molecular modeling study on novel HEMs in the group. Prof. Kyoung Tai No in Yonsei University and Dr. Sung Kwang Lee in Bioinformatics and Molecular Design Research Center (BMDRC) initiated neural network studies of impact sensitivity prediction, and Prof. Chan Kyung Kim in Inha University performed density prediction studies with MSEP scheme. The author wishes to thank them.

Handbook of Material Science Research, Nova Science Publishers, Incorporated, 2010. ProQuest Ebook Central,

REFERENCES

[1] Brennan, M.B. *Chem. and Eng. News* 2000 (June 5th issue), 63.
[2] Gans, W.; Amann, A.; Boeyens, J.C.A., Eds.; *Fundamental Principles of Molecular Modeling*; Plenum Press: New York, NY, 1995.
[3] Wilson, S.R.; Czarnik, A.W. *Combinatorial Chemistry. Synthesis and Application*; John Wiley and Sons, Inc.: New York, NY, 1997.
[4] Sikder, A.K.; Sikder, N. *J. Hazard. Mater*. 2004, *A112*, 1.
[5] Agrawal, J.P. *Prog. Energy Combust. Sci.* 1998, *24*. 1.
[6] Zhang, M.-X.; Eaton, P.E.; Gilardi, R. *Angew. Chem. Int. Ed. Engl.* 2000, *39*, 401.
[7] Eaton, P.E.; Gilardi, R.L.; Zhang, M.-X. *Adv. Mater.* 2000, *12*, 1143.
[8] Christe, K.O.; Wilison, W.W.; Sheedy, J.A.; Boatz, J.A. *Angew. Chem. Int. Ed. Engl.* 1999, *38*, 2004.
[9] Vij, A.; Wilson, W.W.; Vij, V.; Tham, F.S.; Sheehy, J.A.; Christe, K.O. *J. Am. Chem. Soc.* 2001, *123*, 6308.
[10] Engelke, R.; Stine, J.R. *J. Phys. Chem.* 1990, *94*, 5689.
[11] Nguyen, M.T.; Ha, T.-K. *Chem. Phys. Lett.* 2001, *335*, 311.
[12] Li, Q.S.; Wang, L.J. *J. Phys. Chem. A* 2001, *105*, 1979.
[13] Manaa, M.R. *Chem. Phys. Lett.* 2000, *331*, 262.
[14] Christe, K.O. *Propel. Explos. Pyrotech.* 2007, *32*, 194.
[15] Xue, H.; Gao, H.; Twamley, B.; Shreeve, J.M. *Inorg. Chem.* 2005, *44*, 5068.
[16] Gao, H.; Zeng, Z.; Twamley, B.; Shreeve, J.M. *Chem. Eur. J.* 2008, *14*, 1282.
[17] Hammerl, A.; Klapötke, T.M. *Inorg. Chem.* 2004, *41*, 906.
[18] Karaghiosoff, K.; Klapötke, T.M.; Mayar, P.; Piotrowski, H.; Polborn, K.; Willer, R.L.; Weigand, J.J. *J. Org. Chem.* 2006, *71*, 1295.
[19] Geisberger, G.; Klapötke, T.M.; Stierstorfer, J. *Eur. J. Inorg. Chem.* 2007, 4743.
[20] Hyunh, M.H.V.; Hiskey, M.A.; Chavez, D.E.; Naud, D.L.; Gilardi, R.D. *J. Am. Chem. Soc.* 2005, *127*, 12537.
[21] Hehre, W.J.; Radom, L.; Schleyer, P. v. R.; Pople, J.A. *Ab Initio Molecular Orbital Theory*; Wiley: New York, NY, 1986.
[22] Sousa, S.F.; Fernandes, P.A.; Ramaos, M.J. *J. Phys. Chem. A* 2007, *111*, 10439.
[23] *Chemical Applications of Density-Functional Thoery*; Laird, B.B.; Ross, R.B.; Ziegler, T., Eds.; ACS Symposium Series 629; American Chemical Society: Washington, D.C., 1996.
[24] *Modern Density Functional Thoery. A Tool for Chemistry*; Seminario, J.M.; Politzer, P., Eds.; Theoretical and Computational Chemistry Vol. 2; Elsevier: Amsterdam, Netherlands, 1995.
[25] Foresman, J.B.; Frisch, A. *Exploring Chemistry with Electronic Structure Methods*; Gaussian, Inc.: Pittsburgh, PA, 1993.
[26] Anderson, E. In: *Tactical Missile Warheads*; Carleone, J., (Ed.); Prog. in Asteronatics and Aeronautics Vol. 155; AIAA: Washington, D.C., 1993, pp 81-163.
[27] Gavezzotti, A. *Acc. Chem. Res.* 1994, *27*, 309.
[28] Dunitz, J.D. *Chem. Commun.* 2003, 545.
[29] Dunitz, J.D.; Gavezzotti, A. *Cryst. Growth Des.* 2005, *5*, 2180.

Copyright © 2010. Nova Science Publishers, Incorporated. All rights reserved.

Handbook of Material Science Research, Nova Science Publishers, Incorporated, 2010. ProQuest Ebook Central,

[30] Wawak, R.J.; Gibson, K.D.; Liwo, A.; Scheraga, H.A. *Proc. Natl. Acad. Sci. USA* 1996, *93*, 1743.
[31] Gavezzotti, A.; Filippini, G. *Chem. Commun.* 1998, 287.
[32] Perlstein, J. *J. Am. Chem. Soc.* 1994, *116*, 11420.
[33] Beyer, T.; Lewis, T.; Price, S.L. *Cryst. Eng. Commun.* 2001, *44*, 1.
[34] Hulme, A.T.; Price, S.L.; Tocher, D.A. *J. Am. Chem. Soc.* 2005, *127*, 1116.
[35] Williams, D.E.; Gao, D. *Acta Cryst.* 1998, *B54*, 41-49.
[36] Cromer, D.T.; Ammon, H.L.; Holden, J.R. *A Procedure for Estimating the Crystal Densities of Organic Explosives*; Los Alamos National Laboratory, LA-11142-MS, 1987
[37] Sorescu, D.C.; Rice, B.M.; Thompson, D.L. *J. Phys. Chem. B* 2000, *104*, 8406.
[38] Rice, B.M.; Thompson, D.L. *J. Phys. Chem. B* 2004, *108*, 17730.
[39] Lewis, J.P.; Sewell, T.D.; Evans, R.B.; Voth, G.A. *J. Phys. Chem. B* 2000, *104*, 1009.
[40] Eckhardt, C.J.; Gavezzotti, A. *J. Phys. Chem. B* 2007, *111*, 3430.
[41] Stine, J.R. *Prediction of Crystal Densities of Organic Explosives by Group Additivity*; LA-8920, Los Alamos Nat. Lab., NM, 1981.
[42] Ammon, H.L.; Mitchell, S. *Propel. Explos. Pyrotech.* 1998, *23*, 260.
[43] Ammon, H.L. *Struct. Chem.* 2001, *12*, 205.
[44] Murray, J.S.; Brinck, T.; Politzer, P. *Chem. Phys.* 1996, *204*, 289.
[45] Kim, C. K.; Lee, K. A.; Hyun, K. H.; Park, H. J.; Kwack, I. Y. Kim, C. K.; Lee, H. W.; Lee, B.-S. *J. Comput. Chem. 25*, 2073-2079 (2004).
[46] Kim, C.K.; Cho, S.G.; Lee, K.A; Kim, C.K.; Park, H.-Y.; Zhang, H.; Lee, H.W.; Lee, B.-S. *J. Comput. Chem.* in press.
[47] Rice, B.M.; Hare, J.J.; Byrd, E.F.C. *J. Phys. Chem. B* 2007, *111*, 10874.
[48] Habibollahzadeh, D.; Grice, M.E.; Concha, M.C.; Murray, J.S.; Politzer, P. *J. Comput. Chem.* 1995, *5*, 654.
[49] Grice, M.E.; Politzer, P. *Chem. Phys. Lett.* 1995, *244*, 295.
[50] Charlton, M.H.; Docherty, R.; Hutchings, M.G. *J. Chem. Soc., Perkin Trans. 2*, 1993, 2023.
[51] Bathelt, H.; Volk, F.; Weindel, M. *ICT - Database of Thermochemical Values, Fifth Updates (1999)*; Institut fur Chemische Technologie: Karlsruhe, Germary, 1999.
[52] Karelson, M. *Molecular Descriptors in QSAR/QSPR*; Wiley-Interscience: New York, NY, 2000.
[53] Cooper, P.W. *Explosives Engineering*; VCH: New York, NY, 1996.
[54] Fried, L.E.; Howard, W.M.; Souers, P.C. *Cheetah 2.0 User's Manual*; Lawrence Livermore National Laboratory, UCRL-MA-117541, 1998.
[55] Goh, E.M.; Cho, S.G.; Park, B.S. *J. Def. Tech. Res.* 2000, *6*. 91.
[56] Brill, T.B.; James, K.J. *Chem. Rev.* 1993, *93*, 2667.
[57] Zupan, J.; Gasteiger, J. *Neural Networks in Chemistry and Drug Design*, 2nd ed.; Wiley-VCH: Weinheim, Germany, 1999.
[58] *Neural Networks in QSAR and Drug Design*; Devillers, J., Ed.; Academic Press: London, 1996.
[59] Nefati, H.; Cense, J.-M.; Legendre, J.-J. *J. Chem. Inf. Comput. Sci.* 1996, *36*, 804.
[60] Storm, C.B.; Stine, J.R.; Kramer, J.F. *Sensitivity Relationship in Energetic Materials*; Los Alamos National Laboratory, LA-UR-89-2936, 1989.

Copyright © 2010. Nova Science Publishers, Incorporated. All rights reserved.

Handbook of Material Science Research, Nova Science Publishers, Incorporated, 2010. ProQuest Ebook Central,

[61] Storm, C.B.; Stine, J.R.; Kramer, J.F. In *Chemistry and Physics of Energetic Materials*; Bulusu, S.N., Ed.; Kluwer Academic Press: Dordrecht, Netherlands, 1990; p. 605.
[62] Cho, S.G.; No, K.T.; Goh, E.M.; Kim, J.K.; Shin, J.H.; Joo, Y.D.; Seong, S. *Bull. Korean Chem. Soc.* 2005, *26*, 399.

Copyright © 2010. Nova Science Publishers, Incorporated. All rights reserved.

Handbook of Material Science Research, Nova Science Publishers, Incorporated, 2010. ProQuest Ebook Central,

Copyright © 2010. Nova Science Publishers, Incorporated. All rights reserved.

Handbook of Material Science Research, Nova Science Publishers, Incorporated, 2010. ProQuest Ebook Central,

In: Handbook of Material Science Research
Editors: C. René and E. Turcotte, pp.433-443
ISBN 978-1-60741-798-9
© 2010 Nova Science Publishers, Inc.

Chapter 12

THE DEVELOPMENT OF CO-BASED BULK METALLIC GLASSES

Ding Chen[1]* and Gou-zhi Ma[1]
Institute for Materials Research,
Hunan University, Changsha, China

ABSTRACT

Bulk metal glasses (BMGs) are currently the focus of the intense research in the world because of their excellent properties and potential applications as engineering materials and functional devices. Owing to their disordered structure, metallic glasses possess several unique properties that make them attractive for tribological, magnetic and mechanical applications. Most recently, with the development of new Co-based BMG with the highest strength (the compressive true strength is up to 5500 MPa) and unique magnetic characterization, Co-based BMG has become a hot topic in the new material field.

In this review, the preparation, factors contributing to glass-forming ability (GFA), mechanical and magnetic properties, and practical strategies for pinpointing compositions with optimum glass -forming ability of Co-based BMGs were presented. Furthermore, some potential investigation field and application condition about the new BMGs alloys system were also discussed. Our goal is to illustrate the major issues for Co-based BMG, from progressing to structures to properties and applications and from the fundamental science to viable industrial applications.

1. INTRODUCTION

The discovery of the first amorphous alloy in 1960 by Duwez opened a new chapter in the history of materials science[1].From then on, amorphous alloys(metallic glasses) have been attracting considerable attention due to their unique properties, such as high strength, good wear and corrosion resistance, and extraordinary electronic and magnetic properties,

∗E-mail address: ma97chen@hotmail.com.

Copyright © 2010. Nova Science Publishers, Incorporated. All rights reserved.

Handbook of Material Science Research, Nova Science Publishers, Incorporated, 2010. ProQuest Ebook Central,

which are significantly different from the corresponding crystalline alloys due to the different atomic configuration [2].For a long time, however, only thin ribbons, thin films or fine powders with amorphous structure could be prepared since a high cooling rate($>10^4$K/s)is necessary for preparing metallic glasses, and the thickness limitation confined the potential application of these materials[3].since the first bulk metallic glass (BMG) with about 1 mm in size was discovered in Pd-Ni-P alloy by Chen et al[4]in 1974,great efforts have been devoted to search for new BMGs. The effort has been mainly focus on two areas [5]: (1) developing alloy systems that exhibit high resistance to crystallization such as the works of the Chen's and Inoue's groups [6-8];(2) improving the processing method to suppress heterogeneous nucleation in the melt, for example,Turnbull,Greer,and their collaborators used boron oxide fluxing and heating–and-cooling cycles to suppress heterogeneous nucleation[9,10].Over the past decade, a series of multicomponent BMGs have been developed mainly by Inoue's group(IMR, Tohoku University Sendai), including Mg-based [10,11], Ln-based[12,13], Zr-based[14-19], Nd-based [20,21], Pr- based[22], Pd- based[23,24],Pt-based[25],Fe-based [26-31], Co-based [32-34], Ti-based [35],Cu-based[36-40],and so on. Among these BMGs systems, it has been found that some new-developed late transition metal based BMGs (Fe-, Co- and Ni-based BMGs) exhibit various unique properties which have not been obtained for any kind of crystalline alloys. The novelty of these properties enabled us to use BMGs as engineering and functional materials and their application fields have a tendency to be extended widely [41].

As a deputy of these new BMGs materials, Co-based BMGs show the ultrahigh strength (The strength, specific strength and specific Young's modulus of Co-Fe-Ta-B systems BMGs are higher than previous values reported for any bulk crystalline alloys or BMGs [42])and unique magnetic properties [41]. Furthermore, with the small amounts of Nb addition, the GFA of Co-based alloys was improved to form bulk amorphous cylinder with the critical diameter of 4-5mm[43], whereas the traditional Co-based glassy alloys only prepared in an amorphous alloy wire form as high-strength structural materials from the 1980's. Based on these excellent properties, Co-based BMGs have become a hot-topic not only in the BMGs field but also in the whole new material filed in the recently years. Table 1 summarizes typical bulk glassy alloy systems reported up to date together with the calendar years when the first paper or patent on BMG preparation in each alloy system was published. It should be noted that the Co-based BMGs with critical diameters of over 1 cm was obtained in Co-(Cr,Mo)-(C,B)-Ln (Ln=Y, Er, Tm) alloy systems in the past three years[44-46] .

This article intends to make a short review on the GFA, thermal stability, mechanical and magnetic properties of Co-based BMGs. In addition, some potential investigation field and applications about the new BMGs were also discussed.

2. GFA OF CO-BASED ALLOY SYSTEMS AND THERMAL STABILITY OF CO-BASED BMGS

No pure metals and few metallic alloys are natural glass-formers. A major challenge, therefore, is to obtain glassy alloys in bulk form in a simple operation such as casting. The critical size of BMGs is defined as the maximum possible value of the minimum dimension (such as the diameter of a rod) that permits the sample to be fully glassy. BMGs have indeed

Copyright © 2010. Nova Science Publishers, Incorporated. All rights reserved.

Handbook of Material Science Research, Nova Science Publishers, Incorporated, 2010. ProQuest Ebook Central,

been difficult to come by; despite encouraging results on noble-metal–based compositions in the early1980s [10], BMG-forming compositions mostly have been discovered only since 1990[6, 47]. Systematic research has identified the key thermodynamic and kinetic factors that lead to some alloy compositions with particularly good GFA, as analyzed by Busch, Schroers and Wang[48]. In essence, the alloy melt should have (1) a low entropy and enthalpy and therefore a low thermodynamic driving force for crystallization, and (2) low atomic mobility associated with a viscosity that is high and comparatively weakly temperature-dependent, kinetically suppressing the crystallization. These factors are linked, having their origin in a densely packed liquid structure with pronounced short- and medium-range order guided by such insights, and armed with knowledge of phase equilibria from measurements and calculations.

With the elevating cooling rate, the liquid melt will solidify in amorphous phase from metallic glass ribbon to bulk metallic glass. Figure1 shows outer surface and morphology of the cast Co-based glassy alloy rods with diameters of 2 to 4 mm prepared by Professor Inoue's group [49]. In the Figure1, we can see that their as-cast surfaces all appear smooth and lustrous. No apparent volume reductions can be recognized on their surfaces, indicating that there was no drastic crystallization during the formation of these bulk samples.

Table.1 Typical BMG-forming alloy systems reported up to date together with the calendar years when the first paper or patent of each alloy system was published [41,44]

Alloys	Period
Co-(Al,Ga)-(P,B,Si)	1996
Co-(Zr,Hf,Nb)-B	1996
Co-Nd-Al Co-Sm-Al	1996
Co-Ln-B	1998
Co-Ta-B	1999
Co-Fe-Nb-B	2000
Co-Fe-Ta-B	2001
Co-Fe-Si-B-Nb	2002
Co-Fe-Ta-B-Si	2003
Co-(Cr,Mo)-(C,B)-Ln (Ln=Y, Er, Tm)*	2006

*: Co-based BMGs with the critical diameter up to 10 mm

Copyright © 2010. Nova Science Publishers, Incorporated. All rights reserved.

Handbook of Material Science Research, Nova Science Publishers, Incorporated, 2010. ProQuest Ebook Central,



Figure 1. Outer surface and morphology of the cast [(Co1-xFex) 0.75B0.2 Si0.05] 96Nb4 (x=0.1.0.2, 0.3and0.4) glassy alloy rods with critical diameters of 2, 2.5, 3.5 to 4 mm, respectively [49].

As mention above, it have found that the addition of small amounts of Nb to (Fe, Co, Ni)–(B, Si) alloys is very effective for improving the GFA through increasing the stability of supercooled region against crystallization [43]. And the addition of the small amount of Nb as the third element leads to the satisfaction of the three empirical component rules for stabilization of supercooled liquid, which are summarized by Professor Inoue, namely: (1) multicomponent systems consisting of more than three elements; (2) significant difference in atomic size ratios above about 12% among the three main constituent elements; and (3) negative heats of mixing among the three main constituent elements. Furthermore, detailed structure analyses confirm that a new type of glassy structure with a higher degree of dense random packed atomic configuration, new local atomic configurations and long-range homogeneity with attractive interaction were obtained in this condition.

Based on the three empirical component rules, a series of Co-based BMGs were obtained by copper mold casting and the maximum diameter of glassy alloy was up to 10 mm recently. Table 2 shows the thermal stability of some as-casted Co-based BMGs cylinders with the critical diameter up to 10 mm. In this table, T_g, $T_{x,}$ $\triangle T_x$ and d_{max} are the glass transition temperature, the crystallization temperature, the supercooled liquid region and the critical diameter, respectively. The 2at. % Tm(Er) addition was considered to be the dominating reason for great GFA and $\triangle T_x$. The atomic diameter of Tm (Er) is the largest among Co, Cr, Mo, C, B and Er: 0.125 nm, 0.128 nm, 0.140 nm, 0.077 nm, 0.097 nm and 0.175(or0.176) nm, respectively, and it is believed that the addition of a small amount of Tm (Er) can lead to a more densely packed atomic configuration in amorphous phase and liquid phase. Therefore, the undercooled liquid of the Tm(Er)-free alloy is stabilized, as reflected by the reduction of T_x due to the addition of Tm (Er). Furthermore, the addition of Tm element causes the more sequential change in the atomic size in the order Tm(Er) > Mo > Cr > Fe > B > C as well as the generation of new atomic pairs with various negative heats of mixing. This leads to the difficulty in the arrangement of the constituent elements on a long-range scale. Finally, the Tm (Er)-containing alloy exhibits a relatively higher T_{rg} (reduced glass transition temperature, defined as the ration of the glass transition temperature and liquid temperature). The large value of T_{rg} reflects a low nucleating rate in the undercooled liquid, and a low critical cooling rate for glass formation.

Copyright © 2010. Nova Science Publishers, Incorporated. All rights reserved.

Handbook of Material Science Research, Nova Science Publishers, Incorporated, 2010. ProQuest Ebook Central,

Table 2. Thermal stability of Co-based BMGs cylinders with the diameter up to 10 mm reported up to data

Alloys	*Tg* / K	T_x /K	$\triangle T_x$/K	d_{max} /mm
$Co_{48}Cr_{15}Mo_{14}C_{15}B_6Tm_2$[45]	853	943	90	10
$Co_{48}Cr_{15}Mo_{14}C_{15}B_6Er_2$[46]	848	933	85	10

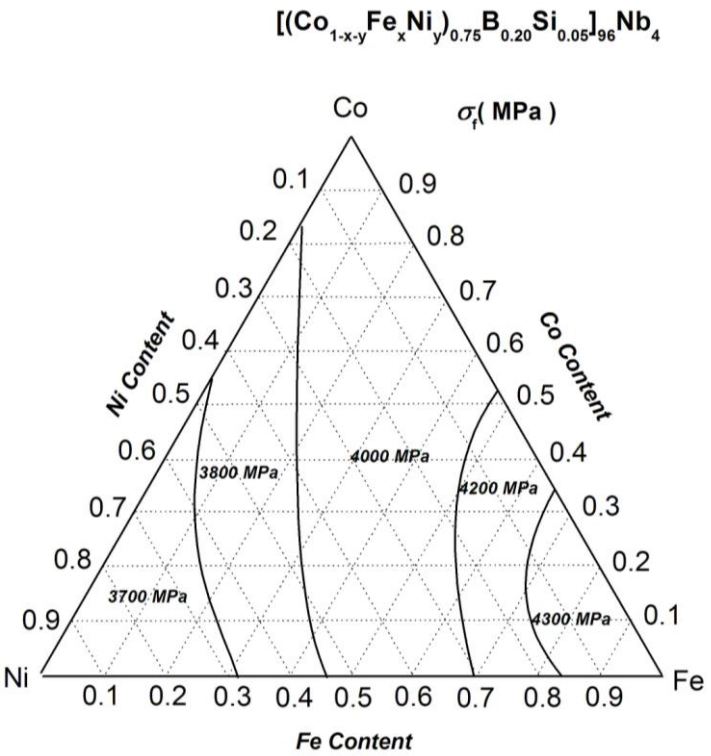


Figure 2. Compositional dependence of compressive fracture strength of [(Co1-x-y FexNiy) 0.75 B0.2 Si0.05]96Nb4 bulk glassy alloy rods produced by the copper mold casting technology.

3. Mechanical And Magnetic Properties Of Co-Based BMGs

It is well-known that BMGs have many unique characterizes, such as excellent mechanical and soft-magnetic properties, which is important to potential engineering and functional application, and Co-based BMGs are typical materials with ultrahigh strength and outstanding soft-magnetic properties. In this section, some important details about these properties were introduced.

Copyright © 2010. Nova Science Publishers, Incorporated. All rights reserved.

Handbook of Material Science Research, Nova Science Publishers, Incorporated, 2010. ProQuest Ebook Central,

3.1. Ultrahigh Strength and High Young's Modulus of Co-Based BMGs

Figure2 shows the compositional dependence of compressive fracture strength of the cast Co –Fe–Ni–B–Si–Nb BMGs rods. From this figure, it can be seen that the high strength of over 4000MPa is obtained in all the composition range of Co element [43], which indicated a good base to obtained ultrahigh strength in these Co-based BMGs system.

Co–Fe–Ta–B based BMGs with a large supercooled liquid region above 70K before crystallization and the critical diameters of glassy rod up to 2mm were developed by Inoue and Shen in 2003 [42]. It has subsequently been reported that the Co–Fe–Ta–B base bulk glassy alloy rods exhibit ultrahigh fracture strength of 5,185 MPa, high Young's modulus of 268 GPa, high specific strength of 6.0×10^5 Nm kg^{-1} and high specific Young's modulus of 31×10^6 Nm kg^{-1} at room temperature as well as high elevated temperature strength of over 2000 MPa in the wide temperature range up to 585℃. In addition, excellent formability is manifested by large tensile elongation of 1,400% and large reduction ratio in thickness above 90% in the supercooled liquid region for this alloy. The ultrahigh strength alloy also exhibited soft magnetic properties with extremely high permeability of 550000. So this alloy is promising as a new ultrahigh-strength material with good deformability and soft magnetic properties. More details about these Co-based BMGs are shown in the Ref. [42]. Most recently, with the small amount of 2 at. % Mo addition, the true fracture strength and Young's modulus *(E)* for Co–Fe–Ta–B glassy alloy systems were improved to 5545 MPa and 282 GPa, respectively [2]. However, The plasticity always is very bad even in a zero-plasticity fracture with a fragmentation mode [50]. It is noteworthy that many investigations have been reported for improving the plasticity of BMGs. The ductility of some composites has been improved by adding elements with high melting points, such as Ta, Nb or Mo, to Zr-, Cu- and Ti-based BMGs by in situ precipitation of ductile micrometer-sized particles [51,52], body-centered cubic(bcc) dendrites [53, 54] or nano-structured dendrites [55,56] upon cooling from the melting stage. Therefore, this gives rise to the scientifically important problem of how to make Co–Fe–Ta–B BMGs ductile by controlling the microstructure to produce a new material with a super-high strength in combination with certain ductility.

Actually,a new $Co_{43}Fe_{20}Ta_{5.5}B_{31.5}$ metallic glass matrix composite with in situ precipitated crystalline dendrite phases was obtained by Fan and his coworkers in 2008[57]. This composite has particular plasticity properties with a large stress rise after yielding under uniaxial compressive test, which offsets the strength loss, together with local shear deformation and plastic flow within the vein-like structure. From the XRD and SEM data, it can be seen that this Co-based BMGs composite is a mixture of the metallic glass matrix and some precipitated crystalline phase, identified as a complex face-centered cubic (fcc) $(Co, Fe)_{21}Ta_2B_6$ phase with a large lattice parameter of 1.055 nm. According to the SEM image, it is interesting to find that the precipitated crystalline phase is clearly dispersed in the metallic glass matrix with some snow-like dendrites. Moreover, there is no any trace of the thick reaction layer at the interface between the precipitated crystalline phase and the metallic glass matrix. Furthermore, neither pores nor voids appear over the whole cross-section of the samples. Therefore, this Co-based metallic glass composite can be considered to have potential to be developed into a high-performance material with both high strength and good plasticity.

Copyright © 2010. Nova Science Publishers, Incorporated. All rights reserved.

Handbook of Material Science Research, Nova Science Publishers, Incorporated, 2010. ProQuest Ebook Central,

3.2. Good Soft-Magnetic Properties of Co-Based BMGs

Since 1995, a series of Co-based BMGs with ferromagnetism at room temperature has been developed by copper mold casting or water quenching [59-60]. Many Co-based BMGs show good soft-magnetic properties, i.e., better combination of lower coercivity and higher electrical resistivity among all soft magnetic metallic alloys. For example, Co-Fe-Ta-B based BMGs show excellent soft magnetic properties, namely, extremely high maximum permeability reaching 500000 and very low coercivity of 0.26A / m, when it was formed in a ring shape with 1mm in thickness,10mm in outer diameter and 5mm in inner diameter[61]. The lower coercivity is presumably due to the smaller magnetic anisotropy and lower internal stress [41].

The extremely low magnetostriction behavior of Co-Fe-B-Si-Nb BMGs was found by Chang *et al* [62]. For example, $[(Co_{0.6}Fe_{0.4})_{0.75}B_{0.2}Si_{0.05}]_{96}Nb_4$ bulk glassy alloys shows a low λs (saturation magnetostriction) of 5.76×10^{-6} and with decreasing Fe content to x=0.1, the $[(Co_{0.9}Fe_{0.1})_{0.75}B_{0.2}Si_{0.05}]_{96}Nb_4$ glass alloy exhibits an extremely low λs of 0.55×10^{-6}. In fact, this BMGs system also exhibits other excellent soft-magnetic properties, i.e., high saturation magnetization of 0.71–0.97 T, low coercive force of 0.7–1.8 A/m, high permeability of 1.48–3.25×10^4.And most recently,zero-magnetostriction bulk metallic glass samples of $(Co_{0.952}Fe_{0.058})_{70}B_{20}Si_8Nb_2$ were prepared in cylindrical form with a diameter of 1.5 mm and in ring form with a thickness of 0.5 mm [63], which exhibited a high glass forming ability and good soft magnetic properties, i.e., a saturation magnetization of 0.6 T, a low coercivity within 0.1–0.2 A/m, and a high permeability of 104 000 at a frequency of 1 kHz and zero magnetostriction. The success of the synthesis of the zero-magnetostriction Co–Fe–B–Si–Nb glassy alloy with good soft magnetic properties and a high glass forming ability is promising for the future development of sensitive magnetic sensors.

Inoue and Takeuchi summarized the advantages for soft magnetic properties of Co-based BMGs, comparing with the traditional Co-based amorphous alloy ribbons. [58], such as high electrical resistivity at room temperature; lower coercive force; higher initial permeability; controllable arrangement of domain wall structure achieved by control of casting and/or cooling processes; and better high-frequency permeability. However, they have lower saturated magnetic flux density due to the addition of large amount of solute elements, which is a serious obstacle to future use in power transformers. Obviously, the high material cost is another limit. Therefore, a lot of effort is still needed for attaining excellent soft magnetic and relative lower cost Co-based BMGs.

4. FUTURE INVESTIGATION FIELDS AND APPLICATION

As the new BMGs system with ultrahigh strength and good soft-magnetic properties, Co-based BMGs have been paid more and more attentions. In this section, some potential investigation fields and application condition about the new BMGs system were discussed and introduced.

Copyright © 2010. Nova Science Publishers, Incorporated. All rights reserved.

Handbook of Material Science Research, Nova Science Publishers, Incorporated, 2010. ProQuest Ebook Central,

4.1. The Crystallization Behavior of Co-Based BMGs

Metallic glass, which is in a metastable state, can crystallize when heated or held at elevated temperature for sufficient time. Crystallization occurs with a change in properties, such as heat capacity, electrical resistivity, volume and magnetic properties [64]. From the 1970's, the crystallization behavior of Co-based metallic glasses has been investigated and many papers were published [65-69]. However, there are few reports about the crystallization behavior about bulk form metallic glasses after the first Co-based BMGs obtained in 1996[41, 70].

It has been reported that either the soft-magnetic properties of BMGs may deteriorate after crystallization or they may be improved if nanocrystalline phases are formed [65]. And recently,the high-temperature magnetic behaviors of $Co_{45}Fe_{28.5}Si_{13.5}B_9Cu_1Nb_3$ and $Co_{36}Fe_{36}Si_4B_{20}Nb_4$ nanocrystalline alloy were investigated [71, 72], in which the two alloys were metallic glasses in the as-cast state. The results show their potential application as the high-temperature soft-magnetic materials and devices. In order to get the optimum microstructure with useful functional properties and practical application, a full understanding of the crystallization behavior of Co-based BMGs is required. Therefore, it can presume that the crystallization behavior research will become an important research topic in the Co-based BMGs field.

4.2. The Corrosion Behavior of Co-Based BMGs

Soft magnetism, high strength and high corrosion resistance are three fundamental properties of Co-based BMGs [41]. But it is seldom reported about the corrosion behavior of this kind of BMGs in the existed literatures, except for limited reports about the corrosion properties of Co-based metallic glasses ribbon in the various solutions [73-76]. Thus, it is very necessary to put more attention to it in the future.

4.3. The Wear Behavior of Co-Based BMGs

For bulk metallic glasses, their high hardness coupled with high strength and corrosion resistance indicates their potential in tribological applications. The distinctive mechanical properties of Co-based metallic glasses make their wear resistance of fundamental interest and many papers were published in this field [77-81]. However, all the existed investigations do not refer to the Co-based bulk metallic glasses materials. So the research about the wear behavior of ultrahigh strength Co-based BMGs has important meaning to the theoretic study and industrial application and it may be promising a new metallic engineering materials in the wear-resistant materials field.

Copyright © 2010. Nova Science Publishers, Incorporated. All rights reserved.

Handbook of Material Science Research, Nova Science Publishers, Incorporated, 2010. ProQuest Ebook Central,

4.4. The Application Condition of Co-Based BMGs

Most recently, the applications condition of BMGs were reviewed in detail by Inoue[44]. For the Co-based BMGs, which are focus on the soft-magnetic materials and devices field, i.e., soft magnetic choke coils, soft magnetic high frequency power coils and so on. However, compared with other late transition metal base systems BMGs (Fe-, Ni, Cu-, and Pb-based), the practical application and industrial productions of Co-based BMGs are relatively limited. The reason may due to their relatively lower glasses-forming ability (GFA), which would be improved by further investigation.

5. CONCLUSION

In the past several years, Co-based BMGs have become a new hot-topic in new materials fields (especially, in BMGs and relative fields). Considering their excellent mechanical and soft-magnetic properties and the continual improving bulk glass-forming ability, it is expected that the subsequent study will lead to the production of Co-based BMGs with diameter up to 30 mm and good combination of mechanical and magnetic properties. It can presume that the Co-based BMGs will obtain wide use in the engineering and functional materials field in the near future.

ACKNOWLEDGMENTS

D. Chen gratefully acknowledged helpful discussion and important information from Dr. C. T. Chang (IMR, Tohoku University, Sendai) and Dr. A. L. Zhang (IMR, Hunan University, Changsha).

Copyright © 2010. Nova Science Publishers, Incorporated. All rights reserved.

REFERENCES

[1] Clement,W., Willwns, R. H.,and Duwez,P.,1960, *Nature*, 48,2560
[2] Shen, B. L., and Inoue, A., 2005, J. Phys.: *Condens. Matter.*, 17, 5647.
[3] Greer, A. L.,1995, *Science*, 267, 1947.
[4] Chen, H.S., 1974, *Acta.metall.*, 22,1505.
[5] Wang, H., and Fu, H., 2007, The world of Bulk metallic glass and their composites, *Research Signpost*, Kerala,74.
[6] Inoue, A., 2000, *Acta. Mater.*, 48, 279.
[7] Wang, W. H., Dong, C., and Shek, C. H., 2004, *Mater. Sci. Eng. R.*, 44, 45.
[8] Inoue, A., 2005, Proc. Japan. Acad., 81(B), 156.
[9] Drehman,A.J.,Greer,A.L.,and Turnbull,D., 1982, *Appl.Phys.Lett.*,41,716.
[10] Kui,H.W.,Greer,A.L.,and Turnbull,D.,1984, *Appl.Phys.Lett.*,45,615
[11] Inoue, A., Kohinata, M., Tsai, A.P., and Masumoto, T., 1989, *Mater. Trans. JIM.*, 30, 378.
[12] Inoue, A., Zhang, T., and Masumoto, T., 1989, *Mater. Trans. JIM.*, 30, 965.

Handbook of Material Science Research, Nova Science Publishers, Incorporated, 2010. ProQuest Ebook Central,

[13] Inoue, A., Yamaguchi, H., and Zhang, T., 1990, *Mater. Trans. JIM.*, 31, 104.
[14] Inoue, A., Zhang, T., and Masumoto, T., 1990, *Mater. Trans., JIM*, 31, 177.
[15] Zhang, T., Inoue, A., and Masumoto, T., 1991, *Mater. Trans., JIM*, 32, 1005.
[16] Zhang, T., Inoue, A., and Nishiyama, N., 1993, *Mater. Trans., JIM*, 34, 1234.
[17] Inoue, A., Nishiyama, N., Amiya, K., Zhang, T., and Masumoto, T., 1994, *Mater. Lett.*, 19, 13 .
[18] Inoue, A., Shibata, T., and Zhang, T., 1995, *Mater. Trans. JIM.*, 36, 1420.
[19] Peker, A. L., and Johnson, W. L., 1993, *Appl. Phys. Lett.*, 63, 2342.
[20] Inoue, A., Zhang, T., Zhang, W., and Takeuchi, A., 1996, *Mater. Trans. JIM.*, 37, 99.
[21] Inoue, A., Zhang, T., Takeuchi, A., and Zhang, W., 1996, *Mater. Trans. JIM.*, 37, 636.
[22] Inoue, A., Zhang, T., and Takeuchi, A., 1996, *Mater. Trans. JIM.*, 37, 1731.
[23] Inoue, A., Nishiyama, N., and Matsuda, T., 1996, *Mater. Trans. JIM.*, 37, 181.
[24] He, Y., Shen, T.D., and Schwarz, R.B., 1998, *Metall. Mater. Trans.*, 29A, 1795.
[25] Zhang, T., Inoue, A., 2003, *Mater. Trans.*, 44, 1143.
[26] Inoue, A., Gook, J. S., 1995, *Mater. Trans. JIM.*, 36, 1180.
[27] Inoue, A., Slfinohara, Y., and Gook, J. S., 1995, *Mater. Trans. JIM.*, 36, 1427.
[28] Inoue, A., Zhang, T., and Itoi, T., 1997, Mater. *Trans. JIM.*, 38, 359.
[29] Inoue, A., Koshiba, M., Zhang, T., and Makino, A., 1997, Mater. Trans. *JIM.*, 38, 577.
[30] Inoue, A., Koshiba, M., Zhang, T., and Makino, A., 1998, *J. Appl. Phys.*, 83, 1967.
[31] Inoue, A., Zhang, T., and Takeuchi, A., 1997, *Appl. Phys. Lett.*, 71, 464.
[32] Inoue, A., Koshiba, M, Itoi. T., and Makino, A., 1998, *Appl. Phys. Lett.*, 73, 744.
[33] Inoue, A., 1999, *Mater. Sci. Forum*, 312-314, 307.
[34] Pang, S.J., Zhang, T., Asami, K., and Inoue, A., 2001, *Mater. Trans.*, 42, 376.
[35] Shen, B.L., Koshiba, H., Inoue, A., Kimura, H.M., and Mizushima, T., 2001, *Mater. Trans.JIM.*, 41, 2136.
[36] Inoue, A., Zhang, W., Zhang, T., and Kurosaka, K., 2001, *Acta Mater.*, 49, 2645.
[37] Inoue, A., Zhang, W., Zhang, T., and Kurosaka, K., 2001, *J. Mater. Res.*, 16, 2836.
[38] Zhang, T., Kurosaka, K., and Inoue, A., 2001, *Mater. Trans.*, 42, 2042.
[39] Inoue, A., Zhang, T., Kurosaka, K., and Zhang, W., 2001, *Mater. Trans.*, 42, 1800.
[40] Zhang, W., and Inoue, A., 2006, *J. Mater. Res.*, 21, 234.
[41] Inoue,A., Shen, B. L., and Takeuchi, A., 2006, *Mater. Trans.*,47,1275.
[42] Inoue.A., Shen, B. L.,Koshiba, H.,Kato, H., and Yavari,A. R., 2003, *Nature materials.*, 2, 661.
[43] Inoue.A., Shen B.L., and Chang,C.T.,2004, *Acta.metall.*,52,4093.
[44] Inoue, A., Wang, X. M., and Zhang, W., 2008, *Rev. Adv. Mater.Sci.*, 18,1.
[45] Amiya, K., and Inoue, A., 2006, *Mater. Trans.*, 47, 1615.
[46] Men,H., Pang, S. J., and Zhang, T., 2007, Mater. *Sci. Eng. A.*, 449-451, 538.
[47] Johnson, W. L., 1999, *MRS Bull.*, 24, 42.
[48] Busch, R., Schroers, J., and Wang, W.H., 2007, *MRS Bull.*, 32, 620.
[49] Shen, B. L., and Inoue, A., 2007, The world of Bulk metallic glass and their composites., *Research Signpost*, Kerala,128
[50] Zhang, Z. F., Zhang, H., Shen, B. L., Inoue, A., and Eckert, J., 2006, *Philosophical Magazine Letters*., 86, 643.
[51] Fan, C., Ott, R.T., and Hufnagel, T.C., 2002, *Applied Physics Letters*, 81., 1020.
[52] Lee, J. C., Kim, Y. C., Ahn, J. P., Kim, H.S., Lee, S. H., and Lee, B.J., 2004, *Acta Materialia*., 52 ,1525.

Copyright © 2010. Nova Science Publishers, Incorporated. All rights reserved.

Handbook of Material Science Research, Nova Science Publishers, Incorporated, 2010. ProQuest Ebook Central,

[53] Hays, C.C., Kim, C. P., and Johnson, W. L., 2000, *Physical Review Letters*., 84, 2901.
[54] Bian, Z., Kato, H., Qin, C. L., Zhang, W., and Inoue, A., 2005, *Acta Materialia.*, 53, 2037.
[55] He, G., Eckert, J., Loser, W., and Schultz, L., 2003, *Nature Materials*., 2, 33.
[56] Kuhn, U., Eckert, J., Mattern, N., Schultz, L., 2002, *Applied Physics Letters*., 80, 2478.
[57] Fan, J., Zhang, Z. F., Shen, B. L., and Mao, S. X., 2008, *Scripta Materialia*., 59, 603.
[58] Inoue.A., and Takeuchi, A., 2002, *Mater. Trans.*, 43. 1892.
[59] Inoue.A., 1998, Bulk Amorphous Alloys, *Tans Tech Publications.*, Zurich.
[60] Inoue. A., Zhang, T., and Takeuchi, A., 1998, *Mater. Sci. Forum*., 269, 855.
[61] Koshiba, H., and Inoue, A., 2001, *Mater. Trans.*, 42, 2572.
[62] Chang, C. T., Shen, B. L., and Inoue. A., 2006, *Applied Physics Letters*., 88, 011901.
[63] Amiya, K., Urata, A., Nishiyama, N., and Inoue, A., 2007, *Journal of Applied Physics*., 101, 09N112.
[64] Scott, M.G., Amorphous Metallic Alloys, Butterworths, London., 1983, 144.
[65] Coleman, E., 1976, *Materials Science and Engineering.*, 23, 161
[66] Quintana, P., Amano, E., Valenzuela, R., and Irvine, J. T. S., 1994, *Journal of Applied Physics*., 75, 6940.
[67] Buttino, G., Cecchetti, A., and Poppi, M., 1997 *Journal of Magnetism and Magnetic Materials*., 172, 147.
[68] Li, H.F., and Ramanujan, R. V., 2004, *Materials Science and Engineering* A., 375–377, 1087.
[69] Kraposhin, V.S., Khmelevskaya, V. S., Yazvitsky, M. Y., and Antoshina, I. A.,*Journal of Non-Crystalline Solids* 353 (2007) 3057–3061.
[70] Mchenry, M.E., Willard, M.A., and Laughlin, D.E., 1999, *Prog. Mater. Sci.*, 44, 291.
[71] Gomez-Polo, C., Marin, P., Pascaul, L., Hernando, A., and Vazquez, M., 2002, *Phys. Rev.* B., 66, 024433.
[72] Panda, A. K., Mohanta, O., Kumar, A., Ghosh, M., and Mitra, A., 2007, *Philosophical Magazine.*, 87, 1671.
[73] Zaprianova V, Raicheff R, Kashieva E, Stefanova S 1995, *Journal of materials science letters*.,14,1643
[74] Pardo, A., Otero, E., Merino, M. C., Lopez, M. D., Vazquez, M., Agudo, P., Escalera, M. D., and M'Hich, A., 2002, *Ritish Corrosion Journal.*, 37, 69.
[75] Pardo, A., Otero, E., Merino, M. C., Lopez, M. D., Vazquez, M., and Agudo, P., 2002, *Corrosion Science*., 44, 1193.
[76] Pardo, A., Merino, M. C., Otero, E., Lopez, M. D., and M'Hich, A., 2006, *Journal of Non-Crystalline Solids*., 352, 3179.
[77] Moreton, R., and Lancaster, J. K., 1985, *Journal of Materials Science Letters.*, 4, 133.
[78] Wege, F.V., Skrotzki, B., and Hornbogen, E., 1988, *Z. Metall.*, 79, 492.
[79] Prakash, B., and Hiratsuka, K., 2000, *Tribol. Lett.*, 8, 153.
[80] Greer, A. L., Rutherford, K. L., and Hutchings, I. M., 2002, *International Materials Reviews.*, 47,87.
[81] Prakash, B., 2005, *Wear*., 258, 217.

Copyright © 2010. Nova Science Publishers, Incorporated. All rights reserved.

Handbook of Material Science Research, Nova Science Publishers, Incorporated, 2010. ProQuest Ebook Central,

Copyright © 2010. Nova Science Publishers, Incorporated. All rights reserved.

Handbook of Material Science Research, Nova Science Publishers, Incorporated, 2010. ProQuest Ebook Central,

In: Handbook of Material Science Research
Editors: C. René and E. Turcotte, pp.445-458
ISBN 978-1-60741-798-9
© 2010 Nova Science Publishers, Inc.

Chapter 13

CONTROL OF MICROSTRUCTURES BY HEAT TREATMENTS AND HIGH-TEMPERATURE PROPERTIES IN HIGH-TUNGSTEN COBALT-BASE SUPERALLOYS

Manabu Tanaka and Ryuichi Kato
Department of Mechanical Engineering
Faculty of Engineering and Resource Science,
Akita University, Akita, Japan

ABSTRACT

Cobalt-base HS-21 (L-605) alloy has high strength and good oxidation resistance at high temperatures, and is widely used for high-temperature components including blades, vanes and combustor parts in the hot sections of jet engines. In this study, effects of microstructures on the creep-rupture properties were investigated on the heat-treated specimens of the HS-25 (L-605) type heat-resistant alloys containing about 14 to 20% (mass %) tungsten (W) at 1089 and 1311 K. Serrated grain boundaries which were formed by precipitation of W-rich phase and M_6C carbide by heat treatment, improved rupture strength without significant loss of creep ductility. Ageing for 1080 ks (300 h) at 1273 K (1000℃) caused similar precipitates on grain boundaries and in grains, and also increased rupture strength in the specimens with normal straight grain boundaries. Improvement of the rupture properties by heat treatments was remarkable in the alloys with the higher W content at 1089 K, while such heat treatments were effective in relatively short-term creep at 1311 K. In the non-aged specimens with straight grain boundaries, the rupture strength increased with increasing W content at 1311 K, although the rupture strength was not improved largely with increasing W content at 1089 K. The principal strengthening mechanism in these alloys was attributed to the strengthening of grain boundaries and grains by precipitates of W-rich phase and carbide phases in addition to solid-solution strengthening by W atoms. The strengthening of grains by high-temperature ageing was comparable with the strengthening by serrated grain boundaries in the high-tungsten cobalt-base alloys at 1089 K. Fracture surfaces of specimens with serrated grain boundaries and those of aged specimens were ductile grain-boundary

Copyright © 2010. Nova Science Publishers, Incorporated. All rights reserved.

Handbook of Material Science Research, Nova Science Publishers, Incorporated, 2010. ProQuest Ebook Central,

fracture surfaces with small dimples and ledges, while the non-aged specimens with straight grain boundaries exhibited brittle grain-boundary facets at 1089 K.

INTRODUCTION

Austenitic cobalt-base HS-21 (L-605) alloy has good formability, high strength up to 1089 K (816℃), and good oxidation resistance up to 1366 K (1093℃). This alloy is widely used for blades, vanes, combustor parts and afterburners in the hot sections of aircraft engines, and is also used in the hot sections of land based gas turbines. In the HS-25 (L-605) type heat-resistant alloys, the increase of tungsten (W) content may raise the high-temperature strength [1], but may also increase the tendency to form topologically close-packed phases (tcp) such as the Laves phase (Co_2W) which is believed to be harmful to ductility [2]. Therefore, it is necessary to prevent such phases by heat treatments in order to utilize beneficial effects of tungsten (W).

Initiation and growth of grain-boundary cracks in polycrystalline materials are governed by grain-boundary sliding at high temperatures, and relative contribution of grain-boundary sliding to total creep strain increases with decreasing creep stress [3, 4]. High-temperature strength can be considerably improved by serrated grain boundaries in the nickel-base superalloys [5-7] and the austenitic heat-resisting steels [8, 9], because grain-boundary sliding which controls the initiation [5, 10] and growth [11] of grain-boundary cracks is inhibited by serrated grain boundaries.

In cobalt-base heat-resistant alloys, serrated grain boundaries are formed by precipitation of $M_{23}C_6$ carbide [12] or a W-rich phase (tungsten solid solution, bcc) and M_6C carbide [13], and improve the creep rupture strength. R. Tanaka et al. [14] previously found the same W-rich phase in the Ni-20Cr-20W alloy. High-temperature ageing at 1273 K also causes precipitates of the W-rich and carbide phases on grain boundaries and in the grains, and leads to an improved rupture life without decreasing creep ductility in the HS-25 alloys [15]. It was found that in high-tungsten HS-25 type cobalt-base superalloys the rupture life increased with increasing W content at 1311 K [16]. In this study, effects of microstructures produced by heat treatments on the creep-rupture properties were investigated using the HS-25 type superalloys containing about 14 to 20 mass % W at 1089 and 1311 K. Precipitated phases, microstructures and fracture mechanisms were also examined in the ruptured specimens of the alloys. Then, the strengthening mechanisms of these alloys were discussed on the basis of experimental results.

EXPERIMENTAL PROCEDURE

Table 1 lists the chemical composition, typical heat treatments, matrix hardness, grain size and grain-boundary configuration of HS-25 (L-605) type cobalt-base alloys used in this study. The alloy bars of 20 mm in diameter were supplied by Mitsubishi Material Company.

Copyright © 2010. Nova Science Publishers, Incorporated. All rights reserved.

Handbook of Material Science Research, Nova Science Publishers, Incorporated, 2010. ProQuest Ebook Central,

Table 1. Chemical composition, typical heat treatments, matrix hardness, grain size and grain-boundary configuration of HS-25 type cobalt-base alloys

Alloys	Chemical composition (mass %)	Typical heat treatments	Matrix hardness (Hv)*	Grain size (μm)	Grain-boundary configuration
14W	Co-0.07%C-19.82%Cr-9.83%Ni-14.37%W-2.22%Fe-1.46%Mn	1473 K, 7.2 ks→W.Q.	253	255	straight
		1473 K, 7.2 ks→W.Q. + 1273 K, 1080 ks→ A.C.	326	255	straight (plus ageing)
		1473 K, 3.6 ks－F.C.→ 1323 K, 72 ks→ W.Q.	249	260	serrated
17W	Co-0.06%C-19.40%Cr-9.89%Ni-17.20%W-2.37%Fe-0.76%Mn	1503 K, 7.2 ks→W.Q.	264	246	straight
		1503 K, 7.2 ks→W.Q. + 1273 K, 1080 ks→ A.C.	344	246	straight (plus ageing)
		1503 K, 7.2 ks－F.C.→ 1323 K, 10.8 ks→W.Q.	255	249	serrated
20W	Co-0.06%C-19.05%Cr-9.54%Ni-19.74%W-2.28%Fe-0.77%Mn	1573 K, 7.2 ks→W.Q.	269	273	straight
		1573 K, 7.2 ks→W.Q. + 1273 K, 1080 ks→ A.C.	379	273	straight (plus ageing)
		1573 K, 7.2 ks－F.C.→ 1323 K, 3.6 ks→W.Q.	256	280	serrated

*: Vickers harness number (load 4.9 N); W.Q.: water-quenched; F.C.: furnace-cooled; A.C.: air-cooled.

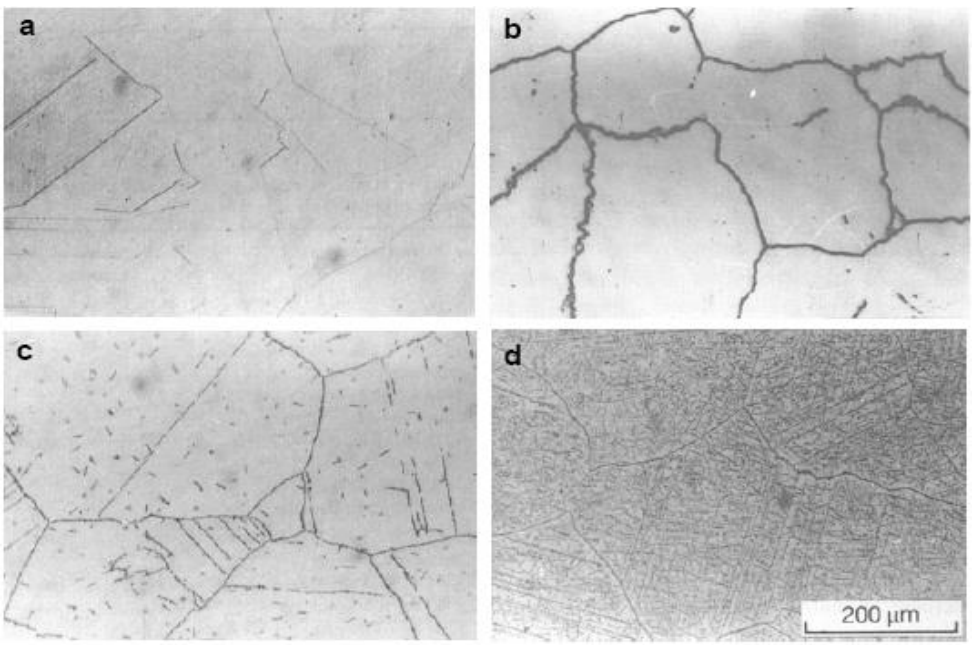


Figure 1. Examples of microstructures in the heat-treated specimens of the cobalt-base alloys. a. 14W (straight grain boundaries) b. 14W (serrated grain boundaries). c. 14W (straight grain boundaries plus ageing) d. 20W (straight grain boundaries plus ageing).

Copyright © 2010. Nova Science Publishers, Incorporated. All rights reserved.

Handbook of Material Science Research, Nova Science Publishers, Incorporated, 2010. ProQuest Ebook Central,

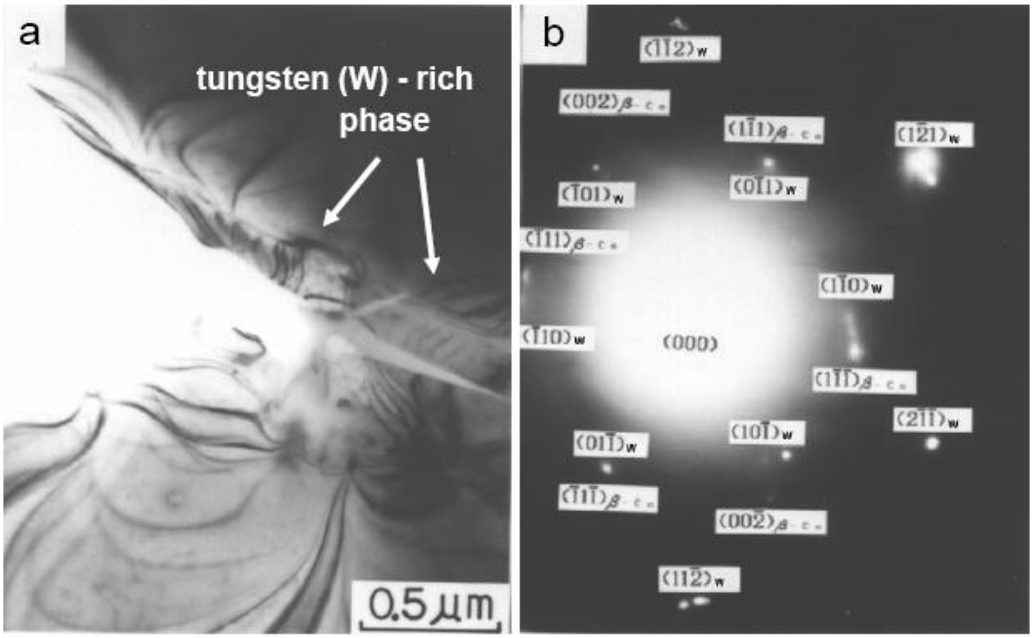


Figure 2. Electron transmission micrographs of the specimen with serrated grain boundaries of the 14W alloy [13]. a. bright field image, b. selected area electron diffraction pattern of a.

These alloys containing about 14 to 20 mass % are designated by approximate tungsten (W) content, such as 14W alloy. Specimens with 'straight' grain boundaries were produced by simple solution treatment. 'Serrated' grain boundaries were formed by precipitation of tungsten (W) - rich phase (tungsten solid solution, bcc) and carbide phases [13] which were caused by solution treatment followed by furnace cooling in these alloys. Some specimens with straight grain boundaries were further aged for 1080 ks at 1273K to cause similar precipitation of W-rich and carbide phases on grain boundaries and in the grains. Heat-treated specimens were machined into creep-rupture test pieces of 30 mm in gauge length and 5 mm in diameter. Creep-rupture experiments were carried out using these specimens at 1089 and 1311 K. All specimens were held for 10.8 ks (3 h) at each test temperature before loading. Microstructures and fracture patterns were examined with optical microscope and scanning electron microscope. Precipitated phases were identified by dint of X-ray diffraction, electron probe microanalysis (EPMA) or transmission electron microscopy on heat-treated specimens or ruptured test pieces.

RESULTS AND DISCUSSION

Effects of Tungsten Content on Creep-rupture Properties at 1089 K

Figure 1 shows examples of microstructures in the heat-treated specimens of the cobalt-base alloys. In the 14W alloy, grain-boundary precipitates are visible in specimen with serrated grain boundaries (Figure 1b), while precipitates are not observed in simply solution-treated specimen with straight grain boundaries (Figure 1a). Figure 2 shows the electron

Copyright © 2010. Nova Science Publishers, Incorporated. All rights reserved.

Handbook of Material Science Research, Nova Science Publishers, Incorporated, 2010. ProQuest Ebook Central,

transmission micrographs of the specimen with serrated grain boundaries of the 14W alloy [13]. Large grain-boundary precipitates of W-rich phase can be observed in the bright field image (Figure 2a). According to the selected area electron diffraction pattern (Figure 2b), there is a crystallographic orientation relationship between the W-rich phase (bcc) and ß-Co matrix (fcc) that $(011)_W$ // $(111)_{ß\text{-}Co}$ and $[1\bar{1}1]_W$ // $[1\bar{1}0]_{ß\text{-}Co}$. Grain-boundary precipitates of M_6C carbide were also detected by the line analysis using EPMA in addition to W-rich phase [13]. Ageing for 1080 ks at 1273K caused similar precipitates in grains in the 14W and 20W alloys (Figs. 1c and 1d).

Figure 3 shows some examples of creep curves of the cobalt-base alloys at 1089 K. The creep curve exhibits primary (transient) creep and tertiary (accelerated) creep terms with very short secondary creep term. The rupture life is relatively longer in the specimens with serrated grain boundaries and in the aged specimens with straight grain boundaries. Figure 4 shows the creep-rupture properties of the 14W and 20W alloys at 1089 K. Serrated grain boundaries and the ageing lead to the increase in rupture life without significantly decreasing ductility, although the creep ductility decreases a little with increasing W content. The aged specimen with straight grain boundaries exhibits the longest rupture life (7946.89 ks) and good creep ductility (0.1499) under the stress of 118 MPa. In non-aged condition, the specimen with serrated grain boundaries has the longer rupture life than the one with straight grain boundaries in the 20W alloy. Similar results were obtained in the 17W alloy. Strengthening by ageing or by serrated grain boundaries was larger in the specimens of the higher W content.

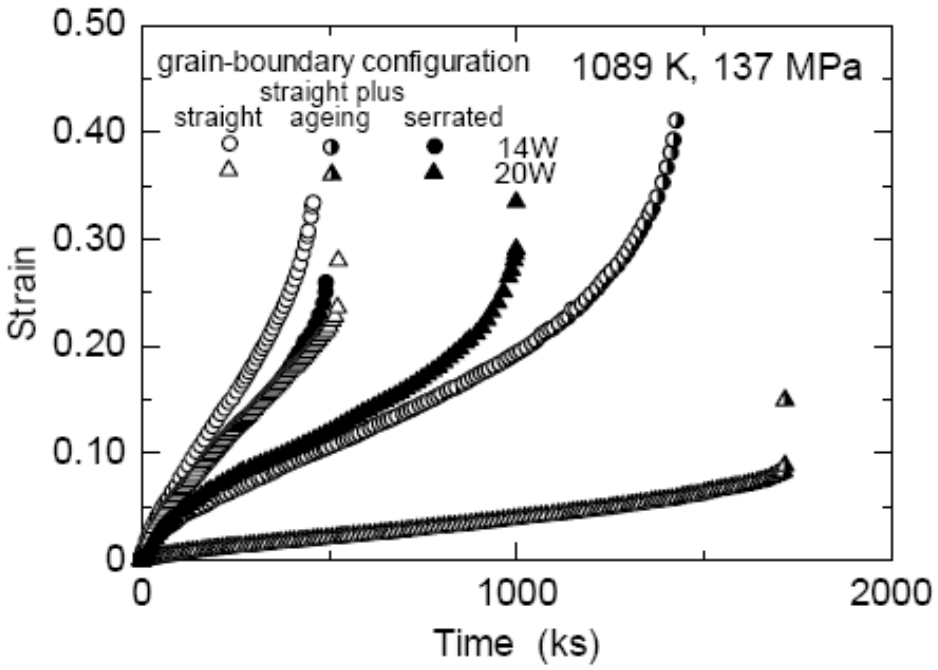


Figure 3. Creep curves of the 14W and 20W alloys at 1089 K.

Copyright © 2010. Nova Science Publishers, Incorporated. All rights reserved.

Handbook of Material Science Research, Nova Science Publishers, Incorporated, 2010. ProQuest Ebook Central,

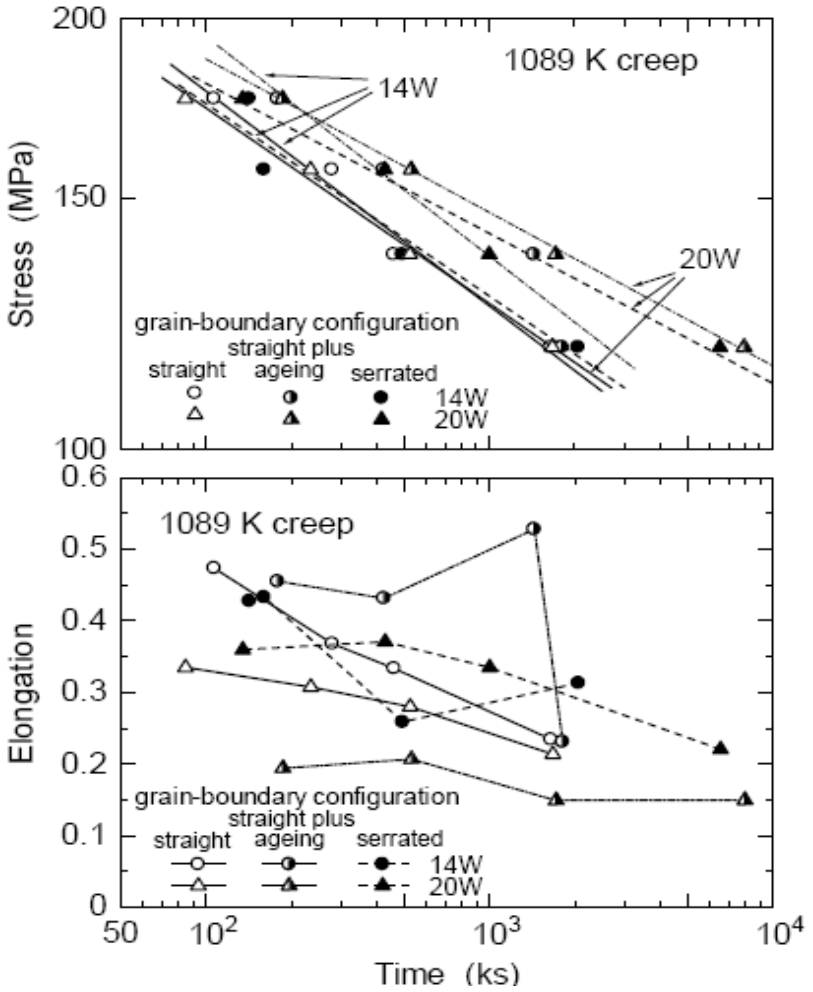


Figure 4. Creep-rupture properties of the 14W and 20W alloys at 1089 K.

Figure 5 shows effects of W content on rupture strength of cobalt-base alloys at 1089K. The rupture strength increases with increasing W content in the specimens with serrated grain boundaries and in the aged specimens with straight grain boundaries except short-term creep. In the non-aged specimens with straight grain boundaries, the rupture strength does not increase largely with increasing W content. The strengthening effect of the ageing seems to be a little larger than that of serrated grain boundaries. Improvement of the rupture properties by heat treatments is remarkable in the alloys with the higher W contents except short-term creep. Precipitation of W-rich phase and carbide phase on grain boundaries contribute to the strengthening of grain boundaries and may retard precipitation of Laves phase (Co_2W) on grain boundaries, which is believed to be harmful to ductility in heat-resistant alloys [11]. Fine precipitates of Laves phase and carbide phases such as M_6C and $Cr_{23}C_6$ were detected by X-ray diffraction on the non-aged specimens ruptured at 1089 K [16]. The precipitates of carbide phases may contribute to the strengthening of the matrix in specimens with serrated grain boundaries. The Laves phase may not decrease the rupture strength in the cobalt-base heat-resistant alloys if it is finely dispersed in the matrix [17].

Copyright © 2010. Nova Science Publishers, Incorporated. All rights reserved.

Handbook of Material Science Research, Nova Science Publishers, Incorporated, 2010. ProQuest Ebook Central,

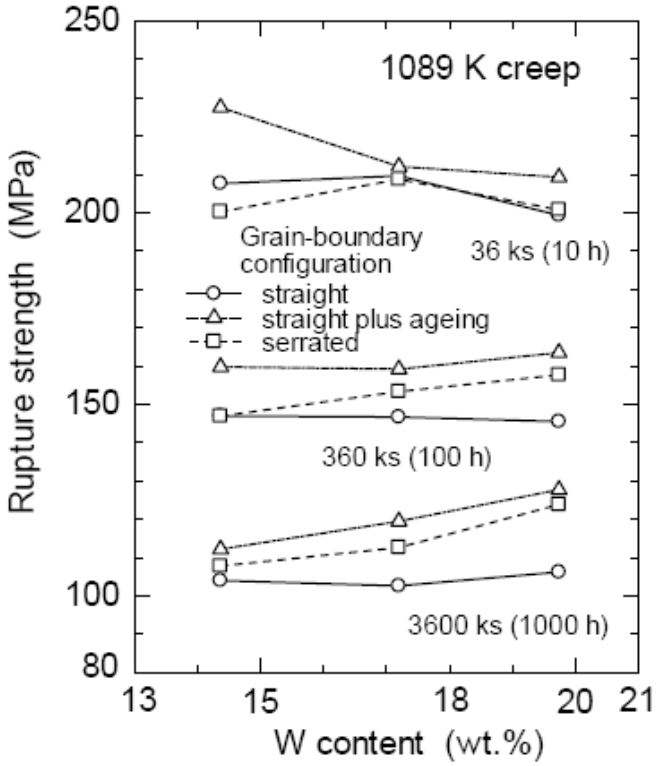
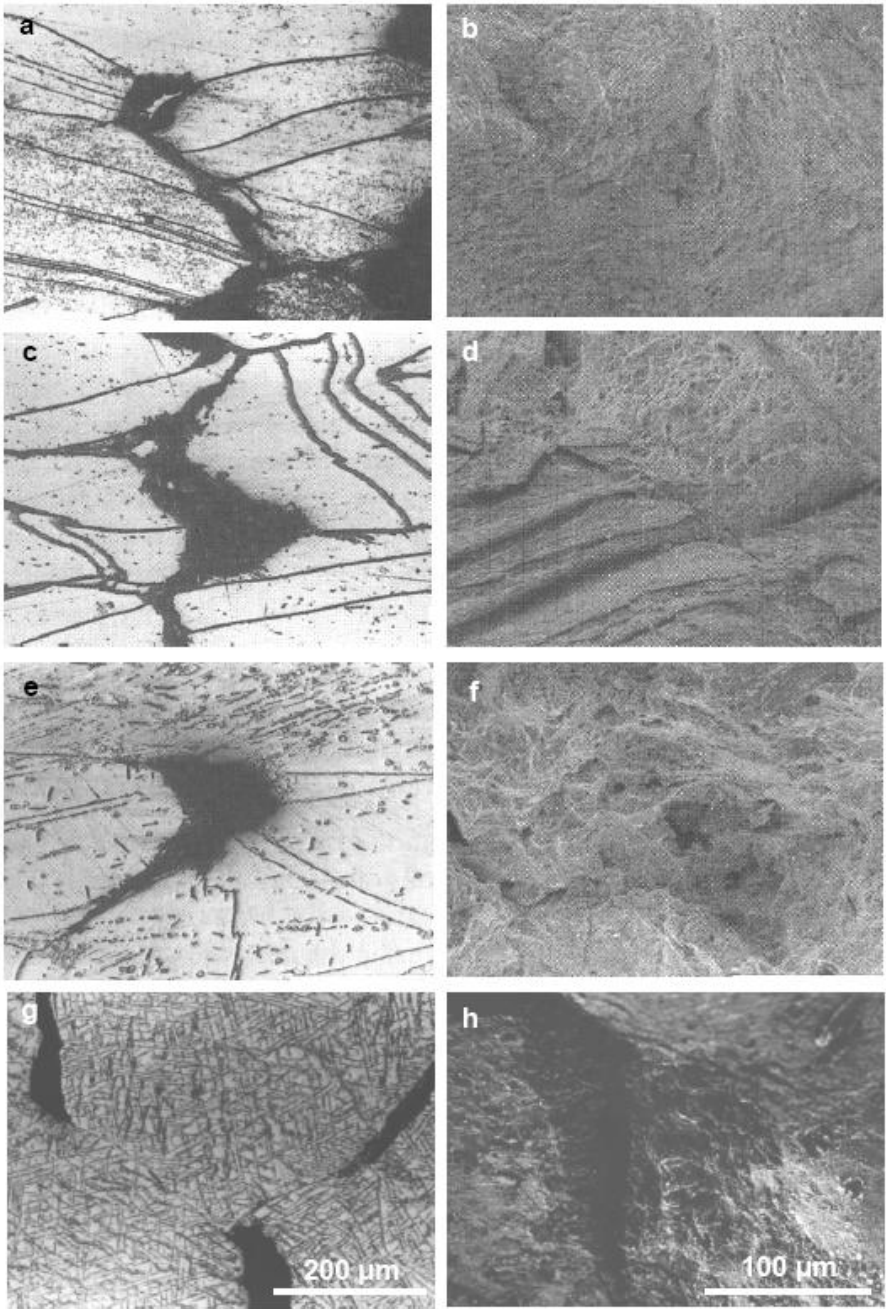


Figure 5. Effects of W content on the rupture strength of cobalt-base alloys at 1089 K.

Figure 6 shows the examples of microstructures and fracture surfaces of the ruptured specimens at 1089 K. The tensile direction is horizontal in the optical micrographs. Grain-boundary cracks are visible near the fracture surface (Figs. 6a, 6c, 6e and 6g). Coarse precipitates of W-rich and carbide phases are formed on grain boundaries in the specimen with serrated grain boundaries (Figure 6c), and on grain boundaries and in the grains in the aged specimens with straight grain boundaries (Figs. 6e and 6g). As a result, improvement of the rupture properties by heat treatments was remarkable in the alloys with the higher W contents. Very fine precipitates which were formed during creep at 1089 K, can be seen on the grain boundaries and in the grains of the specimen with straight grain boundaries (Figure 6a) and in the grains of the specimen with serrated grain boundaries (Figure 6c). These precipitates may be Laves phase and carbide phases such as M_6C and $Cr_{23}C_6$ [16]. In the 14W alloy, small dimples and ledges which are associated with grain-boundary precipitates can be observed in both specimen with serrated grain boundaries (Figure 6d) and aged specimen with straight grain boundaries (Figure 6f), while the non-aged specimen with straight grain boundaries exhibits a brittle grain-boundary fracture surface (Figure 6b). Similar fracture surfaces were observed in the ruptured specimens of the 17W and 20W alloys. In the aged specimen with straight grain boundaries of the 20W alloy that exhibited the longest rupture life at 118 MPa (Figure 6g), small steps and dimples associated with grain-boundary precipitates are visible on the fracture surface (Figure 6h). Thus, the improvement of the rupture life by grain-boundary precipitates may be related to occurrence of ductile grain-boundary fracture with small dimples and ledges.

Copyright © 2010. Nova Science Publishers, Incorporated. All rights reserved.

Handbook of Material Science Research, Nova Science Publishers, Incorporated, 2010. ProQuest Ebook Central,



(σ: stress; t_r: rupture life; ε_r: elongation).

Figure 6. Examples of microstructures and fracture surfaces of the ruptured specimens at 1089 K. a, b. straight grain boundaries (14W, σ=137 MPa, t_r=459.8 ks, ε_r=0.3337) c, d. serrated grain boundaries (14W, σ=137 MPa, t_r=493.60 ks, ε_r=0.2590) e, f. straight grain boundaries plus ageing (14W, σ=137 MPa, t_r=1437.70 ks, ε_r=0.5278) g, h. straight grain boundaries plus ageing (20W, σ=118 MPa, t_r=7946.89 ks, ε_r=0.1499).

Copyright © 2010. Nova Science Publishers, Incorporated. All rights reserved.

Handbook of Material Science Research, Nova Science Publishers, Incorporated, 2010. ProQuest Ebook Central,

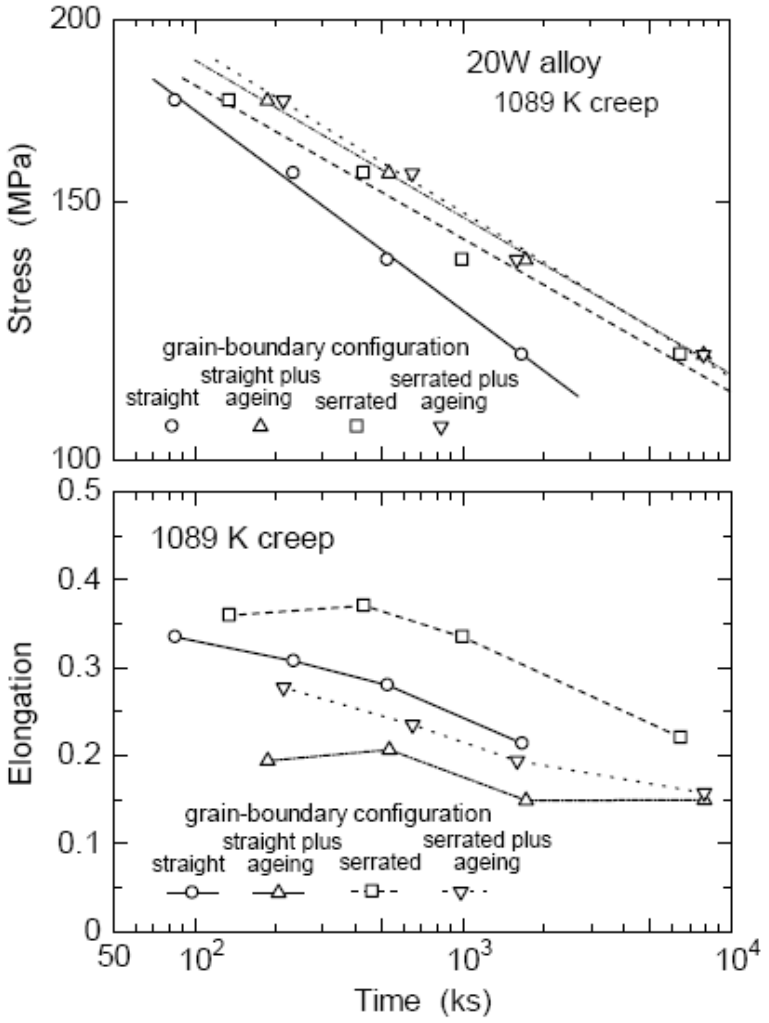


Figure 7. Creep-rupture properties of the 20W alloy at 1089 K.

Kobayashi et al. [9] reported that in the austenitic heat-resisting steels the rupture lives of specimens increase with increasing strength of grains. However, it is still unknown whether the strengthening of grains works 'additive' to the strengthening by serrated grain boundaries in cobalt-base heat-resistant alloys. Improvement of the rupture properties by heat treatments is relatively large in the alloys with the higher W contents under the lower stresses at 1089 K (Figure 5), although high-temperature ageing was less effective under the lower stresses at 1311 K [18]. Figure 7 shows the creep-rupture properties of the 20W alloy at 1089 K. The high-temperature ageing further increases the rupture life of the specimen with serrated grain boundaries. However, the rupture life of the aged specimen with serrated grain boundaries is almost the same as that of the aged specimen with straight grain boundaries, because not only grains but also grain boundaries were strengthened by the precipitation of W-rich and carbide phases in the aged specimen with straight grain boundaries. Thus, the strengthening of grains by high-temperature ageing is comparable with the strengthening by serrated grain boundaries in the 20 W alloy at 1089 K. Similar results were obtained in the 14W and 17W alloys.

Copyright © 2010. Nova Science Publishers, Incorporated. All rights reserved.

Handbook of Material Science Research, Nova Science Publishers, Incorporated, 2010. ProQuest Ebook Central,

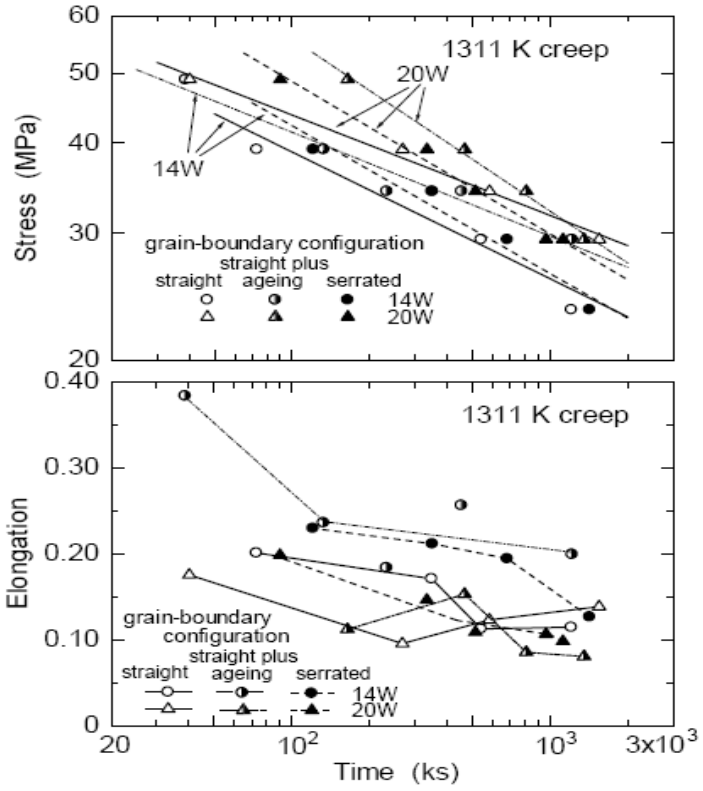


Figure 8. Creep-rupture properties of the 14W and 20W alloys at 1311 K.

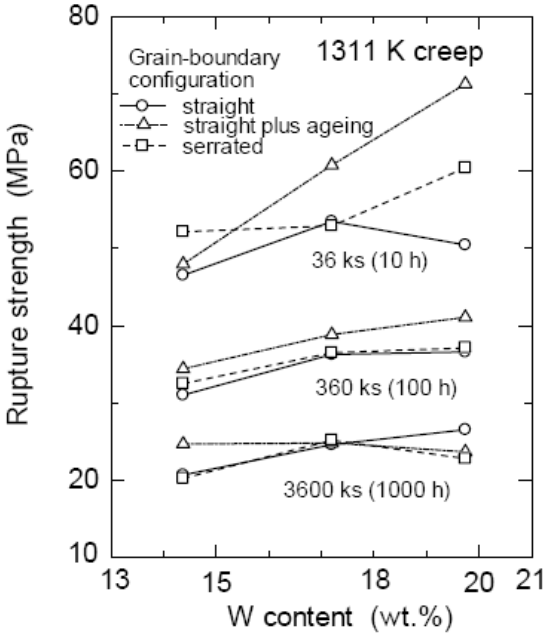
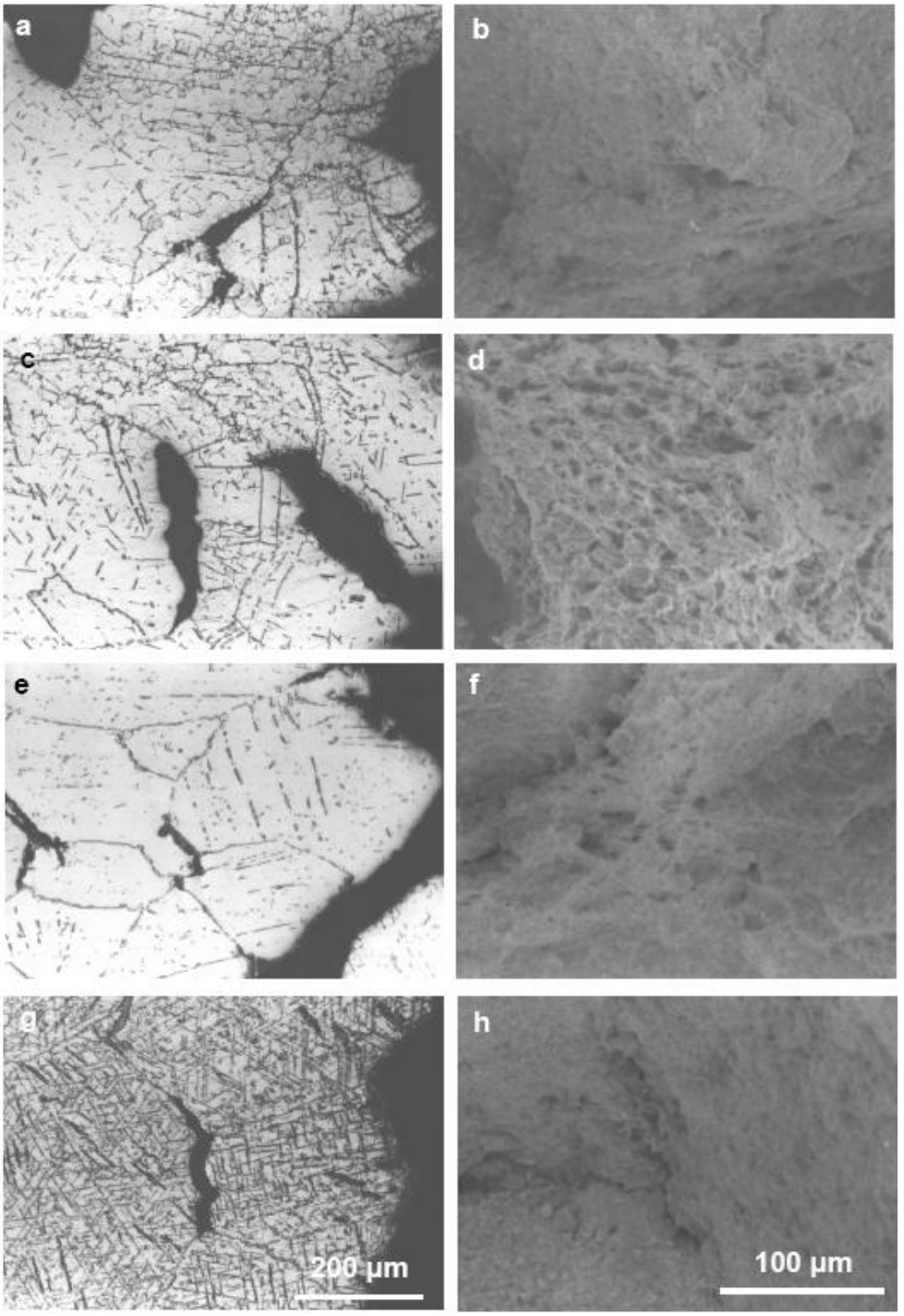


Figure 9. Effects of W content on the rupture strength of cobalt-base alloys at 1311 K.

Copyright © 2010. Nova Science Publishers, Incorporated. All rights reserved.

Handbook of Material Science Research, Nova Science Publishers, Incorporated, 2010. ProQuest Ebook Central,



(σ: stress; t_r: rupture life; ε_r: elongation)

Figure 10. Examples of microstructures and fracture surfaces of the specimens ruptured under a stress of 29.4 MPa at 1311 K. a, b. straight grain boundaries (14W, t_r=541.26, ε_r=0.1127) c, d. serrated grain boundaries (14W, t_r=682.99 ks, ε_r=0.1945) e, f. straight grain boundaries plus ageing (14W, t_r=1218.96 ks, ε_r=0.1996) g, h. straight grain boundaries plus ageing (20W, t_r=1354.44 ks, ε_r=0.0806).

Copyright © 2010. Nova Science Publishers, Incorporated. All rights reserved.

Handbook of Material Science Research, Nova Science Publishers, Incorporated, 2010. ProQuest Ebook Central,

Effects of Tungsten Content on Creep-rupture Properties at 1311 K

Figure 8 shows the creep rupture properties of the 14W and 20W alloys at 1311 K. High-temperature ageing increases the rupture life without decreasing creep ductility in both alloys. Strengthening by serrated grain boundaries has similar effects on the creep-rupture properties, although the strengthening by ageing seems to be more effective than the strengthening by serrated grain boundaries at this temperature. Further, effects of ageing or serrated grain boundaries on the rupture properties was relatively large in the short-term creep, especially in the 20W alloy, because precipitation of W-rich and carbide phases occurred on grain boundaries and in the grains of the non-aged specimens during creep at 1311 K. Similar results were obtained in the 17W alloy. The rupture life is longer in the specimens with the higher W content. Figure 9 shows the effects of W content on the rupture strength of cobalt-base alloys at 1311 K. The rupture strength tends to increase with increasing W content in the non-aged specimens with straight grain boundaries. In relatively short-term creep, the rupture strength also increases with increasing W content of the aged specimens with straight grain boundaries or the specimens with serrated grain boundaries. The W-rich phase, M_6C and $Cr_{23}C_6$ carbides were detected by X-ray diffraction on the non-aged specimens ruptured under a stress of 29.4 MPa at 1311 K [16]. Strengthening of grain boundaries and grains by these precipitates may also have occurred in the non-aged specimens during creep at 1311 K. The amount of the precipitates increased with increasing rupture life of the specimens and with increasing W content in the alloys. These may be the principal reason that there is almost no difference in the rupture strength between the non-aged specimens and the aged specimens or the specimens with serrated grain boundaries.

Figure 10 shows the examples of microstructures and fracture surfaces of the specimens ruptured under a stress of 29.4 MPa at 1311 K. The tensile direction is horizontal and grain-boundary cracks can be seen in the optical micrographs (Figs. 10a, 10c, 10e and 10g). Coarse grain-boundary and matrix precipitates of W-rich and carbide phases are observed in the specimen with serrated grain boundaries (Figure 10c) and the aged specimens with straight grain boundaries (Figs. 10e and 10g) of the 14W alloy. These precipitates can also be seen in the non-aged specimen with straight grain boundaries of the 14W alloy (Figure 10a). Strengthening of grain boundaries and grains may occur in the non-aged specimens with straight grain boundaries during creep at 1311 K. Further, the matrix of the specimen with serrated grain boundaries may also be strengthened by the precipitation of W-rich and carbide phases during creep. These strengthening mechanisms may also have worked in the 17W and 20W alloys. Small dimples and ledges which were associated with coarse grain-boundary precipitates, were observed not only in the specimen with serrated grain boundaries (Figure 10d) and the aged specimen (Figure 10f) of the 14W alloy but also in non-aged specimens with straight grain boundaries of the 14W alloy (Figure 10b) and the 20W alloy (Figure 10h). Such features of the fracture surfaces were common in the alloys with different W contents.

From the experimental results described above, it is considered that in the cobalt-base heat-resistant alloys with high W content the principal strengthening mechanism is the strengthening of grain boundaries and grains by precipitates of W-rich and carbide phases in addition to solid-solution strengthening by W atoms. Improved rupture strength and creep ductility may be associated with occurrence of ductile fracture associated with coarse grain-boundary precipitates. Thus, the control of microstructures by heat treatments is important to utilize favorable effects of W for the improved performance of the cobalt-base HS-25 type

Copyright © 2010. Nova Science Publishers, Incorporated. All rights reserved.

Handbook of Material Science Research, Nova Science Publishers, Incorporated, 2010. ProQuest Ebook Central,

alloys with high W content at high temperatures, while it is also necessary to evaluate the resistance to high-temperature oxidation and corrosion in these alloys.

CONCLUSIONS

Effects of microstructures on the creep-rupture properties were investigated on the cobalt-base superalloys containing about 14 to 20 mass % tungsten (W) at 1089 and 1311 K. The results obtained were summarized as follows.

(1) The rupture strength of the alloys was improved by serrated grain boundaries which were produced by heat treatments, and by ageing for 1080 ks at 1273 K without serious loss of creep ductility. Improvement of the rupture properties by heat treatments was remarkable in the alloys with the higher W content at 1089 K, while such heat treatments were effective in improving rupture properties of the alloys in the relatively short-term creep at 1311 K. In the non-aged specimens with straight grain boundaries, rupture strength increased with increasing W content at 1311 K, although the rupture strength was not improved largely with increasing W content at 1089 K. The high-temperature ageing further increased the rupture life of the specimen with serrated grain boundaries at 1089 K, although the rupture life of the aged specimen with serrated grain boundaries was almost the same as that of the aged specimen with straight grain boundaries.

(2) The principal strengthening mechanism in these alloys was attributed to the strengthening of grain boundaries and grains by precipitates of W-rich and carbide phases in addition to solid-solution strengthening by W atoms. The strengthening of grains by high-temperature ageing was comparable with the strengthening by serrated grain boundaries in the high-tungsten cobalt-base alloys at 1089 K. In the specimen with serrated grain boundaries and the aged specimen with straight grain boundaries, precipitation of the W-rich and carbide phases on grain boundaries probably retarded precipitation of the Laves phase (Co_2W) on grain boundaries. The Laves phase did not lower the strength of the cobalt-base heat-resistant alloys, if it was finely dispersed in the matrix. Precipitation of the W-rich phase and carbides on the grain boundaries and in the grains also occurred and contributed to the strengthening in the non-aged specimens with straight grain boundaries during creep at 1311 K.

(3) Fracture surfaces of non-aged specimens with serrated grain boundaries and those of aged specimens were ductile grain-boundary fracture surfaces with small dimples and ledges at 1089 K, while those of non-aged specimens with straight grain boundaries exhibited brittle grain-boundary facets. Small steps, dimples and ledges were also observed in non-aged specimens with straight grain boundaries ruptured at 1311 K. Occurrence of ductile grain-boundary fracture was associated with the strengthening of grain boundaries by precipitates of W-rich and carbide phases, and led to the improvement of rupture properties at high temperatures. The control of microstructures by heat treatments is important to utilize favorable effects of W for

Copyright © 2010. Nova Science Publishers, Incorporated. All rights reserved.

Handbook of Material Science Research, Nova Science Publishers, Incorporated, 2010. ProQuest Ebook Central,

improvement in performance of components of the cobalt-base HS-25 type alloys with high W content at high temperatures.

ACKNOWLEDGMENTS

The authors thank Mitsubishi Material Company for supplying the cobalt-base alloys used in this study.

REFERENCES

[1] F.R. Morral: *J. Met*., 20 (1968), 52.
[2] S.T. Wlodek: *Trans. ASM*, 56 (1963), 287.
[3] T.G. Langdon and R.B. Vastava: Mechanical Testing for Deformation Model Development, ASTM STP 765, ed. By R.W. Rohde and J.C. Swearengen, American Society for Testing and Materials, Philadelphia, (1982), 435.
[4] H.E. Evans: Mechanisms of Creep Fracture, Elsevier Applied Science Publishers, New York, (1984), 7.
[5] D. McLean, *J. Inst. Metals*, 85 (1956-57), 468.
[6] W. Betteridge and A.W. Franklin, *J. Inst. Metals*, 85 (1956-57), 473.
[7] V. Lupinc, "High Temperature Alloys for Gas Turbines 1982" (Reidel, Dordrecht, 1982), p. 395.
[8] M. Yamazaki, *J. Japan Inst. Metals*, 30 (1966), 1032.
[9] M. Kobayashi, O. Miyagawa and M. Yamamoto, in Proceedings of International Conference on Creep, Tokyo, April 1986, edited by H. Udoguchi et al. (Japan Society for Mechanical Engineers, Tokyo, 1986), p. 65.
[10] M. Tanaka, O. Miyagawa, T. Sakaki, H. Iizuka, F. Ashihara and D. Fujishiro, *J. Mater. Sci.*, 23 (1988), 621.
[11] M. Tanaka, H. Iizuka and F. Ahihara, *J. Mater. Sci.*, 23 (1988), 3827.
[12] M. Tanaka, H. Iizuka and F. Ashihara, *J. Mater. Sci*., 24 (1989), 1623.
[13] M. Tanaka, H. Iizuka and M. Tagami: *J. Mater. Sci*., 24 (1989), 2421.
[14] R. Tanaka, M. Kikuchi, T. Matsuo, S. Takeda, N. Nishikawa, T. Ichihara and M. Kajihara, Proceedings of the Fourth Symposium on Superalloys, Seven Springs Mountain Resort, Champion, Pennsylvania, edited by J.K. Tien, S.T. Wlodek, H. Morrow III, M. Gel and G.E. Maurer (American Society for Metals, Metals Park, Ohio, 1980), p. 481.
[15] M. Tanaka and H. Iizuka: *J. Mater. Sci*., 25 (1990), 5199.
[16] M. Tanaka and H. Iizuka: *Metall. Trans.* A, 23A (1992), 609.
[17] M. Tanaka, Y. Ito and R. Kato: Proceedings of the International Conference on Solid-Solid Phase Transformations '99 (JIMIC-3), May 24-28, 1999, Kyoto, Japan, Edited by M. Koiwa, K. Otsuka and T. Miyazaki, The Japan Institute of Metals, (1999), 277.
[18] M. Tanaka: *J. Mater. Sci*., 29 (1994), 2620.

Copyright © 2010. Nova Science Publishers, Incorporated. All rights reserved.

Handbook of Material Science Research, Nova Science Publishers, Incorporated, 2010. ProQuest Ebook Central,

In: Handbook of Material Science Research
Editors: C. René and E. Turcotte, pp.459-472
ISBN 978-1-60741-798-9
© 2010 Nova Science Publishers, Inc.

Chapter 14

PT-CO SUPPORTED ON POLYPYRROLE-MULTIWALLED CARBON NANOTUBES AS AN ANODE CATALYST FOR DIRECT METHANOL FUEL CELLS

Lei Li*
Shanghai Jiaotong University, Shanghai, China

ABSTRACT

Direct methanol fuel cells (DMFCs) have attracted considerable attention as portable power sources due to their simple system design, low operating temperature, convenient fuel storage and supply. However, poor methanol oxidation at the anode is one of main challenges to limit DMFC applications. In order to solve this challenge, a novel catalyst, Pt-Co alloy supported on polypyrrole (PPy)-multiwalled carbon nanotubes (MWCNTs), was prepared by chemical reduction method. PPy-MWCNTs as catalyst support was prepared by *in situ* polymerization of pyrrole onto MWCNTs. Pt-Co nano-scaled particles with narrow particle size distribution about 2-4nm were uniformly co-deposited onto the PPy-MWCNTs. The physical characterizations of catalyst and catalyst support were measured by SEM, TEM, EDS and XRD, respectively. The electrochemical properties of Pt-Co/PPy-MWCNT catalyst were tested by using cyclic voltammetry, CO stripping voltammetry, and chronoamperometry measurements. It was found that the partial over-oxidation treatment of catalyst support enhanced the catalytic activity of Pt-Co catalyst for methanol oxidation. Under the same Pt loading and experiments conditions, the Pt-Co/PPy-MWCNT catalyst after the over-oxidation activation shows higher catalytic activity toward methanol oxidation compare to commercial Pt-Ru/C catalyst, and potential application for direct methanol fuel cells.

INTRODUCTION

Direct methanol fuel cells (DMFCs), as an important alternative energy source for portable devices, has attracted considerable interest because of their simple system design,

* E-mail: lilei0323@sjtu.edu.cn

Copyright © 2010. Nova Science Publishers, Incorporated. All rights reserved.

Handbook of Material Science Research, Nova Science Publishers, Incorporated, 2010. ProQuest Ebook Central,

low operating temperature, convenient fuel storage and supply [1-4]. However, limited abundance and high cost of noble metal electrocatalysts still is one of major barriers to the application of DMFCs. Apart from the issue of high cost of catalysts, fuel cell catalysts suffer from strong adsorption of monoxide (CO) on platinum, which causes the surface poison of catalyst and hinders further oxidation of methanol [5-8]. As an alternative strategy to reduce the use of platinum and improve the electrocatalytic activity of anode catalysts, multiple-component transition-metal alloy catalysts attract more and more interest. It has been found that Pt-M (M=Ru, Pd, Co, Sn) alloy catalysts have high activity towards methanol oxidation, good tolerance to CO poisoning compared with pure platinum surface [2, 8, 9-12], and the improved noble metal utilization. Similarly, developing suitable supports to achieve high catalyst utilization, stability and activity is also a challenge.

Carbon black has been used as catalyst support broadly and commercially. However, the efficiency of methanol oxidation is low partly due to low platinum utilization on this conventional carbon support, which is, in turn, related to the low electrochemically accessible surface area for the deposition of Pt particles [13-16]. Compared to the carbon black, carbon nanotubes (CNTs) are attractive materials used as the catalyst support for fuel cell applications due to their particular morphologies and properties, such as small nanometer particle size, high accessible surface area, corrosion resistance, good electronic conductivity and high stability [17-18]. There are many different methods to disperse platinum/platinum alloys on CNTs. Since CNTs are chemically inert, activating their surfaces is essential and this has motivated numerous studies to improve metal dispersions on CNTs, mainly through optimization of the metal supporting procedures or functionalization of the CNT surface [19–21]. Unfortunately, functional groups such as –OH and –COOH formed on the surface of carbon nanotube are not homogeneous. These functional groups are easy to adsorb Pt crystal seeds and make most of Pt particles grow on these defects and form agglomerate Pt particles, resulting in the poor dispersion and low utilization of Pt catalysts [20, 21-24]. An alternative method is to modify CNTs with conducting polymers, such as polyaniline and polypyrrole. As polyaniline modified single wall carbon nanotube composite was used as Pt or Au catalyst support, both catalysts showed high catalytic activity towards methanol oxidation due to better dispersion and high catalyst utilization [23-25]. A similar result has also been reported, in which PPy modified multiwalled carbon nanotubes (MWCNTs) was used as catalyst support [9].

Usually, electrochemical over-oxidation treatment was used to remove impurities which were mixed in the catalysts during the synthesis process. A high potential was applied and the impurities were oxidized, even degraded completely. Conducting polymers, such as polyaniline, polypyrrole (PPy) and poly(3,4-ethylenedioxythiophene) (PEDOT), all can be over oxidized partially. After the over-oxidation treatment, the interchain links will be partially broken, the net structure of polymer will be destroyed and therefore the electronic conductivity declines (Fig. 1) [26]. Interestingly, some researchers reported that the over-oxidation treatment is one of activation processes to improve the electrochemical activity of catalysts when conducting PEDOT was used as the catalyst support [27-28].

Copyright © 2010. Nova Science Publishers, Incorporated. All rights reserved.

Handbook of Material Science Research, Nova Science Publishers, Incorporated, 2010. ProQuest Ebook Central,

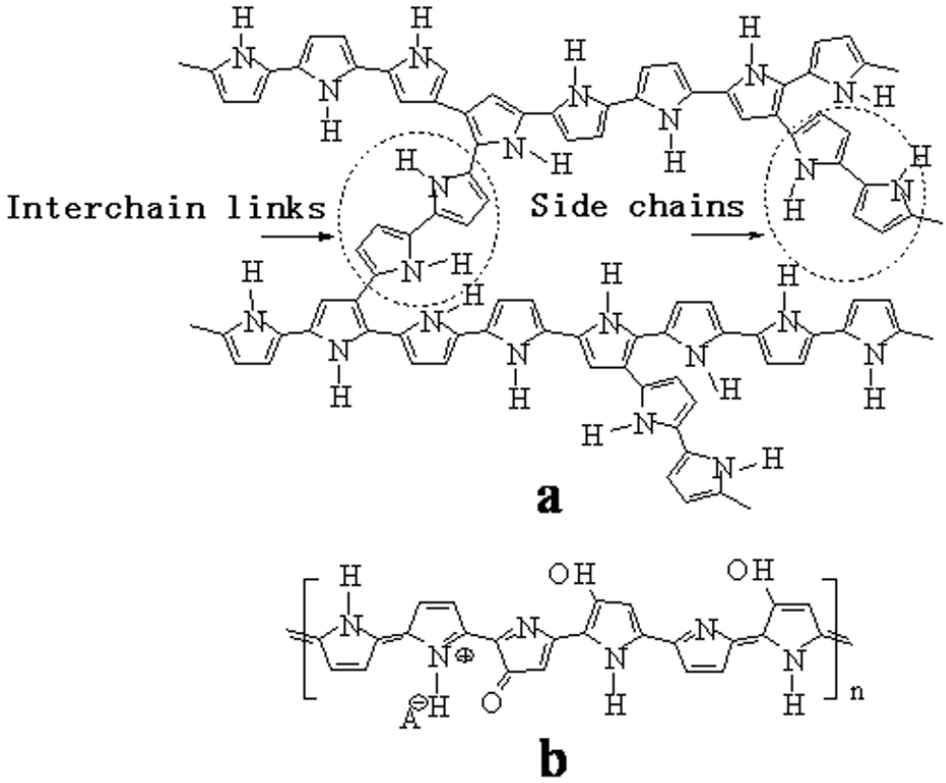


Figure 1. The microstructure of PPy (a) and over-oxidized PPy (b).

In the present work, we prepared a composite of Pt-Co alloy particles dispersed onto the PPy modified MWCNTs as catalyst for methanol oxidation. In our experiments, the functional groups (-COOH) on the surface of MWCNTs can be employed as counter-ions during the polymerization of pyrrole monomers onto the surface of carbon nanotube. Thus the functional groups can be hided and Pt would not grow around these groups. At the same time, $PtCl_6^{2-}$ can be considered as counter ions to dope in the PPy matrix. In further, Pt particles can be deposited on the surface of PPy homogeneously when $PtCl_6^{2-}$ is reduced. By this method, the dispersion and utilization of catalysts was improved. Pt-Ru multi-component metal on PPy modified MWCNTs with a high electrocatalysis has been reported [9, 19]. However, to the best of our knowledge, there have been no reports on Pt-Co alloy nanoparticles dispersed onto PPy-MWCNTs support for methanol oxidation and the influence of over-oxidation treatment of the composite on the catalytic activation.

EXPERIMENTAL

Preparation and Characterization of Catalyst

Pt-Co/PPy-MWCNTs catalyst (molar ratio of platinum : cobalt = 3:1) was prepared as follow: MWCNTs (Chengdu Desilan Technology CO., LTD, China) were treated in 6M

Copyright © 2010. Nova Science Publishers, Incorporated. All rights reserved.

Handbook of Material Science Research, Nova Science Publishers, Incorporated, 2010. ProQuest Ebook Central,

HNO_3 at 100 ^oC for 5 hours and followed washed with DDI water and dried at 80 ^oC. PPy-MWCNTs support was synthesized by an *in situ* chemical polymerization of pyrrole monomers on the surface of MWCNTs. 0.12 g MWCNTs were homogenously dispersed in 100 mL ethanol-water (volume ratio of ethanol to water is 1:5), and then 0.714 mmol $(NH_4)_2S_2O_8$ was added. The obtained mixture was vigorously stirred for 30 minutes with N_2 satuaration. Then 0.443 mmol pyrrole solved in 50 mL ethanol was slowly added to the suspension solution and kept striiring for 8 hours. After the polymerization, a precursor aqueous solution of 0.338 mmol H_2PtCl_6 and 0.113 mmol $Co(NO_3)_2{\cdot}6H_2O$ solved in 50 mL water was added into the mixture with vigorously stirring. Then Pt and Co metals were reduced and co-deposited onto the PPy-MWCNTs support by using 15 wt% formaldehyde aqueous solution as reduction agent at 80 ^oC for 5 hours with N_2 satuarted. Finally, the resultant catalyst was washed with ethanol and DDI water, and dried at 60 ^oC in vaccum condition for 12 hours. For comparison, Pt/PPy-MWCNTs was prepared with the same process.

Physical and Chemcial Characterizations

Characterization of the samples was carried out by the following techniques: Energy-dispersive X-ray spectrometer (EDS) analysis, morphology and particle size distribution of catalyst were obtained by using a JEOL S-520 high resolution transmission electron microscopy (HR-TEM) operating at 200 kV and a JEM-100CX scanning electron microscope (SEM) operating at 20 kV. X-ray powder diffraction (XRD) characterization (Cu Kα X-ray radiation source) was carried out on D/max-2200/PCX-Ray Diffractometer at a scan rate of 6 $^o\,min^{-1}$.

Electrochemical Characterizations

Cyclic voltammetry (CV) measurements were carried out in a three-electrode cell by using a rotating disk electrode (Model 616, Eco Chemie, Netherland) and Autolab PGSTAT 302 electrochemical test system (Eco Chemie, Netherland). The catalyst ink was prepared by mixing a suspension of 50 μL 5 wt% perfluorosulfonic acid (Dongyue Group, Shandong, China) water-ethanol solution with several miligrams catalyst in ultrasonic bath about 5 minutes. The catalyst ink in 5 μL was dropped onto clean glassy carbon (GC) electrode (3 mm diameter) and dried at room temperature. The Pt loading of catalyst in the GC electrode was 0.5 mg cm^{-2}. The GC electrode coating catalyst was used as working electrode, platinum foil (1cm × 1cm) as counter electrode, and an Ag/AgCl as reference electrode (0.242V *vs.* NHE). 0.5 M H_2SO_4 aqueous solution was served as electrolyte for hydrogen oxidation measurements, and 0.5 M H_2SO_4 + 1.0 M CH_3OH aqueous solution for methanol oxidation measurements, respectively. High-purity N_2 was bubbled into the electrolytes during the experiments.

The CO stripping test was carried out as follow. CO was adsorbed by flowing pure CO at a flow rate of 100 mL min^{-1} through the electrolyte for 30 minutes, while holding the electrode potential at 0.1 V. By keeping the potential at the same value the gas was switched to N_2 for 15 minutes to remove physical adsorpted CO from the gas phase. After additional 20

Copyright © 2010. Nova Science Publishers, Incorporated. All rights reserved.

Handbook of Material Science Research, Nova Science Publishers, Incorporated, 2010. ProQuest Ebook Central,

minutes, the potential was scanned with the sweep rate of 50 mV s^{-1} from the starting potential to 1.0 V and then back to -0.3 V.

Fuel Cell Performance

The prepared Pt-Co/PPy-MWCNTs were used as anode catalyst, and commercial Pt/C (40wt% Pt, Johnson Matthey) as cathode catalyst, respectively. The platinum loading for all electrodes used was 1.0 mg cm^{-2}. The reaction layer, for both anode and cathode, was prepared by direct mixing in an ultrasonic bath a suspension of perfluorosulfonic acid ionomer in water with the catalyst powders, the obtained paste was spread on carbon cloth backings. The membrane-electrode assemblies (MEAs) were manufactured by pressing the electrode onto Nafion 117 membrane at 120 ^{o}C and 15.4 MPa for 2 min.

The fuel cell performance was evaluated at a fuel cell test station (Arbin FCTS-PEM-DM) using a single DMFC with active area 4 cm^2 at 60 ^{o}C. 2 M methanol solution was pumped through the anode at a flow rate of 20 ml min^{-1} with atmosphere pressure while humidified oxygen was fed to the cathode at 75ml min^{-1} at a pressure of 0.1 MPa.

RESULTS AND DISCUSSION

The electrochemical performance of the fresh catalyst was first characterized by cyclic voltammetry measurement. An strange phenomenon attracted us that not only the hydrogen oxidation peaks, but also the oxygen reduction peaks were not very obvious. Most research considered that this phenomenon was due to some impurities being mixed in the catalyst during the synthesis process. To deal with this strange phenomenon, a general method to treat catalyst with wide scan potential window, named the over-oxidation treatment, was used [27-28]. However, to the best of our knowledge, there are no any reports about the influence of this activation process on the electrochemical activity of catalysts using conducting PPy modified carbon as the catalyst support. In our experiments, the characterizations and performances of fresh and the over-oxidation treated Pt-Co/PPy-MWCNTs catalysts were investigated. Usualy, pyrrole monomers can be oxidazed and polymerized when the potential reached 0.65 V. In this paper, the over-oxidation activation process was carried out in a wider electrochemical window from -0.3 to 1.4 V vs. Ag/AgCl in 0.5 M H_2SO_4 aqueous solution.

Firstly, with the EDS measurement (Fig. 2), the content of Pt and Co in the Pt-Co/PPy-MWCNTs catalyst was about 29.71 wt% and 3.31 wt%, respectively. This result is accordance to the original reactant stochiometric proportion of 3:1.

Typical SEM images of Pt-Co/PPy-MWCNTs before and after the over-oxidation treatments were shown in Fig. 3. It was obvious found that more metal particles are exposed on the surface of support after the over-oxidation treatment, which means that the over-oxidation process can change the structure of the composite catalyst and the electrochemical active surface of Pt should be improved.

Copyright © 2010. Nova Science Publishers, Incorporated. All rights reserved.

Handbook of Material Science Research, Nova Science Publishers, Incorporated, 2010. ProQuest Ebook Central,

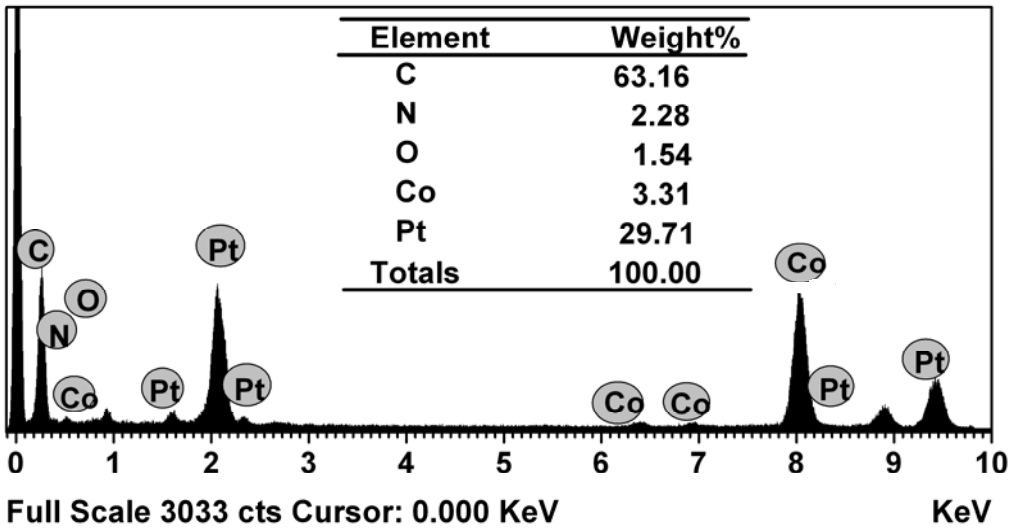


Figure 2. EDS result of Pt-Co/PPy-MWCNTs catalyst.

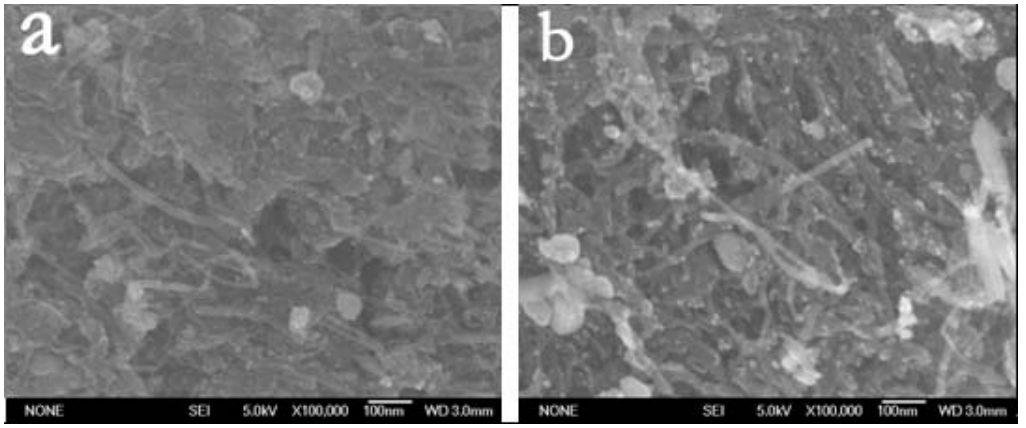


Figure 3. SEM morphologies of Pt-Co/PPy-MWCNTs catalysts before (a) and after (b) over-oxidation treatment.

A further study of the influence of the over-oxidation treatment to the morphology of catalysts was investigated by TEM measurements. Untreated and treated catalysts were first ultrasonically dispersed in ethanol solution, and then coated on ultrathin carbon membrane before TEM measurements. Typical TEM images of catalysts fresh and after the over-oxidation treatments were shown in Fig. 4. It can be found that the metal particle size has not obviously changed. The select area electron diffraction patterns also confirmed that Pt (111) space had not an obviously changed. It indicates that the over-oxidation activation process would not affect the metal particle size markedly. The diffraction ring and lattice distance of Pt on fresh and Pt-Co alloy on the over-oxidation treated Pt-Co/PPy-MWCNTs were quite similar, which means that Pt in the alloy kept the original structure. The lattice distance of Pt (111) space in the untreated and treated catalysts was 2.21 Å and 2.14 Å, respectively. In addition, it can be found that more Pt particles bunched in PPy matrix were exposed after the over-oxidation process. The reason is maybe the PPy geometric configuration changed after

Copyright © 2010. Nova Science Publishers, Incorporated. All rights reserved.

Handbook of Material Science Research, Nova Science Publishers, Incorporated, 2010. ProQuest Ebook Central,

the over-oxidation activation process. During the over-oxidation process, the interchain links and side chains of PPy (as shown in Fig. 1 [26]) could be broken at high potential, which caused the orignal net strucured PPy formed more pores, in further, more Pt was exposed and the specific electrochemical active surface increased.

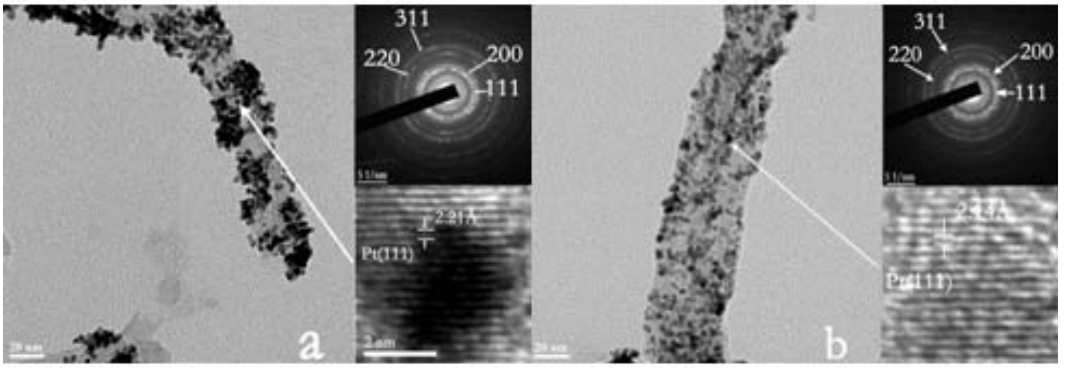


Figure 4. HR-TEM images of Pt-Co/PPy-MWCNTs catalysts before (a) and after (b) over-oxidation treatment.

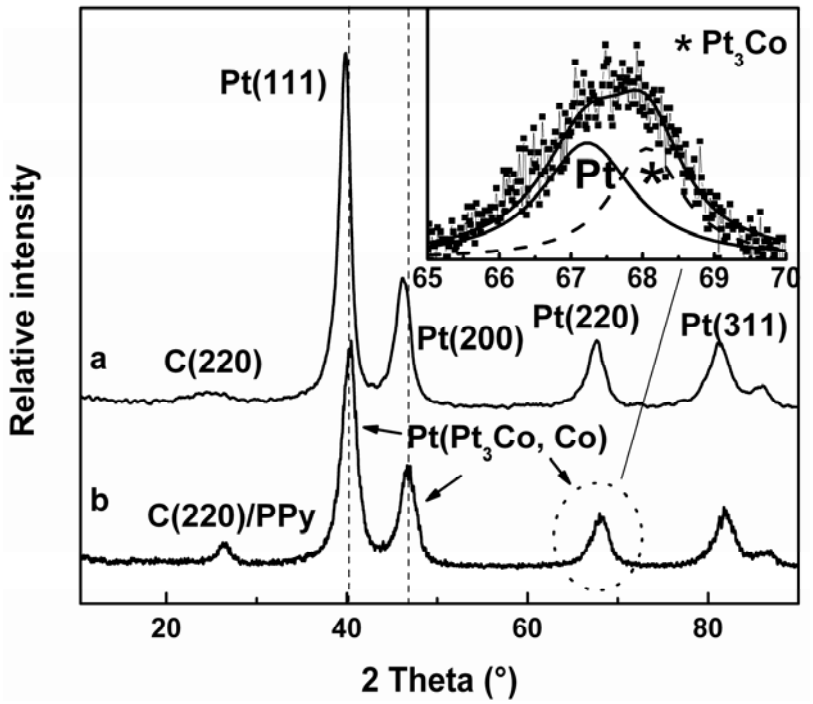


Figure 5. XRD patterns of (a) JM 40 wt% Pt/C and (b) fresh Pt-Co/PPy-MWCNTs catalysts with a scan speed 6 ° sec^{-1}.

The XRD results in Fig. 5 indicate that both commerical 40 wt% Pt/C and the prepared Pt-Co/PPy-MWCNTs catalysts present a typical platinum fcc crystallographic structure. Compared to the commercial Pt/C catalyst, there was a slight shift of the X-ray diffraction peaks of Pt-Co/PPy-MWCNTs catalyst to higher Bragg angles. It means that some bimetallic

Copyright © 2010. Nova Science Publishers, Incorporated. All rights reserved.

Handbook of Material Science Research, Nova Science Publishers, Incorporated, 2010. ProQuest Ebook Central,

interaction or alloying occurred in the catalyst. According to the Scherrer equation, bimetallic catalyst particle size of 3.1 nm was obtained by using Pt (311) response, which is accordant with the result of TEM image. In view of that the main XRD peaks of Pt and Pt_3Co are very close, the broad peak characteristic of Pt-Co/PPy-MWCNTs catalysts is attributed to partial overlap of the respective peaks. It should be noted that small proportion of Co metal should exist in the catalyst, considering of the original reactant stochiometric proportion, but because of its low content, we can not find obvious Co diffraction peaks. The inset in Fig. 5 (scan with 1° min^{-1}) illustrates the peak separation of Pt (220) and Pt_3Co (220) [29].

The CO stripping test was carried out to check the CO-tolerance of Pt-Co alloy on this new composite support in 0.5 M H_2SO_4 solution. In Fig. 6, the dashed line is corresponding to oxidation of chemical absorption state CO, and the solid line represents the CV after CO oxidazed. It is clear that PtRu alloy still is the best CO-tolerance anode catalyst because of its low onset CO oxidation potential and peak potential. In our study, the Pt-Co alloy also shows low onset CO oxidation potential and peak potential compared with the Pt/XC72 and Pt/PPy-MWCNTs catalysts, which means that CO was oxidized easily on the surface of Pt-Co/PPy-MWCNTs catalyst. Also the integral area of CO oxidation peak (represent CO adsorption) was smaller than that of the other two catalysts, which mean low CO adsorption on our catalyst. Such a result is concordant to Mitsuru's report [30]. The reason for the improvement of CO-tolerance is due to that the electronic structures of Pt-Co alloys is apparently different from that of Pt and Pt $4f_{7/2}$ energy bonding is lower than pure Pt, which is benefit to adsorb CO at low potential.

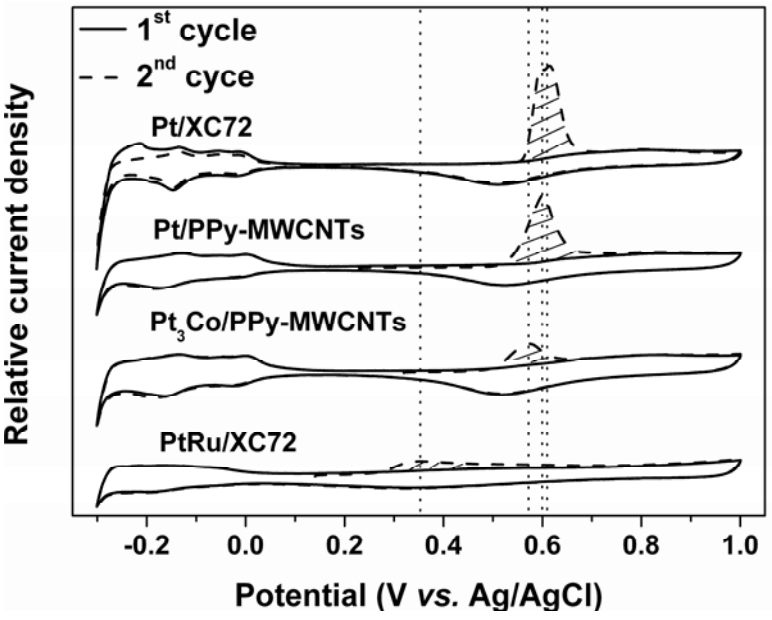


Figure 6. The CO stripping voltammetry of different catalyst, Pt loading of 500 μg cm^{-2}, 0.5 M H_2SO_4 aqueous solution, scan rate: 50 mV s^{-1}, temperature: 25 ^oC. 1st cycle: the chemical adsorbed CO oxidition, 2nd cycle: after chemical adsorbed CO is removed.

Copyright © 2010. Nova Science Publishers, Incorporated. All rights reserved.

Handbook of Material Science Research, Nova Science Publishers, Incorporated, 2010. ProQuest Ebook Central,

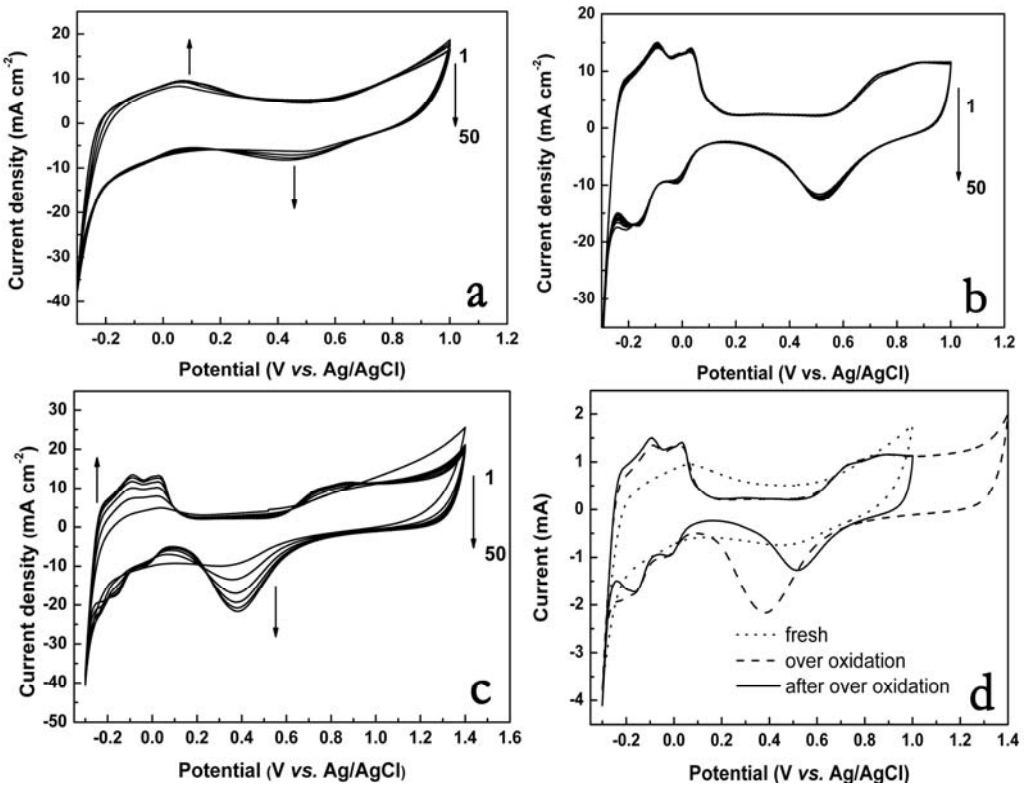


Figure 7. Cyclic voltammograms of Pt-Co/PPy-MWCNTs in 0.5 M H_2SO_4 at 25 °C, a: fresh, b: after the over-oxidation treatment, c: the over-oxidation (a-c all for the first 50 cycles), d: a comparison of the 50th cycle for the different steps.

Fig. 7 shows cyclic voltammograms of Pt-Co/PPy-MWCNTs modified GC electrode in 0.5 M H_2SO_4 before and after the over-oxidized activation treatment under half-cell condition in the range from -0.3 to 1.4 V versus Ag/AgCl. Before the over-oxidation treatement, three pairs of characteristic adsorption and desorption peaks, related to hydrogen oxidation (from -0.3 to 0.1 V) and oxygen reduction (at about 0.7 V) which usually appear on pure Pt electrode were not obvious and the current densities of hydrogen desorption and oxygen reduction were low (Fig. 7a). While the over-oxidized in the range of -0.3 to 1.4 V about 50 cycles as an activation process, the characteristic peak of Pt exhibited obviously and reached stable gradually (Fig. 7c). The electrochemical response of the conducting PPy decreased, while the Pt characteristics became more pronounced, this result was corresponding to the literature [27-28]. In case of the electrochemical activity of Pt-Co/PPy-MWCNTs after the over-oxidation (Fig. 7b), the typical hydrogen and oxygen adsorption-desorption peaks on Pt electrode were obvious and stable. One reason for the continuous diminution of the anodic current plateau is that the potential shift of the PtO reduction peak to more positive potentials and the decrease of the PPy redox charge were associated with the over oxidation and degradation of PPy. This behavior was coherent with that of PEDOT [28]. The other reason for the improved electrocatalysis ability of the over-oxidation treatment maybe is attributed to degradation of PPy. Before the over-oxidized, PPy should be in a reduction state (non-doped state) when $PtCl_6^{2-}$ was reduced to Pt in alkali solution [31-33]. When the catalyst layer was immersed into sulfuric acid aqueous solution, PPy would change its structure from non-doped

Copyright © 2010. Nova Science Publishers, Incorporated. All rights reserved.

Handbook of Material Science Research, Nova Science Publishers, Incorporated, 2010. ProQuest Ebook Central,

state to doped state slowly with time extending and at last reached stable and the conductivity of PPy was improved. Though under high potential (>0.8 V), the long chain of PPy were decomposed to short chain and the net structure of PPy would be destroyed on a certain extent, more loose pore of PPy was obtained and more Pt particle surface exposed simultaneously, then the utilization of catalyst increased. Such a result is accordant to the SEM results (Fig. 3).

Fig. 8 exhibits the electrochemical performance of the resulting catalysts and commercial Pt-Ru/XC72 catalyst for methanol oxidation. The onset potential for methanol oxidation on treated catalyst was about 0.20 V *vs.* Ag/AgCl, which is lower than that of fresh catalyst (0.3 V) and identical to that of Pt-Ru/XC72. In addition, the forward anodic mass activity of the treated Pt-Co/PPy-MWCNTs electrode was higher than that of fresh catalyst and commercial Pt-Ru/XC72. Therefore, the over-oxidation treatment is an activation method to improve the electrochemistry activity of Pt-Co/PPy-MWCNTs catalyst towards methanol oxidation.

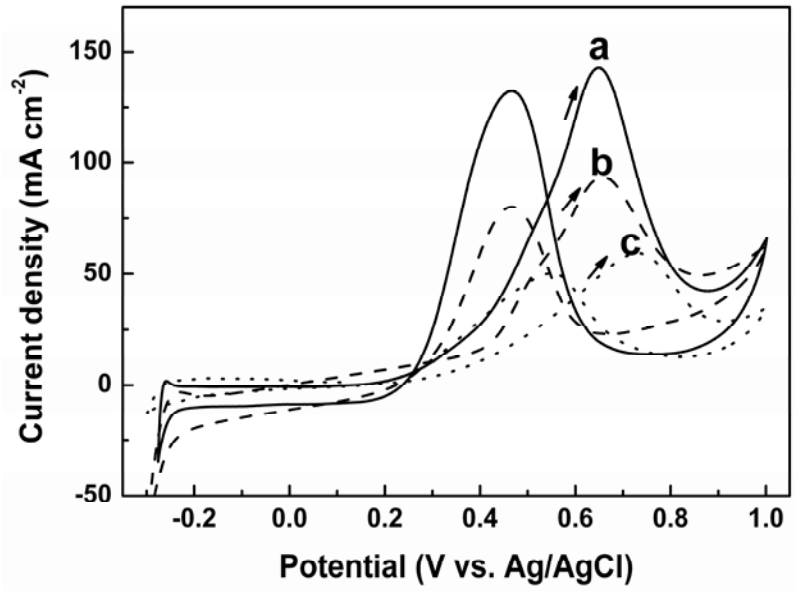


Figure 8. Anodic sweep voltammograms of catalysts modified GC electrode. (a): Pt-Co/PPy-MWCNTs after the over-oxidation treatment, (b): Pt-Ru/XC72 and (c): Pt-Co/PPy-MWCNTs before the over-oxidation treatment. Pt loading of 500 μg cm^{-2}, 0.5 M H_2SO_4 +1.0 M CH_3OH aqueous solution, saturated with N_2, scan rate: 50 mV s^{-1}, temperature: 25 ^oC.

Methanol oxidation stability of our catalysts was investigated by the chronoamperometry measurements as a function of potentials. Fig. 9 shows the chronoamperometry curve of before and after the over-oxidation treated Pt-Co/PPy-MWCNTs and Pt-Ru/XC72 electrode applied at 0.76 V for 200 seconds. It is clearly found that the electrochemical activity of Pt-Co/PPy-MWCNTs to methanol oxidation is significantly improved after the over-oxidation treatment and keep stable methanol oxidation ability. The current density is also higher than that of Pt-Co/PPy-MWCNTs before the over-oxidation and Pt-Ru/XC72 catalyst.

Copyright © 2010. Nova Science Publishers, Incorporated. All rights reserved.

Handbook of Material Science Research, Nova Science Publishers, Incorporated, 2010. ProQuest Ebook Central,

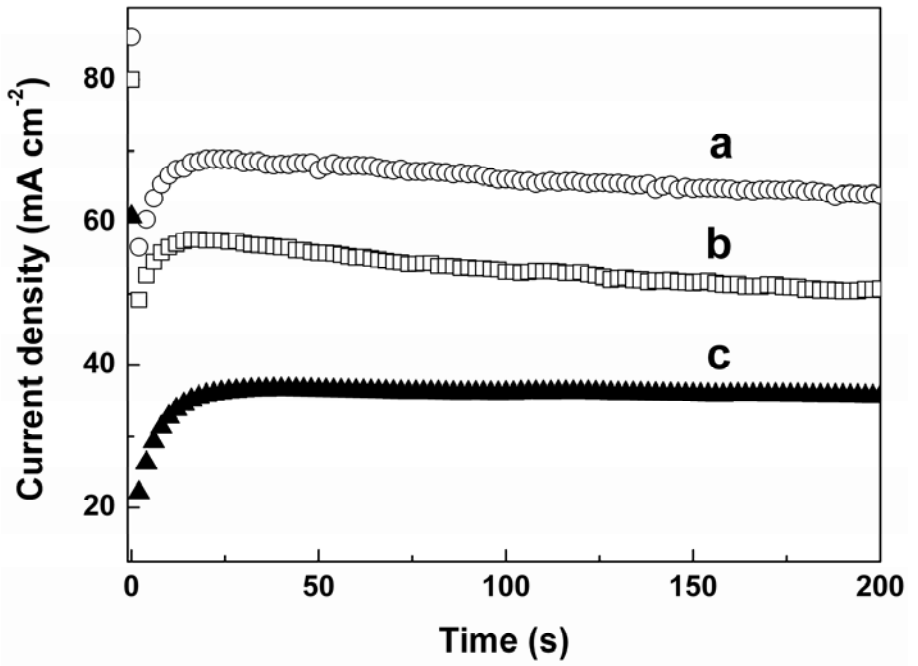


Figure 9. The chronoamperometry curves of catalysts. (a): Pt-Co/PPy-MWCNTs after the over-oxidation treatment, (b): Pt-Ru/XC72 and (c): Pt-Co/PPy-MWCNTs beforeafter over oxidation (c), under 0.76 V. Pt loading of 500 μg cm^{-2}, 0.5 M H_2SO_4 +1 M CH_3OH aqueous solution, saturated with N_2, scan rate: 50 mV/s and 25 ^oC.

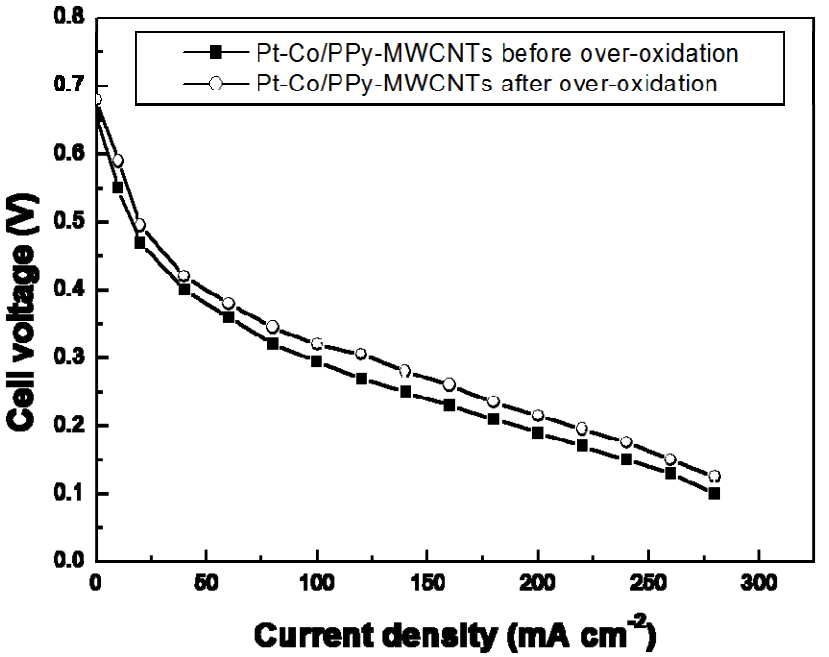


Figure 10. DMFC performances of different MEAs in 2M CH_3OH at 60 ^oC.

Copyright © 2010. Nova Science Publishers, Incorporated. All rights reserved.

Handbook of Material Science Research, Nova Science Publishers, Incorporated, 2010. ProQuest Ebook Central,

The prepared Pt-Co/PPy-MWCNTs as anode catalysts for methaol oxidation was investigated in a single DMFC. The performances of fuel cell were shown in Fig. 10. It can be easily found that the performance of fuel cell using the catalysts after the over-oxidation treatment was higher than that of the no-treated catalyst. A power density of about 45mW cm^{-2} was obtained for an electrochemically activated Pt-Co/PPy-MWCNTs based MEA. This value was hihger than that of a non-activated system (34mW cm^{-2}).

CONCLUSION

Pt-Co nanoparticles decorated polypyrrole (PPy-MWCNTs) composite has been developed for methanol oxidation reaction. This catalyst showed good CO-tolerance ability and stable methanol oxidation electrocatalysis. The influence of over oxidation activation on improving the Pt-Co/PPy-MWCNTs electrocatalysis was studied. XRD result shows that Pt-Co alloy phase formed and the particle size calculated by Sherrer equation is about 3.4 nm. The reason for this stable methanol oxidation should be attributed to that the over-oxidation treatment process would change the arrangement of PPy matrix, companying with more Pt surface was exposed. The Pt-Co/PPy-MWCNTs catalyst shows improved catalytic activity towards methanol oxidation after over oxidation compared to the fresh catalyst and commercial Pt-Ru/XC72, which means that the over oxidation activation can change PPy structure and improve the Pt utilization. The performance of Pt-Co/PPy-MWCNTs after the over-oxidation treatment in a DMFC was better than that of the no-treated catalysts. Therefore, Pt-Co/PPy-MWCNTs catalyst indicates great potential in direct methanol fuel cells.

REFERENCES

[1] Wadmus, S., & Küver, A. (1999). Methanol oxidation and direct methanol fuel cell: a selective review. *J. Electroanal. Chem.*, 461, 14-31.

[2] Antolini, E., Salgado, J.R.C., & Gonzalez, E.R. (2006). The methanol oxidation reaction on platinum alloys with the first row transition metals; The case of Pt-Co and -Ni alloy electrocatalysts for DMFCs: a short review. *Appl. Catal. B-Environ.*, 63, 137-149.

[3] George, A., & Eric, J. (2004). Direct methanol fuel cells - ready to go commercial? *Fuel Cells Bull.*, 11, 12-17.

[4] Reddington, E., Sapienza, A., Gurau, B., Viswanathan, R., Sarangapani, S., Smotkin, E.S., & Mallouk, T.E. (1998). Combinatorial electrochemistry: a highly parallel, optical screening method for discovery of better electrocatalysts. *Science*, 280, 1735-1737.

[5] Golabi, S.M., & Nozad, A. (2002). Electrocatalytic oxidation of methanol on electrodes modified by platinum microparticles dispersed into poly(o-phenylenediamine) film. *J. Electroanal. Chem.*, 521, 161-167.

[6] Mikhaylova, A.A., Khazoova, O.A., & Bagotzky, V.S. (2000). Electrocatalytic and adsorption propertied of platinum microparticles electrodeposited onto glassy carbon and into Nafion® films. *J. Electroanal. Chem.*, 480, 225-232.

Copyright © 2010. Nova Science Publishers, Incorporated. All rights reserved.

Handbook of Material Science Research, Nova Science Publishers, Incorporated, 2010. ProQuest Ebook Central,

[7] Li, W.S., Tian, L.P., Huang, Q.M., Li, H., Chen, H.Y., & Lian, X.P. (2002). Catalytic oxidation of metnanol on molybdate-modified platinum electrode in sulfuric acid solution. *J. Power Sources*, 104, 281-288.

[8] Hubert, A.G., Nenad, M.M., & Philip, N.R.J. (1995). Electrooxidation of CO and H_2/CO mixtures on a well -characterized Pt_3Sn electrode surface. *J. Phys. Chem.*, 99, 8945-8949.

[9] Selvaraj, V., & Alagar, M. (2007). Pt and Pt–Ru nanoparticles decorated polypyrrole/multiwalled carbon nanotubes and their catalytic activity towards methanol oxidation. *Electrochem. Commun.*, 9, 1145-1153.

[10] Li, H., Sun, G., Li, N., Sun, S., Su, D., & Xin, Q. (2007). Design and preparation of highly active Pt−Pd/C catalyst for the oxygen reduction reaction. *J. Phys. Chem. C*, 111, 5605-5617.

[11] Koh, S., Leisch, J., Toney, M.F., & Strasser, P. (2007). Structure-activity-stability relationships of Pt−Co alloy electrocatalysts in gas-diffusion electrode layers. *J. Phys. Chem. C*, 111, 3744-3752.

[12] Baglio, V., Arico, A.S., Stassi, A., D'Urso, C., Di Blasi, A., Castro Luna, A.M., & Antonucci, V. (2006). Investigation of Pt-Fe catalysts for oxygen reduction in low temperature direct methanol fuel cells. *J. Power Sources*, 159, 900-904.

[13] Uchida, M., Fukuoka, Y., Sugawara, Y., Ohara, H., & Ohta, A. (1998). Improved preparation process of very-low-platinum-loading electrodes for polymer electrolyte fuel cells. *J. Electrochem. Soc.*, 145, 3708-3714.

[14] Rao, V., Simonov, P.A., Savinova, E.R., Plaksin, G.V., Cherepanova, S.V., Kryukova, G.N., & Stimming, U. (2005). The influence of carbon support porosity on the activity of PtRu/Sibunit anode catalysts for methanol oxidation. *J. Power Sources*, 145, 178-187.

[15] Wang, Z.B., Yin, G.P., Shi, P.F. (2005). Effects of ozone treatment of carbon support on Pt–Ru/C catalysts performance for direct methanol fuel cell. *Carbon*, 44, 133-140.

[16] Zhou, Z., Wang, S., Zhou, W., Wang, G., Jiang, L., Li, W., Song, S., Liu, J., Sun, G., & Xin, Q. (2003). Novel synthesis of highly active Pt/C cathode electrocatalyst for direct methanol fuel cell. *Chem. Commun.*, 394-395.

[17] Liang, Y., Zhang, H., Yi, B., Zhang, Z., & Tan, Z. (2005). Preparation and characterization of multi-walled carbon nanotubes supported PtRu catalysts for proton exchange membrane fuel cells. *Carbon*, 43, 3144-3152.

[18] Su, J., Wang, G., Deng, H., & Fan, X. (2002). Effect of protonic acids types on the structures and conductivity of polyaniline. *J. Funct. Polym.*, 2, 122-126.

[19] Chandrasekhar P. (1999). *Conducting polymers, fundamentals and applications: a practical approach*. Kluwer Academic Publishers, Boston.

[20] Reddy, A.L.M., Rajalakshmi, N., & Ramaprabhu, S. (2008). Cobalt-polypyrrole-multiwalled carbon nanotube catalysts for hydrogen and alcohol fuel cells. *Carbon*, 46, 2-11.

[21] Liu, Y.C., & Tsai, C.J. (2002). Characterization and enhancement in conductivity and conductivity stability of electropolymerized polypyrrole/Al_2O_3 nanocomposites. *J. Electroanal. Chem.*, 537, 165-171.

[22] Selvaraj, V., Alagar, M., & Kumar, K.S. (2007). Synthesis and characterization of metal nanoparticles- decorated PPY-CNT composite and their electrocatalytic oxidation

Copyright © 2010. Nova Science Publishers, Incorporated. All rights reserved.

Handbook of Material Science Research, Nova Science Publishers, Incorporated, 2010. ProQuest Ebook Central,

of formic acid and formaldehyde for fuel cell applications. *Appl. Catal. B-Environ.*, 75, 129-138.

[23] Shi, J., Guo, D., Wang, Z., & Li, H. (2005). Electrocatalytic oxidation of formic acid on platinum particles dispersed in SWNT-PANI composite film. *J. Solid State Electrochem.*, 9, 634-638.

[24] Wang, Z., Zhu, Z.Z., Shi, J., & Li, H.L. (2007). Electrocatalytic oxidation of formaldehyde on platinum well-dispersed into single-wall carbon nanotube polyaniline composite film. *Appl. Surf. Sci.*, 253, 8811-8817.

[25] Shi, J., Wang, Z., & Li, H. (2007). Electrochemical fabrication of polyaniline/multi-walled carbon nanotube composite films for electrooxidation of methanol. *J. Mater. Sci.*, 42, 539-544.

[26] Joo, J., Lee, J.K., Lee, S.Y., Jang, K.S, Oh, E.J., & Epstein, A.J. (2000). Physical characterization of electrochemically and chemically synthesized polypyrroles. *Macromolecules*, 33, 5131-5136.

[27] Drillet, J.F., Dittmeyer, R., & Jüttner, K. (2007). Activity and long-term stability of PEDOT as Pt catalyst support for the DMFC anode. *J. Appl. Electrochem.*, 37, 1219-1226.

[28] Drillet, J.F., Dittmeyer, R., Jüttner, K., Li, L., & Mangold, K.M. (2006). New composite DMFC anode with PEDOT as a mixed conductor and catalyst support. *Fuel Cells*, 6, 432-438.

[29] Cabri, L.J., & Feather, C.E. (1975). Platinum-iron alloys: a nomenclature based on a study of natural and synthetic alloys. *Can. Mineral.*, *13*, 117-126.

[30] Mitsuru, W., Satoshi, M., Yoshikazu, H., Katsura, K., Hiroyuki, U., & Masahiro, W. (2006). Electronic structures of Pt-Co and Pt-Ru alloys for CO-tolerant anode catalysts in polymer electrolyte fuel cells studied by EC-XPS. *J. Phys. Chem. B*, 110, 23489-23496.

[31] Tian, Y., Li, Z., Xu, H., Wu, Y., & Yang, F. (2008). Effects of different electrolyte solutions on characteristics of Polypyrrole-modified films. *Acta Phys. Chim. Sin.*, 24, 612-617.

[32] Osaka, T., Ouchi, K., & Fukuda, T. (1990). An application of polypyrrole films electropolymerized in NaOH aqueous solution to non-linear MIM devices. *Chem. Lett.*, 19, 1535-1538.

[33] Garfias-García, E., Romero-Romo, M., Ramírez-Silva, M.T., Morales, J., & Palomar-Pardavé, M. (2008). Mechanism and kinetics of the electrochemical formation of polypyrrole under forced convection conditions. *J. Electroanal. Chem.*, 6, 67-69.

Copyright © 2010. Nova Science Publishers, Incorporated. All rights reserved.

Handbook of Material Science Research, Nova Science Publishers, Incorporated, 2010. ProQuest Ebook Central,

In: Handbook of Material Science Research
Editors: C. Rene and E. Turcotte, pp. 473-489
ISBN 978-1-60741-798-9
© 2010 Nova Science Publishers, Inc.

Chapter 15

GRAPH-SKEIN MODULES OF THREE-MANIFOLDS

Nafaa Chbili*
United Arab Emirates University, Al Ain, U.A.E.

Abstract

Our main purpose is to introduce the theory of graph-skein modules of three-manifolds. This theory associates to each oriented three-manifold M an algebraic object (a module or an algebra) which is defined by considering the set of all ribbon graphs embedded in M modulo local linear skein relations. This idea is inspired by Przytycki's theory of skein modules which is also known as algebraic topology based on knots. Historically, this theory appeared as a generalization of the quantum invariants of links in the three-sphere to links in an arbitrary three-manifold. In this paper, we review the construction of the Kauffman bracket skein module and investigate its relationship with our graph-skein modules. We compute the graph-skein algebra in few cases. As an application we introduce new criteria for symmetries of spatial graphs which improve some results obtained earlier. The proof of these criteria is based on some easy calculation in the graph-skein module of the solid torus.

Copyright © 2010. Nova Science Publishers, Incorporated. All rights reserved.

1. Introduction

Throughout this chapter, a graph G is the total space of a finite one-dimensional cell complex. We allow our graphs to have loops and multiple edges. Moreover, the valency of each vertex is assumed to be greater than or equal to three. A spatial graph is the image of an embedding of a graph G into the three-sphere. Spatial graphs are often seen as a natural generalization of the classical knots and links. Thus, the basic problems and methods in knot theory have their counterparts in spatial graph theory. For instance, the study of spatial graphs up to isotopy is equivalent to the study of planar diagrams of graphs modulo a family of moves which generalize the classical Reidemeister moves for links.

*E-mail address: nafaachbili@uaeu.ac.ae

Handbook of Material Science Research, Nova Science Publishers, Incorporated, 2010. ProQuest Ebook Central,

In his seminal paper [14], V. F. Jones introduced a new invariant of links in the three-sphere. This invariant is a Laurent polynomial with integral coefficients which depends only on the isotopy class of the link. The original definition of the Jones polynomial comes from the study of operator algebras. However, the simplest way to define this invariant is via linear skein theory. The Jones polynomial was subsequently generalized to the two-variable HOMFLY polynomial [19] and Kauffman polynomial [15]. These discoveries led immediately to a spectacular progress in low dimensional topology generated by the introduction of quantum invariants of three-manifolds [27, 33].
Another interesting generalization of the newly discovered quantum invariants has been suggested by Przytycki in his project of algebraic topology based on knots.

Przytycki's original motivation was to extend the definition of the quantum link invariants to the general context where we consider links in an arbitrary oriented three-manifold rather than the three-sphere. Let M be an oriented three-manifold, and $\mathcal{R}$ a commutative ring with unit. Let $\mathcal{L}$ be the set of all isotopy classes of all links (there are several different versions, oriented, non oriented, framed ...) in M. A skein module of M with coefficients in $\mathcal{R}$ is the quotient of the free $\mathcal{R}$-module generated by $\mathcal{L}$, divided by properly chosen local skein relations. The Kauffman bracket skein module which corresponds to the skein relations used to define the Kauffman bracket polynomial [15] is so far the most extensively studied object among skein modules. The Kauffman bracket skein module of the solid torus has been used to give a combinatorial definition of the quantum $Su(2)$ invariants of three-manifolds [1], [18].
Inspired by the discovery of the quantum invariants of links in S^3, Yamada [30] introduced a polynomial invariant of spatial graphs which can be defined recursively using skein relations on planar diagrams of spatial graphs. In the spirit of the algebraic topology based on knots, we define a version of skein modules using graphs instead of links. Here is an outline of our construction. Let M be an oriented three-manifold. A *ribbon graph* in M is an oriented surface in M that retracts by deformation on a graph embedded in M. Let $\mathcal{G}$ be the set of all isotopy classes of ribbon graphs in M. Let $\mathcal{R} = [A^{\pm 1}, d^{-1}]$, where $d = -A^2 - A^{-2}$. We define the *graph-skein module* of M with coefficients in $\mathcal{R}$, $\mathcal{Y}(M, \mathcal{R}, A)$ to be the quotient of $\mathcal{RG}$ by the Yamada skein relations depicted in Section 3. Our main goal is to study this new object and explore its relationship with the Kauffman bracket skein module. As an application, we show how to use the graph-skein module of the solid torus to study symmetries of spatial graphs. Namely, we prove criteria for spatial graph periodicity which improve former results obtained in [9].
This paper is outlined as follows. In Section 2, we briefly review some basic results about the Kauffman Bracket skein module. In Section 3, we introduce the graph-skein modules of three-manifolds and compute the algebra structure in few cases. Ultimately, in Section 4 we prove a Theorem which provides obstructions to periodicity of spatial graphs.

2. The Kauffman Bracket skein module

2.1. The Kauffman Bracket polynomial

A knot in the three-sphere is the image of an embedding of a circle S^1 into S^3. A link is a disjoint union of knots which may be linked. As usual, links are considered up to

Copyright © 2010. Nova Science Publishers, Incorporated. All rights reserved.

Handbook of Material Science Research, Nova Science Publishers, Incorporated, 2010. ProQuest Ebook Central,

continuous deformations (isotopies). One of the fundamental results in knot theory shows that the study of links up to isotopy is equivalent to the study of planar diagrams of links up to Reidemeister moves [21]. A framed link in S^3 is the image of an embedding of a finite family of annuli into S^3. Framed links are presented by their projections in the plane with blackboard framing. Two framed links are isotopic if and only if their diagrams are related by a finite sequence of the 3 Reidemeister moves depicted in Figure 1, their inverses and mirror images.

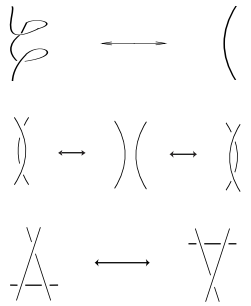


Figure 1

The Kauffman bracket polynomial $\prec, \succ$ is an invariant of framed links in the 3-sphere [15]. This invariant is defined recursively by the following relations:

$$\prec \bigcirc \cup L \succ = d \prec L \succ,$$
$$\prec L \succ = A \prec L_0 \succ + A^{-1} \prec L_\infty \succ,$$

where $d = -A^2 - A^{-2}$, L, L_0 and L_∞ are three links which are identical except in a three-ball where they are like in the following picture.

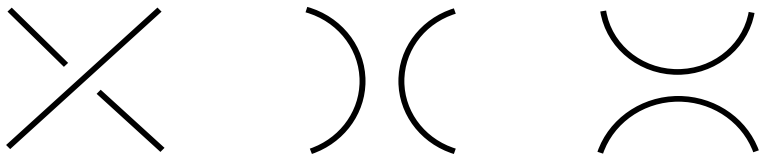


Figure 2

This invariant which is actually a Laurent polynomial in A is known to be related to the Jones polynomial by a simple formula involving the writhe of the link [15]. We shall now introduce the Kauffman bracket skein module of three-manifolds and review some of its fundamental properties.

2.2. Definition and basic properties of the Kauffman Bracket skein module

Let M be an oriented three-manifold. A framed link in M is the image of an embedding of a finite family of annuli into the interior of M. Let $\mathcal{L}$ be the set of all isotopy classes of

Copyright © 2010. Nova Science Publishers, Incorporated. All rights reserved.

Handbook of Material Science Research, Nova Science Publishers, Incorporated, 2010. ProQuest Ebook Central,

framed links in M. Let $\mathcal{R}$=$[A^{\pm 1}, d^{-1}]$, where $d = -A^2 - A^{-2}$. Let $K(M)$ be the free $\mathcal{R}$-module generated by all elements of $\mathcal{L}$. We define the Kauffman bracket skein module of M with coefficients in $\mathcal{R}$, $\mathcal{K}(M, \mathcal{R}, A)$ to be the quotient of $K(M)$ by the smallest submodule containing all expressions of the form:

$$\bigcirc \cup \text{Ł} - dL$$
$$L - AL_0 - A^{-1}L_\infty,$$

where $d = -A^2 - A^{-2}$, L, L_0 and L_∞ are three links which are identical except in a three-ball where they are like in Figure 2. Throughout the rest of this paper and if there is no need for a specific value of A, then we write $\mathcal{K}(M)$ instead of $\mathcal{K}(M, \mathcal{R}, A)$.
It is worth mentioning here that our definition of the Kauffman bracket module is slightly different from the usual definition since we consider the coefficients in $\mathcal{R}$=$[A^{\pm 1}, d^{-1}]$ instead of $[A^{\pm 1}]$. The existence and the uniqueness of the Kauffman bracket polynomial [15] is equivalent to the fact that the Kauffman bracket skein module of § is isomorphic to $\mathcal{R}$ with the empty link $\emptyset$ as a generator. The Kauffman bracket skein module was computed for several three-manifolds. In particular, the case where M is a product of an oriented surface by the unit interval, *i.e.* $M = F_{g,n} \times I$, where $F_{g,n}$ is the oriented surface of genus g with n boundary components and I is the unit interval $[0, 1]$. In this case one may project on the surface and consider diagrams of links on the surface modulo the skein relations. Przytycki [23] proved that the Kauffman bracket skein module of M is generated by all links on $F_{g,n}$ without trivial components but including the empty link. For instance, the skein module of the solid torus $S^1 \times I \times I$ is generated by $\{b^n; n \geq 0\}$ where b^n is the link in the annulus made up of n parallel copies of the boundary component $b = S^1 \times \{0\} \times \{0\}$, see Figure 3.

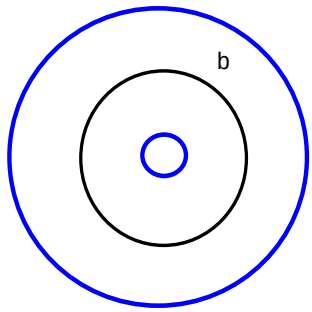


Figure 3

There is an algebra structure on the skein module of $M = F_{g,n} \times I$. The unit of the algebra is the empty link, and if L and L' are two links in M, the product $L.L'$ is obtained by taking a disjoint union of L and L' where L is pushed isotopically into $F_{g,n} \times [1/2, 1]$ and L' is pushed isotopically into $F_{g,n} \times [0, 1/2]$. Since the multiplication depends on the product structure on M, then we will denote the skein algebra of $F_{g,n} \times I$ by $\mathcal{K}(F_{g,n})$.
Bullock [4] proved that the Kauffman Bracket skein algebra of $F_{g,n}$ is finitely generated and gave an upper bound for the minimal number of generators.

Copyright © 2010. Nova Science Publishers, Incorporated. All rights reserved.

Handbook of Material Science Research, Nova Science Publishers, Incorporated, 2010. ProQuest Ebook Central,

Theorem 2.2.1 [4]. *Let F be an oriented surface. Then, the algebra $\mathcal{K}(F)$ is finitely generated and the minimal number of generators is no more than $2^{rankH_1(F)} - 1$.*

In some simple cases $(g, n) \in \{(0, 2), (0, 3), (0, 4), (1, 0), (1, 1)\}$, Bullock and Przytycki [6] succeeded to give nice descriptions of these algebras using generators and relations. In the surface $F_{1,1}$, we consider the curves $x_1 = (1, 0)$, $x_2 = (0, 1)$ and $x_3 = (1, 1)$. For any two curves x and y in $F_{1,1}$, let $[x, y]_A$ denote the deformed commutator $Axy - A^{-1}yx$.

Theorem 2.2.2 [6]. *1) The algebra $\mathcal{K}(F_{0,2})$ is isomorphic to the polynomial algebra $\mathcal{R}[b]$.*
2) The algebra $\mathcal{K}(F_{0,3})$ is isomorphic to the polynomial algebra $\mathcal{R}[x, y, z]$, where x, y and z are the three boundary components.
3) The algebra $\mathcal{K}(F_{1,1})$ is presented as $\mathcal{R} \prec x_1, x_2, x_3 \mid [x_i, x_{i+1}]_A = dx_{i+2} \succ$, where $i = 1, 2, 3$ and subscripts are interpreted modulo three.
4) The algebra $\mathcal{K}(F_{1,0})$ is the quotient of $\mathcal{K}(F_{1,1})$ by the principal ideal $(A^2x_1^2 + A^{-2}x_2^2 + A^2x_3^2 - Ax_1x_2x_3 - 2A^2 - 2A^{-2})$.

The Kauffman bracket skein module has been subject to an extensive literature. In addition to the results mentioned above, Hoste and Przytycki [12] proved that the skein module of the lens space $L(p, q)$ is a free R-module and it has $[p/2] + 1$ generators, where $[p/2]$ denotes the integer part of $p/2$. They also computed the skein module of $S^1 \times S^2$ and showed that this module has torsion [13]. The skein module of the complement of the $(2, k)$-torus knot was computed in [3]. This result was recently generalized by T. Le who computed the skein module for the complements of 2-bridge knots [17]. The connection between the Kauffman bracket skein algebra and the $Sl_2(C)$-character variety has been studied in [5, 26].

3. Graph skein modules

3.1. The Yamada polynomial of spatial graphs

At the beginning of this section, we introduce the invariant of spatial graphs known as the Yamada polynomial [30].

Definition 3.1. *A ribbon graph is an oriented compact surface with boundary that retracts by deformation on a graph.*

A ribbon spatial graph is the image of an embedding of a ribbon graph in the three-sphere. Ribbon spatial graphs are represented by their diagrams in ^{2} with blackboard framing. Here, a diagram is a planar projection with a finite number of multiple points, each of which is the common projection of exactly two non-vertex points where the corresponding edge projection meet transversely, moreover at each such point (called a crossing) the over-crossing and under-crossing arcs are indicated by the standard pictorial convention. Figure 4 below presents a diagram of a ribbon spatial graph obtained by embedding the Peterson graph into S^3.

Copyright © 2010. Nova Science Publishers, Incorporated. All rights reserved.

Handbook of Material Science Research, Nova Science Publishers, Incorporated, 2010. ProQuest Ebook Central,

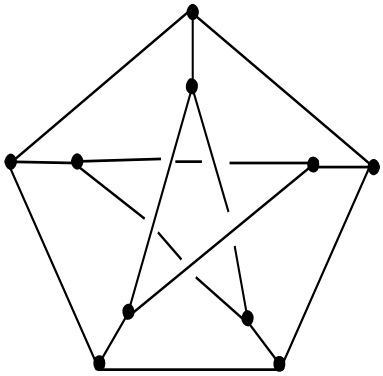


Figure 4

The study of ribbon spatial graphs up to isotopy is equivalent to the study of graph diagrams in ^{2} up to the generalized Reidemeister moves 0, II, III and IV pictured below, see [30].

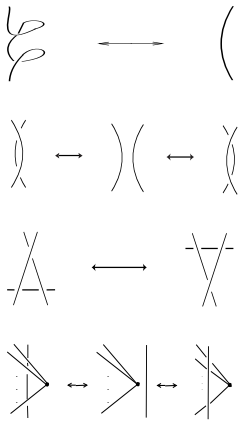


Figure 5

In [30], S. Yamada introduced an invariant R of ribbon spatial graphs. This invariant takes its values in the ring $[A^{\pm 1}]$ and may be defined recursively on diagrams of spatial graphs. A similar invariant of trivalent graphs, with good weight associated with the set of edges, was also introduced by Yamada [31]. This invariant was extended by Yokota [32] using the linear skein theory introduced by Lickorish [18]. For our purposes, we find it more convenient to slightly change the recursive formulas introduced by Yamada. Namely, we define an invariant Y of spatial graphs recursively by the initialization $Y(\emptyset) = 1$ and the four relations in Figure 6. Notice that the vertical dots in our figures mean an arbitrary number of edges. It is also worth mentioning that the following identities hold for diagrams which are identical except in a small disk where they look as indicated below.

Copyright © 2010. Nova Science Publishers, Incorporated. All rights reserved.

Handbook of Material Science Research, Nova Science Publishers, Incorporated, 2010. ProQuest Ebook Central,

In the rest of this chapter, we refer to these relations as the Yamada skein relations.

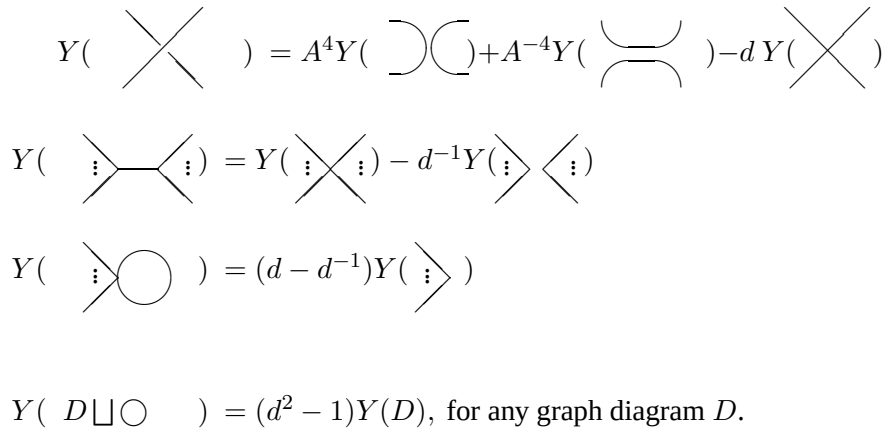


Figure 6

Theorem 3.1.1. *The polynomial $Y \in [A^{\pm 1}, d^{-1}]$ is an invariant of ribbon spatial graphs.*

Proof. Comparing the recursive formulas defining the Yamada polynomial R (see [30], Section 6) with the relations in Figure 6, we can easily see that for any spatial graph $\tilde{G}$ we have:

$$Y(\tilde{G})(A) = (-d)^{\alpha(G)} R(\tilde{G})(A^4),$$

where $\alpha(G)$ is equal to the number of edges of G minus the number of vertices of G. Since R is an invariant of ribbon spatial graphs, then Y is an invariant of ribbon spatial graphs as well.

3.2. The graph-skein module

In spirit of the algebraic topology based on knots defined by Przytycki, our main goal here is to build a kind of algebraic topology based on ribbon graphs. Namely, we would like to extend Przytycki's construction of the Kauffman bracket skein module to a similar theory using ribbon embedded graphs instead of framed links and Yamada skein relations instead of the Kauffman bracket skein relations.

Let M be an oriented three-manifold and let $\mathcal{G}$ be the set of all embeddings of ribbon graphs in M considered up to isotopy. Let $\mathcal{RG}$ be the free $\mathcal{R}$-module generated by $\mathcal{G}$. The graph-skein module of M with coefficients in $\mathcal{R}$, $\mathcal{Y}(M, \mathcal{R}, A)$ is defined to be the quotient of the module $\mathcal{RG}$ by the smallest submodule containing all expressions of the form:

Copyright © 2010. Nova Science Publishers, Incorporated. All rights reserved.

Handbook of Material Science Research, Nova Science Publishers, Incorporated, 2010. ProQuest Ebook Central,

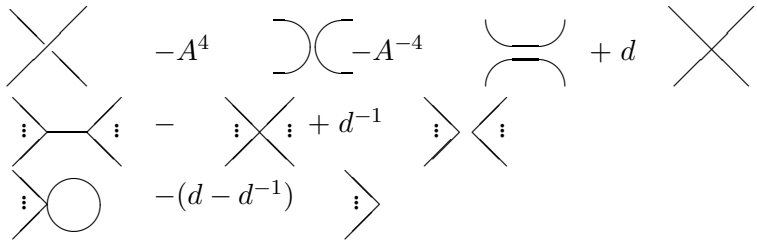


Figure 7

Throughout the rest of the paper and when there is no need to specify the value of A, we write $\mathcal{Y}(M)$ instead of $\mathcal{Y}(M, \mathcal{R}, A)$. The fact that the Yamada polynomial is uniquely determined by the Yamada skein relations [30] translates in the language of graph-skein modules as follows:

Theorem 3.2.1. *The graph skein module $\mathcal{Y}(S^3)$ is isomorphic to $\mathcal{R}$ with the empty graph $\emptyset$ as a generator.*

As an immediate consequence of the definition of the graph-skein modules and the observations in [25], we have the following.

Remark 3.2.2. (Functoriality) Our theory of graph-skein modules defines a functor from category of three-manifolds and orientation preserving embedding (up to isotopy) to the category of $\mathcal{R}$-modules.

Remark 3.2.3.(Universal Coefficient Property) Let $\mathcal{R}'$ be a commutative ring with unit. Let $r : \mathcal{R} \longmapsto \mathcal{R}'$ be a homomorphism of rings. Then the identity map on $\mathcal{G}$ induces an isomorphism between $\mathcal{Y}(M, \mathcal{R}, A) \otimes_{\mathcal{R}} \mathcal{R}$ and $\mathcal{Y}(M, \mathcal{R}', r(A))$. We will need this fact in Section 4.

Remark 3.2.4. (Disjoint union) The graph-skein module of a disjoint union of two three-manifolds $M \sqcup N$ is equal to the tensor product of the graph-skein modules of M and N

$$\mathcal{Y}(M \sqcup N) = \mathcal{Y}(M) \otimes \mathcal{Y}(N).$$

3.3. Computation of $\mathcal{Y}(M)$ and Relationship with $\mathcal{K}(M)$

This section is devoted to study the basic properties of graph-skein modules of three-manifolds. In particular, we show that the module turns to be an algebra in some special cases. We study the algebra structure and explore the relationship between our graph-skein module and the Kauffman bracket skein module.

Let us start by this obvious observation. If M is an oriented three-manifold and A is an eighth root of unity, then one may define an algebra structure on the module $\mathcal{Y}(M, A)$. The unit relative to this product is the empty graph $\emptyset$ and the product of two elements G

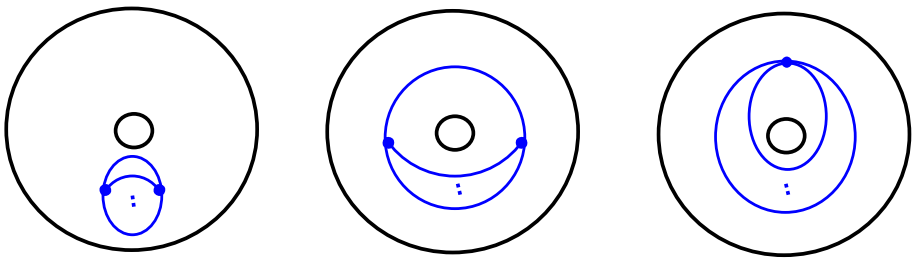
Copyright © 2010. Nova Science Publishers, Incorporated. All rights reserved.

Handbook of Material Science Research, Nova Science Publishers, Incorporated, 2010. ProQuest Ebook Central,

and G' is defined by simply taking the disjoint union $G \bigsqcup G'$. Since $A^4 = A^{-4}$, then the information about the nature of the crossing in the first skein relation is irrelevant. Hence, the algebra $\mathcal{Y}(M, A)$ is commutative.
A more interesting algebra structure is obtained in the case where the manifold is the product of a surface by the unit interval $M = F_{g,n} \times I$ with no restriction on A. Following Bullock [4], we define a multiplication operation in the graph-skein module of M. The unit is the empty graph and the product of two elements G and G' is obtained by taking a disjoint union of G and G' where G is pushed isotopically into $F_{g,n} \times [1/2, 1]$ and G' is pushed isotopically into $F_{g,n} \times [0, 1/2]$. We will denote this algebra by $\mathcal{Y}(F_{g,n})$.

Theorem 3.3.1. *The skein algebra $\mathcal{Y}(F_{0,2})$ is isomorphic to the polynomial algebra $\mathcal{R}[b]$, where b is pictured in Figure 3.*

Proof. In the annulus $F_{0,2} = S^1 \times I$, we denote by $b_n, n \geq 1$ the bouquet which is made up of n non-trivial loops. Notice here that b_1 is nothing other than the generator b of the Kauffman bracket skein algebra of the annulus. Let $S_n, n \geq 1$ be the graph with 2 vertices and $n + 1$ edges as in Figure 8. Finally, let $\theta_n, n \geq 2$ be the graph consisting of two vertices and n-edges, pictured in Figure 8. We can see easily that θ_2 is a trivial circle and that θ_3 is the usual θ-curve.



θ_n S_n b_n

Figure 8

Lemma 3.3.2. *We have the following identities in the graph-skein module $\mathcal{Y}(S^1 \times I \times I)$:*

$$(i) \quad \theta_n = -d^{-1}\theta_{n-1} + (\frac{d^2-1}{d})^{n-2}(d^2-1)\emptyset.$$
$$(ii) \quad S_n = -d^{-1}S_{n-1} + (\frac{(d^2-1)}{d})^{n-2}b.$$
$$(iii) \quad b_n = S_n + d^{-1}\theta_n.$$

Proof. The arguments for proving the three identities in the lemma are similar. We will only explain how to prove the identity (i) and let the two others to the reader. If we write the second Yamada relation relative to deletion-contraction of the upper edge in the graph θ_n in Figure 8, then we get $\theta_n = r_{n-1} - d^{-1}\theta_{n-1}$, where r_n is a bouquet made up of $n-1$ leaves. By the third Yamada relation we have $r_{n-1} = (d - d^{-1})^{n-2}(d^2-1)\emptyset$. This ends

Copyright © 2010. Nova Science Publishers, Incorporated. All rights reserved.

Handbook of Material Science Research, Nova Science Publishers, Incorporated, 2010. ProQuest Ebook Central,

the proof of the first part of Lemma 3.3.2.

Now we return to the proof of Theorem 3.3.1. Let D be a graph diagram in $F_{0,2}$. It is easy to see that one can use the first Yamada skein relation to transform D onto a linear combination of diagrams with no crossings. By using the second Yamada relation (deletion-contraction), it is possible to transform each of those diagrams onto a linear combination of diagrams such that each connected component has only one vertex. Finally, by applying the third and the fourth Yamada relations to those components, the diagram D may be written as a linear combination of disjoint unions of bouquets with no contractible cycles. This means that the set of all disjoint unions of bouquets with no contractible cycles generates the Yamada skein module of the solid torus $F_{0,2} \times I$.
Now, according to (i) and (ii) of Lemma 3.3.2, each of θ_n and S_n may be written as a linear combination of b and $\emptyset$. Since the bouquet with no contractible cycles b_n is equal to $S_n + d^{-1}\theta_n$. Then b_n can be expressed as a linear combination of b and $\emptyset$. Thus, we conclude that the Yamada skein module of the solid torus is generated by all links in the annulus $F_{0,2}$, without trivial components but including the empty diagram. Since each of these links is actually a product of finite number of nontrivial circles parallel to b. Then, the skein algebra of the solid torus is isomorphic to the polynomial algebra $\mathcal{R}[b]$. This ends the proof of Theorem 3.3.1.

Before we give another example of computation, we will try to establish some relationship between our graph module and the Kauffman bracket skein module. We start by introducing the Jones-Wenzel idempotents [16]. Let n be an integer, an n-tangle T is a one-dimensional sub-manifold of $^2 \times I$, such that the boundary of T is made up of $2n$ points $\{(0, i, 1), (0, i, 0)\ 0 \leq i \leq n-1\}$. Let $\mathcal{T}_n$ be the free $\mathcal{R}$-module generated by the set of all n-tangles. We define τ_n to be the quotient of $\mathcal{T}_n$ by the Kauffman bracket skein relations. It is well known that τ_n is isomorphic to the Temperley-Lieb algebra. A set of generators $(U_i)_{0\leq i\leq n-1}$ of τ_n is given as follows.

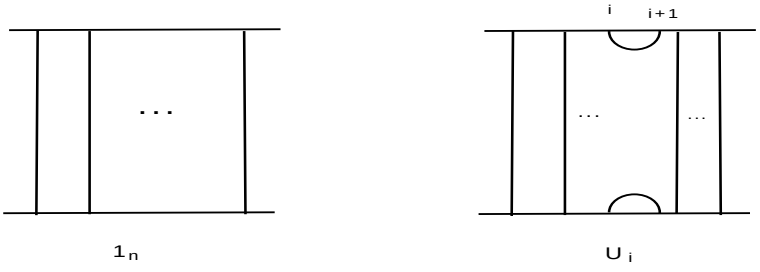


Figure 9

Let $(f_i)_{0\leq i\leq n-1}$ denote the family of Jones-Wenzl projectors in τ_n. This family is defined by the following recursive formulas:
$f_0 = 1_n$,
$f_{k+1} = f_k - \mu_{k+1} f_k U_{k-1} f_k$,
where $\mu_1 = d^{-1}$ and $\mu_{k+1} = (d - \mu_k)^{-1}$.

Copyright © 2010. Nova Science Publishers, Incorporated. All rights reserved.

Handbook of Material Science Research, Nova Science Publishers, Incorporated, 2010. ProQuest Ebook Central,

In particular, we have f_1=$1_n - d^{-1}U_1$. The elements f_k enjoy the following properties: $f_k^2 = f_k$ and $f_iU_j = U_jf_i = 0$ for $j \leq i$. See [16] for more details.

Let G be a graph diagram lying in a given oriented surface. Let f_1 be the Jones-Wenzl projector in τ_2

$$f_1 = \left|\left| - d^{-1} \right.\right.$$

We define G' to be the linear combination of graph diagrams obtained from G by replacing each edge of G by two planar strands with a projector f_1 in the cable, and by replacing each vertex of G by a diagram as follows

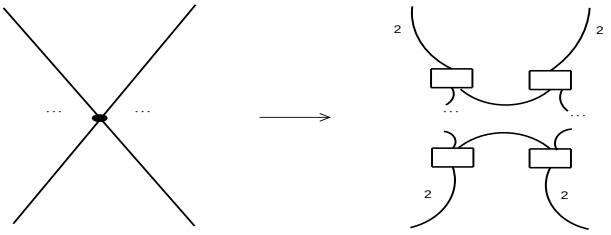
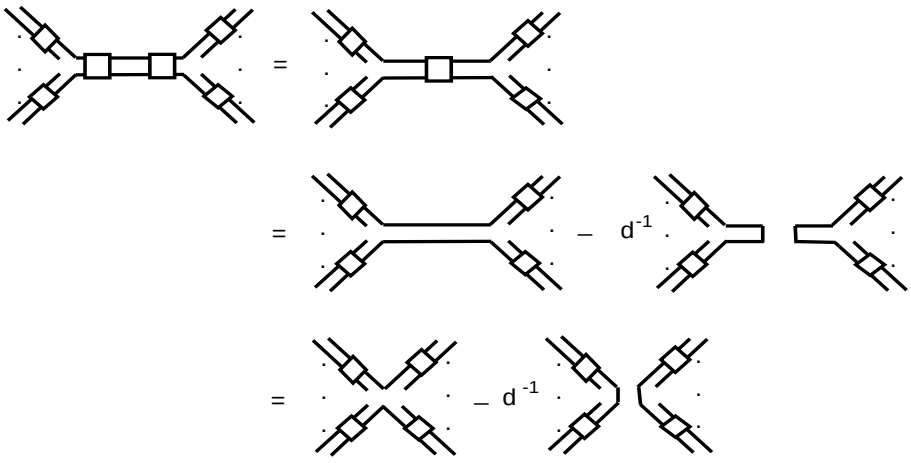


Figure 10

Here, writing an integer n beneath an edge e means that this edge has to be replaced by n parallel ones.
Now, let φ be the map from $\mathcal{R}(\mathcal{G})$ to $\mathcal{K}(F)$ defined on the generators by $\varphi(G) = G'$ and extended by linearity to $\mathcal{R}(\mathcal{G})$, see also [31] and [32].

Lemma 3.3.3. *Let $\mathcal{Q}$ be the sub-module generated by the Yamada skein relations in Figure 7, then $\varphi(\mathcal{Q}) = 0$.*

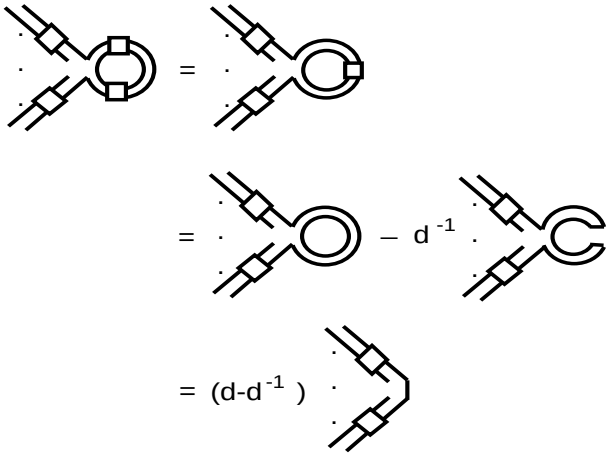
Proof. Arguments needed to prove the first skein relation can be found in [16], page 35. Using the definition of f_1 and the fact that $f_1^2 = f_1$, we should be able to prove the result for the other Yamada relations. This is explained by the calculations below:
the second Yamada relation



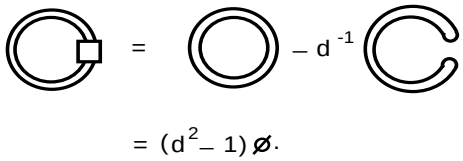
Copyright © 2010. Nova Science Publishers, Incorporated. All rights reserved.

Handbook of Material Science Research, Nova Science Publishers, Incorporated, 2010. ProQuest Ebook Central,

the third Yamada relation



the fourth Yamada relation



Since for every ribbon graph D we have $\varphi(D \cup \bigcirc) = \varphi(D)\,\varphi(\bigcirc)$, then the identity above implies that $\varphi(D \cup \bigcirc - (d^2-1)D) = 0$. This ends the proof of Lemma 3.3.3.

By Lemma 3.3.3, φ defines a map from the graph-skein module $\mathcal{Y}(F \times I)$ to the Kauffman bracket skein module $\mathcal{K}(F \times I)$, we will denote this map by Φ. Obviously, Φ is a homomorphism of algebras.

Example 3.3.4. We have seen that both $\mathcal{K}(F_{0,2})$ and $\mathcal{Y}(F_{0,2})$ are isomorphic to the polynomial algebra $\mathcal{R}[b]$. We can easily see from the calculation above that $\Phi(b) = b^2 - 1$. Thus, Φ is injective. Moreover, it defines an isomorphism between the graph algebra $\mathcal{Y}(F_{0,2})$ and the even part of the Kauffman bracket skein algebra $\mathcal{K}(F_{0,2})$.

Theorem 3.3.5. *The graph-skein algebra $\mathcal{Y}(F_{0,3})$ is isomorphic to the quotient of the polynomial algebra $\mathcal{R}[x,y,z,t]$ by the ideal generated by*

$$\begin{aligned} t^2 - \;& 1 + d^{-2} - 2d^{-1} + (1-2d^{-1})x + (1-2d^{-1})y + z - 2d^{-1}t \\ & + (1-2d^{-2})xy + xz + zy - 2d^{-1}tx - 2d^{-1}ty - d^{-2}x^2 - d^{-2}y^2 + xyz, \end{aligned}$$

where x, y, z and t are as in the following picture.

Copyright © 2010. Nova Science Publishers, Incorporated. All rights reserved.

Handbook of Material Science Research, Nova Science Publishers, Incorporated, 2010. ProQuest Ebook Central,

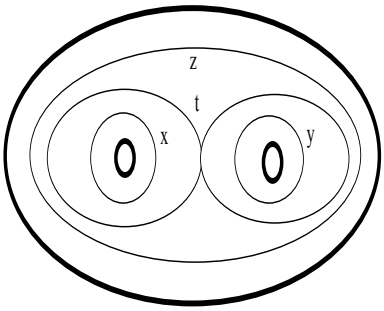


Figure 11

Proof. By the reduction arguments used in the case of the annulus, we can prove that any graph diagram in $F_{0,3}$ can be written as a linear combination of finite disjoint unions of bouquets each of which has no contractible cycles. Arguments similar to the ones used in Lemma 3.3.2 would enable us to prove that the graph-skein module of $F_{0,3} \times I$ is generated by elements of type $x^i y^j z^k t^\epsilon$, where i, j and k are nonnegative integers, and $\epsilon = 0$ or 1.

To prove that the algebra is exactly as depicted in Theorem 3.3.5, we use the fact that the homomorphism Φ is injective. The injectivity of Φ is due to the following identities: $\Phi(x) = x^2 - 1$, $\Phi(y) = y^2 - 1$, $\Phi(z) = z^2 - 1$ and $\Phi(t) = xyz - d^{-1}x^2 - d^{-1}y^2 + d^{-1}$. Let $\mathcal{E} =< x^2, y^2, z^2, xyz >$ be the even part of the algebra $\mathcal{K}(F_{0,3})$. Then, Φ defines an isomorphism between $\mathcal{Y}(F_{0,3})$ and $\mathcal{E}$. The inverse isomorphism Ψ is defined as follows: $\Psi(x^2) = x + 1$, $\Psi(y^2) = y + 1$, $\Psi(z^2) = z + 1$ and $\Psi(xyz) = t + d^{-1}x + d^{-1}y + d^{-1}$.

Using the relations above we can see that:

$$xyz = \Phi(t + d^{-1}x + d^{-1}y + d^{-1}).$$

Hence:
$\Phi(t^2) = \Phi(t)^2 = \Phi((x+1)(y+1)(z+1) + d^{-2}(x+1)^2 + d^{-2}(y+1)^2 + d^{-2}$
$-2d^{-1}(t + d^{-1}x + d^{-1}y + 1)(x + y + 1) + 2d^{-1}(x+1)(y+1) - 2d^{-2}(x + y + 2))$.
Since Φ is injective, then

$$\begin{aligned} t^2 = \;& 1 + d^{-2} - 2d^{-1} + (1 - 2d^{-1})x + (1 - 2d^{-1})y + z - 2d^{-1}t \\ & + (1 - 2d^{-2})xy + xz + zy - 2d^{-1}tx - 2d^{-1}ty - d^{-2}x^2 - d^{-2}y^2 + xyz. \end{aligned}$$

This ends the proof of Theorem 3.3.5.

In a joint work, T. Fleming and the author [10] studied the graph-skein algebras of the torus $F_{1,0}$ and the punctured torus $F_{1,1}$. They determined a set of generators for each of these algebras. It was showed that the graph-skein algebra $\mathcal{Y}(F_{1,0})$ is generated by the 3 torus curves $(1,0), (0,1), (1,1)$ and the graph made up by the wedge $(1,0) \vee (0,1)$. A similar statement was proved for the punctured torus.

4. Application to symmetries of spatial graphs

Let $p \geq 2$ be an integer, G a ribbon graph and $\tilde{G}$ a spatial embedding of G in the three-sphere. The ribbon spatial graph $\tilde{G}$ is said to be *p-periodic* if and only if there exists

Copyright © 2010. Nova Science Publishers, Incorporated. All rights reserved.

Handbook of Material Science Research, Nova Science Publishers, Incorporated, 2010. ProQuest Ebook Central,

an orientation preserving auto-homeomorphism h, of $(\S, \tilde{G})$ such that h is of order p and the set of fixed points of h is an unknotted circle Δ which does not intersect $\tilde{G}$. By the positive solution of the Smith conjecture [2], we know that h is topologically conjugate to an orthogonal action (rotation). If $\tilde{G}$ is a periodic ribbon spatial graph, then we denote by $\underline{\tilde{G}}$ its quotient. It is well known that $\underline{\tilde{G}}$ is a spatial ribbon graph as well since the quotient of S^3 by the orthogonal action defined by h is S^3. Marui [20], used the Yamada polynomial to study the periodicity of spatial graphs with winding number 1 or 2. In [9], we used the criteria of link periodicity introduced by Murasugi [22], Przytyki [24] and Traczyk [28] to obtain a generalization of Marui's result.

Theorem 4.1 [9]. *Let p be a prime and $\tilde{G}$ a ribbon spatial graph. If $\tilde{G}$ is $p-$periodic, then*

(1) $Y(\tilde{G})(A) \equiv (Y(\underline{\tilde{G}})(A))^p$ modulo $p, d^p - d$.

(2) $Y(\tilde{G})(A) \equiv Y(\tilde{G})(A^{-1})$ modulo $p, A^{2p} - 1$.

Where the congruences hold in the ring $[A^{\pm 1}, d^{-1}]$.

It is worth mentioning that the symmetry we consider here is an extrinsic property of the embedding of the graph and not an intrinsic property of the graph itself. However, it is clear that from the symmetries of the graph G itself we get some restrictions on the possible periods for the spatial embedding. E. Flapan [11], studied the relationship between intrinsic and extrinsic properties of graphs and proved that not every automorphism of a graph can be realized by a homeomorphism of $\S$ for some embedding of the graph.
The proof of Theorem 4.1 is based on Murasugi's and Traczyk's criteria for the Kauffman polynomial of periodic links. By considering the graph-skein module of the solid torus we could improve this theorem by establishing similar congruences involving smaller ideals. The congruence relations given by the following theorem hold in the ring $[A^{\pm 1}, d^{-1}]$.

Theorem 4.2. *Let p be a prime and $\tilde{G}$ a ribbon spatial graph. If $\tilde{G}$ is $p-$periodic, then :*

(a) $Y(\tilde{G})(A) \equiv (Y(\underline{\tilde{G}})(A))^p$ modulo $p, d^{2p} - d^2$.

(b) $Y(\tilde{G})(A) \equiv Y(\tilde{G})(A^{-1})$ modulo $p, A^{8p} - 1$.

Proof. We will start by proving the first congruence relation. The idea is to change the coefficients in the skein relations of Yamada in order to define a kind of equivariant graph skein module. We already know that this idea works very well for the study of symmetries of links [7, 8]. Let $\mathcal{R}_p = /p[A^{\pm 1}, d^{-1}]$ and $\mathcal{S}_p$ the free $\mathcal{R}_p$-module generated by all isotopy classes of ribbon graphs embedded in the solid torus. Now, let $\mathcal{Q}_p$ be the submodule of $\mathcal{S}_p$ generated by all elements of the form:

Copyright © 2010. Nova Science Publishers, Incorporated. All rights reserved.

Handbook of Material Science Research, Nova Science Publishers, Incorporated, 2010. ProQuest Ebook Central,

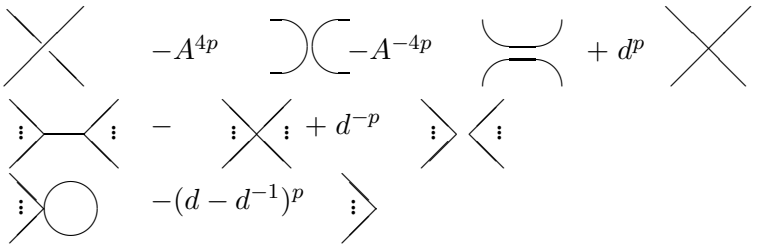


Figure 12

We define $\mathcal{Y}_p$ to be the quotient of $\mathcal{S}_p$ by the submodule $\mathcal{Q}_p$. By the universal coefficient property (Remark 3.3.3), the module $\mathcal{Y}_p$ is isomorphic to $\mathcal{R}_p[b]$. Let $\pi : S^1 \times D^2 \longrightarrow S^1 \times D^2$ denote the p-fold cyclic cover defined by the action of the rotation h on the solid torus. Let F (resp. F') be the map from $\mathcal{S}_p$ to $\mathcal{R}_p$ defined on the set of generators of $\mathcal{S}_p$ by $F(g) = Y(\pi^{-1}(g))$ (resp. $F'(g) = (Y(g))^p$) and extended to $\mathcal{S}_p$ by linearity. Using the fact that p is a prime and that the finite cyclic group of order p acts semi-freely on the set of states of the Yamada resolution of the diagram of the periodic spatial graph $\tilde{G} = \pi^{-1}(g)$, we should be able to easily prove the following lemma (see also Lemma 3.4 in [24]).

Lemma 4.3. $F(\mathcal{Q}_p) = F'(\mathcal{Q}_p) = 0$.

According to this lemma, F (resp. F') defines a map from the skein module $\mathcal{Y}_p$ to $\mathcal{R}_p$. We will denote this map by $\bar{F}$ (resp. $\bar{F}'$).

The module $\mathcal{Y}_p$ is generated by $\{b^k, k \geq 0\}$. Let I be the submodule generated by $\{\bar{F}(b^k) - \bar{F}'(b^k), k \geq 0\}$. Simple computations show that I is equal to the ideal generated by $(d^2 - 1)^p - (d^2 - 1)$. Consequently:

$$\bar{F}(g) = \bar{F}'(g)(d^2 - 1)^p - (d^2 - 1).$$

This ends the proof of the first congruence of Theorem 4.2.

It remains to prove the second congruence in Theorem 4.2. Let $Y!$ be the map defined for every spatial graph $\tilde{G}$ by $Y!(\tilde{G})(A) = Y(\tilde{G}!)(A)$, where $\tilde{G}!$ is the mirror image of $\tilde{G}$. Since $Y(\tilde{G}!)(A) = Y(\tilde{G})(A^{-1})$, then both of the polynomials Y and $Y!$ satisfy the following relations modulo p,

$$Y(\tilde{G}_+)(A) \equiv A^{4p} Y(\tilde{G}_0)(A) + A^{-4p} Y(\tilde{G}_\infty)(A) - d^p Y(\tilde{G}_\times),$$

and

$$Y!(\tilde{G}_+)(A) \equiv A^{-4p} Y!(\tilde{G}_0)(A) + A^{4p} Y!(\tilde{G}_\infty)(A) - d^p Y!(\tilde{G}_\times)(A),$$

where $\tilde{G}_+$, $\tilde{G}_0$, $\tilde{G}_\infty$ and $\tilde{G}_\times$ are respectively the four graph diagrams in the first Yamada skein relation.

It is obvious that if $A^{4p} = A^{-4p}$ then Y and $Y!$ are defined using the same skein relations. Hence, $Y \equiv Y!$ modulo $p, A^{8p} - 1$. This ends the proof of the second part of Theorem 4.2.

Copyright © 2010. Nova Science Publishers, Incorporated. All rights reserved.

Handbook of Material Science Research, Nova Science Publishers, Incorporated, 2010. ProQuest Ebook Central,

References

[1] C. Blanchet, N. Habegger, G. Masbaum and P. Vogel. *Three-Manifold invariants derived from the Kauffman bracket*. Topology, 31 (1992), 685-699.

[2] H. Bass and J. W. Morgan. *The Smith conjecture*. Pure and App. Math. 112, New York Academic Press (1994).

[3] D. Bullock. *The $(2,\infty)$-skein module of the complement of a $(2,2p+1)$-torus knot*, Journal of Knot theory, 4 (1995), pp. 619-632.

[4] D. Bullock. *A finite set of generators for the Kauffman bracket skein algebra* . Math. Z. 231, (1999), pp. 91-101.

[5] D. Bullock. *Rings of $Sl_2(C)$-characters and the Kauffman bracket skein module,* Comm. Math. Helv. 72 (1997), 521-542.

[6] D. Bullock and J. H. Przytycki, *Multiplicative structure of Kauffman bracket skein module quantizations.* Proc. Amer. Math. Soc. 128 (2000), no. 3, 923–931.

[7] N. Chbili. *Les invariants θ_p des 3-variétés périodiques,* Annales de l'Institut Fourier, Fascicule 4 (2001), pp. 1135-1150.

[8] N. Chbili. *The quantum $Su(3)$ invariant of links and Murasugi's congruence,* Topology and its Applications, Volume 122/3 (2002), pp. 479-485.

[9] N. Chbili. *Skein algebras of the solid torus and symmetric spatial graphs* . Fund. Math. 190, (2006), pp. 1-10.

[10] N. Chbili and T. Fleming. *The graph-skein algebras of the torus* . In preparation.

[11] E. Flapan. *Rigidity of graph symmetries in the 3-sphere* , J. Knot Theory Ramif. Vol 4, No 3 (1995) pp. 373-388

[12] J. Hoste and J. H. Przytycki. *The $(2,\infty)$-skein module of lens spaces; a generalization of the Jones polynomial* , Journal of Knot Theory and Its Ramifications, 2(3), 1993, pp. 321-333.

[13] J. Hoste and J. H. Przytycki. *The Kauffman bracket skein module of $S^1 \times S^2$*, Math. Z., 220(1), (1995), 63-73.

[14] V. F. R. Jones. *A polynomial invariant for knots via von Neumann algebras,* Bull. Amer. Math. Soc. 12 (2005) pp. 103112.

[15] L. Kauffman. *An invariant of regular isotopy.* Trans. Amer. Math. Soc. 318 (1990), no. 2, pp. 417471.

[16] L. H. Kauffman and S. L Lins. *Temperley-Lieb recoupling theory and invariants of 3-manifolds*. Ann. Math. Studies. 134, Princeton Univercity Press (1994).

Copyright © 2010. Nova Science Publishers, Incorporated. All rights reserved.

Handbook of Material Science Research, Nova Science Publishers, Incorporated, 2010. ProQuest Ebook Central,

[17] T. T. Q. Le *The Colored Jones Polynomial and the A-Polynomial of Two-Bridge Knots* , Advances Math. 207 (2006) pp. 782-804.

[18] W. B. R. Lickorish. *The skein method for 3-manifold invariants* . J. Knot Th. Ram. 2 (1993), 171-194.

[19] W.B.R. Lickorish, K. C. Millet. *A polynomial invariant of oriented links* . Topology, vol. 26 (1987), pp. 107-141.

[20] Y. Marui. *The Yamada polynomial of spatial graphs with* $_n$*-symmetry*. Kobe J. Math, 18 (2001) pp. 23-49.

[21] K. Murasugi. *Knot Theory and its applications* Birkauser 1996.

[22] K. Murasugi. *The Jones polynomials of periodic links* . Pacific J. Math. 131 (1988) pp. 319-329.

[23] J. H. Przytycki. *Skein modules of 3-manifolds* , Bull. Pol. Acad. Sci.: Math., 39, 1-2 (1991) pp. 91-100.

[24] J. H. Przytycki. *On Murasugi's and Traczyk's criteria for periodic links* . Math. Ann., 283 (1989), pp. 465-478.

[25] J. H. Przytycki. *Fundamentals of Kauffman bracket skein modules* . Kobe Math. J., 16(1), (1999), 45-66.

[26] J. H. Przytycki and A. Sikora. *Skein Algebras and* $Sl_2(C)$*-Character Varieties* . Topology, 39 (1) (2000), 115–148.

[27] N. YU. Reshitikhin and V. Turaev. *Invariants of 3-manifolds via link polynomials and quantum groups.* Invent. Math. 103, (1991), 547-597.

[28] P. Traczyk. 10_{101} *has no period 7: A criterion for periodicity of links* . Proc. Amer. Math. Soc. 108 (1990), pp. 845-846.

[29] V. G. Turaev. *The Conway and Kauffman modules of the solid torus* , Zap. Nauchn. Sem. Lomi. 167 (1988),79-89. English translation: J. Soviet Math.

[30] S. Yamada. *An invariant of spatial graphs.* J. Graph theory, 13 (1989) pp. 537-551.

[31] S. Yamada *A topological invariant of spatial regular graphs.* Proceeding of Knots 90, De Gruyter 1992, pp. 447-454.

[32] Y. Yokota *Topological invariants of graphs in 3-space.* Topology, Vol. 35, (1996), pp. 77-87.

[33] E. Witten. *Quantum field theory and the Jones polynomial* . Comm. Math. Phys. 121 (1989), 351-399.

Copyright © 2010. Nova Science Publishers, Incorporated. All rights reserved.

Handbook of Material Science Research, Nova Science Publishers, Incorporated, 2010. ProQuest Ebook Central,

Copyright © 2010. Nova Science Publishers, Incorporated. All rights reserved.

Handbook of Material Science Research, Nova Science Publishers, Incorporated, 2010. ProQuest Ebook Central,

In: Handbook of Material Science Research
Editor: C. Rene and E. Turcotte, pp. 491-516
ISBN 978-1-60741-798-9
© 2010 Nova Science Publishers, Inc.

Chapter 16

EVALUATION OF METAL FATIGUE CHARACTERISTICS CONSIDERING THE EFFECT OF DEFECTS

Tatsujiro Miyazaki and Hiroshi Noguchi
Faculty of Engineering, University of Ryukyus,
Okinawa, Japan and others

Abstract

When the fatigue strength is evaluated for machine designs, fatigue evaluation methods and fatigue data which match physical phenomena and the design conditions need to be chosen properly. Generally, fatigue tests are performed under stress controlled conditions and controlled conditions. Because the load condition is closely associated with crack closure phenomena, the differences of the load conditions cause the differences of the crack propagation and non-propagation behavior. Then, the fatigue crack is divided into a small and long one depending on a plastic zone size at a crack tip. The propagation and non-propagation characteristics of the small crack are different from those of the long one. Therefore, it should be noted that the fatigue data under the stress controlled conditions are different from those under the controlled conditions, and the propagation and non-propagation characteristics of the small crack are different from those of the long one. The authors proposed the evaluation methods for the fatigue strength of specimens with the various dimensional cracks and notches and applied the methods to the predictions of the fatigue life reliability and the fatigue limit reliability of the inhomogeneous materials. In this paper, it is mentioned that the propagation and non-propagation characteristics of the fatigue crack depends on the relative plastic zone size and the load conditions, and the simple forms which are obtained by formulating these characteristics under a constant stress controlled condition are introduced. Then, their applications to predictions of fatigue life reliability and fatigue strength reliability at $N = 10^7$ of aluminum cast alloy JIS AC4B-T6 which contains various stress concentration parts are roughly introduced.

Copyright © 2010. Nova Science Publishers, Incorporated. All rights reserved.

Handbook of Material Science Research, Nova Science Publishers, Incorporated, 2010. ProQuest Ebook Central,

1. Introduction

In actual machines and structures, there are various stress concentration parts: structural notch and hole, non-metallic inclusion and porosity, defect and so on. Because the stress concentrations degrade the fatigue strength, it is important for a reasonable fatigue design to evaluate them. The physical phenomena of the fatigue crack initiation, propagation and non-propagation are closely associated with sharpness and a size of the stress concentration part in addition to a maximum stress. For example, if the stress concentration part is a blunt notch, the microscopical non-propagating crack limit appears as the fatigue limit [1, 2]. On the other hand, if the part is a sharp notch, the macroscopic non-propagating crack limit appears as the fatigue limit [1, 2]. Therefore, when the fatigue strength is evaluated, the methods and the fatigue data which match the physical phenomena and the design conditions need to be chosen properly.

Generally, the fatigue tests are often performed under stress controlled conditions and controlled conditions. Because the load condition is closely associated with crack closure phenomena, the differences of the load conditions cause the differences of the crack propagation and non-propagation behavior. Then, the fatigue crack is divided into a small and long one depending on a plastic zone size at a crack tip. When the plastic zone size is small against the crack length relatively, the crack is satisfied with the small scale yielding and treated as the long one; when the crack is satisfied with the large scale yielding, it is treated as the small one. Because the propagation and non-propagation characteristics of the small crack are different from those of the long one, the small crack can not be evaluated by the fatigue data of the long crack. Therefore, when the fatigue data are used for the design, it should be also noted that the fatigue data under the stress controlled conditions are different from those under the controlled conditions even if the cracks are similar [3]. Moreover, it is necessary to distinguish the small crack and the long crack [4, 5, 6].

In this paper, it is mentioned that the propagation and non-propagation characteristics of the fatigue crack depends on the relative plastic zone size and the load conditions and it is important for an evaluation of a fatigue strength to grasp these characteristics of both the small and long cracks. Then, the prediction methods for the crack propagation law and the crack non-propagation limit under a constant stress controlled condition are explained. And then, examples of predictions of fatigue life reliability and fatigue strength reliability at $N = 10^7$ of aluminum cast alloy JIS AC4B-T6 which contains various stress concentration parts are roughly introduced.

2. Fatigue Characteristics

2.1. Macro-fatigue Characteristics

A fatigue life consists of a fatigue crack initiation life and a fatigue crack propagation life. The former is the number of stress repetitions to the fatigue crack initiation; the latter is the number of the stress repetitions from the fatigue crack initiation to the fatigue fracture. The fatigue crack initiation life is a few percentages of the fatigue life even if there are no stress concentrations structurally [5]. A large part of the fatigue life is occupied by the fatigue

Copyright © 2010. Nova Science Publishers, Incorporated. All rights reserved.

Handbook of Material Science Research, Nova Science Publishers, Incorporated, 2010. ProQuest Ebook Central,

crack propagation life [5].

When the fatigue life is given as a design condition, a fatigue strength at the fatigue life N_f is used in the design. The fatigue strength at the N_f is stress amplitude at which the fatigue fracture does not occur during the N_f although the fatigue crack propagates. On the other hand, when a specified design life is long remarkably, a fatigue limit is used. The fatigue limit is critical stress amplitude which determines whether or not a fatigue fracture does not occur. When the stress amplitude is smaller than the fatigue limit, the fatigue fracture does not occur. From the viewpoint of physical phenomenon, the fatigue crack at the fatigue limit is in a state of an arrest.

2.2. Macro-fatigue Characteristics and Fatigue Crack Propagation Characteristics

The S-N curve is often used for the design as the macro-fatigue characteristics, and is obtained by the fatigue experiments of the plain and notched specimens under the stress controlled conditions. On the other hand, the da/dN- curve is often used for the maintenance as the fatigue crack propagation characteristics, and is obtained by the fatigue experiments of the CT specimens under controlled conditions. It seems that both curves each show separate fatigue characteristics apparently. However, as mentioned in Section 2.1, the fatigue life of the plain specimen is the propagation life of the microscopical fatigue crack; the fatigue limit of the plain specimen is the non-propagation limit of the microscopical fatigue crack [3, 6]. Therefore, these fatigue characteristics can be unified from the viewpoint of the propagation and non-propagation behavior of the fatigue crack.

2.3. Fatigue Characteristics of Small Defects

Generally, the fatigue experiments of the plain and notched specimens under the stress controlled and CT specimens under the controlled condition often have been performed. In the practical machines and structures, there are various small stress concentration parts: non-metallic inclusion, porosity, surface roughness and so on. When the fatigue strength is assumed to be the weakest link model, it is determined by the competition of propagation and non-propagation behavior of the various fatigue cracks [7, 8, 9]. When there are small stress concentration parts, a matrix can not be assumed to be homogeneous and continuum. Then, for all defects, propagation and non-propagation behavior of the fatigue cracks need to be examined in the viewpoint of the fracture mechanics, in which case the small cracks have to be distinguished from the long ones [4, 5, 6]. Therefore, the fatigue experimental data in earlier studies are not enough for the reasonable fatigue design. It is essential for the practical design to investigate the fatigue characteristics of the specimen with the small artificial defects.

3. Fatigue Crack Propagation Characteristics

The behavior of the fatigue crack propagation is strongly influenced by such crack closures as plasticity induced crack closure [10], oxide induced crack closure [11, 12], roughness induced crack closure [13]. In this section, the characteristics of the fast and stable crack propagations which are governed by the plasticity induced crack closure are mentioned.

Copyright © 2010. Nova Science Publishers, Incorporated. All rights reserved.

Handbook of Material Science Research, Nova Science Publishers, Incorporated, 2010. ProQuest Ebook Central,

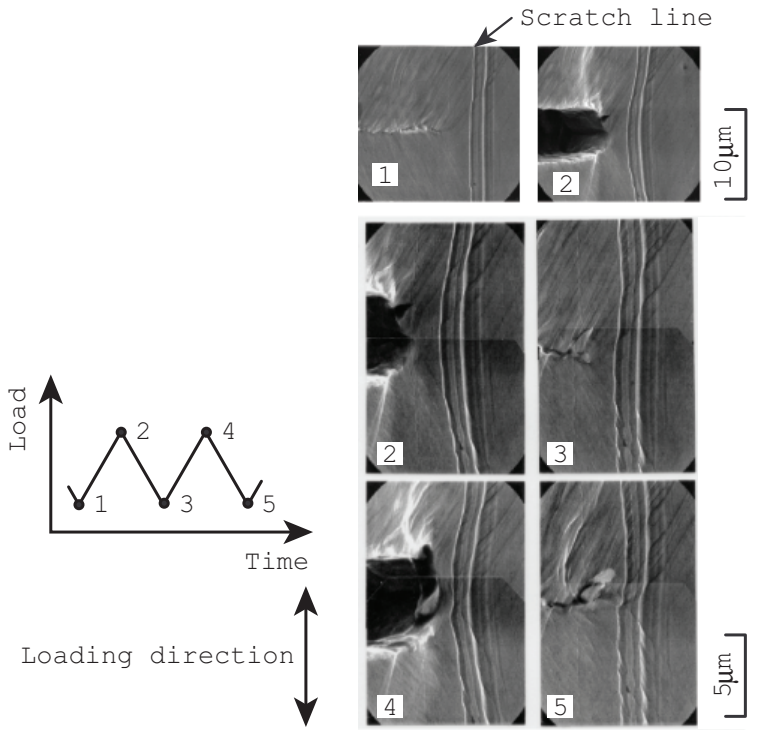


Figure 1. SEM photographs showing the behavior of slip near a crack tip.

3.1. Mechanism of Fatigue Crack Propagation

At a crack tip of which a mode I fatigue crack propagates fast and stably, a plastic blunting and resharpening are continued alternatively. Figure 1 shows SEM photographs of the behavior of slip near a crack tip [14]. Slip steps are detected as scratch line discrepancies in the figures. Slip during loading is alternately activated in a concentrated manner and during unloading in a distributed manner. Figure 2 shows SEM photographs taken during on loading cycle [14]. Figures 2-(1) to (4) show the crack behavior during the unloading process, and Figures 2-(5) and (6) show it during the loading process. The traces of the slips are observed in front of the crack tip. From this figure, the fatigue crack opens by multi-pairs of alternating slip. And, then, V-shaped tip of the fatigue crack closes from the apex to the back little by little.

Figure 3 shows a kinetic model with dislocations [14]. The numbers or letters besides the dislocation symbol correspond to the positions in the load cycle of Figure 3. During a loading process, a pair of concentrated slip is alternately activated by the avalanche of dislocations as shown in Figure 3-(c) and 3-(d). During the unloading process, slip by dislocations of opposite sign move first on a plane adjacent to the last one activated during loading. The flanks of the crack partially contact, and slip alternates in succession as shown in Figure 3-(e) to (h). When next loaded, slip occurs first on the same side as Figure 3-(c),

Copyright © 2010. Nova Science Publishers, Incorporated. All rights reserved.

Handbook of Material Science Research, Nova Science Publishers, Incorporated, 2010. ProQuest Ebook Central,

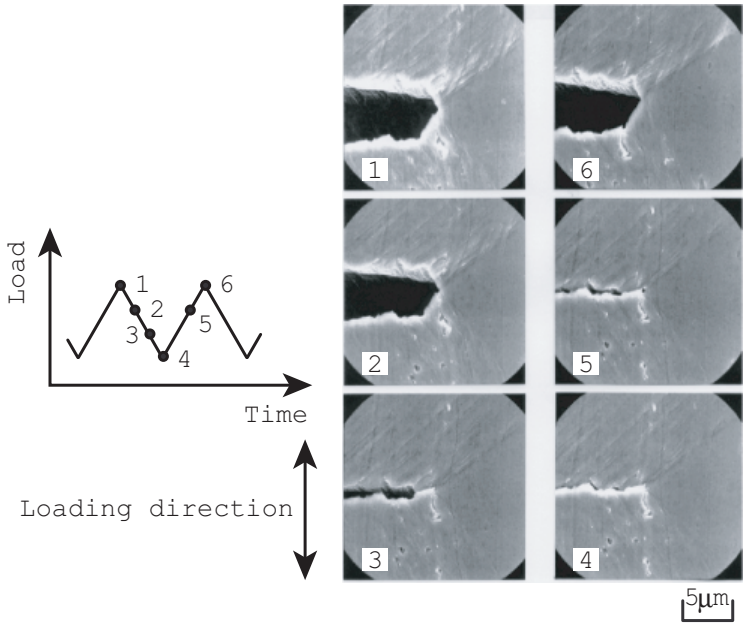


Figure 2. SEM photographs showing the crack growth by multi-pairs of alternating slip.

since the material in this area has not experienced any slip in previous cycle. Moreover, the dislocations in Figure 3-(h) are locally in equilibrium. Thus a crack will continue to grow via the same processes shown in Figure 3-(a) to (h).

In air, when the surface is newly formed during the loading process, it is oxidized immediately. Slip occurs in virgin material during the unloading process. Therefore, monotonic material characteristics is suitable for the evaluations of the propagation and non-propagation of the fatigue cracks [15].

3.2. Fatigue Crack Propagation Law

Let us consider a fact which affects an increment of the crack propagation due to the plastic blunting under a monotonic load. Using CTOD with the Dugdal model [16] concretely, the crack growth due to the plastic blunting of a non-work-hardening material under a monotonic load is expressed with the following equation [15].

$$\Delta a \propto \frac{8\,\sigma_S}{\pi E}\,\ln\Big[\,\sec\Big(\frac{\pi}{2}\cdot\frac{\sigma_a}{\sigma_S}\Big)\,\Big]\,a \tag{1}$$

Here, E is Young's modulus, σ_S is a yield stress, σ_a is a stress amplitude, a is a half crack length, Δa is the increment of a. Because the fatigue crack propagation is affected by the work-hardening and the crack closure phenomena, the crack opening stress σ_{op} does not

Copyright © 2010. Nova Science Publishers, Incorporated. All rights reserved.

Handbook of Material Science Research, Nova Science Publishers, Incorporated, 2010. ProQuest Ebook Central,

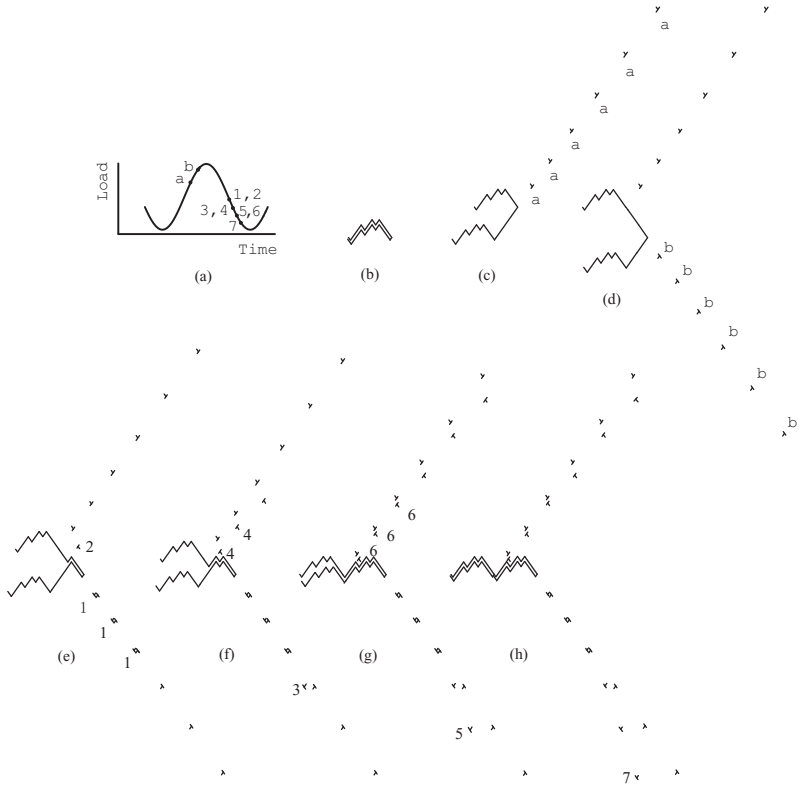


Figure 3. Dislocation model for crack growth.

necessarily correspond to zero even if $R = -1$. Consequently, the effective stress range σ_{eff} $(= \sigma_{max} - \sigma_{op})$ has been greatly used instead of the σ_a. From Equation (1), it is supposed that the crack growth rate law is expressed with the following equation [15].

$$\frac{d\,\ell}{dN} = \frac{8}{\pi}\, C_D \cdot \frac{\sigma_S}{E}\, \ln\Big[\, \sec\Big(\, \frac{\pi}{2} \cdot \frac{\sigma_{eff}}{\sigma_S}\, \Big)\, \Big]\, \ell \tag{2}$$

Here, C_D is a material constant, ℓ is a crack length, N is the number of stress repetitions.

When the crack is long enough and satisfied with $\sigma_a \ll \sigma_S$, the long fatigue crack growth law is approximated with the following equation [10].

$$\frac{d\,\ell}{dN} = C'(eff)^{m'} \tag{3}$$

Here, eff $(= \sigma_{eff}\sqrt{\pi a})$ is the effective stress intensity factor range, C' and m are material constants, respectively. When the crack propagates stably, the crack opening ratio U $(= \sigma_{eff}/\sigma_a)$ is related to the I; in this case, the fatigue crack growth rate is expressed with the following equation [17].

$$\frac{d\,\ell}{dN} = C(I)^m \tag{4}$$

Copyright © 2010. Nova Science Publishers, Incorporated. All rights reserved.

Handbook of Material Science Research, Nova Science Publishers, Incorporated, 2010. ProQuest Ebook Central,

Here, C and m' are material constants, respectively.

When the small fatigue crack propagates stably, the U can be taken as constant irrelevant to the crack growth rate and the crack length [4]. Considering that Equation (2) is fitted to the experimental data and the fatigue life is predicted by Equation (2) practically, the expression $\ln[\sec(\pi/2 \cdot \sigma_{eff}/\sigma_S)]$ is too complex; therefore, the expression is expanded into the polynomial of the (σ_{eff}/σ_S); the polynomial is approximated with the $(\sigma_a/\sigma_S)^n$, where n is a constant which is larger than 2. The small fatigue crack growth law is expressed with the following equation [15].

$$\frac{d\,\ell}{dN} = C_4 \frac{\sigma_S}{E} \left(\frac{\sigma_a}{\sigma_S}\right)^n \ell \tag{5}$$

Here, C_4 is a material constant.

4. Fatigue Crack Non-Propagation Characteristics

4.1. Non-propagation of Fatigue Crack

The eff is decreased by the crack closure phenomena at the early stages of the propagation under a stress controlled condition [3]. If the eff becomes smaller than a certain critical value, the fatigue crack arrests. Using the threshold stress intensity factor range th and the stress intensity factor K_I, the crack non-propagation condition is expressed with the following equation [6].

$$I = th \tag{6}$$

Although the I value is obtained by numerical and theoretical stress analyses, the th value requires the fatigue experiments.

Generally, the th values often have been measured by the decreasing test [18]. Also, the th values can be calculated by the fatigue limit of the cracked specimen, σ_{w2}, under the stress controlled condition [3]. The former primary factor which causes the non-propagation of the fatigue crack is different from the latter one. As a result, the former tendency of the th against the material quality is different from the latter one if materials are same ones [3]. Figures 4 and 5 show the th values by decreasing method and the σ_{w2} under the stress controlled condition, respectively [3]. It is found that both tendencies against Brinell hardness H_B are different. This means that the non-propagation of the fatigue crack is strongly related to the fatigue histories. The primary factor which causes the non-propagation of the fatigue crack of the decreasing test is the oxide induced crack closure [3]; that of the method by using σ_{w2} is the plastic induced crack closure [3]. When the fatigue crack non-propagation is evaluated for the design, the th value need to be chosen appropriately based on the experimental condition which is satisfied with the design condition.

4.2. Threshold Stress Intensity Factor Range, w

Depending on the material and the loading condition, it is difficult to determine whether a crack is a macroscopic or microscopic crack and what a definition of a fatigue crack is. Then, the threshold stress intensity factor range w (nominal stress intensity factor range

Copyright © 2010. Nova Science Publishers, Incorporated. All rights reserved.

Handbook of Material Science Research, Nova Science Publishers, Incorporated, 2010. ProQuest Ebook Central,

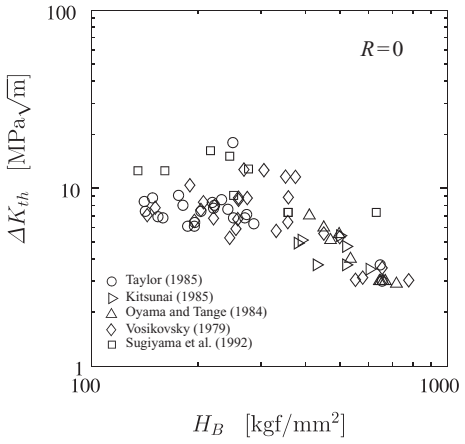


Figure 4. Relation between th measured by decreasing method and H_B.

just after the fatigue test at the fatigue limit; the fatigue crack propagation and the crack closure phenomena are not considered), which doesn't correspond to the phenomenon of crack initiation and crack non-propagation, is introduced as a value to predict the fatigue limit of the cracked metal quantitatively [3].

4.2.1. $w|_{R=-1}$ for a Small Crack

The w values of the macroscopic fatigue crack under the stress controlled condition offer different tendencies depending on the crack length [3]. Figure 6 shows the w by the σ_{w2} of the notched specimen whose the notch root radius ρ is smaller than the branch point ρ_0 [3]. When the notch depth t is smaller than a critical value, the w increase agaist the t. However, when the notch depth t is larger than a critical value, the w becomes constant independent of the t. When the corrected area of a projection of a three dimensional crack to a plane perpendicular to a loading axis is identified with $area_P$ as shown in Figure 7, the w values can be expressed with the following equation [6].

$$w|_{R=-1} = 3.3 \times 10^{-3}(H_V + 120)\sqrt{area_P}^{1/3} \tag{7}$$

$$(w : \text{MPa}\sqrt{\text{m}}\,,\ H_V : \text{kgf/mm}^2\,,\ \sqrt{area_P} : \mu\text{m})$$

Here, H_V is the Vickers hardness of the matrix.

4.2.2. Lower Limit Value of $w|_{R=-1}$, $wLL|_{R=-1}$

When the dislocation is not emitted from the crack tip after the crack finished opening elastically during the loading process, the crack does not propagate. The eff is expressed with the following equation [10].

$$eff = K_{max} - K_{op} \tag{8}$$

Copyright © 2010. Nova Science Publishers, Incorporated. All rights reserved.

Handbook of Material Science Research, Nova Science Publishers, Incorporated, 2010. ProQuest Ebook Central,

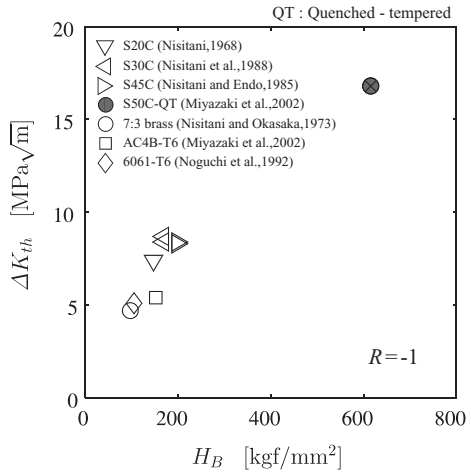


Figure 5. Relation between th predicted by σ_{w2} of specimens with $\rho \leq \rho_0$ and H_B.

Here, K_{max} and K_{op} are stress intensity factors at the σ_{max} and the σ_{op}, respectively. If $K_{max} = K_e$ and $K_{min} = K_{op} = -K_e$, the plastic deformation does not occur at the crack tip during the loading process, where K_{min} is the stress intensity factor at the minimum stress, K_e is the stress intensity factor which determines whether or not a dislocation is emitted from the crack tip [19]. When the crack is satisfied with these conditions, the eff value becomes the threshold value of the eff, eff, th, and the lower limit value of the w, wLL. The wLL is expressed with the following equation [3].

$$wLL = eff, th = 2\,K_e \tag{9}$$

Here, $K_e = 1.05\,\text{MPa}\sqrt{\text{m}}$ for iron; $K_e = 0.25\,\text{MPa}\sqrt{\text{m}}$ for aluminum [19].

4.2.3. Upper Limit Value of $w|_{R=-1}$, $wUL|_{R=-1}$

The upper limit value of the w against the crack length is denoted with the wUL. The wUL value is obtained from the following equation using the σ_{w2} values of the specimens with the deep and sharp notch [3]. For steels, the $wUL|_{R=-1}$ value is approximated by the following equation [20].

$$wUL|_{R=-1} = \begin{cases} wLL|_{R=-1} + 0.04H_B \\ \quad \cdots (105 \leq H_B \leq 582, 0.55 \leq \sigma_S/(3.2H_B) \leq 0.63) \\ wLL|_{R=-1} + 0.027H_B \\ \quad \cdots (124 \leq H_B \leq 615, 0.74 \leq \sigma_S/(3.2H_B) \leq 0.97) \end{cases} \tag{10}$$

Copyright © 2010. Nova Science Publishers, Incorporated. All rights reserved.

Handbook of Material Science Research, Nova Science Publishers, Incorporated, 2010. ProQuest Ebook Central,

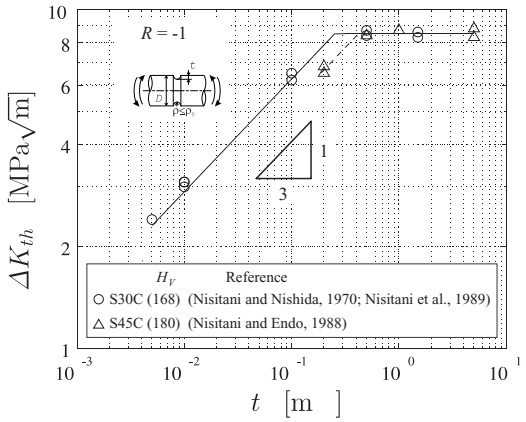


Figure 6. Relation between th predicted by σ_{w2} of specimens with $\rho \leq \rho_0$ and t.

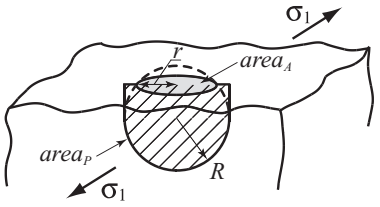


Figure 7. Spheroidal particle cut by the surface.

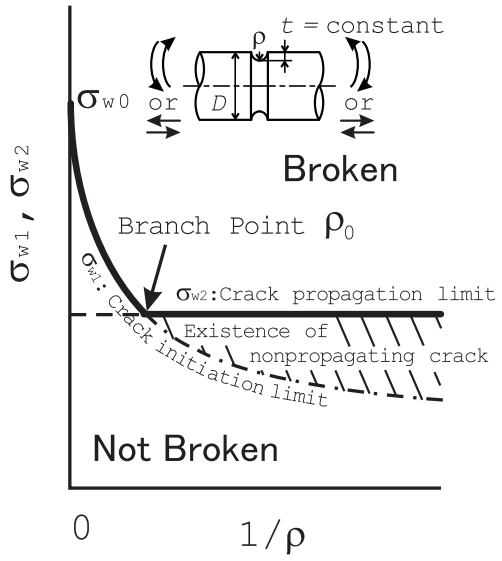


Figure 8. Schematic illustration of a relation between fatigue limit of a notched structure and a notch root radius ρ.

Copyright © 2010. Nova Science Publishers, Incorporated. All rights reserved.

Handbook of Material Science Research, Nova Science Publishers, Incorporated, 2010. ProQuest Ebook Central,

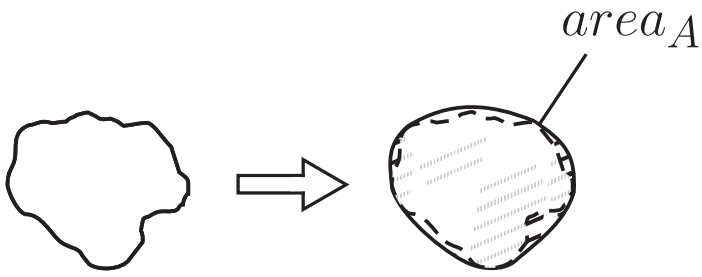


Figure 9. Definition of $area_A$.

$$(wUL, wLL : \text{MPa}\sqrt{\text{m}}\,,\ \sigma_S : \text{MPa}\,,\ H_B : \text{kgf/mm}^2)$$

Here, $wLL|_{R=-1} = 2.1\,\text{MPa}\sqrt{\text{m}}$.

For aluminum alloys, the $wUL|_{R=-1}$ value is approximated by the following equation [9].

$$wUL|_{R=-1} = wLL|_{R=-1} + 0.03H_B \tag{11}$$

$$40 \leq H_B \leq 100$$

Here, $wLL|_{R=-1} = 0.5\,\text{MPa}\sqrt{\text{m}}$.

4.3. Prediction of Fatigue Limit of Notched Specimen

In general, when fatigue tests are carried out on notched specimens with constant notch depth t and various root radii ρ, a typical relation between the fatigue limits and ρ is shown as in Figure 8 [1, 2]. ρ_0 is a critical notch root radius which determines whether or not the non-propagating crack can exist along the notch root, and a material constant which is called the branch point [2]. σ_{w0} is the fatigue limit of the plain specimen; σ_{w1} is the microcrack non-propagation limit; σ_{w2} is the macrocrack non-propagation limit. As shown in Figure 8, although the σ_{w1} decreases with the ρ, the σ_{w2} is constant independent of ρ. Then, the σ_{w1} and σ_{w2} intersect at $\rho = \rho_0$. When $\rho > \rho_0$, the σ_{w1} appears as the fatigue limit; when $\rho \leq \rho_0$, the σ_{w2} appears as the fatigue limit, and the notch can be treated as a crack mechanically. The fatigue limit of the notched specimen, σ_w, is predicted by the following equation.

$$\sigma_w = \min\Big\{\sigma_{w0}, \max(\sigma_{w1}, \sigma_{w2})\Big\} \tag{12}$$

Copyright © 2010. Nova Science Publishers, Incorporated. All rights reserved.

Handbook of Material Science Research, Nova Science Publishers, Incorporated, 2010. ProQuest Ebook Central,

4.3.1. Predictions of σ_{w0} and σ_{w1}

The non-propagation limit stress of the microscopical crack, σ_{w0}, can empirically predicted by the following equation [1, 6].

$$\sigma_{w0}|_{R=-1} = 1.6\, H_B \tag{13}$$

$$(\sigma_{w0} : \text{MPa}\,,\ H_B : \text{kgf/mm}^2)$$

Using Linear Notch Mechanics [21], the non-propagation limit stress of the microscopical crack under the stress gradient, σ_{w1}, can be predicted by the following equation [3].

$$\sigma_{w1}|_{R=-1} = \frac{\sigma_{w0}|_{R=-1}}{K_t}\sqrt{1 + 4.5\,\frac{\varepsilon_0|_{R=-1}}{\rho}} \tag{14}$$

$$(\sigma_{w1} : \text{MPa}\,,\ \rho : \text{mm})$$

Here, ε_0 is a material constant. For steels, the ε_0 is approximated with the following equation [3].

$$\varepsilon_0|_{R=-1} = \frac{51.1}{H_B^{1.46}} \tag{15}$$

$$\rho \geq 0.1,\ 116 \leq H_B \leq 615$$

For aluminum alloys, the ε_0 is approximated with the following equation [9].

$$\varepsilon_0|_{R=-1} = 5.0 \times 10^{-4} H_B - 0.0164 \tag{16}$$

$$\rho \geq 0.5,\ 97 \leq H_B \leq 207$$

4.3.2. Prediction of σ_{w2}

The non-propagation limit of the long macrocrack, σ_{w2L}, can be predicted by the following equation [3].

$$\sigma_{w2L}|_{R=-1} = \frac{wUL|_{R=-1}}{2F\sqrt{\pi\, t}} \tag{17}$$

$$(\sigma_{w2L} : \text{MPa}\,,\ wUL : \text{MPa}\sqrt{\text{m}}\,,\ t : \text{m})$$

Here, F is a modified parameter, t is a crack depth.

On the other hand, the non-propagation limit of the small macrocrack, σ_{w2s}, can be predicted by the following equation [6].

$$\sigma_{w2s}|_{R=-1} = \frac{1.43\,(H_V + 120)}{\sqrt{area_P}^{1/6}} \tag{18}$$

$$(\sigma_{w2s} : \text{MPa}\,,\ H_V : \text{kgf/mm}^2\,,\ \sqrt{area_P} : \mu\text{m})$$

When the notch is assumed to be the long crack with the crack depth t, the fatigue limit is predicted by Equation (17); when the notch is assumed to be the small macrocrack, the fatigue limit is predicted by Equation (18), where $\sqrt{area_P} = \sqrt{10}\,t \times 10^3$. It is difficult to determine whether the notch is deep or shallow. However, because the wUL is the upper limit of the w, the smaller of the σ_{w2s} and σ_{w2L} becomes the σ_{w2} as follows [3].

$$\sigma_{w2} = \min(\sigma_{w2s}, \sigma_{w2L}) \tag{19}$$

Copyright © 2010. Nova Science Publishers, Incorporated. All rights reserved.

Handbook of Material Science Research, Nova Science Publishers, Incorporated, 2010. ProQuest Ebook Central,

5. Evaluation of Fatigue Strength Characteristics of Aluminum Cast Alloy

In this section, the prediction method for the fatigue strength of a inhomogeneous metal based on the distribution characteristics of the defect size and the hardness is explained. And then, an example of an application to an aluminum cast alloy JIS AC4B-T6 (Young's modulus $E = 74\,\text{GPa}$, 0.2 % proof stress $\sigma_{0.2} = 292\,\text{MPa}$, ultimate tensile strength $\sigma_B = 349\,\text{MPa}$) is roughly explained [15].

5.1. Characteristics of Particle Size Distribution

The total number of the particles in a unit volume is denoted with $\bar{N}_{V0}$. The average number of the particles with $R \geq R_0$ in a unit volume, $M_{V0}(R_0)$, is expressed with the following equation [22].

$$M_{V0}(R_0) = \bar{N}_{V0} \exp\left\{-\left(\frac{R_0}{\lambda}\right)^{\nu}\right\} \tag{20}$$

Here, R is a particle radius, λ and ν are material constants, respectively.

When a spheroidal particle whose size distribution is expressed with Equation (20) is cut by a free surface as shown in Figure 7, the average number of the cross-section particles with $r \geq r_0$ in a unit area, $M_{A0}(r_0)$, is given by the following equation [22].

$$M_{A0}(r_0) = 2\int_{\infty}^{r_0} \sqrt{R^2 - r_0^2}\,\frac{dM_{V0}}{dR}\,dR \tag{21}$$

$$\simeq \sqrt{\frac{2\pi}{\nu}}\lambda\left(\frac{r_0}{\lambda}\right)^{1-\frac{\nu}{2}} \bar{N}_{V0} \exp\left\{-\left(\frac{r_0}{\lambda}\right)^{\nu}\right\} \tag{22}$$

Then, the average number of the surface defects with $\sqrt{area_P} \geq \sqrt{area_P}_1$ in a unit area, $M_{S0}(\sqrt{area_P}_1)$, is given by the following equation [7].

$$M_{S0}(\sqrt{area_P}_0) = \lambda\,\bar{N}_{V0}\int_0^1 \frac{t}{\sqrt{1-t^2}}\left\{\Gamma\left(1+\frac{1}{\nu},\left(\frac{\sqrt{area_P}_0}{\lambda\sqrt{\theta^-}}\right)^{\nu}\right) + \Gamma\left(1+\frac{1}{\nu},\left(\frac{\sqrt{area_P}_0}{\lambda\sqrt{\theta^+}}\right)^{\nu}\right)\right\} dt \tag{23}$$

$$\theta^+ = \frac{\pi}{2} + 2\sqrt{1-t^2}\,\overline{\qquad} \tag{24}$$

$$\theta^- = \arcsin(t) - t\sqrt{1-t^2} \tag{25}$$

Here, Γ is the second incomplete gamma function.

The present AC4B-T6 contains three kinds of particles: eutectic Si, Fe compound and porosity [15]. The evaluations of the M_{A0}, M_{V0} and M_{S0} of those particles are concretely mentioned as follows. Because a practical non-metallic inclusion is not perfectly spheroidal, the cross-section plane is not perfectly circular. Enclosing the shape with a convex ~~smooth line~~ as shown in Figure 9, the area is defined as $area_A$ ~~[15,~~ 22]. By using $r = \sqrt{area_A}/\sqrt{\pi}$, the r distribution, $M_{A0}(r_0)$, is obtained from a $\sqrt{area_A}$ distribution. A line of Equation (22) is drawn to best fit the experimental data, and the values of $\bar{N}_{V0}$Cν and λ are determined. The measured r distributions and the fitting lines of Eutectic Si, Fe compound and porosity are shown in Figure 10 [15]. Then, the M_{V0} and M_{S0} of Eutectic Si, Fe compound and porosity are shown in Figures 11 and 12, respectively [15].

Copyright © 2010. Nova Science Publishers, Incorporated. All rights reserved.

Handbook of Material Science Research, Nova Science Publishers, Incorporated, 2010. ProQuest Ebook Central,

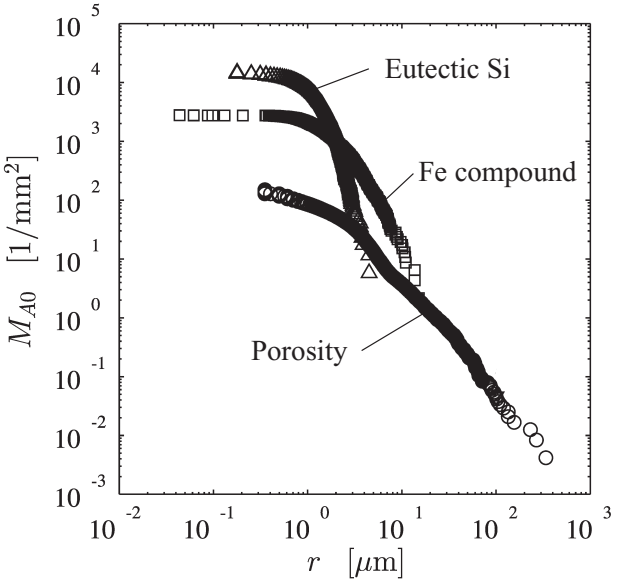


Figure 10. The average number of the cross-sectioned particles whose radii are larger than r in a unit area, M_{A0}.

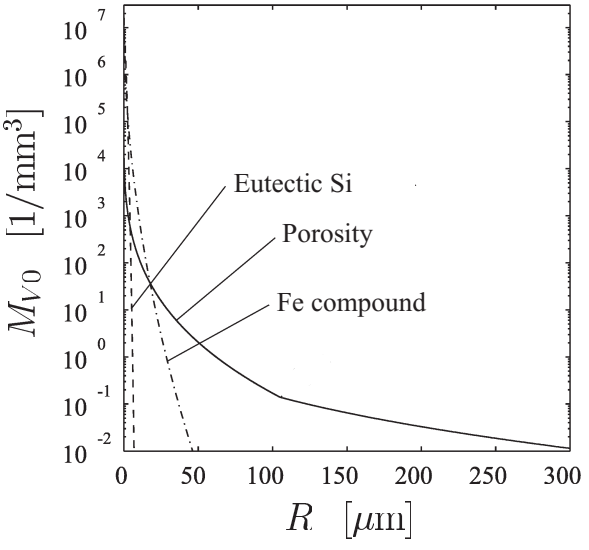


Figure 11. The average number of the particles whose radii are larger than R in a unit volume, M_{V0}.

Copyright © 2010. Nova Science Publishers, Incorporated. All rights reserved.

Handbook of Material Science Research, Nova Science Publishers, Incorporated, 2010. ProQuest Ebook Central,

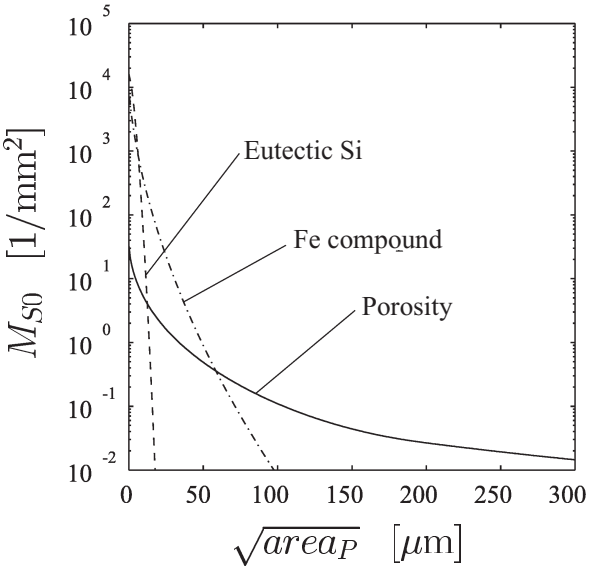


Figure 12. The average number of the cross-sectioned particles whose sizes are larger than $\sqrt{area_P}$ in a unit area, M_{S0}.

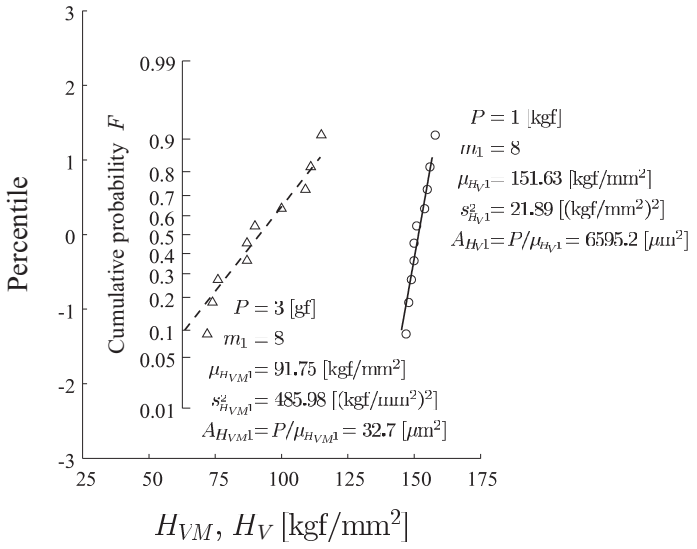


Figure 13. Evaluation of the Vickers hardness distribution of the matrix from a normal probability graph.

Copyright © 2010. Nova Science Publishers, Incorporated. All rights reserved.

Handbook of Material Science Research, Nova Science Publishers, Incorporated, 2010. ProQuest Ebook Central,

5.2. Characteristics of Vickers Hardness Distribution

When m_1 Vickers hardness values are measured by an indentation load P, the values form a normal distribution. Figure 13 shows the Vickers hardness distributions [7]. The open circle is the Vickers hardness of the matrix with the particles, H_V; triangle marks is the Vickers hardness of the matrix without the particles, H_{VM}. A normal probability paper was used to evaluate the distribution; the measured values were plotted on the probability paper. A line was drawn with the values in range from 10% to 85%. then, the average and the variance were determined by the slope and intercept of the line, respectively.

A mean and a variance of the sample distribution are denoted with $\mu 1$ is a mean and $s1$, respectively. A population mean $\mu 0$ is expressed with the following equation [7].

$$\mu 1 = \mu 0 \tag{26}$$

Using the χ^2 distribution with the freedom degree of $n = m_1 - 1$, the population variance $s0$ is expressed with the following equation [7].

$$f_{\chi^2}(\chi^2) = \frac{1}{2\,\Gamma(n/2)}\Big(\frac{\chi^2}{2}\Big)^{\frac{n}{2}-1}\exp\Big(-\frac{\chi^2}{2}\Big) \tag{27}$$

$$\Gamma(t) = \int_0^\infty x^{t-1}e^{-x}\,dx\,,\ \chi^2 = m_1\frac{s_1^2}{s_0^2} \tag{28}$$

The Vickers hardness in an area, A_{npc} which is concerned with a non-propagation crack, can be expressed with the normal distribution from the central limit theorem. The variance sS and mean μS in A_{npc} can be estimated from $s0$ and $\mu 0$ as follows [7].

$$sS = \frac{A_1}{A_{npc}}\,s0 \tag{29}$$

$$\mu S = \mu 0 \tag{30}$$

Here, A_1 is an indentation area of a Vickers hardness under the indentation load P.

5.3. Prediction of High Cycle Fatigue Life Reliability

5.3.1. Prediction Method

The small fatigue crack propagation rate is approximately expressed with the following equation [15].

$$\frac{d\,\ell}{dN} = C_5\,\frac{\sigma_S}{E}\Big(\frac{\sigma_a}{\sigma_S}\Big)^6\,\ell \tag{31}$$

Here, C_5 is a material constant and given by the following equation. [15]

$$C_5 = \begin{cases} \Big(\dfrac{\sigma_S}{500}\Big)^{6.73} \cdots (0.52 \le \sigma_S/\sigma_B \le 0.59, 200 \le \sigma_S\,\text{MPa} \le 400) \\ \Big(\dfrac{\sigma_S}{2092}\Big)^{1.4} \cdots (0.67 \le \sigma_S/\sigma_B \le 0.92, 200 \le \sigma_S\,\text{MPa} \le 1400) \end{cases} \tag{32}$$

Copyright © 2010. Nova Science Publishers, Incorporated. All rights reserved.

Handbook of Material Science Research, Nova Science Publishers, Incorporated, 2010. ProQuest Ebook Central,

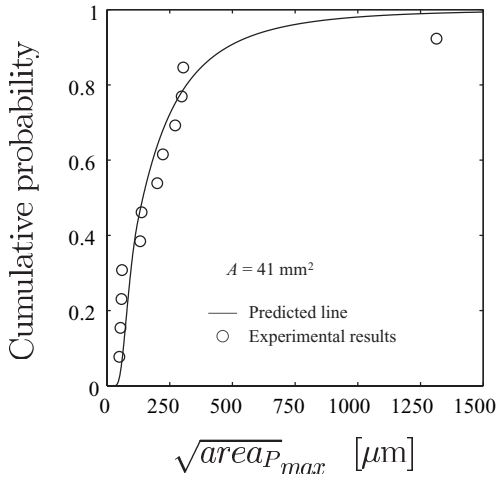


Figure 14. Cumulative probability of maximum surface defect size $\sqrt{area_P}_{max}$.

Integrating Equation (31) from an initial crack length ℓ_0 to a final crack length at the fatigue fracture, ℓ_f, the fatigue life N_f is obtained as follows [15].

$$N_f = \frac{E}{C_5\,\sigma_S}\Big(\frac{\sigma_S}{\sigma_a}\Big)^6 \ln\Big[\sqrt{\frac{\pi}{8}}\cdot\frac{\ell_f}{\sqrt{area_P}_{max}}\Big] \tag{33}$$

Here, $\ell_0 = \sqrt{8/\pi}\sqrt{area_P}_{max}$.

The distribution of the maximum surface crack size $\sqrt{area_P}_{max}$ is obtained by combining Equation (23) with Poisson distribution [15]. Then, the high cycle fatigue life reliability is predicted by applying the $\sqrt{area_P}_{max}$ distribution to the $\sqrt{area_P}_{max}$ of Equation (23) [15].

5.3.2. Predicted Results

All of the fatigue fracture origins were the porosities [15]. Figure 14 shows the cumulative probability distributions of the $\sqrt{area_P}_{max}$ of the porosity [15]. The solid line is the distribution by the present method, and the open mark is the distribution obtained from the $\sqrt{area_P}$ values of the fracture origins by the mean rank method.

Figure 15 shows the S-N curve [15]. The open marks are the experimental results, and the solid lines are 50%, 90% and 99% of reliability which is estimated by the present method. Figure 16 shows the experimental reliability distributions of the fatigue life at $\sigma_a = 160$ MPa. The open mark is the reliability obtained from the fatigue life at $\sigma_a = 160$ MPa by the mean rank method, and the solid line is the reliability estimated by the present method.

Copyright © 2010. Nova Science Publishers, Incorporated. All rights reserved.

Handbook of Material Science Research, Nova Science Publishers, Incorporated, 2010. ProQuest Ebook Central,

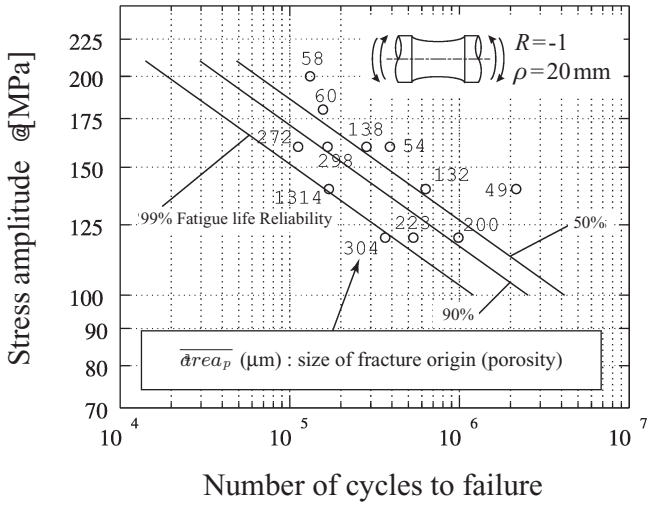


Figure 15. Predicted S-N curves.

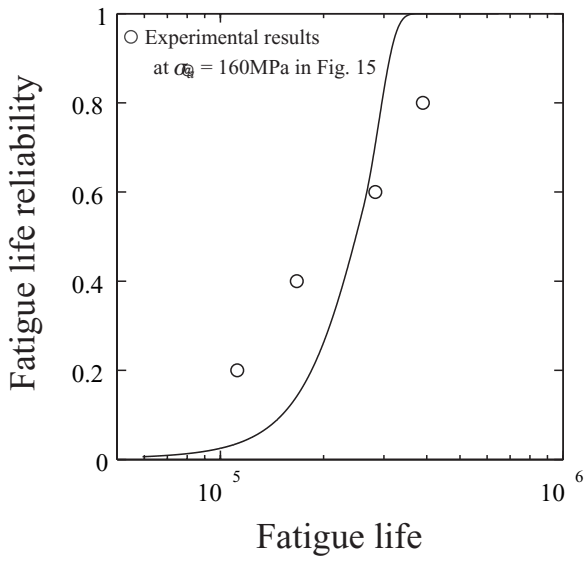


Figure 16. Fatigue life reliability at $\sigma_a = 160\,\mathrm{MPa}$.

Copyright © 2010. Nova Science Publishers, Incorporated. All rights reserved.

Handbook of Material Science Research, Nova Science Publishers, Incorporated, 2010. ProQuest Ebook Central,

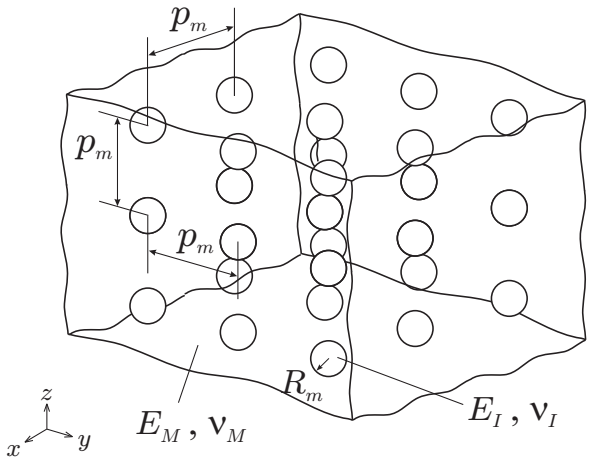


Figure 17. Approximated model of a material with inhomogeneous particles.

5.4. Prediction of Fatigue Strength Reliability at $N = 10^7$ of Notched Specimen

5.4.1. Stress Field Characteristics Near Notch Root

Figure 17 shows a schematic illustration of the inhomogeneous material modeled for the prediction [8, 9]. Average particle radius R_m is given by the following equation [8, 9].

$$R_m = \lambda\,\Gamma\Big(1+\frac{1}{\nu}\Big) \tag{34}$$

Average distance between particles, p_m, is given by the following equation [8, 9].

$$p_m = \Big(\frac{1}{\bar{N}_{V0}}\Big)^{1/3} \tag{35}$$

It is supposed that stress fields $\sigma_z = Z_m$ and $\sigma_x = \sigma_y = \sigma_z = T_m$ are formed around the particle under a monotonic z axial stress $\sigma_{z\infty} = 1$. When the origin is set to a center of a certain particle, the following equations consist at a point $(0, 0, R_m)$ [8, 9].

$$T_m + Z_m = 1 + \sum_{\substack{i,\,j,\,k\,=\,-\infty \\ (i,\,j,\,k)\,\neq\,(0,\,0,\,0)}}^{\infty}\sum\sum \sigma_{zm}(T_m, Z_m)\Big|_{\substack{x_{i,j,k}=-ip_m \\ y_{i,j,k}=-jp_m \\ z_{i,j,k}=R_m\,-\,kp_m}} \tag{36}$$

$$T_m = \sum_{\substack{i,\,j,\,k\,=\,-\infty \\ (i,\,j,\,k)\,\neq\,(0,\,0,\,0)}}^{\infty}\sum\sum \sigma_{ym}(T_m, Z_m)\Big|_{\substack{x_{i,j,k}=-ip_m \\ y_{i,j,k}=-jp_m \\ z_{i,j,k}=R_m\,-\,kp_m}} \tag{37}$$

Here, $\sigma_{ym}(T_m, Z_m)$ and $\sigma_{zm}(T_m, Z_m)$ are y and z axial stresses added at a point $(x_{i,j,k}, y_{i,j,k}, z_{i,j,k})$ when there is a unit particle in the infinite body under $\sigma_{x\infty} = \sigma_{y\infty} =$

Copyright © 2010. Nova Science Publishers, Incorporated. All rights reserved.

Handbook of Material Science Research, Nova Science Publishers, Incorporated, 2010. ProQuest Ebook Central,

Table 1. Area of iso-stress near notch root.

j	1	2	3	4	5	6
$\sigma_{1,j}/\sigma_{max}$	1-0.95	0.95-0.9	0.9-0.8	0.8-0.7	0.7-0.6	0.6-0.5
A_j/ρ^2	0.0083	0.0187	0.0703	0.1442	0.2957	0.6574

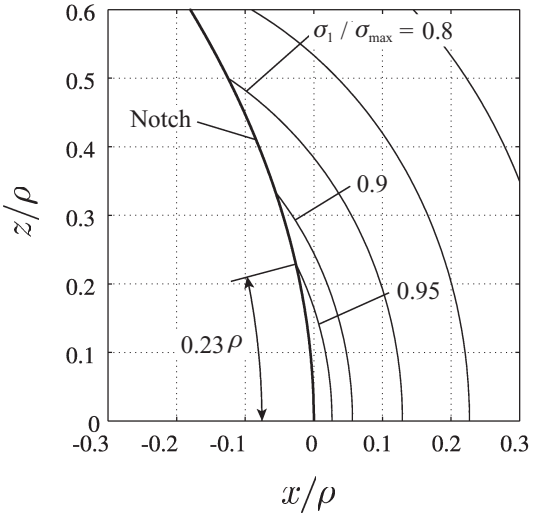


Figure 18. Contour map of a relative first principal stress near notch root.

Copyright © 2010. Nova Science Publishers, Incorporated. All rights reserved.

$\sigma_{z\infty} = T_m$ and $\sigma_{z\infty} = Z_m$, respectively [23]. The relaxation effect of the stress concentration by interference of the particles, γ_m, is defined as the following equation [8, 9].

$$\gamma_m = Z_m + T_m \tag{38}$$

Here, T_m and Z_m are obtained by solving the simultaneous linear equations (36) and (37).

When the first principal stress and the maximum stress under the notch root are denoted with σ_1 and σ_{max}, respectively, a contour line map of σ_1/σ_{max} distribution of a homogeneous notch root is shown in Figure 18 [9]. The j-th stress and the j-th area size are denoted with σ_j and A_j, respectively. In case of two dimensional elastic problem, $\sigma_{1,j}$ and A_j are shown in Table 1, respectively [9]. Considering the relaxation effect of the stress concentration, γ_m, the stress in the A_j becomes $\gamma_m\sigma_{1,j}$ [9]. In the present analysis, a region under the notch root is divided as shown in Figure 18 and Table 1. Then, the divided regions are used as solid elements and plane elements to predict the fatigue limits.

5.4.2. Prediction Method

The fatigue limit of the present AC4B-T6, σ_w, is composed of the microcrack non-propagation limit σ_{w1}, the small crack non-propagation limit σ_{wd} and the macrocrack non-

Handbook of Material Science Research, Nova Science Publishers, Incorporated, 2010. ProQuest Ebook Central,

propagation limit σ_{w2} [8, 9]. Moreover, the σ_{wd} is composed of the internal crack non-propagation limit σ_{wdI} and the surface crack non-propagation limit σ_{wdS} [7, 8, 9]. Because these limit stresses are competitive, the fatigue limit reliability is predicted through a fatigue survival rate and a fatigue fracture rate [7].

First, the survival rates for the microcrack is explained [7]. The microcrack non-propagation limit, σ_{w1}, can be predicted by Equation (14). The limit hardness which determines whether or not the microcrack arrests under a certain stress amplitude is obtained by solving Equation (14) on the hardness, where the $\varepsilon_0|_{R=-1}$ is predicted by Equation (16). The Vickers hardness of the matrix which does not contain the particles, , is expressed with the probability distribution as mentioned in Section 5.2, and the probability that the is larger than the limit hardness becomes equivalent to the fatigue survival rate for the microcrack.

Next, the survival rates for the small crack is explained [7]. The non-propagation limit of the fatigue crack which is initiated from an internal defect of $\sqrt{area_R}$ near the notch of the ρ, σ_{wdI}, can be predicted approximately by the following equation [9].

$$\sigma_{wdI}|_{R=-1} = \frac{1.56 \times 240}{F_R \sqrt{area_R}^{1/6} \ln(240/ + 1)} \tag{39}$$

$$F_R = \frac{4}{\pi^{5/4}} \Big\{ 1 - \Big(\frac{2}{\sqrt{\pi}} - \frac{4}{3\pi} \Big) \frac{\sqrt{area_R}}{\rho \times 10^3} \Big\} \tag{40}$$

$$(\sigma_{wdI} : \text{MPa} , : \text{kgf/mm}^2 , \sqrt{area} : \mu\text{m} , \rho : \text{mm})$$

The distribution of the maximum internal crack size is obtained by combining Equation (20) with Poisson distribution. And then, the distribution of the limit hardness which determines whether or not the small internal crack arrests is obtained by combining the maximum crack size distributions with Equation (39). The survival rate for the small internal crack is obtained by composing the limit hardness distribution and the distribution like the stress-strength model [7].

The non-propagation limit of the fatigue crack which is initiated from an surface defect of $\sqrt{area_P}$ near the notch of the ρ, σ_{wdS}, can be predicted approximately by the following equation [9].

$$\sigma_{wdS}|_{R=-1} = \frac{1.43 \times 240}{F_P \sqrt{area_P}^{1/6} \ln(240/ + 1)} \tag{41}$$

$$F_P = 0.963 - 1.497 \frac{\sqrt{area_P}}{\rho \times 10^3} \tag{42}$$

$$(\sigma_{wdS} : \text{MPa} , : \text{kgf/mm}^2 , \sqrt{area} : \mu\text{m} , \rho : \text{mm})$$

When Equations (23) and (41) are used instead of Equations (20) and (39), respectively, the survival rate for the small surface crack as well as the internal crack is obtained by the similar procedure for predicting the rate for the internal crack.

When the fatigue fracture does not occur in all solid and surface elements, the notched specimen does is not broken by the fatigue. Therefore, the survival rate of the notched specimen is obtained by multiplying the above mentioned survival rates for the microcracks, the small internal and surface cracks together. Then, a complementary event of the survival

Copyright © 2010. Nova Science Publishers, Incorporated. All rights reserved.

Handbook of Material Science Research, Nova Science Publishers, Incorporated, 2010. ProQuest Ebook Central,

rate corresponds to the fracture rate [7]. Finally, the fracture rate which is cut off by the σ_{w2} becomes the fatigue limit reliability. The σ_{w2} is predicted by Equations (11) and (17), where the average Vickers hardness of the matrix which contains the particles, H_V, is used [9].

5.4.3. Predicted Results

Figure 19 shows survival rates of the notched specimens of $\rho = 20$, 5, 1 mm [8, 9]. The thick broken and solid line are σ_{w1} and σ_{w2}, respectively. The fine solid, broken and chained line are σ_{wd} of porosity, Eutectic Si and Fe compound. Figure 20 shows the fatigue limit reliability [8, 9]. The thick solid line in Figure 20-(a) is the σ_w distribution in case of $\rho = 20$ mm; the thick and fine solid lines in Figure 20-(b) are σ_w distributions in case of $\rho = 5$ and 1 mm, respectively. When the ρ is small, the influence of Fe compound becomes large. However, the fatigue limit reliability is governed by the σ_{w1} distribution. Then, when $\rho \leq \rho_0$, the σ_{w1} and σ_{wd} are cut off by the σ_{w2}. Finally, Fe compound almost influences the fatigue limit reliability. Figure 21 shows σ_{w1}, σ_{wd}, σ_{w2} and σ_w against the ρ, where σ_{w1}, σ_{wd} and σ_w are 50 % reliability, respectively [8, 9].

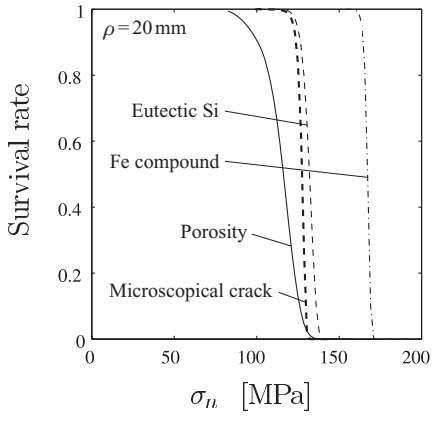
6. Conclusion

In this paper, the characteristics of the crack propagation and non-propagation were explained. When the mechanisms and the mechanical characteristics of the fatigue crack propagation are taken into consideration, the monotonic characteristics of the matrix are suitable for the evaluations of the fatigue propagation and non-propagation, and the cracks are divided into the small and long ones depending on the plastic zone size against the crack size. Then, the simple forms which are obtained by formulating the crack propagation and non-propagation characteristics under $R = -1$ were explained, and their applications to predictions of the fatigue life reliability and the fatigue strength reliability at $N = 10^7$ of aluminum cast alloy AC4B-T6 were roughly introduced.

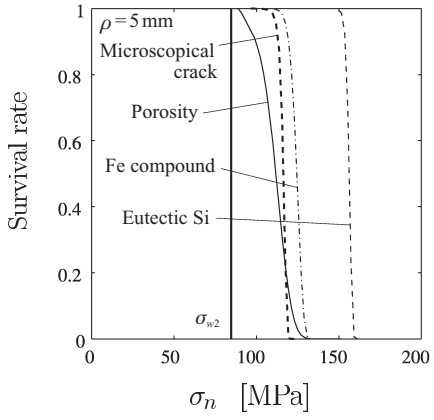
In actual structures, there are various stress concentration parts: structural notch and hole, non-metallic inclusion, porosity, defect and so on. When it is supposed that the structures obey the weakest link model, all stress concentration parts can become the fatigue fracture origins; in this case, because the propagation and non-propagation characteristics of the small crack are different from those of the long one, the attention has to be paid to the evaluation of the fatigue crack from the small particles. It is very important for the reasonable fatigue design to grasp and use these characteristics of both cracks properly. Moreover, if the particles are densely distributed in the material, the characteristics of the matrix also need to be carefully examined based on the particle distribution density in the zone which is affected by the fatigue crack propagation and non-propagation.

Copyright © 2010. Nova Science Publishers, Incorporated. All rights reserved.

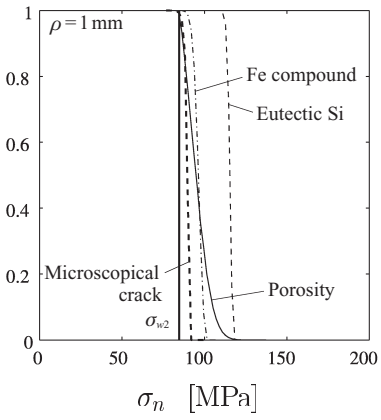
Handbook of Material Science Research, Nova Science Publishers, Incorporated, 2010. ProQuest Ebook Central,



(a) $\rho = 20\,\mathrm{mm}$.



(b) $\rho = 5\,\mathrm{mm}$.

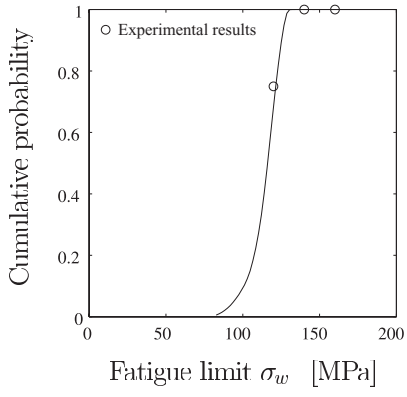


(c) $\rho = 1\,\mathrm{mm}$.

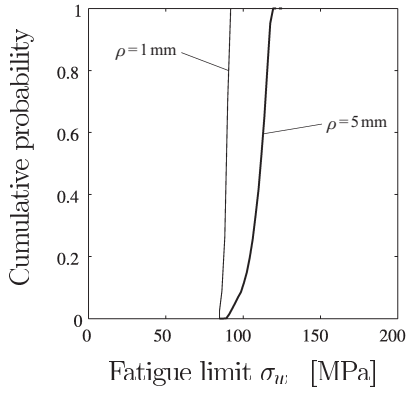
Figure 19. Survival rates for microcrack, small crack and macrocrack

Copyright © 2010. Nova Science Publishers, Incorporated. All rights reserved.

Handbook of Material Science Research, Nova Science Publishers, Incorporated, 2010. ProQuest Ebook Central,



(a) $\rho = 20\,\mathrm{mm}$.



(b) $\rho = 5, 1\,\mathrm{mm}$.

Figure 20. Predicted fatigue strength reliability at $N = 10^7$.

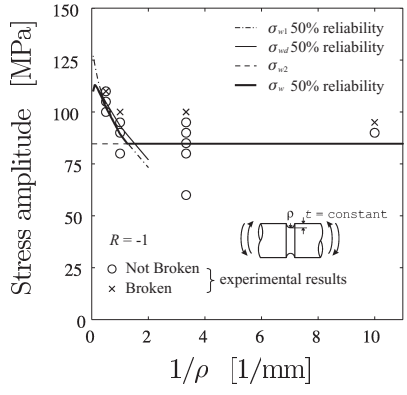


Figure 21. Comparison between experimental results and predicted 50% fatigue strength reliability at $N = 10^7$.

Copyright © 2010. Nova Science Publishers, Incorporated. All rights reserved.

Handbook of Material Science Research, Nova Science Publishers, Incorporated, 2010. ProQuest Ebook Central,

References

1. Isibasi, T., (1954). *Prevention of fatigue and fracture of metals*, (in Japanese), Yokendo.

2. Nisitani, H., (1968), Effects of size on the fatigue limit and the branch point in rotary bending tests of carbon steel specimens. *Bulletin of the JSME*, Vol. 11, No. 47, 947-957.

3. Miyazaki, T., Noguchi, H. and Ogi, K. (2002). Quantitative evaluation of the fatigue limit of a metal with an arbitrary crack under a stress controlled condition (stress ratio $R = -1$). *International Journal of Fracture*, vol. 129, 21-38.

4. Nisitani, H., (1981). Unifying treatment of fatigue crack growth law in small, large and non-propagationg cracks. *Mechanics of Fatigue*, AMD 47, ASME,151-166.

5. Nisitani, H. and Kawagoishi, N., (1983). Fatigue Crack Growth Law in Small Cracks and Its Application to the Evaluation of Fatigue Life. *Transaction of Japanese Society of Mechanical Engineers*, A49-440, 431-440.

6. Murakami, Y., (2002). Metal fatigue: effect of small defects and nonmetallic inclusions. *Elsevier*.

7. Miyazaki, T., Noguchi, H. Kage, M. and Imai, R., (2002). Evaluation for fatigue limit reliability of a metal with inhomogeneities under stress ratio $R = -1$. *International Journal of Mechanical Science*, 47-2, 230-250.

8. Miyazaki, T., Noguchi, H., Ogi, K. and Aono, Y., (2005). Examination of Fatigue Characteristics of Aluminum Cast Alloy from Meso-level Consideration (2nd Report, Prediction for the Fatigue Limit Reliability of Plain Specimen of Metal Containing Different Sorts of Inhomogenities under $R = -1$). *Transaction of Japanese Society of Mechanical Engineers*, A71-712, 1699-1707.

9. Miyazaki, T., Noguchi, H., Miyahara, H. and Aono, Y., (2006). Examination of Fatigue Characteristics of Aluminum Cast Alloy from Meso-level Consideration (3rd Report, Prediction of the Fatigue Limit Reliability of Notched Specimen of Metal Containing Different Sorts of Inhomogenities under $R = -1$). *Transaction of Japanese Society of Mechanical Engineers*, A72-720, 1185-1193.

10. Elber, W. (1971). The Significance of fatigue crack closure, damage torelance in aircraft structure. *ASTM STP*, 486, 230-242.

11. Ritchie, R. O., Suresh, S. and Moss, C. M., (1980). Near-threshold fatigue crack growth in a 2 1/4 Cr-Mo pressure vessel steel in air and hydrogen, *Journal of Engineering Materials and Technology*, ASME, Series H., 102(3), 293-299.

12. Suresh, S., Zimiski, G. F. and Ritchie, R. O., (1981). Oxide-induced crack closure : an explanation for near-threshold corrosion fatigue crack growth behavior. *Metallurgical Transactions A*, 12A, 1434-1443.

Copyright © 2010. Nova Science Publishers, Incorporated. All rights reserved.

Handbook of Material Science Research, Nova Science Publishers, Incorporated, 2010. ProQuest Ebook Central,

13. Minakawa, K. and McEvily, A. J., (1981). On crack closure in the near-threshold region. *Scripta Metallurgica*, vol. 15, 633-636.

14. Oda, Y., Furuya, Y., Noguchi, H. and Higashida, K. (2002). AFE and SEM observation on mechanism of fatigue crack growth in a Fe-3.2% Si single crystal. *International Journal of Fracture*, 113, 213-231.

15. Miyazaki, T., Kang, H. G., Noguchi, H. and Ogi, K., (2008). Prediction of high-cycle fatigue life reliability of aluminum cast alloy from statistical characteristics of defects at meso-scale , *International Journal of Mechanical Sciences*, 50-2, 152-162.

16. Dugdale, D. S. (1960). Yielding of steel sheets containing slits. *Journal of the Mechanics and Physics of Solids*, 8, 100-104.

17. Paris, P. C. and Erdogan, F. (1963). A critical analysis of crack propagation laws, *Journal of Basic Engineering*, 85, 528-534.

18. ASTM E647-095a. Standard test method for measurement of fatigue crack growth rates. *Annual Book of ASTM Standard*, Section 3.

19. Yokobori, A. T. and Yokobori, T., (1981). On Micro- and macro-mechanics of fatigue thresholds, *EMAS*, Fatigue Threshold, 171-189.

20. Miyazaki, T., Noguchi, H. and Kage, M., (2005). Fatigue limit of steel with an arbitrary crack under a stress controlled constant with a positive mean stress, *International Journal of Fracture*, vol. 134, 109-126.

21. Nisitani, H., (1983), Linear notch mechanics as an extension of linear fracture mechanics. *Proceedings of the International Conference on the Role of Fracture Mechanics in Modern Technology*, North-Holland, 25-37.

22. Hashimoto, A., Miyazaki, T., Kang, H.G., Noguchi, H. and Ogi, K., (2000). Estimation for particle size distribution in materials in case of spheroidal particles with quantitative microscopy, *Jounal of Testing and Evaluation*, 28-9, 367-377.

23. Edward, R. H., (1951). Stress Concentrations around Spheroidal Inclusions and Cavities. *Transaction of the ASME Journal of Applied Mechanics*, vol. 18, 19-30.

Copyright © 2010. Nova Science Publishers, Incorporated. All rights reserved.

Handbook of Material Science Research, Nova Science Publishers, Incorporated, 2010. ProQuest Ebook Central,

INDEX

3

3,4-ethylenedioxythiophene, 460

A

Aβ, 13, 14, 196
absorption, 15, 87, 90, 107, 134, 216, 228, 236, 314, 385, 466
absorption spectra, 15
absorption spectroscopy, 314
acceleration, 129, 130, 132
accelerator, 127, 128, 131, 132
acceptor, 422
accidents, 273
accuracy, 34, 39, 41, 42, 43, 97, 243, 245, 289, 357, 418, 419, 422, 423, 428
ACE, 368
acetone, 326, 338
acid, 51, 135, 349, 353, 462, 463, 467, 471, 472
acoustic, 4, 18
acoustic emission, 18
ACS, 429
activation, xii, xvi, 59, 70, 99, 102, 213, 214, 221, 226, 227, 228, 236, 266, 352, 459, 460, 461, 463, 464, 467, 468, 470
activation energy, xii, 59, 70, 99, 213, 214, 221, 226, 227, 228, 236, 266
active site, 355
actuation, 329
additives, 349
adhesion, 353
adiabatic, 17, 282
adjustment, 106
adsorption, 331, 332, 460, 466, 467, 470
adsorption isotherms, 331, 332
aerospace, xiv, 126, 347, 348
Ag, xii, 173, 174, 185, 186, 187, 188, 189, 190, 191, 192, 193, 195, 198, 199, 208, 209, 462, 463, 467, 468
ageing, xvi, 24, 445, 446, 447, 449, 450, 452, 453, 455, 456, 457
agent, 349, 462
agents, 297, 332
aggregates, 378
aggregation, 182
aging, 275
aid, 201, 207, 208
AIP, 119, 344
air, 164, 165, 187, 188, 189, 190, 297, 336, 349, 350, 447, 495, 515
alcohol, 325, 372, 471
alcohol use, 325
algorithm, 44, 47, 282, 283, 286
alkali, 467
alkaline, 349
alternative, xiv, 347, 353, 459, 460
alternative energy, 459
aluminium, 324, 329, 330, 339
aluminum, xvii, 372, 491, 492, 499, 501, 502, 503, 512, 515, 516
aluminum oxide, 372
amino acid, 51
ammonia, 297, 317
ammonium, xv, 6, 325, 395, 397, 414
amorphous, 6, 127, 189, 396, 405, 406, 433, 434, 435, 436, 439
amplitude, 35, 130, 259, 260, 261, 262, 263, 316, 493, 495, 508, 511
analog, 45, 215, 227
analytical techniques, 331, 332, 341
anharmonicity, 216, 260
anisotropy, 22, 185, 255, 260, 292, 296, 308, 310, 319, 390, 439
annealing, 13, 34, 131, 134, 144, 152, 153, 154, 155, 164, 165, 166, 168, 397, 408, 409, 412, 413

Copyright © 2010. Nova Science Publishers, Incorporated. All rights reserved.

Handbook of Material Science Research, Nova Science Publishers, Incorporated, 2010. ProQuest Ebook Central,

anode, xvi, 133, 349, 350, 372, 397, 459, 460, 463, 466, 470, 471, 472
anomalous, xiii, 14, 25, 31, 102, 193, 209, 214, 215, 240, 254, 257, 271, 272, 300, 348, 354, 366, 404
antibonding, 216
antiferromagnetic, 207, 208, 301, 304, 306, 307, 309, 310, 313, 316, 317, 318, 319, 320
APP, 352, 359
application, xi, xiv, xvi, xvii, 12, 23, 35, 126, 167, 262, 263, 273, 301, 304, 316, 320, 323, 324, 325, 329, 342, 343, 348, 390, 396, 413, 427, 433, 434, 437, 439, 440, 441, 459, 460, 472, 473, 474, 503
aqueous solution, 366, 368, 372, 462, 463, 466, 467, 468, 469, 472
aqueous solutions, 366, 368
argon, 131, 397, 413
argument, 32, 241
Arrhenius law, xii, 1, 97, 99, 102, 116, 214, 226, 245, 266, 280
aspect ratio, 325, 326
ASTM, 353, 364, 458, 515, 516
asymmetry, xi, 1, 31, 50, 62, 67, 80, 81, 82, 83, 84, 199, 209, 240, 256, 389
asymptotic, 229
atmosphere, 131, 135, 136, 138, 139, 140, 149, 156, 167, 183, 185, 397, 413, 463
Auger electron spectroscopy, xii, 125, 134

B

backscattering, xii, 125, 134
band gap, 369, 378
bandwidth, 39, 43, 243
barrier, xiv, 62, 63, 152, 347, 348, 359, 360, 363, 383
barriers, 24, 28, 460
batteries, 296, 320
B-cells, 182
beams, 126, 127, 145
bending, 115, 515
benign, 353
beryllium, 128, 278
Bessel, 37, 38, 41, 280
bias, xiii, 103, 213, 260, 261, 262, 263, 265, 266
biophysics, 420
birefringence, 16, 23, 24
boiling, 139, 324
Boltzman constant, 9
bonding, 20, 22, 185, 216, 260, 466
bonds, xv, 14, 22, 26, 51, 52, 62, 73, 77, 84, 215, 417, 423
boundary conditions, 135, 207, 283
brass, 499
Brillouin spectra, 18
broad spectrum, 332
broadband, xi, xii, 1, 31, 33, 34, 35, 52, 67, 85, 87, 213, 240
buffer, 197, 261, 262, 263
building blocks, 369, 390
bulk crystal, 372, 434
bulk materials, 390
burning, 274, 284, 285, 286, 288, 292, 329

C

C++, 47
cadmium, 367, 372
calibration, 36, 39
calorimetric measurements, 133, 159
capacitance, xi, 1, 34, 36, 37, 38
capillary, 350, 397
carbide, xvi, 129, 142, 144, 159, 161, 162, 163, 164, 165, 166, 167, 168, 445, 446, 448, 449, 450, 451, 453, 456, 457
carbon, xi, xii, xvi, 125, 128, 129, 130, 131, 134, 140, 141, 142, 144, 145, 153, 156, 159, 167, 170, 287, 320, 325, 369, 383, 422, 459, 460, 461, 462, 463, 464, 470, 471, 472, 515
carbon cloth, 463
carbon nanotubes, xvi, 320, 369, 383, 459, 460, 471
carrier, 297, 370
cast, xvii, 336, 435, 436, 438, 440, 491, 492, 503, 512, 516
casting, 279, 324, 434, 436, 437, 439
catalyst, xvi, 373, 375, 378, 380, 459, 460, 461, 462, 463, 464, 465, 466, 467, 468, 470, 471, 472
catalytic activity, xvi, 459, 460, 470, 471
category a, 19
cathode, 133, 350, 398, 399, 463, 471
cation, 214, 216, 228, 418
cavities, xiii, 271
CCC, 353, 363
ceramics, xi, 13, 14, 86, 87, 90, 93, 94, 96, 97, 98, 99, 101, 103, 104, 105, 107, 109, 110, 111, 112, 113, 114, 115, 116
channels, 228, 266
charge density, 295, 298
chemical composition, 19, 109, 130, 132, 297, 376, 396, 397, 446
chemical etching, 372
chemical reactions, xiv, 272, 281
chemical vapor deposition, 372, 380, 383, 396
China, 282, 292, 369, 433, 459, 461, 462
chloride, xv, 350, 395, 396, 397
chlorine, 325
chromatography, 331

Copyright © 2010. Nova Science Publishers, Incorporated. All rights reserved.

Handbook of Material Science Research, Nova Science Publishers, Incorporated, 2010. ProQuest Ebook Central,

chromium, 151, 300, 301, 315
circular dichroism, 310
classical, xiii, 5, 14, 63, 86, 201, 203, 204, 205, 221, 271, 272, 273, 281, 286, 385, 473
classification, 423, 424
cleavage, 185, 186, 187
closure, xvii, 491, 492, 493, 495, 497, 498, 515, 516
clouds, 334
clustering, 174, 183, 189, 191, 192, 193, 195, 197, 198, 199, 208, 209
clusters, 15, 21, 22, 102, 103, 111, 112, 158, 174, 178, 192, 193, 197, 202, 209, 254, 366, 418
CNTs, 460
CO2, 423
coagulation, 154, 166
coatings, xiv, 127, 151, 347, 348, 349, 350, 351, 352, 353, 355, 356, 357, 358, 359, 361, 362, 363, 364, 365, 366, 367
cobalt, xi, xv, xvi, 300, 348, 353, 354, 360, 361, 363, 395, 396, 402, 404, 408, 409, 413, 414, 445, 446, 447, 448, 449, 450, 451, 453, 454, 456, 457, 458, 461
codes, 276, 351, 355
coherence, 185
cohesion, 291
collaboration, 210
collisions, 145
combined effect, 129
combustion, 275, 284, 343
compaction, 338
compatibility, 324
competition, 7, 282, 309, 312, 316, 493
components, xiv, xvi, 38, 43, 44, 46, 47, 51, 103, 107, 115, 146, 165, 243, 255, 343, 347, 445, 458, 476, 477, 482
composites, xi, xii, 105, 173, 174, 175, 180, 183, 187, 189, 191, 193, 195, 198, 199, 208, 209, 438, 441, 442
compressibility, 298
compressive strength, 281
computation, xv, 286, 417, 418, 419, 482
concentration ratios, 397, 399, 407
condensation, 21, 22, 327, 396
conducting polymers, 460
conduction, 132, 191, 216, 222, 283, 284, 301, 309, 312, 316, 317
conductive, 189, 262
conductivity, xii, 135, 176, 179, 180, 181, 183, 184, 187, 191, 192, 193, 194, 195, 196, 197, 198, 199, 209, 213, 214, 216, 217, 218, 222, 225, 226, 227, 228, 231, 257, 266, 316, 319, 371, 460, 468, 471
conductor, 35, 38, 178, 180, 189, 195, 197, 200, 360, 472
configuration, 14, 24, 35, 74, 175, 206, 208, 214, 216, 287, 434, 436, 446, 447, 464
confinement, 386
congruence, 486, 487, 488
conjecture, 316, 486, 488
connectivity, 176
constraints, 45, 46
construction, xvii, 280, 473, 474, 479
continuity, 181
control, xi, xiv, 35, 146, 182, 279, 323, 325, 352, 380, 383, 439, 456, 457
convection, 148, 168, 272, 472
convective, 274
conversion, 134, 203, 204, 205, 206, 207, 208, 209, 353
convex, 503
cooling process, 439
copper, xii, 35, 213, 214, 215, 216, 227, 229, 257, 397, 409, 412, 413, 436, 437, 439
correlation, 8, 9, 17, 21, 138, 175, 176, 178, 179, 183, 187, 300, 304, 314, 316, 336, 425
correlation coefficient, 425
correlations, 17, 23, 131
corrosion, xi, xiv, 127, 158, 167, 347, 348, 352, 353, 355, 357, 359, 360, 363, 365, 366, 367, 433, 440, 457, 460, 515
corrosive, 348, 358, 359, 360, 397
Coulomb, 204, 397
coupling, 4, 9, 27, 52, 54, 59, 73, 82, 83, 174, 185, 203, 209, 214, 216, 221, 265, 371
coupling constants, 59, 221
covalent, 20, 22, 222, 296, 299
covalent bond, 20, 22, 222, 296
covering, 373
Cp, 235, 236, 354
crack, xvii, 272, 273, 274, 276, 277, 278, 279, 280, 281, 282, 283, 284, 285, 286, 287, 288, 289, 290, 491, 492, 493, 494, 495, 496, 497, 498, 499, 501, 502, 506, 507, 510, 511, 512, 513, 515, 516
cracking, 272, 279, 282, 289
creep, xvi, 445, 446, 448, 449, 450, 451, 453, 456, 457
critical analysis, 516
critical behavior, 174, 176, 178, 180, 183, 208
critical current, 185, 186
critical current density, 185, 186
critical points, 204
critical temperature, 112, 116, 130, 178, 185, 200, 298, 302, 304, 306, 307, 308, 311, 313, 320
critical value, 20, 128, 129, 173, 273, 280, 498
crystal growth, 14
crystal lattice, 140, 151, 227, 254, 296, 299, 306, 313, 314, 336, 344

Copyright © 2010. Nova Science Publishers, Incorporated. All rights reserved.

Handbook of Material Science Research, Nova Science Publishers, Incorporated, 2010. ProQuest Ebook Central,

crystal structure, xi, xii, xiv, 11, 173, 174, 295, 296, 298, 300, 310, 319, 383, 404, 420
crystalline, xii, xiv, 6, 22, 173, 174, 200, 203, 208, 209, 263, 308, 310, 323, 325, 328, 336, 342, 345, 365, 373, 376, 380, 382, 407, 414, 434, 438
crystallisation, 327
crystallites, 366, 404, 405, 406, 409, 410
crystallization, xiv, 147, 323, 324, 325, 326, 327, 329, 339, 341, 342, 344, 406, 434, 435, 436, 438, 440
CST, 334, 338
cuprate, xi, xii, 173, 174, 183, 185, 186, 187, 191, 193, 194, 197, 198, 205, 208
cuprates, xi, xii, 173, 174, 185, 186, 202, 210
cyanide, 350, 353
cycles, xv, 18, 417, 423, 434, 467, 482, 485, 508
cyclic voltammetry, xvi, 459, 463
cycling, 18
cyclohexanone, 326, 327

D

damping, 18, 74, 106, 216, 274
data analysis, 75
data set, 421, 422
database, 422, 425
dating, 125
DBP, 52, 61
decay, 5, 24, 29, 166, 228, 231, 238, 335, 339
decomposition, 45, 46, 47, 152, 154, 273, 329, 342, 345
deconvolution, 134
defects, xiii, 25, 34, 74, 140, 145, 222, 246, 271, 272, 273, 275, 276, 281, 289, 328, 336, 337, 338, 342, 345, 408, 460, 493, 503, 515, 516
deficiency, 181
definition, 29, 50, 97, 238, 474, 476, 480, 483, 497
deformability, 438
deformation, 19, 128, 186, 187, 214, 273, 276, 277, 278, 282, 283, 285, 288, 300, 314, 334, 396, 438, 474, 477, 499
degenerate, 115
degradation, 189, 467
degrading, 186, 189
degrees of freedom, 6, 71, 274, 284
dendrites, 438
density functional theory, 420
density values, 359, 365, 420
Department of Homeland Security, 342
deposition, xiv, xv, 133, 158, 165, 347, 348, 349, 350, 351, 353, 354, 355, 366, 372, 380, 383, 395, 396, 398, 399, 402, 404, 406, 414, 460
deposits, xiv, xv, 347, 348, 350, 355, 359, 395, 397, 399, 401, 402, 403, 404, 406, 408, 409, 412, 415
desorption, 467
destruction, 39
detection, 125
detonation, xiii, 271, 272, 275, 289, 291, 293, 329, 339, 340, 341, 344, 423, 424, 427
deuteron, 71, 73, 81, 85
deviation, 16, 50, 51, 62, 127, 178, 191, 196, 199, 209, 216, 265, 310
diamagnetism, 207
diamond, 134, 135, 175, 392
dielectric constant, 12, 176, 178, 385
dielectric function, 30, 33, 105, 106, 115, 240, 242
ielectric relaxations, 85, 105
dielectric strength, 106, 234, 236, 238
dielectrics, 34, 60
Dienes, ix, 271, 276, 277, 278, 279, 280, 281, 282, 283, 284, 285, 286, 287, 288, 289, 290, 291, 292, 293
diffraction, 13, 15, 23, 25, 134, 149, 152, 156, 161, 162, 165, 304, 310, 316, 329, 373, 376, 378, 397, 405, 407, 462, 464, 466
diffusion, 13, 21, 128, 131, 135, 136, 140, 141, 145, 147, 148, 149, 152, 156, 159, 162, 168, 222, 273, 352, 399, 471
diffusion time, 168
digital images, 402
dimensionality, 174, 175, 183, 187, 191, 193, 197, 198, 199, 208
diodes, 129, 369
dipole, 2, 4, 5, 9, 11, 17, 20, 21, 23, 24, 25, 26, 28, 33, 59, 62, 65, 75, 82, 214, 221, 242, 386
dipole moment, 4, 5, 11, 17, 21, 25, 26, 62, 65
directionality, 414
discretization, 43, 44, 242
discrimination, 338
dislocation, 128, 129, 132, 136, 139, 282, 494, 498, 499
dislocations, xiv, 128, 139, 140, 254, 323, 324, 328, 336, 342, 409, 413, 494, 495
disorder, xii, 6, 7, 13, 14, 15, 19, 20, 21, 25, 73, 76, 82, 83, 85, 102, 112, 115, 116, 213, 214, 218, 219, 248, 249, 266
dispersity, 144
displacement, 17, 22, 214, 215, 216, 259, 260, 279, 282
distortions, 9, 15, 73, 74
distribution function, xi, 1, 15, 20, 21, 27, 28, 29, 30, 31, 32, 33, 34, 48, 49, 50, 51, 62, 67, 72, 74, 75, 85, 97, 102, 238, 239, 240, 241
disulfide, 306, 310, 312
divergence, 106

Copyright © 2010. Nova Science Publishers, Incorporated. All rights reserved.

Handbook of Material Science Research, Nova Science Publishers, Incorporated, 2010. ProQuest Ebook Central,

domain walls, 19, 414
dominance, 309
donor, 422
dopant, 185, 186, 222
doped, 159, 161, 467
doping, 201
drop test, 276, 289
drowning, 324, 325, 327, 329
drugs, 418
drying, 329, 330
DSC, xv, 395, 397, 407, 408, 410, 412
ductility, xvi, 186, 283, 438, 445, 446, 449, 450, 456, 457
duration, 127, 129, 130, 131, 132, 135, 158
dynamic loads, 288

E

earth, xii, xiv, 173, 174, 200, 201, 206, 295, 296, 317, 319
earthquake, 281, 292
egg, 272, 276, 282
eigenvector, 106, 107
elastic constants, 285
elastic deformation, 277
elasticity, 250, 273, 279
electric conductivity, 225, 226
electric field, xiii, 2, 4, 5, 11, 14, 18, 19, 20, 24, 25, 26, 28, 37, 38, 73, 74, 103, 104, 181, 213, 225, 228, 229, 231, 262, 265, 266, 336, 385
electrical conductivity, 183, 187, 222
electrical properties, 222
electrical relaxation, 225, 228
electrocatalysis, 461, 467, 470
electrocatalyst, 471
electrochemical deposition, 396
electrochemistry, 468, 470
electrocrystallization, 399
electrodeposition, xi, xiv, xv, 347, 348, 349, 350, 351, 353, 354, 395, 396, 397, 404, 406
electrodes, 37, 133, 296, 397, 463, 470, 471
electrolyte, xiv, xv, 347, 349, 350, 351, 353, 354, 355, 358, 360, 367, 395, 397, 398, 399, 401, 402, 403, 404, 405, 406, 407, 409, 410, 412, 414, 462, 471, 472
electromagnetic, 4, 35, 38, 385
electromagnetic waves, 4, 35, 38
electron, xii, xiv, 14, 17, 54, 73, 74, 75, 81, 126, 132, 134, 145, 173, 216, 228, 295, 296, 299, 310, 316, 317, 319, 331, 332, 372, 373, 374, 379, 387, 397, 448, 462, 464
electron beam, 17, 126, 145, 373, 387
electron density, 228
electron diffraction, 374, 379, 464
electron microscopy, xii, 14, 17, 125, 134, 331, 332, 334, 336, 372, 373, 376, 448, 462
electron spin resonance, 73
electron state, 216, 299, 316, 319
electronic structure, 304, 313, 319, 466
electron-phonon, 216
electrons, 133, 174, 204, 301, 304, 306, 309, 311, 312, 313, 314, 315, 316, 317, 319
elongation, 438, 452, 455
emission, 18, 369, 385, 386, 387, 388, 389, 397
emission field, 387
EMP, 127
Empedocles, 392
ENDOR, 73, 74, 75, 81, 82, 83, 84
energetic materials, xi, xiv, 323, 324, 328, 332, 336, 341, 342, 343, 344, 345
energy density, 127, 128, 129, 130, 131, 132, 133, 342
energy transfer, 145, 155
engines, xvi, 445, 446
entropy, 435
environment, 47, 275, 348, 358, 359, 360
environmental regulations, xiv, 347, 348
epitaxial growth, 383
epitaxy, 383
epoxy, 333
equality, 45
equilibrium, xv, 4, 5, 8, 11, 22, 24, 25, 28, 145, 156, 251, 327, 366, 395, 396, 406, 495
ESR, 73, 74, 306
ethanol, xvi, 31, 87, 241, 325, 326, 350, 459, 462, 464
ethylenediamine, 372
ETI, 127
evaporation, 127, 129, 158, 187, 324, 325
evolution, xv, 12, 17, 20, 22, 24, 215, 228, 335, 355, 357, 395, 396, 397, 399
EXAFS, 15
excitation, 23, 260, 387, 388, 389
exciton, 386
experimental condition, 388, 497
explosions, xiii, xiv, 271, 272, 275, 282, 286, 287, 288, 289, 292, 332
explosives, xi, xiii, xiv, 271, 273, 276, 279, 281, 286, 288, 290, 292, 293, 323, 324, 334, 336, 341, 344, 345, 420, 427
exposure, 357, 359
extraction, 67
extrapolation, 319, 359

Copyright © 2010. Nova Science Publishers, Incorporated. All rights reserved.

Handbook of Material Science Research, Nova Science Publishers, Incorporated, 2010. ProQuest Ebook Central,

F

fabrication, 186, 279, 472
fatigue, xi, xvii, 491, 492, 493, 494, 495, 496, 497, 498, 500, 501, 502, 503, 506, 507, 510, 511, 512, 514, 515, 516
FCC, xv, 395, 396, 405, 406, 409, 410, 413, 414
Fermi level, 299, 301, 306, 316, 319
ferrite, 136, 138, 143, 144, 146
ferroelectrics, xi, 1, 2, 6, 11, 13, 14, 17, 19, 21, 25, 28, 35, 52, 54, 55, 58, 59, 63, 66, 71, 85, 86, 87, 105, 115, 116, 218, 219, 233, 236, 238, 248, 249, 267
ferromagnetic, 296, 301, 304, 305, 307, 309, 310, 316, 320, 413
ferromagnetism, 439
ferromagnets, 312
fiber optics, 339
fibers, 334
field theory, 2, 20, 489
film, 102, 149, 150, 158, 159, 178, 396, 397, 470, 472
films, 85, 112, 127, 276, 372, 383, 396, 397, 434, 470, 472
filtration, 324, 325
flow, xii, 125, 132, 135, 156, 158, 160, 163, 165, 167, 283, 407, 408, 411, 438, 462, 463
flow rate, 462, 463
fluctuations, 13, 17, 19, 20, 22, 25, 74, 102, 130, 252, 282, 304, 316, 322
fluid, 284
flux pinning, 185
formaldehyde, 462, 472
Fortran, 47
Fourier, 33, 331, 488
Fourier transform infrared spectroscopy, 331
fractal structure, 175
fracture, xvi, 280, 281, 288, 292, 437, 438, 446, 448, 451, 452, 455, 456, 457, 492, 493, 507, 508, 511, 512, 515, 516
fragmentation, 292, 338, 438
framing, 475, 477
free energy, 2, 3, 23, 251, 252, 253, 410
free volume, 222, 413
freezing, 7, 8, 26, 28, 70, 71, 72, 75, 81, 90, 97, 102, 112, 116, 216, 236, 303, 304, 306, 307, 308, 311
frequency distribution, 27
friction, 165, 167, 278, 281, 282, 286, 289, 290, 291, 292, 323
fuel cell, xvi, 459, 460, 463, 470, 471, 472
function values, 366
functionalization, 460
fusion, 126

G

GaAs, 372, 378, 379, 382, 383, 384, 386, 387
gadolinium, 297, 299
gas, xiii, 132, 133, 145, 271, 274, 284, 292, 297, 369, 396, 421, 446, 462, 471
gas phase, 284, 292, 421, 462
gas turbine, 446
gases, 152, 159, 274, 282
gauge, 334, 336, 448
Gaussian, 8, 10, 26, 62, 84, 377, 378, 429
GAUSSIAN, 420
generalization, xvii, 273, 473, 474, 486, 488
generation, 127, 128, 129, 214, 436
generators, 39, 131, 132, 145, 168, 476, 477, 482, 483, 485, 487, 488
geology, 283
Ger, 391, 392
Germany, 343, 344, 345, 430
glass transition, 10, 74, 75, 436
glass transition temperature, 74, 436
glasses, xi, xiii, xv, 6, 7, 8, 9, 10, 12, 23, 24, 27, 28, 29, 32, 35, 53, 60, 73, 75, 76, 79, 81, 82, 85, 115, 116, 213, 238, 239, 241, 245, 246, 247, 306, 308, 433, 440, 441
glassy state, 6, 75, 84, 85, 257, 258
gold, 373
government, viii
grades, 332, 333, 334, 337, 338, 341
grain boundaries, xvi, 141, 324, 328, 445, 446, 447, 448, 449, 450, 451, 452, 453, 455, 456, 457
grain boundary structure, 408
graph, xvii, 473, 474, 477, 478, 479, 480, 481, 482, 483, 484, 485, 486, 487, 488, 505
groups, 10, 51, 54, 73, 83, 214, 216, 337, 390, 423, 434, 460, 461, 489
growth mechanism, xv, 355, 395
growth rate, 281, 380, 496, 497
growth temperature, 378, 380, 383

H

H1, 22, 41, 73, 502
H_2, 22, 353, 462, 463, 466, 467, 468, 469, 471
Hamiltonian, 6, 8, 9, 21, 22, 26
hardening, xii, 102, 125, 126, 127, 128, 129, 130, 131, 132, 134, 139, 140, 145, 151, 152, 154, 156, 157, 159, 161, 163, 165, 166, 167, 168, 278, 495
hardness, 126, 127, 129, 132, 138, 154, 163, 164, 165, 397, 440, 446, 447, 497, 498, 503, 505, 506, 511, 512
healing, 292

Copyright © 2010. Nova Science Publishers, Incorporated. All rights reserved.

Handbook of Material Science Research, Nova Science Publishers, Incorporated, 2010. ProQuest Ebook Central,

heat, xi, xiv, xv, xvi, 13, 17, 128, 129, 130, 132, 135, 136, 145, 164, 167, 178, 185, 272, 274, 283, 284, 296, 304, 310, 353, 408, 417, 421, 422, 423, 424, 428, 440, 445, 446, 447, 448, 450, 451, 453, 456, 457
heat capacity, 440
heat release, 408
heating, xiii, 12, 99, 100, 102, 103, 111, 112, 116, 127, 129, 130, 131, 215, 222, 253, 255, 257, 258, 262, 264, 271, 272, 274, 278, 281, 282, 283, 287, 289, 303, 329, 397, 407, 408, 409, 411, 412, 413, 414, 415, 434
heating rate, 329, 397, 407, 411, 413
helium, 134
heterocycles, 422
heterogeneity, 24
heterogeneous, 138, 343, 434
heterostructures, 372
hexagonal lattice, 300
high resolution, 376, 462
high temperature, xvi, 3, 11, 15, 17, 20, 25, 26, 59, 90, 97, 99, 102, 127, 130, 164, 168, 216, 221, 248, 266, 380, 445, 446, 457
high-frequency, 31, 35, 42, 44, 54, 105, 107, 111, 218, 222, 225, 229, 240, 243, 439
high-performance liquid chromatography, 331
high-speed, xii, 125, 129, 134, 154, 159, 161, 162, 164, 165, 166, 167, 168, 275
high-Tc, 185, 186, 187
histogram, 33
HNF, 325, 326
homogeneity, 66, 156, 297, 436
homogenized, 87, 297
homogenous, 272
homomorphism, 480, 484, 485
hot spots, xiii, 271, 272, 274, 275, 282, 288
humidity, 55
hybridization, xii, 14, 173, 174, 200, 201, 204, 206, 207, 208, 209, 299, 301, 310, 311, 313, 314, 315, 316, 317, 319
hydrates, 360
hydro, 276, 282, 422
hydrocarbons, 422
hydrodynamics, 286, 288
hydrogen, xi, xv, 1, 51, 52, 54, 62, 67, 73, 74, 75, 81, 83, 133, 139, 140, 320, 353, 355, 366, 395, 396, 397, 399, 422, 462, 463, 467, 471, 515
hydrogen atoms, 51
hydrogen bonds, xi, 1, 51, 52, 67, 73, 74, 75, 81, 83
hydrostatic pressure, 316
hydroxide, 360
hydroxyl, 339
hysteresis loop, 24, 25, 246, 310, 320

I

ICT, 343, 344, 345, 422, 430
idealization, 272, 281, 287
IDP, 341
images, 137, 145, 146, 163, 333, 334, 374, 375, 379, 380, 381, 382, 384, 386, 387, 402, 463, 464, 465, 475
IMF, 367, 368
immersion, 126, 336, 352, 355, 356, 357, 358, 359, 360, 361, 362, 363, 367
impurities, 9, 20, 21, 66, 134, 138, 139, 144, 156, 215, 233, 254, 336, 342, 460, 463
in situ, xvi, 438, 459, 462
inclusion, 73, 333, 492, 493, 503, 512
indication, 261, 264, 266, 298
indicators, 336
indices, 326, 336, 373, 376
indium, xii, 213, 214, 215
industrial, xiv, xvi, 348, 353, 363, 433, 440, 441
industrial application, xvi, 433, 440
industrial production, 441
industry, 126
inequality, 45, 46
inert, 275, 289, 396, 460
inertia, 274
inertness, 186
infinite, 4, 8, 13, 24, 178, 191, 280, 509
infrared, xii, 1, 74, 105, 115, 331
infrared spectroscopy, 331
inhibition, 354, 366
inhomogeneities, 515
inhomogeneity, 208
initial state, 161
initiation, xiv, 272, 273, 274, 281, 284, 286, 288, 289, 293, 323, 324, 328, 334, 335, 336, 338, 339, 341, 344, 446, 492, 498
injection, xii, 125, 158
Innovation, 347, 367
inorganic, 51, 74
InP, 390
inspection, 103, 236
instability, 11, 14, 22, 28, 214, 216, 274, 282, 284, 286, 287, 290
integration, 5, 63
integrity, 275
interaction, 6, 7, 8, 9, 10, 22, 26, 33, 74, 75, 82, 83, 84, 115, 132, 158, 165, 207, 208, 216, 221, 242, 257, 266, 274, 289, 296, 298, 301, 304, 305, 306, 309, 313, 316, 317, 319, 320, 342, 436, 466
intercalation, 296, 297, 299, 300, 304, 306, 310, 312, 313, 314, 317, 319, 320
interface, 39, 273, 282, 290, 438

Copyright © 2010. Nova Science Publishers, Incorporated. All rights reserved.

Handbook of Material Science Research, Nova Science Publishers, Incorporated, 2010. ProQuest Ebook Central,

interference, 378, 381, 510
interphase, 125
interstitial, 131
interval, xv, 14, 18, 21, 22, 26, 54, 133, 216, 228, 257, 263, 309, 320, 395, 413, 476, 481
intrinsic, 9, 132, 181, 186, 202, 389, 486
invariants, xvii, 473, 474, 488, 489
Investigations, 136, 139
ion beam, 126, 127
ion implantation, 126, 128
ionic, xii, 4, 13, 14, 17, 22, 173, 201, 204, 205, 206, 208, 209, 214, 216, 218, 222, 225, 226, 228, 257, 298, 300, 305, 342, 349
ionic conduction, 222
ionic liquids, 342
ionic-covalent, 222
ionization, 128
IOP, 56, 58, 60, 69
IR spectra, 107, 109, 115
IR transmission, 112
iron, xi, xii, 125, 128, 129, 134, 135, 136, 137, 138, 139, 140, 141, 142, 147, 149, 151, 160, 161, 167, 307, 310, 348, 360, 397, 404, 472, 499
irradiation, 17, 127, 132
isolation, 378
isomers, 420
isomorphism, 161, 480, 484, 485
isothermal, 229, 231
isotherms, 331, 332
isotope, 52
isotropic, 14, 15, 73, 105, 277, 385

J

J_c, 185, 186
JEM, 462
joints, 407
Josephson coupling, 174
Joule heating, 282

K

kernel, 43, 44, 243
kinematics, 273
kinetic model, 28, 494
kinetics, xiv, 28, 292, 347, 367, 378, 383, 399, 406, 472
knot theory, 473, 475
knots, xvii, 473, 474, 477, 479, 488

L

L1, 210
Lagrangian, 293
lamella, xii, 173, 185, 187, 193, 197, 199, 208, 209
lamellae, 214
lamellar, 153, 174, 186, 187, 191, 214
Landau theory, 2, 252
laser, 126, 140, 145, 160, 276, 331, 333, 334, 387
lasers, 128
lasing threshold, 369
lattice parameters, 151, 215, 298, 300, 404
lattices, xii, 4, 175, 213
LDP, 45, 46, 47
lens, 477, 488
light-emitting diodes, 369
linear, xvii, 4, 5, 8, 15, 20, 24, 27, 35, 36, 39, 42, 43, 45, 103, 106, 131, 156, 180, 194, 196, 219, 226, 242, 265, 277, 278, 310, 472, 473, 478, 482, 483, 485, 510, 516
linear dependence, 156, 180, 219, 265
linear function, 103
links, xvii, 179, 299, 460, 465, 473, 474, 475, 476, 479, 482, 486, 488, 489
liquid chromatography, 331
liquid nitrogen, 35
liquid phase, 148, 168, 436
liquids, 5, 31, 228, 241, 342
lithium, 255, 261, 296
Lithuania, 1, 213
loading, xvi, 134, 328, 331, 448, 459, 462, 463, 466, 468, 469, 471, 494, 495, 497, 498, 499
localization, 200, 201
losses, 34, 41, 42, 87, 99, 102, 103, 104, 218, 234, 236, 249
low temperatures, xii, 13, 19, 23, 24, 25, 28, 31, 61, 72, 75, 76, 81, 83, 84, 85, 102, 115, 185, 197, 213, 238, 240, 248, 249, 266, 300, 301, 302, 306, 307, 310, 311, 313, 320
low-temperature, 6, 11, 21, 23, 25, 26, 51, 54, 72, 75, 115, 215, 301, 313, 318
LTD, 461

M

M.O., 169
M1, 107
magnesium, 103
magnetic field, 8, 9, 128, 132, 134, 205, 286, 301, 303, 304, 309, 318, 320, 383, 398, 413
magnetic materials, 397, 440, 441

Copyright © 2010. Nova Science Publishers, Incorporated. All rights reserved.

Handbook of Material Science Research, Nova Science Publishers, Incorporated, 2010. ProQuest Ebook Central,

magnetic moment, xiv, 7, 207, 295, 296, 301, 302, 304, 306, 307, 308, 310, 311, 313, 314, 315, 316, 318, 319
magnetic properties, xiv, xv, xvi, 295, 296, 306, 310, 313, 315, 316, 319, 320, 395, 397, 413, 433, 434, 437, 438, 439, 440, 441
magnetic resonance, 75, 83
magnetic sensor, 439
magnetism, 316, 317, 440
magnetization, 9, 23, 301, 304, 305, 309, 310, 318, 319, 413, 439
magnetoresistance, 320
magnetostriction, 439
manganese, 306, 314
manifolds, xvii, 473, 474, 475, 476, 480, 488, 489
Markov, 169, 170, 171
materials science, xi, 433, 443
mathematical methods, 289
matrix, 13, 14, 19, 35, 36, 43, 44, 45, 46, 47, 102, 107, 112, 180, 181, 183, 214, 242, 243, 285, 301, 309, 310, 311, 313, 314, 316, 317, 320, 338, 342, 409, 438, 446, 447, 449, 450, 456, 457, 461, 464, 470, 493, 498, 505, 506, 511, 512
mean-field theory, 8
mean-square deviation, 127
measurement, 34, 35, 71, 75, 82, 83, 103, 129, 154, 187, 218, 265, 351, 355, 357, 359, 363, 375, 381, 387, 463, 516
measures, 35
mechanical behavior, 273
mechanical properties, 128, 130, 144, 145, 146, 152, 154, 158, 160, 286, 440
media, 175, 176, 178, 180, 183, 208, 385
melt, 128, 129, 130, 132, 147, 149, 283, 324, 434, 435
melting, 55, 127, 129, 130, 149, 153, 158, 272, 273, 278, 281, 283, 284, 289, 324, 329, 438
melting temperature, 153, 324, 329
membranes, 329
MEMS, 343, 396
Merck, 349
mesoscopic, 11, 23
metal ions, 311, 404
metal nanoparticles, 471
metallurgy, 171
metals, ix, xi, xiv, 128, 131, 170, 171, 295, 296, 299, 300, 306, 312, 314, 316, 317, 319, 320, 360, 366, 396, 397, 404, 408, 434, 462, 470, 515
methanol, xvi, 325, 326, 459, 460, 461, 462, 463, 468, 470, 471, 472
Mg^{2+}, 13, 14, 15, 19, 20
micro-alloyed, 125
micrometer, 438
microparticles, 470
microscope, 134, 378, 387, 397, 448, 462
microscopy, xii, 14, 17, 125, 134, 331, 332, 333, 334, 336, 341, 372, 373, 376, 448, 462, 516
microstructure, xiv, xv, 129, 130, 347, 395, 397, 438, 440, 461
microstructures, xi, xvi, 445, 446, 447, 448, 451, 452, 455, 456, 457
microwave, 35, 39, 40, 41, 42, 52, 55, 85, 87, 99, 102, 111
microwaves, 87
military, 418, 427
Millennium, 292
millimeter waves, 55
mixing, xii, 125, 132, 145, 146, 148, 158, 166, 168, 274, 289, 325, 329, 436, 462, 463
mobility, 222, 226, 231, 370, 414, 435
MOCVD, 372, 373, 380, 383
modeling, 281, 425, 428
models, 18, 19, 20, 26, 28, 33, 61, 63, 65, 73, 75, 82, 85, 105, 107, 127, 180, 183, 242, 289
modulation, 73, 388
modules, xvii, 473, 474, 477, 480, 489
modulus, 41, 106, 222, 225, 228, 229, 231, 278, 290, 338, 434, 438, 495, 503
molar ratio, 461
molar volume, 420
mold, 436, 437, 439
molecular beam, 383
molecular beam epitaxy, 383
molecular dynamics, 345
molecular structure, xv, 417, 418, 419, 421, 423, 428
molecules, xv, 6, 51, 116, 296, 298, 342, 417, 418, 419, 420, 423, 425
monolayer, 158
monomers, 461, 462, 463
morphological, 181, 191, 380
morphology, xi, xii, xiv, xv, 134, 136, 139, 147, 162, 173, 174, 176, 187, 193, 197, 199, 208, 209, 343, 347, 372, 373, 379, 380, 395, 396, 397, 399, 402, 414, 415, 435, 436, 462, 464
Mössbauer, xii, 125, 134
motion, 13, 25, 76, 216, 219, 220, 228, 231, 273, 284
motivation, 474
mouth, 349
movement, 4, 61, 228, 266
MRD, 397
MRS, 442
multiphase alloys, 366
multiwalled carbon nanotubes, xvi, 459, 460, 471

Copyright © 2010. Nova Science Publishers, Incorporated. All rights reserved.

Handbook of Material Science Research, Nova Science Publishers, Incorporated, 2010. ProQuest Ebook Central,

N

NaCl, 134, 351, 352, 355, 356, 357, 358, 359, 360, 361, 362, 363, 364, 367
Nafion, 463, 470
nanobelts, 369, 374, 386, 390
nanocomposites, 471
nanocrystalline, xv, 127, 395, 396, 397, 408, 409, 410, 413, 415, 440
nanocrystalline alloys, 413
nanocrystals, 369, 370, 385
nanodevices, 379
nanomaterials, 320, 328, 329, 344
nanometer, xii, 11, 14, 23, 173, 174, 205, 208, 407, 409, 460
nanometer scale, 11, 205, 407
nanometers, 370, 372, 373, 379, 385
nanoparticles, 461, 470, 471
nanorods, 369, 379, 380, 381, 382, 383, 386, 390
nanostructured materials, 396
nanostructures, xv, 126, 343, 370, 371, 372, 373, 378, 379, 380, 381, 382, 383, 384, 390
nanotechnology, 328
nanotubes, xvi, 320, 369, 383, 459, 460, 471, 472
nanowires, xv, 369, 371, 372, 373, 379, 380, 383, 384, 385, 386, 387, 388, 389, 390
National Academy of Sciences, 172
Navy, 272
Nb, 14, 15, 17, 20, 21, 22, 183, 184, 317, 320, 434, 435, 436, 438, 439
Nd, 200, 206, 434, 435
negative relation, 198
NEMS, 396
network, xiii, xv, 178, 179, 183, 195, 197, 199, 209, 272, 280, 300, 383, 384, 417, 420, 422, 425, 427, 428
neural network, xv, 417, 422, 425, 427, 428
nickel (Ni), xv, 129, 131, 132, 134, 296, 312, 313, 320, 321, 365, 395, 396, 397, 399, 401, 402, 404, 405, 406, 408, 409, 410, 412, 413, 414, 434, 436, 438, 441, 446, 447, 470
nickel oxide, 408
nitrides, 138, 142, 144, 149, 151, 159, 162, 166, 167
nitrogen, 35, 131, 135, 136, 138, 139, 140, 141, 144, 146, 147, 149, 152, 156, 158, 159, 161, 162, 163, 165, 167, 342, 345, 418
NMR, 15, 25, 27, 28, 73, 86, 102
N-N, 423
nodes, 179
nonequilibrium, 145
non-linearity, 27
non-magnetic, xiv, 295, 304
nonstoichiometric, 13
normal conditions, 372, 378, 383
normal distribution, 506
normalization, 29, 102, 159, 238
novelty, 434
NQR, 331, 334, 336, 338, 341, 344, 345
nuclear, 73, 126, 334
nuclear magnetic resonance, 73
nuclear power, 126
nucleation, 129, 324, 325, 327, 329, 355, 366, 380, 409, 434
nuclei, 22, 324, 325, 336, 402, 409

O

observations, xiii, 271, 280, 298, 336, 379, 384, 386, 480
oil, 134, 278, 279, 462
oil shale, 278
one dimension, 9, 51, 220
opacity, 281
optical, 4, 24, 25, 74, 106, 126, 134, 216, 228, 298, 332, 333, 336, 338, 341, 388, 389, 448, 451, 456, 470
optical anisotropy, 390
optical micrographs, 332, 336, 338, 451, 456
optical microscopy, 134, 332, 336, 341
optical properties, 298
optimization, 33, 324, 421, 460
optoelectronic devices, 369, 390
organic, 51, 275, 291, 325, 380
organic solvents, 325
orientation, 5, 156, 273, 278, 282, 287, 288, 289, 327, 383, 384, 399, 408, 449, 480, 486
oscillation, xiii, 272
oscillations, 61
oscillator, 35, 105, 106, 107, 111
oxidation, xvi, 445, 446, 457, 459, 460, 461, 462, 463, 464, 465, 466, 467, 468, 469, 470, 471, 472
oxide, 87, 152, 222, 349, 360, 372, 408, 434, 493, 497
oxygen, xv, 14, 15, 20, 22, 112, 116, 152, 156, 207, 359, 417, 423, 463, 467, 471
ozone, 471

P

PANI, 472
parabolic, 3
paradox, 280
paramagnetic, 73, 74, 301, 303, 304, 306, 307, 308, 309, 311, 312, 313, 315, 316, 317, 318, 319
particle shape, xiv, 323, 324, 331, 404

Copyright © 2010. Nova Science Publishers, Incorporated. All rights reserved.

Handbook of Material Science Research, Nova Science Publishers, Incorporated, 2010. ProQuest Ebook Central,

particles, xvi, 135, 154, 158, 159, 164, 166, 174, 175, 180, 324, 325, 327, 328, 329, 330, 331, 332, 334, 338, 341, 342, 344, 345, 399, 404, 413, 438, 459, 460, 461, 463, 464, 472, 503, 504, 505, 506, 509, 510, 511, 512, 516
passivation, 348, 359
Pb, 13, 14, 15, 17, 22, 23, 25, 86, 102, 112, 113, 116, 185, 186, 236, 441
PDEs, 273, 284
pearlite, 142, 144, 145, 146, 153
percolation, xi, xii, xiii, 173, 174, 175, 176, 178, 179, 180, 183, 189, 190, 191, 192, 193, 194, 196, 197, 198, 199, 200, 201, 203, 204, 205, 206, 207, 208, 209, 272, 274, 278, 280, 281, 288, 290
percolation cluster, 175, 176, 179, 183
percolation theory, 174, 193, 288
periodic, 207, 286, 485, 486, 487, 489
periodicity, 474, 486, 489
permeability, xv, 279, 396, 397, 413, 414, 415, 438, 439
permittivity, 3, 4, 5, 6, 24, 28, 36, 37, 40, 44, 45, 50, 55, 73, 75, 82, 83, 87, 90, 97, 99, 100, 103, 105, 106, 107, 217, 218, 222, 228, 233, 236, 237, 243, 247, 248
perovskite, 13, 14, 15, 16, 17, 19, 20, 21, 24, 25, 87, 102, 112, 113
perovskites, 11, 12, 13, 14, 15, 20
pH, 349, 350, 351, 353, 359, 360, 362, 364, 396, 397
phase boundaries, 236
phase diagram, 7, 53, 54, 72, 103, 145, 171, 404, 413, 416
phase transformation, 13, 127, 410, 413, 415
phase transitions, xi, xiii, 1, 13, 19, 20, 22, 52, 63, 112, 116, 174, 209, 213, 216, 217, 218, 219, 236, 261, 266, 298
phenomenology, 275
phonon, xii, 1, 4, 6, 21, 22, 27, 74, 83, 99, 105, 106, 107, 111, 112, 115, 216, 260, 371
phosphate, xi, 1, 6, 51, 52, 55, 63, 66, 67, 71, 73, 74, 79, 83, 85, 115, 248
phosphorous, 51
photochemical, 372
photoconductivity, 389
photodetectors, 369
photoelectron spectroscopy, 317
photoemission, 314
photoluminescence, xv, 369, 371, 374, 385
physical properties, xi, xii, 11, 24, 173, 174, 180, 183, 185, 208, 214, 295, 298, 316, 379, 396
physicochemical, 420
physicochemical properties, 420
physics, 28, 170, 204, 280, 295
piezoelectric, xiii, 25, 85, 213, 214, 254, 257, 261, 262, 263, 264, 265, 266
piezoelectricity, 85, 261
PL spectrum, 378
planar, 36, 105, 473, 474, 475, 477, 483
plasma, xii, 106, 107, 125, 126, 128, 129, 130, 131, 132, 133, 135, 145, 156, 158, 160, 163, 165, 167, 168
plastic, xvii, 276, 277, 278, 282, 344, 396, 438, 491, 492, 494, 495, 497, 499, 512
plastic deformation, 396, 499
plastic strain, 276
plasticity, 273, 276, 279, 281, 282, 283, 438, 493
platelets, 397, 399, 413
platinum, 87, 350, 351, 460, 461, 462, 463, 465, 470, 471, 472
plausibility, 39
point defects, 128, 324
poisoning, 460
Poisson distribution, 507, 511
polarity, 74, 214
polarizability, 20
polyaniline, 460, 471, 472
polybutadiene, 339
polycrystalline, 174, 205, 296, 297, 309, 373, 446
polymer, xiv, 292, 323, 324, 336, 338, 460, 471, 472
polymer matrix, 338
polymerization, xvi, 459, 461, 462
polymers, xi, 460, 471
polynomial, 39, 474, 475, 476, 477, 479, 480, 481, 482, 484, 486, 488, 489, 497
polynomials, 487, 489
pores, 161, 187, 372, 438, 465, 468
porosity, 187, 188, 197, 471, 492, 493, 503, 507, 508, 512
potential energy, 229, 419
powder, xv, 23, 158, 185, 187, 215, 329, 334, 395, 396, 397, 399, 404, 406, 408, 409, 410, 414, 462
powders, xi, xv, 296, 329, 395, 396, 397, 399, 402, 407, 414, 415, 434, 463
power, xvi, 30, 39, 126, 131, 176, 177, 178, 180, 183, 185, 186, 191, 192, 193, 194, 195, 196, 197, 199, 208, 209, 215, 226, 239, 329, 420, 427, 439, 441, 459, 470
power transformers, 439
powers, 2, 419
Prandtl, 276
precipitation, xvi, 125, 156, 164, 189, 349, 438, 445, 446, 448, 450, 453, 456, 457
predicate, 9, 30, 85, 103, 222, 240
prediction, 418, 419, 420, 421, 422, 423, 425, 426, 428, 492, 503, 509

Copyright © 2010. Nova Science Publishers, Incorporated. All rights reserved.

Handbook of Material Science Research, Nova Science Publishers, Incorporated, 2010. ProQuest Ebook Central,

pressure, xiii, 27, 128, 132, 133, 148, 152, 159, 163, 165, 183, 214, 271, 272, 274, 275, 277, 284, 285, 286, 288, 316, 334, 335, 336, 338, 339, 423, 424, 427, 463, 515
pressure gauge, 334, 336
probability distribution, 8, 26, 507, 511
probe, 73, 74, 111, 187, 448
production, 324, 325, 329, 331, 339, 342, 344, 396, 404, 441
propagation, xvii, 4, 35, 38, 128, 329, 344, 491, 492, 493, 495, 497, 498, 501, 502, 506, 510, 511, 512, 516
proportionality, 265, 352
proposition, 248
propulsion, 329
protection, xiv, 347, 348, 353, 357, 359, 360, 363
protective coating, xiv, 347, 348
proton exchange membrane, 471
protons, 54, 61, 72, 73, 74, 83, 84
prototype, 175
PST, 13, 15, 85, 109, 111, 113
pulse, xiii, 127, 128, 129, 130, 131, 132, 133, 135, 136, 137, 138, 140, 141, 142, 143, 144, 145, 146, 148, 149, 150, 151, 152, 155, 158, 159, 160, 161, 163, 164, 165, 166, 168, 213, 252, 261, 262, 274, 286, 293, 309, 310, 318
pulsed laser, 387
pulses, xiii, 127, 129, 130, 131, 133, 136, 138, 146, 155, 159, 160, 162, 164, 165, 167, 168, 271, 292
PVA, 372
pyramidal, 373
pyrrole, xvi, 459, 461, 462, 463

Q

QSAR, 430
quadrupole, 73, 134, 143, 331, 334
quantitative technique, 341
quantum, xv, xvii, 61, 369, 370, 385, 389, 417, 428, 473, 474, 488, 489
quantum confinement, 386
quantum dot, 369, 370, 386, 389
quantum groups, 489
quartz, 261, 262, 263, 296, 407

R

radiation, xiv, 134, 272, 274, 289, 365, 397, 462
radical formation, 74
radius, 15, 37, 40, 41, 42, 127, 151, 156, 201, 206, 274, 278, 284, 285, 286, 300, 373, 498, 500, 501, 503, 509
Raman scattering, 112
Raman spectra, 216
Raman spectroscopy, 329
random, xiii, 6, 7, 8, 9, 10, 11, 14, 15, 19, 20, 21, 22, 25, 26, 27, 28, 34, 39, 73, 74, 75, 81, 82, 83, 84, 86, 102, 115, 181, 183, 191, 226, 247, 266, 271, 280, 288, 327, 409, 436
random errors, 39
randomness, 21, 204
rare earth elements, 200, 206, 317
reactant, 463, 466
reaction time, xiii, 271
reactivity, 329
reagents, 349
recrystallization, 129, 338
recrystallized, 338
recursion, 9
redistribution, 148, 152, 159, 165, 216
redox, 467
reflection, 35, 36, 38, 39, 40, 41, 42, 105, 130, 333, 404, 406, 413
reflectivity, xii, 1, 41, 105, 107, 109, 111, 112, 115
refraction index, 15, 18
refractive index, 16, 332, 333, 334, 336, 338
refractive indices, 336
regression, 422
relationship, xvii, 30, 33, 38, 70, 174, 180, 181, 198, 226, 236, 240, 242, 344, 384, 449, 473, 474, 480, 482, 486
relaxation effect, 510
relaxation process, 6, 13, 32, 241, 410
relaxation rate, 54, 71
relaxation times, xi, xii, 1, 8, 24, 29, 30, 32, 33, 43, 48, 50, 51, 58, 59, 61, 62, 67, 71, 72, 75, 77, 79, 85, 90, 96, 97, 98, 99, 103, 115, 116, 219, 238, 240, 242, 243, 244, 266
repetitions, 492, 496
reproduction, 210
resin, 333
resistance, xiv, xvi, 129, 145, 179, 188, 189, 199, 202, 225, 347, 348, 350, 352, 353, 355, 359, 360, 363, 364, 367, 433, 440, 445, 446, 457, 460
resistin, 446, 453
resistivity, 189, 190, 191, 192, 193, 194, 196, 200, 317, 320, 397, 413, 439, 440
resolution, 14, 17, 73, 126, 208, 289, 376, 377, 381, 386, 462, 487
resources, 419, 428
Rho, 391
rhombohedral, 17, 19, 25, 86, 109, 111
rings, 15, 480
risk, 275, 290
rods, 370, 380, 385, 435, 436, 437, 438

Copyright © 2010. Nova Science Publishers, Incorporated. All rights reserved.

Handbook of Material Science Research, Nova Science Publishers, Incorporated, 2010. ProQuest Ebook Central,

roughness, 127, 128, 130, 131, 139, 402, 493
roughness measurements, 402
rubidium, 6
Ruderman-Kittel-Kasuya-Yosida, 309
rust, 353, 363, 365

S

salt, 350, 353, 363, 364, 367, 372
sapphire, 112
saturation, 166, 304, 310, 316, 319, 413, 439
scalar, 45
scaling, 176, 177, 183, 194, 196, 199, 208
scanning calorimetry, xv, 332, 395
scanning electron microscopy, xii, 125, 134, 334, 336, 350, 373
scattering, 14, 17, 18, 23, 35, 36, 112
SDT, xiii, 47, 271, 272, 275, 282, 288
search, 236, 419, 428, 434
seeding, 325
seeds, 460
segregation, 147, 156, 222
selected area electron diffraction, 376, 448, 449
selecting, 379, 418
selenium, xiii, 213, 215, 228, 248, 258, 266, 372
SEM micrographs, 336, 337, 399, 401, 402, 403, 409, 412, 413
semiconductor, 200, 369
semiconductors, 216, 369, 385
sensitivity, xiii, xiv, xv, 213, 257, 263, 265, 271, 275, 282, 283, 284, 323, 324, 331, 332, 334, 336, 337, 338, 339, 341, 342, 343, 344, 345, 417, 418, 422, 425, 426, 427, 428
sensors, 369, 396, 439
separation, 331, 466
September 11, 344
shape, xiv, 3, 14, 17, 23, 27, 28, 39, 42, 50, 51, 73, 75, 135, 140, 147, 193, 197, 199, 209, 237, 272, 276, 278, 282, 297, 304, 323, 324, 326, 327, 331, 336, 342, 373, 378, 379, 380, 383, 389, 399, 404, 439, 503
sharing, 204, 208, 209
sharp notch, 492, 499
shear, xiii, 228, 271, 272, 273, 274, 276, 277, 278, 281, 282, 287, 288, 289, 290, 291, 438
shear deformation, 438
shock, xiii, xiv, 127, 128, 129, 130, 158, 271, 272, 274, 275, 286, 323, 324, 328, 334, 335, 336, 338, 339, 340, 341, 342, 343, 344, 345
shock waves, 127, 128, 129, 130, 342
shocks, 286
short period, 130
short-range, 4, 20, 21, 231
short-term, xvi, 445, 450, 456, 457
shoulder, 189
sign, 82, 209, 304, 494
signals, 35, 264, 335
silica, 6
silicon, 158, 330
silver, 34
simulation, 44, 50, 74, 131, 205, 207, 215, 272, 273, 282, 283, 286, 289, 335
single crystals, 23, 297
single-crystalline, 373, 376, 382
sintering, 14, 87, 183, 186, 187, 188, 189, 190
sites, 12, 13, 14, 73, 74, 102, 112, 115, 176, 215, 355, 380, 383
Sm, 106, 206, 435
SME, 341
smoothing, 43, 128, 243
software, 397, 428
solar cells, 369
solid phase, 422
solid solutions, xi, 1, 13, 53, 74, 77, 81, 85, 86, 87, 99, 138, 140, 149, 151, 166, 228, 257, 406
solid state, 87, 130, 214, 288
solidification, 129
solubility, 149, 156, 324, 325, 341
solvent, 324, 325, 326, 327, 329, 331, 332, 343
solvents, 325, 327, 342
spatial, xvii, 20, 21, 181, 191, 193, 197, 207, 298, 316, 473, 474, 477, 478, 479, 485, 486, 487, 488, 489
specific heat, 17, 313, 371
specific surface, 327
spectroscopy, xi, xii, 1, 14, 33, 34, 35, 52, 75, 83, 84, 85, 99, 112, 116, 120, 125, 134, 213, 216, 242, 267, 299, 330, 376, 388, 389
spectrum, 24, 43, 48, 75, 99, 105, 111, 243, 330, 332, 369, 376, 377, 378
speed, xii, 125, 129, 132, 134, 154, 159, 161, 162, 164, 165, 166, 167, 168, 175, 273, 275, 278, 281, 283, 285, 418, 465
spin, xiv, 6, 7, 8, 9, 10, 11, 23, 24, 28, 53, 65, 73, 74, 75, 82, 83, 205, 208, 247, 295, 296, 300, 301, 304, 306, 308, 310, 311, 315, 316, 319, 320
sputtering, 134, 382, 383
stability, xii, 27, 125, 144, 152, 154, 165, 167, 278, 281, 284, 285, 286, 290, 292, 324, 331, 332, 342, 360, 396, 397, 407, 409, 410, 434, 436, 437, 460, 468, 471, 472
stabilization, 144, 149, 413, 436
stable crack, 493
stable states, 3
stages, 189, 274, 284, 497
stainless steel, 126, 128, 140, 160, 161

Copyright © 2010. Nova Science Publishers, Incorporated. All rights reserved.

Handbook of Material Science Research, Nova Science Publishers, Incorporated, 2010. ProQuest Ebook Central,

standard deviation, 62, 63, 80
standard error, 425
stars, 303
statistical mechanics, 8
statistics, 277, 278, 279, 290, 418
steady state, 285
steel plate, 275, 281
stiffness, 274, 283, 334, 338
stochastic, 74, 225
stoichiometry, 14, 162, 186
storage, xvi, 132, 133, 320, 459, 460
strain, 18, 251, 273, 276, 277, 278, 280, 282, 283, 289, 336, 446
strategies, xvi, 433
strength, xi, xv, xvi, xvii, 23, 25, 59, 71, 106, 221, 234, 236, 238, 278, 280, 281, 338, 350, 353, 433, 434, 437, 438, 439, 440, 445, 446, 450, 451, 453, 454, 456, 457, 491, 492, 493, 503, 512, 514
stress, xvii, 127, 262, 272, 273, 277, 278, 279, 280, 281, 283, 285, 286, 290, 438, 439, 446, 449, 452, 455, 456, 491, 492, 493, 495, 496, 497, 498, 499, 502, 503, 509, 510, 511, 512, 515, 516
stress fields, 509
stress intensity factor, 280, 281, 285, 496, 497, 499
stress level, 286
stretching, 216, 277, 278, 289
structural changes, xv, 23, 300, 395, 408, 414, 415
structural characteristics, 298
structural defect, 324, 331
structural defects, 324, 331
structural dimension, 198
structural relaxation, 408, 410
structural transformations, 397, 408, 412
structural transitions, 51
students, 210, 415
submarines, 289
substances, 236, 324, 325, 342, 418
substitution, 13, 43, 46, 86, 243, 257, 258, 305, 320
substrates, 348, 355, 379, 383, 384
sugar, 275, 288, 289
sulfate, xv, 395, 397, 414
sulfur, 215
sulfuric acid, 353, 467, 471
sulphate, 396
sulphur, xii, 213, 214, 218, 226, 227, 228, 233, 234, 235, 246, 257, 258, 266
superalloys, 446, 457
supercomputers, 284
superconducting, xi, xii, 173, 174, 185, 189, 191, 192, 193, 195, 197, 199, 200, 201, 202, 203, 204, 205, 208, 209, 295
superconductivity, 174, 185, 186, 189, 192, 200, 201, 202, 204, 205, 208, 209
superconductor, xii, 173, 178, 185, 201
superimpose, 273, 276
superlattice, 14, 23, 298
superlattices, 299
superposition, 29, 126, 238, 273, 276, 277, 289
supply, xvi, 130, 459, 460
suppression, 200, 201, 354, 355, 366
surface area, 327, 397, 460
surface energy, 19, 282, 283, 285, 290
surface layer, xii, 125, 126, 127, 128, 129, 130, 132, 133, 134, 135, 136, 138, 139, 143, 144, 145, 146, 148, 149, 150, 151, 152, 153, 154, 156, 157, 158, 159, 161, 162, 163, 164, 165, 166, 167, 168
surface properties, 331
surface roughness, 127, 128, 131, 139, 493
surface structure, 130
surface tension, 148
surface treatment, 126
survival, 511, 512
survival rate, 511, 512
susceptibility, 8, 9, 10, 24, 27, 204, 205, 296, 300, 301, 302, 303, 304, 305, 306, 308, 310, 311, 312, 313, 315, 316, 317, 318, 319, 336
symbols, 285, 302, 303, 305
symmetry, 2, 8, 9, 11, 13, 14, 15, 17, 19, 22, 23, 24, 25, 51, 107, 109, 111, 113, 174, 198, 214, 288, 379, 384, 385, 486, 489
synchronous, 35
synchrotron, 17, 23
synthesis, 87, 126, 127, 186, 296, 320, 323, 324, 327, 336, 341, 383, 396, 418, 439, 460, 463, 471

T

TCC, 353, 363
TEM, xvi, 17, 18, 35, 36, 38, 376, 377, 379, 380, 381, 382, 386, 459, 462, 464, 465, 466
temperature annealing, 19
temperature gradient, 127, 217
Tennessee, 292
tensile, 228, 277, 278, 281, 290, 438, 451, 456, 503
tensile strength, 278, 281, 503
tensile stress, 290
tension, 290
test data, 275
theoretical dependencies, 254
thermal analysis, 332
thermal decomposition, 342
thermal energy, 383
thermal equilibrium, 8
thermal evaporation, 383
thermal expansion, 298
thermal properties, 329, 342

Copyright © 2010. Nova Science Publishers, Incorporated. All rights reserved.

Handbook of Material Science Research, Nova Science Publishers, Incorporated, 2010. ProQuest Ebook Central,

thermal relaxation, 17
thermal stability, xii, 125, 144, 152, 165, 167, 324, 342, 397, 407, 409, 410, 434, 436
thermodynamic, 2, 6, 19, 24, 186, 435
thermodynamic parameters, 24
thermodynamics, 378, 383
thin film, 85, 102, 112, 158, 159, 383, 396, 434
three-dimensional, xiv, xv, 73, 74, 83, 84, 174, 193, 199, 202, 283, 295, 320, 417, 419
threshold, xii, xiii, 131, 173, 174, 175, 176, 183, 190, 191, 192, 193, 194, 197, 198, 199, 204, 207, 208, 209, 272, 274, 278, 280, 281, 290, 497, 499, 515, 516
TiO_2, 36, 156, 397
titanium, xiv, 156, 295, 297, 298, 299, 300, 301, 306, 307, 309, 310, 311, 312, 313, 316, 317, 320
topology, xvii, 473, 474, 479
torus, xvii, 473, 474, 476, 477, 482, 485, 486, 487, 488, 489
total energy, 22, 131
toughness, 283, 369
toxic, xiv, 347, 348
traction, 277, 281, 285, 286
traditional model, 75
transducer, 255, 259, 260, 261, 263, 265
transformation, 11, 13, 144, 153, 161, 164, 410, 413, 414
transformations, 159, 397, 408
transition metal, 298, 300, 320, 322, 434, 441, 470
transition temperature, xiii, 2, 3, 20, 23, 35, 52, 54, 55, 63, 65, 66, 74, 82, 83, 104, 115, 213, 214, 217, 218, 220, 221, 234, 250, 253, 254, 255, 257, 258, 264, 266, 436
transitions, xiii, 19, 22, 74, 82, 213, 216, 217, 218, 269, 276, 295, 299, 385
translation, 489
translational, 13
transmission, 17, 38, 39, 40, 41, 42, 99, 107, 112, 376, 448, 449, 462
transmission electron microscopy, 17, 376, 448, 462
transparent, 99, 112, 333, 336
transport, 130, 131, 148, 175, 176, 178, 179, 208, 209, 217, 225, 256, 297
transport phenomena, 176, 208, 217
tribological, xv, 165, 167, 396, 433, 440
tungsten, xvi, 158, 159, 160, 445, 446, 448, 457
tungsten carbide, 159
tunneling, 54, 61, 74, 202, 203, 204
two-dimensional, xii, xiv, xv, 173, 174, 185, 187, 193, 197, 198, 199, 202, 203, 204, 208, 209, 281, 295, 296, 317, 319, 333, 417, 419

U

ultrasonic waves, 257, 266
ultrasound, 256
ultraviolet light, 372

V

vacancies, 13, 20, 297, 300, 310
vacuum, 34, 37, 41, 128, 129, 133, 144, 156, 159, 163, 183
valence, 216, 317
validation, 276, 287, 288, 425, 426
validity, 99, 276, 286
van der Waals, 185, 216, 296, 297, 298, 420
vanadium, 162, 301
vapor, 297, 372, 380, 383, 396
vapor-liquid-solid, 380
variables, xv, 43, 243, 277, 280, 417, 423
variance, 10, 11, 26, 74, 191, 193, 195, 198, 209, 506
variation, xiv, 16, 35, 38, 126, 155, 158, 189, 216, 228, 256, 259, 260, 262, 299, 300, 310, 339, 347, 354, 355, 380, 423
vector, 4, 5, 10, 43, 44, 45, 46, 47, 181, 243, 275
vein, 438
velocity, 4, 41, 128, 132, 214, 250, 251, 252, 253, 254, 255, 256, 257, 258, 260, 264, 266, 272, 275, 277, 285, 286, 287, 291, 293, 298, 334, 339, 340, 371, 423, 424, 427
vibration, 4, 106, 112, 113, 115, 116
Vickers hardness, 126, 498, 505, 506, 511, 512
violence, xiii, 271, 272, 282, 288
violent, xiii, 271, 272, 275, 287, 288, 289
viscosity, 435
visible, 4, 31, 205, 237, 240, 369, 448, 451
vitreous, 6
VLS, 380

W

water, 31, 35, 241, 279, 297, 326, 327, 338, 349, 407, 439, 447, 462, 463
wave propagation, 128
wave vector, 4
waveguide, 39, 40, 41, 42
wavelengths, 4
weapons, 126
wear, 127, 129, 145, 168, 433, 440
wells, 216, 229, 231
wires, 286

Copyright © 2010. Nova Science Publishers, Incorporated. All rights reserved.

Handbook of Material Science Research, Nova Science Publishers, Incorporated, 2010. ProQuest Ebook Central,

X

XPS, 472
X-ray absorption, 15, 314
X-ray analysis, 146
X-ray diffraction, xii, xv, 23, 25, 87, 125, 134, 187, 215, 310, 331, 373, 395, 404, 405, 406, 407, 413, 448, 450, 456, 465
X-ray diffraction (XRD), xvi, 134, 137, 138, 139, 142, 143, 144, 145, 149, 151, 153, 154, 156, 157, 160, 161, 162, 165, 166, 187, 365, 366, 373, 376, 378, 380, 381, 397, 408, 411, 413, 438, 459, 462, 465, 470

Y

yield, xiv, 86, 130, 134, 175, 186, 187, 189, 208, 216, 278, 290, 323, 341, 363, 383, 495

Z

zero-dimensional structures, 369
zinc (Zn), ix, xiv, 347, 348, 349, 350, 351, 352, 353, 354, 355, 356, 357, 358, 359, 360, 361, 362, 363, 364, 365, 366, 367
zirconium, 147, 148, 149, 150, 151, 152, 165
ZnO, 87, 360, 380, 386
ZnO nanorods, 386

Copyright © 2010. Nova Science Publishers, Incorporated. All rights reserved.

Handbook of Material Science Research, Nova Science Publishers, Incorporated, 2010. ProQuest Ebook Central,